Site U1309[1]

Expedition 304/305 Scientists[2]

Chapter contents

[1]Expedition 304/305 Scientists, 2006. Site U1309. *In* Blackman, D.K., Ildefonse, B., John, B.E., Ohara, Y., Miller, D.J., MacLeod, C.J., and the Expedition 304/305 Scientists. *Proc. IODP,* 304/305: College Station TX (Integrated Ocean Drilling Program Management International, Inc.). doi:10.2204/iodp.proc.304305.103.2006
[2]**Expedition 304/305 Scientists' addresses.**

Principal results

Integrated Ocean Drilling Program (IODP) Site U1309 is located on the central dome of Atlantis Massif, 14–15 km west of the median valley axis of the Mid-Atlantic Ridge (MAR), where the seafloor coincides with what is interpreted to be a gently sloping, corrugated detachment fault surface (Figs. **F1, F2**). Two drill holes at this site (Holes U1309B and U1309D) penetrate a multiply intruded and faulted crustal section, providing core that documents the interplay between magmatism, deformation, and hydrothermal alteration prior to, during, and subsequent to a period of footwall displacement and denudation associated with detachment faulting. Five shallow-penetration holes (Holes U1309A and U1309E–U1309H) were designed to sample the sedimentary carapace and upper few meters of basement, to test the hypothesis that the upper surface coincides with a detachment fault, and to help constrain the temporal history of denudation. Collected sedimentary deposits may provide constraints on the timing of exposure across the dome based on the age and isotopic character of preserved microfossils. Basement rock sampled in these short holes provides initial information on deformation and alteration within the exposed fault and, perhaps, rock adjacent to the fault zone.

Site selection was based on a combination of geological and geophysical data (Figs. **F3, F4**), balancing the details of seafloor character with larger scale objectives attainable if deep penetration of the footwall was successful. Centered within the gently sloping, morphologically corrugated, striated dome (Cann et al., 1997), the site coincides with gravity anomaly and seismic velocity maxima that indicate unaltered ultramafic rocks are likely to be present within several hundred meters of the seafloor (Blackman et al., 1998; Collins et al., 1998, 2001). *Argo II* imagery and *Alvin* dive mapping previously showed that the seafloor is covered by a thin layer of unconsolidated sediment deposited on bedrock and interrupted in places by lineated rubble fields (Blackman et al., 2004). In areas without significant loose sedimentary cover, a thin cover of lithified carbonate caps the underlying low-relief basement. Dredge and *Alvin* sampling (Fig. **F2**) indicate that loose, angular fragments on the central dome include low-grade metabasalt and serpentinite (Blackman et al., 1998, 2004).

Site U1309 comprises eight holes drilled within 2 km of one another along a spreading-parallel corridor (Fig. **F2**). The first five

doi:10.2204/iodp.proc.304305.103.2006

holes, Holes U1309A–U1309E, are located within 30 m of each other in an area with 2–4 m of unconsolidated sedimentary deposits above basement. A 60 m × 50 m survey with the vibration-isolated television camera on the drill string documented a ~2000 m² area where both a single-bit pilot hole and a deep-penetration hole could be initiated within an area free of cobble- to boulder-sized rubble. The area is ~280 m south of an *Argo II* track (run 039) and an *Alvin* dive (3642), both from cruise AT3-60 (Blackman et al., 2004), just south of NOBEL Line 10 and west of EW0102 multichannel seismic (MCS) Line Meg-4 at common midpoint 4100 (Canales et al., 2004) (Fig. **F3**). Towed ocean-bottom instrument (TOBI) and DSL120 side-scan sonar data show spreading-parallel striations crossing this area. A gentle northeast slope coincides with the northern flank of the corrugation that the site penetrates. Principal geologic results from the pilot and deep-penetration holes are presented in subsequent sections.

The series of shallow-penetration holes included in this footwall site are located adjacent to, 280 m northwest of, and 1.6 km northeast of the deep hole (Hole U1309D). The motivation for this series of holes was twofold: first, to check for possible fossils or isotopic signatures in the sedimentary deposits to constrain the exposure age of the hypothesized detachment fault and, second, to attempt recovery of possible fault rock at the top of the domal surface. The first shallow-penetration core was obtained in Hole U1309A. Overcoring in the top interval of the deep-penetration holes (Holes U1309B and U1309D) precluded meaningful recovery of the sedimentary deposits and the upper 20 m of basement immediately below. Additional shallow-penetration holes were drilled in an effort to achieve that goal (Holes U1309E–U1309H).

Hole U1309A

Before initiating coring in Hole U1309A (30°10.11′N, 42°07.11′W; 1642 meters below sea level [mbsl]), we obtained a temperature measurement and seawater sample for microbiology and geochemistry (see **"Appendix A"**). Bottom water at this site has temperature = 5.33° ± 0.6°C, pH = 7.73, alkalinity = 2.16 mM, and salinity = 35.5 g/kg. These values are typical for the water depth and north central Atlantic location of the site (Levitus and Boyer, 1994). A push core in Hole U1309A (Table **T1**) recovered ~2.0 m of unlithified tacky mud above bedrock. This microfossil ooze (with foraminifers and pteropods) includes mineral grains (fresh olivine and pyroxene) and fish remains. A sample of sediment for microbiological study was collected from Section 304-U1309A-1R-2, 48–60 cm, ~20 cm above basement.

Hole U1309B

In an effort to assess drilling conditions and begin geologic characterization of the expected detachment fault zone, a single-bit pilot hole was drilled at Site U1309. Hole U1309B, initiated at the same location as Hole U1309A, was cored to 101.8 meters below seafloor (mbsf). Recovery was good (overall average = 46%), increasing significantly (to an average of 52% for 30–100 mbsf) below the upper, very slow drilling 25 m. The hole deviates from vertical by 7° toward the northeast, and this was probably a factor in the reduced quality for some of the downhole logging measurements (see **"Downhole measurements"**).

Hole U1309C

The attempt to set casing for the hard rock reentry system (HRRS) was not successful in Hole U1309C (30°10.11′N, 42°7.12′W; 1638 mbsl). The hole was abandoned with ~25 m of 13⅜ inch casing pipe standing above the seafloor; it is 20 m east of Hole U1309B and ~30 m southwest of Hole U1309D.

Hole U1309D

Drilling in Hole U1309D (30°10.12′N, 42°07.11′W; 1645 mbsl) took place over four periods for a total of 15 days during IODP Expedition 304 and 34 days during IODP Expedition 305. The hole was spudded using a hammer drill with 13⅜ inch casing in an effort to provide stable reentry for a deep hole. No rock was recovered in the upper 20.5 m of the hole. Below 20.5 mbsf, coring was accomplished using a rotary core barrel (RCB) bit. Despite rough sea conditions during some of the drilling, recovery rates were generally very good. The section from 108 to 126 mbsf (Cores 304-U1309D-18R through 21R) had very low recovery, including one empty core barrel and a second with only 14% recovery. Logging data suggest this low-recovery zone may coincide with a fault zone. Aside from the low-recovery interval and the upper 20.5 m, recovery rates averaged 68% in the upper 400 mbsf (Expedition 304). As drilling conditions in the pilot hole (Hole U1309B) were very good, casing below 20 m in Hole U1309D was deemed unnecessary. This gave us time to core the upper ~130 m during our initial occupation of the hole, providing an opportunity to assess cross-hole correlation of lithologic units and structure between Holes U1309B and U1309D. The second period of coring followed drilling at IODP Sites U1310 and U1311 and deepened the hole to 401.3 mbsf before the first logging run in Hole U1309D completed the work of Expedition 304. Before coring began during Expedition 305, a water sample was obtained from the bottom of the hole (see **"Appendix B"**). After coring to a

depth of ~840 mbsf during Expedition 305, a second logging run was completed. Final coring penetrated to 1415.5 mbsf and was followed by the third set of downhole logging measurements at the end of Expedition 305. Total recovery in Hole U1309D is 1043.3 m (average = 75% below the upper ~20 m).

Hole U1309E

Hole U1309E (30°10.12′N, 42°07.11′W; 1645 mbsl) was offset 10 m east of Hole U1309D for an attempt to recover the sediment and upper meter of basement using the RCB. Disrupted sediments were obtained, as were several fragments of metabasalt.

Hole U1309F

The next attempt at shallow penetration was made in Hole U1309F (30°10.20′N, 42°07.25′W; 1645 mbsl), ~280 m to the northwest of Hole U1309D in an area where unconsolidated sedimentary deposits are less widespread than in Holes U1309A–U1309E and lithified carbonate cap rock was mapped with the *Alvin* and the *Argo II* during cruise AT3-60 in 2000. A brief camera survey confirmed the basic setting, although some loose sediment occurred within a few meters of the first contact of the drill bit at the seafloor. Despite clear indications that we drilled >1 m into hard rock, recovery included only disrupted sediment and a few fragments of metabasalt. No chips of lithified carbonate were recognized. We discontinued RCB shallow-penetration attempts and switched to the extended core barrel (XCB) bit for a further attempt (Hole U1309G).

Hole U1309G

Hole U1309G (30°10.54′N, 42°06.32′W; 1872 mbsl) was sited 1.6 km northeast of Hole U1309D in an area characterized by a broad region of variably lithified carbonate deposits above basement. A brief camera survey confirmed this assessment, and the hole was located within sight of a marker left by the *Alvin* in 2000. The hole was spudded into stepped and platy lithified carbonate sediment. Coring to 3.5 m using an XCB bit recovered 0.91 m of microfossil ooze with three thin (2–3 cm) interlayers of basaltic hyaloclastite. Glass from the hyaloclastite is oxidized palagonite. No lithified carbonate or intact basement rock was recovered. The sequence of fossiliferous ooze, hyaloclastite, and a clayey material with rounded, largely metabasalt clasts may provide useful postexposure data. The latter could be a sedimentary conglomerate, but we cannot rule out significant reworking due to drilling in this lowermost interval.

Hole U1309H

A second attempt at basement recovery from a shallow-penetration hole at the same location as Hole U1309G was possible when logging activities in Hole U1309D were stopped early because of logging tools sticking in the borehole. Rather than risk either tools or hole, the remaining time on site was used to RCB core a few meters at essentially the same location as Hole U1309G. This eliminated the need for a camera survey. Drilling for 4 h penetrated to 4 mbsf; recovery from this hole was 0.19 m and included pieces of basalt and talc-tremolite schist along with one piece of diabase cataclasite (Fig. **F5**). Despite the small return, these samples are significant. The talc-tremolite schist is similar to fault rocks recovered near the top of the Southern Ridge at Atlantis Massif (Schroeder and John, 2004) and at 15°45′N on the MAR (Escartin et al., 2003). Fracture intensity in the diabase is minor, suggesting fairly low strain, but consistent with the sample being part of a process zone associated with a fault system. Although these samples are minimal, they provide direct evidence that the corrugated central dome of Atlantis Massif is an exposed detachment, consistent with the 50–100 m thick brittle deformation zone described along the top of the south face of the massif (Schroeder and John, 2004; Karson et al., 2005). An *Alvin* sample within this spreading-parallel corridor on the central dome showed similar talc rock (Blackman et al., 2004) and there were a few chips of talc-tremolite schist in the top core from Hole U1309B, but neither of these latter samples could be proven to be in place.

Igneous sequence petrology and geochemistry

A total of 770 igneous units were defined in Hole U1309D during Expeditions 304 and 305. Each unit is distinguished on the basis of primary modal mineralogy, igneous contacts, and variations in grain size.

The most abundant rock type is from the gabbro group (Fig. **F6**), comprising 55.7% of the core recovered from Hole U1309D. This group spans a wide range in modal composition, including minor (rarely exceeding a few percent) amounts of olivine, Fe-Ti oxides, and/or orthopyroxene. Gabbroic rocks from Hole U1309D exhibit significant variations in grain size from microgabbro (crystals <1 mm) to seriate medium-grained gabbro to pegmatitic gabbro (grain size >10 cm), in places within a single section (i.e., ~150 cm) of core. Gabbronorite and orthopyroxene-bearing gabbro are included in this group. Because unambiguous identification of orthopyroxene requires careful thin section observation, the amount

of orthopyroxene-bearing gabbro is a minimum estimate (see **"Igneous petrology"**). Gabbronorites show the same textural relationships as the associated gabbros. In the lower part of Hole U1309D (Cores 305-U1309D-243R through 272R), low-Ca pyroxene appears as orthopyroxene and/or inverted pigeonite.

Olivine gabbro is the second most abundant rock type recovered from Hole U1309D (25.5%), with modal olivine varying widely (>5%). The modal composition of this rock type is highly variable on a submeter scale and locally grades into troctolitic gabbro.

Troctolite is commonly spatially associated with olivine and troctolitic gabbros, but it is less common, constituting only 2.7% of the rocks recovered (Figs. **F6, F7**). The texture of troctolite is irregularly seriate, locally with poikilitic clinopyroxene. Troctolite units are commonly intruded by late-stage dikes of both coarse-grained gabbro and microgabbro.

Olivine-rich rocks with relatively low modal plagioclase and clinopyroxene, including dunite, wehrlite, and troctolite, are grouped as olivine-rich troctolite. They represent 5.4% of the recovered rocks in Hole U1309D, with the thickest interval between 1092 and 1236 mbsf (Fig. **F6**). The olivine-rich troctolites contain >70% olivine by mode and are commonly intercalated with olivine and troctolitic gabbro (Fig. **F8**). In contrast to troctolite, olivine-rich troctolite displays subhedral to rounded medium-grained olivine and interstitial to poikilitic plagioclase and clinopyroxene in variable proportions (Fig. **F9**).

Two short intervals of ultramafic rock were recovered in the upper 100 m of both Holes U1309B and U1309D (Fig. **F8C**). Four intervals of serpentinized peridotite (three of which are clearly in place) at ~61, 132.5, 172–173, and 224 mbsf were recovered in Hole U1309D and include both lherzolite and dunite. Peridotites from Hole U1309B (~58 mbsf) have Mg# of 90–91. The low CaO and Al_2O_3 contents of the peridotites suggest that, prior to alteration, they were more refractory than those collected during Ocean Drilling Program (ODP) Leg 153 at 23°N on the MAR (Casey, 1997).

Oxide gabbro, defined by the presence of >2% modal Fe-Ti oxide minerals, makes up 7% of the rocks recovered from Hole U1309D (Fig. **F6**). The most common occurrence of oxide minerals (~80% of the oxide gabbros) is as randomly dispersed patches in undeformed, generally coarse grained gabbro (Fig. **F10A, F10B**). Concentrations of oxide minerals are also present as discrete dikelets/layers cutting other rock types with either sharp or diffuse boundaries. Additionally, oxide mineral concentrations are associated with intervals of ductile deformation (Fig. **F10C, F10D**). Many oxide gabbros contain apatite and zircon as accessory minerals. Common occurrences of oxide gabbros were also noted in ODP Hole 735B, Atlantis Bank (Dick, Natland, Miller, et al., 1999); in the Kane Fracture Zone (MARK) area (Leg 153; Cannat, Karson, Miller, et al., 1995); and at 15°N at the MAR (ODP Leg 209; Kelemen, Kikawa, Miller, et al., 2004).

Where visible, contact relations between gabbro and other rock types (except diabase) at Site U1309 suggest that gabbro is generally intrusive into more olivine rich rock types (olivine gabbro and troctolite) and that it is in turn intruded by felsic ("leucocratic") dikes and oxide gabbro. These relationships are more common between 400 and 650 mbsf than in the lower part of the hole, where gabbro contacts are commonly more diffuse. Contact relations between troctolite and gabbro range from sharp, where thin intervals of gabbro crosscut the serpentine foliation in troctolite, to gradational, where thicker intervals of gabbro are present. Contacts between oxide-bearing rock types and gabbro range from sharp to gradational over centimeters. Felsic dikes in gabbro generally show sharp contacts, but varying degrees of high-temperature reaction between dikes and wallrocks are also observed. These reaction zones commonly have oriented minerals such as oxides, pyroxenes, or plagioclase growing along and across them, suggesting postemplacement reaction.

Holes U1309B and U1309D have interfingered units that vary in thickness from centimeters up to ~100–200 m where intrusive contacts are preserved. The ~140 m thick interval of olivine-rich troctolite from 1094 to 1236 mbsf in Hole U1309D forms an integral lithologic package. The olivine-rich troctolites and minor associated lithologic units that this package comprises have been intruded by numerous crosscutting gabbroic dikes of variable thickness at temperatures below the troctolite solidus. Broader scale contacts with adjacent olivine gabbro appear to be dominantly intrusive and formed under hypersolidus conditions. Interstitial clinopyroxene appears more abundant adjacent to gabbroic dikes, suggesting that oikocrystic clinopyroxene recrystallized during intrusion of the crosscutting dikes.

Diabase intrudes other rock types in several places throughout Holes U1309B and U1309D (Fig. **F6C, F6D**). The intrusive contacts in Hole U1309B and the upper 130 m of Hole U1309D, taken with the relative intensity of alteration and vein development, suggest that the diabase bodies were emplaced late in the intrusive history of the footwall at Site U1309. Subhorizontal magmatic foliations, together with paleomagnetic and logging data, suggest that diabase

in Holes U1309B and U1309D forms groups of subhorizontal sheets or sills. Unit boundaries are locally marked by chilled margins, and in some cases magnetic susceptibility (MS) increases systematically toward the top and base of a unit (Fig. **F11**). Together, these observations suggest individual diabase sheet thicknesses on the order of 2–8 m.

Nearly all gabbroic rock types recovered from Site U1309 are cut by veins/dikes (Fig. **F12**) of variable thickness and composition. These veins and/or dikes range in composition between gabbro, oxide-bearing gabbro, and trondhjemite and may be partly magmatic, partly metamorphic, partly deformation-related, or the result of a combination of all three processes.

Among Deep Sea Drilling Project (DSDP)/ODP/IODP drill holes, Hole U1309D is unique in that it represents a section of primitive to somewhat evolved gabbroic rocks and includes intrusive diabase intervals as well as olivine-rich rocks, which may represent primitive cumulates. Gabbroic rocks from Site U1309 have compositions that are among the most primitive sampled by drilling along the MAR (23°N and 15°20′N; Agar et al., 1997; Kelemen, Kikawa, Miller, et al., 2004) and on the Southwest Indian Ridge (SWIR; Hole 735B) (Dick, Natland, Miller, et al., 1999) (Fig. **F13**). This is reflected in Mg numbers ranging from 67 to 87 (Fig. **F14**) and low TiO_2 (<0.72 wt%), Na_2O, and trace element contents. Site U1309 gabbroic rocks can be interpreted as cumulates related to the basalt and diabase through crystal fractionation processes and a common parental magma.

Basalt and diabase from Site U1309 are tholeiitic basalts and minor basaltic andesite, with compositions that overlap basaltic glasses from the entire MAR (Fig. **F15**). All samples analyzed are slightly CaO and Al_2O_3 poor and Na_2O rich compared to average MAR basaltic glass compositions. These differences may be related to the pervasive greenschist-facies alteration. Samples from the thin diabase units below 130 mbsf are somewhat less evolved in composition than those in the uppermost section. All diabasic rocks show significant variation in incompatible trace elements, including Y and Zr.

Hydrothermal alteration, metamorphism, and metasomatism

Alteration mineral assemblages in rocks from Site U1309 record cooling of mafic plutonic rocks from submagmatic conditions (>1000°C) to the temperatures of zeolite facies (<200°C) during the unroofing and uplift of Atlantis Massif. Individual samples generally display a range of superposed metamorphic conditions, but no single sample records the entire cooling history of the site. Alteration intensity is moderate, tends to decrease downcore, and is commonly related to the intensity of veining (Fig. **F16**). Locally, there are exceptions to the decreasing alteration downhole where, for example, alteration intensity broadly correlates with the modal abundance of olivine in the intercalated olivine-rich troctolite, olivine gabbro, and gabbro recovered between ~1090 and ~1240 mbsf and in the lowermost gabbros and olivine gabbros. Coarser grained gabbro intervals are, in general, more altered than medium- to coarse-grained units. Intervals of olivine-rich troctolite show alteration restricted to heterogeneous serpentine networks, with strong alteration gradients from the contact with intensely veined intercalated gabbros to the fresher cores of the olivine-rich troctolite units (Fig. **F16C**). The latter locally contain intervals of very fresh (as low as 1% serpentinization) olivine-rich (as much as ~90%) rocks.

The metamorphic and alteration history recorded at Site U1309 is summarized as follows:

1. High-temperature, near-solidus, mylonitic deformation and recrystallization of plagioclase + clinopyroxene and brown amphibole at granulite to upper-amphibolite-facies conditions (Fig. **F17**).
2. Replacement of pyroxene by green to brown hornblende in diabase, gabbro (especially oxide gabbro), and mylonite zones. The extent of this largely static event is difficult to estimate because of a greenschist-facies overprint by amphibole and uncertainties over amphibole compositions in thin section.
3. A widespread, largely static upper-greenschist-facies to lower-amphibolite-facies metamorphism manifested by the following:
   - Formation of secondary plagioclase and amphibole and, below 384 mbsf, epidote growth that appears to be related to late magmatic leucocratic intrusions.
   - Replacement of pyroxene by actinolitic amphibole. This is the major effect of the greenschist event in most gabbroic rocks and diabase. In the upper ~300 m of Hole U1309D, this alteration is pervasive and all samples are affected to some extent. At greater depths, the alteration is increasingly associated with the emplacement of amphibole-rich veins and accompanying halo alteration (Fig. **F18**).
   - Development of tremolite-chlorite ± talc corona texture in all rocks containing both olivine and plagioclase (Fig. **F19**). This may include some amphibolite-facies formation of cummingtonite and green hornblende. In the upper 300 m of Hole U1309D, this reaction proceeded to completion in almost all samples,

removing either olivine or plagioclase from the assemblage. At greater depths, the reaction commonly did not proceed to completion and is increasingly localized by amphibole veins and the margins of gabbroic dikelets. At shallower levels, most amphibole veins postdate corona formation.
- Metasomatic talc-tremolite ± chlorite veins and irregular zones in ultramafic rocks, especially near contacts with mafic rock (Fig. F20).
- Talc-tremolite schist with ultramafic protolith (upper 25 m of Holes U1309B and U1309D and fragments in Holes U1309E and U1309H) (Fig. F5).

4. Static, lower-greenschist to subgreenschist metamorphism that includes the following:
   - Serpentinization in olivine gabbro, troctolite, and olivine-rich troctolite with concomitant formation of prehnite and hydrogrossular in associated plagioclase. Above ~300 mbsf, serpentinization is restricted to rocks where olivine was in excess over plagioclase and was therefore still present after the corona-forming reaction went to completion. At deeper levels, serpentine, prehnite, and hydrogrossular are often localized on closely spaced, variably oriented fractures ("ladder veins"). The degree of serpentinization varies widely from >90% to <10% of the olivine. In the simplest case, serpentinization proceeds via the development of kernel texture (O'Hanley, 1996) (Fig. F21). A commonly observed feature in serpentinized rocks is the development of microfracture sets that radiate or extend into plagioclase from neighboring serpentinized olivine grains (Fig. F22). These fractures are commonly filled with chlorite and/or amphibole.
   - Sporadic talc-carbonate metasomatic alteration of olivine-rich rocks.
   - Relatively late emplacement of slip-fiber amphibole veins and associated local metasomatism.
   - Serpentinization of isolated grains in olivine gabbro and relict grains in coronas.
   - Zeolite-facies metamorphism that includes replacement of plagioclase by zeolites throughout the core and emplacement of zeolite-bearing veins below 700 mbsf (Fig. F23, F24). Late, open, irregular fractures commonly contain a clay mineral that may be saponite, along with carbonate and (below 700 mbsf) zeolite minerals.

Structural relationships

The majority of core recovered from Site U1309 records pervasive static alteration of the rocks and shows that pseudomorphs of igneous textures remain largely unmodified. Magmatic deformation fabrics (defined by the preferred orientation of plagioclase) were recorded in 22% of recovered rocks (Fig. F24). These fabrics are weak except in local intervals. Magmatic foliation tends to be better developed in finer grained gabbros than in coarser grained varieties; foliation is also well developed in the rare layered intervals. Textural observations suggest that some foliation may have been destroyed by late growth of pyroxene crystals reaching sizes as large as 20 cm. Magmatic foliations typically dip ~30°–60° but are steeper (e.g., at 400 and 560 mbsf) or more gently dipping (e.g., at 850 and 1150 mbsf) in local intervals. In many places, weak to moderate crystal-plastic deformation seems to overprint magmatic foliations (Fig. F25), as also described in Hole 735B (Shipboard Scientific Party, 1999). This deformation is commonly difficult to identify macroscopically but is evident in thin section.

High-strain crystal-plastic shear zones are rare (recorded in only 3% of the core). The highest densities of crystal-plastic shear zones are at 35–80 mbsf and 670–720 mbsf in Hole U1309D and are typically restricted to clearly defined, mostly granulite grade shear zones ranging in width from millimeters to a maximum of a few meters. Both normal and reverse senses of offset in the core reference frame are observed in such shear zones, and their dips are typically moderate but can be locally steep (e.g., at 700 mbsf). This is in marked contrast to the much larger number of high-strain shear zones recorded in Hole 735B on the SWIR, especially in the upper 500 m (Dick, Natland, Miller, et al., 1999; Dick et al., 2000).

Vein sets defined by mineralogy are found throughout the core. The earliest generation is late magmatic veins. Their occurrence broadly correlates with country rocks with a similar composition, suggesting local derivation (scale = ~100 m). Later generations of veins include dark green amphibolite-facies veins (consisting of amphibole) cut by pale green, fibrous greenschist-facies veins (actinolite/tremolite-chlorite ± talc and epidote). Fiber orientations on the pale green veins are commonly subhorizontal (particularly deeper than ~300 mbsf) independent of vein-dip, indicating strike-slip movement during formation. The latest (and lowest metamorphic grade) vein type is typically open, white veins (carbonate and sulfide ± chlorite; prehnite), possibly associated with unloading. Gray veins (serpentine and chlorite) are spatially restricted to olivine-rich troctolite and both cut and are cut by serpentine foliation. In hand sample, such areas of intense serpentinization form a conspicuous but generally irregular foliation (Fig. F26) with orientations varying on a meter scale or

from one piece of core to the next, and several crosscutting foliations developed in the same piece of core. Subsets of the gray veins have synkinematic fibers. Vein intensities tend to correlate with fault zones on a local scale (Fig. F27), though displacement on veins (vein faults) is not common. Vein intensities decrease significantly below 785 mbsf. The dip of veins is variable but moderate on average, irrespective of the vein type. On the scale of the entire core, there is no systematic, lithology-dependent downhole distribution pattern of specific vein types.

The amount of strain recorded by brittle fracture and cataclasis is negligible overall, except for fault zones concentrated in the upper 50 m of Hole U1309D, at 108–126 mbsf and between 685 and 785 mbsf (Fig. F28), where the boundaries of structural units are defined (Fig. F27). Additional zones of significant cataclasite were found at 250 and 1100 mbsf. Cataclasis is locally associated with oxide gabbro intervals/dikelets, leucocratic veins, and contact zones between diabase intrusions and their gabbroic host rocks. Crosscutting relationships indicate a complex succession of events involving fluid flow and deformation.

Structurally, core from Hole U1309D can be subdivided into three major units (Fig. F27):

- Structural Unit 1 (0–170 mbsf) is marked by a high but decreasing degree of cataclasis downhole; abundant, late, relatively undeformed diabase; a high degree of greenschist-grade alteration; and a near-present-day orientation of the paleomagnetic inclination. The boundary to structural Unit 2 at ~170 mbsf is marked by a subhorizontal to moderately dipping crystal-plastic shear zone within gabbroic rocks, a high intensity of veining, strong cataclasis, and a ~2 m thick interval of altered ultramafic rocks.
- Structural Unit 2 extends from ~170 to ~785 mbsf. It is marked by a relatively high intensity of veining, including the presence of sulfides. Paleomagnetic inclinations are ~10°–30° shallower than present-day values. Lithologically, structural Unit 2 is varied and nondistinct. The base of structural Unit 2 is defined by a series of greenschist-grade cataclastic fault zones occurring between 695 and 785 mbsf. There is a sharp decrease in whole rock Mg# of the gabbros at ~600 mbsf (Fig. F14).
- Structural Unit 3 extends from this boundary to the bottom of Hole U1309D and is characterized by an overall low intensity of cataclastic deformation, veining, and plastic deformation.

Tentative reorientations of structures using paleomagnetic and logging data were performed on structural features from Holes U1309B and U1309D to ~130 mbsf. These data indicate that crystal-plastic foliations dip dominantly to the west, a majority of veins dip toward the east, and several faults strike east-west. Holes U1309B and U1309D are 20 m apart, and thus the local continuity of igneous, metamorphic, and structural units can be evaluated. On a broad scale, lithologic correlations between Holes U1309B and U1309D are possible, but correlation breaks down at a scale of <10 m (see **"Structural geology"**).

The lack of significant structures indicative of high displacement by either ductile or brittle processes severely limits the possible thickness of fault zones that could comprise a detachment system over the central dome. Poor recovery of the upper 20 m of the footwall allows the possibility that this narrow zone accommodated very high strain along a brittle fault. Such extreme strain localization has been documented to occur associated with continental detachments (e.g., John, 1987; Miller, 1996). If this is the case here, the central dome differs from the southern ridge of Atlantis Massif, where seafloor mapping and sample analysis suggest a detachment zone thickness on the order of 50–100 m (Schroeder and John, 2004; Karson, 2003).

Geophysical measurements

Shipboard physical property data in combination with downhole logging data provide an initial means to assess which aspects of the geological characteristics of the domal core of Atlantis Massif might contribute to the regional geophysical data sets. In addition, inherent rock properties can be assessed and related to rock type and alteration.

MS is highest in the olivine-rich troctolites recovered from Hole U1309D but is quite low in most of the gabbros (Fig. F29). Both olivine-rich troctolite and oxide gabbro intervals can have very high MS signals (2,000–10,000 instrument units [IU]), although only the former is consistently at these levels. The olivine-rich troctolites are variously serpentinized, with very strong local gradients, and the susceptibility reflects magnetite produced during the alteration process.

Natural remanent magnetization (NRM) of the rocks from Hole U1309D was determined on board following removal of the drilling-induced overprint. Alternating-field demagnetization (typically 30 mT) was used to remove the overprint, and the bulk of the archive-half sections show negative inclination direction (Fig. F27C), which corresponds to a reversed magnetic polarity epoch. Minicore samples, cleaned of overprint by either alternating-field (up to 100 mT) or thermal demagnetization (to 500°–550°C), generally show very good agreement with the half-core inclination patterns downhole. Five inclination

groups have been identified based on remanence data from archive halves and discrete samples. The boundaries between these groups generally coincide with structural features (faults and shear zones), so structural data have been used to define the precise boundaries.

The upper 180 m is characterized by a mean discrete sample inclination (–49°) that is identical to the expected dipole inclination at the site (Fig. F27C). This suggests that from 0 to 180 mbsf there has not been detectable tectonic rotation since the remanence was acquired, although it should be kept in mind that modest but significant (~20°) counterclockwise rotation about a 10° trending, horizontal axis (i.e., subparallel to the ridge axis) would produce no net change in the inclination of the remanent vector. In contrast, the mean inclinations from all inclination groups deeper than 180 mbsf in the hole are statistically distinct from the expected direction (Fig. F27C). The shallower inclinations in these sections cannot be attributed to artifacts of the drilling and/or measurement process, as they are corroborated by numerous high-quality discrete sample demagnetization data. Inclination Groups III and IV have mean values steeper than those from Groups II and V. This nonsystematic change in remanence inclination downhole is difficult to reconcile with any simple model of denudation. Instead of the footwall behaving as a single block, it appears that different intervals (inclination Groups I–V) may have experienced different tectonic and/or alteration histories. Because structural boundaries generally coincide with the inclination group boundaries (Fig. F27), those deformation zones could provide a mechanism for variation in tectonic rotation within the footwall.

Multicomponent remanences were documented for a few samples in the upper 400 m of Hole U1309D, and this suggests that remanence acquisition spanned multiple polarity intervals. The highest stability reversed polarity magnetizations are typically shallower than the normal polarity overprint (Fig. F30), and the two components are not antipodal. These overprints, distinct from the steep, low-coercivity drilling-induced component, have a mean inclination (53.6° +6.4°/–8.2°) that is not statistically distinguishable from the present-day normal polarity inclination at the site. The difference between the normal and reversed polarity directions may reflect the influence of tectonic tilting after acquisition of the highest stability reversed polarity magnetization. Although less common, such multicomponent magnetizations are also observed in several discrete samples analyzed from the lower 1000 m of the hole.

The physical properties that are most relevant for relating the rocks from Hole U1309D to broader scale geophysical measurements are seismic velocity and density. Shipboard measurements provide an indication of the inherent properties of small samples at room temperature and pressure. Variability in the measured values can be due to a number of factors, including mineralogy, porosity, grain size, and the style and degree of alteration.

A significant change in several core sample and downhole logging properties occurs between ~280 and ~350 mbsf, across an interval dominated by serpentinized, olivine-rich rocks (Fig. F31). Density values have reduced scatter and slightly higher average values below 350 mbsf, increasing from 2.8 g/cm^3 in the interval 280–340 mbsf to 2.9 g/cm^3 in the interval 350–400 mbsf. Average compressional velocity of minicore samples in the 280–340 mbsf interval drops to 5.3 km/s (from 5.5 km/s in the overlying 200 m) before increasing to 5.7 km/s at 340–400 mbsf. Logging compressional velocity increases from ~5.5 to 6.0 km/s between 340 and 370 mbsf. These changes combine to produce an impedance contrast (Fig. F32), and this can be related to the seismic reflection data. Electrical resistivity measured by the Dual Laterolog shows a marked decrease in the ~280–340 mbsf interval and then increases significantly below 350 mbsf in the underlying gabbroic interval (Fig. F31). Overall alteration in the serpentinized, olivine-rich interval is greater than in the overlying section (average = 50%–75%), and it drops steadily to 20%–40% by 400 mbsf. Higher velocity and density values correspond to the underlying gabbroic interval.

A second strong gradient in borehole electrical resistivity is present from 730 to 760 mbsf. Core sample porosity drops from an average of 1.5% (400–700 mbsf) to 1% (700–800 mbsf) and maintains an average of 0.6% at greater depths. These physical property changes approximately coincide with a rapid drop in overall level of alteration (Figs. F16B, F33) across this interval. Intriguingly, below ~925 mbsf, average sample velocities steadily decrease from ~5.9 to ~5.5 km/s at 1415 mbsf, whereas the densities remain stable on average (Fig. F31). The cause of this decrease in compressional velocity is not clear but could be related to microcracking due to unloading during the coring process at these depths.

The check shot experiment extended from 275 to 840 mbsf with average station spacing of ~50 m. Tool failure and high seas combined to preclude collection of any seismic measurements during the final logging run. The check shot data indicate an average velocity in the upper 550 m of the footwall in Hole U1309D of 5.5–5.6 km/s. An increase is indicated for greater depths by higher average velocities (5.8 km/s for stations 580–796 mbsf). Interval velocities computed from the automatic picks on stacked seismo-

grams vary between stations. At this stage, we cannot rule out the determination of a velocity of >7 km/s between 580 and 635 mbsf. Adjustments that could compensate for an error in seismometer position(s) of several meters do not change the basic result of a thin higher-than-average velocity interval. It is possible that a lens of essentially unaltered, olivine-rich rock occurs within the Fresnel zone of the check shot experiment at Hole U1309D (on the order of a few hundred meters), although confidence in this result will require additional seismic measurements.

Temperature in the borehole increases with depth as expected (Fig. **F34**). Because of the significant impact of drilling in the hole, the measurements made provide minimum estimates of what the actual formation temperature is. The Temperature/Acceleration/Pressure (TAP) tool recorded a temperature of 120°C at the bottom of the hole (1415 mbsf). The temperature is somewhat lower than predictions from a simple cooling plate model of a spreading ridge flank with an age of ~2 Ma. However, the measured temperatures are a minimum (owing to hole cooling during coring), and much more careful measurement is required before quantitative interpretation should be made. These initial results suggest that thermally driven flow in the hole is likely to occur. Several drops of a few degrees were recorded in narrow intervals on repeated TAP runs (Fig. **F34**). At least two of these coincide with documented fault zones (~785 and 1107 mbsf), perhaps indicating fluid flow there.

Microbiology

A total of 12 samples for microbiological investigations were collected from whole-round core samples recovered from Holes U1309B and U1309D during Expedition 304. Sample depths ranged from 0.45 to 396.5 mbsf, and all major rock types were included: carbonate sediment, basalt, diabase, gabbro, and serpentinized peridotite. Shipboard cultivation studies indicate growth of matter from two altered gabbro samples at elevated temperature, based on positive fluorescence tests. Shore-based analyses are required to confirm that this is a microbial signature as opposed to being due to inorganic material.

Additional microbiological studies were conducted on 15 whole-round core samples taken from 401 to 1391 mbsf during Expedition 305. Gabbro, olivine gabbro, and olivine-rich troctolite were sampled. In an effort to establish a culture collection of endolithic microbes, four different types of media, as well as agar plates, were inoculated with portions of these core samples. Growth was observed from two samples based on a positive fluorescence test. Again, because of the autofluorescence of rock particles, the presence of microorganisms can neither be confirmed nor denied until a shore-based molecular analysis of cultures is undertaken.

Igneous petrology

This section describes the igneous rock types recovered from the two principal holes drilled at Site U1309: Holes U1309B and U1309D. These holes are 20 m apart, and the upper 132 m of Hole U1309D, cored during the first phase of drilling at Site U1309 (see **"Operations"**), was compared to Hole U1309B in an attempt to correlate rock types. A total of 770 igneous units were defined in Hole U1309D, including 221 in the upper 401.3 m (Expedition 304) and 549 from 401.3 to 1415.5 mbsf (Expedition 305). Each unit is distinguished on the basis of primary modal mineralogy, igneous contacts, and variations in grain size.

Hole U1309B (Expedition 304)

Hole U1309B (Fig. **F35;** Table **T2**) is dominated by two intrusive series separated by a narrow (~2–4 m) interval of relatively undeformed serpentinized harzburgite. The upper intrusive sequence includes diabase and gabbro that show an increase in fracture intensity and alteration downhole. There is an intrusive contact between the lowermost gabbro and the serpentinite. The lower intrusive sequence includes diabase and gabbro that are less altered in appearance and significantly less fractured than those of the upper series. Both the basalt and the gabbro are interpreted to be younger than, and most likely intrusive into, the serpentinized harzburgite, although the key contacts were not recovered.

Upper intrusive series

Upper basaltic sequence

Depth: ~2–21 mbsf
Units: 1–13
Interval: Sections 304-U1309B-1R-3, 25 cm, through 3R-1, 67 cm

The upper basaltic sequence comprises a series of fine- to medium-grained basalt that shows an increase in grain size and ophitic textures downhole. There are a number of intrusive contacts in the core; nowhere in the sequence is there evidence of eruption at the seafloor. With the possible exception of the uppermost basalt unit (interval 304-U1309B-1R-3, 25–150 cm), the entire sequence appears to be intrusive in origin. The total recovered thickness is 4.3 m with a possible maximum thickness of ~19 m.

As seen in hand specimen, the core appears increasingly altered downhole, primarily because of the de-

velopment of greenish, patchy discoloration. The dominant alteration effects seen in thin section are the almost complete alteration of generally sparse olivine to random aggregates of acicular amphibole and of clinopyroxene to acicular green or green-brown actinolite, generally in optical continuity. Plagioclase appears relatively fresh throughout (see **"Metamorphic petrology"** for further description).

The coarser grained units have variably developed subophitic textures, and, in places, the distinction between medium-grained basalt and diabase is somewhat arbitrary. Phenocrysts are rarely abundant, although local concentrations of either olivine or plagioclase are present within Units 6–8. There are no vesicles in Hole U1309B core. In some places, sparse trains of altered plagioclase phenocrysts define weak, near-horizontal laminations.

There is clear evidence of intrusive relationships in two places. Unit 10 displays an aphanitic chilled margin at its horizontal contact with Unit 9. Matrix grain size increases downhole away from the contact, but the size and abundance of sparse plagioclase phenocrysts increase upward, suggesting flow concentration near the margin or, perhaps, that plagioclase has floated in a magma body (Fig. **F36**).

Aphanitic basalt and breccia

Depth: ~21–31 mbsf
Units: 14–19
Interval: Sections 304-U1309B-3R-1, 67 cm, through 5R-1, 42 cm

This distinctive sequence, dominated by aphanitic to fine-grained basalts, has a recovered thickness of ~2 m (maximum = ~10 m). Hand samples have a characteristic dense aphanitic surface texture, reflecting the fine-grained metamorphic recrystallization of the matrix, that is easily recognized on cut surfaces and is distinct from all other Site U1309 rock types. These basalts are characterized by a fine-grained, originally glassy matrix that is now dominated by fine actinolitic amphibole. Within this matrix, fine acicular plagioclase microphenocrysts are preserved (<5%). Cataclastic breccias and fracture networks are common on macro- to microscales throughout the interval, forming a significant fraction of the sequence. At least some of the thicker zones of cataclasite are associated with intrusive contacts. The dominant clast type is the host aphanitic basalt, accompanied by fresh, broken plagioclase phenocrysts and by fragments of more crystalline basalt with subophitic textures. These coarser basalts resemble similar lavas in the overlying upper basalt sequence but differ in grain size and texture from the deeper diabases. The breccia matrix is a complex mixture of highly altered relict clasts and finer material (e.g., Sample 304-U1309B-3R-1, 65–68 cm). The dominant mineral is actinolitic amphibole in a variety of forms, accompanied by lesser chlorite, albite, and opaque minerals (see **"Metamorphic petrology"**).

Where intrusive contacts are clearly visible, they most commonly display grain-size-graded chilled margins against other similar basalts. The only measurable contact is located within Unit 19. It is steeply dipping (Fig. **F37**) (interval 304-U1309B-4R-1 [Piece 5A, 36–42 cm]). Elsewhere, more irregular contacts defining small intrusive basalt dikelets have been identified within some of the breccias. A single piece of gabbro with no recovered contact is located at ~21 mbsf (interval 304-U1309B-3R-1, 105–114 cm).

We interpret this sequence as a suite of mutually intrusive fine-grained basalts that have been brecciated by intrusion and hydrothermal alteration and, subsequently, pervasively recrystallized to a very fine grain size. Its relatively small thickness suggests that it represents a suite of narrow dikes or sills intrusive into a deformed or deforming gabbroic protolith.

Upper diabase

Depth: ~31–35 mbsf
Units: 20–22
Interval: Sections 304-U1309B-1R-3, 14 cm, through 6R-2, 67 cm

The units of this sequence appear to constitute a single <5 m thick medium-grained diabase intrusion (recovered thickness = ~3 m). The upper and lower contacts were not recovered, but a single piece of cataclasite at the lower boundary (interval 304-U1309B-6R-2 [Piece 6, 67–74 cm]) suggests a sheared contact with the underlying gabbro. This interval is characterized by a well-developed medium-grained ophitic texture and by a gradation to finer grain size margins approaching both the upper and lower boundaries. The dominant minerals are plagioclase and clinopyroxene, with only minor olivine. An opaque phase, presumed to be magnetite, varies in abundance from a few percent to as much as 5% over certain 10–20 cm intervals. Magnetite abundance is strongly reflected in higher MS values, particularly close to the fine-grained margins (see **"Physical properties"**). Plagioclase phenocrysts are very sparse through this interval, with rare examples up to 1 cm in length. Occasional sparse trains of a few such crystals locally define a weak subhorizontal magmatic fabric. Similar sparse trains of rounded relict olivine are also present in several places, with a good example in interval 304-U1309B-5R-1 (Piece 12, 72–80 cm) (Fig. **F38**).

The average mineral composition of this basalt is 50% plagioclase, 40% clinopyroxene, 5% olivine, and 5% oxides. Minor apatite in some samples is usually present within large, unusually clear plagioclase grains that are presumed to have recrystallized to more sodic compositions. The majority of the plagioclase is strained but relatively fresh prismatic grains that display zoned and sweeping extinction and are radially oriented to form a classic subophitic to ophitic texture with anhedral clinopyroxene. Euhedral prismatic to equant plagioclase phenocrysts are rare but present throughout. Most display strong zonation, and some are embayed, indicating resorption. Clinopyroxene is 20%–100% altered to amphibole, including tremolite, actinolite, hornblende, and, possibly, chlorite. Olivine is never fresh and is replaced by chlorite, amphibole, and opaques.

Upper gabbro sequence

Depth: ~38–58 mbsf
Units: 38–57
Interval: Sections 304-U1309B-7R-1, 0 cm, through 11R-1, 86 cm

This sequence consists of coarse-grained gabbro with an average grain size of 10–20 mm. No internal contacts or consistent lithologic variations that might indicate multiple intrusions were recovered, and we interpret this to be a single intrusive body with a maximum thickness of ~20 m (recovered thickness = ~7.5 m). The gabbro is extensively altered and fractured throughout, with pervasive crystal-plastic deformation fabric dipping ~50°. Small anorthosite intrusions partially invade the fabric of the gabbro in several places, with prominent occurrences as thick as ~5 cm (Fig. **F39**) (interval 304-U1309B-8R-1, 83–100 cm). Magmatic layering defined by variations in mode and grain size is apparent in both hand samples and thin section beginning in Unit 29 (Section 304-U1309B-10R-1, 102 cm) (Fig. **F40**) and continuing through Unit 29 (Section 304-U1309B-10R-1, 121 cm), where several centimeter-scale troctolitic layers are present.

The primary mineralogy of the coarse-grained gabbros is dominated by subequal but variable proportions of plagioclase and clinopyroxene, with small amounts of olivine and, in rare cases, orthopyroxene and opaques. Olivine gabbros are rare or absent, and minor troctolite or troctolitic layers were only recognized in Unit 29. Alteration is pervasive with virtually complete conversion of clinopyroxene to green-brown actinolite in rough optical continuity and of olivine to randomly oriented clusters of actinolitic amphibole. Plagioclase remains relatively fresh in appearance. In places, lower grade alteration minerals, including chlorite, clays, and, possibly, prehnite are present along or close to fractures. The petrography of the upper gabbros is similar to that of comparable lithologies in the lower gabbros, which is described in **"Lower gabbros and troctolites,"** below.

Serpentinized harzburgite

Depth: ~58–60 mbsf
Unit: 32
Interval: Sections 304-U1309B-11R-1, 86 cm, through 11R-2, 94 cm

Between the upper and lower intrusive series, a thin interval of serpentinized peridotite with a maximum thickness of ~3.5 m (recovered thickness = 1.4 m) begins at 57.86 mbsf (interval 304-U1309B-11R-1, 86 cm, through 11R-2, 94 cm) (Fig. **F41**). The upper boundary is in direct (intrusive) contact with the coarse-grained gabbro from Unit 31. The lower boundary was not recovered.

The unit consists of protogranular harzburgite with overall alteration degree ranging from 60% to >99%. The harzburgite contains ~20% subrounded orthopyroxene, and relict clinopyroxene grains cannot be identified. Equant spinels in Sections 304-U1309B-11R-1, 100 cm, and 11R-2, 88 cm, have a measured Cr# (Cr × 100/[Cr + Al]) of 42, which correlates to a degree of melting of 15%–16% (Hellebrand et al., 2001).

Indicators of deformation in the harzburgite are rare and only weakly developed; lattice-preferred orientation (LPO) and subgrain formation in olivine both record mantle flow (see **"Structural geology"**). Domains with recrystallized olivine are present close to the gabbro/peridotite boundary (Fig. **F42B**). The harzburgite is intruded by narrow gabbroic dikes and dikelets at 109 and 111 cm in Section 304-U1309B-11R-1, as well as at 7, 40, and 76 cm in Section 11R-2. At the upper gabbro/harzburgite boundary, a 2 cm wide zone parallel to the contact differs in texture from the rest of the serpentinized harzburgite. In thin section, this zone has a lower degree of serpentinization, a higher degree of deformation, and a relatively high modal clinopyroxene content that decreases away from the contact. Similar low degrees of serpentinization are a common feature of gabbro/peridotite contacts observed in other oceanic rock samples (Bideau et al., 1991; Cannat, Karson, Miller, et al., 1995).

Talc-tremolite bands of hydrothermal origin formed along the upper harzburgite/gabbro contact (Fig. **F42A**) and at dike contacts within the serpentinite. This suggests that hydrothermal fluids are preferentially channeled along gabbroic intrusions, as previously observed on the MAR (Cannat et al., 1992). Extensive serpentinization of harzburgite postdates

both the intrusion of the gabbroic dikelets and their hydrothermal alteration, as the talc-tremolite bands are cut by serpentine tension cracks filled by lizardite. This is in contrast with results from Leg 209, where pronounced alteration of pyroxene to talc near gabbro contacts was found to postdate serpentinization in Hole 1268A (see Kelemen, Kikawa, Miller, et al., 2004). A variety of characteristics of the serpentinized harzburgite and its contacts with gabbroic intrusions suggest high emplacement temperatures. Both the absence of a chilled margin in the coarse-grained gabbro at the peridotite contact and the medium grain sizes in the dikes suggest emplacement in host rock without a significant temperature contrast to intruding liquid. Crystal-plastic deformation in the gabbro, minor amounts of recrystallization of olivine in peridotite, and deformation (undulose extinction and bent lamellae) of magmatic clinopyroxenes next to the gabbro/peridotite contact (Fig. **F42B**) must have occurred after crystallization of clinopyroxene and above the olivine brittle–ductile transition, ~700°–1000°C, depending on strain rate (Kirby, 1983). Ductile deformation of peridotite away from the contact is subdued, and protogranular textures are preserved. These considerations give a lower limit for the deformation temperature of at least 600°C.

Key indicators of magmatic infiltration into peridotite suggest even higher temperatures. The relatively abundant clinopyroxene (~5%) close to the gabbro/peridotite contact have textures that indicate crystallization as a result of melt infiltration. These include clinopyroxenes crosscutting mantle olivines (Fig. **F42C**) and networks of altered interconnected pyroxenes (Fig. **F42D**). Dark brown interstitial spinel grains in the melt reaction zone (Sample 304-U1309B-11R-1, 87–91 cm) have a Cr# of ~55 and are significantly higher than those in the remainder of the unit. Similar elevated Cr#s are often found in spinels from melt-impregnated peridotites (Dick and Bullen, 1984; Cannat et al., 1997), although they can also form by secondary hydrothermal alteration (Kimball and Evans, 1988).

Apart from a few rare grains close to dike contacts (Fig. **F42E**), clinopyroxene is not present in most of the recovered peridotite. The farthest location of clinopyroxene from a gabbro contact is ~6 cm (Sample 304-U1309B-11R-1, 98–100 cm), where a single relict pyroxene grain is completely altered to bastite + tremolite. A second indication of the extent of melt impregnation is the relative enrichment in iron, sodium, and titanium and depletion in nickel of a sample from interval 304-U1309B-11R-1, 100–104 cm, relative to one from farther downcore (see **"Geochemistry"**). Similar chemical enrichments are reported from peridotites close to gabbroic dikelets recovered during Leg 153 (MARK; Cannat et al., 1997). The apparent restricted range in infiltration depth of the melt suggests temperatures close to the peridotite solidus and potentially provides an upper limit for the emplacement temperature (Cannat et al., 1997; Kelemen, Kikawa, Miller, et al., 2004). Taken together, these indicators suggest a mantle temperature between 1000° and 1100°C is likely for the emplacement of the gabbro unit.

Lower intrusive series

Middle diabase

Depth: ~62–67 mbsf
Units: 33–35
Interval: Sections 304-U1309B-12R-1, 0 cm, through 13R-1, 147 cm

The middle diabase sequence consists of narrow upper and lower fine-grained intervals (~70 and ~30 cm thick, respectively) separated by a uniform medium-grained interval that is 4–5 m thick. The internal contacts were not recovered, and no transitions in grain size are apparent in the core. The upper and lower contacts were not recovered, and there is no information in the core as to their nature (see further discussion of the lower boundary in **"Lower gabbros and troctolites,"** below).

The medium-grained unit (Unit 34) is mineralogically and chemically (see **"Geochemistry"**) very similar to those of the upper and lower diabase sequences. It is characterized by a well-developed ophitic texture, with plagioclase and clinopyroxene as the dominant minerals and only minor olivine. An opaque phase varies in abundance up to 5%. Plagioclase phenocrysts are present very sparsely throughout the core, with rare examples up to 1 cm in length. Plagioclase is relatively fresh, clinopyroxene is pervasively altered to green-brown actinolite in rough optical continuity, and olivine is altered to randomly oriented clusters of actinolitic amphibole.

Lower gabbros and troctolites

Depth: ~68–93 mbsf
Units: 37–59
Interval: Sections 304-U1309B-13R-2, 12 cm, through 18R-3, 87 cm

The lower gabbro sequence is dominated by medium-grained olivine gabbros grading to frequent thin troctolite intervals. Average grain size is ~5 mm, ranging from 2 to 10 mm. Occasional intervals of coarse-grained olivine gabbro range in average grain size up to 20 mm. No internal contacts or consistent lithologic variations that might indicate multiple intrusions were recovered. At its upper boundary, the

gabbro is in contact with and intruded by a fine-grained basalt dike (Fig. F43) (interval 304-U1309B-13R-2 [Piece 1, 0–10 cm]). At its lower boundary, the gabbro adjoins a similar fine-grained basalt, but no contact was recovered. However, ~30 cm above the boundary (Fig. F44) (interval 304-U1309B-18R-3 [Piece 9, 48–53 cm]), a small (<2 cm thick) dikelet of very similar basalt intrudes coarse-grained gabbro. This intrusive relationship suggests the lower gabbro boundary is also marked by basalt intrusion. No contacts were recovered between the middle and lower diabase sequences and either the lower gabbro or the intrusive basalts that are present at its boundaries. We interpret these relationships to indicate that the lower gabbro is a single intrusive body with a maximum downhole thickness of ~24 m (recovered thickness = ~15.6 m). The natures of its boundaries are not known, but they appear to have been loci for later basalt dike emplacement.

The lower gabbros differ from those of the upper series in their finer grain size, the predominance and variety of their olivine-bearing assemblages, and their common magmatic layering. Magmatic layers are typically between five and a few tens of centimeters in thickness. They are defined primarily by variations in clinopyroxene abundance and/or grain size. In some intervals (e.g., interval 304-U1309B-17R-2, 0–120 cm), patchy olivine gabbro and troctolitic domains predominate (Fig. F45). The dominant modal mineralogy of Hole U1309B gabbroic rocks is summarized in Table T2. Minor phases include opaque minerals, brown amphibole, and apatite.

Textures of gabbros from both the upper and lower gabbro sequences are normally equigranular and rarely seriate under the microscope. Plagioclase is present as anhedral to subhedral crystals and is almost always fresh relative to clinopyroxene and olivine, particularly away from shear and/or hydrothermal zones. Overall, plagioclase is 0%–40% altered to chlorite and amphiboles. Small polygonal recrystallized neoblasts are present in shear zones. Olivine was originally present as anhedral crystals in troctolite and troctolitic gabbro and as anhedral to subhedral crystals in olivine gabbro and gabbro. Throughout the lower and upper intrusive series, olivine is usually completely altered to randomly oriented clusters of actinolitic amphibole, typically surrounded by halos of chlorite that appear black in hand specimen. In the troctolites, this style of alteration is particularly well developed; the chlorite halos connect along grain boundaries, forming a distinctive and diagnostic network texture (Fig. F46). The only recognized unaltered olivines are in olivine gabbro (interval 304-1309B-16R-2, 71–73 cm) and troctolite (interval 304-1309B-15R-1, 110–112 cm). Clinopyroxene is anhedral in troctolite and troctolitic gabbro and, most commonly, granular and subhedral to anhedral in olivine gabbro and gabbro. In the most altered and/or foliated samples, clinopyroxene is 60%–100% altered to aggregates of amphibole, including tremolite, actinolite, and hornblende, which tend to maintain crystallographic continuity with the original pyroxene. In some places, primary clinopyroxene is replaced by clear clinopyroxene with wider spaced cleavages, possibly as a result of late magmatic fluid migration (Pettigrew, Casey, Miller, et al., 1999; Maeda et al., 2002) (Fig. F47) (interval 304-1309B-16R-2 [Piece 5, 26–29 cm]). The troctolites and troctolitic gabbros have higher whole-rock Mg# than gabbros from Atlantis Bank (SWIR) and the MARK area (see **"Geochemistry"**).

A strongly deformed and brecciated sample of oxide gabbro from interval 304-U1309B-16R-1, 29–48 cm (Unit 48), is characterized by a medium-grained equigranular texture. Major constituent minerals are 48% plagioclase, 48% clinopyroxene, and 3% ilmenite. Clinopyroxene and plagioclase are both strongly deformed, and recrystallized plagioclase neoblasts are present throughout the thin section. Ilmenite is interstitial between the plagioclase neoblasts and also intimately associated with greenish brown amphibole. In some places, ilmenite has been cut by greenish brown amphibole veins. Small grains of rutile are associated with, or included within, ilmenite (see **"Metamorphic petrology"**), suggesting that ilmenite is formed from magnetite during a late-stage process.

Alteration is pervasive throughout the gabbros, although plagioclase remains relatively fresh in appearance. Most clinopyroxene has been altered to green-brown actinolite in rough optical continuity. Adjacent to the basalt dike at the upper boundary of the lower gabbro, larger grains (5–10 mm) of brown hornblende are present within clusters of fine actinolitic amphibole (interval 304-U1309B-13R-2 [Piece 1, 0–9 cm]). Throughout the lower intrusive series, olivine is commonly altered to randomly oriented clusters of actinolitic amphibole that are usually surrounded by halos of chlorite that appear black in hand specimen. In the troctolites, this style of alteration is particularly well developed; the chlorite halos connect along grain boundaries, forming a distinctive and diagnostic network texture (Fig. F45).

Lower diabase

Depth: ~94–101 mbsf
Unit: 62
Interval: Sections 304-U1309B-19R-1, 13 cm, through 20R-2, 83 cm

This sequence consists of a single intrusive unit of medium-grained diabase, mineralogically and texturally indistinguishable from those of the middle and upper sequences. Its contact with the overlying gabbro was not recovered (see **"Lower gabbros and troctolites"**).

Crosscutting fine-grained basalt dikes

Depths: various short intervals
Units: 36, 40, 42, 54, 57, and 60

Within the lower intrusive series, a distinctive dark-colored sparsely plagioclase (± olivine) phyric basalt was recovered at seven distinct locations. Recovered intervals range from individual small pieces to 50 cm in interval 304-U1309B-18R-3 (Pieces 13–17, 87–138 cm). Two intrusive contacts with underlying gabbro were recovered in intervals 304-U1309B-13R-1 (Piece 1, 0–10 cm) and 18R-3 (Piece 9, 49–51 cm). Both dip at ~60° (Figs. **F43, F44**).

In thin section, fine randomly oriented plagioclase needles are seen to be set in an indeterminate, altered granular groundmass dominated by actinolitic amphibole. Patchy concentrations of rounded altered olivine are present in several locations and are most prominent in the lowermost unit (Unit 60; Section 304-U1309B-18R-3 [Pieces 16–17, 111–139 cm]).

Hole U1309D (Expedition 304)

In the upper 132 m of Hole U1309D, the range of primary igneous rock types is very similar to that of Hole U1309B (Fig. **F35;** Table **T3**). In broad outline, Hole U1309B and the upper part of Hole U1309D are dominated by two gabbroic intrusive series that are separated by a narrow interval of serpentinized peridotite. The gabbroic and ultramafic series are intruded, in turn, by a series of diabase sills and several narrow, steep, fine-grained basaltic dikes. Invasive and discrete felsic veining of magmatic and/or hydrothermal origin is common and accounts for a significant fraction of total volume in some parts of the core. In detail, the upper gabbroic series (gabbro Zone 1) in Hole U1309D is more extensively layered and more variable in composition than the one in Hole U1309B. As in the upper series in Hole U1309B, gabbro Zone 1 in Hole U1309D becomes increasingly more altered and fractured downhole. It is occasionally cut by small (10 cm) dikes of coarse-grained gabbro. Pervasive, irregular yellow-green actinolitic veins are abundant in Hole U1309D but rare or absent in Hole U1309B. The upper basalt sequence of Hole U1309B has no equivalent in Hole U1309D, perhaps because the uppermost 20 m of Hole U1309D was not cored. In both holes, the short serpentinized peridotite interval is intruded by the gabbros above; the lower serpentinite boundaries were not recovered. In Hole U1309D, both gabbro Zones 1 and 2 are complex, layered sequences that include troctolites, troctolitic and olivine gabbros, and gabbros. Both series can be divided into lithologic zones, each with a dominant lithology. Throughout Zone 1, cataclastic deformation and hydrothermal alteration effects are ubiquitous, whereas rocks of Zone 2 appear less altered and significantly less fractured. Gabbro Zone 1 in Hole U1309D, which comprises olivine-rich rock types with fine-scale (5–10 cm) layering, is distinctly different from the upper gabbro sequence of Hole U1309B, which consists mostly of fairly uniform gabbro, becoming layered only close to its lower boundary. Gabbro Zone 2 and the Hole U1309B lower series are, however, quite similar on a scale of one to a few meters, with each series divided into five correlated lithologic zones that are layered on the scale of ten to a few tens of centimeters and internally variable in mineralogy and texture (Fig. **F35**). Finer scale correlations between individual layers or distinctive packets of layers have not been recognized. Correlations between the six diabase intervals recovered in Hole U1309D and the three in Hole U1309B have proven elusive. MS data suggest that upper and lower diabases of Hole U1309B are equivalent to Diabases D-2 and D-5, respectively (see **"Physical properties"**), but petrographic and geochemical data neither support nor refute this hypothesis.

As drilling in Hole U1309D proceeded beyond the reentry depth of 132 m (see **"Operations"**), no further basaltic or diabase intervals were encountered during Expedition 304 and gabbroic rock types predominated, with only minor serpentinized peridotite. As in the shallower part of Hole U1309D, the gabbroic units can be divided into gabbro zones characterized by their dominant rock types (Figs. **F35, F48**). Overall, there are 10 such zones in the core recovered during Expedition 304.

Basalts

Rock types equivalent to the upper basaltic sequence of Hole U1309B were not recovered in Hole U1309D. However, the interval in which correlative lithologies would be expected was not cored above ~20 mbsf (see **"Operations"**).

Aphanitic basalt and breccia

Depths: ~23 and ~32 mbsf
Units: 2, 4, and 7
Intervals: Sections 304-U1309D-1R-2, 2–119 cm, 1R-3, 3–18 cm, and 4R-1, 62–65 cm

In Hole U1309D, basalts and basalt breccias equivalent to the distinctive aphanitic to fine-grained basalt sequence of Hole U1309B (~21–29 mbsf) are

present in three short intervals with a total recovered (and maximum) thickness of ~1 m, significantly less than in Hole U1309B. The basaltic intervals are interspersed between intervals of Diabases D-1 and D-2. Even though some of the basalt breccias contain small diabase clasts, these are finer grained than the adjacent diabase units, which appear to have intruded, and perhaps displaced, the basaltic sequence.

Diabase

There are six "diabase" intervals in Hole U1309D. The majority are medium grained with well-developed ophitic textures, closely resembling those of Hole U1309B, and we have not been able to identify distinctive petrographic characteristics that could establish correlations between the two holes.

Diabase D-1

Depth: ~20–23 mbsf
Unit: 1
Interval: Sections 304-U1309D-1R-1, 0 cm, through 1R-2, 118 cm

This is a single intrusive unit with fine-grained margins grading to a medium-grained interior. Recovered thickness is ~1 m, but because coring began in this interval, the maximum thickness is not known but must be ≤23 m.

Diabase D-2

Depth: ~24–32 mbsf
Units: 5 and 6
Interval: Sections 304-U1309D-1R-3, 55 cm, through 4R-1, 59 cm

Diabase D-2 includes two lithologic units. The diabase of Unit 5 is medium grained throughout, but it is more strongly (almost completely) altered approaching its top and bottom margins than at its center. The diabase of Unit 6 is finer grained, but because of the gap between Cores 304-U1309D-2R and 4R, it is unclear whether it represents a marginal phase of the same intrusion.

Diabase D-3

Depth: ~43–48 mbsf
Units: 12 and 14
Interval: Sections 304-U1309D-6R-2, 50 cm, through 7R-3, 5 cm

Diabase D-3 is 5–6 m thick (5.2 m recovered). It has fine-grained margins at the top and bottom grading over ~0.5 m to a typical medium-grained diabase. Toward the center of the unit, grain sizes are as coarse as 3 mm. Between Units 12 and 14, a narrow interval of olivine gabbro rubble (Unit 13; Section 304-U1309D-7R-1, 6–48 cm) may represent a narrow screen between separate intrusions, but because of the fine-grained top and bottom margins in Units 12 and 14, respectively, it appears more likely that the gabbro pieces are out of place, derived from Unit 11. At the lower boundary of Diabase D-3, an intrusive contact with the underlying gabbro is preserved in interval 304-U1309D-7R-3 (Piece 3, 9–19 cm) (Fig. **F49**).

Diabase D-4

Depth: ~55 mbsf
Unit: 22
Interval: Section 304-U1309D-9R-1, 9–44 cm

Diabase D-4 is a narrow interval (<50 cm recovered; <2 m maximum) within olivine gabbro. It is represented in the core by several small pieces, of which only the lowermost appears to have been cut by the drill bit. It is fine grained and very similar to Unit 6 (Diabase D-3). It is possible that this unit is entirely derived from Unit 6 and out of place.

Diabase D-5

Depth: ~82–94 mbsf
Units: 42, 44, and 46
Interval: Sections 304-U1309D-14R-2, 112 cm, through 16R-4, 124 cm

Diabase D-5, with a recovered thickness of ~10 m (maximum = ~16 m), is the thickest of all Hole U1309D diabases and is comparable to the lower diabase of Hole U1309B. This similarity is consistent with the suggestion, based on MS profiles, that these units are correlated (see **"Physical properties"**). A fine-grained interval (~0.5 m) is present at each margin, whereas the interior has a uniform fine to medium grain size. The upper fine-grained margin, recorded as Unit 13 and described as basalt, was recovered at the base of interval 304-U1309D-14R-2, 112–149 cm, and is not contiguous with the remainder of the diabase. The lower margin is contiguous with the coarser interval above, whereas its lower boundary has been intruded by a fine-grained black basalt dike (see **"Late basalt dikes"**). The contact between this dike and the diabase that lies immediately above was not recovered, but at the lower margin of the dike, a short contact with a very small fragment of fine-grained basalt (very similar to the marginal phase of the basalt above) is preserved (Fig. **F50**) (interval 304-U1309D-16R-4 [Piece 13, 144–147 cm]). At the very top of the next section (Section 304-U1309D-16R-5 [Piece 1, 0–2 cm]; archive half only), what appears to be a very small fragment of the same fine-grained marginal diabase has intrusive contacts, both with an equally small fragment of the basaltic dike material and with the underlying short interval of cataclastically deformed, fine-grained basalt. If

this interpretation is correct, this lowermost deformed diabase was emplaced and deformed before the emplacement of the main body of Diabase D-5 above.

Diabase D-6

Depth: ~117–127 mbsf
Units: 52 and 54
Interval: Sections 304-U1309D-20R-1, 7 cm, through 22R-1, 112 cm

Diabase D-6 is finer grained overall than the other diabases. Sparse aphyric plagioclase phenocrysts are scattered throughout. Recovered thickness is ~4 m, but the maximum possible thickness could be as much as 10 m. At its lower margin, it grades from fine grained to microcrystalline over ~1 m. A finer grained upper margin was not recovered.

Gabbros

Gabbro Zone 1

Gabbro Zone 1 in Hole U1309D is a layered intrusive sequence that includes troctolite, troctolitic gabbro, olivine gabbro, and gabbro (Fig. **F48**). The layered sequence extends from ~32 to 61 mbsf (Fig. **F35**) and is intruded by Diabases D-3 and D-4. The overall recovered thickness (not including the diabase intervals) is ~12 m, with a possible maximum thickness of almost 25 m. Olivine-rich rock types are dominant. Estimated volume proportions, based on lithologic interval lengths, are 28% gabbro, 40% olivine gabbro, and 32% layered troctolite and troctolitic gabbro.

The ~25 m drilled thickness of this upper gabbroic sequence can be divided into five lithologic zones (G1-1 to G1-5 in Fig. **F35**), each between ~2 and 10 m in thickness. Within each zone, one lithology is dominant, although other lithologies are commonly present as gradational, magmatic, and/or intrusive layers ranging from a few centimeters to ten or more centimeters in thickness. In order downhole, the lithologic zones are as follows.

Zone G1-1: gabbro

Depth: ~32–34.5 mbsf
Unit: 8
Interval: Sections 304-U1309D-4R-1, 67 cm, through 4R-3, 8 cm

Zone G1-1 is dominated by coarse-grained, brecciated gabbro lithologically similar to but significantly more altered than the upper gabbro sequence of Hole U1309B. Cataclastic textures and networked yellow-green alteration veins are abundant. The contact between the brecciated gabbro and overlying diabase (D-2) was not recovered, but a single small piece of brecciated, fine-grained basalt (Unit 7) appears to record an intrusive contact of diabase into gabbro.

Zone G1-2: troctolitic gabbro

Depth: ~34.5–40.4 mbsf
Unit: 9
Interval: Sections 304-U1309D-4R-3, 8 cm, through 5R-4, 21 cm

Zone G1-2 is a ~6 m thick interval of medium-grained troctolitic gabbro, within which grain size generally increases downhole and modal compositions are slightly variable. Gabbroic domains (2–3 cm in size) with slightly larger grain size are present in Section 304-U1309D-5R-3 (Pieces 6 and 7, 43–66 cm).

Zone G1-3: olivine gabbro

Depth: ~46–51 mbsf
Units: 11, 13, 16, and 17
Interval: Sections 304-U1309D-7R-1, 6 cm, through 8R-1, 119 cm

Zone G1-3 is characterized by medium- to coarse-grained olivine gabbro (Units 11 and 13) with interlayered gabbro (Units 16 and 17). It is intruded by Diabase D-3 (Units 12 and 14). In several units, downhole coarsening from medium to coarse grain is observed, and there is an irregular, abrupt transition from medium- to coarse-grained gabbro (Units 16–17) in interval 304-U1309D-8R-1 (Piece 4, 19–23 cm). Weak magmatic foliation is overprinted by crystal-plastic deformation in Units 11 and 13. An intrusive contact of Diabase D-3 into gabbroic rocks was recovered in Section 304-U1309D-7R-3 (Piece 3, 11–20 cm) (Fig. **F49**).

Zone G1-4: troctolite and troctolitic gabbro

Depth: ~52–53 mbsf
Units: 18 and 19
Interval: Sections 304-U1309D-8R-1, 120 cm, through 8R-2, 133 cm

Zone G1-4 is characterized by interlayered troctolite and troctolitic gabbro with minor gabbro layers in Unit 18. Unit 18 has been deformed and has a well-developed mylonitic texture. Its contact with the overlying olivine gabbro was recovered in interval 304-U1309D-8R-1 (Piece 15, 126–130 cm). In intervals 304-U1309D-8R-2 (Pieces 1 and 2, 0–27 cm, and Piece 7, 66–79 cm), both magmatic layering and faulted contacts between troctolite and olivine gabbro were recovered (Fig. **F51**).

Zone G1-5: olivine gabbro and gabbro

Depth: ~56–61 mbsf
Units: 23–27
Interval: Sections 304-U1309D-9R-1, 45 cm, through 10R-1, 99 cm

Zone G1-5 is characterized by broader scale interlayering of medium-grained olivine gabbro (Units 23, 25, and 26) with coarse-grained gabbro (Units 24 and 27). Both lithologies are heterogeneous in modal composition and grain size.

Gabbro Zone 2

Gabbro Zone 2 extends from ~61 to 138 mbsf and comprises the same range of rock types as Zone 1, including troctolite, troctolitic gabbro, olivine gabbro, and gabbro (Fig. **F48**). Estimated volume proportions are 13% gabbro, 15% olivine gabbro, and 72% layered troctolite and troctolitic gabbro, suggesting that olivine-rich lithologies are significantly more common than in the first sequence. Diabase intrudes the lower gabbro series at ~82–94 mbsf (Diabase D-5) and ~117–127 mbsf (Diabase D-6).

Gabbro Zone 2 is subdivided into five lithologic zones (G2-1 to G2-5 in Fig. **F35**).

Zone G2-1: layered troctolite (with olivine gabbro and gabbro)

Depth: ~62–75 mbsf
Units: 32–34
Interval: Sections 304-U1309D-10R-2, 0 cm, through 13R-1, 10 cm

This thick (~13 m recovered; 15 m maximum) zone of troctolite and olivine gabbro is characterized by alternating 10–50 mm thick layers of medium-grained troctolite and olivine gabbro with occasional gabbroic bands (Fig. **F52**) (interval 304-U1309D-11R-2, 0–20 cm; see also intervals 10R-2, 55–57 cm, and 12R-1, 69–84 cm).

Zone G2-2: gabbro

Depth: ~75–77 mbsf
Units: 35–37
Interval: Sections 304-U1309D-13R-1, 11 cm, through 13R-2, 142 cm

Gabbros of Zone G2-2 are characterized by coarse grain size (e.g., interval 304-1309D-13R-2, 45–65 cm). Olivine is rare. Orthopyroxene is sporadically present as subhedral to anhedral grains as large as 6 mm in the lower part of Unit 35 (interval 304-U1309D-13R-1, 50–107 cm). In a few patches, modal orthopyroxene exceeds 5%, defining the host rock as gabbronorite (e.g., interval 304-U1309D-13R-1, 68–70 cm).

Zone G2-3: layered troctolite (with olivine gabbro and gabbro)

Depth: ~77–82 mbsf
Units: 38–41
Interval: Sections 304-U1309D-13R-3, 0 cm, through 14R-2, 110 cm

The principal rock types in Zone G2-3 are interlayered troctolites (~30 mm thick) and (olivine) gabbros (~10 mm thick) (e.g., interval 304-1309D-14R-1 [Piece 11, 61–73 cm]). Coarse-grained clinopyroxene as large as 10 mm is observed in interval 304-U1309D-14R-1 (Pieces 8 and 9, 46–56 cm).

Zone G2-4: olivine gabbro

Depth: ~99–103 mbsf
Unit: 49
Interval: Sections 304-U1309D-17R-1, 17 cm, through 13R-3, 131 cm

This 3.5 m thick zone is characterized by coarse-grained gabbro with very variable modal mineral proportions.

Zone G2-5: layered troctolitic gabbro

Depth: ~127–130 mbsf
Unit: 55
Interval: Sections 304-U1309D-22R-1, 112 cm, through 22R-3, 89 cm

Zone G2-5 is dominated by troctolitic gabbro. Its recovered thickness is ~2.5 m. Modal proportions of the dominant minerals are variable, and bands of anorthositic olivine gabbro (e.g., interval 304-U1309D-22R-2, 27–30 cm), anorthositic troctolite (e.g., interval 22R-2, 48–51 cm), and typical troctolitic gabbro (e.g., interval 304-U1309D-22R-3, 39–42 cm) are observed. Narrow, branching, clinopyroxene-rich gabbroic dikes cut the section at relatively high angles in interval 304-U1309D-22R-2, 72–84 cm. Two kinds of clinopyroxene can be distinguished in hand specimen: one is dark in color; the second has brown rims and an unusual pastel green core with apparent exsolution lamellae visible under the binocular microscope.

Gabbro Zone 3

Zone 3 extends between 138 and 180 mbsf (interval 304-U1309D-24R-1, 18 cm, through 33R-3, 108 cm) and is dominated by medium- and coarse-grained olivine and olivine-bearing gabbro that grades locally to troctolitic intervals and patches and, in places, to troctolite (Fig. **F48**). Neither zone boundary was recovered, and the exact relationships of Zone 3 gabbroic units to those of the adjacent zones are unknown. The uppermost unit is dunite that is almost completely serpentinized and grades downhole into serpentinized troctolite, and below this narrow (<2 m) upper subzone, there is an overall downhole increase in modal olivine (Fig. **F53**) within the interval 150–175 mbsf. In several intervals, orthopyroxene, which was only rarely recognized macroscopically elsewhere at Site U1309 during Expedition 304, is present. These include a gabbronorite at ~145.4 mbsf and two orthopyroxene-bearing intervals (145.4–

148.3 and ~160–161 mbsf) in which relatively large (up to ~1 cm) orthopyroxene grains are sporadically present within otherwise olivine-bearing gabbro (Fig. F54). Beginning at ~148 mbsf, an unusual "salt-and-pepper" mottled matrix appears in the core as an interstitial phase between clinopyroxene and/or relict olivine grains (Fig. F55). This feature, which is present at least through gabbro Zone 7, was initially interpreted as invasive fine-grained dioritic material. In thin section, however, it is clear that most or all of it is plagioclase that has recrystallized into small, uniform, 0.1–0.2 mm neoblasts. Pervasive fine fractures in this material are filled with green actinolite. The principal visual effect of this texture appears to be one of contrast between larger transparent plagioclase grains that appear black in hand specimen and smaller aggregates of neoblasts that appear white.

The gabbroic sequence of Zone 3 is frequently interrupted by narrow, late-stage magmatic leucocratic dikes (see also "Metamorphic petrology") that frequently invade and impregnate the surrounding gabbroic material, possibly contributing locally to the development of salt-and-pepper plagioclase alteration. Although dikes of this type are present throughout the gabbroic sections at Site U1309, they appear to be particularly common in Zone 3. Occasional narrow dikes of both coarse gabbro and microgabbro are also present throughout Zone 3. Also interrupting the olivine-bearing sequence are two serpentinite intervals. The first, at ~155 mbsf, is a ~20 cm interval of completely serpentinized harzburgite, for which the contacts with the surrounding gabbroic rocks were not recovered. The second, between 171.5 and 173.5 mbsf, is a complex interval of serpentinized dunite, harzburgite, and olivine-rich troctolite lithologies that appears to have been intruded by a coarse-grained gabbro dike (see "Peridotites").

Gabbro Zone 4

Zone 4 extends from 186 to 208 mbsf (interval 304-U1309D-34R-1, 0 cm, through 34R-1, 58 cm) and is dominated by heterogeneous medium-grained gabbro grading to olivine gabbro and, rarely, to troctolitic gabbro (Fig. F48). Coarser grained patches are common, and, in places, a weak magmatic layering is defined by variations in mode and/or grain size. Coarser clinopyroxene is present, intermittently dispersed in a medium-grained matrix.

A 6 m thick coarse-grained oxide gabbro, the thickest encountered at Site U1309 during Expedition 304, is present in the middle of this zone (Fig. F56). The upper contact is not preserved, but the lower contact appears to be intrusive into the olivine gabbro with a narrow medium-grained chilled margin (Fig. F57). Alternating coarse-grained and pegmatitic intervals are a prominent characteristic of this unit. Oxide minerals throughout the interval are mainly disseminated. The top of Core 304-U1309D-36R has the most abundant oxide, with as much as 20% modal content. Emplacement of this and other oxide gabbros appears to be among the last igneous events recorded, at least in the deeper part of the section recovered during Expedition 304.

Gabbro Zone 5

Zone 5 extends from ~210 to 265 mbsf (interval 304-U1309D-39R-1, 58 cm, through 50R-3, 122 cm) and is dominated by medium- and coarse-grained olivine gabbro that commonly grades to olivine-bearing intervals, to troctolitic intervals and patches, and, occasionally, to troctolite (Fig. F48). From ~255 to 256 mbsf, the olivine-bearing sequence is interrupted by a 1.2 m thick oxide gabbro with 2%–5% oxides, and, from 238 to 244 mbsf, intermittent oxide-bearing patches are present within an otherwise olivine-bearing host gabbro. The gabbro sequence is also interrupted at 224 mbsf by a single piece of serpentinized harzburgite. No contacts are preserved, and, because this irregular piece was recovered at the top of a core (Section 304-U1309D-42R-1), it is most likely not in place. It was noted that a section of alternating olivine gabbro and troctolitic gabbro in Cores 304-U1309D-39R and 40R preceded the occurrence of the harzburgite in Core 41R. Sporadic narrow dikes of both coarse gabbro and microgabbro are present throughout.

At the upper zone boundary, medium-grained olivine gabbro is in sharp intrusive contact with the coarse-grained gabbro of Zone 4. A few centimeters below the contact, a narrow, irregular gabbro dikelet only 1–2 cm thick intrudes the olivine gabbro (Section 304-U1309D-39R-1, 50–52 cm) (Fig. F58). Near the bottom of Zone 5, in Core 304-U1309D-49R, a section of highly deformed olivine gabbro with a minimum thickness of 1.3 m occurs. This deformed section is located between undeformed rocks above and below. The lower boundary of Zone 5 was not recovered.

Gabbro Zone 6

Zone 6 extends from ~268 to 282 mbsf (interval 304-U1309D-51R-1, 17 cm, through 54R-2, 62 cm) and is dominated by coarse-grained gabbros (Fig. F48), characterized by the presence of large (~1 cm) clinopyroxene grains. In some places, the crystal distribution becomes patchy; in others, coarse-grained gabbro grades into a medium-grained matrix with sparsely and randomly dispersed grains (Fig. F59); in a few places, sharp contacts define short, apparently

intrusive intervals (Figs. F60, F61). Similar intrusive gabbros, ranging from the width of a single crystal to 10 cm or more, are present throughout the section below ~180 mbsf and are common in gabbro Zones 8 and 10.

At the base of Zone 6 is a ~1 m thick coarse-grained gabbro. The upper boundary of this unit was not recovered, but a lower intrusive contact with troctolite of gabbro Zone 7 is preserved in interval 304-U1309D-54R-2, 53–62 cm (Fig. F62).

Gabbro Zone 7

Zone 7 extends from ~281 to 310 mbsf (interval 304-U1309D-54R-2, 63 cm, through 59R-4, 16 cm) and is dominated by coarse- and medium-grained olivine gabbro that grades intermittently into both troctolitic and olivine-bearing gabbro (Fig. F48). At the upper zone boundary, troctolite of Zone 7 is in intrusive contact with the apparently younger gabbro of Zone 6. At the lower zone boundary, olivine-bearing gabbro with a narrow, finer grained margin intrudes serpentinized dunite of Zone 8. (Fig. F63).

Modal olivine decreases overall downhole in Zone 7 (Fig. F53); troctolitic variants are more common near the top of the zone. The gabbro sequence is interrupted at ~291 and ~301 mbsf by intervals of serpentinized dunite that are 0.25 and 0.7 m thick, respectively. Beneath the upper dunite, a 3 m interval of troctolitic gabbro that closely matches similar intervals in the underlying zone (Zone 8) represents the shallowest limit of pervasive serpentinization of gabbroic rocks in Hole U1309D. The olivine-bearing gabbro sequence is also interrupted by a number of gabbro dikes ranging in thickness from a few centimeters to ~1 m (Fig. F64).

Gabbro Zone 8

Zone 8 extends from ~312 to 344 mbsf (interval 304-U1309D-60R-1, 0 cm, through 67R-1, 60 cm) and is dominated by troctolitic gabbros (Fig. F48) that are distinctly more olivine rich than those of the other zones (Figs. F53, F65). The upper zone boundary is an interfingering, intrusive contact with olivine-bearing gabbro of Zone 7 (see **"Gabbro Zone 7,"** above). The lower boundary was not recovered. Throughout the zone, where olivine is dominant it has been replaced by serpentine. The troctolitic gabbros are characterized by modal olivine >50% with common interstitial plagioclase (Fig. F66). They belong to the olivine-rich troctolite group (although they were called dunitic troctolites in the Expedition 305 *Preliminary Report*) as defined below in **"Hole U1309D (Expedition 305)."**

Clinopyroxene, frequently occurring as large oikocrysts, is also a common interstitial phase. In several places, troctolitic gabbro grades over a few centimeters to dunite. A 3 m thick oxide gabbro interval (321–324 mbsf; interval 304-U1309D-62R-1, 132 cm, to 63R-1, 10 cm) interrupts, and most likely intrudes, the troctolitic gabbro sequence. There are two significant coarse-grained gabbro intervals, each ~2 m thick, at ~317 and ~336 mbsf. Several narrow coarse-grained dikes and a single microgabbro also intrude the troctolitic gabbro sequence (Fig. F67).

Gabbro Zone 9

Zone 9 extends from ~344 to 356 mbsf (interval 304-U1309D-67R-1, 61 cm, through 69R-2, 124 cm) and consists of a coarse-grained gabbro that is intermittently olivine bearing and an underlying oxide gabbro (Fig. F48). The gabbro, which is 8–9 m thick, is coarser grained (~3 cm) than that of gabbro Zone 6 but otherwise very similar. The upper boundary of Zone 9 was not recovered, but intrusive contact with the underlying troctolitic gabbro of Zone 10 is present in Section 304-U1309D-69R-2, 118–133 cm (Fig. F68). As with other gabbro zones (Zones 4 and 6), an oxide gabbro interval is present at the base of Zone 9. The intrusive relationships of this oxide gabbro are complex; it is separated into two units by intervening short intervals of gabbro (upper) and troctolite (lower), between which an intrusive contact is preserved (Fig. F69). The contact between this troctolite and underlying oxide gabbro is obscured by subsequent alteration, and the contact between this gabbro and the upper part of the oxide gabbro was not recovered.

A tentative interpretation is that coarse-grained gabbro (Zone 9) originally intruded troctolitic gabbro from Zone 10 and a later oxide gabbro intrusion bifurcated at the location of Hole U1309D, isolating the original gabbro/troctolite contact as a narrow screen within the oxide gabbro.

Gabbro Zone 10

Zone 10 extends from ~358 to 402 mbsf (interval 304-U1309D-69R-2, 124 cm, through 78R-4, 100 cm), and the upper portion is dominated by relatively uniform plagioclase-rich (leucocratic) troctolitic gabbros. Beginning in Section 71R-3, olivine gabbro becomes the dominant rock type, with frequent transitions to layers or irregular domains of troctolitic gabbro (Fig. F48). Modal plagioclase exceeds 70% in the leucocratic subzone, but below ~375 mbsf there is a steady downhole decrease in modal plagioclase with this zone. Olivine abundances increase downhole throughout the zone (Fig. F53). In the uppermost troctolitic gabbros, the ser-

pentinization of residual olivine that characterizes gabbro Zone 8 (overprinting the typical high-temperature alteration of olivine to actinolitic amphibole and chlorite) continues through Section 304-U1309D-71R-2, 75 cm; below this level, the intensity of serpentinization appears to be significantly diminished.

The olivine gabbros are medium to coarse grained with large (2–3 cm) prismatic clinopyroxene crystals having a patchy distribution though much of the zone (Fig. F70); presences range from small individual grains and clumps to small dikes with essentially the width of a single crystal to discrete, apparently intrusive small dikes that are typical of those that are present through much of Hole U1309D (Fig. F71).

Late basalt dikes

Depths: ~48, 94 mbsf
Units: 15 and 45
Intervals: Sections 304-U1309D-7R-3, 8–12 cm, and 16R-4, 124–146 cm

Black fine-grained basalt dikes with a distinctive irregular fracture pattern on the outer core surface intrude gabbros from the upper part of Hole U1309D in two places. Lithologically, these dikes appear identical to the more numerous similar intrusions in Hole U1309B. The upper Hole U1309D dike is the only place where this lithology is present in the upper series of either hole. This dike is narrow (~1 cm thick) and branching, with an irregular contact geometry that is best observed in the working half of the core (Fig. F49) (interval 304-U1309D-7R-3, 11–21 cm). It cuts across the boundary between Diabase D-3 and the underlying gabbro of Zone G1-3. The lower dike is actually a composite, with at least one internal intrusive contact displaying both a chilled margin and local brecciation in thin section (e.g., interval 304-U1309D-16R-4, 143–146 cm). In hand specimen, small remnants of basalt at the lowermost end of Section 16R-4 and of both aphanitic basalt and black diabase at the very top of Section 304-U1309D-16R-5 indicate that this basalt dike intruded an earlier intrusive contact between the main body of Diabase D-5 and an earlier, now deformed, finer-grained basalt (see **"Diabase D-5"**).

Peridotites

Ultramafic rocks of probable mantle origin

Ultramafic rocks recovered at Site U1309 are of two types: those that have clearly cumulate textures and those that lack cumulate characteristics. Many of the latter commonly have characteristics that suggest that they originated in the mantle, but some are too completely serpentinized for their origin to be reliably inferred.

Ultramafic rocks that are interpreted to be of mantle origin were recovered at ~60 mbsf in Hole U1309B and at four different depths in Hole U1309D. Total recovered thickness in Hole U1309D is 140 cm. Compositions of these rocks range from dunite to lherzolite, and all show evidences of intensive melt impregnation. The degree of alteration varies from 10% to 100%, but most are extensively altered; dunites are the most severely altered.

- At 61.1 mbsf, close to the depth of the harzburgite recovered in Hole U1309B, ~20 cm of plagioclase-lherzolite (Fig. F72A) was drilled. It has an intrusive contact with the overlying troctolite. The underlying unit is a coarse-grained gabbro dike, but the boundary between these units was not recovered. The sample is cut by several dikes and veins.
- At 155.08 mbsf, plagioclase harzburgite (Fig. F72B) is present at the bottom of Core 304-U1309D-27R. The presence of fault rocks recovered directly above suggests a tectonic emplacement.
- At 171.61 mbsf, serpentinized harzburgite (Fig. F72C) and dunite (Fig. F72D) were recovered in Core 304-U1309D-31R. These ultramafic rocks are intruded by a coarse-grained gabbro dike that shows evidence of brittle deformation. The lower contact to either gabbro or ultramafic rocks is gradational, and cataclastic textures are observed again in the gabbro.
- At 224.3 mbsf, a single piece of serpentinized harzburgite (Fig. F72E) was recovered at the top of Core 304-U1309D-42R. Because of its small size, this sample is probably not in place and may have fallen downhole. However, it does not closely match any of the earlier recovered material and is described individually.

Within all of these samples, distinct modal variations provide evidence of intensive melt impregnation. These include interstitial plagioclase, scattered melt-derived clinopyroxenes, and olivine chadacrysts in larger clinopyroxene oikocrysts. Similar textural features in samples from the MAR (DSDP Leg 37; ODP Legs 153 and 209), Hess Deep, and the Oman ophiolite have been interpreted as originating from impregnation with a plagioclase-wehrlite melt.

Impregnated lherzolite

Gabbro Zone 1
Depth: 61.1–61.31 mbsf
Interval: Section 304-U1309D-10R-1, 90–111 cm

The uppermost mantle peridotite in Hole U1309D resembles the harzburgite from Hole U1309B in hand specimen. It contains abundant (35%), rounded pyroxenes that form clusters in the (former)

olivine matrix. The degree of serpentinization varies from <10% to as much as 100%. Modal amount of spinel is low (<1%).

The lherzolite is in direct contact with the overlying medium-grained troctolite. Several crosscutting dikes and veins intrude the peridotite. The earliest is of gabbroic composition, followed by magmatic hornblende. Both are cut by a steeply dipping talc-tremolite vein and by randomly oriented carbonate veins. In thin section, the contact between peridotite and the adjoining troctolite interfingers with distinct alteration styles in each lithology. The troctolite appears to be intrusive into peridotite. Olivine in the peridotite is serpentinized (Fig. F73A), whereas olivine in the troctolite is completely replaced by talc (Fig. F73B). Interstitial plagioclase in both areas is almost completely altered to chlorite that appears dark in hand specimen. Residual olivine often has undulose extinction, and subgrain boundary formation is common. These characteristics are typical of mantle peridotites that have undergone mantle flow.

Several textural characteristics are typically indicative of melt impregnation in mantle peridotites. Unstrained olivine grains, and sometimes equant chromite, are often enclosed by poikilitic clinopyroxene that is, in turn, surrounded by interstitial plagioclase (Fig. F73C). Other pyroxene and plagioclase grains are heterogeneously distributed but increase in abundance toward the contacts with both the troctolite country rock and the gabbro dike (Fig. F73D). This is consistent with impregnation by intruding magmatic fluid(s). Finally, in one thin section (Sample 304-U1309D-10R-1, 99–102 cm), clinopyroxene forms a vermicular intergrowth with plagioclase (Fig. F73E) and sometimes replaces earlier clinopyroxene (Fig. F73F).

Plagioclase-harzburgite

Gabbro Zone 3
Depth: 155.08–155.26 mbsf
Interval: Section 304-U1309D-27R-3, 0–18 cm

A single piece and small pebbles of plagioclase-bearing peridotite were recovered at the bottom of Core 304-U1309D-27R (interval 27R-3, 0–18 cm). Plagioclase and olivine are completely altered, but pyroxenes are commonly fresher. No evidence for crystal-plastic deformation was observed. Coarse orthopyroxene often contains clinopyroxene exsolution lamellae. Fresh clinopyroxene is present as single grains as well as blebs and exsolution lamellae in orthopyroxene (Fig. F74A). One clinopyroxene contains inclusions that may have been olivine prior to alteration (Fig. F74B). Those are completely altered and often contain euhedral oxides. Spinel is equant and almost opaque. Plagioclase is present in small amounts, mostly along a discontinuous train in the matrix.

Dunite and plagioclase harzburgite

Gabbro Zone 3
Depth: 171.61–173.63 mbsf
Intervals: Sections 304-U1309D-31R-1, 11 cm, and 31R-2, 67 cm

The longest recovered section of peridotite in Hole U1309D (overall = 88 cm) was drilled at 171.61 mbsf (interval 304-U1309D-31R-1, 11 cm, to 31R-2, 67 cm). It consists of two intervals separated by a 0.7 m interval of deformed coarse-grained gabbro. The uppermost peridotite interval consists of dunite that is almost completely serpentinized, with almost no relict features. However, some coarse spinel grains remain, and these often contain olivine inclusions that have been partly protected from alteration.

The lower interval of harzburgite is in direct contact with gabbro, and talc-tremolite veins are present along the contact and within the harzburgite. Two thin section billets were cut from the harzburgite interval, one next to the contact to gabbro in Section 304-U1309D-31R-1 (and within the talc-tremolite zone) and the other in Section 31R-2; the latter was chosen in an attempt to avoid most of the alteration veins. The thin section from the contact area reveals strong talc alteration of all silicate phases. Carbonate is abundant and present in the serpentine mesh. Pyroxene grains are heavily altered to talc except for rare clinopyroxene exsolutions and blebs in altered orthopyroxene. Spinels are equant to interstitial in shape and often have olivine inclusions. Plagioclase is widespread in thin section but is invariably altered to chlorite and seems to be randomly distributed. Pyroxenes and olivine appear to be undeformed, but static replacement during alteration may have obliterated deformation textures. Some less altered pyroxenes show no preferred orientation and straight extinction, and spinel is undeformed with serrated grain boundaries.

Thin section Sample 304-U1309D-31R-2, 46–48 cm, from the bottom part of the interval, contains fresh cores of orthopyroxene and olivine that are mostly cut by serpentine veins but are not completely altered. Olivine exhibits subgrain boundaries and a weak LPO indicative of mantle flow. Two grains of clinopyroxene are fresh and contain olivine inclusions. They show corrosive boundaries with each other (Fig. F75A). Coarse spinels have mostly equant shapes and dark red colors. Plagioclase is confined to a narrow zone along the long axis of the thin section, where it is present in the matrix (Fig. F75B). Within this zone, spinels are often rimmed by plagi-

oclase, whereas farther away, no plagioclase coronas could be observed. Pyroxenes have very elongated grains with length:width ratios >1:3.

Impregnated harzburgite

Gabbro Zone 5
Depth: 224.3–224.39 mbsf
Interval: Section 304-U1309D-42R-1, 0–9 cm

This sample is serpentinized (~70%) harzburgite with a talc-tremolite vein cutting along one edge. Olivine grains are commonly cut by serpentine veins, but grain boundaries, including some subgrain boundaries, are still recognizable. Pyroxene is present as oikocrysts enclosing olivine (Fig. F76A) and often forms heterogeneously distributed clusters (Fig. F76B) or trails. It has been mostly replaced by alteration phases. No plagioclase or plagioclase relics could be identified. The significant number of clinopyroxenes enclosing olivine and the absence of plagioclase are notable features in this sample, which differs from the peridotites previously described.

Hole U1309D (Expedition 305)

The gabbroic rocks recovered during Expedition 305 seamlessly form the continuation of the lithological sequence at the bottom (401.3 mbsf) of Hole U1309D from the end of Expedition 304. The downhole igneous stratigraphy for the entire hole is shown in Figure F77. The rock types and their proportions for the entire hole (and separated by expedition) are shown in Figures F77 and F78. Between 401.3 and 1415.5 mbsf, the most common lithology is medium- to coarse-grained (rarely pegmatitic) gabbro, which forms 60.8% of the rocks recovered during Expedition 305. The gabbroic rocks have a broad range in modal composition, commonly including minor quantities (rarely exceeding 10%) of olivine, Fe-Ti oxides, and/or orthopyroxene. Intercalated with these gabbros are medium-grained olivine gabbros, which have modal olivine that nearly always exceeds 20%. The modal composition of olivine-bearing rocks is highly variable on a submeter scale as well and, in places, frequently grades into rocks of troctolitic gabbro composition. Together, olivine and troctolitic gabbro form 23.1% of the section, the second most abundant lithology (Figs. F78, F79A). Spatially associated with the olivine- and troctolitic gabbros are troctolites with a dominantly seriate texture. The troctolites are less common and only contribute 2.2% of the lithologies recovered during Expedition 305.

A rarely recovered lithology at mid-ocean ridges is olivine-rich troctolite that contains >70% olivine and, in contrast to troctolite, has a cumulate-like texture with subhedral to rounded olivine and interstitial to poikilitic plagioclase and clinopyroxene in variable proportions. In places, these rare primitive rocks are very fresh. The downhole abundance of the olivine-rich troctolites is 5.4%, and they are restricted to very confined intervals.

Oxide gabbro (7.7% of the rocks recovered) is defined by the occurrence of >2% modal Fe-Ti oxide minerals (Fig. F79B). The oxide-bearing gabbros are most common within the gabbro sequence, and the Fe-Ti oxides are present as heterogeneously distributed patches or seams. The oxide gabbros can be discrete dikelets crosscutting other rock types or can display strong enrichment in ductile deformation zones. In general, oxide gabbros appear to be a common lithology along slow-spreading mid-ocean ridges, and in addition to Hole U1309D, they have been reported from other drilling locations along the MAR (Legs 153 and 209) and the SWIR (Hole 735B).

Finally, the gabbroic rocks have been crosscut by a number of diabase intrusions.

Olivine-rich troctolites

The term "olivine-rich troctolite" is assigned to olivine-rich rocks with relatively low modal abundance of plagioclase and clinopyroxene and a classic cumulate texture. They form a volumetrically minor component (5.4%) of the section of Hole U1309D recovered during Expedition 305 (Fig. F78). Their modal composition is 70%–90% olivine, 5%–20% plagioclase, 0%–15% clinopyroxene (Fig. F80), and, in places, up to 2% chromian spinel. Their modes commonly change on a decimeter scale, mainly as a result of variable plagioclase and clinopyroxene proportions. Typical features of each olivine-rich troctolite interval are shown in Figures F81, F82, F83, F84, F85, F86, F87, and F88. Representative photomicrographs are shown in Figures F89 and F90. Applying the International Union of Geological Sciences (IUGS) terminology, they can be classified as olivine gabbro, troctolite, wehrlite, or, locally, even dunite. Texturally, they consist of a medium-grained subhedral to rounded olivine matrix and interstitial to poikilitic plagioclase and clinopyroxene (e.g., Figs. F89, F90).

We have adopted the informal descriptive term "olivine-rich troctolite" as a practical tool to facilitate core description and subsequent statistical analysis. This approach is needed for four reasons:

1. To avoid recombining four different rock names that would inevitably result from an IUGS-conforming classification;
2. To clearly distinguish olivine-rich troctolites from true dunites from the olivine gabbros and associated "modifier-free" troctolites. The latter have far

less modal olivine and clearly distinct equigranular to seriate texture;
3. To avoid the process-related term "cumulate," which imposes a subjective and premature interpretation; and
4. To avoid the much-debated term "plagioclase-wehrlite," as seen in many deep crustal sections of ophiolites, which is commonly inferred to have process-related implications.

Olivine-rich troctolites are present in eight discrete intervals recovered during Expedition 305 (Fig. F77):

1. Interval 305-U1309D-100R-1, 0–128 cm (495.30–496.58 mbsf),
2. Sections 305-U1309D-136R-1 to 136R-2, 58 cm (669.44–671.35 mbsf),
3. A complex interval intruded by a highly altered network of oxide gabbro and diabase dikes in Sections 305-U1309D-140R-2, 56 cm, to 140R-3, 84 cm (689.51–690.98 mbsf),
4. Sections 305-U1309D-227R-2, 32 cm, to 228R-4, 58 cm (1093.75–1101.28 mbsf),
5. Sections 305-U1309D-233R-1, 51 cm, to 238R-1, 123 cm (1093.75–1101.28 mbsf),
6. Sections 305-U1309D-240R-1, 115 cm, to 243R-1, 39 cm (1154.65–1168.29 mbsf),
7. Sections 305-U1309D-247R-1, 2 cm, to 248R-4, 58 cm (1187.12–1196.50 mbsf), and
8. Sections 305-U1309D-256R-1, 4 cm, to 257R-1, 74 cm (1230.34–1235.84 mbsf).

Olivine-rich troctolites form the dominant lithology between 1092 and 1236 mbsf. In the remainder of the hole drilled during Expedition 305, they represent only a minor component (Figs. F77, F78). In the sequence dominated by olivine-rich troctolite, the rocks are mainly intercalated with olivine and troctolitic gabbro and, in places, crosscut by sharply bounded medium- to coarse-grained olivine gabbro dikes. The olivine gabbro consists of subequal proportions of clinopyroxenes and plagioclase with variable low olivine and/or orthopyroxene (e.g., Fig. F85A). A second set of crosscutting gabbro dikes have similar modal contents, but their contacts with the surrounding olivine-rich troctolite are diffuse and difficult to discern.

In hand specimen, most olivine-rich troctolites are easily identified by the presence of fine black serpentine veins or a fine serpentine network, due to their (originally) high modal olivine (e.g., Fig. F88A). Most troctolites contain abundant, irregularly distributed, large (up to 30 mm), undeformed clinopyroxene oikocrysts that enclose olivine and, to a lesser extent, plagioclase (Figs. F81, F90A). Plagioclase commonly fills the interstitial spaces between olivine and pyroxene. In places, the interstitial plagioclase displays a preferred dominantly subhorizontal orientation.

Thin section observations generally confirm the coarse grain size and optical continuity of the clinopyroxene oikocrysts. Within the oikocrysts, plagioclase abundance is generally very low. Occasionally, plagioclase also forms oikocrysts enclosing olivine, but its predominant mode of occurrence is a continuous network of moderately annealed individual grains. Olivine is generally only partially surrounded by plagioclase; 10%–40% of olivine grain boundaries are olivine/olivine contacts. Olivine connectivity is significantly reduced among clinopyroxene-hosted olivines, where olivine/olivine contacts are scarce. Overall, the olivine grain size does not change significantly between clinopyroxene- and plagioclase-hosted texture.

Chromian spinel is a common accessory phase in olivine-rich troctolites. It is present as fine-grained (50–100 µm) subhedral to euhedral, rarely holly leaf shaped crystals, either enclosed within olivine grains or within the plagioclase matrix. In plagioclase-rich, clinopyroxene-free zones, the modal content of chromian spinel is as high as 2%, whereas in clinopyroxene-rich zones, spinel as olivine-hosted inclusions is rare. Roughly one out of twenty chromian spinels is orbicular, containing olivine, plagioclase, or, rarely, brown amphibole inclusions, around which it presumably nucleated.

Each olivine-rich troctolite has different contact relationships with the surrounding lithologic units. Given their potentially crucial importance for the interpretation of the igneous evolution of Atlantis Massif, each contact is described below in stratigraphic order.

Contact 1

The first occurrence of olivine-rich troctolite during Expedition 305 is in Section 305-U1309D-100R-1. Its contact with the lowermost coarse-grained gabbro of Section 305-U1309D-99R-3 at 494.92 mbsf (Fig. F81) was not recovered. The exact length of this interval is not accurately constrained, as a result of an overrecovery of Core 305-U1309D-101R that exceeded the cored interval. In order to avoid two cored intervals with the same depth, the overlying Core 305-U1309D-100R was shifted upward accordingly. The effect of this shift is that the nonrecovered interval is reduced from 168 to 38 cm. Neither this lowermost gabbro nor the uppermost olivine-rich troctolite are significantly deformed. Nevertheless, there is no evidence to either support or discount stratigraphic continuity.

Contact 2

A medium-grained olivine-rich troctolite in Section 305-U1309D-100R-1 grades through troctolitic gabbro to coarse-grained olivine gabbro (Fig. **F81B**), and details of the transition are obscured by a pervasive metamorphic overprint. The distribution of corona textures suggests that modal olivine decreases gradually as modal plagioclase increases.

Contact 3

The upper contact of the olivine-rich troctolite at 669 mbsf in Section 305-U1309D-136R-2 is missing, but the lower one is well preserved (Fig. **F82**). Between the lowermost undeformed coarse-grained gabbro of Section 305-U1309D-135R-2 at 667.05 mbsf and the underlying, equally undeformed olivine-rich troctolite of Section 136R-1, there is a no-recovery zone of 230 cm. The lower contact between the olivine-rich troctolite and an almost anorthositic clinopyroxene-poor gabbro is sharp. Included in this underlying plagioclase-rich gabbro are irregular 1–5 cm sized troctolitic patches (Fig. **F82B**). Along the contact between the anorthositic interval and the olivine-rich troctolite, a trail of well-preserved chromian spinel can be seen in thin section (Fig. **F91**). The primary igneous plagioclase microstructure in the anorthositic interval is obliterated by plastic deformation. In the olivine-rich troctolite, plagioclase is poikilitic and only weakly strained. In contrast, clinopyroxene in both intervals is largely undeformed.

Contact 4

The upper contact between the olivine-rich troctolite of Section 305-U1309D-140R-2 (Fig. **F83**) and the oxide-bearing gabbro of the section above is not well preserved; it is marked by deformed and highly altered serpentine-rich rubble. The recovery of Core 305-U1309D-140R is >100%, suggesting that the contact between two lithologies does not represent a significant displacement zone. This conclusion is supported by the presence of a network of crosscutting, small oxide-bearing gabbro and diabase dikes postdating the strong metamorphic overprint within the olivine-rich troctolite. In other words, the olivine-rich troctolites at 670 and 690 mbsf may represent a continuous lithologic "package."

Contact 5

At 1127 mbsf, a well-preserved contact between coarse-grained olivine gabbro and fine- to medium-grained clinopyroxene-free, olivine-rich troctolite (85% modal olivine) is sharp, wavy, and undeformed (interval 305-U1309D-227R-2, 34–36 cm) (Fig. **F84A**). There is no gradual transition toward the contact within the olivine-rich troctolite, but within the overlying olivine gabbro modal olivine gradually increases from <5% at the top of the section to 30% near the contact without any significant change in grain size. Thirteen 0.5–20 cm wide gabbroic dikes crosscut this nearly 6 m long section of olivine-rich troctolite (Fig. **F84B**). Within the fine-grained olivine-rich troctolite, the plagioclase content increases strongly toward the contact. The lower contact to a medium- to coarse-grained troctolitic gabbro (20%–30% olivine; 15% clinopyroxene) is similarly well preserved, subvertical, and relatively sharp (interval 305-U1309D-228R-3, 64–76 cm) (Fig. **F84C**).

Contact 6

The next olivine-rich troctolite interval >1 m thick starts at Section 305-U1309D-233R-2, 51 cm, and ends at Section 305-U1309D-238R-1, 123 cm (Fig. **F85**). A diffuse upper contact with coarse-grained troctolite is well preserved; the lower contact is missing. It is likely, however, that the upper contact is with a crosscutting dike that has sharp contacts similar to the other crosscutting gabbroic dikes within this and other olivine-rich troctolite intervals (Fig. **F85A, F85C**).

Contact 7

At Section 305-U1309D-240R-1, 115 cm, the upper contact is missing, but an olivine-rich troctolite has generally sharp boundaries with coarse-grained gabbro dikes (Fig. **F86A, F86B**). Olivine-rich troctolite fragments are seen within the gabbro dike (Fig. **F86C**). The lower contact with olivine gabbro is similarly well preserved (Section 305-U1309D-243R-1, 34 cm) and relatively sharp (Fig. **F86D**). There is a gradual decrease of modal olivine approaching the contact within the olivine gabbro. This contact is distinct from those of the crosscutting gabbro dikes described above; it more closely resembles the gradual upper contact of Section 305-U1309D-227R-2.

Contact 8

The upper contact of an olivine-rich troctolite interval between the top of Section 305-U1309D-247R-1 and Section 248R-4, 59 cm (Fig. **F87**) was not recovered, and the lower contact with olivine-bearing gabbro is poorly preserved and strongly altered but appears to be sharp. Two coarse-grained gabbro dikes with sharp contacts crosscut the olivine-rich troctolites in Section 305-U1309D-247R-1 (Fig. **F87A, F87B**).

Contact 9

The lowermost olivine-rich troctolite interval recovered during Expedition 305 starts at the top of Section 305-U1309D-256R-1, below diabase rubble, and

ends at Section 257R-1, 74 cm (Fig. F88). Neither the upper nor the lower contact was recovered, but the contacts with an olivine gabbro dike are relatively sharp (Fig. F88B, F88C). Thin gabbro dikes (<1 cm thick) intrude subvertically into the olivine-rich troctolite through interval 305-U1309D-256R-3, 64 cm, to 257R-4, 45 cm (Figs. F88C, F90B).

The overall olivine-rich troctolite-dominated interval from Section 305-U1309D-227R-2 through 257R-1 (1093.75–1235.84 mbsf) forms an integral lithologic package. The olivine-rich troctolites and minor associated lithologic units that comprise this package have subsequently been intruded, at temperatures below the olivine-rich troctolite solidus, by numerous crosscutting gabbroic dikes of variable thickness. The larger scale contacts with the surrounding olivine gabbro units seem, however, to be dominantly intrusive and to have formed under hypersolidus conditions. There is currently no evidence concerning possible genetic relationships between the olivine-rich troctolites and the surrounding gabbroic rocks.

Troctolite

Troctolite is relatively abundant in the interval 400–600 mbsf but occurs only sporadically through the remainder of the core (Fig. F79). Overall, troctolite constitutes only 2.7% of the rocks recovered from Hole U1309D. The deepest recovered troctolite is in interval 305-U1309D-268R-1, 78–93 cm (1290 mbsf). Primary mineral modes in troctolite are 30%–70% olivine, 30%–50% plagioclase, and up to 5% clinopyroxene. Plagioclase/olivine ratios vary on a decimeter scale, and there are frequent irregular gradations into troctolitic gabbro and even olivine gabbro. Texturally, olivine-rich troctolites are characterized by cumulate textures defined by discrete rounded olivine grains with interstitial plagioclase and/or clinopyroxene. In contrast, troctolite textures are more irregularly seriate with local poikilitic clinopyroxene occurrences.

Olivine crystals vary in size. They are mostly present as continuous networks of millimeter-sized grains, but they are also present as subrounded centimeter-sized grains. Olivine chadacrysts, sometimes with aligned olivine kink bands, also occur in plagioclase and clinopyroxene.

Within the troctolite, clinopyroxene shapes range from interstitial to pegmatitic oikocrysts 2–50 mm in size. Their mode is highly variable, and troctolitic gabbro patches are developed locally. Interstitial clinopyroxene seems more abundant close to gabbroic dikes, suggesting that primary oikocrystic clinopyroxene is recrystallized during later intrusion of the crosscutting dikes. In many cases, interstitial orthopyroxene and clinopyroxene are present as fine rims around olivine or as thin films at olivine/plagioclase contacts. Clinopyroxene oikocrysts enclose olivine and plagioclase chadacrysts. Less frequently, clinopyroxene is present as chadacrysts in plagioclase oikocrysts.

Plagioclase is present as subhedral to anhedral crystals and is fine to coarse grained. Plagioclase is present as interstitial crystals and oikocrysts enclosing clinopyroxene and olivine chadacrysts. In some cases, early plagioclase is possibly replaced by olivine. Both plagioclase-rich veins/zones and olivine-rich patches are observed. Spinel is seen as euhedral to anhedral crystals enclosed in both plagioclase and olivine.

The troctolite units are commonly crosscut by late-stage dikes of both coarse-grained gabbro and microgabbro (Fig. F92A, F92B). Dike orientations are highly variable from horizontal to vertical, and contacts range from diffuse to sharp. Along the diffuse contacts, locally abundant sulfides and patches of clinopyroxene suggest infiltration into the host.

One particular example showing the textural contrast to the olivine-rich troctolites occurs in interval 305-U1309D-111R-3 through 112R-1, at 545–557 mbsf. Both the upper and lower contacts for the ultramafic interval around 650 mbsf are gradual and not clearly defined at all. The upper contact is probably characterized by the first presence of a pegmatitic troctolite patch enclosed in coarse-grained gabbro (interval 305-U1309D-110R-1, 113–128 cm). After an interval of interfingering coarse-grained gabbros and minor troctolitic patches in Sections 305-U1309D-110R-2 and 110R-3, olivine-rich troctolite with variable grain size becomes dominant. A zone of bimodally sized olivine in Sections 305-U1309D-112R-1 and 112R-2 accompanies the gradual change to more gabbro dominated zones. Occasionally, subrounded centimeter-sized olivines appear in addition to the millimeter-sized continuous olivine network that is typical of these troctolites. At the bottom of Section 305-U1309D-112R-3, the large olivines become dominant prior to a transition to coarse equigranular olivine gabbro.

Troctolitic gabbro and olivine gabbro

Olivine gabbro is abundant in Hole U1309D. Within this lithology, decimeter- to meter-scale variations in clinopyroxene content lead to local gradations to troctolitic gabbro. Together, olivine gabbro and troctolitic gabbro constitute 23.1% of the material recovered during Expedition 305 (Figs. F77, F78).

Olivine gabbro is the dominant lithology in the intervals 400–600, 1000–1100, 1200–1300, and 1380–

1415 mbsf. The intervals are characterized by fine- to coarse-grained olivine and olivine-bearing gabbros that locally grade to troctolitic intervals and patches and, in places, to troctolite (Fig. F7). The modal composition varies widely from 5%–50% olivine, 25%–80% plagioclase, and 10%–70% clinopyroxene. Grain size, texture, and modal composition are heterogeneous and vary highly throughout this sequence.

Like the troctolites, the olivine gabbros are frequently interrupted by late-stage magmatic leucocratic dikes and by dikes of both coarse gabbro and microgabbro. Patches and zones of coarser grained clinopyroxene in a medium-grained matrix are also common. In the upper part of the interval cored during Expedition 305, intrusive contacts are sharp and commonly wavy, accompanied by tiny interstitial clinopyroxene grains that suggest infiltration into the host. Downhole, both obvious igneous contacts and more diffuse boundaries are seen. Owing to centimeter-scale variations in mineral proportions, lithologies determined from thin sections sometimes differ from those determined from hand samples. The olivine gabbros show strong modal variability. Plagioclase-, pyroxene-, and olivine-rich intervals and patches are irregularly distributed, leading to local variations in lithology ranging from troctolite to olivine-bearing gabbro. Occasionally, olivine is concentrated in variably oriented bands (vertical, oblique, and horizontal) separating medium- and fine-grained zones in the center of the core.

There is no systematic downhole variation in primary modes or textures of olivine gabbros. Olivine is present in the upper portion of the hole as subhedral to interstitial crystals. Down to ~1000 mbsf, olivine is usually pervasively altered by a hydration reaction with plagioclase to mesh-textured serpentine and/or fine-grained talc-tremolite intergrowths. In pervasively altered samples, the resulting coronitic texture delineates the original olivine grain boundaries, allowing a first-order approximation of primary olivine abundance (see also **"Metamorphic petrology"**) (Fig. F93A). In places, however, a similar texture surrounding altered clinopyroxene can be seen in thin section. In some places, this effect may lead to a small overestimation of olivine mode and a complementary underestimation of clinopyroxene in hand sample.

Olivine-rich zones also appear to correlate generally with MS highs (as measured with the whole-core multisensor track [MST]; see **"Physical properties"**). This correlation is presumed to reflect the formation of dispersed iron oxides during serpentinization of olivine. Olivines are seen as chadacrysts in plagioclase and clinopyroxene (Fig. F93B) but are also present as oikocrysts enclosing plagioclase. Below 1000 mbsf, olivine encloses spinel and is less altered, with abundant trails of (possibly) secondary fluid inclusions. Kink bands, which occur frequently in the upper part of the hole, are absent below 1000 mbsf.

Clinopyroxene most commonly occurs as anhedral primary grains ranging from 1 to 10 mm with an average grain size of 5 mm. In many samples, it is interstitial with interlocked contacts between plagioclases (Fig. F93C, F93D), as thin films between olivine and plagioclase, or as thin (50 µm) films rimming olivine. In places, large oikocrysts poikilitically enclose subhedral to rounded olivine (Fig. F93B), plagioclase, and spinel chadacrysts. Clinopyroxene is usually ~20% altered, with tremolite/actinolite forming rims around primary clinopyroxene (see **"Metamorphic petrology"**). In some cases, clinopyroxene is partially or completely replaced by acicular colorless amphibole, particularly along exsolution lamellae. Exsolved interlocking clinopyroxene/orthopyroxene contacts are also abundant.

Plagioclase is present as euhedral to anhedral crystals and appears relatively fresh compared to clinopyroxene and olivine. It is rarely present as oikocrysts enclosing rounded clinopyroxene and olivine chadacrysts. The most altered plagioclases are ~20% altered to tremolite and chlorite rims. The plagioclase crystals commonly show recrystallized textures and abundant trails of fluid inclusions.

Orthopyroxene is sporadically present as interstitial films between olivine and plagioclase and rarely as clinopyroxene/plagioclase contacts. The films are ~20–50 µm thick and up to 200 µm in length. They seem most abundant in the upper part of the hole.

Spinel appears as euhedral to anhedral small (~1 mm) crystals enclosed in olivine and plagioclase. In some cases, the spinels are oxidized, although some relics exist.

Trace amounts of sulfide and oxide are locally enriched, usually in the vicinity of nonmagmatic veins.

In the troctolitic gabbros, the olivines are, in some cases, widely spaced and show few weak kink bands compared to troctolite and olivine gabbro. In some cases, plagioclase is present as chadacrysts in olivine. Large olivines and clinopyroxene- and plagioclase-rich concentrations, together with grain size variation, lead to modal variations in the units.

Gabbro group (gabbro, olivine-bearing gabbro, microgabbro, and disseminated oxide gabbro)

In this section, we describe several rock types together. Gabbros are dominated by plagioclase and clinopyroxene with <5% olivine or orthopyroxene. Gabbronorites contain >5% modal orthopyroxene.

Consistent with Expedition 304, we use the term "olivine-bearing gabbro" for modal olivine between 1% and 5%. These rock types are discussed together because modal olivine in the core fluctuates over short length scales. Modal variations from 0% to 5% are common in gabbros and from >5% to <5% olivine within olivine gabbro units. Thus, the term "olivine-bearing gabbros" is a descriptive term, not a genetic one. Microgabbros generally have subequal modal abundances plagioclase and clinopyroxene. It should be noted that many of the rocks identified as gabbros in the visual core descriptions actually contain significant modal orthopyroxene that could only be identified in thin section. Because the generally grayish orthopyroxene is very difficult to distinguish from clinopyroxene and groundmass plagioclase in hand sample, sections of core described as gabbro are in some places gabbronorites or olivine gabbronorites (see the more detailed discussion in **"Gabbronorites and orthopyroxene-bearing gabbros"**).

In terms of cumulative length, the gabbro group (gabbro, olivine-bearing gabbro, microgabbro, disseminated oxide gabbro, and gabbronorite) is the dominant lithologic group, encompassing 60.75% of material recovered during Expedition 305 and 55.7% over the entire depth of Hole U1309D (Figs. **F67, F77, F78**).

Gabbros vary considerably in grain size from microgabbro through seriate medium grained to pegmatitic, in places within a single core section. Gabbros commonly contain pegmatitic or coarse-grained clinopyroxene over tens of centimeters long (Fig. **F94**). Pegmatitic clinopyroxenes are commonly undeformed, between 50 and 150 mm in size, and can be oikocrystic. From 650 mbsf to the bottom of the hole, pegmatitic intervals are shorter; the grain size in gabbro is typically medium to coarse. Plagioclase crystals are generally anhedral and form interlocking textures with pyroxene and other plagioclase grains. Olivines are commonly interstitial in olivine-bearing gabbros and rimmed by alteration coronas (Fig. **F95**). Olivine-bearing gabbros show variable grain sizes and downhole distribution.

Microgabbro (including microgabbronorite) grades in grain size from fine grained to cryptocrystalline. It exhibits high-temperature equigranular crystallization textures (Fig. **F96B**), and along some contacts plagioclase has recrystallized at high temperature (Fig. **F96C**). In many cases, microgabbro and diabase are difficult to distinguish in hand sample because of similar grain size. In thin section, microgabbro is distinguished by its equigranular textures from diabase (Fig. **F96**), which has glassy, intersertal, or cryptocrystalline textures with acicular plagioclase. In some intervals, diabase intrusions have fine-grained chilled margins, whereas microgabbros do not exhibit chilled margins.

Microgabbros are also distinguishable from diabase on the basis of their chemical compositions. Plots of Na_2O against TiO_2 provide a useful discriminant; microgabbros plot with other cumulate rocks at lower TiO_2 for a given Na_2O content, whereas diabases follow a distinct liquid line of descent that is also followed by the basalts (Fig. **F97**).

Microgabbro is present intermittently as dikes throughout the hole but increases in abundance in association with a prominent ductile shear zone at ~575–675 mbsf. It occurs in three modes: in intrusive contact with surrounding rocks (Fig. **F96A, F96B**), in plastically deformed zones (Fig. **F96D**), and in zones that grade in grain size and apparent magmatic continuity to medium- and coarse-grained gabbro.

Where visible, the contact relationships of gabbro with other lithologies suggest that gabbro is generally intrusive into olivine-rich lithologies (olivine gabbros and troctolites) and is intruded by felsic (leucocratic) dikes and oxide gabbros. These relationships are more common between 400 and 650 mbsf than in the lower part of the hole, where gabbro contacts are diffuse. Contacts between troctolite and gabbro range from sharp, where thin intervals of gabbro crosscut the serpentine foliation in the troctolite, to gradational, where thicker intervals of gabbro are present. Contacts between oxide-bearing lithologies and gabbro range from sharp to gradational as well. True felsic dikes in gabbro generally show sharp contacts, but varying degrees of high-temperature reaction between dikes and wallrocks are also observed. These reaction zones commonly have oriented minerals such as oxides, pyroxenes, or plagioclase growing along and across them, indicating postemplacement reaction.

Gabbros are present in varying proportions throughout the hole, but there are long (tens of meters) intervals in which gabbro is the overwhelmingly dominant lithology. One of these gabbro zones is bounded above by oxide gabbro at ~600–650 mbsf and below by olivine gabbro and troctolite at ~1030 mbsf (Fig. **F77**). The gabbro sequence is punctuated only by a short interval in which oxide gabbros and more olivine rich lithologies appear at 870–900 mbsf. Gabbronorite abundance also peaks in the interval 760–1050 mbsf, tailing off where the abundance of olivine-rich lithologies begins to increase at ~1000 mbsf. A second, shorter gabbro-dominated interval from 1300 to 1360 mbsf is bounded above by a ~10 m interval of oxide gabbro and below by troctolite and olivine gabbro. It is punctuated at ~1340

mbsf by narrow intervals of oxide gabbro and olivine gabbro (Figs. F77, F79).

Downhole variations in lithology and modal composition define two similar intrusive packages (at ~600–1240 mbsf and ~1240–1415 mbsf) within the 600–1415 mbsf portion of Hole U1309D. In both packages, an interval of olivine-rich lithologies (troctolite and olivine-rich troctolite) occurs below a relatively thick interval of gabbro and gabbronorite with oxide gabbro and olivine-bearing gabbro units. These are overlain, in turn, by ~10–12 m upper intervals of oxide gabbro. Microgabbros are present as dikes in gabbro or in deformation zones. From 0 to 400 mbsf, olivine-rich lithologies are more abundant than below 400 mbsf.

Gabbronorites and orthopyroxene-bearing gabbros

Gabbronorites are defined as gabbroic rocks in which the total amount of orthopyroxene ± inverted pigeonite is >5%, but in practice, they are difficult to identify in the core because of significant local modal fluctuation and because orthopyroxene is difficult to consistently identify in hand specimen. For these reasons, reported gabbronorite abundances are minimum estimates and contact relationships are unconstrained. In the lower part of the hole (from Core 305-U1309D-243R through Core 272R), low-Ca pyroxenes include both orthopyroxene and inverted pigeonite (see below). Compositionally, gabbronorites partially overlap the gabbro field, with slightly higher average Na_2O (Fig. F97). This observation suggests that the parent liquids of the orthopyroxene-bearing gabbros are slightly more evolved than those of the orthopyroxene-free gabbros. Gabbronorites occur in contact with all other lithologies, but their contact relationships are not readily observable in the core.

Gabbronorites have similar textural relationships to those of the gabbros and olivine gabbros. Primary magmatic fabrics are usually absent but sometimes weakly developed. Weak high-temperature deformation is irregularly present as kink bands in olivine and rarely in orthopyroxene. Plagioclase usually shows wavy extinction and tapered twins. In strongly sheared to mylonitic gabbronorites, orthopyroxene is characteristically replaced by aggregates of tabular neoblasts (see **"Structural geology"**).

Plagioclase is the dominant phase; it is usually anhedral in the granular groundmass and is also present as rounded chadacrysts enclosed either in clinopyroxene and orthopyroxene oikocrysts.

Clinopyroxene is anhedral and rarely subhedral; it is frequently present as fine interstitial aggregates associated or directly connected with large oikocrystic grains.

Olivine is always anhedral, in places enclosed as rounded chadacrysts in large clinopyroxene and orthopyroxene oikocrysts.

Orthopyroxene occurs as large subhedral grains in the coarser gabbro and gabbronorite but is more commonly anhedral, particularly in the fine-grained microgabbro or microgabbronorite. Orthopyroxene oikocrysts enclose plagioclase with less clinopyroxene and olivine (Fig. F98). These chadacrysts are generally rounded and resorbed, suggesting that oikocrystic orthopyroxene is the last phase to crystallize. In the more olivine poor assemblages (<20% olivine), olivine and orthopyroxene are commonly present together with primary nonreactive contacts (Fig. F99A). A 100–400 µm thick orthopyroxene film that mantles olivine in almost all thin sections appears most commonly at olivine/plagioclase contacts (Fig. F99B). In places, both orthopyroxene and clinopyroxene films occur. Rarely, orthopyroxene films extend from a large anhedral grain into clinopyroxene-olivine and plagioclase-clinopyroxene interstices (Fig. F99B).

Inverted pigeonite is present between Cores 305-U1309D-243R and 272R, dividing the lower gabbronorite into two zones (see below). It is identified on the basis of its characteristic exsolution pattern, following (001) and (100) (Fig. F99C). In places, inverted pigeonite is seen in thin section to be associated with late-stage magmatic impregnations (oxide-rich gabbroic veins). This association may suggest that pigeonite inversion occurs only under restricted thermal conditions. Because inversion simplifies pigeonite detection, this situation may lead to underestimation of pigeonite content.

Gabbronorite abundance increases downhole below ~400 mbsf (Fig. F100). Between Cores 305-U1309D-80R and 156R, gabbronorites occur only as rare fine- to medium-grained (micro)gabbronorite and orthopyroxene-bearing gabbro. The uppermost appearance of a gabbronorite is a narrow (8–10 mm) fine-grained dike that intrudes olivine-bearing gabbro (Unit 213, ~404 mbsf) (Sample 305-U1309D-80R-2, 123–143 cm). A narrower (up to 0.4 mm) amphibole-bearing gabbronorite dike cuts olivine gabbro at Unit 314 (582 mbsf).

Based on the continuity of gabbronorite recovery and modal mineralogy, six gabbronorite zones can be defined in Hole U1309D (Fig. F100).

Gabbronorite Zone 1

Depth: ~400–625 mbsf
Interval: Cores 304-U1309D-80R to 126R
Lithology: occasional fine- to medium-grained (micro)gabbronorite and orthopyroxene-bearing gabbro.

Gabbronorite Zone 2

Depth: ~650–682 mbsf
Interval: Cores 305-U1309D-132R to 138R
Lithology: fine- to coarse-grained olivine-bearing to olivine gabbro and gabbronorite in the upper part and fine- to medium-grained orthopyroxene-bearing microgabbro and gabbronorite in the lower part; Unit 379 shows mylonitic deformation and oxide impregnation during the late stage of deformation.

Gabbronorite Zone 3

Depth: ~704–729 mbsf
Interval: Cores 305-U1309D-143R to 149R
Lithology: orthopyroxene-bearing gabbro and gabbronorite alternating with olivine gabbro in the upper part and with medium- to coarse-grained gabbro in the lower part.

Gabbronorite Zone 4: main gabbronoritic zone

Depth: ~760–1100 mbsf
Interval: Cores 305-U1309D-156R to 230R
Lithology: plagioclase- and clinopyroxene-bearing gabbro. This zone constitutes the main body of the gabbro sequence. Plagioclase and clinopyroxene average 62% and 30%, respectively. Olivine and orthopyroxene average 7% and 5%, respectively. There is no correlation between olivine and orthopyroxene content. Their modes fluctuate downhole in an apparently random way. Relative enrichments in the two phases are commonly observed (Fig. **F100**). The maximum orthopyroxene content, indicated by the modal spikes in Figure **F100,** decreases downhole to the base of the main gabbronoritic zone, thus showing an inverse correlation with the increasing trend of the olivine-rich gabbros (Fig. **F79**).

Gabbronorite Zone 5: pigeonitic gabbronorite zone

Depth: ~1168–1310 mbsf
Interval: Cores 305-U1309D-243R to 272R
Lithology: gabbronorite and olivine gabbronorite (olivine as high as 7%) are intercalated with troctolite and troctolitic gabbro in the upper part of this zone, with oxide gabbro in the central part and olivine-rich gabbro in the lower part. Low-Ca pyroxene is commonly represented by inverted pigeonite. In places, orthopyroxene, clinopyroxene, and inverted pigeonite coexist (Core 305-U1309D-264R).

Gabbronorite Zone 6: lower gabbronoritic zone

Depth: ~1317–1415 mbsf
Interval: Cores 305-U1309D-274R to 295R
Lithology: in the lower part of the hole, gabbronorites are continuous; Orthopyroxene varies from a few percent to 45% in Core 305-U1309D-293R (norite).

Oxide gabbro

Oxide gabbros consist mainly of plagioclase and clinopyroxene but are defined by >2% modal Fe-Ti oxide; disseminated oxide gabbros contain between 1% and 2% modal oxides. Oxide gabbro forms 7.7% of material recovered from Hole U1309D during Expedition 305. Apart from their oxide contents, the mineralogical characteristics of the oxide gabbros are similar to those of the coarse-grained gabbros (Fig. **F101A**).

Oxide gabbros can be distinguished from other gabbros by their high bulk MS, and this property can be used to help constrain their contacts with surrounding oxide-free rock types. In some cases, ilmenite may be present in oxide-bearing zones of low MS.

In many oxide-rich gabbros, accessory apatite as large as 6 mm can be identified in thin section (Fig. **F102**). Bulk rock analyses indicate that the apatite content can locally exceed 7 wt%. Euhedral elongate prismatic zircons, up to 3 mm, also occur in oxide gabbros, but they are much less common than apatite (Fig. **F102**). Titanite is also associated with oxide-bearing rock types, particularly when the oxide gabbro is strongly altered. It is not clear whether titanite crystallized from a melt or is the product of a metamorphic reaction.

Oxide gabbros, and especially oxide-bearing dikelets, display a broad range of compositions and complex mineral assemblages and disequilibrium textures. They can be divided into five end-member magmatic types.

Type 1: normal oxide gabbros

Randomly dispersed oxide-bearing patches in undeformed, generally coarse-grained gabbro represent ~80% of all oxide gabbros. Their modal compositions are variable, with ~25%–75% clinopyroxene and complementary amounts of plagioclase, 0%–2% olivine, and, commonly, several percent orthopyroxene. Subhedral to anhedral plagioclase and clino-

pyroxene range in grain size from coarse to pegmatitic, as large as 50 mm. The oxide minerals are very irregularly distributed, commonly in interstitial patches between plagioclase and clinopyroxene. An example of an oxide-rich gabbro dikelet is shown in Figure **F103.** This sharply bound vertical dikelet crosscuts a gabbro that has undergone weak high-temperature recrystallization. The host gabbro contains coarse heterogeneously distributed oxide patches but is otherwise devoid of Ti-bearing oxides.

Type 2: amphibole-bearing gabbros

Amphibole-rich gabbros occur as intercalations within which are present amphibole-free oxide gabbros and orthopyroxene-bearing gabbros and gabbronorites. This second type of oxide gabbro is coarse grained and amphibole rich, with elongate, bladed green amphiboles and dominantly tabular plagioclase (Fig. **F104**). Amphibole is commonly saussuritized, giving it a leucocratic appearance in places. Sharp, abundant, arrow-shaped, low-angle contacts between two bladed amphiboles and plagioclase suggest an igneous origin. In thin section, secondary green to brown amphibole is commonly seen to have replaced original amphibole. A significant fraction of the secondary green amphiboles may, however, have replaced clinopyroxene, and it is unclear how much, if any, of the amphibole in most samples is of primary igneous origin. The total abundance of trace element–rich accessory minerals, including apatite, titanite, and zircon, can exceed 1%. The modal composition of coarse-grained amphibole-rich oxide gabbros includes 40%–70% plagioclase and as much as 50% possibly magmatic amphibole. Fe-Ti oxides are always present, from a few percent to >10%.

The presence of primary amphibole within this rock type was a matter of debate within the igneous and metamorphic petrology teams: resolution of this issue will require shore-based studies. In this report, the amphibole gabbros are not treated as a separate lithology but are grouped with the oxide gabbros. Between Cores 305-U1309D-128R and 140R, the amphibole-rich oxide gabbros form a significant portion (between 16% and 100% per core) of the core, but they contribute <4% of total core recovered during Expedition 305.

Type 3: oxide bands

Discontinuous oxide bands may be a special subset of the Type 1 normal oxide gabbros. They have been mainly observed in thin section. Figure **F105B** shows a whole thin section scan of a subvertical 3–8 mm wide oxide-rich band. The oxide minerals, along with minor sulfides, apatite, and secondary green amphibole occur along grain boundaries. It seems that silicates were not crystallized along with these oxides because there is no distinct crosscutting oxide-bearing lithology; the modal proportions and grain size of the primary silicate minerals appear to be entirely unaffected by the presence of the oxides. Zircon and titanite do not accompany oxides of this type. Type 3 oxide bands are very rare and represent far less than 1% of the oxide gabbros. Nevertheless, they may yield additional information about the formation of oxide gabbros in general and, in particular, why their occurrence is commonly not associated with variations in the modal composition of their host.

Type 4: oxide-enriched gabbros near undeformed contacts

Fe-Ti oxide minerals are strongly enriched at and near several undeformed contacts of Type 1 oxide gabbros with any of several other lithologies. This type includes the highest local oxide abundances and is associated with the highest local peaks in MS. For example, Figure **F101C** shows an undeformed contact between coarse-grained oxide-free gabbro and a Type 2 amphibole-bearing oxide gabbro. Within the Type 2 amphibole-bearing oxide gabbro, a 2–5 cm band is extremely oxide rich and there is no indication of significant deformation or displacement along the contact. A second example, in which sulfides accompany an extreme enrichment in Fe-Ti oxides, is shown in Figure **F101B.** This particular subtype of oxide enrichment is not very common.

Type 5: oxide gabbro shear zones

This type of oxide gabbro is characterized by oxide enrichment within narrow zones of intense ductile deformation. A distinctive characteristic of this type is the apparent replacement of clinopyroxene by Fe-Ti oxides (Fig. **F106A, F106E**). Figure **F106A** shows a whole thin section scan of a ductile shear zone containing 10% oxides and minor apatite that crosscuts a largely undeformed coarse-grained gabbro. Figure **F106A** and **F106B** shows a remarkably narrow oxide-bearing mylonite zone within an unstrained gabbro host. The mylonitic zone is lithologically distinct from its oxide-free host. Enclosed within the oxide gabbro matrix are neoblasts or porphyroclasts (20–50 µm) of clinopyroxene and plagioclase. A close-up of an apatite-clinopyroxene-plagioclase shear zone aggregate is shown in Figure **F106D.**

Type 6: Fe-Ti-bearing oxides

Relatively abundant oxides also occur in zones of focused metamorphic overprint, where the presence of albitized plagioclase and epidote give the rock a leu-

cocratic appearance (see "Metamorphic petrology"). In this type, the oxides are commonly intergrown with stubby, irregularly shaped, strongly pleochroic titanite.

Diabase

Diabase and basalt intervals of variable thickness cut gabbroic rocks in several places throughout Hole U1309D and form 0.93% of the lithologies recovered during Expedition 305. Basalts occur as thin dikelets (<1 cm) or thin, discontinuous, irregularly shaped intrusive bodies with chilled margins to wallrock gabbro (Fig. F107). They are characterized by a fine-grained sparsely phyric to intersertal texture, few phenocrysts, and a glassy matrix (Fig. F108) with minor clinopyroxene. The modal phenocryst abundance never exceeds 1%–2%. Diabase intrusions range up to at least 3.5 m in thickness (Sections 305-U1309D-154R-1, 75 cm, through 155R-2, 124 cm) and are characterized by fine- to medium-grained ophitic to subophitic texture (Fig. F108) (Units 242 and 412). The dominant minerals are clinopyroxene and plagioclase with minor olivine. Modal compositions are variable (Unit 242 is 40% plagioclase, 10% olivine, 1% oxide, and 30% secondary amphibole, but Unit 412 is 40% plagioclase, 40% clinopyroxene, and 20% other, mainly altered, material). The degree of alteration is variable but usually high, making the estimation of primary modal composition difficult.

The following diabase intervals were cored during Expedition 305; in many cases, igneous contacts were not recovered and exact thicknesses are not known:

- 471–472 mbsf (Sections 305-U1309D-94R-3, 12 cm, through 95R-1, 7 cm),
- 626–628 mbsf (intervals 125R-2, 106–128 cm, and 127R-1, 44–73 and 108–150 cm),
- 751–761 mbsf (intervals U1309D-153R-1, 58–70 cm, and 154R-1, 75 cm, through 155R-2, 124 cm),
- 843 mbsf in a narrow (10 cm) interval (Section 304-U1309D-173R-1),
- 875 mbsf (Sections 179R-4 through 180R-1), and
- 990 mbsf (Sections 205R-4 through 206R-1).

The deepest diabase was recovered at 1377.6 mbsf (interval 305-U1309D-287R-1, 0–48 cm) without igneous contacts and a recovered thickness of only 50 cm. In this interval, the diabase includes wallrock xenoliths—aggregates of plagioclase, olivine, and pyroxene (Fig. F109).

Dikelets and veins of possible magmatic origin

Almost all gabbroic rock types are cut by dikelets or veins of variable thickness and composition. The origins of these features are complex, as they combine magmatic, metamorphic, and deformation-induced attributes. Both Expedition 304 and 305 igneous teams described many of these dikelets and veins using the term "leucocratic," which encompasses a wide variety of light-colored veins and alteration fronts. Thus, the term "leucocratic" has no single meaning other than referring to color and general mode of occurrence. The centers of leucocratic veins commonly contain abundant subhedral to euhedral accessory minerals, including apatite, titanite, and zircon. However, these minerals are absent from the leucocratic halo of altered, commonly fractured, and albitized (saussuritized) plagioclase that is commonly present around veins or along some intrusive contacts. These accessory minerals are interpreted to have been derived from evolved melts that crosscut the gabbros, with the melt pathways subsequently acting as focusing zones for nonmagmatic fluids. However, less abundant, millimeter-sized crosscutting fine-grained amphibole-bearing dikelets also contain zircon and/or apatite, but they lack saussurite halos and were interpreted initially as nonmagmatic. A further complicating factor that inhibits a clear distinction of magmatic from metamorphic characteristics, especially in the smaller dikelets, is the commonly associated cataclastic deformation.

Finally, some "normal" vein-free gabbros, selected for inductively coupled plasma–atomic emission spectroscopy (ICP-AES) whole-rock analysis, contained extremely high phosphorus concentrations, possibly caused by localized concentrations of apatite. The following samples collected from Hole U1309D during Expedition 305 contain >2 wt% calculated apatite:

- 93R-1, 11–16 cm
- 116R-3, 67–77 cm
- 127R-2, 81–93 cm
- 128R-3, 38–48 cm
- 130R-1, 32–42 cm
- 137R-2, 132–136 cm
- 140R-3, 93–103 cm

These observations gradually became evident after at least a week of core description, although modal apatite was not visually identified in all samples that had high phosphorus. Unambiguously identifying all magmatic dikelets of this scale is not possible based on visual core description. The reported examples can only be interpreted as a minimum estimate.

Thin section descriptions of end-member vein or dike lithologies are summarized below.

Gabbro dikes

Crosscutting dikes of fine- to coarse-grained equigranular gabbro usually have sharp contacts

with their hosts and are undeformed. They consist of subequal proportions of plagioclase and clinopyroxene, rarely with minor olivine or orthopyroxene, closely resembling the coarse-grained gabbros that predominate in Hole U1309D. Apatite and zircon are not present, suggesting that they crystallized from relatively unevolved melts. Dike thickness ranges from millimeter size to as much as several meters.

Gabbro dikelets intrude fine- to medium-grained olivine-rich troctolite, ranging in thickness from <5 mm to >1 m. Contacts range from diffuse, irregular, and discontinuous to sharp, straight, and continuous (Fig. **F88C**). Based on their textures, the diffuse dikelets can be interpreted as either local zones of melt segregation from a compacting olivine-supported mush or as focused infiltration zones that spread diffusely into the host from intrusive dikes or dikelets. Whether these features formed by infiltration or extraction, the temperature of the surrounding troctolite must have been at or near its solidus to allow for such pervasive grain boundary melt migration. The more sharply bound dikes may, in principle, have formed by the same process and subsequently traveled over a limited distance within the olivine-rich troctolite body as it cooled.

Medium-grained orthopyroxene (10% modal) occurs in the center of a diffuse olivine-free gabbro dikelet at 629 mbsf. In this and some other dikelets, clinopyroxene oikocrysts cross the boundary between the dikelet and the host olivine-rich troctolite. The apparent immediate crystallization of orthopyroxene from a liquid derived from a primitive troctolite can only have occurred at high pressure. Crystallization of the troctolite along an olivine-plagioclase cotectic requires relatively low pressures, whereas crystallization of magnesian orthopyroxene requires pressures exceeding 4 kbar (Ghiorso and Sack, 1995). If, on the other hand, the melt was significantly evolved prior to infiltration, orthopyroxene stability would be enhanced at crustal pressures. Resolution of this issue requires more detailed shore-based studies.

Oxide-bearing dikelets

The association of Fe-Ti oxides and their detection on the basis of MS peaks is described in the **"Oxide gabbro"** section. An example of a vertical oxide-rich dikelet crosscutting a gabbro with minor contents of heterogeneously distributed oxide patches is shown in Figure **F103**, where a vertical 2–3 cm wide oxide-rich dikelet is clearly visible. However, many oxide-bearing dikelets are too thin to be recognized in hand specimen.

Trondhjemites and late-magmatic leucocratic dikelets

Extremely evolved quartz-bearing granitoid rocks occur in Hole U1309D only in rare, narrow trondhjemite dikes. Six such dikes have been identified in thin section, three in the upper part of the hole (Samples 305-U1309D-89R-2, 130–133 cm, 89R-3, 42–44 cm, and 93R-1, 16–18 cm) and three in the lower part (Samples 212R-2, 50–53 cm, 216R-1, 73–76 cm, and 262R-4, 84–87 cm) (Fig. **F110**). The three trondhjemites in the upper part of the hole are affected by cataclastic deformation and a strong metamorphic overprint. The three lower ones are undeformed and their primary mineralogy is better preserved. These dikes consist of medium-grained albitic plagioclase, (magmatic?) amphibole, minor quartz, and accessory minerals. All samples contain apatite in various sizes and five contain zircon and allanite (identified optically and by energy dispersive X-ray analyzer in Sample 305-U1309D-212R-2, 50–53 cm).

Two possible trondhjemites were analyzed for whole-rock major and trace element compositions (Samples 305-U1309D-93R-3, 11–16 cm, and 158R-1, 11–17 cm, at 463 and 770 mbsf, respectively). They have the lowest MgO contents of the entire sample set and very low iron content, resulting in a misleadingly high Mg#. At the same time, their incompatible lithophile trace element concentrations (P, Zr, and Y) are exceedingly high, indicating significant apatite and zircon contents.

Downhole distribution of accessory zircon and apatite

Zircon and apatite are not restricted to quartz-bearing rocks. Apatite coexists with Fe-Ti oxides in oxide gabbros (see **"Oxide gabbro"**). Zircon is less common. Figure **F111** shows the downhole occurrences of zircon and apatite, as observed in thin section. The presence of significant apatite (six samples exceed 2% modal) and zircon was also inferred from high P and Zr in whole-rock ICP-AES analysis. Apatite and zircon appear to be concentrated in four zones, based on thin section observation:

1. Sporadically above 200 mbsf;
2. 440–470 mbsf, where they occur in evolved dikelets that crosscut intercalated olivine gabbro and olivine-bearing gabbro;
3. 620–690 mbsf, where they occur in evolved Type 2 oxide gabbros, in association with possible primary magmatic amphibole (see **"Oxide gabbro"**); and
4. 840–910 mbsf, where they are found in oxide gabbro, which occurs both as massive bodies and as dikes crosscutting orthopyroxene-bearing gabbro.

Between 1020 and 1182 mbsf, neither zircon nor apatite has been observed, and below 1182 mbsf, apatite and zircon occur only sporadically within small, Type 5 oxide gabbro shear zones (see **"Oxide gabbro"**).

Discussion

The intrusive emplacement history of Hole U1309D is complex and is reflected in the relationships between the various rock types. Where visible, the contact relationships of gabbros with other rock types suggest that gabbro is generally intrusive into olivine-rich rock types (olivine gabbros and troctolites) and are themselves intruded by felsic (leucocratic) dikes and oxide gabbros. These relationships are more common between 400 and 650 mbsf than in the lower part of the hole, where gabbro contacts are diffuse. Contacts between troctolite and gabbro range from sharp, where thin intervals of gabbro cut the serpentine foliation in the troctolite, to gradational, where thicker intervals of gabbro are present. Contacts between oxide-bearing rock types and gabbro range from sharp to gradational as well. The sharpness of contacts probably reflects temperature contrast between the country rock and the intrusive unit. True felsic dikes in gabbro generally show sharp contacts, but varying degrees of high-temperature reaction between dikes and wallrocks are also observed. These reaction zones commonly have oriented minerals such as oxides, pyroxenes, or plagioclase growing along and across them, suggesting postemplacement reaction.

The olivine-rich troctolite interval from 1093.75 to 1235.84 mbsf forms an integral lithologic package. The olivine-rich troctolites and minor associated lithologic units that comprise this package have subsequently been intruded, at temperatures below the olivine-rich troctolite solidus, by numerous crosscutting gabbroic dikes of variable thickness. The larger scale contacts with the surrounding olivine gabbro units seem, however, to be dominantly intrusive and to have formed under hypersolidus conditions. Interstitial clinopyroxene seems more abundant close to gabbroic dikes, suggesting that primary oikocrystic clinopyroxene is recrystallized during later intrusion of the crosscutting dikes. There is currently no evidence concerning possible genetic relationships between the olivine-rich troctolites and the surrounding gabbroic rocks, but this will be a focus of postcruise research.

The presence of inverted pigeonite in the lower parts of the hole may have thermal implications for the intrusion. Inverted pigeonite is identified only in thin section and is associated with late-stage magmatic impregnations (oxide-rich gabbroic veins). This association may suggest that pigeonite inversion occurs only under restricted (lower temperature) thermal conditions of this lower intrusive sequence.

Ultramafic rocks from the upper portion of Hole U1309D appear to be true mantle peridotites that have been intensively impregnated by melts of variable composition. In the Hole U1309D samples, pyroxene oikocrysts enclosing olivine differ from textures commonly seen in impregnated peridotites. Similar textures have been previously described along the MAR (DSDP Leg 37, Girardeau and Mercier, 1992; Leg 153, Cannat, Karson, Miller, et al., 1995) and at Hess Deep (Francheteau et al., 1990), as well as ophiolites like Oman (Hopson et al., 1981; Boudier and Nicolas, 1995), where they are related to intrusions of or impregnation by wehrlitic melts. Similar textures were also reported from Site 1275 during Leg 209, where they were explained by addition of interstitial basaltic liquid to a peridotite (Kelemen, Kikawa, and Miller, 2004). A high melt/rock ratio resulted in separation and isolation of most olivine grains that were surrounded by a gabbroic matrix and mimic a wehrlitic texture.

Several locations of wehrlites have been reported from the MAR, but the origin of wehrlitic intrusions into crustal gabbros is still a matter of debate. If their presence is more common than previously thought, we assume it has important implications for mid-ocean-ridge processes, as proposed, for example, in the Oman ophiolite (e.g., Jousselin and Nicolas, 2000). Clinopyroxenes from wehrlites are in equilibrium with mid-ocean-ridge basalt liquids (Koga et al., 2001), but it requires additional water in the melt to bring clinopyroxene before plagioclase on the solidus at a temperature of <1150°C. As normal tholeiites contain only ~1000 ppm water, an additional source is needed. Evidence for bursts of seawater into magma chambers has been proposed recently from Oman (Bosch et al., 2004), and this may provide the crucial water to form the wehrlitic melt.

Metamorphic petrology

General observations

During Expeditions 304 and 305, two deep holes were drilled at Site U1309 (Atlantis Massif): Hole U1309B (to 101.8 mbsf) and the upper 401.3 m of Hole U1309D were drilled during Expedition 304, and Hole U1309D from 401.3 to 1415.5 mbsf was drilled during Expedition 305. In general, the mineral assemblages of the rocks recovered during both expeditions at Site U1309 record the cooling of mafic plutonic rocks from magmatic conditions to zeolite facies during the unroofing and uplift of Atlantis Massif. Individual samples generally display a range of superposed metamorphic conditions, but no single sample records the entire cooling history of the site. The assemblages encountered in any sample depend on at what point in its cooling history the rock underwent deformation or hydration. It is only by studying the assemblages recorded in a large number

of samples from this site that the whole cooling history can be inferred.

Metamorphic history at Site U1309 can be summarized as follows:

1. Granulite facies, probably near-solidus, mylonitic deformation, and recrystallization of plagioclase + clinopyroxene and brown amphibole.
2. Amphibolite-facies replacement of pyroxene by green to brown hornblende in diabases, gabbros (especially oxide gabbros), and mylonite zones. The extent of this largely static event is hard to judge because of overprinting by greenschist-facies amphiboles and uncertainties over amphibole compositions in thin section.
3. Widespread, largely static upper-greenschist-facies to lower-amphibolite-facies metamorphism manifested by the following:
   - Formation of secondary plagioclase and secondary amphibole and, below 384 mbsf, epidote growth that appears to be related to late magmatic leucocratic intrusions.
   - Replacement of pyroxene by actinolitic amphibole. This is the major effect of the greenschist event in most gabbroic rocks and diabases. In the upper 300 m of Hole U1309D, this alteration is pervasive and all samples are affected to a greater or lesser extent. At greater depths, the alteration is increasingly associated with the emplacement of amphibole-rich veins and accompanying halo alteration.
   - Development of tremolite-chlorite ± talc corona texture in all rocks containing both olivine and plagioclase. This may include some amphibolite-facies formation of cummingtonite and green hornblende. In the upper 300 m of Hole U1309D, this reaction went to completion in almost all samples, removing either olivine or plagioclase from the assemblage. At greater depths, the reaction commonly did not go to completion and is increasingly localized by amphibole veins and the margins of gabbroic dikelets. At shallower depths, most amphibole veins postdate corona formation.
4. Mainly static lower-greenschist to subgreenschist metamorphism including the following:
   - Serpentinization of olivine in olivine gabbro, troctolite, and olivine-rich troctolite, with concomitant formation of prehnite and hydrogrossular in associated plagioclase. Above 300 mbsf, serpentinization is restricted to rocks where olivine was in excess over plagioclase and was therefore still present after the corona-forming reaction went to completion. At deeper levels, serpentine, prehnite, and hydrogrossular are often localized on closely spaced, variably oriented fractures (ladder veins).
   - Metasomatic talc-tremolite ± chlorite veins and irregular zones in ultramafic rocks, especially near contacts with mafic rock. These veins and zones overprint serpentine.
   - Talc-tremolite-chlorite schist with ultramafic protolith (upper 25 m of Holes U1309B and U1309D and fragments in Holes U1309E and U1309H). This is assumed to be the same age as the talc-tremolite-chlorite veins and zones deeper in the hole, although the relationship to serpentinization is not observed. It is inferred to reflect the main deformation on the detachment fault that forms the surface of the massif.
   - Sporadic talc-carbonate metasomatic alteration of olivine-rich rocks.
   - Relatively late emplacement of slip-fiber amphibole veins and associated local metasomatism.
   - Serpentinization of isolated grains in olivine gabbro and relict grains in coronas.
5. Zeolite-facies metamorphism that includes replacement of plagioclase by zeolites throughout the core and emplacement of zeolite-bearing veins below 700 mbsf. Late, open, irregular fractures commonly contain a clay mineral that may be saponite, along with carbonate and (below 700 mbsf) zeolite minerals.

Hole U1309B

Three rock types with distinct chemical compositions were encountered in Hole U1309B. In order of decreasing abundance, these are

1. Mafic igneous rocks,
2. Peridotite, and
3. Talc-tremolite-chlorite rocks of mainly ultramafic protolith.

Mafic igneous rocks

Mafic rocks varying from gabbro and troctolite through diabase to basalt form the major rock types within the core. All rocks evidence some degree of hydration, with the effects of hydration decreasing downhole. Traces of fresh augite appear in the gabbros at ~40 mbsf, and relics of fresh olivine appear in the troctolite at 82 mbsf. Assemblages indicative of conditions from amphibolite- to zeolite-facies hydration are found within the core (Fig. **F112**). Traces of brown pleochroic hornblende are found in some rocks (Fig. **F112A**), indicating that, in places, amphibolite-facies alteration preceded pervasive greenschist alteration. Some grains of brown hornblende may have formed during late-stage crystallization of fractionated gabbroic magma. Other grains are

zoned to green margins or show metamorphic fabrics in ductile shear zones; these probably formed in response to postmagmatic hydration. Cummingtonite is found in a number of gabbro samples, where it probably formed by hydration of orthopyroxene or olivine. Cummingtonite is best recognized where it is adjacent to calcic amphibole because in these locations the difference in extinction angle between the two amphiboles is obvious (Fig. **F112B**). Although patches of albite with or without actinolite and chlorite are seen to replace plagioclase in a few samples, in most rocks the primary plagioclase appears to be fresh, even in breccias. Zeolite replaces feldspar locally (Fig. **F112C**) but was not detected in X-ray diffraction (XRD) spectra (Table **T4**) (e.g., Sample 304-U1309B-5R-2, 55–56 cm) and appears to be a minor phase. Saponite is present in some XRD spectra.

Although the metamorphism in Hole U1309B extends over a wide range of temperatures, the most abundant alteration is in greenschist facies. This is marked by the abundance of actinolite and tremolite in the mafic rocks. Chlorite and albite are present in many thin sections but are subordinate to amphibole. The amphibole shows a wide range of pleochroism, ranging from deep green actinolite in diabase and basalt to colorless tremolite in some gabbros. Because tremolite and actinolite have similar stability fields in mafic rocks, when we use the term "actinolite" in this report we refer to any presumed low-temperature amphibole, regardless of its pleochroism. We use the term "tremolite" to refer to colorless amphibole in ultramafic rocks and in tremolite-chlorite schists.

In most rocks, actinolite replaces pyroxene and olivine. In the basaltic rocks, fine-grained actinolite has replaced the matrix and, if it had been present, glass. In all rocks, the actinolite replacing pyroxene is texturally distinct from that replacing olivine. Single grains of actinolite may grow epitaxially on augite so that the host mineral and the pseudomorph share the same c-axis orientation. The amphibole produced by this process is coarse grained and can only be distinguished from the original augite by its small extinction angle. Actinolite pseudomorphs after pyroxene are less well developed in diabase, where the actinolite replacing pyroxene may form clusters rather than single grains (Fig **F112D**).

Amphiboles replacing olivine in gabbros and troctolites are texturally distinctive from those replacing pyroxene. In the plutonic rocks, the reaction between olivine and surrounding plagioclase produces a cluster of minerals with a distinct corona structure (Fig. **F112E, F112F**). In samples where olivine has been completely altered, the cluster has two zones. The outer rim consists of chlorite, which was probably formed from plagioclase. The core of the cluster, which probably marks the extent of the original olivine, contains a complex intergrowth of chlorite and amphibole. The amphibole appears to be mostly actinolite or tremolite, but the possible presence of cummingtonite in the core cannot be ruled out. In two samples (304-U1309B-15R-1, 110–112 cm, and U1309B-16R-2, 71–73 cm), fresh olivine remains and the cluster consists of three zones: a rim of chlorite, a zone of tremolite, and an inner zone of talc.

Amphibole replacing olivine in diabase is also texturally distinct. In diabases, olivine pseudomorphs form as rounded clusters of small, randomly oriented actinolite (rarely, cummingtonite is present) as well as chlorite (Fig. **F112D**). Commonly, the only chlorite found in an altered diabase is present in these structures. However, the distinct chlorite rims against plagioclase that are common in troctolitic rocks are rarely observed in the diabase.

The static greenschist (or possibly low-amphibolite)-facies alteration described above occurs to a greater or lesser degree in all the mafic rocks examined. Alteration involves influx of water but appears to be otherwise isochemical and predominantly affects pyroxene and olivine. Except where it was originally in contact with olivine, primary plagioclase is largely unaffected in many basalts and diabases and some gabbros. Also prominent in the core are zones of brecciation, cataclasis, or intense veining (Fig. **F113**) where the host rock, usually gabbro, is cut by yellow-green veins rich in calcic amphiboles. In one instance, the breccia contains a clast of chromite-bearing tremolite schist inferred to be of ultramafic origin (Fig. **F113A;** see **"Talc-tremolite-chlorite rocks,"** below). Breccia matrix varies from weakly (Fig. **F113B, F113C**) to intensely (Fig. **F113E, F113F**) foliated. In most breccias, the amphibole is a weakly pleochroic actinolite, but in some, brown amphibole is present (Fig. **F113F**). In some intensely deformed areas, the amphibole is a colorless tremolite, suggesting that the influx of Mg-enriched fluids accompanied deformation. In most instances, these "breccia veins" show halos of milky secondary plagioclase, turbid in thin section, containing abundant solid and fluid inclusions (Fig. **F113D**). Deeper in the hole the breccia veins become less common, but intense hydrothermal alteration is seen in Core 304-U1309B-14R in the vicinity of a late leucocratic magmatic dikelet (Fig. **F114**). Dark green patches as long as 8 cm are filled almost entirely with fine-grained actinolite and have milky margins as wide as 2 cm, in which turbid secondary plagioclase net-veined by actinolite is developed. One patch appears to contain clinopyroxene relics.

Serpentinized peridotite

Approximately 1.5 m of serpentinite was recovered from Core 304-U1309B-11R. The rock is variably hydrated, producing characteristic ribbon and mesh textures. In rocks where serpentinized pseudomorphs (i.e., bastites) indicate the presence of original orthopyroxene, both the pyroxene and the olivine are completely serpentinized. Locally, where the major pyroxene is diopside, substantial amounts of both olivine and diopside remain. Also present in the serpentinite are small amounts (up to a few percent) of chromite, magnetite, and magnesite. Primary chromite grains are invariably rimmed by magnetite. In many grains, magnetite also grows on fractures cutting the chromite grains. These textures indicate that chromite was out of equilibrium with the serpentinizing fluid. Magnetite forms both as rims on chromite and as trains of fine crystals in the serpentinite. The metaperidotite is cut by veins at all scales (Fig **F115**). Fine-grained carbonate, probably magnesite, is commonly associated with serpentine veins and also partially replaces serpentinite ribbon textures (Fig. **F115E**). Calcite (or aragonite) veins are also present locally, particularly at contacts with gabbro.

Talc-tremolite-chlorite rocks

Pale green tremolite ± talc ± chlorite rocks were recovered as small clasts sampled from just beneath the carbonate ooze in Section 304-U1309B-1R-3 (Pieces 2 and 3) and from a clast in basaltic breccia in Section 3R-1 (Fig. **F113A**). These samples are variably schistose with isotropic to brecciated and intensely foliated fabrics. Included in these samples is one piece that was marked by the bit and, therefore, was possibly drilled in situ. These rocks generally contain chromite grains and "cuspate textures" inferred to be relict orthopyroxene pseudomorphed by talc and magnetite and are inferred to have an ultramafic protolith. This is supported by shipboard geochemical analysis of Section 304-U1309B-1R-3 (Piece 3) (see **"Geochemistry"**). Some samples from Section 304-U1309B-1R-3 contain rutile, suggesting that they have mafic components. Similar rocks have been described from the detachment fault zone on the Southern Ridge of the massif (Schroeder and John, 2004) and from a detachment fault in the 15°45′N area of the MAR (Escartín et al., 2003). We infer that the top of the central dome of Atlantis Massif includes poorly recovered talc-tremolite schists from a detachment fault that caps the massif. This inference is supported by recovery of tremolite schist in a short core (Core 304-U1309H-1R) from the top 4 m of the central dome, 1.6 km to the east (see **"Hole U1309H"**).

Similar rocks are present in a steeply dipping sheared vein cutting peridotite in Section 304-U1309B-11R-2 (Fig. **F115A, F115B**) and give a clue to the geochemical origin of talc-tremolite rocks. This zone roots in a poorly recovered interval containing altered gabbroic fragments and tremolite schists. The zone tapers upward and has an outer talc-rich zone with an isotropic fabric replacing serpentinite (Fig. **F115C, F115D**) and an inner tremolite-rich zone with highly schistose talc bands. Dark grains within the talc alteration are bastites containing serpentine + magnetite assemblages. In contrast, several former orthopyroxene grains beyond the talc front are completely pseudomorphed by talc and magnetite, giving a pseudoschistose texture. We infer that these were pyroxenes that had not been serpentinized and, therefore, had Mg:Si ratios more suitable for talc replacement, whereas the bastites within the band were already serpentinized when the talc alteration occurred.

The tremolite-talc rocks are clearly metasomatic and require introduction of a fluid with higher Si/Mg and Ca/Mg activities than that in equilibrium with serpentine. The most likely local source for such a fluid is mafic layers or veins within the peridotite. Another interesting observation is the lack of magnetite in the talc rock. Reduction of Fe^{3+} to Fe^{2+} is required, suggesting reducing fluids (perhaps CH_4 bearing). Apparently, alteration of serpentine to tremolite is reversible, because in Section 304-U1309B-11R-3, we find a tremolite vein that has been cut by serpentine veins (Fig. **F115F, F115G**). Adjacent to the serpentine veins, the tremolite vein has been altered to serpentine.

Metamorphic conditions and degrees of alteration

The main hydration event occurred in the greenschist facies, as indicated by the presence of actinolite in the gabbros and diabases throughout the core. The preservation of early brown hornblende in some gabbro and diabase samples indicates that, locally, hydration occurred at temperatures corresponding to amphibolite facies. Similarly, local zeolite replacing plagioclase and the presence of yellow to brown saponite veins cutting the gabbroic rocks indicates that, in places, hydration occurred under conditions at or below those of zeolite facies. Unlike the clay- and zeolite-bearing assemblages, which are present around isolated veins and fractures, the greenschist assemblages are pervasive. This indicates that the whole sequence of rocks was open to pervasive fluid flow (probably low flux) at temperatures ~350°–450°C but has been relatively impermeable since.

Although there is a tendency for increased survival of primary pyroxene and olivine downhole, there appears to be no systematic gradient in the intensity of alteration through Hole U1309B (Fig. F116). Figure F116A shows that the total degree of alteration depends largely on rock type. Where olivine is abundant (in the peridotite and the troctolites), the degree of alteration can reach 100% because of the reaction between olivine and plagioclase. Because primary plagioclase was stable during the greenschist hydration event and because plagioclase generally makes up 50% of the rocks, most olivine-poor gabbro and diabase intervals show no more than 50% alteration. Gabbros and diabases that show >50% alteration invariably have undergone deformation or intense veining. This is shown in Figure F116B, which estimates the degree of vein-related alteration (veins and halos). The most intense alteration is associated with zones of brecciation and veins in gabbro and diabase above 60 mbsf and in the serpentinite, which is cut by talc-tremolite veins. Below 60 mbsf, the extent of vein-related alteration is much less and is mainly associated with late magmatic leucocratic dikelets. Diabase intrusions away from zones of brecciation generally show little or no vein-related alteration, suggesting that they were intruded after the hydrothermal event that produced actinolite-rich veins.

Hole U1309D

Gabbroic rocks (gabbro, olivine gabbro, oxide gabbro, gabbronorite, and troctolite) constitute >90% of the rocks recovered from Hole U1309D. Several large diabase intrusions occur in the upper 130 m, but diabase is uncommon below this depth. Ultramafic and near ultramafic rocks (wehrlite, dunite, and olivine-rich troctolite) are present sporadically, with large concentrations between 300 and 350 mbsf and 1100 and 1225 mbsf and narrower occurrences near 175 and 700 mbsf. Talc-chlorite schists with an ultramafic protolith are restricted to the upper 25 m of Hole U1309D. Although restricted in abundance and occurrence, these rocks are important for the interpretation of the structural history of Site U1309.

Although some types of metamorphism in Hole U1309D are restricted to certain rock types (serpentinization, for example), by and large all rocks experienced the same range of metamorphic conditions. In particular, the dominance of vein-related alteration in the lower 1100 m of the core lends itself to description by metamorphic type as opposed to rock type. In contrast to Hole U1309B, the discussion of metamorphism in Hole U1309D is organized according to metamorphic type.

Hole U1309D was drilled ~20 m north of Hole U1309B. Not surprisingly, the alteration seen in the upper ~100 m of Hole U1309D is similar to that encountered in Hole U1309B. Alteration is intense with alteration >90% common. Greenschist-facies metamorphism in which calcic plagioclase is stable and where actinolite is the main metamorphic mineral predominates. The major difference between the holes is that the rocks in the upper portion of Hole U1309D record a high-temperature deformation and metamorphism event that is poorly represented in cores from Hole U1309B.

XRD analyses

Selected vein material and all samples chosen for whole-rock ICP-AES analysis were analyzed by XRD (Tables T4, T5, T6; Figs. F117, F118, F119). Diabase and basalt from the upper 400 m of the hole show actinolite, plagioclase, and, sometimes, chlorite as discernable peaks (the main peaks for clinopyroxene coincide with some amphibole peaks, so a separation is often difficult). In addition, a number of late veins and alteration patches were sampled and consist mainly of amphibole + clays (possibly saponite in most cases). A few more unusual spectra are shown in Figure F117, some of which remain to be identified. No zeolites were identified in any spectra from the upper 400 m of the hole.

The whole-rock spectra from the lower 1000 m of the core are dominated by plagioclase and clinopyroxene. Locally, olivine, serpentine, amphibole, and ilmenite are also found. Orthopyroxene was found in fewer samples than expected, probably because of peak overlap problems. The most significant finding from whole-rock XRD was the detection of brucite in one serpentinized olivine-rich troctolite (Fig. F118). Significant findings from XRD examination of veins include the identification of anhydrite in Sample 305-U1309D-150R-3, 22–23 cm (Fig. F119A), zeolites (analcime and thomsonite) (Fig. F119B, F119C), and a green, waxy, translucent clay mineral (possibly saponite).

Metamorphism

Granulite-facies metamorphism associated with deformation

This is the highest temperature metamorphism recognized in the core and is directly related to plastic deformation (see "Structural geology"). It is characterized by recrystallization of pyroxene and plagioclase (and, more rarely, brown hornblende) into an equigranular, mosaic texture (for example, Samples 304-U1309D-13R-1, 68–70 cm, 30R-1, 26–28 cm, 44R-4, 16–18 cm, and 305-U1309D-110R-3, 46–49 cm) (Fig. F120). Less common is the presence of nar-

row (~0.2 mm) undeformed zones of recrystallized pyroxene and plagioclase (see Sample 304-U1309D-50R-1, 52–56 cm). Granulite-facies shear zones are most common at igneous contacts in the upper 150 m in the core but do occur at greater depths.

Amphibolite-facies replacement of pyroxene by green and brown hornblende

Textural evidence from mafic rocks in Hole U1309D indicates that amphibolite-facies recrystallization accompanied ductile deformation, brittle deformation, and static hydration (Fig. **F121A, F121B**). Brown hornblende surrounded by brown hornblende neoblasts in the mylonitic portion of Sample 304-U1309D-8R-2, 26–28 cm, indicates that hornblende was stable in this rock during ductile deformation. In an entirely different texture, green-brown hornblende in Sample 304-U1309D-4R-2, 108–110 cm, fills fractures formed during brittle deformation. In an unusual sample (304-U1309D-16R-5, 1–4 cm), brown hornblende has replaced pyroxene in the matrix of a brecciated diabase and has also grown in the deformed zones between the clasts.

The replacement of pyroxene by green and/or brown hornblende postdates granulite-facies recrystallization, as some deformed pyroxenes in the mylonites are replaced by hornblende. Brown hornblende has been found growing as tails on deformed pyroxene (Fig **F121B**), as well as forming adjacent to narrow felsic dikelets. Brown hornblende is commonly associated with upper-amphibolite-facies and granulite-facies conditions. The extent of amphibolite-facies recrystallization is uncertain and may have been underestimated in shipboard studies. Many thin sections contain small amounts of brown or green-brown hornblende, often overprinted by much more abundant green amphiboles. Initial shore-based electron microprobe work shows that some of these green amphiboles are hornblende and others are actinolite.

Late magmatic leucocratic dikelets, breccia zones, and associated formation of secondary plagioclase, secondary amphibole, and epidote

A "bleaching" alteration in which plagioclase is converted to albite and pyroxene is converted to amphibole, commonly in the vicinity of late magmatic leucocratic dikelets (also referred to as "magmatic veins"), was first observed in Hole U1309B (Fig. **F114**) and is common below 140 mbsf in Hole U1309D (Fig. **F122A, F122B**). The largest and most voluminous individual veins in Hole U1309D are these magmatic intrusions, some of which have thicknesses of tens of centimeters. As such, they can locally dominate modal "vein" abundance. Several of the most conspicuous alteration zones in Hole U1309D are associated with late magmatic leucocratic dikelets. Most of the vein-related alteration between 60 and 400 mbsf is attributable to these veins, as are several prominent zones of bleaching farther downhole. Typically, the late magmatic leucocratic dikelets contain euhedral plagioclase, often zoned, surrounded by fine-grained actinolite mats or amorphous patches (Fig. **F122A, F122B**). Brown hornblende is generally present but is extensively replaced by actinolite. Brown hornblende and secondary white (turbid in thin section) plagioclase are commonly developed in the wallrocks of the vein, together with extensive actinolite mats. Epidote is an important phase in the alteration assemblage between 380 and 950 mbsf but is scarce both below and above this interval. Bleaching alteration is rare below 1000 mbsf. Many of the late magmatic leucocratic dikelets are overprinted by intense amphibole veining and brecciation (Figs. **F121D, F123**) and in some cases are recognizable only by the presence of zircon and apatite in breccia zones (Fig. **F113F**).

This alteration is linked to the intrusion of late, relatively leucocratic (and rarely quartz-bearing) melts. Difficulties in ascertaining the exact nature of the link arise because the primary beneficiary of the alteration is usually the intrusion itself. In most instances (i.e., where the intrusion lacks quartz), it is difficult to distinguish between the bleached intrusion and the bleaching in the surrounding gabbro. In some cases, the contacts of the leucocratic areas with the adjacent gabbro are gradational, either as alteration fronts or as zones of microbreccia with or without recrystallization of the breccia fragments (e.g., Fig. **F123**). On the other hand, minerals that appear igneous, especially zoned plagioclase, brown hornblende, and zircon, are commonly associated with the bleached zones.

We suggest that the late magmatic veinlets exsolved significant amounts of fluid in the latter stages of crystallization, forming brown hornblende. As cooling occurred, remaining magmatic fluid in fractures and fluid inclusions led to lower effective stress, localizing brittle failure. Further influx of fluid produced greenschist-facies alteration. The "magmatic" veins are almost always associated with (and crosscut by) the green amphibole veins described below.

Corona texture formation by reaction of plagioclase and olivine

In olivine-bearing gabbro, olivine gabbro, and troctolite, the most widespread alteration products are the aggregates of tremolite, talc, chlorite, and (tentatively identified) cummingtonite that form corona

texture or coronitic pseudomorphs after primary olivine and plagioclase (Fig. F124A). Corona textures are not seen in olivine diabase. In thin section, the corona texture in Hole U1309D is very similar to that recorded in Hole U1309B (Fig. F112E, F112F). The most common texture consists of partial or complete replacement of olivine by tremolite (and/or cummingtonite) ± talc and replacement of the edges of neighboring plagioclase by chlorite. Chlorite is also present as fracture filling within plagioclase, often forming radial crack networks where olivine grains were completely surrounded by plagioclase (Fig. F124C, F124D). These textures are indicative of volume increase during the reaction. Tremolite may either entirely replace olivine or be restricted to its margins and may be intergrown with chlorite or talc. Cummingtonite (tentatively identified on the basis of twinning) has the same paragenesis as tremolite. Where relatively fresh olivine cores are present, an annulus of talc may separate it from the outer tremolite zone. Complex coronas containing carbonate, serpentine, and sulfides have also been recognized (Fig. F124E, F124F). Serpentine is generally present only as relics within fractures in olivine, as a late replacement of olivine cores (usually "oxidized serpentine"), or, rarely, as a replacement of tremolite. In a few cases, calcite is also found associated with serpentine, talc, or tremolite (Fig. F125A, F125B). Magnetite and sulfides (pyrite, pyrrhotite, and chalcopyrite) are often dispersed within the olivine pseudomorphs and locally form concentric patterns. Orthopyroxene, where present in the gabbros, alters to talc (Fig. F126B). In some samples, chlorite and actinolite form a reaction zone between orthopyroxene and plagioclase (Fig. F126C). This is analogous to the corona textures found between olivine and plagioclase, but it is usually not as well developed around orthopyroxene as it is around olivine. Coronas of tremolite and chlorite are not produced between clinopyroxene and plagioclase (Fig. F127B, F127C). In coronitic rocks, clinopyroxene is overgrown by actinolite or partially replaced by brown amphibole and appears to be uninvolved in the corona-forming reactions.

Corona texture is observed in hand specimen and thin section throughout the hole. Above 280 mbsf, the corona-forming reactions commonly went to completion, with all olivine being replaced by tremolite with or without small amounts of chlorite and talc. In olivine-rich troctolites, plagioclase is completely replaced by chlorite, leaving relict olivine which may be serpentinized (Fig. F127A). Below this depth, relict olivine becomes increasingly common in coronitic alteration zones. Below 350 mbsf, rocks appear where olivine and plagioclase are in direct contact (Fig. F126A). Rocks where the corona-forming reaction did not go to completion can often be recognized because characteristic "ladder vein" textures are developed in which olivine and plagioclase are replaced by serpentine and prehnite/hydrogarnet, respectively (Fig. F124B). In the lower part of the hole (below 350 mbsf), there is a correlation between focused fluid flow and corona formation. Most coronas are associated either with dark green amphibole veins or with igneous contacts between gabbro and olivine gabbro (Fig. F128). Above this depth, coronitic alteration is pervasive and the coronitically altered rocks are notable for their lack of veining.

Actinolitic amphibole replacement of pyroxene

In most rocks cored in Hole U1309D, the principal metamorphism is a greenschist-facies event manifested by the replacement of pyroxene by green fibrous to acicular amphibole tentatively identified as actinolite. The replacement may be complete (i.e., pseudomorphic), but in less altered rocks, partial replacement along grain margins and cleavage or exsolution planes is more common (Fig. F112B). This amphibole is petrographically distinct from the colorless tremolitic amphibole that is common in the coronas developed during plagioclase-olivine reaction. In diabases, green amphibole, some of which is hornblende, replaces both pyroxene and olivine (Fig. F112D).

Actinolite replacement of pyroxene occurs in all pyroxene-bearing rock types and often occurs in the same thin section as corona texture. The intensity of pyroxene replacement in gabbros is often related to the presence of amphibole veins, particularly below 400 mbsf. In diabase, pyroxenes are often completely replaced without any macroscopic veining.

Green amphibole veins

Green amphibole veins are the most common vein type in Hole U1309D. Above ~200 mbsf, the most important vein set (Type 2 veins in the "Expedition 304 vein log" in **"Supplementary material"**) contains yellow-green actinolite and is often associated with breccia zones and late magmatic leucocratic dikelets. These veins are commonly braided and typically associated with an alteration halo 5 mm to 2 cm wide. The halo is usually much wider than the vein itself. At greater depths, dark green veins logged by the Expedition 305 scientists are interpreted as the same vein set. In some cases, dark green veins form dense networks (Fig. F129A), but they are also present in relative isolation. In other cases, the veins can be seen in thin section to be a zone of deformation that has been permeated by fibrous green am-

phibole. True amphibole veins commonly extend outward from these deformation zones.

In thin section, most dark green veins consist of 90%–100% colorless, pale brown, or pale green amphibole (probably actinolite). This amphibole is generally acicular to fibrous and is present as mats of needles or as needles aligned parallel or perpendicular to the vein. In many thin sections, colorless to pale green amphibole fills numerous small veins and fractures. It is especially conspicuous in fractures in plagioclase (Fig. **F129B**). Chlorite is the common accessory phase in the dark green veins, but it is not found in all veins and is almost always subordinate to amphibole. Turbid plagioclase containing abundant fluid and solid inclusions is commonly associated with actinolite veins (Fig. **F121D**).

Green amphibole veins show different relationships to other forms of alteration at different depths in the core. Above 330 mbsf, the coronitic reaction mostly went to completion, and amphibole veins appear to postdate this reaction. The main new alteration in vein halos is alteration of plagioclase to turbid plagioclase (probably albite) filled with solid and fluid inclusions. Corona-textured intervals are often notably free of macroscopic veins, but in some cases, amphibole in the coronas shows yellow-green discoloration in the vicinity of amphibole veins. Below 330 mbsf, the dark green amphibole veins are closely associated with localized development of corona textures and replacement of pyroxene by actinolite (Fig. **F129B**). Plagioclase close to the veins is altered to a variety of minerals that may include chlorite, albite, and prehnite. Orthopyroxene, when present, shows alteration to both amphibole and talc.

Our interpretation is that the pervasive alteration in the upper part of the hole predated the main phase of vein development. At deeper levels, the veining event introduced hydrous fluid into rocks containing unreacted igneous minerals and therefore caused localized occurrences of the reactions that had already occurred above. An important conclusion is that any or all alteration assemblages in the core may be diachronous in their development.

Serpentinization in olivine-rich rocks

The main mode of alteration of the most olivine-rich rocks (harzburgite, dunite, and olivine-rich troctolite) is serpentinization. The degree of serpentinization varies widely from >90% to <10% of original olivine. In the simplest case, serpentinization proceeds via the development of kernel texture (O'Hanley, 1996) (Fig. **F130A**). Olivine grains are penetrated and surrounded by serpentinite veinlets, leaving isolated fragments of olivine. In hand sample, areas of more extensive serpentinization form a conspicuous but generally irregular foliation. In places, this foliation reflects an original magmatic foliation defined by aligned olivine. The veinlets that define the foliation appear black because of included opaque phases (mostly magnetite, but some sulfides [pyrrhotite and, more rarely, pyrite]). Some brownish serpentine (possibly oxidized) is also locally found replacing olivine (Fig. **F130B**). Wehrlitic rocks generally show lower degrees of serpentinization than dunites and harzburgites at similar levels in the core. In a few samples, tremolite has grown on the margin of clinopyroxene (Fig. **F127B**). In general, however, clinopyroxene oikocrysts are fresh and have sharp boundaries against olivine and serpentine (Fig **F127C**).

Plagioclase in the serpentinized rocks ranges from virtually unaltered to partially altered (usually to prehnite) to complete replacement by hydrogarnet and/or prehnite (Fig. **F127E**). This is a rodingitic assemblage normally interpreted as being due to introduction of Ca into a mafic rock, although it can equally well be modeled by removal of silica. The coupled serpentinization and rodingitization are spectacularly developed in ladder veins seen below 330 mbsf (Fig. **F124B**). Black seams of serpentine contain white "bridges" of prehnite and hydrogarnet replacing plagioclase. In thin section, it is clear that hydrogarnet postdates prehnite in the local metasomatic sequence and that serpentine, prehnite, and hydrogarnet all postdate a chlorite rim that formed in an earlier corona-forming event (Fig. **F127F**). Serpentine is also seen to replace tremolite (Fig. **F127D**). Ladder veins can vary rapidly in orientation over a few meters of core and sometimes occur parallel to gabbroic veins, where they continue as prehnite veins. Hydrogarnet appears to be most common in highly serpentinized rocks, whereas the plagioclase is essentially fresh in the one known brucite-bearing sample. One commonly observed feature in serpentinized rocks is the development of fracture sets that radiate or extend into plagioclase from neighboring serpentinized olivine grains (Fig. **F131**). These fractures appear to be filled with prehnite and/or hydrogarnet and demonstrate that volume increase accompanied the reaction. Above 330 mbsf, the coronitic reaction has mostly gone to completion and prehnite and hydrogarnet are rarely developed even in plagioclase-rich rocks. This is further evidence for the coupled nature of the serpentinization and rodingitization reactions.

Veins

Talc-tremolite-chlorite rocks

Talc-tremolite-chlorite rocks are a minor but important component of the rocks encountered in Hole U1309D. A pale green tremolite + talc + chlorite rock

was recovered as a 10 cm thick horizon in Section 304-U1309D-1R-3 (Fig. F132A), and veins with similar assemblages were found cutting peridotitic rocks sporadically throughout the core. Two thin sections from interval 304-U1309D-1R-3, 0–11 cm (Samples 1R-3, 0–4 cm, and 1R-3, 9–11 cm), display relations that are important for understanding the origin of these rocks. Sample 304-U1309D-1R-3, 0–4 cm, contains abundant tremolite and talc with ~20% chlorite. This talc-rich composition, along with the presence of large chromite grains (Fig. F132B, F132C), indicates that this rock was derived, at least in part, from metaperidotite. Sample 304-U1309D-1R-3, 9–11 cm, in contrast, contains far more chlorite (up to 50%), as well as tremolite pseudomorphs after pyroxene and minor amounts of brown hornblende (Fig. F132D). All these factors suggest that this rock was formed to a large extent from gabbro (Fig. F132E). These samples may correlate with the piece of tremolite schist found in a breccia at about the same level in Hole U1309B (Fig. F113A, F113B). Similar rocks were recovered from Hole U1309H and collected from the detachment fault on the Southern Ridge of the massif (Schroeder and John, 2004). A likely explanation for their present location is that the detachment fault was intruded by basaltic and diabasic intrusions.

Clues to the origin of the talc-tremolite schists are found in tremolite ± chlorite ± talc veins that cut peridotitic rocks in intervals 304-U1309D-10R-1, 90–100 cm, 31R-1, 130–138 cm, and 63R-3, 1–4 cm, and talc-tremolite assemblages that are commonly seen at contacts between ultramafic and mafic rocks. Extensive talc metasomatism associated with tremolite in two narrow zones below 500 mbsf also deserves mention. The first zone is observed in interval 305-U1309D-111R-2, 79–103 cm (~550 mbsf), and the second one is in interval 140R-2, 110–113 cm (~691 mbsf). These two zones are evidence of extensive replacement of the initial troctolitic gabbro (intervals 305-U1309D-111R-2, 79–103 cm, and 140R-2, 110–113 cm, respectively) by a secondary mineral assemblage dominated by talc. In Section 305-U1309D-111R-2, the metasomatism is present as 1–10 cm wide alteration halos around amphibole-chlorite veins (Fig. F133A). In Section 305-U1309D-140R-2, olivine-rich troctolite exhibits a striking banded appearance and talc metasomatism is developed at several contacts between olivine-rich troctolite and gabbro. All these cases represent greenschist-facies metasomatism of peridotite by fluids rich in Si and Ca that have passed through mafic rocks. The reciprocal metasomatic reaction in mafic rocks leads to complete chloritization of plagioclase and replacement of actinolite by tremolite. A very similar vein from Hole U1309B (Fig. F115) has been described in detail and consists of a tremolite core and talc margins replacing serpentine and olivine. The tremolite-talc rocks are clearly metasomatic and require introduction of a fluid with higher Si/Mg and Ca/Mg activity ratios than that in equilibrium with serpentine. The most likely local source for such a fluid is adjacent mafic rocks. We believe that the same metasomatic reactions produced the talc-tremolite-chlorite schists found in the uppermost cores of Holes U1309B, U1309D, and U1309F and on the Southern Ridge of Atlantis Massif (Schroeder and John, 2004).

The talc-tremolite veins show ambiguous relationships to serpentinization. Figure F115D shows that talc replaces serpentine on the margin of veins, whereas Figure F115G shows serpentine replacing tremolite. The corona textures, which reflect a similar reaction, clearly predate serpentinization. We have tentatively placed the talc-tremolite alteration in both the schists at the top of the massif and in ultramafic layers within the core after the main serpentinization event, recognizing that both alteration processes are almost certainly diachronous, may occur at different rates in different lithologies, and may overlap in time.

Talc-carbonate veining and alteration in olivine-rich rocks

Some carbonate veins are associated with talc-carbonate alteration of the peridotite in the upper 350 m of the core (Fig. F134) (Sample 304-U1309D-56R-1, 20–23 cm). Talc-carbonate alteration is characterized by the replacement of olivine by carbonate (presumably magnesite) and talc. This type of alteration is very rare below 350 mbsf. Carbonate veins and replacement zones are also present in serpentinites close to gabbro contacts and may be related to Lost City hydrothermal vent field–type fluids.

Slip-fiber amphibole veins and associated metasomatism

Some amphibole veins consist of white to brownish tremolite/actinolite in a slip-fiber configuration. Where crosscutting relationships are observed, these veins invariably cut the dark green amphibole veins. The core commonly breaks along slip-fiber veins, revealing, in many cases, a strong lineation in hand sample (Fig. F133A) (see **"Structural geology"** for a detailed discussion of this lineation). Some slip-fiber veins in more olivine-rich lithologies contain talc and/or serpentine. A few veins also contain carbonate. Slip-fiber veins are usually pale green, pale bluish green, or white in hand sample. Serpentine and talc-rich examples may be darker or brighter green. In thin section, the amphibole may be pale green,

colorless, brown, or, in many cases, very dark brown. Other light green amphibole veins have the optical peculiarity of appearing pale green or bluish green in hand sample and dark honey-brown in thin section (Fig. **F133C**). These veins can contain a substantial amount of isotropic and/or very fine grained material that may include hydrogarnet. At shallower levels in the core, isolated veins (Type 3 in the Expedition 304 vein log in **"Supplementary material"**) containing actinolite ± chlorite ± titanite occur in diabase and gabbro and postdate the green amphibole veins described above. These may be the same age as the slip-fiber veins described by the Expedition 305 scientists.

There are some large alteration halos, as wide as 10 cm, associated with slip-fiber veins. Many of these veins, however, pass through the rock with little apparent effect except for local brecciation (Fig. **F133C**). The most spectacular halos tend to be present in olivine-rich rocks. In several sections (e.g., Sections 305-U1309D-140R-2 and 111R-2) (Fig. **F133A, F133C**), slip-fiber veins are associated with wide zones of talc metasomatism, where rocks for as much as 10 cm on either side of the vein are replaced almost entirely by talc. Other metasomatic zones are more complex and resemble rodingites. In the latter areas, olivine is completely replaced by tremolite and/or talc, pyroxene is completely replaced by amphibole (occasionally, clinopyroxene remains unaltered), and plagioclase is completely replaced by chlorite, albite, prehnite, zeolites, or hydrogarnet for up to 10 cm around a 2 mm vein. As with the more abundant dark green veins, the signature of this alteration seems to be the transport of silica into olivine-rich lithologies.

Quartz veins

Quartz veins are dispersed sparsely through the core but are more abundant in a few intervals between 200 and 300 mbsf. They disappear from the vein assemblage below 800 mbsf. They are sometimes associated with trondhjemite intrusives but also occur as isolated veins, sometimes containing chlorite. Quartz shows unusual sector extinction and contains fluid inclusions (Fig. **F121E, F121F**).

Zeolite and other late veins

These veins postdate the greenschist-facies metamorphism. They have variable mineralogy that, at least in part, correlates with depth. Late carbonate veins are common in ultramafic rocks from the upper 350 m of Hole U1309D. These commonly parallel the contacts between the ultramafic rock and late gabbroic and dioritic dikes (Fig. **F134A**). Although some carbonate veins are associated with talc-carbonate alteration of the peridotite (see Fig. **F134B, F134C**) (Sample 304-U1309D-56R-1, 20–23 cm), others (Fig. **F134D**) leave the serpentinite completely unaltered and appear to be replacive. Carbonate and, possibly, zeolite (commonly with small amounts of sulfide minerals) are constituents of the white veins in the upper 400 m of Hole U1309D. Confirmed zeolites are absent between 0 and 700 mbsf. They become increasingly common below 700 mbsf. Zeolites identified from the lower part of the hole include analcime and natrolite-thomsonite. In some veins, the zeolites are associated with prehnite (Fig. **F23**) and, in one case, anhydrite. Note that anhydrite solubility in seawater is retrograde (Mills et al., 1998); it dissolves in seawater with a temperature of <160°C. Thus, the hydrothermal system from which the anhydrite precipitated must have been closed to direct seawater input at temperatures >160°C. Alteration associated with the white veins varies widely from little or no discernable halo to irregular halos in which plagioclase seems especially susceptible to alteration (usually to albite, prehnite, and/or zeolites).

Clay (saponite) veins

The youngest vein set in Hole U1309D consists of a waxy, translucent, pale to dark green clay mineral (easily mistaken for talc) that may be saponite. The combination of the friable, hydroscopic nature of the clay vein material and the propensity of the core to break along clay-filled fractures makes shipboard thin sectioning impossible, so identification is based on XRD data. A more complete characterization of the clay will be a shore-based activity. The clay is present along with calcite and/or zeolites (especially thomsonite) in broad, uneven fractures in the rock. In the few cases where an alteration halo is present, it is likely that the halo is left over from an earlier vein fluid that passed through the same conduit. The clay veins seem to be most commonly associated with olivine-rich rocks and are notably abundant in gabbroic rocks intercalated with olivine-rich troctolite between 1100 and 1230 mbsf.

Although we have no firm temperature constraints on the formation of the clay veins, bottom hole temperatures measured during Expedition 305 (120°C) (see **"Downhole measurements"**) provide a minimum temperature constraint.

Oxide and sulfide mineralogy

The main oxide phases are ilmenite and magnetite (Fig. **F135A, F135C, F135D**). Rutile is present in association with titanite in some altered ilmenites. Ilmenite is found in all lithologies, with the highest amount (up to 8 vol%) observed in oxide gabbros and olivine gabbros. Ti-rich magnetite in the oxide gabbros has recrystallized to a mixture of ilmenite

and magnetite. Magnetite is also found as a secondary phase resulting from the serpentinization of olivine in most olivine-bearing rocks.

The sulfides present as primary and secondary phases are pyrrhotite, pyrite, chalcopyrite, and, less commonly, bornite and pentlandite (Fig. **F135**). Sulfides occur both as a primary phase in the gabbros and as a metamorphic mineral. Pyrrhotite and pyrite are found in alteration products after both serpentinized and corona-textured olivine and in pyroxene altered to amphibole. Some pyrrhotite is present in veins associated with calcite. Chalcopyrite generally occurs with igneous pyrrhotite (Fig. **F135B–F135D**). In a few cases, "flame textured" pentlandite was observed as exsolutions in pyrrhotite (Figs. **F135B, F135C**). One possible occurrence of a Ni-Fe alloy (awaruite) was noted in the olivine-rich troctolite (interval 305-U1309D-247R-3, 97–98 cm) associated with serpentinized olivine. The sulfide phases in the gabbro, oxide-gabbro, troctolite, and olivine-rich troctolite are mainly low-sulfur assemblages. They suggest low fS_2 and low fO_2 for the rocks recovered in Hole U1309D.

Downhole variation of modal alteration intensity

Hole U1309D shows a heterogeneous alteration profile, ranging from fresh (<2%) to highly altered (up to 100%); however, most of the cores below 350 mbsf show a low to moderate alteration. The overall alteration, shown in Figure **F136,** is the estimate from visual examination of the core for the modal abundance of secondary hydrous minerals. An expanded version of this figure from the top 400 m of Hole U1309D (Fig. **F137A**) shows a general decrease of alteration downhole, with peaks corresponding to olivine-rich horizons.

The degree of alteration of rocks from the uppermost ~350 mbsf is relatively high (as much as 100%) and reflects the pervasive alteration of all rock types high in the core (Fig. **F137A**). At depths less than ~100 mbsf, all rocks in the core display some degree of hydration, and hydration and metamorphism are essentially pervasive to a depth of 350 mbsf. Traces of fresh clinopyroxene appear at ~40 mbsf and become more abundant downhole. Fresh gabbro with essentially no alteration is found below ~135 mbsf, and some fresh pyroxene is found in most samples below that depth. Fresh olivine appears in the troctolites at ~150 mbsf, and fresh troctolite with only minimal alteration of olivine appears at 380 mbsf. Prehnite alteration of plagioclase occurs locally below 300 mbsf, where it is most commonly associated with serpentinization of neighboring olivine. Epidote-bearing veins were found in intervals 304-U1309D-75R-2, 77–80 cm, and 77R-3, 112–118 cm.

Above 400 mbsf, vein-related alteration is generally superimposed on more pervasive alteration. Vein-related alteration (Fig. **F137B**) peaks from 0 to 50 m, where it is associated with breccia zones, and between 150 and 300 mbsf, where it is mostly associated with late leucocratic magmatic dikelets. Below 400 mbsf, virtually all alteration appears to be vein related, and hence this has not been plotted separately. From ~350 to 840 mbsf, the rocks recovered show moderate alteration. Zones 0.2–3 m wide with low alteration (total alteration = ~10 vol%) alternate with zones 0.4–3 m wide with moderate alteration (total alteration = >40 vol%). Higher alteration intensity in this interval is mainly in coarse-grained gabbro, later intrusions (leucocratic magmatic rocks and oxide gabbro), and zones of high deformation (cataclasite or mylonite). Two peaks showing a total alteration of >80 vol% (Cores 305-U1309D-152R and 162R at 746 and 789 mbsf, respectively) correspond to zones of highly altered gabbro with a cataclastic fabric. In both places, alteration is characterized by near-complete replacement of pyroxene by fibrous green amphibole. Core 305-U1309D-162R at 789 mbsf also shows a strong bleaching alteration with formation of secondary plagioclase and epidote. The highest peak of alteration (>90 vol% at 551.7 mbsf) corresponds to serpentinized olivine-rich troctolite, where olivine is completely replaced by serpentine.

From 841 to 1094 mbsf, the recovered rocks (mostly gabbro) generally show very low overall alteration (~2–3 vol%). Extensive alteration is restricted to zones with a high density of veins and to contacts between gabbro and diabase (Cores 305-U1309D-205R and 206R). There are some local peaks of higher alteration (50 vol%) corresponding to zones of high deformation (Section 305-U1309D-173R-1; 842 mbsf). Zones with total alteration amounts between 20 and 30 vol% are related to alteration halos around veins and fractures.

From 1095 to 1415.15 mbsf, the alteration is heterogeneous, showing increased degree of alteration between 1095 and 1200 mbsf. This high alteration zone (locally >90 vol%) corresponds to highly deformed zones of protomylonite (see **"Structural geology"**) and to zones of rodingitization within the olivine-rich troctolite (Sections 305-U1309D-231R-2, 234R-2, 237R-1, and 248R-2). The rodingites are strongly altered gabbroic rocks that appear to have undergone metasomatic reaction, possibly with serpentinizing fluids derived from nearby olivine-rich troctolites. The former gabbros now consist largely of chlorite, tremolite, and talc. The lowermost 200 m of Hole U1309D shows decreased alteration (~30 vol%), similar to the interval 841–1094 mbsf. The last high peak of alteration corresponds to zones of

intense veining associated with bleaching alteration (green amphibole replacing pyroxene and crystallization of secondary plagioclase).

Most of the rock types exhibit the entire range of alteration, from 0% to 100%, except for the diabase, which mainly is from 0% to 40% altered (Fig. F138A, F138B). Gabbro is the main lithology recovered in Hole U1309D and exhibits a range of alteration from 0% to 100%, but most rocks (~90% of the recovered gabbros) are altered within the range 0–40 vol%. The oxide gabbros and the olivine and troctolitic gabbros show the same moderate alteration range as the gabbros, within the 0%–40% range. The troctolites and olivine-rich troctolites show variation in alteration from 0% to 100%; ~10% have alteration >60%, and 1% of them have alteration >80% that is related to the serpentinization process of these olivine-rich rocks.

Downhole variation in alteration mineralogy

The secondary mineralogy for cores collected during Expedition 305, as identified in thin section, is given in Table T7. Total alteration estimated in thin section (Fig. F139B) mirrors the hand specimen–based alteration log but contains a built-in bias toward altered samples deeper in the core. We have sought to remove this bias by plotting only the mineral abundances in thin sections from geochemical samples (Fig. F139C), which were generally selected to be the least altered parts of the core. Plots of the abundances of the secondary minerals in thin section show some systematic variations downhole. The second diagram in Figure F139 includes data only from the geochemical samples and clearly shows the presence of almost unaltered rock between 700 and 1100 mbsf. Green to colorless (actininolitic) amphibole (Fig. F139E) is the most abundant secondary phase in the rocks in thin section. It replaces pyroxene, occurs in corona textures, and is present in veins; thus, the percentage of actinolitic amphibole correlates closely with total alteration except in serpentinized horizons. Brown amphibole is present in minor amounts as patches in pyroxene throughout the core. The abundance of brown amphibole (Fig. F139D) is greatest high in the hole and decreases markedly downhole from 400 mbsf, with peaks in oxide gabbro layers where it may be of primary origin. Talc (Fig. F139J) and chlorite (Fig. F139F) are involved in the formation of corona texture and are present in varying amounts, but they are most common in the upper part of the hole and in intervals of higher intensity of veining. Peaks in talc also correspond to some ultramafic horizons. Serpentine (Fig. F139K) is present at least as a very minor component of almost all rocks containing olivine below 330 mbsf, although it may make up only a very small percentage of secondary minerals (as fine veinlets along fractures in olivine grains). Serpentine abundance peaks in several intervals that correlate with some higher degrees of alteration of olivine-rich rocks. Prehnite (Fig. F139L) and hydrogarnet (Fig. F139M) are almost absent above 330 m because of the corona-forming reaction going to completion. Prehnite is most common between 330 and 430 mbsf, where it is present in ladder veins, whereas the main occurrence of hydrogarnet is below 1100 mbsf. Epidote (Fig. F139H) and titanite (Fig. F139I) appear in association with zones of leucocratic alteration, but epidote is also observed as zoned, euhedral crystals in veins. Epidote is rare in cores shallower than 380 mbsf and deeper than ~910 mbsf. Zeolite (Fig. F139N) appears below 751 mbsf. Albite and titanite appear in zones of leucocratic alteration throughout the cores, but albite is most common above 300 mbsf.

Downhole variation in vein composition and abundance

Veins containing dark green and slip-fiber amphibole are the most common type observed in hand sample (Fig. F140). Other vein types include secondary plagioclase, serpentine, clay, and white secondary minerals (usually zeolite + carbonate). The vein data recorded during visual inspection of the core and plotted in the following figures are available in the vein log (see **"Site U1309 core descriptions"** in "Core descriptions"). Vein mineralogy constrained by XRD and petrography is given in Table T8. Although there are several distinct maxima in the number and volume of veins per core, there is no consistent correlation between depth or rock type and number or volume of veins (Fig. F141). There is a correlation between both number and volume of veins and the location of faults in the core. In particular, major maxima in vein count are present in close association with faults at 695, 746, 989, 1070, and 1337 mbsf. Smaller maxima are associated with faults at 785 and 960 mbsf. Of particular note is the lack of correlation between magmatic veins and faults. Only one magmatic vein maximum, at 695 mbsf, is present in conjunction with a fault, but there is also a peak in nonmagmatic veining at this point. No faults have been recognized that correspond to peaks at 440, 550, 1190, and 1230 mbsf.

Faults also correlate with abundance of the two major amphibole-bearing vein groups: dark green amphibole veins and slip-fiber amphibole veins (Fig. F142). Serpentine veins are present, not surprisingly, at depths dominated by olivine-rich rocks (Fig. F142). Magmatic veins are most abundant near the top of the hole (above 700 mbsf) (Fig. F143). They are particularly abundant, as indicated by the peak

in secondary plagioclase, between 150 and 350 mbsf (Figs. F142, F144). A major increase in vein abundance is associated with the olivine-rich troctolites between 1100 and 1230 mbsf. Although veins in the olivine-rich troctolites themselves are mostly restricted to veining/foliation associated with the early serpentinization, intercalated gabbroic rocks are highly fractured and intensely veined. Slip-fiber and clay (saponite?) veins, in particular, show a strong spike associated with alteration of gabbros intercalated with the olivine-rich troctolites between 1100 and 1230 mbsf (Figs. F141, F142, F143).

The components of the "white" veins vary significantly with depth. Above 400 mbsf, sulfide-bearing veins are abundant and quartz-bearing veins occur (Fig. F145). Quartz is rare below 400 mbsf, and little sulfide is found in veins below 800 mbsf. Zeolite appears at ~700 mbsf and increases in abundance downhole to the deepest penetration of Hole U1309D (Fig. F145). Carbonate is present in veins throughout the hole. A peak between 700 and 850 mbsf reflects the presence of calcite in many slip-fiber veins through that interval (Fig. F144).

Metamorphic conditions at Site U1309

Granulite-facies recrystallization

Granulite-facies shear zones occur mainly above 350 mbsf. In one shear zone studied during preliminary shore-based electron microprobe studies (Fig. F146A; Table T9; see "Glass" in "Supplementary material"), pyroxene neoblasts have similar Al and Ti contents to large grains in the host gabbro and brown amphibole grains in the shear zone contain 3.5% TiO_2. The texture and mineralogy are both indicative of granulite facies and likely reflect formation at near-solidus conditions (probably 800°–900°C). Undeformed zones of recrystallized pyroxene and plagioclase occur locally and may mark zones of high-temperature fluid flow (Maeda et al., 2002). Pyroxene has also been observed filling microveins in igneous pyroxenes (Fig. F146B; Table T9), although the temperature at which this occurred is uncertain.

In some gabbros, especially oxide gabbro, there is substantial static replacement of clinopyroxene by green and brown amphibole. In general, such textures are interpreted as magmatic, having formed by incongruent, vapor-absent reaction between hydrous melt and pyroxene (e.g., Beard et al., 2004).

clinopyroxene + Fe-Ti oxides + hydrous melt ± plagioclase (calcic) = hornblende + SiO_2 (solid or melt) ± plagioclase (sodic). (1)

The similarity of igneous brown amphibole in the oxide gabbros and metamorphic amphibole in the mylonites suggests that igneous activity overlapped deformation and metamorphism.

Amphibolite-facies recrystallization

Statically grown brown to green-brown amphibole has been found partially replacing pyroxene at all levels in Holes U1309B and U1309D, and amphibole neoblasts are observed in some shear zones. Electron microprobe analysis of one diabase sample (Fig. F147; Table T9; see "Glass" in "Supplementary material" for analyses) reveals a wide range of amphibole compositions ranging from fluorine-rich ferroedenite to magnesiohornblende and actinolite, accompanied by a range of plagioclase compositions including labradorite, andesine, oligoclase, and albite. These observations indicate that hydration of the diabases, and probably the gabbros, occurred in both the amphibolite and greenschist facies and that the extent of amphibolite-facies metamorphism may have been underestimated on board ship.

A model for the formation of hornblende from pyroxenes is Reaction 2:

plagioclase + augite + orthopyroxene + H_2O = hornblende. (2)

Because the composition of hornblende changes as a function of temperature and pressure, the exact stoichiometry of Reaction 1 is difficult to determine. Despite this, the location of the reaction in pressure-temperature space (Fig. F148A) is fairly well known (Spear, 1981). The experimental location of this curve shows the conditions at which hornblende begins to break down during heating of a typical metabasite. For a retrograde situation, this reaction marks the conditions at which pyroxene in a metabasite would be completely altered to amphibole if the rock were open to the movement of H_2O. Because the substitution of H and Cl for OH and of Ti and Fe^{3+} into hornblende stabilize it to higher temperature, the temperature at which hornblende would start forming during cooling of a metabasite may be significantly higher than that at which reaction 1 takes place.

Corona-forming reactions

In the simplified system CaO-MgO-Al_2O_3-SiO_2-H_2O, reactions involving the phases olivine, anorthite, tremolite, and chlorite are divariant. Reactions among these phases can only be written assuming that one component is mobile. We have chosen to use CaO and SiO_2 as mobile components because Al_2O_3 has limited mobility in most low-temperature environments and because oceanic fluids have notoriously low Mg contents. Using mobile components of SiO_2 and CaO, we have calculated the stability re-

lations between olivine, tremolite, talc, anorthite, and chlorite for 1 kbar and 450°C (Fig. F149). We have used α-quartz and lime as standard states for SiO_2 and CaO. It is important to note that, if one chose different standard states (such as aqueous species) for the calculations, only the numbers on the coordinates would change; the topology would stay the same.

Figure F149 shows that the coronas around olivine could have been produced by a gradient in the activity of CaO and SiO_2 between plagioclase and olivine. Because Al_2O_3 has low mobility, chlorite produced by this reaction will be concentrated adjacent to plagioclase, whereas tremolite will form adjacent to olivine (see arrow A in Fig. F149). Where the fluid gradient was relatively richer in SiO_2 and poorer in CaO (arrow B in Fig. F149), a zone of talc will appear between olivine and tremolite.

There are two ways to write the reaction between olivine and plagioclase, depending on whether silica or CaO is the mobile component:

$$\underset{\text{plagioclase}}{4CaAl_2Si_2O_8} + \underset{\text{olivine}}{15Mg_2SiO_4} + \underset{\text{silica in fluid}}{5SiO_2} + \underset{\text{fluid}}{18H_2O} =$$

$$\underset{\text{amphibole}}{2Ca_2Mg_5Si_8O_{22}(OH)_2} + \underset{\text{chlorite}}{4Mg_5Al_2Si_3O_{10}(OH)_8}, \quad (3)$$

and

$$\underset{\text{plagioclase}}{11CaAl_2Si_2O_8} + \underset{\text{olivine}}{35Mg_2SiO_4} + \underset{\text{fluid}}{47H_2O} =$$

$$\underset{\text{amphibole}}{3Ca_2Mg_5Si_8O_{22}(OH)_2} + \underset{\text{chlorite}}{11Mg_5Al_2Si_3O_{10}(OH)_8} +$$

$$\underset{\text{Ca in fluid}}{5CaO}. \quad (4)$$

Reactions 3 and 4 both involve large volume increases for the solid phases—24% and 19%, respectively. This explains why intense fracturing is commonly associated with the corona-forming reactions. In feldspar-dominated rocks, chlorite-filled cracks radiate from pseudomorphs of olivine and across the surrounding plagioclase and follow curved paths from one olivine pseudomorph to another (Fig. F124C, F124D).

Because of the multivariant nature of Reactions 3 and 4, we cannot calculate the breakdown temperature of the assemblage olivine + anorthite directly; however, natural assemblages place clear constraints on the occurrence of this assemblage. Frost (1976) noted that plagioclase never appears in the presence of chlorite in peridotitic hornfelses; spinel is the aluminous phase instead. From this, he concluded that plagioclase appears in peridotitic rock a few tens of degrees above the terminal reaction for chlorite. This means that, during hydration, plagioclase + olivine will react out of a rock near the upper limits for amphibolite facies (see heavy gray line on Fig. F148A). Of course, if the reaction between olivine and plagioclase occurred at such high temperatures, the product would be hornblende, rather than chlorite + actinolite. We do see traces of brown hornblende in some coronas, but most consist of chlorite + actinolite. In mafic rocks, chlorite + actinolite is a typical greenschist assemblage, indicating that the coronas probably formed under the same conditions as the actinolite alteration of the gabbros—approximately 400°C. Note that, if the presence of cummingtonite is confirmed, it is likely that at least some corona-forming reaction occurred at substantially higher amphibolite-facies temperatures.

Serpentinization and prehnite-hydrogrossular assemblages

Serpentine can form in the presence of pyroxene via

$$\underset{\text{olivine}}{Mg_2SiO_4} + \underset{\text{orthopyroxene}}{MgSiO_3} + \underset{\text{fluid}}{H_2O} = \underset{\text{serpentine}}{Mg_3Si_2O_{10}(OH)_2}, \quad (5)$$

and

$$\underset{\text{olivine}}{6Mg_2SiO_4} + \underset{\text{tremolite}}{Ca_2Mg_5Si_8O_{22}(OH)_2} + \underset{\text{fluid}}{9H_2O} =$$

$$\underset{\text{serpentine}}{5Mg_3Si_2O_5(OH)_4} + \underset{\text{diopside}}{2CaMgSi_2O_6}. \quad (6)$$

Brucite was detected by XRD (Fig. F118) in one serpentinized olivine-rich troctolite (Sample 305-U1309D-111R-3, 131–138 cm). This suggests the straightforward serpentinization reaction:

$$\underset{\text{olivine}}{2Mg_2SiO_4} + \underset{\text{fluid}}{3H_2O} = \underset{\text{serpentine}}{Mg_3Si_2O_5(OH)_4} + \underset{\text{brucite}}{Mg(OH)_2}. \quad (7)$$

Although we were unable to find brucite in a thin section (305-U1309D-111R-4, 22–25 cm; thin section number 328) near the XRD sample, this thin section contains no tremolite or talc, both of which are common in most olivine-bearing rocks in Hole U1309D and are normally unstable in the presence of brucite. Brucite is commonly finely intergrown with serpentine and is notoriously hard to determine in thin section. Because olivine is typically more Fe rich than coexisting serpentine, magnetite typically forms as a consequence of serpentinization Reaction 5 with the iron end-member (fayalite) of the olivine (O'Hanley, 1996; Frost, 1985).

Serpentine can also form directly from olivine in the presence of a Si-rich fluid via the reaction:

$$\underset{\text{olivine}}{3Mg_2SiO_4} + \underset{\text{silica in fluid}}{SiO_2} + \underset{\text{fluid}}{4H_2O} = \underset{\text{serpentine}}{2Mg_3Si_2O_5(OH)_4}. \quad (8)$$

It is possible that serpentines in rocks that contain prehnite and hydrogrossular formed via reactions of

this sort, possibly with Si derived from the reaction of plagioclase to the rodingitic assemblage.

Reaction 5 marks the highest temperature that serpentine can form in a rock that has not previously been hydrated (i.e., one that lacks talc) (Fig. **F148B**). Using the compositions of phases usually found in peridotite (Trommsdorff and Evans, 1974), we calculate that, at 1 kbar, Reaction 5 takes place at ~460°C (see Fig. **F148B**). Reaction 6 marks the lowest temperature stability for tremolite in serpentinites; at 1 kbar this is 415°C. Reaction 7 is the lowest temperature at which olivine is stable in the presence of pure water. At 1 kbar, this temperature is 354°C (Fig. **F148B**).

In a number of rocks from Hole U1309D, we find tremolite growing from clinopyroxene in the presence of olivine (Fig. **F127B**). Tremolite is too silica rich to form by direct hydration of clinopyroxene in peridotite; its formation requires the input of silica or the expulsion of CaO. Because of this, we argue that textures in which tremolite grows on clinopyroxene must have formed in the presence of free water, and, therefore, this texture must have formed at temperatures above those of Reaction 6. Otherwise, the influx of water would have hydrated the olivine, not the clinopyroxene. In contrast, there are many serpentinites in which the clinopyroxene is still fresh (Fig. **F127C**). In these rocks, hydration could have occurred at temperatures below those of Reaction 6 or even at temperatures below those of Reaction 7.

The association of prehnite, hydrogrossular, and chlorite (Fig. **F127F**) constrains the formation of the prehnite alteration to temperatures below Reaction 9:

$$26\underset{\text{prehnite}}{Ca_2Al_2Si_3O_{10}(OH)_2} + \underset{\text{garnet}}{Ca_3Al_2Si_3O_{12}} + \underset{\text{chlorite}}{3Mg_5Al_2Si_3O_{10}(OH)_8} =$$

$$15\underset{\text{diopside}}{CaMgSi_2O_6} + 20\underset{\text{clinozoisite}}{Ca_2Al_3Si_3O_{11}(OH)} + 28\underset{\text{water}}{H_2O}. \quad (9)$$

At 1 kbar, this reaction in the pure system CaO-MgO-Al_2O_3-SiO_2 occurs at 350°C (Fig. **F148B**). The prehnite-forming reaction must have occurred at temperatures below this; thus, fluid must have been flowing through the olivine-rich troctolites at least to temperatures <350°C.

The distribution of epidote in the core presents an interesting problem. Reaction 10 gives the upper limit for clinozoisite stability in the presence of chlorite (~350°C at 1 kbar; Fig. **F148**). Epidote is clearly incompatible with the corona-forming reaction, where Fe contents of minerals are low. High Fe contents expanding the stability field may account for the formation of epidote at intermediate levels of the core:

$$10\underset{\text{plagioclase}}{CaAl_2Si_2O_8} + \underset{\text{tremolite}}{Ca_2Mg_5Si_8O_{22}(OH)_2} + 6\underset{\text{fluid}}{H_2O} =$$

$$6\underset{\text{epidote}}{Ca_2Al_3Si_3O_{12}(OH)} + \underset{\text{chlorite}}{Mg_5Al_2Si_3O_{10}(OH)_8}$$

$$+ 7\underset{\text{quartz}}{SiO_2}. \quad (10)$$

Movement of late magmatic and hydrothermal fluids

Above 330 mbsf, an early pervasive fluid flow event under low-amphibolite to upper-greenschist conditions affected most rocks in Holes U1309B and U1309D. Metamorphic reactions appear to have played an important role in creating permeability in these rocks. Focused fluid flow in amphibole veins and breccia zones and along late magmatic leucocratic dikelets was superimposed on this event. At greater depths, most of the alteration is related to veins. The gabbroic rocks in Hole U1309D show only minor evidence for prehnite-pumpellyite-facies alteration. Prehnite below 330 mbsf is clearly related to serpentinization and formed above 350°C. This relation suggests that, following the last greenschist hydration event, the rocks in the upper part of the core became closed to the movement of fluids until they had cooled below temperatures of ~100°–200°C. At these temperatures, fracturing formed the clay-bearing veins that cut many of the sections of the core. The main clay mineral detected by XRD is saponite (Table **T4;** Fig. **F117**). It is likely that much of the clay and zeolite observed in fractures below 700 mbsf formed under essentially ambient conditions because temperatures at the bottom of the hole were at least 120°C. The lack of zeolite above this level may reflect rapid cooling through the appropriate temperature interval during unroofing, rather than a lack of fluid flow.

In contrast to the upper parts of the hole, there is a close correspondence between veining, zones of cataclasis, and fluid movement in the lower 1000 m of Hole U1309D. The correspondence ranges from thin section–scale observations of the relationship between cataclasis and veining to an overall correlation of downhole alteration with major faults (see **"Structural geology"**).

Although some zones of cataclasis are unaltered at the thin section scale, more commonly they are pervaded by secondary minerals, especially fibrous amphibole, to the extent that they resemble dark green veins on visual inspection of the core. In some cases, there is an apparent history of fluid flow in these zones. Early high-temperature fluids, probably hy-

drous silicate melts, crystallize euhedral zircon, titanite, zoned plagioclase, and, more rarely, blocky green amphibole that is locally zoned. Later, and presumably at lower temperature, fibrous amphibole has grown as intergranular stringers and patches and as a replacement of pyroxene (Fig. **F150A**). Dark green amphibole veins may branch out from the zone of cataclasis into surrounding undeformed rock. Alteration of plagioclase in the zone of cataclasis at this stage may produce albite, prehnite, and, especially lower in the core, zeolites. The latest fluids crystallize, thus filling void space into which earlier higher temperature minerals have grown (Fig. **F150B**).

The composite talc-tremolite veins seen in some ultramafic layers (Fig. **F115**) may be a manifestation of the same greenschist-facies fluid flow event as the actinolite breccia veins. The intense metasomatic alteration is due to the movement of fluid rich in Si and Ca from mafic to ultramafic rocks. Similar zones where plagioclase is completely altered to chlorite (Fig. **F132E**) reflect flow from ultramafic into mafic rocks.

Fluid flow also seems to have been localized by gabbroic intrusions. Below 300 m, coronitic alteration of olivine and plagioclase in olivine gabbros or troctolites is often associated with zones within a few centimeters of late pegmatitic gabbros (Fig. **F128**) This could be a result either of exsolution of magmatic fluid or localization of fracturing and fluid infiltration into more competent gabbros. The fluid influx that produced the serpentine-prehnite alteration was also localized. Although the reasons for this are not entirely clear, the alteration is clearly fracture related and serpentine-prehnite ladder veins often appear to follow stress trajectories (e.g., rotating to be perpendicular to lithological boundaries), so a tectonic control appears probable.

Larger scale structures also influence the movement of metamorphic fluids. In particular, there is a close correspondence between veining, alteration, and the location of identified faults. Most major maxima in vein abundance are associated with these faults (Fig. **F141**). In addition, the overall downhole decrease in alteration is interrupted twice, once between 600 and 800 mbsf and once between 1100 and 1200 mbsf. In the first case, there are major faults near the bottom of the highly altered section. These faults may have acted as conduits, releasing metamorphic fluids into the overlying rocks, leading to increased veining and alteration.

In the second case, things may be somewhat more complex. There are faults beneath this interval, but much of the fluid flow may have been focused, not by fault zones but by relatively impermeable intervals of fine-grained, partially serpentinized, olivine-rich troctolite.

Summary

Rocks in Hole U1309D experienced metamorphism at grades ranging from granulite to zeolite facies, reflecting the cooling and deformation of a gabbro body. Granulite-facies metamorphism is restricted to mylonite zones in which plagioclase and pyroxene are recrystallized to an equigranular mosaic texture. This deformation may have been syn–late magmatic. Amphibolite-facies metamorphism includes hornblende-forming reactions in diabase, oxide gabbro, and mylonites. Some amphibolite-facies metamorphism may have been coincident with the latest stages of magmatism in Hole U1309D. In particular, late leucocratic dike injection and crystallization and late crystallization in the oxide gabbros appear to be continuous across the transition between fluid-rich late magmatism and amphibolite (and, ultimately, greenschist)-facies hydrothermal metamorphism.

The dominant metamorphic event in Hole U1309D is greenschist-facies hydration of gabbroic, ultramafic, and diabasic rocks. In the upper 350 m of the hole, this alteration is nearly pervasive and does not generally reflect focused fluid flow. With increasing depth, greenschist-facies hydration is almost always related to veins, igneous contacts, and other fluid conduits.

In all pyroxene-bearing rocks, the greenschist-facies event is reflected by partial to complete replacement of pyroxene by actinolitic amphibole, sometimes with subsidiary formation of sodic plagioclase and chlorite. This replacement event is sometimes static, especially in diabase and in the uppermost core, and sometimes clearly related to cataclasis and/or veining (gabbros and the core below 350 mbsf).

In olivine gabbros and troctolites, the greenschist event is most prominently manifested by corona-forming reactions between olivine and plagioclase. In their simplest guise, the coronas consist of a rim of chlorite around plagioclase and a rim of tremolite around (formerly) adjacent olivine. In more complex manifestations, talc and other minerals may form within the coronas. Cummingtonite has been tentatively identified in some coronas, suggesting some form at amphibolite-facies conditions. Unlike other greenschist-facies rocks in Hole U1309D, the formation of coronas appears to be nonisochemical, requiring addition of silica and/or removal of lime. Talc-tremolite-chlorite alteration zones formed at ultramafic/gabbro contacts suggest that these metasomatic rocks may simply reflect exchange of fluids between gabbros and ultramafic rocks.

In ultramafic and near-ultramafic rocks (dunites and olivine-rich troctolites), the dominant low-temperature alteration event is serpentinization. This is generally accompanied by local alteration of plagioclase to prehnite and hydrogarnet. Relict olivine in corona-textured rocks, as well as isolated olivine grains in gabbros and troctolites, may also be serpentinized.

The lowest temperature of metamorphism is manifested by zeolite veins in the lower (below 700 mbsf) core and by various carbonate and clay veins throughout the core. These may be forming under ambient conditions (e.g., ~120°C measured at bottom of hole).

The degree of alteration downhole changes significantly, decreasing between ~375 and 400 mbsf in the last few cores recovered during Expedition 304. Alteration increases again with depth until 841 mbsf. The interval of freshest rock recovered during Expedition 305 is from 841 to 1094 mbsf. Between 1095 and 1200 mbsf, a zone of high alteration reflects highly deformed, localized zones of protomylolite and rodingitization within the olivine-rich troctolites. Below 1094 mbsf, the gabbros and troctolites again are characterized by low to moderate degrees of alteration.

The overall trends in alteration and the changes in secondary mineralogy suggest that there may be two separate secondary processes at work in Hole U1309D. In the upper 841 m, we suggest that a seawater–rock interaction may pervade the sequences, finding downward access along high-angle structural pathways. If an "alteration front" is present in the in the rocks at Site U1309, we suggest that it reaches a depth of 841 mbsf. Below that depth, the nature of and the fluctuations in degree and style of metamorphism are related to fluids of a different composition percolating along fault zones and zones of deformation. We suggest that the fluid composition records an extensive history of rock–fluid interaction, may include magmatic fluids, and is reflected in the secondary mineralization of the rocks. In essence, alteration below 841 mbsf records the cooling of a relatively isolated magma body.

Structural geology

Site U1309 is located at the surface of a low-angle detachment fault exposed at the seafloor on Atlantis Massif. Holes U1309B and U1309D are located at the base of a <20° north-facing slope and in close proximity to the point of inflection of the exposed fault surface. The breakaway of the fault is inferred to be ~5 km to the west, and the termination of the fault (point where the fault intersects the seafloor) is ~5 km to the east. The dip of the fault at its termination is ~11°; this value provides a minimum estimate for footwall rotation at Site U1309, where the fault is approximately horizontal. Atlantis Massif exhibits heterogeneities in both the lithology of the footwall and its physical properties. Extensive peridotite outcrops and an active hydrothermal system venting by serpentinization fluids (Lost City hydrothermal vent field) are found ~5 km to the south. In contrast, ~1.4 km of primarily gabbroic rocks were recovered at Site U1309. Near-bottom NOBEL seismic refraction analysis (Collins et al., 2001, 2003; Collins and Detrick, 1998) ~1 km northwest of Hole U1309D indicates that seismic velocities >7.5 km/s occur at ~900 mbsf. This is in contrast with the lower velocities inferred from both samples and borehole measurements at this site. This section describes local structures observed at Site U1309, which must be part of the larger scale structures of Atlantis Massif.

Summary of structural observations

Hole U1309D was subdivided into three major structural units:

- Structural Unit 1 from 0 to ~170 mbsf;
- Structural Unit 2 from ~170 to ~785 mbsf; and
- Structural Unit 3 from ~785 to ≥1404 mbsf).

Structural Unit 1 is marked by a high but downhole-decreasing intensity of cataclasis, an abundance of late, relatively undeformed diabase, a high intensity of greenschist-grade alteration (see **"Metamorphic petrology"**), and a near-present-day orientation of the paleomagnetic inclination (see **"Paleomagnetism"**). The majority of core recovered records a pervasive static alteration of the rocks, and pseudomorphs of igneous textures remain largely unmodified. The boundary to structural Unit 2 at ~170 mbsf is marked by a low to moderately dipping crystal-plastic shear zone within gabbroic rocks, a high intensity of veining, strong cataclasis, and a ~2 m thick interval of altered ultramafic rocks including mantle harzburgite.

Structural Unit 2 extends from ~170 to ~785 mbsf. It is marked by a high intensity of veining, including the presence of sulfides. Paleomagnetic inclinations are ~10°–30° shallower than present-day values. Lithologically, structural Unit 2 is varied and nondistinct. The base of structural Unit 2 is also defined by a series of greenschist-grade cataclastic fault zones occurring between 695 and 785 mbsf; there is an abrupt decrease in the intensity of both veining and cataclastic deformation below this fault zone. Finally, there is a sharp decrease in whole-rock Mg# of the gabbros near the base of structural Unit 2 below ~600 m (Fig. **F14**).

Structural Unit 3 extends from this boundary to the bottom of Hole U1309D and is characterized by an overall low intensity of cataclastic deformation, veining, and plastic deformation. It comprises one fault zone at ~1107 mbsf.

Magmatic fabrics were recorded in 22% of the recovered rocks and are weak except for local intervals. Magmatic foliation is, in general, better developed in finer grained gabbros than in those with a coarse grain size; foliation is also well developed in the rare layered intervals. Magmatic foliations were strongest in microgabbroic intrusions. Textural observations suggest that foliation may be overprinted in some cases by late growth of pyroxene crystals with grain size up to 20 cm. Magmatic foliations typically dip ~30°–60° but can be steeper (e.g., at 400 and 560 mbsf) or more gently dipping (e.g., at 850 and 1150 mbsf) in local intervals.

High-strain crystal-plastic shear zones are spatially more restricted than magmatic fabrics and are recorded in only 3% of the core. Crystal-plastic deformation typically occurs in clearly defined, mostly granulite grade shear zones ranging in width from a few millimeters to a maximum of a few meters. They have both normal and reverse sense of offset in the core reference frame, and their dips are typically moderate and locally steep (e.g., at 700 mbsf). These shear zones are most abundant in the upper ~320 mbsf of Hole U1309D and typically have a shallow dip.

Magmatic contacts range from gradational to sharp and are defined by variations in modal minerology, grain size, or both. More evolved rocks (e.g., oxide gabbro) always crosscut less evolved rocks (e.g., troctolite). Magmatic banding defined by variation in grain size or mode occurs locally.

Various vein sets are found throughout the core (see also **"Metamorphic petrology"**). The earliest generation is late magmatic veins. Their occurrence broadly correlates with country rocks that have similar rock types, suggesting a local derivation (scale of 100 m). Later vein generations include dark green amphibolite-facies veins (consisting of amphibole) cut by pale green, fibrous greenschist-facies veins (actinolite/tremolite-chlorite ± talc and epidote). Fiber orientations on the pale green veins are often subhorizontal (particularly below ~300 mbsf) independent of vein dip, indicating at least local oblique-slip movement during formation. The latest vein type is typically open, white veins (carbonate and sulfide ± chlorite, prehnite), possibly associated with unloading and of lowest metamorphic grade. Gray veins consisting of serpentine ± chlorite are restricted to olivine-rich rock types. They either crosscut or are crosscut by the serpentine foliation. There is also a subset of the gray veins having synkinematic fibers. Vein intensities tend to correlate with fault zones on a local scale, though displacement on veins (vein faults) is not common. On a whole-core scale, vein intensities decrease significantly below structural Unit 2. The dip of veins is variable, but the mean dip is moderate irrespective of vein type. On the scale of the entire core, there is no systematic, lithology-dependent downhole distribution pattern of specific vein types.

Olivine-bearing rocks are commonly serpentinized (see **"Metamorphic petrology"**). The orientation of the serpentine foliation varies on a meter scale or even from one piece of core to the next. Several crosscutting serpentine foliations may occur in the same rock piece.

In addition to the faults mapped at ~170 mbsf and between ~685 and ~785 mbsf (marking structural unit contacts), more significant zones of cataclasis were found at ~110, ~250, and ~1107 mbsf. Cataclasis is locally associated with the formation of oxide gabbro intervals/dikelets, leucocratic veins, and the contact zones between diabase intrusions and their gabbroic host rocks.

The relatively undeformed nature of the plutonic section recovered from Atlantis Massif allows an unprecedented opportunity to study crustal emplacement processes for a wide range of magmatic conditions. The observation of layering in more primitive cumulates suggests formation by igneous processes within a magma chamber. In contrast, the observations of gabbro dikes and late magmatic leucocratic veins that crosscut more primitive rock types indicate that melt migration was controlled by brittle mechanisms during the latter stages of the fractionation and crystallization processes. At the grain scale, the role of melt in promoting brittle processes is indicated by pyroxene crystals in oxide gabbros that are cut by veins filled with magmatic oxide and hornblende. Similarly, a preferred orientation of cuspate-shaped, interstitial plagioclase crystals in some olivine-rich troctolites suggests that the orientation of melt pockets was controlled by stress state. Finally, the observation of crystal-plastic shear zones within narrow intrusions/dikes and at contacts between gabbroic intervals suggests that the presence of melt promoted strain localization during extension at the ridge axis. On a more speculative note, the lack of a clear internal fractionation stratigraphy and the observation that we rarely, if ever (note wehrlite-vein-cutting gabbro found during Expedition 304), observe primitive gabbroic rocks cutting more fractionated units suggest that the changes in melt migration style described above occurred when the

partially molten crust became impermeable, thus halting magma migration through the crust.

Tentative conclusions can be made based on reorientations of structures using paleomagnetic and logging data performed in Holes U1309B and U1309D to a depth of 130 mbsf. These data indicate that crystal-plastic foliations dip dominantly to the west, a majority of veins dip toward the east, and several faults strike east-west. Holes U1309B and U1309D are 20 m apart, and thus, the local continuity of igneous, metamorphic, and structural units can be evaluated. On a broad scale, both holes can be correlated, but correlation breaks down below a scale of ~10 m.

Models for the formation and denudation of the central dome of Atlantis Massif need to account for the following observations:

- There is little magmatic deformation associated with the intrusive history. This observation suggests that the plutons were "shielded" from deformation, owing to emplacement within the mantle lithosphere. Alternatively, the lack of significant magmatic deformation may simply reflect differences in the timing of deformation and plutonism at the spreading axis.
- The observation that primitive rock types are always cut by more evolved rocks suggests that this plutonic sequence may have formed partly by underplating nearby.
- The drilled gabbro section is mostly continuous and structurally homogeneous, except for zones of increased crystal-plastic and brittle deformation in the upper ~320 mbsf and between ~650 and ~800 mbsf. It is not straightforward to kinematically relate these deeper structures to the zone of detachment associated with the detachment fault system at depths <170 mbsf. Following the granulite grade deformation, there is a relative paucity of evidence for deformation at amphibolite facies. Evidence for deformation related to denudation in the shallow parts of Holes U1309B and U1309D suggests that faulting initiated at greenschist-grade conditions. These observations indicate that the footwall cooled considerably between pluton emplacement and denudation.
- In conjunction with the apparent lack of significant net tectonic rotation indicated by the paleomagnetic data for the upper 120 m of the massif (see **"Paleomagnetism"**), the relative paucity of deformation fabrics suggests that structures with significant slip on the detachment fault were localized within the unrecovered upper 20 m or cored at low temperature within the brittle regime.

Magmatic and crystal-plastic deformation

Peridotite

The earliest structural history of rocks from Site U1309 is constrained by magmatic and crystal-plastic deformation fabrics preserved in peridotites. A few pieces of mantle peridotite were recovered in Hole U1309B and the upper part of Hole U1309D, the deepest recognized mantle rock being a wehrlitic peridotite at 224 mbsf. Serpentinized peridotite recovered in Core 304-U1309B-11R (~59 mbsf) exhibits deformation fabrics consistent with high-temperature mantle flow. The relict olivine and pyroxene grains in this interval display a coarse granular texture with a grain size in the range of 1–5 mm. Numerous low-angle subgrain boundaries and undulatory extinction within olivine are observed microscopically (Fig. **F151A**). In addition, examination of extinction angles relative to vertical, combined with relative refractive indexes (i.e., gypsum plate analysis), indicates that there is a relatively strong LPO of olivine within this sample (Fig. **F151B**). There is not a strong foliation preserved in these rocks; however, a weak spinel lineation was tentatively identified to plunge 0°–30° in Sections 304-U1309B-11R-1 and 11R-2. Two very small intervals of possible residual mantle rock were also recovered in Hole U1309D in Sections 304-U1309D-31R and 42R; these rocks are severely altered but also appear to preserve a coarse granular texture.

In addition to the minor intervals of likely residual ultramafic rock recovered in the upper 224 m of Hole U1309D, an interval of serpentinized peridotite was recovered from Section 304-U1309D-10R-1. This rock exhibits textures indicative of intercumulus growth of clinopyroxene (Fig. **F151C**), and the olivines show fewer subgrain boundaries than the residual harzburgite recovered in Hole U1309B. However, a cursory optical analysis of extinction angles suggests that there is a relatively strong olivine LPO in the wehrlite. This observation, combined with the lack of evidence for deformation of the intercumulus clinopyroxene, suggests that the olivine experienced high-temperature crystal-plastic deformation prior to the crystallization of the clinopyroxene. These textures indicate that the wehrlite may have formed by high-temperature melt impregnation of mantle peridotite. However, we emphasize that the presence of subgrain boundaries in olivine is not, by itself, good evidence for residual mantle olivine. For example, some mostly unaltered troctolitic rocks from Hole U1309D preserve clearly igneous textures with equant olivine grains that exhibit subgrain boundaries (Fig. **F151D**); cursory analysis of extinction angles in this sample (from Section 304-U1309D-7R-3) indicates that there is not a strong LPO of olivine.

Gabbroic rocks

Gabbroic rocks from Holes U1309B and U1309D display a full range of high-temperature structures developed at magmatic and granulite conditions. These include grain size and modal layering (Fig. **F152A**), foliation developed under magmatic conditions (Fig. **F152A–F152C, F152F**), intrusive relations between different magmatic units (Fig. **F152D, F152E, F152G, F152J, F152L**), and crystal-plastic foliations developed during high-temperature solid-state flow (Fig. **F152H, F152I, F152K**). We discuss these features in more detail in the following sections.

Magmatic fabrics

The majority of rocks in Hole U1309D, particularly below 250 mbsf, have no discernible plastic or magmatic fabric (i.e., mineral-defined foliation and lineation). A magmatic foliation could be identified only in ~22% of the recovered core. The foliation identified as magmatic is either defined by single-mineral-preferred shape orientation or as aggregates of minerals that define vague bands (Fig. **F153E–F153H**). The single-mineral foliation is best expressed by elongate plagioclase laths, much more rarely by elongate clinopyroxene, or, in olivine-rich troctolites, by olivine. The foliation is generally weak. In nearly all cases, the core was not cut parallel to the foliation plane. Thus, we cannot make a clear statement about the presence and trend of the mineral lineation. The observation of elongate olivine pseudomorphs in gabbroic rock in an otherwise magmatic fabric (Fig. **F152B, F152C**) might be attributable to crystal-plastic deformation. Similar textures have been observed in gabbros from the Oman ophiolite (Boudier et al., 1996). Some troctolites also display an alignment of cuspate grain edges in intercumulus plagioclase crystals (Fig. **F152F**). Very few indications of coherent magmatic foliation were observed in either the diabase or basaltic units.

The development of magmatic fabrics appears to be grain-size dependent and is most obvious where grain size changes occur along the core. Specifically, we typically observe that in a section of gabbro showing grain-size banding, a magmatic fabric is much more readily identified in the fine-grained parts. Remarkably, such grain size changes are not necessarily parallel to the magmatic foliation. Magmatic foliation is locally overprinted by incipient plastic deformation (Fig. **F153A–F153D**).

Crystal-plastic fabrics

Microstructural observations indicate that the crystal-plastic deformation of gabbros occurred at granulite- to upper-amphibolite-grade conditions in both deep holes at Site U1309. Numerous deformation fabrics indicate that solid-state deformation initiated at near-solidus conditions in the gabbroic rocks. For example, oxide-filled bands cut granulite-grade recrystallized gabbro at a high angle in Section 304-U1309D-44R-2 (Fig. **F152L**). Typical criteria to discriminate plastic from magmatic fabrics are the rounded nature of single minerals, the recognition of porphyroclasts in a fine-grained matrix in more strongly deformed intervals, and the presence of an anastamozing fabric (Fig. **F154A, F154B**). All these features are best expressed in high-strain plastic shear zones that are either pervasive over several decimeters (Fig. **F155**) or, more commonly, very localized and restricted to a few centimeter-wide intervals (Fig. **F156**). Plastic strain mineral foliations were only identified in <3% of the core. Mineral stretching lineations were difficult to determine because of a lack of appropriate exposure of foliation planes.

Mylonitic shear zones are characterized by bands of recrystallized plagioclase and augite (Fig. **F154C**). In many cases, the ferromagnesian phases are completely altered to assemblages of tremolite-actinolite (likely alteration of augite) or chlorite-tremolite (likely alteration of olivine). In general, the bands of dynamically recrystallized plagioclase show optical evidence for a strong LPO. In the least altered examples of the high-temperature mylonites, we observed fresh recrystallized augite together with minor brown hornblende (Fig. **F154D**). In some highly altered rocks, elongate pseudomorphs of olivine suggest that deformation occurred at temperatures high enough to promote relatively easy creep of olivine. Mylonitic foliations are, in places, observed at the contacts between two igneous units. For example, a strong crystal-plastic foliation is observed within a gabbro that cuts a troctolite body in Core 304-U1309D-8R (Fig. **F152I, F152J**). In this case, magmatic layering in troctolite is cut by the contact. Structures resulting from strain localization are also observed within narrow intrusive units. For example, two narrow gabbro dikes with similar orientations are observed to cut a dunite within Section 304-U1309D-64R-2; strong crystal-plastic fabric indicates that one of these dikes is strongly deformed (Fig. **F152G**).

Kinematic indicators in mylonites are difficult to quantify. Those that can be determined unequivocally (~10%) do not show any systematic variations with depth. Mylonitic shear zones with reverse-sense motion in the core reference frame were observed in Cores 304-U1309B-8R and 9R. In Hole U1309D, reverse sense of shear (core reference frame) was observed in Cores 304-U1309D-4R, 8R, 44R, and 64R, and normal sense of shear (core reference frame) was observed in Cores 4R, 8R, 29R, and 49R. For the

shear zones at 670 mbsf, a normal sense of movement in the core reference frame was inferred.

Crosscutting relationships indicate that crystal-plastic deformation occurred over a relatively narrow range of temperatures. Mylonitic foliations are cut by undeformed brown hornblende veins (Fig. F154E), which likely formed at temperatures near 700°C, late-magmatic leucocratic dikes (Fig. F154B), and oxide-rich bands (Fig. F152L). The liquidus temperatures of the leucocratic rocks (largely composed of hornblende + albitic plagioclase) are difficult to estimate without mineral composition data but are likely in the range of 750°–850°C.

In the lower part of Hole U1309D, plastic shear zones are not common. The plastic shear zone at 670 mbsf has an apparent thickness of ~2 m in the core, which translates, for an average dip of 70°, to a true thickness of 70 cm. Another shear zone, ~50 cm true thickness, was recovered at 1300 mbsf. The relatively thin shear zones and general lack of high-strain features (ultramylonite) suggest that the shear zones in the lower part of the core accommodated minor displacement.

Microstructural inventory of gabbroic rocks

Microstructures of gabbroic rocks from Hole U1309D were classified into different intensities of magmatic and plastic foliation development, according to the guidelines given in the "Methods" chapter (see also Figs. F157, F158).

The majority of rocks recovered from Hole U1309D are fine- to coarse-grained gabbros that may or may not contain olivine, clinopyroxene, orthopyroxene, or oxides. The dominance of gabbro is an advantage for studying downhole variation, as plagioclase can serve as a common denominator for microstructural classification. There is some bias in the data collection because of the oversampling of particular features like shear zones, fractures, and veins. However, such a statistical bias can be weakened if averages are considered for a certain depth range (as is done here). For example, five thin sections from a shear zone between 620 and 625 mbsf are averaged as one value for this depth range.

Plagioclase displays the typical range of microstructures from lower temperature (undulose extinction, small and perhaps variable neoblast size, and serrated grain boundaries) to higher temperature plastic strain (coarser, mosaic type neoblasts, straight grain boundaries, and tapered twins) to magmatic fabrics (aligned, elongated laths) (Fig. F158A). S-C mylonitic fabrics (Berthé et al., 1979) are well developed in shear zones associated with oxides.

Clinopyroxene exhibits a similar range of microstructures with a few important differences. Alignment of elongated clinopyroxene grains is rare, perhaps because primary elongate clinopyroxene grains are also rare. Poikilitic clinopyroxene is extremely abundant, with dimensions that can exceed 20 cm. Also, for any given type of plastic strain, clinopyroxene relict grains tend to be more abundant than plagioclase relict grains. Neoblast sizes of clinopyroxene and plagioclase are similar.

Of particular interest are textural relations between plagioclase and clinopyroxene. Plagioclase with an boundary that appears to be strongly resorbed (Fig. F158D) or with an unusually elongate, acicular shape (Fig. F158E) is present within poikilitic clinopyroxene. Extensive films of completely unstrained clinopyroxene are present between olivine and plagioclase, sometimes merging into more massive clinopyroxene grains (Fig. F158J). Microstructural observations demonstrate equilibrated plagioclase enclosed in a poikilitic clinopyroxene (Fig. F158B) or, rarely, even olivine (Fig. F158C).

Olivine is present either as isolated grains within olivine gabbro or as grains with rounded shape in troctolite and olivine-rich troctolite. Most olivine grains have a near-straight extinction or some tilt walls, suggesting only minor strain (except in rocks of inferred mantle origin; see Fig. F151). In troctolites and olivine-rich troctolites, ovoid-shaped olivine dominates. A small grain size (~1 mm) is characteristic in olivine-rich troctolites. An overall LPO on the scale of the thin section is not present. However, in olivine-rich troctolites, adjacent olivine grains can share the same optical extinction pattern (Fig. F158F) despite separation by unstrained poikilitic plagioclase. Larger olivine grains can have ovoid shapes adjacent to poikilitic clinopyroxene (Fig. F158G).

Orthopyroxene shows little deformation throughout Hole U1309D but may deform by internal slip, resulting in elongated grains (Fig. F158H).

As previously mentioned, Fe-Ti oxides are either deformed or undeformed (see also "Igneous petrology"). Between 400 and 800 mbsf, oxide-bearing zones have undergone high shear strains with associated small silicate neoblast sizes whereas the oxide-free gabbro host is apparently strain free (Fig. F158K). However, oxides are also often present in completely undeformed rocks (Fig. F158L). Spinel present in the rare mantle rocks above 400 mbsf and in troctolites and olivine-rich troctolites is typically massive and equant.

Microstructural classification into strain intensities is based primarily on neoblast abundance, with discrimination between neoblast sizes that likely reflect different temperature, stress conditions, and/or re-

crystallization. For neoblast sizes between 200 and 600 µm, it is suggested that a large proportion of primary magmatic plagioclase grains may have undergone recrystallization based on the polygonal, optically related adjacent grains. This is at variance with the observation of negligible plastic strain in most gabbros based on macroscopic description. Closer inspection typically reveals that no significant foliation development is associated with this recrystallization. It is possible that largely preserved outlines of magmatic plagioclases are pseudomorphed as recrystallized plagioclase (e.g., Sample 304-U1309D-40R-1, 52–55 cm). The inference is that, in most cases, accumulated strain was small and that dynamic recrystallization started at low strains. In contrast, for small neoblast sizes (typically <100 µm), recrystallization is typically accompanied by foliation development.

Downhole distribution of magmatic and crystal-plastic foliation

To gain an understanding of the structural characteristics of the rock, the dips and intensity of both magmatic and crystal-plastic foliations are plotted as a function of depth in Figures **F159, F160, F161, F162,** and **F163.** In Hole U1309B, the highest intensity of magmatic foliation—indicated by 1–10 cm scale compositional banding and cumulate foliations—is observed in the lower gabbro unit in Cores 304-U1309B-14R through 16R. By contrast, the upper gabbro unit is largely isotropic, although a few igneous layers are observed. Very few indications of coherent magmatic foliation were observed in either the diabase or basaltic units.

In Hole U1309D, zones of magmatic fabric were encountered between 100 and 250 mbsf, 400 and 450 mbsf, 550 and 580 mbsf (representing a zone of steep foliations; see below), and 800 and 1100 mbsf (an interval that covers diverse rock types). As recognized mainly later in thin sections, microgabbroic intervals are also characterized by strong magmatic fabrics. Intensity of magmatic foliation is lowest in the interval between 580 and 660 mbsf and below 1300 mbsf.

Crystal-plastic deformation is apparently localized into narrow shear zones in Holes U1309B and U1309D. In general, the intensity of crystal-plastic deformation decreases with depth in Hole U1309D. On the scale of the entire core from Hole U1309D, the highest density of shear zones is observed between 35 and 80 mbsf, 170 and 310 mbsf, 670 and 730 mbsf, and 1290 and 1320 mbsf (Fig. **F163**). In the lower portions of the core, the most pronounced group of shear zones is located at the base of the zones with virtually no magmatic fabrics at 670 mbsf. Other less pronounced zones of crystal-plastic deformation are present at ~420, 720, 880, and 1000 mbsf.

Microscopic downhole observations of magmatic and plastic foliation development

The microscopic rating of intensity of crystal-plastic and magmatic fabrics (see the **"Methods"** chapter) is given in Figure **F162.** The following trends can be discerned:

- Intensities of magmatic foliation development as estimated in the core and in thin section (Fig. **F162A** and **F162B,** respectively) broadly correlate. Microscopically determined intensities are highest at 100 to 250 mbsf and ~600 mbsf and gradually increase over the interval from 700 to 1100 mbsf.
- Strain associated with the smaller neoblast size (i.e., higher stress/lower temperature conditions typical for discrete shear zones) correlates well with the occurrence of plastic strain described macroscopically (Fig. **F162D** and **F162E,** respectively). It is recalled that the macroscopic plastic shear strain largely reflects the presence of discrete shear zones.
- Strain, as related to the coarser neoblast size (i.e., lower stress/higher temperature conditions; Fig. **F162C**), is not easily related to either magmatic or plastic foliation development described macroscopically.

Dips of magmatic and crystal-plastic foliation

Dips of the foliation plane in the interval from 0 to 350 mbsf (Expedition 304) are diverse, but median values cluster in the 30°–50° dip range. The dip of the magmatic foliations is remarkably constant in cores from Expedition 305 and typically ranges from 35° to 60°. Exceptions are as follows (Fig. **F163**):

- Between 360 and 400 mbsf, magmatic foliation planes dip steeply, between 60° and 90°.
- In the interval between 540 and 580 mbsf, magmatic foliation planes dip steeply, between 60° and 90°; intensity is higher than in the 400–540 mbsf interval and mineral lineations are subhorizontal.
- Between 800 and 1100 mbsf, a gradual increase in the dip relative to 580–800 mbsf is observed, reaching a maximum of 60°. Between 1100 and 1200 mbsf, a sharp decrease in dip from 60° to 10°–20° is noted. This latter zone is characterized by alternating olivine-rich troctolites, troctolites, and olivine gabbro.

The dip of crystal-plastic foliation in the intensely sheared zone between 35 and 80 mbsf is diverse. In the interval with more abundant plastic strain and

shear zones at 670 mbsf, and again at 1300 mbsf, the foliations are steeply dipping, between 60° and 80°. The two shear zones at 670 and 1300 mbsf are characterized by steeply plunging mineral lineations.

Relation between rock type and fabrics

Data from both Expedition 304 and Expedition 305 indicate that magmatic foliations are most commonly recorded in olivine-rich rocks (olivine gabbros to troctolites) and most rarely in oxide gabbros (Figs. **F163A, F164A, F164B**). In contrast, crystal-plastic deformation is most commonly recorded in oxide gabbros (Figs. **F163A, F164C, F164D**). The partitioning of crystal-plastic deformation by rock type is shown in Figure **F164.** The microscopic classification of fabric intensity conveys a similar picture (Fig. **F165**). If rock types are ordered by their degree of magmatic evolution (i.e., olivine-rich troctolite → troctolite → [olivine-] gabbro → gabbronorite → oxide gabbros), the following observations are noted:

- Magmatic fabrics are poorly developed in more evolved rock types and in olivine-rich troctolites.
- Crystal-plastic strain resulting in development of small neoblasts tends to increase in more evolved rocks.
- Plastic strain resulting in large neoblasts first increases and then decreases toward more evolved rocks.

It is not clear why olivine-rich troctolites show weak magmatic foliations. Perhaps the reason is that their magmatic strain classification is based mainly on olivine, not plagioclase. It may also point to distinct crystallization processes. Microgabbros show the highest magmatic foliation intensity.

Magmatic layering

Two main types of igneous layering are recognized in core recovered from Site U1309. The first is a grain size layering, typically between coarse- and fine-grained gabbro. The second is a compositional (modal) banding, typically with a variation from mafic to more felsic zones (Fig. **F152A**). Both types of layering are commonly present together. Two further examples of layering are shown in Figure **F166.** The more subtle, repeated layers (see also **"Igneous petrology"**) are not shown in Figure **F166** because they show poorly in the photographic documentation. In Figure **F166A–F166E,** a coarse, clinopyroxene-rich band is present in a finer grained olivine-bearing gabbro. In Figure **F166F–F166J,** grain size and compositional layering are shown between a coarse-grained olivine-bearing gabbro and a fine-grained gabbronorite. Dip values of magmatic layering are shown in Figure **F163C.** Magmatic layers are also abundant in Sections 304-U1309B-10R-1 and 15R-1 through 16R-1 and Sections 304-U1309D-10R-2 through 11R-1. Below 800 mbsf, dips range between 35° and 60° (i.e., are overall subparallel to the foliation plane, even though local obliquities are observed in the core).

Igneous contacts

For descriptions of the different rock types on either side of igneous contacts, we refer to **"Igneous petrology."** Many of the unit contacts defined in that section are too diffuse to assign a reliable orientation. Invariably, orientation data on igneous contacts (Fig. **F163D**) are biased toward better defined, sharper contacts rather than the more gradational contacts. Two well-defined contacts are shown in Figure **F167.** In Figure **F167A–F167D,** gabbro in contact with microgabbronorite shares the same magmatic flow fabric. In Figure **F167E** and **F167F,** the microphenocrysts of the diabase exhibit a random texture and show no relationship to the igneous contact. In Figure **F152D,** the igneous contact between gabbro and troctolite was later exploited by a leucocratic vein. In Figure **F152E,** clasts of coarse gabbro float within micrograbbro along their diffuse contact. The intermingled region is then infiltrated by a leucocratic vein.

In general, where clear crosscutting relationships could be determined, more fractionated rocks were observed to cut more primitive rocks. These contacts commonly have orientations similar to the "local" magmatic fabric, though as a whole, their orientations are more scattered (Fig. **F168**). The appearance of only rare intact igneous contacts in some regions (between 100 and 150 mbsf, between 950 and 1050 mbsf, and below 1250 mbsf) is, in part, due to poor recovery. Macroscopic observations of the core suggest that diabases and gabbro dike contacts observed below 300 mbsf in Hole U1309D tend to cut the local magmatic fabric (Fig. **F168B**).

Preferred phenocryst alignment could be measured for a small number of basaltic and diabase units. The observation of 10°–40° dips of aligned phenocrysts in both the top and bottom of the diabase intervals in Cores 304-U1309B-19R through 20R and 15R through 16R supports correlating these units between the holes. The generally low angle dip of the phenocryst alignments suggests that the diabase units are sills. By contrast, the orientations of sharp "dike" contacts in basalt observed in Hole U1309B tend to be significantly steeper (with the notable exception of the horizontal contact in Core 304-U1309B-2R).

Magmatic veins

Veins are classified as magmatic when they are clearly tabular features with a high-temperature mineral assemblage and, preferably, where they display a contact showing interlocking grains with the host. Two examples are shown in Figure F169. They are both marked by a plagioclase-amphibole assemblage, suggesting a link to leucocratic gabbros present elsewhere in the core. Leucocratic veins are the most abundant lithology, but other vein types are present (i.e., pyroxenites, gabbros, troctolites, and Fe-Ti oxides). The oxide-rich veins are separated into two categories: deformed and undeformed (see also "Oxide gabbro" in "Igneous petrology" for a detailed description of the modes of occurrence of oxide gabbros). The boundaries of the undeformed oxide-rich zones can be, at times, diffuse; therefore, we can only show a highly limited data set (Fig. F163D). Two examples, the first of a deformed oxide vein (Fig. F170A–F170D) and the second of an undeformed oxide-rich vein (Fig. F170E–F170H), are given. The mean dip of all veins (Fig. F163D) is typically in the 30°–60° range that also characterizes the magmatic fabrics.

We describe below seven distribution maxima of magmatic veins downhole (Figs. F141, F143). In the upper 400 mbsf, maxima are observed at ~200–240 mbsf, ~270 mbsf, and ~300–350 mbsf. In the core logged during Expedition 305, there are four distinct maxima in the concentration of magmatic veins. The first, at 430–450 mbsf, commonly contains coarse pyroxene-rich veins, and seems to be associated with similar coarse magmatic intrusions in the same depth range. The second local maximum, at 560–580 mbsf, coincides with the steep magmatically foliated gabbros and troctolites and includes several gabbroic to troctolitic, schlieren-type veins and segregations. The third local maximum, between 620 and 650 mbsf, represents largely leucocratic veins associated with leucocratic and oxide gabbros with abundant epidotite alteration present in a zone with very poorly developed ductile fabrics. The fourth maximum is between 1050 and 1200 mbsf and is linked to the presence of olivine-rich troctolite and olivine-rich gabbro. These veins are similar to those between 560 and 580 mbsf (i.e., they are of schlieren/segregation type but may also be distinct grain-scale, sharply defined, more felsic veins than the host). Finally, the oxide-rich veins also appear spatially linked to oxide gabbros.

Threshold ductile brittle behavior

Crosscutting relationships involving more fractionated rock types demonstrate that melt migration is partly controlled by brittle processes at the later stages of crystallization. At the grain scale, the observation of veins filled with magmatic oxide and hornblende indicate that the presence of melt promoted microcracking during deformation of oxide gabbros (Fig. F152L). At a larger scale, late-magmatic leucocratic dikes are observed to crosscut deformed gabbroic rocks (Fig. F152E).

The gabbroic intervals in both holes (Holes U1309B and U1309D) show evidence for semibrittle deformation where both brittle and crystal-plastic mechanisms are active (e.g., Fig. F154F). The observation of schistose tremolite-actinolite, together with plagioclase that exhibits extreme undulatory extinction and very fine recrystallized grains, suggests that semibrittle deformation occurred under relatively high stresses at upper-greenschist-grade conditions.

Alteration fronts

Alteration fronts represent zones that exhibit a marked gradient of alteration and are normally associated with leucocratic intrusions. The mineralogy of the alteration fronts is detailed in "Metamorphic petrology." Most of the 14 measured alteration fronts have dips of 20°–60° but show no systematic relationship between dip angle and depth (Fig. F163D). Two well-defined alteration fronts are shown in Figure F171. In both cases, alteration decreases from the leucocratic vein zone toward the olivine gabbro.

Lower temperature deformation

Expedition 304 vein description

Alteration veins, fractures, breccias, and cataclasites record the lower temperature brittle deformation history of Site U1309. During Expedition 304, three vein types—referred to as Types 1, 2, and 3—are distributed throughout the recovered core in Hole U1309B and the upper 400 mbsf of Hole U1309D. As illustrated in Figure F172, veins consisting of carbonate, talc-tremolite (occasionally with slickensides), quartz, serpentine, and hydroscopic minerals (clays?) were also observed. Vein types are listed in Table T1 in "Metamorphic petrology" in the "Methods" chapter.

Type 1 veins

Type 1 veins are dark green and consist of high-temperature amphibole (Fig. F173A–F173C). These record the early brittle deformation history beginning in amphibolite facies at temperatures >650°C.

Type 2 veins

Type 2 veins are coeval with brecciation, cataclasis, and mineralization at greenschist grade. They are most abundant in brecciated zones, consist of actinolite and clays (saponite), and exhibit a distinctive yellow-brown color (e.g., Fig. **F173D**). The color may be derived from the presence of clays forming much later in permeable zones, at temperatures <150°C.

Type 3 veins

The third and most pervasive type of veins are green to light green in hand sample, have fibrous textures, and consist of actinolite-tremolite and, possibly, minor talc and smectite (Fig. **F173E, F173F**). Tremolite and talc-tremolite (Fig. **F173G**) veins likely formed during the same alteration event as Type 3 veins and record a greenschist alteration event that affects nearly the entire section of recovered core.

The remaining vein types include carbonate (Fig. **F173H**), quartz, serpentine, and clays. These make up the latest and lowest temperature vein sets and crosscut all other types.

Expedition 305 vein description

Examples of the types of veins observed during Expedition 305 are shown in a series of core photographs and thin section photomicrographs (Figs. **F174, F175, F176, F177, F178, F179, F180, F181**). During Expedition 305, veins were classified into four types based on color: dark green (Fig. **F174**), pale green (Fig. **F177**), white (Fig. **F178**), and gray (Fig. **F180**). The first three types are present in mafic rocks, and the latter is present in ultramafic rock. This classification is not the same as that described in **"Metamorphic petrology."**

Dark green veins (probably correlative with Expedition 304 Type 1 veins)

The dark green veins occur individually, in groups (Fig. **F174A–F174D**), and in parallel sets over a few tens of centimeters (Figs. **F174E, F178C**). They are commonly crosscut by the other types of veins. In thin section, the dark green veins commonly consist of amphibole and plagioclase (Fig. **F179A, F179B**), indicating that they formed in the amphibolite-facies regime. In the deeper sections of the core, these green veins are associated with more pervasive cataclasitic deformation of the surrounding rock (Fig. **F175**). Later brittle shear deformation tends to occur along the dark green veins, in which alteration minerals and plagioclase were fractured (Fig. **F176**). Some green veins have fibrous mineral infilling, indicating that they are fault veins.

Pale green veins (probably correlative with Expedition 304 Type 2 and Type 3 veins)

The pale green veins may be further divided into two types based on the presence of alteration halos. The orientation of the pale green veins without alteration halos varies from subhorizontal to steeply dipping, with both alteration zones having subparallel sets and randomly distributed sets of veins (Fig. **F177A–F177C, F177E**). The pale green veins with alteration halos sharply cut the gabbro, and alteration halos are typically a few centimeters thick (Fig. **F177F**). Apart from the alteration halos, the pale green veins are characterized by fiber textures of the mineral infilling, primarily talc and tremolite (Fig. **F177B**). Despite the variable dip of these veins, the fiber orientations are primarily subhorizontal (Fig. **F177B**) (see **"Fault rocks,"** below). In thin section, some pale green veins are observed to consist of epidote, chlorite, and actinolite (Fig. **F179C, F179D**). These mineral assemblages indicate that the veins formed at greenschist-grade conditions.

White veins

The white veins are present dominantly as sets of open cracks with carbonate and local sulfide infillings (Fig. **F177A**). The white veins crosscut the pale green (Fig. **F178B**) and dark green veins (Fig. **F178C**). Locally, large, steeply dipping white veins are present in Section 305-U1309D-136R-3 (Fig. **F178D**). The white veins are also associated with cataclasis (Fig. **F178E, F178F**). In thin section, white veins commonly crosscut pale green veins (Fig. **F179C, F179D**). Although most white veins are filled with carbonate, some are crack-seal veins with fibrous chlorite and, locally, prehnite (Fig. **F179D**). These mineral assemblages represent formation conditions that are at a lower temperature than the pale green veins described above, suggesting that they formed at the latest stage of the evolution history.

Gray veins and related fibrous veins in olivine-rich troctolites

Gray veins are present locally in olivine-rich troctolites. They do not show evidence for distinct deformation features (Fig. **F180**). In thin section, the veins consist of serpentine and chlorite, with chlorite present locally (Fig. **F180F–F180J**). These veins show little evidence for deformation, suggesting that they formed by replacement reactions along microcracks. The gray veins either crosscut or are crosscut by serpentine foliation.

Some fibrous gray veins have alteration halos, for example at ~1126 mbsf (Fig. **F181**). The fibrous minerals consist of tremolite, and the fibers are oriented obliquely from the wall toward the vein center (e.g., broken white line in Fig. **F181**), suggesting synkine-

matic shear during vein opening. For the example shown in Figure F181D, a normal sense of shear in the core reference frame was determined from the fibrous growth. In addition, some fibrous minerals exhibit weak plastic deformation.

Downhole distribution and orientation of veins

As illustrated in Figure F182, vein intensity generally decreases with depth in Hole U1309D, with superimposed "peaks" observed throughout. As described below, these peaks are present at depths where other data sets also indicate structural boundaries. In the upper 400 mbsf of Hole U1309D, intervals of relatively high vein intensity also coincide with the presence of ultramafic rocks and olivine-rich troctolites in Cores 304-U1309D-10R, 32R, and 56R. Based on the degree of alteration, these rock types apparently were more reactive than gabbroic rocks under the same conditions. A somewhat abrupt decrease in the overall vein intensity is observed below the sequence of faults in the interval between ~750 and ~785 mbsf (Fig. F182) and corresponds to the transition from structural Unit 2 to structural Unit 3.

Downhole plots comparing the intensity of veining in Hole U1309B and the upper 130 mbsf in Hole U1309D are shown in Figure F183. For the correlative depths, the vein intensity is greatest (1–3.5) in the upper gabbros of both holes (gabbro Zone 1 in Hole U1309D as defined in "Igneous petrology") and then decreases (intensity ≤ 1) in gabbroic and troctolitic units (~64–94 mbsf in Hole U1309B and ~62–83 mbsf in Hole U1309D). In Hole U1309B, inferred faults separate regions with different vein intensity. The variation in vein intensity in the upper 130 mbsf of Hole U1309D is closely associated with the presence of Type 2 veins, which are present throughout the gabbro and troctolite and are most common in zones that experienced intense brittle deformation (Fig. F184). Vein intensity is also closely related to rock type, especially diabase. In both holes, diabase units show the least intense brittle deformation and vein intensity. Vein type in the diabase from both holes is restricted to Type 3 veins, blue-green actinolite + smectite veins (similar to Type 3), and a few Type 2 veins (Fig. F184). The presence of Type 2 veins in diabase is restricted to regions where brecciation was observed at the diabase margin in Cores 304-U1309B-5R and 6R and 304-U1309D-1R. These observations indicate that diabase units postdate Type 1 veins, are synchronous with Type 2 veins, and predate Type 3 veins.

For the core logged during Expedition 304, the compositional variability of veins with depth is shown in Figures F172 and F184. Type 1 veins are most abundant between 20 and 80 mbsf and absent between ~240 and 400 mbsf (Fig. F172A). By contrast, late-magmatic leucocratic dikes are most abundant between 195 and 400 mbsf (see also Fig. F141). The Type 2 and 3 veins are distributed throughout the upper 400 m of the core, although there are no Type 2 veins observed between ~80 and 130 mbsf (Fig. F172B, F172C). Talc-tremolite veins on fractures are generally restricted to depths of 140–290 mbsf; however, this vein type is similar to the "late tremolite (± talc) associated with olivine-rich rocks" shown in Figure F172C. Type 2 veins associated with brecciation are present throughout the upper 400 mbsf. The lowest temperature veins (serpentine, talc-tremolite, and late carbonate veins) are plotted on Figure F172D.

The vein sets record retrograde metamorphism, and crosscutting relationships indicate that some veins act as sites for fluid migration over a wide range of temperatures. The intrusion of thin leucocratic dikes (plagioclase + hornblende assemblages) was followed closely by Type 1 vein formation. These late-magmatic leucocratic dikes apparently acted as fluid pathways for much of the alteration history; they are commonly overprinted by Type 1 and Type 3 veins. Based on a limited number of observations, Type 2 veins predate Type 3 and talc-tremolite veins. Serpentine, carbonate, and quartz veins are younger and cut all other fabrics and vein types. Talc and carbonate veins commonly cut serpentine veins; these, together with prehnite and clay veins, are the youngest.

Histograms of vein dips for the upper 132 mbsf of Hole U1309D show a weak concentration in the range of 40°–75° (Fig. F185). To simplify the presentation of data for the upper 400 mbsf of Hole U1309D, average dip and the standard deviation are plotted on Figure F172E–F172G. Standard deviations about the mean dip orientation are 15°–23°. However, there is a suggestion that the dips of Type 2 and 3 and talc-tremolite veins covary across inferred fault zones at depths of ~255 and ~285 mbsf.

For the core logged during Expedition 305, the identified vein types (Fig. F186) show no clear trend in dip between 400 and 1415 mbsf. Figure F187 shows the dip distribution of fault veins (Fig. F187A, F187B), open cracks, cataclastic veins (Fig. F187C), and dark green (Fig. F187D), pale green (Fig. F187E), and white veins (Fig. F187F) logged during Expedition 305. The average dip of all fault veins is ~55°, and there is a progressive increase of the average dip from white to pale green to green and to faults with fibers, which have a steeper plunge (Fig. F187B). All veins, open cracks, and cataclastic veins have aver-

age dips of ~40°–55°, with large standard deviations and no clear trend (Fig. F187C–F187F).

Cataclastic deformation

Cataclastic deformation is divided into five categories:

1. Relatively thick zones of brecciation/cataclasis, including faults and semibrittle shear zones (Fig. F188A–F188D, F188E–F188G);
2. High-temperature diffuse cataclastic bands associated with late-magmatic leucocratic intrusions (Fig. F173D);
3. Low-temperature diffuse cataclastic bands associated with greenschist-grade (Type 2 and Type 3) veins (Fig. F188A);
4. Open fractures along low-temperature veins; and
5. Microfractures and veins associated with serpentinization (i.e., serpentine foliation) (Fig. F188H).

Fault rocks

Description of fault rocks from Expedition 304

In Hole U1309B, three fault zones are recognized. Two are at the boundaries between diabase and gabbro (lithologic Unit 23) and between peridotite and diabase (Units 32–33); the other is in the lower gabbro unit (Unit 48). Similar cataclasites were also observed in Core 304-U1309D-1R. However, there are also numerous examples of rocks that deformed by semibrittle mechanisms at greenschist-grade conditions (Fig. F188D, F188E, F188F). Most of the cataclastic deformation in gabbro units is associated with the intrusion of late-magmatic leucocratic veins with subsequent overprinting by greenschist-grade vein networks. Synmagmatic cataclastic deformation in diabase is associated with greenschist-grade hydrothermal brecciation (Fig. F188B, F188C). Microfracturing associated with alteration of both ultramafic rocks and olivine-rich gabbroic rocks resulted in the formation of a serpentine foliation (Fig. F188H).

High-temperature cataclasites are associated with late-magmatic leucocratic intrusions, which are almost always overprinted by greenschist-grade vein networks (Fig. F188G). Plagioclase is usually present as fine-grained, subhedral crystals (<0.2 mm in size). These breccias display a clast-matrix texture that formed during amphibolite- or greenschist-grade deformation. The clasts in these breccias range in size from 10 µm to 5 mm and comprise plastically deformed or brecciated gabbro and hornblende veins. In addition to these gabbro clasts, clasts of diabase and basalt are found in breccia zones in Hole U1309B and the upper 130 m of Hole U1309D (Fig. F188C). The matrix contains <10 µm diameter plagioclase and actinolite grains that locally form a weak cataclastic foliation. In contrast to intense cataclastic zones, diffuse zones of cataclasis do not show clast-matrix texture but instead display pervasive microcracking and incipient brecciation. Evidence for semibrittle deformation and alteration of plagioclase is commonly observed in high-temperature late-magmatic leucocratic zones of cataclasite (Fig. F188G), whereas in low-temperature cataclastic zones, isotropic growth of tremolite is common (Fig. F188F).

Description of fault rocks from Expedition 305

Four fault zones were identified during Expedition 305 by the presence of coherent cataclasite (Fig. F189). Apart from the brittle deformation associated with the detachment zone in the upper part of the core, the fault zone at ~750 mbsf represents the zone with the most significant slip recovered in Hole U1309D.

The most shallow fault zone recovered during Expedition 305 appears at 695 mbsf in Section 305-U1309D-141R-1. The recovered cataclasite is ~2 cm thick. It is well developed and indicates apparent reverse movement along the fault in the core reference frame. The lower boundary of the fault zone shows a sharp contact against cataclastic gabbro (Fig. F189A). In thin section, plagioclase fragments are present in a matrix of mostly chlorite and actinolite, suggesting that the related alteration occurred under greenschist-facies conditions.

A structurally deeper fault zone is located at 746 mbsf in Section 305-U1309D-152R-1 (Fig. F189B, F189C). Two pieces with well-developed ultracataclasite are present in Section 305-U1309D-152R-1. Foliation in the first cataclasite dips 55°, with overall reverse displacement in the core reference frame (Fig. F189B). The fault zone is at least 10 cm thick, but poor recovery precludes a precise measurement. The deeper fault zone is a minimum of several centimeters thick and shows well-developed planar fabrics. Reverse movement (core reference frame) can be determined from geometries of fragments similar to S-C fabrics in mylonite (Fig. F189C). In thin section, microstructural evidence also suggests reverse sense of movement in the core reference frame (Fig. F190A, F190B). Coarse plagioclase grains are highly fractured with moderate undulatory extinction, suggesting that the cataclasite developed by semibrittle mechanisms. Within the fault zone, plagioclase and, locally, amphibole fragments are present in a chlorite and actinolite matrix (Fig. F190C, F190D), indicating that alteration occurred under greenschist-facies conditions similar to those associated with the formation of pale green veins with chlorite and actinolite infilling. In this interval, only 0.8 m of core was recovered from 4.8 m of drilling. This poor recovery is probably related to the presence of lightly

fractured fault rocks. It is therefore likely that a substantially wider zone of brittle deformation exists in this interval. Formation MicroScanner (FMS) images of the borehole walls acquired during logging show a south-dipping structure at ~765 mbsf slightly deeper in the hole, and an east-dipping structure is also recognized (see **"Downhole measurements"**). These structures may be related to the fault zone.

The third zone of cataclasis is located at 785 mbsf in Section 305-U1309D-161R-1 (Fig. **F189D**). It consists of 90% matrix with tiny fragments. The zone is subhorizontal, is a few centimeters in thickness, and has reverse-zone movement in the core reference frame. In thin section, pyroxene and plagioclase fragments are present in a carbonate matrix, indicating that the latest slip occurred under very low temperature conditions, probably <100°C.

The deepest zone of significant cataclasite was recovered at 1107 mbsf in Section 305-U1309D-230R-2 (Fig. **F189E**). The zone of very high strain ultracataclasite is thin (<10 mm), but the cataclasite zone is >10 cm thick and associated with veining around the fault zone. In thin section, protolith minerals are intensely fractured and bent/kinked with local calcite infilling. The mineral assemblages in the fault zone are similar to those in the fault zone at 785 mbsf.

Cataclasis is common along contacts between diabase intrusions and the adjacent gabbro (Fig. **F191**). In thin section, previously formed amphibole and plagioclase grains were fractured along the chilled margin of the diabase dikelet (Fig. **F191B–F191E**).

Serpentinization

Olivine-rich rock types are variably serpentinized; no systematic alteration of pyroxene to serpentine was observed (e.g., bastites). At scales ranging from core pieces (Fig. **F192**) to thin sections (Fig. **F193**), the degree of serpentinization is highly variable, ranging from <10% to >70%. Microstructural observations of moderately (<50%) serpentinized rocks indicate that alteration of olivine to serpentine initiated along irregular microfracture networks within coarse-grained olivine crystals (Fig. **F193B**). The serpentine-filled cracks in olivine commonly extend into adjacent pyroxene and plagioclase grains, where they may also be marked by serpentine infill. Serpentinization results in an irregular foliation, consisting of networks of branching and anastomosing serpentine veins with associated oxides (Fig. **F193C**). Some serpentinites are cut by talc-tremolite shear zones. One steeply southeast-dipping fault zone recognized in Hole U1309B (Figs. **F115A, F188E**) displays offset cleavages and oblique foliations that indicate a reverse sense of shear (in the core reference frame).

The process of serpentinization appears to be nominally static. Weakly altered or fresh olivine-bearing gabbros exhibit pervasively cracked olivine grains that are crosscut by an irregular network of fractures and little associated strain. Water percolation along these microfractures promoted serpentinization, with a progression from thin veins of serpentine along microcracks to progressive growth of these veins and, finally, a mesh texture. Fully serpentinized zones show pseudomorphs of olivine, and the magmatic textures, when recognizable, show no apparent shear displacement (Fig. **F193A**). In addition, microstructural observations suggest little or no dilation associated with serpentine vein formation in weakly altered rocks (Fig. **F193B, F193D**), as the magmatic texture of the surrounding, unaltered minerals (plagioclase and pyroxene) is not affected. Thus, serpentinization appears to have occurred without significant volume increase at the thin section scale, suggesting dissolved material was removed by the serpentinizing fluids during the hydration process.

Downhole distribution and orientation of fault rocks

The average intensity of cataclastic deformation is highest near the top of Hole U1309D, presumably related to detachment faulting, and becomes quite low (5 m average = <1) at depths below the fault zone at ~785 mbsf (Fig. **F182**). In the upper 100 m of Holes U1309B and U1309D, cataclastic deformation with an intensity of 3 and greater is concentrated in the upper gabbro units (Cores 304-U1309B-7R through 11R and 304-U1309D-4R through 8R) (Fig. **F194**), where many late-magmatic leucocratic dikes and low-temperature veins are present. Most diabase units have a cataclastic fabric intensity <1; a few diabase units in Cores 304-U1309B-2R through 4R and 304-U1309D-1R have an intensity >2. Although fault rocks with gouge or healed breccia cataclasite that are similar to those observed in Hole U1309B were not as abundant in Hole U1309D, the presence of a few locations with intense cataclastic deformation implies the existence of faults. These zones are shown as dotted lines in downhole figures. Deeper in Hole U1309D, several intervals with cataclastic fabric intensities ≥3 are present from 140 to 290, 600 to 650, 700 to 800, and at ~1100 mbsf.

Figure **F195** shows the downhole dip magnitude of cataclastic fabrics above 130 mbsf in both holes. Diffuse late-magmatic leucocratic cataclastic zones are most abundant at depths above 60 mbsf in both holes. By contrast, the low-temperature diffuse cataclastic zones are distributed evenly. In general, the dips of low-temperature diffuse cataclastic zones are widely scattered, although local concentrations with more restricted dips are observed. For example, there is a local concentration of dips between ~20° and 60°

at depths between 65 and 80 mbsf in Hole U1309D, which may correlate with a similar group observed at depths between 80 and 90 mbsf in Hole U1309B.

Figure F196 shows the downhole dip magnitude of cataclastic fabrics and rakes of mineral striae on low-temperature veins in Hole U1309D to ~400 mbsf. Dips of fault and semibrittle zones range from 10° to 60°, whereas striated fault veins dip as much as 85°. The fault veins are primarily distributed in the interval between 140 and 350 mbsf and show oblique slip to dip-slip displacement. Normal sense displacement is observed for almost all oblique slip faults. Dips of late-magmatic leucocratic cataclastic zones and low-temperature cataclastic zones are widely scattered; late-magmatic leucocratic intrusions are primarily distributed in three intervals: from 35 to 80 mbsf, 190 to 250 mbsf, and 290 to 400 mbsf.

Veins with fibers are good indicators of late-stage shear sense and slip. During Expedition 305, fault veins were identified (Fig. F197) corresponding to the dark and pale green veins (see **"Expedition 305 vein description"**). Although there is no apparent systematic dip or variation of dip with depth (Fig. F197A, F197B), >60% of the observed plunges of fibers are <30° and only ~15% of them plunge at angles >60°. Assuming no significant rotation since the formation of these fibers, these fault veins indicate primarily oblique-slip deformation, with no clear indicators of sense of shear.

Downhole distribution and orientation of open cracks and drilling-induced fractures

Open cracks identified along the core as not being related to drilling show a very low overall intensity (predominantly values of <1; see **"Structural geology"** in the "Methods" chapter), with no marked trends (Fig. F198). In several intervals of the core, open fracture intensity (particularly the 5 m running average) shows an anticorrelation with rock recovery (Fig. F198A) and correlation with the intensity of drilling-induced fractures (Fig. F198C). The intensity of open and drilling-induced fractures is relatively high in the interval between 720 and 750 mbsf, where the average recovery is low (<50%) and where several fault zones are identified. A zone of intense drilling-induced fractures is also found at ~1200–1300 mbsf, below the olivine-rich troctolite unit at ~1200 mbsf; this interval also coincides with a zone of low recovery (Fig. F198). There is no correlation between the intensity of open fractures and recovery in this interval. Open fractures appear to be one of the latest deformation events, and in the interval between 575 and 775 mbsf they are often associated with sulfides.

Downhole distribution and orientation of serpentine foliation

The vertical distribution of the dip and intensity of serpentine foliation are shown in Figure F199. Zones with low-to-moderate values (intensity ≤ 3) are concentrated in the upper part of the borehole (300–530 mbsf), along a broad zone ~30 m thick at ~560 mbsf and over the interval between ~1090 and 1235 mbsf corresponding to olivine-rich rock types (Fig. F199A). Between 675 and ~1000 mbsf, serpentine foliation is scarce and more localized and has very low intensity values. The dips of serpentine foliation are random, showing variations in orientation at scales <1 m (i.e., along individual core pieces). Similarly, the degree of serpentinization varies at length scales <1 m in intervals with similar olivine content. This heterogeneity in the structure and degree of serpentinization is also observed at the thin section scale (Fig. F193). There is little or no correlation between the degree of total alteration (see **"Metamorphic petrology"**) and serpentinization in the upper 900 m of the Hole U1309D, but the zone with intense serpentine foliation at ~1090–1235 mbsf corresponds to overall alterations of >50% with very strong local alteration gradients.

Correlation of cataclastic fabrics and rock type

Histograms of cataclastic fabric intensity (Cf) illustrate the relationships between rock types and cataclastic deformation (Figs. F200, F201). Whereas the majority of plutonic rocks of Hole U1309B are cataclastically deformed, the diabase and basalt units are largely undeformed. This suggests that diabases and basalts formed late with respect to detachment faulting. In contrast, below 400 m in Hole U1309D, diabase and oxide gabbro show higher intensities of cataclastic strain than other rock types (Fig. F201). The intensity of cataclastic deformation diminishes below the fault zone recovered at ~785 mbsf, suggesting that rocks above and below this boundary accommodated different magnitudes of brittle strain.

Locally, cataclasis also concentrates along leucocratic veins. Enhanced cataclasis in diabase, oxide gabbro, and leucocratic veins appears to reflect the semibrittle mode of emplacement for these rock types, which formed relatively late in the magmatic history. In Hole U1309D below 400 mbsf, olivine-rich rock types have undergone less overall cataclastic deformation than gabbros, which, in turn, bear less cataclastic deformation than oxide gabbros (Fig. F201). A significant proportion of the gabbro and olivine gabbro logged during Expedition 304 have Cf = >1, whereas oxide gabbros and ultramafic rocks are less cataclastically deformed (~20% have Cf = >1) and troctolites are even less. At this stage it is not clear

whether this reflects the proximity of certain rock types to the detachment fault or another model needs to be invoked.

Correlation of cataclastic fabrics and logging data

We investigated the correlation between cataclastic deformation intensity and downhole logging results in Holes U1309B and U1309D (see **"Downhole measurements"**). Owing to the lack of paleomagnetic data in zones of poor recovery, we have few orientation data on fault zones, per se, to compare with logging data. However, several fault zones inferred from core observations in Hole U1309B (especially those at 60 and 80 mbsf) correspond to fault zones inferred from FMS images. In Figure **F202A,** we show the intensity of cataclastic fabrics in Hole U1309D averaged over 5 m intervals; the depths of possible fault zones are shown based on core observation. These locations correlate relatively well with the depths of faults inferred from resistivity and porosity data (Fig. **F202B**). In several cases, no rocks were actually recovered at the exact depth of the fault identified from the logging data. For example, the fault observed at 108 mbsf in the logging data corresponds to a depth where there was no recovery in Hole U1309D. However, in these cases, high cataclastic intensity, involving local brecciation, is observed in the adjacent rock.

Reorientation of structure data using paleomagnetic data

Paleomagnetic data were used to constrain the orientation of structural features in a geographic reference frame. The average inclinations of the remanent paleomagnetic vectors in samples recovered from the upper parts of both holes (all of Hole U1309B and the upper ~180 m of Hole U1309D) are amazingly consistent with that expected for the latitude of Atlantis Massif (Figs. **F203, F204**), suggesting that only modest tectonic rotations on a presumed ridge-parallel horizontal axis have occurred since the remanence was attained. Based on this hypothesis, we rotated cores for which both structural and paleomagnetic data were obtained about a vertical axis such that the declination of the remanent vector in each core was the same; only data from Hole U1309B and the upper 120 m of Hole U1309D were used in this analysis. The orientations of structures were placed in geographic coordinates by assuming that this vector plunges upward to the south (for reversed polarity) or downward to the north (for normal polarity). Caveats regarding this analysis must be kept in mind:

- Logging data indicate that Hole U1309B deviated 7° from vertical (it plunges 83° toward an azimuth of ~42°), but we did not account for this deviation in this preliminary analysis.
- The orientations of high-temperature structures may have rotated significantly between their formation (at magmatic temperatures) and the time when magnetic remanence was obtained (at ~520°–600°C). Modest counterclockwise rotations on axes subparallel to the ridge axis would not change the inclination of the remanent vector significantly. For example, a counterclockwise rotation of 20° about an axis oriented at 00°/010° (plunge/trend) would produce no net change in the inclination of the remanent vector. Thus, significant rotation of structures can occur below the remanence acquisition temperature, although they are not detectable using paleomagnetic data. By contrast, a counterclockwise rotation of ~60° would produce a ~20° shallowing of the remanent inclination; such rotations would be resolved by paleomagnetic data.
- On a sample by sample basis, there may be as much as 20° uncertainty in the orientation of the remanent vector relative to the geographic poles owing to secular variation.

The orientations of crystal-plastic and magmatic structures reoriented using the paleomagnetic data are shown in Figure **F205.** No strong preferred orientation of magmatic fabrics is observed. This observation is consistent with our macroscopic examination of the core, through which we documented relatively large changes in the orientation of compositional banding across narrow intervals within individual pieces (e.g., in Sections 304-U1309D-12R-1 [Piece 6] and 12R-2 [Piece 9]). For crystal-plastic deformation, fabrics dip toward the west-southwest; lineations, where observed (the best examples of which were in Core 304-U1309D-8R), plunge down-dip.

Stereonet diagrams displaying vein orientations from selected samples rotated into a common geographic reference frame using paleomagnetic data are shown in Figure **F206.** Type 1 veins in Hole U1309D preferentially dip to the north at ~25°, but no preferred orientation of Type 1 veins is evident. The orientations of Type 2 veins are apparently random in the upper 40–50 m of both holes. In contrast, at depths between 50 and ~80 mbsf, Type 2 veins dip ~35° to the east-northeast in both holes (Fig. **F207**). Type 3 veins dip predominantly toward the east in Hole U1309B (Fig. **F207A**); a similar concentration of Type 3 veins is observed for Hole U1309D, in addition to a small population of possibly conjugate veins that dip to the west (Fig. **F207B**). The orientations of Type 3

veins do not change significantly with depth. The similar orientations of Type 2 and Type 3 veins suggest that they formed in approximately the same stress field during upper to lower greenschist-grade conditions.

Cataclastic fabrics reoriented using paleomagnetic data are shown in Figure F208. Cataclastic zones generally dip shallowly to the north, whereas a majority of low-temperature cataclastic bands dip northeast. The orientations of late-magmatic leucocratic cataclastic bands are widely scattered. These trends are consistent between Holes U1309B and U1309D.

Summary of crosscutting relationships

Below we provide a summary of crosscutting relationships based on a combination of core description and thin section observations (from oldest to youngest; in this list, the symbol ≤ indicates "younger or the same age as"):

a. High-temperature (~1200°C) deformation of peridotite
b. Impregnation of residual peridotite by basaltic melt to form wehrlite
c. Formation of cumulate dunites and magmatic flow of layered gabbros and troctolites
d. ≤ c. Intrusion of coarse-grained gabbro cutting harzburgite in Hole U1309B
e. Gabbro cutting troctolite (e.g., Core 304-U1309D-8R)
f. Intrusion of oxide gabbros
g. ≤ f. High-temperature, granulite-grade crystal-plastic flow concentrated in gabbros
h. Late-magmatic leucocratic dikes and high-temperature hornblende veins cut crystal-plastic foliation
i. Relatively widespread but low-strain veining and semibrittle deformation of gabbros (predominantly lower amphibolite through greenschist grade)
j. Intrusion of diabase sills (predominantly lower amphibolite through greenschist grade)

(somewhere between i and k) Serpentinization of harzburgite

k. ≤ j. Greenschist-facies brecciation and faulting
m. ≤ l. late talc, prehnite, and carbonate veins
n. Exhumation and denudation at low temperatures

Definition of structural units

Based on a combination of the spatial distribution of structural observations and other shipboard data, we defined structural units for the core logged during Expeditions 304 and 305. These structural units are intended to (1) be used as guides to evaluate which structures played a larger role in the tectonic evolution of the region and (2) define intervals of the cores that shared common deformation histories. Each of the structural unit boundaries coincides with a boundary identified through petrological or geochemical observations, relatively high cataclastic deformation intensity, and the location of faults identified in the logging data.

Hole U1309B

Hole U1309B contains three structural units (from bottom to top):

- Structural Unit 1a, a basalt-diabase brecciated unit;
- Structural Unit 1b, a generally coarse grained gabbro unit, which includes an intrusive contact with serpentinized peridotite; and
- Structural Unit 1c, a magmatically layered gabbro unit.

Hole U1309D

Upon drilling the rock below 130 mbsf in Hole U1309D, the scale of observations provides a different perspective for the definition of structural units. Based on the observations in Hole U1309D, three structural units were identified. In Figure F209, we illustrate the downhole intensity plots for magmatic, crystal-plastic, vein, and cataclastic fabrics averaged over 5 m intervals to 400 mbsf (Expedition 304). In addition, we show the faults that were identified by comparison of the cataclastic deformation intensity and the logging data during Expedition 304. Finally, we show the depths where there are significant concentrations of the different vein types by vertical bars. The boundary between the units (red lines in Figs. F209, F210, F211) are

- Structural Unit 1, 0–176.3 mbsf;
- Structural Unit 2, 176.3–785 mbsf (structural Unit 2 may be split into Subunits 2a and 2b with a boundary at 257.2 mbsf) (pink line in Fig. F209);
- Structural Unit 3, 785–1415.5 mbsf (structural Unit 3 may be split into Subunits 3a and 3b with a boundary at ~1100 mbsf).

In all cases, the boundaries should be considered as approximate.

As illustrated in Figure F209, the base of structural Unit 1 is defined by a relatively thick zone of crystal-plastic deformation and a zone of high vein and cataclastic fabric intensity. It also marks the initiation of a second zone of relatively high crystal-plastic and magmatic deformation intensity. The boundary between structural Units 1 and 2 includes the fault ob-

served at 170 mbsf, which is well located by the logging data and marks the initiation of a new zone of high-temperature amphibole veins. The base of structural Unit 1 is coincident with the base of gabbro Zone 3 as defined in **"Igneous petrology"** (Expedition 304). Finally, the base of structural Unit 1 also defines the depth where a significant decrease in the inclination of the remanent paleomagnetic vector begins.

The base of structural Subunit 2a is defined by the depth at which the zone of relatively high crystal-plastic deformation stops and a zone of relatively high cataclastic deformation intensity that correlates well with the logging data. The base of structural Subunit 2a is also marked by an abrupt increase in the inclination of the remanent paleomagnetic vector (Fig. **F210**) and the base of gabbro Unit 5. The remainder of structural Unit 2 (Subunit 2b) is characterized by a generally low intensity of deformation fabrics.

The boundary between structural Units 2 and 3 at ~785 mbsf (Fig. **F211**) is defined by the base of a sequence of faults identified between ~700 and ~785 mbsf. This zone also marks the location of an abrupt decrease in both the intensity of veins and cataclastic deformation and a relatively abrupt decrease in Mg# (~600 mbsf). Structural Unit 3 is characterized by very low intensity of both high- and low-temperature deformation. The boundary between structural Subunits 3a and 3b (~1120 mbsf) is marked by a fault zone, a down-temperature deflection in the data recorded by the TAP tool (see **"Downhole measurements"**)—which suggests fluids are moving along this fault zone—and another rather abrupt decrease in the inclination of the remanent paleomagnetic vector (see **"Paleomagnetism"**).

Correlations between Holes U1309B and U1309D

Below are listed, in order of confidence, the pro and con arguments to correlate structures and rock types recovered in Hole U1309B and in the upper 130 m of Hole U1309D (Fig. **F212**).

1. Diabase units in Cores 304-U1309B-19R through 20R and 304-U1309D-15R through 16R.
   - Pro: Correlation of MS and orientation of phenocryst alignment.
2. Lower layered gabbro sequence in Cores 304-U1309B-15R through 18R and gabbro Zone 2 in Cores 304-U1309D-11R through 14R (and perhaps 17R).
   - Pro: both units have similar vein and brittle deformation fabrics, lithology, and magmatic deformation fabrics.
   - Con: the sequence in Hole U1309D has a slightly higher crystal-plastic deformation intensity.
3. Upper gabbro sequence in Cores 304-U1309B-8R through 11R and gabbro Zone 1 in Cores 304-U1309D-4R through 10R.
   - Pros: both units have similar intensities of cataclastic fabric, vein intensity, and crystal-plastic fabric. In addition, the orientations of veins and crystal-plastic foliations are similar in these two sequences.
   - Cons: gabbros in Hole U1309D are more primitive and exhibit a higher intensity of magmatic fabric.
   - Cross-examination: the observation that crystal-plastic deformation appears to postdate intrusion of gabbro into "troctolites" indicates that differences in lithology predate most of the deformation, and therefore juxtaposition, of these gabbro sequences.
4. Ultramafic rock in Cores 304-U1309B-11R and 304-U1309D-10R.
   - Pros: similar structural position; similar lithology; the base of both units appears to mark a major change in deformation style and orientation of brittle fabrics.
   - Cons: Although we have evidence for a fault beneath Core 304-U1309B-11R from both examination of the core and logging data, no evidence for a fault was observed at the base of either Core 304-U1309D-10R or the top of Core 304-U1309D-11R. Although these units represent the only ultramafic rocks recovered above 130 mbsf and they both show evidence for high-temperature mantle deformation, they are not strictly the same rock type (as described in **"Geochemistry"** and **"Igneous petrology"**).
5. Diabase units in Cores 304-U1309B-5R through 6R and 304-U1309D-2R through 3R.
   - Pro: some correlation of phenocryst alignment, parallel to lower diabase unit.
   - Con: correlation of phenocryst alignment is better between Cores 304-U1309B-5R through 6R and Core 304-U1309D-7R.
6. Diabase units in Cores 304-U1309B-12R through 13R and 304-U1309D-7R.
   - Pro: general structure parallel to diabase units described above.
   - Con: parallel phenocryst alignment is not obvious.

Based on these observations, we present a schematic cross section of this region in Figure **F212.** There is evidence for relatively large "brittle" faulting with offsets of tens of meters. The prominent zone of cataclasite at 81 mbsf in Hole U1309B correlates with a

conductive horizon in the downhole FMS log. This fault dips 50°–64° southeast, with an apparent dip of up to 50° in the north-south direction. Cataclastic deformation and low-temperature alteration is observed near 36 mbsf in Hole U1309D (near the updip projection of the fault). In this case, using the uppermost and lowermost diabase units in Hole U1309B as markers, the diabase between 44 and 48 mbsf requires either a steeper dip than the other two diabases or a normal offset by the fault. Although the exact trace and timing of this fault is not resolvable from the core data, this fault is probably the best example of a steeply south-dipping fault and, possibly, part of an extensional system controlling syn- to post-greenschist-grade denudation of the central dome.

Discussion

Hole U1309D penetrated 1415.5 m into the footwall of a major oceanic detachment fault system. Some of the major structural questions which will eventually have to be resolved concerning the formation of Atlantis Massif are as follows:

- Did the initial unroofing of plutonic rocks occur along a shallow or steeply dipping detachment system (Karson, 1991; Tucholke et al., 1998)?
- Did the detachment system root deeply and undergo deformation at high temperatures (Tucholke et al., 1998) or at a gentle dip at low temperatures (MacLeod et al., 2002; Escartin et al., 2003)?
- Can denudation be explained by a single master fault, or is a system of faults required; does the plutonic history of the footwall block reflect the operation of a syntectonic normal fault?

Research results from Expeditions 304 and 305 should eventually help to resolve these problems.

Near-surface structures (upper 170 mbsf)

The upper ~170 mbsf of Hole U1309D shows several characteristics that differ from the rest of the hole:

1. The presence of fault schist with residual mantle origin (i.e., relict spinels) (see **"Igneous petrology"**).
2. An abundance of fine- and coarse-grained undeformed diabase and basalt.
3. More abundant plastic deformation at granulite facies.
4. Greater lithologic heterogeneity, including the presence of mantle rocks (upper 170 mbsf). None of these features are present farther downhole in Hole U1309D.

The history of faulting at lower-amphibolite through upper-greenschist conditions is not well represented in the upper 170 mbsf. Very low strain semibrittle deformation in the gabbros is primarily amphibolite to upper greenschist grade. Rare samples of talc-tremolite schist preserve semibrittle fault textures and provide evidence for syntectonic alteration of ultramafic units. These schists are preserved either within or near diabase sheets and basaltic breccias that postdate the alteration. In some cases, these deformation fabrics are cut by coarse-grained, isotropic tremolite, suggesting that fault zones became more localized at lower temperatures. Most greenschist-grade alteration is static, including post-tectonic actinolite distributed throughout the gabbros and younger diabase.

We cannot ascertain at this stage if the relative abundance of granulite grade deformation in the upper 170 mbsf is an early expression of the detachment faulting or if it possibly relates to strain gradients during intrusion of a pluton into an ultramafic environment.

Deformation below 170 mbsf

There is a lack of major discontinuities below 170 mbsf. Prominent zones of magmatic fabric and low deformation are located at ~220 mbsf (magmatic foliation; 40° dip), 560 mbsf (magmatic foliation; 60° dip), 660 mbsf (high crystal-plastic strain; 70° dip), 685–790 mbsf (three greenschist cataclastic fault/shear zones; 50°–60° dip), 1107 mbsf (greenschist grade, cataclastic), and 1300 mbsf (crystal-plastic strain, 70° dip). For a surprisingly large number of the plastic and cataclastic shear zones, reverse senses of shear in the core reference frame could be inferred.

Shear-zone indicators do not allow a simple relationship between the exposed detachment at the surface of Atlantis Massif (which presumably has a shallow dip and normal fault geometry). Internal deformation below 170 mbsf in Hole U1309D is localized along shear zones and developed as cataclasites, but these structures appear to be minor compared to the detachment fault and are not easily related to the deformation history of the detachment fault system. We conclude that relative to the presumably extremely high strain of the exposed detachment fault, the footwall block behaved as a generally coherent block, at least below ~170 mbsf. The detachment-related deformation appears confined to the upper 170 m; the rest of the structures observed correspond to either deformation prior to the detachment (i.e., emplacement in the lithosphere of the different rock types) or to local zones accommodating differential

strain during denudation and/or flexure of the footwall.

High-temperature history

Only a minor fraction of all gabbroic rocks recovered from Hole U1309D shows a magmatic foliation (i.e., ~22%). This suggests a tectonically stable environment, unlike the dynamic environment of mantle flow turnover inferred by some for fast-spreading ridges and as mapped, for example, in the Oman ophiolite (Nicolas et al., 2000). Whether this implies a setting within the lithosphere or at the base of the lithosphere cannot be resolved at this stage. To this end, the resolution of the pressure of formation of the igneous rocks will be important.

Within the overall low strain history of the igneous environment, strain variations can nevertheless be discerned. Both macroscopic and microscopic observations lead to the conclusion that troctolites (excepting the olivine-rich troctolites) record the highest and oxide gabbros record the lowest magmatic foliation. Beyond this, the combined igneous lithology and microstructural evolution (Fig. **F162**) (see **"Igneous petrology"**) can be interpreted in such a way that between 400 and 1400 mbsf there are two major zones of troctolite at ~560 and ~1100 mbsf, both of which lie above highly evolved oxide gabbro. The lithology between ~650 and ~1100 mbsf may be interpreted as an intrusive sequence ranging, on the first order, from troctolite, olivine gabbro, and (noritic) gabbro to oxide gabbro. In this interval, magmatic foliation intensity decreases and crystal-plastic strain increases (combined log of coarser and finer grained neoblast sizes in Fig. **F162**) upward. Whether olivine-rich troctolite intervals below 1100 mbsf are part of this sequence is unresolved. The top of this interval is marked by steep shear zones and oxide gabbro. The base (including the olivine-rich troctolite) is marked by a recurrence and intrusion of oxide gabbro from below and is associated with higher crystal-plastic strain.

Observations of igneous contacts suggest that more fractionated rocks generally intrude more primitive rocks. This lends support to a model where magmatic accretion occurred by progressive underplating of igneous units as opposed to a model where new melt batches are sandwiched between existing plutons.

From microscopic to macroscopic scale, there is an abundance of features suggesting a late formation of clinopyroxene with respect to plagioclase (but not with respect to the oxide formation): the additional observation that clinopyroxene does overgrow a magmatic unit contact at interval 305-U1309-190R-1, 86 cm, plus more circumstantial evidence of abundant megacrystic clinopyroxene and the poor magmatic fabric development in coarse-grained gabbros compared to fine-grained gabbros. The relative timing between intrusion of oxide gabbro and clinopyroxene growth suggests that oxide gabbro emplacement was late.

Magmatic veins are present throughout the hole, but their abundance and lithology seems broadly related to the host rock, although local exceptions do occur. Plagioclase-rich veins are present near troctolitic gabbros, oxide-rich veins are present near oxide gabbros, pyroxenite veins are present near coarse pyroxene gabbros, and leucocratic veins are present near more trondhjemitic bodies.

Strain localization

To provide an initial estimate of the amount of strain accommodated by crystal-plastic deformation at depths above ~130 mbsf, we assigned the following strain magnitudes to rocks with different deformation intensities in a semiquantitatively manner:

- CPf-4 and CPf-3, shear strain (γ) = 10 (the aspect ratio of recrystallized plagioclase and augite bands suggests that this is a conservative estimate)
- CPf-2, $\gamma = 2$
- CPf-1 and CPf-0.5, $\gamma = 0.25$.

The largest uncertainty in these calculations is likely the strain magnitude in high-strain regions. With these assumptions, we estimate a total displacement accommodated by crystal-plastic deformation of 6 m (~10% of the recovered core) in Hole U1309B and 35 m (~60% of the recovered core) in U1309D. By comparison, using the same relationships of strain to CPf and the deformation intensity measured for gabbros in the top 50 m of Hole 735B on the SWIR, >500 m of displacement was accommodated by crystal-plastic deformation directly beneath the hypothesized detachment at Atlantis Bank (Dick, Natland, Miller, et al., 1999; MacLeod et al., 1999).

Brittle history

A major observation at Site U1309 is that footwall rocks have undergone independent low- and high-temperature deformation histories, with little overlap in regional amphibolite-grade deformation events within Hole U1309D. There are, however, instances of syntectonic brown amphibole grains within gabbroic shear zones in the upper part of Hole 1309D, as well as associated with oxide gabbro. The relative scarcity of strain in the amphibolite facies indicates that there is a gap in the deformation history through the entire section between the history related to igneous events (excluded here are the

late diabases) and lower temperature, subamphibolite-facies deformation.

One of the most consistent indicators of internal deformation is veins with fibers that indicate direction of movement (vein faults). In most cases (>75%), these fault veins display oblique-slip deformation, with scant evidence for dip slip (normal or reverse) below 600 m. This episode of veining is likely to be late and associated with the uplift of the footwall and may indicate internal shear during uplift or relative lateral motion of structural blocks within the footwall.

Geochemistry

During Expedition 304, chemical analyses were performed on 1 piece of ultramafic rubble, 2 harzburgites, 7 basalts, 1 basaltic breccia, 7 diabases, and 6 gabbroic rocks from Hole U1309B and on 2 basalts, 11 diabases, 59 gabbroic rocks, 2 peridotites, and 1 wehrlite from Hole U1309D. During Expedition 305, 8 olivine-rich troctolites, 119 gabbroic rocks, and 4 diabases were analyzed. Gabbros, olivine, and olivine-bearing gabbros are the most common rock types at Site U1309. Sample selection was based on discussion among representatives from all expertise teams within the expedition scientific party. ICP-AES was used for determining major and trace element concentrations, and gas chromatography was used for H_2O and CO_2. Samples are representative of the rocks recovered from Site U1309 (see **"Igneous petrology"** and **"Metamorphic petrology"** for characterization of the lithologic units). Tables **T10** and **T11** list all analytical data (including H_2O and CO_2 contents) collected during Expeditions 304 and 305.

One water sample was taken at seafloor at the beginning of Expedition 304 (see **"Operations"**) and analyzed onboard for chemical composition (see **"Appendix A"**). Two water samples were taken at the bottom of Hole U1309D at the beginning of each logging session during Expedition 305 (at ~2396 and ~1215 mbsf; see **"Operations"**) and analyzed onboard for physical properties and chemical composition (see **"Appendix B"**).

Basalts and diabases

Basalts were recovered from the upper sections of Holes U1309B and U1309D. Two basalt and diabase intervals are present in Hole U1309B, and three are present in Hole U1309D above 401.3 mbsf (see **"Igneous petrology"**). Above 401.3 mbsf, Site U1309 basalts are characterized by loss on ignition (LOI) values ranging from –0.05 to 1.45 wt% and H_2O contents ranging from 0.56 to 2.00 wt% (Fig. **F213**). Site U1309 upper diabases are distinguished by more variable, but still low, LOI and H_2O contents (LOI = –0.28–1.90 wt%; H_2O = 0.79–2.33 wt%). LOI and H_2O contents are positively correlated; however, LOI slightly underestimates the total volatile content due to the conversion of Fe^{2+} to Fe^{3+} during heating of the sample powders to ~1000°C (see the **"Methods"** chapter). The relatively low LOI and H_2O values are consistent with the thin section descriptions and XRD results (see **"Metamorphic petrology"**) that show that Site U1309 basalts and diabases are modified to different extents by alteration with secondary precipitation of tremolite and actinolite and, more rarely, chlorite. Because tremolite and actinolite have low H_2O contents (<2.3 wt%) relative to chlorite (>10 wt%), the volatile content of Site U1309 basalts and diabases is not a direct reflection of the degree of alteration of the rock but more likely reflects the mode of the secondary assemblage. Site U1309 diabases sampled above 401.3 mbsf have low CO_2 (<0.01–0.1 wt%), except for Sample 304-U1309B-5R-2, 90–94 cm, which has slightly higher CO_2 (0.13 wt%). Site U1309 basalts sampled above 401.3 mbsf have higher but variable CO_2 contents ranging from 0.02 to 0.49 wt% (Table **T10**). These slightly higher CO_2 contents do not correlate with LOI, H_2O, or any major elements. In addition, thin section descriptions and XRD results (see **"Metamorphic petrology"**) do not show evidence of a different type of alteration, such as carbonate precipitation, that could explain a higher CO_2 contents in these samples. Therefore, we interpret this difference in CO_2 contents as a primary feature of these rocks.

Diabases sampled below 401.3 mbsf (Expedition 305) have high H_2O contents (1.8 and 2.7 wt%) (Fig. **F213**) compared with diabases from the upper part of Hole U1309D, whereas their CO_2 contents are relatively low (0.01–0.05 wt%) (Table **T11**). The relatively high H_2O contents of Sample 305-U1309-94R-3, 22–26 cm (2.7 wt%), is consistent with the thin section descriptions (Sample 94R-3, 34–36 cm), showing a total alteration of ~30%.

Most basalts and diabases sampled in Hole U1309B and in the upper part of Hole U1309D to 401.3 mbsf (during Expedition 304) are similar in SiO_2 and alkali contents (SiO_2 = 49–53 wt%; $Na_2O + K_2O$ = 2.2–3.7 wt%). They have 5.7–10.4 wt% MgO, 7.1–15.8 wt% Fe_2O_3, 12.7–15.7 wt% Al_2O_3, 9.5–12.8 wt% CaO, and 1.1–2.6 wt% TiO_2. These values are typical of tholeiitic basalt compositions, except for two samples from Hole U1309B that have a slightly more andesitic composition (Figs. **F15, F214**). Basalt and diabase trace element contents range 62–184 ppm Zr, 240–400 ppm V, 38–47 ppm Sc, and 30–71 ppm Y (Fig.

F215). These elements are considered immobile during alteration (e.g., Hébert et al., 1990). Zr and Y are incompatible elements, preferentially partitioned into the liquid during partial melting or fractional crystallization. The increase in these incompatible elements in Site U1309 diabases and basalts at relatively constant Zr/Y ratio (1.6–3) suggests an increasing degree of fractionation of silicate phases, the most Zr- and Y-enriched diabases and basalts being the most differentiated (Fig. F215). Moderately incompatible elements such as Ti, V, and Sc show a more complex evolutionary trend. Figure F216 shows that V and Sc both show a strong positive correlation with Ti. Ti, V, and Sc concentrate in clinopyroxene; however, Ti and V also have a strong affinity for oxide minerals, especially for magnetite. The increases in Ti and V correlate with an increase in Fe content and may result from local increases in the abundance of titanomagnetite (Fig. F215). These observations are consistent with visual core and thin section descriptions (see "Igneous petrology") and with physical property measurements (see "Physical properties") that show that high Fe diabases and basalts were sampled in areas where MS, as measured by the MST, was high (Fig. F217) and where magnetite was more abundant. Site U1309 basalts and diabases have Sr ranging from 80 to 130 ppm and Ba <38 ppm. These elements are highly incompatible, but they are also mobile in hydrothermal fluids, which may explain some scattering in Ba content. Sr contents correlate with Ti, Y, and Zr, but they are low compared to MAR volcanic glasses (Fig. F215).

Using the classification of Le Maitre et al. (1989), the diabases sampled during Expedition 305 from 471 to 1378 mbsf have basaltic compositions (Fig. F15). Trace element concentrations are somewhat scattered (compatible elements: 159–357 ppm Cr and 82–125 ppm Ni; moderately incompatible elements: 0.63–1.72 wt% Ti, 179–383 ppm V, and 30–45 ppm Sc; incompatible elements: 50–160 ppm Zr and 22–60 ppm Y), probably because of slight degrees of fractionation (Fig. F214; Table T11).

Major and trace element compositions of Site U1309 diabases and basalts sampled during Expeditions 304 and 305 span most of the field of basalt glasses from the entire MAR (Figs. F214, F215). All samples are slightly CaO and Al_2O_3 poor and Na_2O rich compared to basaltic glass compositions from the MAR (Fig. F214). These variations may be related to the pervasive greenschist alteration observed, to different extents, in all diabases and basalts in Holes U1309B and U1309D (see "Metamorphic petrology"). Major elements in diabases show the largest scatter. The analyzed diabases are fine to medium grained and sparsely plagioclase phyric (see "Site U1309 thin sections" in "Core descriptions"), and their compositional variability may reflect the primary mode of the selected sample and/or the degree of differentiation of the crystallizing melt, in addition to alteration. For example, two diabases from igneous Unit 20 (Expedition 304) plot outside the field defined by the other Site U1309 basalt and diabase (Fig. F214). Sample 304-U1309B-5R-1, 127–129 cm, is distinguished by slightly higher SiO_2 (52 wt%) and Al_2O_3 (14.5 wt%) and low MgO (6.85 wt%), whereas Sample 5R-2, 90–94 cm, has lower SiO_2 (48.9 wt%) and Al_2O_3 (12.7 wt%) and higher MgO (9.91 wt%). These variations are explained, in part, by small variations in modal compositions; Sample 304-U1309B-5R-1, 127–129 cm, has a higher plagioclase/clinopyroxene ratio than Sample 5R-2, 90–94 cm, and is therefore relatively Al rich and Mg poor compared to the latter. These variations are also correlated with TiO_2 and trace element values, indicating that Sample 304-U1309B-5R-1, 127–129 cm, is relatively more evolved. We also observe a decrease in trace element content from fine-grained margins to the coarser grained centers of diabase bodies, such as in Diabase D-5 (Unit 42 and 44, Hole U1309D) (see "Igneous petrology"). We interpret these variations as reflecting the mode of the samples selected in the coarser grained areas.

Sample 304-U1309B-14R-1, 107–109 cm, a plagioclase-phyric basalt (Unit 40), differs from the other Site U1309 basalts and diabases in having slightly higher SiO_2 (53.11 wt%) and Na_2O (3.2 wt%) and lower Fe_2O_3 (7 wt%), although other major and trace element contents plot in the same field as that of the other basalt and diabase samples from Site U1309. The high SiO_2 together with high MgO (8.5 wt%) is poorly understood. Detailed studies on more samples should provide a means to explain these slight differences in composition.

Basaltic breccia

We analyzed a basaltic breccia from Hole U1309B (Unit 15), Sample 304-U1309B-3R-1, 71–74 cm. This sample is composed of relatively fresh clasts of basalt and diabase in a heavily altered matrix (see "Site U1309 thin sections" in "Core descriptions"). It displays LOI and volatile contents similar to those of the diabase and basalt samples (LOI = 1.99 wt%; H_2O = 2.57 wt%; CO_2 = 0.10 wt%). It is characterized by high MgO (13.1 wt%) and low Al_2O_3 (10.4 wt%). Compared to Site U1309 diabases and basalts, it displays, on average, lower incompatible element contents (Fig. F215). However, in contrast to Site U1309 basalts and diabases, Cr and Ni contents are above the detection limit in this sample (Cr = 480 ppm and Ni = 370 ppm). Cr and Ni are compatible elements

concentrated in the most primitive melts. Sample 304-U1309B-3R-1, 71–74 cm, is composed of basaltic clasts embedded in a matrix composed mainly of secondary tremolite and actinolite (see **"Metamorphic petrology"**). These minerals are depleted in Al but have high Mg contents compared to the average composition of Site U1309 basalts and diabases. The high MgO, Ni, and Cr contents of Sample 304-U1309B-3R-1, 71–74 cm, suggests either that primitive material could have been mixed within the primary assemblage that formed this matrix and/or that the hydrothermal fluids that flowed through the basalt breccia and induced its alteration were in equilibrium with serpentinite.

Gabbroic rocks

We analyzed 6 gabbroic rocks from Hole U1309B and 59 from Hole U1309D (to 401.3 mbsf) during Expedition 304, as well as 119 gabbroic samples from Hole U1309D (to 1378 mbsf [Core 305-U1309D-287R]) during Expedition 305. Gabbroic rocks include olivine-rich troctolite, troctolite, olivine gabbro, olivine-bearing gabbro, gabbro and gabbronorite, microgabbro, oxide gabbro, and leucocratic gabbro. For simplicity, some rock types classified in the visual core and thin section descriptions were grouped: gabbro, cataclastic gabbro, medium-grained gabbro, and coarse-grained gabbro are referred to as gabbro; troctolitic gabbro, olivine gabbro, medium-grained troctolitic gabbro, layered olivine-gabbro and troctolite, troctolite with olivine-gabbro bands, medium-grained olivine-gabbro, and alternating troctolite and olivine-gabbro sequence are referred to as olivine gabbro. Olivine-bearing gabbros are referred to as gabbros, except for samples having ≥5% olivine based on thin section descriptions, which are referred to as olivine gabbros. Thin section estimates of modal composition indicate that Sample 304-U1309D-8R-2, 123–129 cm, is a troctolitic interval in an interval of troctolitic gabbro; it is referred to as a troctolite. Orthopyroxene-bearing gabbro and gabbronorite are plotted with gabbro in all figures. Olivine-rich troctolite intervals that comprise olivine-rich troctolite and dunite are described separately.

Gabbro and troctolite

From Hole U1309B, we selected two gabbro samples from Unit 28 above a serpentinized peridotite interval (Unit 32; 61 mbsf), one gabbro below this interval (Unit 56), and one olivine gabbro sample each from Units 46, 50, and 53. From Hole U1309D, we selected 17 gabbro samples, 25 olivine gabbros, 5 troctolites, 2 orthopyroxene-bearing gabbros, 3 oxide gabbros, and a late magmatic leucocratic dike crosscutting an olivine-bearing gabbro unit (Unit 89; Expedition 304).

Gabbroic rock comprises abundant plagioclase and clinopyroxene with various amounts of olivine (see **"Igneous petrology"**). Major and trace element compositions mainly reflect the mode of these phases in the rocks. For example, high plagioclase abundance leads to elevated Al_2O_3 at lower MgO, whereas high olivine contents cause high MgO at low CaO.

Site U1309 gabbros and orthopyroxene-bearing gabbros down to 401.3 mbsf (Expedition 304) are characterized by LOI values ranging from 0.3 to 1.74 wt% and H_2O ranging from 0.6 to 1.9 wt% (Fig. **F213**). Oxide gabbros have comparable H_2O (0.70–1.07 wt%) but lower LOI (–0.28–1.05 wt%). The conversion of Fe^{2+} to Fe^{3+} during heating of the sample powders to ~1000°C (see the **"Methods"** chapter) leads to a strong underestimation of the volatile contents in these Fe-rich samples (Fe_2O_3 > 22 wt%). Olivine gabbros and troctolites are characterized by more scattered and higher LOI and H_2O values, with LOI ranging from 0.2 to 9.6 wt% and H_2O contents ranging from 0.55 to 10.6 wt%. These LOI and H_2O values are consistent with the thin section descriptions and XRD results (see **"Metamorphic petrology"**) that show that the analyzed gabbro samples were modified to different extents by alteration, as shown by secondary crystallization of tremolite, actinolite, and, more rarely, brown hornblende in all gabbroic rocks. Alteration of olivine to talc and/or chlorite is commonly complete in olivine gabbros and in troctolites. All gabbroic rocks display low CO_2 contents (<0.23 wt%).

Hole U1309D gabbros below 401.3 mbsf (Expedition 305) have H_2O contents between the detection limit of 0.15 and 7.3 wt% (Figs. **F213, F218**), which reflects differences in the style and degree of alteration (see **"Discussion"**). Most gabbroic rocks display CO_2 contents near the detection limit of 0.04 wt% (Table **T11**). Only Samples 305-U1309D-101R-3, 0–14 cm, 111R-2, 6–14 cm, and 158R-1, 11–17 cm, have CO_2 contents of ~0.2 wt%, consistent with carbonate veining in those parts of the core (see **"Metamorphic petrology"**). The volatile data are consistent with thin section descriptions and XRD results (see **"Metamorphic petrology"**) that show that the analyzed gabbro samples were modified to different extents by alteration, as shown by secondary formation of talc, tremolite, actinolite, chlorite, zeolite, and serpentine minerals.

Gabbroic rocks sampled in Hole U1309B and above 401.3 mbsf in Hole U1309D (Expedition 304) comprise gabbros, orthopyroxene-bearing gabbros, olivine gabbros, troctolites, and olivine-rich troctolites.

The gabbros have 47.5–53.5 wt% SiO_2, 5–12 wt% MgO, 0.14–0.49 wt% TiO_2, 15.2–23.5 wt% Al_2O_3, and 2.9–7.4 wt% Fe_2O_3. Orthopyroxene-bearing gabbros have similar compositions to gabbros: 51.8–53 wt% SiO_2, 10.4–12.2 wt% MgO, 0.2–0.3 wt% TiO_2, 15.6–16.45 wt% Al_2O_3, and 4.4–6.4 wt% Fe_2O_3. Olivine gabbros overlap in composition with the gabbros, having 4.5–26.5 wt% MgO, <0.3 wt% TiO_2, 10.5–26.4 wt% Al_2O_3, and 2.8–9.9 wt% Fe_2O_3. The troctolites have the most primitive compositions, with 9–36.8 wt% MgO, <0.18 wt% TiO_2, 8–26.9 wt% Al_2O_3, and 3.3–10.4 wt% Fe_2O_3 (Fig. **F219**). Texturally and compositionally, all of these samples represent cumulate compositions and comprise abundant plagioclase and clinopyroxene, with various proportions of olivine (see **"Site U1309 thin sections"** in "Core descriptions"). The most extreme variations due to variations in plagioclase content are in Sample 304-U1309D-48R-1, 111–119 cm, an anorthositic troctolite (Unit 108; see **"Igneous petrology"**) that has 29.2 wt% Al_2O_3 and 4.25 wt% MgO.

Below 401.3 mbsf (Expedition 305), the gabbros have 41.8–53.2 wt% SiO_2, 3.0–36.1 wt% MgO, 0.07–7.9 wt% TiO_2, 7.1–23.6 wt% Al_2O_3, and 4.0–29.1 wt% Fe_2O_3 (Figs. **F219, F220**). Troctolites have the most primitive compositions (Figs. **F219, F220**). Al_2O_3 (7.1–21.9 wt%), MgO (11.9–36.1 wt%), CaO (4.1%–10.5%), and Na (0.4–2.3 wt%) show a large range of concentrations due to the modal variations in olivine and plagioclase, whereas SiO_2 (41.8–46.6 wt%), Fe_2O_3 (6.7–11.1 wt%), and TiO_2 (0.07–0.14 wt%) are less scattered. Olivine gabbros show the largest range in major element composition among the gabbroic rocks. They tend to have more primitive compositions than gabbros and are more evolved than troctolites (43.6–50.9 wt% SiO_2, 10.4–23.6 wt% Al_2O_3, 7.2–24.0 wt% MgO, 7.2–15.1 wt% CaO, and 0.11–0.36 wt% TiO_2) (Figs. **F219, F220**) but still overlap with the other gabbroic rocks. Olivine-bearing gabbros (48.1–52.3 wt% SiO_2, 14.1–21.4 wt% Al_2O_3, 8.9–12.9 wt% MgO, 13.1–15.2 wt% CaO, and 0.18–0.56 wt% TiO_2) (Figs. **F219, F220**), in general, overlap the compositional field defined by the gabbros (49.0–53.2 wt% SiO_2, 14.0–22.2 wt% Al_2O_3, 7.4–11.8 wt% MgO, 10.7–14.7 wt% CaO, and 0.19–1.72 wt% TiO_2) (Figs. **F219, F220**) but have, on average, more primitive compositions. Orthopyroxene-bearing gabbros, which are included here for simplicity in the gabbro group, overlap the gabbros in composition but tend to be slightly more SiO_2 rich. Four microgabbros were analyzed (Samples 305-U1309D-103R-1, 15–23 cm, 113R-2, 145–149 cm, 117R-4, 23–27 cm, and 181R-1, 56–62 cm) from 511 and 881 mbsf. They fully overlap the compositional range defined by the gabbros and olivine gabbros (Figs. **F219, F220**).

Compared to gabbros sampled during Leg 153 (Agar et al., 1997) and Leg 209 (Kelemen, Kikawa, Miller, et al., 2004) from the MAR and from Hole 735B (Dick, Natland, Miller, et al., 1999) on the SWIR, Site U1309 gabbroic rocks have mostly highly primitive compositions indicated by high Mg# (molar Mg/[Mg + Fe]) from ~52 to 90 and low TiO_2 (<0.49 wt%) and Na_2O (0.1–3.7 wt%) (Fig. **F219, F220**). The only exceptions are the oxide gabbros and leucocratic gabbros.

The oxide gabbros and oxide-bearing gabbros have compositions similar to other Site U1309 gabbroic rocks, except for the high TiO_2 (up to 7.9 wt%) and Fe_2O_3 (up to 29.2 wt%) and low Al_2O_3 (<13.2 wt%) and SiO_2 (<47.72 wt%) in the most oxide rich samples. The positive correlation between Fe_2O_3 and TiO_2 (Figs. **F221**) indicates that the variation in these two elements is primarily related to oxide abundance in Site U1309 gabbroic rocks.

Leucocratic gabbros are outstanding in terms of major and trace element composition. They show evolved, highly variable compositions.

The late magmatic leucocratic dike (Sample 304-U1309D-36R-3, 80–82 cm) sampled during Expedition 304 clearly stands out in comparison to the different gabbroic groups, having lower MgO (4.85 wt%) and CaO (4.8 wt%) and much higher SiO_2 (63.1 wt%) and Na_2O (7.95 wt%). This sample comprises mainly plagioclase and actinolite with minor oxides and carbonates (see **"Site U1309 thin sections"** in "Core descriptions"), and its chemical composition reflects the modal abundance of these minerals. The average plagioclase composition was calculated using a mass balance equation relating modes and whole-rock and typical mineral compositions (Deer et al., 1992) in the system comprising the elements CaO-FeO-MgO-Al_2O_3-SiO_2. The calculated plagioclase composition is An_{07}. This value is consistent with extinction angles of plagioclase twins, which give anorthite contents of ~10 (see **"Site U1309 thin sections"** in "Core descriptions"), and this observation suggests that plagioclase in Sample 304-U1309D-36R-3, 80–82 cm, was anorthite poor before alteration (and albitization).

The four leucocratic gabbros (Samples 305-U1309D-93R-1, 11–16 cm, 116R-3, 67–77 cm, 128R-3, 38–48 cm, and 158R-1, 11–17 cm) sampled during Expedition 305 display elevated concentrations of Na_2O (3.3–5.0 wt%), K_2O (0.05–0.10 wt%), and P_2O_5 (1.3–2.8 wt%) (Figs. **F219, F220;** Table **T11**).

Trace element geochemistry of olivine gabbros, orthopyroxene-bearing gabbros, and gabbros sampled during Expedition 304 is consistent with the primitive compositions defined by the major elements.

They have high concentrations of compatible elements, with Ni up to 840 ppm and Cr ranging from 150 to 1400 ppm; Sample 304-U1309D-48R-1, 44–53 cm, an olivine gabbro, has the highest Cr content of all gabbroic rocks (3060 ppm). In contrast, oxide gabbros and the late magmatic leucocratic dikes have low Cr (<190 ppm) and Ni (<166 ppm). The troctolites have, on average, higher Ni and Cr contents (1040–1625 ppm and 1075–2980 ppm, respectively). Ni is concentrated in olivine, and the whole-rock composition in the gabbroic rocks mainly indicates the abundance of this mineral. Cr contents are variable, although we note that the highest Cr contents are found among the most primitive olivine gabbros and troctolites. Cr is mainly concentrated in oxides and, more particularly, in spinels, although clinopyroxene may also contain Cr (up to 0.4 wt% Cr_2O_3). Shipboard thin section descriptions do not show evidence for spinel in these samples. Cr may reflect variations in the Cr content in clinopyroxenes and/or in the modal fraction of this mineral. However, there is no correlation between Cr and any other major and trace elements. This suggests that spinel may be present as a microphase that is not evenly distributed in these samples.

Moderately incompatible elements V and Sc covary positively with TiO_2 in Site U1309 gabbros, orthopyroxene-bearing gabbros, olivine gabbros, and troctolites sampled during Expedition 304, with V ranging from 19 to 201 ppm and Sc from 3 to 53 ppm (Fig. **F216**). Oxide gabbros have significantly higher V (615–1287 ppm), an element that is highly compatible in oxides. Sc shows a very good anticorrelation with Al_2O_3 in Site U1309 gabbroic rocks (Fig. **F222**). The Sc budget in Site U1309 gabbroic rocks is primarily controlled by the abundance of clinopyroxene, given the compatibility of Sc in clinopyroxene. The Al_2O_3 budget of Site U1309 gabbroic rocks is primarily related to the modal abundance of plagioclase. The negative correlation between Sc and Al_2O_3 is, therefore, an indicator of changes in the clinopyroxene/plagioclase ratio of these rocks. When the plagioclase/pyroxene ratio is low, bulk rock Sc content is higher and Al_2O_3 content is lower. Together with positive Sc-Ti covariation (Fig. **F216**), these relations are consistent with a simple mass balance involving corresponding increases in the proportion of clinopyroxene plus oxides as plagioclase proportion decreases. Interestingly, Sc does not covary with Al_2O_3 in Site U1309 troctolites. In these rocks, Al_2O_3 decreases at more or less constant Sc values. This is consistent with the increase of the proportion of olivine when plagioclase decreases in these rocks (see **"Site U1309 thin sections"** in "Core descriptions"). Sample 304-U1309D-4R-2, 112–113 cm, a gabbro, is slightly Ti rich compared to gabbros with similar Sc and V contents. This is consistent with thin section descriptions that show that rutile, a Ti-rich microphase, is present in this sample.

Except for three samples from the upper part of Hole U1309D (gabbro Zone 1; see **"Igneous petrology"**), Site U1309 gabbroic rocks from Expedition 304 have low incompatible element content with Y < 16 ppm and Zr < 17 ppm that covary with TiO_2. Oxide gabbros are slightly enriched in some trace elements, with ~25 ppm Zr and 23–86 ppm Y. The three Zone 1 gabbros are Sample 304-U1309D-5R-3, 114–118 cm, an olivine gabbro that has 28 ppm Y and 22 ppm Zr, and two gabbros, Samples 4R-2, 112–113 cm, and 7R-3, 102–105 cm, that have 71 and 120 ppm Y and 97 and 20 ppm Zr, respectively. These samples show significant scatter in Zr and Y contents (Figs. **F223, F224**). The scattered diverging trends indicate that there could be (at least) two controls on their trace element concentration. One control may simply be enrichment in each of these incompatible elements due to increasing concentration of both elements in the parental melts during fractional crystallization. The variability of Y and Zr contents may also be related to the presence of minor phases concentrating these elements (e.g., zircon, titanite, and xenotime).

Site U1309 gabbros from Expedition 304 (including oxide gabbros) have Ba contents of less than the detection limit to 21 ppm and Sr contents of 27–166 ppm (Table **T10;** Fig. **F223**). Sr and Ba are incompatible elements, although Sr is more concentrated in plagioclase than in other silicate phases. These elements are also highly mobile during alteration. Sr variations correlate with Al_2O_3, an element abundant in plagioclase. Variable Ba content in the Site U1309 mafic rock suite is probably due to postemplacement processes (see **"Metamorphic petrology"**).

One leucocratic dike (Sample 304-U1309D-36R-3, 80–82 cm) was sampled during Expedition 304. It has low Sc (~1 ppm) but V content close to those of other Site U1309 gabbroic rocks. The low Sc is consistent with the absence of clinopyroxene in this sample. This sample has significantly higher Zr (328 ppm), Y (141 ppm), Ba (83 ppm), and Sr (94 ppm) contents than other gabbroic rocks sampled during Expeditions 304 and 305. The high Zr is consistent with the observation of zircon in this sample (see **"Site U1309 thin sections"** in "Core descriptions"). These concentrations are much higher than Y and Zr concentrations observed for mid-ocean-ridge basalt magmas. These high concentrations suggest that this sample was in equilibrium with an evolved trace-element-enriched melt (Fig. **F224**).

In general, the trace element geochemistry of Hole U1309D gabbroic rocks below 401.3 mbsf (Expedi-

tion 305) is similar to gabbros recovered during Expedition 304 and consistent with the primitive compositions defined by major elements. Troctolites and olivine gabbros have relatively high concentrations of compatible elements, with Ni from 150 to 1575 ppm and Cr ranging from 4090 to 120 ppm (Fig. F225; Table T11). In contrast, oxide gabbros and leucocratic gabbros have very low Cr (below detection limit to 195 ppm) and Ni (below detection limit to 140 ppm). Olivine-bearing gabbros and gabbros fall in between the olivine gabbros and oxide gabbros in Ni and Cr concentration. Oxide gabbros have significantly higher V (85–1980 ppm). Sc shows a very good anticorrelation with Al_2O_3 in Site U1309 gabbroic rocks (Fig. F226).

Except for leucocratic gabbros, most Hole U1309D gabbroic rocks below 401.3 mbsf (Expedition 305) have low incompatible element content with <24 ppm Y and Sr contents of 32–287 ppm (Fig. F223). Leucocratic gabbros are characterized by high incompatible trace element contents, with concentrations up to 1180 ppm Zr and 12–301 ppm Y. They also show significant scatter in Zr and Y contents. Leucocratic gabbros have extremely high incompatible trace element concentrations, like Y and Zr (Figs. F224, F226; Table T11), compared with the other gabbroic rocks and MAR-basalts, pointing to the highly fractionated compositions of those liquids.

On average, olivine gabbro and troctolite display lower incompatible element concentrations than gabbro, although they overlap in composition. The oxide gabbros overlap in composition with the most trace element enriched gabbros (Fig. F226). These compositions fall into the range of concentrations previously observed in gabbros in Hole 735B (Dick et al., 2000) and from Legs 153 (Casey, 1997) and 209 (Kelemen, Kikawa, Miller, et al. 2004) (Figs. F223, F224). Overall, the compositions of most of the gabbros analyzed at Site U1309 plot at the most primitive end of the field defined by comparable oceanic gabbros. Based on their major and trace element compositions, Site U1309 gabbros form a coherent suite with diabase and basalts sampled at the same site. This suggests a cogenetic origin for these mafic rocks.

Olivine-rich troctolite

Fourteen samples were selected from lithologic units comprising olivine-rich troctolites. Samples from these intervals, cored during Expedition 304, grade from serpentinized dunite with small amounts of interstitial clinopyroxene and/or plagioclase to wehrlitic and olivine-rich troctolitic intervals at ~132 (Units 57–58), ~300–311 (Units 136–147), and ~330 (Units 167–173) mbsf. They comprise three dunites with variable amounts of interstitial plagioclase, one wehrlite, and two olivine-rich troctolites. Eight olivine-rich troctolite samples were analyzed in two intervals, between 670 and 690 mbsf (Samples 305-U1309D-136R-2, 4–14 cm, and 140R-2, 11–19 cm) and 1095 to 1233 mbsf (Samples 227R-3, 73–78 cm, 234R-2, 63–68 cm, 240R-2, 84–92 cm, 242R-2, 84–92 cm, 248R-2, 5–11 cm, and 256R-2, 88–94 cm) during Expedition 305.

The H_2O and CO_2 contents in the olivine-rich troctolitic samples range between 0.7 and 14.94 wt% and 0.09 and 0.75 wt%, respectively (Figs. F213, F218; Table T11). High H_2O contents in most samples from olivine-rich troctolite intervals point to the presence of serpentine minerals replacing olivine (Fig. F213). Samples 305-U1309D-227R-3, 73–78 cm, and 248R-2, 5–11 cm, have the lowest H_2O contents of all olivine-rich rocks recovered during Expeditions 304 and 305. Carbon dioxide contents are low in the olivine-rich troctolites (<0.14 wt% CO_2), with the exception of Sample 305-U1309D-140R-2, 11–19 cm, which has 0.75 wt% CO_2 (Table T11).

The olivine-rich rocks sampled in Units 57–58, 136–147, and 167–173 during Expedition 304 have low SiO_2 (41.6–42.8 wt%) and TiO_2 (<0.07 wt%), similar to peridotites sampled during Expedition 304. They have 0.9–8.4 wt% Al_2O_3 and 0.8–5.8 wt% CaO. These elements concentrate in plagioclase and clinopyroxene, and their variations reflect the modes of these minerals. They overlap in composition in MgO and Fe_2O_3 contents with peridotites sampled during Expedition 304, although they have more variable MgO (34.5–42.2 wt%) and higher Fe_2O_3 (10–15 wt%), with the highest Fe_2O_3 characterizing the dunites (12.45–15 wt%). MgO concentrates in olivine, and ultramafic rock samples with significant amounts of plagioclase and clinopyroxene (high Al_2O_3 and CaO content) have lower olivine contents and therefore display the lowest MgO. However, Fe_2O_3 variations are not associated with modal changes. This suggests that the Fe composition of the minerals that compose the olivine-rich troctolitic rocks and, in particular, that of olivine, varies.

The olivine-rich rocks sampled in Units 57–58, 136–147, and 167–173 have high Cr (2422–3140 ppm) and overlap in composition with Expedition 304 peridotites, but they have lower Ni (1750–2310 ppm). The Cr values are consistent with thin section observations that show the presence of various amounts of spinels in these samples. Ni concentrates in olivine, and the low Ni content of these samples may reflect their low olivine mode. The ultramafic rocks have ~4 ppm Ba, 3–16 ppm Sr, 28–36 ppm V, 6–14 ppm Sc, and <5 ppm Y. These trace element contents are similar to those of the most olivine rich gabbroic rocks sampled during Expedition 304.

Below 401.3 mbsf (Expedition 305), the olivine-rich troctolites have low SiO_2 (40.8–47.4 wt%), Al_2O_3 (3.3–6.4 wt%), and TiO_2 (0.05–0.46 wt%) contents and high MgO (30.0–38.4 wt%) and Fe_2O_3 (10.5–14.2 wt%) contents compared to the gabbroic rocks from Hole U1309D (Figs. **F219, F220**). The Mg# of these rocks is homogeneously high (Figs. **F220, F225**), ranging only between 84.3 and 86.0 (except for Sample 305-U1309D-140R-2, 11–19 cm). Compatible trace element concentrations are high, with Ni ranging from 1170 to 2008 ppm and Cr ranging from 248 to 3219 ppm (Fig. **F225**). The extremely high Cr contents point to the presence of abundant spinel, which is confirmed by hand specimen and thin section descriptions (see **"Igneous petrology"**). In Sample 305-U1309D-227R-3, 73–78 cm, abundant chromite was identified by XRD (see **"Metamorphic petrology"**). Moderately incompatible and incompatible trace element contents are, in general, low (<73 ppm V, <20 ppm Sc, <30 ppm Sr, <7.8 ppm Y, and less than detection limit of Zr) and very similar to the ultramafic rocks recovered during Expedition 304 (Figs. **F225, F226;** Table **T11**). The primitive composition of the olivine-rich troctolites may indicate that they are cumulates marked by higher concentrations of compatible trace elements such as Mg, Cr, and Ni. However, these samples have significantly higher Ni content than gabbroic rocks with similar Mg#, which suggests either a different magmatic crystallization trend or a more Ni enriched parent magma.

The olivine-rich troctolitic intervals have compositions intermediate between the most primitive gabbroic rocks and peridotites sampled during Expedition 304. Alternatively, they may represent the most extreme product of melt-rock interaction with (or impregnation by) a basaltic melt as proposed by Kelemen, Kikawa, Miller, et al. (2004) for Site 1275 troctolites.

Ultramafic rocks

We selected one piece of ultramafic rubble and two serpentinized harzburgite samples from Hole U1309B. The two serpentinized harzburgites (Unit 32) are representative of a 4 m thick interval that represents the only presence of peridotites in Hole U1309B (see **"Igneous petrology"** and **"Downhole measurements"**). We also sampled three ultramafic samples in Hole U1309D. The uppermost sample in Hole U1309D, Sample 304-U1309D-10R-1, 107–111 cm, was taken from a 15 cm long interval composed of ultramafic material cut by several altered gabbro dikes at ~61 mbsf (Unit 28). This sample was taken as far as possible from the gabbroic dikes, from the leftovers of the microbiology sample. The modal composition of this sample, determined in hand specimen, is that of a wehrlite with >60% olivine, ~35% pyroxene (probably mostly clinopyroxene), and <2% plagioclase. A serpentinized dunite (Unit 77) and a serpentinized harzburgite (Unit 79) were sampled in a ~2.50 m ultramafic interval within the gabbro section at ~171 mbsf.

Bulk rock analyses of ultramafic rocks from Site U1309 show that the composition of these samples was modified by hydrothermal alteration, which added variable amounts of volatile constituents to the original ultramafic assemblage (Fig. **F213**). The peridotites sampled in Holes U1309B and U1309D have LOI ranging from 8.9 to 11.73 wt%. These values are consistent with visual core descriptions and XRD results (see **"Metamorphic petrology"**) that show that these samples have abundant lizardite. Sample 304-U1309D-31R-1, 25–28 cm, a dunite, and Sample 31R-2, 11–17 cm, a harzburgite, have higher LOIs (12.78 and 12.85 wt%, respectively) and CO_2 (1.24 and 1.28 wt%, respectively). High CO_2 may indicate late precipitation of carbonates. This is consistent with visual core description and thin section descriptions that show evidence for carbonate veinlets cutting the peridotites and carbonate secondary precipitation within the serpentine mesh (see **"Metamorphic petrology"**). The ultramafic rubble (Sample 304-U1309B-1R-3, 17–21 cm) sampled at the top of Hole U1309B, which also shows evidence of alteration to talc, has a significantly lower LOI value (7.5 wt%). Unit 28 wehrlite from Hole U1309D has the same LOI value (7.5 wt%) but much higher CO_2 (1.19 wt%) compared to the Hole U1309B ultramafic samples (0.14–0.19 wt%). These relatively low H_2O and high CO_2 contents are consistent with thin section descriptions that show the presence of carbonate veins as well as pervasive talc alteration, although the sample was less altered than Sample 304-U1309B-1R-3, 17–21 cm, as relics of olivines are preserved in the latter. LOI is positively correlated with water content in the alteration intervals in ultramafic rocks, with H_2O ranging between 10.89 and 13.15 wt% where lizardite is predominant and 8.2 and 7 wt% where talc is predominant.

Hole U1309B harzburgites

In spite of their high volatile content, bulk rock compositions of Hole U1309B harzburgites primarily reflect the relative abundance of their primary phases, olivine and pyroxene (Fig. **F227**). They have low Al_2O_3 (~0.8 wt%) and CaO (0.2–0.42 wt%) compared to Leg 153 peridotites (Casey, 1997) (Fig. **F228**). Both Al_2O_3 and CaO are concentrated in pyroxenes, with CaO primarily in clinopyroxene, so variations in Al_2O_3 and CaO reflect clinopyroxene

content and, therefore, the relative degree of fertility of peridotites. The low CaO and Al_2O_3 contents of Hole U1309B harzburgites suggest that, prior to alteration, these peridotites may have been more refractory than Leg 153 peridotites. Together with low clinopyroxene contents, high Mg# is considered as an indicator of high degrees of partial melting of peridotite, yet Hole U1309B harzburgites have the same Mg# as Leg 153 peridotites (90–91) (Fig. F229). Hole U1309B harzburgites are characterized by higher Fe_2O_3 contents (9–10.1 wt%) compared to tectonically emplaced and abyssal peridotites with the same MgO contents (44.5–45.6 wt%) (Fig. F230). This slight Fe enrichment explains their relatively low Mg# and may result from melt-rock reactions involving Fe-Mg exchange with an olivine-saturated basaltic melt. Sample 304-U1309B-11R-1, 100–104 cm, which displays the highest Fe content, was sampled <5 cm from a gabbroic dike.

Harzburgite from Hole U1309B has ~40 ppm V, ~10 ppm Sc, 2500–2650 ppm Ni, and 125–150 ppm Co (Fig. F231). Ni and Co are preferentially partitioned into olivine, and V and Sc are preferentially partitioned into clinopyroxene. Variations in these elements in Hole U1309B harzburgites mainly reflect the modal proportions of olivine and clinopyroxene. V and Sc contents in Hole U1309B harzburgites are high compared to those of Leg 209 peridotites with the same Al content. Other trace element concentrations in Hole U1309B harzburgites fall in the range of Leg 209 peridotites. Hole U1309B harzburgites are depleted in TiO_2 (<0.02 wt%), Zr (<1.5 ppm), and Sr (<2 ppm) compared to Leg 153 peridotites (Fig. F231). These elements are moderately to highly incompatible, and their range in concentration suggests that Hole U1309B harzburgites underwent degrees of partial melting similar to Leg 209 peridotites and higher than Leg 153 peridotites. V and Sc partition preferentially into clinopyroxene, and their correlation with CaO and Al_2O_3, both proxies for the proportion of pyroxene present, suggests the presence of a small amount of clinopyroxene preserved in these rocks. This is consistent with thin section descriptions that show a small amount of relict clinopyroxene.

Hole U1309B ultramafic rubble

Sample 304-U1309B-1R-3, 17–21 cm (Unit 1), is a fragment recovered at the top of the drilled section in Hole U1309B. It is altered to talc and serpentine (see **"Metamorphic petrology"**), and its composition primarily reflects the relative abundance of these alteration phases (Fig. F227). It is significantly enriched in SiO_2 (60 wt%) and depleted in MgO (33 wt%) and Fe_2O_3 (6.7 wt%) relative to harzburgite from the same hole. It is also strongly depleted in CaO, suggesting that serpentinization removed Ca from the pyroxene that was originally present in the peridotite protolith. Sample 304-U1309B-1R-3, 17–21 cm, is depleted in trace elements that are mobile during alteration, such as Sr (below detection limit), relative to peridotites from Legs 153 and 209. Like Ca, these elements appear to have been removed from the peridotite by alteration. This sample is also depleted in Y (<1 ppm), Zr (<1.5 ppm), and, to a lesser extent, TiO_2 (0.03 wt%), V (21 ppm), and Sc (7 ppm). It has high values in Cr (1940 ppm) and Ni (2400 ppm). These elements are considered to be relatively immobile during alteration (e.g., Hébert et al., 1990). Therefore, they can be used as indicators of protolith composition. V, Sc, and Cr variations and, to a lesser extent, Zr, Ti, and Y variations correlate with Al_2O_3 variations in Hole U1309B harzburgites (Fig. F231). Zr, V, Sc, Ti, and Y behave as incompatible elements during partial melting, whereas Cr and Ni behave as compatible elements and Al_2O_3 may be used as an indicator of the protolith pyroxene content. The low Al_2O_3 (0.62 wt%) and trace element contents of Sample 304-U1309B-1R-3, 17–21 cm, suggest that the protolith was composed of a depleted peridotite, probably more similar to or slightly more refractory than Hole U1309B serpentinized harzburgite found at 60 mbsf.

Hole U1309D wehrlite (~61 mbsf, Unit 28)

Sample 304-U1309D-10R-1, 107–111 cm (~61 mbsf; Unit 28), is a wehrlite with low SiO_2 (42.9 wt%), Al_2O_3 (1.2 wt%), and TiO_2 (<1 wt%) and high Fe_2O_3 (15 wt%) and MgO (36.4 wt%) compared to those of Expedition 304 gabbroic rocks (Fig. F219), although Expedition 304 gabbroic rocks have similar Mg# (83). It is grouped together with the olivine-rich troctolites (see **"Igneous petrology"**). Its composition may indicate that this wehrlite is a primitive cumulate distinguished by higher concentrations of compatible trace elements such as Cr (2670 ppm) and Ni (1240 ppm). Its incompatible trace element contents (98 ppm V, 6 ppm Y, 17 ppm Zr, and <25 ppm Sc) are similar to those of Site U1309 olivine gabbros and troctolites. The high concentrations of V and Sc can be attributed to the presence of significant amounts of cumulate clinopyroxene. Spinel is observed in thin sections of wehrlite (see **"Igneous petrology"** and **"Metamorphic petrology"**), which accounts for the high Cr concentration. The high Ni content of Hole U1309D wehrlite may reflect, in part, its high olivine content. However, it should be noted that this sample plots outside of the Ni-Mg# trend shown by the most primitive of Site U1309 gabbroic rocks, suggesting mixing between a peridotite and a more

mafic material (Fig. F229). In addition, thin section description suggests that olivines were deformed at high temperature. This suggests that Hole U1309D wehrlite could have formed as a product of reaction between peridotite and a basaltic melt, as proposed for peridotites with gabbroic impregnation from ODP Site 1271 and for Site 1275 troctolites, which are similarly characterized by low Mg# (as low as 85) but have relatively high Ni contents compared to cumulate rocks of the same Mg# (Kelemen, Kikawa, Miller, et al., 2004).

Hole U1309D Unit 77 dunite and Unit 79 harzburgite

Two serpentinized peridotites were sampled in a ~2.50 m ultramafic interval within the gabbro section at ~171 mbsf. This ultramafic interval is cut by several altered gabbro dikes. Sample 304-U1309D-31R-1, 25–28 cm, a dunite (Unit 77), and Sample 31R-2, 11–17 cm, a harzburgite (Unit 79), were taken as far as possible (>20 cm) from these gabbroic dikes.

The bulk rock compositions of these samples primarily reflect the relative abundance of their primary phases, olivine and pyroxene. They have 43.8–44.16 wt% SiO_2, 43.39–43.46 wt% MgO, and 0.02–0.04 wt% TiO_2. The dunite is distinguished by lower Al_2O_3 (~0.2 wt%) compared to the harzburgite (0.87 wt% Al_2O_3). Al_2O_3 is concentrated in pyroxenes and, to a lesser extent, in spinel in plagioclase-depleted samples, so its variations between the dunite and harzburgite samples mainly reflect pyroxene content. Both samples have high CaO content (1.15 wt%) compared to Hole U1309B harzburgites. Together with high CO_2, these relatively high CaO contents probably indicate late carbonate precipitation, as shown by visual core description and thin section descriptions. Both samples display relatively high Fe_2O_3 content (10.03–10.84 wt%) and low Mg# (88.9–89.6), the more Fe rich sample being the dunite.

Sample 304-U1309D-31R-2, 11–17 cm, the harzburgite, has trace element compositions comparable to Hole U1309B harzburgites, with 0.6 ppm Y, 52 ppm V, 12 ppm Sc, 2350 ppm Ni, 2603 ppm Cr, and 125–150 ppm Co. The dunite, Sample 304-U1309D-31R-1, 25–28 cm, has higher Ni content (3080 ppm) but lower Cr and V contents (1009 ppm and 19 ppm, respectively). Ni concentrates in olivine, whereas Cr and V concentrate in spinel. According to thin section descriptions, Sample 304-U1309D-31R-1, 25–28 cm, is composed of 98% olivine and 2% spinel. Whereas the high Ni content of Sample 304-U1309D-31R-1, 25–28 cm, is consistent with thin section description, the sample's low Cr and V contents suggest that a smaller amount of spinel was present in the geochemistry sample. Both samples have higher Sr contents (5–32 ppm) than Hole U1309B harzburgites. This Sr enrichment may be related to the carbonate alteration observed in these two samples.

Except for chemical variations related to carbonate alteration, the compositions of Samples 304-U1309D-31R-1, 25–28 cm, and 31R-2, 11–17 cm, are comparable to those of Hole U1309B peridotites (Fig. F231). The low Al_2O_3 and incompatible element contents of the two samples suggest that, prior to alteration, these peridotites were more refractory than Leg 153 peridotites. However, like Hole U1309B harzburgites, they are enriched in Fe compared to tectonically emplaced and abyssal peridotites with the same MgO contents, the dunite being the more Fe enriched (Fig. F230). This slight Fe enrichment explains their relatively low Mg#. We interpret these variations as resulting from melt-rock interactions involving Fe-Mg exchange with an olivine-saturated, basaltic melt.

Discussion

Basaltic rocks

Basalt and diabase sampled at Site U1309 are tholeiitic basalts to basaltic andesites with compositions that overlap basalt glasses from the entire MAR. One of the most striking features of Site U1309 basalts and diabases is their wide range of compositions, compared to the full suite of MAR volcanic glasses. All Site U1309 basalts and diabases were modified to different extents by alteration to tremolite and actinolite. This process may explain part of the compositional variation, especially for mobile elements including Ba, K, Sr, and, to a lesser extent, Na and Ca (for example, when plagioclase is albitized). However, elements such as Zr, Ti, Y, Sc, and V, which are assumed immobile during hydrothermal alteration (e.g., Staudigel et al., 1996), also show a wide range of compositions. These variations can be present within the same diabase (Fig. F232). In spite of their large range in composition, Site U1309 diabase and basalt have relatively constant trace element ratios (e.g., Zr/Y varies from 1.6 to 3) and are interpreted to reflect relatively uniform parental magma compositions (Fig. F214). The analyzed diabases are fine to medium grained and sparsely plagioclase phyric (see "Site U1309 thin sections" in "Core descriptions"), and their compositional variability may reflect the phenocryst abundance of the selected sample and/or the degree of differentiation of the crystallizing melt. Plagioclase-rich diabases have higher trace element contents, suggesting that these samples crystallized from a more evolved melt.

Ti and Fe contents in Site U1309 diabases are also affected by oxide abundance, as shown by the correla-

tion between Ti and V, which concentrate in oxides, and Fe content (Fig. F217). This is consistent with higher magnetic susceptibilities measured in these intervals, suggesting high magnetite contents in high-Fe basalts and diabases.

Gabbroic rocks

Site U1309 gabbroic rocks including gabbro, olivine gabbro, troctolite, and gabbronorite have compositions that are among the most primitive sampled anywhere along the MAR, as indicated by high Mg# (67–87) and low TiO_2 (<0.72 wt%), Na_2O (0.3–3.6 wt%), and trace element contents (e.g., ~11 ppm Y and ~17 ppm Zr) on average. Most of the compositional variations observed in Site U1309 gabbroic rocks are consistent with a simple mass balance involving corresponding increases in the proportion of clinopyroxene plus oxide as plagioclase proportion decreases, except in the most olivine rich gabbroic rocks (essentially in troctolites). In these rocks, the proportion of olivine increases when plagioclase decreases. Site U1309 gabbroic rocks can be interpreted as cumulates, which are related, together with Site U1309 basalts and diabases, through crystal fractionation processes to a common parental magma (see "Petrogenesis of gabbroic rocks").

Three gabbroic rocks, all sampled from the upper part from Hole U1309D, show distinctive enrichments in Zr, Y, and, to a lesser extent, Ti. These enrichments are not correlated to major or other trace element variations. On the basis of the thin section description, they are interpreted as being associated with the presence of minor phases concentrating these elements (e.g., zircon, rutile, and titanite).

Oxide gabbros are distinguished by their high TiO_2 (up to 7.9 wt%) and Fe_2O_3 (up to 29.2 wt%) contents and low Mg# (23–62). The strong variations in Fe at constant Mg observed in oxide gabbros mainly reflects the modal content of Fe-rich oxides in these samples (Fig. F233). These gabbros also have slightly higher trace element contents (~25 ppm Zr and 23–86 ppm Y), which suggest they may have crystallized from a slightly more evolved melt.

The gabbroic section is cut by several leucocratic gabbros. The composition of these samples clearly stands out in comparison to the other gabbroic groups having low MgO (3–6 wt%) and high alkali (3.4–8 wt%). Sample 304-U1309D-36R-3, 80–82 cm, a late magmatic leucocratic dike, is further distinguished by its low CaO (4.8 wt%) and much higher SiO_2 (63.1 wt%) and Na_2O (7.95 wt%) contents. The composition of this sample reflects its modal assemblage, which is mainly albite-rich plagioclase and actinolite. The high Zr is consistent with the observation of zircon in this sample (see "Site U1309 thin sections" in "Core descriptions"). Leucocratic gabbros are also characterized by their high trace element contents, with 141–301 ppm Y and 190–1180 ppm Zr. These values are significantly higher than Y and Zr concentrations observed in Site U1309 gabbroic rocks and in mid-ocean-ridge basaltic glass. This suggests that these samples were in equilibrium with an evolved trace element–enriched melt. Highly evolved dikes were also observed at Site 1275, indicating that rocks with such enriched compositions are present elsewhere in the oceanic crust (Kelemen, Kikawa, Miller, et al., 2004).

Several olivine-rich intervals comprising olivine-rich troctolite, dunite, and wehrlite are observed below 300 mbsf. The olivine-rich troctolitic intervals and the wehrlite sampled at ~61 mbsf in Hole U1309D (Unit 32) have compositions intermediate between the most primitive gabbroic rocks and peridotite sampled from the core. They have low SiO_2 (<45 wt%) and TiO_2 (<0.1 wt%), similar to other peridotites sampled from Site U1309. They have highly variable Al_2O_3 (0.9–8.4 wt%) and CaO (0.8–5.8 wt%) that reflects the mode of plagioclase and clinopyroxene in these rocks. They overlap in composition in MgO and Fe_2O_3 contents with Site U1309 peridotites, although they have more variable MgO (30–42.2 wt%) and higher Fe_2O_3 (10–15 wt%), with the highest Fe_2O_3 characterizing the dunites (12.45–15 wt%). All of these olivine-rich samples have higher trace element contents than the peridotites (2–8 ppm Y and 7–17 ppm Zr). They have high but variable Cr and Ni contents (1200–3127 ppm Cr and 1170–2311 ppm Ni). Texturally and compositionally, these olivine-rich rocks are similar to the ultramafic rocks sampled at Site 1275 (Kelemen, Kikawa, Miller, et al., 2004). They are interpreted either as ultramafic cumulates or, alternatively, the most extreme product of melt-rock interaction with (or impregnation by) a basaltic melt (see "Petrogenesis of gabbroic rocks").

Ultramafic rocks

Ultramafic rocks sampled at Site U1309 have strikingly different compositions, and, for several samples, their origin is uncertain. Bulk rock analyses show that their compositions were modified by hydrothermal alteration, which added variable amounts of volatile constituents to the original ultramafic assemblage. The highest LOI (10.35–12.52 wt%) and H_2O (10.89–13.15 wt%) contents are observed where lizardite is predominant, yet the bulk rock compositions of these ultramafic rocks primarily reflect the relative abundance of their primary phases, olivine and pyroxene. In contrast, where volatile contents are lower and talc is predominant (H_2O = 7–8.2 wt%), the bulk rock compositions mainly reflect the alteration phases, as in Sample

304-U1309B-1R-3, 17–21 cm, the ultramafic rubble sampled at the top of Hole U1309B. When a small amount of carbonate is present, the ultramafic rocks have slightly higher CO_2 and CaO contents than the other ultramafic samples.

Four of the ultramafic samples, two serpentinized harzburgite samples from Hole U1309B and two serpentinized peridotites (Units 77 and 79) sampled in a ~2.50 m ultramafic interval within the gabbro section at ~171 mbsf in Hole U1309D, have highly depleted compositions similar to those of serpentinized peridotites sampled during Leg 209. They have low Al_2O_3 (<0.8 wt%) and CaO (0.2–0.42 wt%; except for carbonate-altered samples) (Fig. F228), suggesting that, prior to alteration, these peridotites were poor in clinopyroxene. These samples are characterized by higher Fe_2O_3 values (9–10.8 wt%) compared to tectonically emplaced and abyssal peridotites with the same MgO contents (43.4–45.6 wt%) (Fig. F230). All of these samples have high Ni contents (2360–3080 ppm) and low incompatible element contents (<1.7 ppm Y and <1 ppm Zr). They likely represent residual peridotites that, prior to alteration, had chemical compositions comparable to those of Leg 209 peridotites, apart from relative FeO enrichment. Their high Fe contents may result from melt-rock reactions involving Fe-Mg exchange with an olivine-saturated, basaltic melt. It should be noted that these peridotites were sampled in ultramafic intervals crosscut by multiple gabbroic dikes.

Alteration (downhole variation in H_2O and CO_2)

As water in the primary rocks is only present in "trace amounts," the water content of the altered rocks mirrors the extent of alteration and/or the assemblage of secondary water-bearing phases, which are mainly a product of olivine alteration. In detail, tremolite and actinolite have low H_2O contents (<2.3 wt%), talc has intermediate H_2O contents (~5 wt%), and chlorite and serpentine minerals have high H_2O contents (>10 wt%) (Fig. F213).

In general, olivine gabbros are more volatile rich than the pyroxene- and plagioclase-rich gabbros. Figure F218 shows a clear decrease in water contents from 400 to 500 mbsf. High water contents of >2.5 wt% are always correlated to primary olivine-rich rock types like olivine gabbros and olivine-rich troctolites. This suggests that serpentine minerals are the main water-bearing phases in these altered rocks. The upper 401.3 m of Hole U1309D drilled during Expedition 304 shows, on average, much higher and more scattered water contents than the lower 1000 m, where the average water content is <0.5 wt%. This is consistent with visual core and thin section descriptions showing that the total degree of alteration decreases downhole. It has to be noted that the samples taken for the geochemical analysis are usually taken from the least altered core intervals and therefore show a bias to more unaltered compositions compared to the average degree of alteration.

Compared to other serpentinized ultramafic rocks from Legs 153 and 209 (Casey, 1997; Kelemen, Kikawa, Miller, et al., 2004), the CO_2 contents of the ultramafics in Hole U1309D are very low. Because pervasive carbonate precipitation is commonly related to late-stage hydrothermal alteration, it is likely that the serpentinized olivine-rich rock types from Hole U1309D are relatively unaffected by seawater.

Overall geochemical variations of Hole U1309D gabbroic rocks from troctolite to gabbro

Figures F220 and F225 show covariation of Mg# and selected major and minor elements in Hole U1309D gabbros and peridotites, respectively. Whole-rock geochemical composition of gabbros reflects modal contents and elemental compositions of constituent minerals. Whole-rock Mg# can be used as a first-order indication of the degree of differentiation with some caution, as in the case of oxide gabbros. MgO and Fe_2O_3 contents of other gabbroic rocks correlate well (Fig. F233). Their Mg#s decrease in order of olivine-rich troctolite, troctolite, olivine gabbro, and gabbro. This decrease correlates with a decrease of modal content of olivine and reflects a decrease in Mg# of these constituent phases.

SiO_2 contents of the gabbroic rocks increase with decreasing Mg#. SiO_2 contents of main constituent minerals increase in order of olivine, plagioclase, and pyroxenes (Fig. F220A). Therefore, the increasing trend of the SiO_2 of gabbroic rocks is interpreted as a decrease in modal content of olivine and an increase in plagioclase and pyroxenes with a decrease of Mg#.

TiO_2 and MnO contents broadly increase with decreasing Mg# (Fig. F220B, F220D). Because TiO_2 and MnO are basically incompatible elements, these elements concentrate in the liquid phase as a result of differentiation. Thus, these trends are appropriate for cumulates of normal fractional crystallization. It is also noted that olivine gabbros show relatively large scattering of both elements, which is probably caused by modal variation of constituent minerals. MnO contents of the olivine gabbros are more scattered than TiO_2 contents. TiO_2 partitions only into clinopyroxene, whereas MnO partitions into olivine and clinopyroxene, except in oxide gabbros. Therefore, scattering of the MnO content in the gabbroic rocks, except for oxide gabbros, reflects modal variations of both olivine and clinopyroxene. However, there is also a possibility of scattering of Mg# at the same MnO (and TiO_2) content, caused by significant modification of the Mg# of those rocks by later mag-

matic or hydrothermal processes, or change in MnO by alteration at constant Mg#.

Al_2O_3 variations of Hole U1309D gabbroic rocks show an essentially similar tendency with CaO variations. Al_2O_3 and CaO contents increase with decreasing Mg# in relatively primitive lithologies (i.e., peridotite, olivine-rich troctolite, and troctolite) and relate to the (clinopyroxene + plagioclase)/olivine ratios. Al and Ca contents decrease with decreasing Mg# in gabbros (Fig. **F220C**). CaO contents increase with decreasing Mg# in order of peridotite, olivine-rich troctolite, and troctolite (Fig. **F220E**). This tendency corresponds to a modal increase of plagioclase within those lithologies (see **"Igneous petrology"**), but CaO contents of gabbros decrease with decreasing Mg#. Although the decreasing trend of CaO in the Hole U1309D gabbros can be explained by enrichment of the albite component in plagioclase with advance of differentiation, modal content of plagioclase also increases with decreasing Mg# (see **"Downhole chemical variation within Hole U1309D,"** below). Therefore, decrease of modal content of clinopyroxene is probably the main cause of CaO and Al_2O_3 decreases for the gabbros. Olivine gabbro shows significant scattering due to modal variation of plagioclase.

Cr and Ni contents show clear fractional crystallization trends from ultramafic rocks to evolved lithologies (Fig. **F225A, F225C**). Because Cr partitions into spinel and clinopyroxene, spinel-containing lithologies (i.e., olivine-rich troctolites and troctolites) show the highest contents of Cr (>2000 ppm).

V and Y contents increase with decreasing Mg# and show normal trends of cumulates with differentiation of magma (Fig. **F225B, F225D**). Some of the olivine gabbros show trends of lower contents in Y and V compared to the main trend. Because V and Y partition into clinopyroxene in olivine gabbros, this low V and Y trend may correspond to lower modal content of clinopyroxene in those rocks. Oxide gabbros show significantly higher contents of V and Y. In basaltic systems, V strongly partitions into oxide minerals; hence, higher content of V in the oxide gabbros directly correlates to higher abundance of oxide minerals. Y also partitions toward the oxide minerals and clinopyroxenes.

Downhole chemical variation within Hole U1309D

Figures **F234** and **F235** show the downhole variation of Mg#, TiO_2, MnO, and Al_2O_3 over the whole 1415.5 m section drilled during Expeditions 304 and 305. The figure is based on 219 whole-rock analyses. Gabbroic rock compositions are characterized by significant variations in Mg# at ~600 and ~1100 mbsf. Mg# variations are correlated to abrupt changes in TiO_2 and MnO content and in lithology. In the upper part of the section, Mg# and TiO_2 do not show a significant downhole trend, although MnO increases continuously downhole. From 600 to 1100 mbsf, Mg# increases downhole but TiO_2 and MnO do not show significant downhole trends. Below 1100 mbsf, gabbroic rocks are dominantly olivine-rich troctolites that are characterized by high Mg#, low TiO_2, and high MnO.

At a smaller scale, TiO_2 shows variable downhole contents, increasing from 0 to ~300 and from ~300 to ~1020 mbsf. In the simple case of differentiation of one magma body, a reverse chemical trend would be expected. These variations probably correspond to modal content of clinopyroxene in the gabbroic rocks. Numerous crosscutting relations are observed throughout the entire section; the observed chemical variations may be related to these intrusive relations. However, because of the limited sampling, the correspondence between the descriptive units and detailed geochemical features is uncertain. At the base of structural Unit 2 (see **"Structural geology"**), three fault zones have been described (at 695, 746, and 785 mbsf). Although the Mg# shows scattering around those fault zones, systematic change is not observed across the fault zones. The major change in MG# occurs above, at ~600 mbsf.

Al_2O_3 content decreases from 0 to 600 mbsf and shows broadly constant values from 600 to 1120 mbsf, although the downhole variation shows relatively large scatter. Because plagioclase is the only main phase that contains significant amounts of Al_2O_3, the downhole variation probably corresponds to modal content of plagioclase. Figure **F235** is a comparison between whole-rock Al_2O_3 content and modal content of plagioclase based on thin section observations. Although modal content of plagioclase shows broad variability, it broadly corresponds to downhole Al_2O_3 variation.

Petrogenesis of gabbroic rocks

The range of composition of the gabbroic rocks sampled at Site U1309 spans highly primitive olivine gabbros with Mg# >85 to highly evolved leucocratic gabbros with high SiO_2 and trace element contents.

In general, whole-rock geochemical evolution of gabbroic rocks is the result of complex changes in modal composition and changes in compositions of individual constituent minerals with advance of differentiation. Therefore, precise examination of crystallization processes without mineral chemistry is difficult. However, whole-rock geochemical varia-

tions correlate with whole-rock Mg# as mentioned above, suggesting that whole-rock compositions (except for Fe-rich oxide gabbro) are useful for examination of first-order crystallization processes.

The order of fractional crystallization of olivine tholeiite magmas under anhydrous conditions at relatively low pressures (Green and Ringwood, 1967; Walker et al., 1979; Grove and Bryan, 1983; Tormey et al., 1987; Juster et al., 1989) is

ol + spl – ol + pl + spl – ol + cpx + pl – cpx + opx + pl,

where

ol = olivine,
spl = spinel,
pl = plagioclase,
cpx = clinopyroxene, and
opx = orthopyroxene.

These modes are consistent with the modal composition evolution from olivine-rich troctolites to gabbros. Low-pressure conditions for Hole U1309D gabbroic rocks are also supported by the cotectic crystallization of olivine and plagioclase as observed in troctolites (although not in all olivine-rich intervals). In basaltic systems, the cotectic relation of olivine and plagioclase disappears at ~7 kbar (Kushiro and Yoder, 1966; Presnall et al., 1978).

This suggests that the suite of gabbroic rocks sampled at Site U1309 may represent a single crystallization suite, the olivine-rich troctolites representing the first crystallization product of an olivine tholeiite magma. Yet olivine-rich troctolites have, on average, higher Ni contents than olivine-rich gabbros with similar Mg#, which is not consistent with a simple crystallization model. In addition, it should be noted that the texture of these samples with rounded olivine in a plagioclase-rich matrix (see **"Igneous petrology"**) suggests that these samples were formed by a complex multistage magmatic process. Alternatively, in these rocks, olivine and spinel may represent relics of mantle minerals. Texturally and compositionally, the most olivine rich rocks sampled in Site U1309 olivine-rich troctolite intervals are similar to the ultramafic rocks sampled at Site 1275 (Kelemen, Kikawa, Miller, et al., 2004).

Orthopyroxene-bearing gabbro and gabbronorite were sampled in Hole 1309D, mainly between ~800 and ~1000 mbsf. They may have formed as the late product of crystallization from an olivine tholeiite liquid following the olivine-clinopyroxene-plagioclase crystallization. Yet the Mg# of orthopyroxene-bearing gabbros and gabbronorites overlap the same range of values as olivine gabbros and gabbros, which is inconsistent with crystallization from a more evolved melt. In addition, they do not show trace element enrichments compared to gabbros as expected for late products of differentiation.

Comparison with other oceanic gabbros

Figure **F236** is a whole-rock molecular Mg/(Mg + Fe) and Ca/(Ca + Na) diagram of Hole U1309D gabbros. Fields of other drill cores from MAR gabbros (Casey, 1997; Kelemen, Kikawa, Miller, et al., 2004) and the SWIR (Dick et al., 2000) are also shown in the figure for comparison. The gabbroic rocks from Hole U1309D plot on the primitive end of MAR gabbros, suggesting that Hole U1309D gabbros and other MAR gabbros could have been derived from relatively similar parent magmas and crystallized under similar conditions. One of the most significant aspects of Hole U1309D gabbros in terms of geochemical features is the presence of a series of rock types that span a compositional range from very primitive to moderately evolved. The expanded range in composition has rarely been noted in oceanic settings.

A second salient feature is the ubiquity of oxide gabbros throughout Hole U1309D (Fig. **F233**). A similar presence has been reported for Hole 735B, Atlantis Bank (Dick et al., 1999), in the MARK area (Cannat, Karson, Miller, et al., 1995), and at 15°N at the MAR (Leg 209; Kelemen, Kikawa, Miller, et al., 2004). Oxide gabbros may make up a common component of gabbroic rocks at slow-spreading ridges.

Paleomagnetism

Basaltic, diabasic, gabbroic, and troctolitic rocks and minor serpentinized peridotite were recovered from Site U1309 (see **"Igneous petrology"**). Holes U1309B and U1309D penetrated to ~100 and ~1415 mbsf, respectively, and recovery was sufficient that both holes were well suited for continuous measurements of archive halves. Approximately 1700 core pieces yielded well-defined remanence directions, with ~1400 of these directions defined by averages of multiple measurements. In addition, remanence measurements were made on 35 discrete samples from Hole U1309B and 477 discrete samples from Hole U1309D. During Expedition 304, the combined remanence data from archive halves and discrete samples were used to estimate average declinations (for ~100 core pieces from Hole U1309B and 400 pieces from the upper 400 m of Hole U1309D) that may be used for reorientation studies. Because of the high core recovery rate during Expedition 305, a number of errors in the shipboard data could not be corrected on board. Therefore, all data from Expedition 305 were checked for errors and reprocessed during the postcruise meeting to make the data sets from the two expeditions as compatible as possible.

The data from Expeditions 304 and 305 are described separately below, and the two data sets are then combined to review the overall distribution of remanence directions and their tectonic significance.

Expedition 304

Samples from both holes are characterized by dominantly negative inclinations that are taken to represent a reversed polarity remanence. However, there are important downhole fluctuations in the inclination from both archive halves and discrete samples. Samples from the uppermost ~200 m have a mean inclination (–48°) that is essentially identical to that expected from a geocentric axial dipole (±49°), suggesting little tectonic tilt has occurred since the remanence was acquired. In contrast, samples from deeper levels in Hole U1309D have significantly shallower reversed polarity inclinations, suggesting a more complicated tectonic history. In addition, multicomponent remanences (with up to four well-defined components) have been documented from thermal demagnetization studies. These results provide compelling evidence for the influence of later normal polarity magnetizations in several intervals of the core. The presence of both polarities is not entirely unexpected, given the location of the site near magnetic Anomaly 2 (Zervas et al., 1995). With further detailed thermal demagnetization studies, the multicomponent magnetizations should provide important information on the thermal history of the site.

Some intervals in the holes, particularly within diabase and oxide-rich gabbroic units, have positive inclinations and, therefore, may be of normal polarity. These positive inclinations are, however, significantly steeper than the present field inclination (48°) or the geocentric axial dipolar inclination at the site. A detailed discussion of these data is presented below and demonstrates that data from intervals with positive inclinations must be treated with caution. No single-component magnetizations of normal polarity of unequivocal geomagnetic origin were observed.

Remanence data

Continuous measurements

Remanence measurements were made at 2 cm intervals on all archive-half pieces longer than ~7 cm. All archive halves were subjected to stepwise alternating-field demagnetization at 5–10 mT steps up to maximum peak fields of 60 mT, with some core pieces also treated at 70 and 80 mT if significant remanence remained. Whole core and archive-half susceptibility data obtained from the MST and the archive MST (AMST; see **"Physical properties"**) were filtered to preserve only data corresponding to the intervals where remanence measurements were made. Thus, the resulting remanence and susceptibility data sets (Fig. **F237**) are significantly less affected by artifacts resulting from small core pieces than are the original unfiltered data sets.

The characteristic remanent magnetization (ChRM) directions were calculated by principal component analysis (PCA) (Kirschvink, 1980) at all measurement points along the core pieces where stable vector components could be identified on Zijderveld plots. Initially, this was done by manually picking directions for each 2 cm interval through Hole U1309B and the uppermost 130 m of Hole U1309D. Approximately 1500 vector endpoint diagrams were individually examined in this manner. This procedure allowed recognition of the demagnetization characteristics of different rock types. Based on these characteristics, we developed a semiautomated method of identifying linear segments on the demagnetization plots using the MacPaleomag software for the Macintosh. Such an automated procedure was necessary because, ultimately, demagnetization data from >5500 intervals were analyzed. Principal components were calculated for each of three overlapping coercivity ranges (40–80, 30–60, and 20–50 mT) at each 2 cm measurement point. Only principal components with maximum angular deviation (MAD) angles <5° were considered acceptable. The highest stability linear component found in this way for each measurement point was retained for further analysis (a significant number of points had no linear segment that passed our selection criteria). These data were then averaged at a piece level for plotting and interpretation.

Various basaltic rocks (aphyric, plagioclase-phyric, olivine-phyric, olivine-plagioclase-phyric, and fine-grained basalt), diabasic rocks (diabase and microdiabase), gabbroic rocks (layered gabbro, microgabbro, gabbro, olivine-bearing gabbro, olivine gabbro, troctolitic gabbro), troctolitic rocks (troctolites and olivine-rich troctolites), and serpentinized harzburgite were described from Site U1309 during Expedition 304 (see **"Igneous petrology"**). For simplicity, we have grouped these various rock types into seven primary lithologies:

1. Ultramafic rocks
2. Troctolite
3. Olivine gabbro and troctolitic olivine gabbro
4. Oxide and disseminated-oxide gabbro
5. Gabbro, including olivine-bearing gabbro
6. Diabase
7. Basalt

These divisions are sufficiently distinct to be meaningful in terms of their magnetic properties.

The most significant variations in the NRM intensity and susceptibility for archive halves from Site U1309 are well correlated with lithology (Figs. F237, F238; Table T12). Gabbro and troctolite samples are characterized by low susceptibilities and natural remanent intensities. The mean NRM values are considerably lower than geometric mean values for gabbroic samples (~1 A/m) from the MARK area, Hole 735B, or Site 1275 (Gee et al., 1997; Dick, Natland, Miller, et al., 1999; Kelemen, Kikawa, Miller, et al., 2004). Basalt samples from Site U1309 generally have higher susceptibilities (by approximately a factor of 3–5) than those of the gabbros or troctolites. The remanent intensities of basalt samples are higher than those of the gabbros, although both lithologies show considerable variation. In contrast, diabase samples have much higher NRM intensities (up to 20 A/m) and correspondingly higher susceptibilities. Serpentinized peridotites are the most highly magnetic lithology recovered, with a range of susceptibilities suggesting magnetite concentrations of 1%–3% by volume and remanent intensities, on average, three times those observed in the diabases. Although olivine gabbros have a relatively low average NRM intensity (0.7 A/m), this group also includes very high intensities, presumably reflecting variable degrees of serpentinization of the more olivine-rich lithologies (Fig. F238).

Inclinations of NRMs vary widely downhole from –73° to 89°, but generally migrate to lower values during initial demagnetization steps (Fig. F237). Nearly all samples show evidence of a drilling-induced magnetization, evident from the consistently steep positive NRM inclinations. In many lithologies, this drilling overprint is easily removed by alternating-field demagnetization to 15–30 mT, revealing natural components of lower and dominantly negative inclination.

Demagnetization characteristics are strongly dependent on lithology. Most gabbro intervals are dominated by a low-intensity, high-coercivity reversed component (e.g., Fig. F239A). Similar high-stability reversed components are also observed in many basalt samples. Diabase intervals are dominated by normal polarity components and exhibit three types of behavior:

1. Type A intervals have a low-coercivity, steeply inclined component that is removed by fields of 10–15 mT, leaving a stable, more shallowly inclined normal polarity component that contributes a significant proportion of the natural remanence and that persists to 60 mT or above (e.g., Fig. F239B).
2. Type B intervals have a low-coercivity, steeply inclined component that dominates the remanence, and no stable endpoint is reached (e.g., Fig. F239C).
3. Type C intervals have an extremely weak reversed component of high coercivity that is isolated following removal of the strong normal component (e.g., Fig. F239D).

A number of lines of evidence suggest that the normal polarity components observed as the dominant remanence in the diabase intervals (and as low-stability overprints in all lithologies) represent drilling-induced remanences and/or artifacts of the measuring and demagnetizing process. Perhaps the best indication that most normal polarity components recovered from archive halves have no geomagnetic significance comes from comparison of declinations for samples with positive and negative inclinations (Fig. F240). Principal components with negative inclinations (reversed polarity) show an essentially random distribution of declinations, as expected for azimuthally unoriented core pieces (Fig. F240A, F240B). In contrast, positive inclination remanence components from nearly all archive halves are biased toward the +x coordinate axis in the core reference frame (x on stereo plot; Fig. F240C, F240D), suggesting the measured remanence is dominated by some spurious magnetization or artifact. A small number of archive-half pieces have shallower positive inclinations and more random declinations, suggesting they may preserve some record of geomagnetic field behavior. Demagnetization results from discrete samples provide additional information concerning the origin and significance of these apparently normal polarity components, and we will therefore return to this below.

Discrete samples

Stepwise demagnetization data (from either alternating-field or thermal treatment) were acquired for 35 discrete samples from Hole U1309B and 142 discrete samples from Hole U1309D (Table T13). The demagnetization behavior of discrete samples from Site U1309 varies considerably with lithology, as noted for archive halves. Although a low-stability (presumably drilling related) component is evident in nearly all samples, this drilling component is a relatively small fraction of the remanence (<25%) in most gabbroic samples and is readily removed by alternating-field demagnetization at 10–20 mT (Fig. F241A, F241C). The ChRM of gabbroic samples is uniformly of reversed polarity and shows linear decay toward the origin on vector endpoint diagrams over a range of peak alternating-field values extending as high as 120–150 mT. The median destructive fields (MDFs; the alternating-field value necessary to reduce the NRM intensity [expressed as vector difference sum to account for multicomponent remanence] to one-half

its original value) for gabbroic samples average 30 mT, indicating the remanence is very stable.

Numerous gabbroic samples were subjected to stepwise thermal demagnetization (Fig. F241B, F241D). The ChRM direction is typically isolated above 500°–550°C, and median destructive temperatures (calculated in an analogous fashion as the MDF) range from 530° to 560°C for all samples except one. Where multiple discrete samples were taken from the same core piece, alternating-field and thermal demagnetization isolate essentially the same characteristic magnetization direction (cf. Fig. F241A, F241B). The maximum unblocking temperature of 580°–590°C, the discrete range (dominantly 500°–580°C) of unblocking temperatures, and high coercivity all suggest that the remanence is carried by fine-grained magnetite.

Negative inclinations are also characteristic in most other lithologies, although this reversed polarity component is, in some cases, obscured by a substantial drilling-related normal polarity magnetization. The substantial drilling overprint in diabase, basalt, and serpentinized harzburgite samples is reflected in the low MDF values (average = ~3 mT) for these lithologies. After removal of the drilling overprint, the small interval of serpentinized harzburgite recovered in Core 304-U1309B-11R showed well-defined ChRM directions of reversed polarity (Fig. F241E). Altered basaltic breccia samples have remanence characteristics very similar to those of gabbroic samples (i.e., low NRM intensities and high stability [average MDF = 39 mT])—nearly univectorial remanence decay (Fig. F241F). Basalt samples generally have substantial low-stability overprints, but reversed polarity ChRM directions were isolated for all discrete samples from this lithology. As noted above for archive-half measurements, discrete samples from diabase units are characterized by substantial low-stability drilling-related overprints that, in many cases, obscure the primary remanence (discussed more fully below).

The characteristic remanence inclinations of discrete samples are in general agreement with the results from archive halves (Fig. F242). The reversed polarity components are distributed along a small circle (Fig. F240A, F240B), as expected from azimuthally unoriented core pieces and similar to the pattern of reversed polarity ChRMs from the archive halves. Unexpectedly, and similar to the observations from the archive halves, the low-stability normal polarity components from the discrete samples are clustered about the –x-coordinate axis in the core reference frame (Fig. F240C, F240D). A possible explanation of this bias is that discrete samples may acquire a small remanence parallel to the sample –x-direction during laboratory drilling of the working half (see also "Appendix C").

Discrete samples reveal a strong clustering of inclinations near –40°–50°; however, a small number of discrete samples have positive or shallow inclinations. Steep positive inclinations (>65°) were isolated primarily from thermal demagnetization of diabase and some gabbroic samples. The remanence in these samples (red dots in Fig. F240C) initially is very similar to the direction of the steep low-stability component isolated by alternating-field demagnetization (blue dots in Fig. F240C, F240D) and decays univectorially to the origin. Thus, the steep positive inclinations recovered by thermal demagnetization likely reflect samples in which the remanence was essentially entirely reset by the drilling process. A small number of samples have moderate positive inclinations that apparently represent true normal polarity magnetizations (i.e., unrelated to the drilling process).

Downhole inclination variations in archive halves are corroborated by characteristic remanence directions determined from discrete samples. For the shallowest interval (0–180 mbsf, including data from both Holes U1309B and U1309D), discrete samples with negative inclinations have an average value of –48.7° (+3.4°/–1.7°; n = 76; κ = 38.3; calculated using the inclination only method of McFadden and Reid [1982]). The interval from 180 to 260 mbsf shows more scattered inclinations that average –31.5° (+8.5°/–6.2°; n = 25; κ = 14.9). This interval includes subhorizontal remanent inclinations with high magnetic stability (as judged from both alternating-field and thermal demagnetization studies). Discrete samples from 260 to 400 mbsf in Hole U1309D have intermediate inclinations (–38.0°, +4.2°/–2.9°; n = 43; κ = 34.7) similar to those observed in the more abundant archive-half data. Downhole variations in magnetic remanence and their tectonic significance are discussed more fully at the end of this section in conjunction with results from Expedition 305.

Results from discrete sample demagnetization also provide an opportunity to evaluate the accuracy of the archive-half remanence data that are used (in combination with the discrete sample results) to reorient core pieces to a common geographic framework (Table T14). Numerous core pieces have stable remanence directions identified in both the archive-half data and a discrete sample from the same core piece. Comparison of the declinations of these two types of data (Fig. F243) shows that most pairs of data agree within ~10° (note that points in the upper

left and lower right of this diagram are not, in fact, discrepant but simply reflect the discontinuity at 360°).

Origin and significance of normal polarity remanence components

Most normal polarity data from Site U1309 (whether derived from the archive halves or discrete samples) have a number of characteristics that invalidate their use in tectonic studies.

Declination bias

Samples with positive inclinations (whether from the archive or working half) show a bias along the x-axis in core coordinates (Fig. **F240**) that is unexpected for core pieces that are free to rotate in the core barrel. An attempt is made to align the dominant fabric elements between core pieces prior to core splitting. However, this strategy should be most successful in lithologies with strongly developed petrofabrics (e.g., deformed gabbros). The clustering of normal polarity components is predominantly observed in diabase intervals, which have relatively weak petrofabrics. Thus, it is difficult to attribute the clustering of normal polarity components to accurate alignment of petrofabric elements between diabase pieces. A series of experiments conducted to characterize the response functions of the magnetometer (outlined in **"Appendix C"**) indicate that the X-superconducting quantum interference device (SQUID) (and, to a lesser extent, the Y-SQUID) sensor picks up a signal from the axial (z)- component of magnetization. Thus, samples with strong, steeply inclined normal components (e.g., drilling remanence) generate declinations biased toward the north or south, depending on the sample position in the sensor region.

Low stability of multidomain magnetite

Figure **F244** shows a clear relationship between the inclination of magnetization vectors (determined from PCA of demagnetization data from archive halves) and volume susceptibility (determined on the AMST system). Samples with reversed polarities are strongly clustered around low susceptibilities of ~30 × 10^{-5} to 40 × 10^{-5} SI and display a range of inclinations consistent with that expected from geomagnetic secular variation. In contrast, steep normal polarities of magnetization predominantly cluster at inclinations greater than the present-day magnetic field and are present in samples with the highest magnetic susceptibilities (two orders of magnitude higher than that of the reversed polarity samples). This correlation presumably reflects the abundance of coarse, multidomain magnetite grains in the diabase and serpentinized, olivine-rich intervals that are more susceptible to acquiring a drilling-induced remanence. This is also indicated by the rapid decrease in remanence intensities of these lithologies during the initial stages of alternating-field demagnetization, with MDF values that average 3 mT.

Comparison of the results of different demagnetization treatments on discrete samples from a single diabase interval provides further insight into the nature of the magnetization of these rocks (Fig. **F245**). The remanence of these samples is dominated by the steeply inclined drilling-induced component of magnetization. For the sample shown in Figure **F245A** and **F245B,** alternating-field demagnetization successfully removes this component and isolates a high-coercivity reversed polarity component. Curvature of the demagnetization path indicates partial overlap of the coercivity spectra of the grains carrying natural and drilling-induced magnetizations. Substantial loss of remanence during low-temperature demagnetization (Fig. **F245C, F245D**) provides further evidence that the low-coercivity component is carried by unstable multidomain magnetite, with subsequent alternating-field treatment isolating a poorly defined reversed polarity component. Thermal demagnetization indicates distributed unblocking and a maximum unblocking temperature close to the Curie temperature of magnetite. The magnetization decays univectorially to the origin (Fig. **F245E, F245F**), with a direction identical to the drilling-induced component observed during alternating-field treatment and with no indication of any reversed polarity component. This indicates complete overlap of the unblocking temperature spectra of magnetite grains carrying the natural and drilling-induced magnetizations.

The presence of multidomain magnetite grains (which are particularly susceptible to acquisition of high-intensity drilling-induced remanences) and the partial to complete overlap of demagnetization spectra of natural and artificial components combine to make recovery of natural components of magnetization of geological significance problematic in the diabase intervals, particularly from the more abundant archive-half (continuous) data. These difficulties are further illustrated in Figure **F30,** which shows demagnetization results from two diabase intervals where both archive-half and discrete sample data are available. Here, alternating-field demagnetization isolates a high-coercivity, reversed polarity component in both discrete samples (Fig. **F30A, F30C**), in contrast to corresponding points in the archive-half data where either the alternating-field data are too noisy at high field levels to detect stable components

(Fig. F30B) or (more rarely) where only a weak reversed component is observed during the last stages of demagnetization (Fig. F30D).

As a result of the remanence characteristics and analytical difficulties described above, there are insufficient discrete samples or archive-half intervals at Site U1309 where high-coercivity, nondrilling-related components of magnetization have been successfully isolated to allow robust directional characterization of these components in diabase, serpentinized peridotite, and some oxide-rich gabbroic intervals. We note, however, that where such components are identified in discrete samples (e.g., Figs. F245B, F245D, F30A, F30C), they are invariably of reversed polarity and may have some utility in reorienting core pieces. Diabase intervals with Type B behavior during archive-half demagnetization are also observed to migrate to lower inclinations and, eventually, to reversed inclinations during demagnetization at higher fields (Fig. F239C). Together, these data suggest that both the diabase and serpentinized peridotite recovered from Site U1309 held reversed polarity magnetizations prior to drilling, in keeping with the reversed polarity magnetizations documented in most other intervals.

Multicomponent remanence in gabbroic rocks from Hole U1309D

Magnetic results from olivine gabbro and troctolite from Section 304-U1309D-22R-2 provide compelling evidence for the reheating of some gabbroic rock from Site U1309 during a normal polarity interval. Archive-half data from Section 304-U1309D-22R-2 (Piece 1) have ChRM directions with negative inclinations but progressively become shallower toward the bottom of the piece (Fig. F246C, F246D). These shallow inclinations continue through the upper 20 cm of Section 304-U1309D-22R-2 (Piece 2), where an abrupt shift in direction occurs. A ~20 cm wide interval with positive inclinations and nearly antipodal declinations (relative to the top and bottom of the piece) is roughly centered on a small pyroxene-rich vein cutting the olivine gabbro (Fig. F246A). This interval is also marked by high stability to alternating-field demagnetization (Fig. F246E) and an increase in MS (Fig. F246B), though the latter feature appears to correlate more closely with a ~10 cm wide troctolite band. It is worth noting that the low susceptibility values throughout this section preclude a significant amount of magnetite (e.g., from serpentinization of olivine). For example, the highest susceptibility values within the troctolite (~24 × 10^{-5} SI) could be entirely explained by the paramagnetic contribution from iron in silicate minerals if the bulk rock has ~4%–5% FeO (at the low end of values measured for troctolites during Expeditions 304 and 305). Given the susceptibility of magnetite (3 SI), the troctolite would have a maximum of ~80 ppm magnetite even if no iron-bearing silicates were present in the rock.

Two discrete samples (one from Section 304-U1309D-22R-2 [Piece 1] and the second from Piece 2 near the pyroxene-rich vein) were thermally demagnetized to further investigate this apparent normal polarity magnetization. The upper sample (Sample 304-U1309D-22R-2, 8–10 cm) (Fig. F247B) exhibits a high-stability reversed polarity remanence that is unblocked from 520° to 600°C. In addition, this sample shows a well-defined normal polarity magnetization component (inclination = +57°) removed at temperatures from 350° to 520°C. Results from the corresponding interval of the archive half (Fig. F247C) recover a similar high-stability reversed polarity remanence but show little evidence of the nearly antipodal normal polarity overprint isolated by thermal demagnetization.

The lower sample (Sample 304-U1309D-22R-2, 79–81 cm) (Fig. F247D) also shows a high-stability reversed polarity remanence isolated at temperatures >550°C. This sample, however, shows a much larger normal polarity overprint (inclination = +43°), such that the initial NRM direction has a positive inclination. In this case, the archive-half data show a normal polarity ChRM after removal of a steep drilling-related component, although the peak alternating-field of 80 mT is insufficient to demagnetize the sample. Finally, the outer chip from the minicore sample was also alternating-field demagnetized (Fig. F247F). As with the archive-half data, this sample has very high coercivity and a normal polarity ChRM (inclination = +40°).

The normal polarity components in these thermally demagnetized discrete samples are distinct from the steep, low-coercivity component normally associated with a drilling-induced remanence. Indeed, a steep component with positive inclination (removed by ~300°C) that likely represents a drilling-induced component is evident as a distinct magnetization component in both samples. Thus, the moderate-inclination normal polarity component isolated by thermal demagnetization appears to reflect reheating during a normal polarity interval. Although the normal polarity interval in the archive-half data coincides with a small (1 cm wide) pyroxene-rich intrusion, this small intrusion is unlikely to be responsible for the normal polarity overprint throughout the section. Rather, we suggest that a larger intrusion not sampled by the drill core is more likely responsible for this reheating episode.

In addition to the localized example of reheating described above, thermal demagnetization data elsewhere indicate that such complex multicomponent remanences are widespread in Hole U1309D (Fig. F248), although these complexities are not readily detected by alternating-field demagnetization. The directions and temperature stability of these various magnetization components provide valuable information on the thermal and, potentially, the tectonic history of the samples. The sharp breakpoints between the high-temperature components are most compatible with a simple thermoremanence because chemical remanence should be accompanied by a broad range of unblocking temperatures. An initial steeply inclined component present in some samples is removed by temperatures of 100°–350°C (blue arrows in Fig. F248) and is interpreted as a drilling-induced overprint. A normal polarity component (orange arrows in Fig. F248) is commonly observed between temperatures of 350° and 530°C, with a mean inclination of 53.6° (+6.4°/–8.2°; n = 11; κ = 40.3). This moderate-inclination component is, therefore, distinct from the steep, low unblocking temperature (and low coercivity) drilling-induced component. The highest temperature component (red arrows in Fig. F248) is consistently of reversed polarity and unblocks between 530° and 590°C. This component typically has a shallower inclination than the normal polarity overprint, and the two components are not antipodal. These samples are therefore characterized by two components of geomagnetic significance that were acquired over sharply defined blocking temperature intervals. A sample from Section 304-U1309D-71R-2 (Fig. F248C) reveals an additional lower unblocking temperature reversed component between 200° and 350°C, providing evidence of a (presumably later) reversed overprint in at least this section.

Magnetic fabric

The anisotropy of MS (AMS) was determined for most discrete samples from Holes U1309B and U1309D during Expedition 304 (Table T15). The remaining samples had susceptibilities too low to reliably measure onboard. Most susceptibility tensors are moderately anisotropic (P' < 1.10, where P' is the corrected degree of anisotropy) (Jelinek, 1981), but significantly higher degrees of anisotropy (P' up to 1.37) were noted for several very coarse grained gabbroic samples (Fig. F249E). The majority of samples have triaxial susceptibility ellipsoids, with a range of ellipsoid shapes. In the core reference frame, the only discernable pattern is a concentration of minimum principal axes at moderate to steep inclinations (Fig. F249A).

In order to compare the orientations of magnetic fabrics from different samples, some common reference frame is required. Under the assumption that the stable remanent magnetization approximates the time-averaged reversed polarity direction, the magnetic fabric data have been restored to a common reference frame by a simple vertical axis rotation that restores the remanent declination to the presumed reversed polarity direction (180°). After this restoration, the largest concentration of minimum eigenvectors lie in the southwest quadrant, with a corresponding cluster of maximum eigenvectors in the northeast quadrant (Fig. F249B). To a large extent, these concentrations of eigenvectors can be attributed to diabase and basaltic samples (Fig. F249C). Eigenvectors from gabbroic samples are much more variable but also show a concentration of minimum eigenvectors in the southwest quadrant (Fig. F249D). Two samples from the serpentinized harzburgite in Core 304-U1309B-11R have relatively consistent fabrics, with a shallow east-dipping magnetic foliation.

The orientation of the maximum eigenvector of the susceptibility tensor for mafic dikes typically has been interpreted as parallel to the magmatic flow or emplacement direction, with the minimum eigenvector approximating the pole to dike plane (e.g., Knight and Walker, 1988; Tauxe et al., 1998). Although a minority of dike samples have AMS fabrics that do not conform to this simple model, the AMS results from diabase samples from Site U1309 may provide valuable structural information for the site. The principal axis directions from multiple diabase samples taken from the same core piece are well grouped, as emphasized by the small 95% error bounds of three samples from Section 304-U1309B-19R-2 (Piece 4) (Fig. F249C). We note that a sample (Sample 304-U1309D-15R-2, 126–128 cm) from a potentially correlative diabase in Hole U1309D has a very similar magnetic fabric (maximum eigenvector = 359°/21°). To the extent that the interpretive model for AMS in mafic dikes outlined above is applicable, the minimum eigenvectors should approximate the pole to the dike plane (i.e., the diabase units would represent sills dipping gently to the northeast). Although the number of specimens is small, the consistency of the maximum eigenvectors in diabase and basalt samples may indicate a northeast–southwest flow lineation.

Comparison of core magnetic data and logging results

The General Purpose Inclinometry Tool (GPIT) incorporates a three-axis fluxgate magnetometer that is primarily used to provide azimuthal information for

the FMS images (see "Downhole measurements"). In principle, these fluxgate sensors also can provide valuable information on the intensity and direction of the magnetization of the borehole wallrocks. The horizontal and vertical magnetic anomalies from the first FMS/GPIT run in Hole U1309B are shown in Figure F250 (note that north and east magnetic anomalies cannot be resolved because there is no independent estimate of the azimuth of the logging tool string). At first glance, this anomaly pattern appears remarkably consistent with the magnetic inclination measured on the recovered core. The vertical anomaly is positive and the horizontal anomaly is negative, as expected for reversely magnetized material, and the average values (approximately +5000 nT for the vertical and –2000 nT for the horizontal) correspond to an inclination value of about –50°.

Comparison of the borehole anomaly data with remanence intensity data from the cores indicates that this correspondence is simply fortuitous. We constructed a simple forward model of the borehole magnetic field based on horizontal, uniformly magnetized layers with intensities based on average values from the core. Average remanence intensities were calculated for seven intervals corresponding to large-scale lithologic changes in the core (Fig. F250). Intensity data from the archive halves after 10 mT demagnetization were used to minimize the influence of drilling-induced remanence (which should not be present in the borehole walls except in the immediate vicinity of the borehole). The calculated anomalies in gabbroic sections of the core are typically less than a few hundred nanotesla, in contrast to the values of several thousand nanotesla measured by the GPIT. This discrepancy is most readily attributed to improper calibration of the fluxgate sensors.

Despite these calibration problems, there is useful information in the borehole magnetometer data. After adjusting the baseline levels and subtracting a model for the magnetic effect of the pipe on the vertical anomaly, the calculated and observed anomalies are similar in character. The observed anomaly data indicate a highly magnetic interval near 73 mbsf in an interval with incomplete recovery. The magnitude of this anomaly suggests that a significant interval of strongly magnetic material (possibly serpentinized peridotite or diabase) was not recovered. In contrast, the near constant and low anomaly amplitudes in other intervals (e.g., 40–57 and 68–94 mbsf) suggests that the recovered materials are representative of the entire drilled interval. Regions such as the interval from 27 to 37 mbsf, where the modeled (based on reversed polarity remanences) and observed anomalies are of opposite sign, may indicate large induced magnetizations or possibly normal polarity of the natural remanence.

Expedition 305

Expedition 305 deepened Hole U1309D to ~1415 mbsf. Shipboard paleomagnetic studies during Expedition 305 consisted of continuous measurements of archive-half sections and progressive demagnetization measurements of discrete samples, in a manner similar to that performed during Expedition 304 (with the exceptions described in the "Methods" chapter). A total of 335 minicore samples were stepwise thermally or alternating-field demagnetized to evaluate the directional stability and coercivity/unblocking temperature spectra of each sample. The Königsberger ratio, which is defined as the ratio of remanent magnetization to the induced magnetization in the Earth's magnetic field, was also calculated using the volume MS for these samples. AMS was measured on 216 minicore samples with the Kappabridge KLY-2 using the standard 15-position measuring scheme. The remaining samples had susceptibilities that are too low to measure their AMS reliably onboard.

Remanence data

Continuous measurements

Within the recovered rocks, there are considerable variations in magnetic properties and demagnetization behavior among the various lithologies, which are similar to what was observed during Expedition 304 (see "Expedition 304"). The most important observations during Expedition 305 are summarized as follows:

1. The NRM intensities of the archive halves span more than four orders of magnitude (ranging from 0.001 to >10 A/m) (Fig. F251). Variations in magnetic susceptibility are consistent with the variations in NRM intensity. Susceptibility data from the core sections provide important information on the Fe-Ti oxide content in the rocks recovered from Hole U1309D. Magnetic susceptibility measurements revealed sharp peaks in numerous oxide gabbro core sections (e.g., Sections 305-U1309D-113R-1, 114R-2, 254R-1, 270R-3, 272R-3, 276R-1, and 277R-1), olivine-rich troctolite zones (Sections 305-U1309D-111R-4, 112R-1, 227R-2, 228R-2, 238R-1, 242R-2, 243R-1, and 247R-2), and olivine-bearing gabbro (Sections 305-U1309D-135R-1, 139R-1, 159R-4, and 241R-1). These susceptibility peaks were verified by further measurements of corresponding discrete samples.

2. A remagnetization imparted by the coring process is commonly encountered, as noted during previous DSDP, ODP, and IODP cruises (e.g., Gee et al., 1989). This remagnetization is characterized by NRM inclinations that are strongly biased toward vertical (toward +90°) in a majority of cores as is largely removed by alternating-field demagnetization to 30 mT (Fig. **F251**). In some intervals with relatively low magnetic susceptibility (e.g., ~930–970 mbsf), the remagnetization appears to have only affected inclination and little effect on NRM intensity is apparent (Fig. **F251**). Interestingly, some intervals in the holes (e.g., Core 305-U1309D-101R, ~505 mbsf), particularly within medium- to coarse-grained gabbro sections, show little drilling-induced overprinting both in NRM intensity and inclinations.
3. Data remanence inclinations obtained in Hole U1309D can be correlated with lithology. As shown in Figure **F252** and Table **T16,** gabbroic samples (Fig. **F252A–F252C**) are characterized by dominantly negative inclinations (reversed polarity) and low NRM intensity and susceptibility, whereas diabases, troctolites, and olivine-rich troctolites have higher NRM intensity and susceptibility and, apparently, dominantly positive inclinations (normal polarity) (Fig. **F252D–F252F**). These rocks with positive inclinations typically have one order of magnitude higher NRM intensity and magnetic susceptibility than those of fresh gabboric rocks and commonly have much lower coercivity, as indicated by a rapid decrease in intensity during lower steps of alternating-field demagnetization experiment. In a majority of cases, the positive inclination zones correspond to olivine-rich intervals where the concentration of serpentine is high (e.g., Fig. **F251,** 1120–1200 mbsf where troctolite and olivine-rich troctolite are recovered). Interestingly, olivine-rich gabbro and troctolite samples in Hole 735B also recorded apparently opposite magnetic polarity than those of surrounding metagabbros (Kikawa and Pariso, 1991). These observations of normal polarity with serpentinization are intriguing and may have rock magnetic (drilling-induced overprint) or geologic implications (hydrothermal alteration in a normal polarity field). Borehole magnetic measurement results and more complete paleomagnetic and rock magnetic studies are needed to further address this problem (see discussion in **"Expedition 304"**).
4. Although the timing of remanence acquisition is uncertain, the presence of both polarities is not unexpected because of the age and location of the site near magnetic Anomaly 2 (Olduvai normal epoch; 1.66–1.88 Ma) (Zervas et al., 1995; Gee and Blackman, 2004). However, the inclinations for the recovered rocks during Expedition 305 (depth range = 400–1415 mbsf) are significantly shallower than expected from a geocentric axial dipole (±49°), suggesting some tectonic tilt occurred after the remanence was acquired, as discussed below.
5. There is an apparent relationship between the inclination (determined from the 30 mT demagnetization data from archive halves) and volume susceptibility (determined with the AMST system). As shown in Figure **F253,** samples with reversed polarity are strongly clustered around low susceptibilities of ~100 × 10^{-5} SI. In contrast, no low-susceptibility samples with unambiguous positive inclinations have been noted.

In summary, preliminary pass-through paleomagnetic data revealed important magnetic signatures that await further verification in terms of age and origin. Results from discrete sample demagnetization allow evaluation of the accuracy of the archive-half pass-through data, as described below.

Discrete samples

To investigate the nature of the remanent magnetization of the discrete samples from Hole U1309D rocks, 335 samples were stepwise thermally (266) or alternating-field (69) demagnetized. The demagnetization behavior of discrete samples from Site U1309 varies widely with lithology, as outlined above for archive halves. The ChRM of various gabbroic samples (medium-grained, coarse-grained, amphibole-bearing, olivine-bearing, and oxide gabbros) is mainly of reversed polarity, whereas troctolitic gabbro, olivine-rich troctolite, and diabase samples mainly have normal polarity. The MDF for gabbroic samples averages >30 mT, suggesting the remanence is of high stability. For many troctolite samples, however, the MDF value is often <10 mT. Stepwise thermal demagnetization isolates the ChRM direction typically >500°–550°C, suggesting that the remanence is carried by fine-grained magnetite.

As mentioned above, the vertically directed drilling-induced magnetization is commonly present in Expedition 305 cores. In most cases, this steep downward component of magnetization is not very resistant to alternating-field demagnetization. Examples are shown in Figure **F254A;** alternating-field demagnetization to 15 mT on Sample 305-U1309D-82R-2, 114–116 cm, effectively removed the drilling overprint to reveal negative inclination of the ChRM. Thermal demagnetization of minicore samples also successfully removed this drilling-induced magnetization component. Figure **F254B** illustrates that the drilling-induced remagnetization component is re-

moved after 400°C (Sample 305-U1309D-119R-1, 40–42 cm) or 500°C (Sample 126R-1, 27–29 cm) demagnetization, and a characteristic component decaying linearly toward the origin can be identified. Two representative samples of normal polarity (Samples 305-U1309D-143R-2, 72–74 cm, and 160R-3, 104–142 cm) are also shown in Figure **F254B.** It is interesting to note that in both cases, thermal demagnetization to temperatures >400°C is required to isolate the highest-stability magnetization component.

Rock magnetic characterization

Königsberger ratio

In general, the Königsberger ratio is used as measure of stability to indicate a rock's capability of maintaining a stable remanence. The International Geomagnetic Reference Field value at Site U1309 (40,918 nT = 32.56 A/m) was used for calculating *Q*, where, in the equation

$$Q = \text{NRM [A/m]}/(k\ \text{[SI]} \times \text{H [A/m]}),$$

k = magnetic susceptibility and
H = the intensity of the local geomagnetic field.

The variation of the Königsberger ratios is listed in Table **T17** and plotted in Figure **F255.** The *Q* ratio, in general, resembles that of the NRM. For example, diabase Sample 305-U1309D-287R-1, 8–10 cm, has a higher intensity of remanence than overlying gabbro Sample 305-U1309D-286R-2, 134–136 cm, and, consequently, the Königsberger ratio of the former (68.7) is much higher than that of the latter (7.8) (see Table **T17**). Similar examples of this correlation are also seen in samples from other rock types. In general, the Königsberger ratios throughout the hole are >1.0 (Fig. **F255**), indicating that remanent magnetization is greater than the induced magnetization.

Anisotropy of magnetic susceptibility

AMS was measured on 216 minicore samples (Table **T18**). The remaining samples have susceptibilities that are too low to measure their AMS reliably on board. The degree of anisotropy (*P*, where *P* = maximum/minimum eigenvalue of the susceptibility tensor) ranges from 1.034 to 1.895 (Fig. **F255**). In general, the degree of anisotropy is <1.2. Toward the bottom of the hole (1150–1415 mbsf), where several ultramafic zones were recovered, rock samples have relatively consistent degrees of anisotropy. Because of the high noise levels of these shipboard measurements compared to shore-based laboratory environments, however, the AMS results obtained on the ship are preliminary and need to be verified by post-cruise study. The directional data from Expedition 305 shipboard AMS measurements have not been reoriented to a common reference frame and are not discussed further here.

Tectonic significance of remanence data

The deep penetration and high core recovery (particularly of gabbroic rocks containing fine-grained magnetite) at Site U1309 provide a unique opportunity to examine the thermal and tectonic history of lower crust denuded at an oceanic core complex. Although drilling-induced overprints are a significant problem in some lithologies, the high-quality magnetic data obtained from gabbroic (sensu lato) rocks should provide a record of the geomagnetic field during construction and uplift of Atlantis Massif. Two aspects of the remanence data set, in particular, must be accounted for in any valid tectonic model for the massif.

First, several depth intervals with distinctly different mean inclinations can be identified from the shipboard data. Five inclination groups have been identified based on remanence data from archive halves and discrete samples (Fig. **F203**). The boundaries between these groups generally coincide with structural features (faults, shear zones) and so structural data have been used to define the precise boundaries (see **"Structural geology"**). The upper 180 m is characterized by a mean discrete sample inclination (~47°) that is nearly identical to the expected dipole inclination at the site (Fig. **F204**). A simple possible explanation of this result is that the interval has not experienced detectable tectonic tilt since the remanence was acquired, although this inference depends on the rotation axis and history (see discussion in **"Reorientation of structure data using paleomagnetic data"**). In contrast, the mean inclinations from all inclination groups deeper in the hole are statistically distinct from the expected direction. The shallower inclinations in these sections cannot be attributed to artifacts of the drilling and/or measurement process, as they are corroborated by numerous high-quality discrete sample demagnetization data. An example of a near-horizontal characteristic magnetization identified from thermal demagnetization of a sample from inclination Group II is shown in Figure **F248D.** The extremely narrow range of unblocking (550°–590°C) in this sample and the corresponding high-coercivity remanence (and identical direction) recovered by alternating-field demagnetization of a companion sample from the same core piece suggest the shallow inclination represents a primary thermoremanence. Inclination Groups III and IV have mean values steeper than those from Groups II and V and closer to the expected dipole inclination at the site. This nonsystematic change in remanence inclination downhole is difficult to rec-

oncile with any simple model of denudation and likely reflects a more complex thermal and unroofing history (relative motions between multiple fault blocks and/or reheating by later intrusions).

Second, well-defined multicomponent remanences noted during Expedition 304 suggest that remanence acquisition spanned multiple polarity intervals. In addition, we note that the highest stability reversed polarity magnetization is typically shallower than the normal polarity overprint and the two components are not antipodal. Although the number of samples with well-defined normal polarity overprints is small (n = 11), these overprints have a mean inclination (53.6° +6.4°/–8.2°; κ = 40.3) that is not statistically distinguishable from the present-day normal polarity inclination at the site. The directional difference between the normal and reversed polarity components may reflect the influence of tectonic tilting after acquisition of the highest stability reversed polarity magnetization. Although less common, such multicomponent magnetizations are also observed in several discrete samples analyzed during Expedition 305.

The origin and significance of remanence throughout the core will clearly require more detailed shore-based studies (particularly thermal demagnetization of discrete samples) in order to more fully understand the thermal and tectonic history at the site. Further rock magnetic and petrographic analyses are required to establish the likely timing of acquisition of magnetization.

Physical properties

The physical properties of basalt, diabase, gabbro, and peridotite cored at Site U1309 were characterized through a series of measurements on whole-core sections, split-core sections and pieces, and discrete samples as described in **"Physical properties"** in the "Methods" chapter. Natural gamma radiation (NGR) was not measured in Hole U1309B or between 40.5 and 131.1 mbsf in Hole U1309D because of a malfunction of the NGR data acquisition program.

Evaluation of physical properties at Site U1309 included nondestructive measurements of bulk density by gamma ray attenuation (GRA; for Hole U1309D core from >400 mbsf only), bulk magnetic susceptibility, noncontact resistivity (NCR), and NGR on whole cores using the MST as described in **"Physical properties"** in the "Methods" chapter. Sampling parameters for GRA, magnetic susceptibility, NCR, and NGR are summarized in Table **T11** in the "Methods" chapter. Horizontal (x- and y-direction) and vertical (z-direction) *P*-wave velocities were measured on cubes, and they were measured in the x-direction only on minicores, cut from half-core samples. Porosity and bulk density were also determined from the cubes or minicores. Thermal conductivity was measured on polished half-core samples immersed in saltwater (and for Hole U1309D samples below 400 mbsf in an insulated box). Relatively high core recovery facilitated acquisition of an excellent physical properties data set.

Hole U1309B

Density and porosity

Measured values of bulk and grain density are summarized in Table **T19** and Figure **F256.** Measured samples of basalt, diabase, and gabbro in this hole all have the same mean density, ~2.9 g/cm^3, within their respective standard deviations of 0.05–0.08 g/cm^3. The peridotite has a barely significantly lower density of 2.66 ± 0.08 g/cm^3. The porosities are somewhat more variable, averaging 1.9% ± 1.4% for basalt, 2.1% ± 0.6% for diabase, 2.0% ± 0.8% for gabbro, 2.1% ± 1.6% for olivine and troctolitic gabbro, and 3.2% ± 0.3% for peridotite.

P-wave velocity is plotted against density in Figure **F257.** In this uppermost part of the section of the footwall at Site U1309, the points generally lie on the same linear trend as reported in the Leg 209 *Initial Reports* volume (Shipboard Scientific Party, 2004) for gabbro and peridotite data from Leg 153 (Cannat, Karson, Miller, et al., 1995) (Fig. **F257**).

Compressional wave velocity

Figure **F256** shows the axial (x) component of compressional wave velocity plotted downhole with lithology indicated. We were not able to consistently measure velocity along the other two directions; where we did, uncertainties were relatively large and the velocities were not significantly different from the axial ones. The values are only moderately correlated with lithology (Figs. **F257, F256**). The average velocities for basalt and diabase are close (5.14 ± 0.33 km/s and 5.20 ± 0.27 km/s, respectively). The gabbros have slightly lower velocities, 4.99 ± 0.16 km/s, and olivine and troctolitic gabbros have slightly higher velocities of 5.54 ± 0.30 km/s. Peridotite velocity is significantly lower at 4.59 ± 0.12 km/s. The low velocity value for the peridotite reflects the high degree (60%–100%) of serpentinization observed in the samples and emphasizes the problem of identifying rock type from seismic velocity.

Thermal conductivity

Thermal conductivity was measured as described in **"Physical properties"** in the "Methods" chapter (Ta-

bles T20). Measurements were made with the heating needle parallel and 35° to the core axis, and each run consisted of four measurements that were averaged for each data point. The standard deviation for these four measurements, averaged over all the Hole U1309B data points, is 0.08–0.09 W/(m·K), and only two data points (both in apparently isotropic basalts) had individual standard deviations >0.12 W/(m·K). The maximum difference between the 0°, +35°, and –35° measurements, also averaged over all the Hole U1309B data points, is 0.1 W/(m·K). We conclude that we are unable to detect any significant anisotropy of thermal conductivity within the precision of our measurements. We therefore averaged the three (or occasionally only one or two) directional measurements to yield each value reported in Table T19 and plotted in Figure F256.

Thermal conductivity is closely correlated with rock type in Hole 1309B (Table T20). Diabase shows the least thermal conductivity variation throughout the hole, whereas harzburgite has values of 3.7 ± 0.1 W/(m·K) and 4.1 ± 0.1 W/(m·K) measured at locations only 11 cm apart in the same piece. Alteration appeared in hand specimen to differ significantly between the two locations.

Magnetic susceptibility

Magnetic susceptibility was recorded on the MST. Measurements were taken every 2 cm on whole-round sections of core (Table T11 in the "Methods" chapter). The quality of these data tends to be degraded in RCB sections because the core is usually undersized with respect to liner diameter and is commonly disturbed by drilling. Volume susceptibility has therefore not been calculated, and all magnetic susceptibility data are presented in terms of IU (where 1 IU is on the order of 0.7×10^{-5} SI). The lack of an exact relationship between IU and SI is due to fact that hard rock cores are not perfectly cylindrical and the diameter of individual pieces varies. Magnetic susceptibility is sensitive to variations in the type and concentration of magnetic grains in rocks and is thus an indicator of compositional variations and magnetic mineralogy. One major contribution to the magnetic susceptibility comes from ferro- and ferrimagnetic minerals such as magnetite, hematite, goethite, and titanomagnetite. Magnetic susceptibility can therefore be used to identify magnetite-rich zones, including oxide gabbros. Also, because magnetite is a by-product of serpentinization of olivine rich rocks, high magnetic susceptibility can indicate serpentinite intervals. Raw (i.e., unfiltered; see "Physical properties" in the "Methods" chapter) magnetic susceptibility amplitudes range from ~10 to >10,000 IU downhole (Fig. F256).

In Hole U1309B, susceptibility is related to rock type because of variations in concentration of magnetic minerals that vary with whole-rock composition. Figure F257 and subsequent plots show the MST measurements, made at 2 cm intervals along whole sections, in gray; "filtered" values, measured >5 cm from the ends of large pieces, are in red. Generally, the same trends are seen in both the 2 cm and the filtered data sets, although many low values measured near the ends of pieces have been removed. Occasionally, peaks in the 2 cm data have no corresponding value in the filtered data (i.e., were made near ends of pieces). An example is at 46.6 mbsf in Hole U1309D Unit 14, where the two highest points (7000–8000 IU) are missing from the edited data. Nevertheless, these removed data should not be ignored but simply recognized as being underestimates of the true values.

The highest susceptibility values measured in Hole U1309B are present in the serpentinite of Core 304-U1309B-11R, which has mean susceptibility of 5700 IU and maximum of ~9500 IU. The next highest values are in diabase, especially that of Core 304-U1309B-6R, Unit 22, and Cores 19R and 20R, Unit 62 (mean = 1800 IU; maximum = 6100 IU). The basalts generally have lower susceptibility (mean = 300 IU; maximum = 4600 IU). The lowest susceptibilities are located in the gabbros, with mean and maximum values of ~100 and 3000 IU, respectively. In fact, most gabbros have susceptibility <100 IU, with the following exceptions: short intervals of gabbro in Units 28 (Section 304-U1309B-9R-2, 49.84 mbsf) and 31 (Section 304-U1309B-10R-1, 53.46 and 53.82 mbsf) have susceptibility peaks of up to 300 IU. Unit 50 shows a more substantial increase, though again over a short interval, to just over 1000 IU in Section 304-U1309B-16R-2 at 82.49 mbsf. Aside from these intervals, the gabbros in Hole U1309B have uniformly very low magnetic susceptibility.

Most of the basalt and diabase have relatively uniform susceptibilities within each unit, but a few diabase units show marked transitions from one fairly uniform (and commonly very low) level to another within what is petrologically described as the same lithologic unit. Such transitions are listed in Table T21 and illustrated in Figure F258.

These variations in susceptibility reflect the proportion of magnetic minerals present (primarily magnetite; see "Paleomagnetism") that may result either from variations in chemical composition or in subsequent alteration. In some instances, particularly in Unit 20, and on a larger scale in Unit 62, there is a symmetric pattern of moderate susceptibility at the unit margins (sometimes recognized by finer grain size) and much lower susceptibility in the interior,

suggesting possible influence of emplacement mechanism (e.g., emplacement of multiple sheets with cryptic boundaries or flow-banding). The harzburgite (Unit 32) also displays some internal variability (Section 304-U1309B-11R-2 [e.g., ~58.89 mbsf]).

Electrical resistivity

The trends of the electrical conductivity and susceptibility curves are quite similar (Fig. F256). This suggests that the same minerals are responsible for both the magnetic susceptibility and the electrical conductivity. The mineral primarily responsible for the susceptibility is probably magnetite, which has the highest susceptibility of all minerals (6.0 SI) (Telford et al., 1976; Blum, 1997, quoting Thompson and Oldfield, 1986) and has been documented in many of the rocks from Hole U1309B. Magnetite can also be strongly electrically conductive compared to silicates, with a mean conductivity in the range 2×10^{-4} to 2×10^{4} Siemens/m (S/m) (Telford et al., 1976). Ilmenite may also contribute; it tends to occur with magnetite in basalt and diabase, though not in serpentinite, and has susceptibility of 2.0 SI and conductivity of 0.02 to 10^{3} S/m. Pyrrhotite and pyrite, though magnetic and electrically conductive, might contribute in places but are not pervasively present in the rock recovered in Hole U1309B.

Hole U1309D

Density and porosity

Bulk density, grain density, and porosity in Hole U1309D (Fig. F259; Table T22) were calculated from the wet mass, dry mass, and dry volume of discrete rock cubes using moisture and density method C for igneous rocks (see "Physical properties" in the "Methods" chapter) in Cores 304-U1309D-1R through 78R and 305-U1309D-80R through 295R (20.5–1415.3 mbsf). Although GRA density was acquired on some whole-round sections of core (with a sampling rate of 2 cm) (Table T11 in the "Methods" chapter), these data should not be used for analytical applications; they are consistently too low because the RCB core did not fill the core liner and the core was commonly broken. GRA density has an important practical application in that rapid decreases in this parameter can be used to map the location of breaks along the core. The moisture and bulk density data are substantially more accurate, and we use these data in describing the downhole density variations.

Bulk density is a measure of the bulk weight divided by the sample volume. To introduce some redundancy into the measurement process (in case of problems with the pycnometers), the wet volume was also estimated using a caliper to measure the cube dimensions (which we refer to as method D). This and method C should give similar values. A plot of bulk density by caliper versus bulk density by pycnometer gives an error of –0.018 ± 0.0007 g/cm³ (Fig. F260). Although both methods accurately represent bulk density, we continue to use the moisture and density–calculated bulk density for description. The caliper-calculated bulk density is more inaccurate with cubes that have nonparallel sides or are chipped, as demonstrated, for example, by a cube that plots around 3.3 g/cm³ (caliper) and 3.45 g/cm³ (pycnometer) and whose corners were chipped because of the fractured nature of the source material.

For the combined Expedition 304 and 305 data, bulk density varies between 2.45 and 3.56 g/cm³ (Fig. F259B). There is a general slight increase in density downhole from 0 to 1100 mbsf, after which the scatter increases significantly. Below 1230 mbsf, the density is constant or slightly decreasing to the bottom of the hole. High densities correlate with fresh oxide gabbros and olivine-rich troctolites. Bulk density scatter tends to decrease with depth, except for a notable increase in scatter between 1100 and 1230 mbsf associated with the presence of olivine-rich troctolites. There is no obvious and consistent correlation with rock type. The increased bulk density scatter within the 1100–1230 mbsf interval relates to the alternation of relatively lower density gabbros with higher density olivine-rich assemblages.

Porosity reflects a combination of crystal fabric, stress history, volume changes induced by metamorphic alteration, vertical unloading, and cracking of the rocks during drilling. Porosity is calculated from the volume of pore water, assuming complete saturation of the rocks (Blum, 1997) (see "Physical properties" in the "Methods" chapter). For the combined Expedition 304 and 305 data, the porosity ranges between 0.0% and 6.4% with a mean of 1.1% ± 0.94% (Fig. F259D). Porosity and bulk density vary similarly downhole, showing a change from increased scatter and porosities generally 1%–2.5% in the upper part of Hole U1309D to significantly reduced scatter and decrease from ~700 mbsf to the bottom of the hole. The discrete zones of relatively high porosities and low bulk densities at 30–85, 420–450, 560–575, 635–645, 685–700, and 1095–1135 mbsf correlate with zones of cataclastic deformation and fault zones (see "Structural geology").

Compressional wave velocity

Compressional wave velocities were measured at 1 atm with the *P*-wave sensor (PWS3) contact probe system on minicores for depths <400 mbsf (Expedition 304) and ~10 cm³ rock cubes for greater depths (Expedition 305). Velocity was measured along axis of the minicores (x-direction), whereas the cubes

were used to measure velocities in the horizontal (x- and y-) and vertical (z-) directions. Apparent seismic anisotropy was calculated from the measured velocities of the cubes (Fig. F261). A test was performed to evaluate the precision of velocity measurements using the PWS3 Hamilton Frame. Sample 305-U1309D-107R-4, 48–50 cm, was measured ~80 times in the x-direction, and a running average was calculated (Fig. F262). Eventually, after ~50 measurements, the running mean converged to a value of 6.07 km/s, although the rate of convergence may have been slowed because of the progressive drying of the cube during the experiment. (The small kink at 72 measurements marks the rewetting and retightening of the caliper at this point). These statistics suggest a measurement error of <1%. It is recommended that the acquisition program be modified to average 20–40 values rather than relying on a single value.

Downhole variations in velocity (Fig. F263) are scattered in the upper 150 m of Hole U1309D, show a slight decrease from ~150 to 350 mbsf, and increase between 350 and 450 mbsf. This is followed by another generally constant value from 400 to 800 mbsf, after which there is a steady decrease in velocity to the bottom of the hole. The velocities between 20 and 350 mbsf average ~5.5 km/s, and those between 600 and 800 mbsf average ~6.0 km/s, whereas the velocities between 1200 and 1400 mbsf show a decreasing trend and an average of ~5.5 m/s. Density is either constant or slightly increasing over the same interval, so no definite conclusions can be made without further work. Velocities measured along the x-axis in the minicores range from 4.0 km/s (in serpentinized peridotite) to 6.2 km/s in olivine gabbro. Velocity of the rock cubes from Hole U1309D range between 4.65 and 6.83, 4.81 and 6.77, and 4.80 and 6.67 km/s in the x-, y-, and z-directions, respectively (Fig. F261).

Superimposed on the long-wavelength velocity trend are a number of smaller, local variations. Downhole variations are not simply related to rock type (Fig. F263). Abrupt velocity variations occur at 325, 440, 468, 547, 584, 642, 690, 810, 942, 1000, 1190, 1251, and 1362 mbsf. The largest velocity variations are located between 350 and 450 (an increase), 600 and 650 (a decrease), and 920 and 950 mbsf (a decrease) and are associated with intervals of massive olivine gabbro and troctolitic gabbro. Despite these local associations of velocity variation with lithology, the bulk of the measurements are not simply related to rock type, including the olivine-rich troctolite, but also to alteration and/or deformation.

The x-y velocity anisotropy ranges between –9% and 14% with an average not statistically different than zero (Fig. F261). There does not appear to be any systematic variation with x-y anisotropy with depth, although the scatter increases significantly between 1000 and 1200 mbsf. In contrast, the vertical-horizontal velocity anisotropy ranges principally between –6% and 11%. There appears to be a systematic variation in the vertical-horizontal anisotropy from a zero or slightly negative value between 400 and 700 mbsf, changing to a few percent positive anisotropy from 750 to 1000 mbsf. Below this, the scatter increases significantly (Fig. F261), probably as a consequence of strong variations in alteration in the olivine-rich troctolite and associated gabbros (see "Metamorphic petrology").

The relationship between *P*-wave seismic velocity and bulk density measured during Expeditions 304 and 305 is compared to results from Leg 209 in Figure F264. A large amount of highly serpentinized peridotite was recovered during Leg 209, which explains the spread to lower density and velocity values compared to Hole U1309D samples. A significant subset of gabbro and diabase samples from Leg 209 show higher densities for a given velocity. This is related to the occurrence of abundant Fe-Ti oxides in numerous 209 samples (Shipboard Scientific Party, 2004). Hole U1309D data also follow a trend similar to gabbro and peridotite recovered in the MARK area during Leg 153 (see Fig. F88 in Shipboard Scientific Party, 2004), although they are more scattered, likely reflecting the wider spectrum of primary lithology and alteration.

Changes in velocity do not show any systematic correlation with trends from other Expedition 304 and 305 igneous, metamorphic, or structural data sets, including alteration, modal olivine content, or Fe_2O_3 variation. Figure F265 explores the relationships between Expedition 304 and 305 PWS velocities (z-velocity), logging velocities, porosity, and fracture intensity (see "Structural geology" for details on calculating fracture frequency). Between 0 and 350 mbsf, the logging velocities, which approximate an in situ velocity estimate, are systemically lower than the measured PWS velocities. Over this same depth range, moisture and density porosities range from 1% to 6%, reaching a local minimum at ~400 mbsf. The qualitative fracture frequency distribution, similar in scale to the PWS and moisture and density data estimates, likewise shows that the degree of macroscopic fracturing is a maximum in the upper part of the section and systematically decreases to 380–400 mbsf (Fig. F265). Between 400 and 800 mbsf, the PWS and logging velocities are coincident. Below 800 mbsf, there is a hint of the logging veloci-

ties increasing relative to the PWS velocities, but the lack of deeper logging data (see **"Downhole measurements"**) makes it impossible to know if the trend is real or just local variability. Porosity is a minimum between 800 and 1200 mbsf. Fracture frequency falls rapidly to values mostly <0.5 below 800 mbsf, following a trend similar to porosity which averages 0.6% for this lower portion of the core.

The interrelationship between logging and PWS velocity, porosity, and degree of fracturing suggests that the velocity behavior with depth is primarily a function of the reduction in opening of fractures and microcracks that is related to increasing overburden pressure. The pattern in the upper ~220 m can be explained by fewer open/visible fractures, consistent with the fracture intensity and porosity variability (given that the fractured, and thus higher porosity, rocks are unlikely to be sampled by drilling). Between 600 and 800 mbsf, the reduction in the amount of open microcracks is suggested by the coincidence of logging and PWS velocities. Below ~800 mbsf, we expect a systematic decrease in rock volume determined by Poisson's ratio and overburden stress. Without a continuous sonic data set from the lowermost 600 m of Hole U1309D, it is impossible to test this hypothesis or to determine if the measured cube velocities (not measured at in situ pressures) are accurately representing the velocity deeper in the hole.

Thermal conductivity

Thermal conductivity measurements were done on intact pieces of archive-half core at least 10 cm in length (Table **T23**). Silicon carbide powder (120 grit) was used to polish most rocks from Expedition 304 and all rocks from Expedition 305 prior to their being measured for thermal conductivity, which, coupled with isolating the experiment from drafts, significantly increased the precision of the measurements. Because the majority of the rocks did not show preferred fabric or crystal alignments, and based on the conclusion of Expedition 304 experiments, no attempt was made to measure thermal conductivity anisotropy.

Measured thermal conductivity in Hole U1309D rocks ranges between 1.71 and 4.34 W/(m·K), with an average value of 2.43 ± 0.45 W/(m·K) (Fig. **F266**). There is an overall decrease in the scatter of the thermal conductivity measurements with depth between seafloor and 1100 mbsf, primarily reflecting the reduction in igneous rock lithologic variability with depth (see **"Igneous petrology"**). The thermal conductivities show a subtle relationship with lithology. In particular, the olivine-rich troctolites have consistently high thermal conductivities. Average values for all measurements in Hole U1309D are given in Table **T22** (Fig. **F266**).

Temperature

Because the oceanic crust of Atlantis Massif is young (1.5–2 Ma), there was a concern that maximum temperatures at depths of 800–1400 mbsf might damage the downhole logging tools. Attempts to measure ambient bottom hole temperatures proved to be difficult because of a malfunctioning Water Sampling Temperature Probe (WSTP). Furthermore, flushing of the bottom of the hole with cold surface waters during drilling meant that any temperature measurement would necessarily be a minimum. A set of "thermal tabs" was placed around the core catcher during a dedicated (noncoring) core barrel run (see **"Operations"**). These simple devices measure the maximum bottom hole temperature by registering a color change in the tab. To test and calibrate this device, a thermal tab was placed in the Physical Properties oven, which is kept at a constant 105° ± 5°C. Figure **F267** shows the before and after color state of the thermal tab. The color change indicates that the maximum temperature experienced by the tab was between 98° and 104°C, consistent with its rating. These thermal tabs were used to estimate minimum bottom hole temperatures when deployed.

Figure **F268** shows the results of modeling crustal temperatures in Hole U1309D. Theoretical temperatures versus depth curves were generated using basal heat fluxes of 226 and 206 mW/m^2, consistent with oceanic crust of 1 and 2 Ma, respectively, for a cooling plate model (thick red and blue lines, Fig. **F268**). The age range was selected to approximate the conductive temperature distribution of the crust (neglecting any effects of hydrothermal fluid circulation in the crust). The temperature structure at the spreading center was assumed to be consistent with a 5 km crust and a 14.5 km thick lithosphere. The anomalous basal heat flow, $q(t)$, is calculated by assuming a lithosphere of 125 km at thermal equilibrium (i.e., a linear geothermal gradient between the surface at 5°C and an asthenosphere temperature of 1333°C) and crustal thickness of 31.2 km; crustal and mantle extension factors of 6.24 and 10, respectively, mimic the structure and thermal state of young oceanic lithosphere.

Fourier's law was then used to calculate the temperature as a function of depth for the range in basal heat flows and the observed thermal conductivity distribution in Hole1309D (Fig. **F266**):

$$T(z_0,t) = \int_0^{z_0} q(t)/\kappa_r(z)\,dz$$

where $T(z_o,t)$ is the rock temperature as a function of depth, z_o, and time t since the initiation of cooling, and $\kappa_r(z)$ is the measured thermal conductivity structure of the basement rocks.

Maximum estimated temperature (disregarding cooling effects by water circulation during drilling) at the base of Hole U309D is ~142°C. Measured temperatures are offered by three methods (Fig. F268):

1. Thermal tabs, giving a minimum temperature of 70° and 108°C at 1171 and 1220 mbsf (red circles), respectively.
2. Temperature estimates from the downhole logging tool (triple combination [triple combo] TAP tool; 52°C at 562 mbsf, 57°C at 700 mbsf, and 69°C at 754 mbsf; yellow circles).
3. From the Goettingen Borehole Magnetometer (GBM), which monitors temperature as a function of time both during descent (purple curve) and ascent (pink curve) of the tool.

It is concluded that a conductive gradient generally characterizes the temperature structure of the hole, at least in the upper ~1 km (see **"Downhole measurements"**) now modified by drilling water circulation, and that maximum temperature may be in the range of 130°–145°C.

Magnetic susceptibility

As in Hole U1309B, magnetic susceptibility is related to lithology because of the occurrence of magnetic minerals being more common in certain rock types than others (Fig. F269).

The basalts in the upper section of Hole U1309D have low susceptibility. Diabase units have high susceptibility intervals. Figure F270 shows the variation of susceptibility along each of the major diabase units (Units 1, 12, 14, and 44; see **"Igneous petrology"**). The pattern of variation itself is quite variable: in Unit 1, moderate peaks straddle a 1 m thickness with very low susceptibility, in large parts of Units 12 and 44, susceptibility increases fairly steadily downcore, and in Unit 14, it decreases downcore. However, there are more local variations; for example, in a single 30 cm long piece at 44.5 mbsf (Section 304-U1309D-6R-3 [Piece 3]), susceptibility increases 16-fold from 350 to 5770 IU within a 20 cm interval. These variations in magnetic susceptibility do not correlate with any of the changes noted in the lithologic descriptions. Although variations in grain size up- or downcore or from unit center to edges have been noted, usually magnetic susceptibility is invariant to changes in grain size. It is likely that the observed susceptibility changes reflect both varying magnetic mineral content (Fig. F271) and varying degrees of alteration of magnetite (Fig. F272).

The highest susceptibilities measured in Hole U1309D were in the oxide gabbro units. In several intervals, values exceed the maximum range of the sensor. However, in some intervals, a relatively simple signal and moderate downhole susceptibility gradient allow the full signal to be reconstructed by adding multiples of 10,000 IU to the logged value, and the required multiple can be verified by using the excellent correlation between electrical conductivity and susceptibility (Fig. F273). Performing such an adjustment to the logged susceptibility from the oxide gabbros in Hole U1309D Cores 304-U1309D-35R and 36R shows that the true susceptibility probably peaks at 24,700 IU at 193.08 mbsf (Fig. F274). If all the susceptibility is carried in magnetite, this requires a volume fraction of 8% magnetite. Other oxide gabbros also have high and variable measured susceptibility values, suggesting true susceptibilities >10,000 IU in places, although we have not attempted to adjust other parts of the data. As with the other rock types cored in Hole U1309D, the susceptibility in the oxide gabbros can vary significantly within a single unit.

Gabbros (including olivine- and orthopyroxene-bearing gabbros) in Hole U1309D mostly have low susceptibility (<500 IU), although there are local decimeter-scale bands of higher susceptibility. Olivine and troctolitic gabbros in Hole U1309D mostly have low susceptibility (<500 IU). However, there are local bands of higher susceptibility with peaks up to 7500 IU. Troctolites carry low to moderate susceptibility.

Ultramafic rocks (olivine-rich troctolite, dunite, and harzburgite) in Hole U1309D can have very high susceptibilities, with a maximum of 12,100 IU estimated at 173.12 mbsf by adjusting the logged values as described above. These high values are associated with intervals that are highly serpentinized.

A feature of the susceptibility values recorded from the mafic and ultramafic rocks at Site U1309 is the extreme variability over a short vertical distance. In Hole U1309D, this is well exemplified in Units 147–163 (310–328 mbsf; Fig. F275). The very high values 321–322 mbsf reach and may locally exceed the maximum recording level of 10,000 IU, compared to very low values near the top and bottom of the unit. Many detailed correlations between susceptibility change and lithologic boundaries can be seen in this interval. The detailed variations in susceptibility patterns also provide a possible means of stratigraphic correlation. For example, the correlation between the diabase units in Hole U1309B, 94–101 mbsf, and Hole U1309D, 85–94 mbsf, and that between the diabase unit in Hole U1309B, 62–78 mbsf, and the one in Hole U1309D, 43–48 mbsf, are based on the

similarity of the magnetic susceptibility pattern along each pair of units (see **"Correlations between Holes U1309B and U1309D"**).

Extreme magnetic susceptibility amplitudes correlate with zones of serpentinization (and the production of magnetite), oxide- and sulfide-bearing gabbros, and troctolites and olivine-rich troctolites. There is, therefore, an excellent relationship between magnetic susceptibility and those lithologies rich in ferro- and ferrimagnetic minerals.

Electrical resistivity

Noncontact resistivity was derived from voltages measured on the MST. Measurements were taken every 2 cm on whole-round sections of core (Table **T11** in the "Methods" chapter). NCR measurements, in volts (and as stored in the IODP database), were converted to resistivity using the calibration done during Expedition 304 (see notes on limitations of NCR data in **"Physical properties"** in the "Methods" chapter). The reciprocal of electrical resistivity (NCR) is electrical conductivity (NCC) with units of S/m. The magnetic susceptibility, NCR, and NCC data tend to be highly variable, so, to see the general variation and interrelationships, the data have been filtered using a 51-point running average (Fig. **F276**). A caution, however: some of the extreme magnetic susceptibility variations are a function of the 10,000 IU wrap-around problem documented in **"Physical properties"** in the "Methods" chapter. Nevertheless, a strong correlation exists between conductivity and magnetic susceptibility (Fig. **F276**). This suggests that the same minerals are responsible for both the magnetic susceptibility (high magnetic susceptibility) and the electrical conductivity (high NCC). Likely candidates are oxides and sulfides. The primary mechanism for noncontact electrical conductivity here is likely to be electronic via conducting minerals (oxides and sulfides), rather than ionic through pore fluids (especially seawater).

We attempted to test whether high NCR values reflected an electronic source versus an ionic source on two large pieces of olivine-bearing gabbro—Section 304-U1309D-57R-1 (Pieces 6 and 7)—by measuring resistivity on the MST following saturation for different times in seawater (Fig. **F277**). Measurements (at atmospheric pressure) were made on nominally dry rock (following curation in the Core Laboratory for several days) and then after the indicated periods of saturation in seawater. No significant variation was observed up to 34 h of saturation, implying that ionic conduction is not an important mechanism in these samples. This is probably due to a combination of low porosity and high volume percent of conducting minerals.

Three main magnetic susceptibility and NCC responses are recognized (Fig. **F276**):

1. Very low magnetic susceptibility and NCC amplitudes (0–500 IU and less than ~0.1 mS/m, respectively) associated with diabase, coarse- and medium-grained gabbros, and locally very fresh olivine-rich troctolite;
2. Intermediate amplitudes (1000–2000 IU and ~0.2–0.4 mS/m) associated with olivine gabbros; and
3. Extreme amplitudes (6,000–10,000 IU and less than ~1.5 mS/m) associated with oxide gabbros and serpentinized troctolites (Fig. **F276**).

Although variations in grain size up- or downcore have been noted, usually susceptibility is invariant to changes in major lithologic grain size. It is likely that the observed susceptibility changes reflect a combination of varying Fe content, magnetite/ilmenite ratio, and degrees of alteration. More than 90% of the magnetic susceptibility values are between 0 and 2000 IU (with corresponding NCC values of ~0–0.5 mS/m), which is associated with the various nuances of gabbroic compositions observed in the core (coarse-, medium-, and fine-grained gabbro, olivine gabbros, olivine-bearing olivines, amphibole-bearing olivines, gabbronorite gabbros, etc.). Even larger olivine-rich troctolite intervals (669.5–671.5 and 1100–1250 mbsf) are not always associated with significant and unambiguous magnetic susceptibility and NCC amplitudes. Small-scale variations relate to variable degrees of serpentinization.

The location of most of the major oxide gabbros and troctolites are obvious from the magnetic susceptibility/NCC signals (Fig. **F276**). In contrast, the opposite extreme is represented by rocks between 460 and 491 mbsf and 731 and 772 mbsf, which are characterized by extremely low magnetic susceptibility and NCC signatures. These regions consist of coarse-grained gabbro, olivine gabbro, diabase, and olivine-bearing gabbro. In marked contrast, the same rock types can also be associated with relatively high magnetic susceptibility and NCC values, such as the regions between 780 and 800 mbsf and 856 and 862 mbsf (in this case, massive gabbros).

Natural gamma radiation

The variations of natural gamma ray counts along the core are shown in Figure **F278.** Measurements were taken every 10 cm on whole-round sections of core with a 30 s sampling period (Table **T11** in the "Methods" chapter). The relatively large sampling interval was selected because a low NGR was expected; the low-resolution acquisition rate was simply to monitor NGR amplitude and trend to help with calibration of the logging tools. As seen in Fig-

ure F278, the NGR response is not significantly different from the background level.

Conclusions

- Susceptibility shows a general increase with magnetic mineral content, consistent with the conclusion that it is mostly carried in iron-rich oxides, probably mainly magnetite.
- Alteration often contributes to the decreased susceptibility in diabase (magnetite converted to ilmenite) and increased susceptibility in olivine-rich lithologies (production of magnetite during serpentinization).
- Highest susceptibility (>10,000 IU) is frequently present in oxide gabbros; ultramafic rocks generally have high susceptibility (approximately <10,000 IU), probably carried in magnetite produced by serpentinization; basalts and diabases have variable to high susceptibility; gabbros generally have very low susceptibility, but with some moderate- to high-susceptibility zones—the latter perhaps reflecting higher olivine/serpentine content.
- High susceptibility is not present uniformly through lithologic units but tends to concentrate in zones and narrow bands—often near tops or bottoms of units.
- Magnetic susceptibility and electrical conductivity are highly correlated, implying that the same minerals carry each signal.
- Electrical conductivity is not strongly dependent on water saturation, implying that conduction is mostly electronic (in oxide or possibly sulfide minerals), not ionic (in pore water).
- Thermal conductivity is generally highest and most variable in peridotites and olivine-rich troctolites. Gabbros generally have thermal conductivity of 2.0–3.0 W/(m·K). Olivine and troctolitic gabbros can range to higher values similar to the ultramafic rocks (3.0–3.5 W/[m·K]). Basalts and diabases consistently have lower conductivity (generally 2.0–2.3 W/[m·K]).
- *P*-wave velocity is most variable (4.0–5.7 km/s) in ultramafic rocks, presumably dependent on degree of serpentinization.
- *P*-wave velocity and density show no simple relation to rock type.
- *P*-wave velocity variation with depth probably reflects reduced opening of fractures and microfractures with increasing overburden, but our sample measurements do not show a simple monotonic or step increase.
- NGR shows no significant anomalies.

Microbiology

Lost City, an extensive hydrothermal field, was recently discovered near the MAR at 30°N (Kelley et al., 2001). This example of an ultramafic hosted hydrothermal system is postulated to be driven by the heat of the exothermic serpentinization reaction (Kelley et al., 2001), as opposed to the cooling of basaltic material, which drives the hydrothermal flow in younger basaltic crust (Fornari and Embley, 1995). Serpentinization reactions produce significant volumes of hydrogen, methane, and, possibly, low molecular weight organic compounds (Allen et al., 1998; Shock and Schulte, 1998; Berndt et al., 1996; Janecky and Seyfried, 1986; Neal and Stanger, 1983). At the Lost City site, an analysis of the microbial communities revealed the predominance of a single group of methane-metabolizing Archaea (Schrenk et al., 2004). The results of this study suggest that a microbial niche may exist for hydrogen-utilizing methanogens and that the high level of methane (as compared to seawater) measured at Lost City may be produced as a direct result of microbial metabolism. In addition to the microbial niche potentially occupied by methanogens, the hydrogen produced from serpentinization reactions and the iron present in ultramafic rocks may also support other microbial populations, including iron-reducing bacteria.

To further elucidate the microbial communities present in a system possibly similar to the Lost City, a microbiological analysis of the rocks cored at Atlantis Massif, 30°N, was undertaken during Expeditions 304 and 305. A culture collection of anaerobic sediment and endolithic microbes was established and monitored throughout both expeditions. Additionally, core samples from Hole U1309D were frozen at –80°C for shore-based molecular analysis. Unfortunately, only minor amounts of ultramafic rocks were recovered and Hole U1309D is lithologically defined as a mafic system. Even though only a small proportion of the rocks recovered during Expeditions 304 and 305 had an ultramafic protolith, fluids circulating through the massif potentially reacted with substantial volumes of ultramafic rock. Thus, a comparison of microbial communities present at the Lost City hydrothermal vent field and Site U1309 is warranted. Regardless of the lithology, microbiological analyses of Expedition 304 and 305 samples will provide an unprecedented body of knowledge of the deep subsurface biosphere from the seafloor to 1400 mbsf.

Sample information

Carbonate sediment was sampled from 0.45 mbsf in Hole U1309A (Sample 304-U1309A-1R-2, 45–58 cm). Three types of igneous rocks (Samples 304-U1309B-2R-1, 18–26 cm, basalt; 12R-2, 34–43 cm, diabase;

and 16R-2, 0–8 cm, gabbro) were sampled in Hole U1309B from the depths of 15.8, 61.9, and 80.4 mbsf, respectively. In Hole U1309D, five types of igneous rocks were sampled. Serpentinized peridotites (Samples 304-U1309D-10R-1, 107–112 cm, and 58R-1, 67–73 cm) were sampled from 60.20 and 300.40 mbsf, respectively. Olivine gabbros (Samples 305-U1309D-80R-1, 18–28 cm, 90R-1, 30–36 cm, 184R-1, 78–85 cm, and 250R-1, 0–11 cm) were sampled from depths of 401.48, 448.90, 895.78, and 1201.50 mbsf, respectively. Olivine-bearing gabbros (Samples 305-U1309D-82R-1, 27–39 cm, 102R-2, 67–78 cm, 122R-2, 76–89 cm, 142R-3, 0–13 cm, and 290R-3, 136–145 cm) were sampled from depths of 410.47, 508.31, 604.24, 701.05, and 1391.01 mbsf, respectively. Olivine-rich troctolites (Samples 305-U1309D-100R-1, 80–89 cm, and 235R, 52–63 cm) were sampled from depths of 497.40 and 1131.28 mbsf, respectively. Gabbros (Samples 304-U1309D-12R-3, 46–54 cm, 28R-4, 43–56 cm, 37R-2, 94–102 cm, 53R-1, 100–111 cm, 68R-1, 88–101 cm, and 78R-1, 82–90 cm, and 305-U1309D-133R-3, 122–132 cm, 164R-1, 60–74 cm, 208R-4, 0–12 cm, and 273R-1, 116–132 cm) were collected at depths of 69.80, 160.93, 201.90, 276.40, 348.40, 396.50, 658.73, 799.60, 1004.79, and 1313.06 mbsf, respectively.

In addition to rock samples, 5 mL of seawater was collected using a sterile WSTP from 5 m above the seafloor (see **"Appendix A"**) and at 390 and 1215 mbsf (see **"Appendix B"**). Water samples will serve as a control for molecular analysis to constrain the degree of contamination of core samples by microorganisms from the surrounding seawater.

In situ cell densities

Interior portions of core samples were stained with 4′,6-diamidino-2′-phenylindole-dihydrochloride (DAPI) (Expedition 304) and acridine orange (Expedition 305) and viewed using bright-field illumination and epifluorescence microscopy to determine in situ cell densities. The cell densities in carbonate sediment were determined. The density in the exterior and interior of carbonate cores were $1.1 \times 10^4 \pm 0.9 \times 10^4$ cells/mL and $1.2 \times 10^4 \pm 1.0 \times 10^4$ cells/mL, respectively. Because of the overwhelming autofluorescence of rock material, it was not possible to quantify cell densities of igneous rock samples. The question as to whether microbial communities are present in rock samples will be addressed by shore-based molecular analysis of core sections frozen at –80°C.

Cultivation experiments

Expedition 304

Cultures that were established during Expedition 304 were monitored for cell growth using phase-contrast and epifluorescent microscopy (Table **T24**). A subsample extracted from the interior of the carbonate ooze was used as the innoculum in enrichment experiments to bring into culture methanogenic and sulfate-reducing microbes at 5°C. No positive growth was observed in these cultures. Portions from the interiors of basalt, gabbro, and serpentinized peridotite core samples were used as innoculum to bring into culture methanogens, sulfate-reducing microorganisms, and organic matter–utilizing microbes. After 2 days of incubation at 65°C, fluorescing particles were observed in a culture bottle containing methanogen enrichment media (Section 304-U1309B-16R-2). These particles radiated green light under the blue filter of wavelength 450–490 nm (Fig. **F279**). A methanogen is able to radiate green light because the absorption spectrum of methyl-coenzyme M reductase, which is the terminal enzyme of methanogenesis (Thauer, 1998). After 5 days of incubation at 85°C, fluorescence of cell-like particles from Section 304-U1309B-16R-2, stained with DAPI, were observed in a culture containing methanogen enrichment media (Fig. **F279C**).

Molecular analysis is required to confirm that the observed fluorescence is caused by the presence of microbes and not by the presence of minerals that fluoresce when exposed to ultraviolet light. Two gabbro incubations at 37°C (Sections 304-U1309B-16R-2 and 12R-3) resulted in growth of organic matter–utilizing microorganisms after 6 and 7 days, respectively (Fig. **F279D;** Table **T24**).

Expedition 305

In an effort to establish a culture collection of endolithic microbes from Site U1309, four different types of media (~300 cultures established), as well as agar plates, were inoculated with interior portions of core samples. Growth was observed in samples from Sections 305-U1309D-80R-1 (Fig. **F280**) and 82R-1 on marine agar 2216. To begin the process of isolation, a portion of each of the two colonies was transferred from the original plate to a second marine agar 2216 plate. Subsequently, an additional transfer was made from the second plate to a third marine agar 2216 plate. Additionally, using a sterile innoculating loop, tubes of each of the four types of liquid media discussed above were innoculated with a small portion of the viable colony and incubated at 30°C. Growth in liquid media and on marine agar 2216 plates was monitored.

Liquid cultures were monitored for growth via increased turbidity. Cultures that appeared more turbid with time were subsampled, stained with acridine orange, and observed using epifluorescence microscopy (Fig. **F281**). Several cultures contain fluorescing

spheres and small rods, both on and off the rock surfaces; however, because of the autofluorescence of rock particles, the presence of microorganisms will not be confirmed until a shore-based molecular analysis of cultures is undertaken.

Contamination experiments

Expedition 304

The extent of contamination of the carbonate sediment sample was determined by presence/absence of fluorescent microspheres. One microsphere was detected from the exterior of the core sample. No microspheres were detected in the interior of the sample. This result suggests that the exterior of the carbonate sediment sample was potentially contaminated by microorganisms from ambient seawater during the drilling process. Perfluorocarbon tracer (PFT) was not used as an indicator of contamination for the sediment sample. A contamination test of igneous rocks was conducted both with bacterial-sized fluorescent microspheres and PFT. A perfluorocarbon analysis with a gas chromatograph (Hewlett Packard 8059) revealed that all subsamples had PFT concentrations that were below detection limits. A maintenance inspection on the PFT system during the Expedition 305 transit to Site U1309 revealed that both the primary and secondary PFT pumps had suffered a failure (for different reasons). The storage tank for PFTs was depleted, but it cannot be determined if this was caused by use or evaporation through the damaged systems. This is the first occurrence of a system failure, and it cannot be determined whether PFTs were introduced into the drill water system during Expedition 304. However, because no PFTs were detected in any of the samples collected, we presume that PFTs were not incorporated into the drill water circulation system during Expedition 304.

Fluorescent microspheres were detected in seawater used for rinsing the surface of the samples. No microspheres, however, were detected from the interior of igneous rock samples. This result suggests that interior rock samples were not contaminated by microorganisms from surface seawater used for circulation during the drilling.

Samples from Sections 304-U1309D-12R-3 and 58R-1 were not initially intended for microbiological sampling; therefore, neither PFT tracer nor microspheres was used as a contamination indicator.

Expedition 305

To determine the extent of contamination in core samples, fluorescent microspheres were deployed in the core catcher for samples intended for microbiological sampling. The exterior of each core sample was rinsed with nanopure water. This water sample was collected, filtered, and viewed using epifluorescence microscopy. All core samples had detectable levels of microspheres on the exterior. Interior portions of each core were also viewed using epifluorescence, and it was determined that no microspheres were present from the interior subsamples. This initial contamination assay indicates that if seawater penetrated rock samples, microorganisms >0.5 µm were excluded. PFTs were not used during this expedition because of an inability to process samples.

In addition to microspheres, deoxyribonucleic acid will be extracted from water samples collected in Hole U1309D at 390 and 1215 mbsf and used to conduct a comparison of the microbes present in seawater versus those found on the interior of core samples. This comparison will serve as the ultimate control in determining the extent of contamination of rock samples by seawater microorganisms.

Downhole measurements

Operations

Hole U1309B

After reaching a depth of 101.8 mbsf, Hole U1309B was conditioned and filled with freshwater and the bit released at the bottom of the hole. The pipe was pulled to 35.7 mbsf, and three tool strings were deployed (Fig. F282A). The first deployment consisted of the triple combo tool string, which contained the Hostile Environment Natural Gamma Ray Sonde (HNGS), the Accelerator Porosity Sonde (APS), the Hostile Environment Litho-Density Sonde (HLDS), the Dual Laterolog (DLL), and the Lamont-Doherty Earth Observatory (LDEO) TAP tool. The APS was not used on the first pass because it would activate the formation during the neutron capture phase as gamma rays are emitted. For the second pass, the pipe was pulled up to 21.6 mbsf. The second pass was logged to the seafloor with the APS minitron on.

The second tool string deployment consisted of the Scintillation Gamma Ray Tool (SGT), the General Purpose Inclinometry Tool (GPIT), the FMS, and the Dipole Sonic Imager (DSI). The first pass proceeded without difficulty, and the FMS arms were closed several meters before the logging head entered pipe. During the second pass, when the bottom of the FMS began coming into the pipe, some overpull was recorded. The tool string was brought to the surface to check for damage. It appeared that the outer cover of the caliper that serves as housing for the pad wiring was broken and the arm expansion springs were fully extended.

The third tool string consisted of the GPIT and the SGT with spacers. This last run was devoted to the Offshore Service Unit-F-model Modular Configuration MAXIS Electrical Capstan Capable (OSU-FMEC) heave compensator tests. For reference, a first pass with the LDEO-Borehole Research Group wireline heave compensator (WHC) at 900 feet/h and a station log was run. Next, the OSU-FMEC was used, and three passes were performed at different speeds (900, 300, and 1800 ft/h), followed by stationary logs. These data will be used to evaluate and improve the new heave compensator system.

All logging passes reached 96 mbsf, or 7 m above the maximum penetration. Borehole conditions were excellent during the three runs, and no ledges or obstructions were encountered. Additionally, the drill pipe was held a depth of 21.6 mbsf before tool string reentry into pipe during each run, except for the first triple combo pass.

Hole U1309D

Three phases of logging operations were performed in Hole U1309D (Fig. **F282B**). During Expedition 304, Phase 1 (0–400 mbsf) was accomplished. Phases 2 (400–836 mbsf) and 3 (836–1414.5 mbsf) were accomplished during Expedition 305.

Phase 1 (0–400 mbsf)

A first attempt to log Hole U1309D with the triple combo was made on 31 December 2004. The drill pipe was set inside the casing. We could not get past an obstruction at 39 mbsf. A second run was made by using a short tool string (DLL and HNGS), but we could not pass the same obstruction. As we were using an 11⅞ inch bit, there was no way to move the pipe to pass the obstruction in the 9⅞ inch hole. This logging attempt ended on 1 January 2005 at 0600 h.

After doing some shallow spot coring with the 11⅞ inch bit (see **"Operations"**), a round trip was made to replace the bit with a 9⅞ inch cleanout bit. On 2 January at 0700 h, the second logging attempt started with the triple combo (Fig. **F282B**). The pipe was set at 64 mbsf so it would be below the known obstruction zone. While exiting the pipe, the triple combo set down at 74 mbsf. The pipe was moved up to 54 mbsf, and, after working the tool string, it went past 74 mbsf. It shortly set down at 79 and 96 mbsf, but finally went to bottom. After we had a problem with the Schlumberger Minimum Configuration Maxis acquisition software while coming off bottom, the computer was rebooted. There was some activation over the first 5 m from the APS on the subsequent logs. A repeat pass was performed at the bottom of the hole to minimize the effect of APS activation.

The second tool string deployed was the FMS-sonic, which went to bottom with no problems. On the first pass, we had some overpull at 129 mbsf and the tool was partially closed before it became free. Calipers were opened again and there was more overpull at 99 mbsf, where we had planned to close the calipers to enter pipe. The second FMS-sonic pass proceeded without difficulty.

After changing over to the accelerometer to test the Schlumberger heave compensator, the tool stopped at 67 mbsf. Working for 30 min, the tool string advanced to ~69 mbsf. At that point, we decided to make sure we could still come back uphole. It appears that a piece of the borehole wall had probably fallen in and wedged the tool in place. Half the tool was in pipe and we could not go up or down. We finally freed the tool after working it for an additional 30 min. Any further attempts to log the hole were cancelled. A 15 min OSU-FMEC heave compensator test in pipe at 900 feet/h up and a stationary test were performed.

During all logging runs in both holes, the WHC was turned on following the exit from pipe and used continuously while the tool strings were in the open hole. Following acquisition, logging data were transmitted to LDEO for depth and environmental correction processing and subsequently returned to the ship. All data presented in this chapter have been processed and depth-shifted as described in **"Processing and data quality."**

Phase 2 (400–836 mbsf)

After reaching a depth of 837.4 mbsf, Hole U1309D was conditioned and filled with freshwater for logging operations. The pipe was tripped, and a logging bottom-hole assembly (BHA) with logging bit was run into the hole. To avoid obstructions and to allow an overlap with the previous logging runs from Expedition 304, the pipe was set at 170 mbsf, and a total of five tool strings were deployed (Fig. **F282B**). The first deployment consisted of the triple combo tool string, which contained the HNGS, the APS, the HLDS, the DLL, and the LDEO TAP. The first pass covered the interval from the bottom of the hole at 836.4 mbsf to the pipe. The pipe was identified in the logs at 170 mbsf. For data quality check, a short repeat pass was run in the lowermost 120 m. The second tool string deployment consisted of the DSI, the SGT, the GPIT, and the FMS. The first pass covered the interval from 836.4 to 350 mbsf, and the second pass logged the entire open hole up to the pipe. Because of time constraints and the need to wait for daylight for marine mammal watch associated with

the seismic check shot work, 3 h was devoted to heave compensator tests with the OSU-FMEC. One joint of the pipe was removed, and the pipe was set to a depth of 161 mbsf before tool string reentry. The third tool string consisted of the three-component Well Seismic Tool (WST-3). The tool was lowered to the end of the pipe and halted in a safe position. No marine mammals were sighted during a 1 h watch, so the air gun was soft-started by increasing pressure levels over 0.5 h. After clearance and during the soft-start, the tool was lowered to the bottom of the hole and subsequently clamped. In 50 m intervals, a total of 13 stations were occupied for check shot recording (Table T25). For the two lowermost stations, no clear arrival could be identified in the seismograms, but all other stations had good signal-to-noise ratio for many individual and all stacked seismograms. The fourth run included the Ultrasonic Borehole Imager (UBI), the GPIT, and the SGT. A sinker bar was added to speed up lowering of the tool in the pipe. The tool was not lowered to total depth but only to 824.4 mbsf to protect the sensor at the end of the tool string. The first pass from 824.4 to 724 mbsf was acquired in high-resolution mode at a speed of ~120 m/h. Subsequently, the tool was lowered again to 824.4 mbsf and the normal mode, at a speed of ~260 m/h, was started. However, because of software problems in detecting the first arrival of the signal, no consistent data could be obtained with normal mode. It was decided to abandon this acquisition mode and to conduct additional high-resolution measurements in the depth interval (704–503.2 mbsf) where good hole conditions had been documented by caliper data and where lithology is significantly variable. The GBM was deployed in the fifth run. A low-magnetic sinker bar was added and the tool had no problems reaching total depth. The tool obtained data for the downhole, as well as the uphole pass at a speed of 360 m/h. The tool also measures temperatures within the housing, which are within ±2°C of ambient borehole temperatures. Prior to and after logging, the gyrocompass of the tool was oriented with the vessel heading. Vessel heading parameters at those times were provided by the bridge. The data from the GBM were sent to Goettingen (Germany) for further processing, and preliminary results were returned to the ship. All data presented in this chapter have been processed and depth-shifted as described in **"Processing and data quality."**

Phase 3 (836–1414.5 mbsf)

After reaching a final depth of 1415 mbsf, Hole U1309D was conditioned and filled with freshwater for logging operations. The pipe was tripped, and a logging BHA with logging bit was run into the hole. The pipe was set at 194 mbsf and three tool strings were rigged up, but only two were successfully deployed (Fig. F282B). The first deployment consisted of the triple combo tool string. The first pass covered the interval from the bottom of the hole at 1415 mbsf to the pipe. The pipe was identified in the logs at 194 mbsf. For data quality check, a short repeat pass was run in an interval of low recovery (1270–1096 mbsf). The second tool string deployment consisted of the DSI, the SGT, the GPIT, and the FMS. After reaching the bottom of the hole, communication to the lower part of the tool was lost. It was concluded that the joint between transmitter and receiver section in the DSI must have been damaged, and the tool was pulled back to the rig floor. The broken joint was identified, and the DSI was removed. Hence, no sonic data were acquired during this phase. The remaining SGT, the GPIT, and the FMS string were lowered back into the hole. A successful first pass was recorded from total depth to 734 mbsf, and a second pass was run from total depth to 629 mbsf. The third tool string consisted of the WST-3. The tool was lowered to the end of the pipe and halted in a safe position. After 1 h of marine mammal watch, the air gun was soft-started by increasing pressure levels >0.5 h. After clearance and during the soft-start, the tool was lowered to the bottom of the hole. After reaching total depth, communication to the tool was problematic, and high temperatures were suspected to have caused electronic problems. The tool was pulled to shallower depth, but the problems remained. The tool was pulled out of the hole and replaced by the single-component WST. After lowering the tool into the hole, one test position at 328 mbsf was chosen for a tool check. It recorded successfully, and lowering of the tool to total depth was begun. Midway downhole, heave had increased beyond safe deployment conditions, and it was decided to terminate the logging operation.

When pulling back the tool, a sudden increase in tension (1500 lb over normal) was registered and continued to be erratic, indicating a problem with the wireline. When approaching the surface, the tool speed was reduced at ~600 meters below rig floor (mbrf) and approach to rig floor was slowed to prevent any damage to the oil-saver/circulation sub in the top of the drill pipe. At 570 mbrf, the tension increased to 6000 lb and the tool was stopped; tension was released, and the oil-saver was removed. It was decided to recover the wireline with T-bars by pulling it up in ~30 m intervals and cutting it in sections. A series of wireline knots was subsequently recovered. The WST was pulled back to the rig floor without any damage.

During all logging runs, the WHC was turned on following the exit from pipe, and it was used continuously while the tool strings were in open hole. Following acquisition, logging data were transmitted to the LDEO for depth and environmental correction processing (see **"Downhole measurements"** in the "Methods" chapter); these data were then returned to the ship.

Processing and data quality

Hole U1309B

The original logs were shifted to the seafloor depth given by the drillers (1653.4 mbrf) and depth-matched to the gamma ray log and FMS images from pass 2 of the FMS-GPIT-SGT-DSI tool string. The density log from the triple combo tool string was depth-matched to the FMS images because the extremely low gamma ray values (<10 gAPI) made matching by gamma ray data alone difficult. The seafloor depth could not be determined from gamma ray values, also because of the very low values; therefore, the seafloor depth given by the drillers was used. The quality of the data was assessed by checking against reasonable values for the logged rock types, by repeatability between different passes of the same tool. Hole U1309B diameter was recorded with the caliper on the HLDS (LCAL) and on the FMS (C1 and C2) (Fig. **F283**) tools. The borehole was in good condition, typically 10 inches wide except for occasional small enlargements, the largest of which is at 61 mbsf, where the calipers reach 15 inches.

The excellent hole conditions resulted in particularly good measurements in the contact tools, such as density, porosity, and FMS. Good repeatability is observed between the two passes. Hole deviation, as measured by the GPIT, reached 7° (hole azimuth 040°–045°) in the lower 40 m of the hole, which contributed to the poor sonic data. The DSI was operated in the following modes: for pass 1, *P*- and *S*-wave mode monopole and for pass 2, *P*- and *S*-wave mode monopole, lower dipole, and Stoneley mode. The acoustic velocities from pass 1 seem to be in reasonable value range for gabbroic rocks but do not match the patterns in the other physical property logs (density, electrical resistivity, and FMS). Further processing postcruise may improve data usefulness. No TAP data could be recovered from the tool in Hole U1309B, and the reasons for tool failure are unclear. The quality of the FMS images recorded in Hole U1309B is excellent. Flushing with resistive freshwater mud improved FMS response as it reduced conductivity contrast between the borehole fluid and the wallrock. The contact between the FMS pads and the borehole wall is confirmed because maximum aperture measured by the calipers is 15.2 inches, less than the maximum possible aperture (16 inches).

Hole U1309D

Phase 1 (0–400 mbsf)

A selection of logs acquired during Phase 1 is presented in Figure **F284A.** Their uppermost limit corresponds to the pipe depth, as indicated by the dashed horizontal line. Their lowermost limit represents the deepest depth achieved by the various probes.

In Hole U1309D, FMS images were recorded between 400 and 96 mbsf. For the majority of the borehole, the walls are relatively smooth and uniform with a typical diameter of ~11 inches (~28 cm). More irregular sections of the borehole are located within the upper interval, especially in the intervals between 113 and 145, 222 and 230, and 243 and 249 mbsf. Within these zones, there are several intervals where the diameter of the borehole exceeds the limits of the FMS calipers, and in these locations, image quality is expected to be low. Within the remainder of the borehole, data are continuous and of very high quality. Furthermore, in some intervals (for example, at 96–117, 236–248, and 273–400 mbsf), the two passes did not follow the same path, which increases the wall coverage.

The original logs were shifted to the seafloor depth given by the drillers (1656 mbrf). Caliper data indicate that Hole U1309D is generally in good shape, especially between 286 and 400 mbsf with a gauge hole (C1 and C2) (Fig. **F284A**). The top section is in good shape but has several irregular sections ranging from 13 to 18 inches, especially in the intervals between 113 and 145, 222 and 230, and 243 and 249 mbsf. The DSI data were good in some sections but very noisy throughout the irregular areas of the hole. The hole deviation, as measured by the GPIT, reaches 1.75° at 125 mbsf and smoothly decreases to <1° from 196 mbsf to the bottom of the hole.

Phase 2 (400–836 mbsf)

Conditions in Hole U1309D continued to be very good, particularly in the deepened part from 400 to 836 mbsf (Fig. **F284B**). The excellent conditions allowed particularly good measurements for contact tools such as density, porosity, and FMS. No TAP data could be recovered from the tool, and the reason for tool failure was suspected internal connection problems. Comparing the caliper data from the Phase 1 and Phase 2 logging runs of the upper 400 m, progressive enlargement with continued drilling is evident (Fig. **F284B**). This supports the strategy of implementing intermediate logging runs to ensure good data quality for contact measurements.

The logs were shifted to the seafloor depth given by the drillers (1656 mbrf) and depth-matched to the Phase 1 logging run of the upper 400 m. As in the topmost interval, the resistivity log from the triple combo tool string was depth-matched to the FMS images. The GBM data were depth-matched to the total magnetic field data recorded by the GPIT.

The measurement quality of natural gamma ray data is good; however, the natural radioactivity of the formation measured with this tool is overall very low (<5 gAPI). As with Phase 1 data, potassium, thorium, and uranium concentrations derived from the spectrum are below the detection limit, so quantitative values for these three elements should not be trusted.

Magnetic field intensity and direction were recorded by the GBM and GPIT (here GPIT data are taken from the Expedition 305 FMS-sonic tool string). The GBM setup did not allow direct depth measurement, only magnetic field versus time. We obtained the corresponding logging depth by correlation with the Schlumberger time-depth log output from the logging winch. The GBM tool recorded data during both the downhole and uphole run (Fig. F285). Because of tool rotation, the horizontal field components x and y oscillate around the zero line. The vertical field component z shows a high level of repeatability for the downhole and uphole logs. In addition to the GBM fluxgate sensors, the angular rate of the GBM tool around the x-, y-, and z-spin axes was measured using three fiber-optic gyros. The rotation record of the tool is determined by the accumulation of the angular rate during the logging run. Rotation data will be used for reorientation of the magnetic data. Gyro temperature and telemetry temperature were also recorded in order to allow temperature correction for the gyros and to obtain chassis temperature, which closely relates to borehole temperature. Inclinometer data around x- and y-axes were also recorded. Because there are no centralizers used, the inclinometer data are required to determine what, if any, correction is required for trade-off between horizontal and vertical component.

Onshore processing of the gyro data is required to correct for the orientation of the tool. This will allow determination of the horizontal field components. The magnetic field intensity derived from GBM logging differs slightly from the International Geomagnetic Reference Field expected at this latitude (horizontal field = 27,483 nT; vertical field = 30,313 nT; total field = 40,918 nT; inclination +47.8°) (Fig. F286). The in situ magnetic field inclination (raw data) averages +51.11° (downhole run median = +51.36°) and +52.04° (uphole run median = +51.79°) for the open hole depth interval. The GPIT inclination averages +51.42° (median = +52.13°). The two magnetic tool logs agree well with respect to the sequence of magnetic variations, although they show differences in magnitudes (Fig. F286) and a slight offset in the vertical component.

The FMS and UBI data were processed to correct for acceleration and sticking that occurred during the uphole logging. The two passes of the FMS were depth-matched, with the second pass as reference. Although the FMS images could be corrected with confidence, the UBI images show artifacts of sticking even after speed correction. One possible explanation is that because of the low tool speed, the heave of ~3 m during the data acquisition was not entirely compensated. Depth-matching the UBI data to the FMS passes alleviated some of those effects. All resistivity scan data sets were statically and dynamically normalized during conversion to color images. In most intervals, the coverage of the borehole wall by the FMS is excellent and is complemented by the UBI images.

Phase 3 (836–1414.5 mbsf)

Data recorded during the last logging run have been depth-matched to the upper logging curves. Triple combo data show high data quality and allow an excellent overlap with the previous logging run. Between 630 and 655 mbsf, the triple combo caliper (LCAL) recorded borehole diameter data smaller than the bit size, which may be due to electronic failure within this depth interval because no obstruction could be detected while lowering the triple combo. Two FMS passes were acquired, and overall images repeated very well. Caliper data registered no obstruction in the interval mentioned above. Poor data quality was typical between 1275 and 1180 mbsf within the first pass. The second pass had no problems, and high-quality images were gained. The check shot station recorded by the WST will be discarded because of wireline problems that occurred during this run. Because depth is measured by cable length and there were knots in the wireline, the exact depth determination of this check shot station is unreliable (see **"Operations,"** above).

In general, logging data and core petrophysical data compare very well (Fig. F287). The density and velocity data are in the same range for core samples and logging measurements. The main difference is between the sample porosity (see **"Physical properties"**) and the neutron porosity logs. The logging values are much higher than the core sample data; however, they follow similar trends. The reason is that neutron porosity measurement is sensitive to all hydrogen (such as in pore water or bound in minerals) present in the formation (Serra, 1984), whereas sam-

ple porosity reflects only pore water. Neutron porosity curves are calibrated to limestone porosity, which may further contribute to some discrepancies.

Results

Natural radioactivity

Formation natural radioactivity was measured during each run with two different tools. The high-resolution curve from the SGT and spectral data from the HNGS are shown in Figure **F283.** The different gamma ray tools show the same general patterns throughout the logged interval. Total gamma ray values (HSGR) obtained with the triple combo tool string range from 0 to 12 gAPI in both holes. Such very low gamma ray measurements are expected in oceanic crust. Significant increases observed on the total gamma ray log occur at 56.5, 64.1, and 73.4 mbsf in Hole U1309B and correlate with minor tool responses in electrical resistivity, porosity, and density measurements. In Hole U1309D, several significant increases in gamma ray are recorded, for example at 172, 373, 632–638, 742–756, and 866–872 mbsf (Fig. **F284A**). The spectral gamma ray measurements also show very low values that, in many instances, are below the tool detection limits for Th (0.7 ppm), U (0.35 ppm), and K (0.18 wt%). Potassium values are low, between 0 and 0.1 wt%. Thorium and uranium values are mostly between 0 and 1 ppm.

Neutron porosity and capture cross section

The neutron porosity in the logged section of the hole ranges from 56.6% to 3.2%. Absolute values in the neutron porosity log do not match the discrete laboratory porosity measurements, which are lower. This may be caused by the presence of bound water in the wallrock and/or sampling bias due to the fact that fractured intervals commonly result in poor recovery and the rocks recovered have veins and fractures that are rarely sampled for physical property measurements. In Hole U1309B, neutron porosity maxima occur at 36.8, 41.6, 46.4, 52.6, and 66.9 mbsf (Fig. **F283**). These high values may correspond to the tool losing contact with the borehole wall, a high degree of fracturing, the presence of hydrous alteration minerals such as clay minerals in veins, or altered groundmass (see **"Metamorphic petrology"**). These high neutron porosity values generally correlate with lows in the density log and low resistivities. Within the logging interval 57.6–61.5 mbsf, high neutron porosity values may correspond to depths where peridotites were recovered (Fig. **F284A**). High neutron porosity in this particular interval could be explained by the high content of bound water in the serpentine minerals (10 wt% H_2O; see **"Geochemistry"**). In Hole U1309D, numerous neutron porosity maxima occur, especially in the intervals 100–290, 410–500, 550, and 1100–1150 mbsf, where the borehole shape is the most irregular (Figs. **F284B, F284C**). However, in some intervals, such as 311–343, 740–755, and 1090–1200 mbsf, where the borehole is in gauge, high neutron porosity values are related to the presence of serpentinized rocks with high contents of bound water in the serpentine minerals.

The capture cross section ranges from 11.8 to 40 capture units (cu). Capture cross section values are ~10–30 cu for most silicate minerals and up to 100 cu for Fe-Ti oxides (Serra, 1984). High values are recorded in diabase, oxide-rich gabbros, and serpentinized rock. However, sigma values can also be caused by large borehole conditions because the tool is sensitive to bad borehole wall contact.

Density and photoelectric factor

Density values range from 1.6 to 3.1 g/cm^3 over the entire logged section in Hole U1309B and from 1.2 to 3.7 g/cm^3 in Hole U1309D. In both holes, very low density values correspond to borehole washouts or fractures in igneous rocks and generally correlate with high values in the neutron porosity log. Density measured downhole shows excellent correlation with density values from discrete laboratory measurements (see **"Physical properties"**).

The photoelectric effect (PEFL), which varies from 1.1 to 5.2 b/e$^-$ in Hole U1309B and from 0.4 to 9.4 b/e$^-$ in Hole U1309D, is commonly a good indicator of lithologic variations. In Hole U1309B, PEFL values tend to be slightly higher in two intervals (29.4–34.7 and 61.7–69.8 mbsf) than in the rest of the section. These two intervals appear to correspond to the diabases crossed within the logged section. In Hole U1309D, PEFL maxima are recorded in several intervals (675, 880–886, 1182–1183, and 1301–1303 mbsf) corresponding to diabase and oxide-rich gabbros (Fig. **F284A**).

Electrical resistivity

In Hole U1309B, the electrical resistivity curves range between 3 and 400 Ω·m, most likely due to changes in fracture intensity and alteration. The lowest resistivity intervals are well correlated with the lowest density and highest neutron porosity values (Figs. **F283, F284**).

In Hole U1309D, the electrical resistivity values are locally extremely high (up to 40,000 Ω·m) between 1190 and 1195 mbsf, most likely in fresh olivine-rich troctolites. The bulk of the data varies between 30 and 3000 Ω·m with lithology (e.g., occurrence of oxides), fracture intensity, and alteration.

Lithological and structural interpretation

The logging data reflect the overall variability of the rock types drilled, comprising diverse gabbroic rocks, diabase, and olivine-rich troctolites (Fig. F284) (see "Igneous petrology"). Logging data also reflect structural changes and alteration modes. Based on density, velocity, PEFL, neutron porosity, and resistivity logs, we are able to distinguish characteristics that may correspond to lithology changes. The FMS images visualize the structural as well as partly textural variation downhole.

In the gabbroic rock intervals, logging bulk density varies between 2.8 and 3.2 g/cm^3 and resistivity ranges from 50 to 2000 Ω·m. In general, the PEFL is <4 b/e$^-$ and it averages ~3.1 b/e$^-$. Logged compressional velocity ranges between 5.5 and 6.5 km/s. Gabbros and olivine gabbros are characterized on the FMS images by high resistivities that correspond to light-colored zones (for example, the interval between 360 and 400 mbsf) (Fig. F288).

Most intervals of oxide gabbro, as identified in the visual core descriptions (see "Igneous petrology"), can be recognized in the logging data. They are generally characterized by elevated values of density (3.0–3.2 g/cm^3), PEFL (4–8 b/e$^-$), and capture cross section (>30 cu) and low electrical resistivity (<100 Ω·m). PEFL is increased because of the presence of Fe in the formation. PEFL is proportional to the atomic radii of the atoms in the formation. Among the common elements, Fe has high PEFL (Serra, 1984). The intervals of oxide gabbro inferred from logs are intervals 191–196, 351–355, 642–645, 672–677, 719–720, 880–886, 989–998, 1182–1184, 1268–1274, and 1300–1302 mbsf. Although oxide gabbros have been described between 235 and 243 mbsf and 400 and 560 mbsf, there are no significant peaks in the PEFL log. The gabbros in these intervals contain disseminated oxides in lower concentrations (see "Igneous petrology"), and low PEFL values, ~4 b/e$^-$, match this observation.

Most olivine-rich rocks, such as olivine gabbro, troctolite, or olivine-rich troctolite, show high levels of serpentinization, and they contain more structurally bound H_2O than olivine-poor gabbros (see "Igneous petrology" and "Geochemistry"). Based on this relation, we interpret intervals with neutron porosities of <5% as the least altered gabbro. In concert with low neutron porosity are high resistivities (>500 Ω·m). The slightly altered gabbros, on the other hand, show neutron porosities between 5% and 15% and intermediate resistivities (50–500 Ω·m). The olivine-rich troctolite at 689–691 mbsf is highly altered and has H_2O contents of 8 wt% (see "Geochemistry"). For this section, neutron porosity averages 20%.

The recovered diabases have varying thicknesses. They are mostly very thin (<1 m) and show log responses reminiscent of oxide gabbros. The reason for that is that most diabases have a Fe_2O_3 content ranging between 11 and 13 wt%, which is comparable to that of oxide gabbro (see "Geochemistry").

Structural features like discrete, open faults and fracture zones are portrayed by enlarged borehole diameter (>11 inches), which causes sudden apparent drops in density (1.5–2 g/cm^3), resistivity (10–50 Ω·m), and velocity (4–5 km/s) and an increase in neutron porosity to values >40%. In addition, FMS and UBI images (Figs. F281, F290) show structural variations as well as textural variations of gabbroic rocks. FMS sections with patchy appearances correspond to intervals of coarse-grained gabbro (resistive patches) (Fig. F289A) or oxide-rich gabbro (conductive patches) (Fig. F290).

The continuous structural information gained from the FMS images with respect to dip and azimuth of conductive fractures is a crucial contribution to the understanding of the tectonic evolution of Atlantis Massif (see also "Structural geology"). On FMS and UBI images, mapping structural features consists of connecting a perfect plane (sinusoid) through the presumed geological object (mainly conductive features on FMS images or low-amplitude features on UBI images).

In Hole U1309B, 142 planar structures have been manually mapped (Fig. F291; "Supplementary material"). These features correspond to veins, fractures, faults, foliation, or lithologic boundaries. Dip magnitudes range between 5° and close to 85°, with most dips ranging from 20° to 60°. The number of subvertical planes (60°–90°) is much lower than subhorizontal (0°–30°) and intermediate (30°–60°) planes. This difference in detected plane abundance is linked to the borehole verticality, as the probability of encountering a horizontal fracture is higher than the probability of encountering a vertical one. Preliminary structural analyses of features (Fig. F291) show features dipping mostly southeast (mean dip direction = 130.4°). These orientations are consistent with orientations of a majority of veins measured on the core face and rotated into a geographical reference frame using paleomagnetic data (see "Reorientation of structure data using paleomagnetic data"). Within the interval 79.4–80 mbsf, FMS images show conductive rocks with a series of resistive clasts (white round features) that may be correlated to the breccia samples recovered in Section 304-U1309B-16R-1 (Fig. F292). At 58 mbsf, there is a change from a resistive to more conductive formation that can be correlated to the transition from gabbro to peridotite (Fig. F293). Below this contact,

many conductive features inferred to be fractures are also present, although the overall resistive nature of the formation is still apparent below 62 mbsf.

Figure F294 shows an example of how consistent the dip of structures is in short depth intervals. Between 772 and 783 mbsf, the shallow structures in the gabbro dip toward the north, whereas the steep structures dip toward the south. The combination of FMS and UBI images is well suited to depiction of steep or complicated structures (Figs. F289B, F295).

Figure F296 compares conventional logging data to results from structural observations of brittle features (see "Structural geology"). The borehole enlargements seen in the caliper data are an expression of the local weakness in the formation caused by intense brittle deformation. Most borehole enlargements and the associated reduction in density, for example, correlate with peaks in the intensity of cataclastic features or large numbers of veins. Interestingly, the peaks in cataclastic and vein intensity at ~690 and ~745 mbsf show only slight decreases in wallrock density and no significant borehole enlargement. The fault zone at ~785 mbsf is not associated with any borehole enlargement. The lower two zones contain fault gouge that has been cemented by fluids (see "Structural geology" and "Metamorphic petrology").

There is not only a good correlation of logging data with cataclasis and vein occurrence but also with alteration intensity; these are commonly genetically related. Here, it appears that alteration most strongly affects the neutron porosity. High intensities of alteration are associated with three fault zones between 690 and 785 mbsf (Fig. F297). The interval between 788 and 790 mbsf shows distinct logging responses (Fig. F298), indicating alteration. The FMS portrays it as a discrete layer with abrupt upper and lower boundaries and from which core has probably not been recovered. Overall, the most conductive intervals are well correlated with the oxide gabbro, troctolite, and serpentinized lithologic units defined in the core description (Fig. F299).

The interval between 729 and 760 mbsf shows a complex interaction of alteration and structural features. Between 729 and 735 mbsf and 740 and 750 mbsf, neutron porosities as high as 20% indicate intense alteration, probably chloritization (Fig. F300) (see "Metamorphic petrology"). Low values in resistivity (<100 Ω·m) and velocity (<5 km/s), as well as high values of natural gamma ray (~4 gAPI) and capture cross section (~30 cu), not only support this interpretation but indicate fluid flow in the past. In previously drilled ODP holes, an uptake in potassium with increased time of alteration and fluid flow has been observed (e.g., ODP Holes 504B, 395A, and 1137A). Below 765 mbsf, an increase in resistivity (>1000 Ω·m) and a drop in neutron porosity (0%–5%) occur, and values remain more or less constant down to 1092 mbsf. This agrees well with the observation of low core alteration in this interval. Between 1092 and 1170 mbsf and 1185 and 1195 mbsf, neutron porosity sharply increases locally to values >20% and resistivity decreases to <100 Ω·m. These intervals correspond to the olivine-rich troctolites, when highly serpentinized (see "Metamorphic petrology").

The vertical magnetic field variations recorded by the GBM correlate well with magnetic susceptibility measurements on whole cores (Fig. F301). The differences in the magnetic behavior are observable in intervals containing altered olivine-rich troctolites. Between 300 and 350 mbsf, the magnitude of the vertical component strongly increases. Within this interval, the recorded PEFL remains low. Oxide gabbros are characterized by high magnetic susceptibility, minor to high variation in the magnetic field component, and an increase in PEFL. The magnitude of these anomalies may depend on the presence of disseminated or massive oxides. Gabbroic rock intervals between 400 and 600 mbsf are associated with more or less constant field intensity at ~32,000 nT. In the lower part of the interval logged with the GBM, there is an overall increase in the magnetic field strength that may be caused by changes in lithology. Below 680 mbsf, less olivine gabbro is present but there are more oxide gabbros.

During the uphole logging run, the maximum recorded temperature of the gyros was 71.09°C (743 mbsf), which is close to the instrument operating limit. A second temperature sensor in the telemetry module, which measures close to the ambient borehole temperature, had a maximum of 71.35°C at 808 mbsf. The downhole measurement on the GBM tool is slightly lower than the uphole measurement. This is probably because of time needed for the tool to reach equilibrium in a positive downward gradient.

Seismic stratigraphy

Site U1309 is located 350 m west of MCS Line Meg-4, being closest to common depth point 4136 (Fig. F302). The site is positioned on a slightly higher elevation (20–40 m) than the projected position on the seismic line. The time-depth conversion for Hole U1309D was calculated from a check shot survey. Velocity information was provided by the downhole sonic logging data and, in the upper 53 mbsf where the pipe in the hole prevented downhole measurements, by *P*-wave velocity measurements on core samples (see "Physical properties"). The resulting traveltime-to-depth curves are shown in Figure F303.

Comparing the core-, log-, and check shot–derived relations, one can see an excellent agreement. Because of the high core recovery, the lithologies are adequately sampled (see **"Physical properties"**).

Average velocities computed from automatic picks on stacked seismograms generally fall in the range 5600–5800 m/s (5.6–5.8 km/s), but interval velocities can vary considerably between stations, particularly between 623 and 673 mbsf with 7971 and 5055 m/s, respectively (Table **T25**). Two errors might have occurred during check shot data acquisition. First, an error in station depth of a few meters cannot be ruled out. Second, the vertical movement of the air gun due to heave can contribute a small shift in time. However, stacking of several shots made at each station should have averaged the heave uncertainties. Adjusting the depths of the two stations (623 and 673 mbsf) by 2–4 m (which is probably beyond the potential station location error) would change these two interval velocity values; however, the high and low values (>7000 and <6000 m/s, respectively) would still be preserved at these stations. Despite our overriding caution with these initial results, it is possible that a lens of relatively unaltered, high-velocity, relatively olivine rich rock a few tens of meters thick occurs within the Fresnel zone of the vertical seismic profile (VSP) experiment (of the order of several meters).

A reversed polarity, zero-phase wavelet of 150 ms length was statistically extracted from the migrated seismic Line Meg-4 and used for convolution with the downhole impedance curve derived from logging *P*-wave velocity and density in order to calculate a synthetic seismogram (Fig. **F32**).

Hole U1309D transected a series of strong reflections seen in the seismic lines (Fig. **F302**). The lowermost reflection in seismic Line Meg-10 was identified as Reflector D by Canales et al. (2004). One interpretation put forward by those authors was that it coincided with the transition from shallower altered peridotite to underlying unaltered peridotites. In Line Meg-4, this reflector is at ~2.346 s two-way traveltime (TWT). Based on initial drilling results, several explanations for Reflector D are possible. This reflection could coincide with an apparent closure of fractures below ~295 mbsf and can be seen by the disappearance of low density and velocity peaks. Alternatively, density continues to increase monotonically until the base of the olivine-rich troctolite interval (310–360 mbsf), which may cause the reflector by its velocity contrast with underlying units. The lowermost reflection seen at 2.5 s TWT might be associated with the transition from a major fault zone, located at ~745–780 mbsf, to relatively unaltered gabbros below (see **"Metamorphic petrology"**). This inference is supported by an increase in both velocity and density logging data at 760 mbsf and a reduction in porosity as measured on core samples (see also Fig. **F300**).

Temperature profile

During the final logging run, the temperature of Hole U1309D was recorded using the TAP tool during the downhole and uphole runs, as well as the main log and the repeat log (Fig. **F34**). The borehole temperature measured uphole is slightly higher than downhole, and the second pass is higher than the first because the TAP tool sensor takes time to equilibrate. Logging curves show a slight change in the temperature gradient below 375 mbsf and at 720 and 1100 mbsf. These changes are recorded in each pass. The depth intervals coincide with changes in lithology (presence of olivine-rich troctolites) and/or structural events (fault zone). The maximum recorded temperature is 118.9°C at 1415 mbsf.

Operations

Expedition 304

Port call

Expedition 304 began at Ponta Delgada, Portugal, with the first line ashore at 0816 h on 17 November 2004, which ended Expedition 303. Cores from the previous expedition were offloaded for transfer to the IODP Bremen Core Repository (Germany), and the hardware for our HRRS deployments and the advanced diamond core barrel was brought aboard. Cores from Leg 209 (MAR at 15°45′N) were taken aboard to use as instructional material for Expedition 304 scientists. Maintenance on the active heave compensator (AHC) corrected an intermittent control problem, and the port call was completed in 3.5 days.

Transit to Site U1309

Our transit began with the last line away at 2012 h, 21 November 2004. The pilot was dispatched at 2024 h, and we were under way at full speed to our first site. During the transit, we averaged 11.1 kt over the 939 nmi distance. The vessel arrived at location (based on global positioning system [GPS] coordinates), and we launched a beacon at 0830 h on 24 November 2004, initiating operations at Site U1309.

Hole U1309A

Operations began with a subsea camera survey of the seafloor (Fig. **F304**) to locate suitable places to drill the pilot hole and install the HRRS. The survey was completed in <2 h, and an appropriate area (devoid

of large boulders or rubble) was selected for drilling. A water sample and a temperature measurement were collected for microbiology and geochemistry with the WSTP just above the mudline. The first hole (Hole U1309A; 30°10.11′N, 42°07.11′W; 1642 mbsl) was a punch core with the RCB coring assembly that captured the seafloor sediments (Table T26). Hole U1309A was terminated when the bit cleared the seafloor at 2230 h on 24 November 2004.

Hole U1309B

Rotary coring commenced in Hole U1309B (same coordinates as Hole U1309A) at 0050 h on 25 November 2004. From our punch test at Hole U1309A, we determined there was ~2 m of sediment covering hard rock. Because we were effectively attempting a hard rock spud, we began with low weight on bit (4000 lb) and slow bit rotation (30 rpm) to minimize the potential of drill collar failure. Penetration rates started at <1 m/h, but by 25 mbsf increased to as much as 2 m/h, as we were able to increase weight on bit and rotation speed while advancing the hole. Final penetration was 101.8 m with 46.7 m of recovery. All coring in Hole U1309B (Cores 304-U1309B-1R through 20R) recovered nominally 4.5 m increments (half cores) to maximize recovery. Owing to excessive vessel heave (4–5 m), only passive heave compensation was used during coring operations at Hole U1309B.

Penetration in Hole U1309B was terminated when the bit ceased rotation and penetration after 86.25 rotating h. The mechanical bit release was activated, and the bit was released at the bottom of the hole. The hole was displaced with drill (fresh) water for logging (to minimize resistivity contrast between the formation and the fluid in the borehole), and the end of the pipe was set 25 mbsf for logging. The logging operation consisted of three tool string deployments, one each with the triple combo and the FMS-sonic and a third run to test the new logging winch heave compensation system. Logging results indicate that Hole U1309B deviated ~7° to the northeast (N43E). Hole U1309B ended at 0805 h on 1 December when the mechanical bit release cleared the rotary table.

Hole U1309C

The HRRS was deployed with three joints of 13.375 inch casing with a designed penetration of 31.6 mbsf. The hammer-in-casing design utilizes a bit style that engages the hammer to a cutting shoe welded onto the bottom of the casing. All components were assembled starting at 0805 h on 1 December 2004. The assembly was tested at the rig floor and construction completed at 0230 h on 2 December. The vessel was offset ~20 m west of Hole U1309B to a location where the subsea camera survey showed seafloor characteristics similar to our pilot hole location (30°10.11′N, 42°07.12′W; 1638 mbsl). The subsea camera was deployed as we ran the HRRS to just above the seafloor, and after a comparison of active and passive heave compensation behavior, we decided to initiate the hole with the passive system (again because of high heave). Hole U1309C was initiated at 0945 h on 2 December. Hammer drill operations continued to 1655 m (drill pipe measurement), or 6 mbsf. This depth was reached shortly after noon on 2 December, at which time penetration and rotation effectively stopped. High torque, slow penetration rates, and low bit rotation speed during this deployment made for challenging drilling, and the drillers noted that each time weight was applied to the drill string, rotation would cease. Raising the pipe off bottom allowed rotation, but even after 8 h of attempts, no new penetration was possible, even while employing the active heave compensation system.

Because it seemed apparent we could not make sufficient penetration to install our casing string, we decided to abandon the attempt in this hole and move to another location. The subsea camera was deployed to inspect the HRRS as we cleared the seafloor and to aid us in selecting the next drilling target. Once the camera was near bottom, we could see that the casing running tool had released from the casing. Our operations team concluded that the release had probably occurred early in the deployment and that penetration effectively stopped at the time of release. The casing was firmly stuck in the seabed, with >25 m of casing standing proud above seafloor, and because it did not fall over when we extracted the pipe, we surmise that it is still upright. The BHA was pulled back to the surface, and the pilot bit from the HRRS cleared the rotary table at 0755 h on 3 December, ending Hole U1309C. Disassembly of the running tool revealed no detectable reason for early release.

Hole U1309D

A new drilling location was selected within our subsea camera survey area with similar seafloor appearance to the earlier drilling locations but outside the potential falling radius of the abandoned casing string and outside of the area of influence of the deviation of Hole U1309B. The HRRS was deployed for the second time, now with two joints of 13.375 inch casing for a designed penetration of ~22.45 mbsf. We

utilized the same hammer-in-casing design as deployed at Hole U1309C. We elected to use a shorter casing string on this attempt to reduce installation time but still provide a viable reentry system.

All components were assembled and ready for deployment by 1915 h on 3 December 2004. Hole U1309D (30°10.12′N; 42°07.11′W) was initiated at 0120 h on 4 December with a tagged drillpipe measurement of 1645 mbsf. Hammer drilling commenced, and at 0630 h, at a depth of 5 mbsf, penetration seemed to stop. The subsea camera was deployed to see if the running tool had prematurely released again, but everything appeared to be intact. Drilling continued with slow penetration until 0900 h on 5 December.

After penetration of 20.5 m, rotation on the drill pipe stalled, with excessive torque only relieved by lifting the bit off the bottom of the hole. Our engineers suspected the possibility of another premature release of the casing running tool, which was confirmed after deployment of the subsea camera. Fortunately, the running tool did not release until we had nearly achieved our target depth in Hole U1309D, leaving 4.5 m of casing above the seafloor (within the design parameters for HRRS deployment). The reentry cone was released, and a subsea camera survey indicated successful deployment of the reentry system.

As per our operations plan, we elected to open the hole beneath the reentry funnel to ~100 mbsf before moving to our second drilling site. Because drilling parameters and logging data indicated a clean gauge borehole at the pilot hole, we determined a nested casing system would not be required at this time. We elected instead to deploy a coring system to provide additional core as well as a head start for future deepening operations. The first reentry into Hole U1309D was accomplished in 10 min at 0240 h on 6 December. Cores 304-U1309D-1R through 22R were cut from 20.5 to 131.0 mbsf. The majority of the cores were nominally 4.5 m penetrations (half cores), but two ~9.5 m cores were cut to compare recovery to half cores. Penetration rates and operating parameters were similar to pilot Hole U1309B. The BHA was pulled after 60.75 rotating h. The bit cleared the rotary table at 1520 h on 10 December, suspending operations at Site U1309. Even though we attempted to be conservative on bit rotating hours, inspection after pulling the bit indicated excessive wear, with numerous missing teeth and three loose cones. The excessive wear might be attributed to coring through several intervals of diabase.

Following operations at Sites U1310 and U1311, we returned to Hole U1309D to continue deepening the hole. Reentry with a new RCB bit took about an hour, and was completed by 1305 h on 22 December. At 1705 mbrf (~49 mbsf), we encountered an obstruction in the hole. After installing the top drive, only a short rotation was required to pass the obstruction, and the hole was cleared to the depth of our previous penetration (131.0 mbsf). Coring began with Core 304-U1309D-23R and continued in nominally 4.8 m increments through Core 47R to 252.4 mbsf.

After a pipe trip to install a new RCB bit, the pipe was deployed into Hole U1309D, encountering the same obstruction at 48–49 mbsf. Again, it was easy to pass this obstruction with rotation. Coring continued from Core 304-U1309D-48R through Core 78R (252.4–401.3 mbsf), with total recovery for the hole in excess of 64%. With 56 rotating h on the bit and only a few days left in the expedition, we tripped the pipe out of the hole after conditioning the hole for logging and filling it with freshwater (to improve resistivity contrast between the formation and the borehole fluid for logging). Obstructions in the hole were encountered at 1704 and 1690 mbrf (~48 and ~34 mbsf).

Before pulling the pipe, we attempted two shallow penetrations with the used RCB bit.

Hole U1309E

Hole U1309E was initiated with the RCB system after our last full coring run in Hole U1309D. After the pipe was withdrawn from the HRRS, we moved the ship in dynamic positioning mode ~10 m east of Hole U1309D and cored without circulation to a depth of 3.8 mbsf (Core 304-U1309E-1R). Drilling-disturbed unlithified microfossil ooze with coarse sand and a few pieces of rock were recovered.

Hole U1309F

Continuing with efforts to capture the oldest sediments draping the central dome of Atlantis Massif, as well as the detachment surface itself, we moved the vessel in dynamic positioning mode to a site 275 m northwest of Hole U1309D. This location was selected to attempt to core through thin lithified carbonate and into basement, as was determined to be present based on seafloor images from an *Argo* still camera survey (*Argo II* run 039, cruise AT3-60). A short subsea camera survey revealed a surface with the characteristics of lithified carbonate, and Hole U1309E was cored to 4.8 mbsf (Core 304-U1309F-1R); ~6 m of drilling-disturbed, unlithified microfossil ooze was recovered. Because RCB coring was not successful in recovering material we could recognize as intact basement rock in either Hole U1309E or U1309F, we tripped the pipe in preparation for logging. Hole U1309F ended when the RCB coring bit

cleared the rotary table at 1450 h on 31 December 2004.

Logging in Hole U1309D

A new advanced piston corer (APC)/XCB BHA was assembled for logging. We selected this assembly to log Hole U1309D and provide the possibility of attempting two more coring systems (XCB and APC) on a transect of shallow-penetration holes across the central dome. The bit was positioned in the 13⅜ inch casing, but after 6 h, the logging tool would not pass the obstruction at ~48 mbsf and the logging run was terminated. Shallow-penetration holes were attempted with the XCB/APC coring system (see **"Hole U1309G,"** below) before tripping the pipe to install a logging BHA.

With the logging BHA installed, we were able to set the bit below the obstruction at ~48 mbsf in Hole U1309D. Triple combo and FMS tool string runs were successful, but the UBI run was not attempted because the second FMS pass ended with fallen rock briefly trapping the tool in the hole. The tool was extracted with no significant damage, and the logging BHA was pulled.

Hole U1309G

With the XCB/APC BHA in place, we made the short transit from Hole U1309D to Hole U1309G. Our target was an area of extensive lithified carbonate identified during a seafloor submersible survey (cruise AT3-60, *Alvin* dive 3642) in 2000. We deployed the subsea camera and encountered a marker deployed during the submersible survey. The navigation offset between AT3-60 and Expedition 304 is 11 m, the 2000 position of the marker is registered slightly to the north of the position determined during Expedition 304. Hole U1309G was cored to 3.5 m, recovering just under a meter of sediment and drilling-disturbed hard rock. An APC barrel was deployed to see if we could recover an intact section through the sediment and into basement, but the core barrel parted and no core was recovered. Because the result of XCB/APC coring was inconclusive regarding the nature of the uppermost basement at this location, we elected to trip the pipe to complete logging in Hole U1309D.

Hole U1309H

After logging operations were concluded, there was sufficient time left in the expedition for a short bit run. We elected to attempt a shallow RCB core at the same location as Hole U1309G. Using the retired bit from our last coring run, we attempted coring to a depth of just >2 m below the soft sediment blanket, but the core barrel returned empty. With ~5 h of operations time left in the expedition, the bit was returned to the seafloor and Core 304-U1309H-1R was cut without circulation in the upper 0.5 m and low pump pressure for the remainder of coring (~3.5 m). The pipe was pulled and inspected, and we were under way for Ponta Delgada by 0700 h on 4 January 2005.

Expedition 305

Port call

Expedition 305 began when the first line was placed ashore at Pier 12 in Ponta Delgada on the island of São Miguel, Azores, Portugal, at 2120 h on 7 January 2005. The vessel arrived slightly ahead of schedule and was able to clear customs and immigration the evening before the scheduled crew change. The US Implementing Organization and Transocean personnel crossover took place on the morning of 8 January. In addition to the routine freight transfer and the loading of fuel (999.6 MT), there were three pacing items for this port call: an American Bureau of Shipping (ABS) Annual and Statutory survey, an overhaul of the drawworks transmission, and the replacement of the AHC hydraulic hose bundle.

The ABS survey was completed by the morning of 11 January. Also on 11 January, the new AHC hose bundle was filled with oil and tested. After testing, the return hose had stretched in length by ~1.5 m. The return hose appeared to be either defective or inappropriately rated. Because repair was not possible within the port call schedule, the AHC was not operational during Expedition 305. The completion of the drawworks transmission repair was dependent upon the arrival of hardware from the Transocean warehouse in Houston (Texas, USA). Customs clearance in Lisbon, Portugal, delayed arrival of these parts until ~1530 h on 12 January.

At 1715 h on 12 January, the last line was released from the dock, and after clearing the harbor entrance, the pilot was released at 1721 h and the vessel began the journey to Site U1309. The duration of the port call was 4.8 days.

Transit to Site U1309

The transit to Site U1309 covered 1002 nmi at an average speed of 10.7 kt. Weather-related course deviations resulted in a somewhat longer transit than the one during Expedition 304. During the transit, the ship's clocks were retarded 2 h to –3 h UTC. On approach to Site U1309, we conducted a 17.8 nmi towed magnetometer survey near the site. The survey line began at 30°4.7′N, 41°47.0′W, and extended west-northwest to 30°07.9′N, 42°07.1′W.

Initial deepening of Hole U1309D

The vessel was positioning over Hole U1309D at 1600 h on 16 January 2005 using the GPS and the beacon that was deployed during Expedition 304. The drill crew made up a 10-collar RCB BHA affixed with a new C-7 rotary bit. At 0027 h on 17 January, we reentered Hole U1309D and deployed the WSTP to the bottom of the hole. To minimize contamination or disturbance of the borehole water column, the drill string was lowered to ~10 m off the bottom of the hole with minimum rotation and no circulation. After the WSTP was retrieved, a fresh core barrel was dropped and ~3 m of fill was cleaned from the bottom of the hole. The recovered core barrel was curated as Core 305-U1309D-79G (numbering continuing serially from Expedition 304), as no new penetration was achieved.

Between 17 January and 30 January, we cored from 401.3 to 837.4 mbsf (Table **T26**) using four C-7 rotary core bits. The average rate of penetration steadily decreased downhole, from 2.6 to 1.6 m/h, averaging 2.2 m/h for the 14 day coring operation, with recovery averaging >80%. Based on a conservative estimate of bit life, we elected to change bits after nominally 50 h of rotation. At the end of each bit run, the bits returned worn but essentially undamaged. Mud sweeps (20 bbl) were circulated every 10 m of advance to clean the hole. Fluorescent microspheres and PFTs were deployed episodically during cored intervals at depths where microbiology samples were requested. However, PFT use was discontinued after Core 305-U1309D-90R at the request of the shipboard microbiologist, owing to insufficient time to rapidly process samples. At the end of the fourth bit run (837.4 mbsf), the hole was conditioned for logging, including displacing the borehole fluid with freshwater to improve the logging signal.

Logging Run 1, Hole U1309D

In preparation for logging, the bottom of the pipe was set at 170 mbsf. This allowed overlap with previous logging runs performed during Expedition 304 and positioned the pipe below an interval where minor obstructions were encountered in the borehole during reentry. The first logging run with the triple-combo tool string covered the full length of open hole. Logging with the FMS-sonic tool string also covered the interval from the bottom of the hole to 170 mbsf. Following the completion of the FMS-sonic log, we completed a test of the WHC to evaluate the performance of the new drum-compensator and compare it with the performance of the older LDEO wireline compensator. The third logging run was a VSP utilizing the WST-3 and the generator-injector air gun. In accordance with IODP policy, prior to the VSP, a 1 h visual survey of the water within a 700 m radius of the vessel was undertaken to ensure that no marine mammals were present prior to the start of the VSP experiment. Also consonant with the policy, the generator-injector gun was soft-started (gradually increased intensity for the first 30 min of operation) at the initiation of testing. The marine mammal watch was maintained until the VSP was secured, and no marine mammals were sighted during the experiment. A single joint of pipe was removed from the string, placing the bit at 161 mbsf before deploying the tool. The fourth logging run utilized the UBI. The UBI was deployed with a sinker bar to enhance deployment speed. Owing to an inconsistent borehole geometry in some intervals of the hole and poor tool performance in the high-speed, low-resolution mode, only intervals from 824 to 724 mbsf and 704 to 503 mbsf were imaged with the UBI. A final logging pass was made with the GBM. The internal gyrocompass of the tool was oriented with the vessel heading prior to lowering into the pipe. The GBM recorded data in both directions as it traversed from 170 to 837 mbsf and back. The drill string was raised 10 m as the GBM approached the pipe. The internal gyrocompass was oriented a second time when the tool was recovered. Logging operations were completed at 1040 h on 2 February 2005.

Deepening Hole U1309D

Between 2 and 23 February 2005, we cored from 837.4 to 1415.5 mbsf (Table **T26**), using one C-7 and five C-9 bits. The C-9 bits are designed for harder formation coring. We elected to use C-9 bits in order to preserve the last two C-7 bits in inventory in the event we encountered softer rock at depth. Average rate of penetration continued at 1.6–2.4 m/h, with recovery averaging 78%. We experienced no significant difference in bit performance between the styles of coring bits employed. Our routine procedure included 20 bbl mud sweeps after every other cored interval to clean the hole. Coring in Hole U1309D concluded with the last core on deck at 1015 h on 23 February.

Over the entire coring program, there were only a couple of irregularities of note in routine operations. Shortly after initiation of the second coring interval (at ~929 mbsf), the pump pressure decreased from 1000 to 900 psi, indicating that the core barrel may have become unseated. After the core barrel was recovered, a bit deplugger was deployed and normal pressure was restored. In addition, at 1373 mbsf, 0.5 m penetration required 1.5 h, and the core barrel was recovered empty. Because we suspected the bit might be jammed, we ran a bit deplugger. The ensu-

ing coring interval still proceeded quite slowly (2 h for 1.5 m of penetration), so the core barrel was again recovered early, this time returning fine-grained diabase. The hard formation was eclipsed during the subsequent coring interval, and our rate of penetration increased to routine values.

During our midcruise logging run, a temperature of ~60°C was measured by one of the magnetometer tool's sensors. After communication with the manufacturer to confirm the configuration of the temperature measurement system (to ensure the thermistor was not simply registering the internal temperature of the tool, which is heated to maintain instrument stability), we elected to attempt to verify the borehole temperature in preparation for our next logging run. In our first attempt, an assortment of calibrated, heat-sensitive, adhesive strips were affixed to a modified APC brass core catcher spacer deployed in a dedicated core barrel run. The core barrel was deployed at 1162 mbsf (a few meters above the bottom of the hole at the time) and allowed to equilibrate for 17 min without circulation. Upon recovery, the temperature strips indicated a minimum temperature of ~70°C. During the ensuing bit trip, we decided to deploy the WSTP to collect a water sample and temperature measurement. Before deploying the sampler, our technicians determined the thermistor on the WSTP was broken and no exact replacement was available. The shipboard electrical technician fabricated an ad hoc arrangement of the APC temperature (APCT) tool on the WSTP and found an uncalibrated thermistor to install on the WSTP. In addition to these two temperature measuring devices, an assortment of the adhesive temperature recording strips were also affixed to the WSTP. Owing to a failed O-ring, the APCT failed to record a temperature. The thermistor on the WSTP recorded a maximum temperature of ~60°C. A subsequent bench test determined 60°C was the maximum recording temperature for the new WSTP thermistor/datalogger assembly. The adhesive temperature strips indicated a minimum temperature of 110°C.

Logging Run 2, Hole U1309D

After hole conditioning on 23 February 2005 (once coring operations were completed), the borehole was filled with drill water to improve the logging signal. A logging BHA was deployed, and the bit was set at 194 mbsf. Two passes were completed with the triple combo tool string, the first from the bottom of the hole to the logging bit (1415–194 mbsf) and a repeat pass (as a calibration check) from 1284 to 1094 mbsf. The second logging run utilized the FMS-sonic tool string, but the telemetry link failed when the tool reached the bottom of the hole. The tool string was pulled to the rig floor, where the logging team determined the sonic tool had broken. The sonic tool was removed from the logging string, and the FMS was redeployed. Two logging passes were completed with the FMS. The first pass covered the interval from the bottom of the hole to 754 mbsf (to overlap with our midcruise logging run), and the second covered the interval from the bottom of the hole to 629 mbsf. At this point, the FMS tool string was recovered to allow time for a daylight VSP experiment.

A marine mammal watch was instituted at daybreak on 24 February, and after an hour with no marine mammal sightings, the generator-injector gun was hung from the port aft crane and a gradual power increase firing process was initiated. The WST-3 was deployed to the bottom of Hole U1309D, but voltage at the tool head was intermittent. The tool was raised to ~1200 mbsf, but only brief continuous communication could be established. A final attempt to communicate with the WST was attempted at ~700 mbsf, but when this attempt failed the tool was recovered. The single-component WST was deployed, but shortly after the tool was into the open borehole, sea state (heave in excess of 5 m) had deteriorated to the point where the logging heave compensator could not operate within safety limits. Only a single station was occupied with shots recorded before logging operations were terminated. The drill string was recovered and we began preparations for our transit back to Ponta Delgada. Operations in Hole U1309D concluded on 26 February.

Transit to Ponta Delgada

Prior to departure from Site U1309, a towed magnetometer survey was conducted. A survey line was laid out from 30°09.0′N, 42°14.2′W to 30°07.8′N, 42°06.3′W to complete the flowline path begun during arrival at Site U1309 at the start of Expedition 305. Initial problems with the port winch and with the logging software delayed acquisition of useful data until ~2.5 nmi along the line. Acquisition with the starboard magnetometer was successful and continued beyond the endpoint of the first line, along a track toward Ponta Delgada, until 1200 h on February 26. The 950 nmi transit required 104 h at an average speed of 9.1 nmi/h. Expedition 305 concluded with the first line ashore at Ponta Delgada on 1805 h on 2 March 2005.

Shallow-penetration cores

Among our scientific objectives at the central dome of Atlantis Massif was capturing the sediment cover draping the top of the dome and recovering rock from the uppermost part of the basement directly below this cover. We reasoned that the denudation history of the footwall via detachment faulting might

be constrained by paleoceanographic indicators within sedimentary deposits, if they could provide limits on age of exposure of this surface at the seafloor. In addition, the lithified carbonate cap previously observed and sampled in submersible dives was known to contain microfossils. If the exposure of the western domal surface occurred significantly earlier than exposure at the eastern edge (the termination at the hanging wall block), sampling along a spreading-parallel transect across the top of the dome might document the denudation history of the dome. In addition, the uppermost basement could preserve the fault rock formed while the domal surface was exposed during unroofing along the detachment.

Although rotary coring was an effective approach to recovering basement at Atlantis Massif, in order to keep the rotary bit in the hole while recovering the first cored interval, it is commonly necessary to core to >10 mbsf with the first core barrel. As a result of pipe flexure and slow penetration rates in this initial coring interval, recovery in hard rock is generally poor (commonly <20%). In addition, circulation of drilling fluid, used to keep the bit clear of impacted sediment, tends to flush away thin surface sediments during RCB coring.

During operations at Site U1309, we tested several methods to improve recovery from the sediment cover and uppermost basement. These included pushing the RCB BHA into the sediment without rotation or circulation (Hole U1309A), routine RCB coring with rotation and circulation to sufficient depth to ensure the pipe did not pull out of the hole after the first cored interval (Hole U1309B), shallow penetration (1–2 m after contact with hard formation) with rotation but no circulation (Holes U1309E and U1309F), shallow XCB coring with rotation and no circulation (Hole U1309G), and APC piston coring (same location as Holes U1309G and U1309H). The core barrel separated during the APC coring attempt, and no core was recovered. The other coring attempts recovered intervals of drilling disturbed, unlithified, unconsolidated sediment and small fragments of basement from beneath the sediment cover. Brief descriptions of these cores are summarized below.

Core 304-U1309A-1R

Core 304-U1309A-1R (0.0–2.0 mbsf) was a push core without rotation or circulation; 1.77 m of drilling-disturbed calcareous microfossil ooze was recovered. The upper 25 cm of Section 304-U1309A-1R-1 is normally graded drilling slurry, with subcentimeter chips of basalt and serpentinite with mineral grains near the base of the interval. From 25 cm to the base, Section 304-U1309A-1R-2 consists of tacky, light tan calcareous ooze with abundant microfossils. Section 304-U1309A-1R-CC is completely disturbed, but also contains subcentimeter chips of basalt and serpentinite.

Core 304-U1309B-1R

The first core from Hole U1309B was cut with rotation and circulation to 15.5 mbsf. A total of 2 m of drilling-disturbed calcareous microfossil ooze was recovered above several cobbles of basalt (see **"Igneous petrology"**). The upper 120 cm of sediment is normally graded drilling slurry, with millimeter-sized chips of basalt, serpentinite, and, possibly, carbonate. From 120 to 135 cm is light tan, soupy sediment. To 10 cm in Section 304-U1309B-1R-3 is light tan ooze with abundant microfossils.

Core 304-U1309E-1R

Core 304-U1309E-1R was cored 10 m east of Hole U1309D to 1 mbsf with rotation but no circulation. A total of 5.6 m of soupy to tacky, severely drilling-disturbed, light tan calcareous microfossil ooze was recovered. Two intervals in Section 304-U1309E-1R-1 (0–8 and 20–28 cm) are stiff, silty clayey fine sand. Section 304-U1309E-1R-2 is soupy mud, with a thin interval at 8–13 cm of stiff, silty sand. At 93 cm are thin laminae of green, sandy silt. At 6–20 cm in Section 304-U1309E-1R-3 is a smear of green silty, clayey sand with rare subcentimeter fragments of greenschist-facies-altered basalt. Overall, Section 304-U1309E-1R-3 is soupy and has a slightly greener cast than sections above with disseminated black sand. The interval from 0 to 6 cm in Section 304-U1309E-1R-4 is similar to the green silty sand in Section 1R-3. The rest of the section is similar to the soupy to tacky, severely disturbed mud from Section 304-U1309E-1R-3. The upper part of the core catcher contained stiff clayey silt with abundant foraminifers and fine sand-sized black particles. The bottom of the section contains a 7 cm rounded fragment of highly altered metabasalt with tremolite and chlorite. Ghosts of stretched fragments are discernible in hand specimen. One edge of the basalt is in contact with foliated tremolite schist with rare chlorite.

Core 304-U1309F-1R

Core 304-U1309F-1R was cored with rotation but no circulation to 5.6 mbsf (1 m into hard formation); 6.09 m of light tan, soupy, severely disturbed calcareous ooze was recovered. At 45 cm in Section 304-U1309F-1R-2 is a small interval of semi-indurated sandy clay.

Two thin intervals (58–62 and 67–72 cm) in Section 304-U1309F-1R-4 are coarser grained, semi-indurated sandy mud that crushes easily with light pressure. At 60 cm in Section 304-U1309F-1R-4 are several centimeter-sized fragments of Mn-encrusted rock. On one side of the largest piece are radiating fans of minerals that may have been amphibole. Below 4 cm in Section 304-U1309F-1R-6 is a distinct color change to darker tan, and the sediment has a denser texture (which may have been imparted by packing mud in the core liner with a plunger). A centimeter-sized fragment of brown-green, pervasively altered basalt is in the top of this section. The lower part of the core catcher contains abundant fragments of Mn-encrusted rock and several pieces of pervasively altered, brown-green basalt. Some possible amygdules are present, and a few blades of amphibole are preserved along a fracture.

Core 304-U1309G-1X

Hole U1309G is located within a few meters of a submersible-deployed marker where lithified carbonate was observed to drape basement. Core 304-U1309G-1X was cut with the XCB and cored to 3.5 mbsf without circulation. The recovered core is dark tan silty clay with abundant microfossils, dark sand-sized rock fragments, and mineral grains. Rare disturbed streaks of gray-green clay and rare millimeter-sized green metabasalt fragments are also present. At 38–40 cm in Section 304-U1309G-1X-1 is a 3 cm clast of indurated ooze and red-brown hyaloclastite. Two 2–3 cm thick intervals of carbonate-free hyaloclastite bracket a 4 cm thick interval of light tan calcareous ooze with abundant subcentimeter sized fragments of gray-green metabasalt. A thin (<0.5 cm) layer of calcareous ooze with sharp, subhorizontal contacts separates the lower hyaloclastite layer from a 3 cm thick layer of densely packed gray-green silty clay. Below the clay interval is a clayey silt matrix-supported conglomerate of rounded, mostly metabasalt fragments. This material was packed into the XCB shoe and appears to be drilling-reworked sedimentary deposit.

Core 304-U1309H-1R

Hole U1309H was cored at the same location as Hole U1309G, based on GPS coordinates. A single RCB core was recovered (Core 304-U1309H-1R; 0.0–4.0 mbsf).

The upper few centimeters of this core includes several 1–3 cm sized rounded pieces of hyaloclastite and Mn-encrusted, semilithified microfossil-bearing ooze. The pieces contain submillimeter-sized basalt fragments and fresh and palagonitized basaltic glass. Beneath these fragments in the core catcher is a rounded piece of talc-tremolite schist.

This schist has a strong foliation with apparent folds, suggesting that it formed during ductile or semibrittle deformation. The schist is overprinted by a brecciation event, resulting in minor disruption of the foliation. The lowermost part of the core recovered from Hole U1309H is a highly altered brecciated basalt or diabase. The brecciation is localized, separating regions that are relatively undeformed. This texture suggests that the rock did not experience significant shear displacement, although it may represent part of the brittle process zone adjacent to a fault.

References

Agar, S.M., Casey, J.F., and Kempton, P.D., 1997. Textural, geochemical, and isotopic variations in gabbroic shear zones from the MARK area. *In* Karson, J.A., Cannat, M., Miller, D.J., and Elthon, D. (Eds.), *Proc. ODP, Sci. Results,* 153: College Station, TX (Ocean Drilling Program), 99–121.

Allen, D.A., Berndt, M.E., Seyfried, W.E., Jr., and Horita, J., 1998. Inorganic reduction of CO_2 to HCOOH, CH_4, and other reduced carbon compounds with application to subseafloor hydrothermal systems. *Eos, Trans. Am. Geophys. Union,* 79:58–59.

Beard, J.S., Ragland, P.C., and Rushmer, T., 2004. Hydration crystallization reactions between anhydrous minerals and hydrous melt to yield amphibole and biotite in igneous rocks: description and implications. *J. Geol.,* 112:617–621. **doi:10.1086/422670**

Berman, R.G., 1991. Thermometry using multiequilibria calculations: a new technique with petrologic applications. *Can. Mineral.,* 29:833–855.

Berman, R.G., 1988. Internally-consistent thermodynamic data for minerals in the system Na_2O-K_2O-CaO-MgO-FeO-Fe_2O_3-Al_2O_3-SiO_2-TiO_2-H_2O-CO_2. *J. Petrol.,* 292:445–522.

Berndt, M.E., Allen, D.E., and Seyfried, W.E., Jr., 1996. Reduction of CO_2 during serpentinization of olivine at 300°C and 500 bar. *Geology,* 24:351–354. **doi:10.1130/0091-7613(1996)024<0351:ROCDSO>2.3.CO;2**

Berthé, D., Choukrome, P., and Jegouzo, P., 1979. Orthogneiss, mylonite and non-coaxial deformation and granites: the examples of South American shear zone. *J. Struct. Geol.,* 1:31–42.

Bideau, D., Hebert, R., Hekinian, R., and Cannat, M., 1991. Metamorphism of deep-seated rocks from the Garrett ultrafast transform (East Pacific Rise near 13°25′S). *J. Geophys. Res.,* 96:10079–10099.

Blackman, D.K., Cann, J.R., Janssen, B., and Smith, D.K., 1998. Origin of extensional core complexes: evidence from the MAR at Atlantis Fracture Zone. *J. Geophys. Res.,* 103:21315–21334. **doi:10.1029/98JB01756**

Blackman, D.K., Karson, J.A., Kelley, D.S., Cann, J.R., Früh-Green, G.L., Gee, J.S., Hurst, S.D., John, B.E. Morgan, J., Nooner, S.L., Ross, D.K., Schroeder, T.J., and Williams, E.A., 2004. Geology of the Atlantis Massif (Mid-Atlantic Ridge, 30′N): implications for the evolution of an ultramafic oceanic core complex. *Mar. Geophys. Res.,* 23(5–6):443–469. **doi:10.1023/B:MARI.0000018232.14085.75**

Blum, P., 1997. Physical properties handbook: a guide to the shipboard measurement of physical properties of deep-sea cores. *ODP Tech. Note,* 26 [Online]. Available from World Wide Web: **http://www-odp.tamu.edu/publications/tnotes/tn26/INDEX.HTM**.

Bodinier, J.-L., 1988. Geochemistry and petrogenesis of the Lanzo peridotite body, Western Alps. *Tectonophysics,* 149:67–88. **doi:10.1016/0040-1951(88)90119-9**

Bosch, D., Jamais, M., Boudier, F., Nicolas, A., Dautria, J.M., and Agrinier, P., 2004. Deep and high-temperature hydrothermal circulation in the Oman ophiolite—petrological and isotopic evidence. *J. Petrol.,* 45(6):1181–1208. **doi:10.1093/petrology/egh010**

Boudier, F., and Nicolas, A., 1995. Nature of the Moho Transition Zone in the Oman ophiolite. *J. Petrol.,* 36:777–796.

Boudier, F., Nicolas, A., and Ildefonse, B., 1996. Magma chambers in the Oman ophiolite: fed from the top and the bottom. *Earth Planet. Sci. Lett.,* 144:239–250. **doi:10.1016/0012-821X(96)00167-7**

Canales, J.P., Tucholke, B.E., and Collins, J.A., 2004. Seismic reflection imaging of an oceanic detachment fault: Atlantis megamullion (Mid-Atlantic Ridge, 30°10′N). *Earth Planet. Sci. Lett.,* 222(2):543–560. **doi:10.1016/j.epsl.2004.02.023**

Cann, J.R., Blackman, D.K., Smith, D.K., McAllister, E., Janssen, B., Mello, S., Avgerinos, E., Pascoe, A.R., and Escartin, J., 1997. Corrugated slip surfaces formed at ridge-transform intersections on the Mid-Atlantic Ridge. *Nature (London, U. K.),* 385:329–332. **doi:10.1038/385329a0**

Cannat, M., Bideau, D., and Bougault, H., 1992. Serpentinized peridotites and gabbros in the Mid-Atlantic Ridge axial valley at 15°37′N and 16°52′N. *Earth Planet. Sci. Lett.,* 109:87–106. **doi:10.1016/0012-821X(92)90076-8**

Cannat, M., Karson, J.A., Miller, D.J., et al., 1995. *Proc. ODP, Init. Repts.,* 153: College Station, TX (Ocean Drilling Program).

Cannat, M., Lagabrielle, Y., Bougault, H., Casey, J., de Coutures, N., Dmitriev, L., and Fouquet, Y., 1997. Ultramafic and gabbroic exposures at the Mid-Atlantic Ridge: geological mapping in the 15°N region. *Tectonophysics,* 279:193–213. **doi:10.1016/S0040-1951(97)00113-3**

Casey, J.F., 1997. Comparison of major- and trace-element geochemistry of abyssal peridotites and mafic plutonic rocks with basalts from the MARK region of the Mid-Atlantic Ridge. *In* Karson, J.A., Cannat, M., Miller, D.J., and Elthon, D. (Eds.), *Proc. ODP, Sci. Results,* 153: College Station, TX (Ocean Drilling Program), 181–241.

Collins, J., Canales, J.-P., and Tucholke, B., 2003. Seismic velocity structure of mid-Atlantic core complexes. *Geophys. Res. Abstr.,* 5:10390. (Abstract)

Collins, J.A., and Detrick, R.S., 1998. Seismic structure of the Atlantis Fracture Zone megamiullion, a serpentinized ultramafic massif. *Eos, Trans. Am. Geophys. Union,* 79(45):800. (Abstract)

Collins, J.A., Tucholke, B.E., and Canales, J.-P., 2001. Structure of Mid-Atlantic Ridge megamullions from seismic refraction experiments and multichannel seismic reflection profiling. *Eos, Trans. Am. Geophys. Union,* 82:F1100. (Abstract)

Deer, W.A., Howie, R.A., and Zussman, J., 1992. *An Introduction to the Rock-Forming Minerals* (2nd ed.): Harlow, United Kingdom (Longman Scientific Technical).

Dick, H.J.B., and Bullen, T., 1984. Chromian spinel as a petrogenetic indicator in abyssal and alpine-type peridotites and spatially associated lavas. *Contrib. Mineral. Petrol.,* 86:54–76. **doi:10.1007/BF00373711**

Dick, H.J.B., Natland, J.H., Alt, J.C., Bach, W., Bideau, D., Gee, J.S., Haggas, S., Hertogen, J.G.H., Hirth, G., Holm, P.M., Ildefonse, B., Iturrino, G.J., John, B.E., Kelley, D.S., Kikawa, E., Kingdon, A., LeRoux, P.J., Maeda, J., Meyer, P.S., Miller, D.J., Naslund, H.R., Niu, Y.-L., Robinson, P.T., Snow, J., Stephen, R.A., Trimby, P.W., Worm, H.-U., and Yoshinobu, A., 2000. A long in situ section of the lower ocean crust: results of ODP Leg 176 drilling at the Southwest Indian Ridge. *Earth Planet. Sci. Lett.,* 179:31–51. **doi:10.1016/S0012-821X(00)00102-3**

Dick, H.J.B., Natland, J.H., Miller, D.J., et al., 1999. *Proc. ODP, Init. Repts.,* 176 [CD-ROM]. Available from: Ocean Drilling Program, Texas A&M University, College Station, TX 77845-9547, U.S.A. [**HTML**]

Dilek, Y., Coulton, A., and Hurst, S.D., 1997. Serpentinization and hydrothermal veining in peridotites at Site 920 in the MARK area. *In* Karson, J.A., Cannat, M., Miller, D.J., and Elthon, D. (Eds.), *Proc. ODP, Sci. Results,* 153: College Station, TX (Ocean Drilling Program), 35–59.

Escartín, J., Mével, C., MacLeod, C.J., and McCaig, A.M., 2003. Constraints on deformation conditions and the origin of oceanic detachments, the Mid-Atlantic Ridge core complex at 15°45′N. *Geochem., Geophys., Geosyst.,* 4(8):1067. **doi:10.1029/2002GC000472**

Fornari, D.J., and Embley, R.W., 1995. Tectonic and volcanic controls on hydrothermal processes at the mid-ocean ridge: an overview based on near-bottom and submersible studies. *In* Humphris, S.E., Zierenberg, R.A., Mullineaux, L.S., and Thomson, R.E. (Eds.), *Seafloor Hydrothermal Systems, Physical, Chemical, Biological, and Geological Interactions*. Geophys. Monogr., 91:1–26.

Francheteau, J., Armijo, R., Cheminée, J.L., Hekinian, R., Lonsdale, P.F., and Blum, N., 1990. 1 Ma East Pacific Rise oceanic crust and uppermost mantle exposed by rifting in Hess Deep (equatorial Pacific Ocean). *Earth Planet. Sci. Lett.,* 101:281–295. **doi:10.1016/0012-821X(90)90160-Y**

Frost, B.R., 1976. Limits to the assemblage forsterite-anorthite as inferred from peridotite hornfelses, Icicle Creek, Washington. *Am. Mineral.,* 61:732–750.

Frost, B.R., 1985. On the stability of sulfides, oxides, and native metals in serpentine. *J. Petrol.,* 26:31–63.

Früh-Green, G.L., Kelley, D.S., Bernasconie, S.M., Karson, J.A., Ludwig, K.A., Butterfield, D.A., Boschi, C., and

Proskurowksi, G., 2003. 30,000 years of hydrothermal activity at the Lost City vent field. *Science,* 301:495–498. **doi:10.1126/science.1085582**

Gee, J., and Blackman, D., 2004. Lineated near bottom magnetic anomalies over an oceanic core complex, Atlantis Massif (Mid-Atlantic Ridge at 30°N). *Eos, Trans. Am. Geophys. Union,* 85(17), Joint Assembly Suppl.:GP314-N15. (Abstract)

Gee, J., Staudigel, H., and Tauxe, L., 1989. Contribution of induced magnetization to magnetization of seamounts. *Nature (London, U. K.),* 342:170–173. **doi:10.1038/342170a0**

Gee, J.S., Lawrence, R.M., and Hurst, S.D., 1997. Remanence characteristics of gabbros from the MARK area: implications for crustal magnetization. *In* Karson, J.A., Cannat, M., Miller, D.J., and Elthon, D. (Eds.), *Proc. ODP, Sci. Results,* 153: College Station, TX (Ocean Drilling Program), 429–436.

Gerbert-Gaillard, L., 2002. Caractisation gés chimique des peridotites de l'ophiolite d'Oman: processus magmatiques aux limites lithosphere/asthenosphere [Thèse Doctorat d'Etat]. Univ. Montpellier 2.

Ghiorso, M.S., and Sack, R.O., 1995. Chemical mass transfer in magmatic processes, IV. A revised and internally consistent thermodynamic model for the interpolation and extrapolation of liquid-solid equilibria in magmatic systems at elevated temperatures and pressures. *Contrib. Mineral. Petrol.,* 119(2–3):197–212.

Girardeau, J., and Mercier, J.-C.C., 1992. Evidence for plagioclase-lherzolite intrusion in the Mid-Atlantic Ridge, DSDP Leg 37. *In* Parson, L.M., Murton, B.J., and Browning, P. (Eds.), *Ophiolites and their Modern Oceanic Analogues*. Spec. Publ.—Geol. Soc. London, 60:241–250.

Godard, M., Jousselin, D., and Bodinier, J.-L., 2000. Relationships between geochemistry and structure beneath a paleo-spreading centre: a study of the mantle section in the Oman ophiolite. *Earth Planet. Sci. Lett.,* 180:133–148. **doi:10.1016/S0012-821X(00)00149-7**

Green, D.H., and Ringwood, A.E., 1967. The genesis of basaltic magmas. *Contrib. Mineral. Petrol.,* 15:103–190. **doi:10.1007/BF00372052**

Grove, T.L., and Bryan, W.B., 1983. Fractionation of pyroxene-phyric MORB at low pressure: an experimental study. *Contrib. Mineral. Petrol.,* 84:293–309. **doi:10.1007/BF01160283**

Hart, S.R., and Zindler, A., 1986. In search of a bulk Earth composition. *Chem. Geol.,* 57(4):247–267. **doi:10.1016/0009-2541(86)90053-7**

Hébert, R., Adamson, A.C., and Komor, S.C., 1990. Metamorphic petrology of ODP Leg 109, Hole 670A serpentinized peridotites: serpentinization processes at a slow spreading ridge environment. *In* Detrick, R., Honnorez, J., Bryan, W.B., Juteau, T., et al., *Proc. ODP, Sci. Results,* 106/109: College Station, TX (Ocean Drilling Program), 103 15.

Hellebrand, E., Snow, J.E., Dick, H.J.B., and Hofmann, A.W., 2001. Coupled major and trace elements as indicators of the extent of melting in mid-ocean-ridge peridotites. *Nature (London, U. K.),* 410:677–681. **doi:10.1038/35070546**

Hopson, C.A., Coleman, R.G., Gregory, R.T., Pallister, J.S., and Bailey, E.H., 1981. Geologic section through the Semail ophiolite and associated rocks along a Muscat-Ibra transect, southeastern Oman Mountains. *J. Geophys. Res.,* 86(4):2527–2544.

Irvine, T.N., and Baragar, W.R.A., 1971. A guide to the chemical classification of the common volcanic rocks. *Can. J. Earth Sci.,* 8:523–548.

Jagoutz, E., Palme, H., Baddenhausen, H., Blum, K., Cendales, M., Dreibus, G., Spettel, B., Lorenz, V., and Waenke, H., 1979. The abundances of major, minor and trace elements in the Earth's mantle as derived from primitive ultramafic nodules. *Proc. 10th Lunar Planet. Sci. Conf.,* 2031–2050.

Janecky, D.R., and Seyfried, W.E., Jr., 1986. Hydrothermal serpentinization of peridotite within the oceanic crust: experimental investigations of mineralogy and major element chemistry. *Geochim. Cosmochim. Acta,* 50:1357–1378. **doi:10.1016/0016-7037(86)90311-X**

Jelinek, V., 1981. Characterization of the magnetic fabric of rocks. *Tectonophysics,* 79:63–67. **doi:10.1016/0040-1951(81)90110-4**

John, B.E., 1987. Geometry and evolution of a mid-crustal extensional fault system: Chemehuevi Mountains, southeastern California. *In* Coward, M.P., Dewey, J.F., and Hancock, P.L. (Eds.), *Continental Extensional Tectonics,* Spec. Publ.—Geol. Soc. Am., 28:313–335.

Jousselin, D., and Nicolas, A., 2000. The Moho transition zone in the Oman ophiolite-relation with wehrlites in the crust and dunites in the mantle. *Mar. Geophys. Res.,* 21:229–241. **doi:10.1023/A:1026733019682**

Juster, T.C., Grove, T.L., and Perfit, M.R., 1989. Experimental constraints on the generation of FeTi basalts, andesites, and rhyodacites at the Galapagos Spreading Center, 85°W and 95°W. *J. Geophys. Res.,* 94:9251–9274.

Karson, J.A., 1991. Accommodation zones and transfer faults: integral components of Mid-Atlantic Ridge extensional systems. *In* Peters, T.J., Nicolas, A., and Coleman, R.G. (Eds.), *Ophiolites Genesis and Evolution of Oceanic Lithosphere:* Dordrecht (Kluwer Academic), 21–37.

Karson, J.A., 2003. Unconformities in slow-spread oceanic crust: implications for spreading processes and dismembered ophiolites, *Eos, Trans. Am. Geophys. Union,* 84:F1506. (Abstract)

Kelemen, P.B., Kikawa, E., Miller, D.J., et al., 2004. *Proc. ODP, Init. Repts.,* 209 [CD-ROM]. Available from: Ocean Drilling Program, Texas A&M University, College Station TX 77845-9547, USA. [**HTML**]

Kelley, D.S., Karson, J.A., Blackman, D.K., Früh-Green, G.L., Butterfield, D.A., Lilley, M.D., Olson, E.J., Schrenk, M.O., Roe, K.K., Lebon, G.T., and Rivizzigno, P., 2001. An off-axis hydrothermal vent field near the Mid-Atlantic Ridge at 30°N. *Nature (London, U. K.),* 412(6843):145–149. **doi:10.1038/35084000**

Kikawa, E., and Pariso, J.E., 1991. Magnetic properties of gabbros from Hole 735B, Southwest Indian Ridge. *In* Von Herzen, R.P., Robinson, P.T., et al., *Proc. ODP, Sci. Results,* 118: College Station, TX (Ocean Drilling Program), 285–307.

Kimball, K.L., and Evans, C.A., 1988. Hydrothermal alteration of peridotite from the Galicia margin, Iberian Peninsula. *In* Boillot, G., Winterer, E.L., et al., *Proc. ODP, Sci. Results,* 103: College Station, TX (Ocean Drilling Program), 241–251.

Kirby, S.H., 1983. Rheology of the lithosphere. *Rev. Geophys.,* 21:1458–1487.

Kirschvink, J.L., 1980. The least-squares line and plane and the analysis of palaeomagnetic data. *Geophys. J. R. Astron. Soc.,* 62(3):699–718.

Knight, M.D., and Walker, G.P.L., 1988. Magma flow directions in dikes of the Koolau complex, Oahu, determined from magnetic fabric studies. *J. Geophys. Res.,* 93:4301–4319.

Koga, K.T., Kelemen, P.B., and Shimizu, N., 2001. Petrogenesis of the crust–mantle transition zone and the origin of lower crustal wehrlite in the Oman ophiolite. *Geochem., Geophys., Geosyst.,* 2(9). **doi:10.1029/2000GC000132**

Kushiro, I., and Yoder, H.S., Jr., 1966. Anorthite-forsterite and anorthite-enstatite reactions and their bearing on the basalt-eclogite transformation. *J. Petrol.,* 7:337–362.

Le Maitre, R.W., Bateman, P., Dudek, A., Keller, J., Lameyre Le Bas, M.J., Sabine, P.A., Schmid, R., Sorensen, H., Streckeisen, A., Woolley, A.R., and Zanettin, B., 1989. *Classification of Igneous Rocks and Glossary of Terms:* Oxford (Blackwell).

Levitus, S., and Boyer, T.P., 1994. *World Ocean Atlas 1994* (Vol. 4): *Temperature*. NOAA Atlas NESDIS 4.

MacLeod, C.J., Dick, H.J.B., Allerton, S., Robinson, P.T., and JR31 Scientific Party, 1999. Structure of Atlantis Bank, SW Indian Ridge: an eroded megamullion surface? *Geophys. Res. Abst.,* 1:186.

MacLeod, C.J., Escartin, J., Banerji, D., Banks, G.J., Gleeson, M., Irving, D.H.B., Lilly, R.M., McCaig, A.M., Niu, Y., Allerton, S., and Smith, D.K., 2002. Direct geological evidence for oceanic detachment faulting: the Mid-Atlantic Ridge, 15°45′N. *Geology,* 30(10):879–882. **doi:10.1130/0091-7613(2002)030<0879:DGEFOD>2.0.CO;2**

Maeda, J., Naslund, H.R., Jang, Y.D., Kikawa, E., Tajima, T., and Blackburn, W.H., 2002. High-temperature fluid migration within oceanic Layer 3 gabbros, Hole 735B, Southwest Indian Ridge: implications for the magmatic-hydrothermal transition at slow-spreading mid-ocean ridges. *In* Natland, J.H., Dick, H.J.B., Miller, D.J., and Von Herzen, R.P. (Eds.), *Proc. ODP, Sci. Results,* 176 [Online]. Available from World Wide Web: **http://www-odp.tamu.edu/publications/176_SR/chap_04/chap_04.htm**.

McFadden, P.L., and Reid, A.B., 1982. Analysis of paleomagnetic inclination data. *Geophys. J. R. Astron. Soc.,* 69:307–319.

Miller, M.G., 1996. Ductility in fault gouge from a normal fault system, Death Valley, California: a mechanism for strengthening and relevance to paleoseismicity. *Geology,* 24:603–606. **doi:10.1130/0091-7613(1996)024<0603:DIFGFA>2.3.CO;2**

Mills, R.A., Teagle, D.A.H., and Tivey, M.K., 1998. Fluid mixing and anhydrite precipitation within the TAG mound. *In* Herzig, P.M., Humphris, S.E., Miller, D.J., and Zierenberg, R.A. (Eds.), *Proc. ODP, Sci. Results,* 158, 119–127 [CD-ROM]. Available from: Ocean Drilling Program, Texas A&M University, College Station, TX 77845-9547, U.S.A. [**PDF**]

Monnier, C., 1996. Mécanismes d'accrétion des domaines océaniques arrière-arc et géodynamique de l'Asie du sud-est: pétrologie et géochimie des ophiolites d'Indonesie [Thèse de doctorat]. Univ. Bretagne Occidentale, Brest.

Neal, C., and Stanger, G., 1983. Hydrogen generation from mantle source rocks in Oman. *Earth Planet. Sci. Lett.,* 66:315–320. **doi:10.1016/0012-821X(83)90144-9**

Nicolas, A., Boudier, F., Ildefonse, B., and Ball, E., 2000. Accretion of Oman and United Arab Emirates ophiolite—discussion of a new structural map. *Mar. Geophys. Res.,* 21(3–4):147–179. **doi:10.1023/A:1026769727917**

Niu, Y., and Hekinian, R., 1997. Basaltic liquids and harzburgitic residues in the Garrett Transform; a case study at fast-spreading ridges. *Earth Planet. Sci. Lett.,* 146(1–2):243–258. **doi:10.1016/S0012-821X(96)00218-X**

O'Hanley, D.S., 1996. Serpentinites: records of tectonic and petrological history. *Oxford Monogr. Geol. Geophys.,* Vol. 34.

Parker, R.L., and Gee, J.S., 2002. Calibration of the pass-through magnetometer—II. Application. *Geophys. J. Int.,* 150:140–152. **doi:10.1046/j.1365-246X.2002.01692.x**

Parkinson, I.J., and Pearce, J.A., 1998. Peridotites from the Izu-Bonin-Mariana forearc (ODP Leg 125): evidence for partial melting and melt-mantle interactions in a suprasubduction zone setting. *J. Petrol.,* 39(9):1577–1618.

Pettigrew, T.L., Casey, J.F., Miller, D.J., et al., 1999. *Proc. ODP, Init. Repts.,* 179 [CD-ROM]. Available from: Ocean Drilling Program, Texas A&M University, College Station, TX 77845-9547, U.S.A. [**HTML**]

Presnall, D.C., Dixon, S.A., Dixon, J.R., O'Donnell, T.H., Brenner, N.L., Schrock, R.L., and Dycus, D.W., 1978. Liquidus phase relations on the join diopside-forsterite-anorthite from 1 atm to 20 kbar: their bearing on the generation and crystallization of basaltic magma. *Contrib. Mineral. Petrol.,* 66:203–220. **doi:10.1007/BF00372159**

Rampone, E., Hofmann, A.W., Piccardo, G.B., Vannucci, R., Bottazzi, P., and Ottolini, L., 1996. Trace element and isotope geochemistry of depleted peridotites from an N-MORB type ophiolite (Internal Liguride, N. Italy). *Contrib. Mineral. Petrol.,* 123:61–76. **doi:10.1007/s004100050143**

Schrenk, M.O., Kelley, D.S., Bolton, S.A., and Baross, J.A., 2004. Low archaeal diversity linked to subseafloor geochemical processes at the Lost City hydrothermal field, Mid-Atlantic Ridge. *Environ. Microbiol.,* 6:1086–1095. **doi:10.1111/j.1462-2920.2004.00650.x**

Schroeder, T., and John, B.E., 2004. Strain localization on an oceanic detachment fault system, Atlantis Massif, 30°N, Mid-Atlantic Ridge. *Geochem., Geophys., Geosyst.,* 5:Q11007. **doi:10.1029/2004GC000728**

Serra, O., 1984. *Fundamentals of Well-Log Interpretation* (Vol. 1): *The Acquisition of Logging Data:* Dev. Pet. Sci., 15A: Amsterdam (Elsevier).

Shipboard Scientific Party, 1999. Site 735. *In* Dick, H.J.B., Natland, J.H., Miller, D.J., et al., *Proc. ODP, Init. Repts.,* 176 [Online]. Available from World Wide Web: **http://www-odp.tamu.edu/publications/176_IR/CHAP_03/Output/chap_03.htm**.

Shipboard Scientific Party, 2004. Site 1275. *In* Kelemen, P.B., Kikawa, E., Miller, D.J., et al., *Proc. ODP, Init. Repts.,* 209, 1–167 [CD-ROM]. Available from: Ocean Drilling Program, Texas A&M University, College Station TX 77845-9547, USA. [**HTML**]

Shock, E.L., and Schulte, M.D., 1998. Organic synthesis during fluid mixing in hydrothermal systems. *J. Geophys. Res.,* 103:28513–28527. **doi:10.1029/98JE02142**

Snow, J.E., and Dick, H.J.B., 1995. Pervasive magnesium loss by marine weathering of peridotite. *Geochim. Cosmochim. Acta,* 59(20):4219–4235. **doi:10.1016/0016-7037(95)00239-V**

Spear, F.S., 1981. An experimental study of hornblende stability and compositional variability in amphibolite. *Am. J. Sci.,* 281:697–734.

Staudigel, H., Plank, T., White, B., and Schminke, H.U., 1996. Geochemical fluxes during seafloor alteration of the basaltic upper oceanic crust: DSDP sites 417 and 418. *In* Bebout, G.E., Scholl, D.W., Kirby, S.H., and Platt, J.P. (Eds.), *Subduction Top to Bottom.* Geophys. Monogr., 96:19–38.

Tauxe, L., Gee, J.S., and Staudigel, H., 1998. Flow directions in dikes from anisotropy of magnetic susceptibility data: the bootstrap way. *J. Geophys. Res.,* 103:17,775–17790. **doi:10.1029/98JB01077**

Telford, W.M., Geldart, L.P., Sheritt, R.E., and Keys, D.A., 1976. *Applied Geophysics:* Cambridge (Cambridge Univ. Press).

Thauer, R.K., 1998. Biochemistry of methanogenesis: a tribute to Marjory Stephenson. *Microbiology,* 144:2377–2406.

Thompson, R., and Oldfield, F., 1986. *Environmental Magnetism:* London (Allen and Unwin).

Tormey, D.R., Grove, T.L., and Bryan, W.B., 1987. Experimental petrology of normal MORB near the Kane Fracture Zone: 22°–25°N, Mid–Atlantic Ridge. *Contrib. Mineral. Petrol.,* 96:121–139. **doi:10.1007/BF00375227**

Trommsdorff, V., and Evans, B.W., 1974. Alpine metamorphism of peridotitic rocks. *Schweiz. Mineral. Petrogr. Mitt.,* 54:33–352.

Tucholke, B.E., Lin, J., and Kleinrock, M.C., 1998. Megamullions and mullion structure defining oceanic metamorphic core complexes on the Mid-Atlantic Ridge. *J. Geophys. Res.,* 103(B5):9857–9866. **doi:10.1029/98JB00167**

Walker, D., Shibata, T., and Delong, S.E., 1979. Abyssal tholeiites from the Oceanographer Fracture Zone, II. Phase equilibria and mixing. *Contrib. Mineral. Petrol.,* 70:111–125.

Zervas, C.E., Sempere, J.-C., and Lin, J., 1995. Morphology and crustal structure of a small transform fault along the Mid-Atlantic Ridge: the Atlantis Fracture Zone. *Mar. Geophys. Res.,* 17:275–300. **doi:10.1007/BF01203466**

Publication: 3 June 2006
MS 304305-103

Appendix A

Water sampling at seafloor

On 24 November 2004, a water sample was taken at the seafloor in Hole U1309A. Water samples from the overflow container were sampled in Nalgene 125 mL bottles previously prewashed in 10% trace metal grade HNO_3. The sampling procedure was as follows:

1. The bottle was prerinsed with sampled water,
2. The bottle was filled to the top and sealed, and
3. The sample was refrigerated.

The water samples were curated as "Sample 304 Site U1309—Nov 24, 04 sample from seafloor." They were numbered from 1 to 6 (in order of sampling). In bottle 1, 2.5 mL of saturated $HgCl_2$ + deionized H_2O was added. A blank of the added saturated $HgCl_2$ + deionized H_2O was preserved. In bottle 2, 2.5 mL of concentrated trace metal grade HNO_3 was added. A blank of the added concentrated HNO_3 was preserved. Nothing was added to bottles 3–5. Bottle 6 was filled to the top. This water was used for onboard analyses. Results of onboard analyses for alkalinity, salinity, and pH were measured on the overflow water sample (bottle 6) and on a 3.5 mL batch of water from the coil. The leftovers of bottle 6 were thrown away after the analyses. The water sample from the coil, to which 0.09 mL of HCl was added during onboard analyses, was sealed and refrigerated (as "Coil acidified in 0.09 mL of HCl—304 U1309 Nov 24, 04"). A blank of the HCl was preserved. Results are given in Table **AT1.**

Appendix B

Water sampling at bottom of hole

To investigate the physical properties and chemical composition of water in Hole U1309D, two water samples were taken from near the bottom of the hole at ~396 mbsf on 17 January 2005 and at ~1215 mbsf on 16 February.

At the end of Expedition 304, the hole was filled with freshwater to potentially improve resistivity contrast for logging. The pipe was pulled out on 30 December 2004, and the hole was equilibrated for 17 days before the first reentry of Expedition 305. After reentering Hole U1309D, the pipe was lowered without circulation to 5 m above the bottom of the hole (~396 mbsf). Between 0500 and 0715 h on 17 Janu-

ary 2005, the WSTP was deployed. After recovery of the probe, 800 mL of water was drained from the overflow chamber and ~10 mL of water was recovered from the titanium sampling tube within the WSTP. The 10 mL water sample was transferred by the shipboard microbiologist to a sterile container, a 3 mL aliquot was passed to the geochemists, and a 2 mL aliquot was analyzed on board for salinity, alkalinity, and pH. Both samples had a brownish milky color. The water from the overflow container was, therefore, filtered through 0.45 µm cellulose filters, and the filterate was kept for further analyses. After filtration, the sample was split into two 0.5 L polyethylene bottles; one contained 1 mL concentrated HNO_3 (trace metal grade) to acidify the sample.

The second water sample was taken after a regular pipe trip on 16 February, 5 m above the bottom of the hole (~1215 mbsf). After recovery of the probe, 300 mL of water was drained from the overflow container and ~15 mL of water was recovered from the sterile titanium sampling tube within the WSTP. The water from the coil was colorless, and the water from the overflow container had a light brownish color. The water from the overflow container was, therefore, filtered over 0.45 µm cellulose filters, and the filterate was kept for further analyses. The 15 mL water sample was transferred by the shipboard microbiologist to a sterile container, and a 5 mL aliquot was handed to the geochemists. A 2 mL aliquot of the overflow container was analyzed onboard for salinity, alkalinity, and pH.

Salinity was measured with a handheld-refractometer (Reichert), and pH and alkalinity were acquired using a autotitrator (Brinkmann). The onboard measurements showed that the borehole water, in both cases, was similar to seawater in salinity and pH (Table **AT2**). The salinity was measured to be 36‰ in both samples. The pH of the sample from 396 mbsf was 7.7, and the sample from 1215 mbsf showed a slightly lower pH of 7.4. The alkalinity of the water sample from 396 mbsf was 6.1 mM and was very different from seawater. The second water sample from 1215 mbsf had an alkalinity of 2.0 mM, which is close to seawater. Because of problems with the temperature tool and the data recording, the measured temperature profile seems to be unreliable for both sampling runs.

The similarity of the bottom water to seawater argues against a significant influx of formation water. Furthermore, crustal fluids derived from a serpentinization front in peridotite (Früh-Green et al., 2003) would increase the pH. However, a minor influx of formation water can not necessarily be detected using the employed methods. The hole was filled with freshwater (low salinity) and it reequilibrated within 17 days back to seawater salinity. This could be due to the density difference between seawater and freshwater or could be due to convection driven by the geothermal gradient. Most interesting is the high alkalinity of 6.1 mM measured for the water sample from 396 mbsf, taken on 17 January.

Appendix C
Declination bias

The data presented in **"Paleomagnetism"** (Fig. **F240**) indicate a bias of normal polarity declinations for both archive halves (toward +x, or an azimuth of 360°) and for discrete samples (toward –x, or an azimuth of 180°). The origin of these directional artifacts apparently lies in the crosstalk between the SQUID sensors (i.e., a dipole moment along one sensor axis generates a signal on the other sensors). The magnitude of the off-axis response may represent a significant fraction (more than half of the axial dipole moment) near the outside of the cylindrical sample region (Parker and Gee, 2002). Most off-axis components would be effectively cancelled for a whole-core measurement. In contrast, significant asymmetries remain for the half-core measurements typically made on the 2G magnetometer onboard the *JOIDES Resolution*.

To investigate this declination bias, we measured two (nearly) axial dipole standards in the standard measurement position for discrete samples and in the bottom of the sample tray (to estimate the bias when half cores are measured). The standard moment was aligned along the +z-axis of the magnetometer and measured during a series of clockwise rotations about the +z-axis of the magnetometer (Fig. **AF1**). When the standard is approximately centered in the measurement region (as are discrete samples), the y-magnetic moment describes a sinusoid with approximately zero mean and an amplitude reflecting the small deviation of the standard sample from a purely axial dipole. In contrast, the x-magnetic moment is significantly offset toward negative values. When the same standard is placed in the bottom of the sample region, the resulting measurement bias is exactly reversed (i.e., the x-magnetic moment is significantly offset to positive values).

These results provide a qualitative explanation for the observed bias in normal polarity components both on discrete samples and from the archive-half data. Multiple measurements (e.g., with the moment directed along –z) indicate that, for an axial moment parallel to +z (as is the drilling induced magnetiza-

tion), a spurious signal along –x is generated for samples in the center of the measurement region and a spurious signal along +x is generated for samples near the bottom of the sample region. Although a small component is generated along the y-coordinate axis, this component is substantially smaller (by up to an order of magnitude) than is the spurious signal along the x-coordinate axis (Fig. **AF1**). These off-axis components result in a declination bias toward 180° (–x in the core reference frame) for discrete samples and a corresponding bias toward 360° (+x) for archive halves. The bias for discrete samples should be averaged for samples measured in multiple positions but will be present if samples are measured in a single position (the standard measurement protocol).

This bias is most pronounced for samples in which the +z magnetization is much larger than the components in the horizontal (x-y) plane. This is precisely the case for diabase samples from Hole U1309B that acquire a very substantial drilling-induced remanence. The same effect, though less pronounced, is evident in the normal polarity overprints in other lithologies as well. It is important to note that, upon demagnetization, little declination bias should remain when the drilling remanence is no longer substantially larger than the primary magnetization.

Figure F1. Tectonic and morphologic setting of Atlantis Massif. Bathymetric contours illustrate the deep median valley of the Mid-Atlantic Ridge and its intersection with the Atlantis transform fault. The shallow, corrugated dome composing the core of Atlantis Massif has two structural components: the central dome, where IODP footwall drilling was focused, and the Southern Ridge.

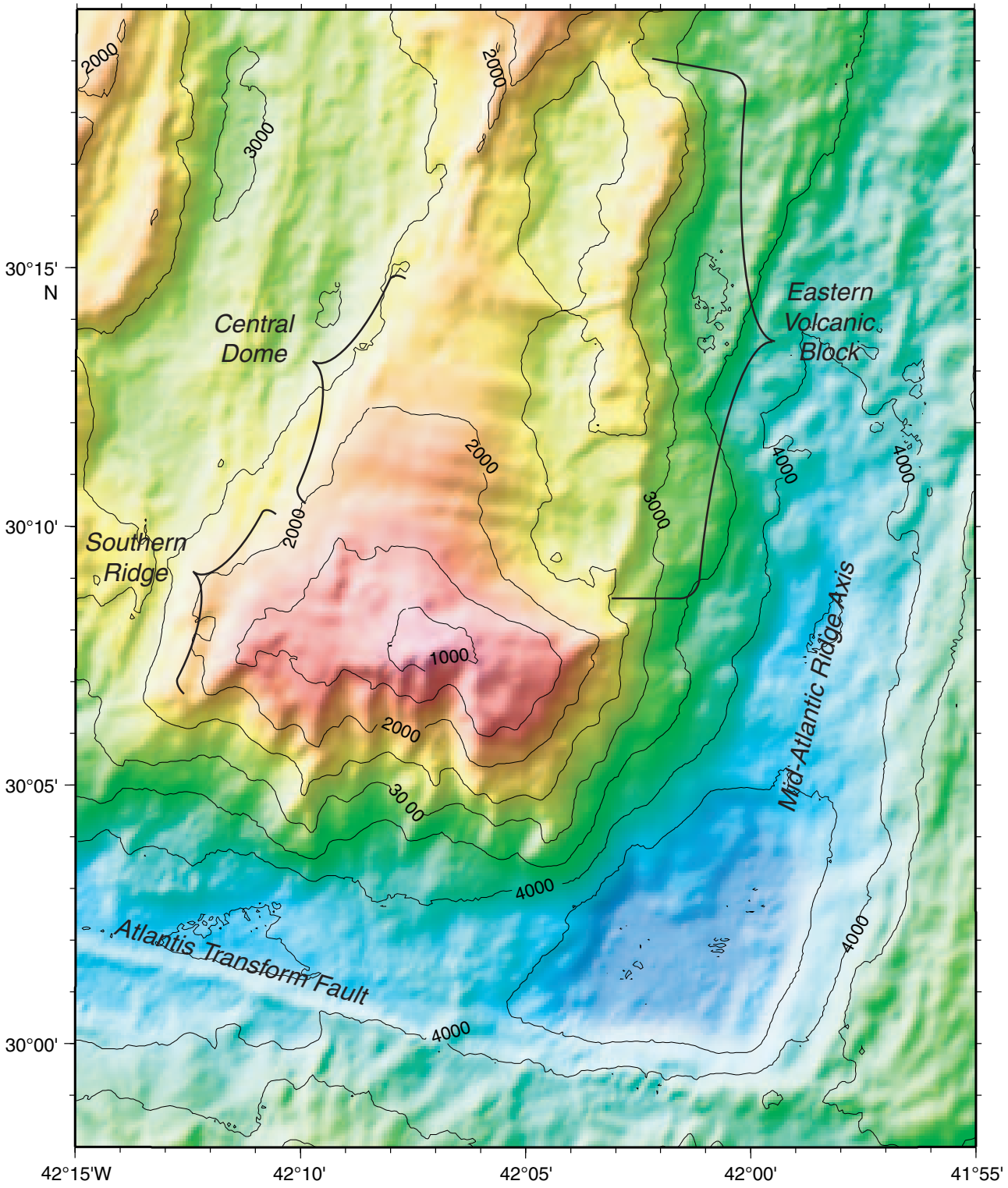

Figure F2. Base map of Atlantis Massif showing prior geological and geophysical data coverage and the location of Integrated Ocean Drilling Program (IODP) drill sites (circles). Bathymetry is contoured at 100 m intervals, based on a 100 m grid. Seismic reflection and refraction lines and seafloor mapping/sampling sites are shown. The corrugated detachment surface capping the central dome is inferred to extend beneath the eastern block, thereby making the upper crustal deposits part of the hanging wall to the fault. MCS = multichannel seismic. OBH = ocean bottom hydrophone.

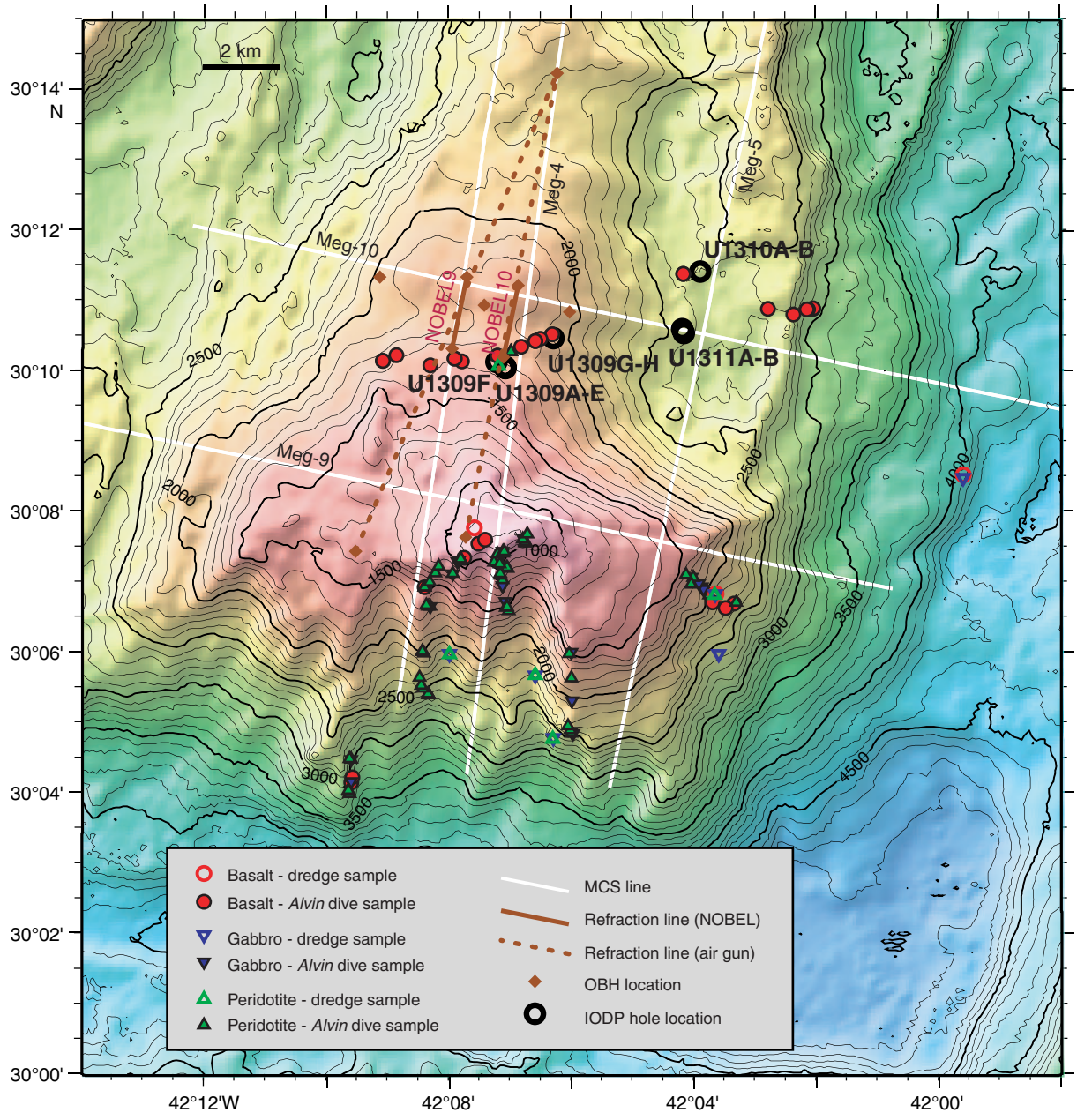

Figure F3. Seismic sections indicate subsurface structure of Atlantis Massif. **A.** Deep source refraction (Line NOBEL9; Fig. F2) recorded by an ocean bottom hydrophone shows arrivals indicating a high-velocity body (8 km/s, assuming plane-layered structure) at very short range. **B.** Velocity gradient determined from refraction analysis at Atlantis Massif (from Collins et al., 2001) is similar to that determined near ODP Site 920, where serpentinized peridotite was recovered. The gradient near Hole 735B, where only gabbro has been recovered, is not as strong. MARK = Mid-Atlantic Ridge (MAR) just south of Kane Fracture Zone, MCS = multichannel seismic, SWIR = Southwest Indian Ridge. **C.** A portion of MCS Line Meg-10 across the central dome. CMP = common midpoint. **D.** A portion of MCS line Meg-4, north–south across the central dome.

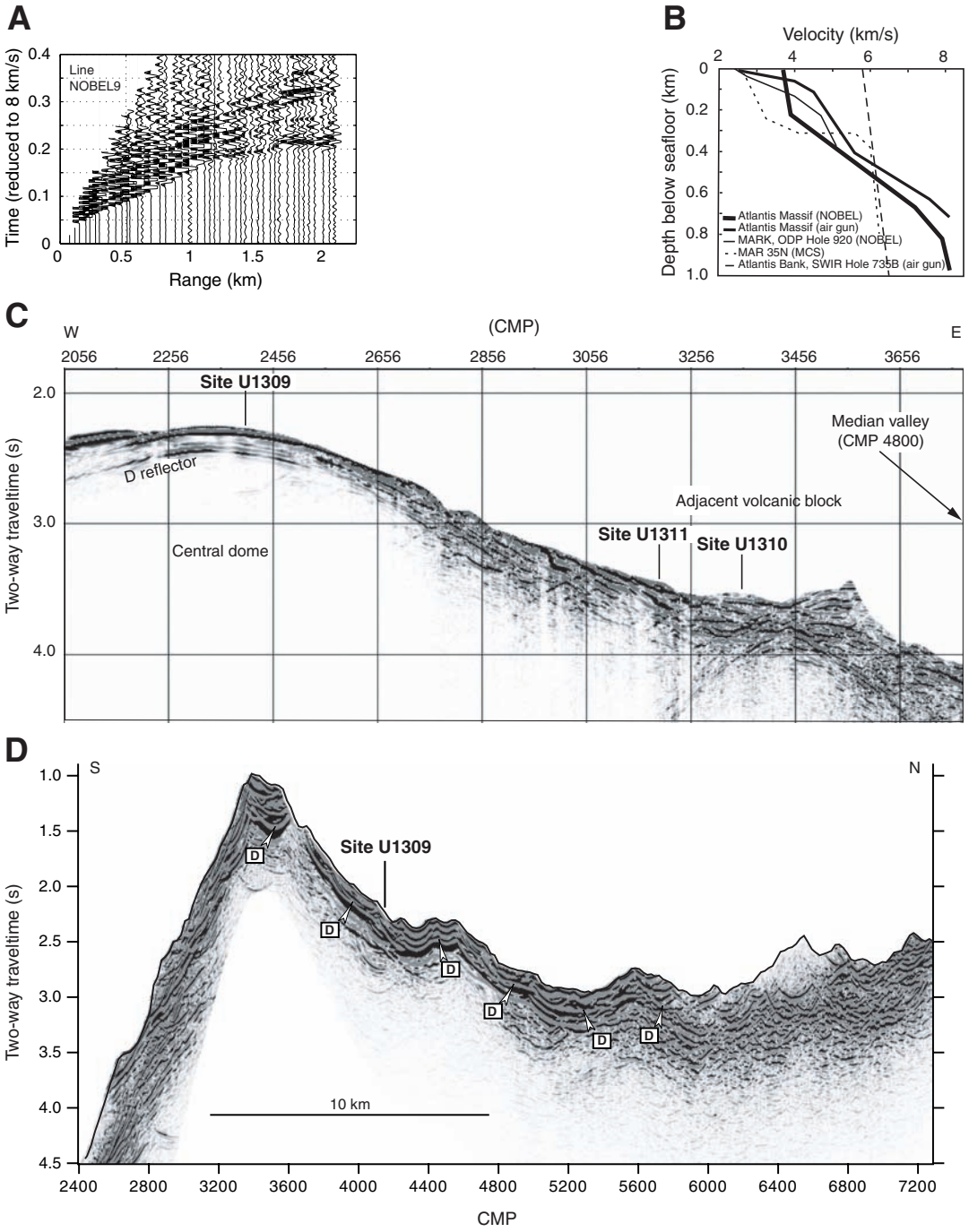

Figure F4. Bouguer gravity anomaly map of the ridge-transform intersection (30°N, MAR). Contribution of seafloor topography has been removed from the Free Air anomaly, assuming a density contrast between seawater and ocean crust of 1700 kg/m³. Trackline data from EW0102 and EW9212 have been added to the compilation presented in Blackman et al. (1998). Anomalously high densities occur within Atlantis Massif. Lower than average density (thicker crust?) characterizes the outside corner region near the fracture zone. Broader scale thermal contribution of subaxial upwelling (gravity low in northern portion of rift valley) and plate cooling have not been removed.

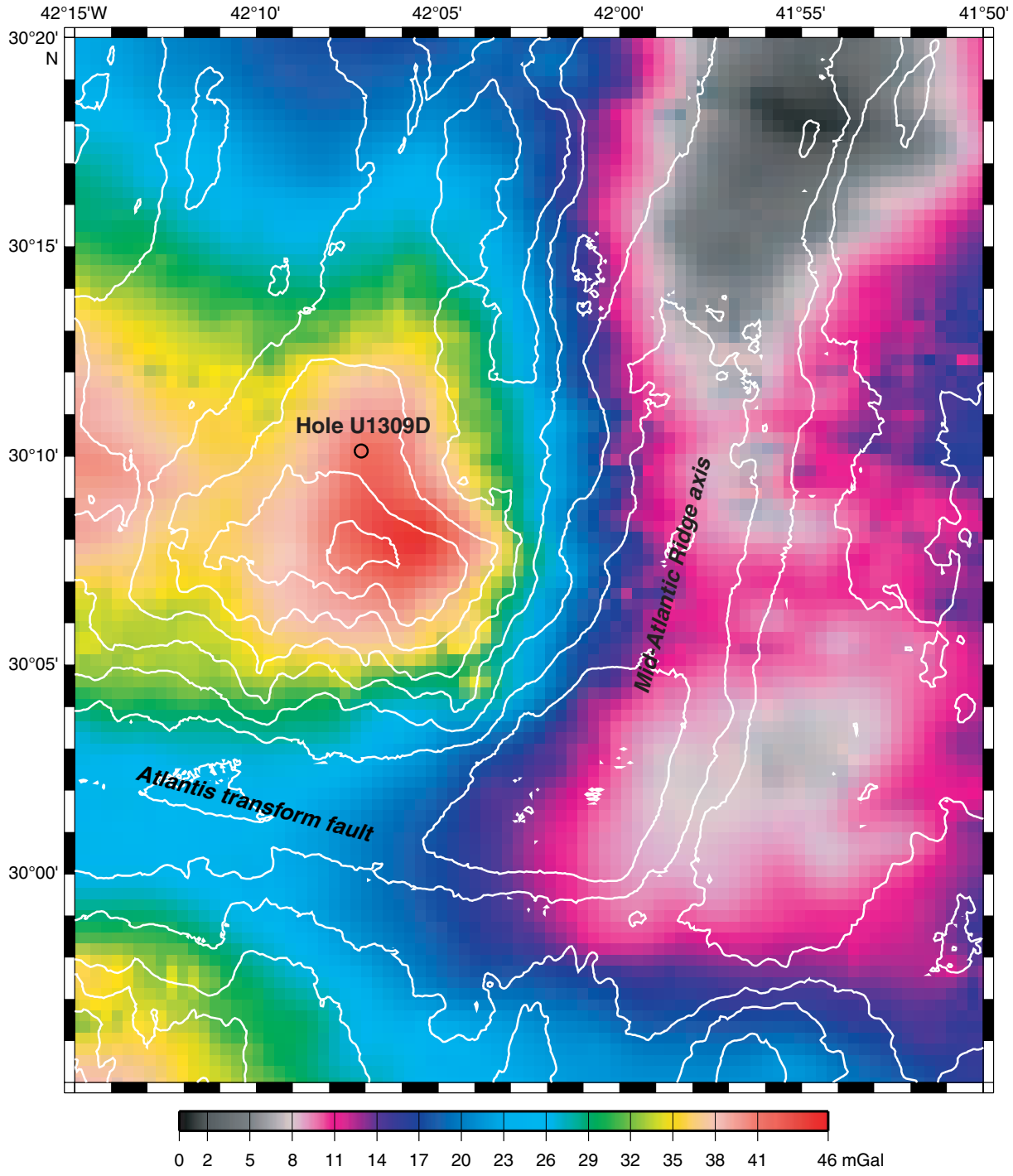

Figure F5. Rocks recovered from shallow-penetration Hole U1309H include basalt, talc-tremolite schist, and fractured diabase (Section 304-U1309H-1R-1).

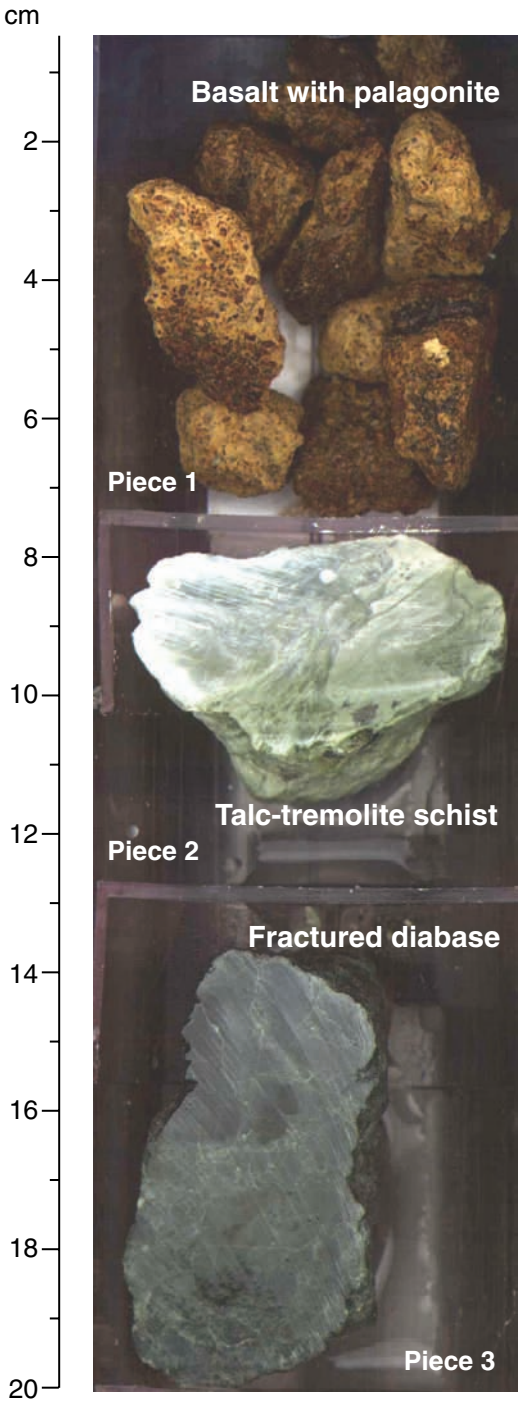

Figure F6. Lithology of core recovered from deep holes at Site U1309. **A.** A 20 m running average of lithologic proportions from Hole U1309D (white = no recovery). **B.** Lithology proportions (in percent) for Hole U1309D. (Continued on next page.)

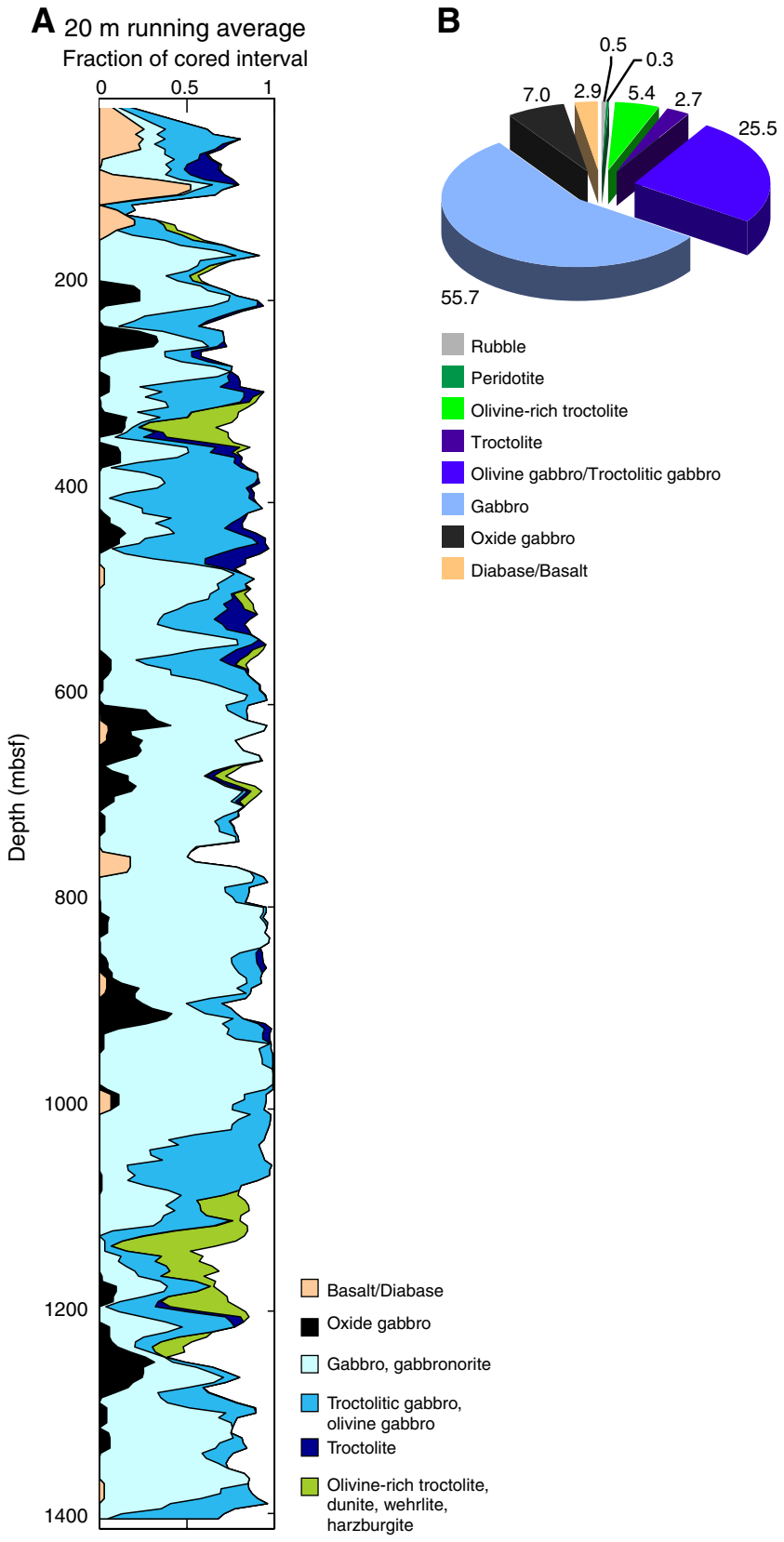

Figure F6 (continued). **C.** Lithostratigraphy of Hole U1309B. **D.** Lithostratigraphy of Hole U1309D.

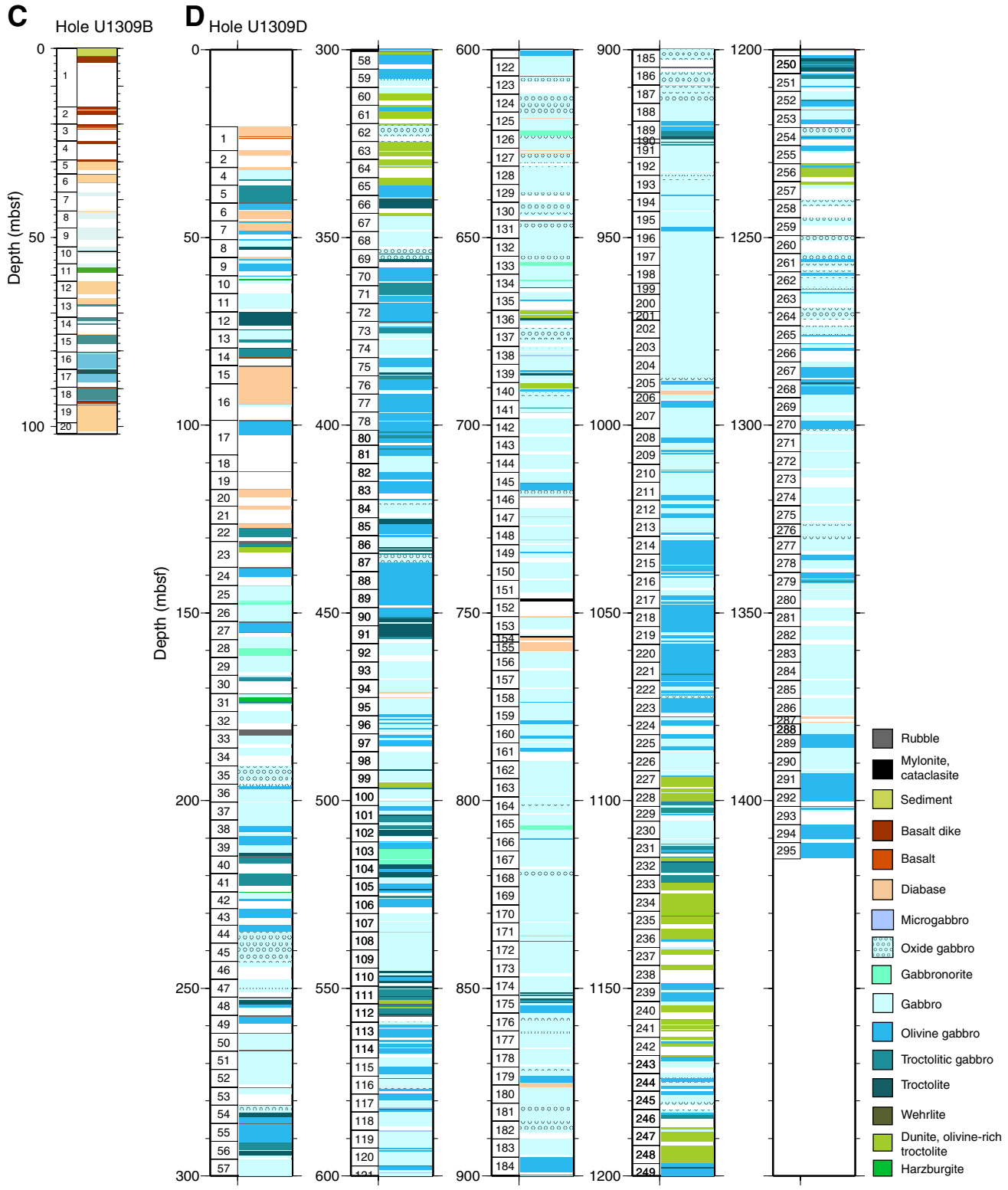

Figure F7. Contact between olivine gabbro and troctolite (interval 305-U1309D-251R-1, 44–65 cm).

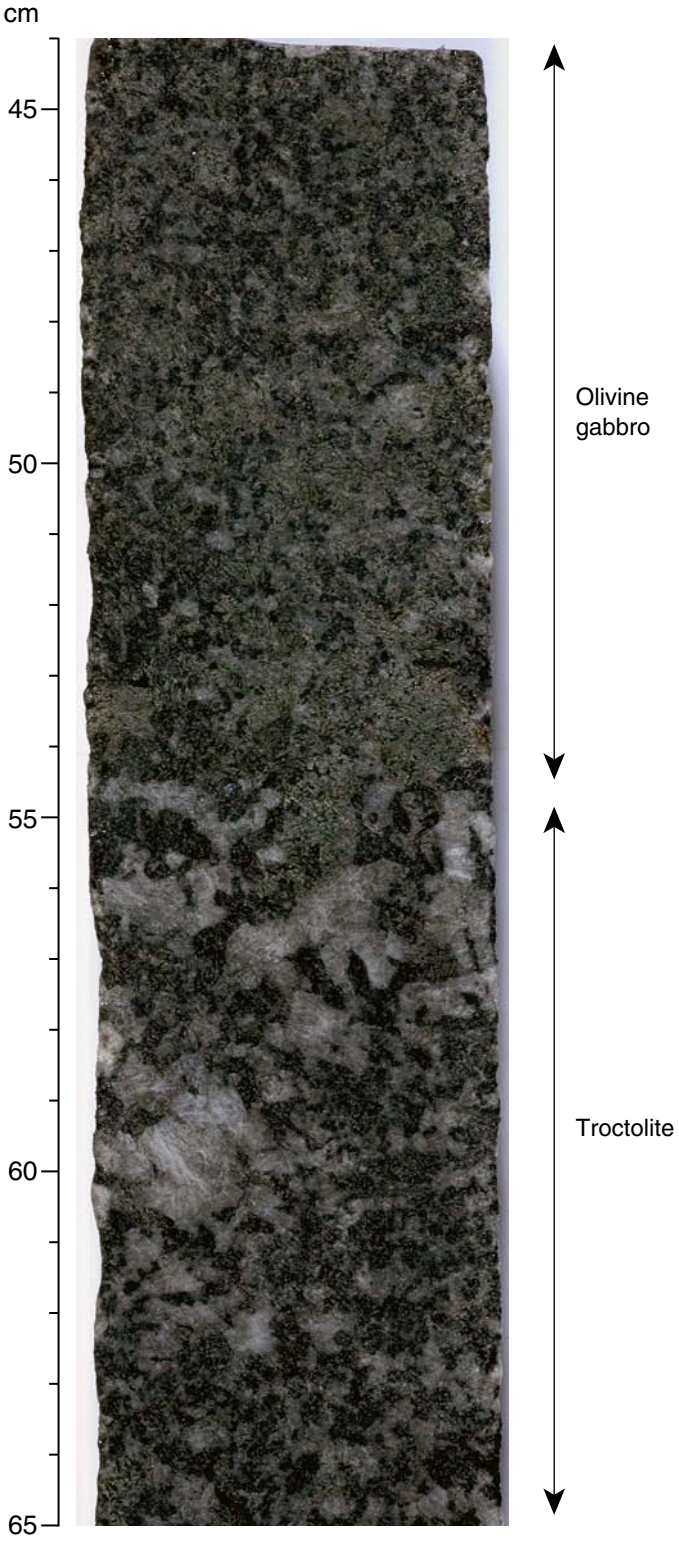

Figure F8. Mode of occurrence of olivine-rich rocks. **A.** Partially serpentinized olivine-rich troctolite in contact with olivine gabbro (interval 305-U1309D-227R-2, 22–45 cm). **B.** Fresh olivine-rich troctolite, cut by a gabbroic dikelet (interval 305-U1309D-248R-2, 2–26 cm). **C.** Residual mantle peridotite (interval 304-U1309B-11R-2, 87–94 cm).

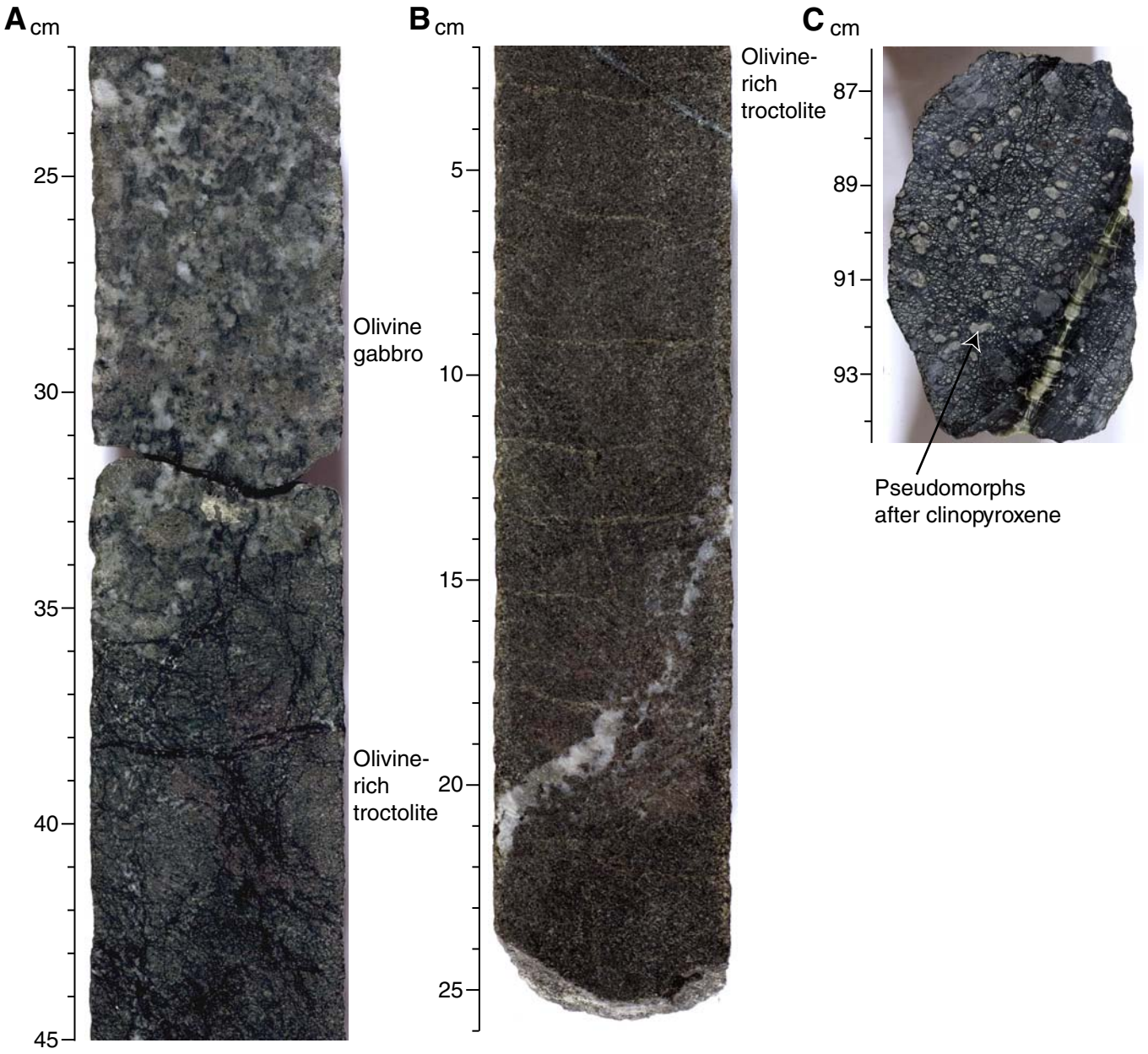

Figure F9. A. Plagioclase-bearing websterite (Sample **305-U1309D-100R-1, 10–13 cm**) (cross-polarized light; field of view [FOV] = 22 mm). **B.** Olivine-rich troctolite (Sample **305-U1309D-227R-3, 70–72 cm**) (cross-polarized light; FOV = 22 mm). **C.** Olivine-rich troctolite (Sample **305-U1309D-248R-2, 7–9 cm**) (cross-polarized light; FOV = 22 mm). **D.** Dunite (Sample **305-U1309D-248R-2, 96–99 cm**) (cross-polarized light; FOV = 22 mm). **E, F.** Fresh olivine and plagioclase in olivine-rich troctolite (Sample **305-U1309D-248R-2, 7–9 cm**) (cross-polarized light; FOV = 11 mm).

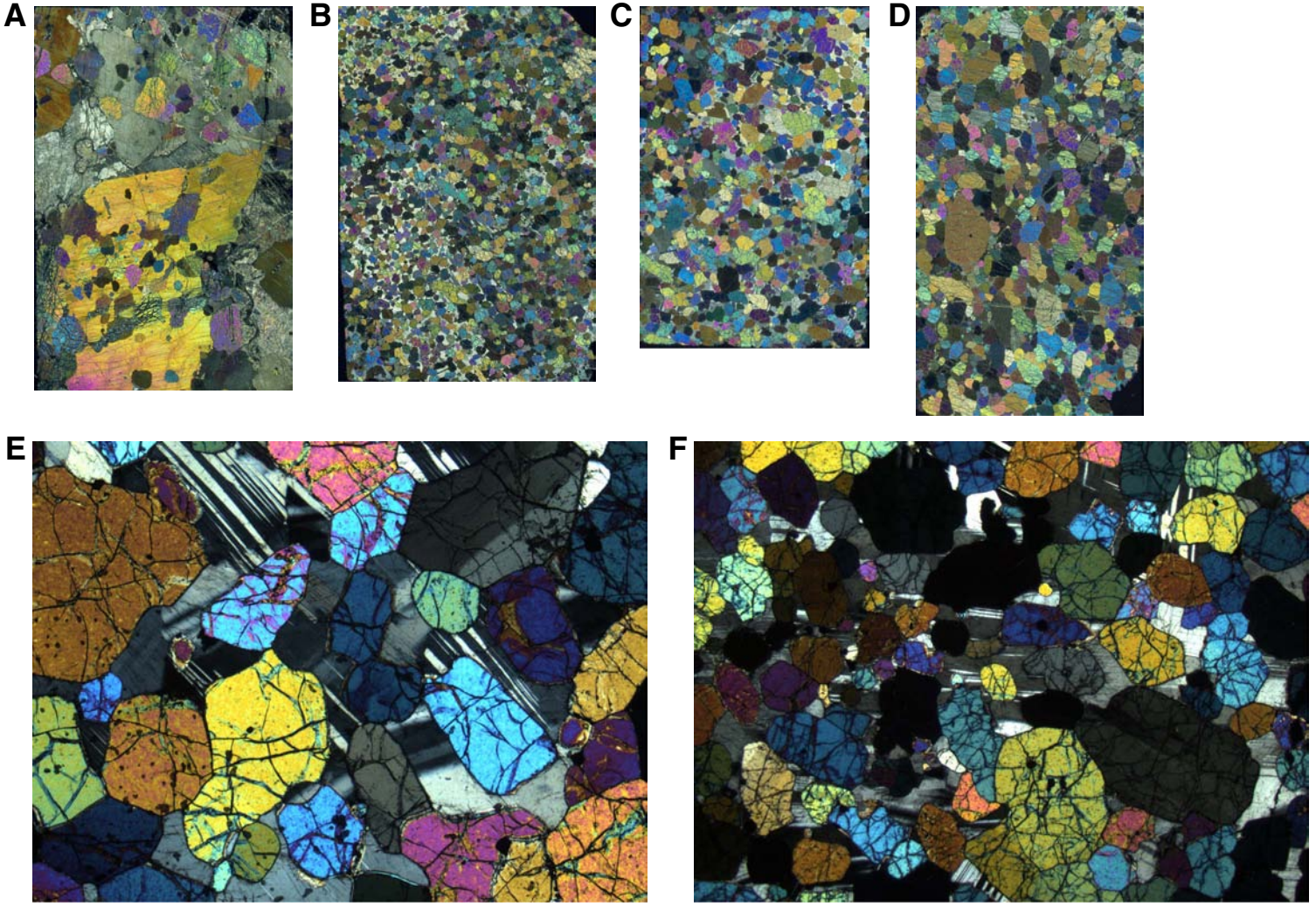

Figure F10. Modes of occurrence of oxide-rich gabbros. **A.** Oxide patches in magmatic texture (Sample **305-U1309D-254R-1, 34–36 cm**) (plane-polarized light; field of view [FOV] = 2 cm). **B.** Same as A; cross-polarized light. **C.** Oxide-rich shear zone (Sample **305-1309D-183R-2, 32–34 cm**) (plane-polarized light; FOV = 2 cm). **D.** Same as C; cross-polarized light.

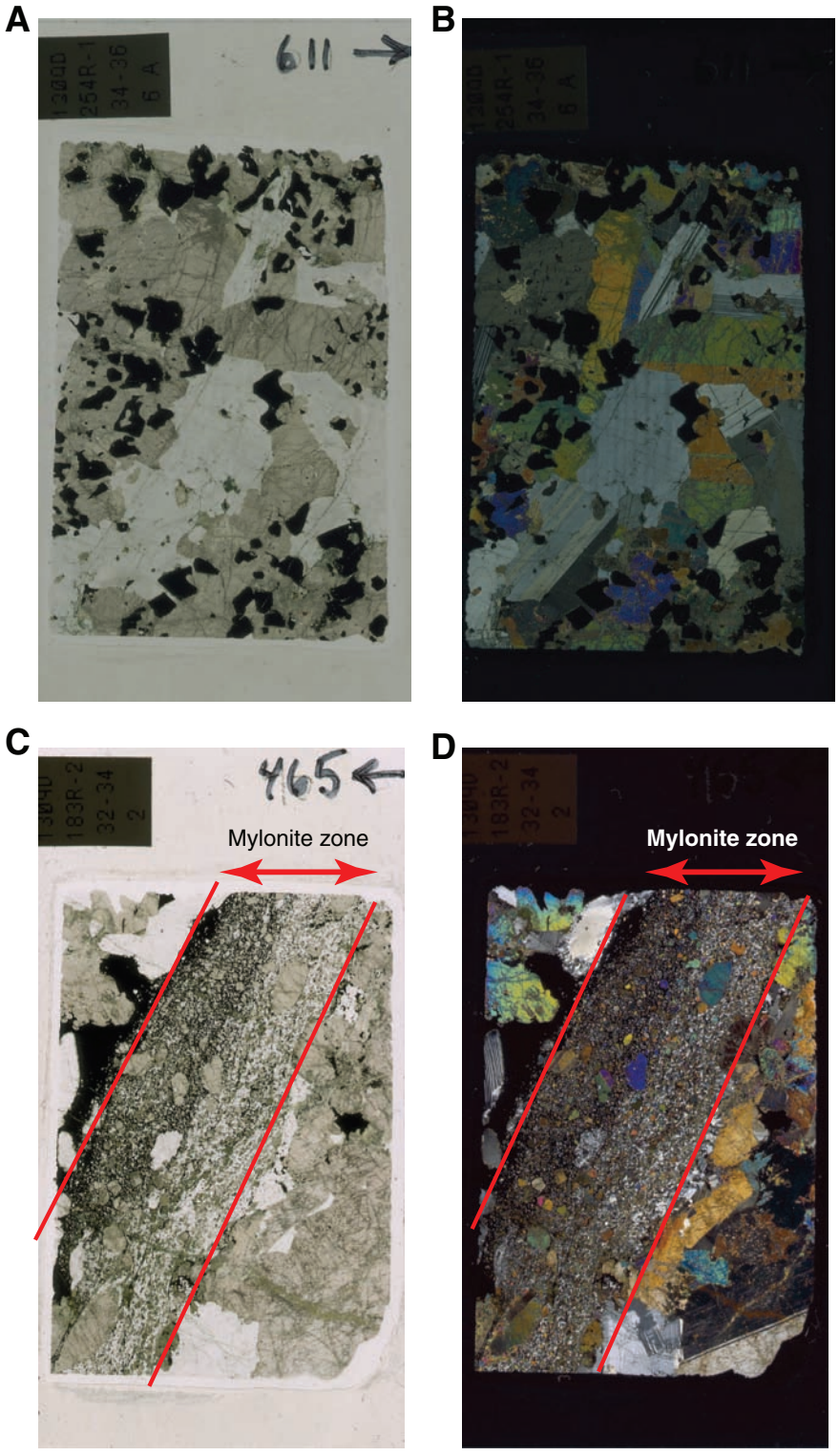

Figure F11. Magnetic susceptibility (MS) measured along half cores from Hole U1309B in diabase Unit 20 (Core 305-U1309D-19R). Edited data (blue) are measurements made >5 cm from the edge of a core piece, so values are most reliable; however, overall pattern is essentially the same as for all data (gray). Note the lower MS in the middle of this diabase unit (MS remains high in Core 305-U1309D-20R below 99 mbsf).

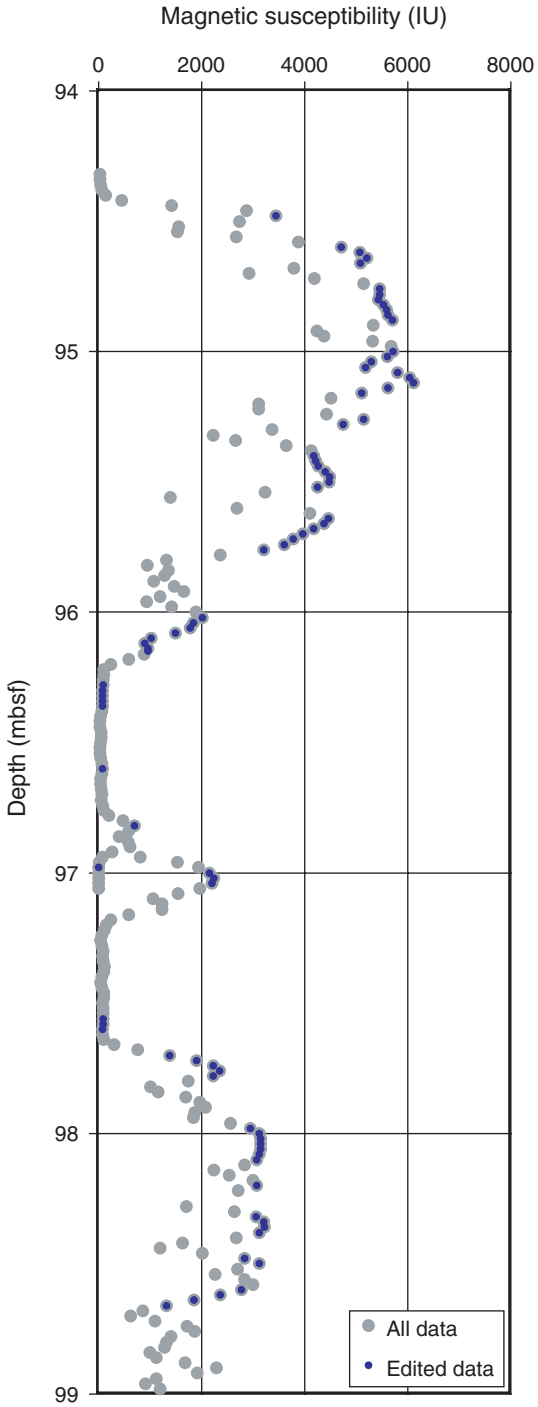

Figure F12. Termination of a late magmatic leucocratic vein in Core 304-U1309D-62R.

Figure F13. Ni versus Mg# (molar Mg/[Mg + Fe]) for gabbros, olivine gabbros, troctolites, orthopyroxene-bearing gabbros, oxide-gabbros, ultramafic rocks, and peridotites from Site U1309. Shaded fields represent data from Leg 153 (peridotite = upper purple field; gabbro = lower purple field), Leg 209 (peridotite = upper yellow field; gabbro = lower yellow field), and Hole 735B (green field).

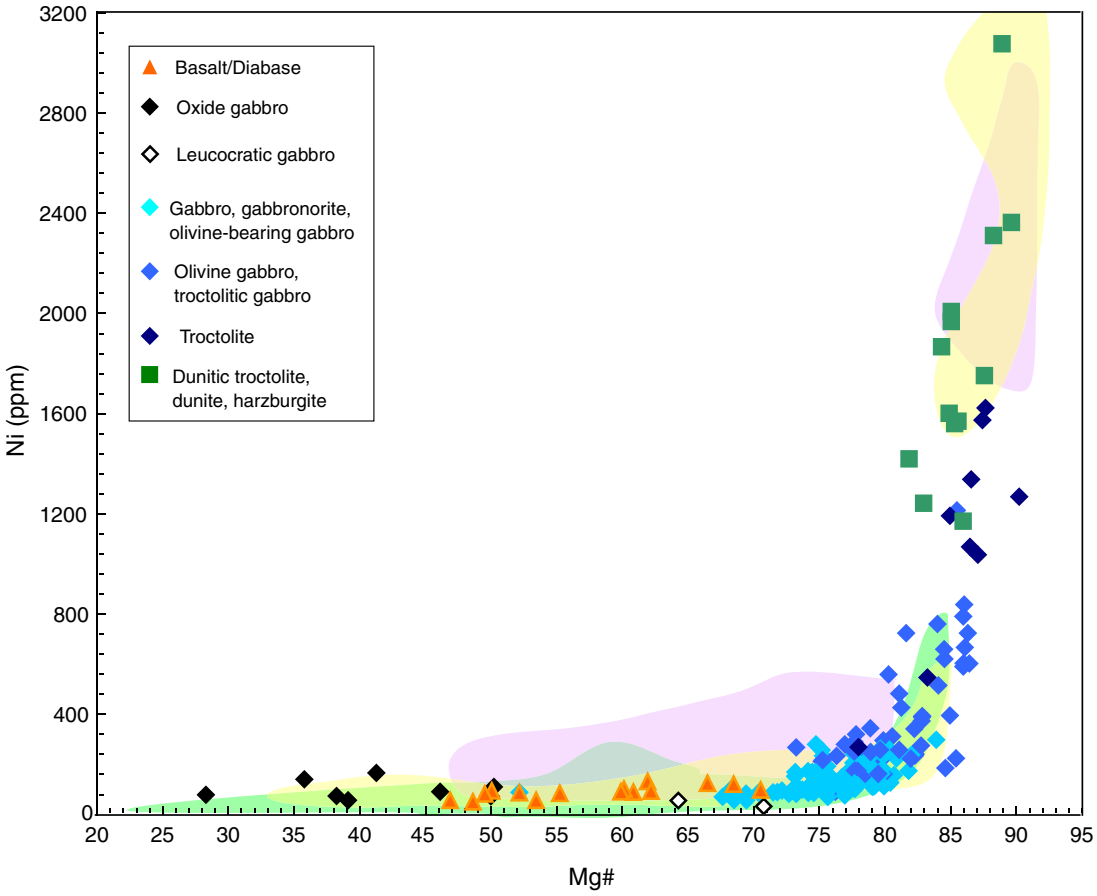

Figure F14. Downhole variations in whole-rock Mg# for Hole U1309D core samples. Dashed lines = fault zones.

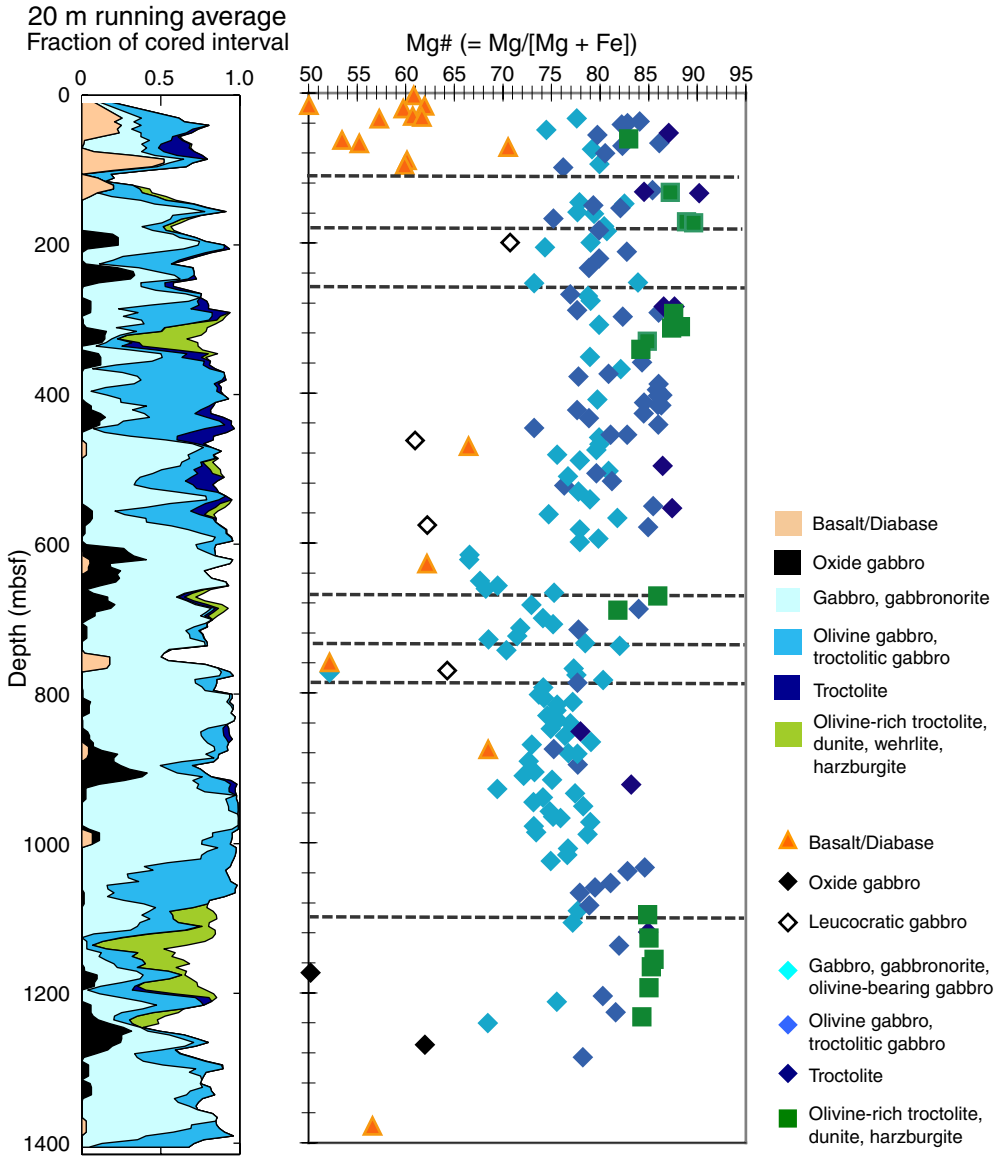

Figure F15. Total alkalis, $Na_2O + K_2O$, versus SiO_2 (after Le Maitre et al., 1989). Data are plotted on a volatile-free basis for basalts, diabases, and basalt breccia from Holes U1309B and U1309D. Compilation of the compositions of Mid-Atlantic Ridge (MAR) glasses (PetDB, December 2004; **beta.www.petdb.org**) is shown for comparison. The continuous line represents the alkalic/tholeiitic boundary of Irvine and Baragar (1971). Ol = normative olivine, Q = normative quartz.

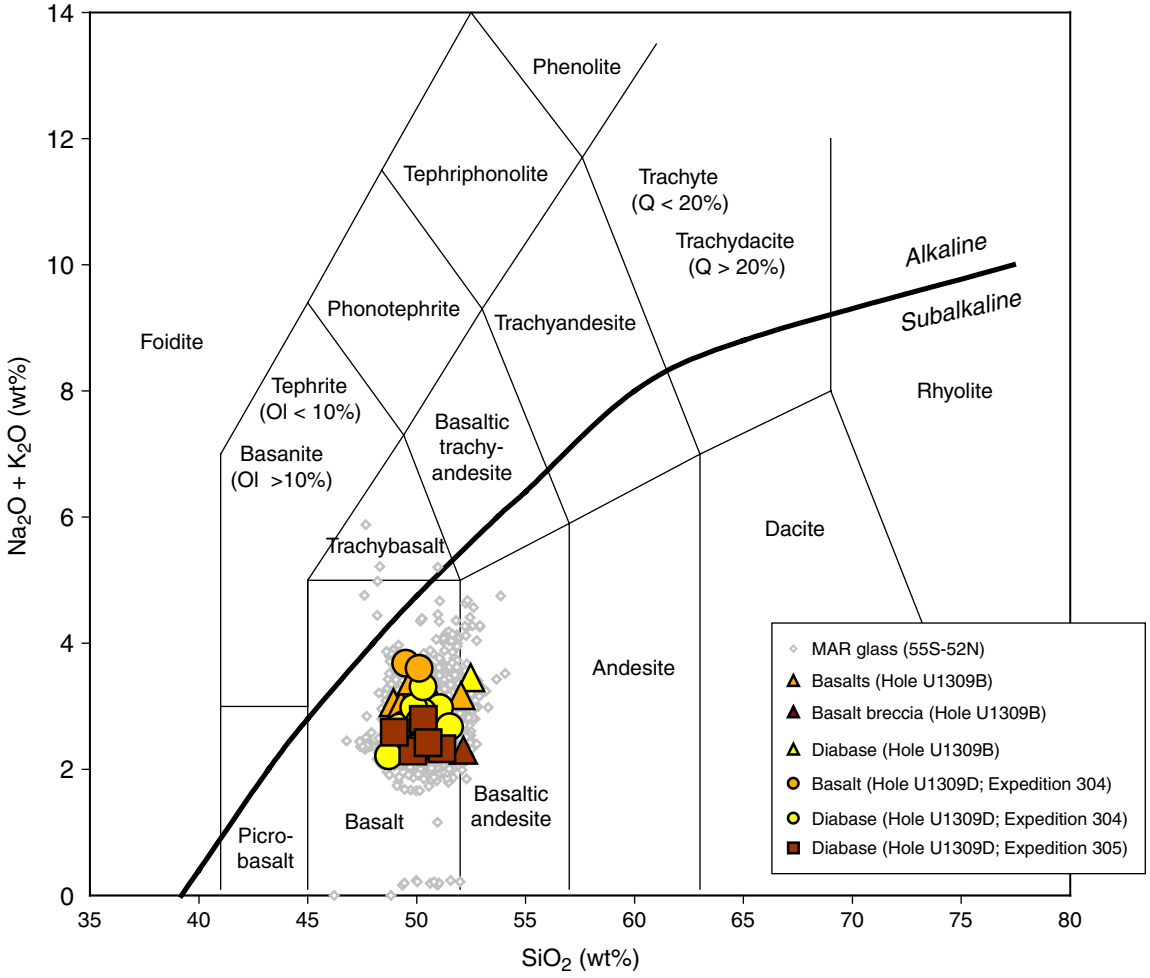

Figure F16. Downhole alteration and veining in Hole U1309D. **A.** Igneous lithology **B.** Overall alteration logged during visual core description (percent per core). **C.** Total number of veins per core.

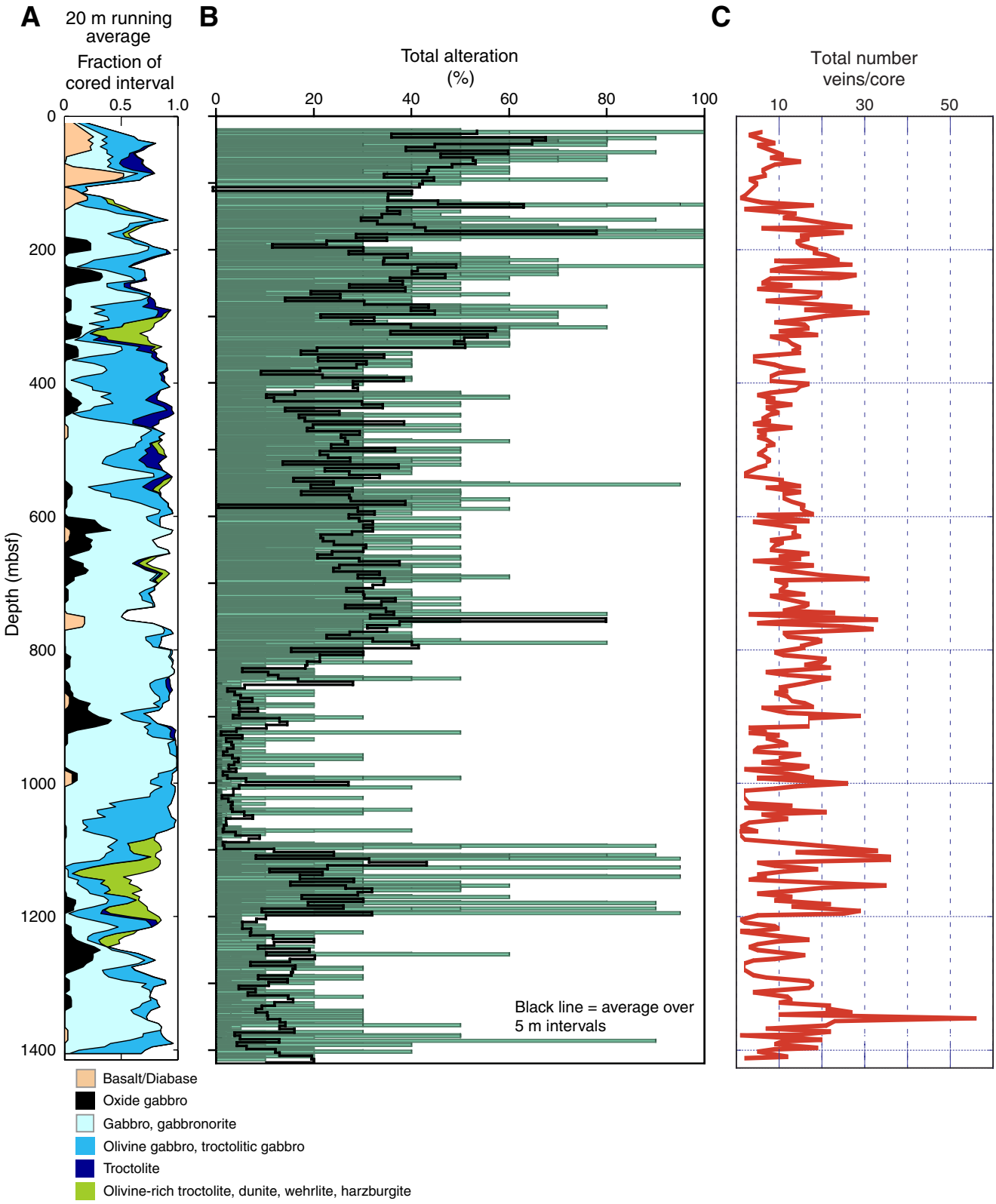

Figure F17. Examples of high-temperature, ductile deformation structure that is recorded in some Hole U1309D rocks. **A.** Well-defined gabbro mylonite cut by a fracture (**Sample 304-U1309D-8R-1, 68–71 cm**) (plane-polarized light; field of view [FOV] = ~2 cm). **B.** Brown amphibole vein crosscuts localized mylonite shear zone with domains of recrystallized plagioclase and pyroxene (**Sample 304-U1309D-9R-1, 71–73 cm**) (cross-polarized light; FOV = 4 mm).

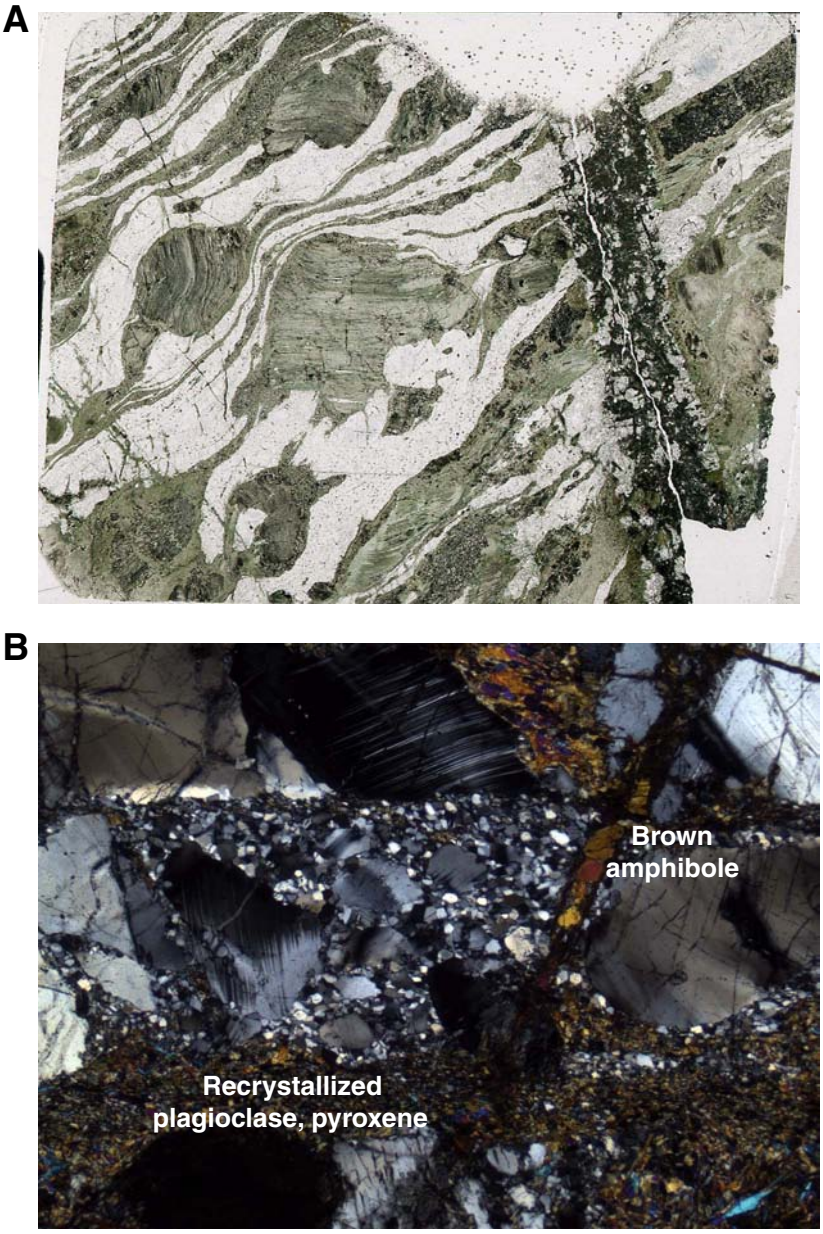

Figure F18. A. Dark green amphibole veins cutting gabbro (interval 305-U1309D-294R-2, 30–44 cm). **B.** Gabbro cut by parallel set of dark green amphibole veins (interval 305-U1309D-160R-4, 0–23 cm). The density of such sets locally approaches that of a foliation. Note development of corona texture in the alteration halo of these veins.

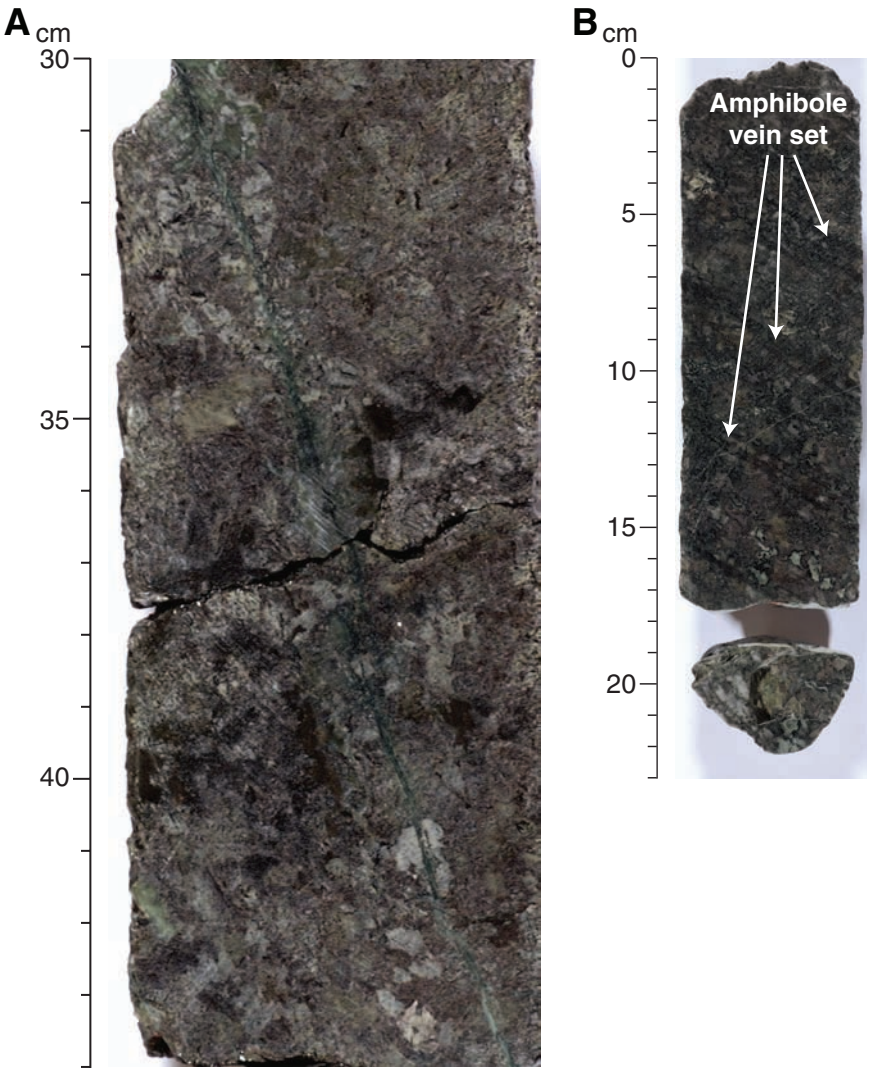

Figure F19. A. Troctolite layer showing well-developed corona mesh texture (interval 304-U1309B-15R-2, 53–64 cm). Lighter green areas are actinolite after relict clinopyroxene. Original grain boundaries are outlined by dark green (appears black) chlorite. **B.** Corona texture in olivine gabbro consisting of talc, tremolite, oxides after olivine, and chlorite after plagioclase where the two original minerals were in contact (Sample **305-U1309D-80R-2, 16–19 cm**) (cross-polarized light; field of view = 1.4 mm).

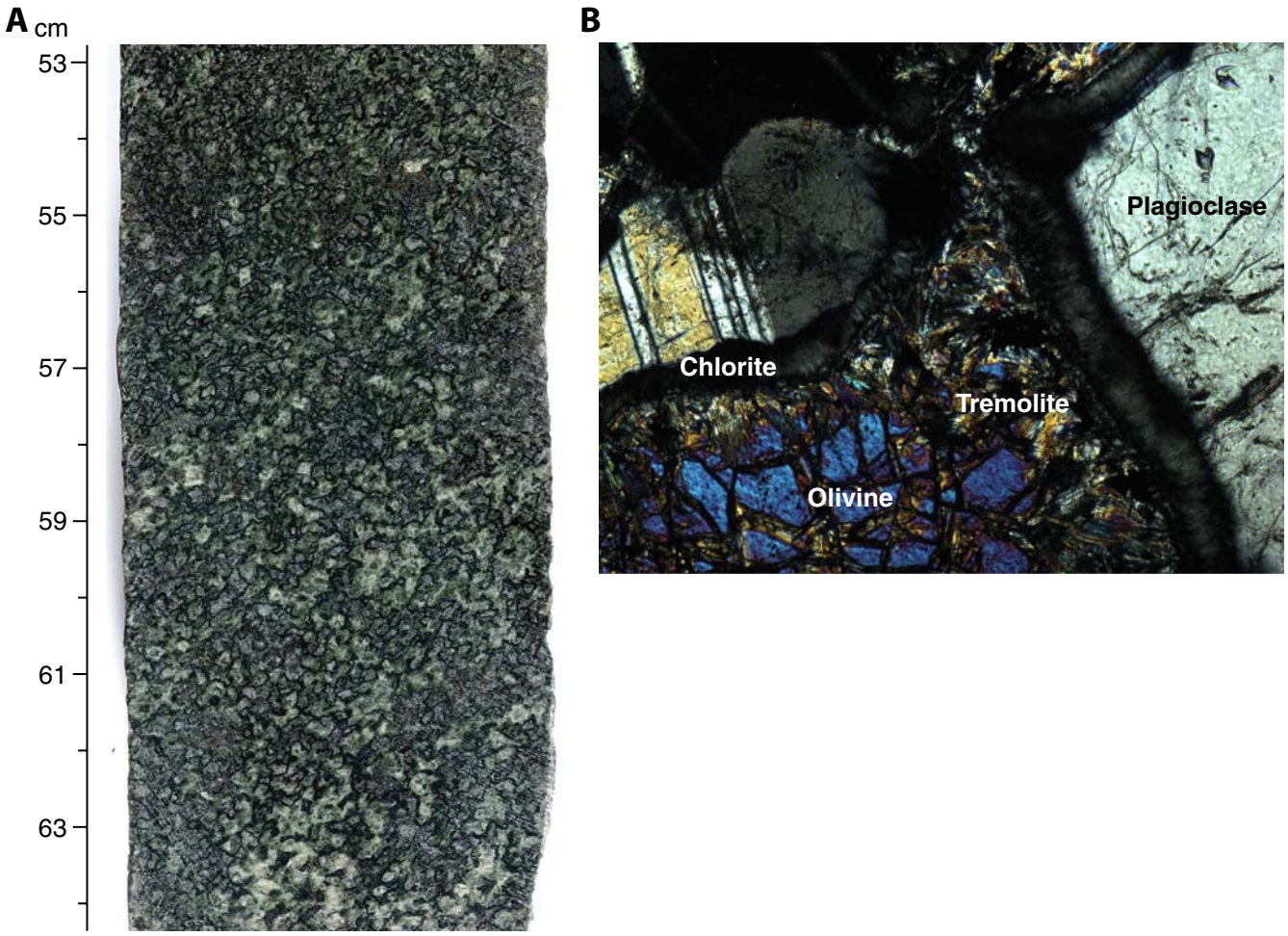

Figure F20. Contact between coarse-grained gabbro and harzburgite (interval 304-U1309B-11R-1, 86–99 cm). Note the talc-tremolite band between the two rock types and variations in style of serpentinization.

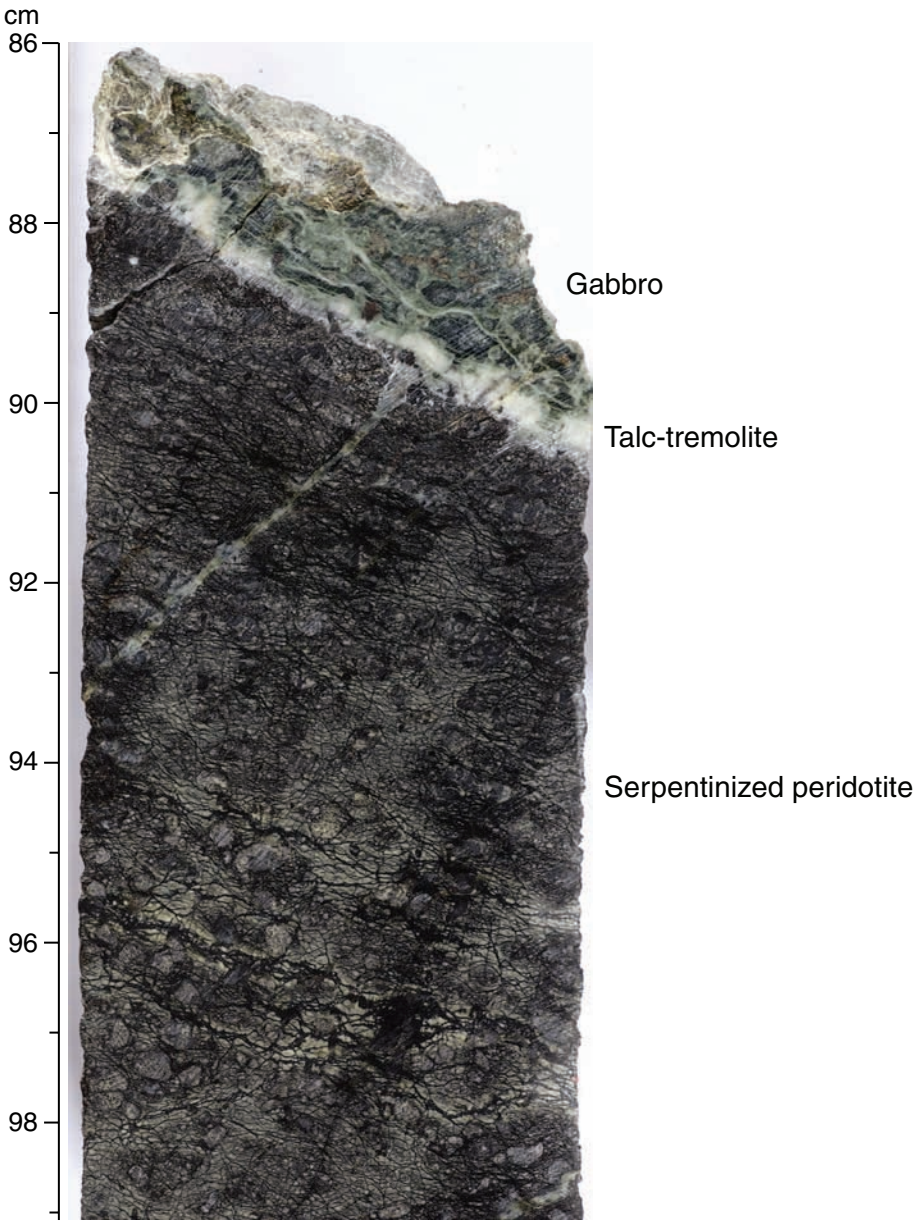

Figure F21. A. Serpentinized olivine with kernel texture (Sample **305-U1309D-80R-1, 39–41 cm**) (plane-polarized light; field of view [FOV] = 5.5 mm). **B.** Serpentine vein with dusty magnetite in olivine (Sample **305-U1309D-236R-2, 10–13 cm**) (cross-polarized light; FOV = 700 µm).

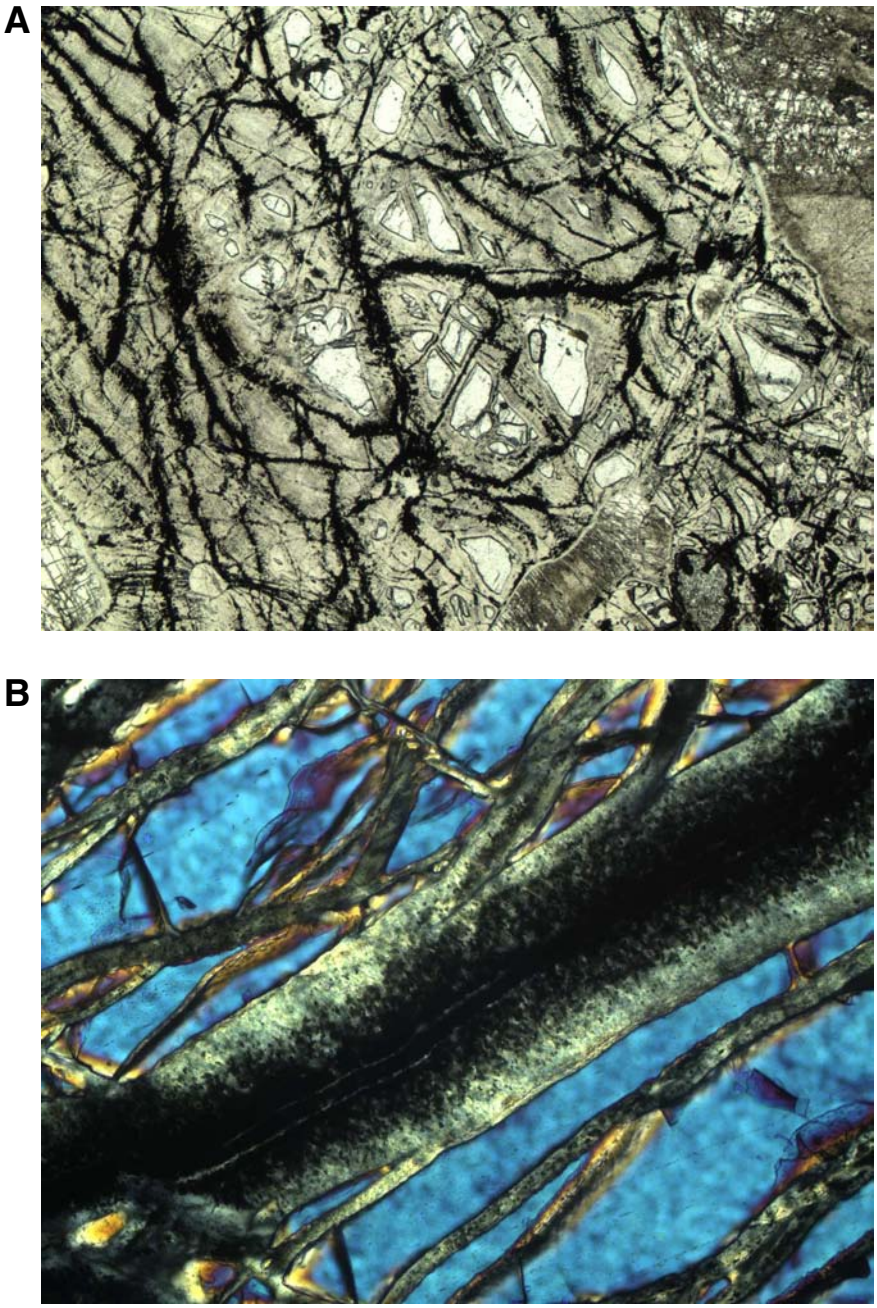

Figure F22. A. Metamorphic expansion microfractures in plagioclase adjacent to serpentinized olivine (Sample **305-U1309D-82R-2, 110–112 cm**) (cross-polarized light; field of view [FOV] = 5.5 mm). **B.** Serpentinization-induced microfracturing (Sample **305-U1309D-232R-1, 102–105 cm**) (cross-polarized light; FOV = 5.5 mm).

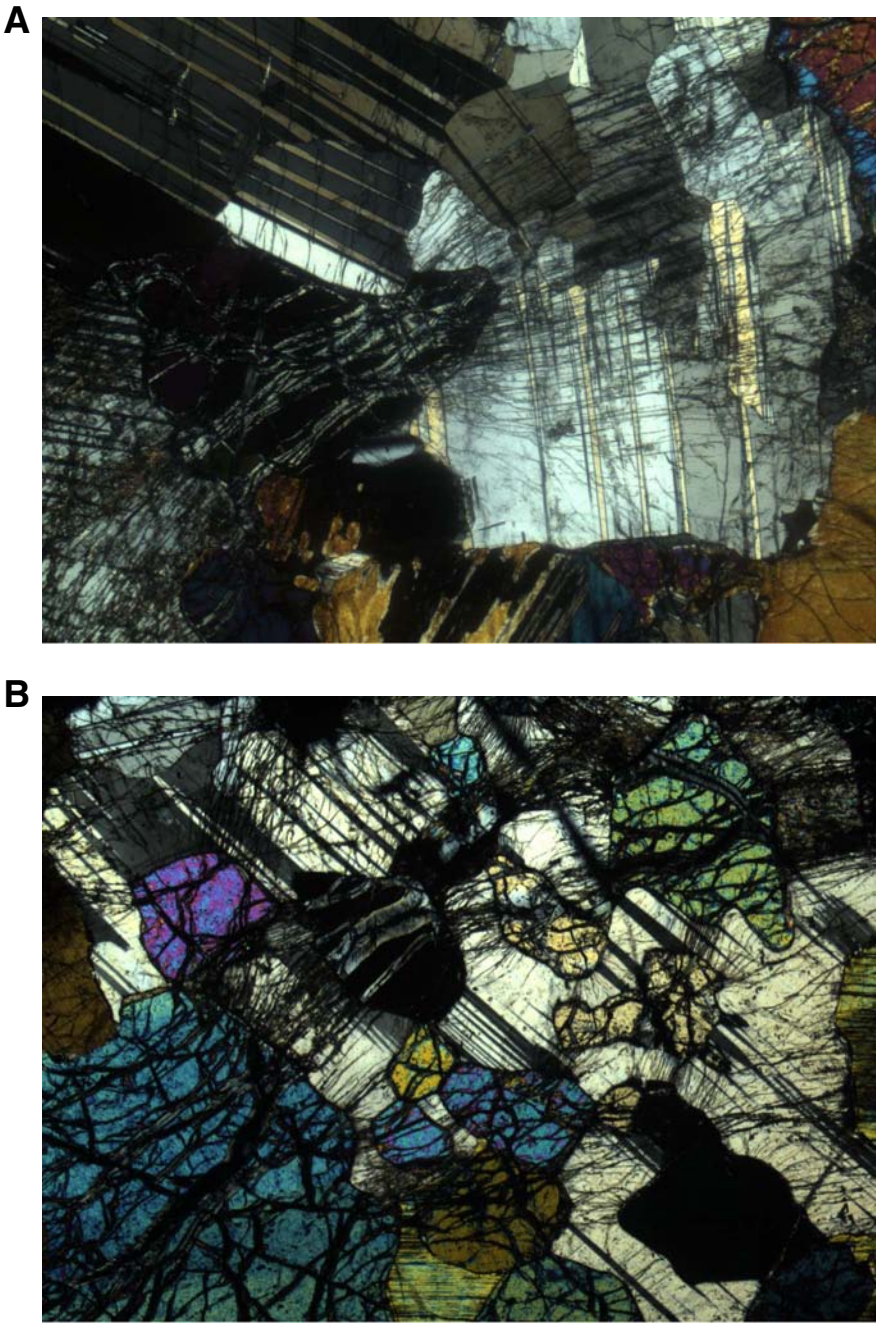

Figure F23. Prehnite vein with zeolite spherules projecting from the vein wall (Sample **305-U1309D-192R-1, 80–82 cm**) (cross-polarized light; field of view = 1.4 mm).

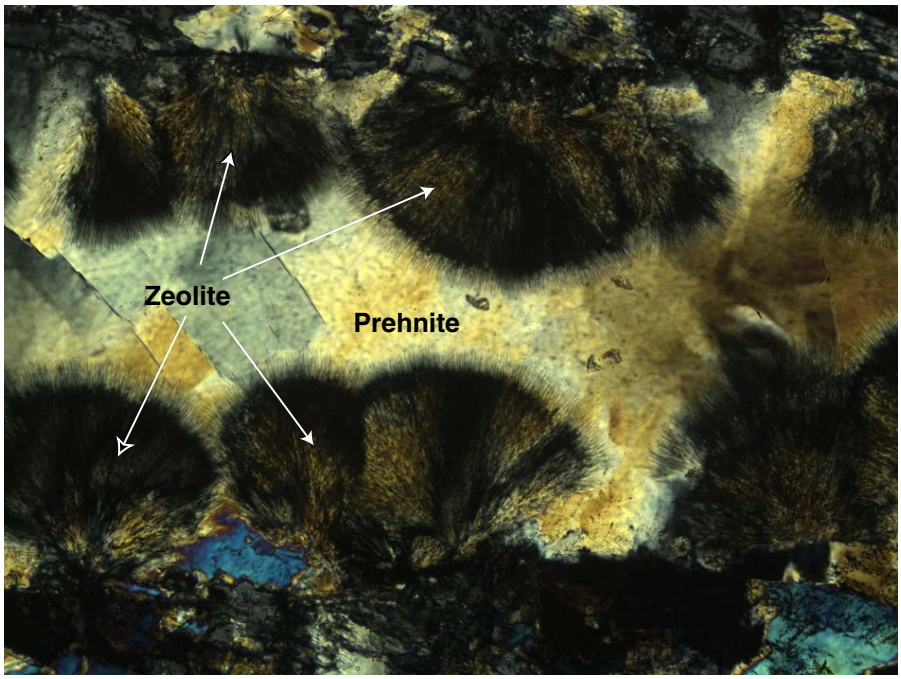

Figure F24. Example of magmatic foliation (Sample **305-U1309D-222R-2, 84–87 cm**) (cross-polarized light; field of view = 22 mm). About 22% of all recovered rocks show a weak magmatic foliation.

Figure F25. High-temperature plastic deformation foliation (Sample **305-U1309D-263R-2, 34–37 cm**) (cross-polarized light; field of view = 22 mm). Although core descriptions suggest an absence of plastic deformation except for local shear zones, microstructural observations commonly indicate a weak to moderate crystal-plastic strain overprint in samples selected to be representative of primary igneous texture.

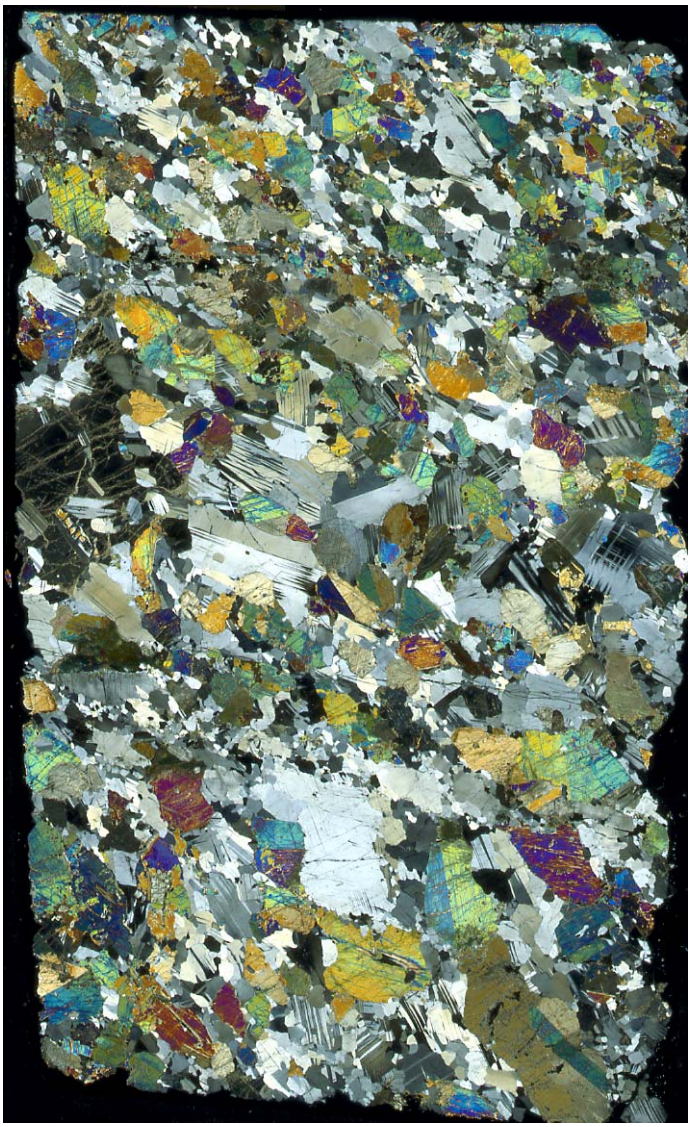

Figure F26. Serpentine foliation (interval 305-U1309D-235R-2, 98–113 cm).

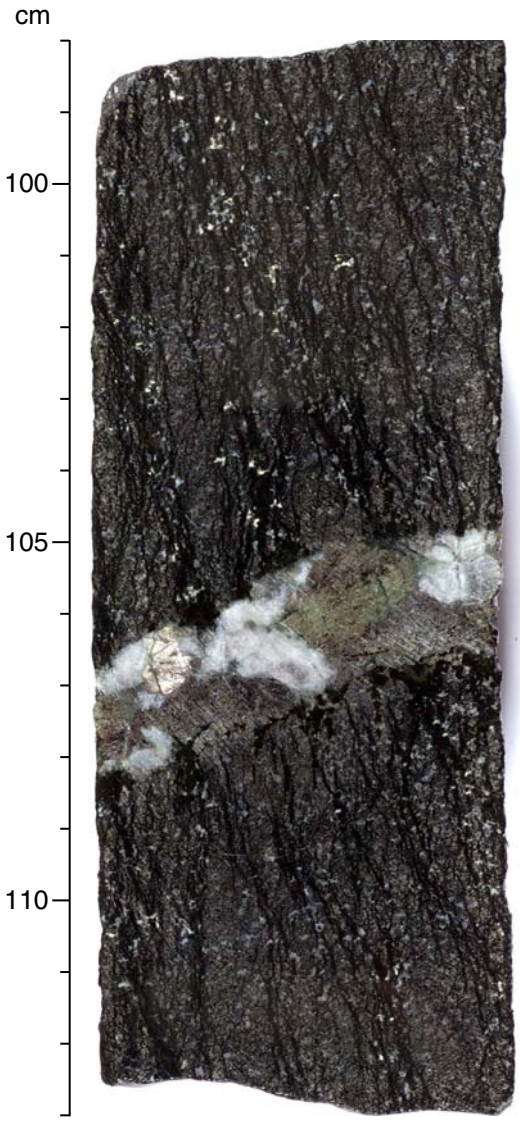

Figure F27. Downhole plots of structural features of Hole U1309D. **A.** Lithostratigraphy. **B.** Average intensity of magmatic and plastic foliation from core observations. **C.** Paleomagnetic inclination from archive-half and discrete samples. Groups I–V correspond to zones with distinct average inclinations. Parts D–I are a summary of deformation in the upper 400 m (top of scale given for each category). **D.** Lithology. **E.** Intensity of magmatic fabrics (3 = strong shape-preferred orientation). **F.** Intensity of crystal-plastic fabrics (4–5 = mylonitic–ultramylonitc). **G.** Frequency of alteration veins (5 = >20/cm). **H.** Intensity of cataclastic fabrics (5 = cataclasite). **I.** Magnetic inclination deduced from core samples that have been demagnetized to remove drilling overprint.

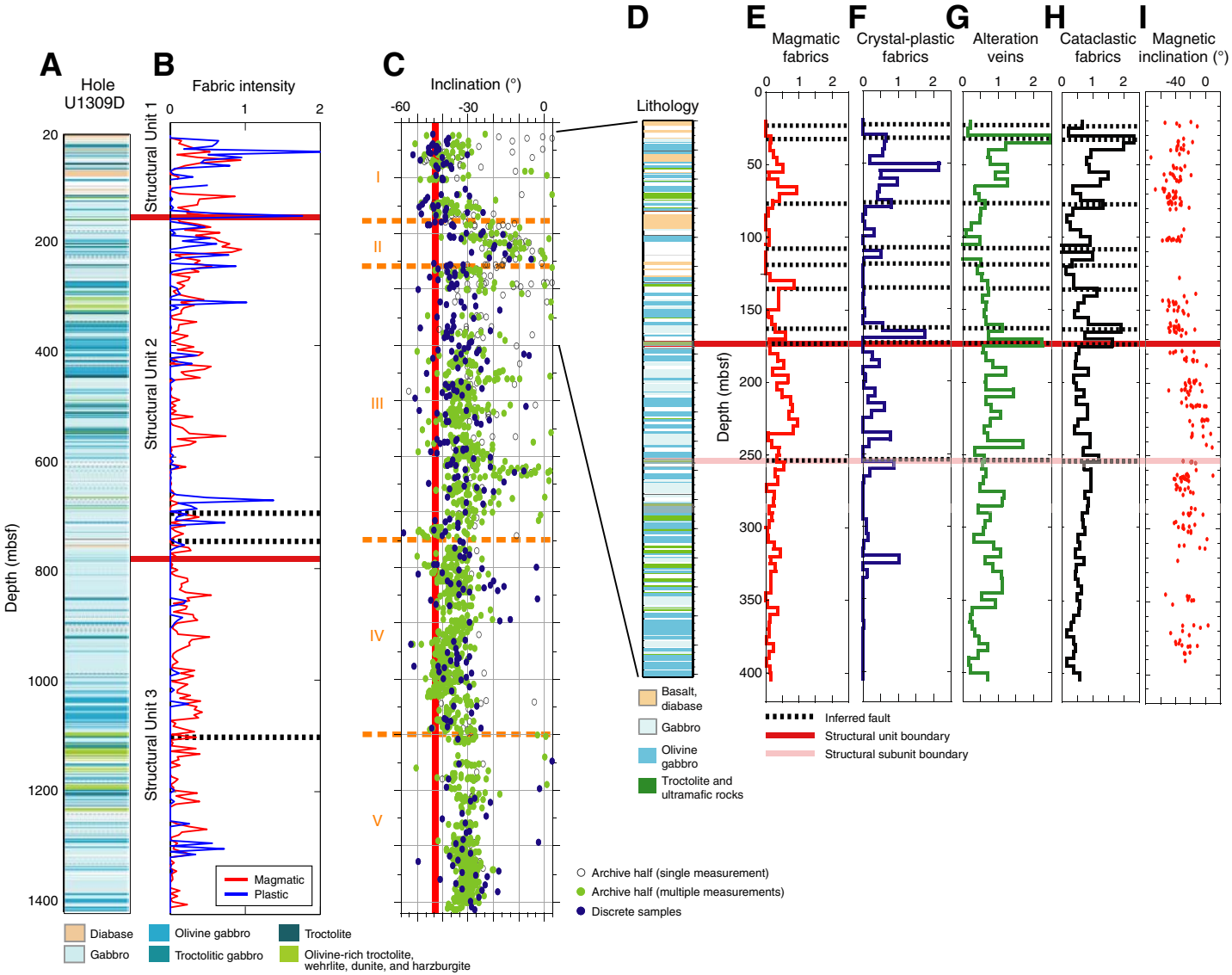

Figure F28. Section of moderately dipping, reverse sense zone of cataclasis at 760 mbsf (interval 305-U1309D-152R-1, 1–22 cm). The zone is overprinted by greenschist-facies mineralogy.

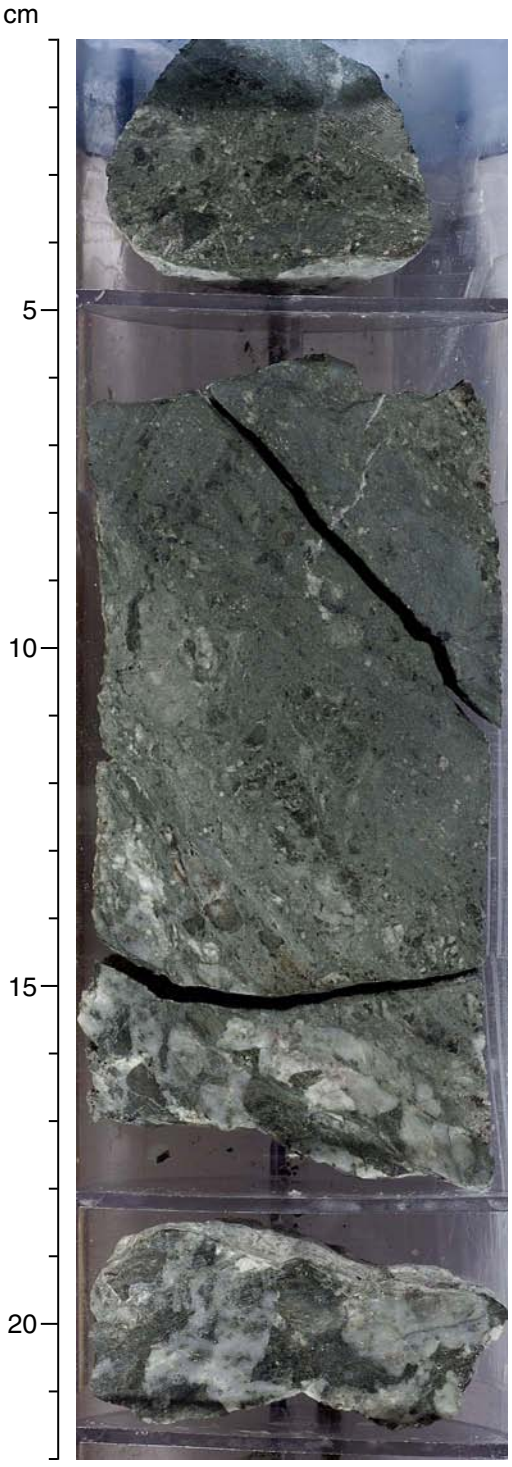

Figure F29. Downhole variation in magnetic properties and relationship to lithology and alteration. **A.** Lithology. **B.** MST magnetic susceptibility. **C.** Serpentinization foliation intensity measured by the structural team illustrates regions where degree of serpentinization is high.

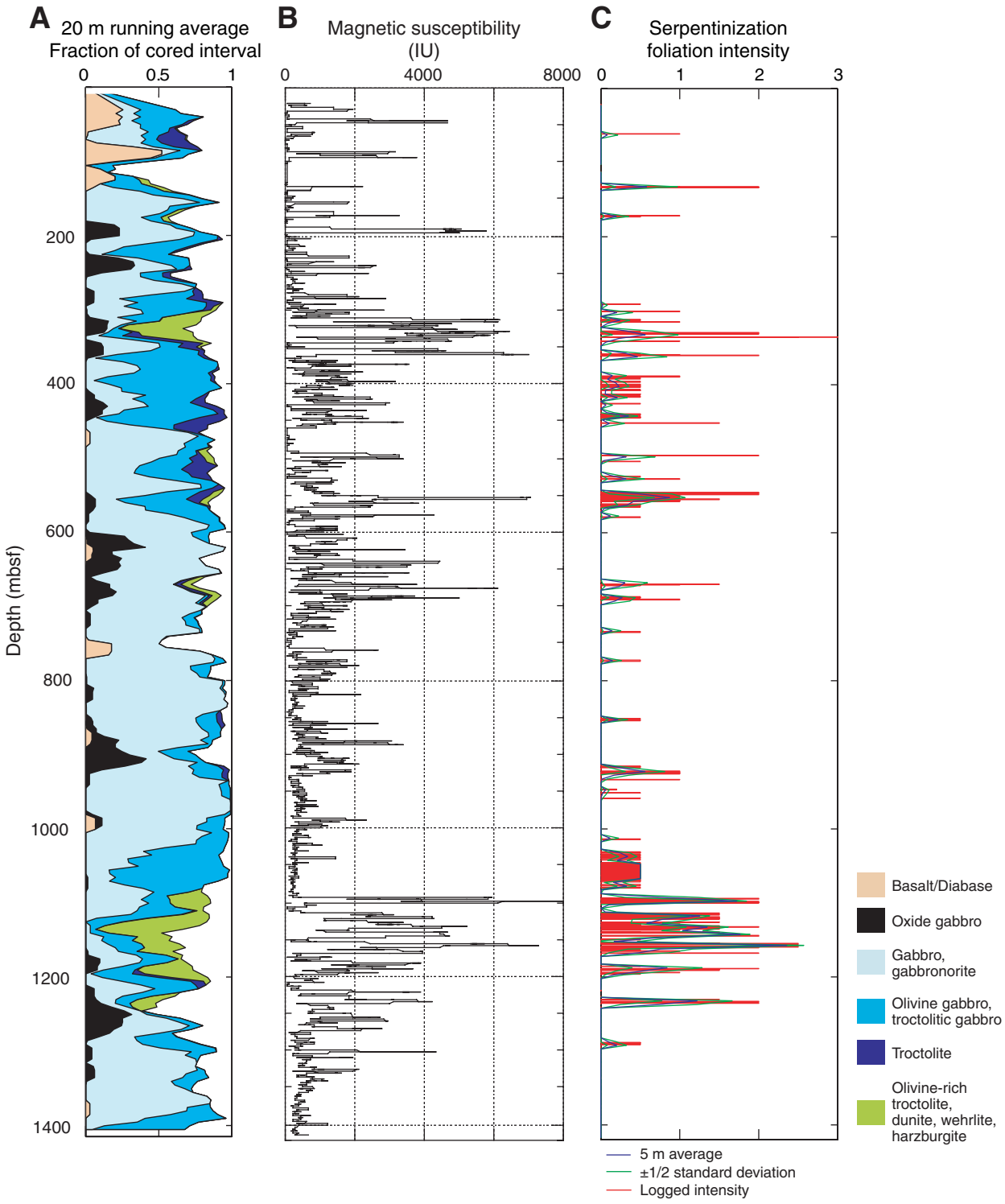

Figure F30. Demagnetization results from two diabase intervals illustrating the difficulty of isolating stable remanence directions in this lithology. In some intervals, a high-stability reversed polarity component is (**A**) readily identified in the discrete sample but (**B**) cannot be isolated from the corresponding point in the archive half. In other intervals, a high-stability reversed component is isolated in both (**C**) discrete sample and (**D**) archive-half data, but this only represents a small fraction of the natural remanent magnetization (NRM). Open circles = projections of the remanence onto the north-south vertical plane, solid circles = projections of the remanence onto the horizontal plane.

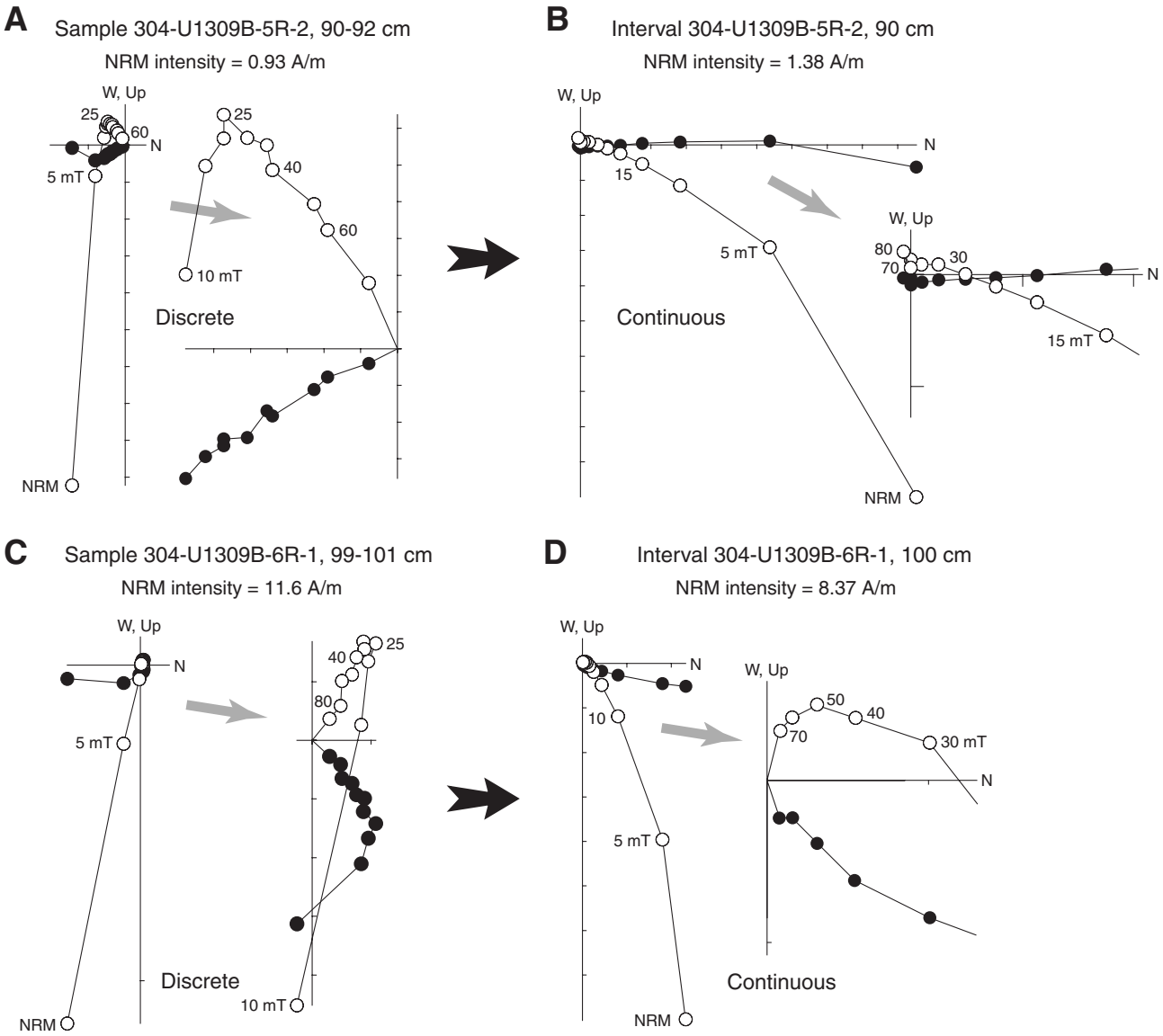

Figure F31. Downhole variations in physical properties in Hole U1309D. **A.** Lithology. **B.** Bulk density of core samples. Data from Expedition 304 are not color-coded based on lithology. **C.** *P*-wave velocity of core samples. **D.** Bulk density measured by logging. **E.** *P*-wave velocity measured by logging. **F.** Electrical resistivity measured by the Dual Laterolog borehole tool.

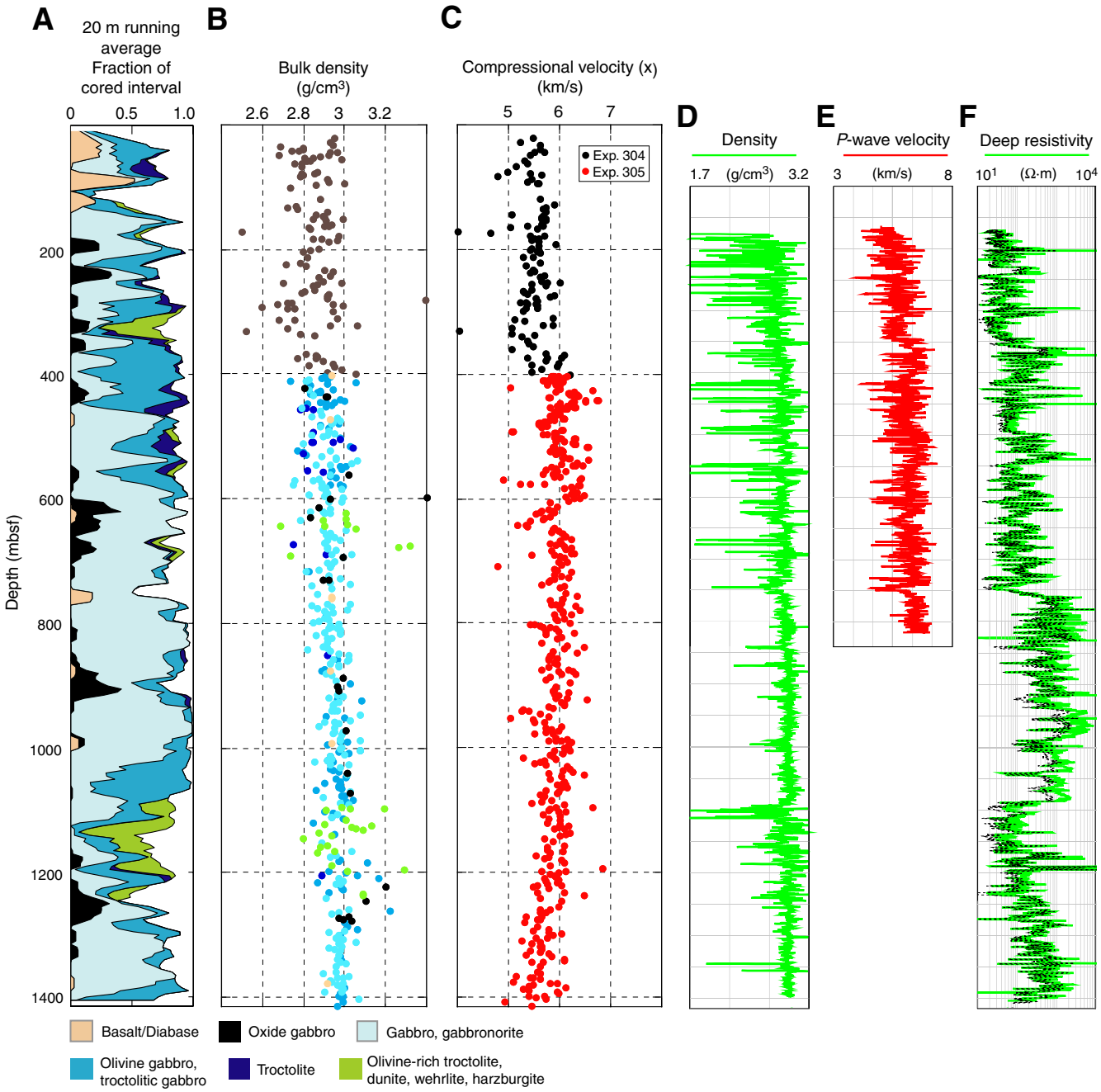

Figure F32. Synthetic seismogram model derived from Hole U1309D logging measurements and comparison to a section of MCS reflection Line Meg-4. **A.** Two-way traveltime-to-depth based on VSP check shot data to 750 mbsf and an assumed value at 1415 mbsf. **B.** Conversion of logging *P*-wave velocity to traveltime at depth. **C.** Logging bulk density. **D.** Time-depth scales. **E.** Reflectivity model derived from data from B and C with bottom velocity value assumed. RC = reflectivity coefficient, which indicates impedance contrast. **F.** Wavelet that is convolved with reflectivity model to calculate synthetic seismogram. **G.** Resulting synthetic seismogram. **H.** Synthetic seismogram trace overlain on section of MCS Line Meg-4 at projected location of Hole U1309D. SP = shotpoint.

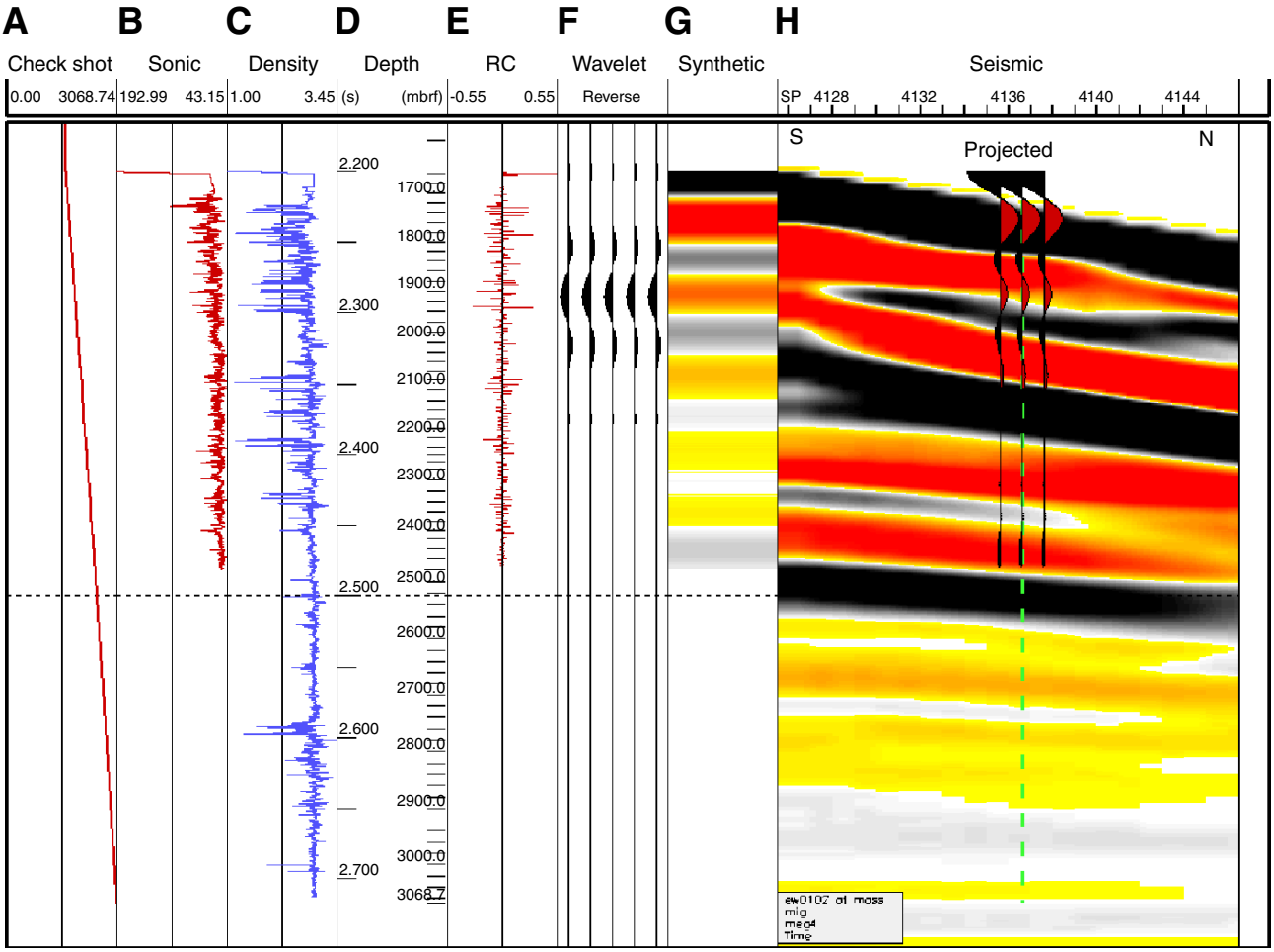

Figure F33. Downhole variation of vein mineralogy plotted with running average of lithology. The overall downcore distribution of veins is relatively homogeneous. Except for a possible occurrence shallow in the hole (not confirmed by XRD or thin section), zeolites first appear near 700 mbsf and then increase regularly to the bottom of the hole. Secondary sulfide minerals are most common in the upper 400 m of Hole U1309D.

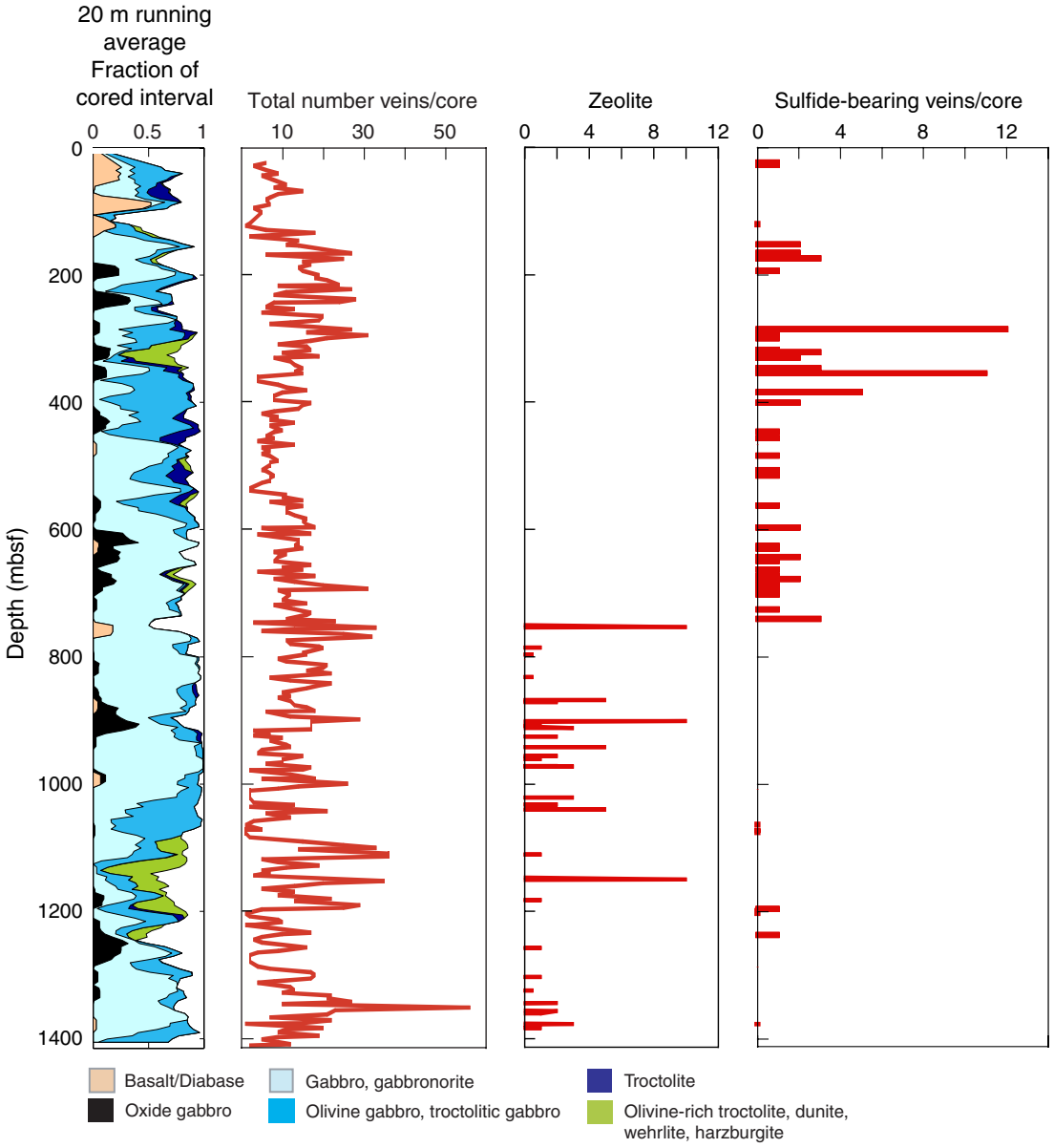

Figure F34. Temperature recorded by the TAP tool. Increase in borehole temperature with time can be seen in downhole versus uphole logging runs and between the main and repeat logging passes. Dashed lines indicate the location of consistent dips in temperature, the lower two of which are located where a fault zone is inferred to occur.

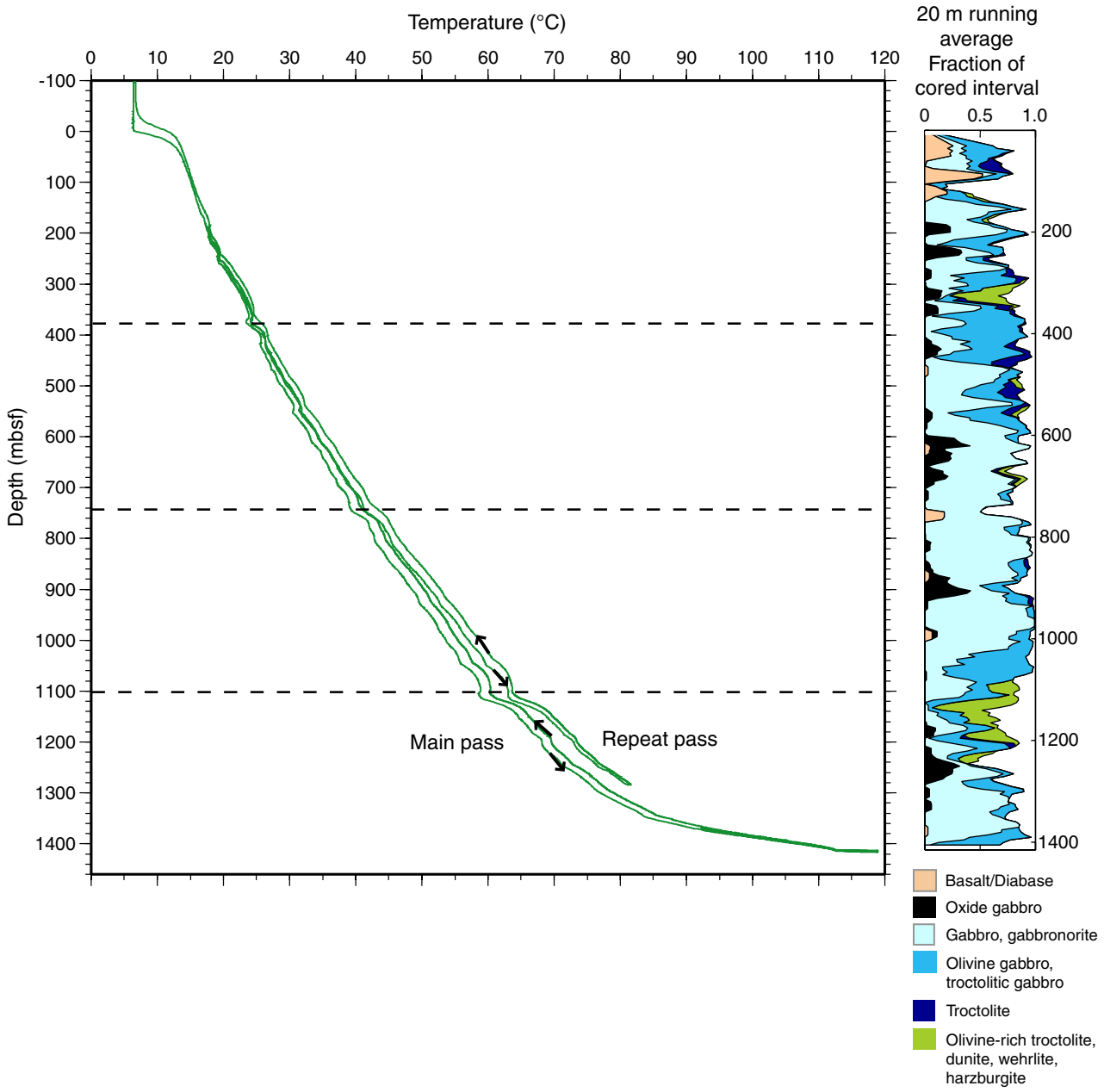

Figure F35. Comparative stratigraphy of Holes U1309B and U1309D, 20–132 mbsf. Core numbers are in red; groups of associated units are labeled igneous rock.

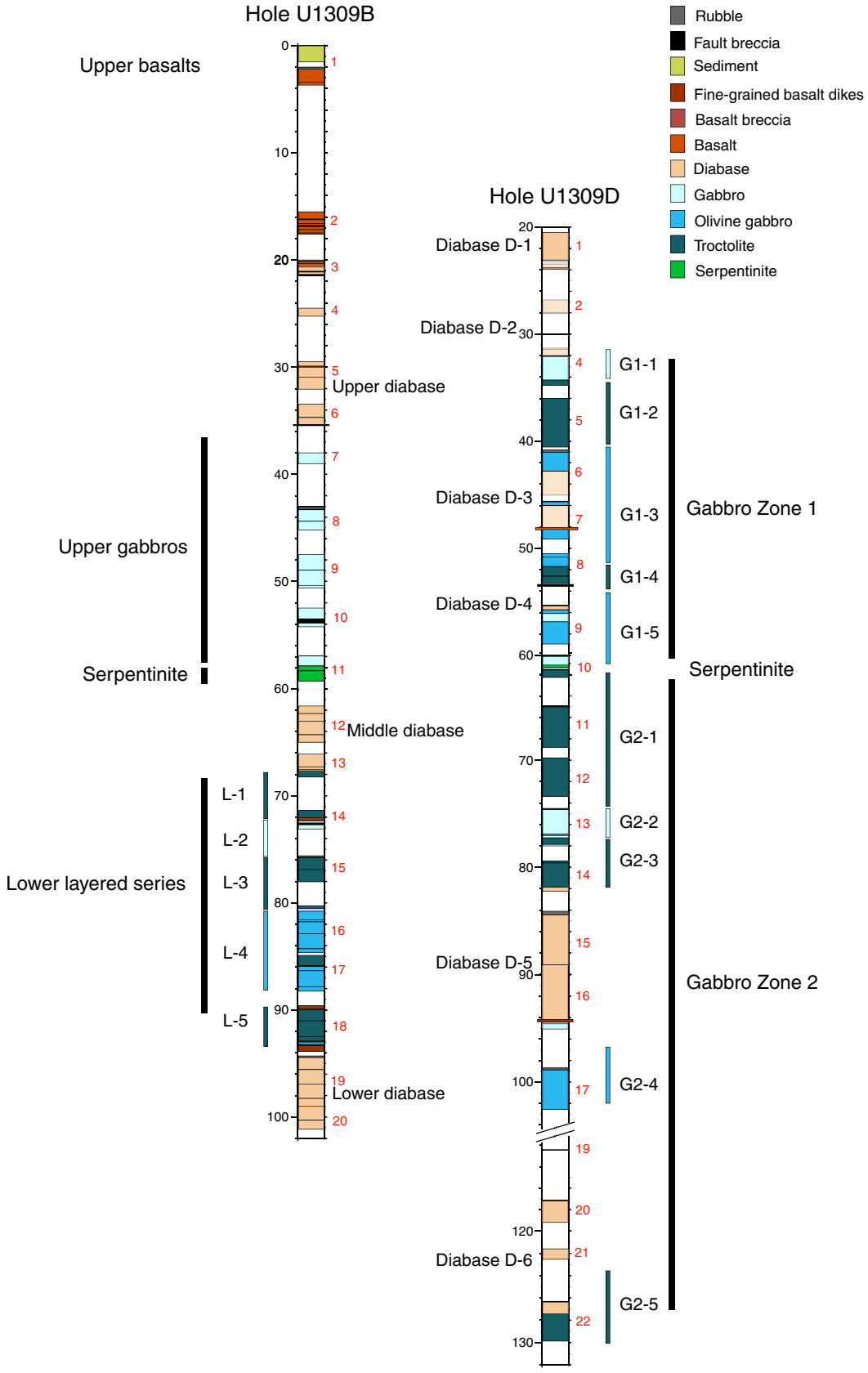

Figure F36. Igneous contact in Unit 10. Note the sharp contact, the downward increase in grain size over the 10 cm interval below the contact, and the upward increase in size and abundance of plagioclase phenocrysts (interval 304-U1309B-2R-2, 24–44 cm).

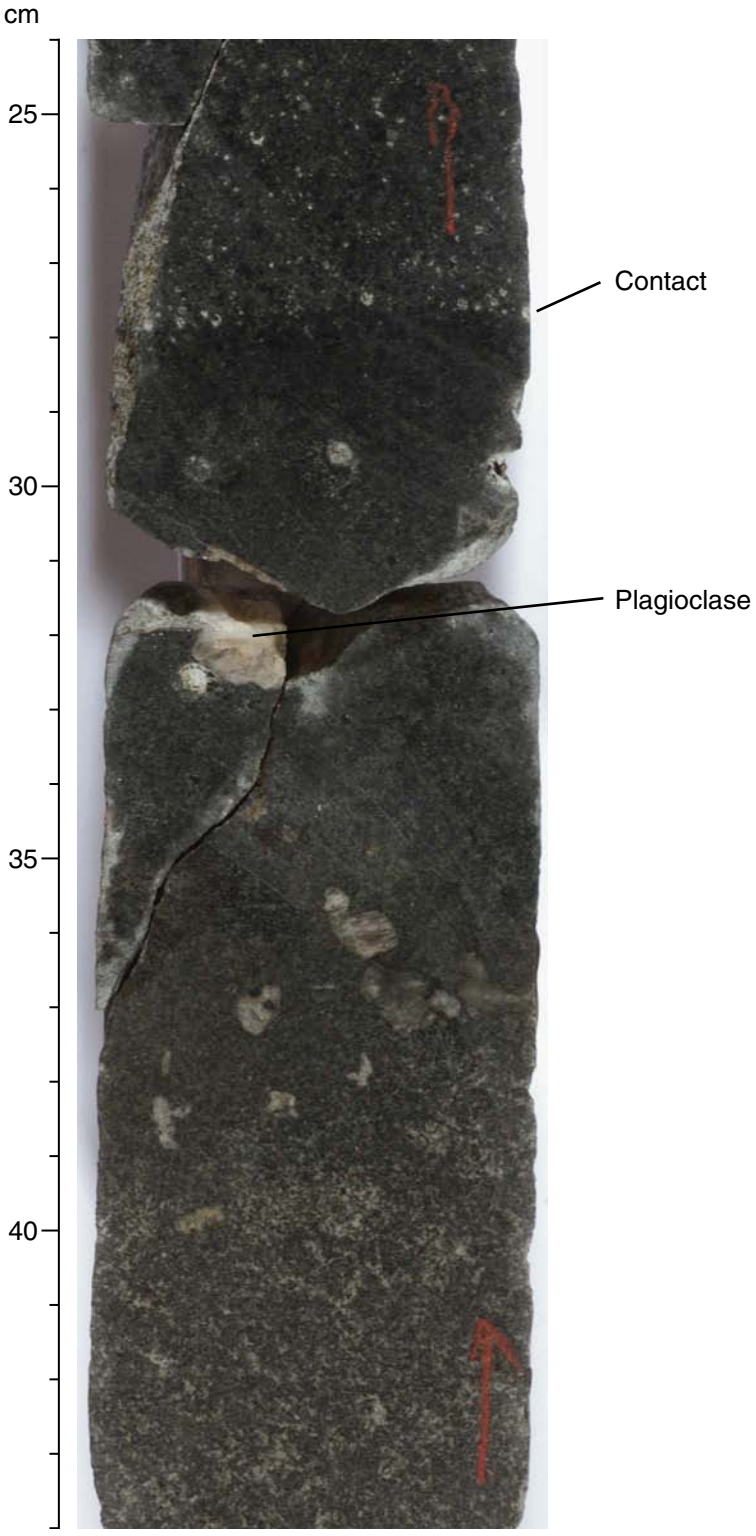

Figure F37. Dipping contact (indicated by arrows) between fine-grained basalt and basaltic breccia of Unit 2 (interval 304-U1309B-4R-1, 31–41 cm).

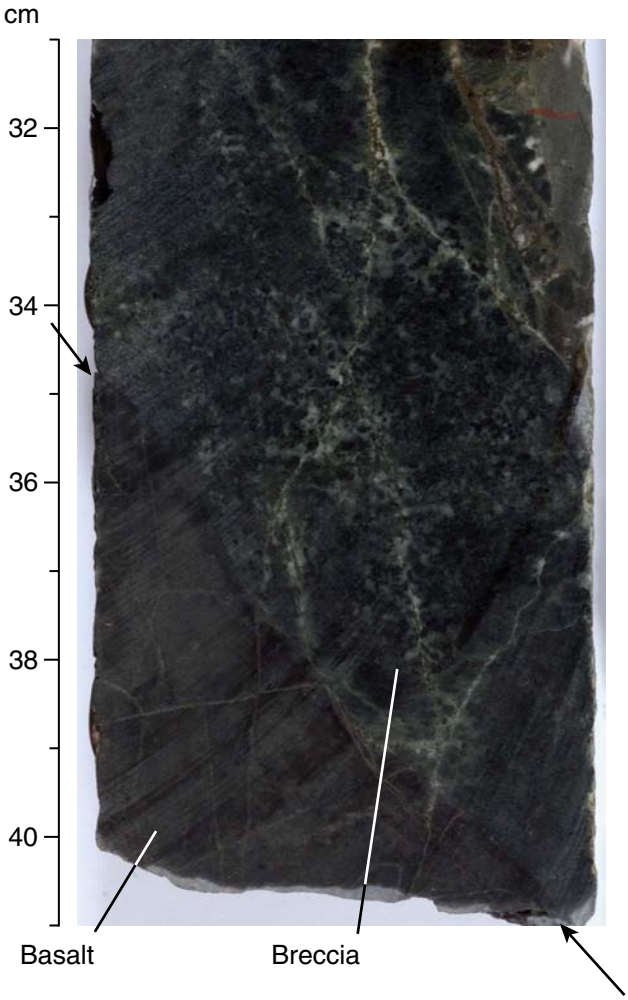

Figure F38. Trains of olivine phenocrysts (indicated by arrows) from the upper diabase that have been completely altered to friable aggregates of actinolite with minor chlorite (interval 304-U1309B-5R-1, 71–84 cm).

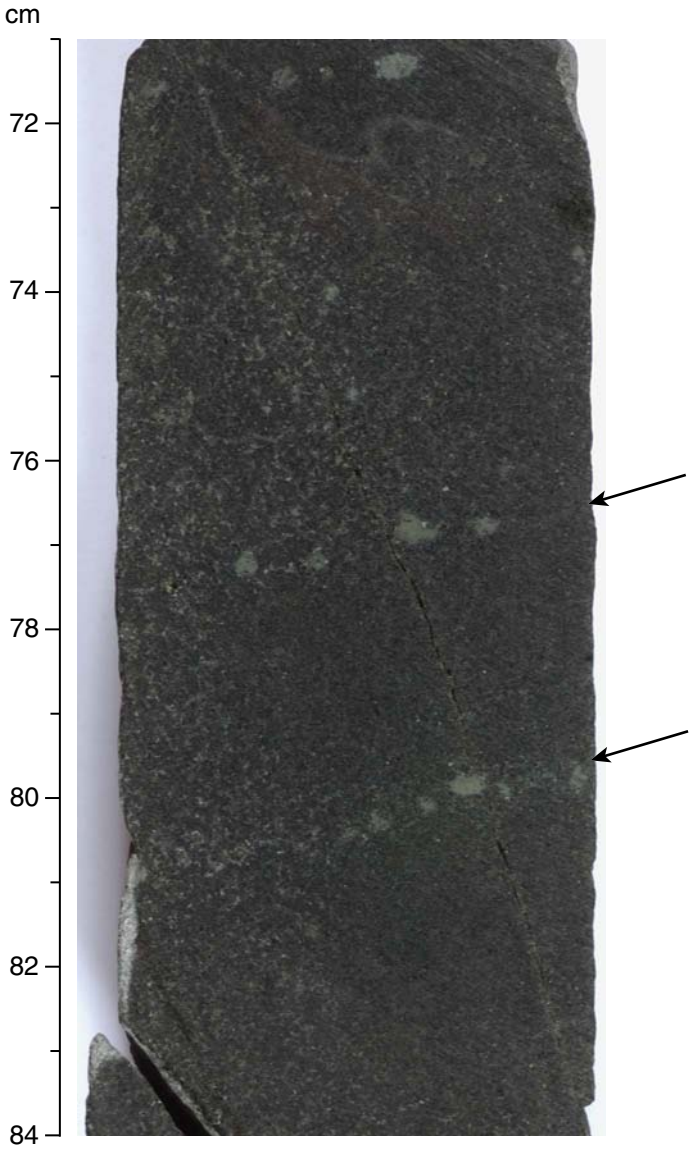

Figure F39. Anorthosite veins in upper gabbro. **A.** Anorthosite impregnating Unit 28 gabbro (interval 304-U1309B-8R-1, 83–90 cm). **B.** Discrete anorthosite vein in Unit 28 gabbro (interval 304-U1309B-8R-1, 93–100 cm).

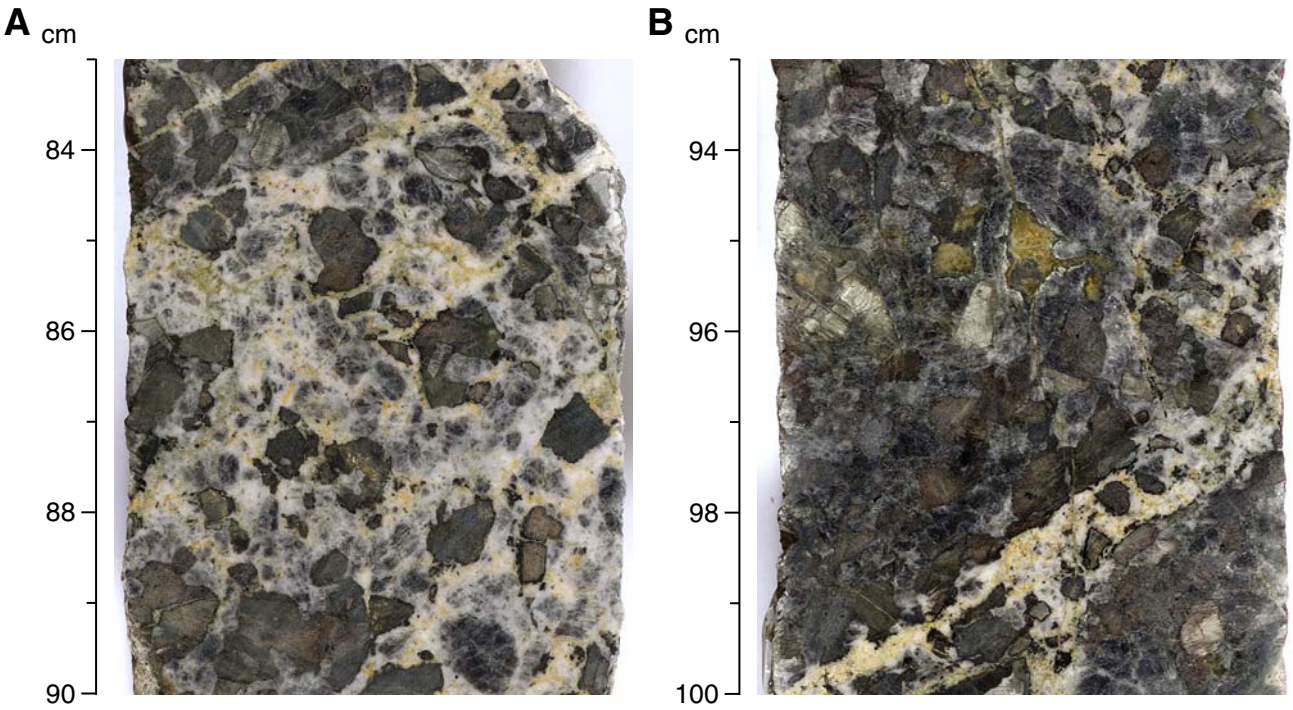

Figure F40. Magmatic layering in Unit 29 of the upper gabbros. Olivine gabbro at the top is richer in plagioclase than troctolite layer on the bottom, which is characterized by green altered olivine with dark green (black) chlorite rims (interval 304-U1309B-10R-1, 113–121 cm).

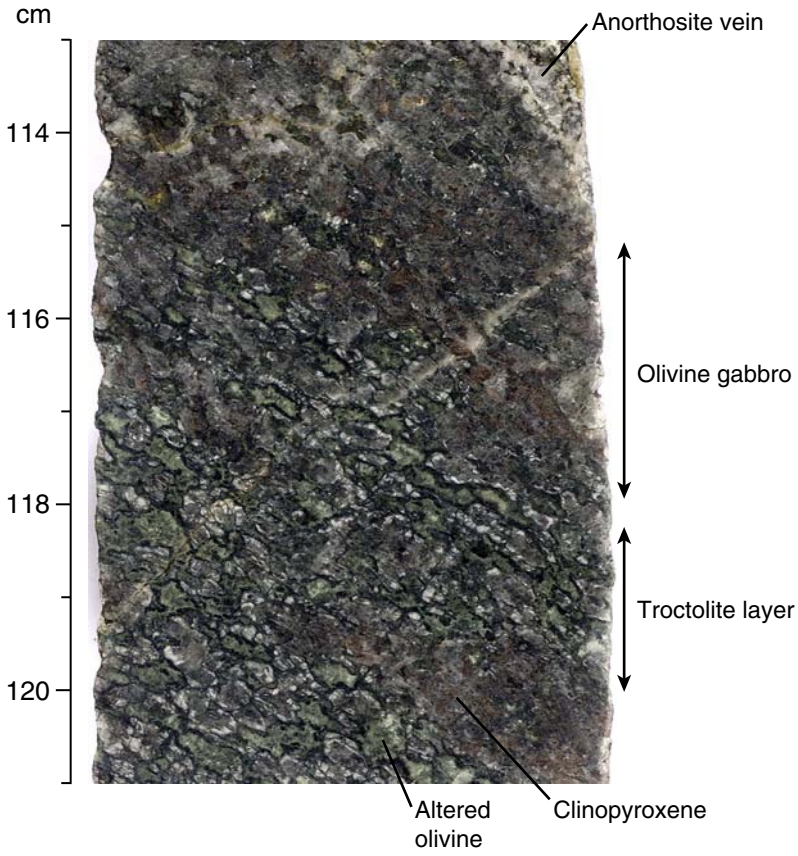

Figure F41. Core 304-U1309B-11R. **A.** Contact (indicated by arrows) between coarse-grained gabbro (Unit 31) and harzburgite (Unit 32) (interval 304-U1309B-11R-1, 86–99 cm). Note the talc-tremolite band between the two rock types and the variations in style of serpentinization. **B.** Gabbro dike crosscutting harzburgite (interval 304-U1309B-11R-2, 0–15 cm). Note the serpentine-filled cracks cutting the hydrothermally altered gabbro dike and the change in extent of serpentinization adjacent to the dike. **C.** Serpentine vein cutting protogranular harzburgite from the bottom (interval 304-U1309B-11R-2, 86–94 cm). Coarse brownish spinel grains within the white ellipse are visible in hand specimen.

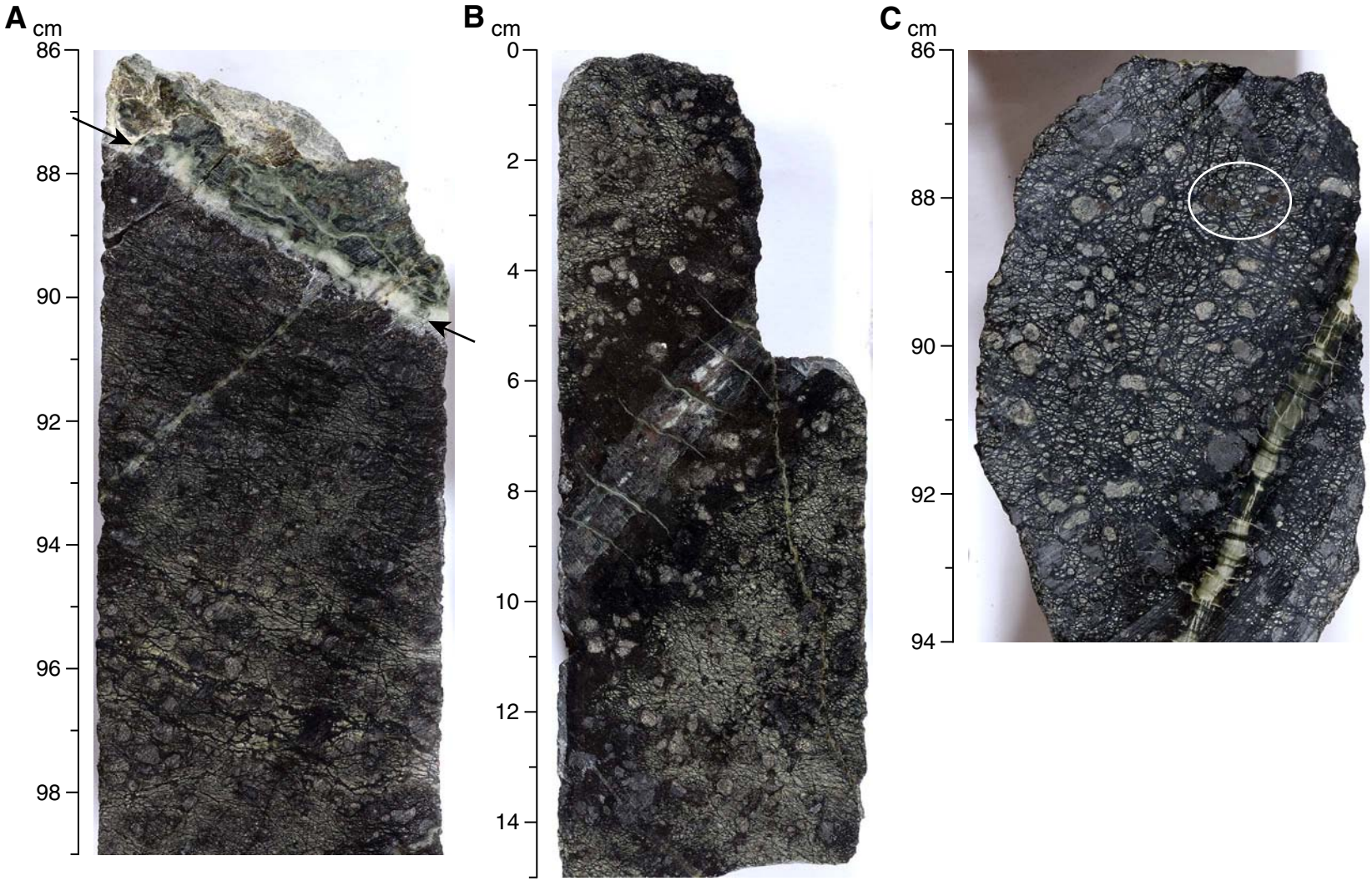

Figure F42. Sample 304-U1309B-11R-1, 98–100 cm. **A.** Talc band in contact with peridotite and penetrating along cracks (cross-polarized light; field of view [FOV] = 5 mm). **B.** Deformed clinopyroxene with bent lamellae surrounded by recrystallized olivine grains (cross-polarized light; FOV = 2.5 mm). **C.** Clinopyroxene (cpx) along grain boundaries and cutting a mantle olivine (ol) grain (cross-polarized light; FOV = 2.5 mm). **D.** Altered pyroxene (px) forming an interconnected network (plane-polarized light; FOV = 5 mm). **E.** Fresh clinopyroxene corroding an altered orthopyroxene (cross-polarized light; FOV = 5 mm).

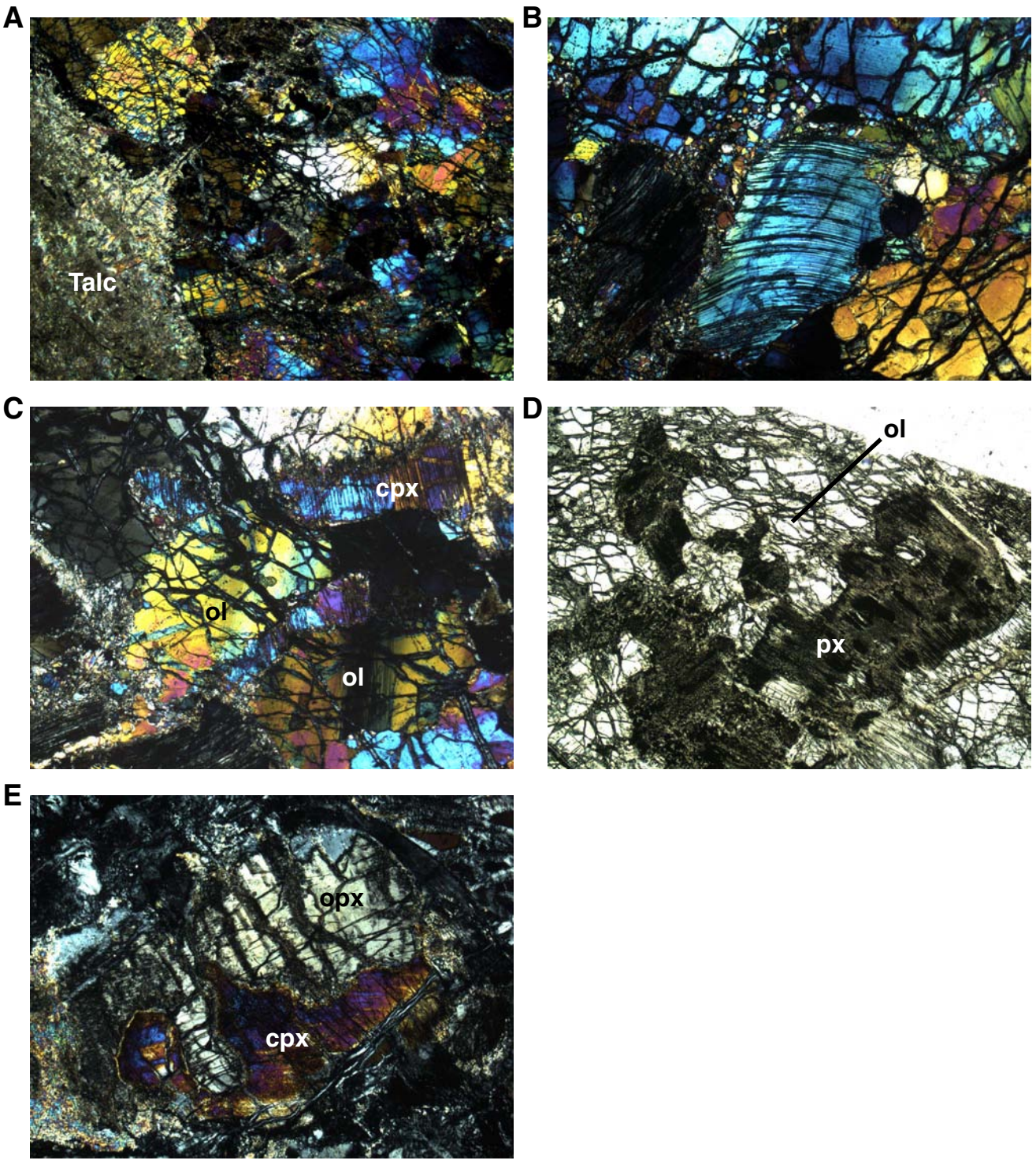

Figure F43. Fine-grained black microcrystalline basalt intruding troctolitic gabbro at the top of lower gabbro sequence (interval 304-U1309B-13R-2 [Piece 1, 1–11 cm]).

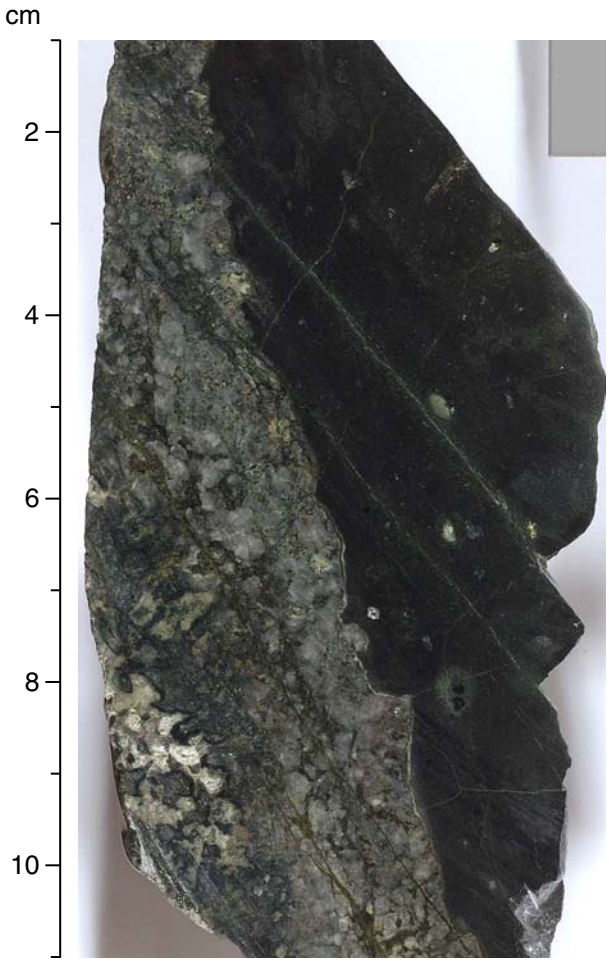

Figure F44. Narrow basalt dike intruding coarse-grained lower gabbro 30 cm above bottom boundary of lower gabbro (interval 304-U1309B-18R-3, 48–56 cm). Shiny black area is not glass. cpx = clinopyroxene.

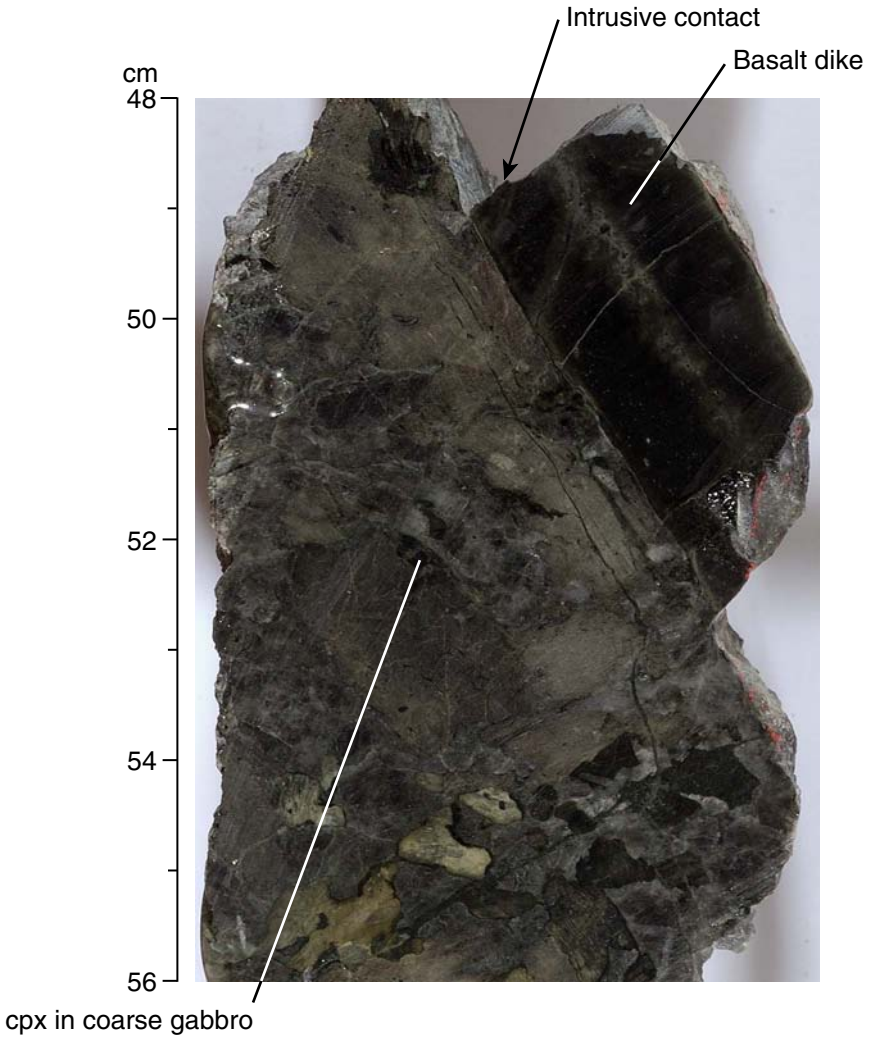

Figure F45. Olivine gabbro from lower gabbro sequence showing mottled pattern of clinopyroxene-rich (red-brown tones) and troctolitic domains (green-black tones) (interval 304-U1309B-17R-2, 14–28 cm).

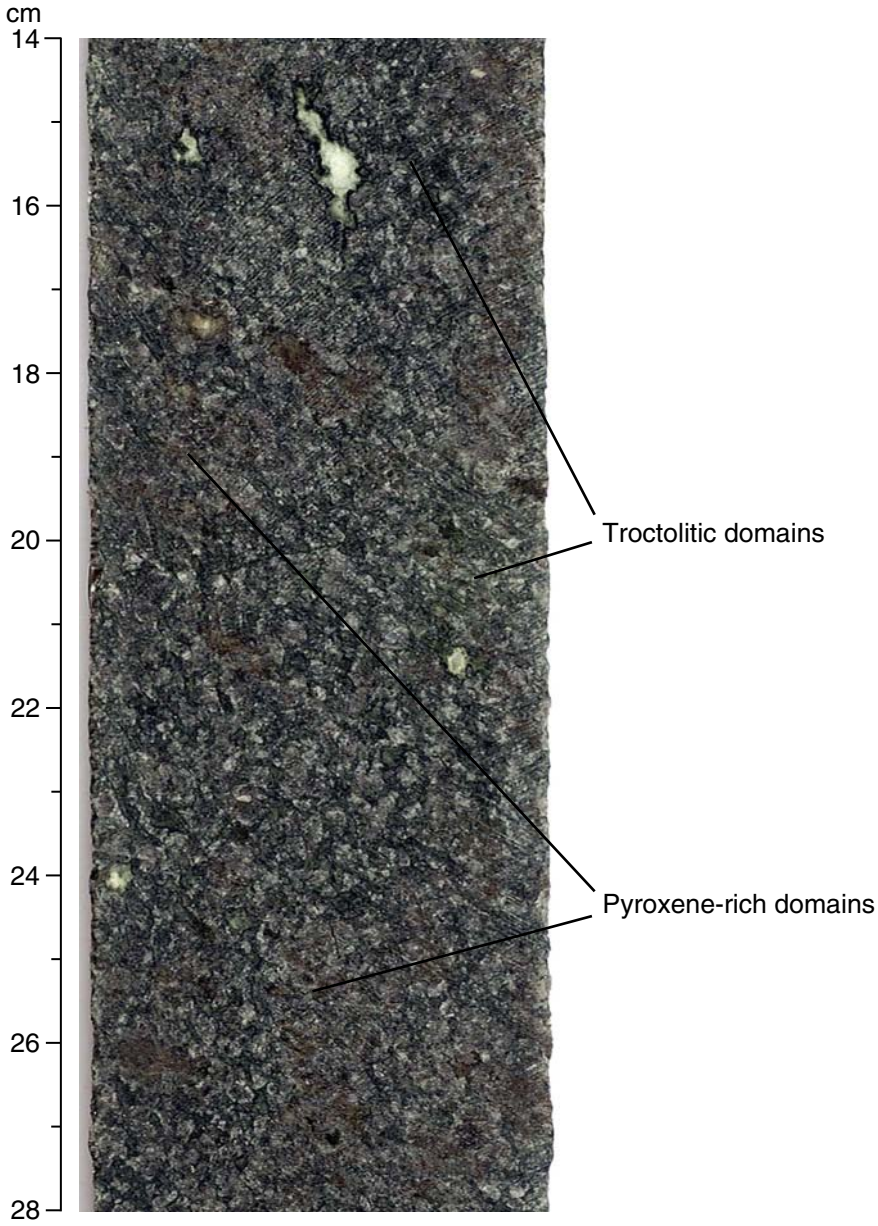

Figure F46. Troctolite layer from lower gabbro showing well-developed corona mesh texture (interval 304-U1309B-15R-2, 53–64 cm). Lighter green areas are actinolite after relict clinopyroxene. Original grain boundaries are outlined by dark green (appears black) chlorite.

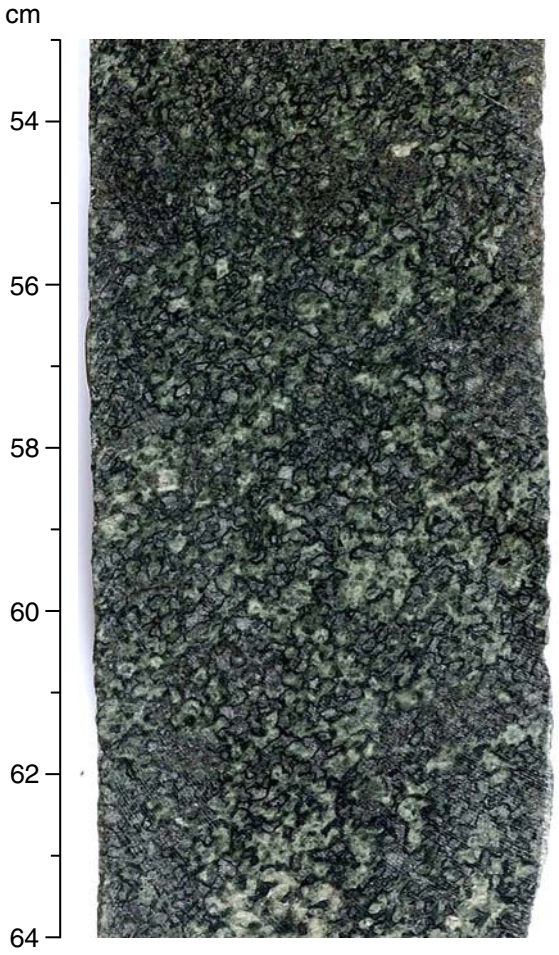

Figure F47. Primary clinopyroxene (P-cpx) replaced by clear secondary clinopyroxene (S-cpx) with more widely spaced cleavages (Sample **304-U1309B-16R-2 [Piece 5, 26–29 cm]**) (plane-polarized light; magnification = 2.5×). This texture is very similar to that described in gabbros from Atlantis Bank, Southwest Indian Ridge (Pettigrew, Casey, Miller, et al., 1999; Maeda et al., 2002).

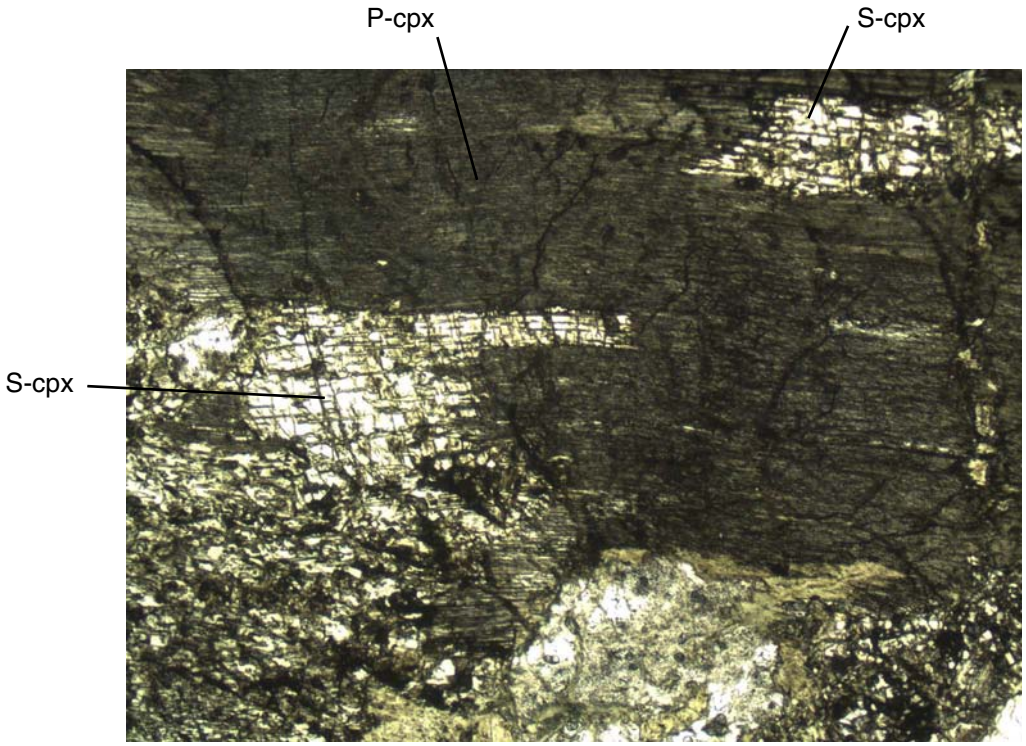

Figure F48. Stratigraphic column for Hole U1309D (Expedition 304). Color bars indicate the extent of, and dominant rock type in, each of the 10 gabbro zones. L = leucocratic intrusions.

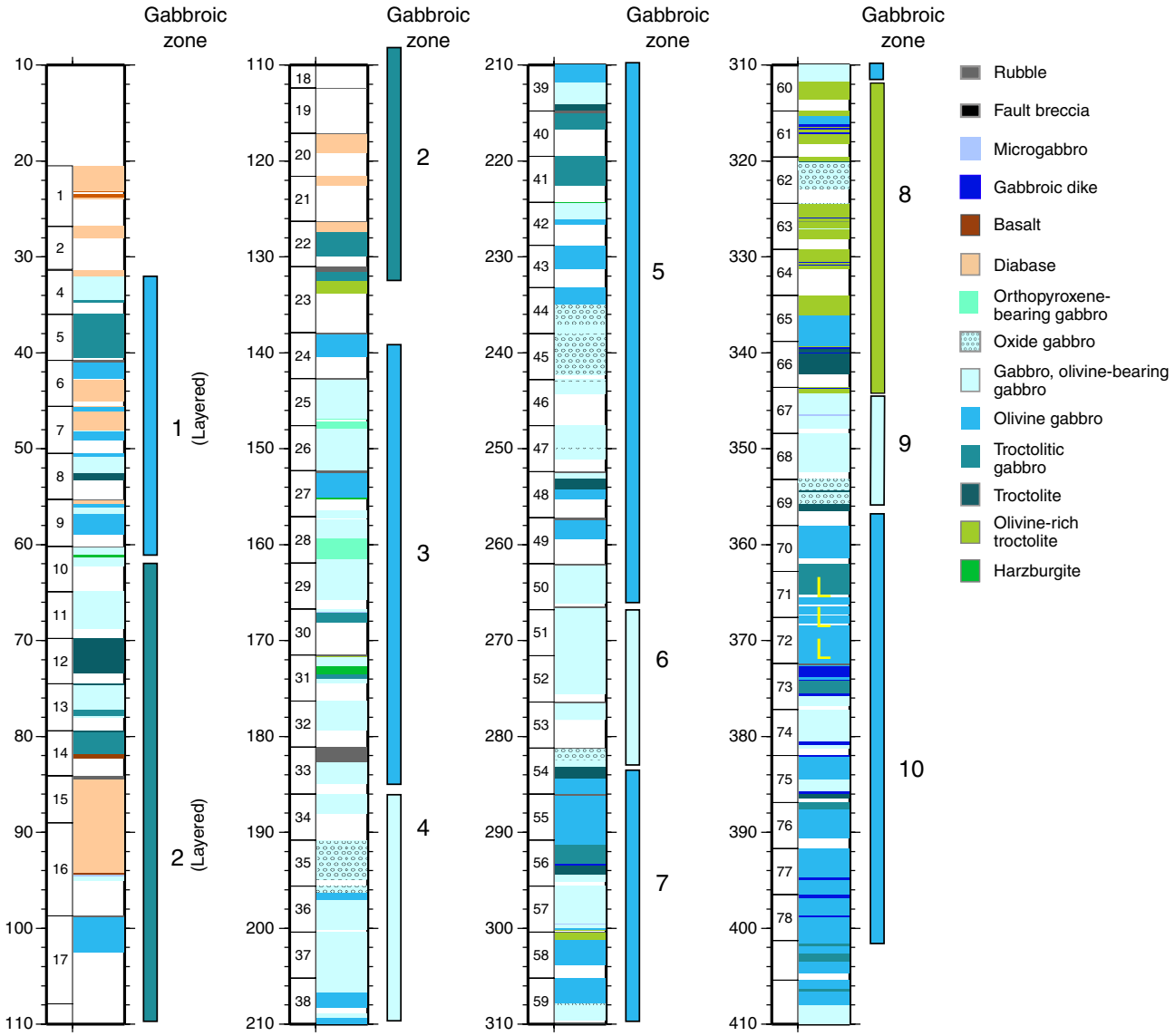

Figure F49. Igneous contact between Diabase D-3 and olivine gabbro (interval 304-U1309D-7R-3, [Piece 3, 9–19 cm]). Also visible are parts of a branching late basalt dike.

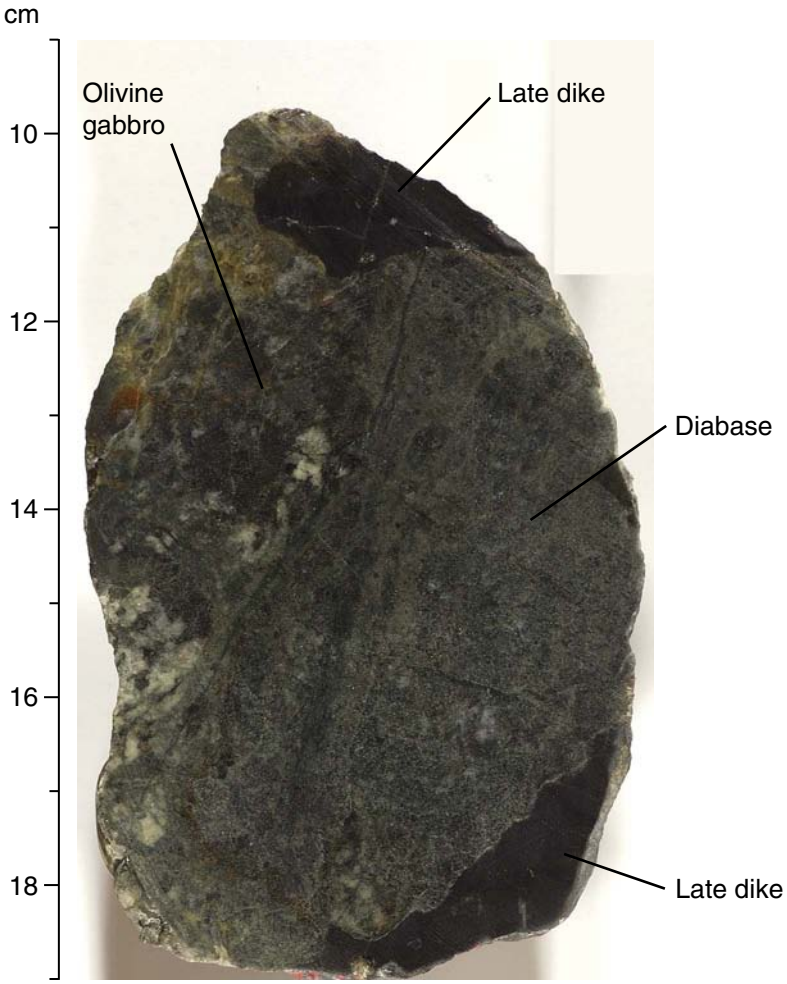

Figure F50. Chilled and brecciated intrusive contact between late basaltic dike and aphanitic basalt at the lower boundary of Diabase D-5 (interval 304-U1309D-16R-4 [Piece 13, 143–147 cm]). The relationship of the aphanitic basalt to the main body of Diabase D-5 is unclear.

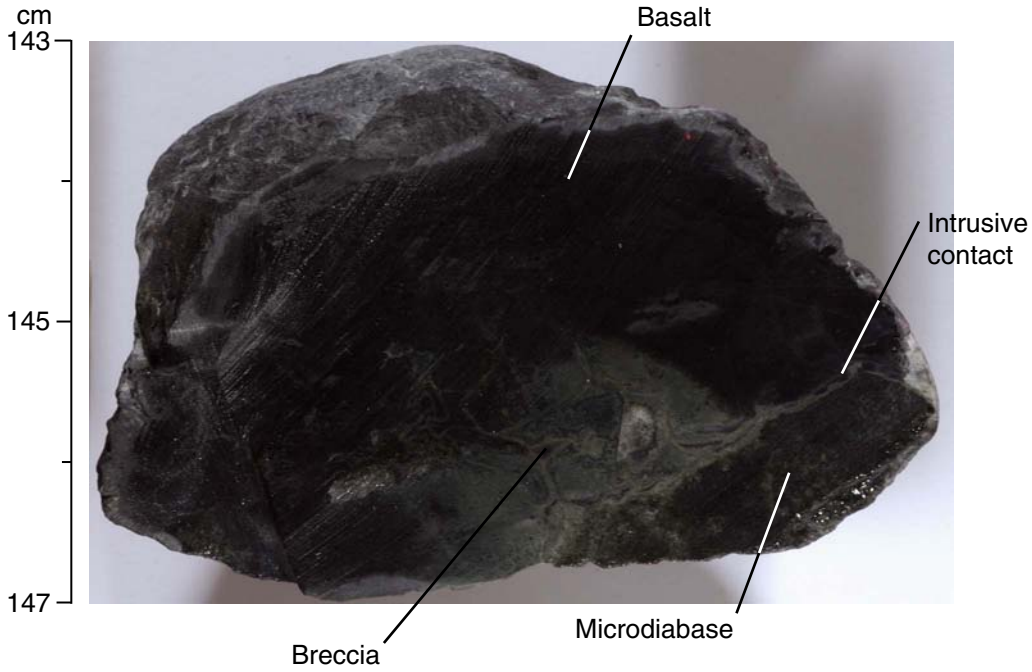

Figure F51. Faulted magmatic contact between troctolite and olivine gabbro in lithologic Zone G1-4 (interval 304-U1309D-8R-2 [Piece 7, 65–78 cm]).

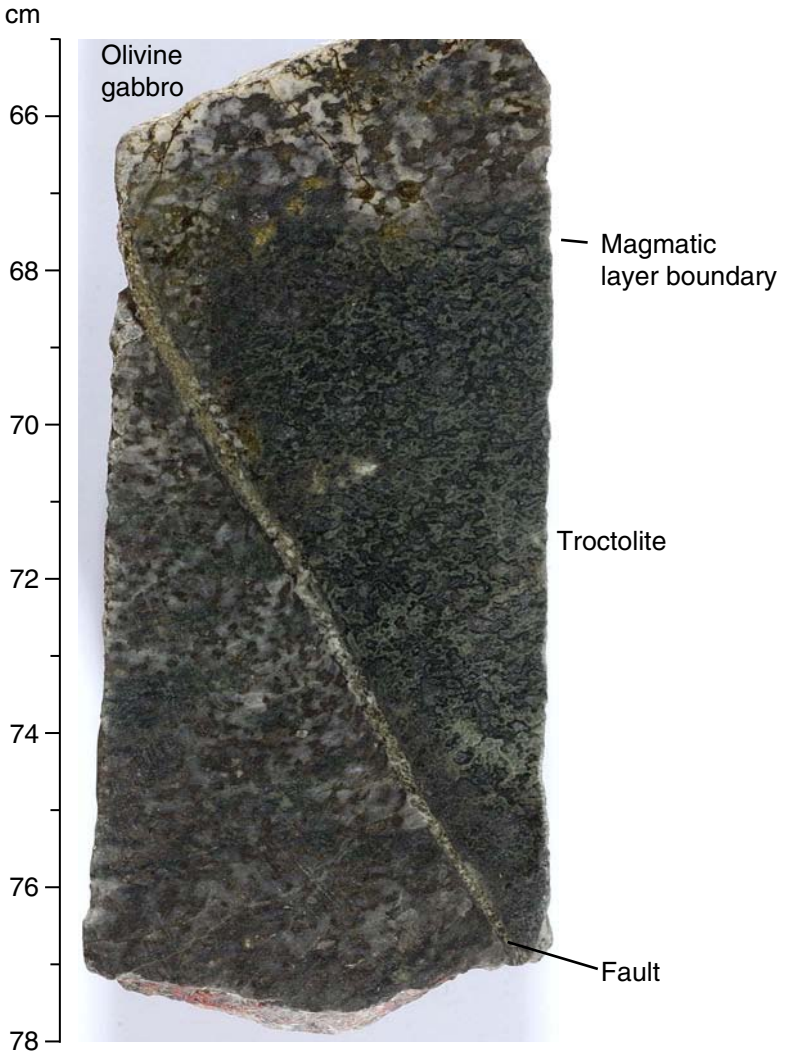

Figure F52. Magmatic layering in lithologic Zone G2-2 in gabbro Zone 2 (interval 304-U1309D-11R-2, 0–20 cm). Note that there are both sharp and gradational layer boundaries. Corona texture diagnostic of troctolitic lithologies at this site forms when olivine is altered to light green actinolite surrounded by dark black/green chlorite.

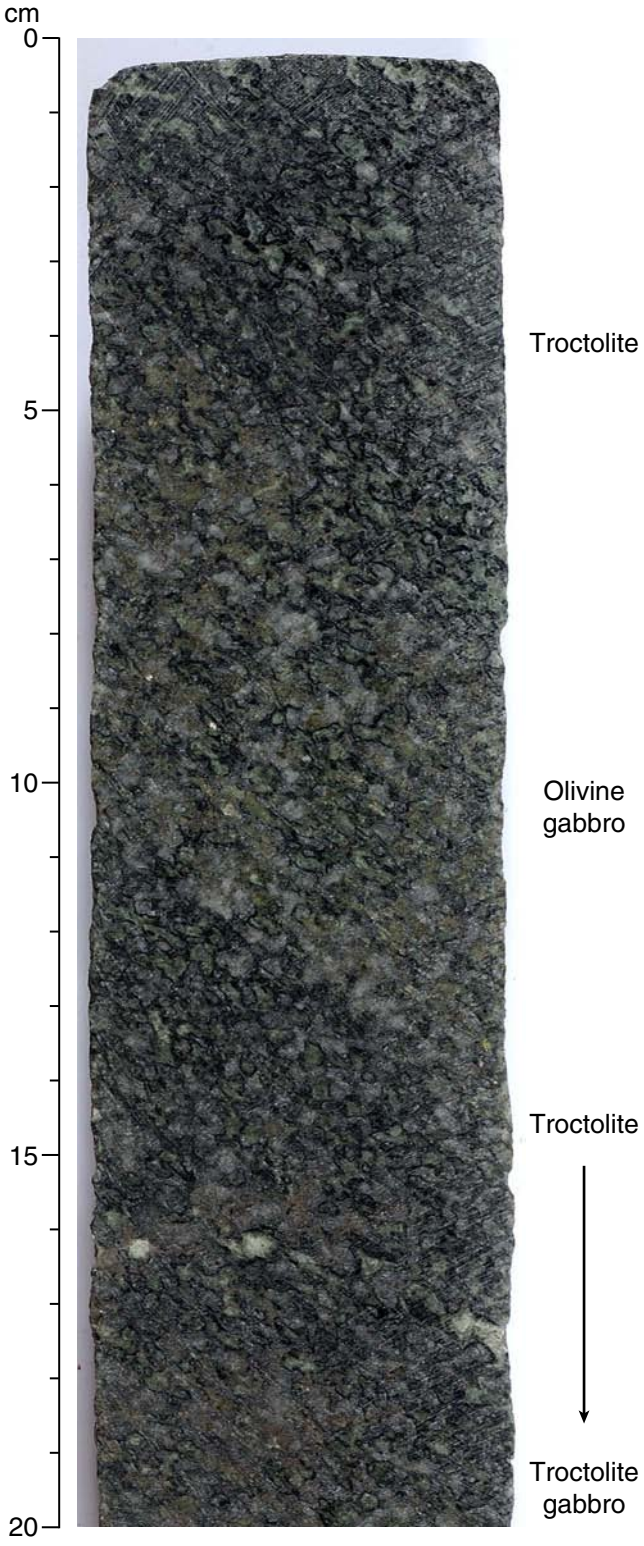

Figure F53. Downhole plot of modal olivine percentages for upper 400 m in Hole U1309D. Black bars = gabbro zone boundaries (Fig. F48), numbers = number of gabbro zone. Arrows = probable within-zone trends. Blue = dominantly gabbros, green = dominantly dunite and olivine-rich troctolite.

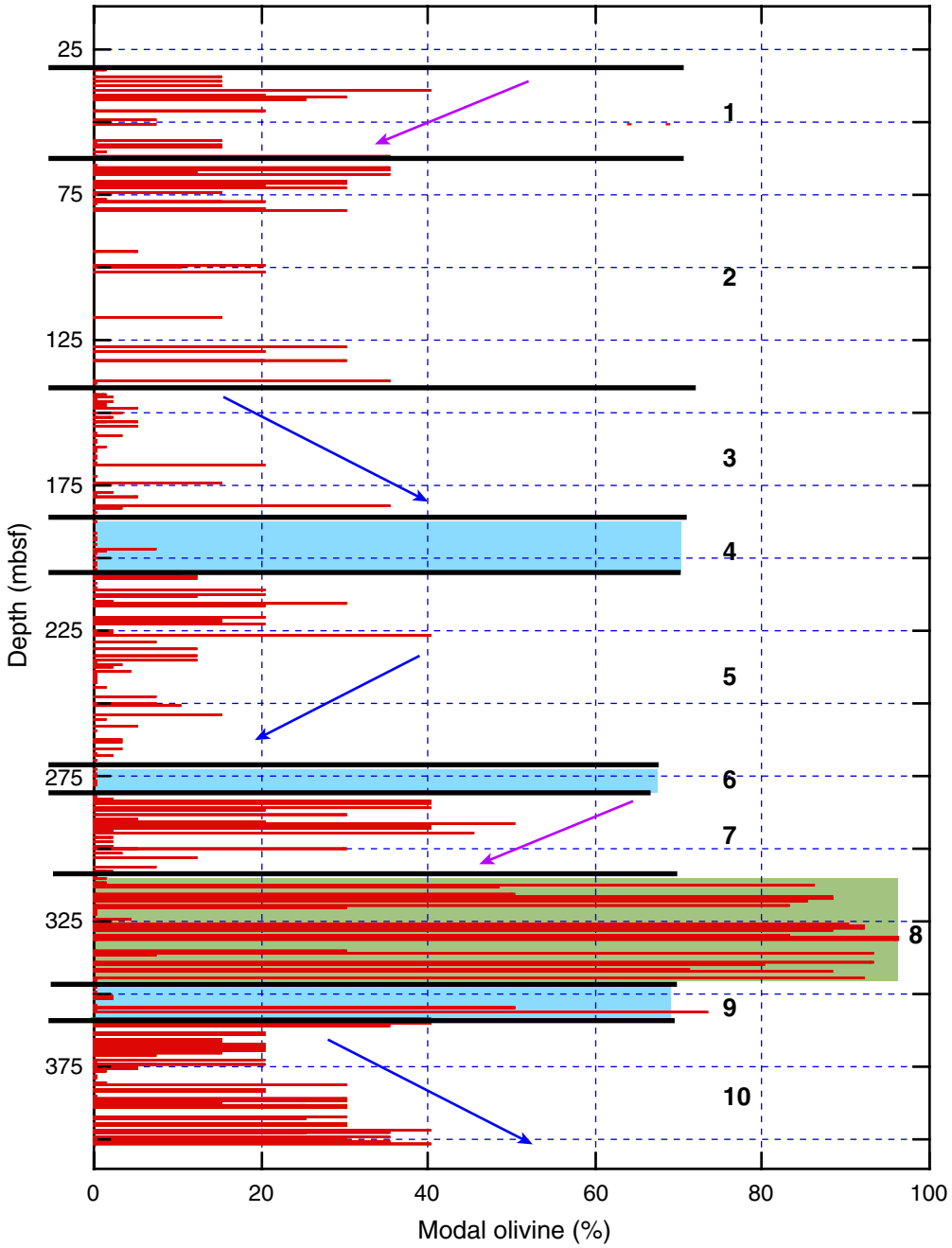

Figure F54. Orthopyroxene-bearing gabbro intruded by a late magmatic leucocratic dike (interval 304-U1309D-25R-2, 115–138 cm).

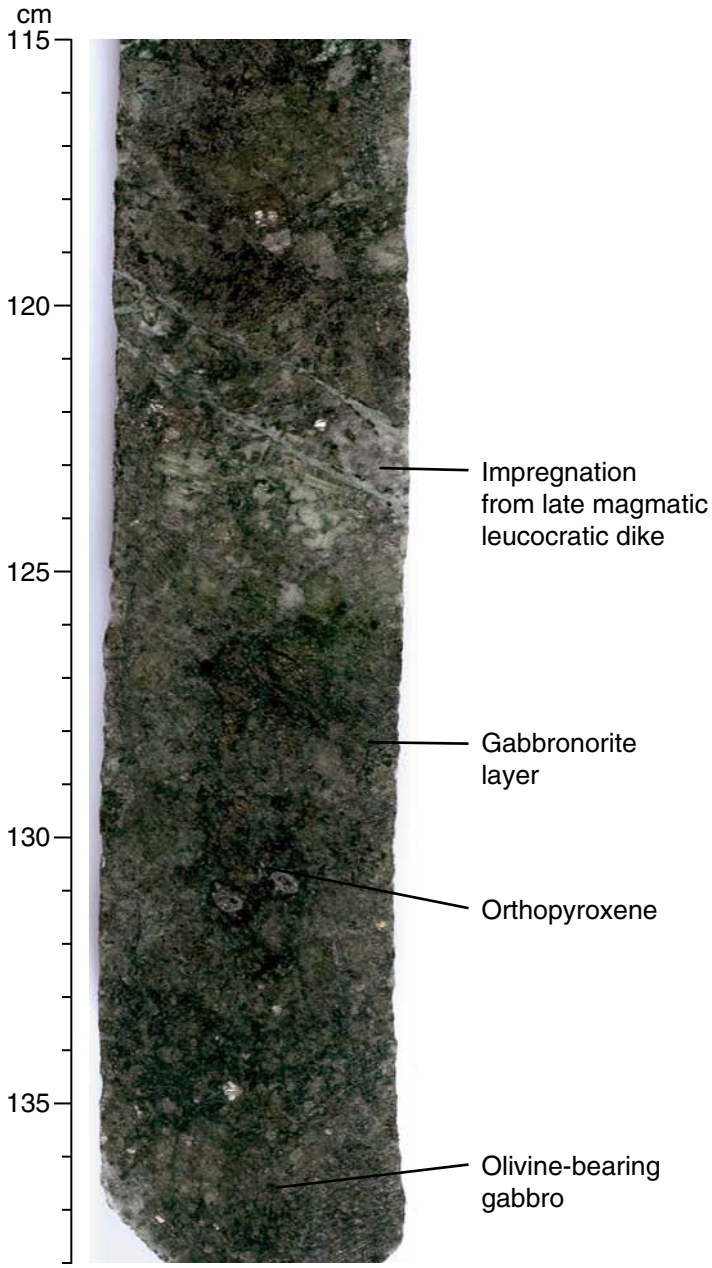

Figure F55. Pegmatitic clinopyroxene oikocryst (interval 304-U1309D-26R-4, 20–38 cm). Note "salt-and-pepper" mottling in matrix.

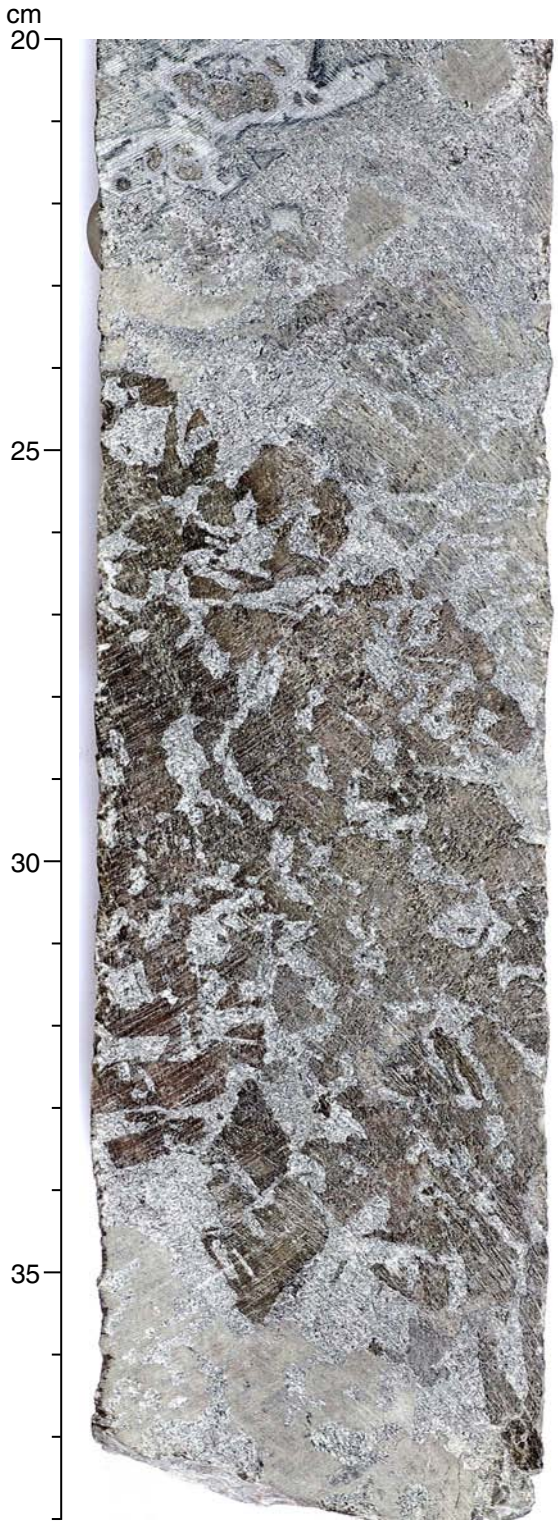

Figure F56. Coarse-grained oxide gabbro ~20 cm from contact with olivine gabbro (interval 304-U1309D-36R-1, 40–58 cm).

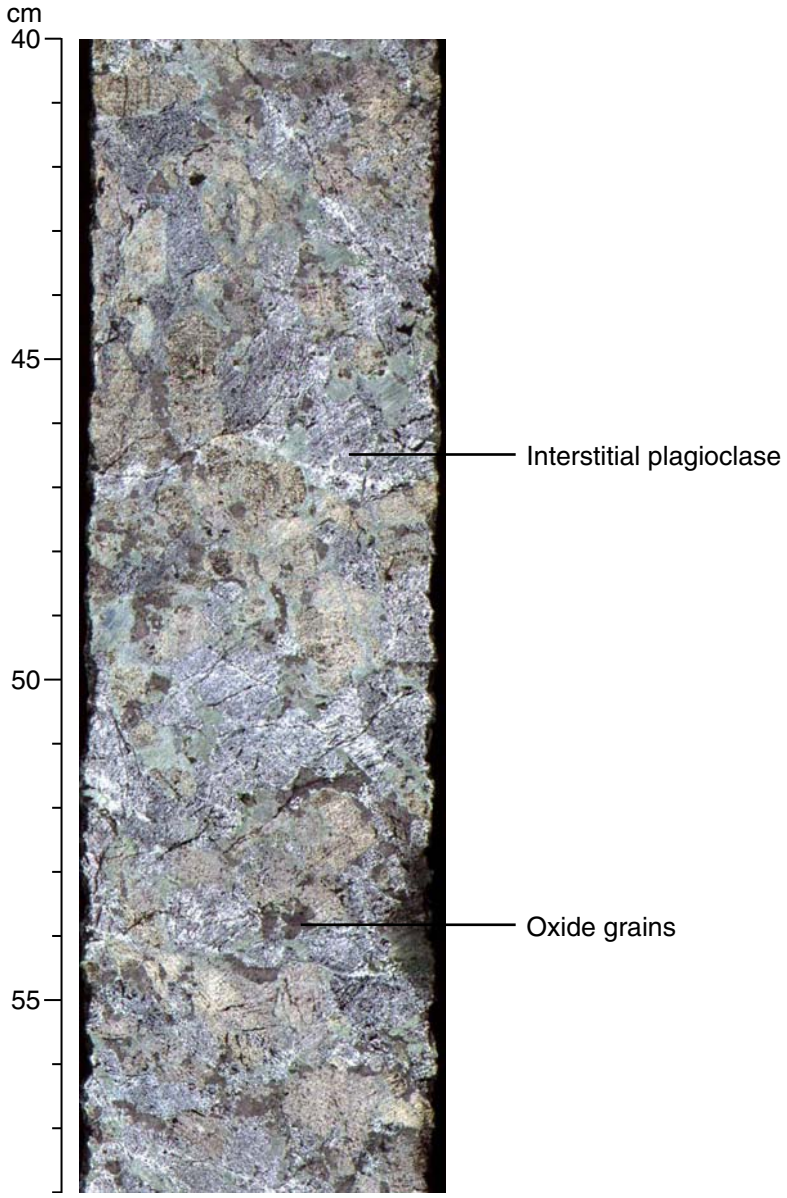

Figure F57. Contact of oxide gabbro with olivine gabbro in plane- and cross-polarized light (Sample **304-U1309D-36R-1, 76–78 cm**) (field of view = 2 cm). A = coarse-grained oxide gabbro, B = medium-grained oxide gabbro contact, C = coarse-grained olivine gabbro. Arrows indicate upcore direction.

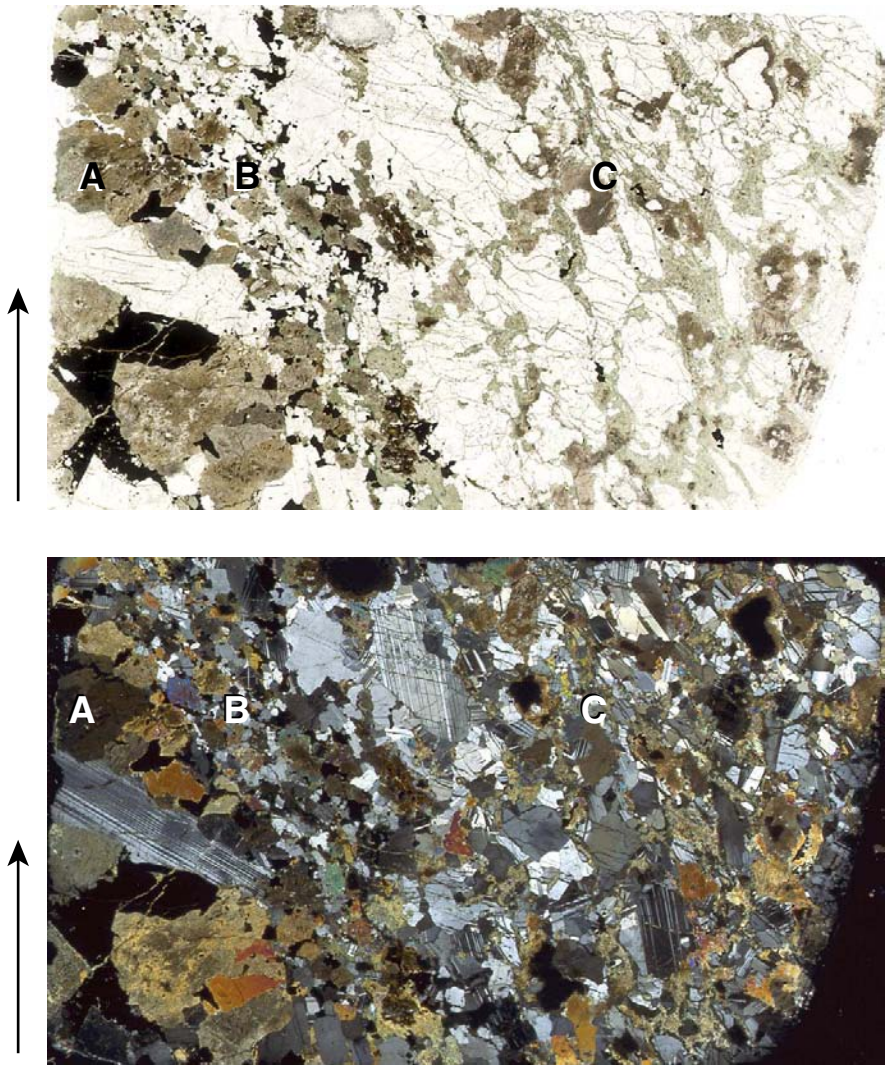

Figure F58. Intrusive contact between gabbro and olivine gabbro, with contact intersected by vein (interval 304-U1309D-39R-1, 45–57 cm).

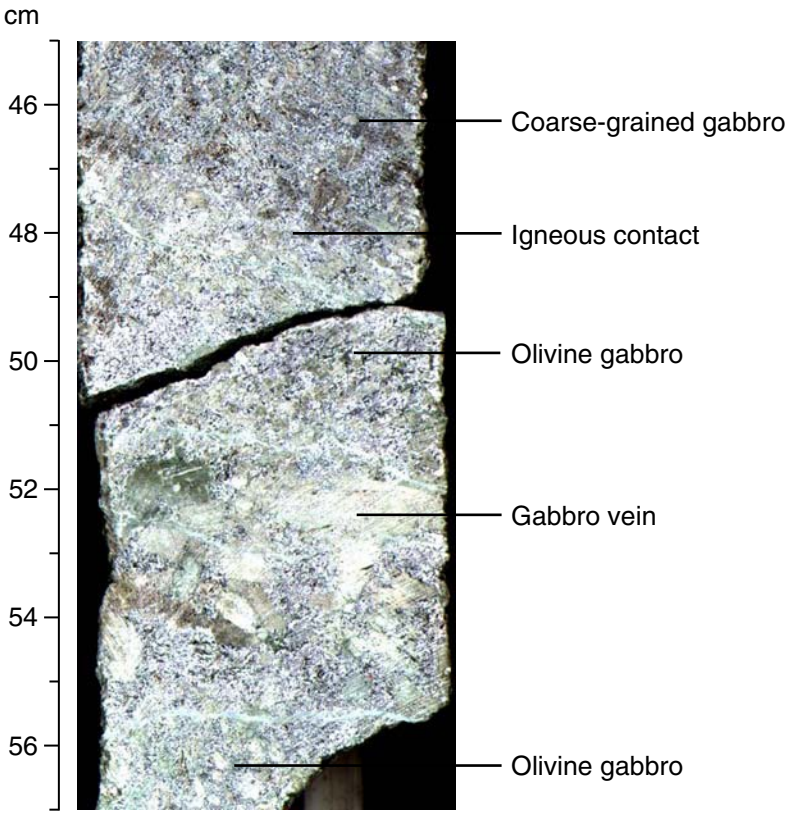

Figure F59. Irregular distribution of clinopyroxene in medium-grained gabbro (interval 304-U1309D-51R-2, 65–85 cm).

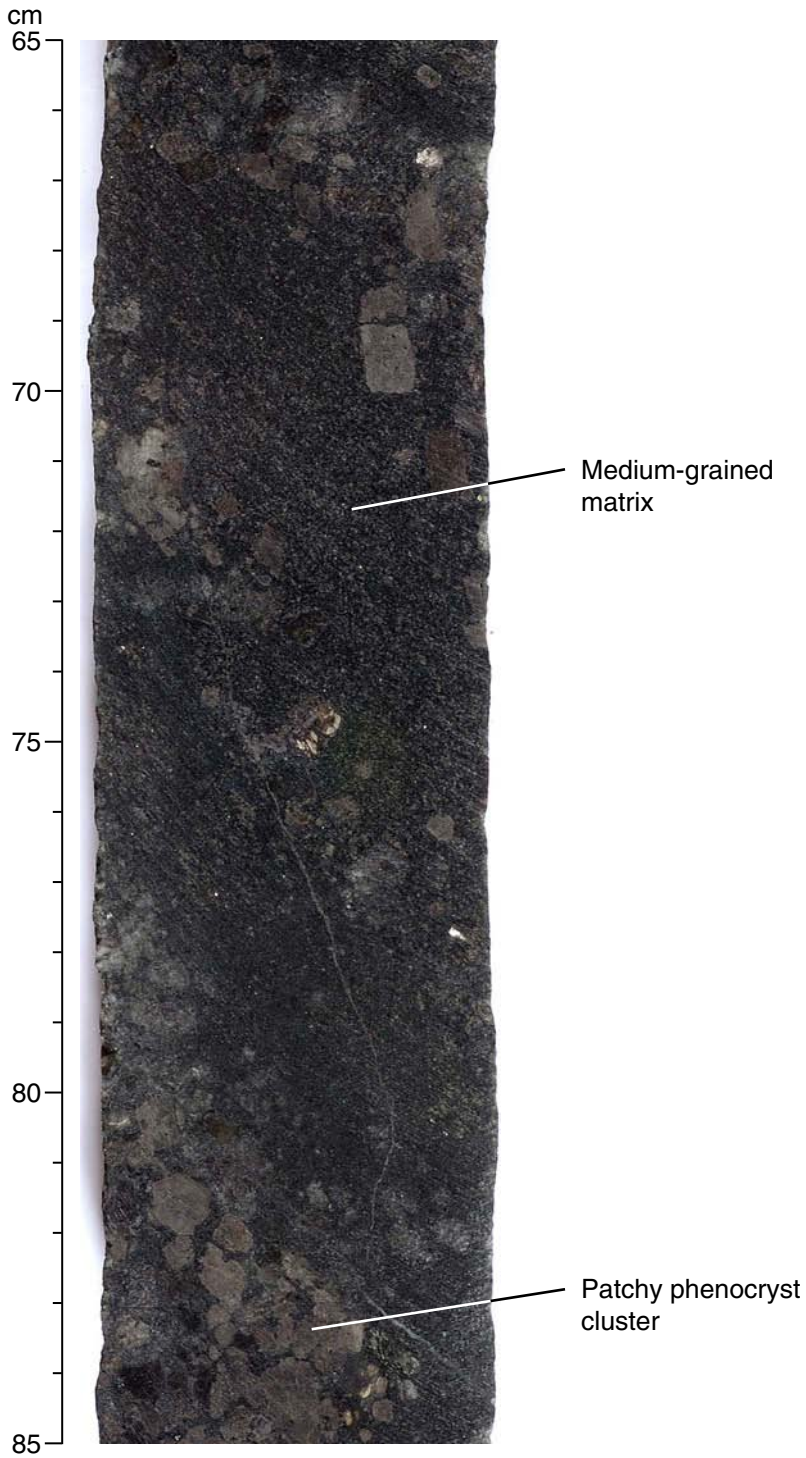

Figure F60. Intrusive layers in medium-grained gabbro showing magmatic foliation (interval 304-U1309D-51R-1, 58–93 cm).

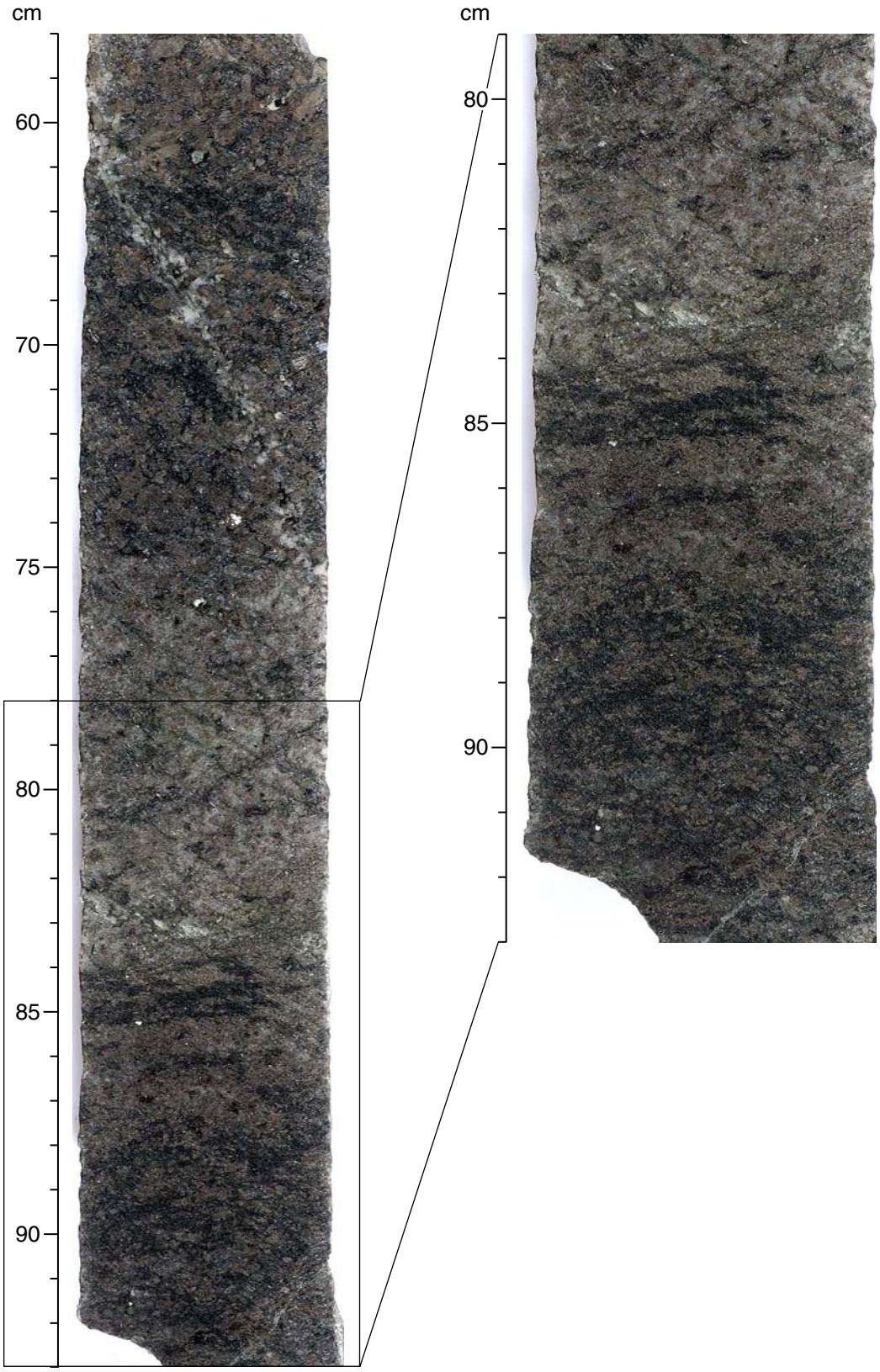

Figure F61. Magmatic layering and variation in grain sizes. **A.** Sample **304-U1309D-51R-2, 77–80 cm** (cross-polarized light; field of view [FOV] = 2 cm). **B.** Same as A; plane-polarized light. **C.** Sample **304-U1309D-51R-1, 82–85 cm** (cross-polarized light; FOV = 2 cm). **D.** Same as C; plane-polarized light.

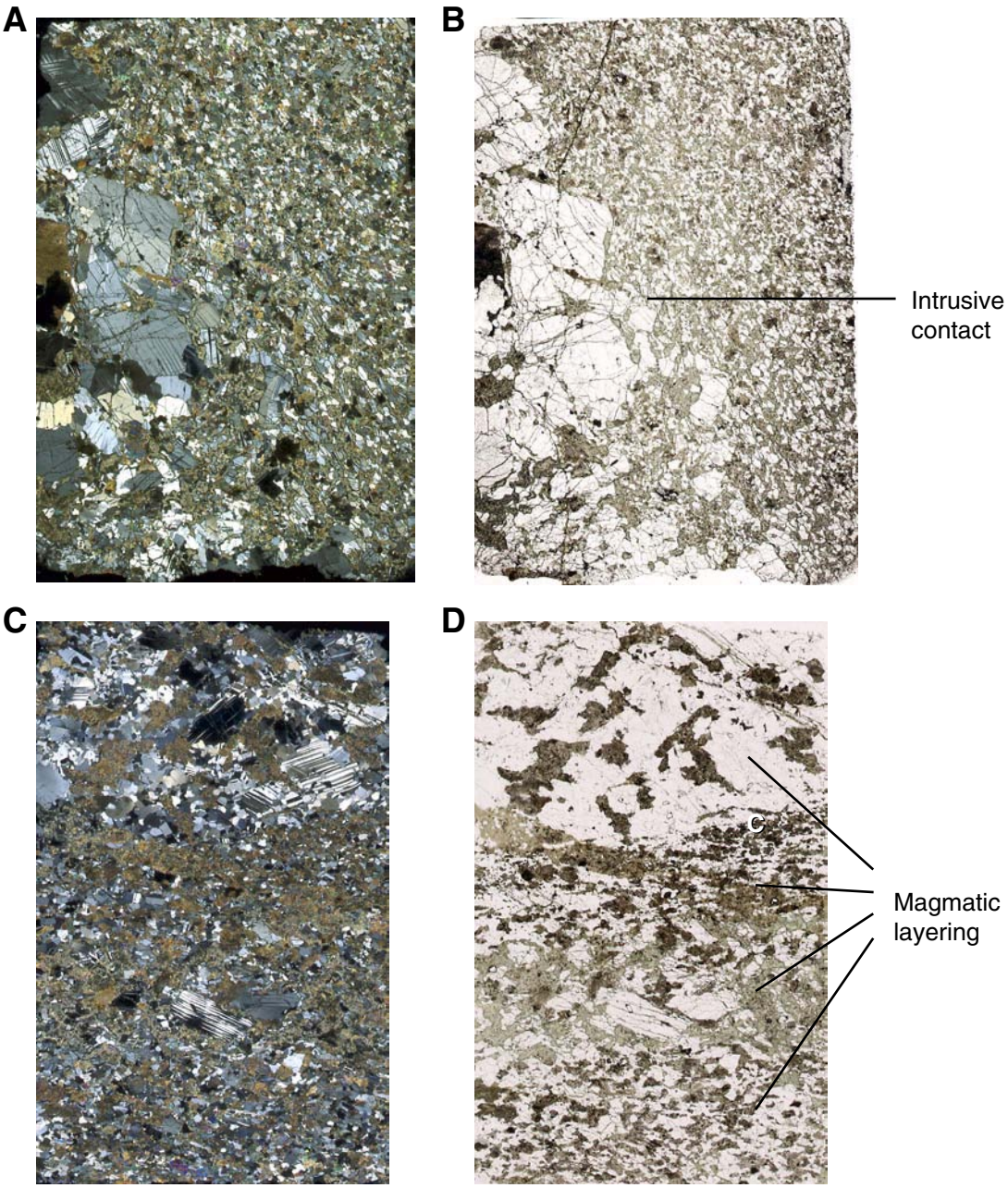

Figure F62. Intrusive contact between coarse-grained gabbro and medium-grained troctolitic gabbro (interval 304-U1309D-54R-2, 53–62 cm).

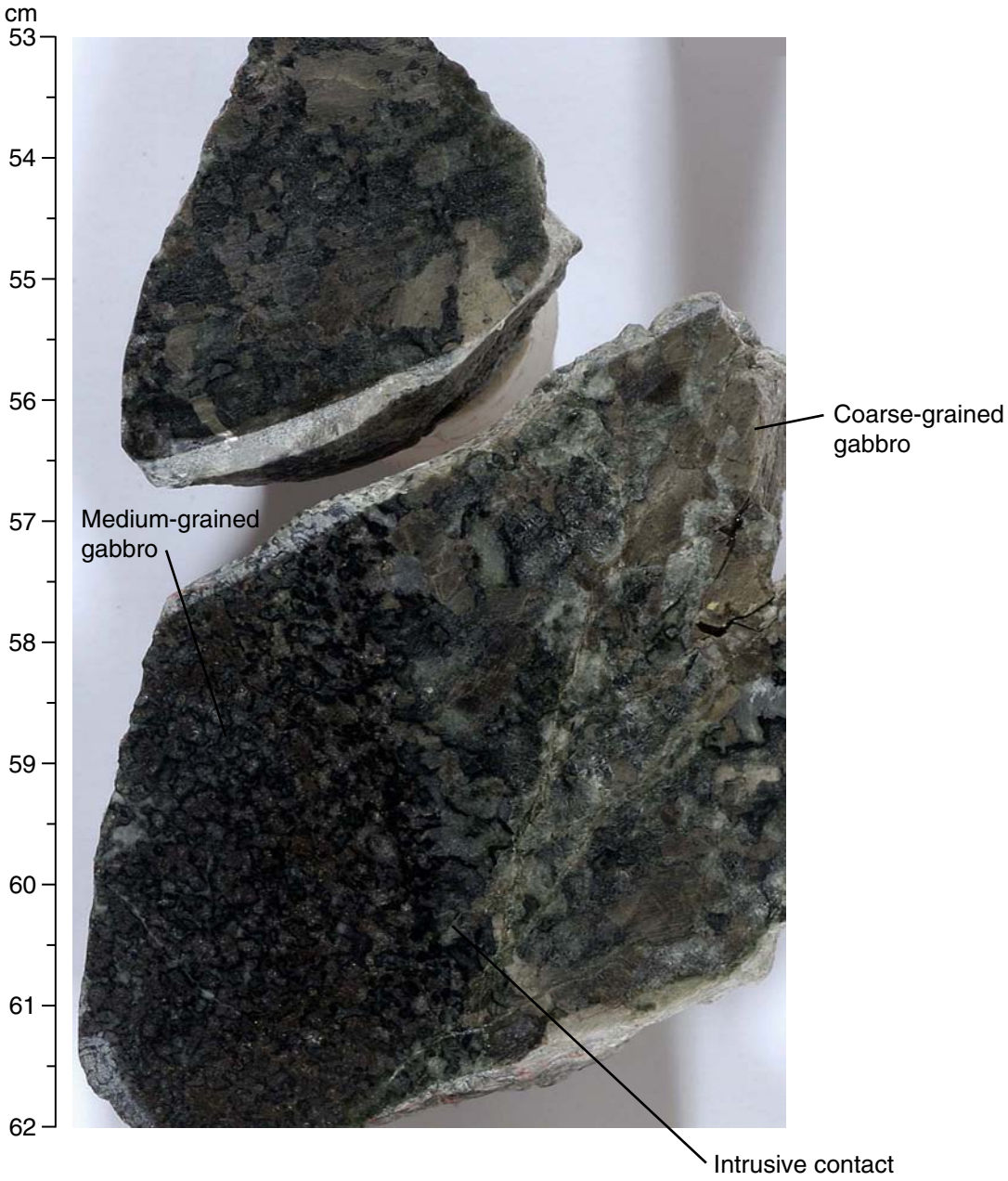

Figure F63. Intrusive contact between olivine-bearing gabbro and serpentinized dunite (interval 304-U1309D-60R-2, 34–47 cm).

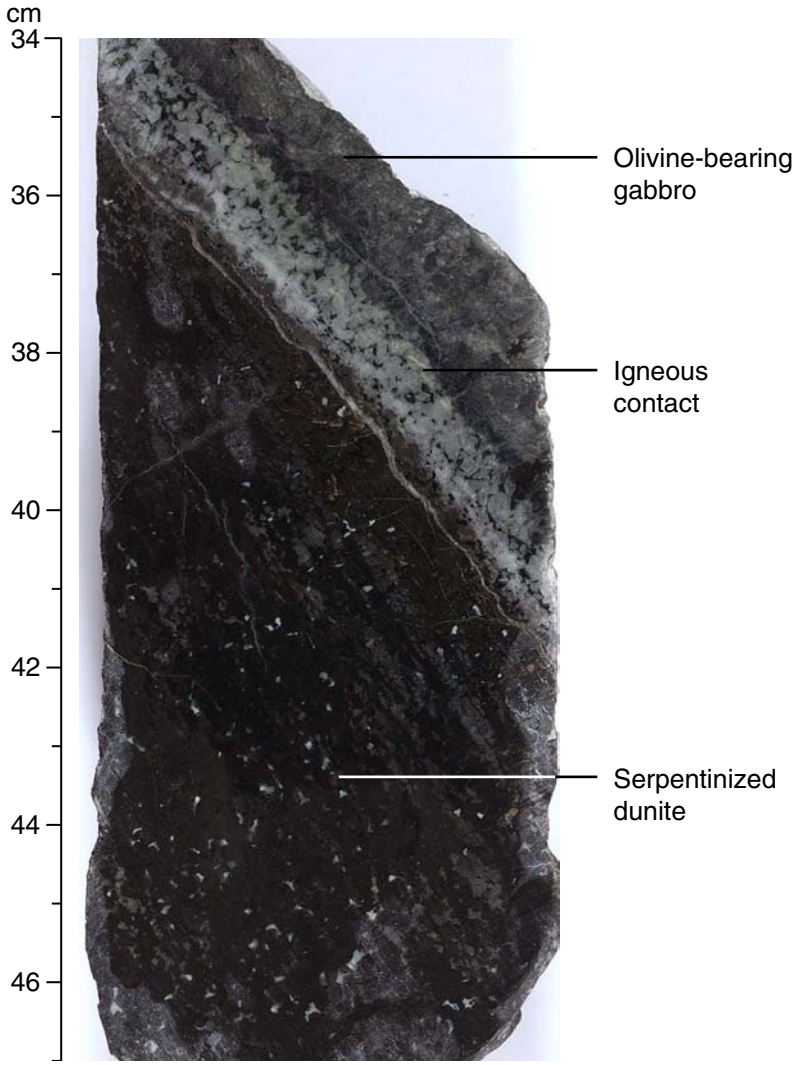

Figure F64. Coarse-grained gabbroic dikes intruding olivine gabbro. **A.** Interval 304-U1309D-56R-3, 2–21 cm. **B.** Interval 304-U1309D-56R-3, 107–127 cm. **C.** Interval 304-U1309D-54R-3, 6–17 cm. **D.** Interval 304-U1309D-54R-3, 59–76 cm.

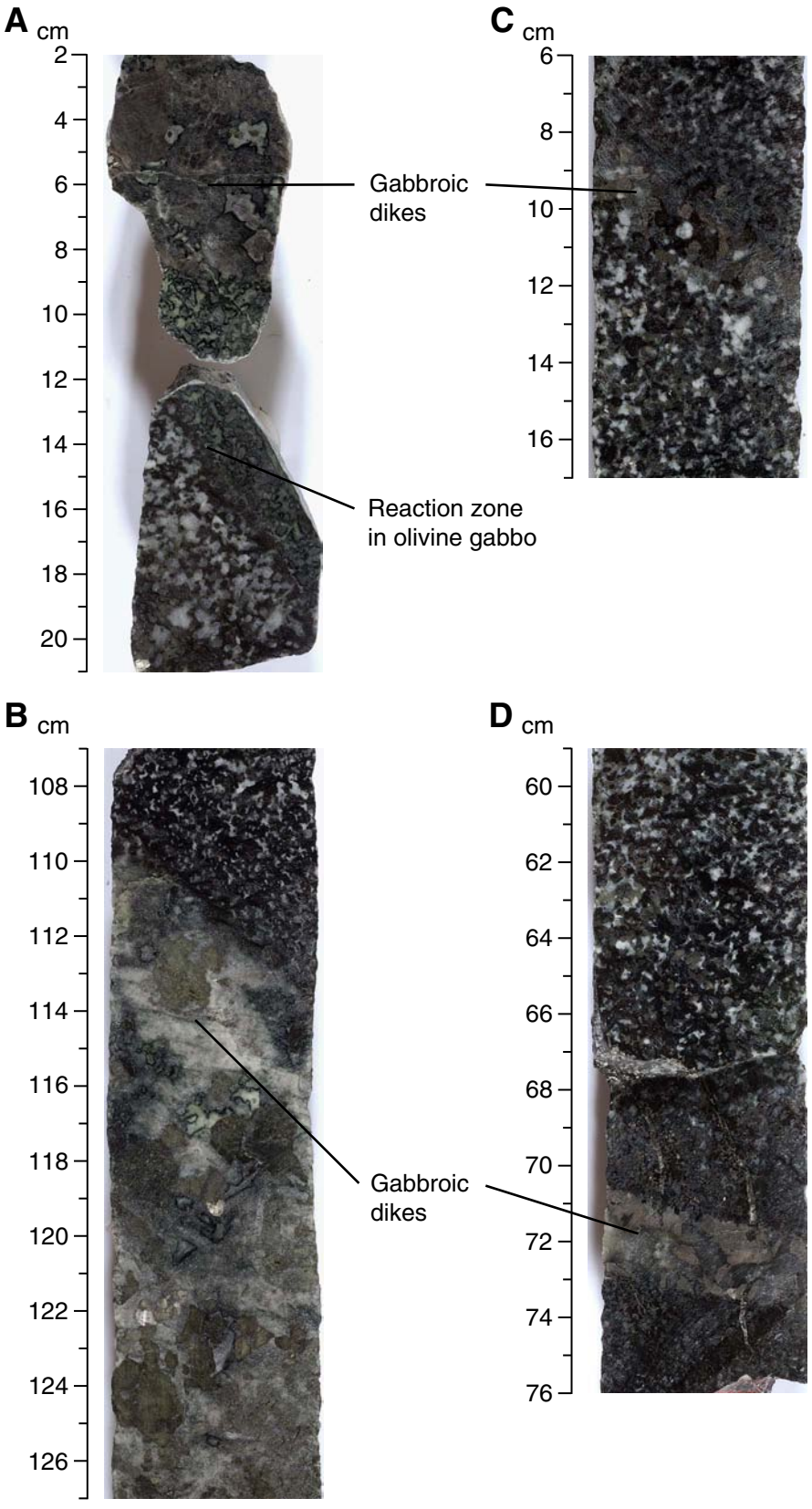

Figure F65. Ternary plots showing relative modal abundances, determined from hand specimens, of olivine, plagioclase, and clinopyroxene for each lithologic unit described during Expedition 304 in Hole U1309D. Color of each ternary diagram = the dominant lithology of that gabbro zone.

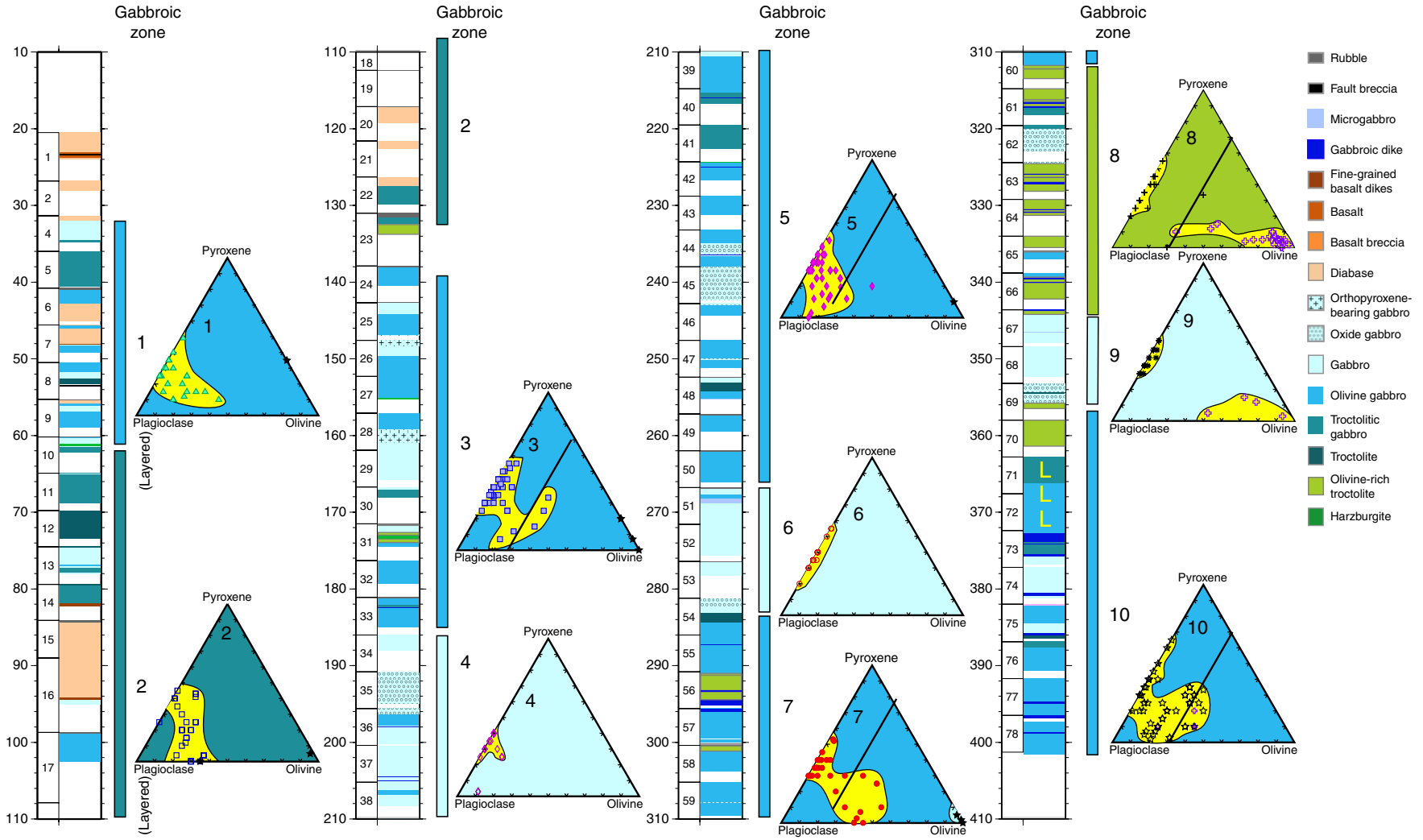

Figure F66. Plagioclase (white) segregation in troctolite (interval 304-U1309D-61R-1, 1–16 cm).

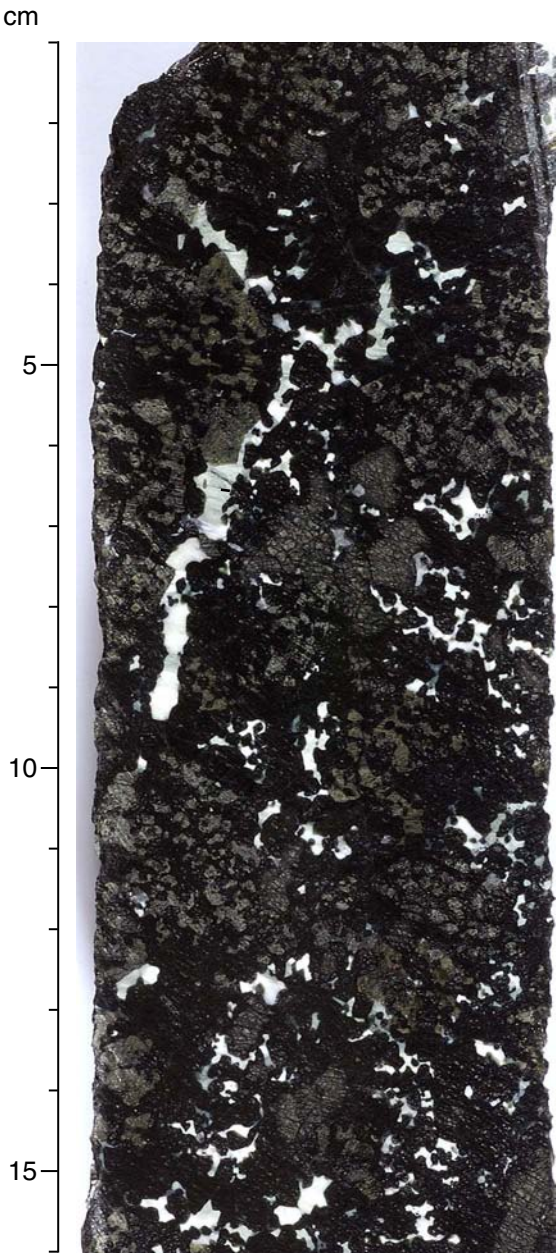

Figure F67. Gabbroic dikes in troctolites and olivine gabbros. **A.** Interval 304-U1309D-63R-2, 33–50 cm. **B.** Interval 304-U1309D-64R-1, 32–48 cm. **C.** Interval 304-U1309D-64R-2, 3–17 cm. **D.** Interval 304-U1309D-66R-1, 120–130 cm.

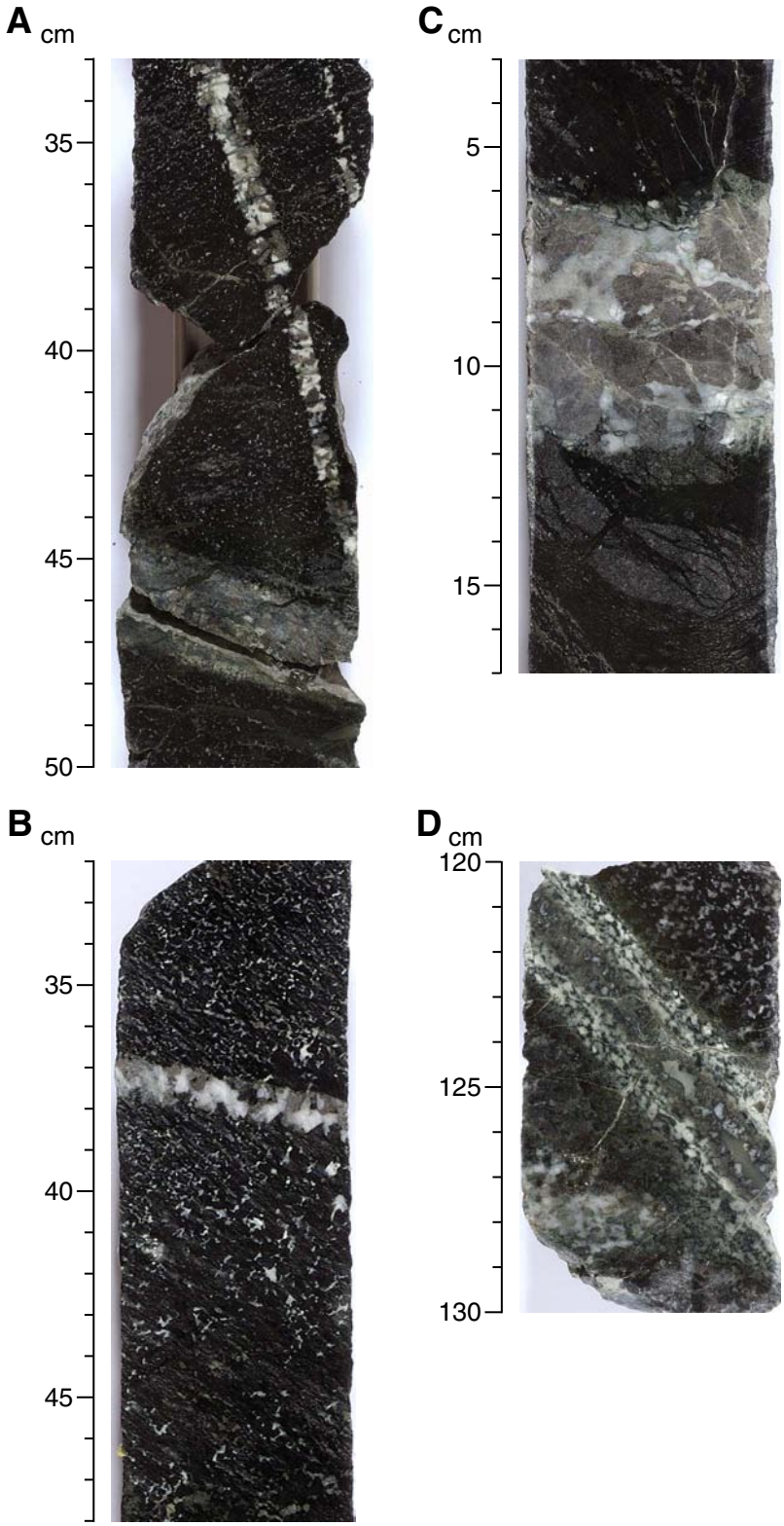

Figure F68. Intrusive contact between oxide gabbro and troctolitic gabbro (interval 304-U1309D-69R-2, 119–132 cm).

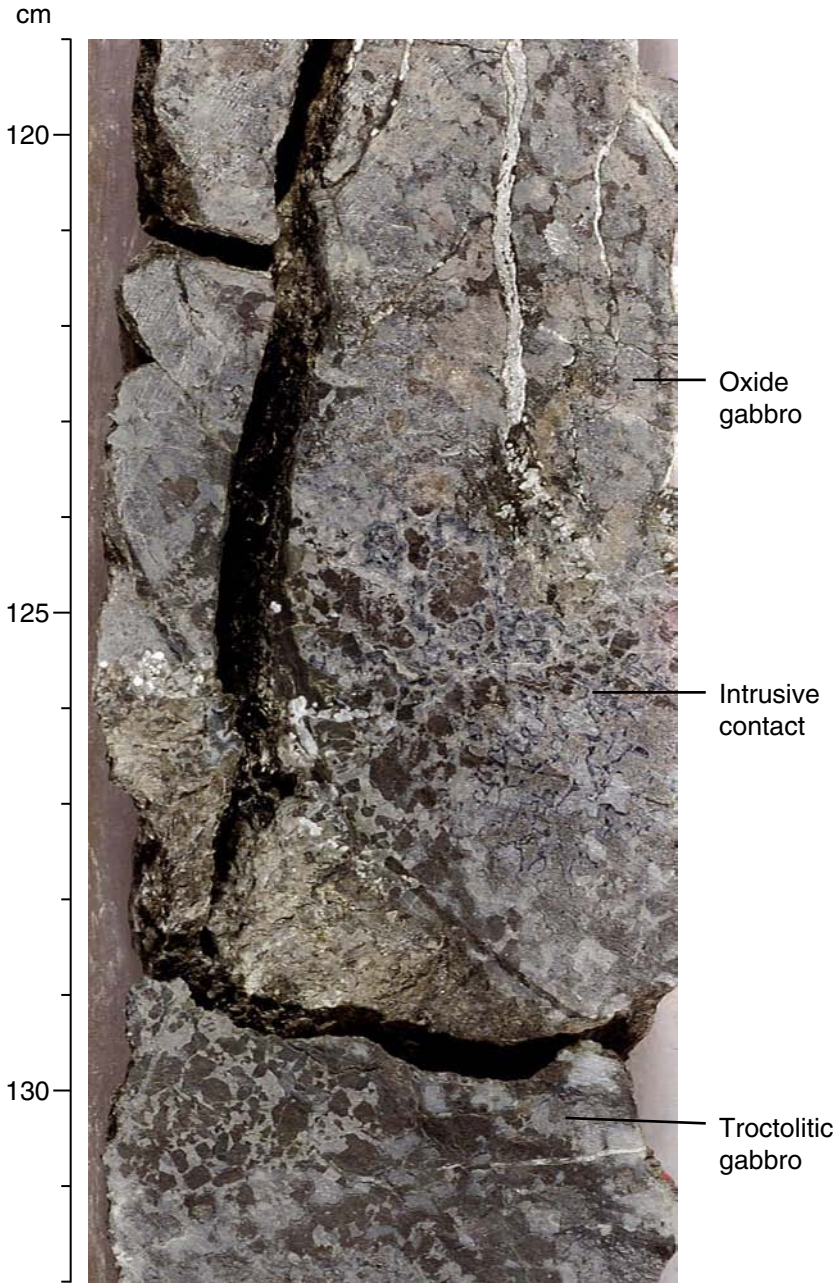

Figure F69. Intrusive contacts between gabbro, troctolite, and oxide gabbro (interval 304-U1309D-69R-1, 116–133 cm).

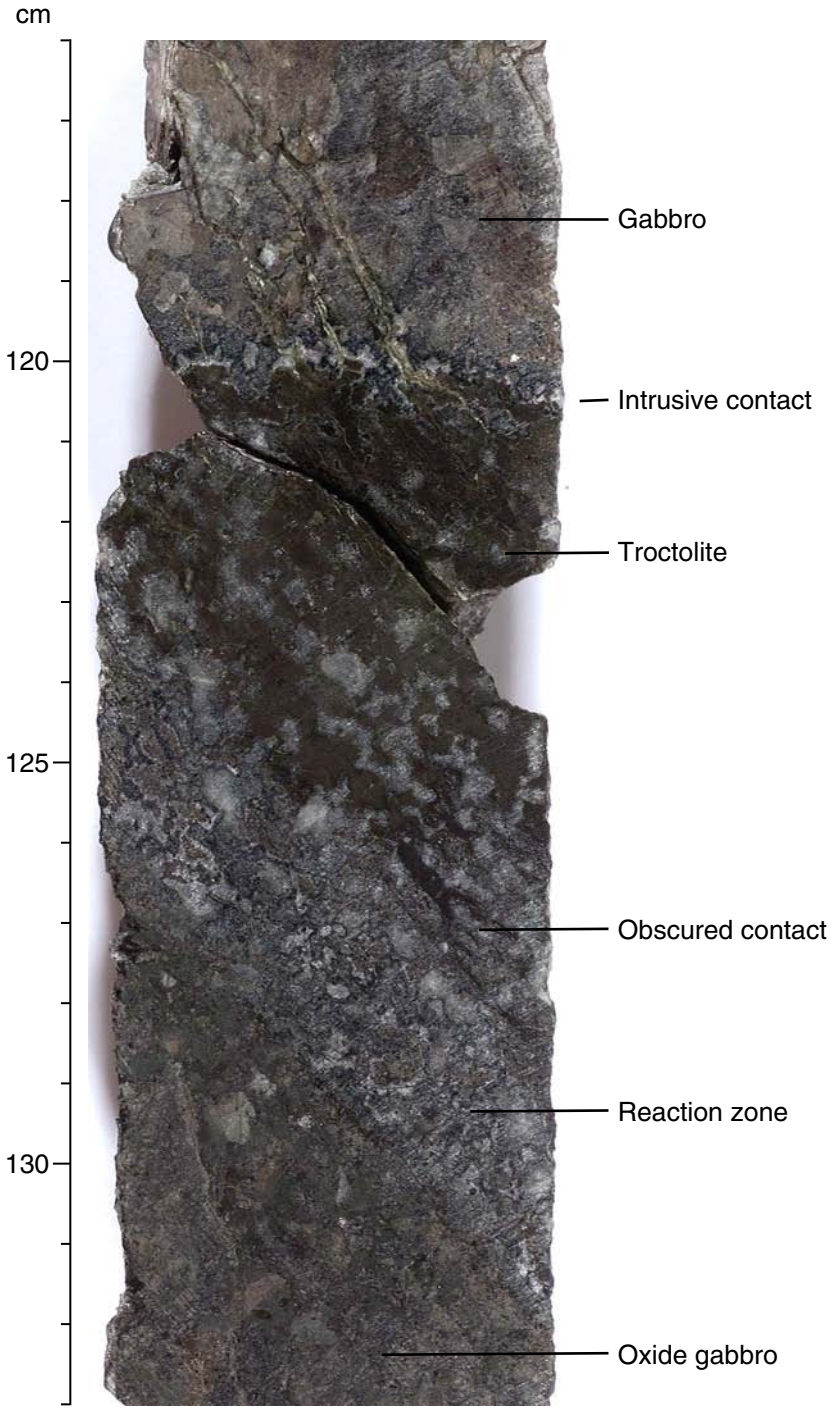

Figure F70. Heterogeneous distribution of clinopyroxene in olivine gabbro (interval 304-U1309D-77R-3, 86–97 cm).

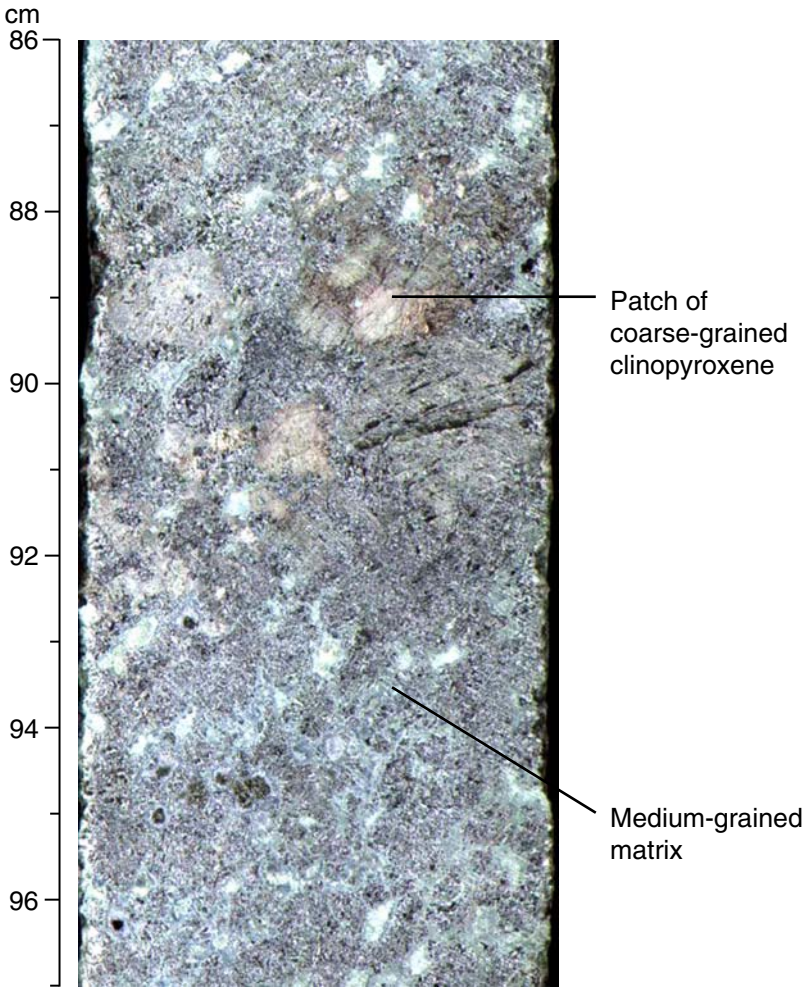

Figure F71. Vein of coarse-grained clinopyroxene (1.5 cm) with a width of ~1 grain (interval 304-U1309D-77R-3, 23–33 cm).

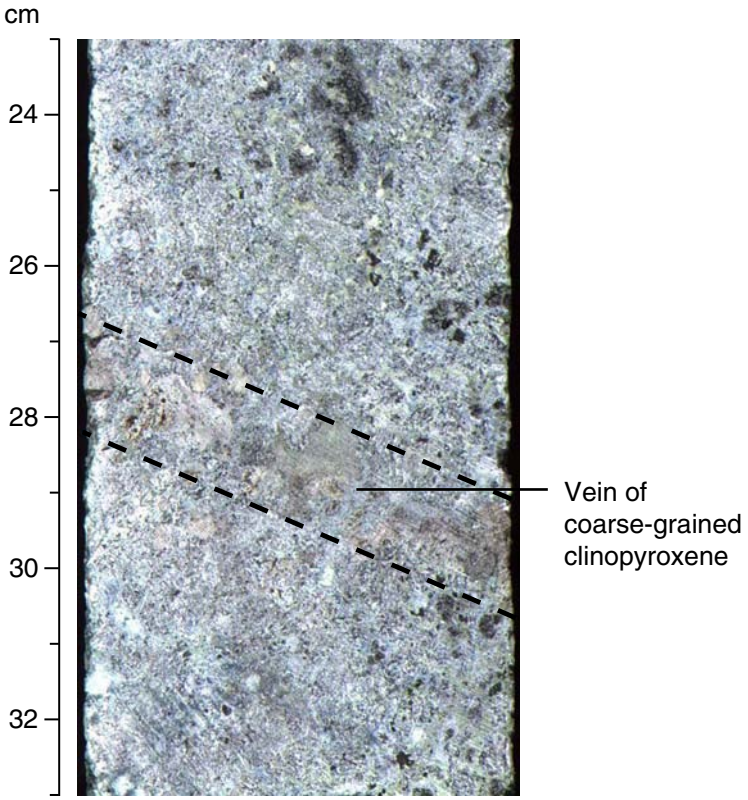

Figure F72. Representative samples for each peridotite unit in Hole U1309D. **A.** Plagioclase lherzolite (interval 304-U1309D-10R-1, 90–106 cm). **B.** Plagioclase harzburgite (interval 304-U1309D-27R-3, 0–8 cm). **C.** Plagioclase harzburgite (interval 304-U1309D-31R-2, 27–49 cm). **D.** Dunite (interval 304-U1309D-31R-1, 24–33 cm). **E.** Harzburgite (interval 304-U1309D-42R-1, 0–10 cm).

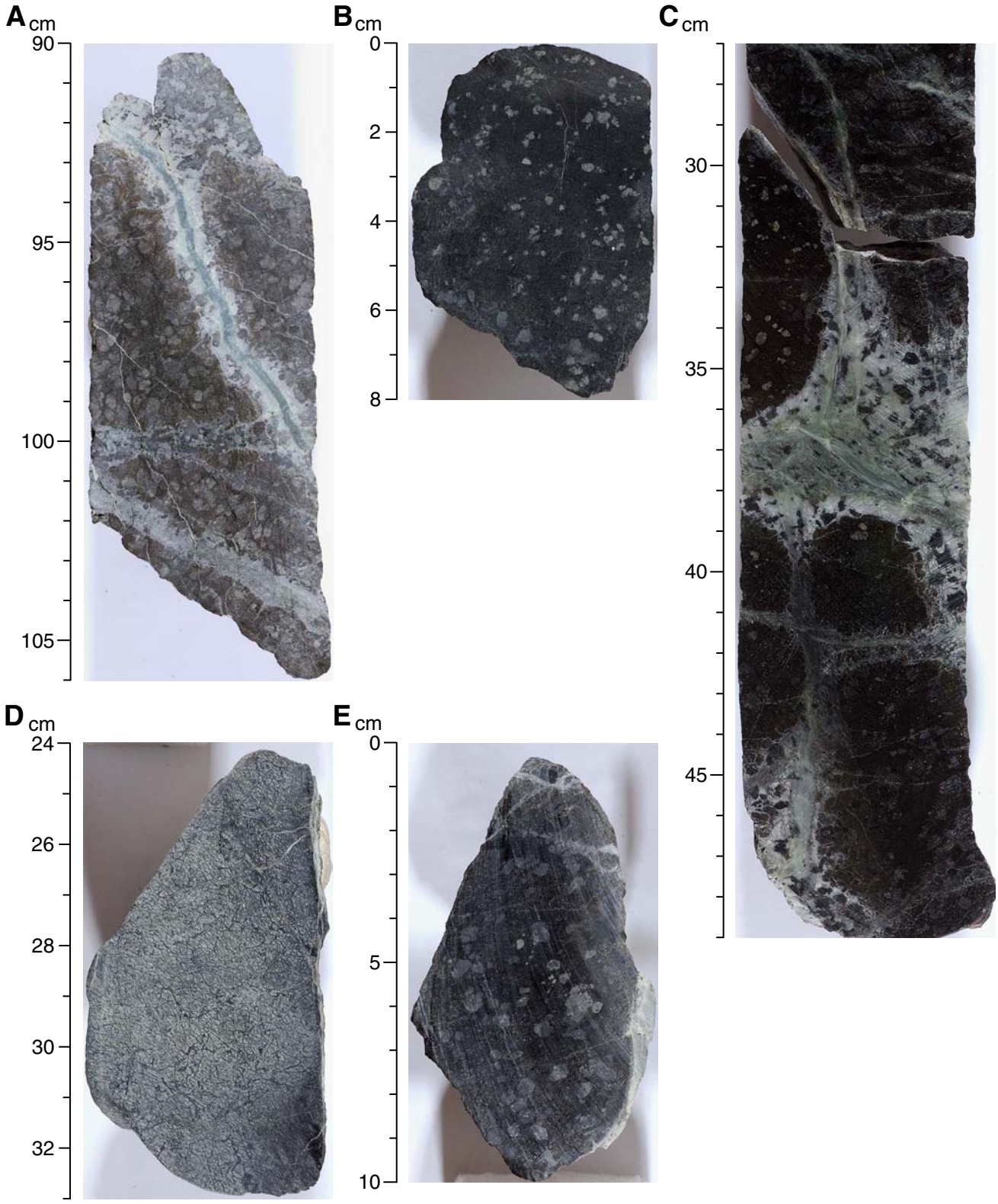

Figure F73. Sample 304-1309D-10R-1, 91–94 cm (cross-polarized light). **A.** Serpentinized olivine (ol) with pyroxene (px) in lherzolite with evidence of melt impregnation as interstitial plagioclase (plag) (field of view [FOV] = 5 mm). **B.** Troctolitic area with olivine altered to talc and plagioclase altered to chlorite (gypsum plate; FOV = 5 mm). **C.** Altered pyroxene oikocryst with olivine chadacryst and interstitial plagioclase (altered to chlorite) (gypsum plate; FOV = 5 mm). **D.** Altered plagioclase interstitial to olivine (gypsum plate; FOV = 2.5 mm). **E.** Fresh clinopyroxene with vermicular intergrowth of plagioclase (FOV = 1.25 mm). **F.** Clinopyroxene with plagioclase bleb (cpx1) corroded by another clinopyroxene (cpx2) (FOV = 1.25 mm); note the olivine inclusion.

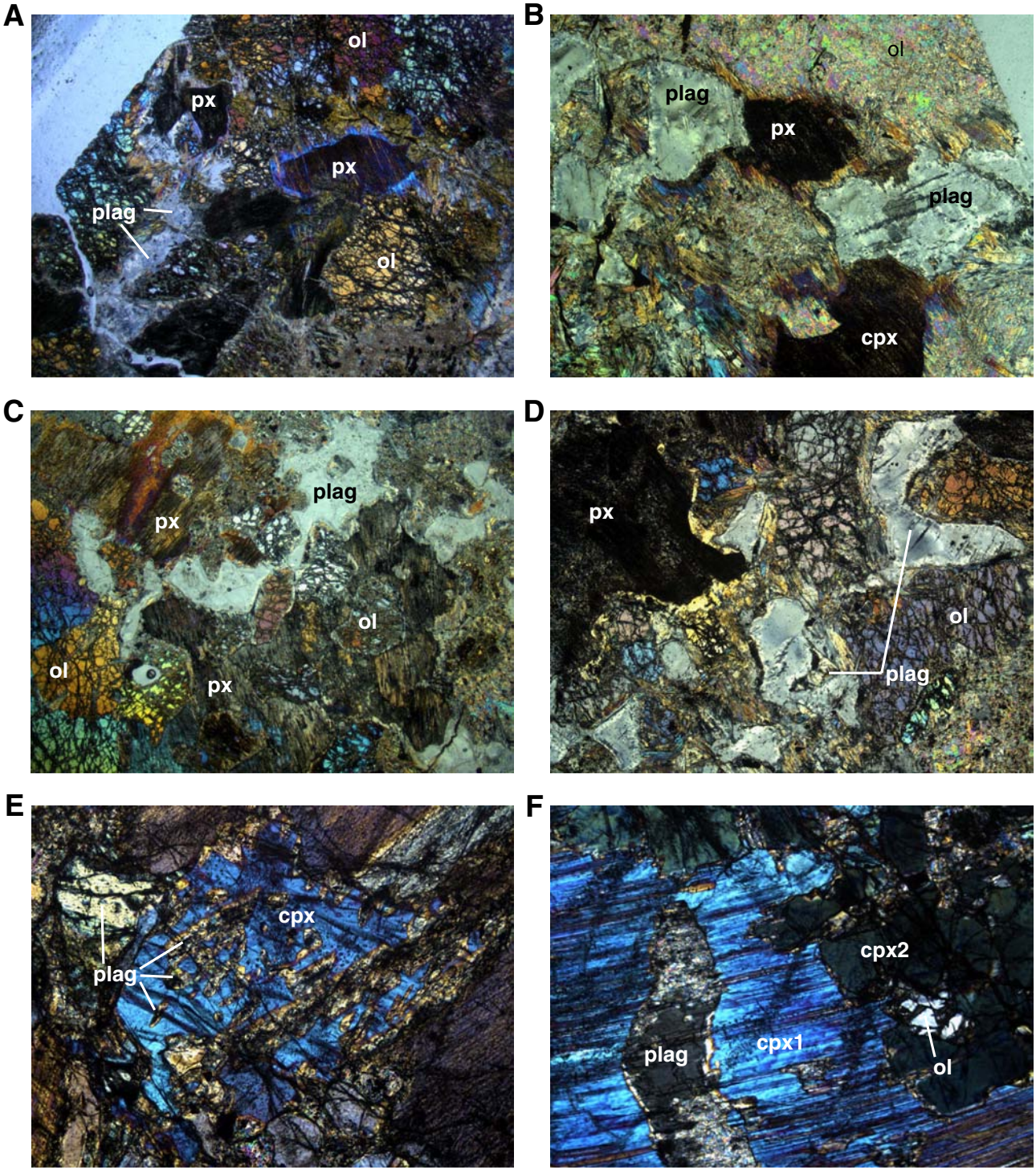

Figure F74. Sample 304-U1309D-27R-3, 4–7 cm. **A.** Relatively fresh orthopyroxene (opx) and clinopyroxene (cpx) grains (cross-polarized light; field of view [FOV] = 5 mm). Orthopyroxene shows a small clinopyroxene inclusion or bleb. serp = serpentine. **B.** Inclusions (of altered olivine? [ol?] and euhedral oxides [spinels?]) in pyroxene (px) (FOV = 1.25 mm).

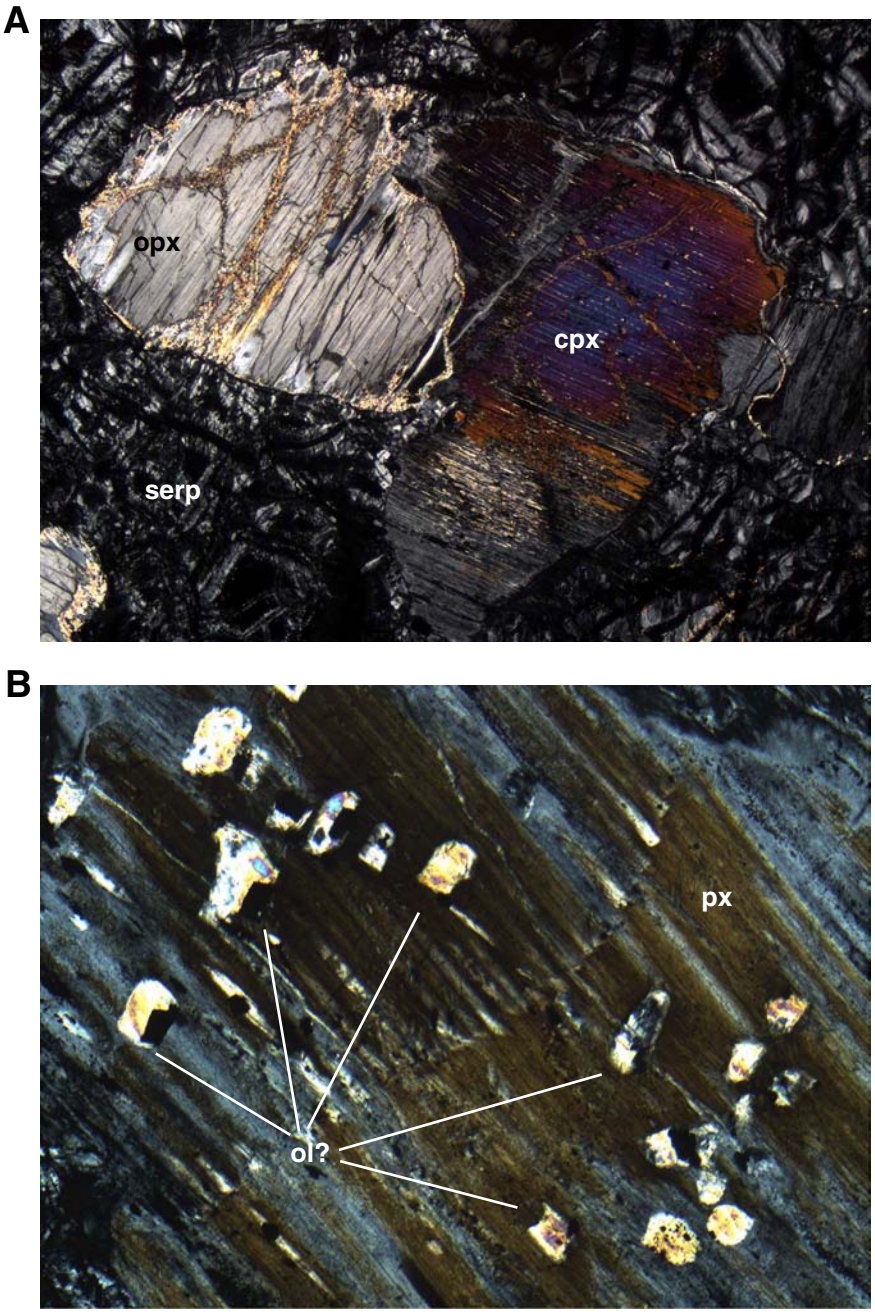

Figure F75. A. Clinopyroxene (cpx1, cpx2) with interpenetrative, corrosive boundaries (Sample **304-U1309D-31R-1, 16–19 cm**) (cross-polarized light; field of view [FOV] = 1.25 mm). Both contain altered olivine (ol) chadacrysts (only those in px2 are shown). **B.** Altered plagioclase (plag) in serpentine (serp) matrix (Sample 304-U1309D-31R-2, 2 cm) (gypsum plate; cross-polarized light; FOV = 5 mm). px = pyroxene.

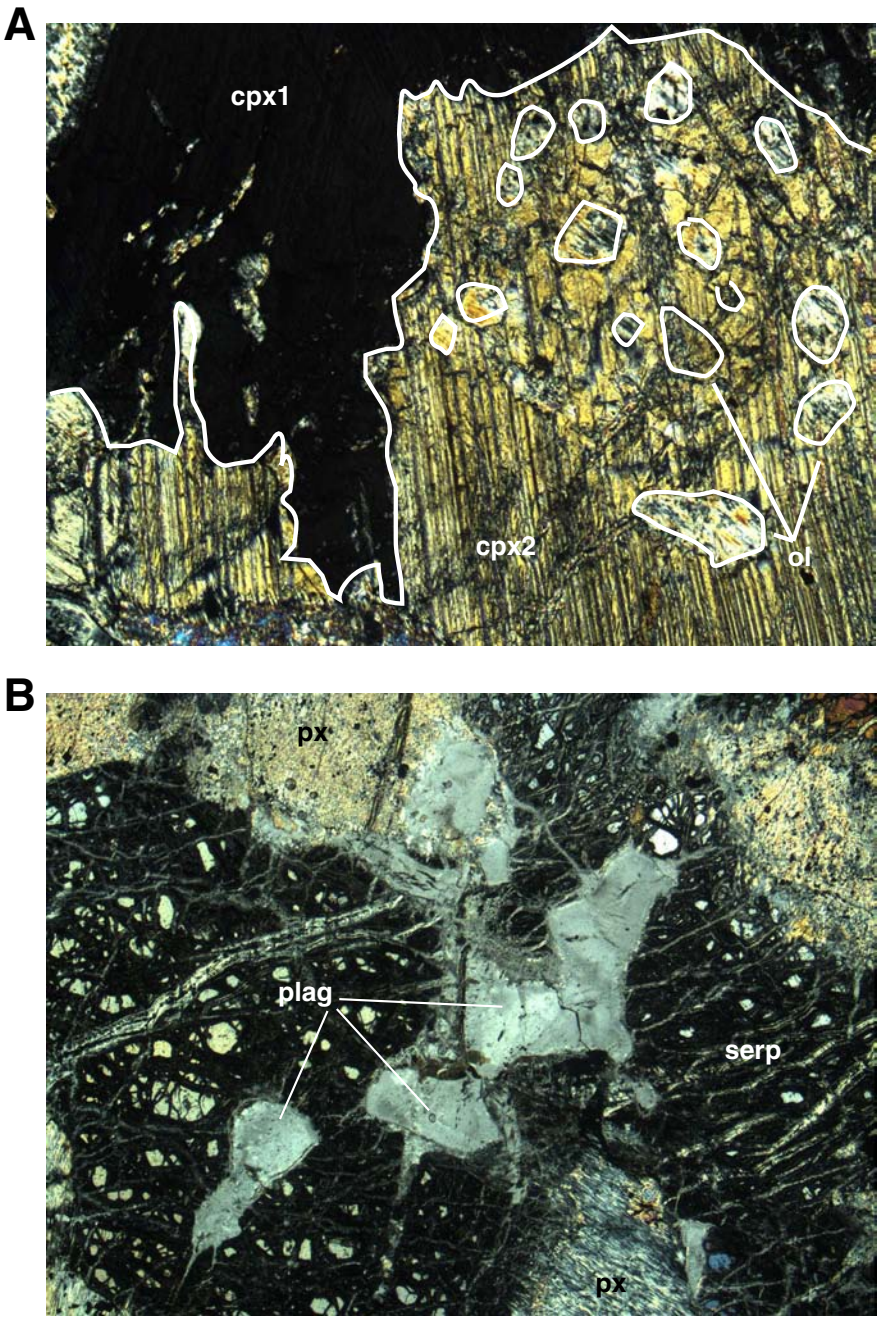

Figure F76. Sample 304-U1309D-42R-1, 7-9 cm (gypsum plate; cross-polarized light; field of view = 5 mm). **A.** Altered pyroxene oikocryst enclosing olivine chadacryst. **B.** Pyroxene cluster with rounded olivine (ol) inclusions. cpx = clinopyroxene, serp = serpentine.

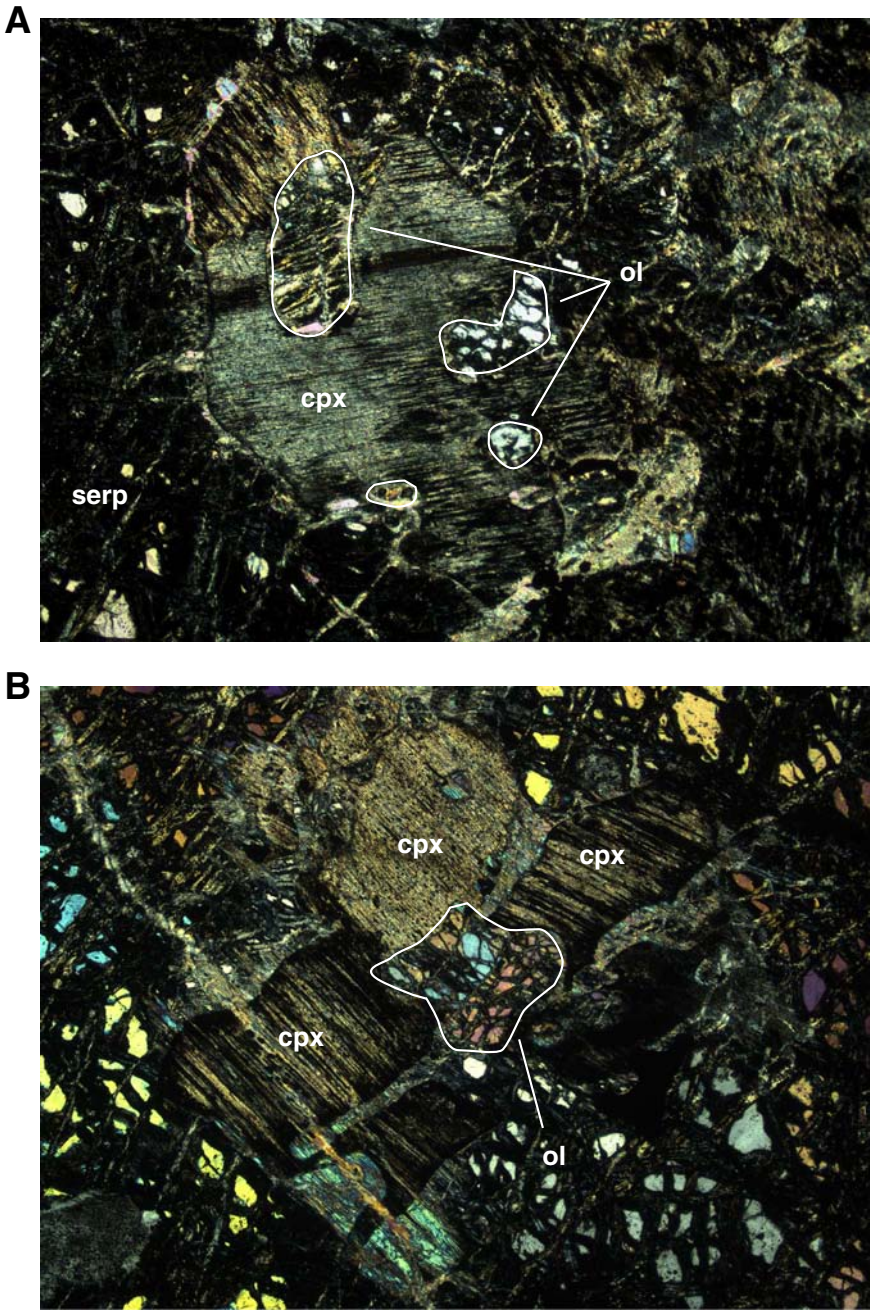

Figure F77. Stratigraphic distribution of lithologic proportions of cores recovered from Hole U1309D. **A.** 20 m running average. White = no recovery. **B.** Individual bars represent the percentage of each rock type per core.

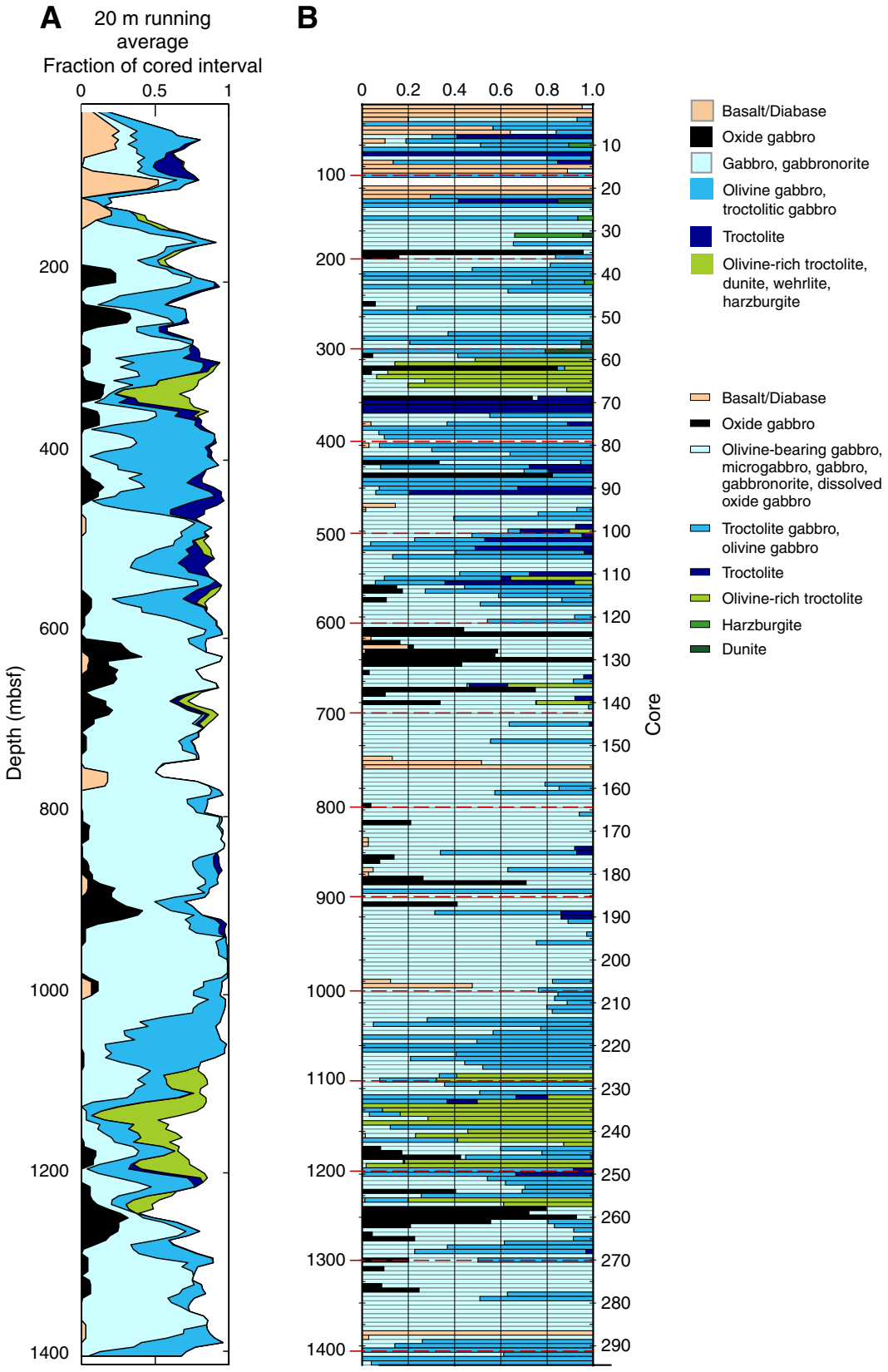

Figure F78. Proportions of recovered rock types in Hole U1309D. Each number refers to the lithologic proportions in percentages. **A.** Interval 0–401.3 mbsf (Cores 304-U1309D-1R through 78R, Expedition 304). **B.** Interval 401.3–1415.5 mbsf (Cores 305-U1309D-80R through 295R, Expedition 305). **C.** Hole U1309D.

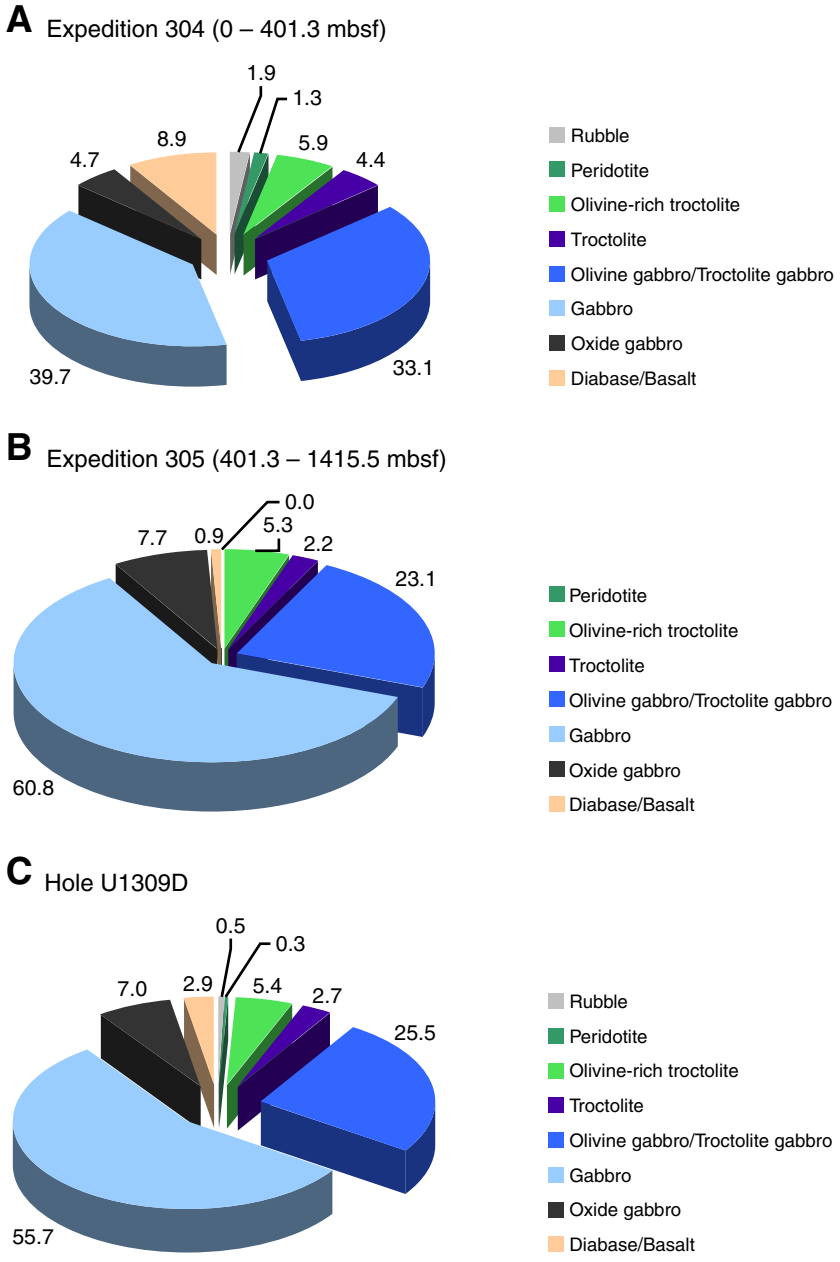

Figure F79. Downhole modal variation in Hole U1309D. **A.** Olivine. **B.** Oxide. **C.** Pyroxenes, including both clinopyroxene and orthopyroxene. **D.** Orthopyroxene. Data from visual core description except for orthopyroxene, for which modes were estimated from thin section (TS) observation. Olivine and oxide modal amounts correspond to lithologic variation in the stratigraphic column. Pyroxene mode is relatively constant, except for the olivine-rich troctolite interval. Orthopyroxene is distributed in almost the entire hole and modal amount varies related to total pyroxene mode variation.

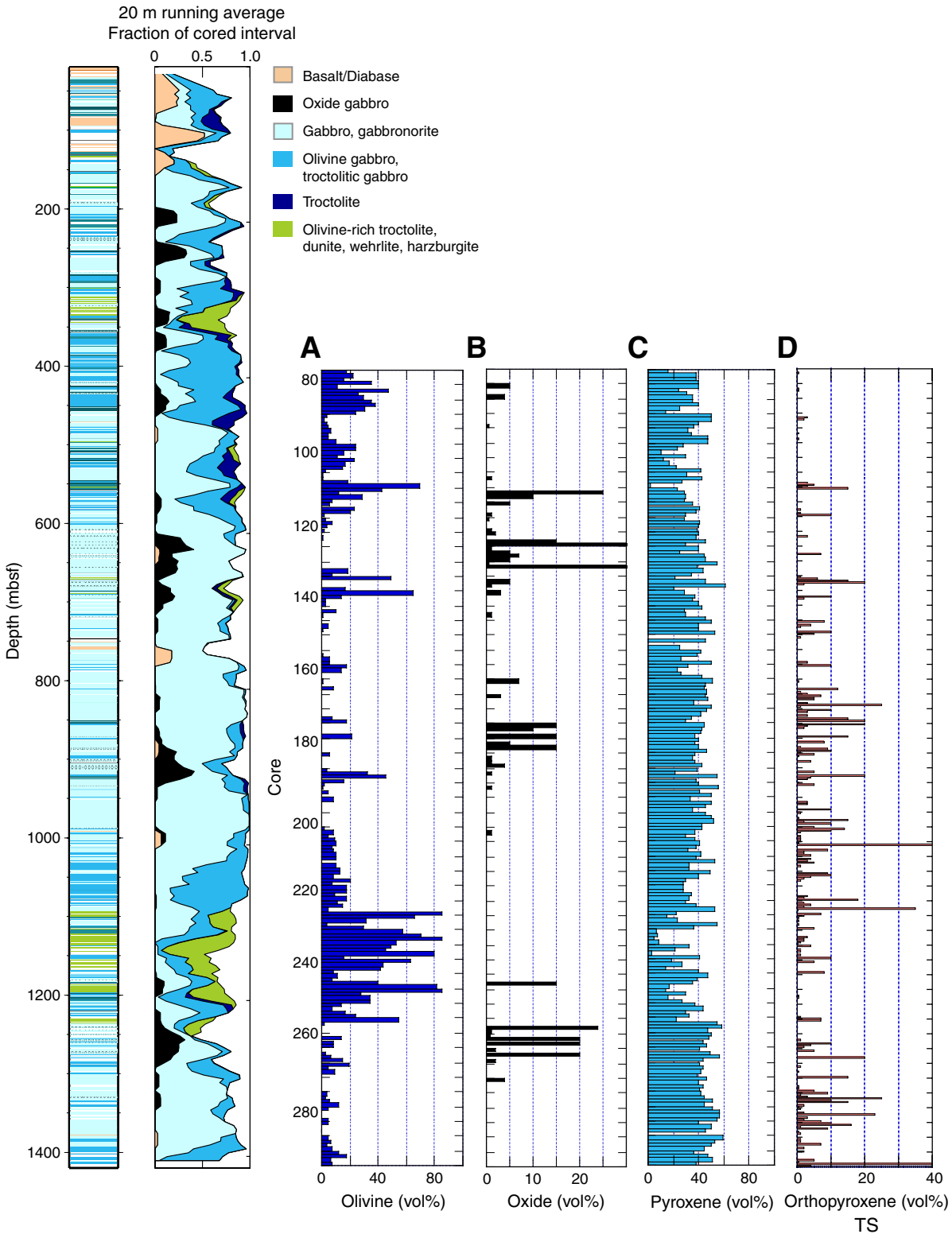

Figure F80. Modal proportions of olivine, pyroxenes (clino- and orthopyroxene), and plagioclase in gabbros from Expedition 305. The modal proportions used for the classification of (olivine-bearing) gabbro, troctolite and troctolitic gabbro, and olivine-rich troctolite are highlighted for Cores 305-U1309D-80R through 295R in the box area. See Figure **F65** for the upper part of the hole (Expedition 304). Blue = gabbro, purple = troctolite and troctolitic gabbro, green = olivine-rich troctolite; all others are classified as olivine gabbro. Py = pyroxene, Pl = plagioclase, Ol = olivine.

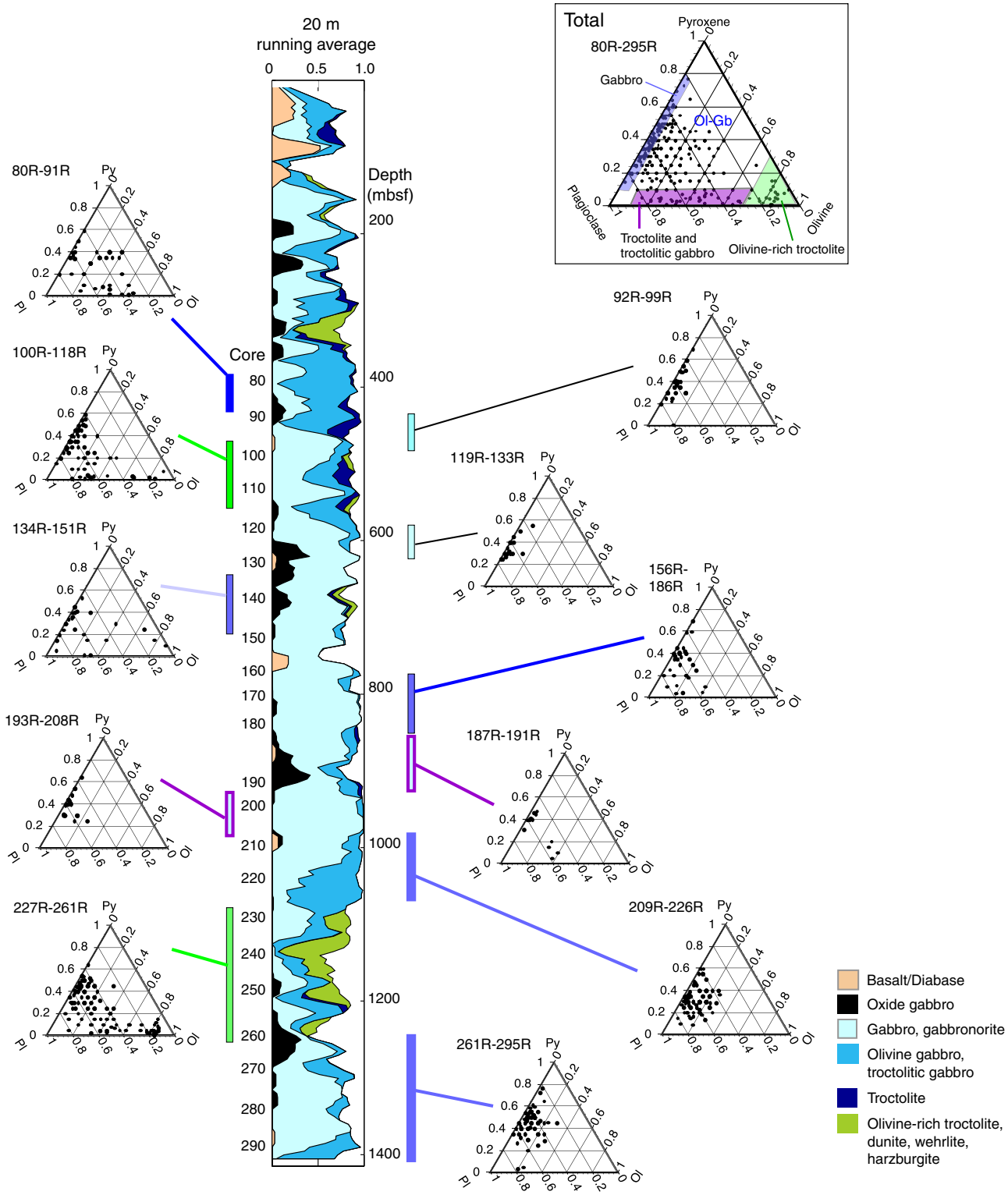

Figure F81. Modes of occurrence of olivine-rich troctolite in Core 305-U1309D-100R. **A.** Interval 305-U1309D-100R-1, 8–23 cm. Red box = location of thin section Sample 305-U1309D-100R-1, 10–13 cm (see Fig. F90A). **B.** Interval 305-U1309D-100R-1, 35–65 cm.

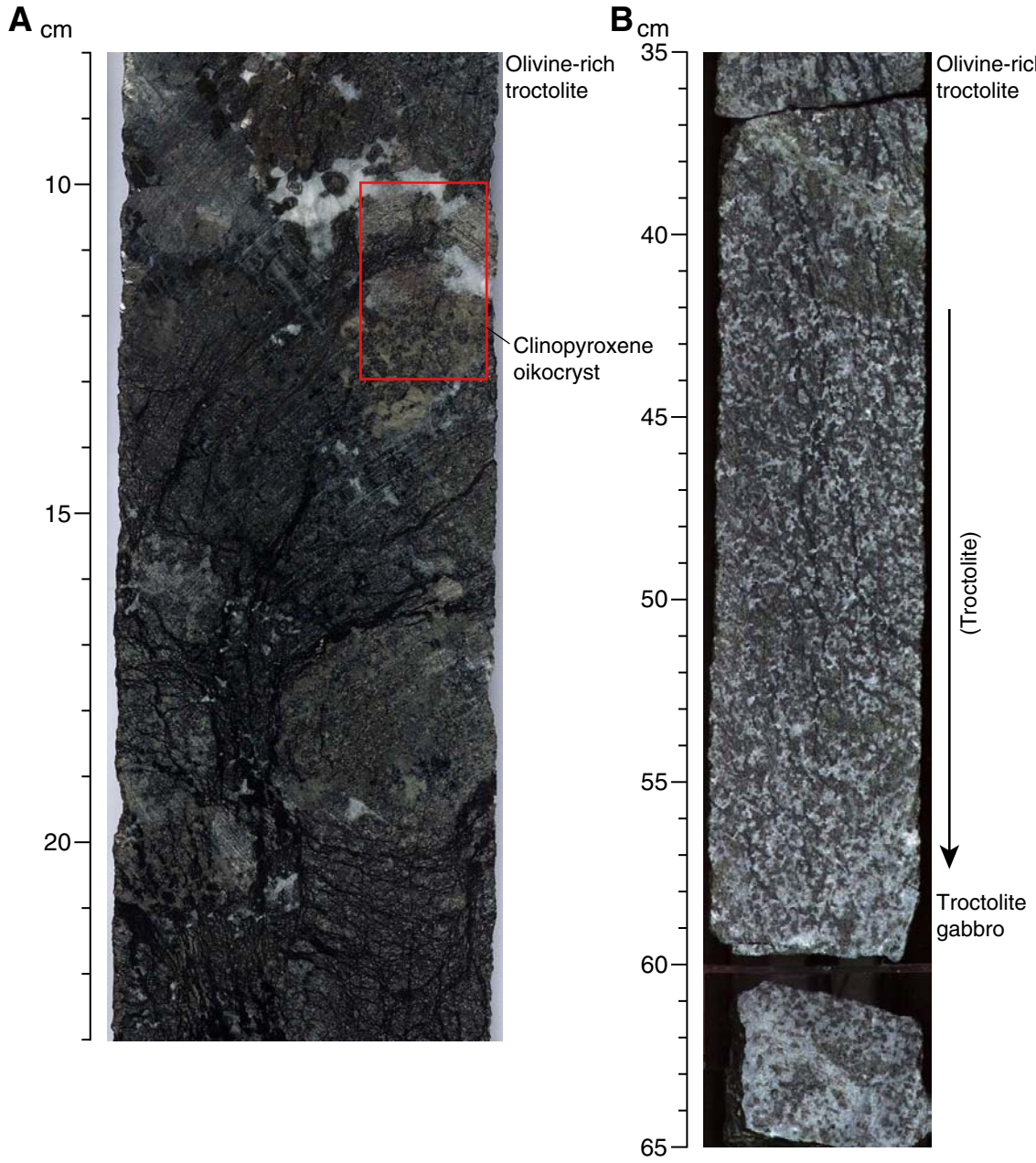

Figure F82. Modes of occurrence of olivine-rich troctolite in Core 305-U1309D-136R. **A.** Interval 305-U1309D-136R-1, 14–28 cm. **B.** Interval 305-U1309D-136R-2, 49–70 cm.

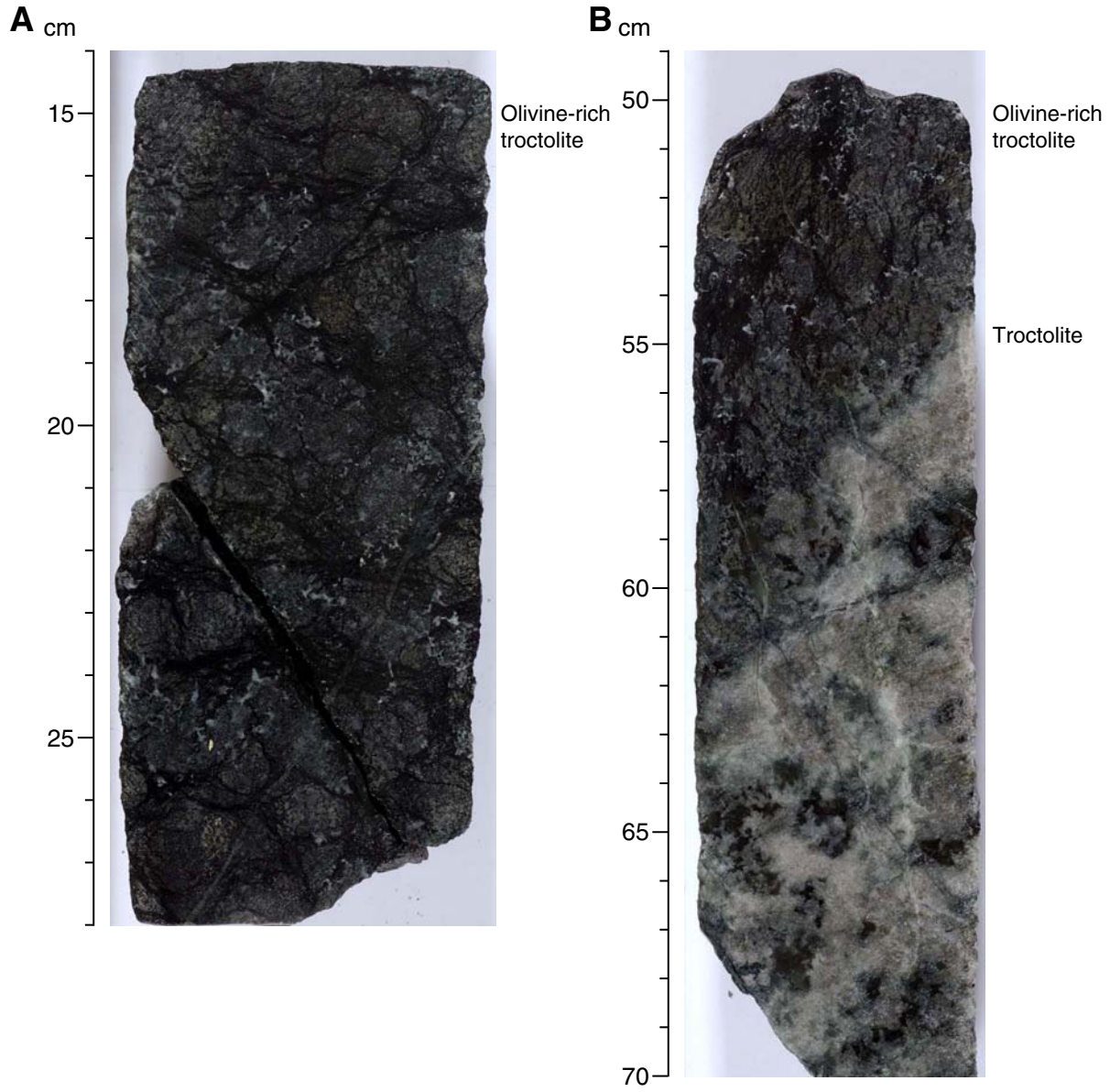

Figure F83. Modes of occurrence of olivine-rich troctolite in Core 305-U1309D-140R. **A.** Interval 305-U1309D-140R-2, 40–56 cm. **B.** Interval 305-U1309D-140R-2, 102–122 cm.

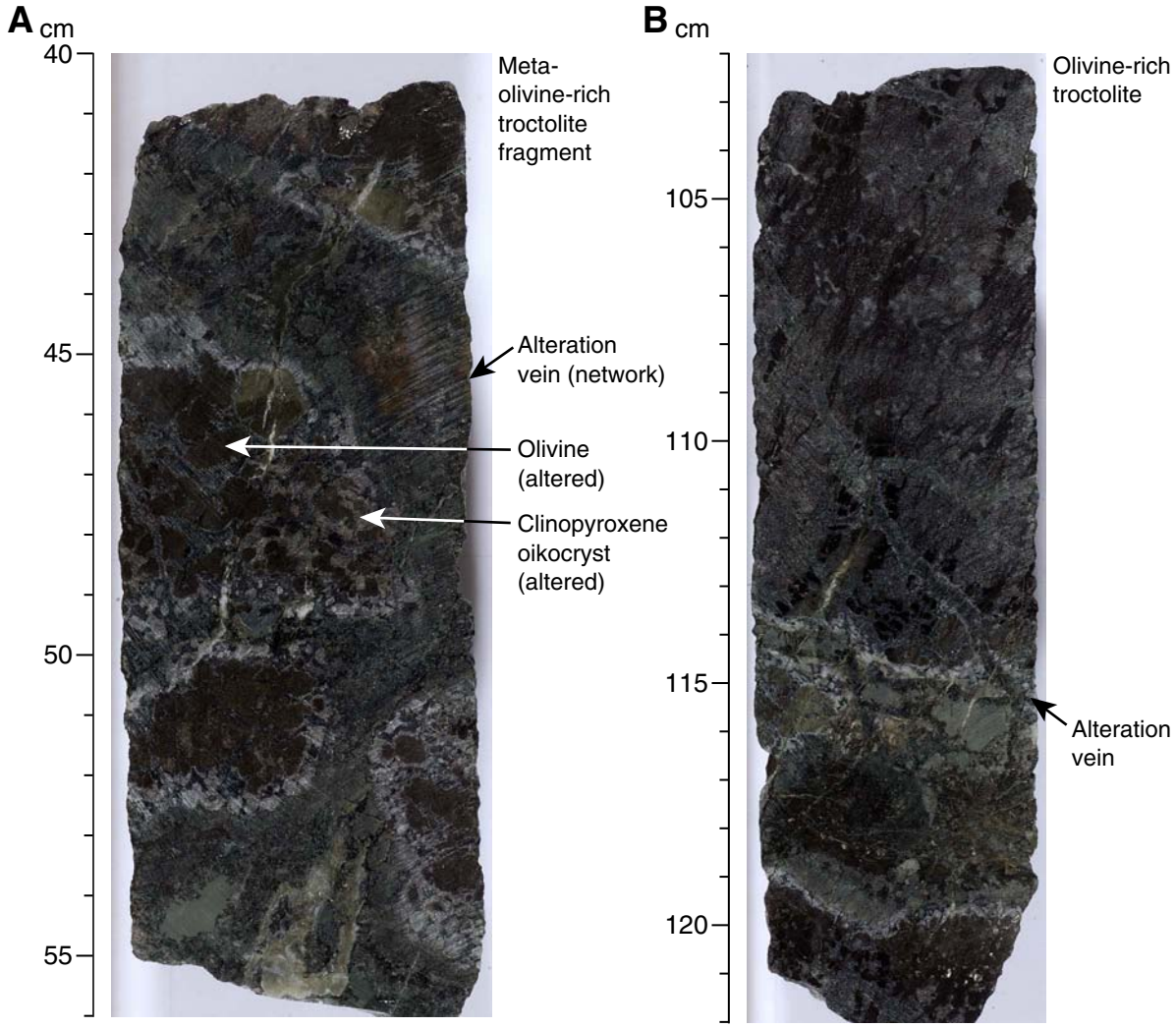

Figure F84. Modes of occurrence of olivine-rich troctolite in Cores 305-U1309D-227R and 228R. **A.** Interval 305-U1309D-227R-2, 21–45 cm. **B.** Interval 305-U1309D-227R-3, 21–51 cm. **C.** Interval 305-U1309D-228R-3, 59–76 cm.

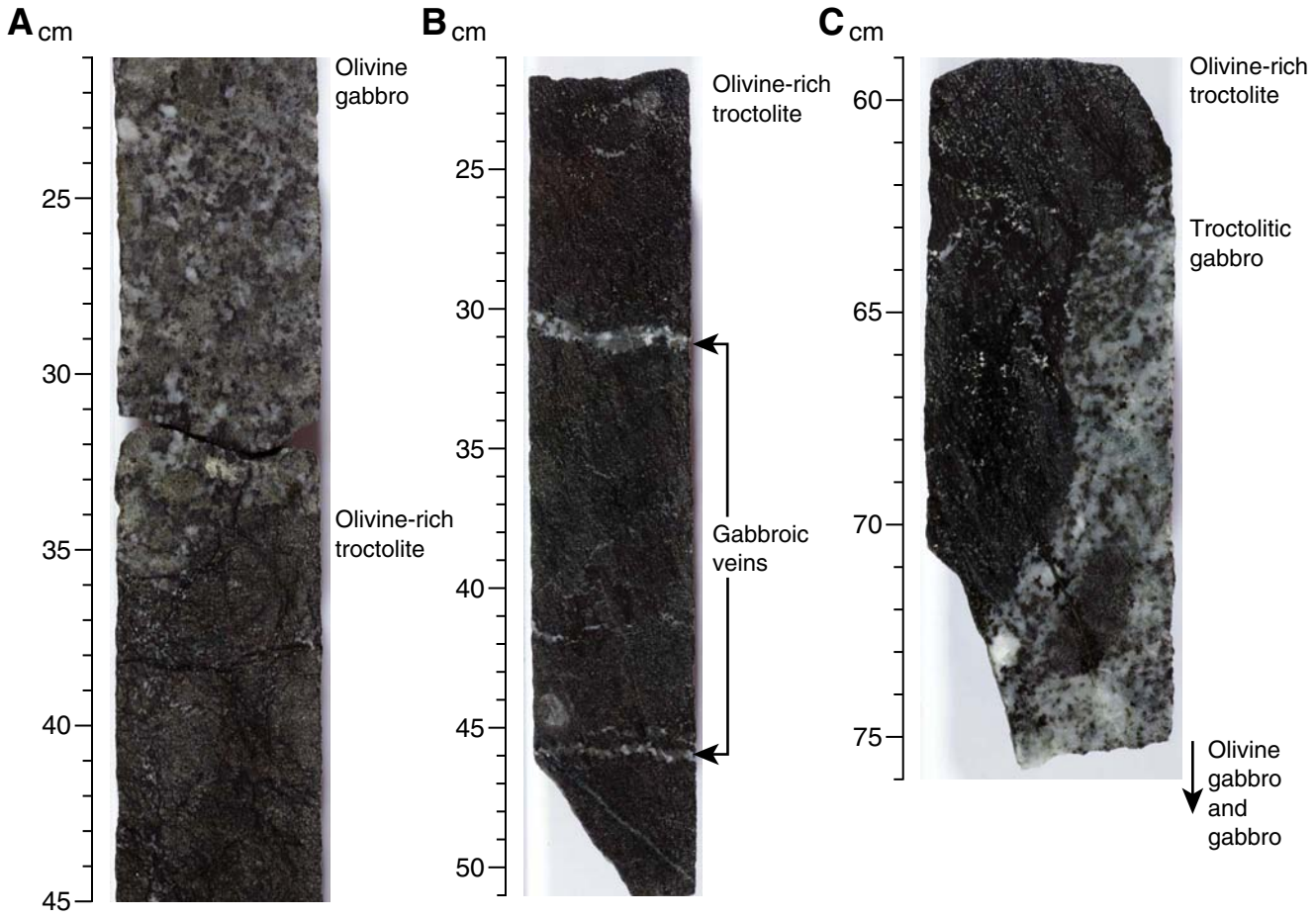

Figure F85. Modes of occurrence of olivine-rich troctolite in Cores 305-U1309D-235R, 236R, and 237R. **A.** Interval 305-U1309D-236R-2, 98–113 cm. **B.** Interval 305-U1309D-236R-1, 25–50 cm. Red box = location of thin section Sample **305-U1309D-236R-1, 45–47 cm** (Fig. **F89B**). **C.** Interval 305-U1309D-237R-1, 57–79 cm.

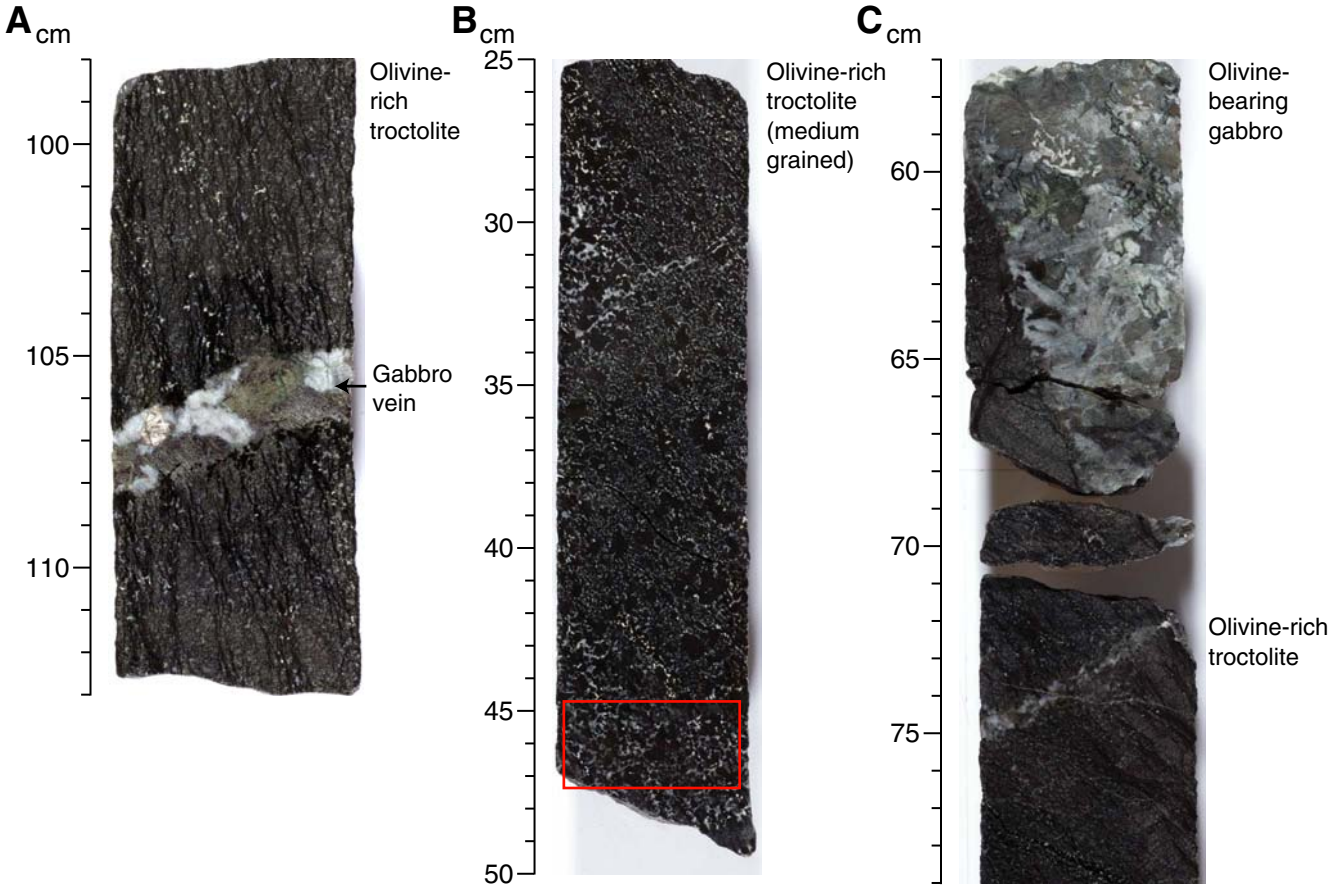

Figure F86. Modes of occurrence of olivine-rich troctolite in Cores 305-U1309D-240R, 241R, and 243R. **A.** Interval 305-U1309D-240R-2, 0–19 cm. **B.** Interval 305-U1309D-241R-1, 63–83 cm. **C.** Interval 305-U1309D-241R-2, 8–26 cm. **D.** Interval 305-U1309D-243R-1, 25–47 cm.

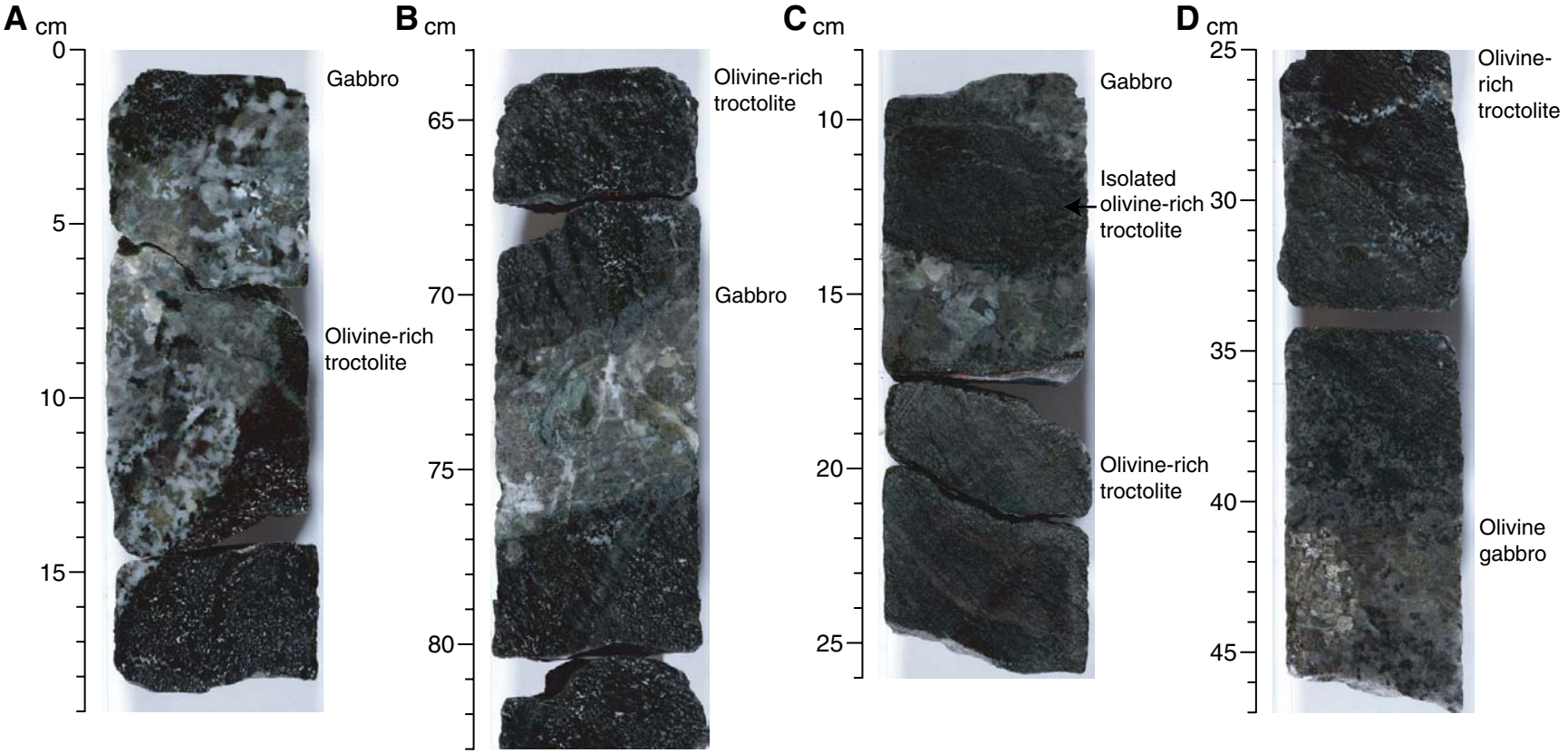

Figure F87. Modes of occurrence of olivine-rich troctolite in Cores 305-U1309D-247R and 248R. **A.** Interval 305-U1309D-247R-1, 82–102 cm. **B.** Interval 305-U1309D-247R-1, 111–125 cm. **C.** Interval 305-U1309D-248R-2, 0–26 cm.

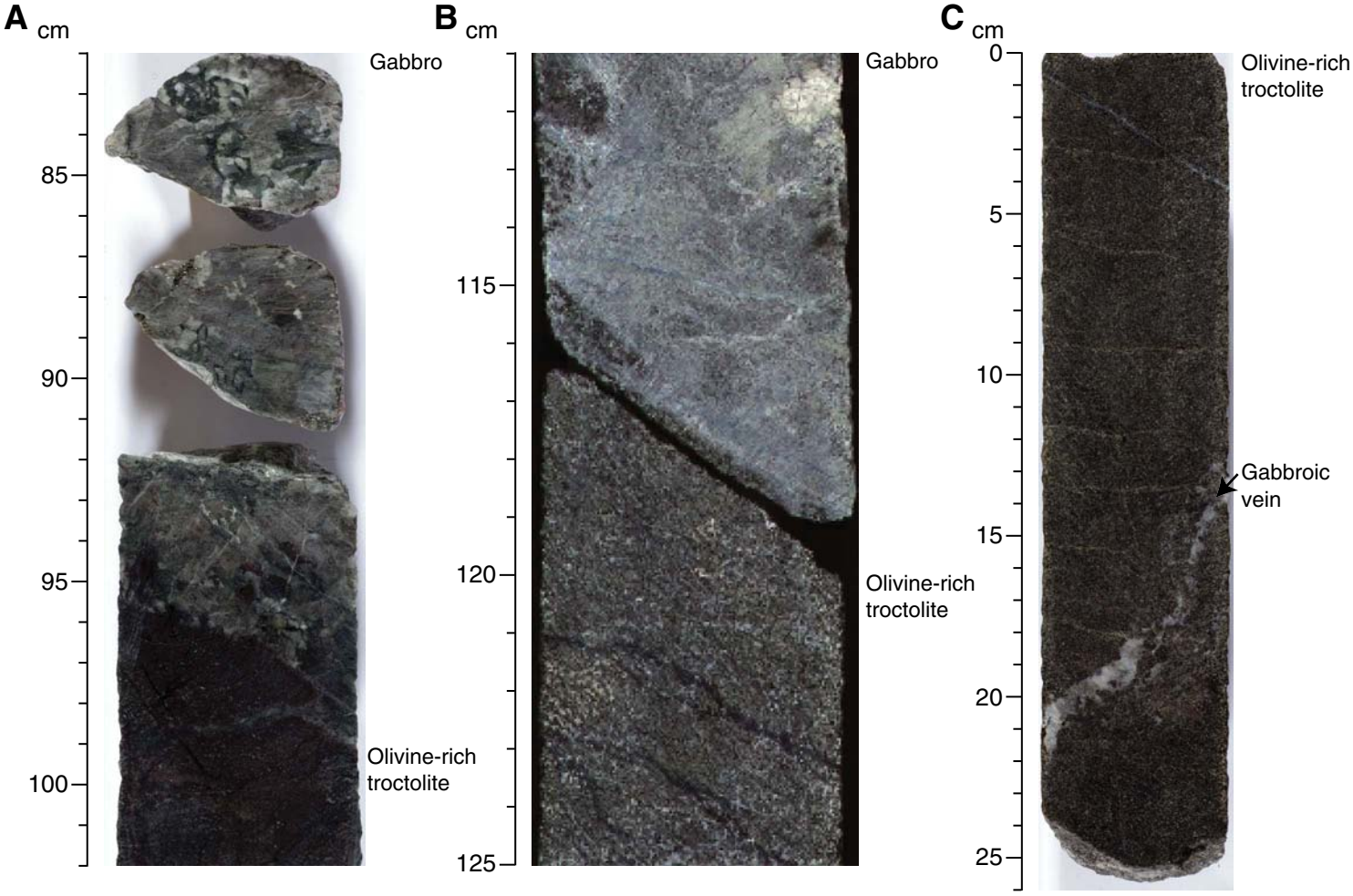

Figure F88. Modes of occurrence of olivine-rich troctolite in Cores 305-U1309D-256R and 257R. **A.** Interval 305-U1309D-256R-1, 9–30 cm. **B.** Interval 305-U1309D-256R-1, 92–113 cm. Red box = location of thin section Sample **305-U1309D-256R-1, 110–112 cm** (Fig. **F90C**). **C.** Interval 305-U1309D-257R-1, 10–37 cm. Red box = location of thin section Sample **305-U1309D-257R-1, 25–28 cm** (Fig. **F90B**).

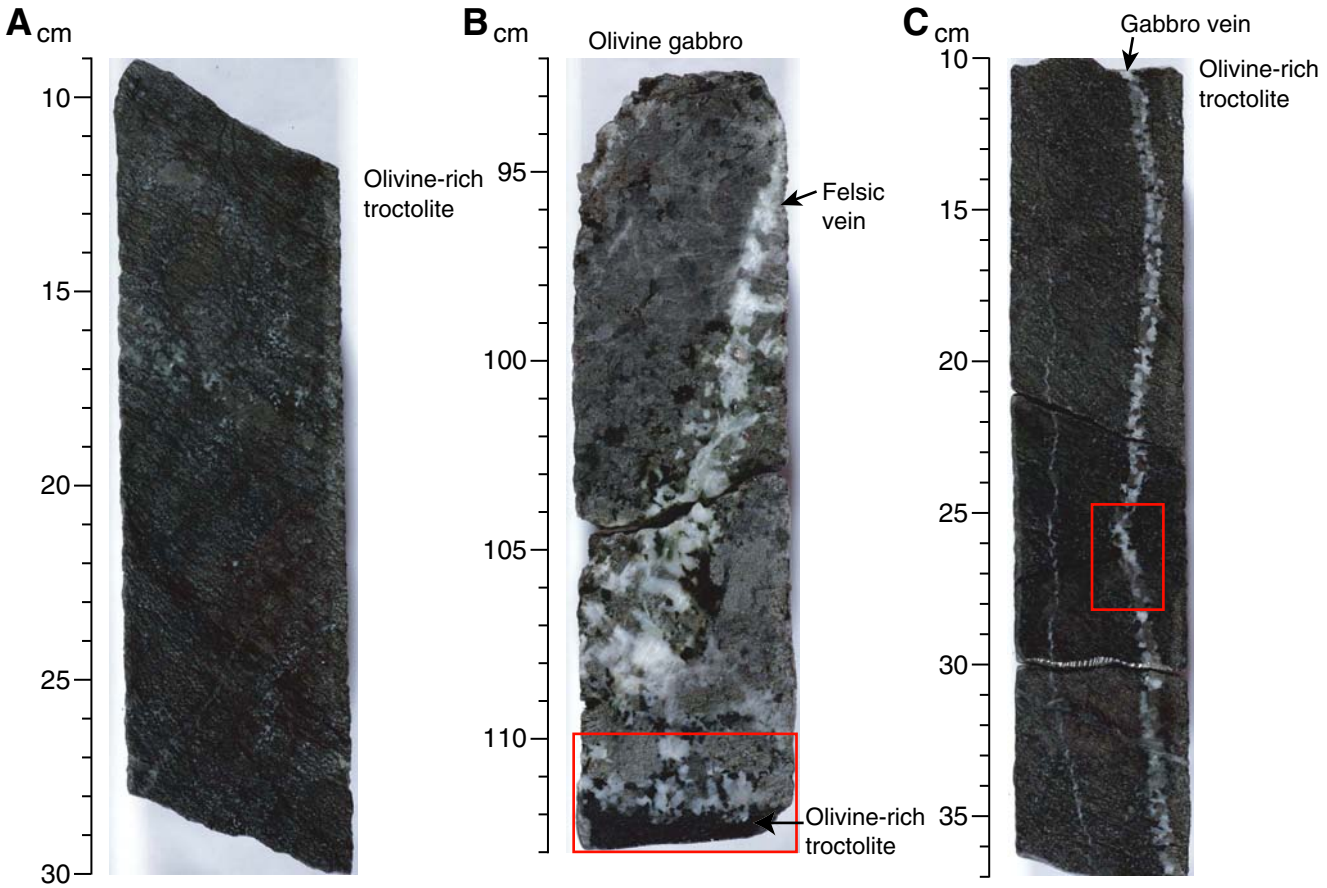

Figure F89. Representative thin sections of olivine-rich troctolite in plane-polarized and cross-polarized light. **A.** Sample **305-U1309D-227R-3, 70–72 cm** (field of view [FOV] = 2 cm). **B.** Sample **305-U1309D-236R-1, 45–47 cm** (FOV = 2 cm) (see Fig. **F85B**).

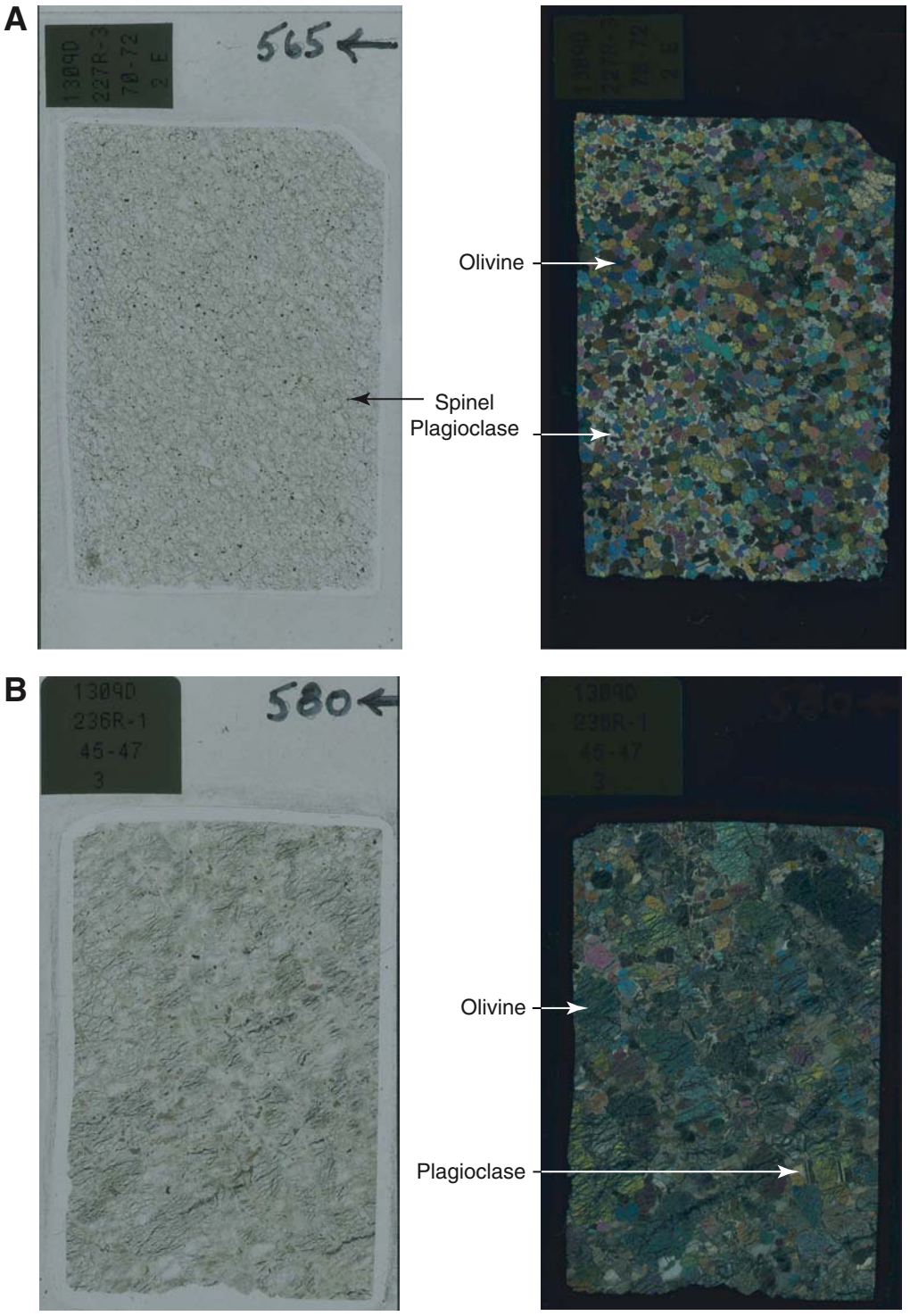

Figure F90. Texture and dikelet within an olivine-rich troctolite in plane-polarized and cross-polarized light. **A.** Sample **305-U1309D-100R-1, 10–13 cm** (field of view [FOV] = 2 cm) (see Figure **F81A**). **B.** Sample **305-1309D-257R-1, 25–28 cm** (FOV = 2 cm) (see location in Fig. **F88C**). **C.** Sample **305-U1309D-256R-1, 110–112 cm** (FOV = 2 cm) (see location in Figure **F88B**).

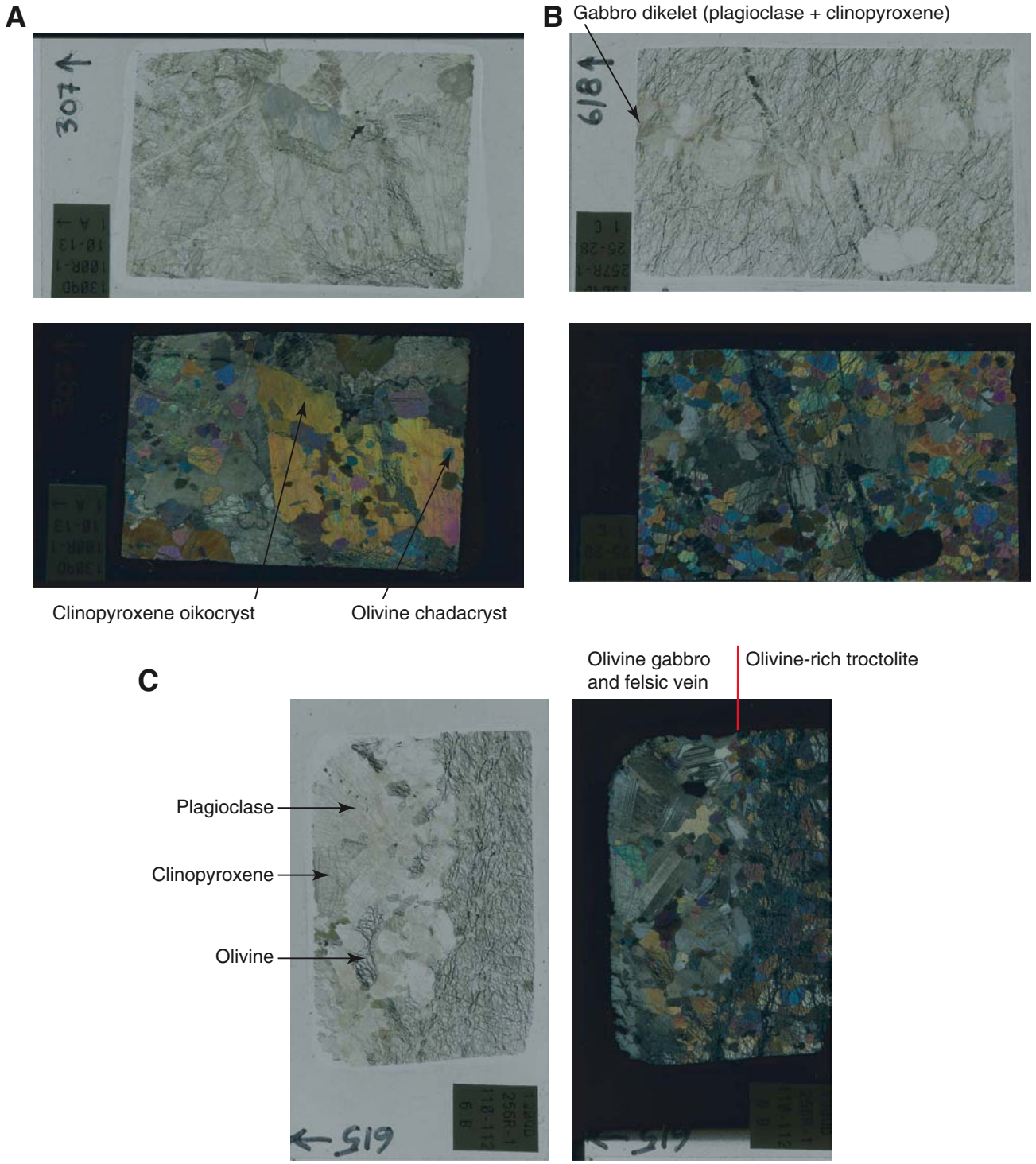

Figure F91. Chromian spinel enrichment at the boundary between olivine-rich troctolite and plagiolase-rich troctolite (Sample **305-U1309D-136R-2, 57–60 cm**) (field of view = 5 mm). Ol = olivine, Pl = plagioclase, Sp = chromian spinel.

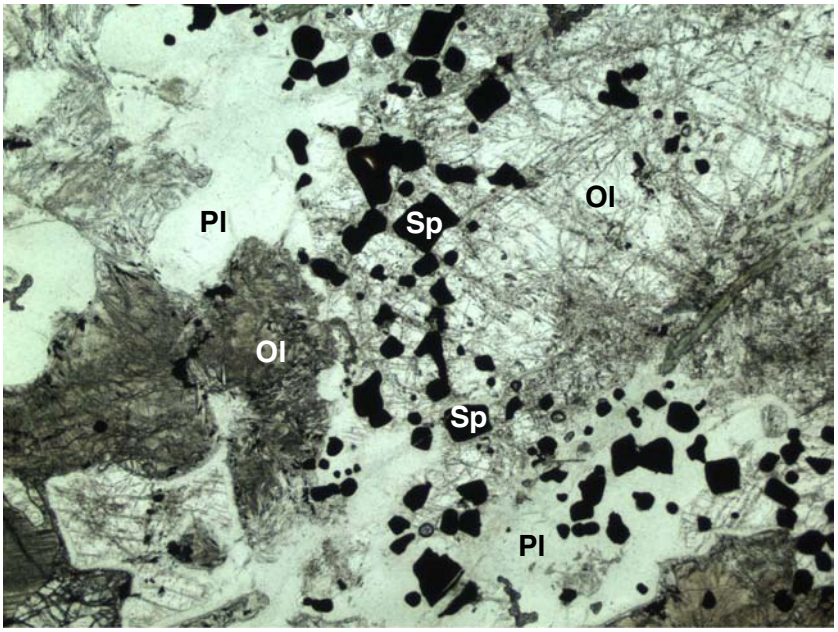

Figure F92. Contact between troctolite and gabbro (interval 305-1309D-111R-3, 12–29 cm) **A.** Troctolite (12–18 cm) cut by coarser grained olivine gabbro (18–27 cm). **B.** Contact between troctolite and coarse-grained gabbro (18–21 cm) (cross-polarized light; field of view = 2 cm).

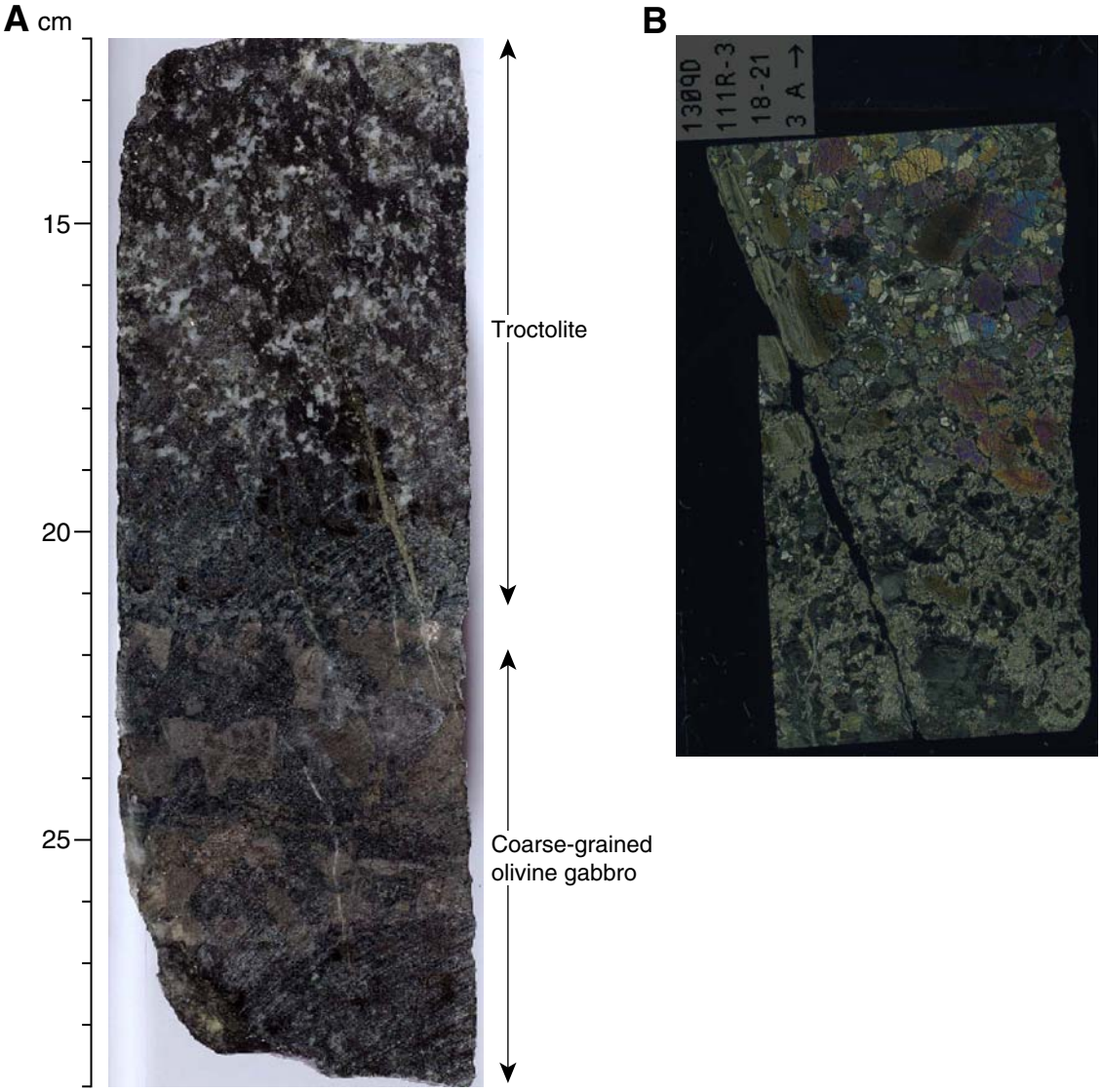

Figure F93. Troctolitic gabbro and olivine gabbro in cross-polarized light. **A.** Coronitic texture (Sample **305-U1309D-150R-1, 70–72 cm**). **B.** Olivine chadacrysts in clinopyroxene oikocryst (Sample **305-U1309D-256R-2, 90–92 cm**). **C.** Interlocked contacts between clinopyroxene and plagioclase (Sample **305-U1309D-120R-2, 41–43 cm**). **D.** Interstitial clinopyroxene between plagioclase (Sample **305-U1309D-81R-3, 12–14 cm**).

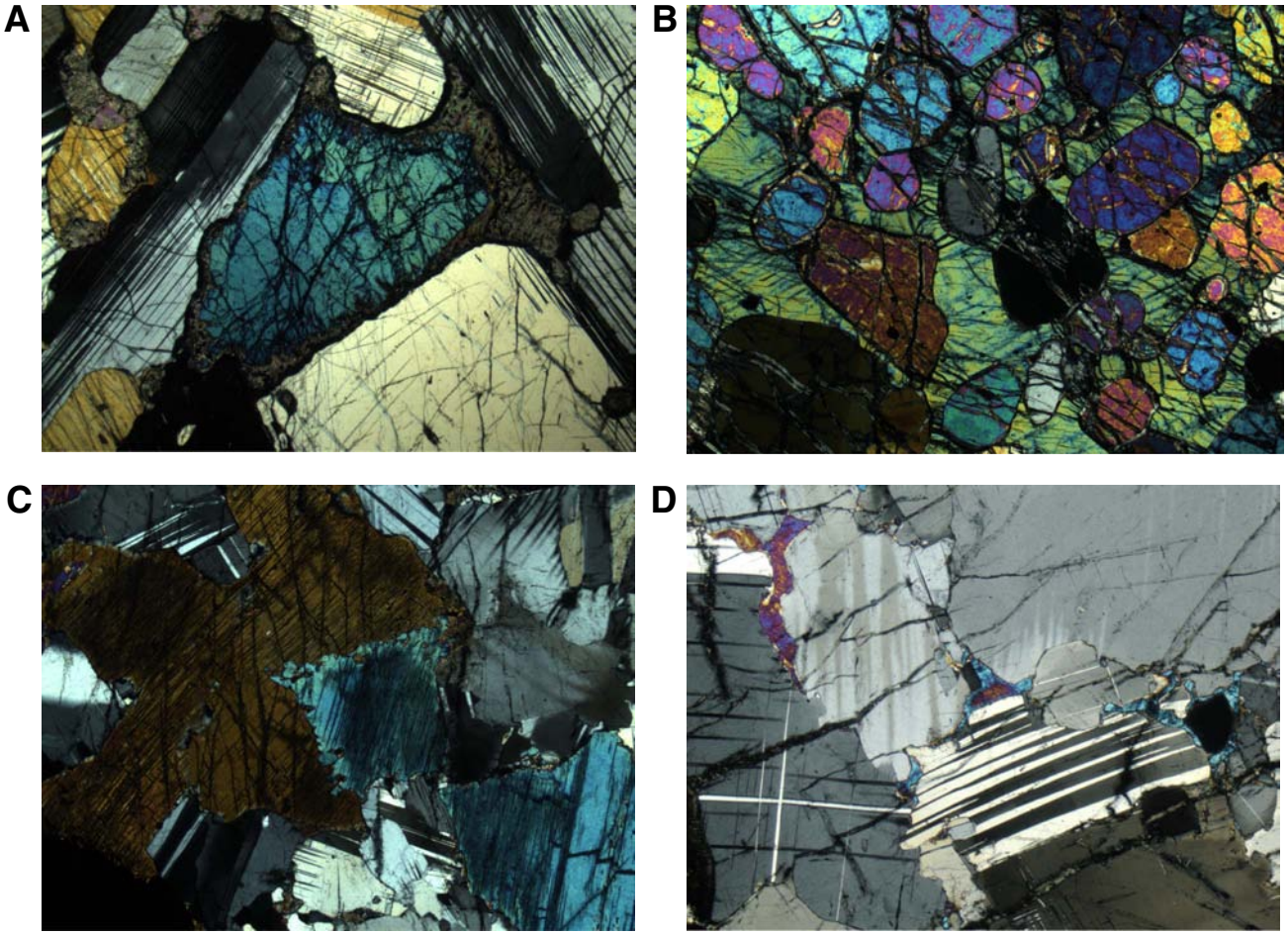

Figure F94. Pegmatitic gabbro (interval 305-U1309D-82R-2, 55–67 cm).

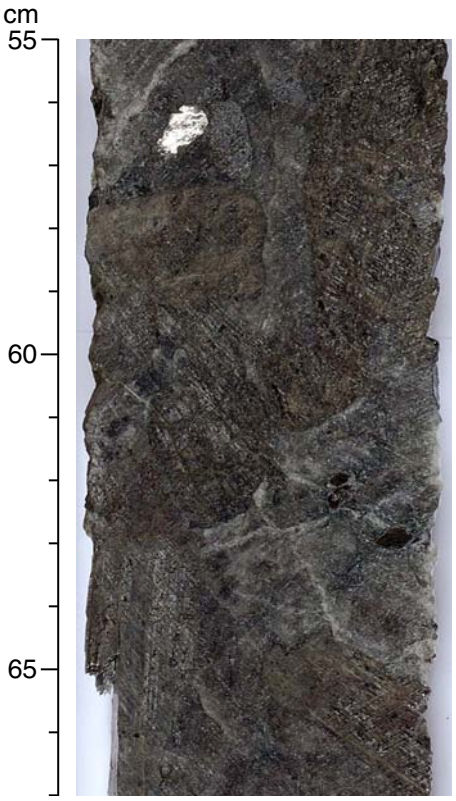

Figure F95. Olivine-bearing gabbro. **A.** Interval 305-U1309D-107R-2, 34–48 cm. **B.** Corona alteration around olivine (Sample **305-U1309D-107R-2, 38–41 cm**) (cross-polarized light; magnification = 1×).

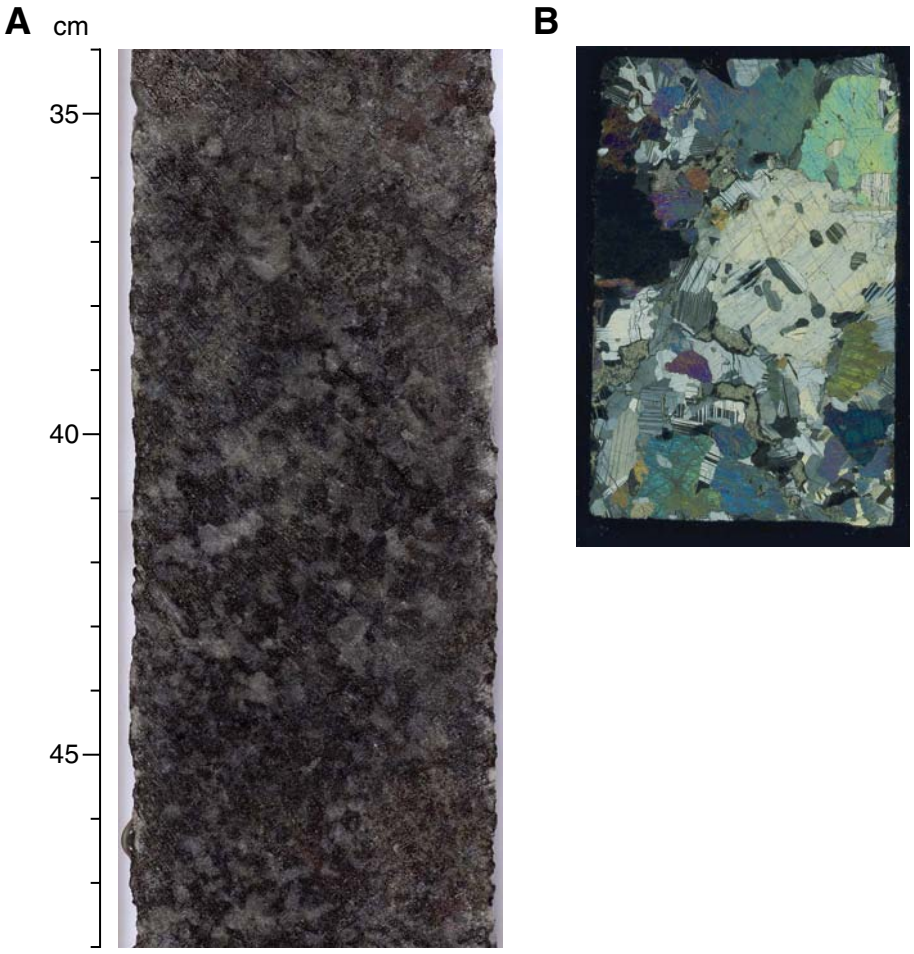

Figure F96. A. Sharp contact between equigranular microgabbronorite and surrounding gabbronorite (interval 305-U1309D-165R-1, 37–57 cm). **B.** Sharp contact and little noticeable deformation in either microgabbronorite or wallrock (Sample **305-U1309D-165R-1, 44–47 cm**) (cross-polarized light; field of view [FOV] = 2 cm). **C.** Sharp yet uneven contact between microgabbronorite and gabbronorite (Sample **305-U1309D-264R-1, 111–114 cm**) (cross-polarized light; FOV = 2 cm). **D.** High-temperature plagioclase recrystallization along the microgabbronorite contact (Sample **305-U1309D-165R-1, 44–47 cm**) (cross-polarized light; magnification = 2.5×).

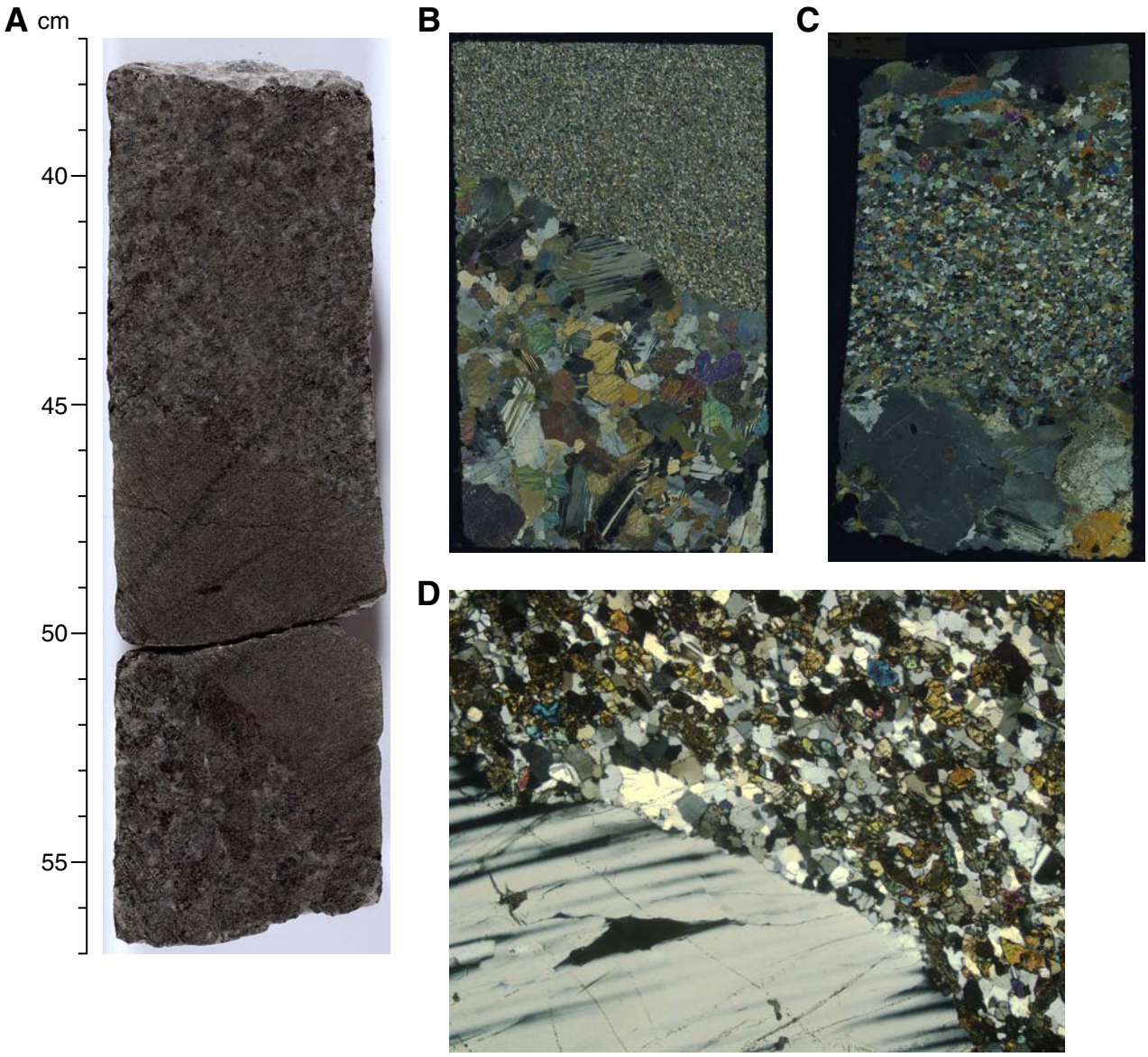

Figure F97. Na_2O versus TiO_2 variation in the lithologies from Hole U1309D. Ti-rich oxide gabbros are not reported because they mainly plot out of this scale. A strong Ti enrichment separates the basalt-diabase trend from the gabbro trend. Gabbroic rocks are progressively enriched in the order of olivine-rich troctolites to troctolites to gabbros to gabbronorites.

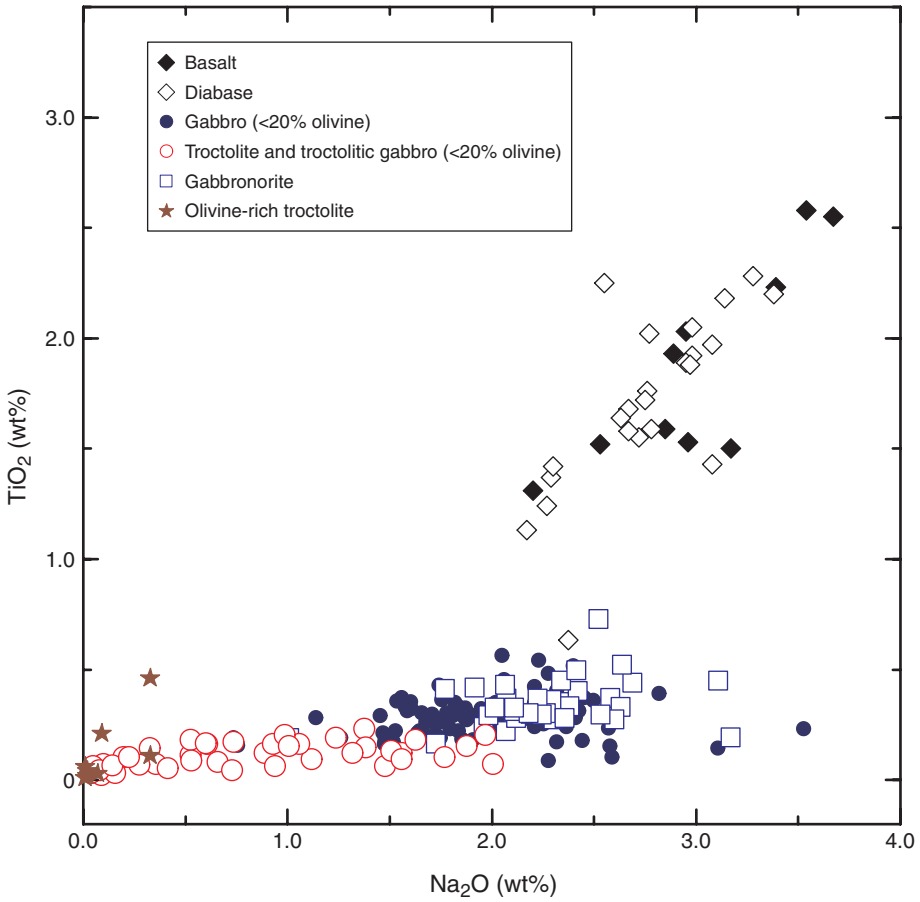

Figure F98. A. Olivine-bearing microgabbronorite (Sample **305-U1309D-133R-2, 50–53 cm**) (cross-polarized light). Anhedral orthopyroxene oikocryst encloses rounded plagioclase chadacrysts. Two plagioclase grains also enclose rounded clinopyroxene microphenocrysts. **B.** Oxide gabbronoritic mylonite (Sample **305-U1309D-137R-2, 133–135 cm**) (cross-polarized light). Subidiomorphic clinopyroxenes enclosed in orthopyroxene oikocryst. **C.** Olivine-orthopyroxene-bearing gabbro (Sample **305-U1309D-188R-1, 6–9 cm**) (cross-polarized light). Olivine chadacrysts in optical continuity enclosed in a large amoeboidal orthopyroxene oikocryst.

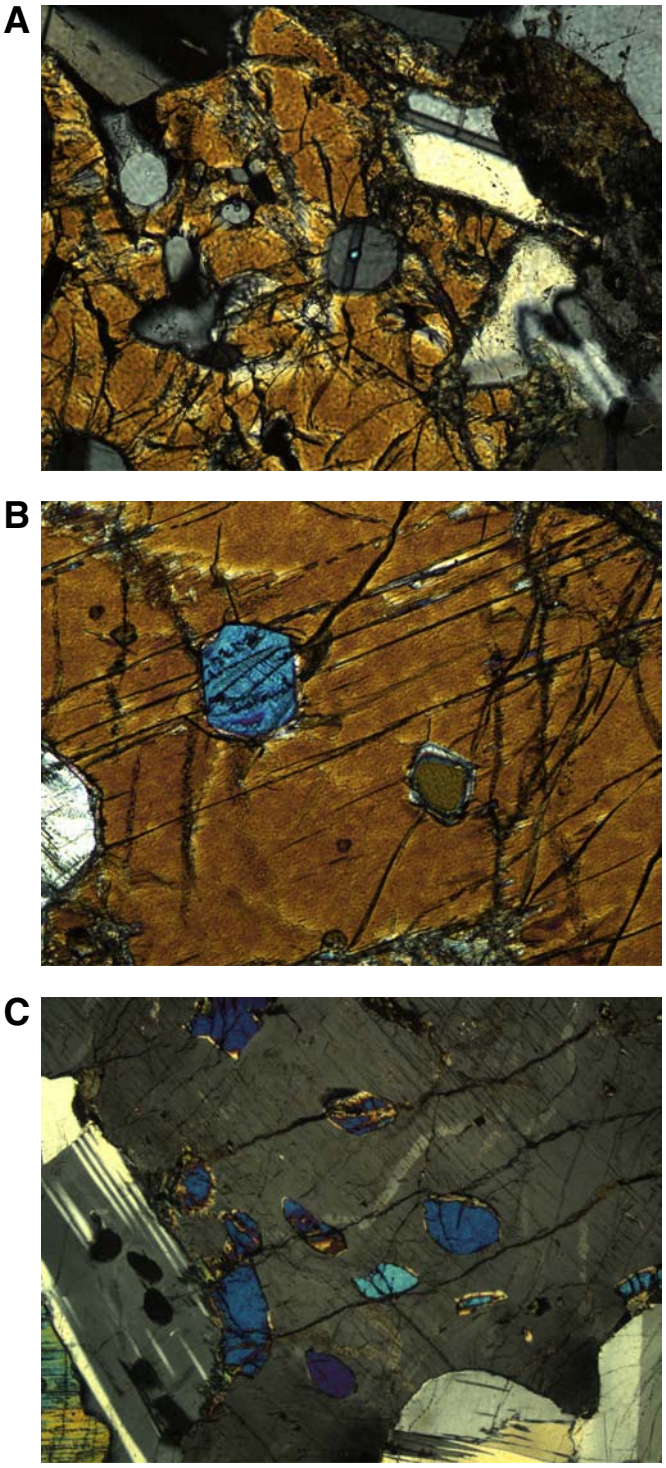

Figure F99. A. Olivine gabbronorite (Sample **305-U1309D-161R-2, 50–53 cm**) (plane-polarized light). Primary nonreactive olivine (right)/orthopyroxene contact (upper left). Olivine is partially replaced by tremolite-talc-oxide. **B.** Olivine-orthopyroxene-bearing gabbro (Sample **305-U1309D-166R-3, 55–57 cm**) (cross-polarized light). A 200–300 µm thick orthopyroxene film rims olivine at the contact with plagioclase. A thinner discontinuous film is also visible between clinopyroxene and olivine (lower right olivine grain). **C.** Pigeonitic gabbronorite (Sample **305-U1309D-254R-2, 33–35 cm**) (cross-polarized light). Two inverted pigeonites show a (001) primary exsolution pattern. A double (100) twinning in the larger central grain possibly reflects high-temperature kink banding.

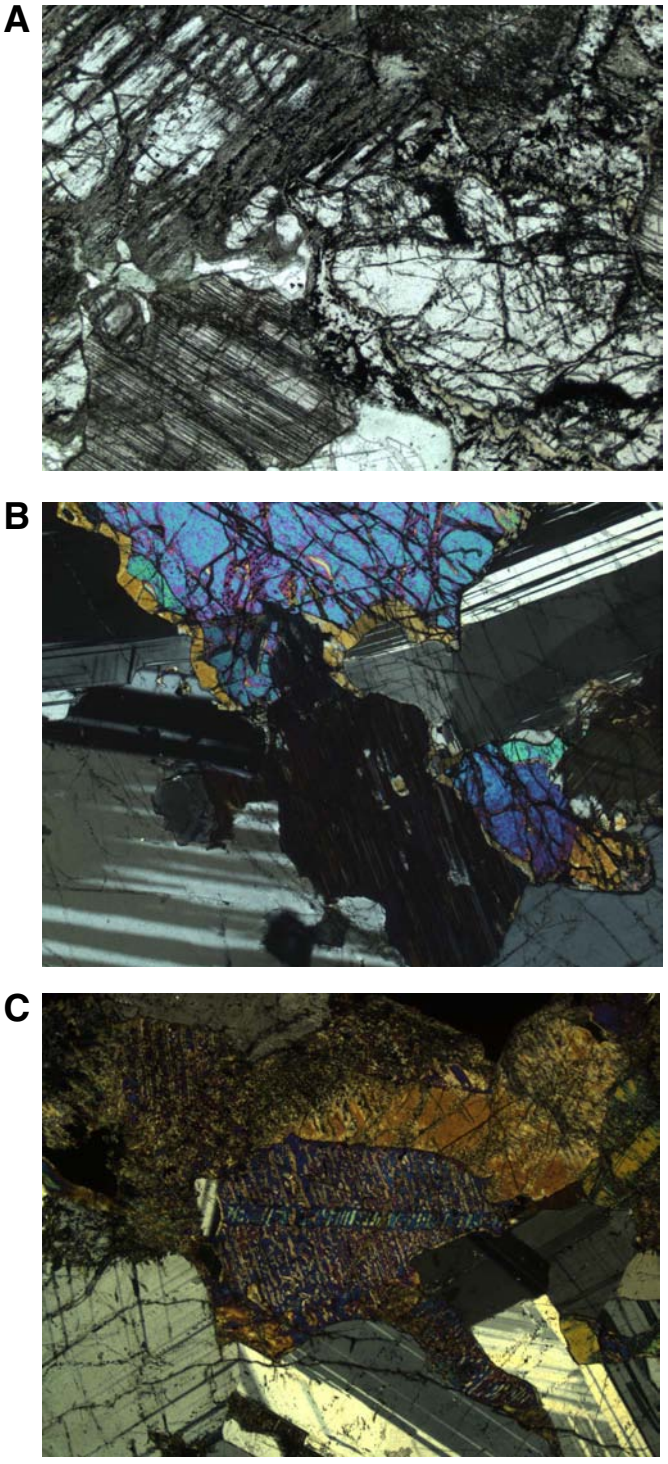

Figure F100. Downhole modal variation of orthopyroxene (red circles) and olivine (brown squares) versus depth. Modes are thin section estimates. Zones are subdivided based on gabbronorite occurrence and mineralogical assemblage (presence of pigeonite).

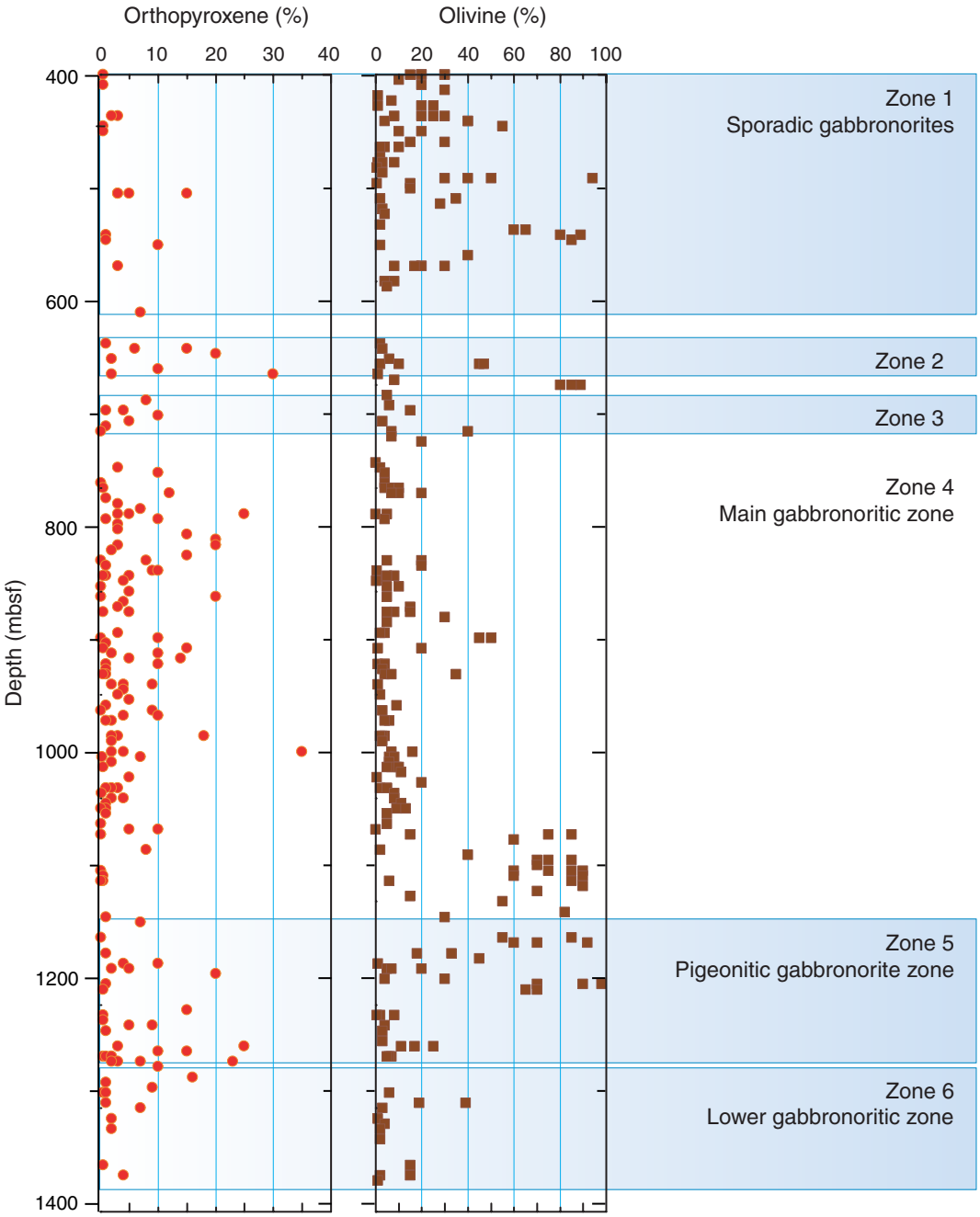

Figure F101. Modes of occurrence of oxide gabbro. **A.** Diffuse boundary between coarse-grained gabbro, oxide gabbro, and oxide concentrations (interval 305-U1309D-127R-3, 74–99 cm). **B.** Oxide concentration at the boundary with coarse-grained gabbro (interval 305-U1309D-244R-2, 102–111 cm). Arrow represents the zone of oxide concentration in this sample. **C.** Sharp boundary between olivine gabbro and oxide gabbro (interval 305-U1309D-114R-1, 41–56 cm).

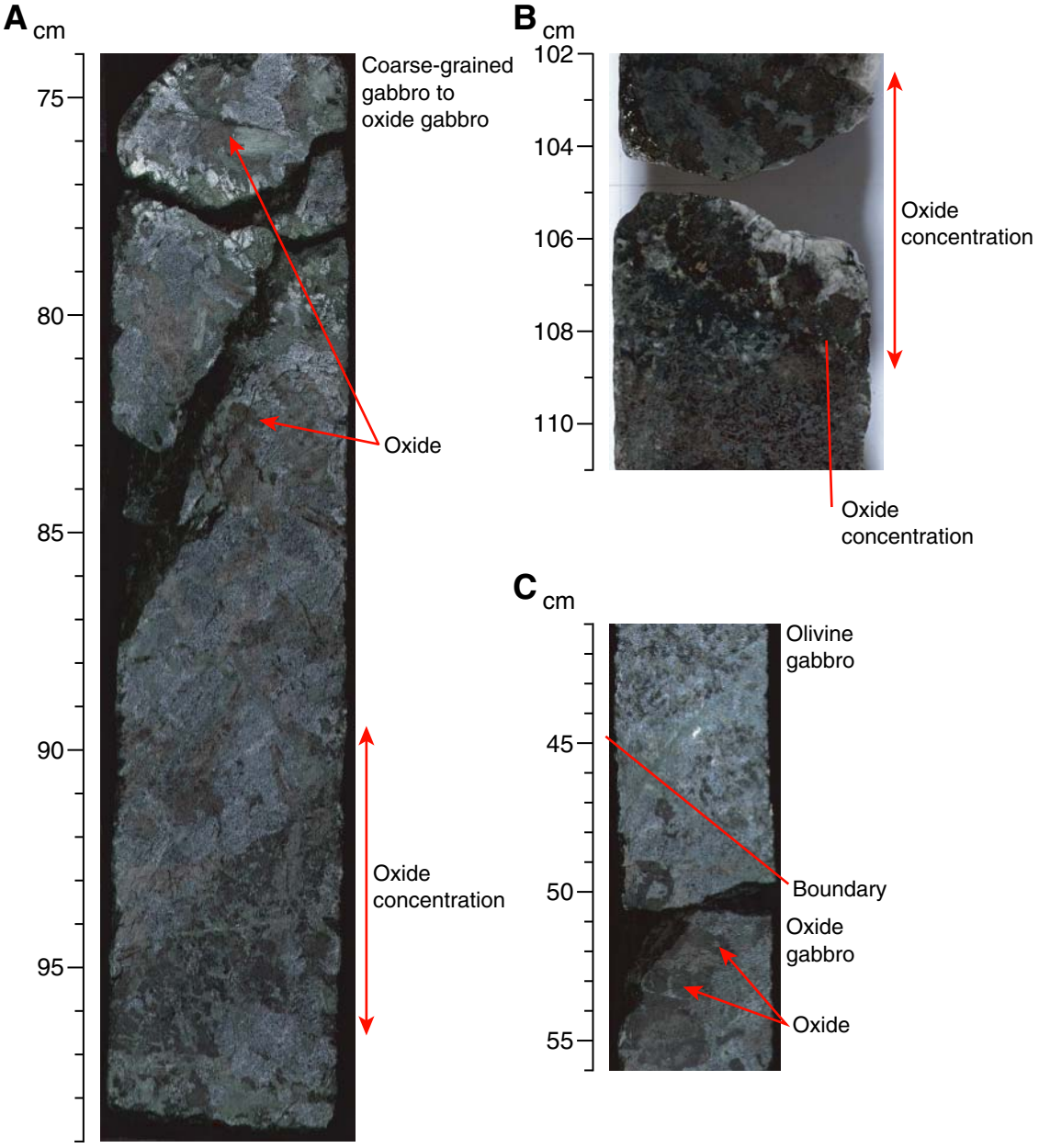

Figure F102. A. Euhedral to subhedral apatite (Ap)-rich part in oxide gabbro (Sample **305-U1309D-133R-1, 24–26 cm**) (plane-polarized light; magnification = 10×). **B.** Euhedral long-prismatic zircons (Sample **305-U1309D-186R-3, 87–90 cm**) (cross-polarized light; magnification = 2.5×). Pl = plagioclase.

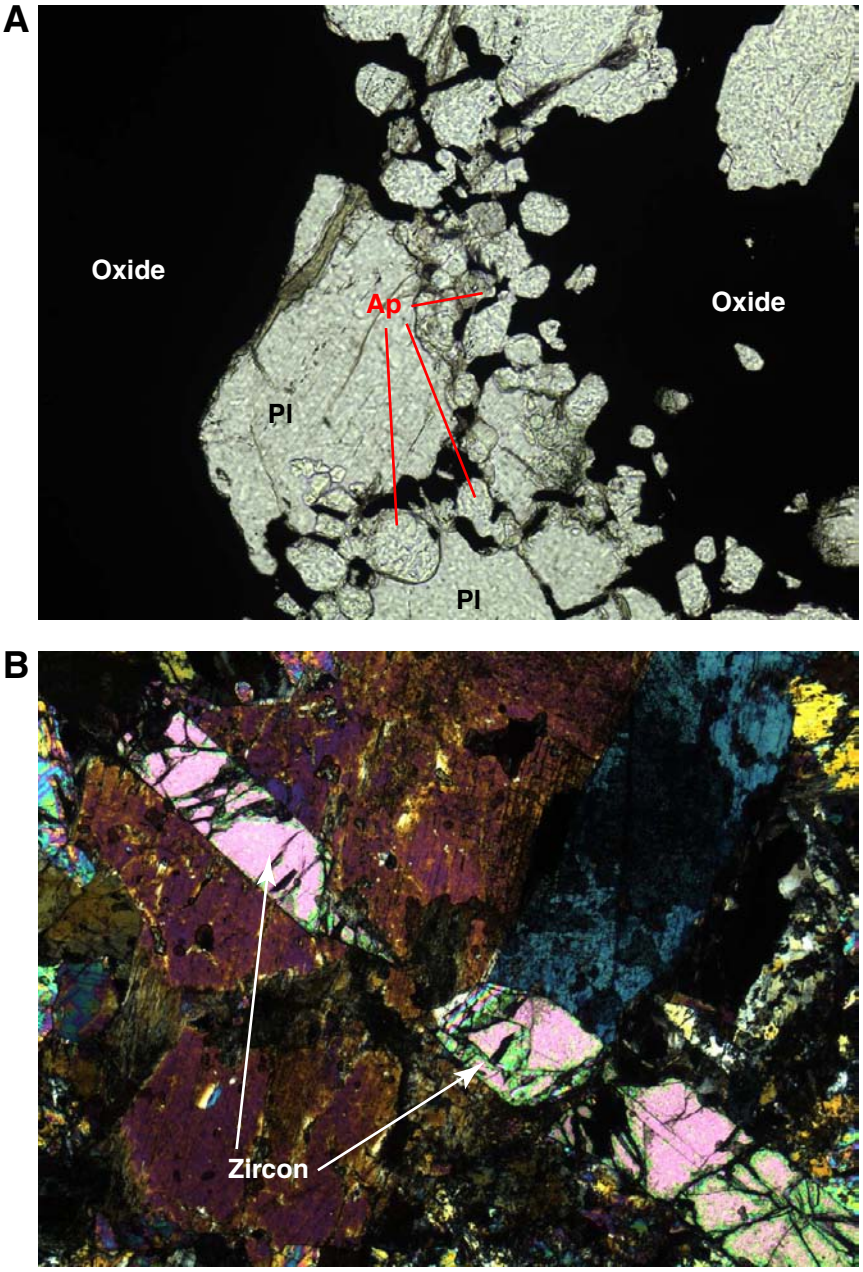

Figure F103. A. Subvertical oxide-rich band in oxide gabbro (interval 305-U1309D-133R-1, 9–31 cm). **B.** Vein in cross-polarized and plane-polarized light (Sample **305-U1309D-133R-1, 24–26 cm**) (field of view = 2 cm).

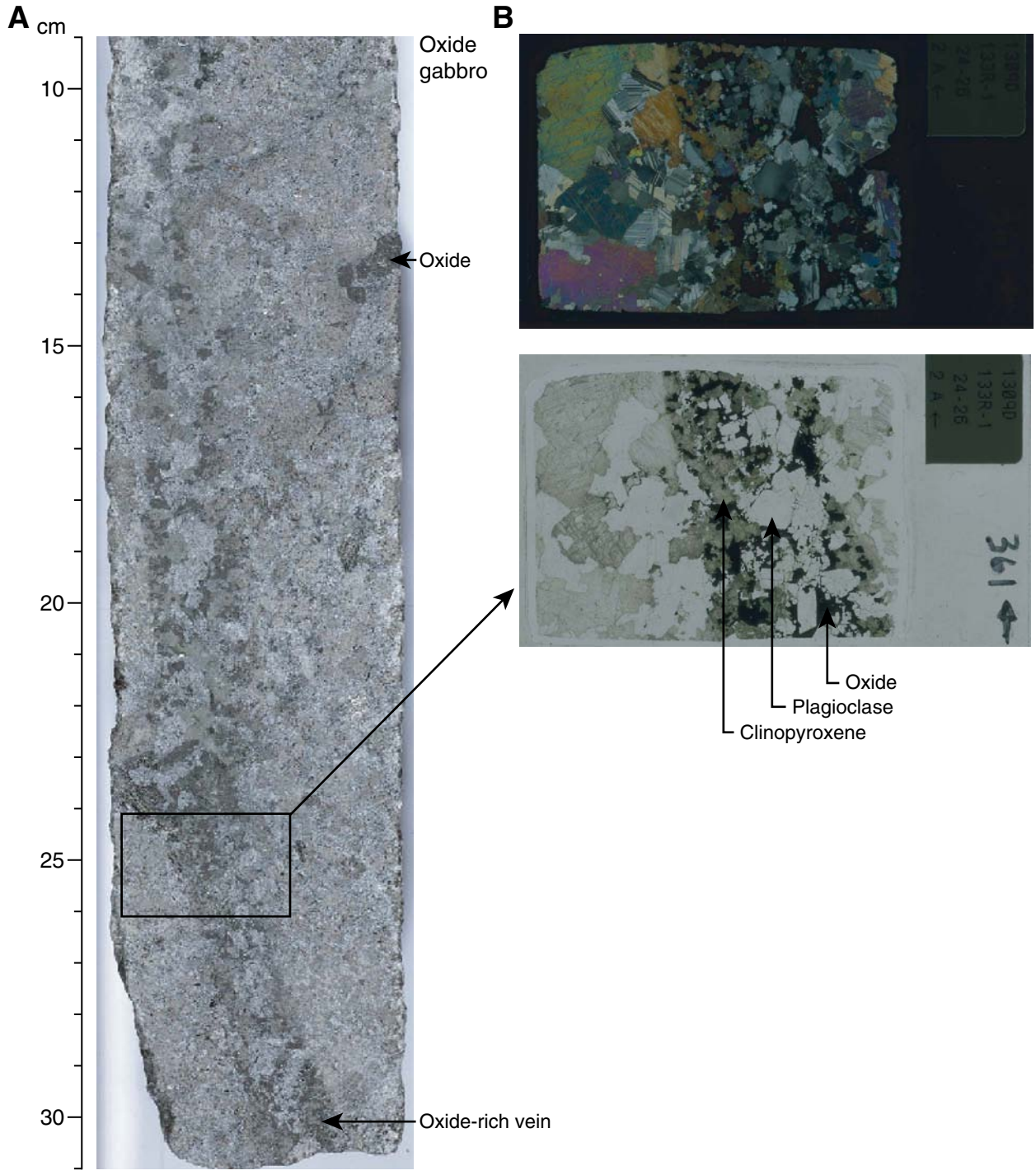

Figure F104. A. Primary mineral assemblage in coarse-grained oxide gabbro (interval 305-U1309D-87R-2, 59–76 cm). **B.** Typical amphibole-bearing oxide gabbro (interval 305-U1309D-130R-1, 43–63 cm). Green amphiboles have an elongate bladed shape and may be partly replacing primary magmatic amphiboles and partly replacing clinopyroxene.

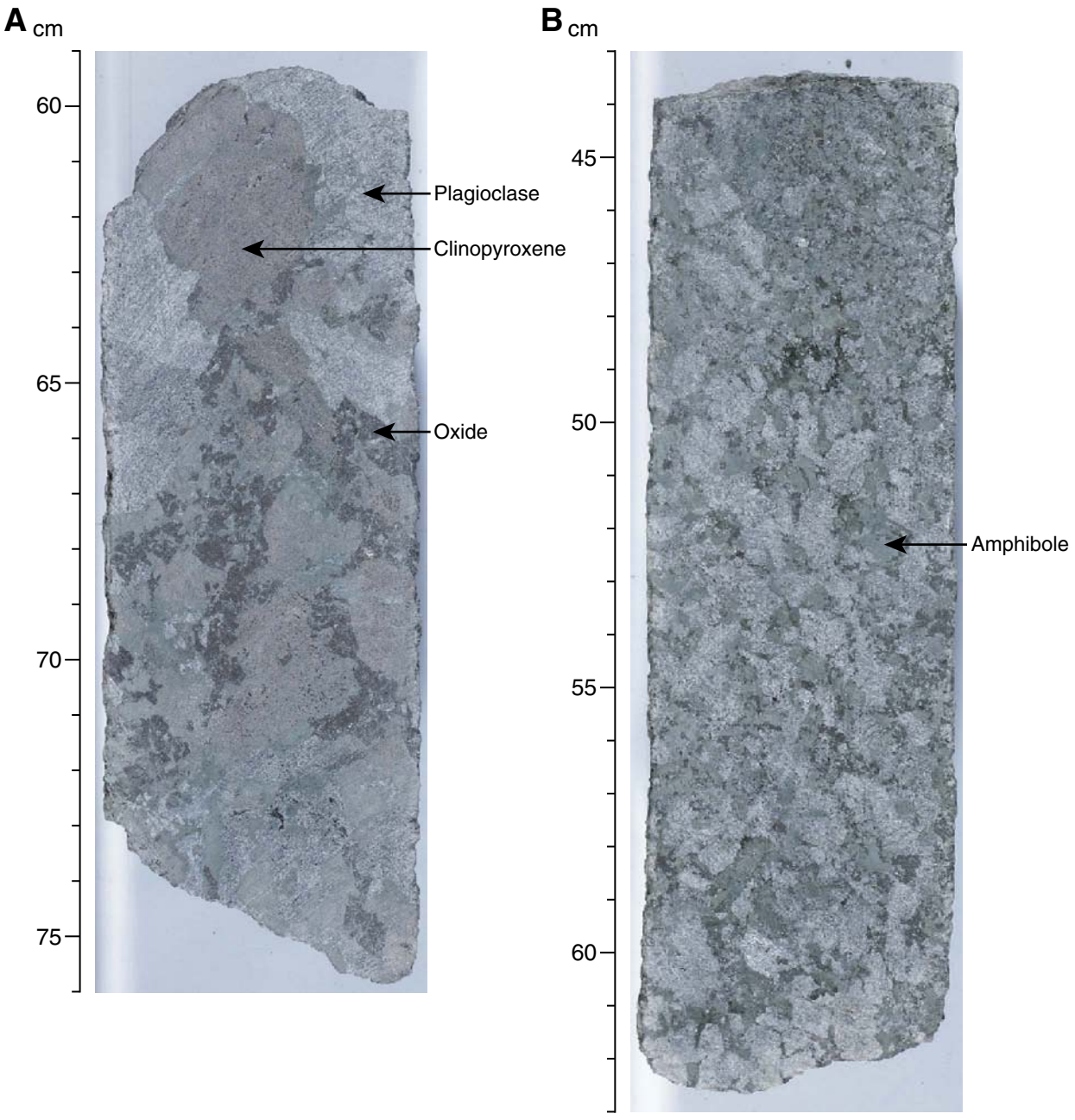

Figure F105. A. Oxide-bearing shear zone in mostly undeformed gabbro (Sample **305-U1309D-271R-1, 68–70 cm**) (plane-polarized light; field of view [FOV] = 2 cm). **B.** Strongly localized oxide-rich band, deposited in an undeformed gabbro (Sample **305-U1309D-272R-3, 10–13 cm**) (plane-polarized light; FOV = 2 cm). Oxide enrichment appears not to affect silicate modes.

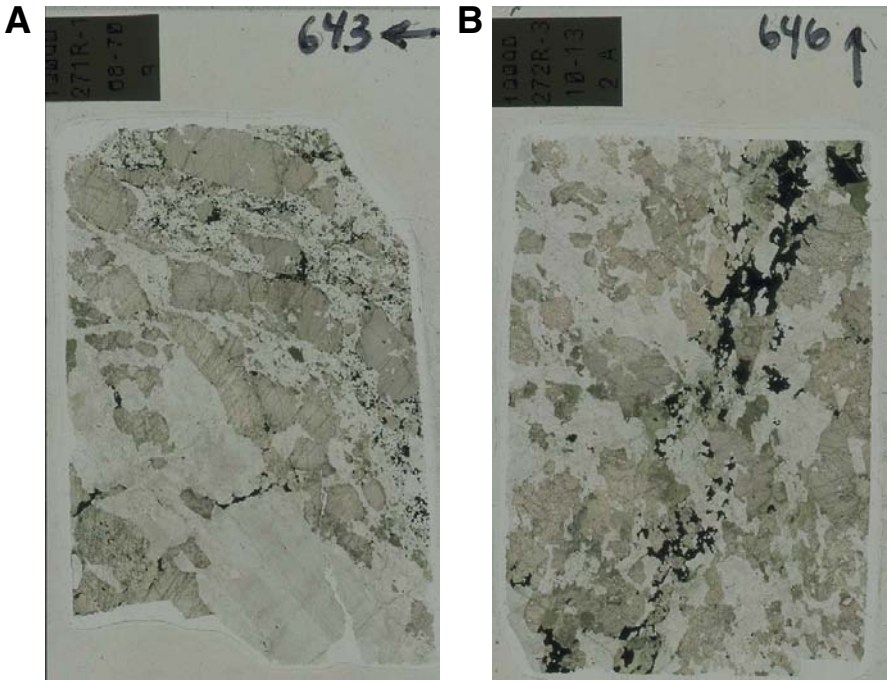

Figure F106. Sample 305-U1309D-183R-2, 32–34 cm. **A.** Whole thin section (plane-polarized light; field of view [FOV] = 2 cm). **B.** Oxide-rich shear zone (cross-polarized light; FOV = 2 cm). **C.** Extreme grain size reduction in the oxide-rich zone of the shear zone. Cathodoluminescence imaging using the Mainz CL-EDX device revealed that ~30% of all the dark to bright gray clasts in the shear zone are apatite. **D.** Approximately 30% of the white-gray minerals are apatite, showing oxide replacing a coarse host-gabbro clinopyroxene at the contact. **E.** Apatite-rich part of C.

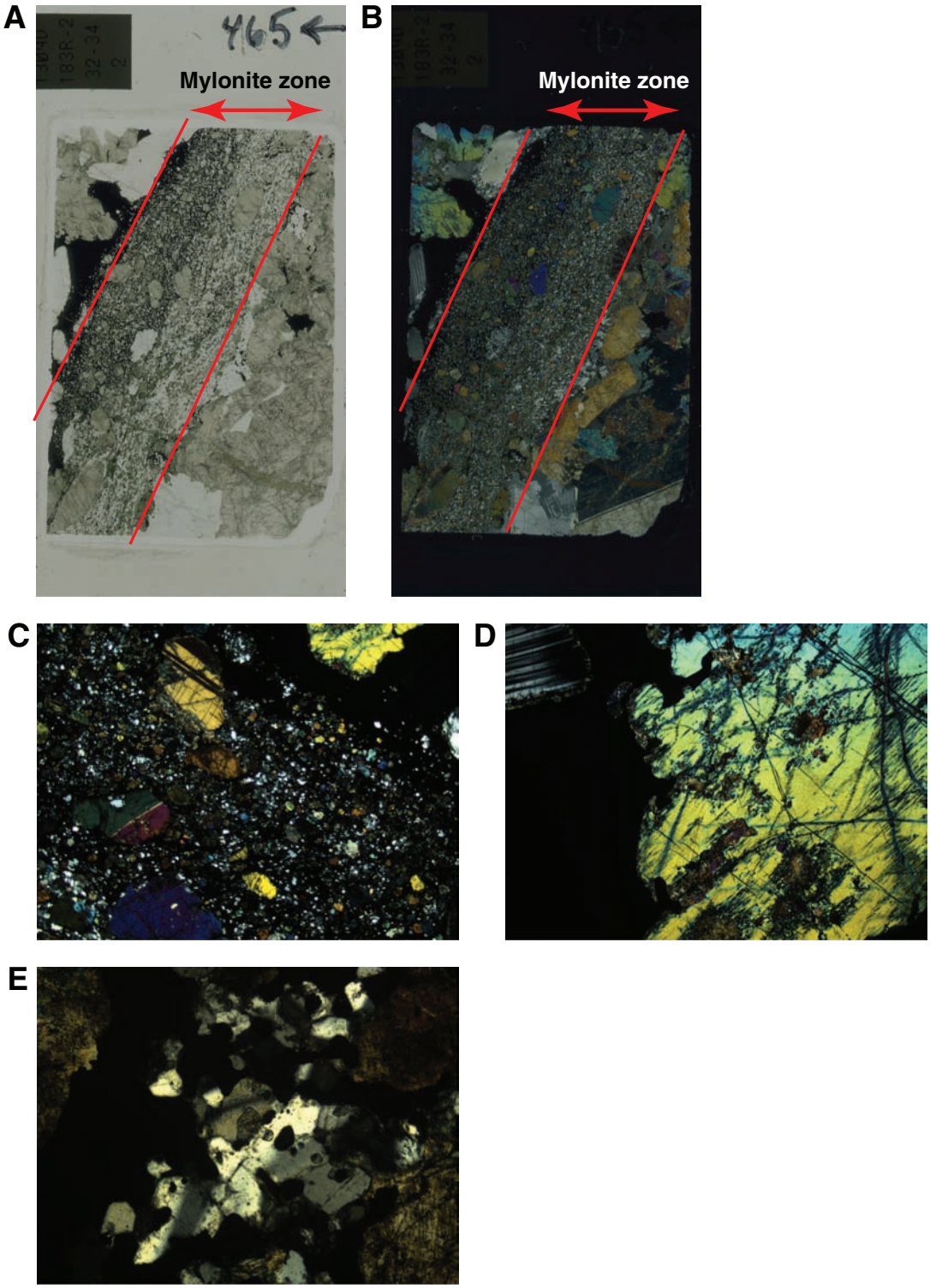

Figure F107. A. Diabase dike intruded in disseminated oxide gabbro (interval 305-U1309D-124R-2, 37–56 cm). **B.** Contact between diabase dike and gabbro (interval 305-U1309D-127R-1, 107–144 cm).

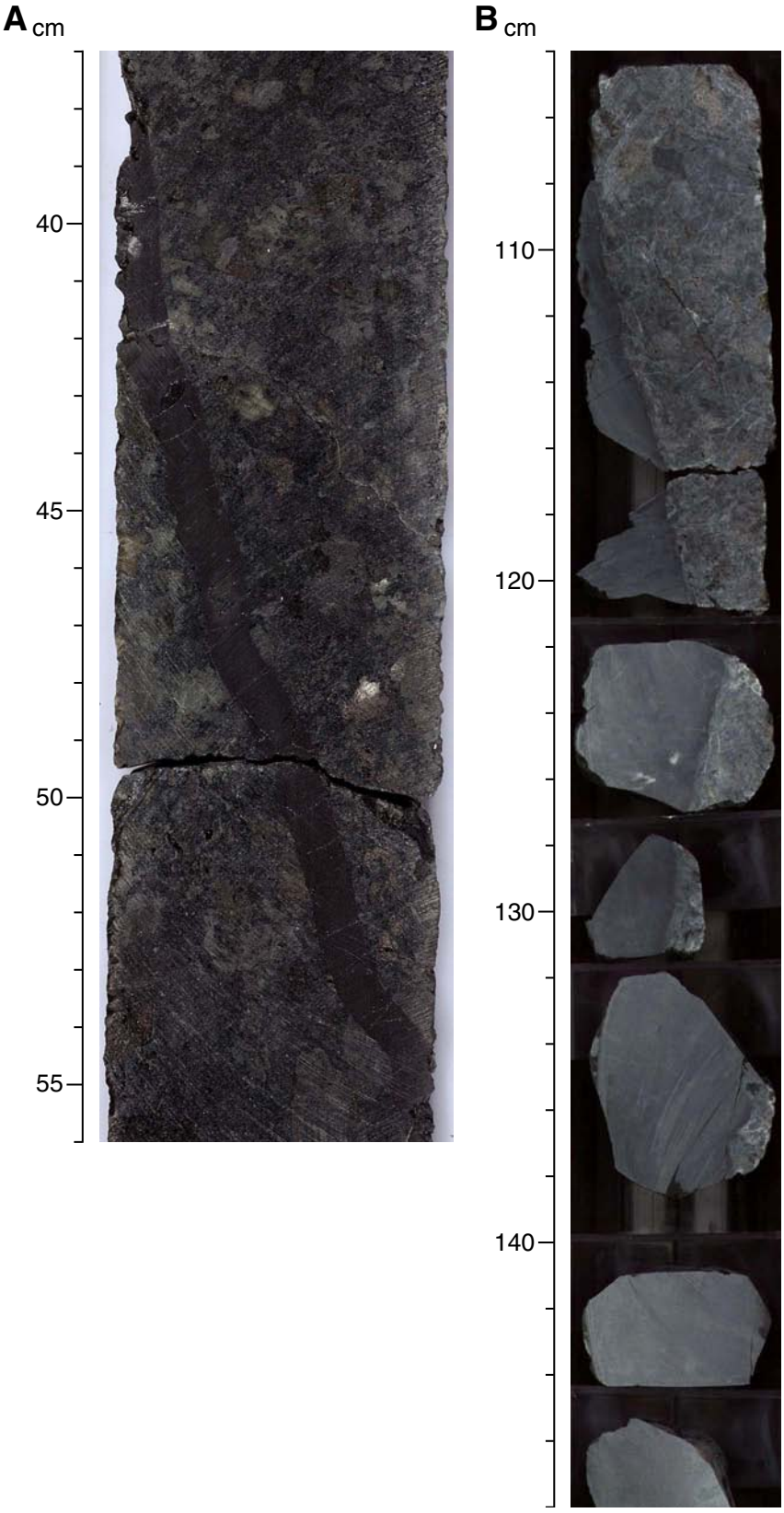

Figure F108. Diabase dikes and diabase in plane-polarized light. The textures are obviously different, regardless of the chilled margin. **A.** Diabase dike intruded in gabbro (Sample **305-U1309D-124R-2, 45–47 cm**). **B.** Contact of diabase dike and gabbro (Sample **305-U1309D-125R-2, 104–106 cm**). **C.** Medium-grained diabase showing ophitic texture (Sample **305-U1309D-155R-2, 38–40 cm**) (field of view = 2 cm).

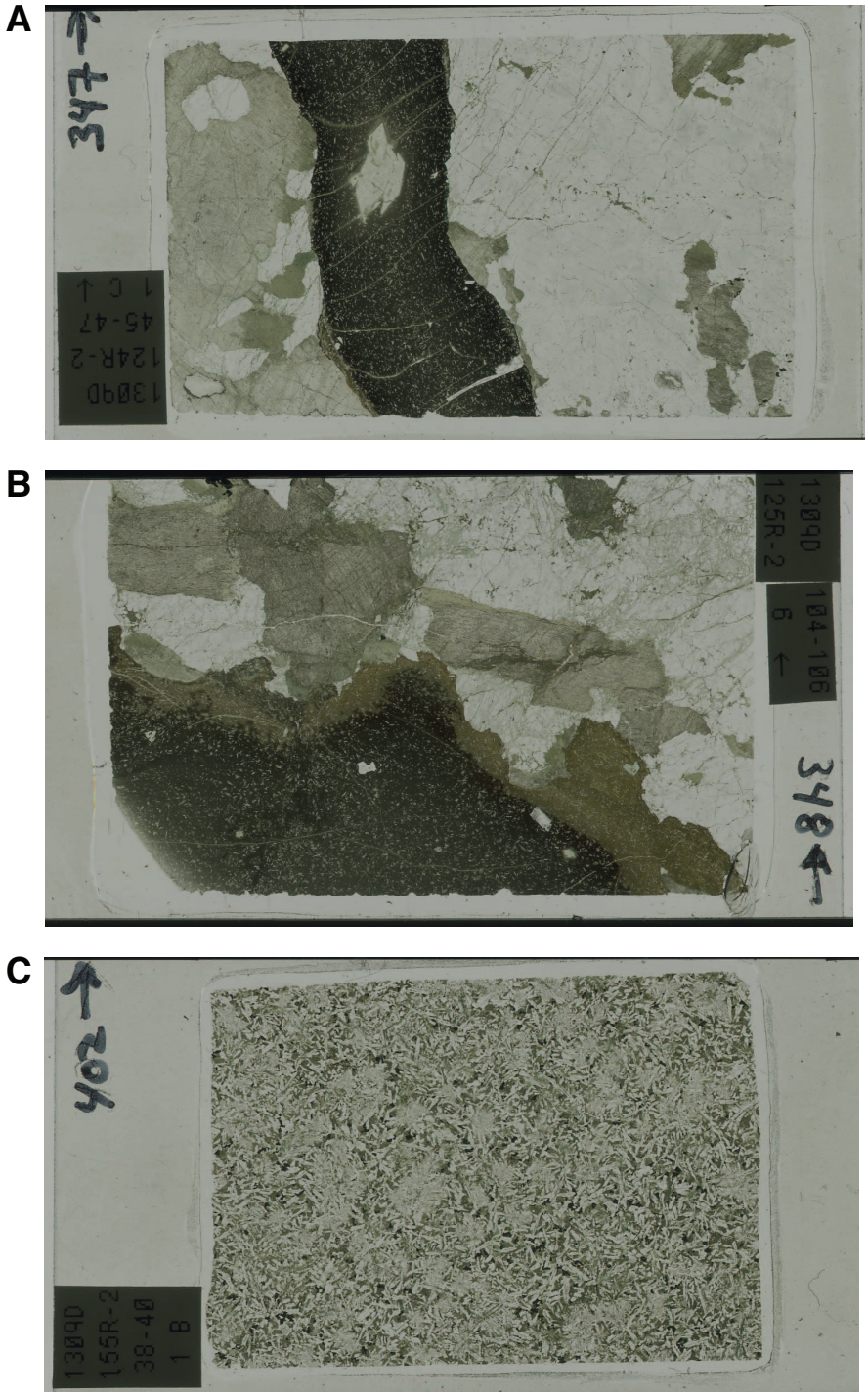

Figure F109. Gabbroic xenolith-bearing diabase. **A.** Interval 305-U1309-287R-1, 26–48 cm. Red box = location of B, C. **B.** Sample **305-U1309-287R-4, 42–44 cm** (plane-polarized light; field of view = 2 cm). **C.** Same as B; cross-polarized light.

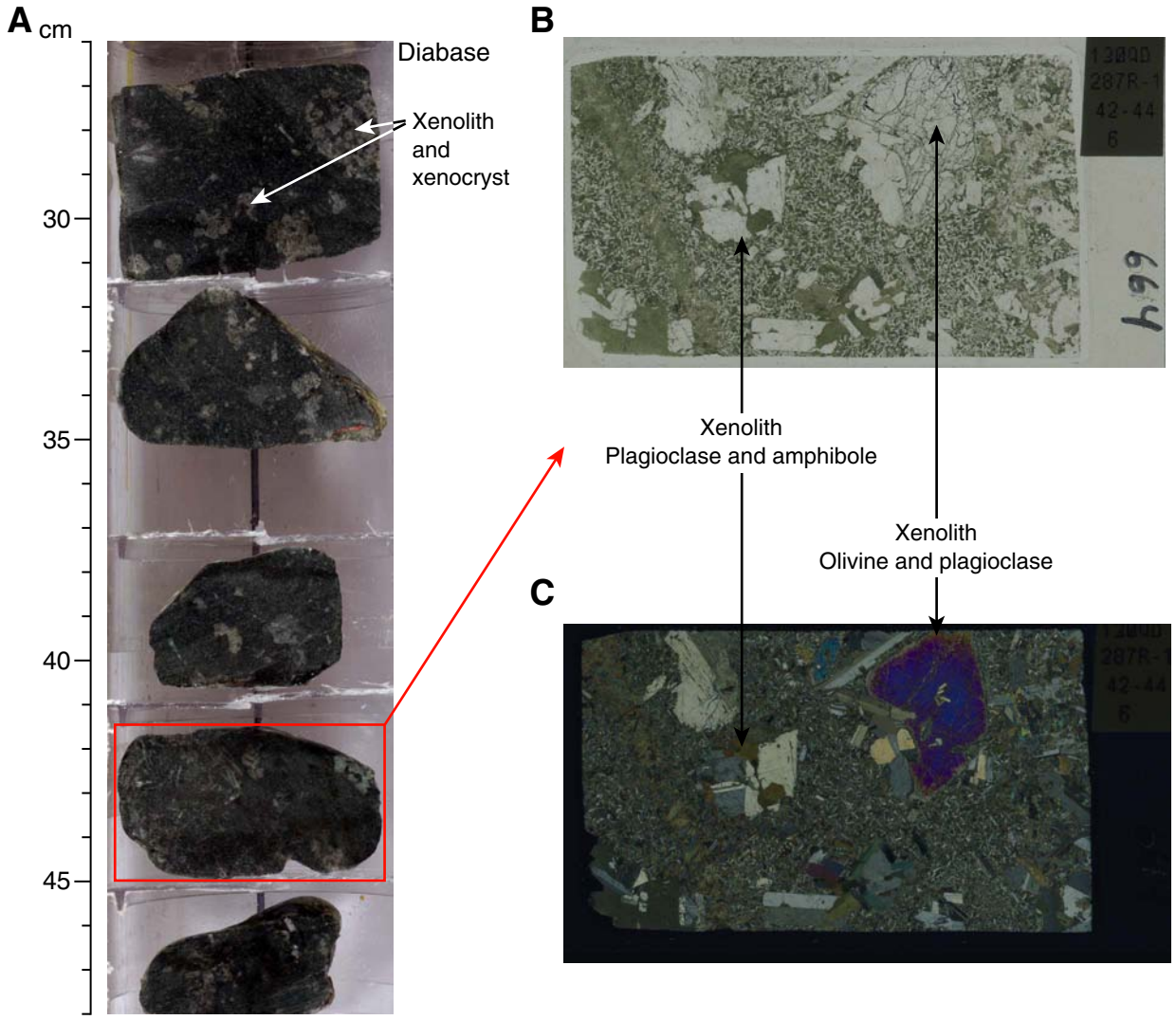

Figure F110. Small trondhjemite veins within gabbro and olivine gabbro. **A.** Trondhjemitic felsic vein with subvertical jigsaw boundary fringed by coarse amphibole grains between gabbro. Amphibole is probably replacing primary clinopyroxene (interval 305-U1309D-216R-1, 53–83 cm). Red box = location of B, C. **B.** Sample **305-U1309D-216R-1, 73–76 cm** (field of view = 2 cm; plane-polarized light). **C.** Same as B; cross-polarized light. **D.** Trondhjemitic felsic vein on olivine gabbro with obscure contact (interval 305-U1309D-262R-4, 68–87 cm). Red box = location of E, F. **E.** Sample **305-U1309D-262R-4, 84–87 cm** (Field of view = 2 cm; plane-polarized light). **F.** Same as E; cross-polarized light.

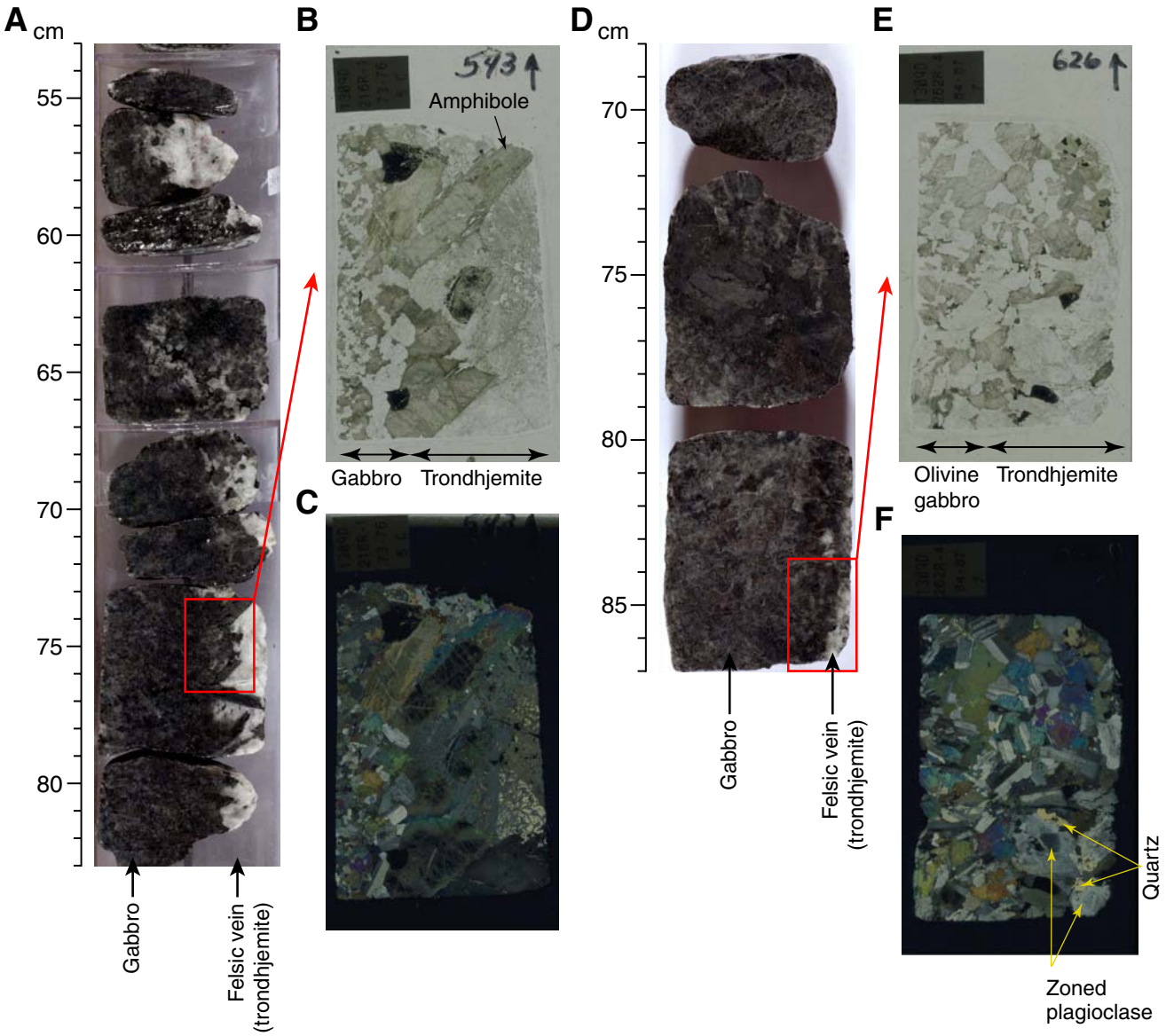

Figure F111. Downhole distribution of zircon and apatite, as observed in thin section (diamonds) and estimated from P and Zr concentrations in whole-rock analyses (squares). These accessory minerals are mainly associated with oxide gabbro, crosscutting oxide-bearing dikelets and shear zones, and rare trondhjemites. The apatite-barren interval between 1020 and 1190 mbsf coincides with the longest oxide-free interval of the core.

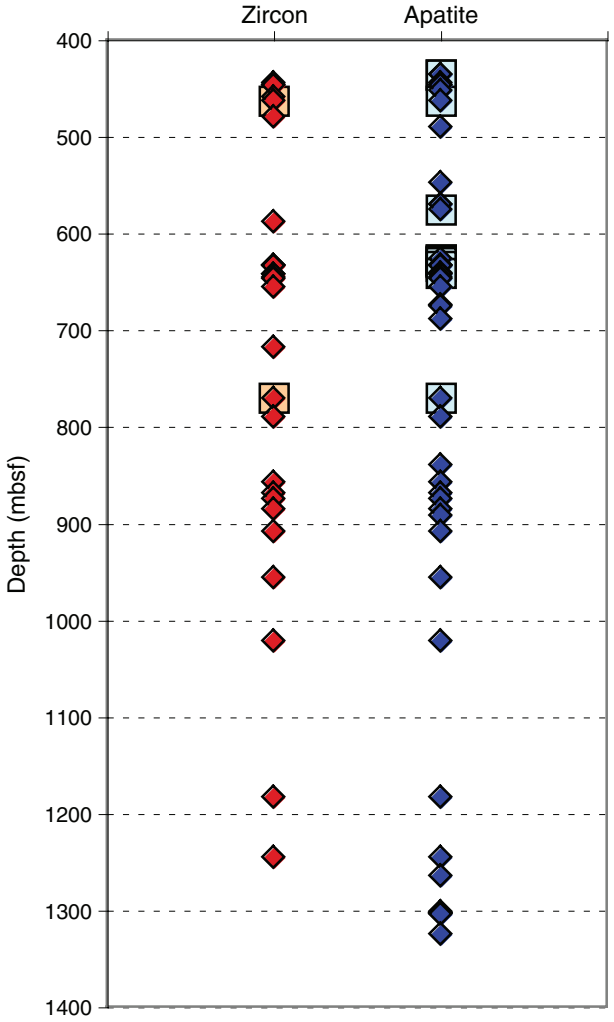

Figure F112. Textures commonly found in Site U1309 gabbros and diabases. **A.** Brown hornblende (Hbl) in metagabbro (Sample **304-U1309B-9R-1, 38–41 cm**) (plane-polarized light; field of view [FOV] = 2.4 mm). cpx = clinopyroxene. **B.** Cummingtonite (Cum) rimmed by actinolite (Act) in metagabbro (Sample **304-U1309B-10R-1, 111–113 cm**) (cross-polarized light; FOV = 1.2 mm). **C.** Zeolite (Zeo) forming after plagioclase (Plag) in gabbro (Sample **304-U1309B-4R-1, 30–31 cm**) (cross-polarized light; FOV = 1.2 mm). **D.** Textures of actinolite replacing (1) clinopyroxene and (2) olivine in diabase (Sample **304-U1309B-3R-1, 18–19 cm**) (plane-polarized light; FOV = 2.4 mm). **E.** Pseudomorphs of chlorite (Chl) and tremolite (Trm) after olivine in troctolite, forming a corona structure (Sample **304-U1309B-15R-2, 84–85 cm**) (plane-polarized light; FOV = 1.2 mm). **F.** Same as E; cross-polarized light.

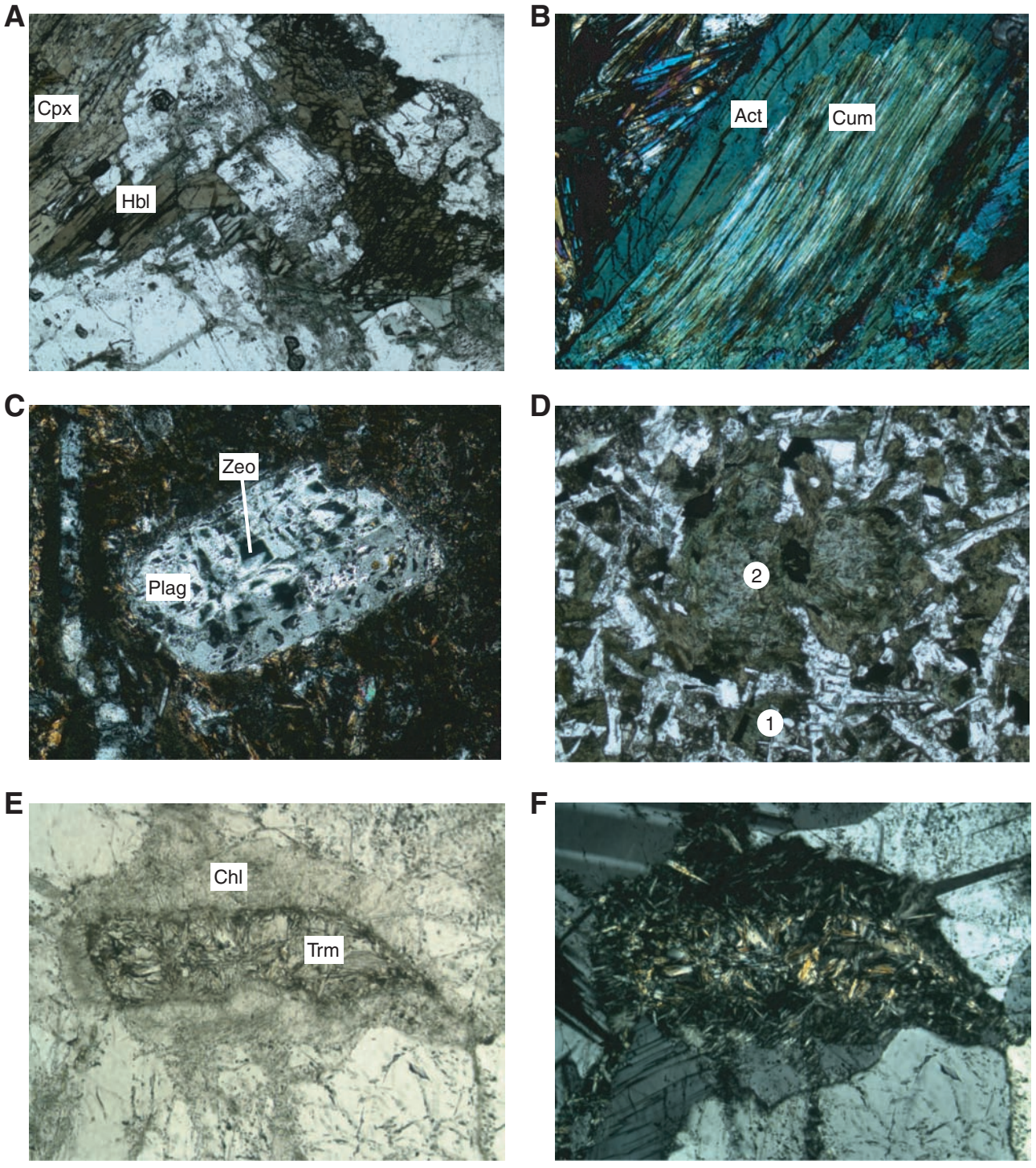

Figure F113. Greenschist-facies breccias and shear zones. **A.** Tremolite schist clast (pale green) in breccia consisting of metabasalt fragments in an actinolite-rich sheared matrix (Sample **304-U1309B-3R-1, 80–82 cm**) (field of view [FOV] = 4.1 cm). **B.** Chromite at the edge of the tremolite schist clast (as seen in A), suggesting an ultramafic origin, together with the actinolite-rich breccia matrix and a clast of altered basalt (plane-polarized light; FOV = 5.1 mm). **C.** Actinolite-rich breccia zone cutting altered gabbro with plagioclase-rich veins of probable igneous origin (Sample **304-U1309B-7R-1, 0–16 cm**) (FOV = 7.3 cm). **D.** Detail of cataclastic actinolite zone at the edge of the gabbro, showing plagioclase with a fresh core altering to albite and cut by stringers of actinolite (Sample **304-U1309B-7R-1, 6–8 cm**) (plane-polarized light; FOV = 1.3 mm). **E.** Porphyroclast of pale amphibole folded in an extremely fine grained actinolite shear zone (Sample **304-U1309B-7R-1, 67–69 cm**) (plane-polarized light; FOV = 2.6 mm). **F.** Euhedral zircon crystals (probably inherited from the protolith) surrounded by albite + chlorite/actinolite after plagioclase in gabbro. Note the presence of both brown and green amphiboles (Sample **304-U1309B-7R-1, 6–8 cm**) (plane-polarized light; FOV = 1.3 mm).

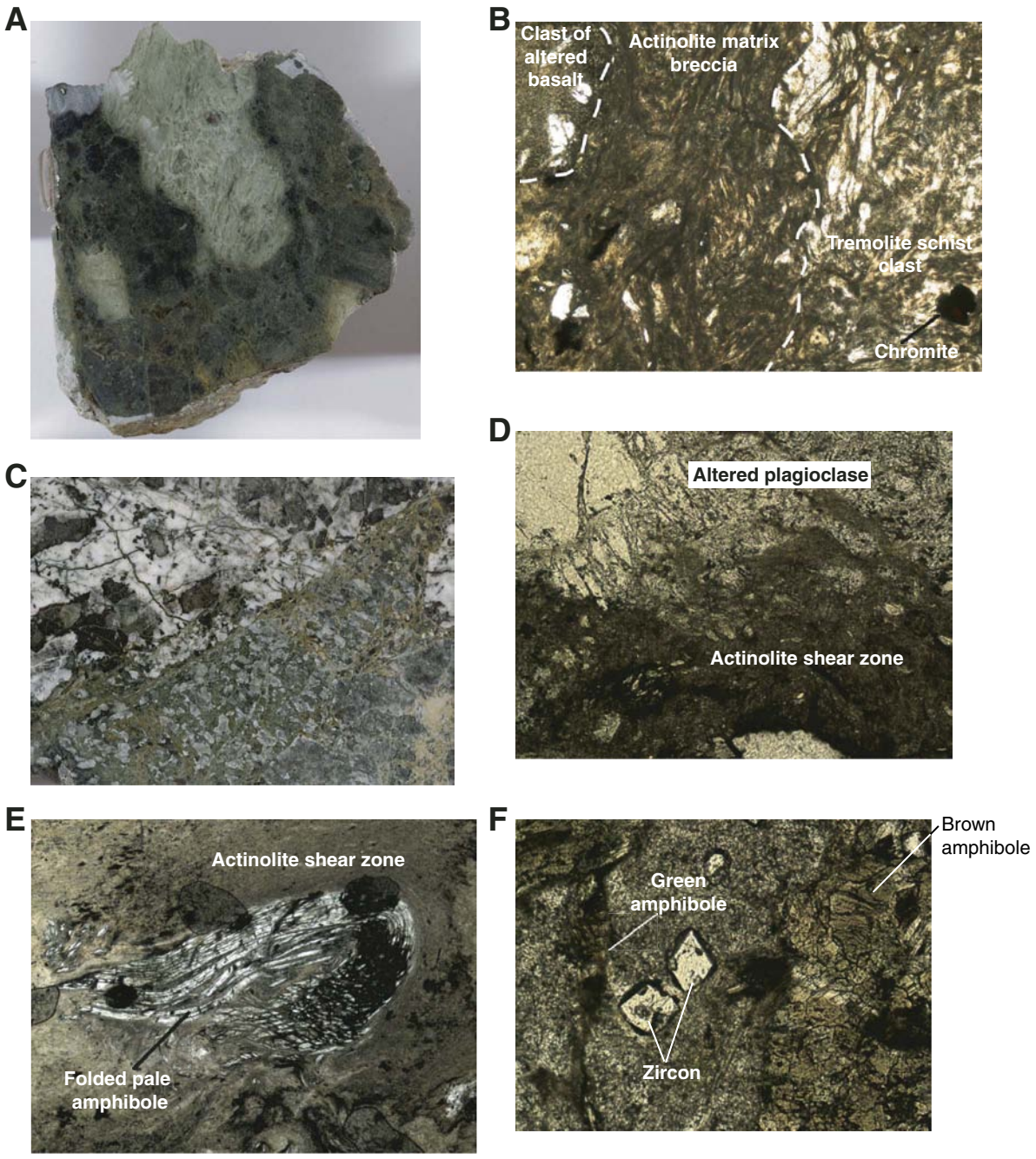

Figure F114. Prominent "vugs" filled with tremolite-actinolite surrounded by a pale zone rich in plagioclase (interval 304-U1309B-14R-1, 51–95 cm). At point A, the pale zone consists of coarse-grained calcic plagioclase with interstitial green amphibole and cuts a high-temperature ductile shear zone. At the bottom of the pale zone (point B; 89–91 cm), an actinolite-rich area containing relict clinopyroxene is surrounded by highly altered plagioclase with many inclusions; it is not clear where the character of the pale zone changes.

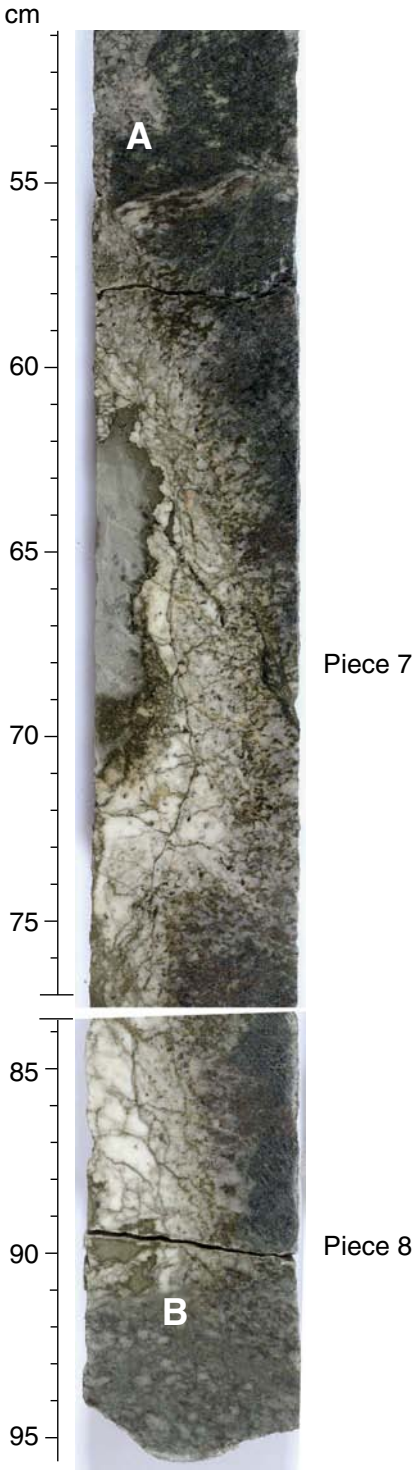

Figure F115. Alteration of peridotite. **A.** Zone of green tremolite and pale talc replacing serpentinized harzburgite (interval 304-U1309B-11R-2, 25–50 cm) (field of view [FOV] = 25 cm). This zone has undergone reverse shear along talc-rich horizons, but the margin of talc alteration against serpentinite is unsheared, overprinting the preexisting serpentinite foliation defined by magnetite seams and serpentine ribbons. Boxes = location of B and D. **B.** Same as A; FOV = 4.4 cm. **C.** Collage showing the transition from the tremolite-rich core of the zone to talc-rich material replacing serpentinite. Relict bastites preserve serpentine + magnetite mineralogy (plane-polarized light; FOV = 9.6 cm). **D.** Detail of talc front against serpentinite. An orthopyroxene crystal within the serpentinite is pseudomorphed by talc + magnetite (cross-polarized light; FOV = 5.2 cm). **E.** Detail of lozenge-shaped carbonate (inferred to be magnesite) replacing interlithon microlithons in serpentinite ribbon texture (cross-polarized light; FOV = 4 cm). **F.** Tremolite vein cutting serpentinized harzburgite (Sample **304-U1309B-11R-2, 88–90 cm**) (plane-polarized light; FOV = 5.3 cm). Vein is cut by chrysotile veins and zones of serpentine. **G.** Detail from F (cross-polarized light; FOV = 4.9 mm).

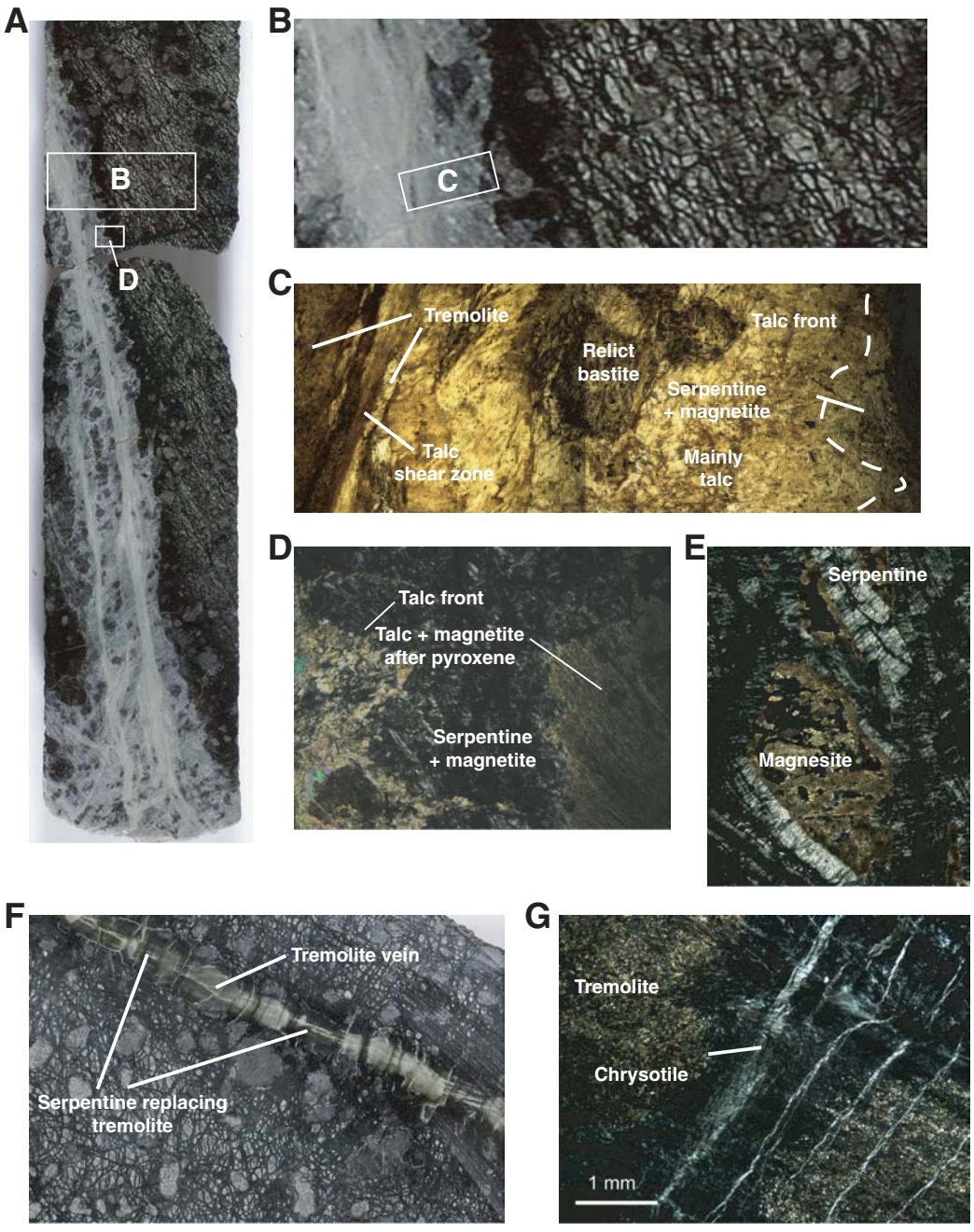

Figure F116. Alteration intensity in Hole U1309B. **A.** Overall degree of alteration in the recovered rock. **B.** Vein-related alteration and brecciation. Light gray indicates intervals of no recovery.

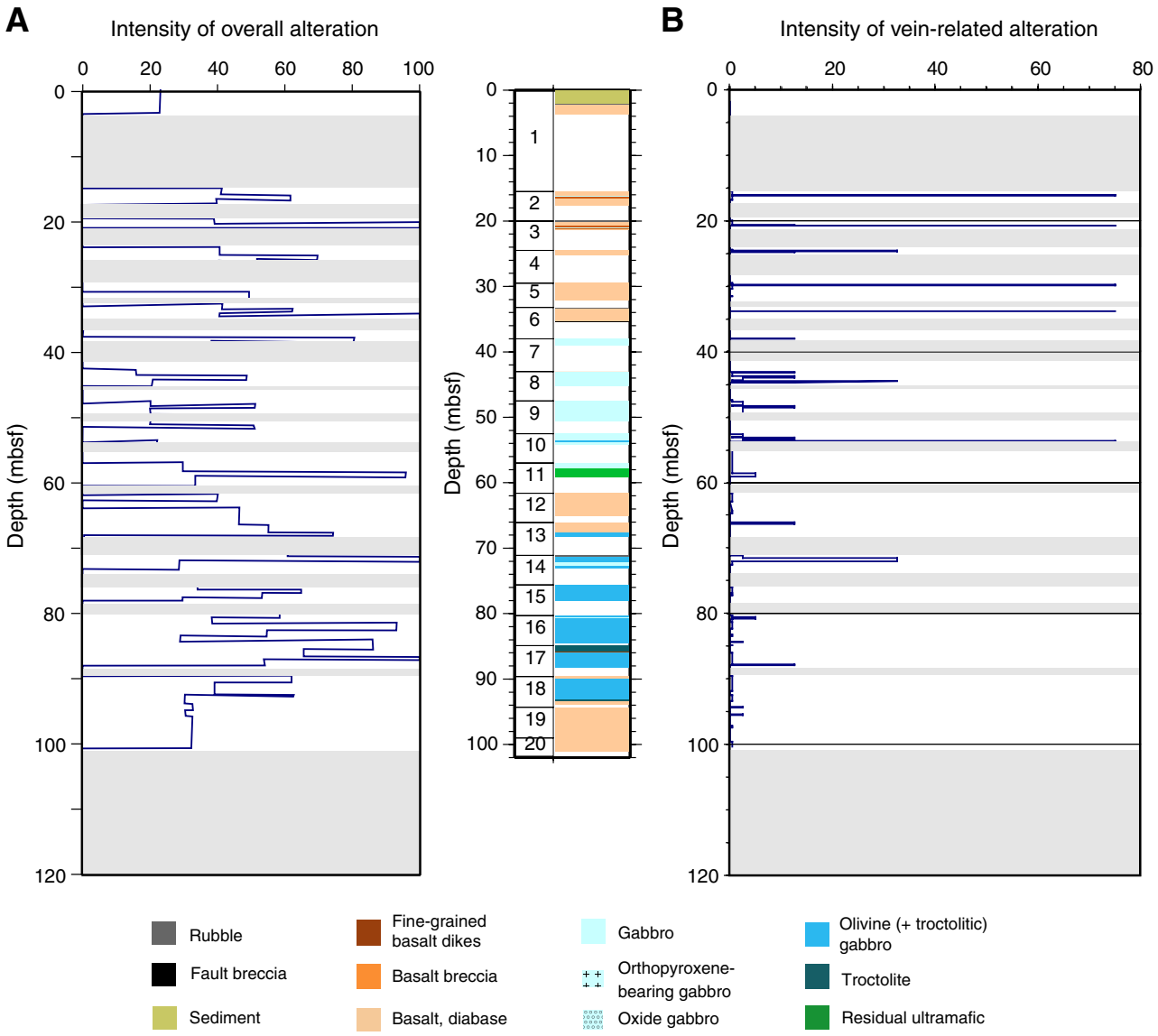

Figure F117. A. Unidentified pink-white mineral in a cavity from a troctolitic gabbro (interval 304-1309D-5R-4, 11–20 cm) (field of view [FOV] = 5 cm) and its XRD spectra. **B.** Beige-green cavity next to a felsic area in a troctolitic gabbro (interval 304-1309D-8R-2, 56–57 cm) (FOV = 4.5 cm) and its XRD spectra. The filling minerals have been identified by XRD and consist mainly of amphibole with the presence of few clays (possibly saponite), as suggested by the diffraction peak at ~4°2θ. amph = amphibole. (Continued on next page.)

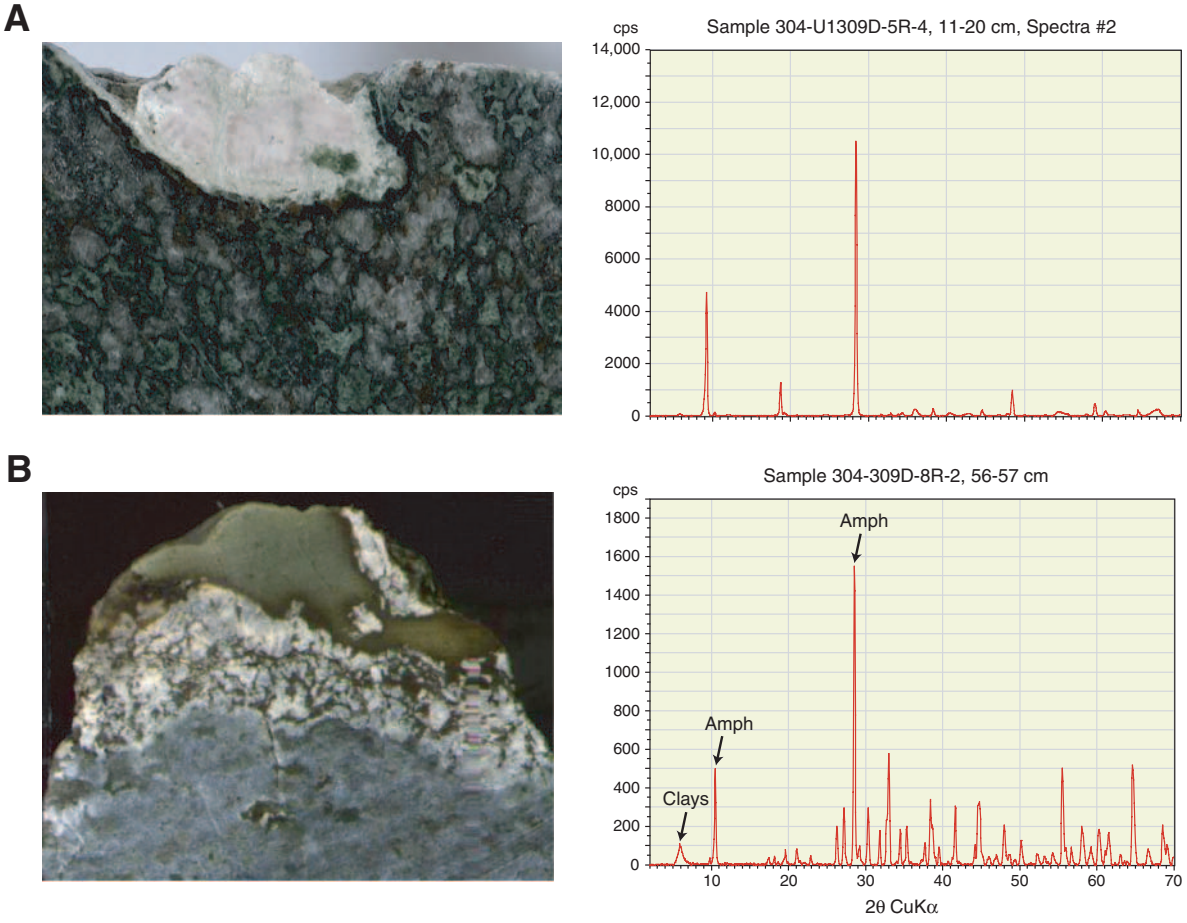

Figure F117 (continued). **C.** Blue-green vein cutting a diabase (interval 304-U1309D-15R-2, 72–74 cm) (FOV = 5 cm) and its XRD spectra. The vein-filling mineral(s) is not clearly identified, but the XRD spectra suggests the presence of amphibole (possibly cummingtonite), as suggested by the diffraction peaks at 10.8 and 28.9°2θ. **D.** Brown-green vein cutting a fine-grained diabase (interval 304-1309D-15R-1, 140–142 cm) (FOV = 5 cm) and its XRD spectra. XRD analysis allows the identification of amphibole and clays (diffraction peak at ~4–5°2θ) as the vein-filling minerals.

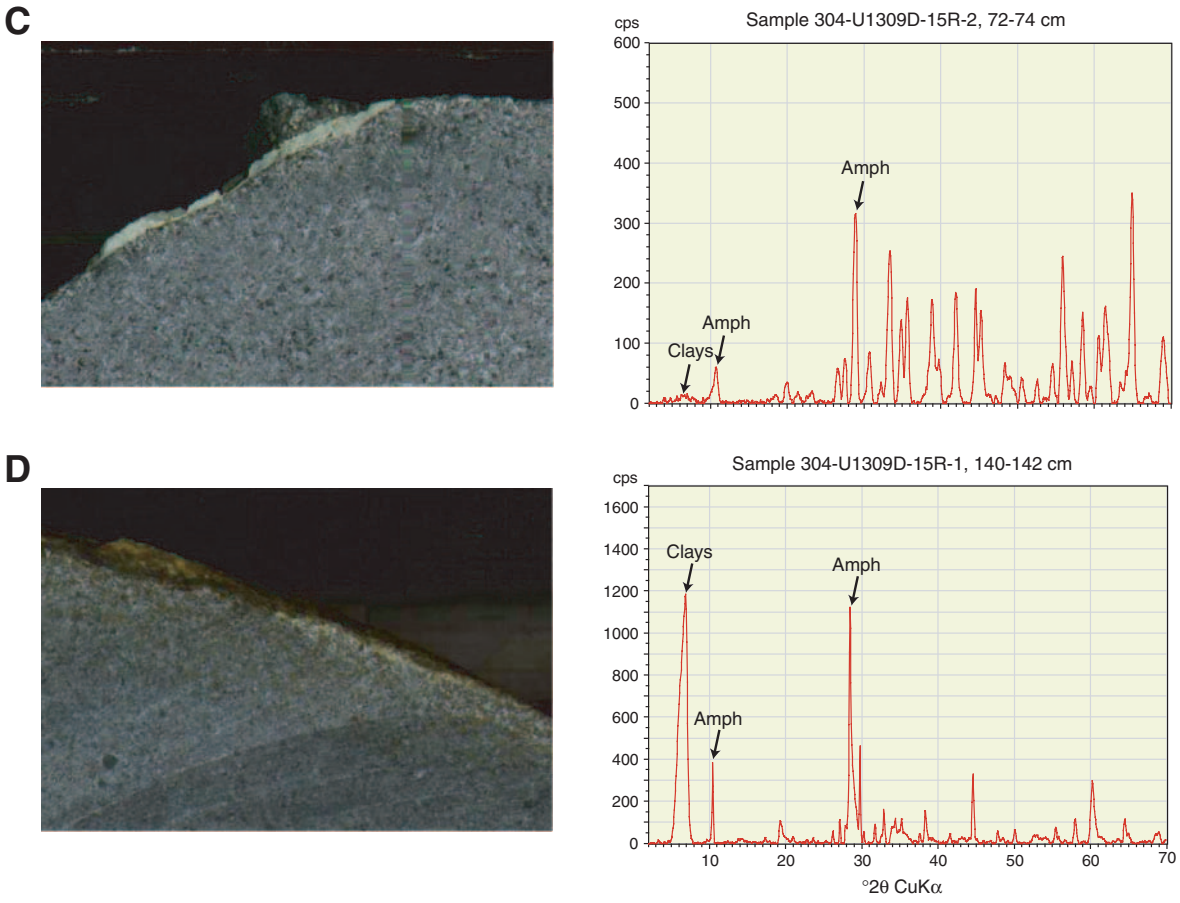

Figure F118. XRD pattern showing brucite peaks (marked with black lines) for ICP-AES Sample 305-U1309D-111R-3, 131–138 cm.

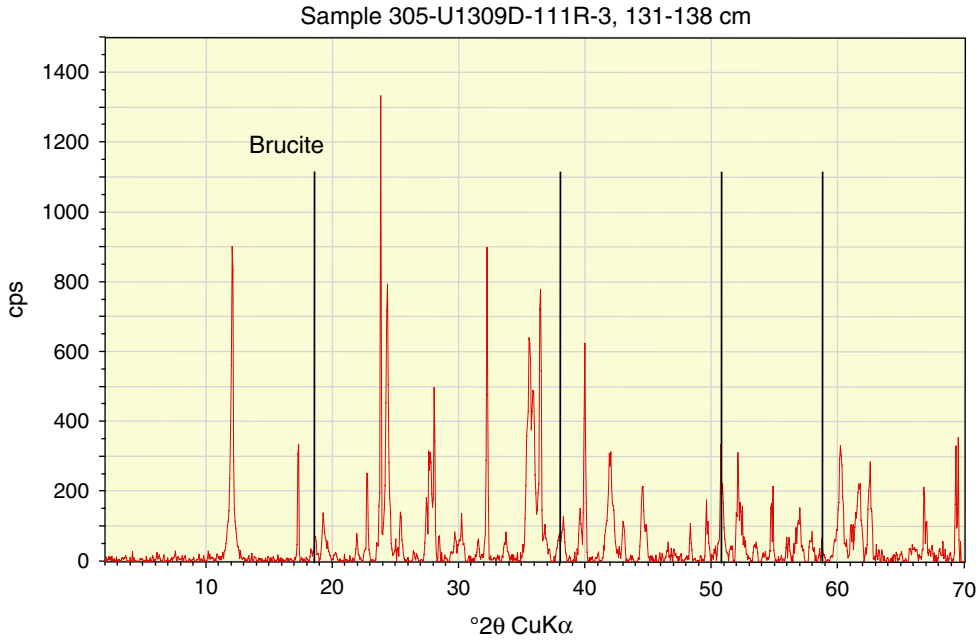

Figure F119. XRD patterns. **A.** Anhydrite (Sample 305-U1309D-150R-3, 22–23 cm). **B.** Analcime (Sample 305-U1309D-165R-2, 143–145 cm). **C.** Thomsonite (Sample 305-U1309D-165R-2, 143–145 cm). JCPDS = Joint Committee on Powder Diffraction Standards.

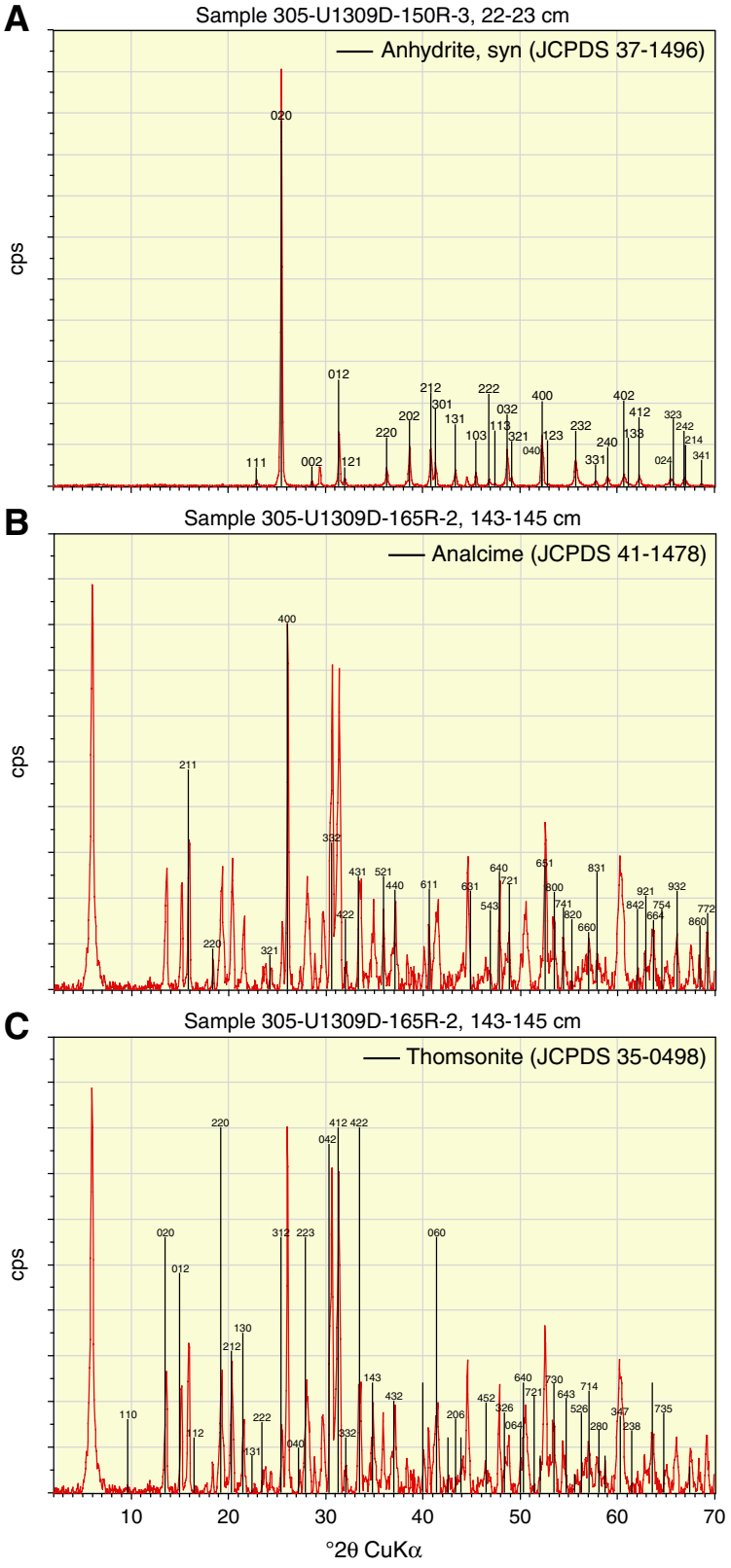

Figure F120. Neoblasts of plagioclase around edges of original plagioclase grain and pyroxene (Sample **305-U1309D-110R-3, 46–49 cm**) (cross-polarized light; magnification = 2.5×).

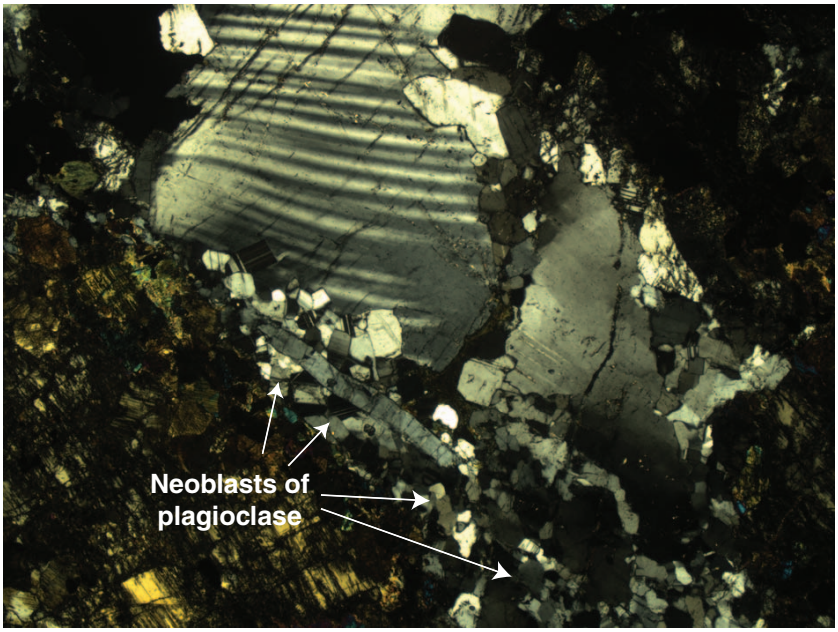

Figure F121. A. Green-brown hornblende (Brown Hbl) veins in gabbro (Sample **304-U1309D-4R-2, 108–110 cm**) (plane-polarized light; field of view [FOV] = 4.8 mm). The hornblende veins are cut by an almost perpendicular actinolite vein. **B.** Clinopyroxene (Cpx) with hornblende growing in strain shadow in deformed gabbro (Sample **304-U1309D-9R-2, 50–53 cm**) (plane-polarized light; FOV = 1.2 mm). **C.** Intense breccia (fault?) zone in gabbro (Sample **304-U1309D-4R-2, 20–23 cm**) (FOV = 6 cm). Matrix is yellow-green actinolite with minor clay alteration. **D.** Turbid plagioclase (Plag) cut by actinolite (Act) veins in gabbro (Sample **304-U1309D-6R-1, 121–124 cm**) (plane-polarized light; FOV = 1.2 mm). The secondary plagioclase contains abundant solid and fluid inclusions. **E.** Quartz (Qtz)-chlorite (Chl) vein in diabase (Sample **304-U1309D-1R-1, 41–44 cm**) (cross-polarized light; FOV = 4.8 mm). Note unusual sector twinning in quartz. **F.** Fluid inclusion in quartz-chlorite vein (Sample **304-U1309D-1R-1, 41–44 cm**) (cross-polarized light; FOV = 120 µm).

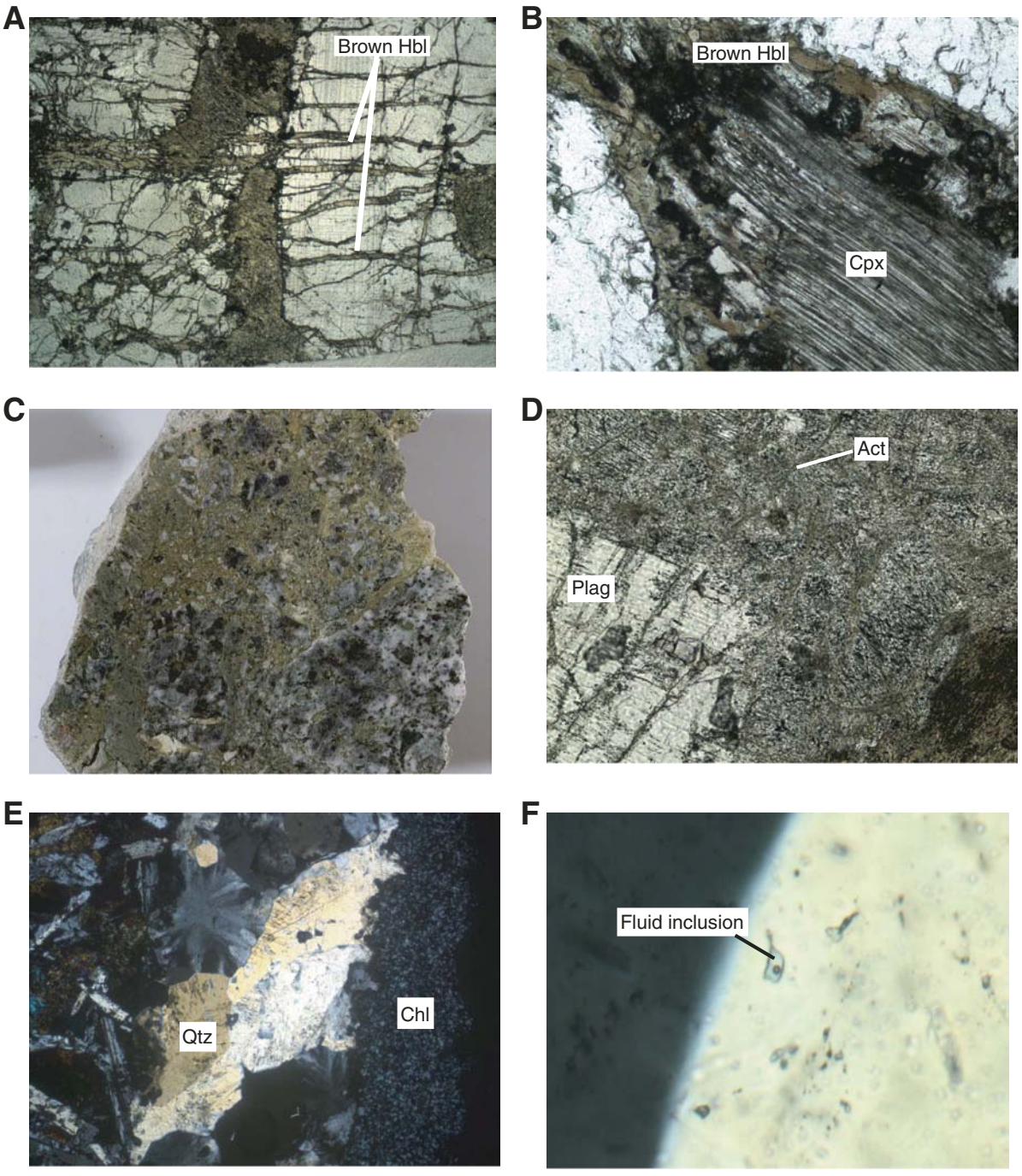

Figure F122. A. Example of late magmatic leucocratic dike cutting gabbro (interval 304-U1309D-62R-1, 82–94 cm). Box = location of B. **B.** Detail of A. Tip of dike, showing termination in a shear zone (plane-polarized light; field of view [FOV] = 9.6 mm). Actinolite mat is replacing an interstitial phase, possibly brown hornblende. **C.** Gabbro dike containing epidote and bladed pyroxenes growing inward from the margin (interval 304-U1309D-75R-2, 74–82). Box = location of D. **D.** Detail of C. Gabbro dike, showing brecciated texture with epidote, titanite, actinolite, and secondary plagioclase (cross-polarized light; FOV = 4.8 mm).

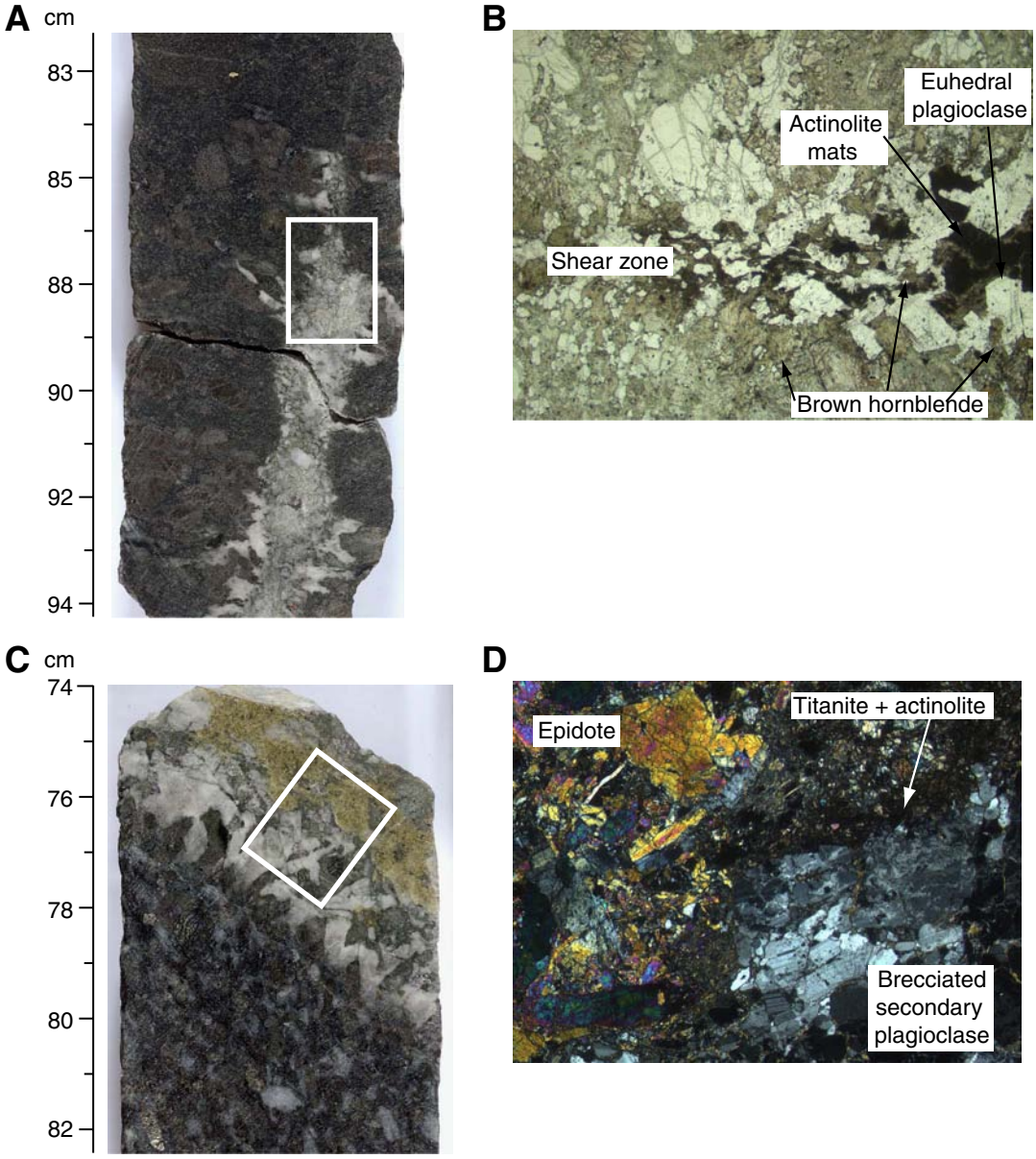

Figure F123. A. Contact between leucocratic zone and gabbro (interval 305-U1309D-128R-3, 69–83 cm). Epidote is also present in some of these zones. **B.** Leucocratic alteration near gabbro showing green amphibole replacing clinopyroxene (interval 305-U1309D-128R-3, 73–76 cm) (plane-polarized light; magnification = 1×). **C.** Same as B; cross-polarized light. Pl = plagioclase.

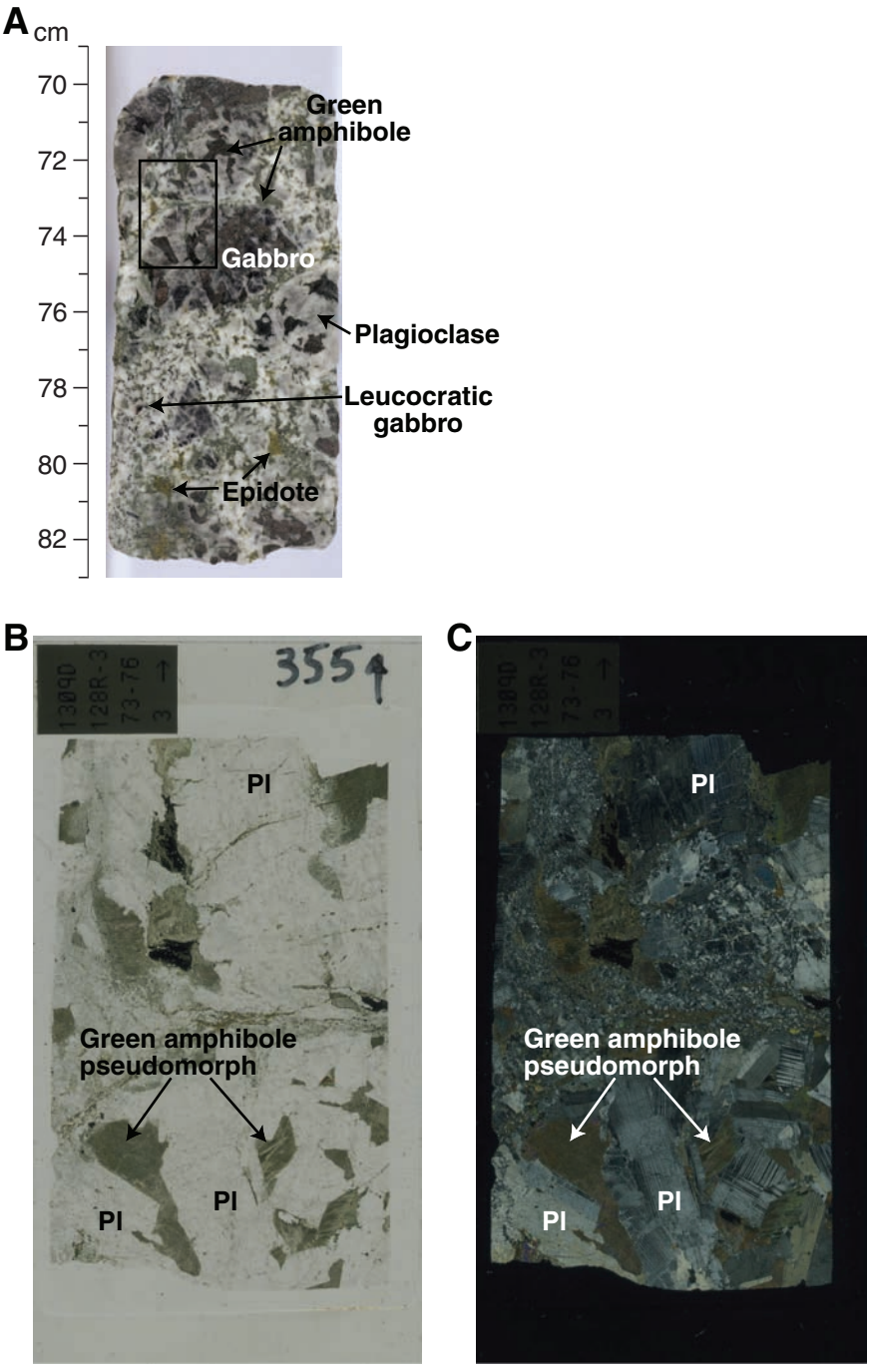

Figure F124. A. Troctolite with coronitic texture (interval 304-U1309D-13R-3, 0–10 cm) (field of view [FOV] = 6 cm). Dark chlorite rims around plagioclase and dark to light green spots of tremolite/actinolite + chlorite after olivine can be seen. **B.** Serpentine "ladder" veins in fresh troctolite (interval 304-U1309D-70R-3, 80–88 cm). Black serpentine veins have white "bridges" of prehnite/hydrogarnet replacing plagioclase. **C.** Radial cracks around chlorite-actinolite coronas after olivine in troctolite (Sample **304-U1309D-12R-1, 65–67 cm**) (plane-polarized light; FOV = 9.6 mm). **D.** Same as C, inverted and contrast-enhanced to emphasize veins of chlorite and actinolite, as well as turbid alteration zones in plagioclase (plane-polarized light). **E.** Complex corona around olivine, showing a talc zone between the tremolite zone and olivine (Sample **304-U1309D-26R-2, 12–14 cm**) (cross-polarized light; FOV = 4.8 mm). Olivine has been converted to serpentine and carbonate. Box = location of F. **F.** Detail of E (cross-polarized light; FOV = 2.4 mm). Carb = carbonate, Serp = serpentine, Trem = tremolite.

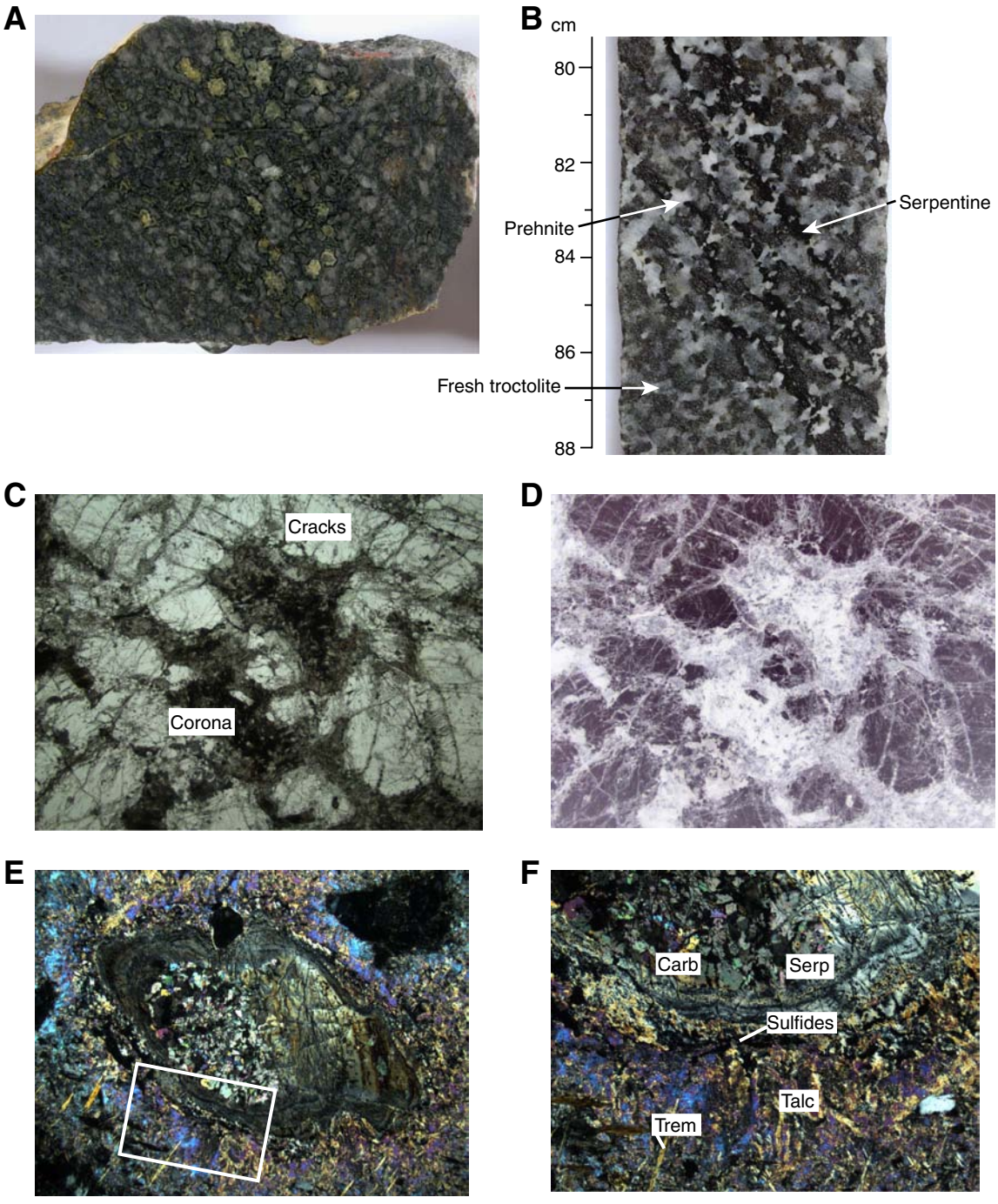

Figure F125. A. Corona texture in olivine gabbro consisting of talc, tremolite, and oxides after olivine and chlorite after plagioclase where the two original minerals were in contact (Sample **305-U1309D-80R-2, 16–19 cm**) (cross-polarized light; magnification = 10×). **B.** Corona texture with pseudomorphic talc/tremolite/serpentine with accompanying late calcite in the core of the pseudomorph (Sample **305-U1309D-115R-2, 89–91 cm**) (cross-polarized light; magnification = 1×).

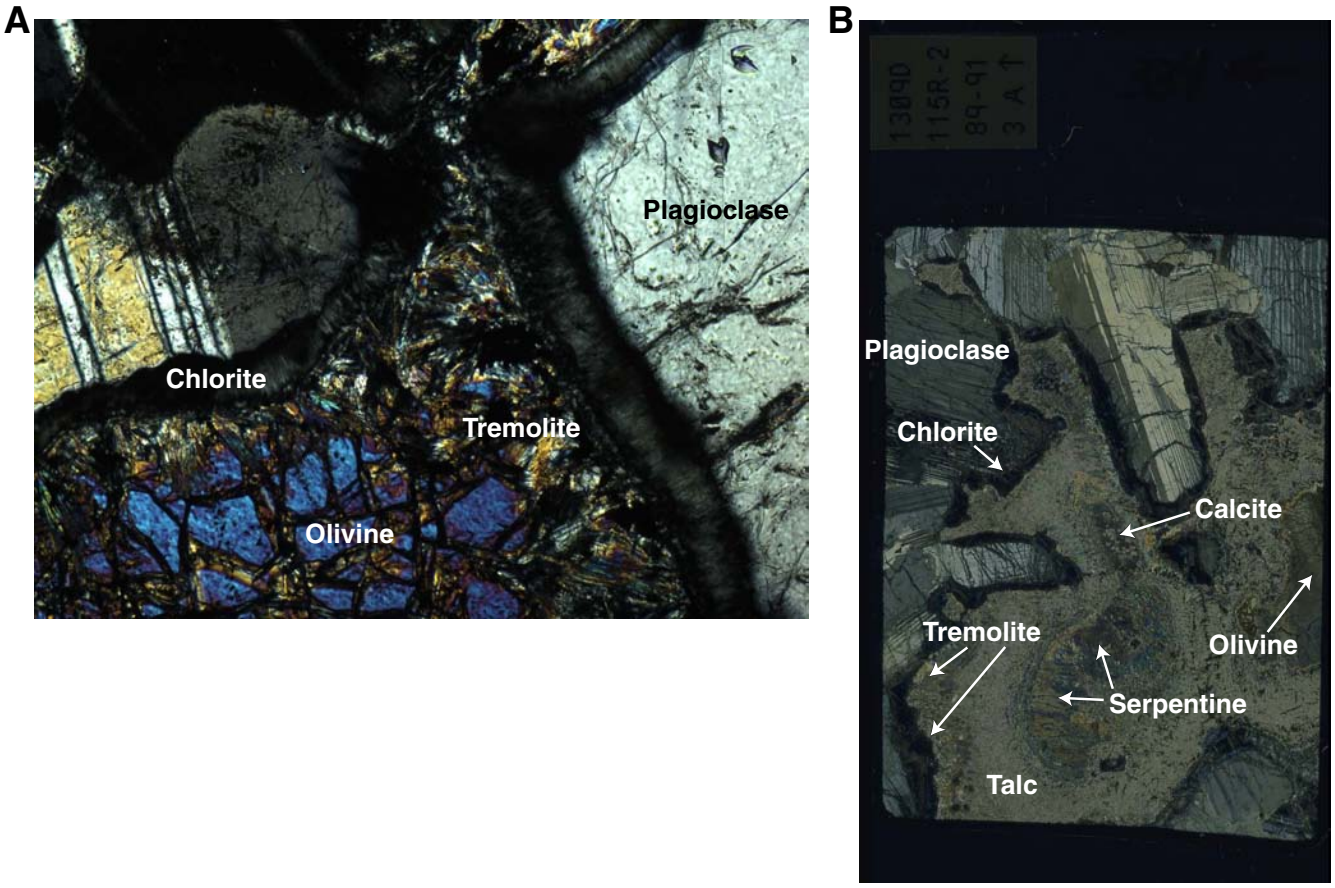

Figure F126. A. Olivine touching plagioclase with no trace of reaction (Sample **304-U1309-78R-4, 73–75 cm**) (cross-polarized light; field of view [FOV] = 2.5 mm). **B.** Orthopyroxene altered to talc and actinolite in deformed gabbronorite (Sample **304-U1309D-13R-1, 68–70 cm**) (cross-polarized light; FOV = 4.8 mm). Opx = orthopyroxene. **C.** Reaction corona between orthopyroxene and plagioclase (Sample **304-U1309D-74R-1, 102–105 cm**) (cross-polarized light; FOV = 2.5 mm).

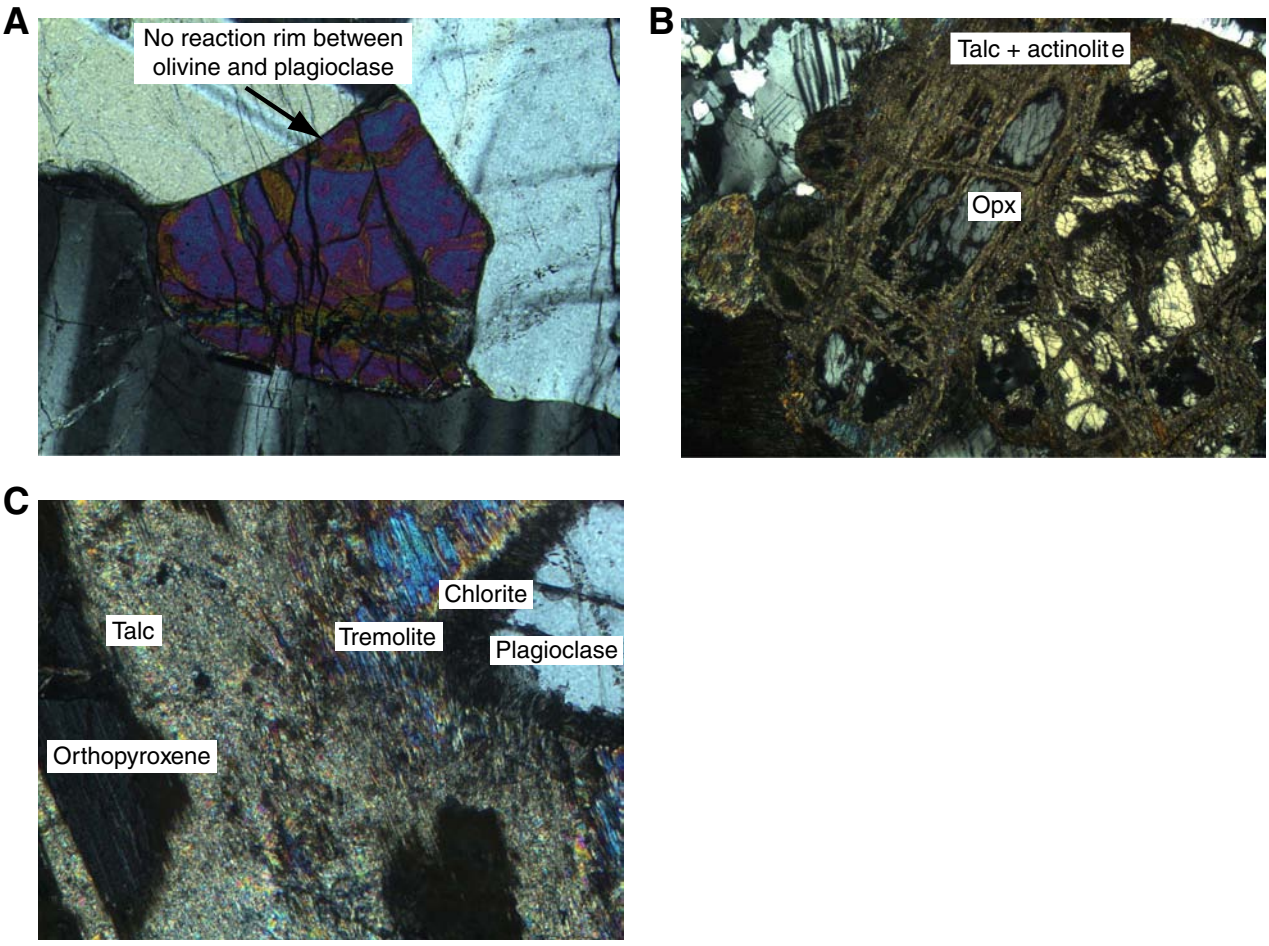

Figure F127. A. Chlorite pseudomorphs after plagioclase in olivine-rich troctolite (Sample **304-U1309D-66R-2, 10–13 cm**) (cross-polarized light; field of view [FOV] = 10 mm). **B.** Tremolite growing between olivine and clinopyroxene in olivine-rich troctolite (Sample **304-U1309D-23R-2, 98–101 cm**) (cross-polarized light; FOV = 1.25 mm). **C.** Fresh clinopyroxene associated with partially serpentinized olivine (Sample **304-U1309D-60R-2, 34–37 cm**) (cross-polarized light; FOV = 4.8 mm). **D.** Tremolite on a coronal reaction rim that has been replaced by serpentine (Sample **304-U1309D-63R-3, 54–57 cm**) (plane-polarized light; FOV = 0.5 mm). **E.** Plagioclase in olivine-rich troctolite cut by prehnite vein (Sample **304-U1309D-63R-3, 54–57 cm**) (cross-polarized light; FOV = 4.8 mm). **F.** Plagioclase in olivine-rich troctolite that has been partially replaced by prehnite and hydrogrossular (Sample **304-U1309D-63R-3, 54–57 cm**) (plane-polarized light; FOV = 10 mm). Note how the fresh plagioclase lies adjacent to fresh olivine, whereas the altered plagioclase touches serpentinite.

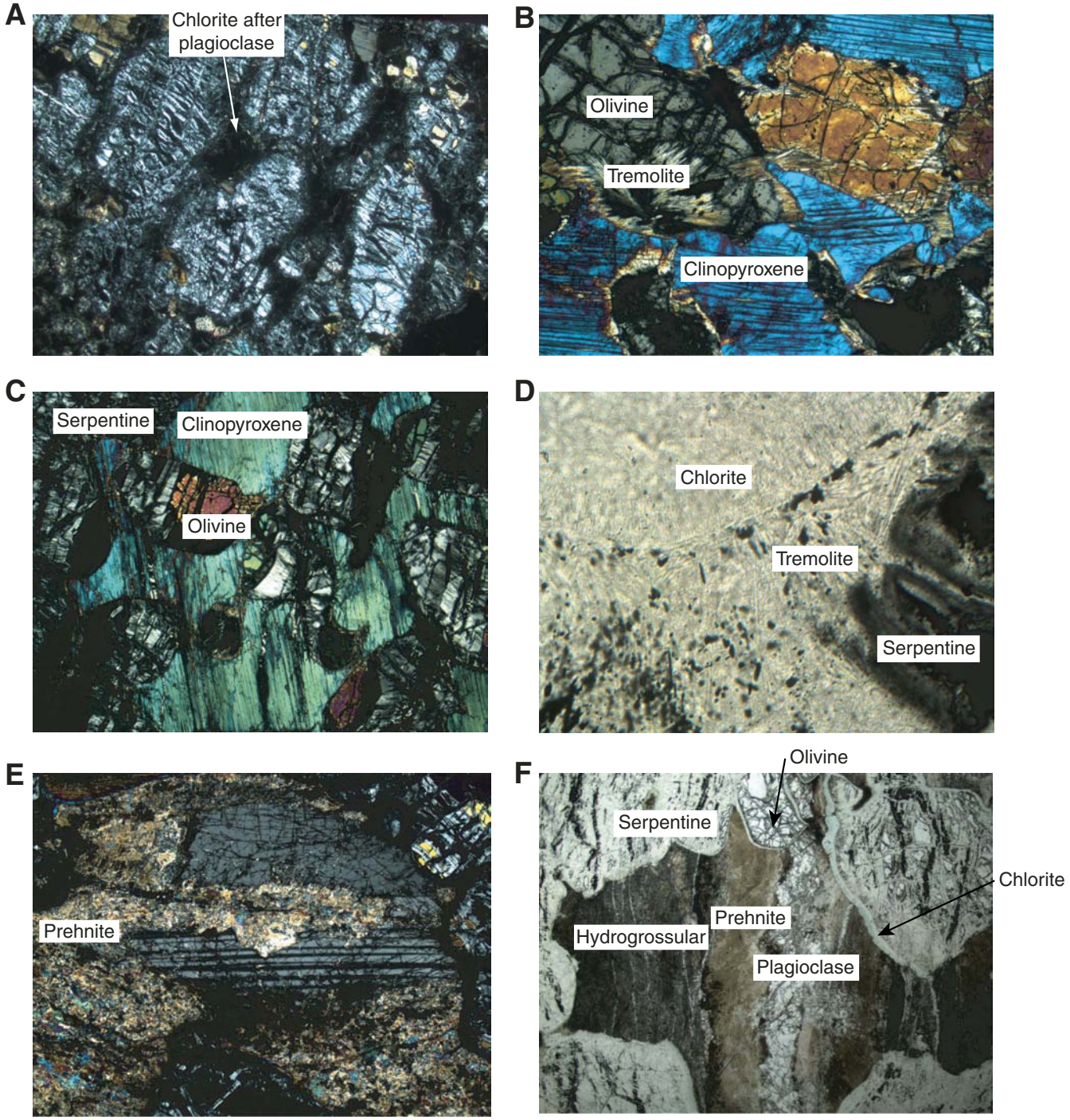

Figure F128. Coronas of tremolite and chlorite produced in troctolite near the contact with pegmatitic gabbro (interval 305-U1309D-86R-3, 108–119 cm).

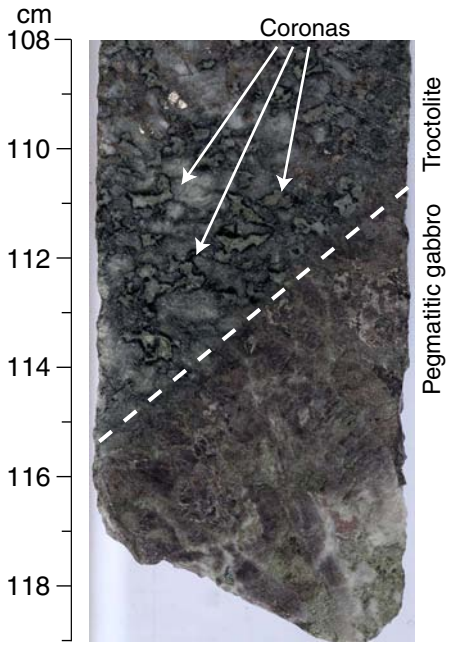

Figure F129. A. Gabbro cut by parallel set of dark green amphibole veins (interval 305-U1309D-160R-4, 0–23 cm). The density of such sets locally approaches that of a foliation. Note development of corona texture in the alteration halo of these veins. **B.** Dark green fibrous amphibole veins (Sample **305-U1309D-145R-1, 62–64 cm**) (plane-polarized light; magnification = 2.5×). Note alteration of proximal clinopyroxene to amphibole very similar to that in the veins. Also note pervasive veining of nearby plagioclase (Pl).

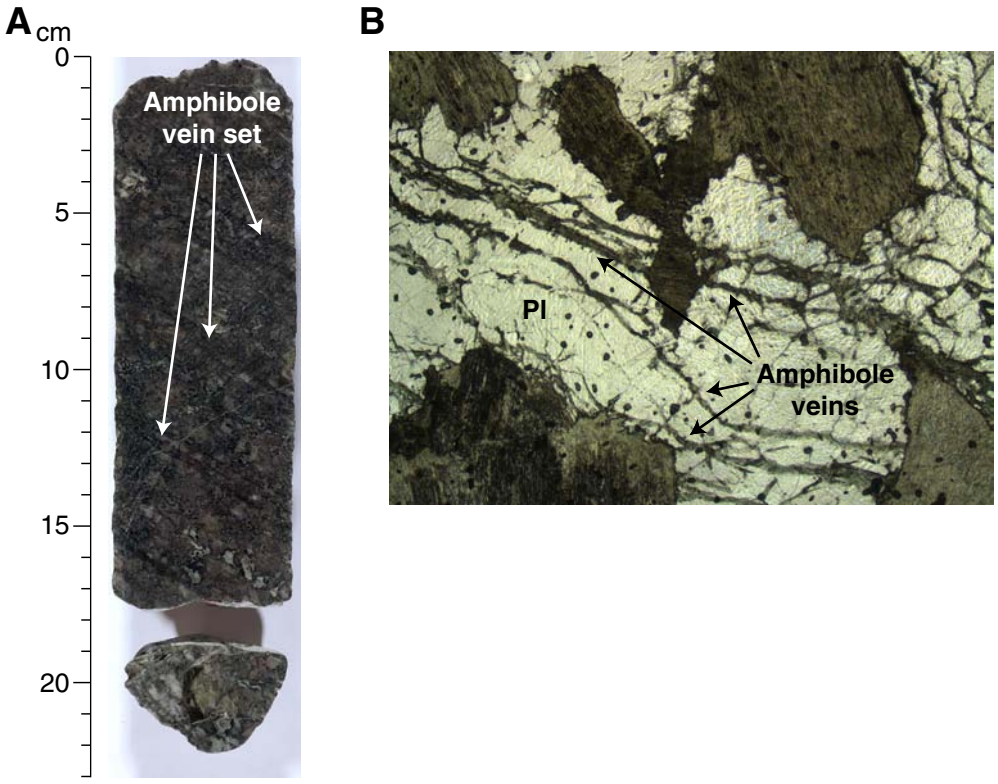

Figure F130. A. Kernel structure developing in serpentinized olivine (Sample **305-U1309D-80R-1, 39–41 cm**) (plane-polarized light; magnification = 2.5×). **B.** Oxidized serpentine after olivine (Sample **305-U1309D-80R-1, 110–113 cm**) (plane-polarized light; magnification = 2.5×).

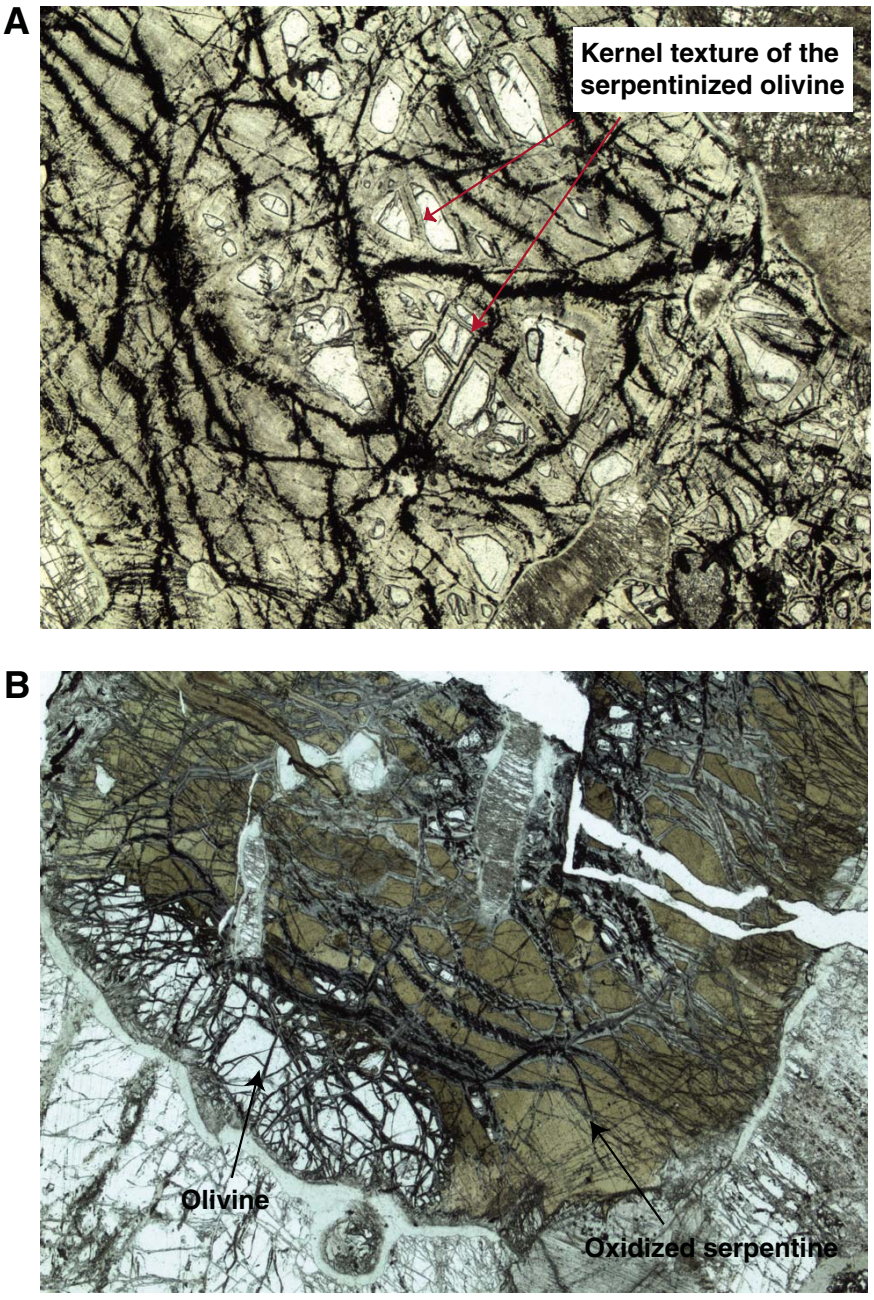

Figure F131. A. Fractures radiating into adjacent plagioclase grain from serpentinized olivine (Sample **305-U1309D-82R-2, 110–112 cm**) (cross-polarized light; magnification = 2.5×). **B.** Fractures extending between serpentinized olivine grains through adjacent plagioclase grains (Sample **305-1309D-232R-1, 102–105 cm**) (plane-polarized light; magnification = 10×).

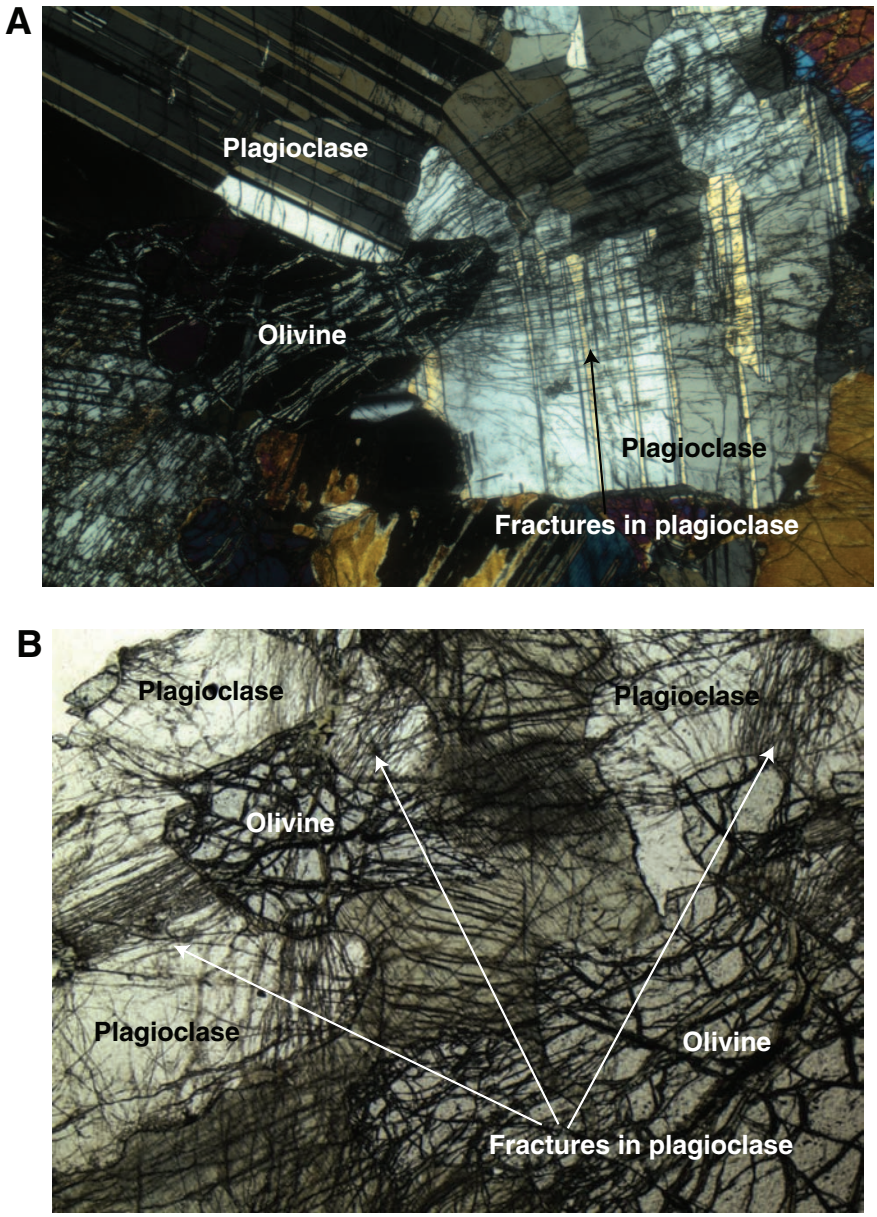

Figure F132. A. Chromite-bearing tremolite-talc-chlorite schist of partly ultramafic origin (Sample **304-U1309D-1R-3, 0–4 cm**) (field of view [FOV] = 5.6 cm). Cross cutting veins are tremolite; dark patches are chlorite rich and may be of mafic (plagioclase) origin. Photo is oriented in the core reference frame. **B.** Tremolite-talc-chlorite schist (Sample **304-U1309D-1R-3, 0–4 cm**) (plane-polarized light). The upper part contains patches of talc, overgrown by random tremolite grains, together with chlorite-rich patches. In the center is a tremolite shear zone, and the lower part of the slide is a breccia with a schistose matrix made of materials similar to those in the upper part. Photo is oriented in the core reference frame (FOV = 2.7 cm.). **C.** Detail of B. Extended chromite grains in tremolite-talc-chlorite schist (FOV = 4.8 mm). The fracturing is clearly contemporary with growth of tremolite. **D.** Metagabbro sample immediately beneath the tremolite-talc-chlorite schist in A (interval 304-U1309D-1R-3, 10–18 cm) (FOV = 6 cm). One edge of the sample is a pure tremolite schist. **E.** Chlorite (Chl) replacing plagioclase and brown hornblende (Brown Hbl) replacing pyroxene in tremolite-chlorite schist (Sample **304-U1309D-1R-3, 9–11 cm**) (cross-polarized light; FOV = 1.2 mm). Note that plagioclase is completely replaced in this sample.

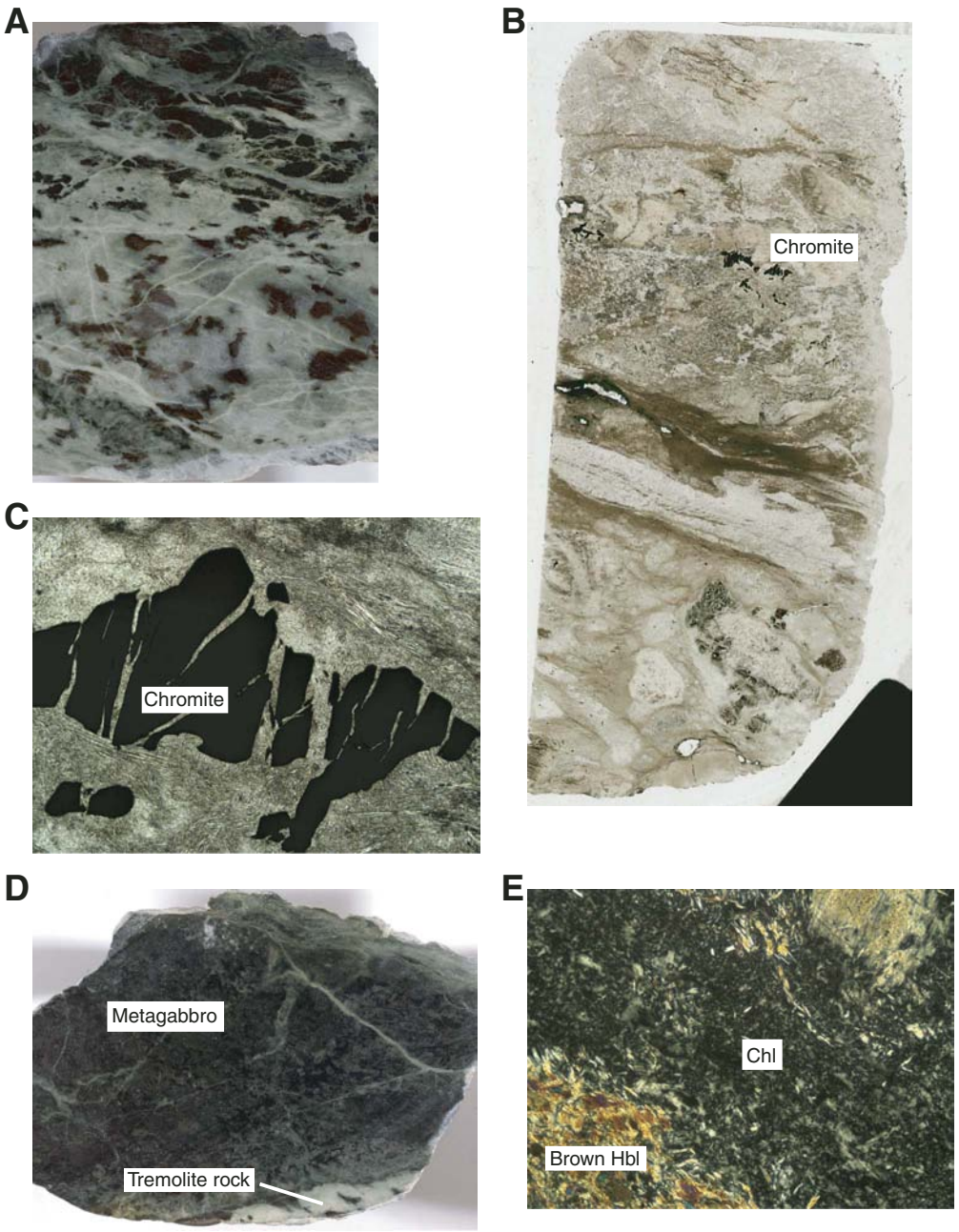

Figure F133. A. Pale green amphibole vein with associated talc alteration zone (interval 305-U1309D-111R-2, 45–74 cm). Note slip-fiber texture on exposed surface. **B.** Banded structure, possibly related to altered intrusive contacts, in pervasive talc alteration zone (interval 305-1309D-140R-2, 57–77 cm). **C.** Brown slip-fiber amphibole (Sample **305-U1309D-128R-3, 73–76 cm**) (plane-polarized light; magnification = 10×). Note lack of alteration.

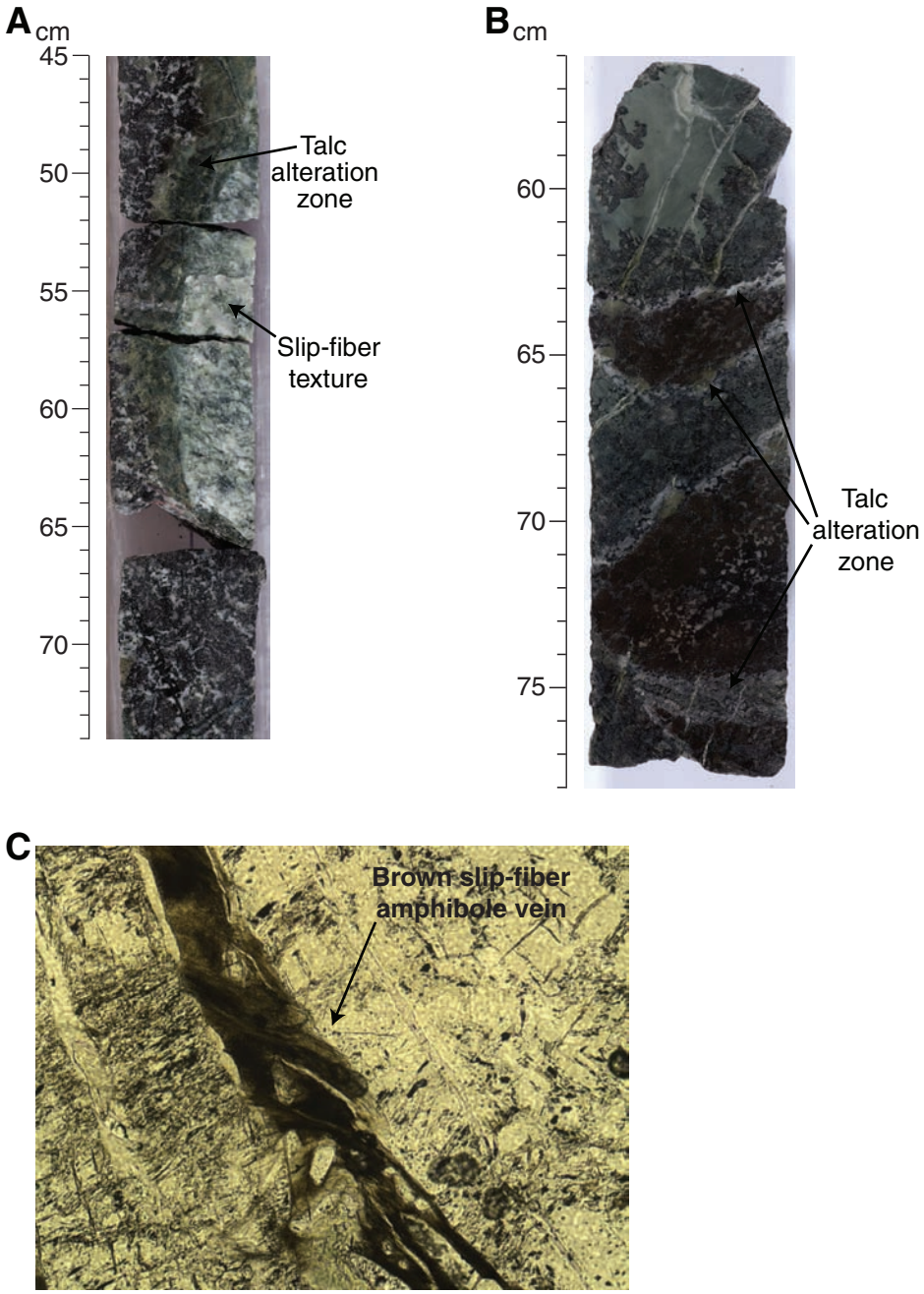

Figure F134. A. Carbonate vein cutting contact between olivine-bearing gabbro and olivine-rich troctolite (interval 304-U1309D-60R-2, 34–45 cm). **B.** Detail of A. Carbonate-talc alteration of diopside with tremolite (Trem) rim (cross-polarized light; field of view [FOV] = 1.25 mm). Px = pyroxene. **C.** Chlorite (Chl) pseudomorph after plagioclase in olivine-rich troctolite that has otherwise been altered to talc + carbonate (Carb) (cross-polarized light; FOV = 1.25 mm). **D.** Carbonate vein, possibly aragonite, that has partially inverted to calcite, cutting serpentinite (Sample **304-U1309D-31R-1, 16–19 cm**) (cross-polarized light; FOV = 5 mm).

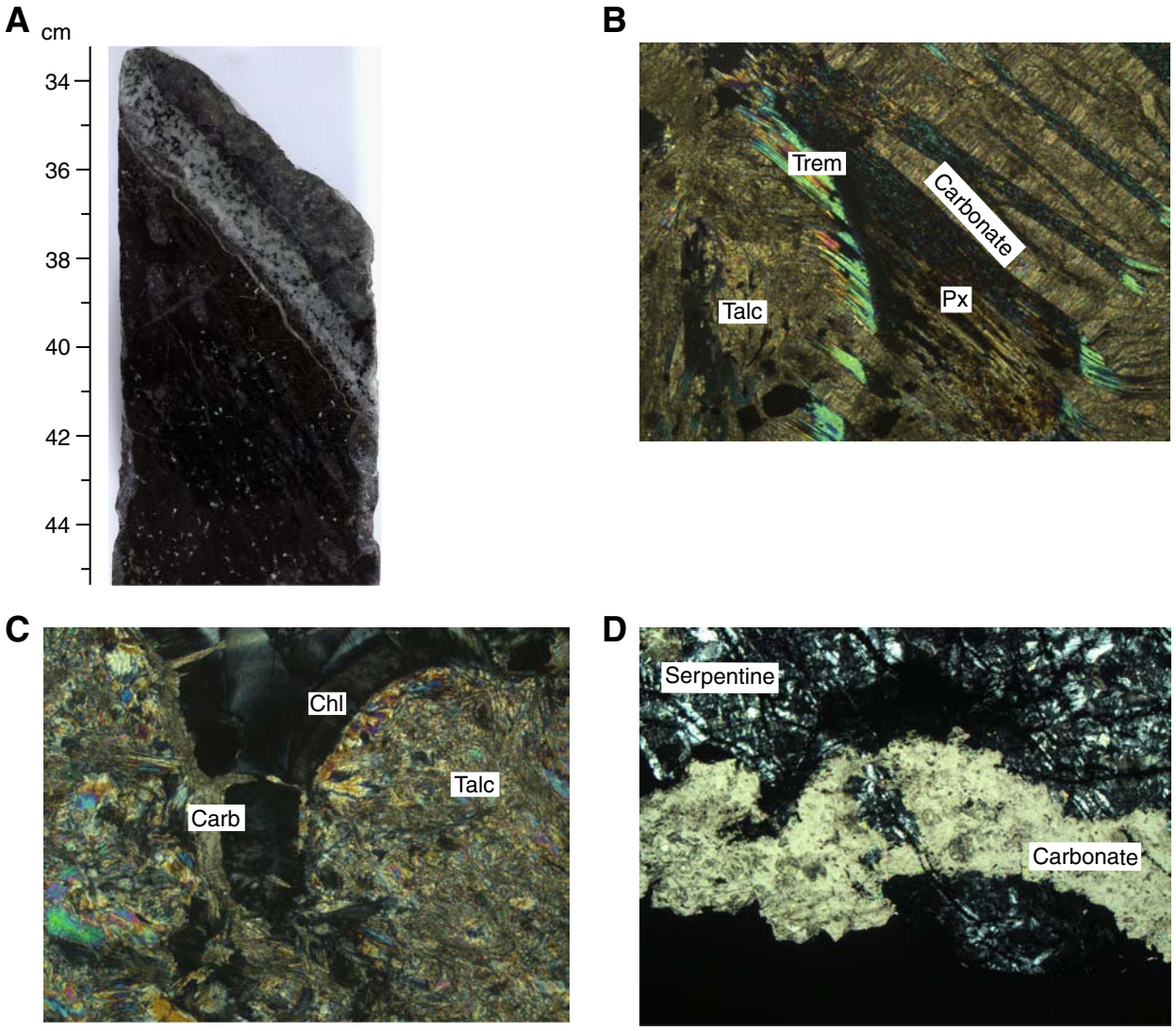

Figure F135. A. Magnetite with ilmenite exsolution, ilmenite, and sulfides (Sample **305-U1309D-183R-2, 32–34 cm**) (plane-polarized light; magnification = 20×). **B.** Chalcopyrite and pyrrhotite with exsolved flames of pentlandite (Sample **305-U1309D-183R-2, 32–34 cm**) (plane-polarized light; magnification = 20×). **C.** Pyrrhotite, chalcopyrite, ilmenite (bottom), pentlandite (Sample **305-U1309D-204R-4, 64–67 cm**) (plane-polarized light; magnification = 20×). **D.** Magnetite, pyrrhotite, and bornite (Sample **305-U1309D-256R-3, 85–88 cm**) (plane-polarized light; magnification = 20×).

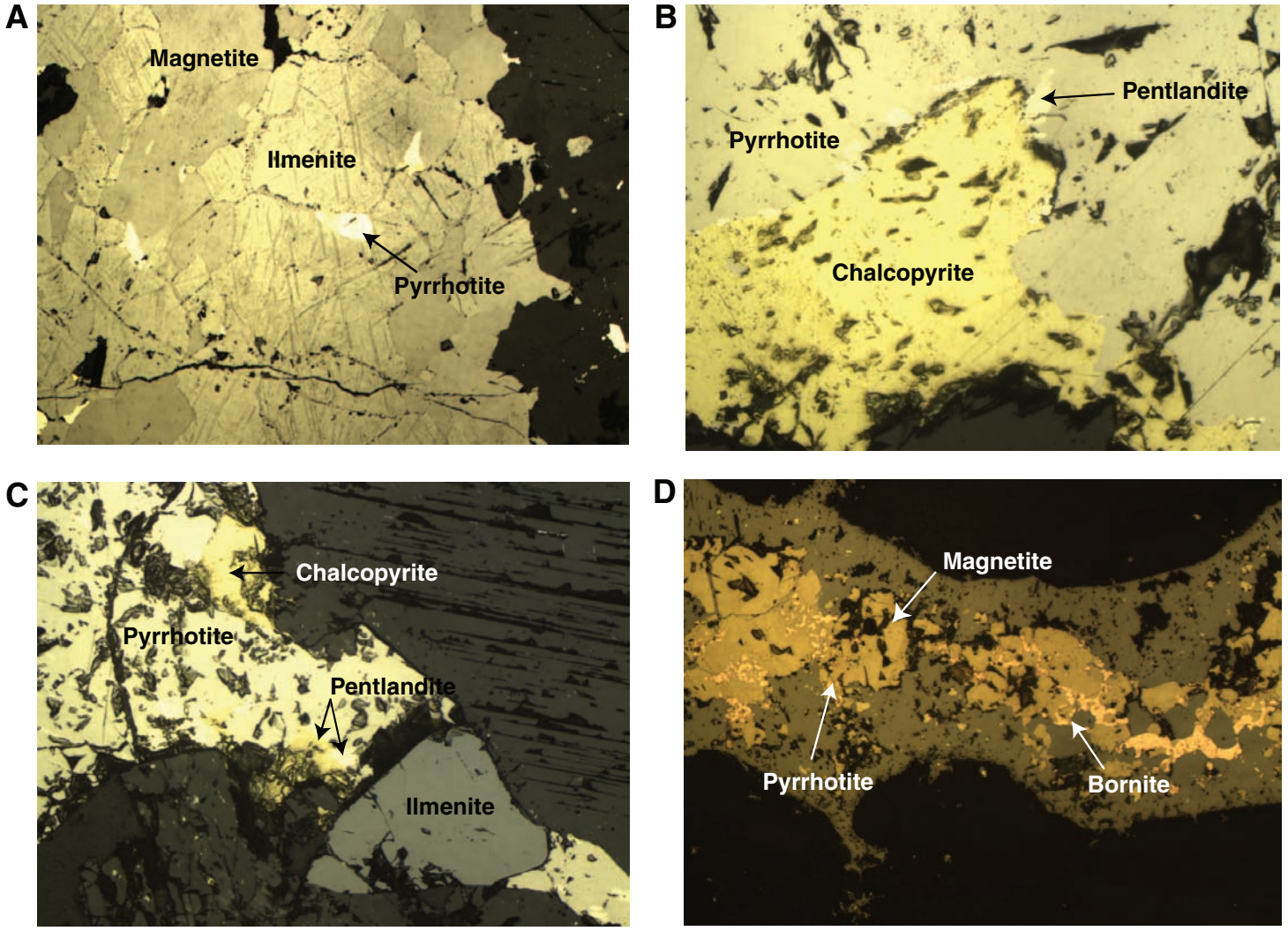

Figure F136. Plot of downhole alteration compared with lithostratigraphic column, Hole U1309D.

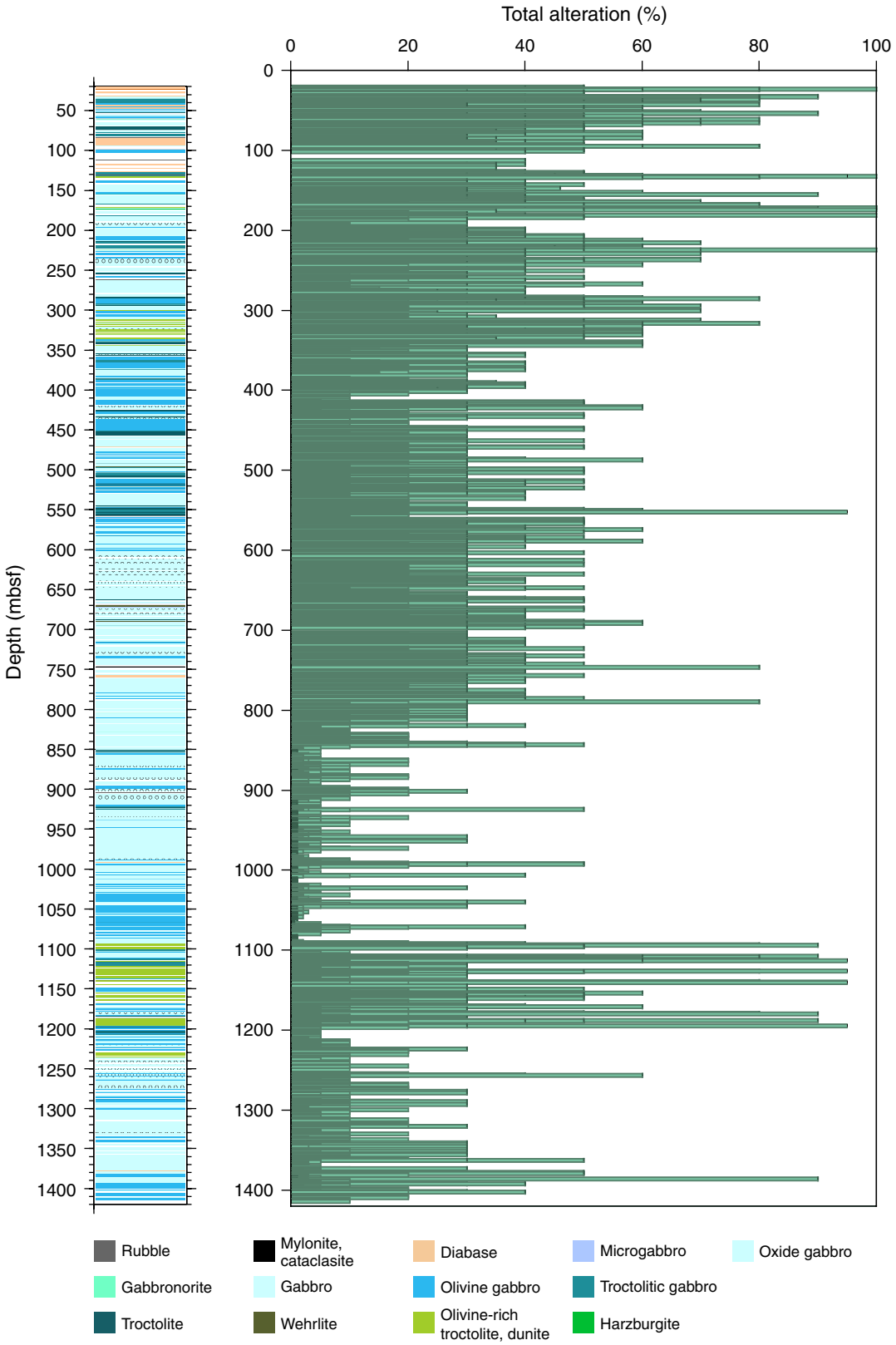

Figure F137. Variation in alteration intensity with depth in Hole U1309D (Expedition 304). **A.** Overall degree of alteration in recovered rock. **B.** Vein-related alteration and brecciation.

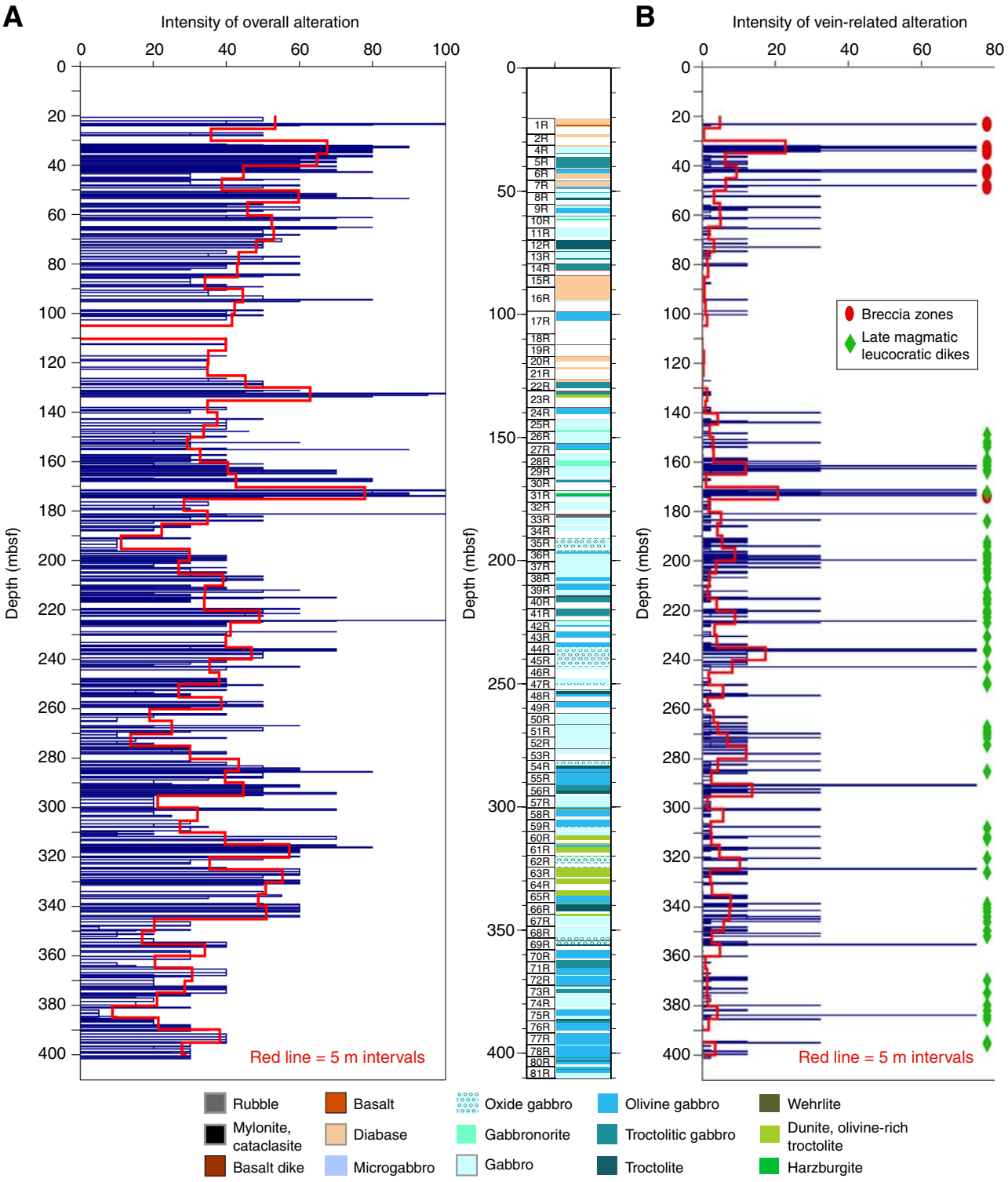

Figure F138. A. Variations of alteration depending on lithology, showing the cumulative length for each lithology and for a defined alteration range. **B.** Proportions of the different ranges of alteration for each lithology recalculated to 100%.

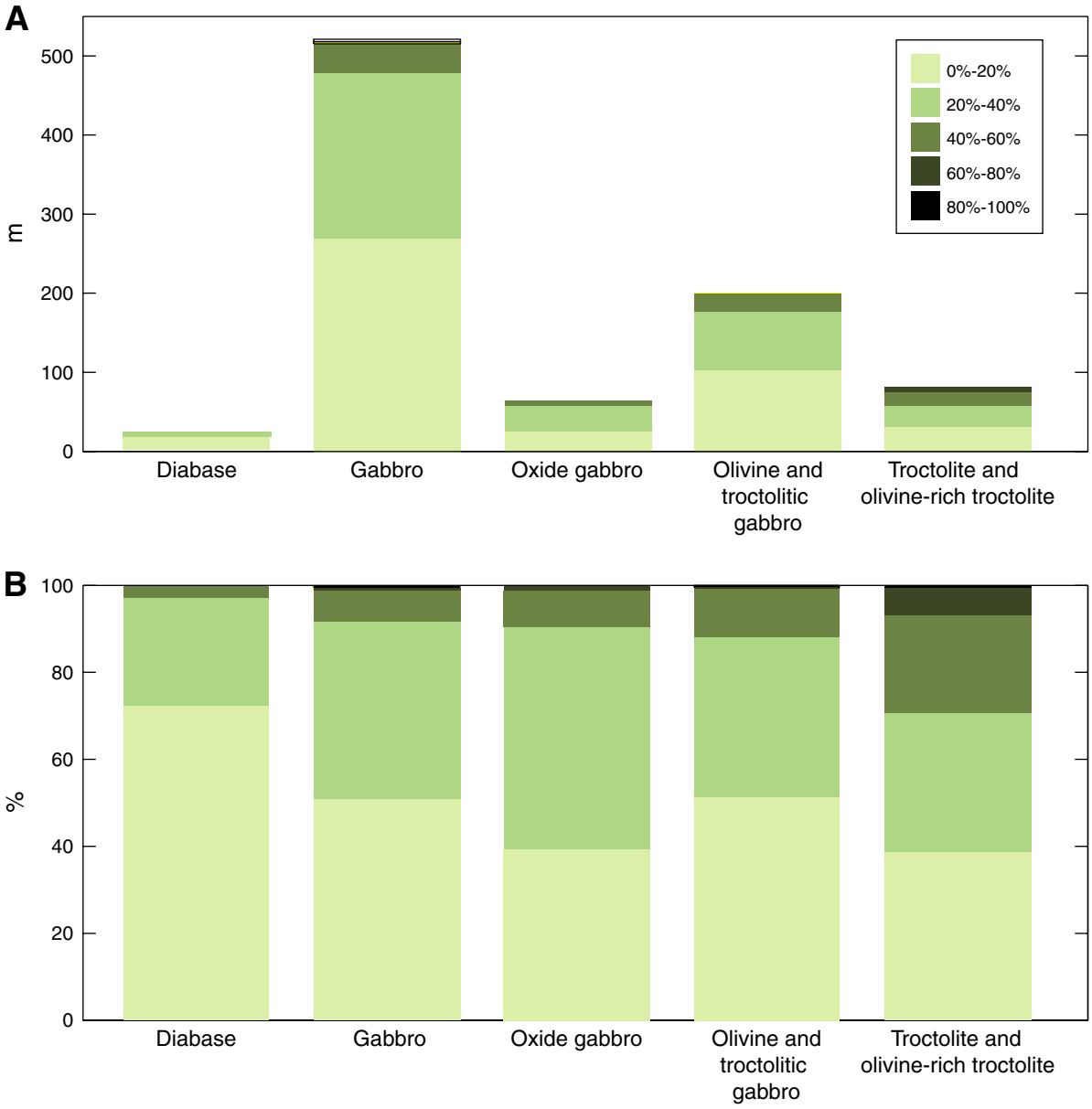

Figure F139. A–N. Percentages of secondary minerals identified in thin section (including vein minerals). (Continued on next three pages.)

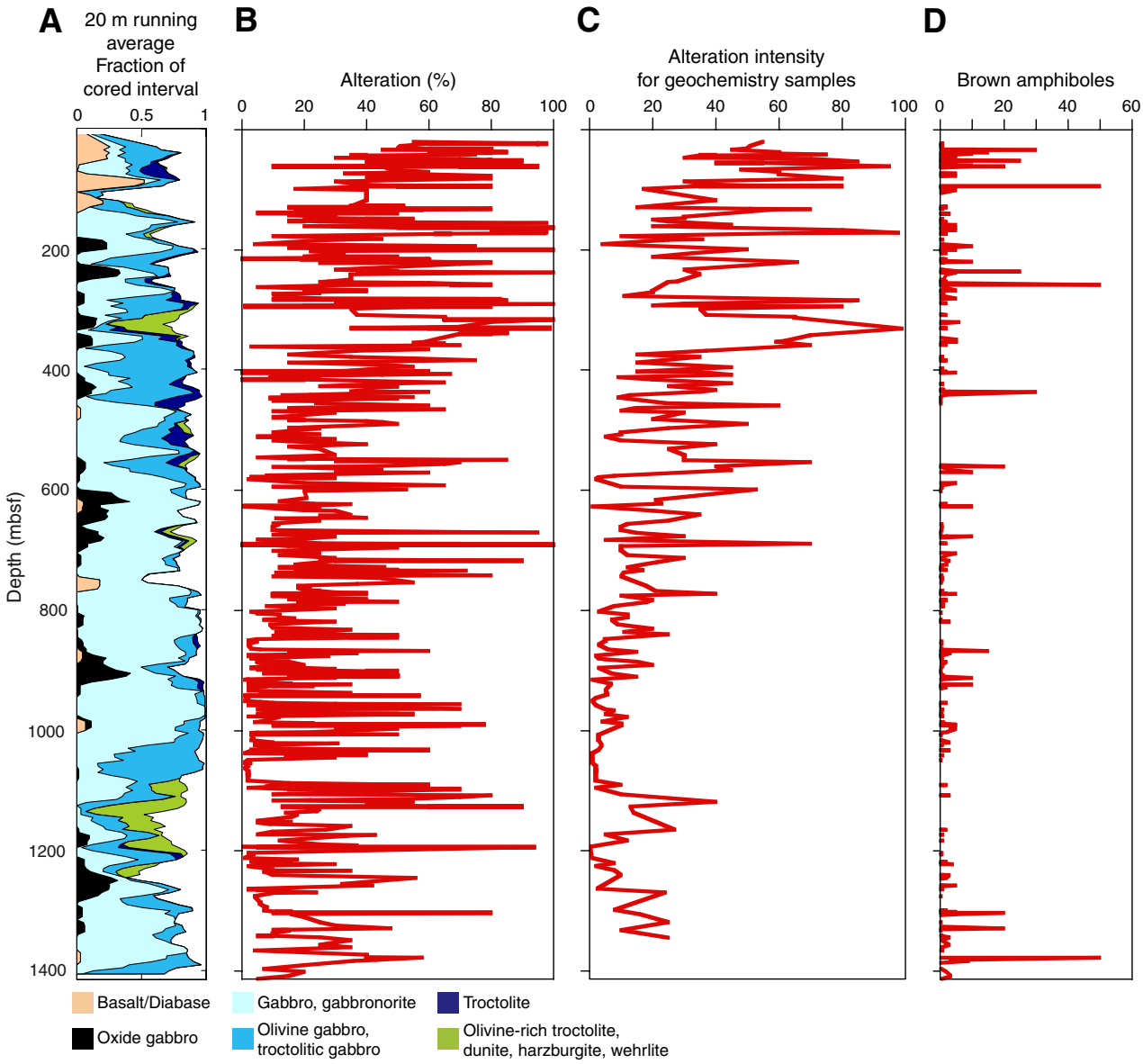

Figure F139 (continued).

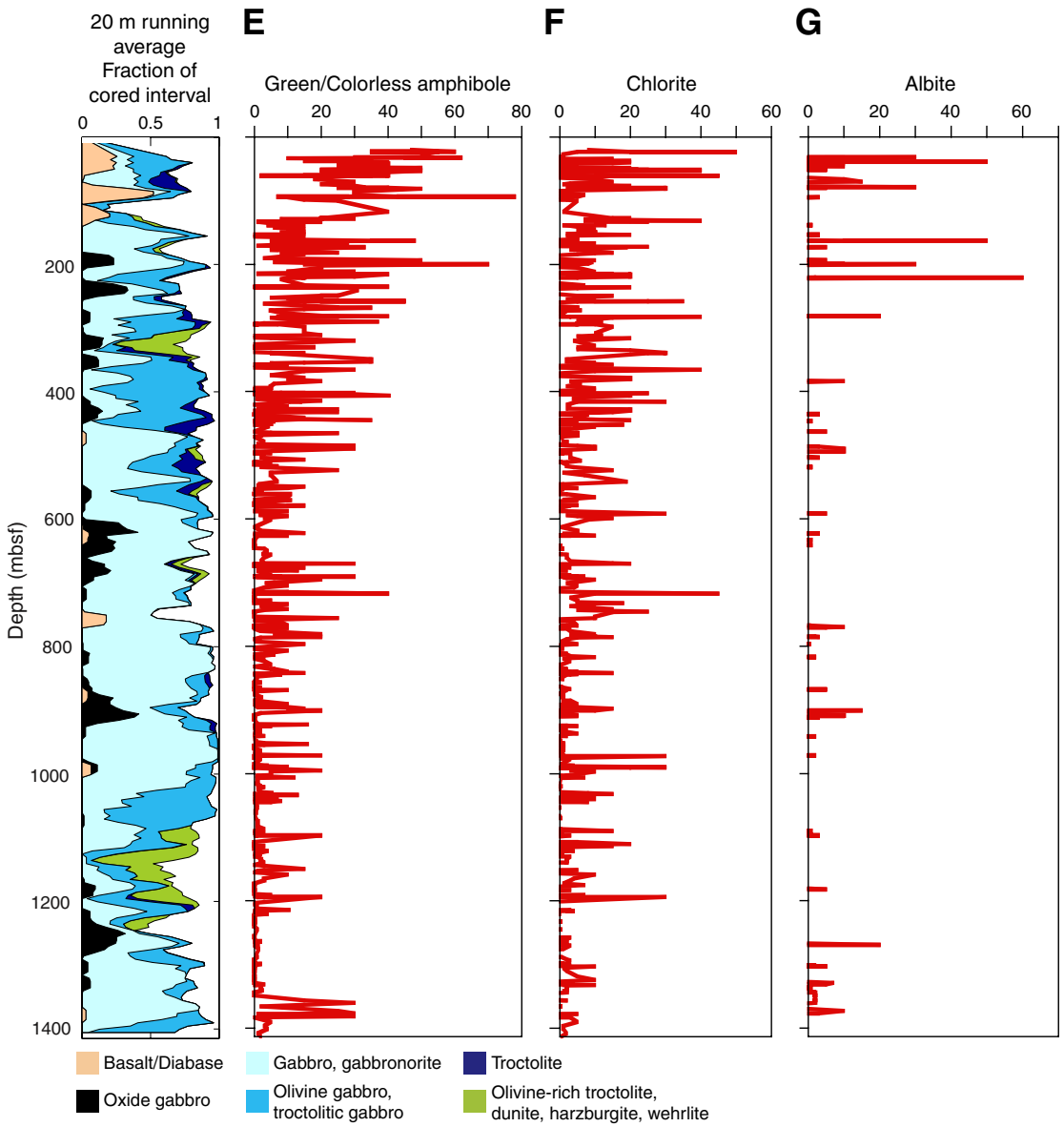

Figure F139 (continued).

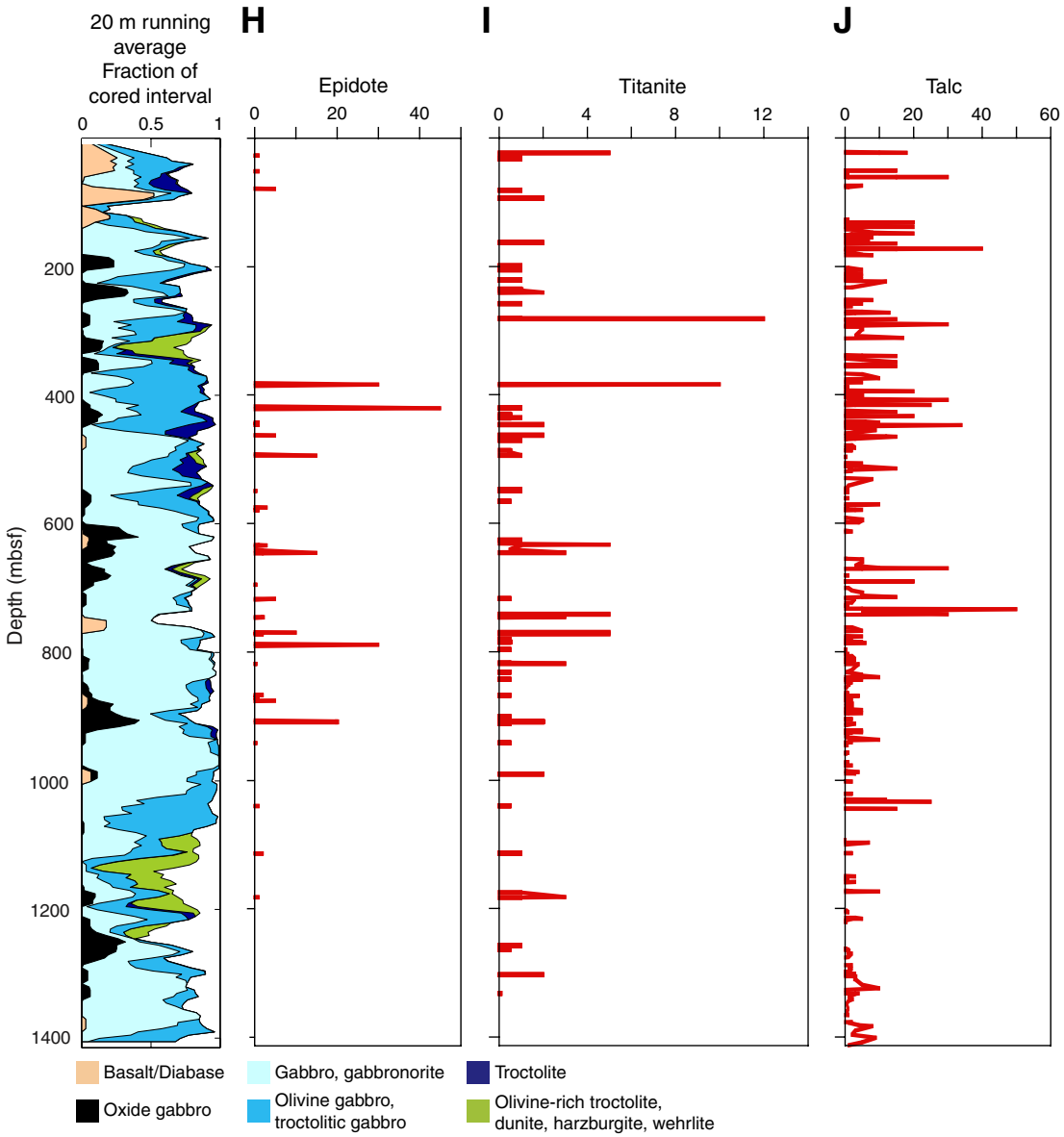

Figure F139 (continued).

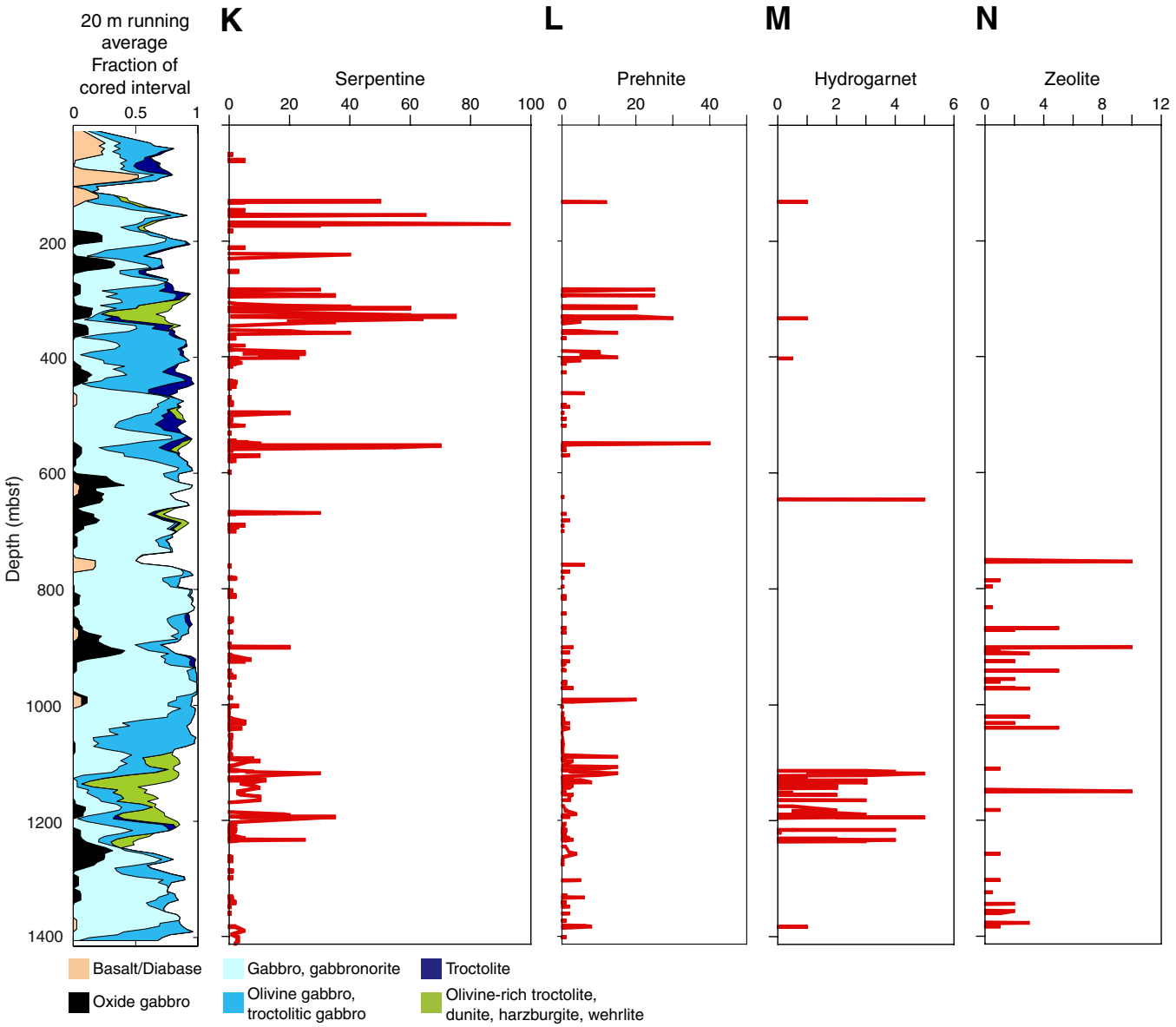

Figure F140. Pie diagram showing the various vein types in cores from Hole U1309D from 401.3 to 1415.5 mbsf (Expedition 305).

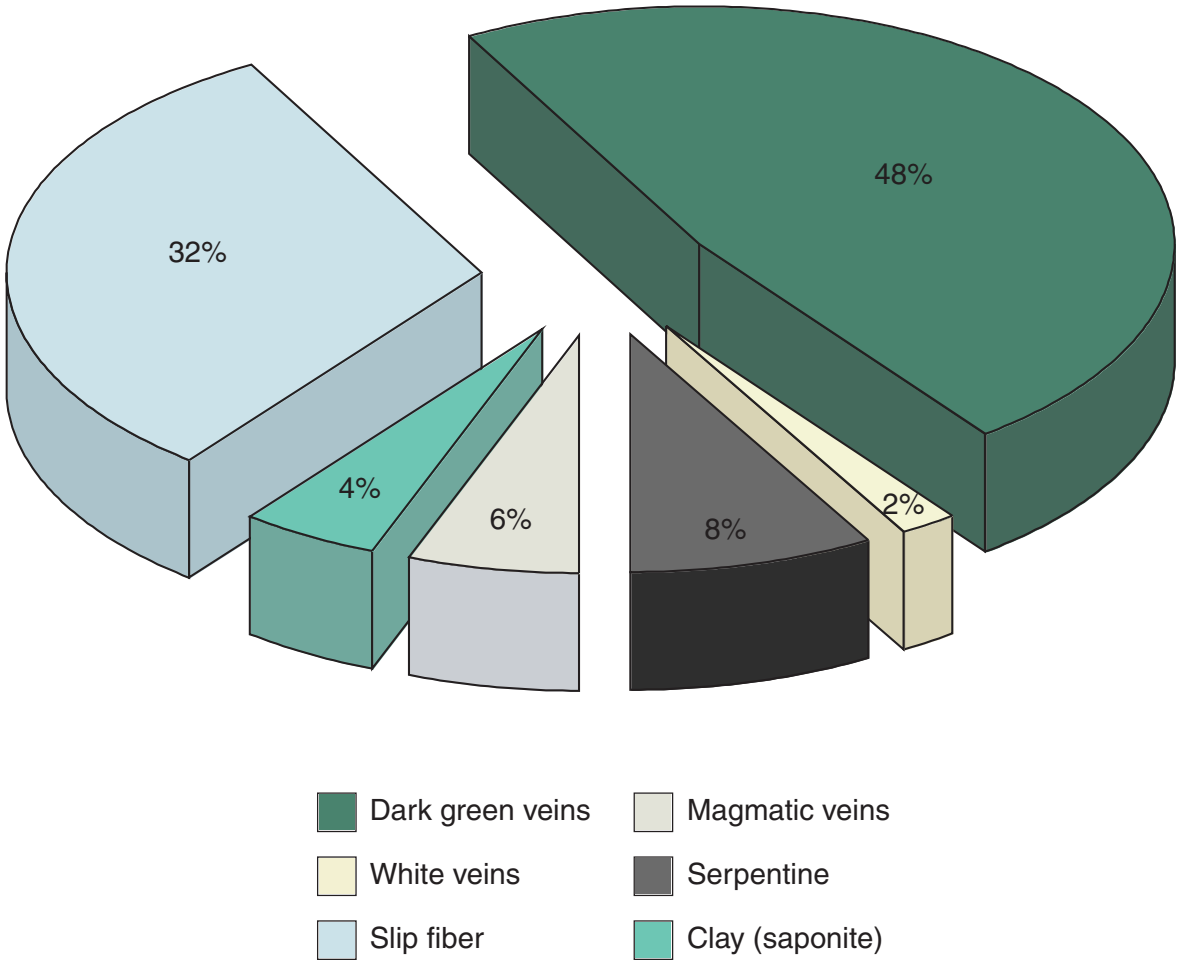

Figure F141. Downhole variation in total number of veins, plotted with running average of lithology. Dark lines are locations of identified fault zones below 400 mbsf.

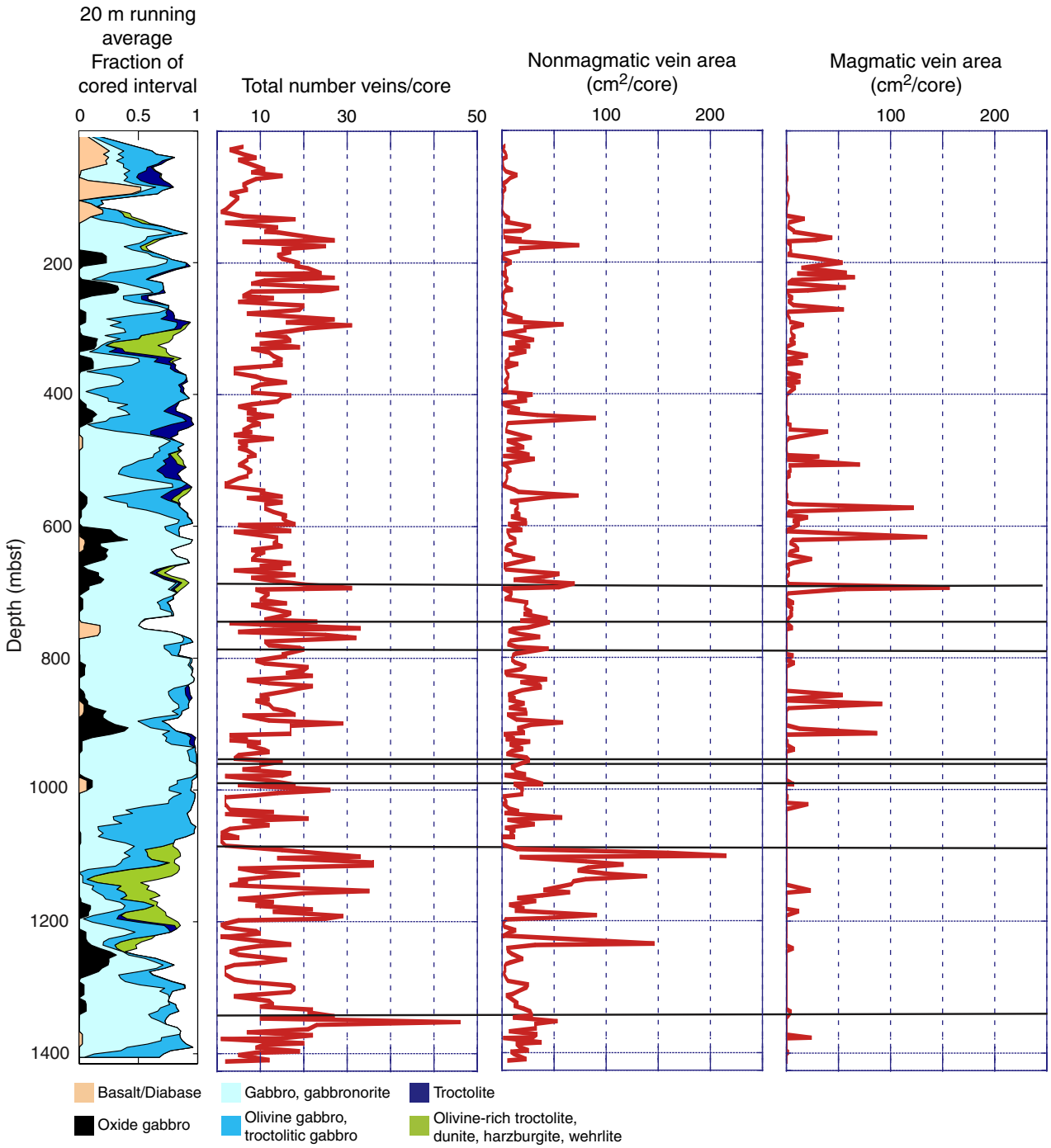

Figure F142. Downhole variation of vein types from Table T7 plotted with running averages of lithology for the lower 1000 m of Hole U1309D. Dark lines are locations of identified fault zones. Serpentine correlates most strongly with olivine-rich rocks. High counts of both amphibole vein types align with or are bracketed by faults.

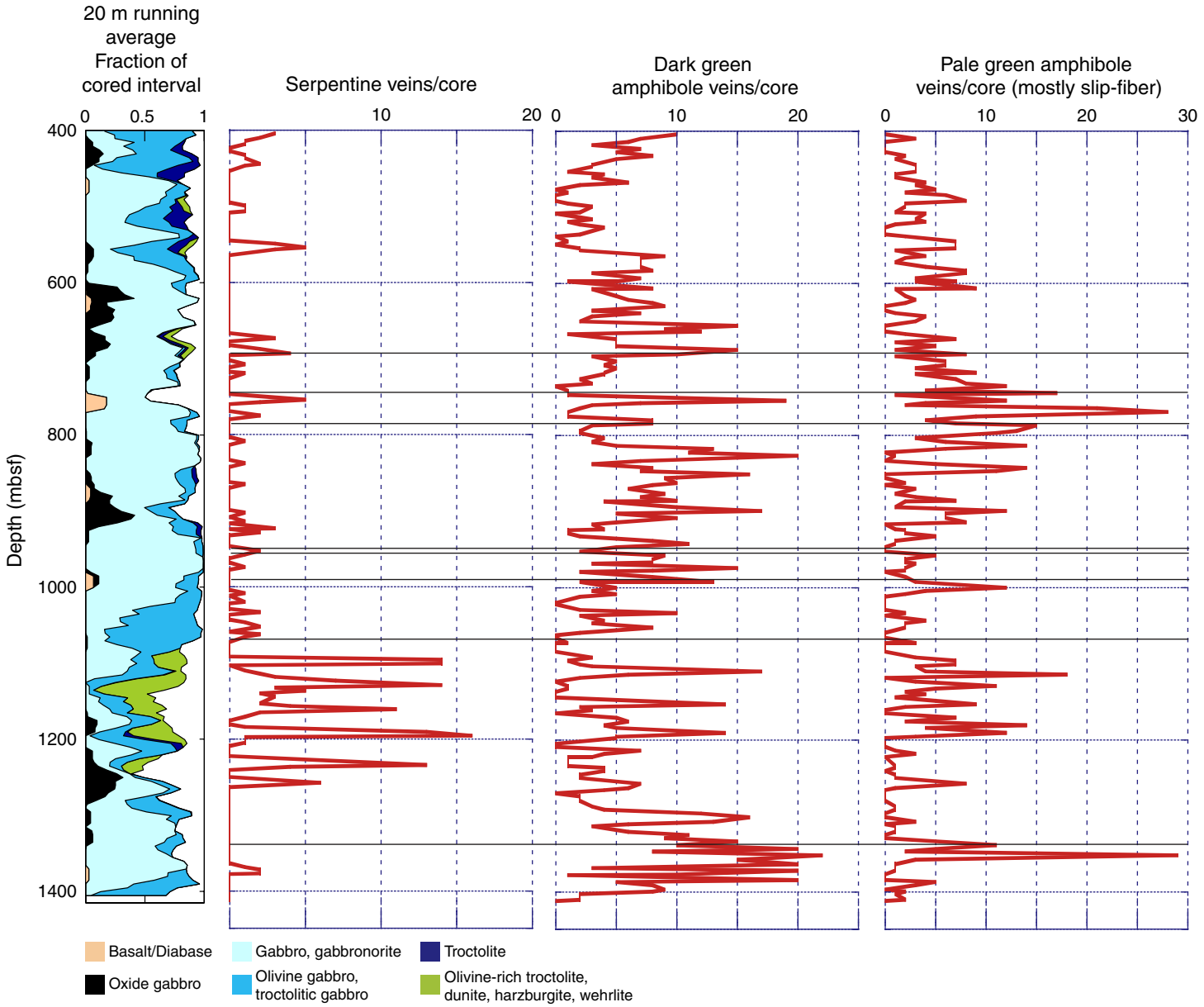

Figure F143. Downhole variation of vein types from Table T7 plotted with running averages of lithology for the lower 1000 m of Hole U1309D. Dark lines are locations of identified fault zones. Magmatic veins are concentrated toward the top of the section (including the top 400 m cored during Expedition 304). Clay veins are concentrated in gabbroic rocks intercalated with olivine-rich troctolites, especially below 1100 mbsf.

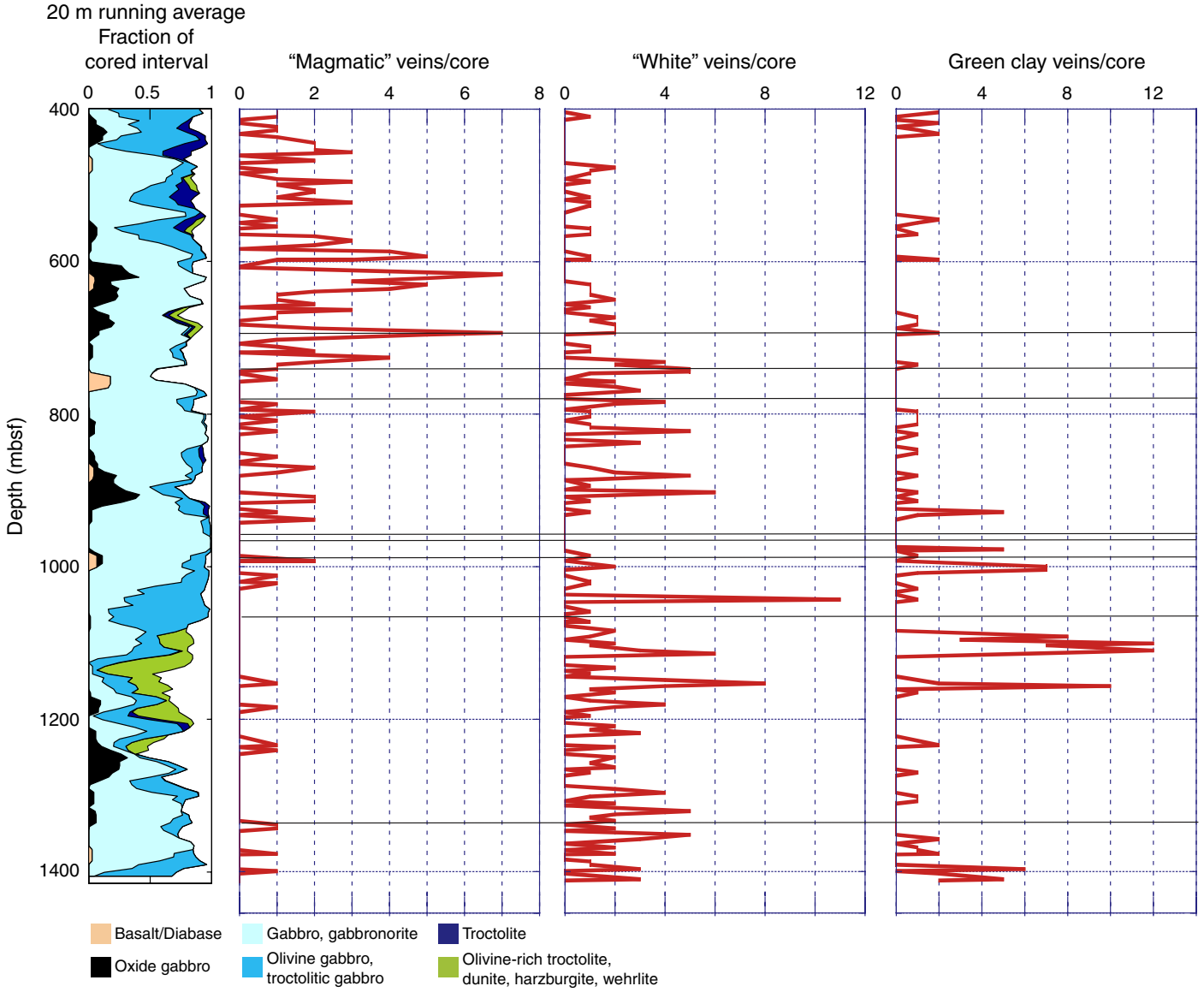

Figure F144. Downhole variation of vein mineralogy plotted with running averages of lithology. Concentration of plagioclase-rich veins, especially in the top 400 m, largely reflects the occurrence of magmatic veins. Serpentine veins are largely restricted to olivine-rich rock types.

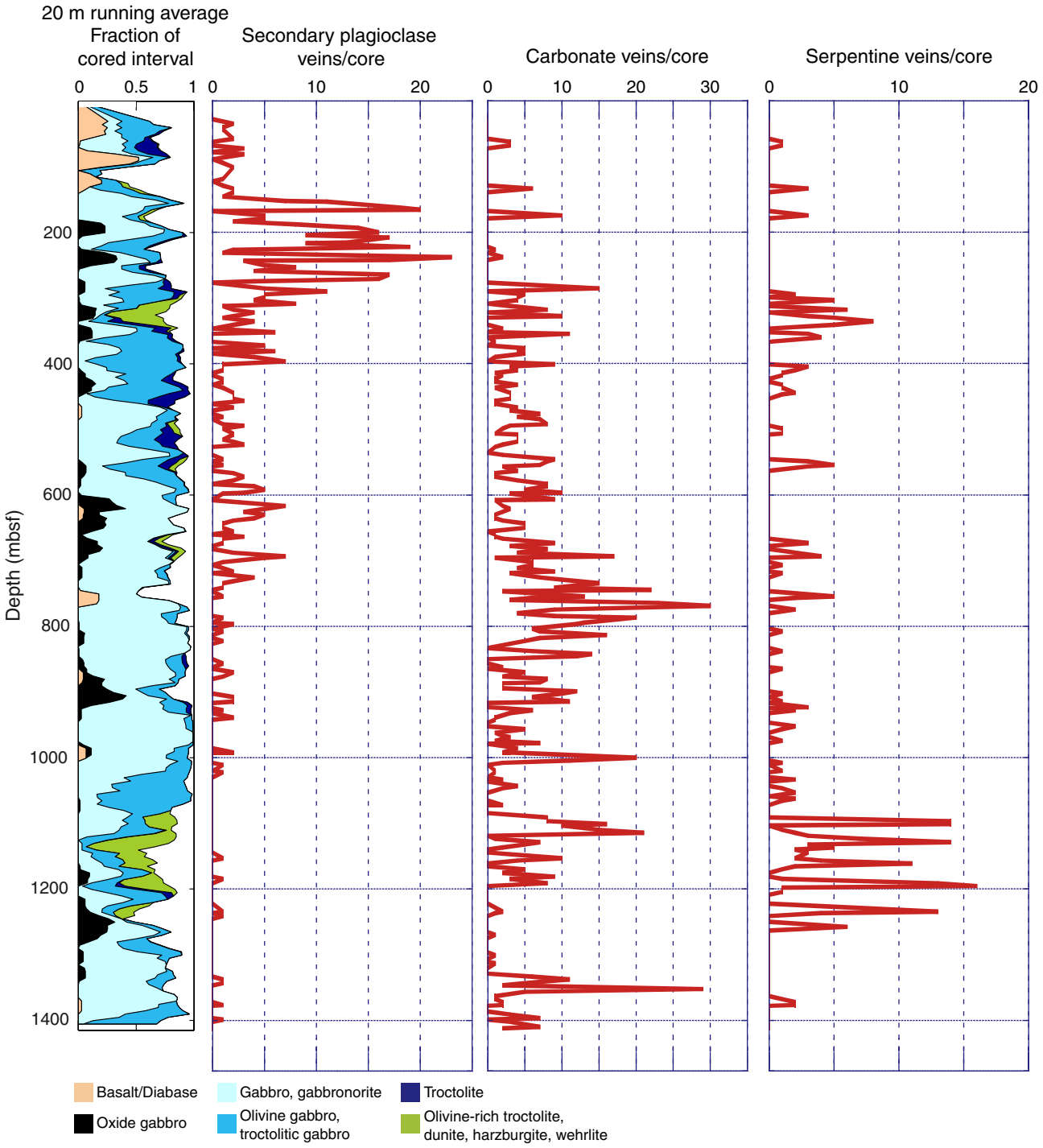

Figure F145. Downhole variation of vein mineralogy plotted with running averages of lithology. Quartz is common in the top 400 m of the hole but essentially disappears by 800 mbsf. Except for a possible spike early in the hole (not confirmed by XRD or thin section), zeolites first appear near 700 mbsf and increase regularly to the bottom of the hole. Sulfides are most common in the uppermost 400 m of Hole U1309D.

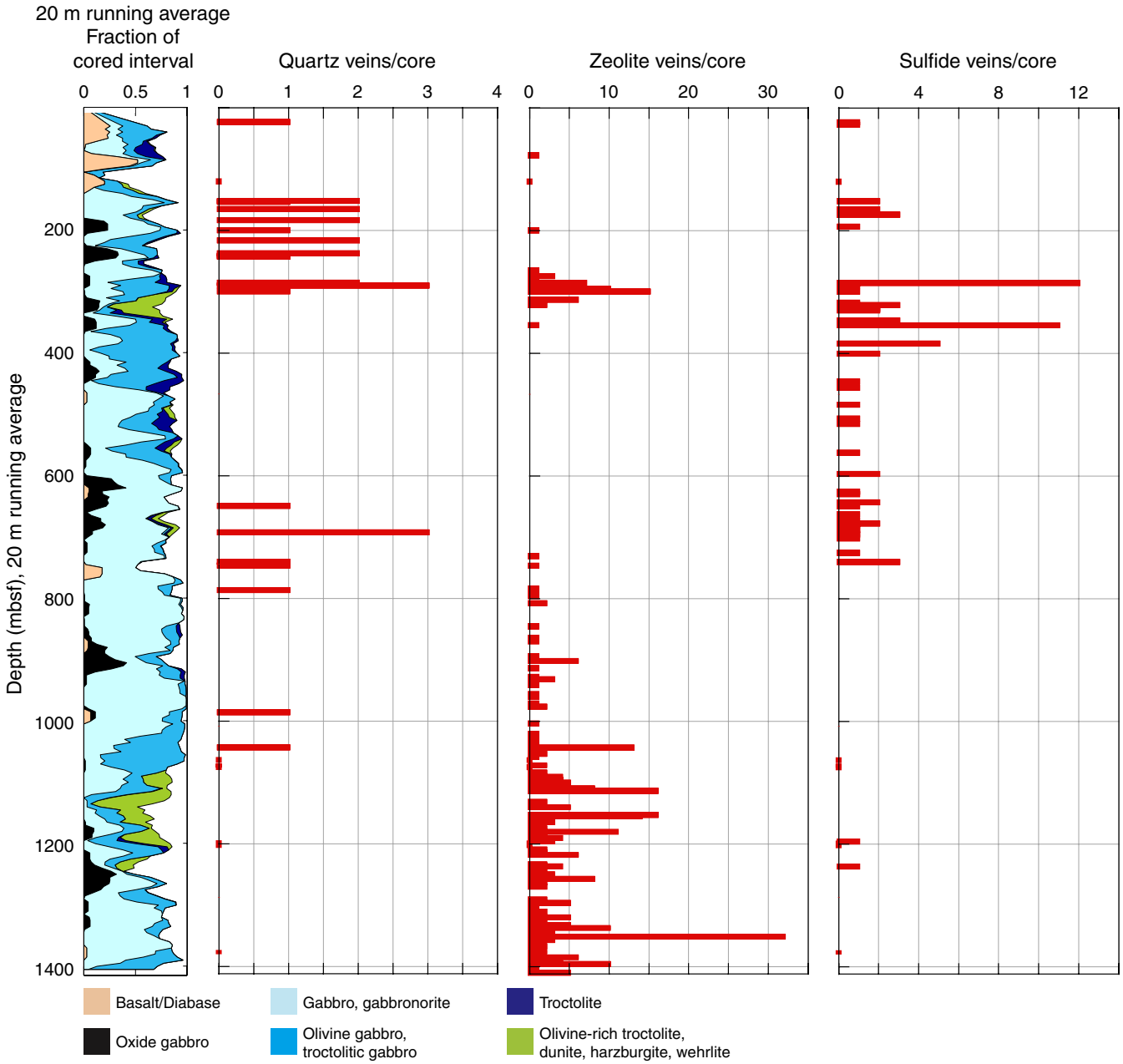

Figure F146. A. Backscatter SEM photo of slightly zoned dynamically recrystallized clinopyroxene in a granulite-facies shear zone cutting gabbro (Sample **304-U1309D-16R-5, 48–50 cm**). Note equant Ti-amphibole (Ti amph) grains probably deformed with the clinopyroxene (Cpx) and later actinolite pervading grain boundaries. For electron microprobe data from this sample, see Table **T9.** **B.** Backscatter SEM photo of Fe-rich clinopyroxene veins cutting large clinopyroxene grain with thin orthopyroxene exsolution lamellae in a coronitic-textured olivine gabbro (Sample 305-U1309D-26R-2, 21–24 cm). Note slight sinistral shear across veined zone and probable fluid inclusions. Dark phase at lower right is plagioclase, with a feathery hornblende alteration rim on the clinopyroxene. (Photographs taken by Eric Condliffe, Leeds University.)

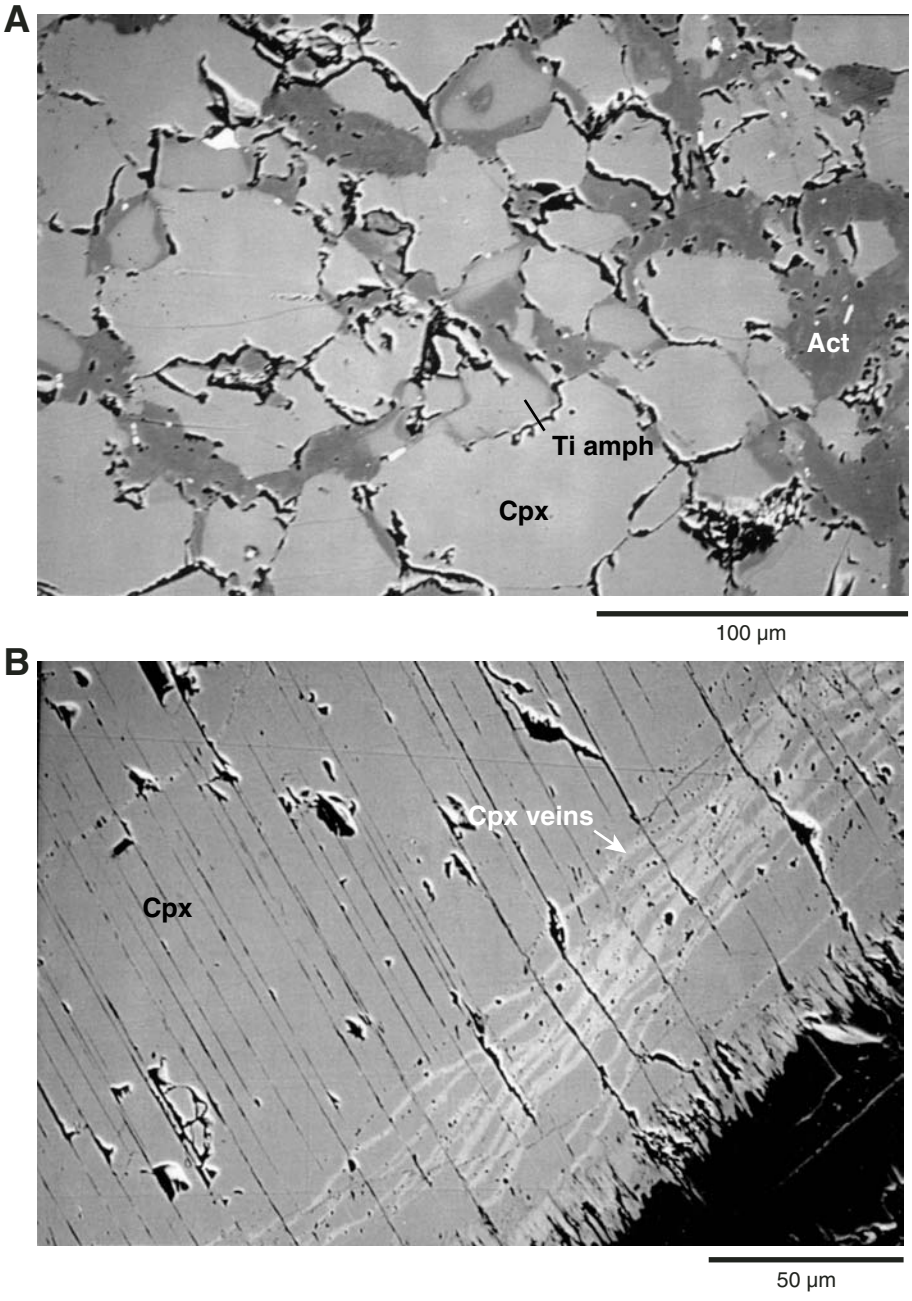

Figure F147. A. Backscatter SEM image of amphiboles replacing clinopyroxene in diabase (Sample **304-U1309D-16R-2, 58–61 cm**). For electron microprobe data, see Table **T9.** Anorthite (An) content of plagioclase (Plag) is marked on the photo. Amphibole compositions are ferroactinolite at A, fluorine-rich ferroedenite at B, and magnesiohornblende at C. **B.** Complex zoning in secondary amphibole replacing clinopyroxene (Cpx). Note that the cleavage traces show that this is a single crystal. No electron microprobe data are available from this area, but the main reason for contrast is probably variations in Fe/Mg ratio. The complex truncated zoning suggests generation of open porosity during reaction. (Photographs taken by Eric Condliffe, Leeds University.)

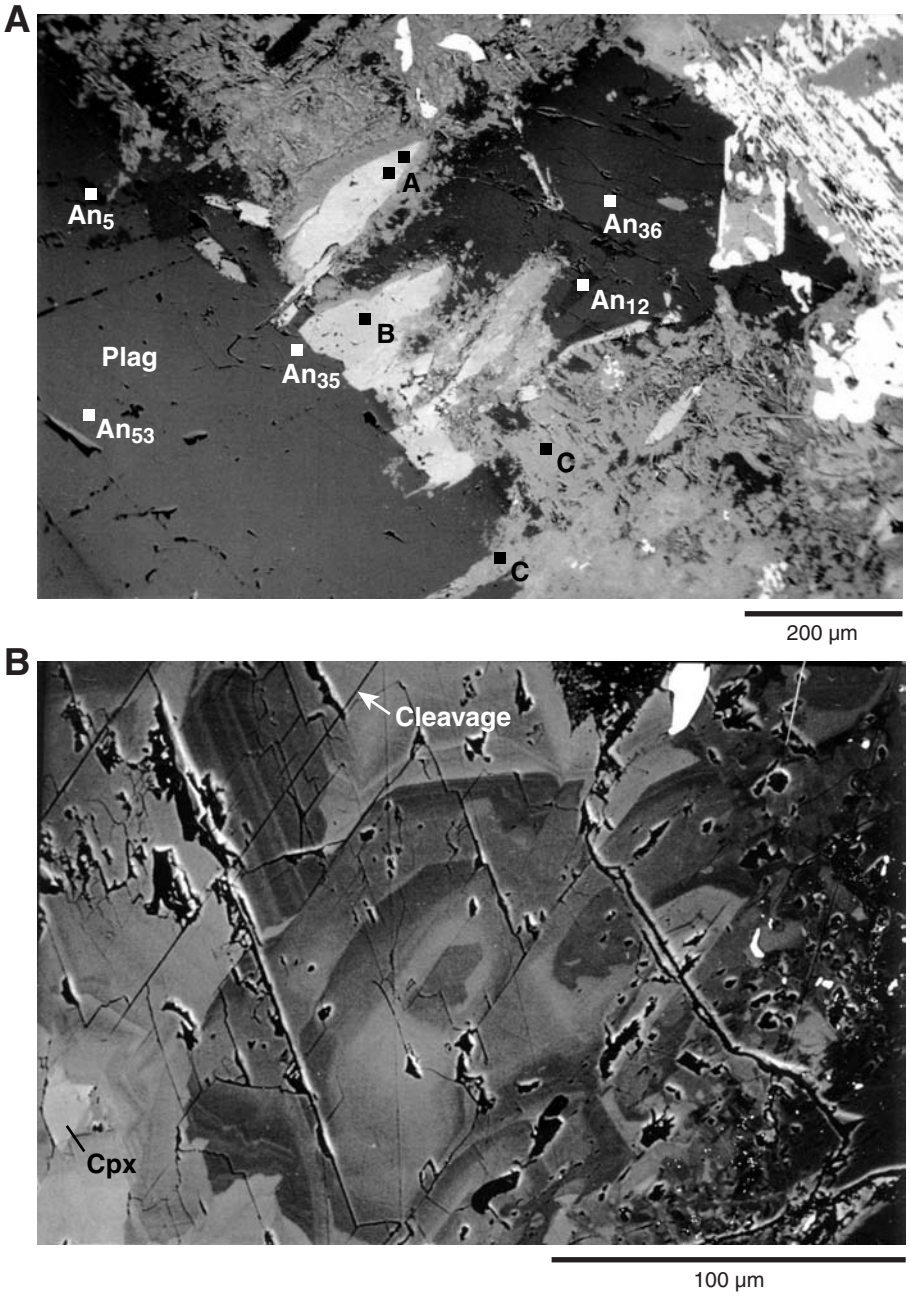

Figure F148. Pressure-temperature diagrams showing the possible cooling path for rocks at Site U1309. Reaction numbers correspond to equations in text. **A.** Reactions in gabbroic rocks. Reaction 1: beginning of hornblende breakdown in amphibolite (Spear, 1981). Reaction 2 = disappearance of epidote in metabasites calculated from TWEEQ program (Berman, 1991), using the database of Berman (1988). Heavy gray line gives approximate low-temperature (T) limit for the stability of olivine + plagioclase after Frost (1976). Blue area gives approximate pressure and temperature conditions for the static hydration seen in gabbroic rocks from Hole U1309B and the upper levels of Hole U1309D. Chl = chlorite, Cz = clinozoisite, Qz = quartz, An = anorthite, Trem = tremolite. **B.** Reactions found in ultramafic rocks. Location of Reactions 5 through 8 calculated from the database of Berman (1988). Green area shows the temperature range over which reactions proceeded in the ultramafic rocks. Gr = garnet, Pr = prehnite, Di = diopside, Serp = serpentinite, Br = brucite, Fo = forsterite, En = enstatite.

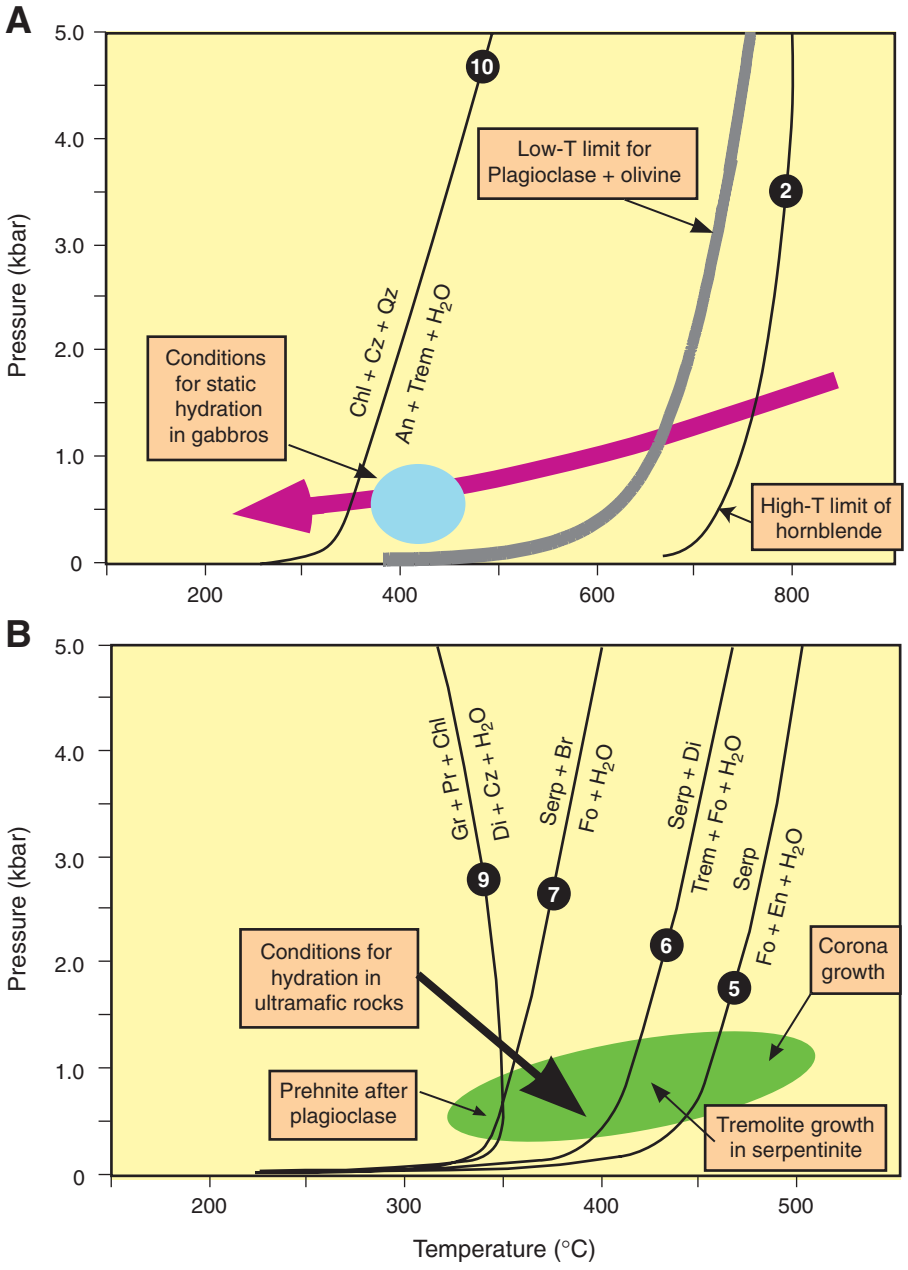

Figure F149. Activity-activity diagram for the formation of corona textures between olivine and plagioclase in troctolites, olivine gabbros, and ultramafic cumulates. Arrow A shows the likely path of fluid composition that accompanied the formation of the coronas with the zonation plagioclase-chlorite-tremolite-olivine. Arrow B shows the path for a corona that contains a talc zone as well. *P* = pressure, *T* = temperature.

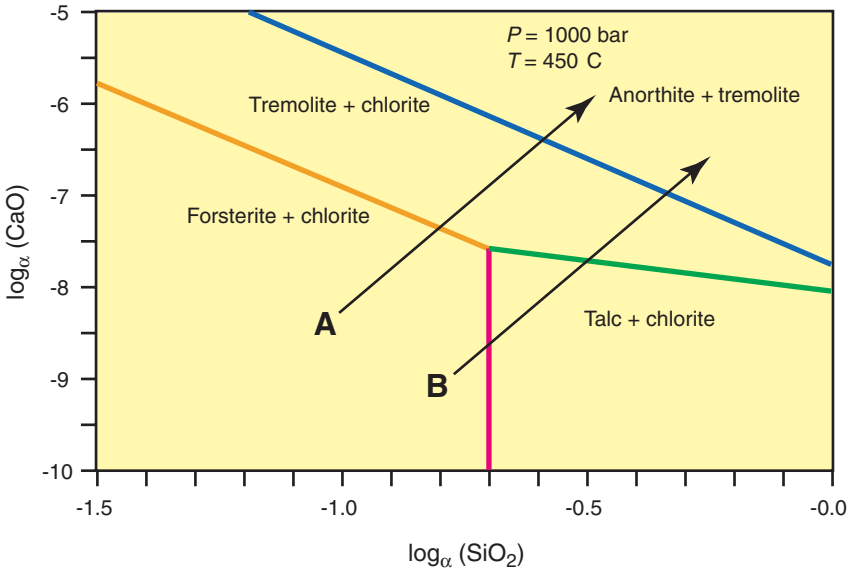

Figure F150. A. Cataclastic (fault) zone pervaded by fibrous green amphibole (Sample **305-U1309D-141R-2, 75–78 cm**) (magnification = 2.5×). Note green amphibole veins emanating from fault zone. **B.** Late interstitial calcite in cataclastic zone (Sample **305-U1309D-161R-1, 84–87 cm**) (magnification = 10×).

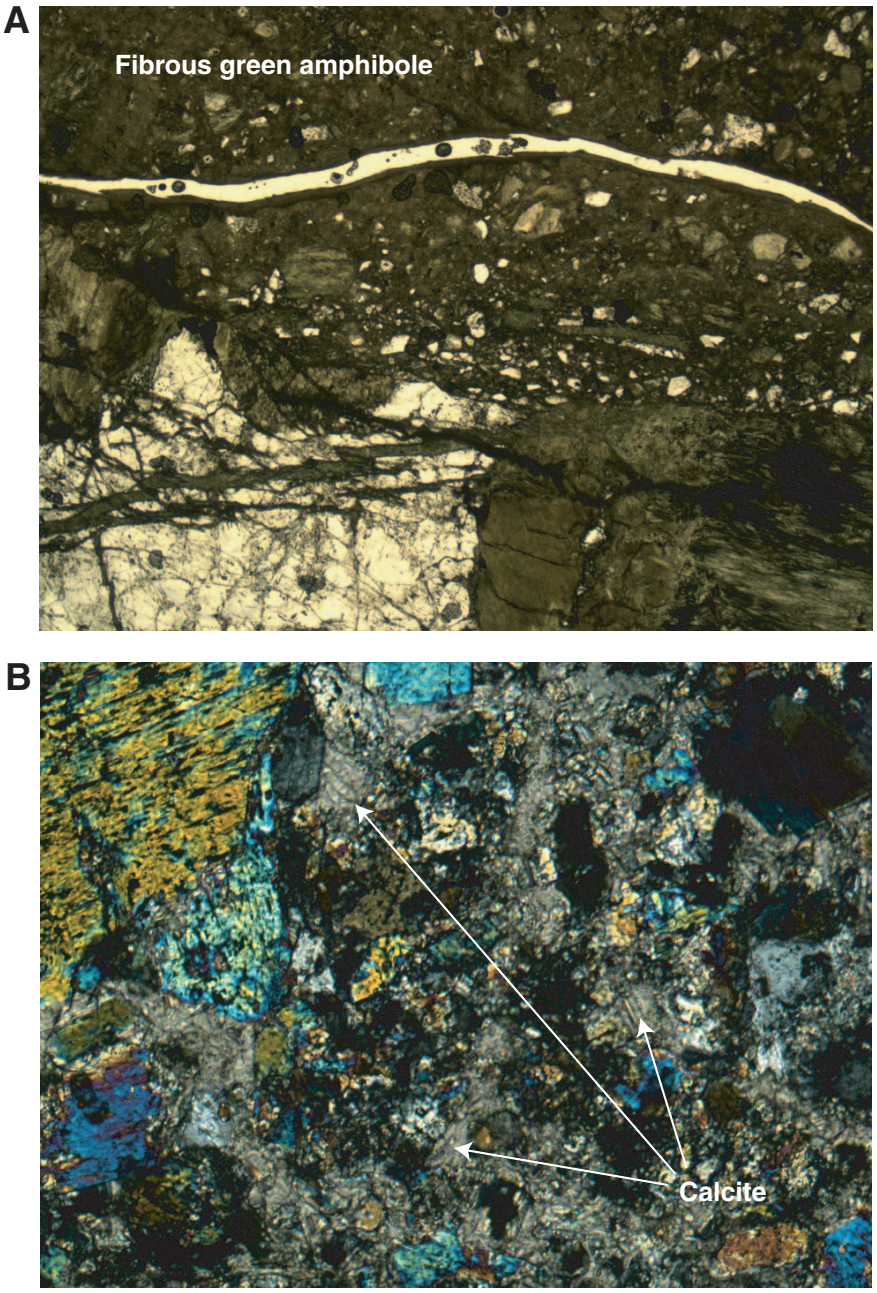

Figure F151. A. Olivine with subgrain boundaries (Sample **304-U1309B-11R-1, 98–100 cm**) (cross-polarized light; field of view [FOV] = 4 mm). **B.** Lattice-preferred orientation in olivine (Sample **304-U1309B-11R-1, 98–100 cm**). Angle to extinction of fast direction (rotation counterclockwise from vertical) in the crystal is plotted versus number of occurrences (N = 34). **C.** Olivine grains in wehrlite showing common extinction behavior as compared to the harzburgite in Hole U1309B (Sample **304-U1309D-10R-1, 91–94 cm**) (cross-polarized light; FOV = 8 mm). **D.** Olivine in troctolite showing well-defined deformation lamellae (Sample **304-U1309D-70R-3, 86–88 cm**) (cross-polarized light; FOV = 4 mm).

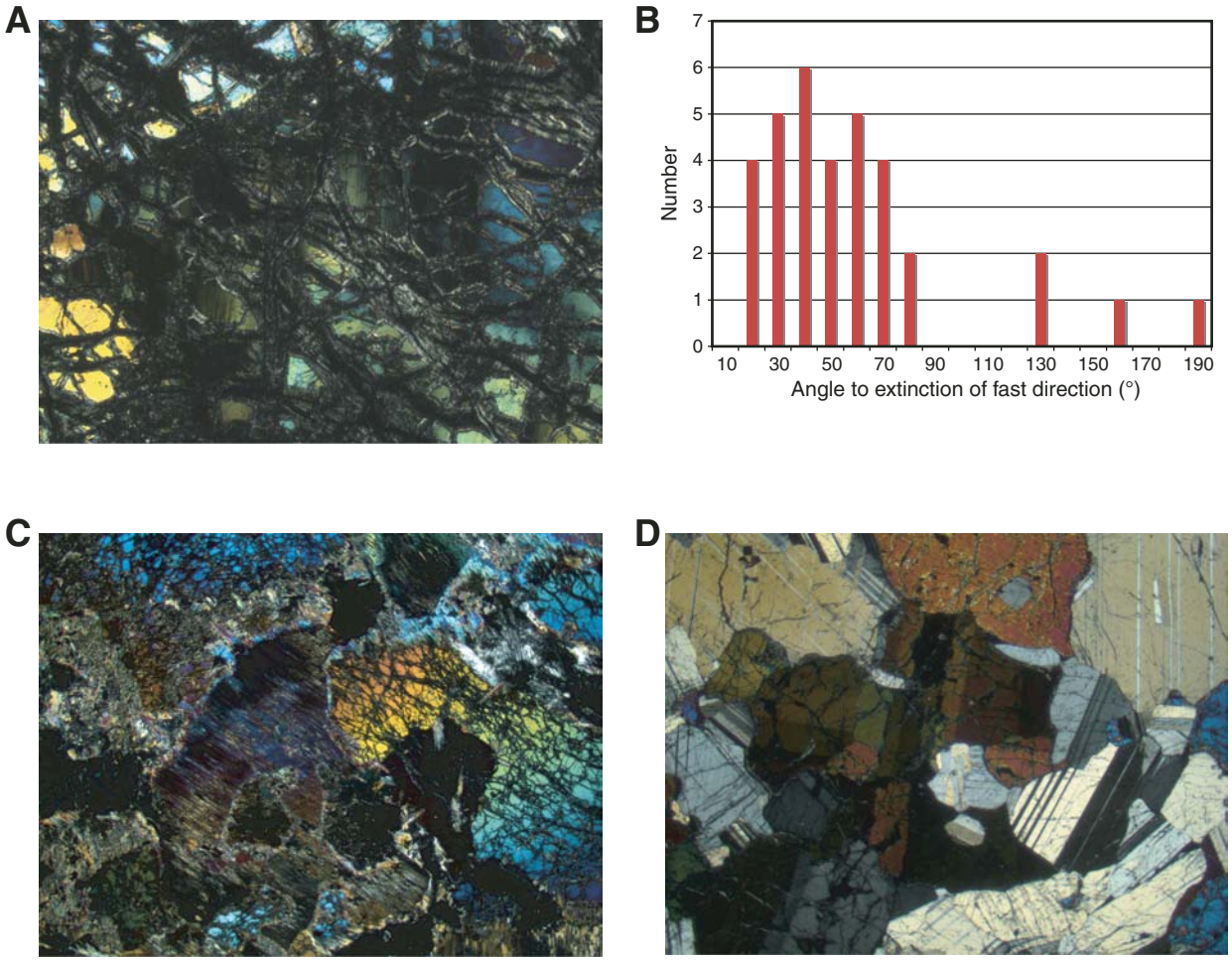

Figure F152. A. Magmatic layering in gabbro (interval 304-U1309B-15R-1, 16–32 cm). **B.** Troctolite exhibiting a magmatic foliation defined by elongated corona-texture olivine (interval 304-U1309D-22R-2, 32–45 cm). **C.** Elongated corona texture olivine (Sample **304-U1309D-22R-3, 39–42 cm**) (cross-polarized light; field of view [FOV] = 8 mm). **D.** Contacts between gabbro and troctolite (interval 304-U1309D-8R-2, 65–77 cm). (Continued on next two pages.)

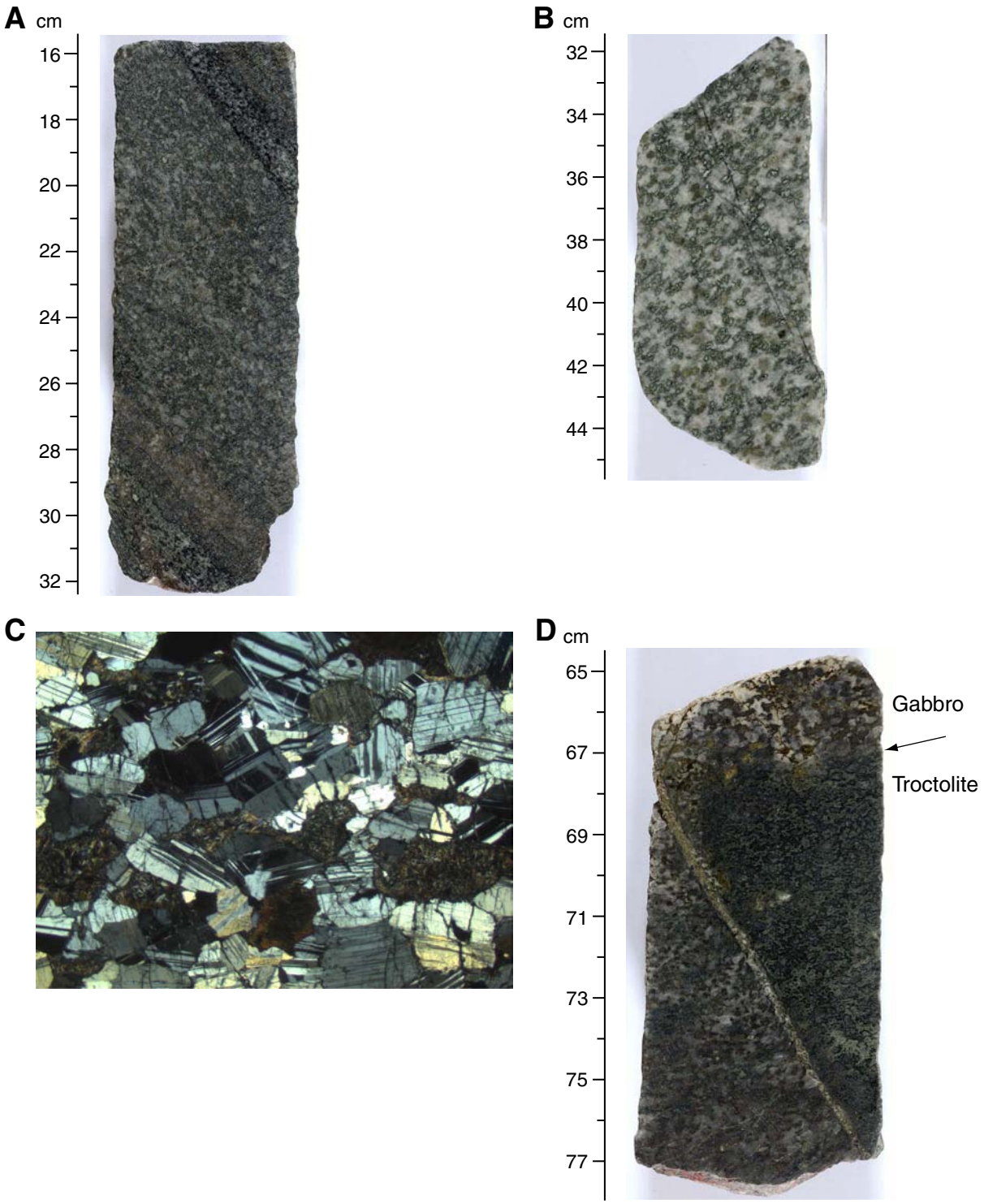

Figure F152 (continued). **E.** Microgabbro intruding coarser grained gabbro across this transitional contact (interval 304-U1309D-62R-1, 81–93 cm). A leucocratic dikelet cuts both units. **F.** Magmatic foliation defined by aligned plagioclase feldspar (interval 304-U1309D-66R-2, 10–21 cm). **G.** Coarse-grained, plagioclase-rich gabbro intrudes serpentinite without related deformation (interval 304-U1309D-64R-2, 4–18 cm). **H.** Coarse-grained gabbro is intensely strained, producing a mylonite with mixed pyroxene, feldspar and plagioclase, along with a xenolith of an ultramafic rock (interval 304-U1309D-64R-2, 41–49 cm).

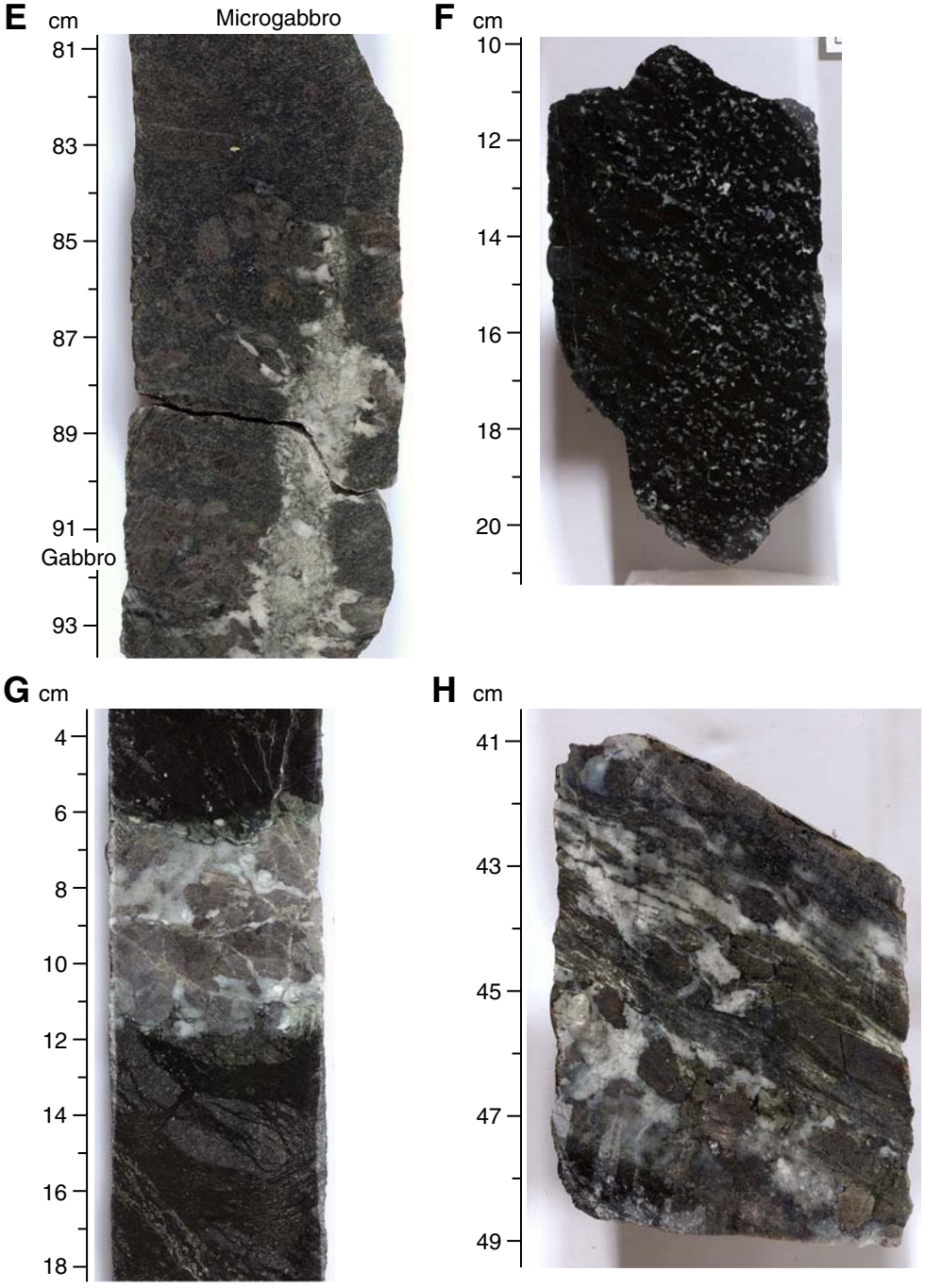

Figure F152 (continued). I. Aligned plagioclase exhibiting a primary magmatic fabric alignment surrounded by grains of dynamically recrystallized plagioclase (Sample **304-U1309D-30R-1, 55–58 cm**) (cross-polarized light; FOV = 8 mm). **J.** Steeply dipping contact of gabbro intruding troctolite showing some crystal-plastic deformation (interval 304-1309D-8R-2, 20–29 cm). **K.** Localized deformation zone between more olivine rich gabbro deformed crystal plastically and less intensely strained gabbro (Sample **304-U1309D-8R-2, 26–28 cm**) (plane-polarized light; FOV = 4 mm). **L.** Recrystallized pyroxene and plagioclase cut by a fracture filled with oxides; fracture was possibly coeval with dynamic recrystallization (Sample **304-U1309D-44R-2, 106–109 cm**) (cross-polarized light; FOV = 8 mm).

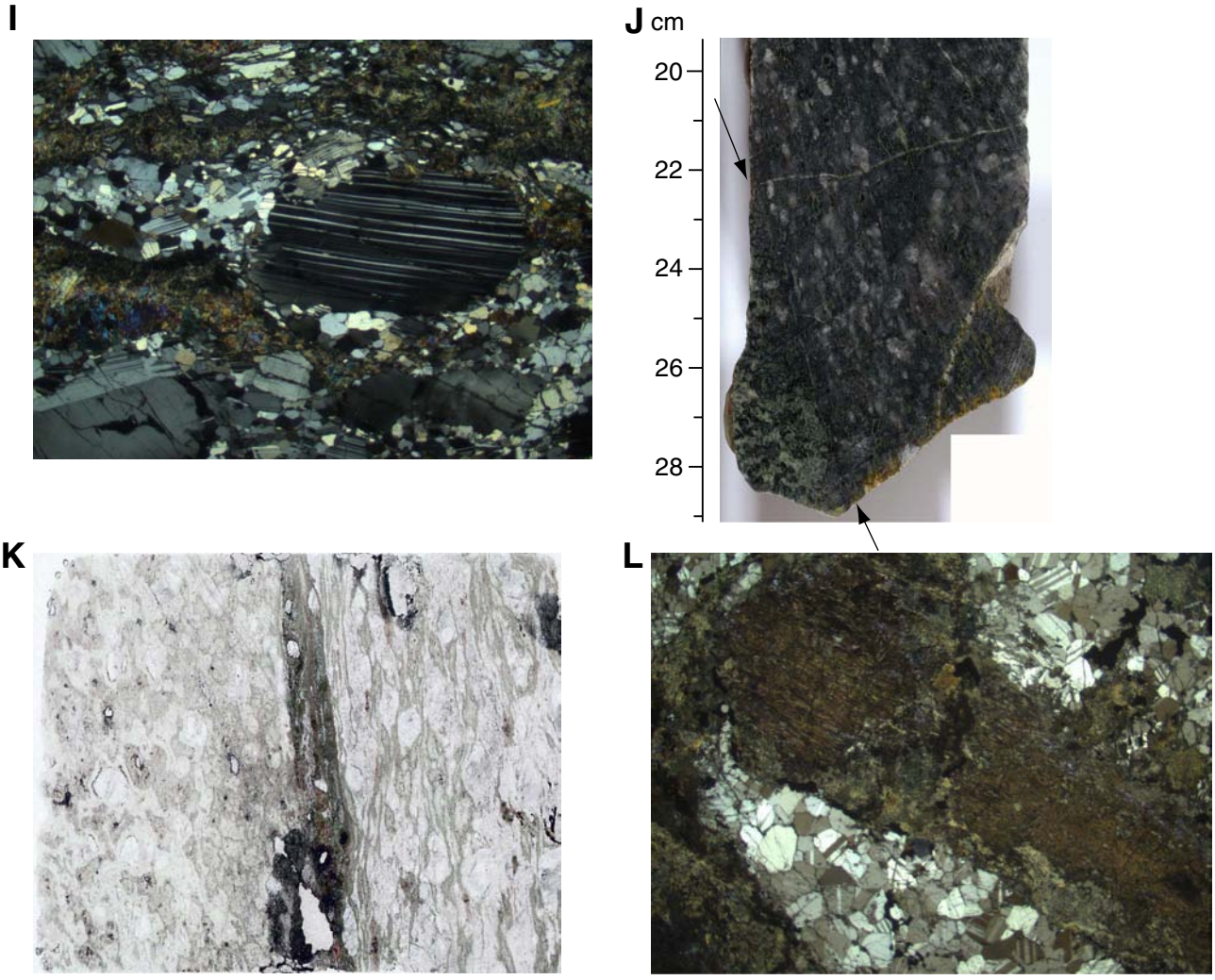

Figure F153. A. Magmatic foliation overprinted by incipient plastic deformation in olivine gabbro (interval 305-U1309D-110R-3, 40–52 cm). Yellow box = location of B and C. **B.** Magmatic foliation with aligned plagioclase overprinted by incipient plastic deformation (Sample **305-U1309D-110R-3, 46–49 cm**) (plane-polarized light; field of view [FOV] = 2 cm). **C.** Same as B; cross-polarized light, FOV = 2 cm. Yellow box = location of D. **D.** Aligned plagioclase crystals showing well-defined deformation lamellae indicating slight crystal-plastic overprint (cross-polarized light; FOV = 11 mm). (Continued on next page.)

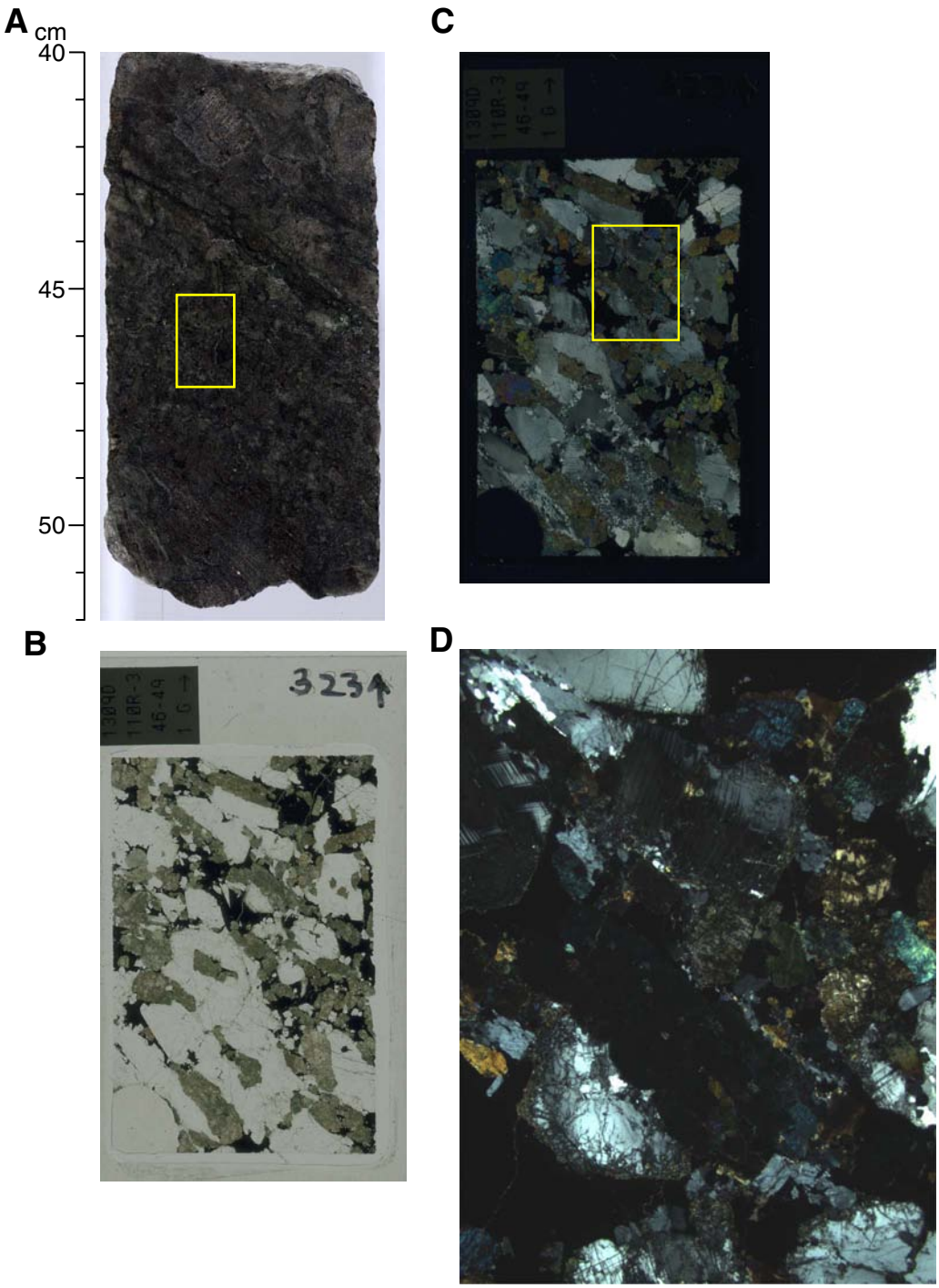

Figure F153 (continued). **E.** Weak magmatic foliation in olivine gabbro (interval 305-U1309D-142R-2, 115–130 cm). Yellow box = location of F and G. **F.** Magmatic foliation with aligned plagioclase and clinopyroxene crystals (Sample **305-U1309D-142R-2, 123–125 cm**) (plane-polarized light; FOV = 2 cm). **G.** Same as F; cross-polarized light, FOV = 2 cm. Yellow box = location of H. **H.** Aligned clinopyroxene and plagioclase crystals showing a well-defined deformation lamellae (cross-polarized light; FOV 11 = mm).

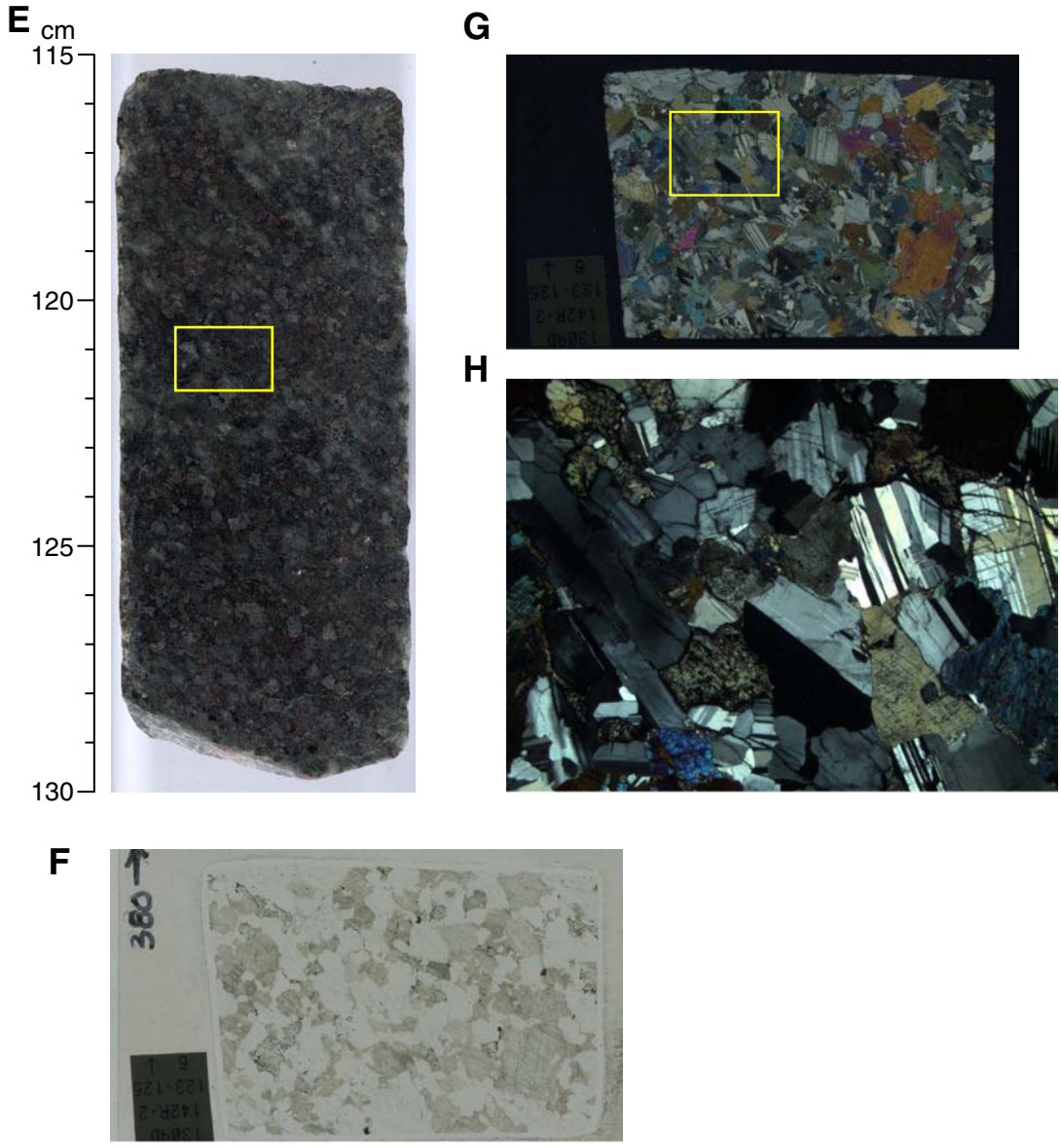

Figure F154. A. Crystal-plastic deformation in gabbro (interval 304-U1309B-8R-1, 46–50 cm) (field of view [FOV] = 14 cm). **B.** Well-defined mylonite in gabbro cut by a fracture (Sample **304-U1309D-8R-1, 68–71 cm**) (plane-polarized light; FOV = 2 cm). **C.** Mylonite (Sample **304-U1309D-8R-1, 68–71 cm**) (cross-polarized light; FOV = 8 mm). **D.** Same as C; recrystallized plagioclase and pyroxene (plane-polarized light; FOV = 1 mm). **E.** Brown amphibole vein crosscuts highly localized shear zone in a mylonite with domains of recrystallized plagioclase and pyroxene (Sample **304-U1309D-9R-1, 71–73 cm**) (cross-polarized light; FOV = 4 mm). **F.** Annealed microcracks in feldspar (Sample **304-U1309B-9R-1, 38–41 cm**) (plane-polarized light; FOV = 4 mm).

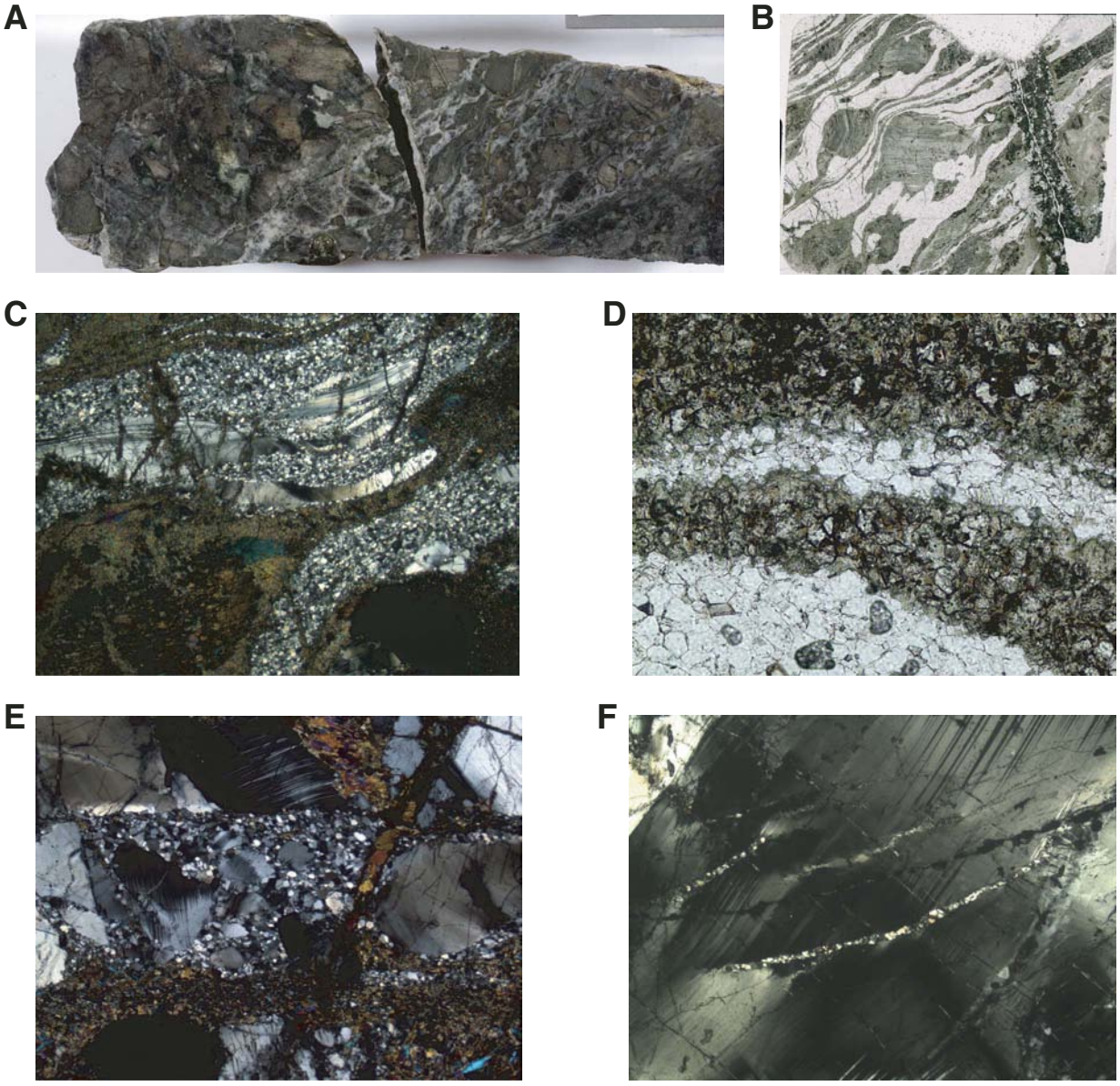

Figure F155. A. Crystal-plastic deformation in oxide gabbro; shear zone = ~2 m (interval 305-U1309D-137R-1, 40–57 cm). Yellow box = location of B and C. **B.** Boundary of a mylonite in oxide gabbro (Sample **305-U1309D-137R-1, 45–47 cm**) (plane-polarized light, field of view [FOV] = 2 cm). **C.** Same as B; cross-polarized light, FOV = 2 cm. (Continued on next two pages.)

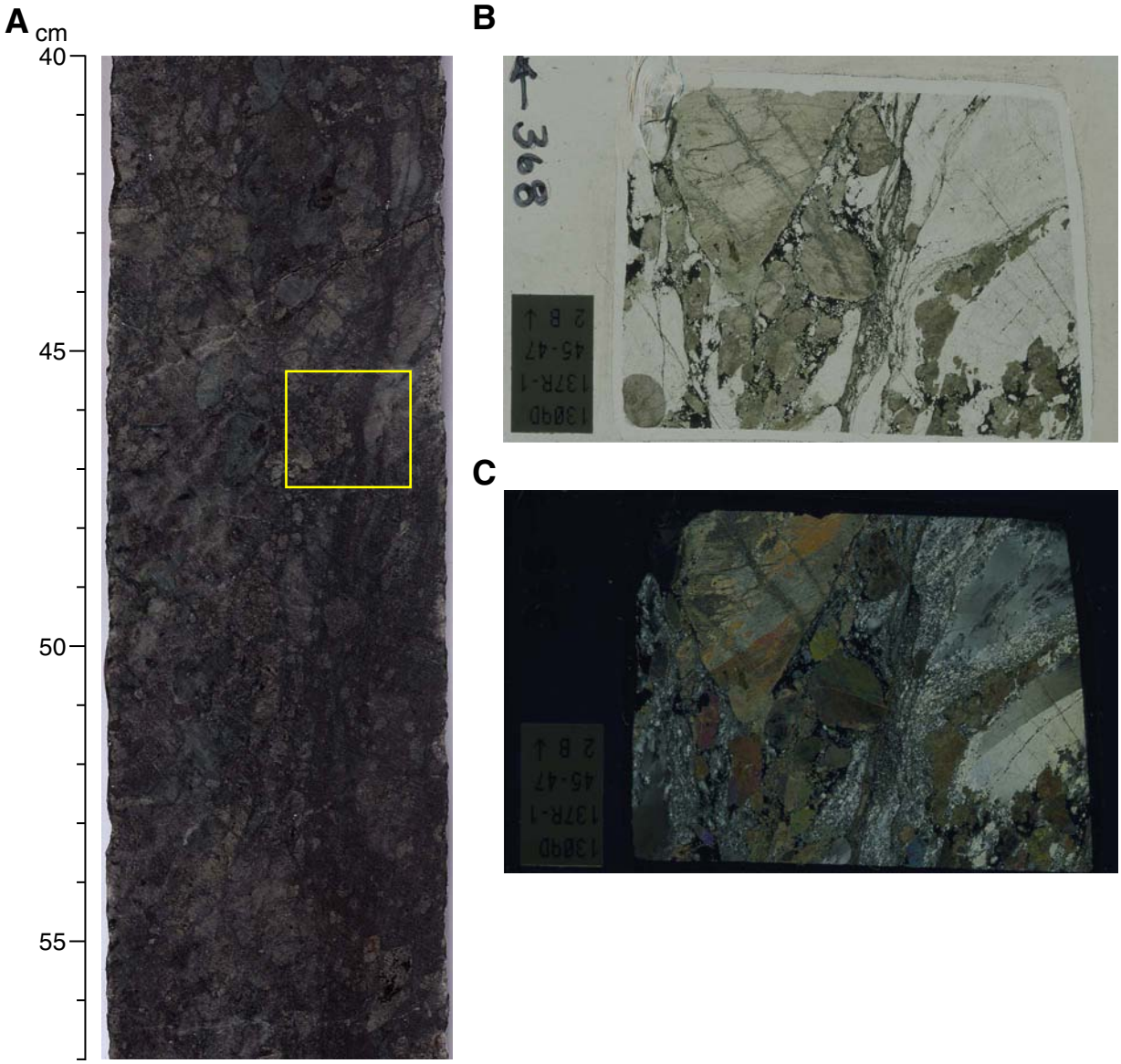

Figure F155 (continued). D. Crystal-plastic deformation of moderate strain in the same oxide gabbro, shear zone = ~2 m (interval 305-U1309D-137R-2, 75–92 cm). Yellow box = location of E and F. **E.** Moderate strain section of the mylonite (Sample **305-U1309D-137R-2, 96–98 cm**) (plane-polarized light, FOV = 2 cm). **F.** Same as E; cross-polarized light, FOV = 2 cm.

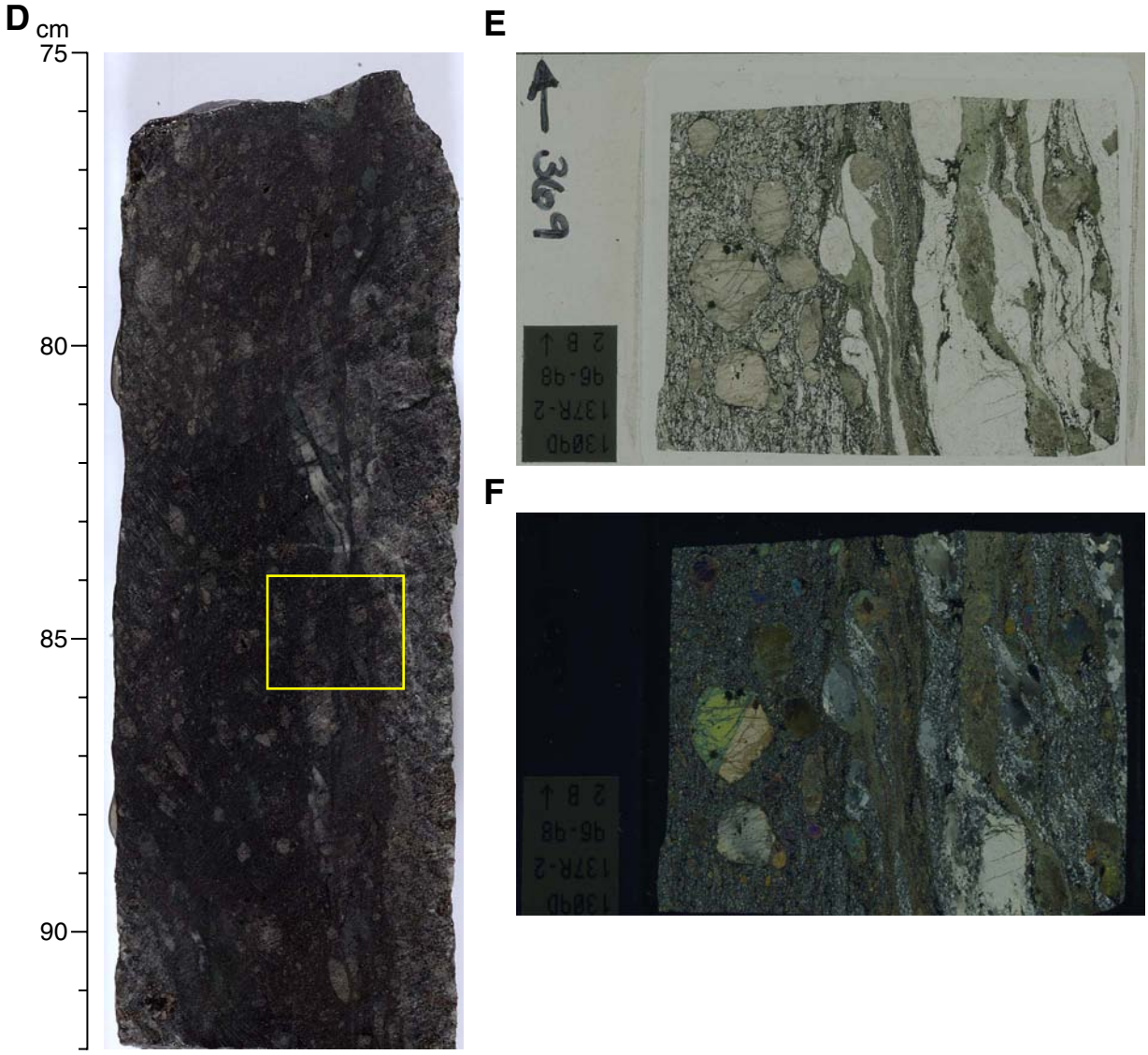

Figure F155 (continued). G. Crystal-plastic deformation of high strain in the same oxide gabbro; shear zone = ~2 m (interval 305-U1309D-137R-2, 125–140 cm). Yellow box = location of H and I. **H.** High-strain center of the mylonite (Sample **305-U1309D-137R-2, 133–135 cm**) (plane-polarized light, FOV = 2 cm). **I.** Same as H; cross-polarized light, FOV = 2 cm.

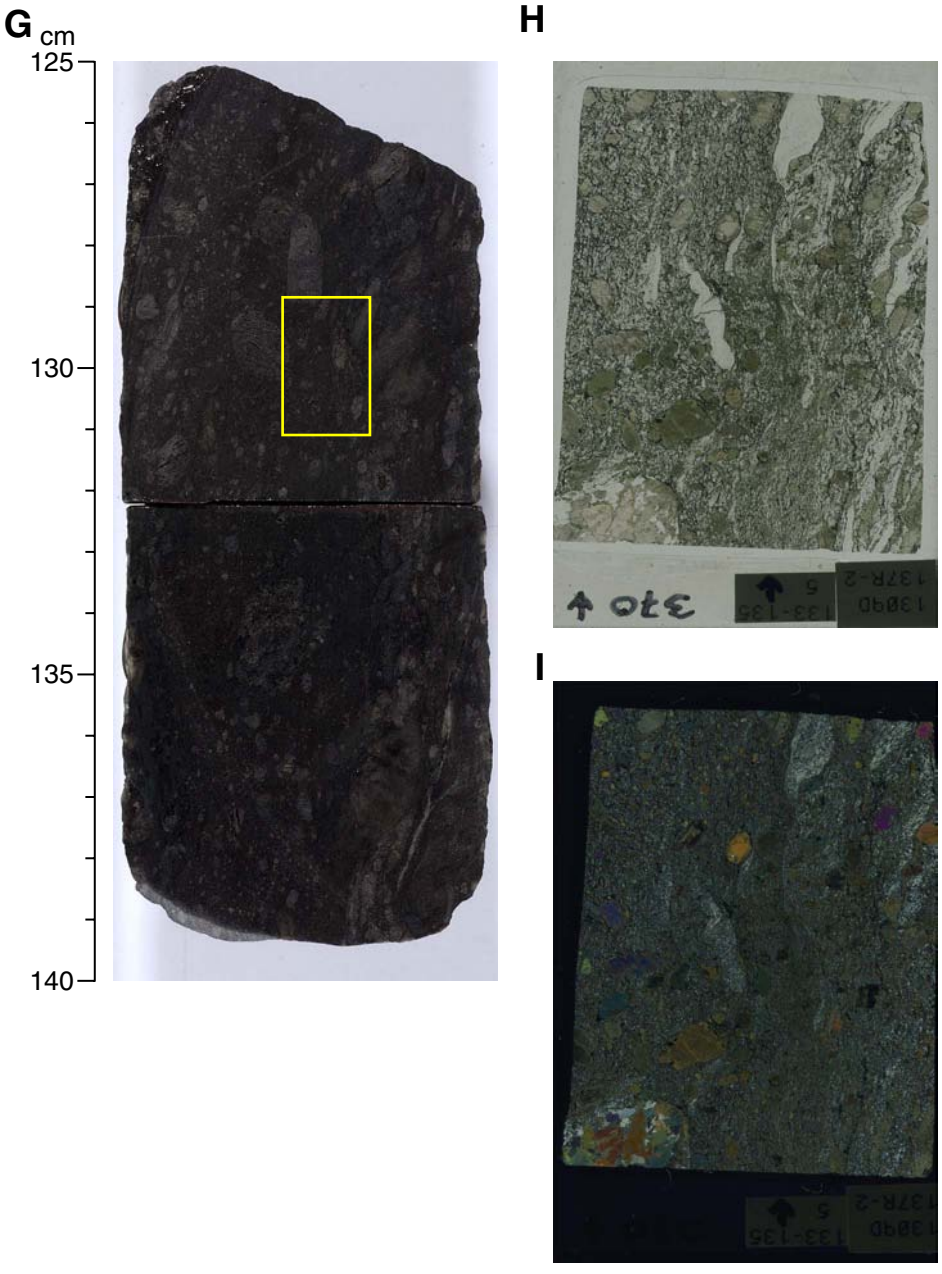

Figure F156. A. Crystal-plastic deformation in oxide gabbro exhibiting a very sharp contact with less deformed zone (interval 305-U1309D-138R-3, 45–57 cm); shear zone = 2 cm at neck. Yellow box = location of B and C. **B.** Sharp boundary to the shear zone (Sample **305-U1309D-138R-3, 55–59 cm**) (plane-polarized light; FOV = 2 cm). **C.** Same as B; cross-polarized light, FOV = 2 cm. Yellow box = location of D. **D.** Difference in the microstructure between the area affected by the shear zone and outside the shear zone margin (cross-polarized light; FOV = 11 mm). (Continued on next page.)

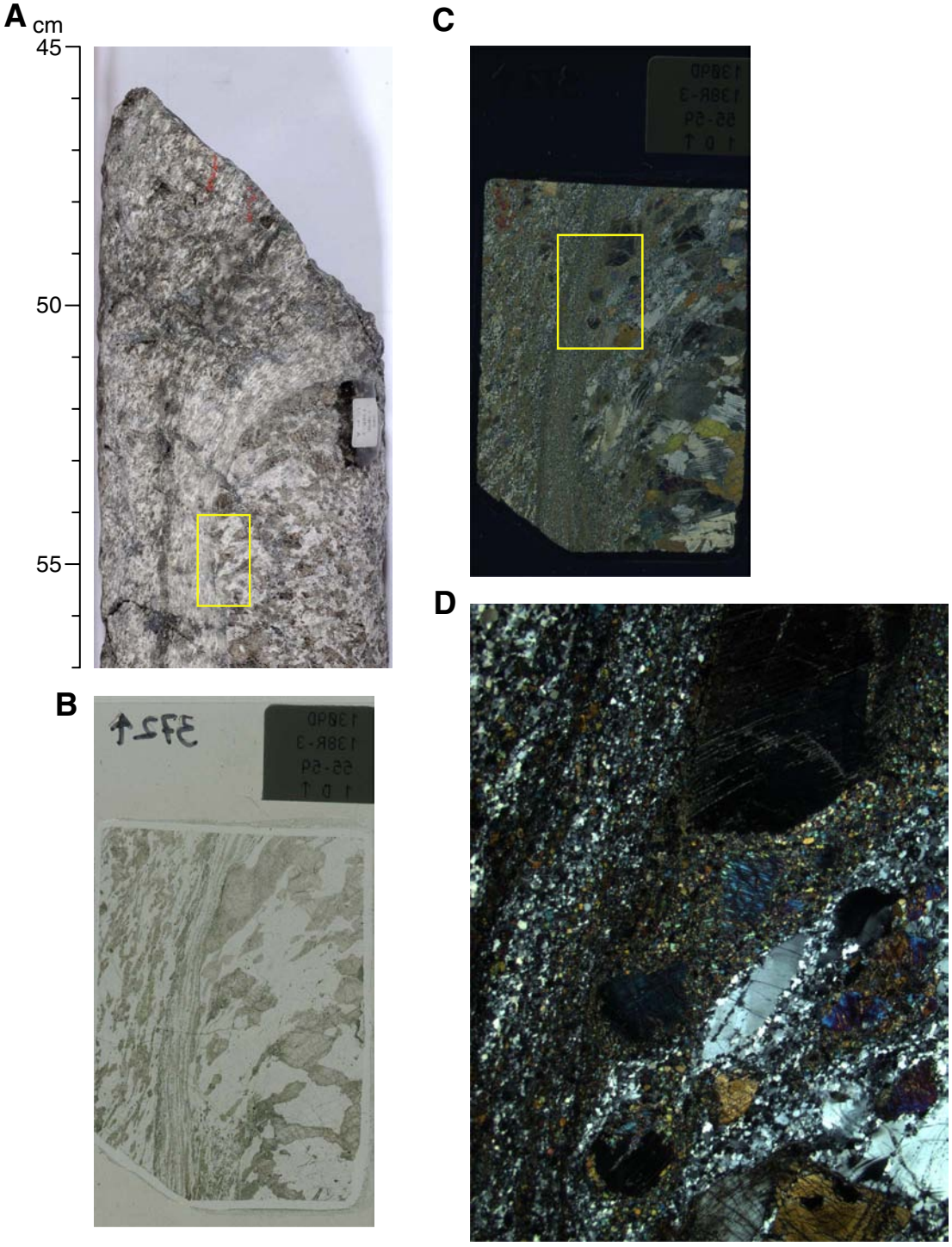

Figure F156 (continued). **E.** Crystal-plastic deformation in gabbro exhibiting a very sharp contact with the undeformed zone (Sample 305-U1309D-143R-2, 53–61 cm); shear zone = 2 cm at neck. Yellow box = location of F and G. **F.** Sharp boundary to the shear zone (Sample **305-U1309D-143R-2, 58–61 cm**) (plane-polarized light, FOV = 2 cm). **G.** Same as F; cross-polarized light, FOV = 2 cm. Yellow box = location of H. **H.** Difference in microstructure between the area affected by the shear zone and the unstrained zone (cross-polarized light; FOV = 11 mm).

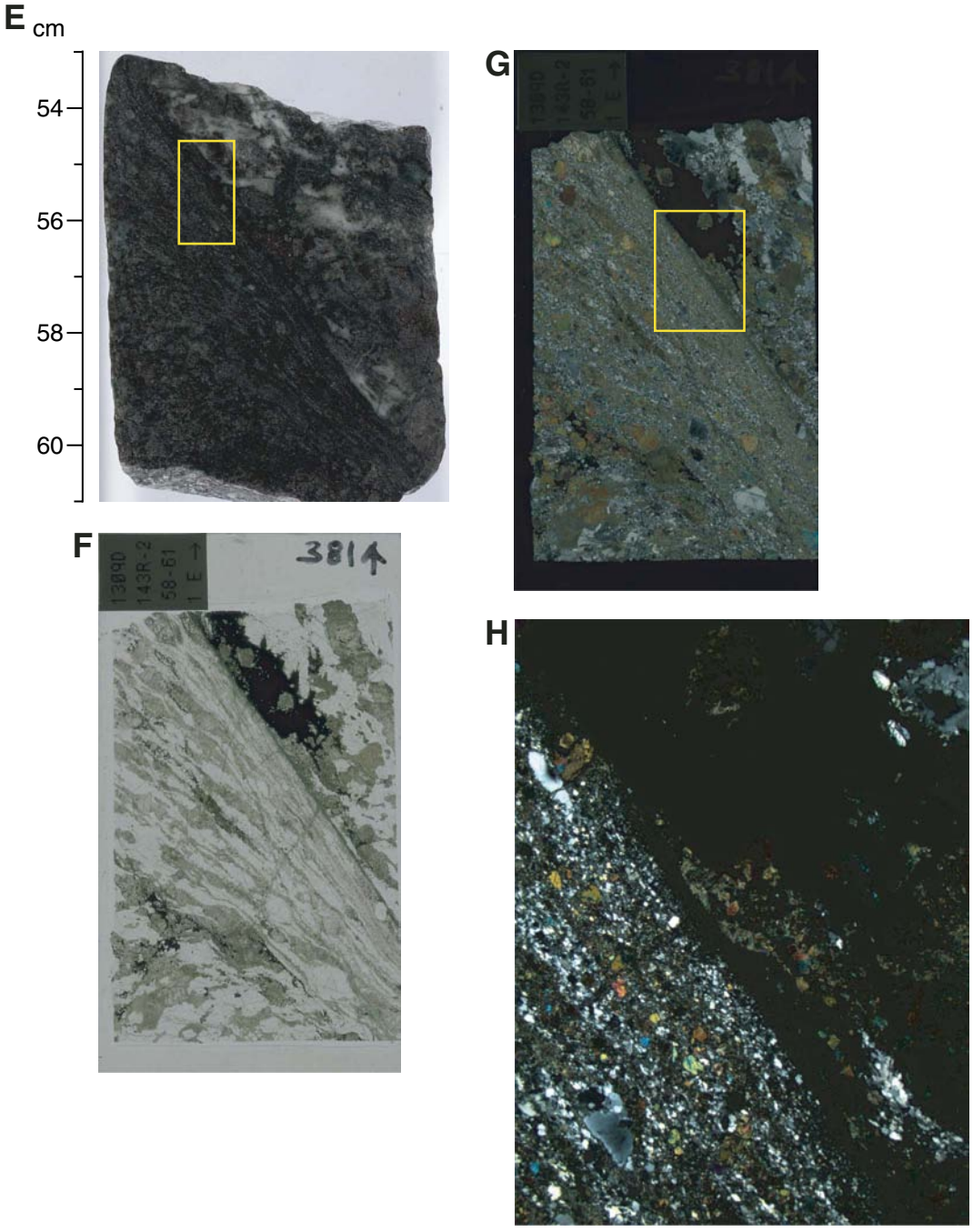

Figure F157. Microstructural characters of magmatic and plastic foliations. **A.** Magmatic foliation with no crystal-plastic overprint (Sample **305-U1309D-189R-3, 103–105 cm**) (cross-polarized light; field of view [FOV] = ~2 cm). See also Figure **F24**. **B.** High-temperature/low-stress crystal-plastic foliation (Sample **305-U1309D-212R-1, 111–113 cm**) (cross-polarized light; FOV = ~2 cm). Note dynamic recrystallization of plagioclase and olivine. Crystal-plastic strain probably overprints a preexisting magmatic foliation. See also Figure **F25.** **C.** Mylonitic foliation (low temperature/high stress) with relict plagioclase and clinopyroxene porphyroclasts (Sample **305-U1309D-137R-2, 96–98 cm**) (cross-polarized light; FOV = ~2 cm). Note dextral sense of shear. **D.** Olivine-rich troctolite with alignment, probably magmatic, of weakly elongated olivines (Sample **305-U1309D-248R-2, 107–110 cm**) (cross-polarized light; FOV = ~2 cm). Note that poikilitic plagioclase and clinopyroxene grains are not elongated parallel to the foliation.

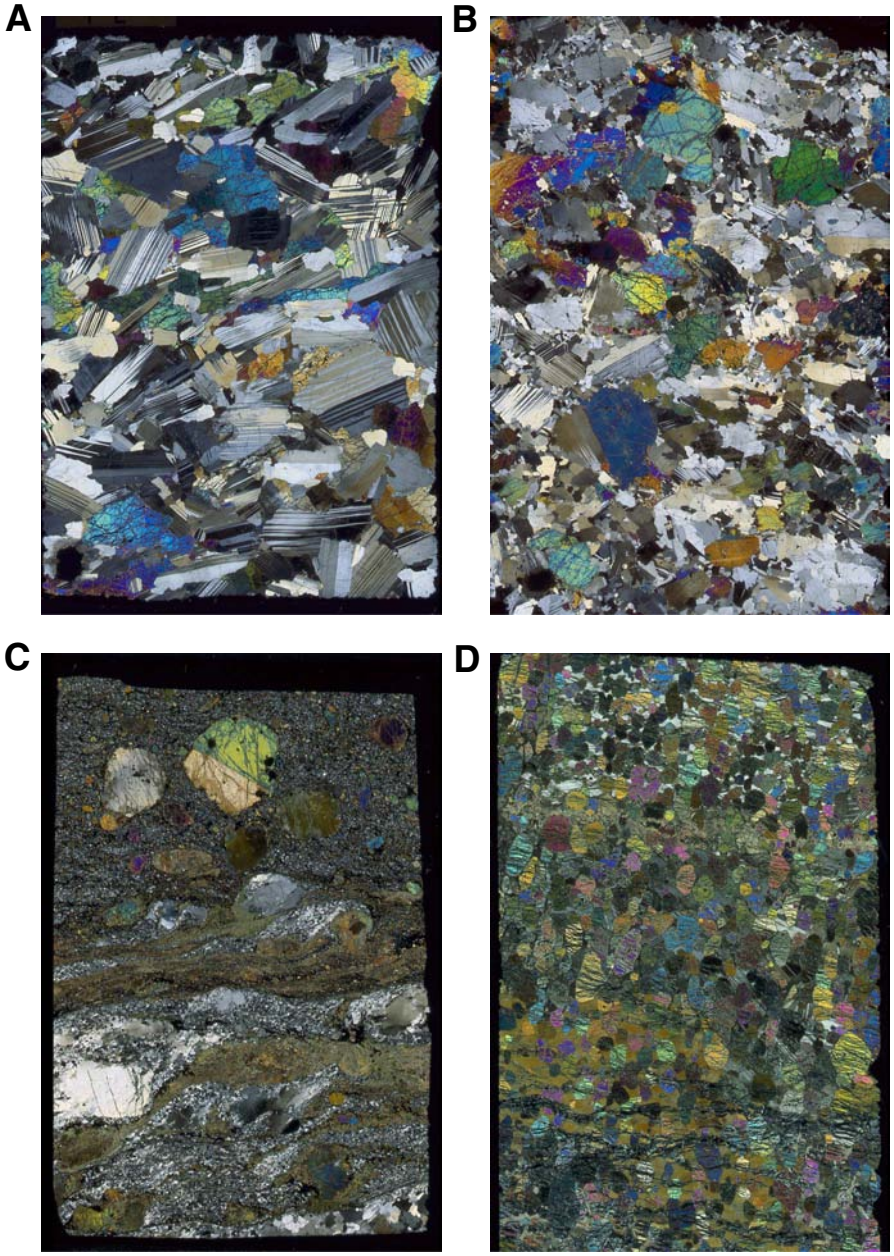

Figure F158. A. Equilibrated plagioclase next to poikilitic clinopyroxene in troctolite (Sample **305-U1309D-112R-2, 67–70 cm**) (cross-polarized light; field of view [FOV] = 1.37 mm). **B.** Well-equilibrated plagioclase crystals are present in an undeformed clinopyroxene oikocryst (Sample **305-U1309D-160R-2, 133–135 cm**) (cross-polarized light; FOV = 5.5 mm). **C.** Plagioclase grains are enclosed by a continuous rim of clinopyroxene (Sample **305-U1309D-251R-1, 74–77 cm**) (cross-polarized light; FOV = 5.5 mm). This association is trapped within an oikocrystic olivine grain. **D.** Plagioclase within poikilitic clinopyroxene grain (Sample **305-U1309D-94R-2, 27–30 cm**) (cross-polarized light; FOV = 5.5 mm). **E.** Two prismatic plagioclase grains enclosed by clinopyroxene oikocryst (Sample **305-U1309D-184R-3, 50–53 cm**) (cross-polarized light; FOV = 5.5 mm). **F.** Dunitic troctolite, showing only subtly misoriented grains of olivine separated by continuous plagioclase grain (Sample **305-U1309D-248R-2, 7–9 cm**) (FOV = 5.5 mm). (Continued on next page.)

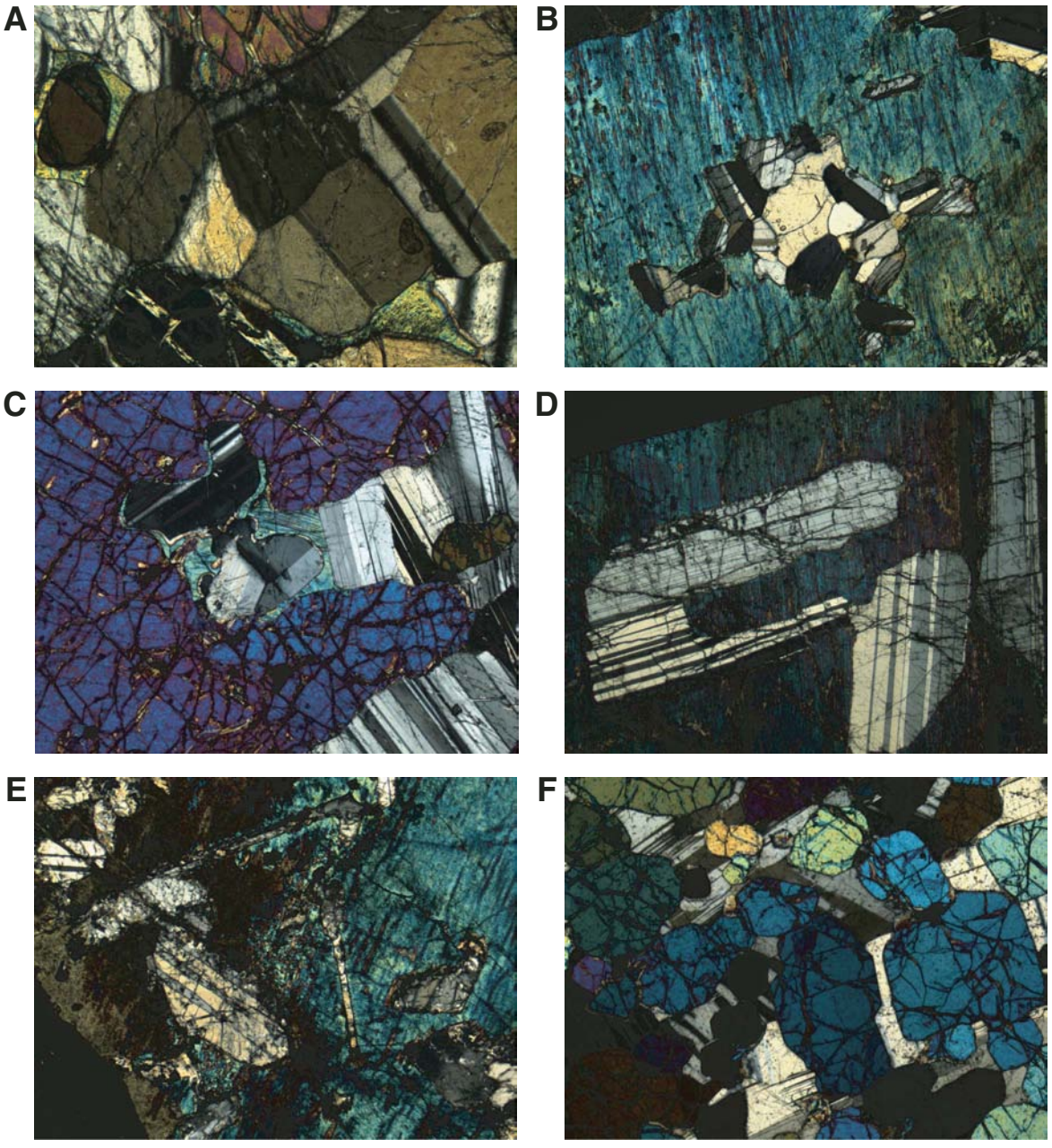

Figure F158 (continued). G. Olivine separated from plagioclase by clinopyroxene with highly concave shape toward olivine, perhaps indicating corrosion of olivine, as a possible process for generating smaller, optically continuous olivine grains (Sample **305-U1309D-250R-4, 17–20 cm**) (cross-polarized light; FOV = 5.5 mm). **H.** Elongate orthopyroxene grains enclosed in a matrix of neoblastic plagioclase (Sample **305-U1309D-269R-1, 3–5 cm**) (cross-polarized light; FOV = 5.5 mm). Note the absence of any orthopyroxene neoblasts. **I.** Tabular-equigranular-shaped neoblasts of orthopyroxene around an orthopyroxene porphyroclast (Sample **305-U1309D-269R-1, 3–5 cm**) (cross-polarized light; field of view = 1.75 mm). **J.** Delicate film of clinopyroxene between olivine and plagioclase, continuous from a larger clinopyroxene grain, and changing to orthopyroxene on the right of the picture (Sample 305-U1309D-222R-4, 82–84 cm) (cross-polarized light; FOV = 1.75 mm). **K.** Contact of an oxide-rich gabbro with an anorthositic gabbro (Sample **305-U1309D-270R-3, 93–95 cm**) (cross-polarized light; FOV = 5.5 mm). The local contact zone is marked by an enrichment in oxide. Note a layer of neoblasts adjacent to the plagioclase porphyroclast in the contact zone to the oxide gabbro and very small neoblasts of plagioclase in the oxide gabbro. **L.** Fe-Ti oxide penetrating along what were possibly former neoblast boundaries of clinopyroxene (in microcracks), partially resorbed and followed by recovery of the entire clinopyroxene grain (Sample **305-U1309D-110R-3, 46–49 cm**) (cross-polarized light; FOV = 5.5 mm).

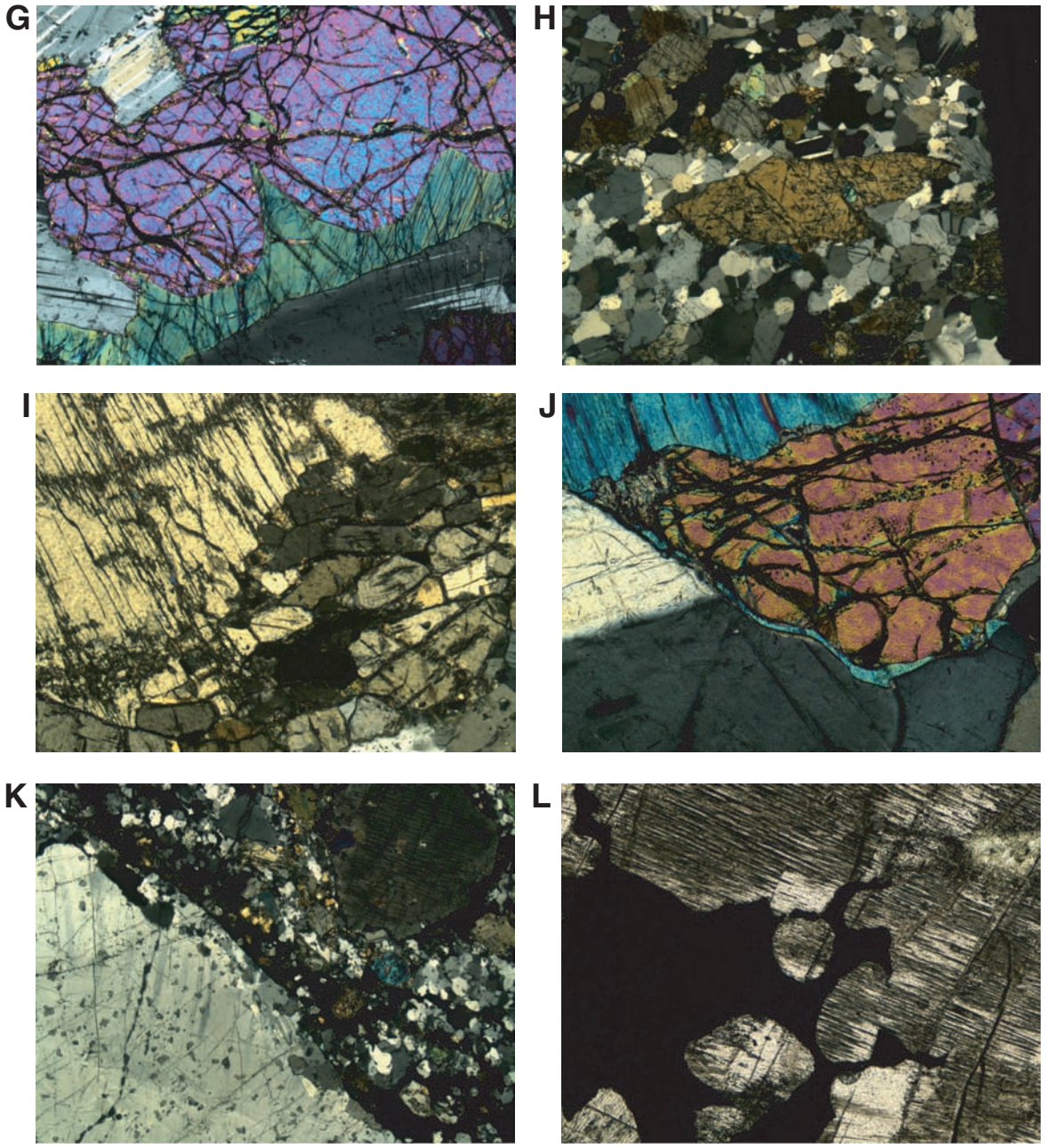

Figure F159. Downhole plots showing the intensities of crystal-plastic and magmatic deformation in (**A**) Hole U1309B and (**B**) Hole U1309D to 132 mbsf. Dotted lines indicate where faults are inferred based on cataclastic fabrics. Arrows = sense of shear where the kinematics of deformation could be determined, tan bands = intervals dominated by diabase, numbers = igneous units.

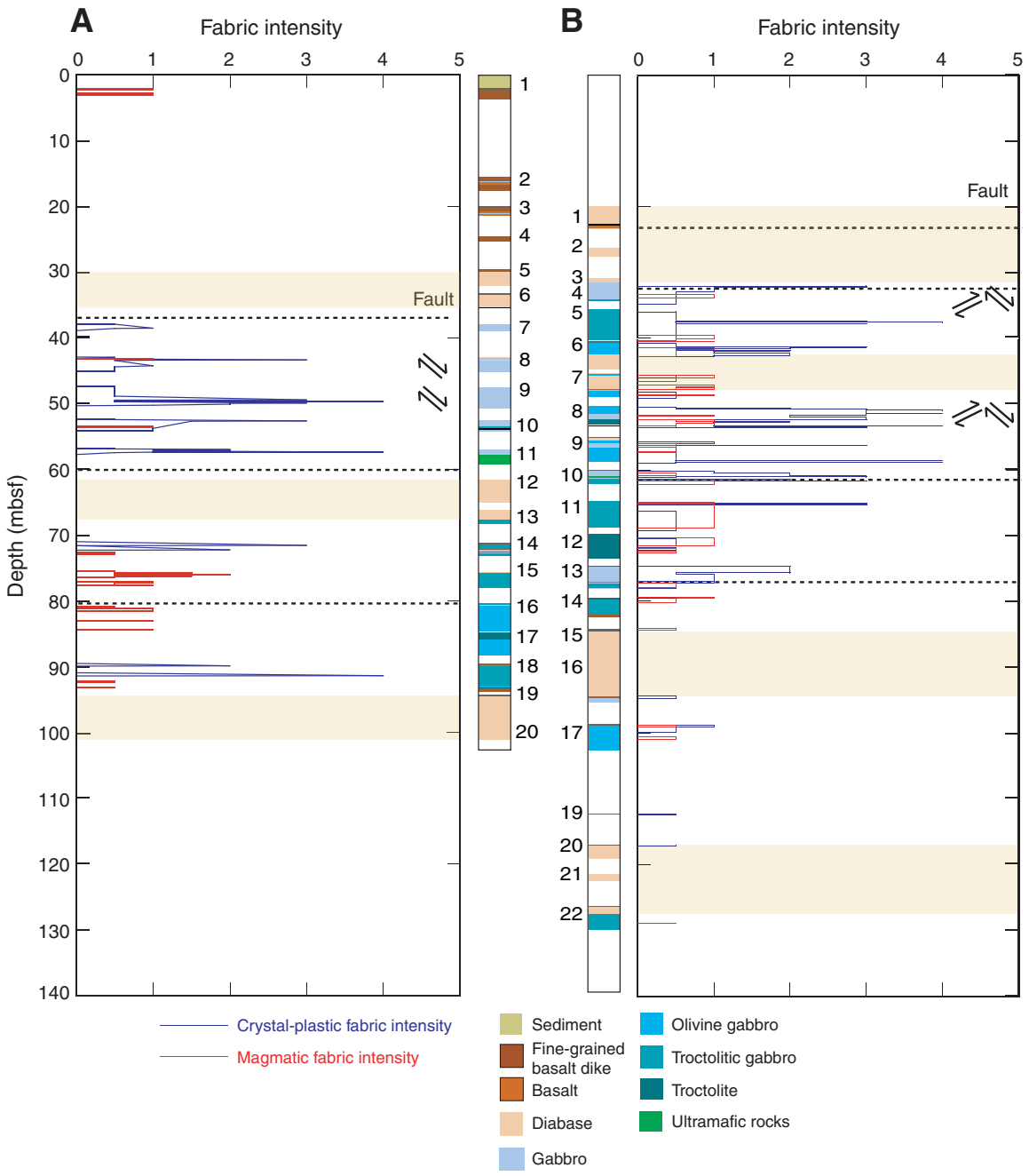

Figure F160. Downhole plot showing the dip of magmatic fabrics in (**A**) Hole U1309B and (**B**) U1309D to 132 mbsf. Dotted lines = location of inferred faults based on cataclastic fabrics, tan bands = intervals dominated by diabase, numbers = igneous units.

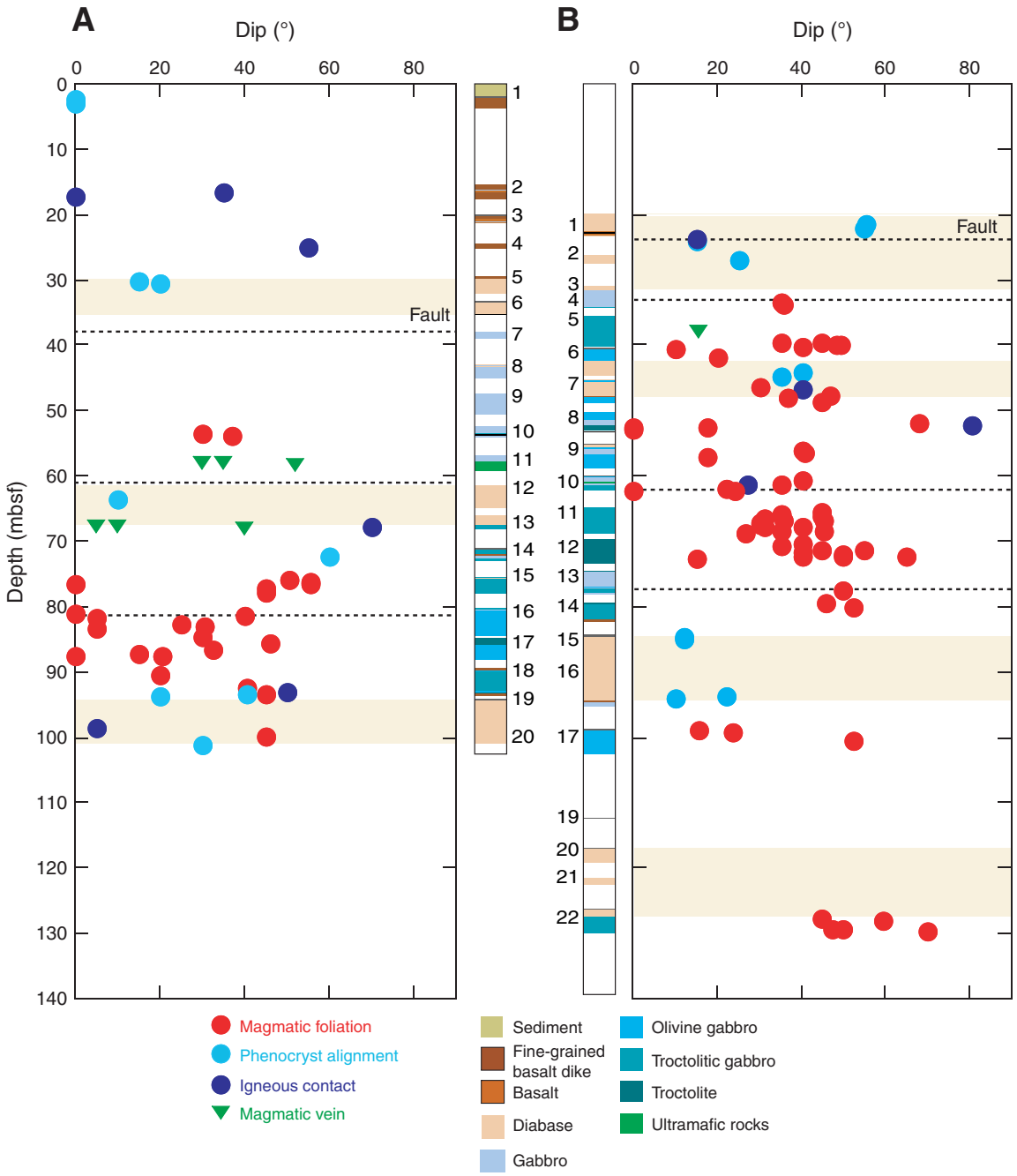

Figure F161. Downhole plot showing the dip of crystal-plastic deformation fabrics in (**A**) Hole U1309B and (**B**) U1309D to 132 mbsf. Dotted lines = location of inferred faults based on cataclastic fabrics, tan bands = intervals dominated by diabase, numbers = igneous units.

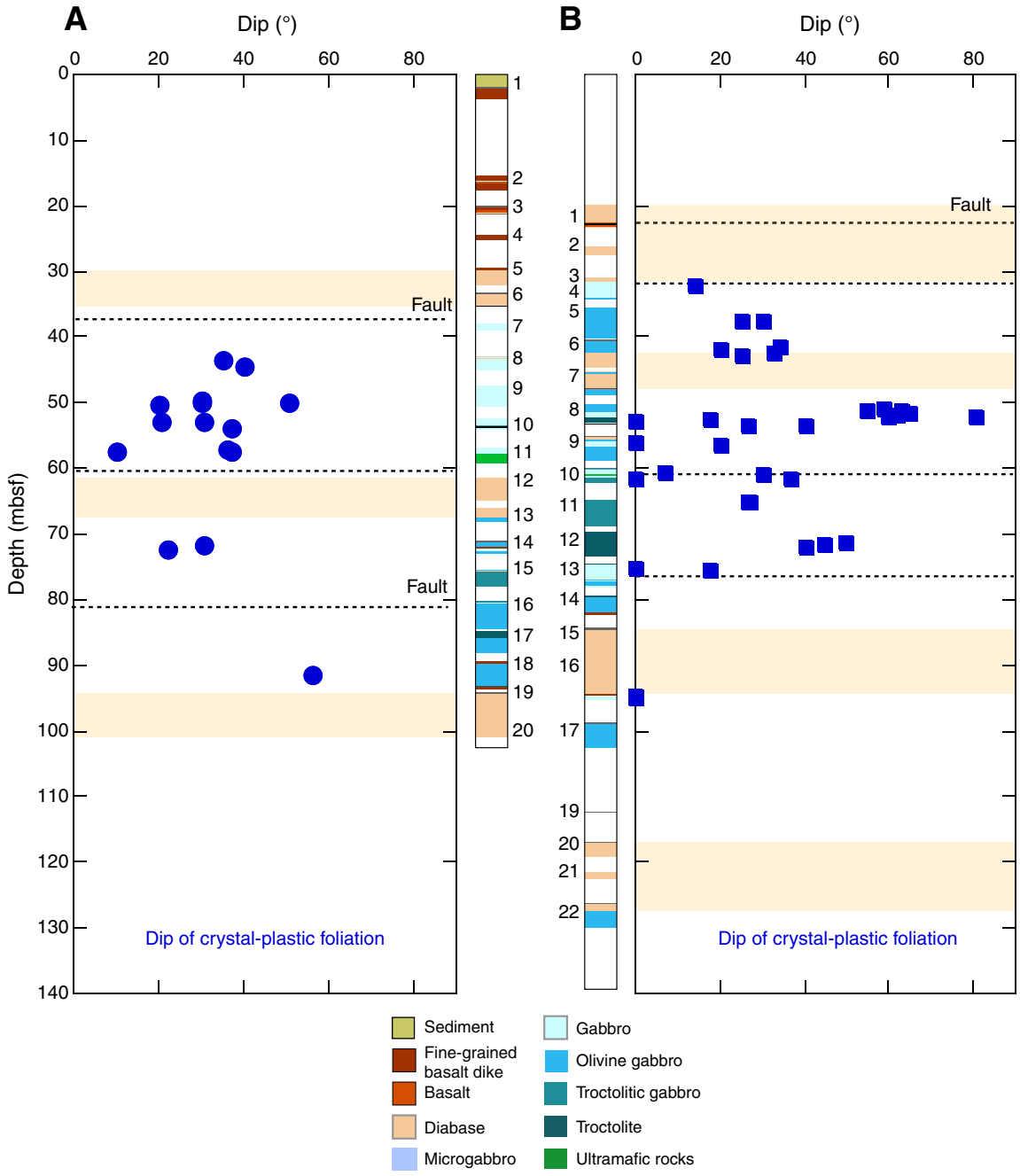

Figure F162. Downhole plots showing the variation of (**A**) macroscopic magmatic foliation; (**B**) microscopic magmatic foliation; (**C**) microscopic crystal-plastic deformation, high temperature (T)/low stress; (**D**) macroscopic crystal-plastic deformation; and (**E**) microscopic crystal-plastic deformation intensity estimated both from core and thin section observations (Hole U1309D). SD = standard deviation.

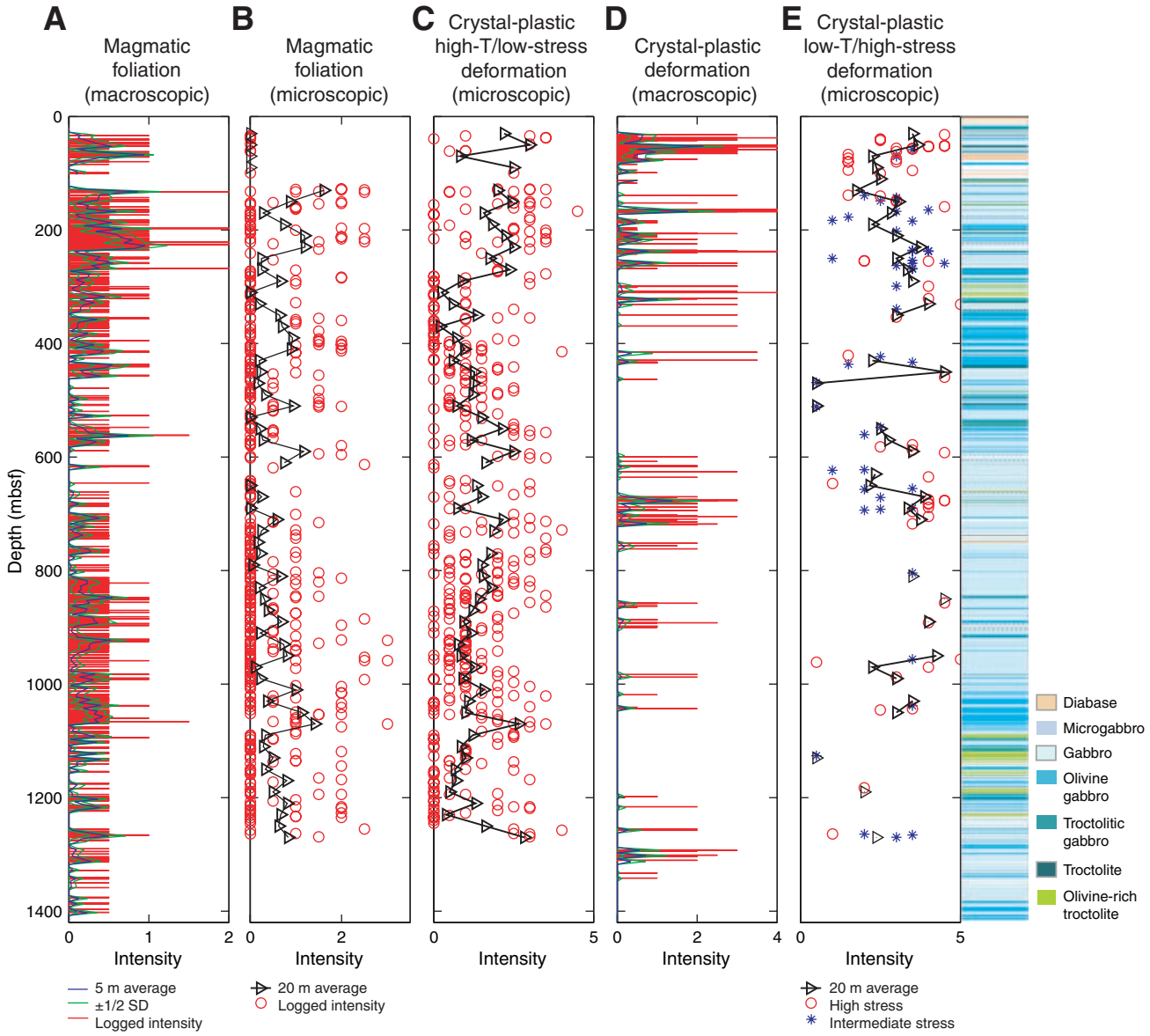

Figure F163. Downhole plots of structural measurements in Hole U1309D. **A.** Average intensities for magmatic and crystal-plastic foliation from core observations. **B.** Dip of magmatic and plastic foliations. **C.** Dip of compositional layers and grain size layers. **D.** Dip of magmatic veins, igneous contacts, alteration fronts, and oxide bands.

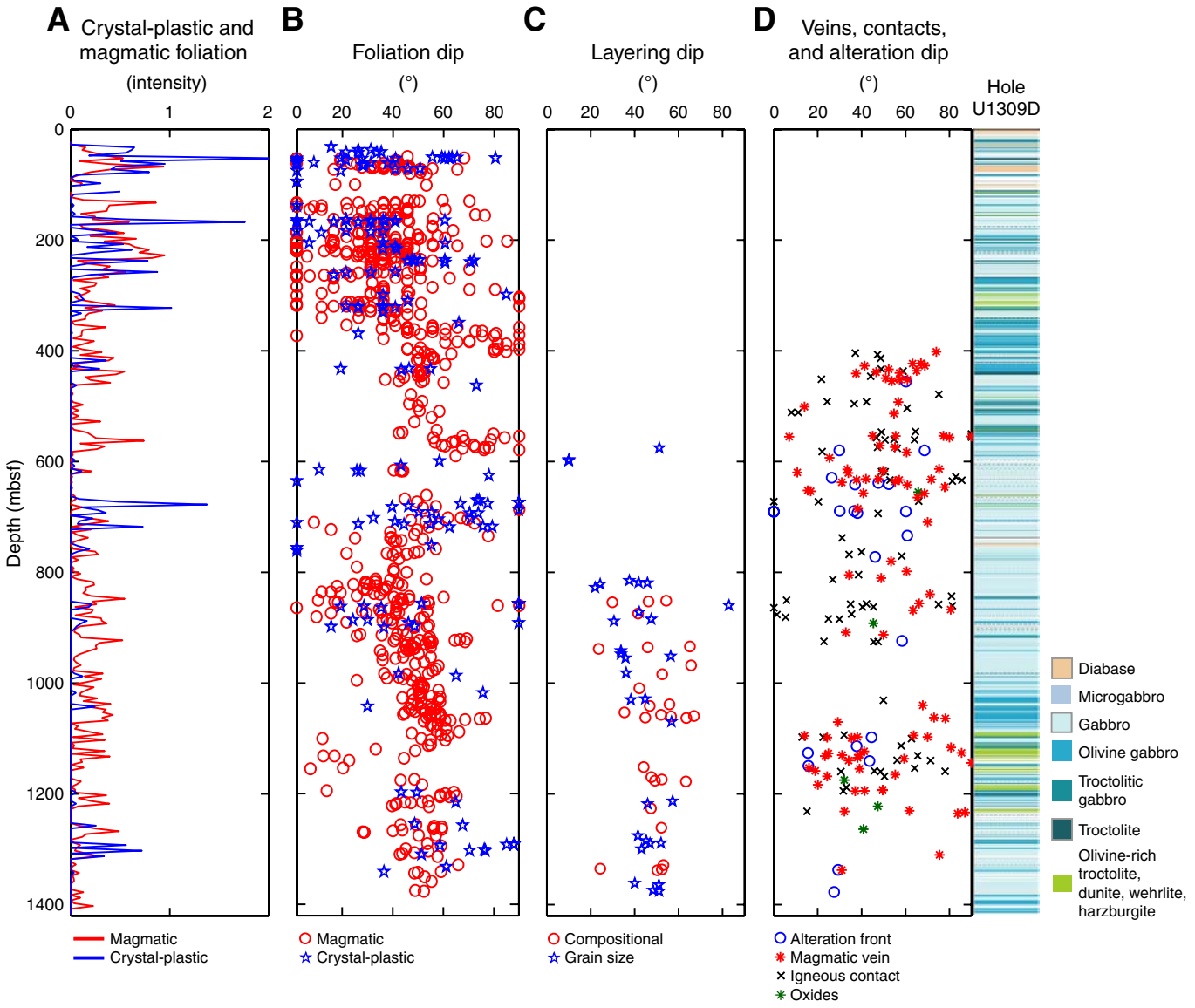

Figure F164. **A.** Intensity of magmatic foliation in each lithologic group per total cored length in Hole U1309D. **B.** Intensity of plastic foliation in each lithologic group per total cored length in Hole U1309D. **C.** Intensity of magmatic foliation in each lithologic group as a percentage of core recovery in Hole U1309D. **D.** Intensity of plastic foliation in each lithologic group as a percentage of core recovery in Hole U1309D.

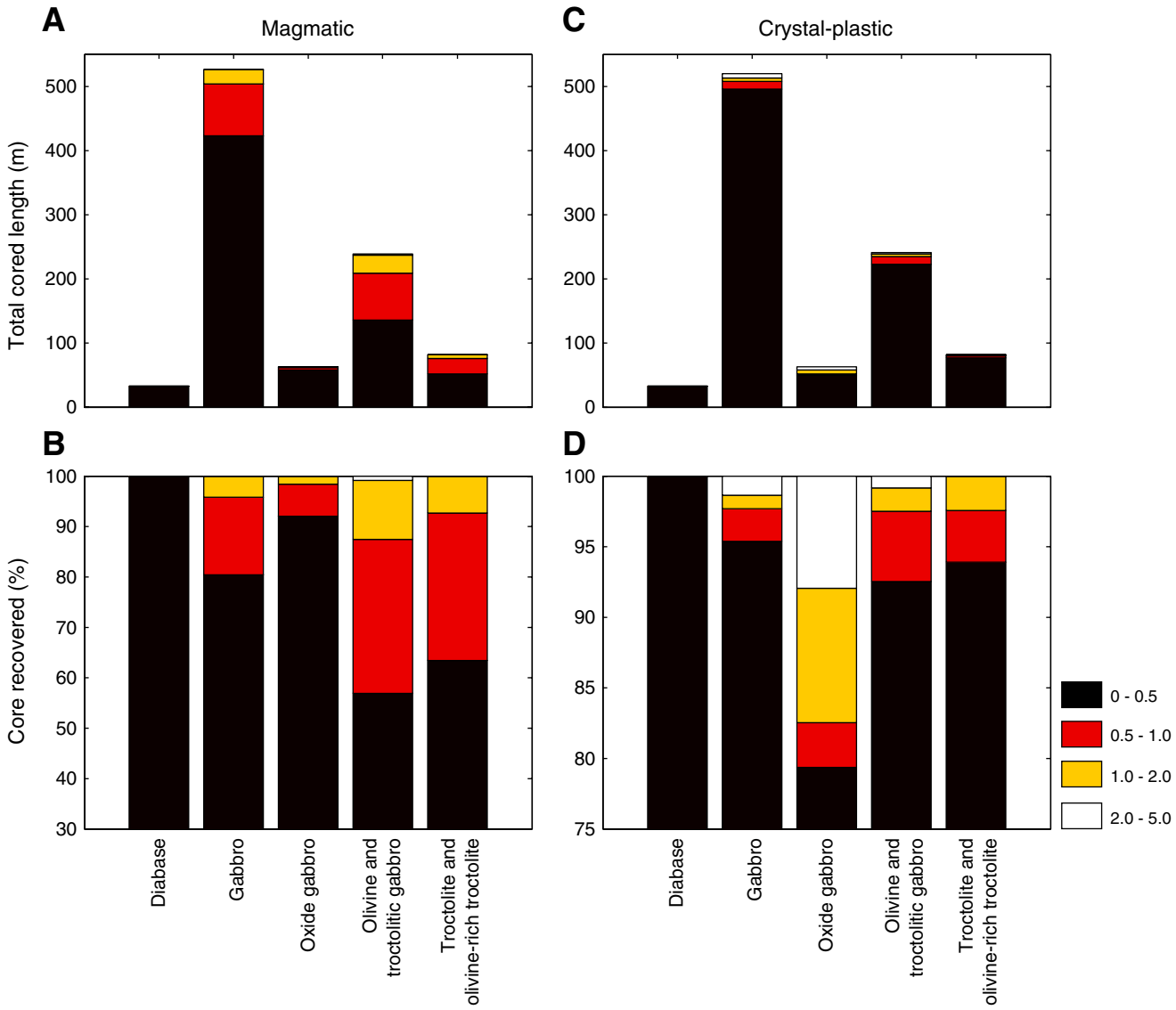

Figure F165. Microscopic strain intensity sorted by rock type and three different fabric regimes (i.e., magmatic, high-temperature [T]/low-stress crystal-plastic, and low-temperature crystal-plastic).

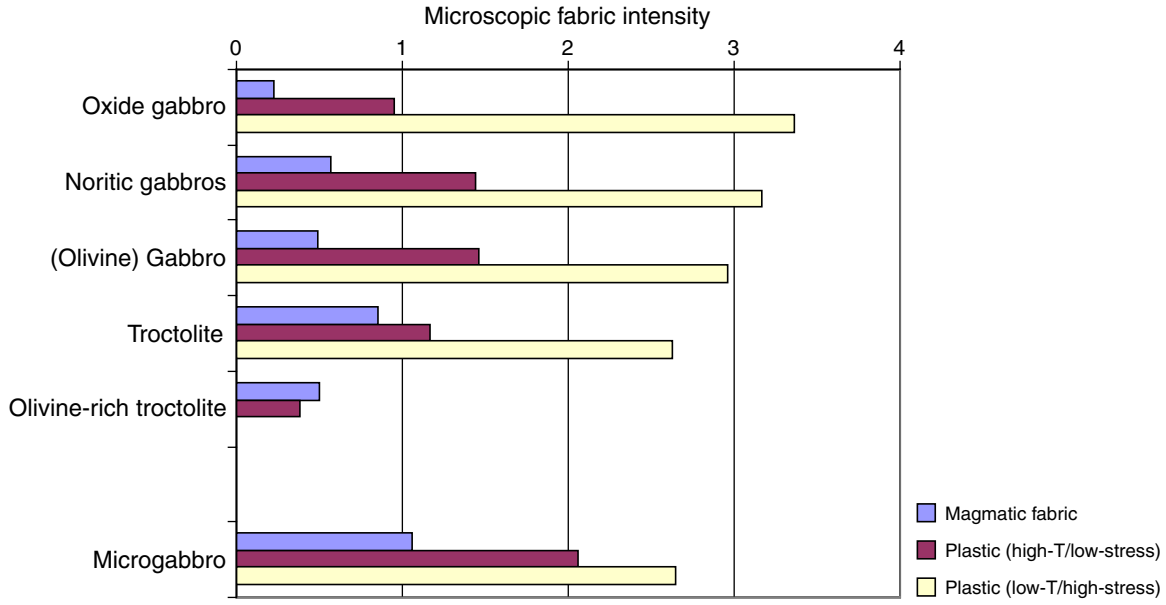

Figure F166. A. Grain-size and compositional layering shown by a coarse-grained pyroxene-rich band within a medium-grained olivine-bearing gabbro (interval 305-U1309D-208R-3, 41–66 cm). Yellow box = location of C and D. **B.** Backside view of A. **C.** Coarse-grained pyroxene band surrounded by medium-grained olivine-bearing gabbro (Sample **305-U1309D-208R-3, 55–58 cm**) (plane-polarized light; field of view [FOV] = 2 cm). **D.** Same as C; cross-polarized light. Yellow box = location of E. **E.** Boundary between coarse-grained pyroxene band and medium-grained olivine-bearing gabbro (cross-polarized light; FOV = 11 mm). (Continued on next page.)

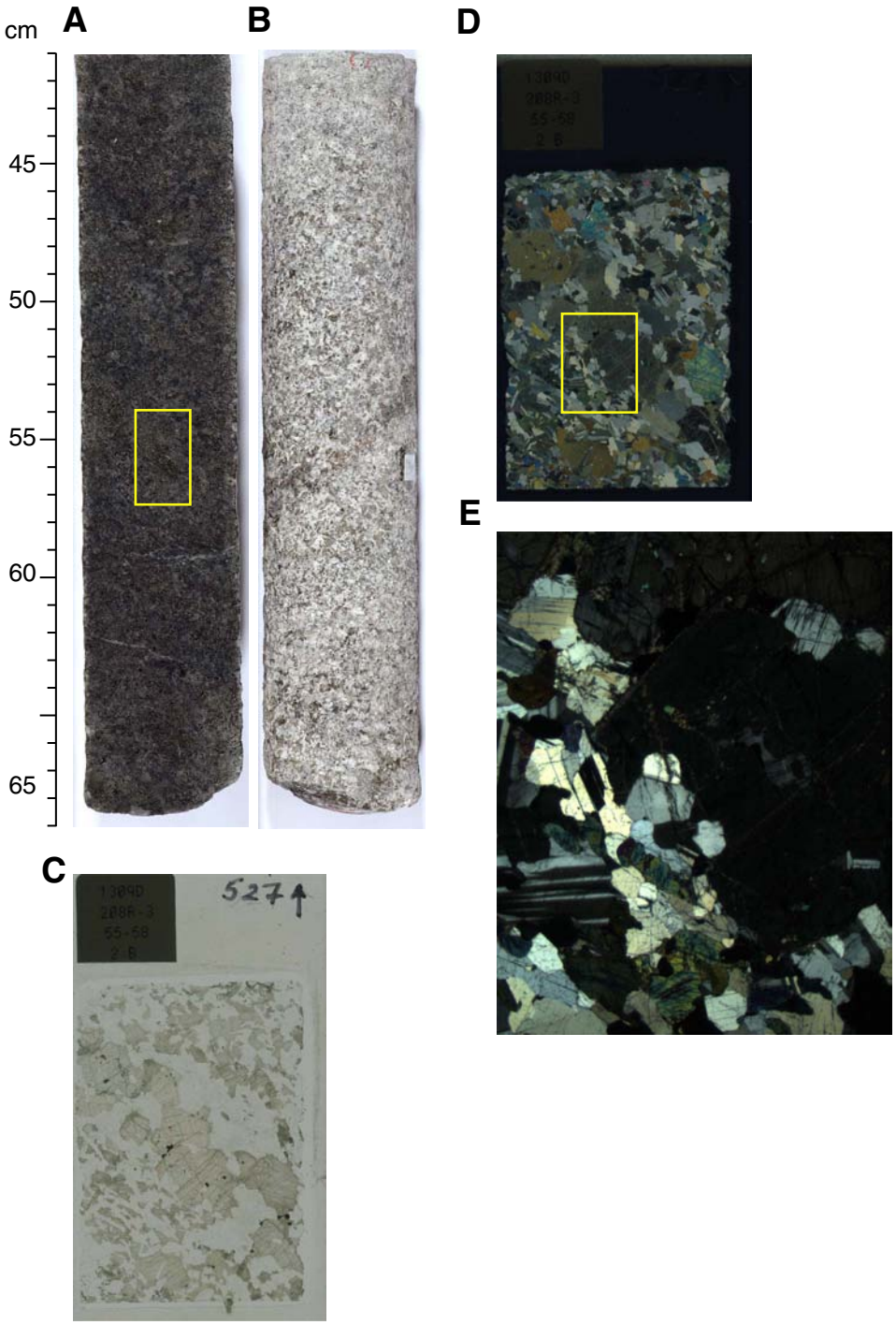

Figure F166 (continued). **F.** Grain-size and compositional layering between a medium-grained olivine bearing gabbro and fine-grained gabbronorite (interval 305-U1309D-220R-3, 113–134 cm). Yellow box = location of H and I. **G.** Backside view of F. **H.** Medium-grained olivine gabbro surrounding a fine-grained gabbronorite (Sample **305-U1309D-220R-3, 123–125 cm**) (plane-polarized light; FOV = 2 cm). **I.** Same as H; cross-polarized light. Yellow box = location of J. **J.** Boundary between medium-grained olivine-bearing gabbro and fine-grained gabbronorite (cross-polarized light; FOV = 11 mm).

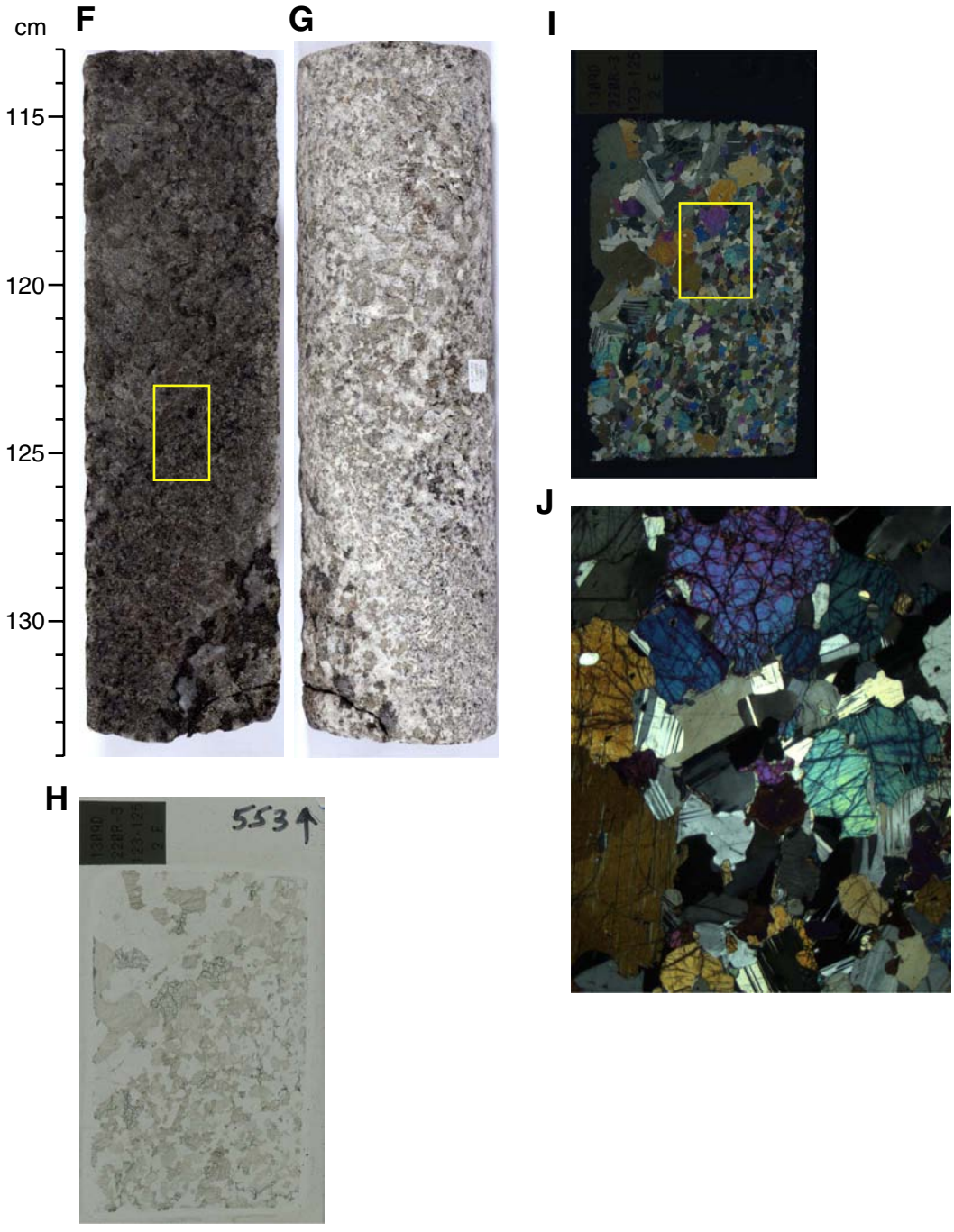

Figure F167. A. Contact between gabbro and microgabbronorite (interval 305-U1309D-103R-1, 5–20 cm). Yellow box = location of B and C. **B.** Contact between gabbro and microgabbronorite (Sample **305-U1309D-103R-1, 11–14 cm**) (plane-polarized light; field of view [FOV] = 2 cm). **C.** Same as B; cross-polarized light. Yellow box = location of D. **D.** Contact between medium grain size gabbro and fine grained microgabbronorite (cross-polarized light; FOV = 11 mm). (Continued on next page.)

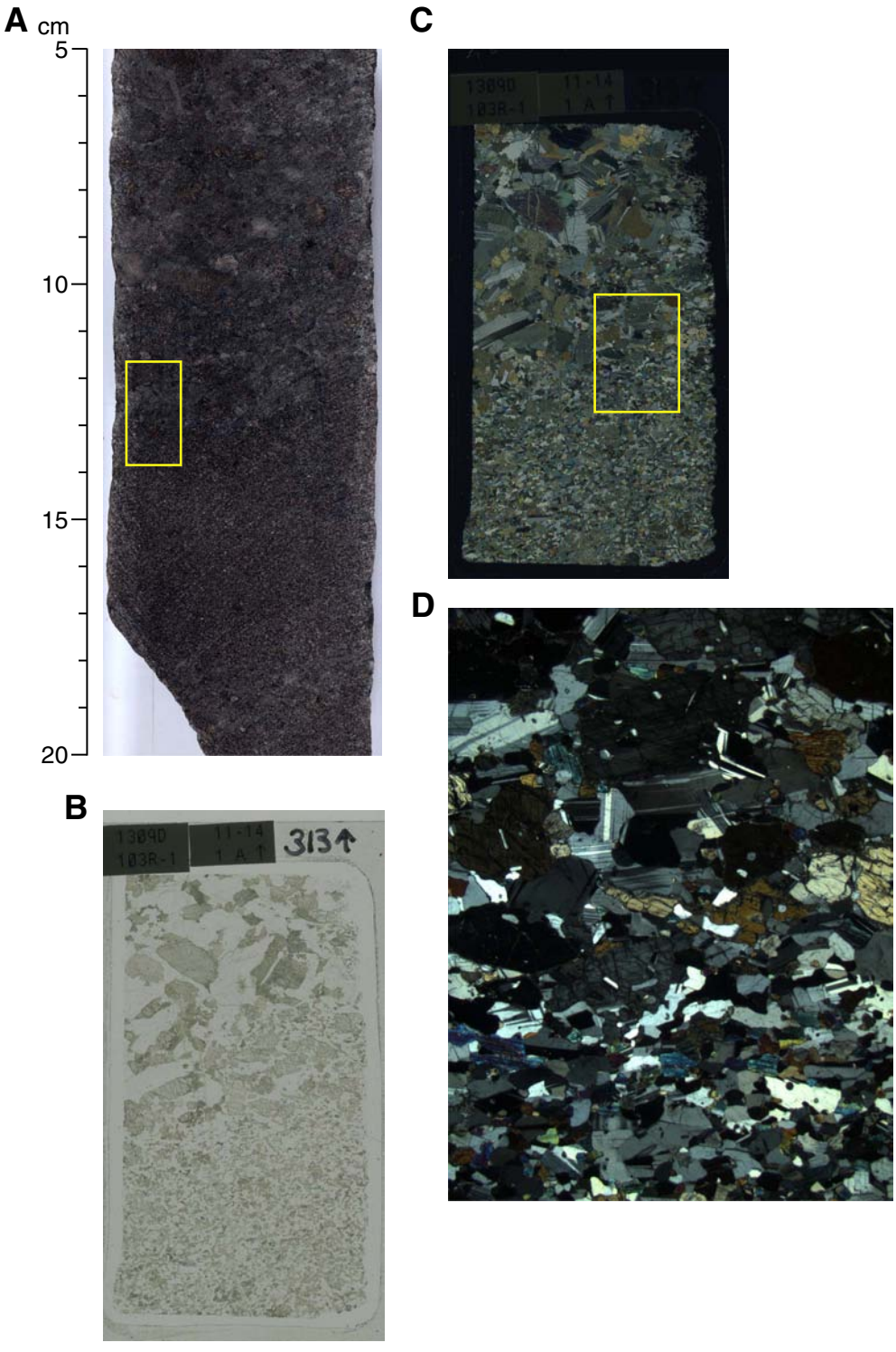

Figure F167 (continued). E. Contact between gabbro and diabase (interval 305-U1309D-125R-2, 100–110 cm). Yellow box = location of F and G. **F.** Undulating boundary between gabbro and diabase (Sample **305-U1309D-125R-2, 104–106 cm**) (plane-polarized light, FOV = 2 cm). **G.** Same as F; cross-polarized light. Yellow box = location of H. **H.** Undulating contact between gabbro and diabase (cross-polarized light; FOV = 11 mm). Microphenocrysts inside diabase show random texture.

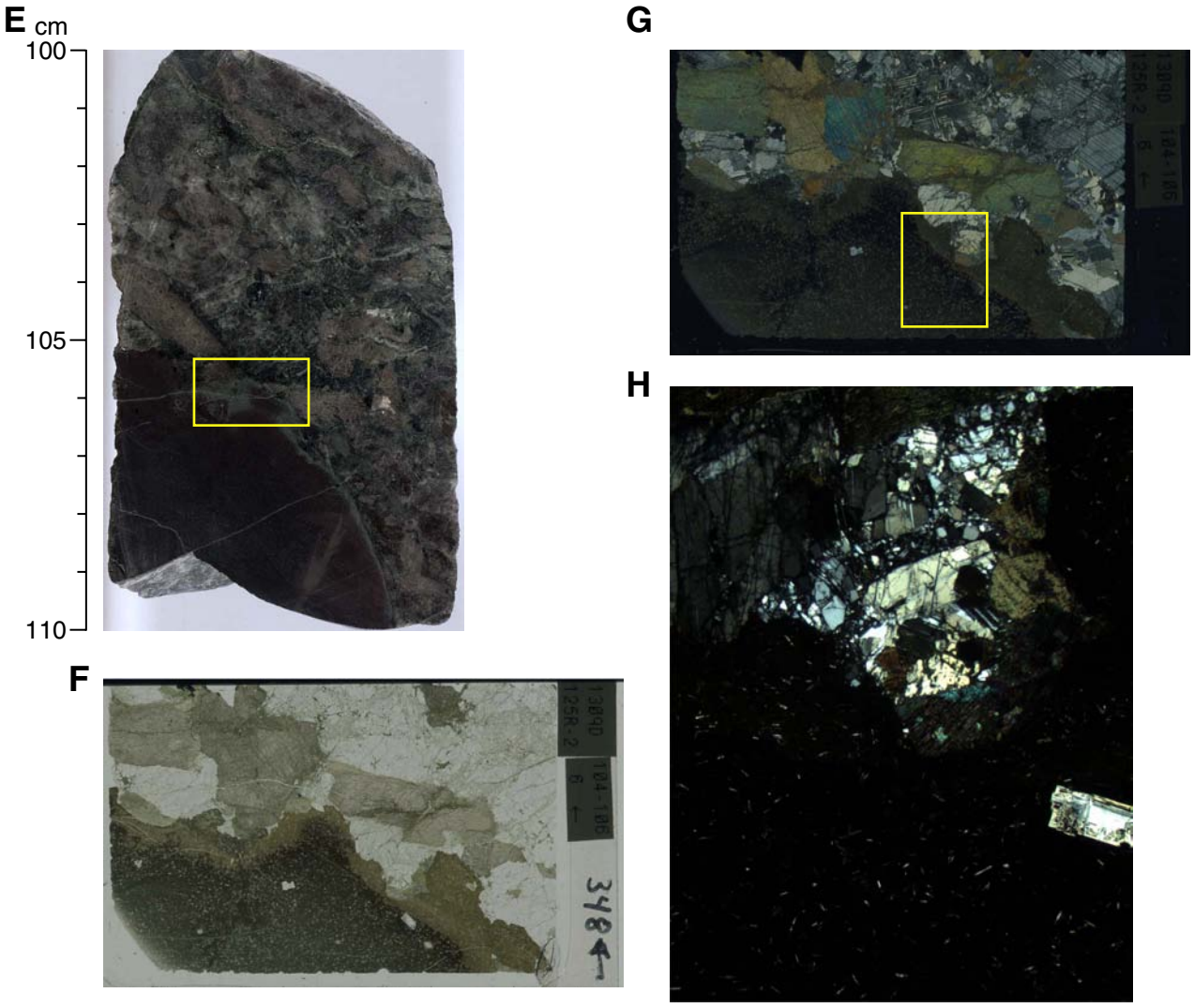

Figure F168. Downhole plot showing the dip of (**A**) magmatic and crystal-plastic fabrics and (**B**) igneous contacts and phenocryst alignment in the upper 400 m of Hole U1309D (Expedition 304). Dotted lines = location of inferred faults based on cataclastic fabrics.

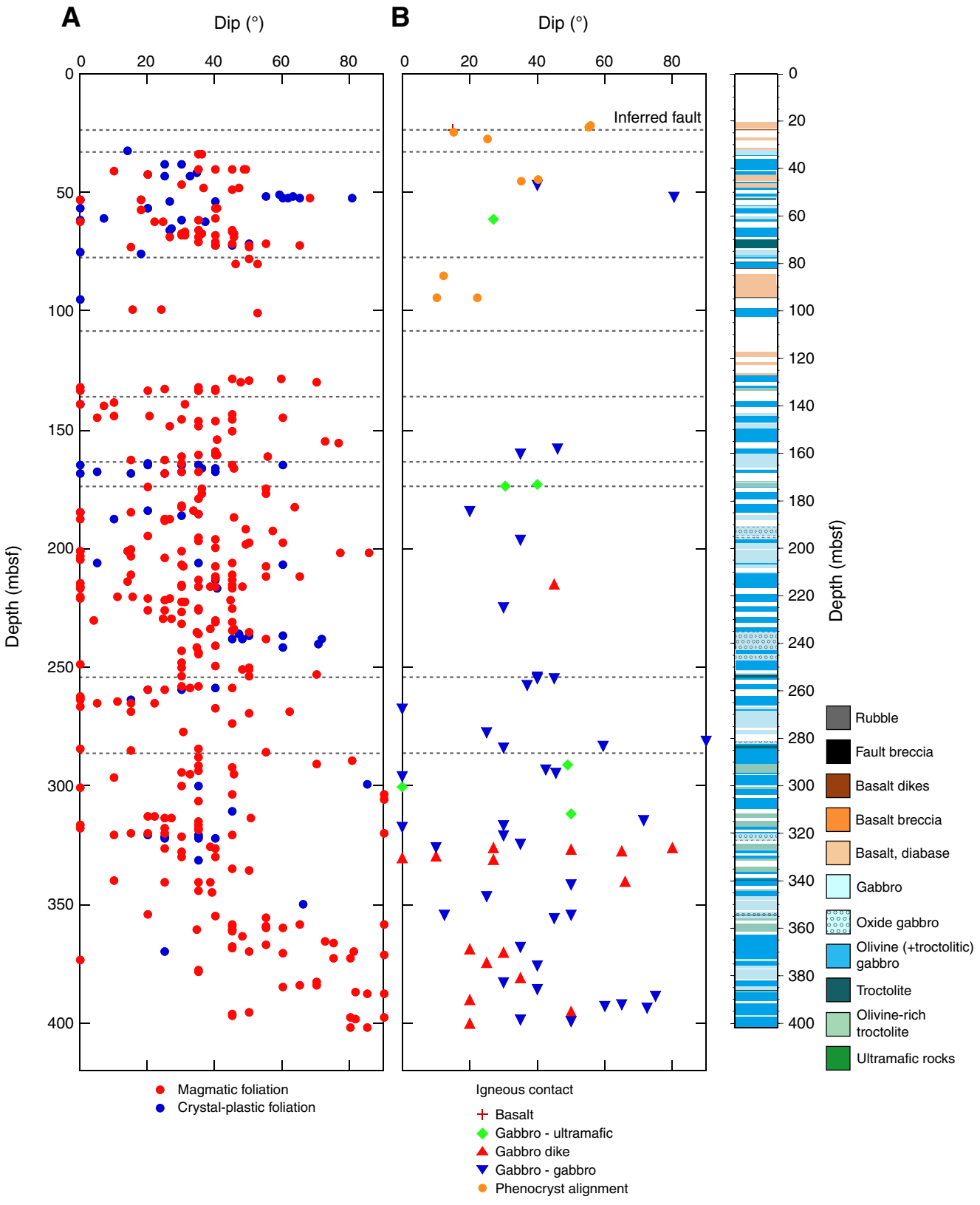

Figure F169. A. Magmatic vein crosscutting olivine gabbro (interval 305-U1309D-85R-2, 100–120 cm). Yellow box = location of B and C. **B.** Boundary between the magmatic vein and the olivine gabbro (Sample **305-U1309D-85R-2, 111–113 cm**) (plane-polarized light; field of view [FOV] = 2 cm. **C.** Same as B; cross-polarized light. Yellow box = location of D. **D.** Boundary of the magmatic vein between plagioclase crystals and green amphibole crystals (cross-polarized light; FOV = 11 mm). (Continued on next page.)

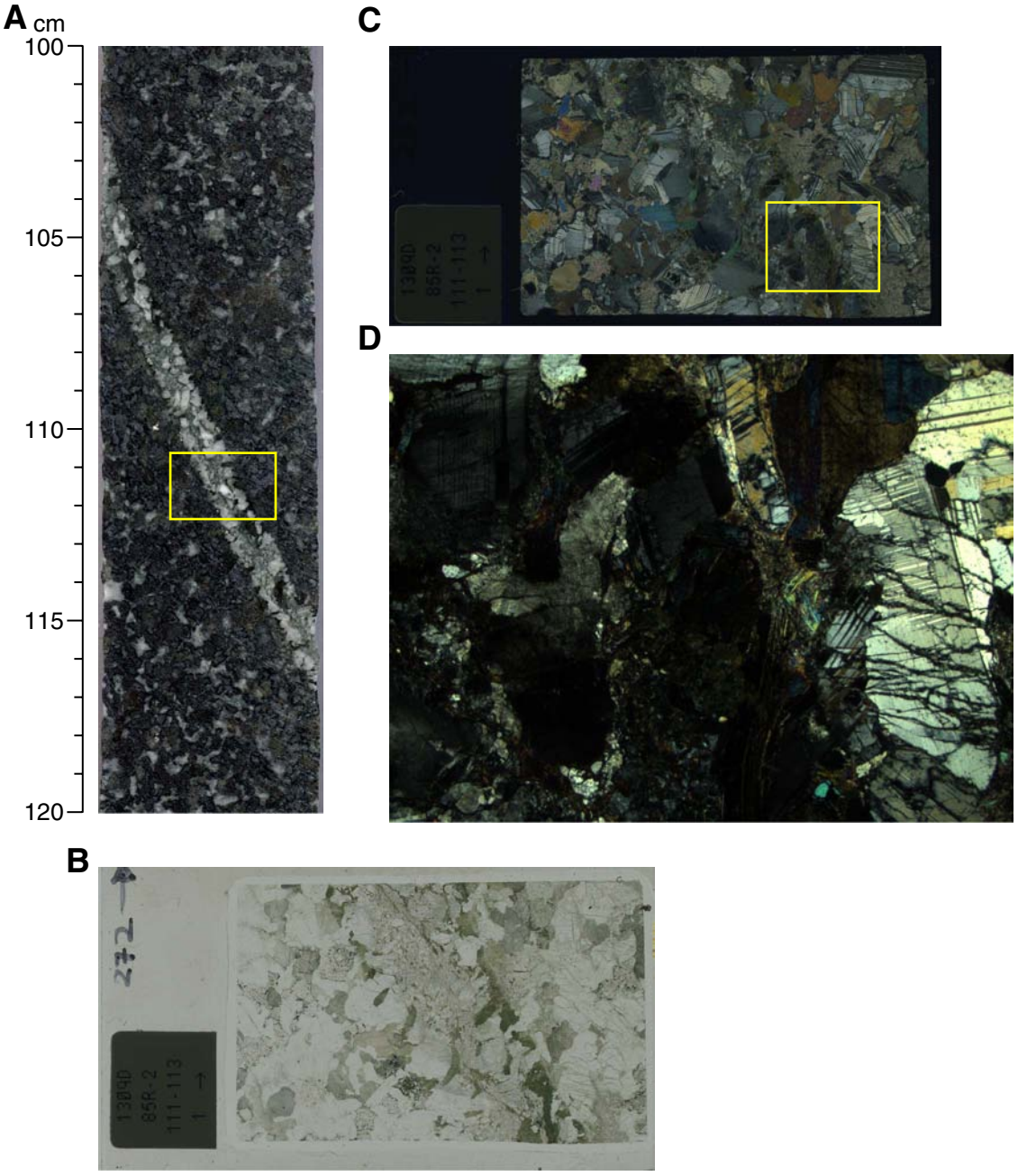

Figure F169 (continued). E. Magmatic vein crosscutting pegmatitic gabbro (interval 305-U1309D-165R-1, 87–107 cm). Yellow box = location of F and G. **F.** Boundaries of the magmatic vein surrounded by the pegmatitic gabbro (Sample **305-U1309D-165R-1, 90–93 cm**) (plane-polarized light; FOV = 2 cm. **G.** Same as F; cross-polarized light. Yellow box = location of H. **H.** Interaction of the magmatic vein boundary with the pegmatitic gabbro (cross-polarized light; FOV = 11 mm). Center of the vein is made up of amphibole crystals.

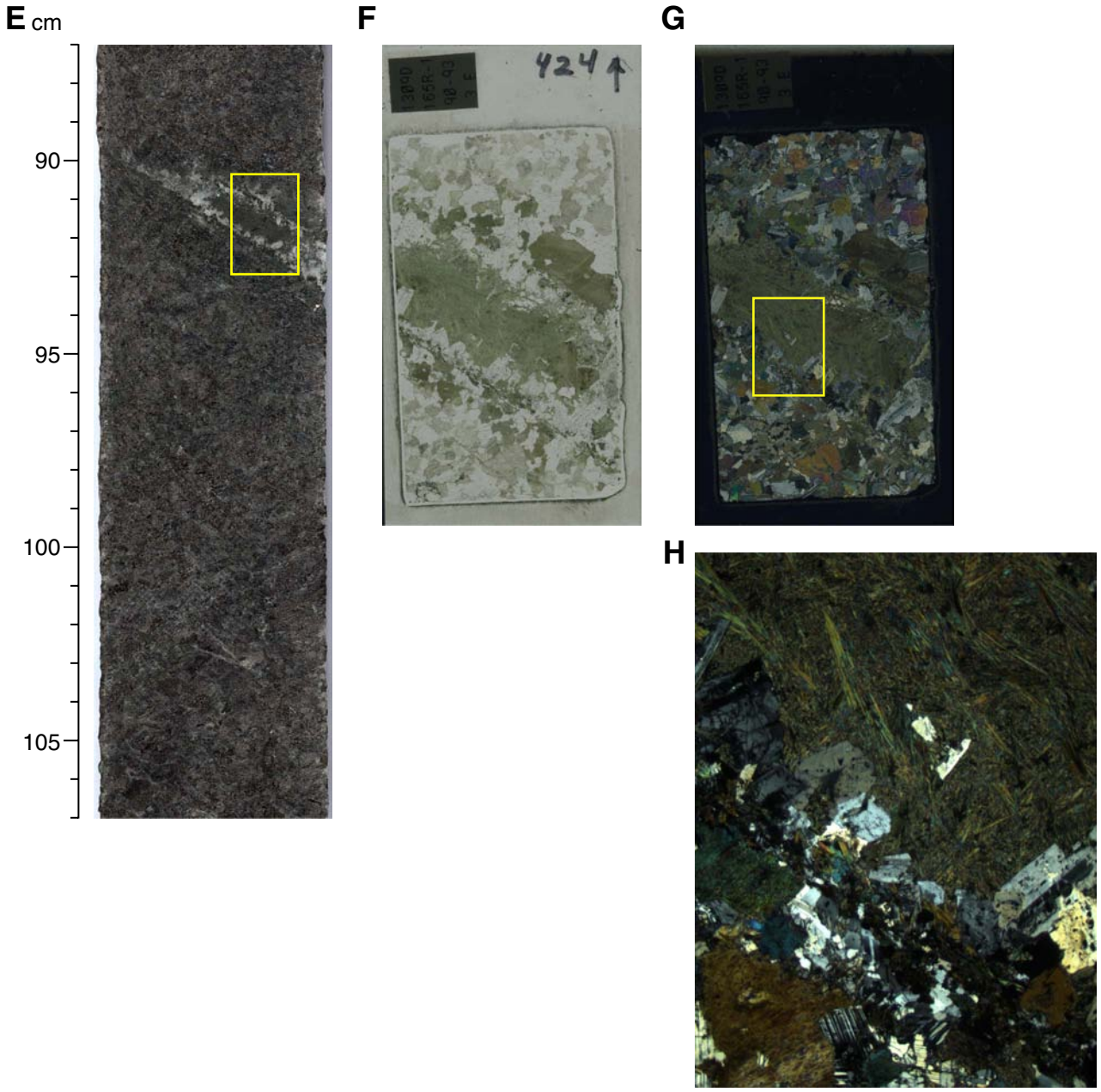

Figure F170. A. Deformed oxide band cutting through a medium-grained gabbro (interval 305-U1309D-183R-2, 21–45 cm). Yellow box = location of B and C. **B.** Sheared oxide band in contact with the medium-grained gabbro (Sample **305-U1309D-183R-2, 32–34 cm**) (plane-polarized light; field of view [FOV] = 2 cm). **C.** Same as B; cross-polarized light. Yellow box = location of D. **D.** Highly sheared oxide band (cross-polarized light; FOV = 11 mm). Porphyroblasts of clinopyroxene (Cpx) + plagioclase (Plg) are seen. (Continued on next page.)

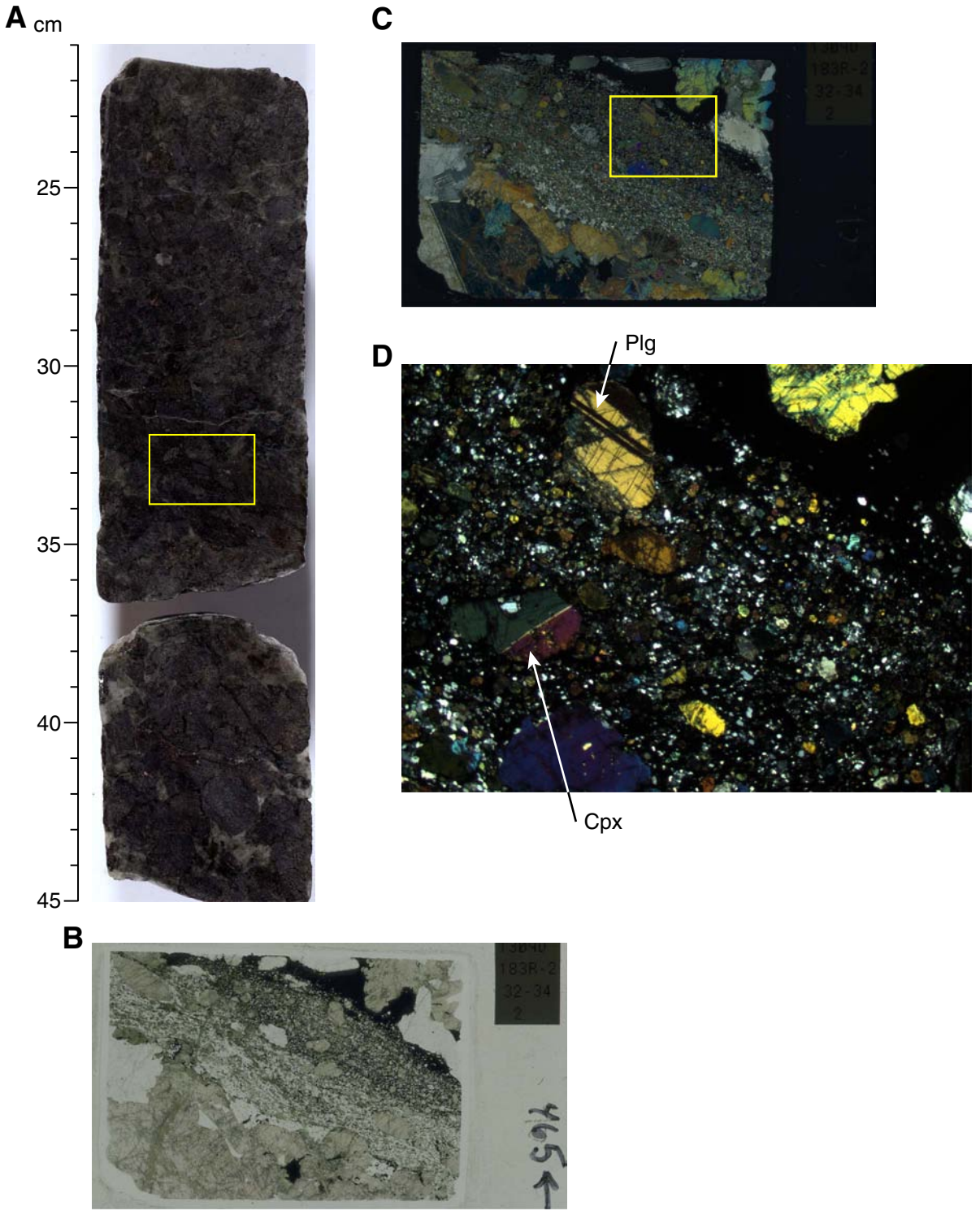

Figure F170 (continued). E. Undeformed oxide-rich band cutting through a medium-grained olivine bearing gabbro (interval 305-U1309D-244R-2, 91–118 cm). Yellow box = location of F and G. **F.** Oxide band in contact with the medium-grained gabbro (Sample **305-U1309D-244R-2, 105–108 cm**) (plane-polarized light, FOV = 2 cm). **G.** Same as F; cross-polarized light. Yellow box = location of H. **H.** Undeformed boundary between the oxide-rich band and the medium-grained olivine-bearing gabbro (cross-polarized light; FOV = 11 mm).

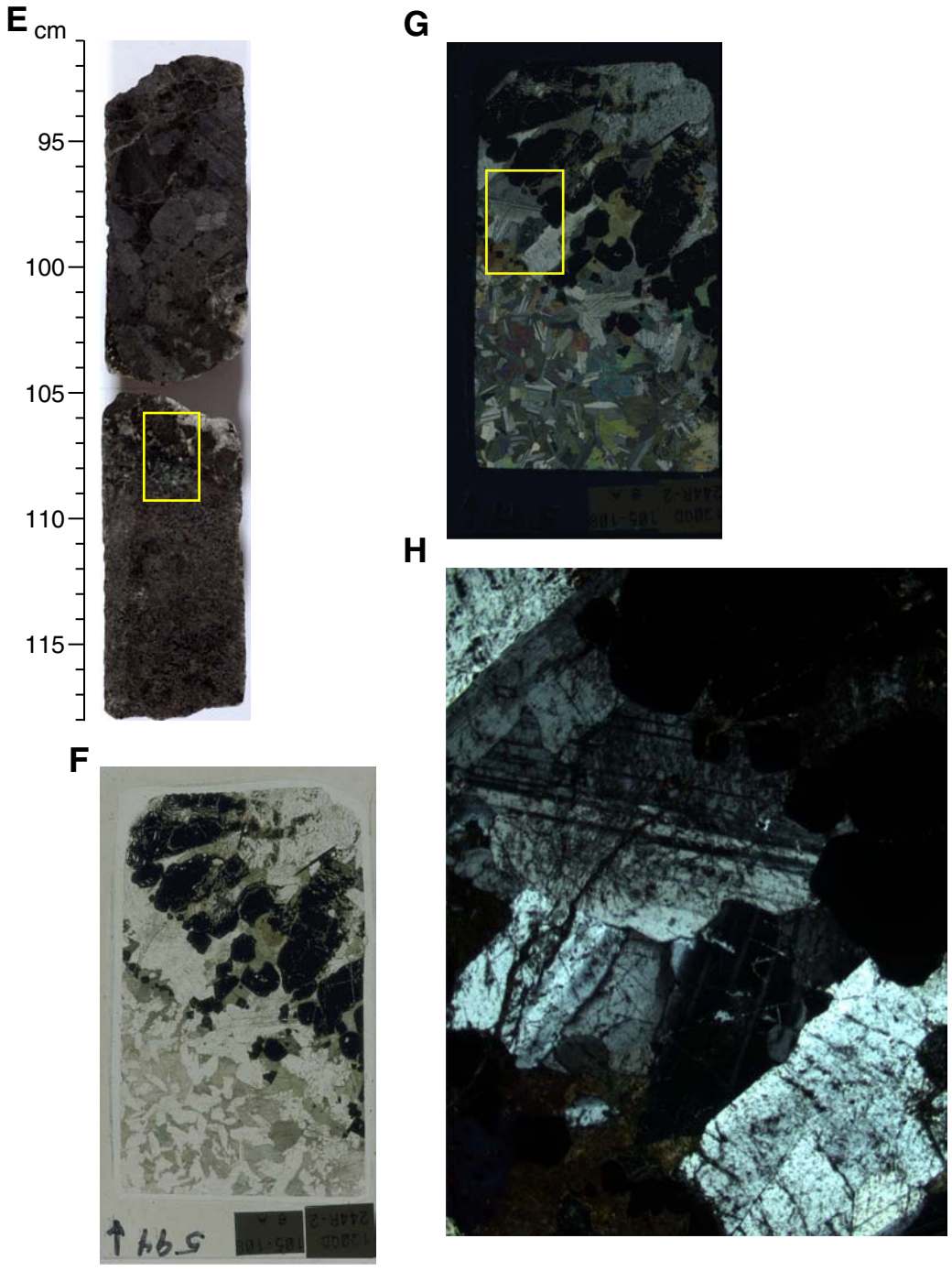

Figure F171. A. Alteration front between a leucocratic zone and gabbro (interval 305-U1309D-99R-3, 10–25 cm). Yellow box = location of B and C. **B.** Gradient of the amount of alteration from the leucocratic zone into the gabbro (Sample **305-U1309D-99R-3, 13–16 cm**) (plane-polarized light, field of view [FOV] = 2 cm). **C.** Same as B; cross-polarized light. Yellow box = location of D. **D.** Varying degrees of alteration from the leucocratic zone to the plagioclase-rich gabbro (cross-polarized light; FOV = 11 mm). (Continued on next page.)

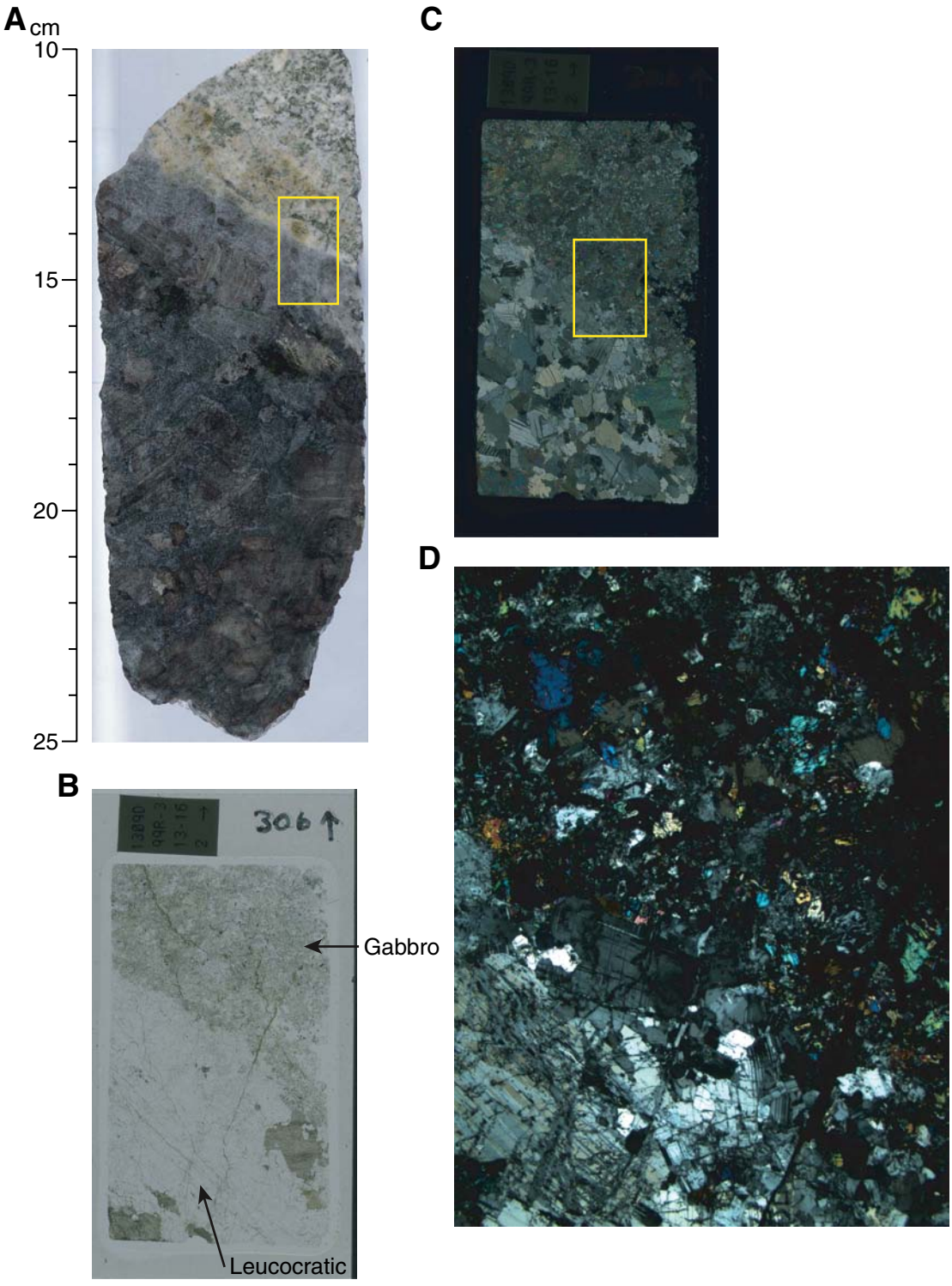

Figure F171 (continued). E. Alteration front between leucocratic zone and olivine gabbro (interval 305-U1309D-149R-2, 42–54 cm). Yellow box = location of F and G. **F.** Gradient of the amount of alteration from the leucocratic zone to the olivine gabbro (Sample **305-U1309D-149R-2, 44–47 cm**) (plane-polarized light, FOV = 2 cm). **G.** Same as F; cross-polarized light. Yellow box = location of H. **H.** Variations in the amount of alteration coronas from the leucocratic zone to the olivine gabbro left to right (cross-polarized light; FOV = 11 mm).

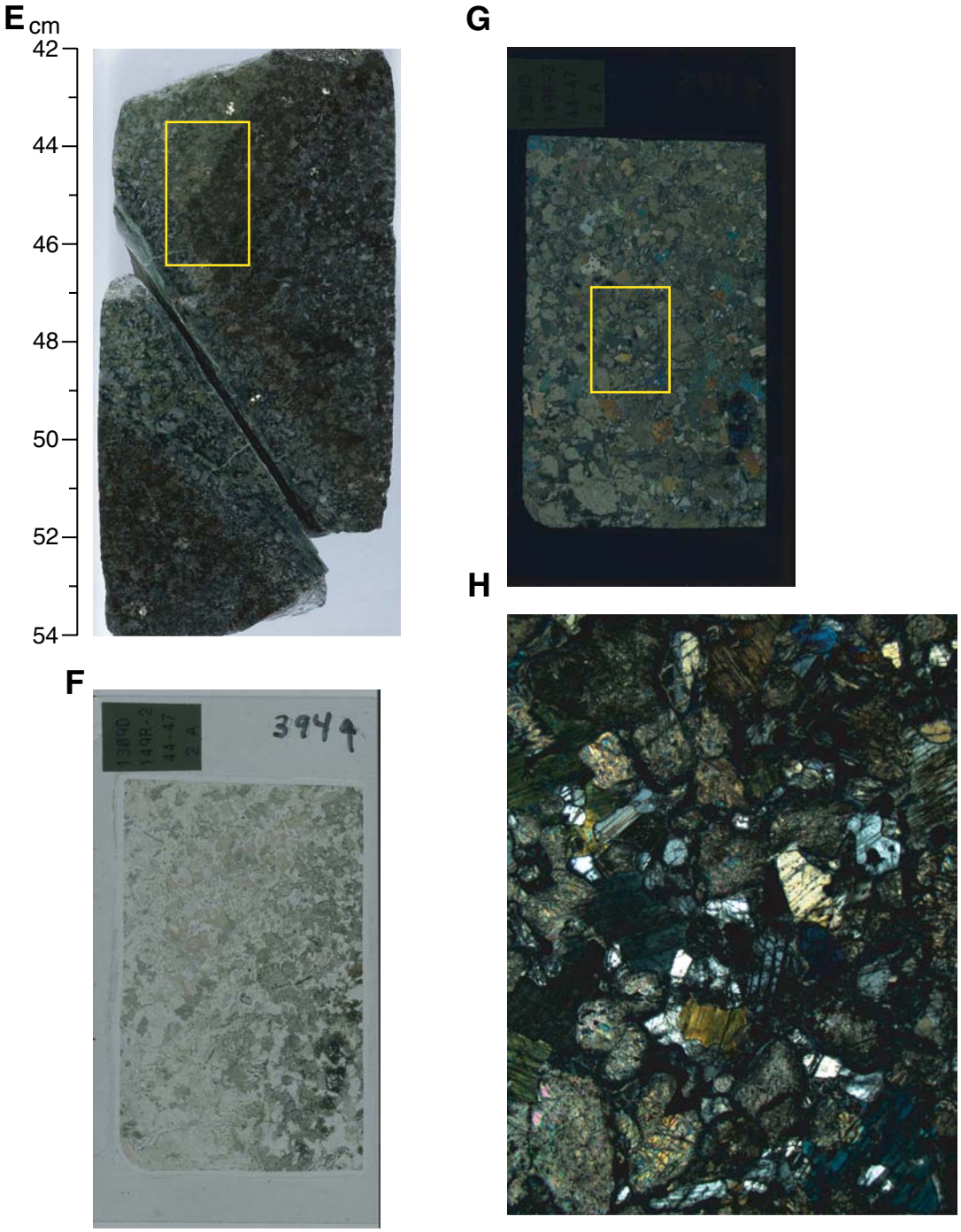

Figure F172. A–D. Downhole plot of alteration vein dip magnitude and vein type distribution in Hole U1309D (Expedition 304). (Continued on next page.)

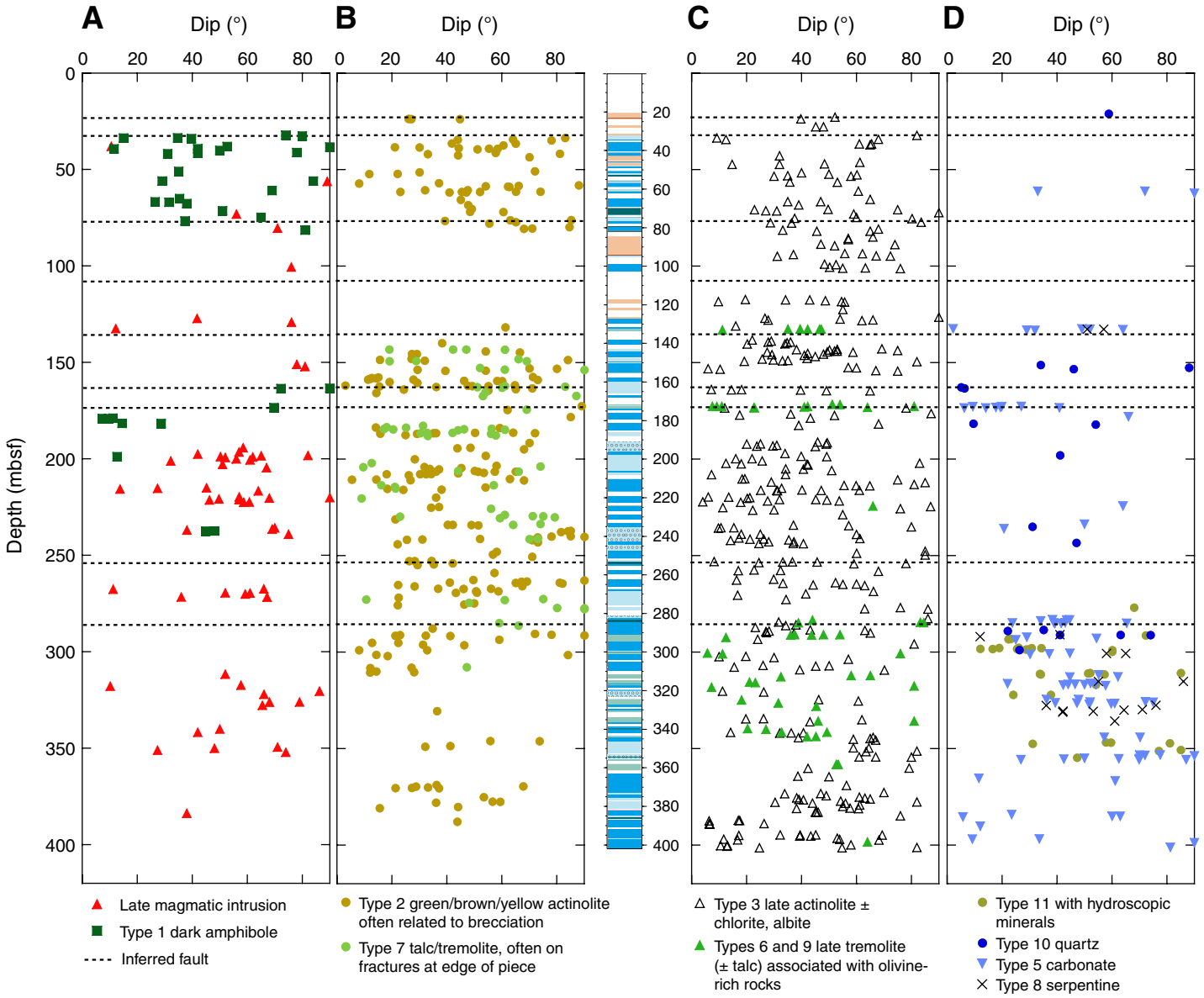

Figure F172 (continued). E–G. Downhole plots of vein dips averaged over structural intervals in Hole U1309D (Expedition 304). Data from A–D were used to calculate an average dip and the standard deviation for points within a defined structural interval. Average dips were then plotted at the average depth for the population of points used for each calculation. Standard deviation shown by bars.

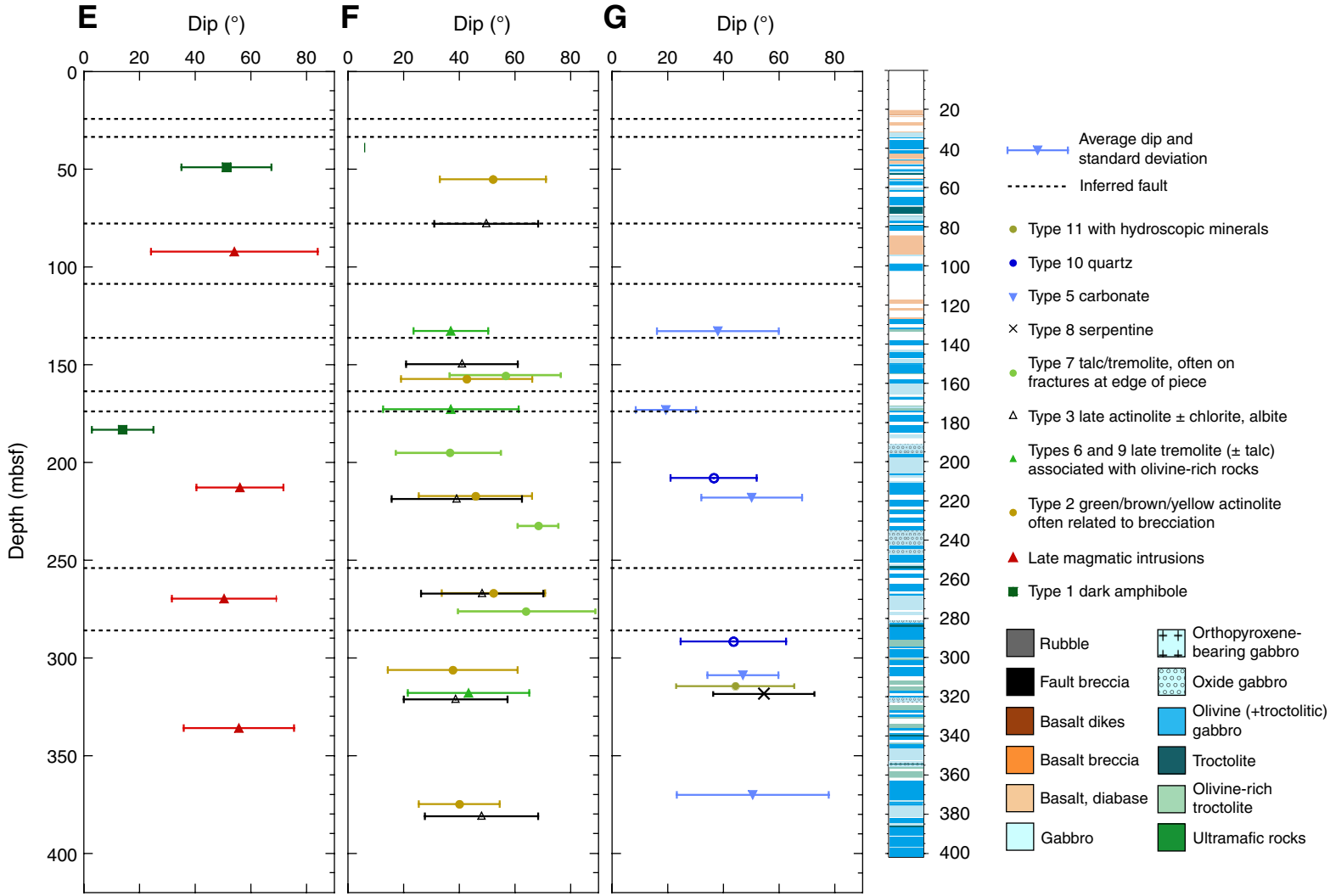

Figure F173. A. Type 1 hornblende alteration veins (interval 304-U1309D-7R-3, 91–103 cm). **B.** Type 1 hornblende vein (Sample **304-U1309D-7R-3, 101–102 cm**) (plane-polarized light; field of view [FOV] = 1 mm). **C.** Multiple Type 1 hornblende veins cutting plagioclase grains and disappearing into matrix of hornblende (altered pyroxene) (Sample **304-U1309D-4R-2, 108–110 cm**) (plane-polarized light; FOV = 4 mm). **D.** Type 2 yellow/brown actinolite veins in a cataclastic band at 44 cm (interval 304-U1309D-9R-2, 43–56 cm). Deformed late-magmatic leucocratic dikes intersect at 52 cm. (Continued on next page.)

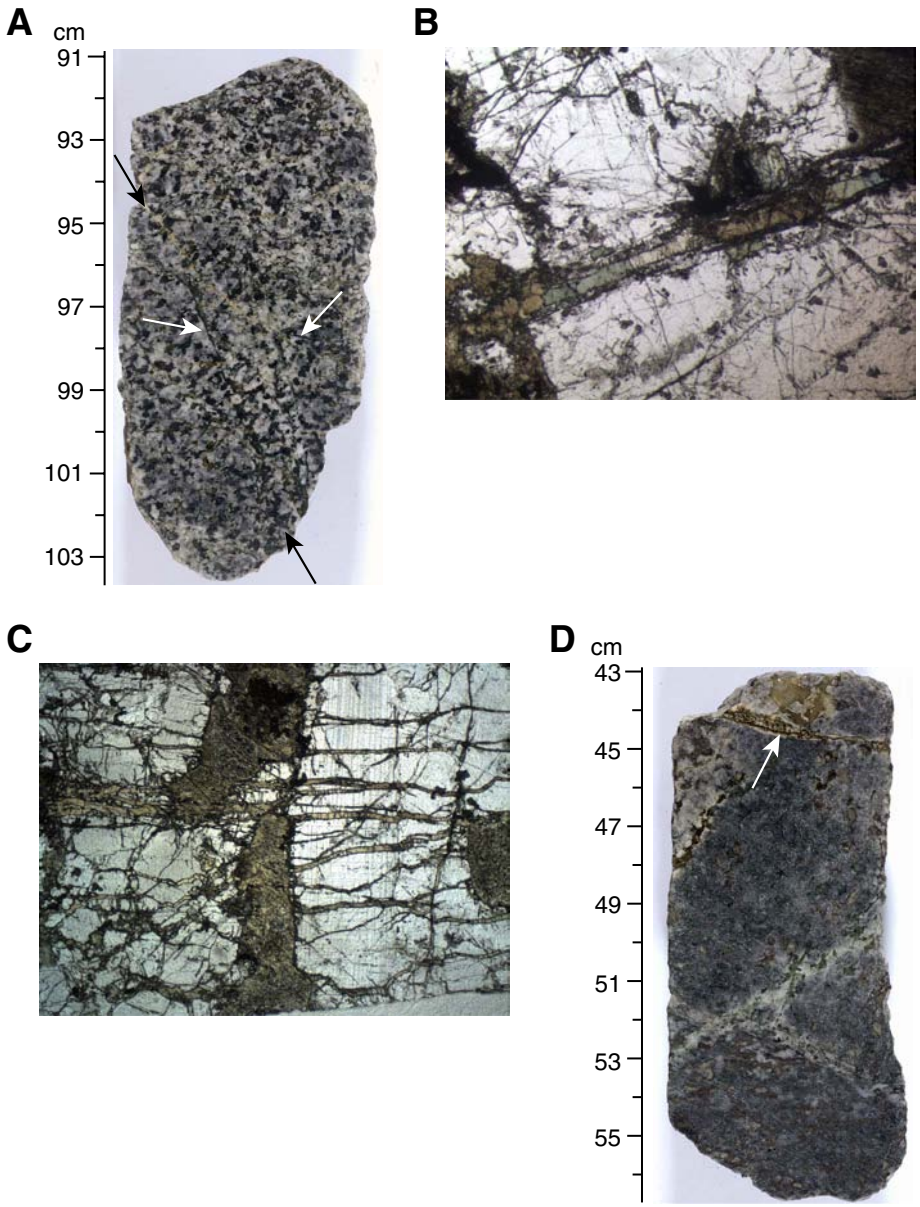

Figure F173 (continued). **E.** Type 3 late actinolite ± chlorite, albite veins (interval 304-U1309D-13R-1, 18–34 cm). **F.** Type 3 actinolite ± chlorite, albite veins cutting diabase (Sample **304-U1309D-1R-3, 46–48 cm**) (plane-polarized light; FOV = 1 mm). Dark, high-relief crystal is titanite. **G.** Type 7 talc-rich vein with lineated surface (interval 304-U1309D-29R-1, 70–76 cm). **H.** Type 5 carbonate vein cutting across a magmatic contact (interval 304-U1309D-61R-1, 140–147 cm).

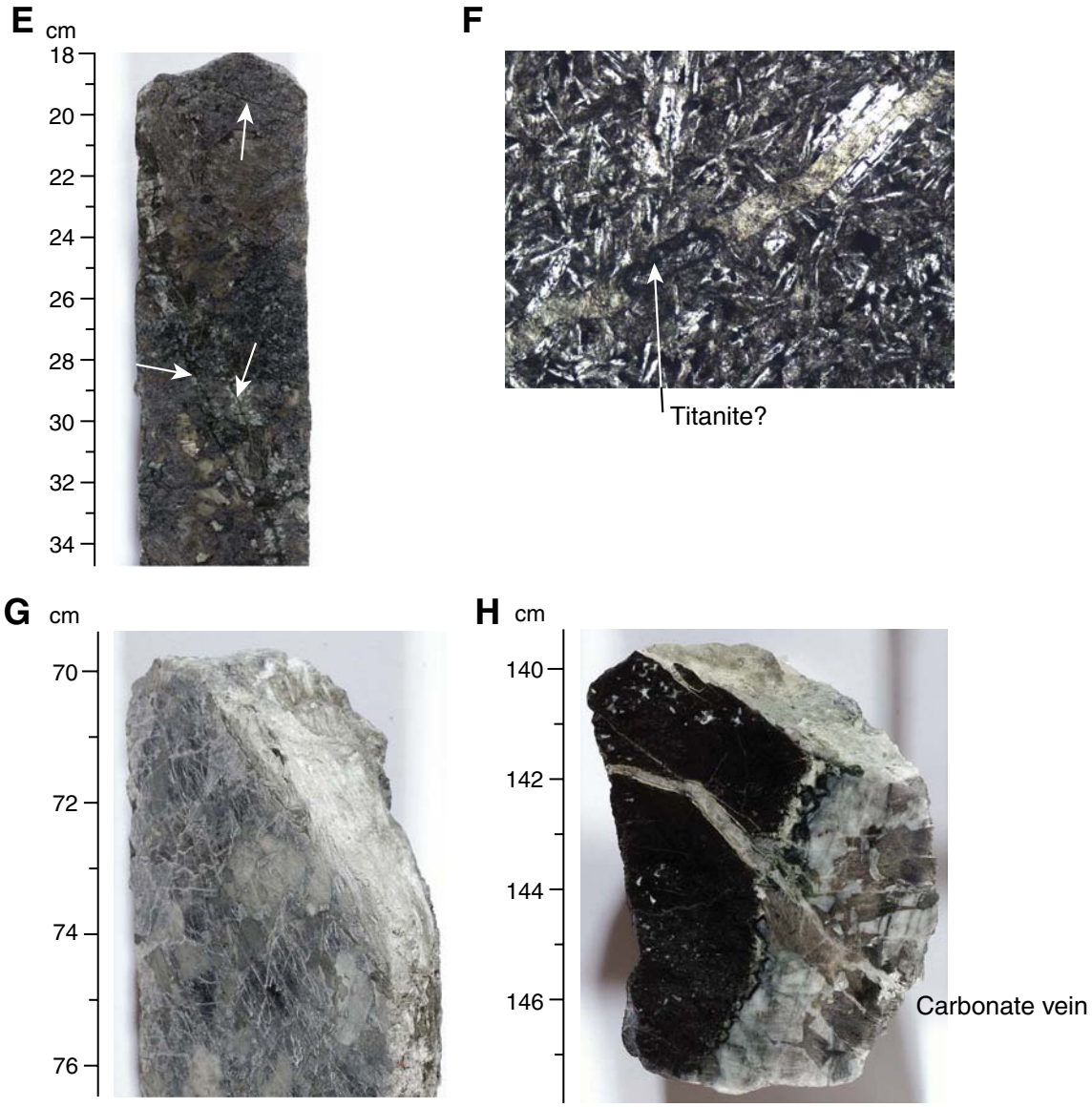

Figure F174. **A.** Moderately dipping dark green vein in olivine gabbro (Sample 305-U1309D-89R-2, 125–137 cm). **B.** Moderately dipping dark green vein in amphibole gabbro (Sample 305-U1309D-130R-2, 7–20 cm). **C.** Set of green subparallel dark green veins dipping steeply in coarse gabbro (Sample 305-U1309D-132R-3, 20–36 cm). **D.** Set of dark green subparallel veins crosscut by late pale green veins in fine-grained gabbro (Sample 305-U1309D-138R-2, 80–93 cm). **E.** Set of high-density parallel dark green veins at <5 mm spacing over a 20 cm interval crosscut by a hairline white vein (Sample 305-U1309D-160R-4, 0–23 cm). A horizontal white vein is present at 17.5 cm.

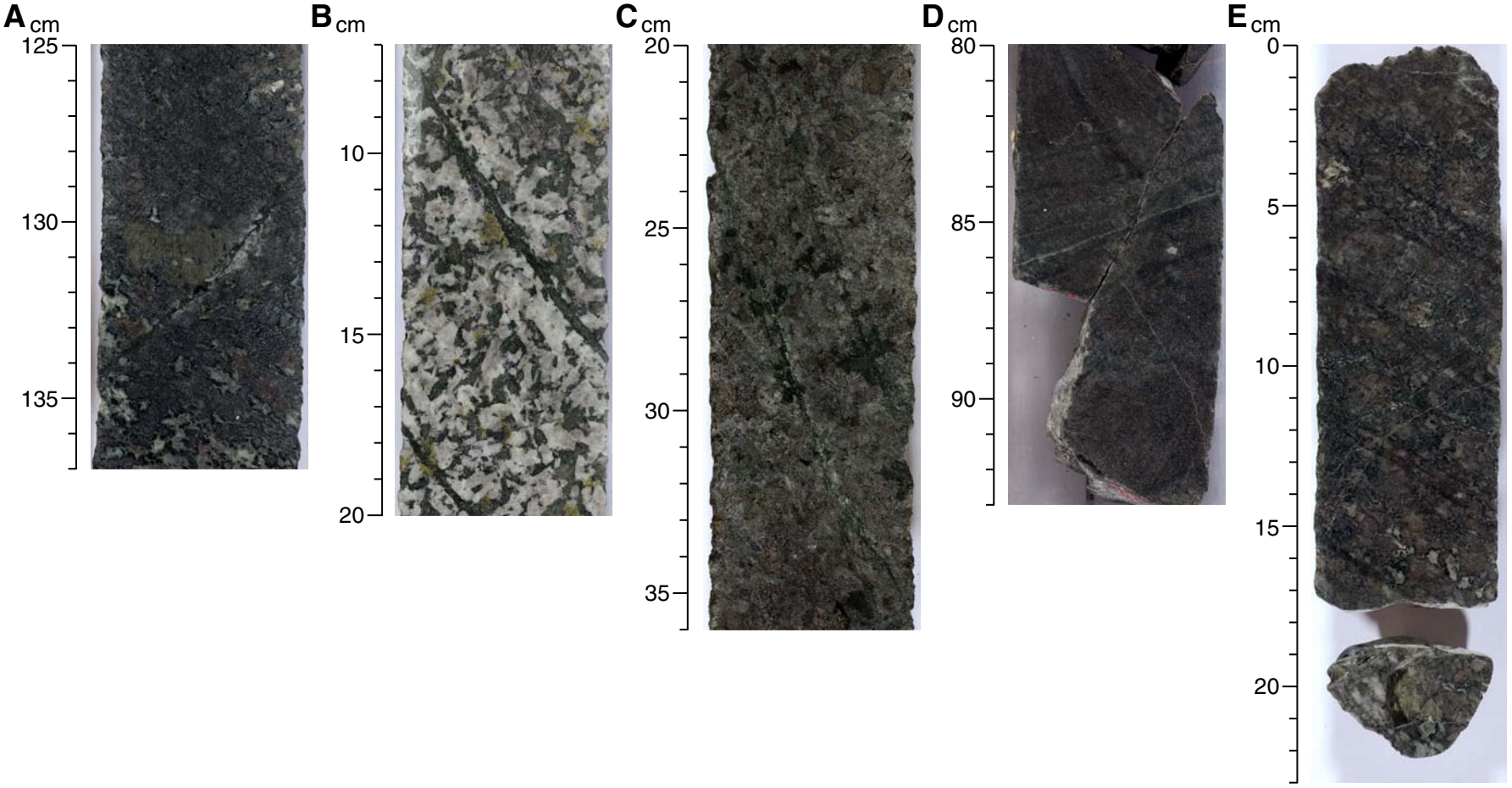

Figure F175. A. Dark green vein associated with sheared fractures in gabbro (interval 305-U1309D-277R-2, 64–75 cm). Yellow box = location of B and C. **B.** Dark green sheared vein (Sample **305-U1309D-277R-2, 69–71 cm**) (plane-polarized light, field of view [FOV] = 2 cm). Yellow box = location of D. **C.** Same as B; cross-polarized light. Yellow box = location of E. **D.** Fractured plagioclase and clinopyroxene grains that have been intensely bent and fractured along the vein networks (plane-polarized light; FOV = 5.5 mm). **E.** Same as D; cross-polarized light. (Continued on next page.)

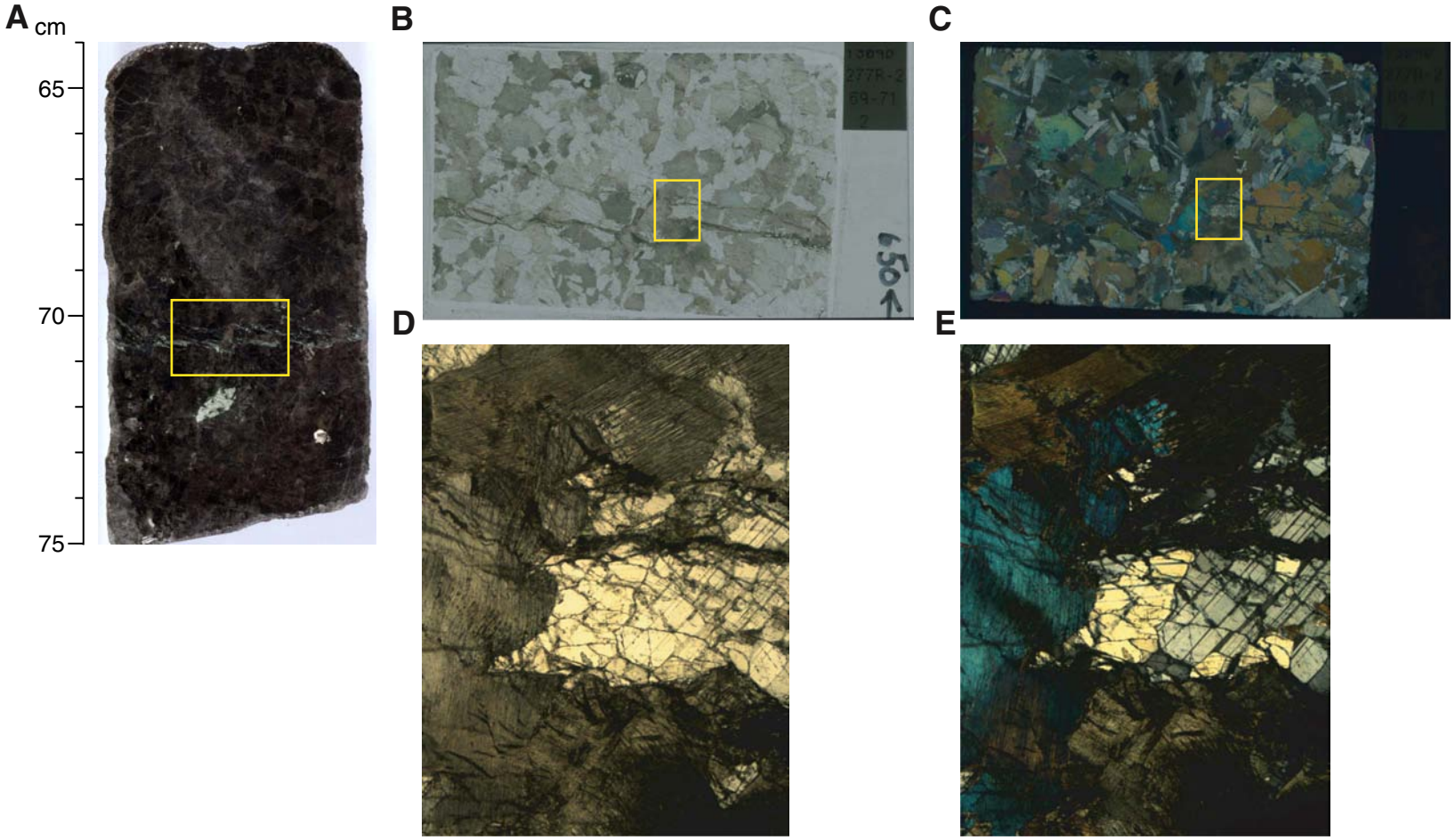

Figure F175 (continued). **F.** Dark green vein associated with sheared fractures in gabbro (interval 305-U1309D-277R-3, 1–24 cm). Yellow box = location of G and H. **G.** Dark green sheared vein in gabbro (Sample **305-U1309D-277R-3, 2–4 cm**) (plane-polarized light, FOV = 2 cm). Yellow box = location of I. **H.** Same as G; cross-polarized light. Yellow box = location of J. **I.** Plagioclase grains adjacent to the vein are fractured and contain altered mineral infilling (plane-polarized light, magnification = 2.5×). Within the vein, replacement minerals such as chlorite and tremolite/actinolite appear to be further deformed into finer grains by a small offset along the vein. **J.** Same as I; cross-polarized light.

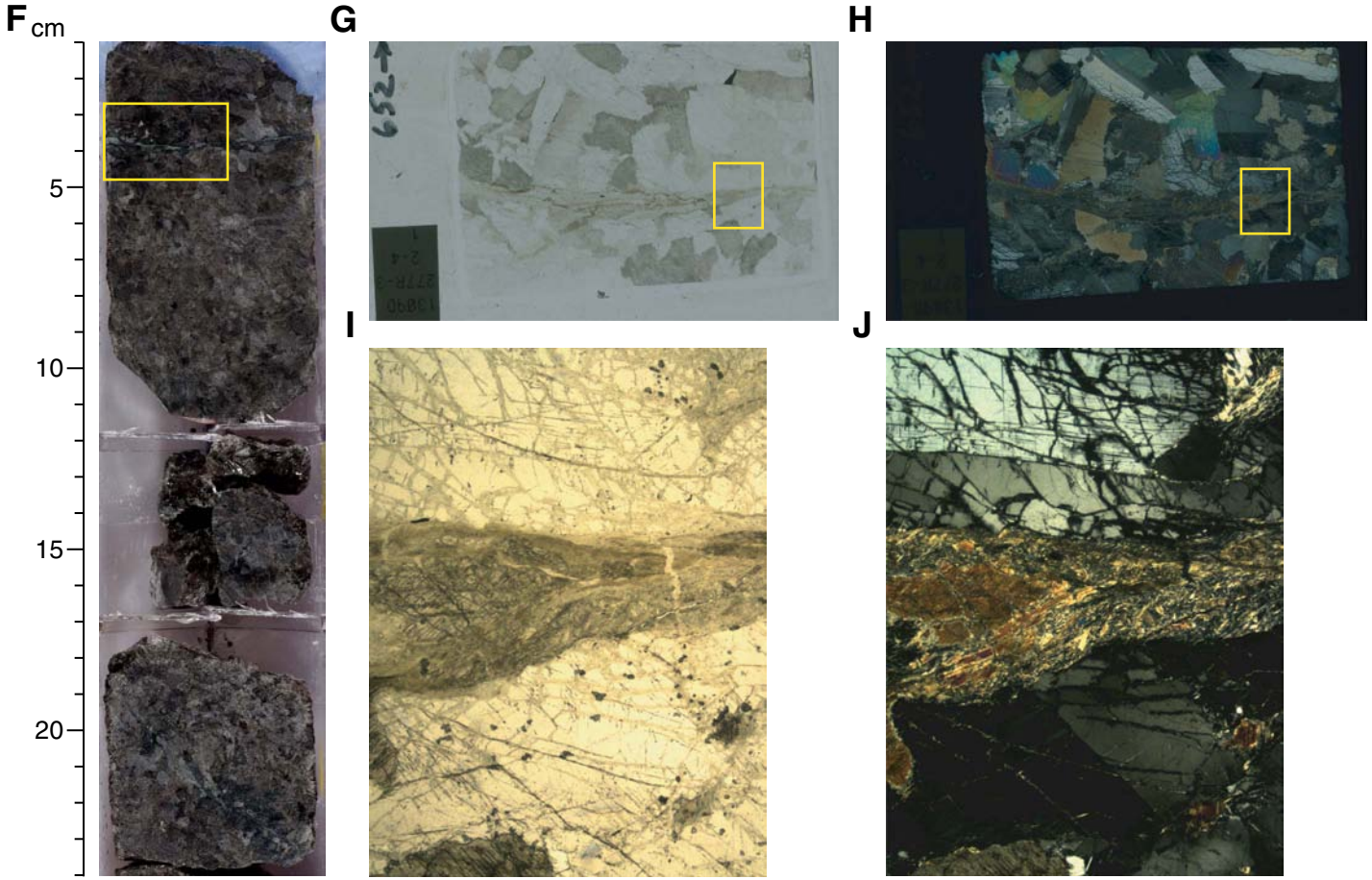

Figure F176. A. Dark green vein overprinted by cataclasis in gabbro (interval 305-U1309D-187R-1, 66–88 cm). Yellow box = location of B and C. **B.** Dark green vein associated with cataclasite (Sample **305-U1309D-187R-1, 69–72 cm**) (plane-polarized light; field of view [FOV] = 2 cm). Yellow box = location of D. **C.** Same as B; cross-polarized light. Yellow box = location of E. **D.** Cataclastic zone along green vein (plane-polarized light; magnification = 7.5×). Also shown are fragmented plagioclase grains with alterationed mineral infilling. **E.** Same as D; cross-polarized light. Note the amphibole grains as fracture infilling with no deformation between fragmented plagioclase grains (arrow) apart from the cataclasite zone.

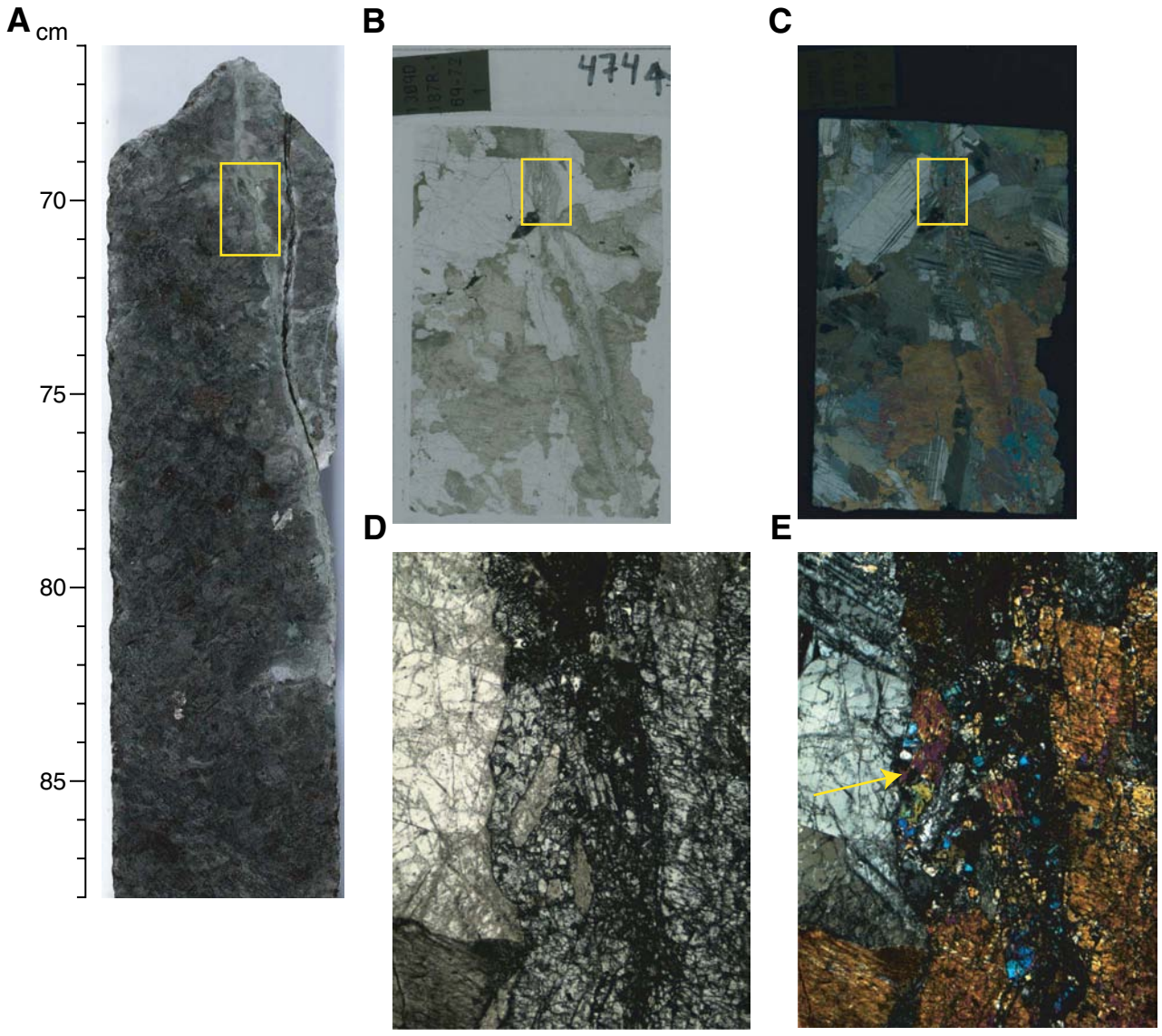

Figure F177. A. steeply dipping pale green vein with talc fibers in coarse-grained gabbro (Sample 305-U1309D-95R-2, 119–133 cm). Shallow-dipping cracks with white infills emanate from the pale green vein. **B.** Same as A; view of vein surface talc fibers plunging 20° along the pale green vein. **C.** Two steeply dipping pale green veins with horizontal talc fibers, indicating strike-slip movement, and thick alteration halo in dunite (Sample 305-U1309D-136R-1, 70–90 cm). **D.** Subhorizontal pale green vein with subhorizontal talc fibers crosscutting earlier steeply dipping magmatic vein in olivine-rich troctolite (Sample 305-U1309D-136R-2, 1–18 cm). **E.** Steeply dipping but irregular pale green vein with subhorizontal talc fibers in medium-grained gabbro (Sample 305-U1309D-145R-2, 100–116 cm). **F.** Steeply dipping pale green vein with talc fibers plunging 60° and alteration halo in fine-grained gabbro (Sample 305-U1309D-149R-2, 42–54 cm).

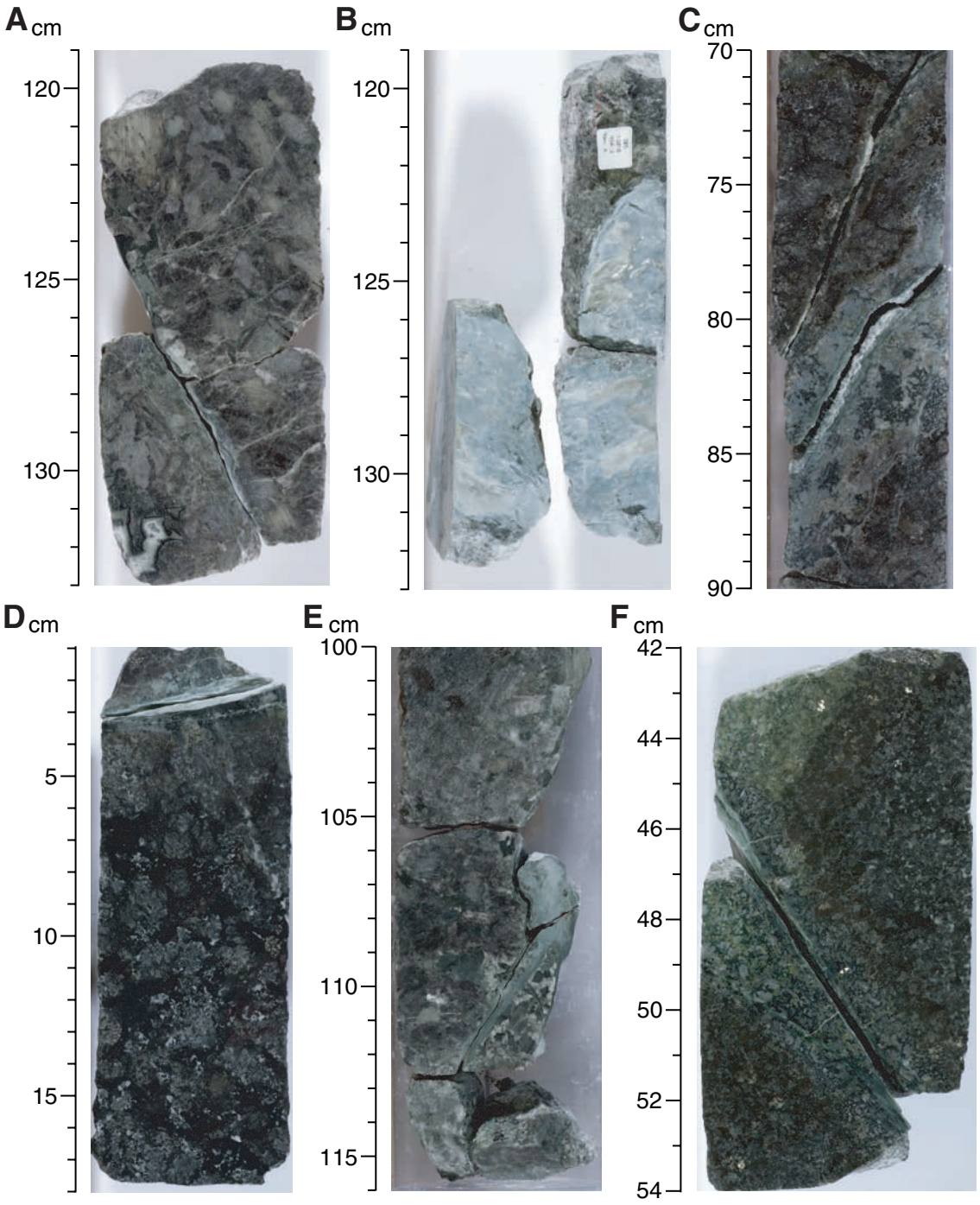

Figure F178. A. Subhorizontal white veins in olivine gabbro (Sample 305-U1309D-90R-4, 27–42 cm). **B.** Subhorizontal white veins crosscutting steeply dipping pale green vein in coarse gabbro (Sample 305-U1309D-104R-3, 27–39 cm). **C.** Thin white vein subparallel to a set of numerous, subparallel dark green veins, closely spaced and dipping moderately in medium gabbro (Sample 305-U1309D-115R-3, 50–70 cm). **D.** Steeply dipping white veins with sulfides cutting dark green veins in fine gabbro (Sample 305-U1309D-136R-3, 0–16 cm). **E.** Subhorizontal white vein crosscutting leucocratic zone with weak cataclasis (Sample 305-U1309D-128R-2, 119–130 cm). **F.** Irregular network of white veins with many minor cracks due to cataclastic deformation in coarse gabbro (Sample 305-U1309D-148R-3, 107–115 cm).

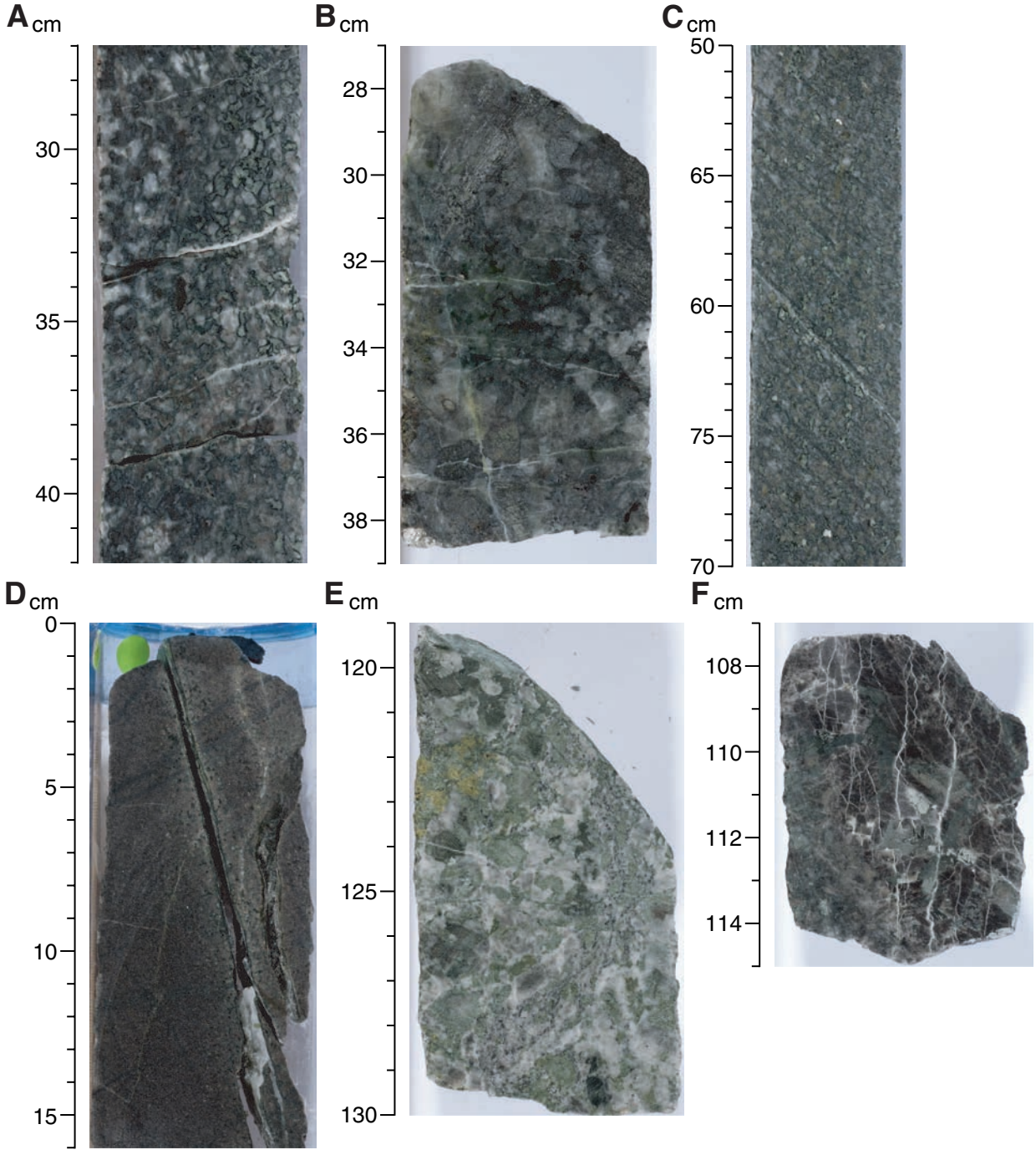

Figure F179. A. Rare evidence of deformation in a dark green vein, which consists of amphibole and plagioclase, within olivine gabbro (Sample **305-U1309D-89R-2, 130–133 cm**) (plane-polarized light; field of view [FOV] = 5.5 mm). A tiny open crack with chlorite infilling occurs in the center of the vein. **B.** Same as A; cross-polarized light. **C.** Subvertical pale green vein with epidote, chlorite, and actinolite infillings cut by a subhorizontal white vein with prehnite and chlorite infillings within troctolite (**Sample 305-U1309D-104R-3, 33–36 cm**) (plane-polarized light; FOV = 5.5 mm). **D.** Same as C; cross-polarized light.

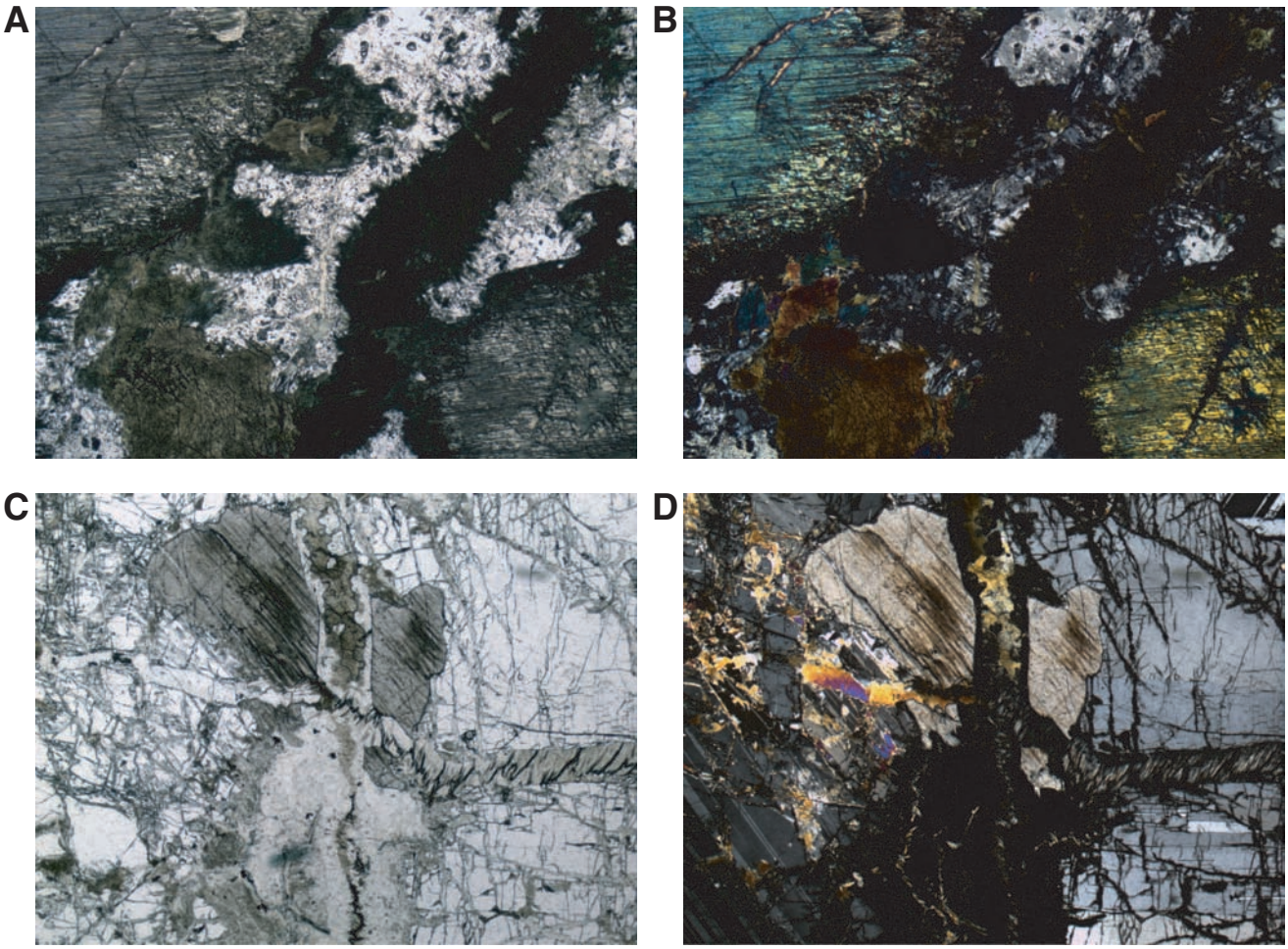

Figure F180. A. Gray vein in troctolite (interval 305-U1309D-233R-2, 51–75 cm). Yellow box = location of B and C. **B.** Gray veins crosscut by serpentine foliations (Sample **305-U1309D-233R-2, 70–73 cm**) (cross-polarized light; field of view [FOV] = 2 cm). Yellow box = location of D. **C.** Same as B; plane-polarized light. **D.** Gray vein consists of serpentine, chlorite, and tremolite (or actinolite), with little evidence of deformation, and is crosscut by serpentine foliation (cross-polarized light; field of view [FOV] = 5.5 mm). **E.** Same as D; plane-polarized light. (Continued on next page.)

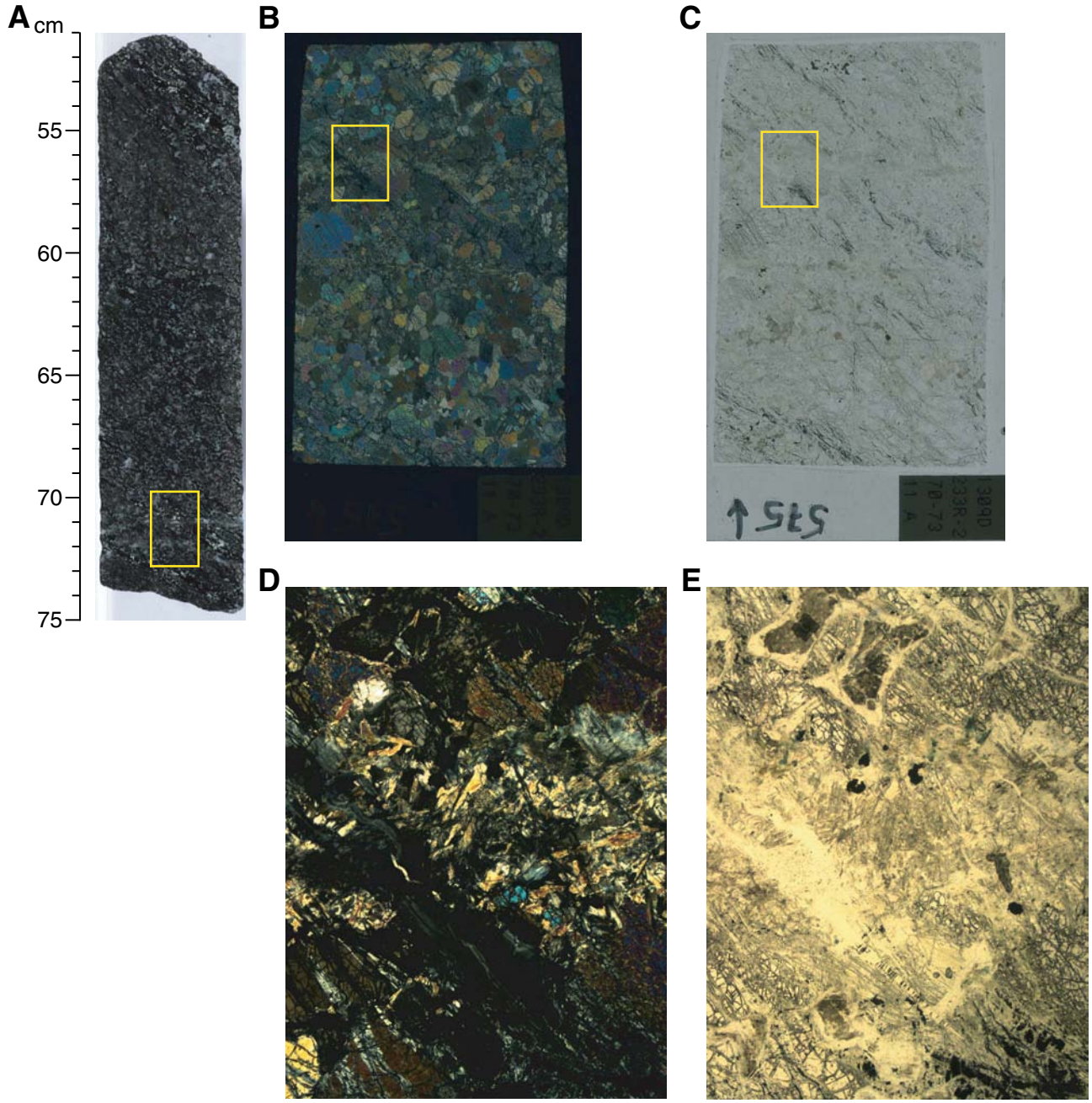

Figure F180 (continued). F. Light gray vein crosscutting gabbro dikelet in olivine-rich troctolite (interval 305-U1309D-257R-1, 10–37 cm). Yellow box = location of G and H. **G.** Gray vein cross cutting magmatic vein in olivine-rich troctolite (Sample **305-U1309D-257R-1, 32–34 cm**) (plane-polarized light; FOV = 2 cm). Yellow box = location of I. **H.** Same as G; cross-polarized light. Yellow box = location of J. **I.** Light gray vein consisting mostly of serpentine and calcite with little deformation (cross-polarized light; FOV = 5.5 mm). **J.** Same as I; plane-polarized light.

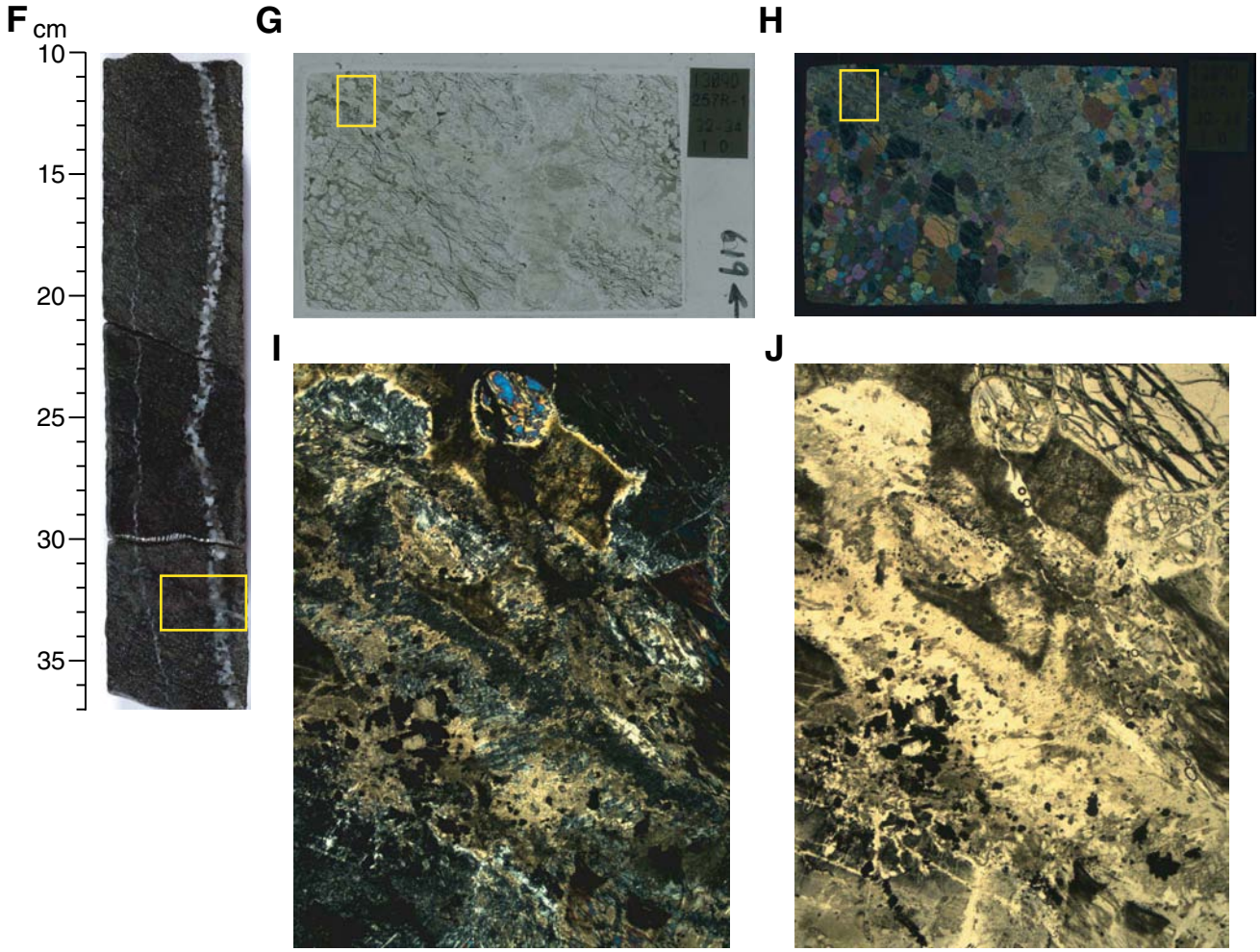

Figure F181. A. Fiber vein with intense alteration halo in olivine-rich troctolite (interval 305-U1309D-234R-2, 0–18 cm). Trend of fiber is subparallel to the vein. **B.** Trend of fibers inside a vein (Sample **305-U1309D-234R-2, 9–12 cm**) (plane-polarized light; field of view [FOV] = 2 cm). Yellow box = location of D. **C.** Same as B; cross-polarized light. Yellow box = location of E. **D.** Broken line traces fiber orientations from the wall toward the vein (plane-polarized light; FOV = 5.5 mm). **E.** Same as D; cross-polarized light.

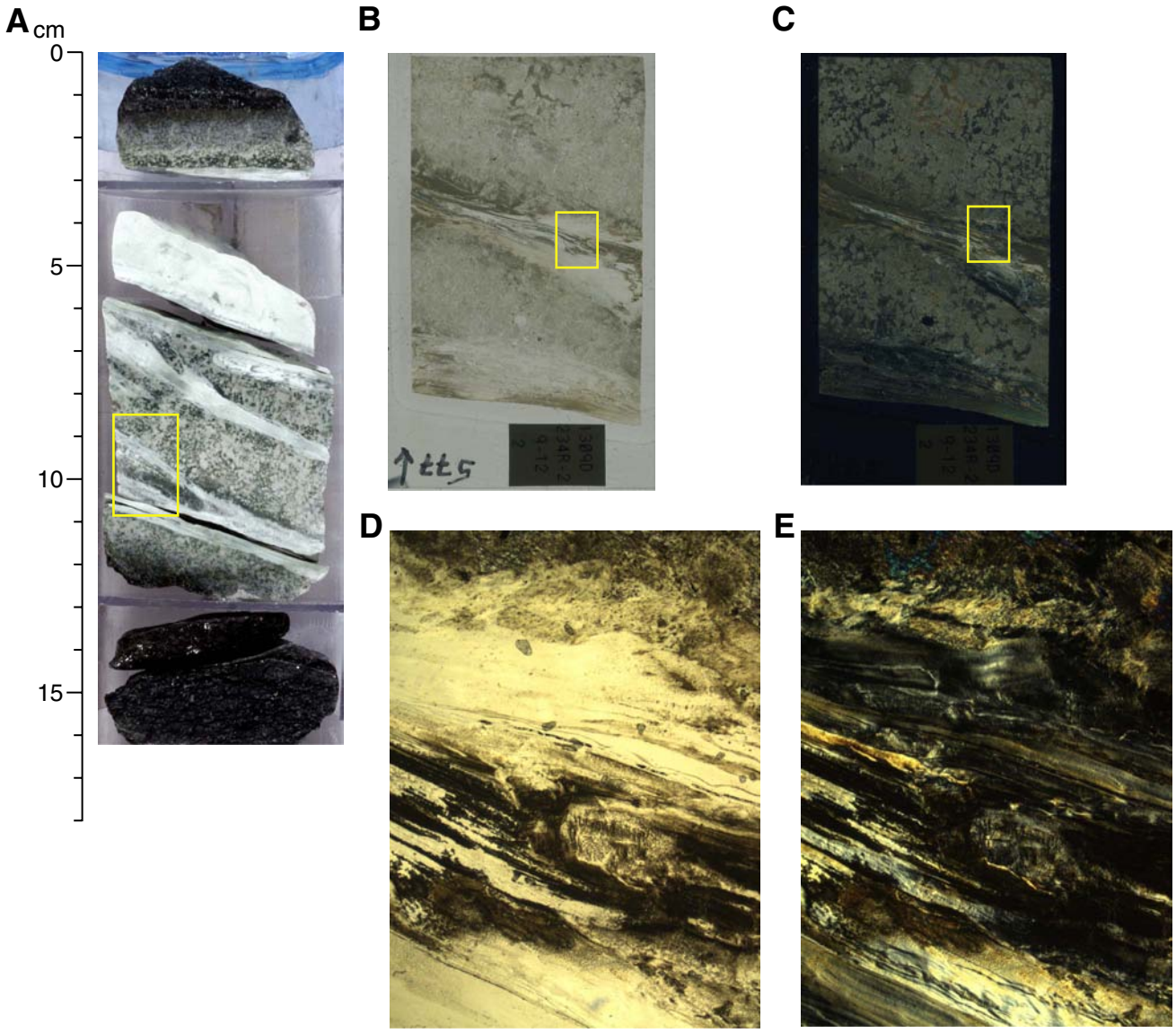

Figure F182. Downhole plots of brittle features in Hole U1309D. **A.** Vertical distribution of vein abundance, estimated from core observations, is relatively constant throughout the interval cored during Expedition 305, with possible vein intensity peaks at ~575 mbsf and at 700–750 mbsf. There is a relatively abrupt decrease in the background vein intensity below the fault zone at ~750 mbsf. This vein intensity log does not include the serpentine foliation. **B.** Cataclastic deformation, estimated from core observations, is overall very low. Similar to the veins, there is an increase between 450 and 750 mbsf, followed by a relatively abrupt decrease in the intensity of cataclastic deformation at ~750 mbsf. **C.** Average number of logged veins (blue) and fault veins (red) per meter, using a 10 m averaging window determined from the metamorphic petrologists during Expedition 305. This log includes the serpentine foliation. Fault zones identified during Expedition 305.

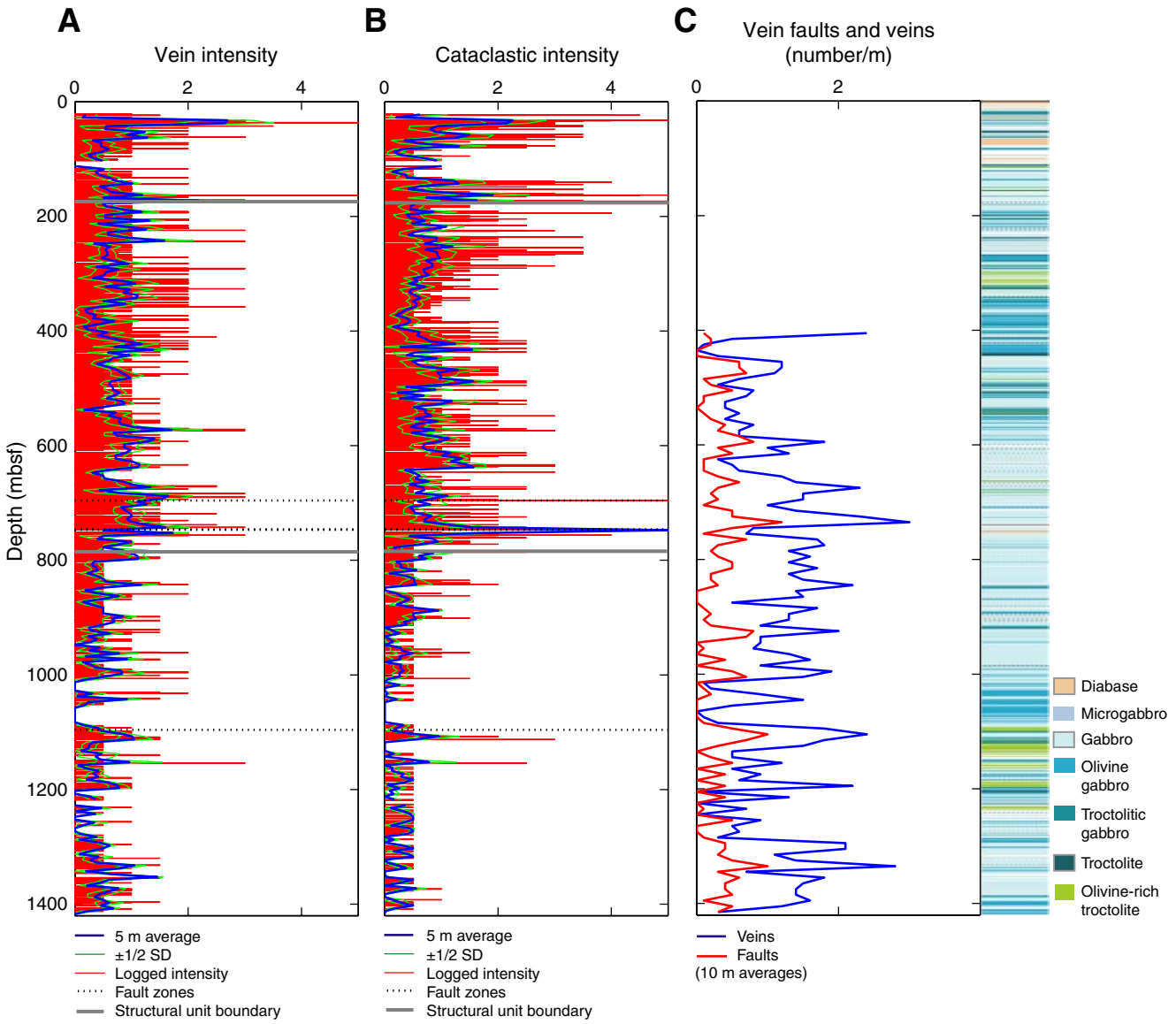

Figure F183. Downhole plot of absolute intensity of alteration veins in Holes (**A**) U1309B and (**B**) U1309D to 132 mbsf (Expedition 304). Diabase is highlighted (beige) across the figures to depict the generally lower intensity in those intervals. Dotted lines = location of inferred faults based on cataclastic fabrics.

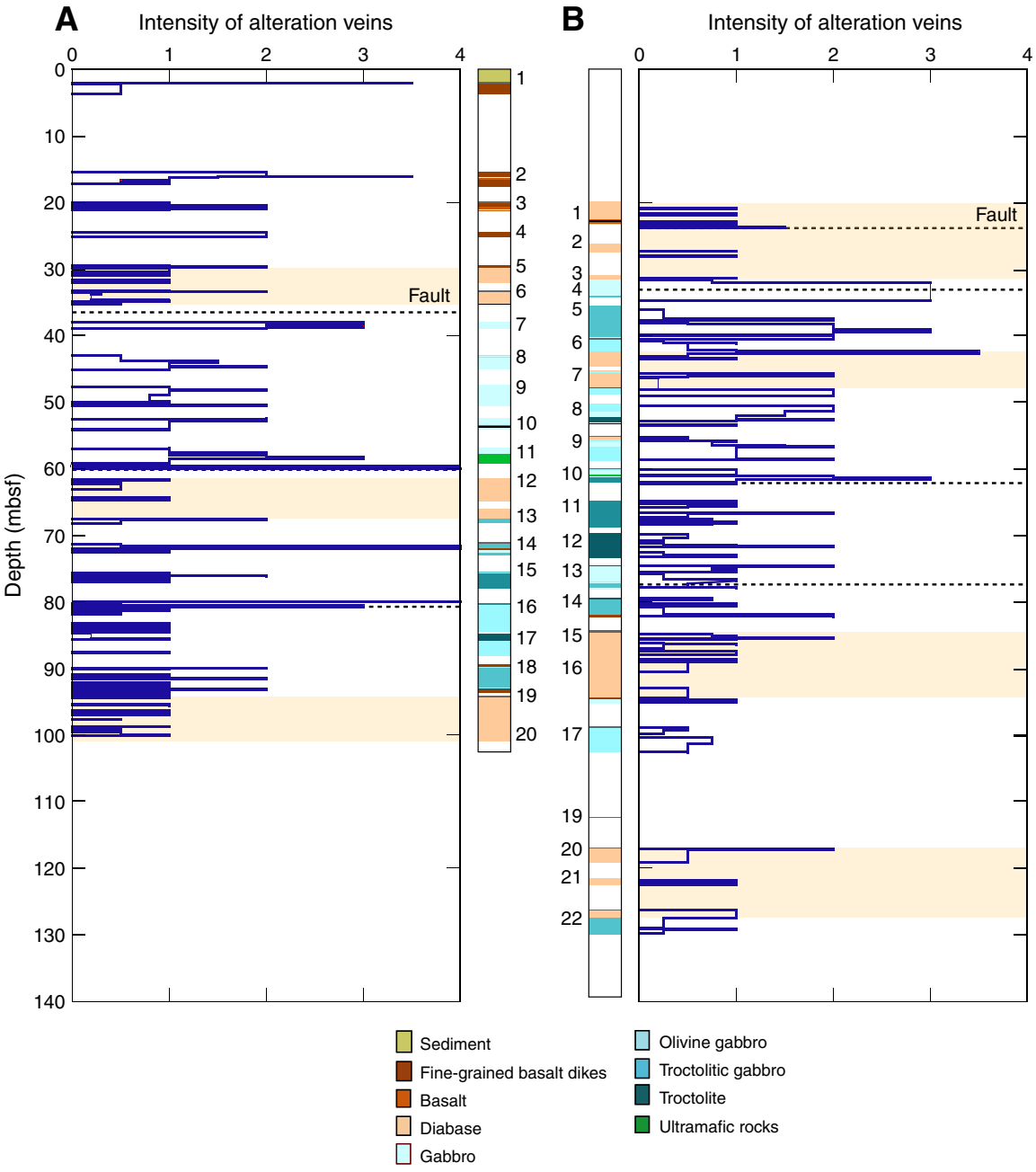

Figure F184. Downhole plot of alteration vein dip magnitude and vein type distribution of Holes (**A**) U1309B and (**B**) U1309D to 132 mbsf. Diabase is highlighted (beige) across the figures to illustrate the lack of vein diversity within those intervals. Dotted lines = location of inferred faults based on cataclastic fabrics.

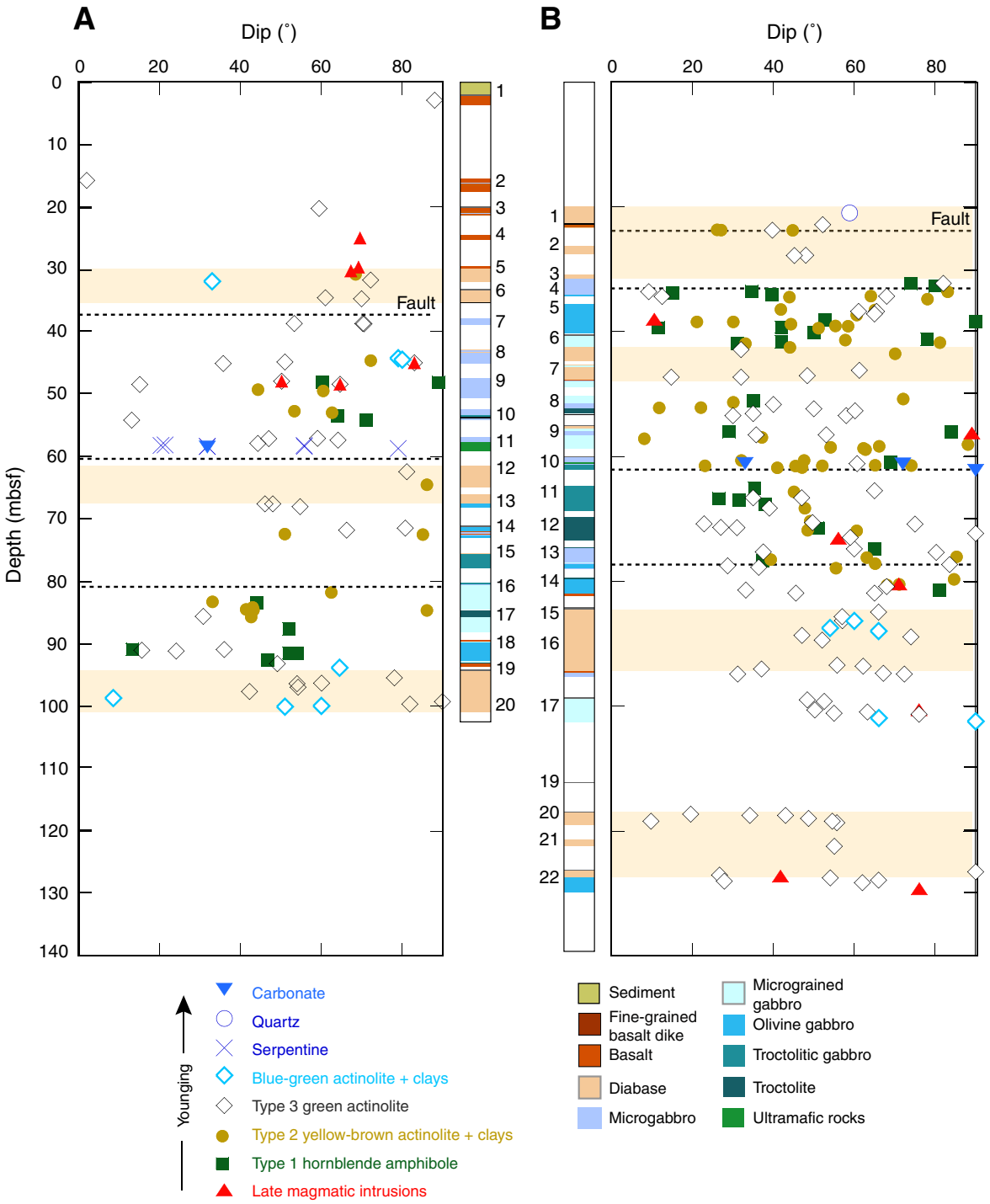

Figure F185. Histograms showing vein type versus dip magnitude in Holes (**A**) U1309B and (**B**) U1309D to 132 mbsf. Bin size = 5°.

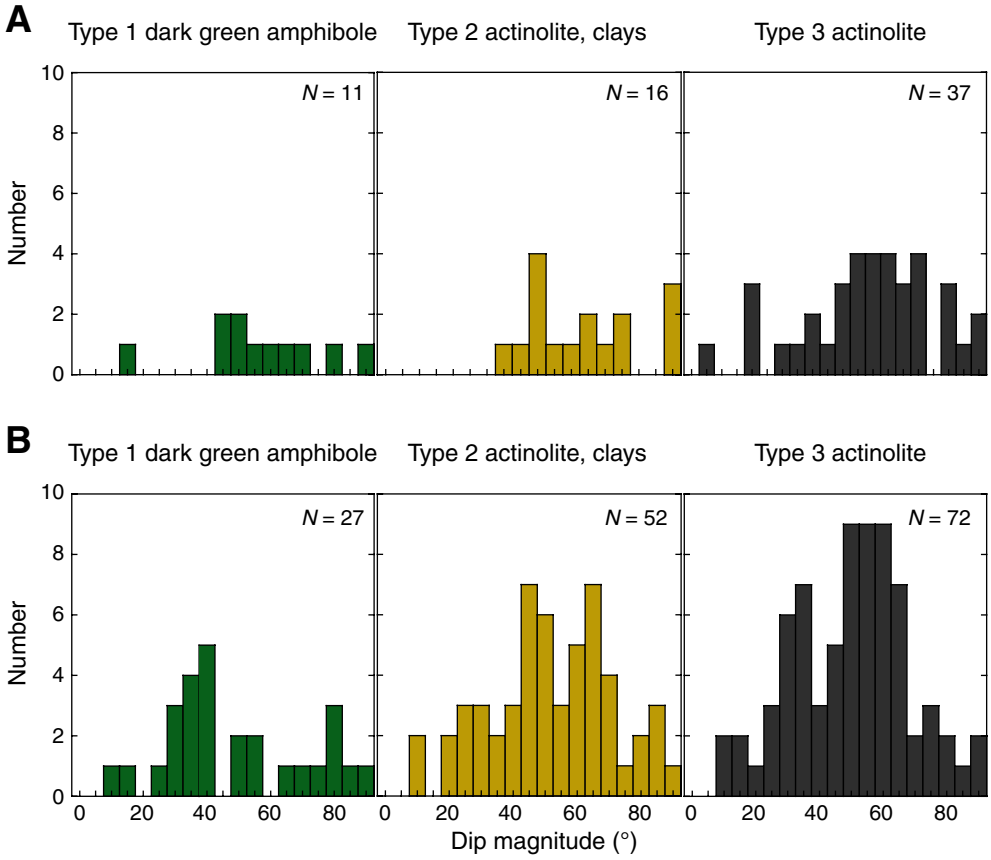

Figure F186. A. Average cataclastic and veining intensity in Hole U1309D (5 m average from Fig. F182). Presence of sulfide along open cracks is also indicated. **B.** Dip of dark green and gray veins (Expedition 305). **C.** Dip of pale green and white veins (Expedition 305). The column on the right corresponds to the lithostratigraphy in Hole U1309D.

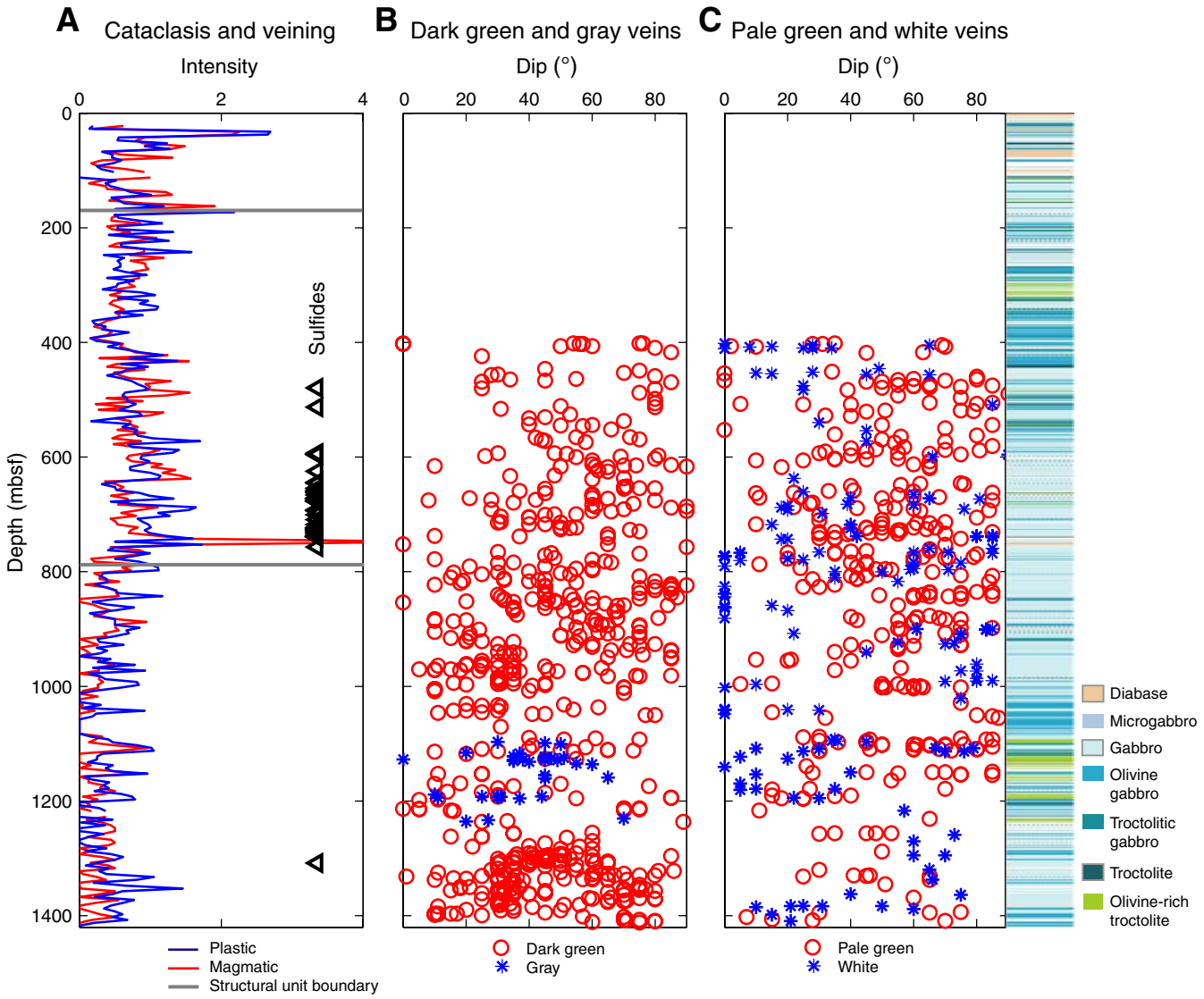

Figure F187. Measured vein dips in Hole U1309D below 400 mbsf (Expedition 305). **A.** All fault veins. Blue line = mean value, green lines = standard deviation. **B.** Fault veins with plunge measurements. Bold lines = average values, dotted lines = standard deviation. **C.** Cataclastic and open fractures. **D.** Dark green veins. Red lines = mean, green lines = standard deviation. **E.** Pale green veins. **F.** White veins.

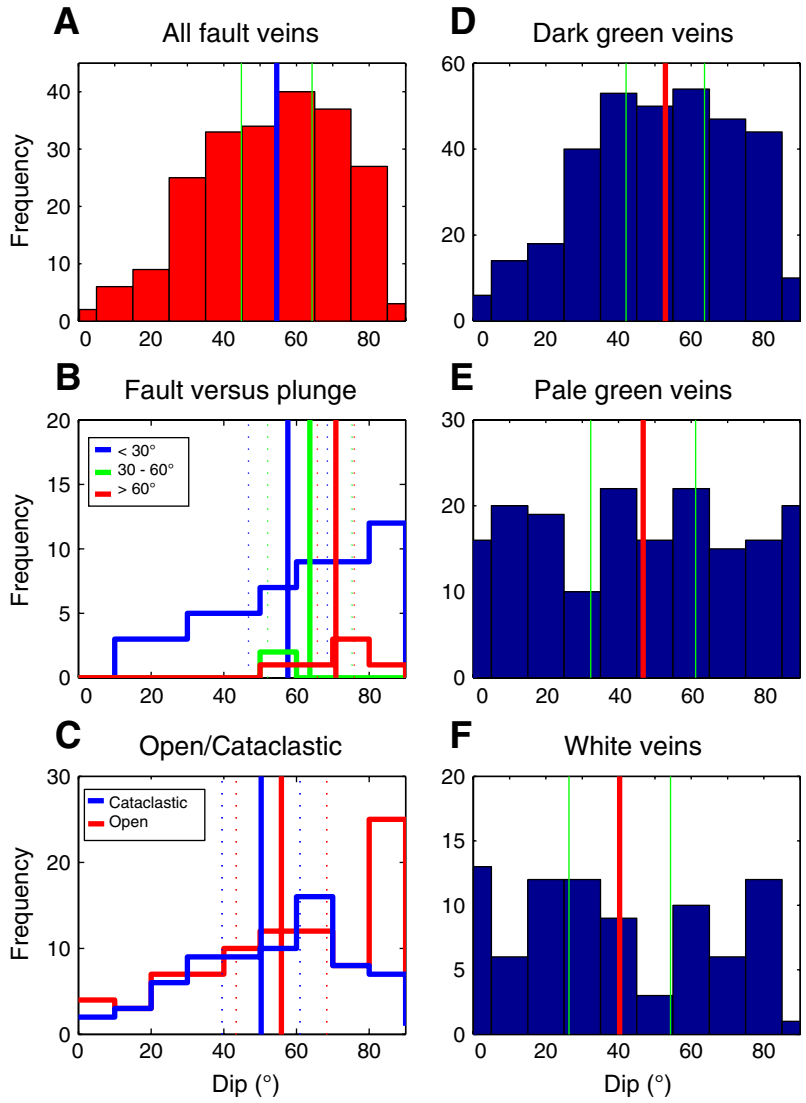

Figure F188. Examples of cataclastic deformation fabrics. **A.** Cataclastic/breccia zones (interval 304-U1309B-16R-1, 39–51 cm). **B.** Breccia in basalt unit (interval 304-U1309B-4R-1, 10–26 cm). **C.** Breccia formed at greenschist grade (Sample **304-U1309B-16R-1, 31–33 cm**) (cross-polarized light; field of view [FOV] = 8 mm). **D.** Brittle shear bands cutting across mylonite (Sample **304-U1309D-29R-2, 131–133 cm**) (gypsum plate; cross-polarized light; FOV = 8 mm). (Continued on next page.)

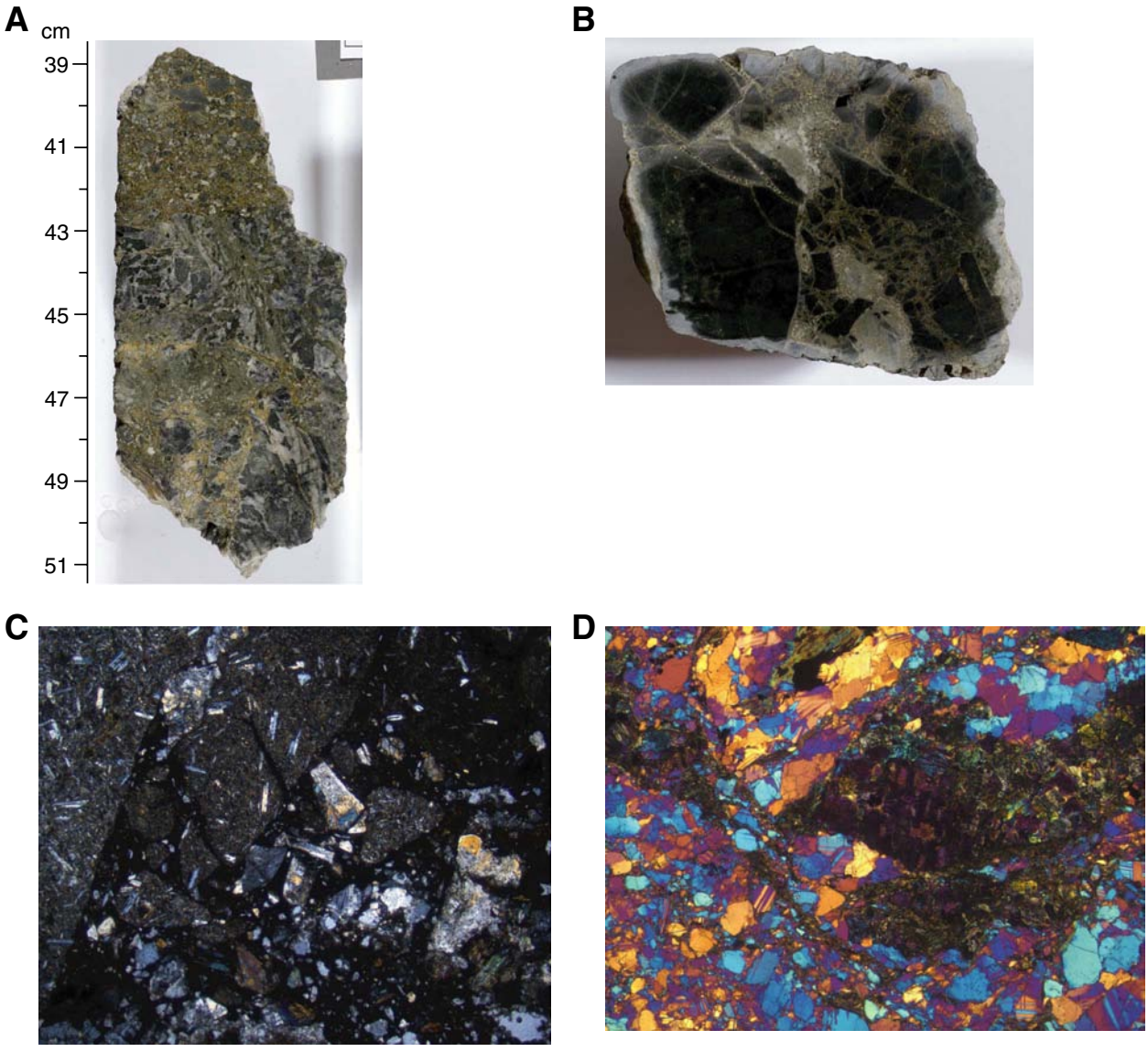

Figure F188 (continued). **E.** Talc schist shear zone showing sinistral (reverse sense in core reference frame) displacement (Section 304-U1309B-11R-2, 32 cm) (cross-polarized light; FOV = 4 mm). **F.** Talc-tremolite schist shear zone, showing overprinting texture of aligned tremolites (Sample **304-U1309D-1R-3, 0–4 cm**) (cross-polarized light; FOV = 4 mm). **G.** Breccia zone associated with late-magmatic leucocratic intrusion (interval 304-U1309B-16R-1, 35–49 cm). **H.** Serpentinite foliation (top) grades into gabbroic texture (bottom) (interval 304-U1309D-70R-3, 77–96 cm).

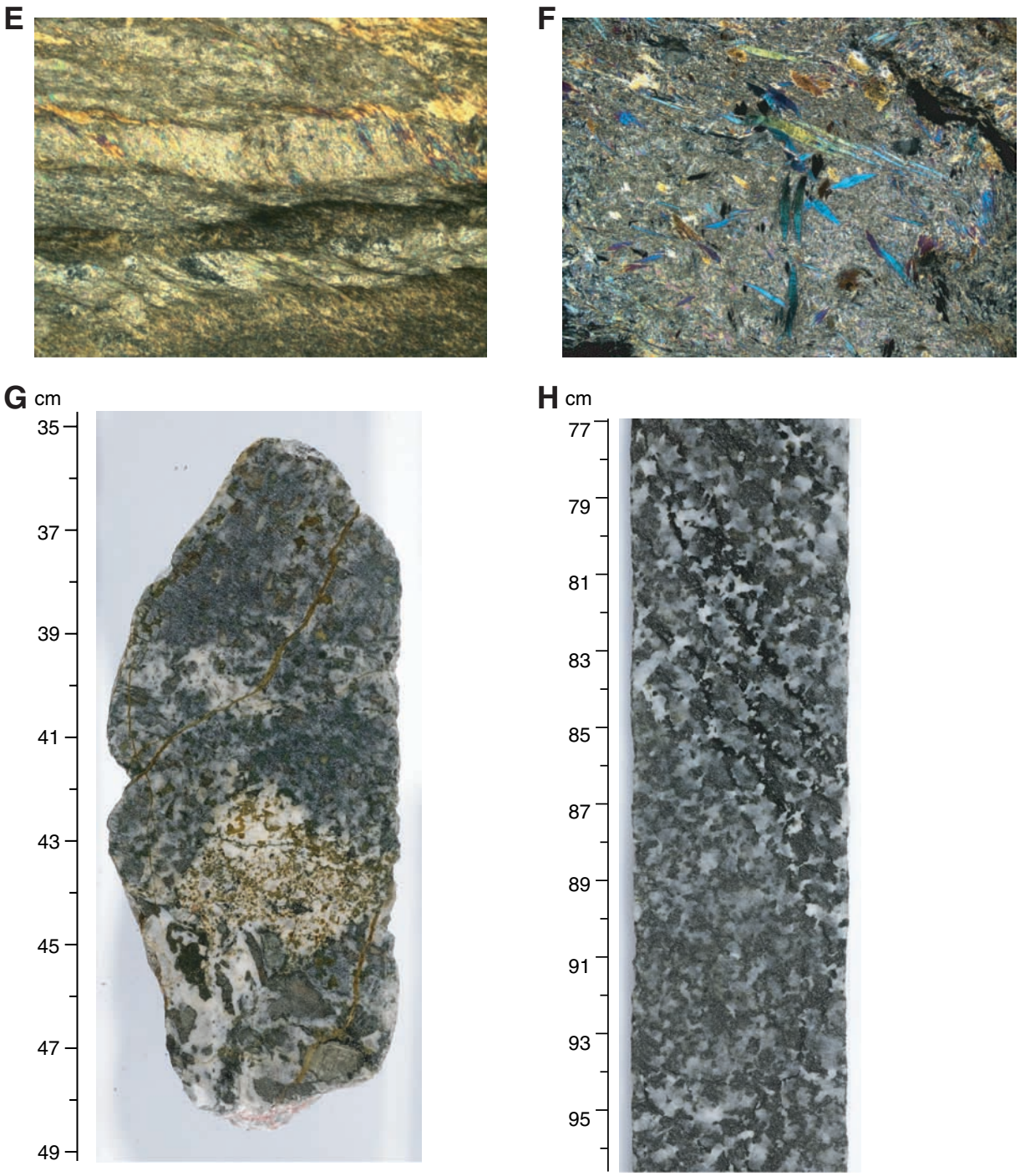

Figure F189. A. Green fault gouge dipping 20° defines a fault zone in gabbro (Sample 305-U1309D-141R-2, 68–80 cm). Cataclasite with planar fabric between 72 and 74 cm shows a reverse sense of apparent shear in the core reference frame and very sharp contact with adjacent fragmented gabbro. **B.** Well-developed foliated cataclasite dipping 55° shows a reverse sense of apparent shear in the core reference frame (Sample 305-U1309D-152R-1, 5–18 cm). **C.** Steeply dipping (55°) cataclasite in gabbro (Sample 305-U1309D-152R-1, 32–43 cm). Apparent sense of shear is reverse in the core reference frame. **D.** Pale green fault gouge between 82.5 and 85 cm in medium-grained gabbro (Sample 305-U1309D-161R-1, 76–96 cm). Apparent sense of shear is reverse in the core reference frame. **E.** Steeply dipping light gray cataclasite between 65 and 75 cm in gabbro (Sample 305-U1309D-230R-2, 64–94 cm).

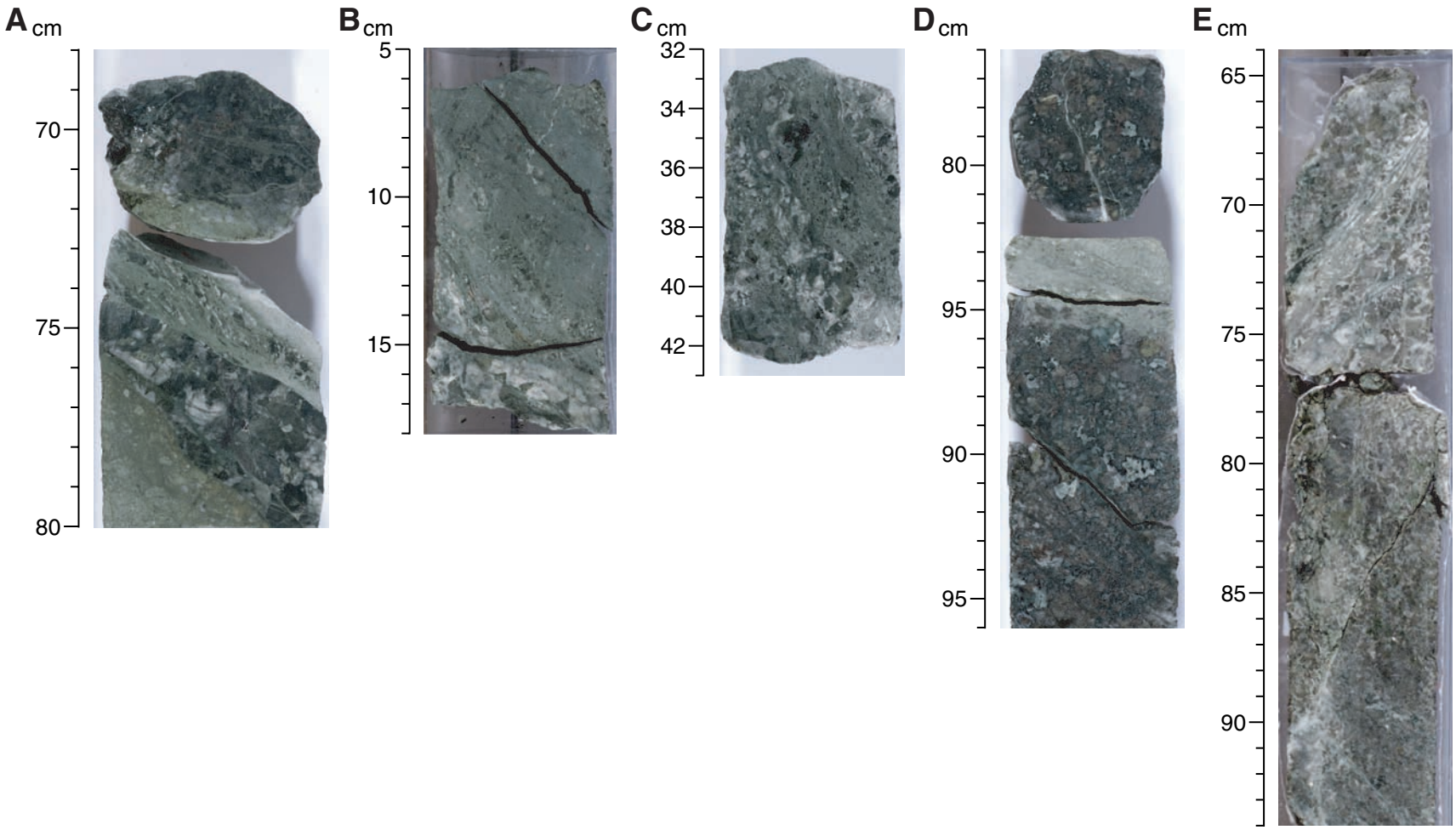

Figure F190. A. Well-developed foliated cataclasite showing apparent reverse sense displacement in the core reference frame (arrows) (Sample **305-U1309D-152R-1, 11–13 cm**) (plane-polarized light, field of view [FOV] = 2 cm). **B.** Same as A; cross-polarized light. Yellow box = location of C and D. **C.** Ultracataclasite (plane-polarized light; FOV = 5.5 mm). A relatively large plagioclase grain at top right corner shows intense microfractures with undulatory extinction. **D.** Same as C; cross-polarized light. Very fine grained fragments of plagioclase + ? are present in the chlorite matrix. **E.** Fractured clinopyroxene and plagioclase grains in carbonate matrix within fault breccia/cataclasite in the fault zone (Sample **305-U1309D-161R-1, 84–87 cm**) (plane-polarized light; FOV = 5.5 mm). **F.** Same as D; cross-polarized light.

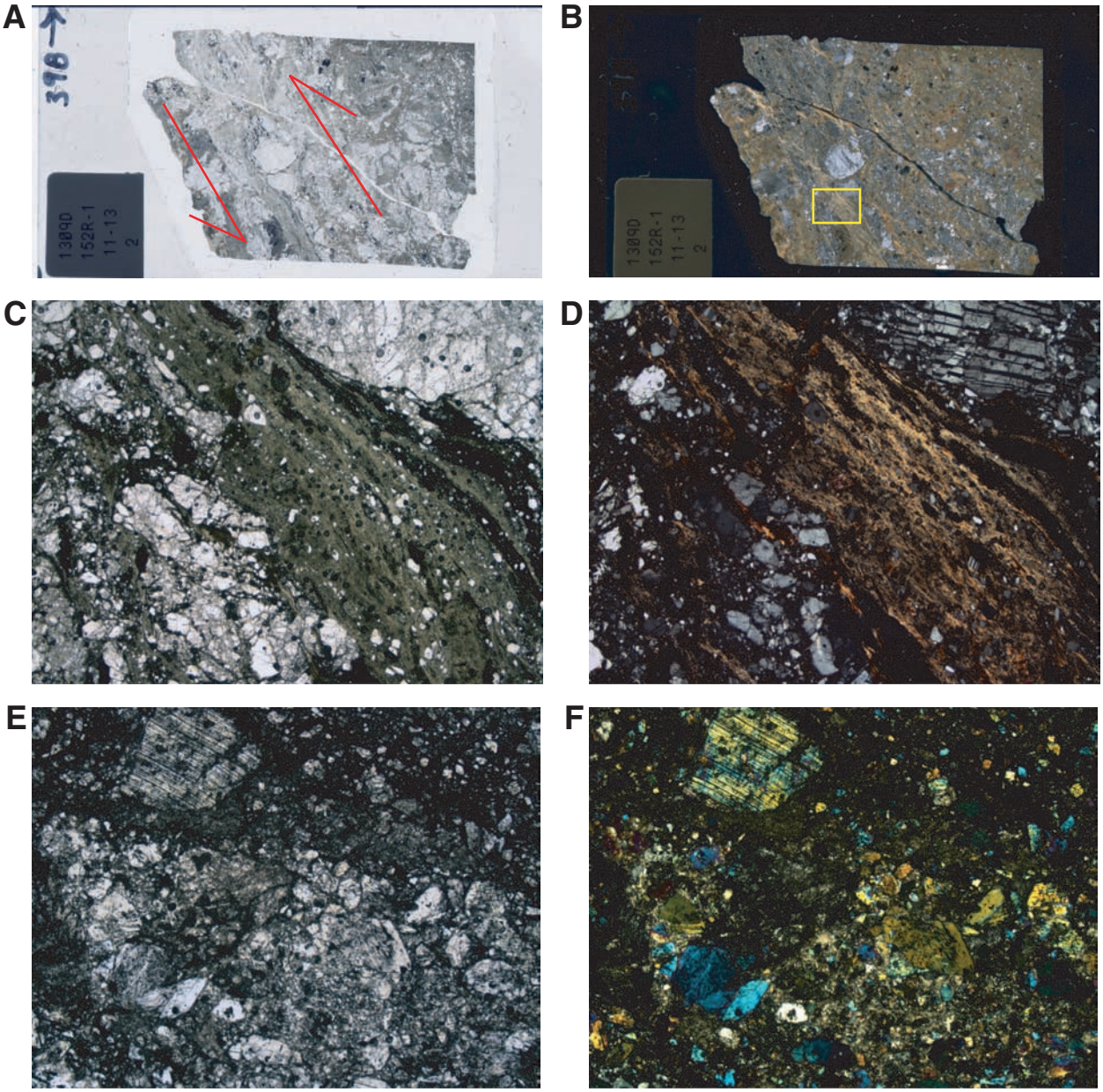

Figure F191. A. Diabase dikelet in brittlely deformed gabbro (interval 305-U1309D-184R-3, 47–57 cm). Yellow box = location of B and C. **B.** Chilled margin of diabase (Sample **305-U1309D-184R-3, 50–53 cm**) (plane-polarized light; field of view [FOV] = 2 cm). Minerals were fractured and fragmented along the margins of the dikelet. Yellow box = location of D. **C.** Same as B; cross-polarized light. Yellow box = location of E. **D.** Fragmented plagioclase grains with alteration mineral infilling (plane-polarized light; magnification = 2.5×). **E.** Same area as D; cross-polarized light.

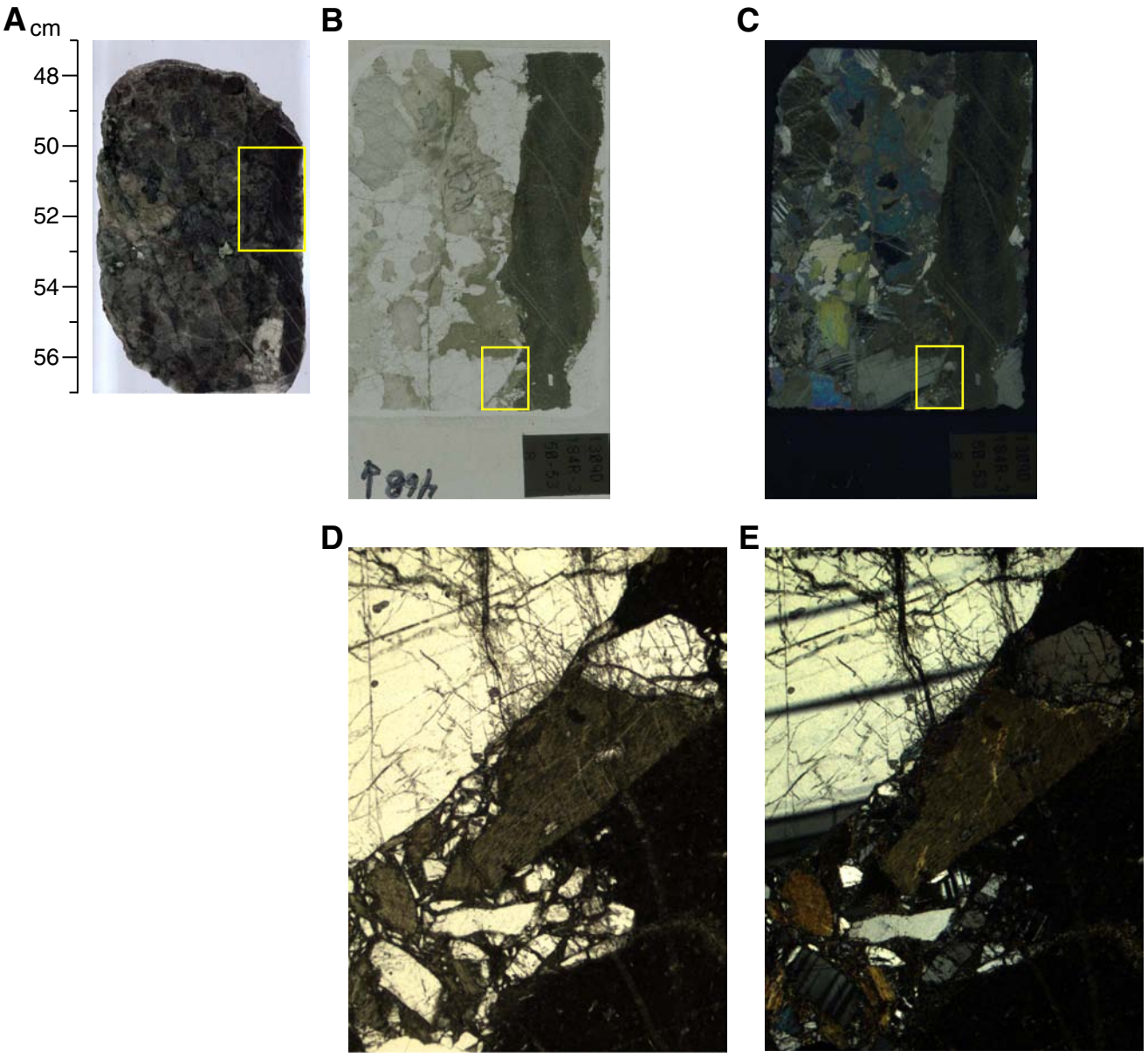

Figure F192. A. Weakly developed serpentine foliations dipping moderately in olivine gabbro (Sample 305-U1309D-90R-3, 3–18 cm). **B.** Olivine-rich troctolite with locally strong serpentinization foliation (Sample 305-U1309D-140R-2, 102–122 cm). Alteration veins crosscut the serpentine foliations, but some serpentine foliation also crosscuts the veins. Late, irregular, brittle veins occur with talc infills. **C.** Troctolite with intense serpentine foliation (Sample 305-U1309D-110R-4, 105–128 cm). Plagioclase grains show intense sets of microcracks subparallel to the adjacent serpentine foliation in olivine. (Continued on next page.)

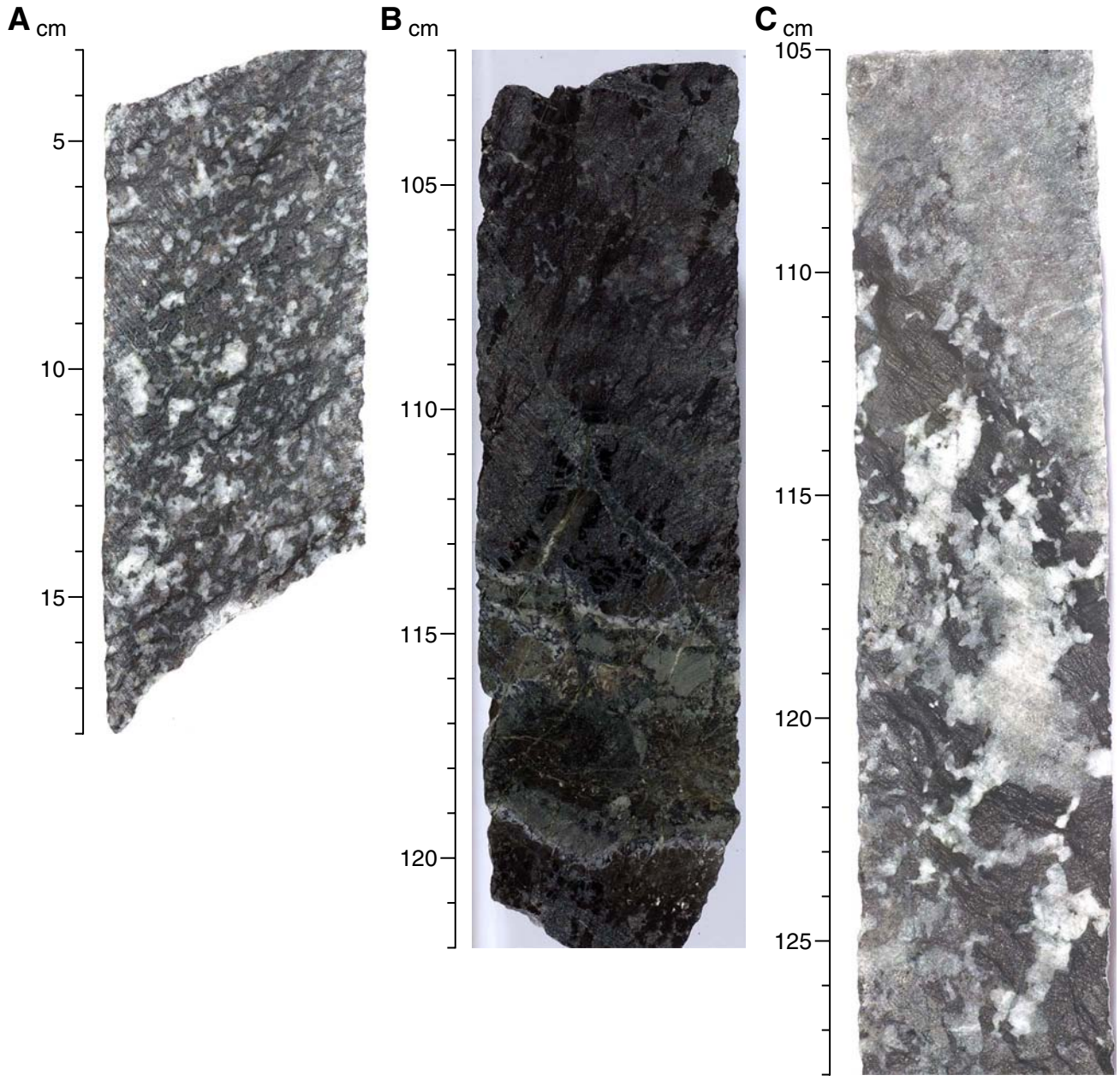

Figure F192 (continued). D. Troctolite with moderate intensity of serpentine foliation dipping steeply (Sample 305-U1309D-110R-3, 79–92 cm). Later fault veins with subhorizontal talc fibers are present subparallel to the serpentine foliation. **E.** Weak serpentine foliation dipping steeply in troctolite (Sample 305-U1309D-111R-4, 0–27 cm). Earlier thin magmatic veins are crosscut by the serpentine foliation. **F.** Steeply dipping serpentine foliation in troctolite, crosscutting earlier magmatic veins (Sample 305-U1309D-112R-2, 53–71 cm).

Figure F193. A. Intensely serpentinized zone in olivine-rich troctolite (Sample **305-U1309D-100R-1, 26–28 cm**) (cross-polarized light; field of view [FOV] = 2 cm). **B.** Serpentine foliation in very large olivine grain within leucocratic troctolite (Sample **305-U1309D-110R-1, 104–107 cm**) (cross-polarized light; FOV = 2 cm). **C.** Moderately developed serpentine foliations in troctolite (Sample **305-U1309D-110R-3, 89–91 cm**) (plane-polarized light; FOV = 2 cm). **D.** Serpentine foliation in troctolite (Sample **305-U1309D-110R-3, 90–91 cm**) (plane-polarized light; FOV = 5.5 mm). Intense microfractures in plagioclase grains are subparallel to the serpentine foliation in adjacent olivine grains. **E.** Same as D; cross-polarized light.

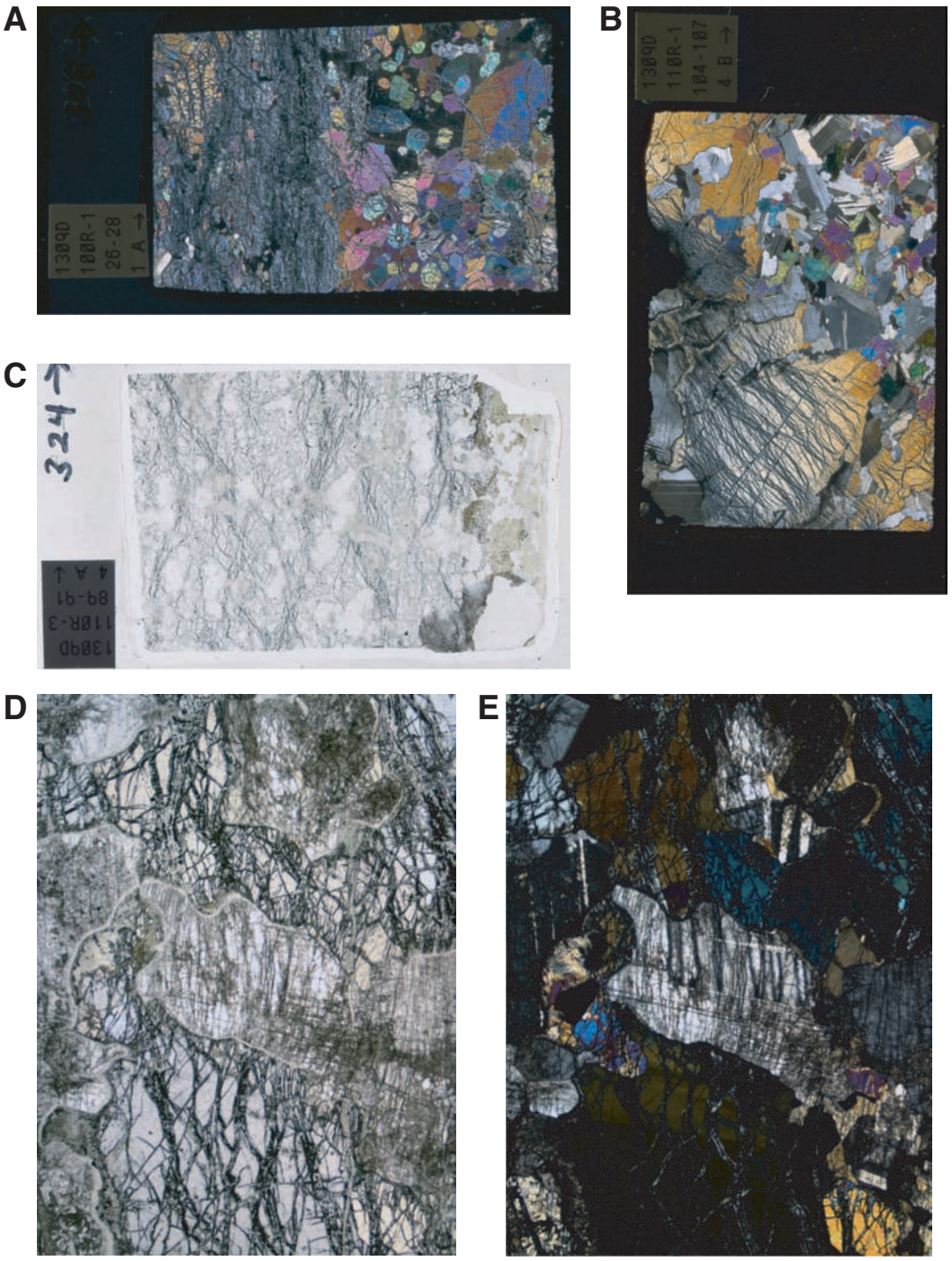

Figure F194. Absolute intensity of cataclastic fabrics in Holes (**A**) U1309B and (**B**) U1309D to 132 mbsf plotted with orientation data (north strike is vertical for strike/dip symbols) of intense cataclastic zones. Diabase is highlighted (beige) across the figures to depict the decrease in intensity in those intervals. Dotted lines = locations of faults inferred based on cataclastic fabrics.

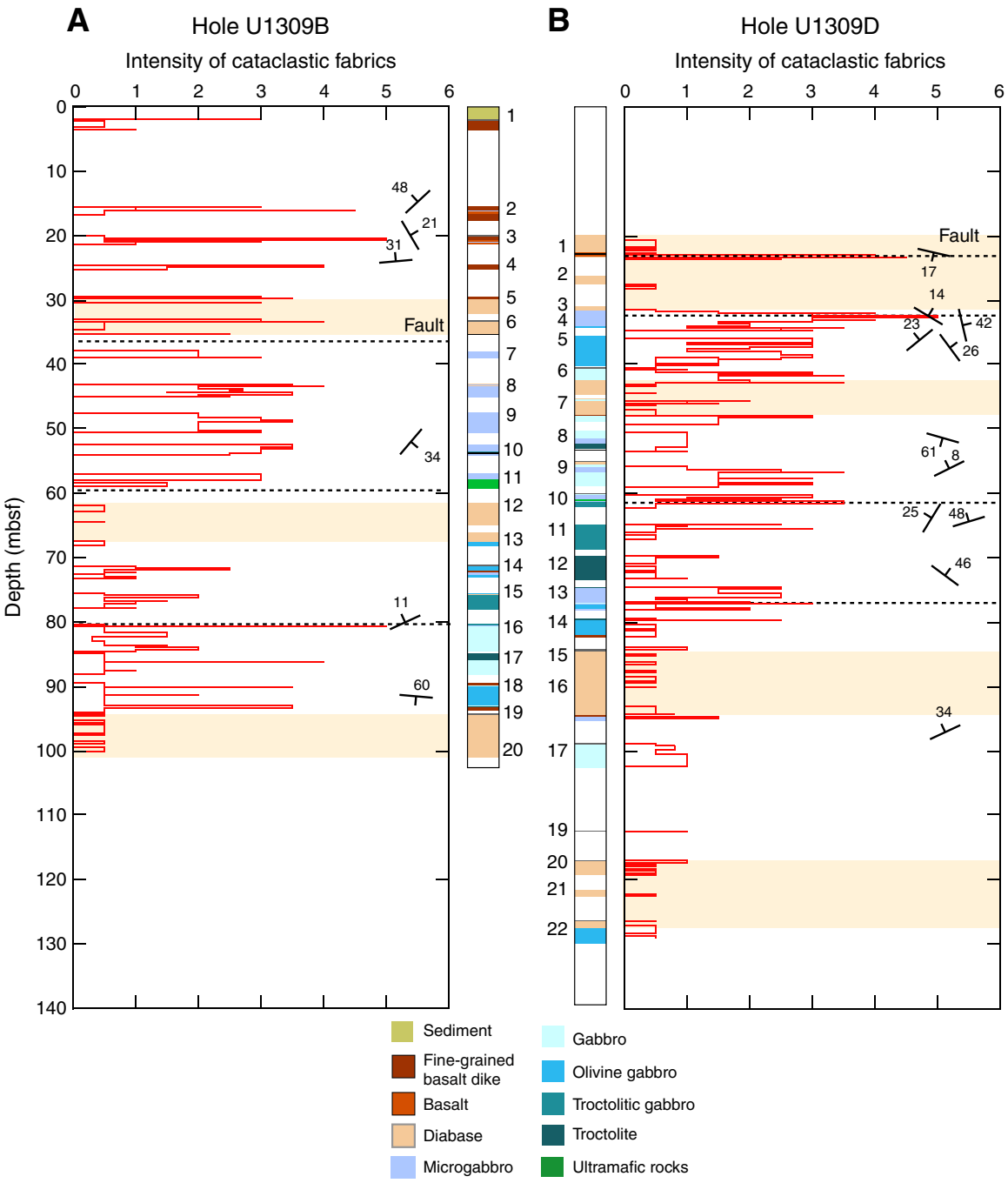

Figure F195. Dip magnitude of cataclastic fabrics and type distribution of cataclastic zones in Holes (**A**) U1309B and (**B**) U1309D to 132 mbsf. Diabase is highlighted (beige) across the figures to illustrate the lack of cataclastic deformation intensity within those intervals. Dotted lines = locations of inferred faults based on cataclastic fabrics or lack of recovery in core.

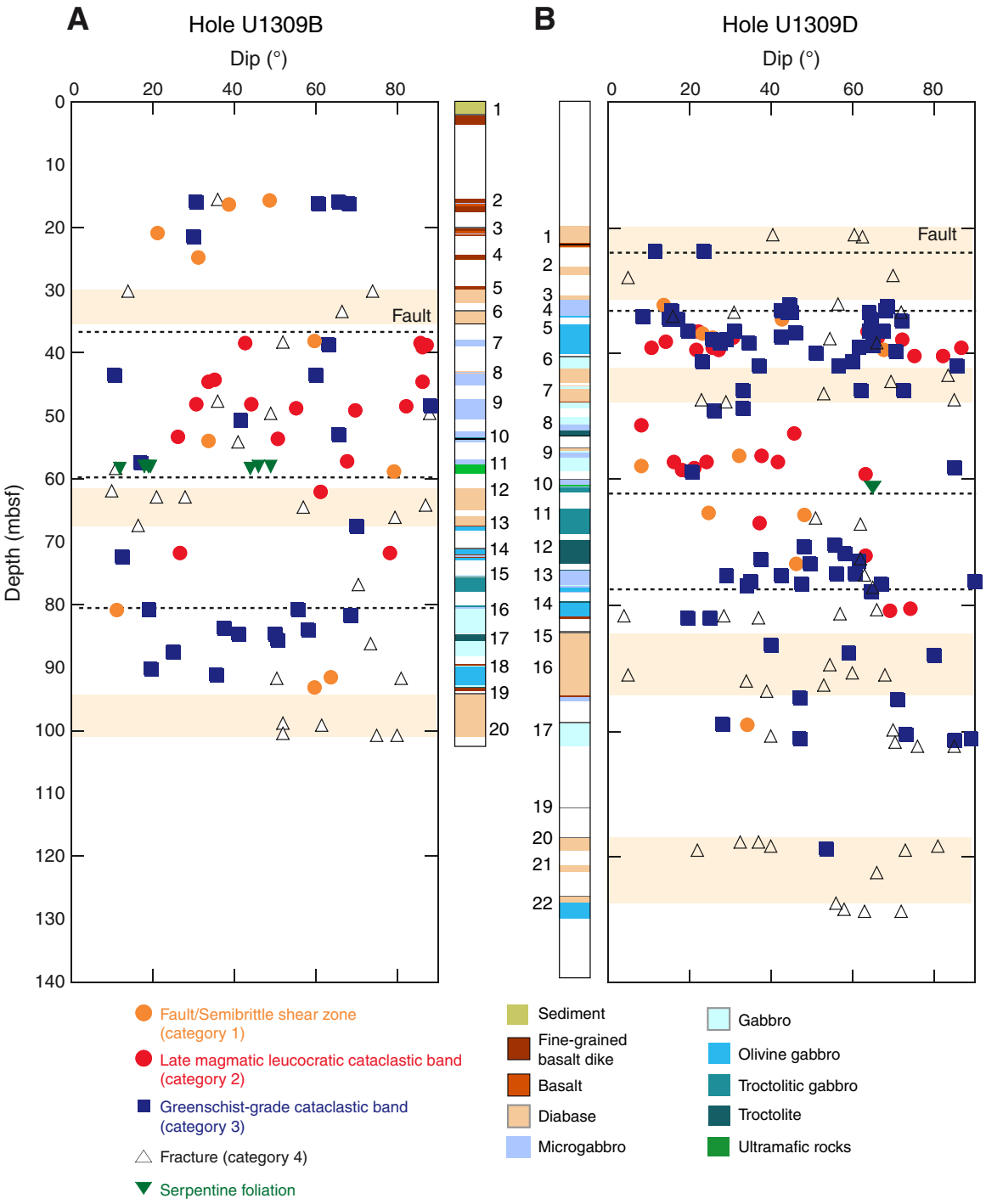

Figure F196. Downhole plots showing (**A**, **C**) dip magnitude of cataclastic fabrics and (**B**) rake of slickenlines observed on low-temperature fault veins. Dotted lines = locations of faults inferred based on cataclastic fabrics, or lack of recovery in core.

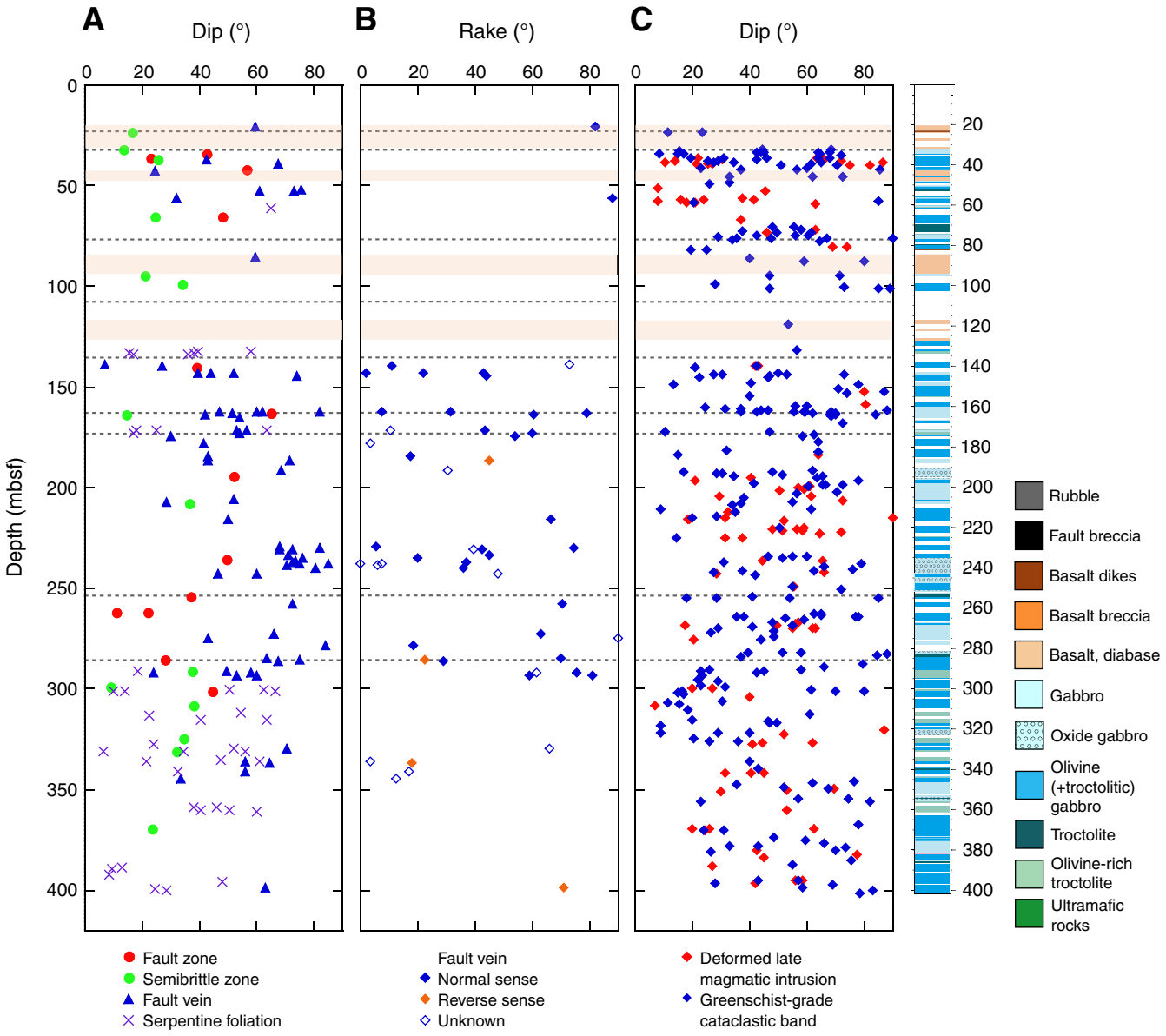

Figure F197. A. Average cataclastic and veining intensity in Hole U1309D (5 m average from Fig. F182). **B.** Dip of dark green fault veins, with indication of measured plunges. **C.** Dip of pale green fault veins, with indication of measured plunges. The column on the right corresponds to lithostratigraphy in Hole U1309D.

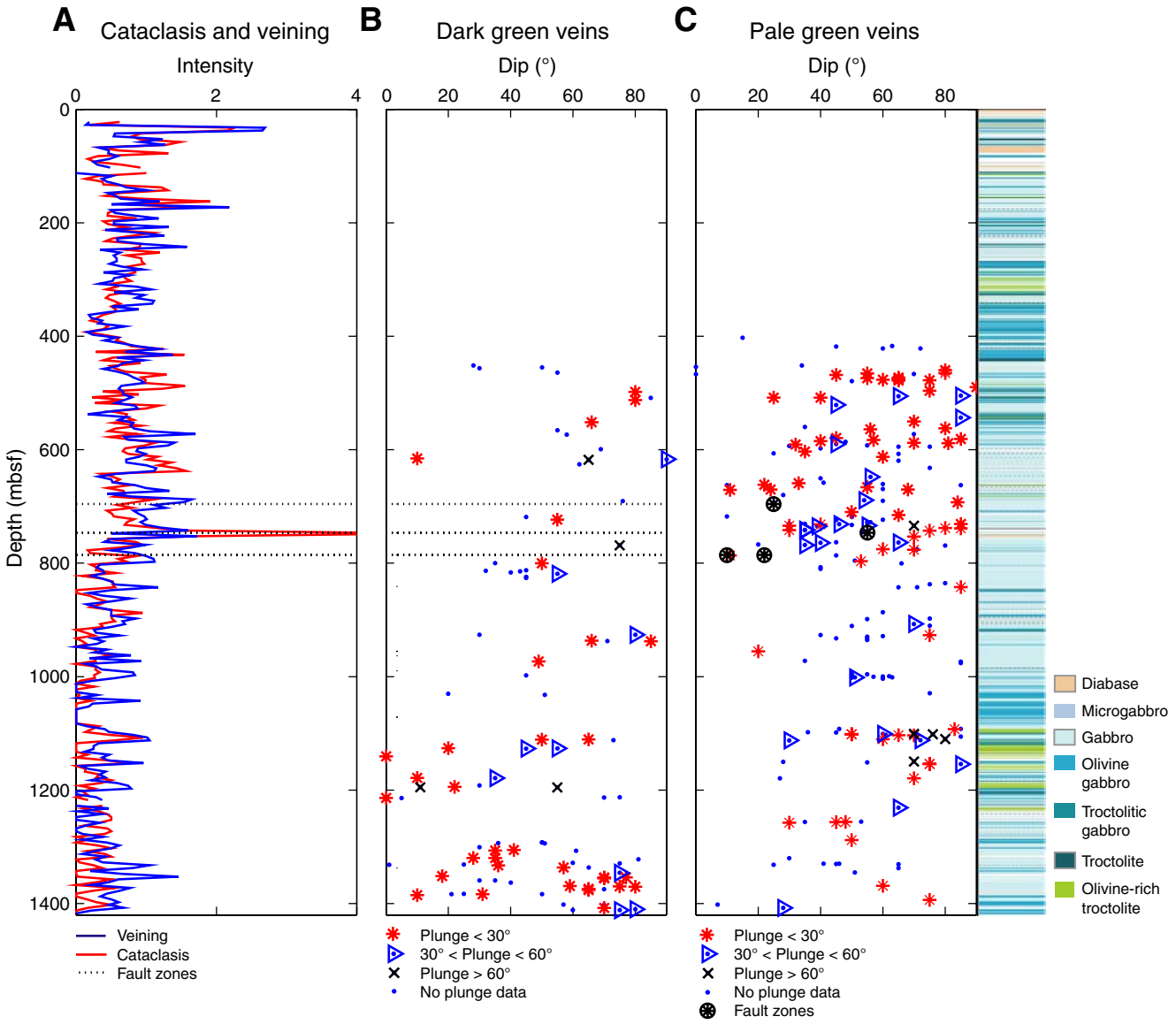

Figure F198. **A.** Variation of percent rock recovery. **B.** Variation of open crack intensity. **C.** Drilling-induced fractures, estimated from core observations in Hole U1309D. The column on the right corresponds to lithostratigraphy in Hole U1309D. SD = standard deviation.

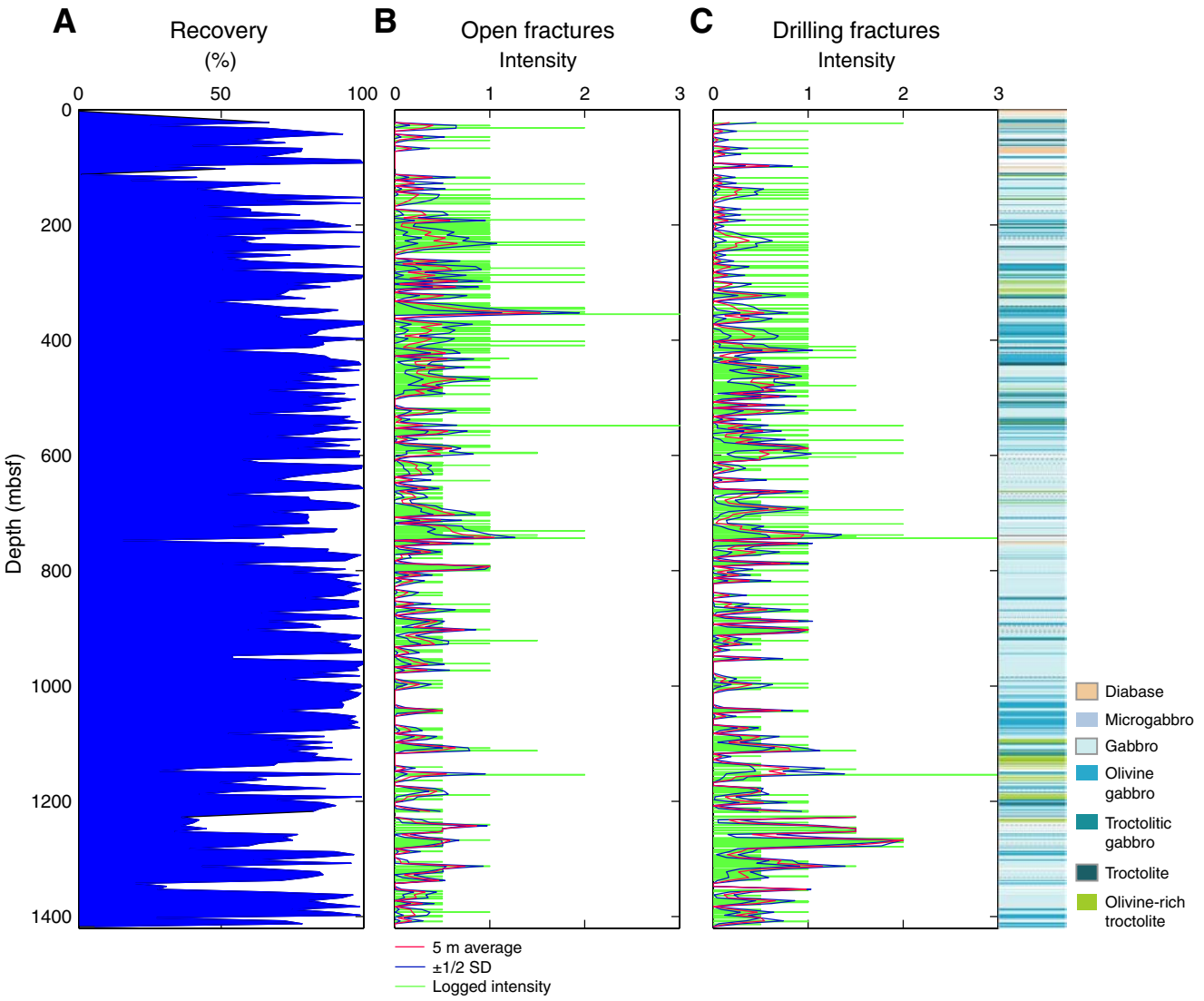

Figure F199. A. Variation of serpentine foliation intensity. **B.** Dip of serpentine foliation. 5 m average is indicated by the thick blue line. Thin green lines correspond to the mean half standard deviation (SD) for each 5 m interval. The column on the right corresponds to lithostratigraphy in Hole U1309D. Triangles indicate the presence of serpentinite foliation for which no measurement was possible.

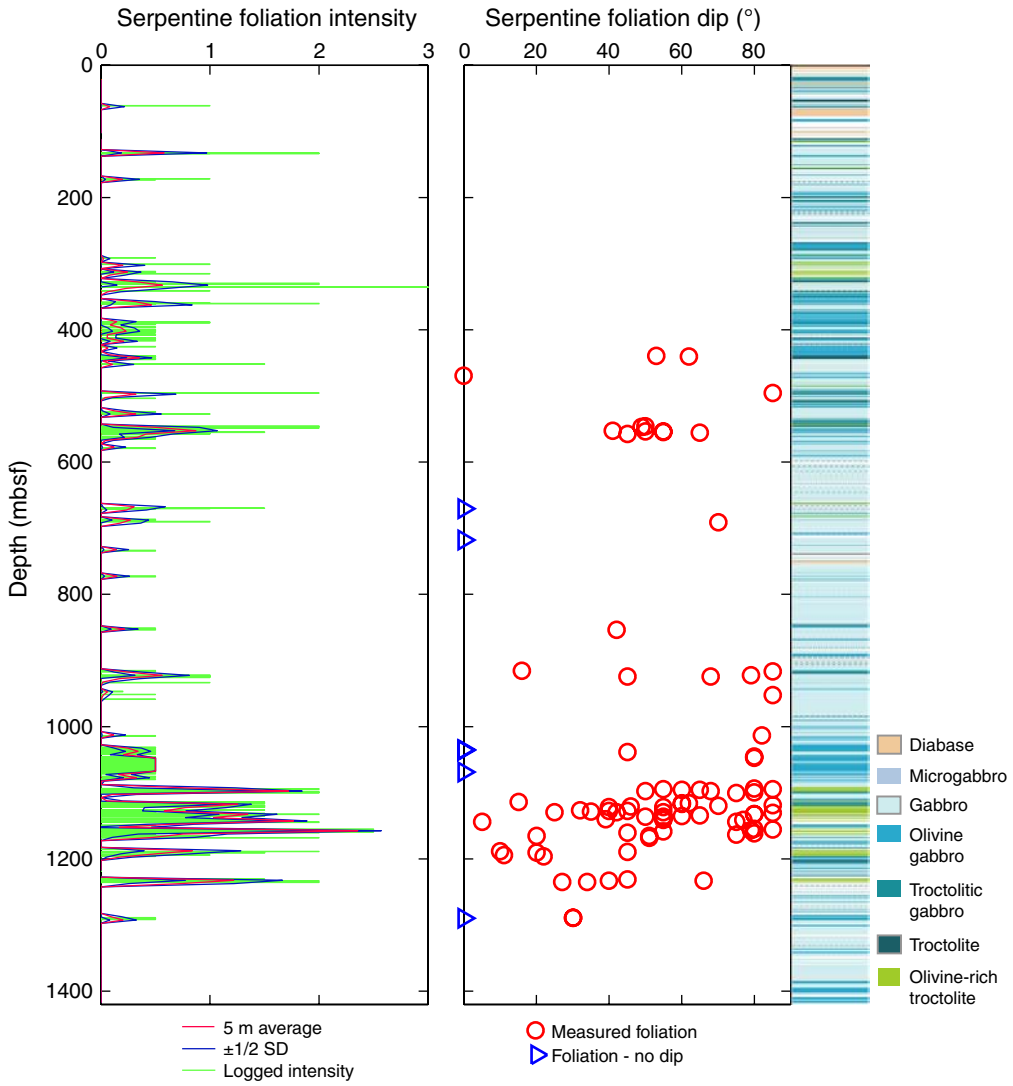

Figure F200. Variation in cataclastic intensity with rock type. **A.** Hole U1309B. **B.** Hole U1309D logged during Expedition 304 (to ~400 mbsf).

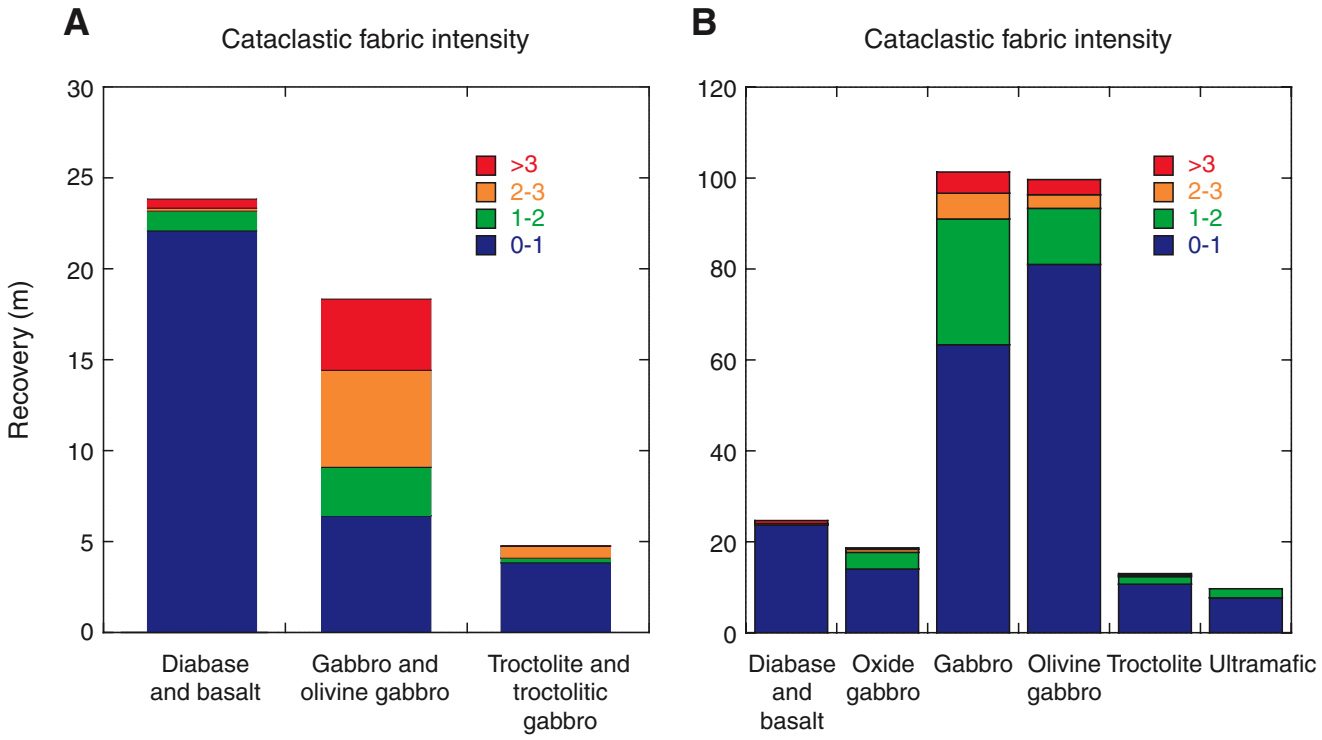

Figure F201. Variations in logged cataclastic intensity as a function of lithology for the core recovered during Expedition 305 (Hole U1309D, ~400–1415 mbsf).

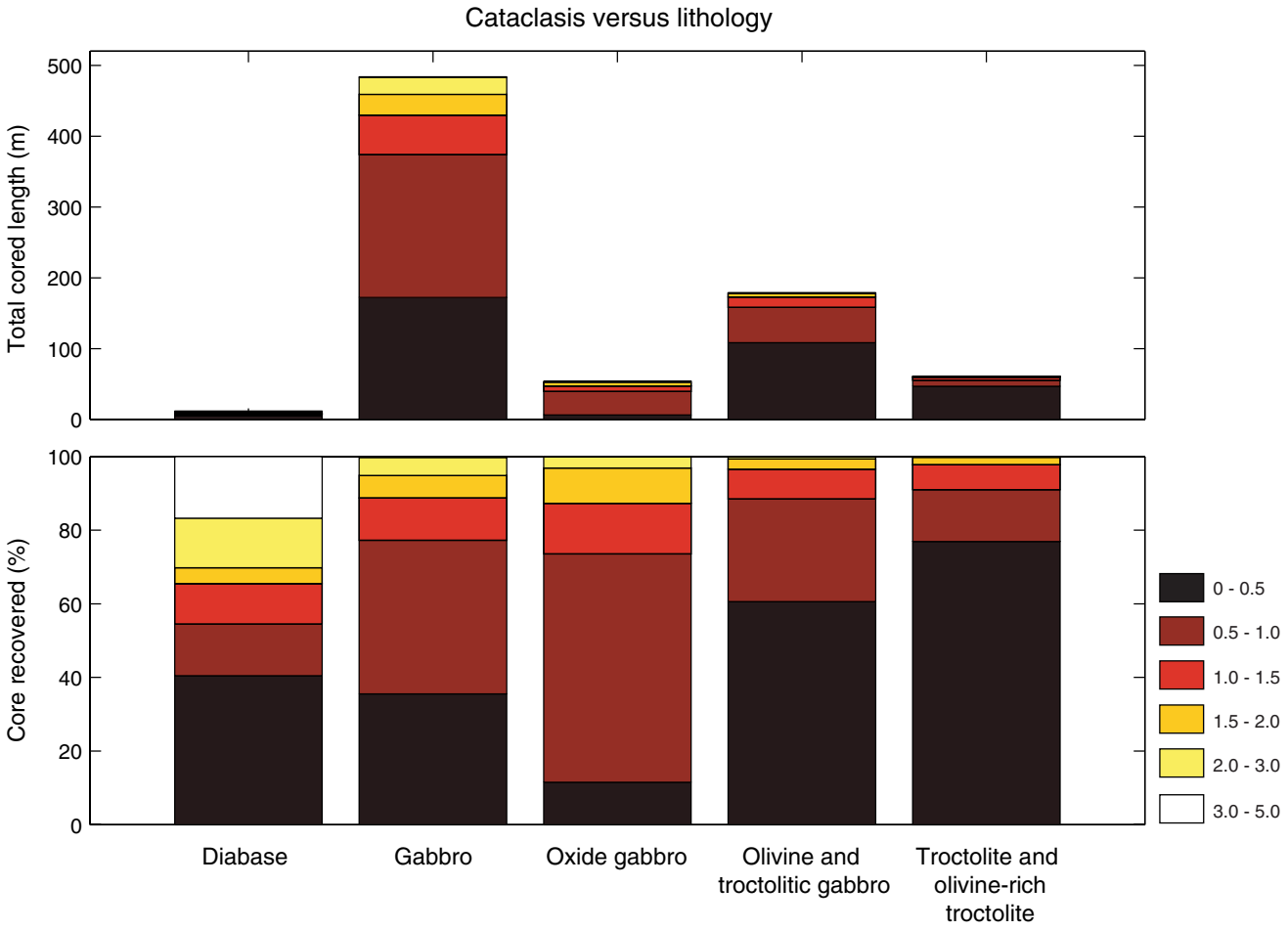

Figure F202. A. Cataclastic fabric intensity averaged over 5 m intervals. Green lines indicate faults inferred on the basis of structural observations of the core. **B.** Fault zones inferred from borehole resistivity and porosity data. Confidence in fault identification is shown on the horizontal axis.

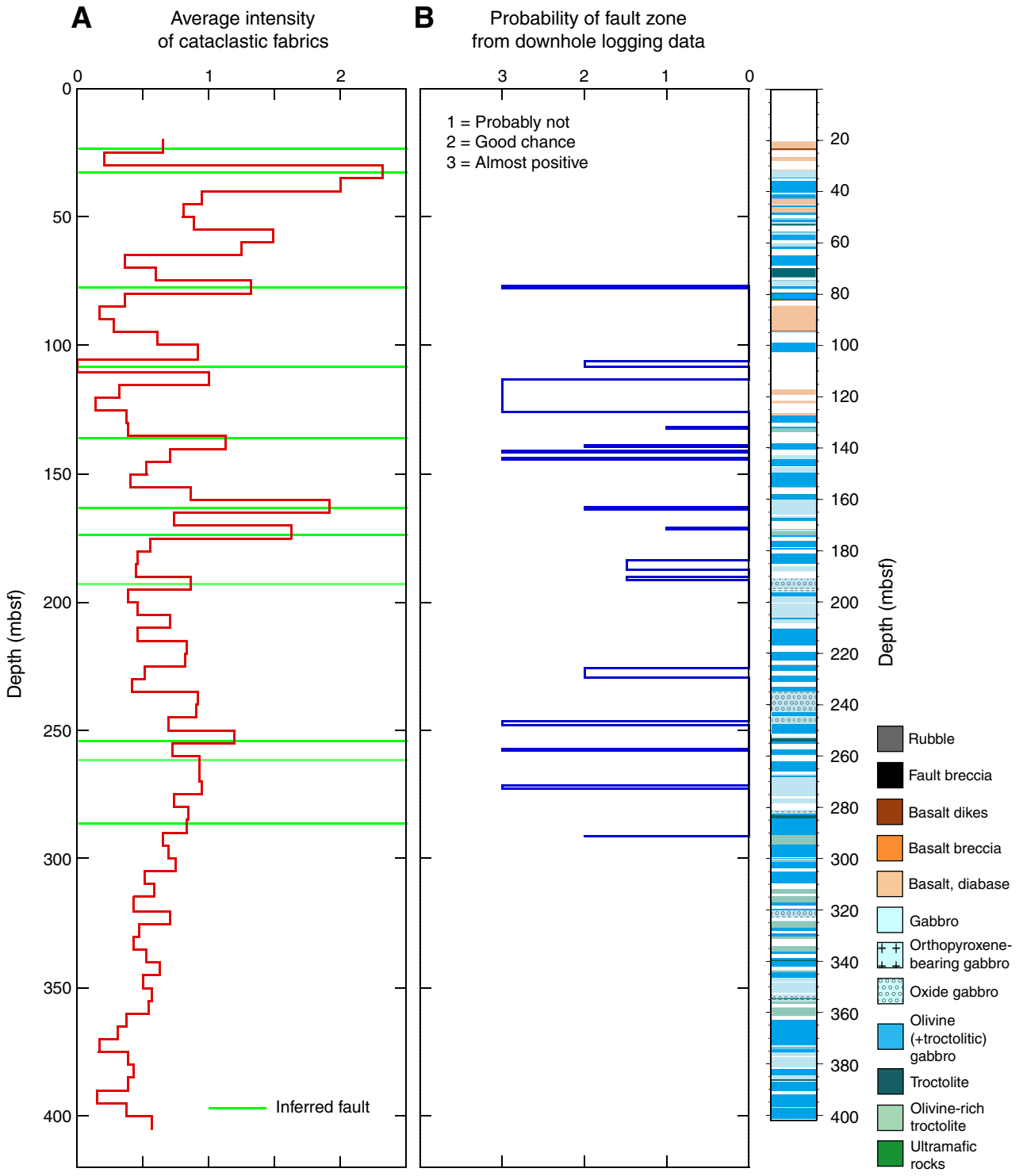

Figure F203. Downhole remanence inclination in Hole U1309D (see **"Paleomagnetism"** for detailed explanations). Column 1 shows average remanent inclinations from archive-half pieces and discrete sample data. Archive-half data represent the highest stability magnetization component (isolated at alternating-field treatments >30–40 mT). For core pieces with multiple measurements, only average inclinations with CSD angles <5° are shown. For discrete samples and core pieces with only a single measurement (open circles), only data with MAD angles <5° are plotted. Column 2 shows expanded version of data in Column 1. Vertical red bar indicates the expected reversed polarity inclination at the site. Five inclination groups (labeled I–V) have been identified based on the inclination data and structural features. Column 3 shows lower stability (typically 20–40 mT) magnetization components from archive-half pieces where no well-defined high-stability magnetization component could be isolated. Selection criteria for piece averages are the same as for data in Column 1. Note that the data in Column 3 are mutually exclusive with data in Column 2 (i.e., only a single magnetization component is plotted for any core piece). Data from Expedition 305 were reprocessed during the first postcruise meeting to ensure compatibility with Expedition 304 data.

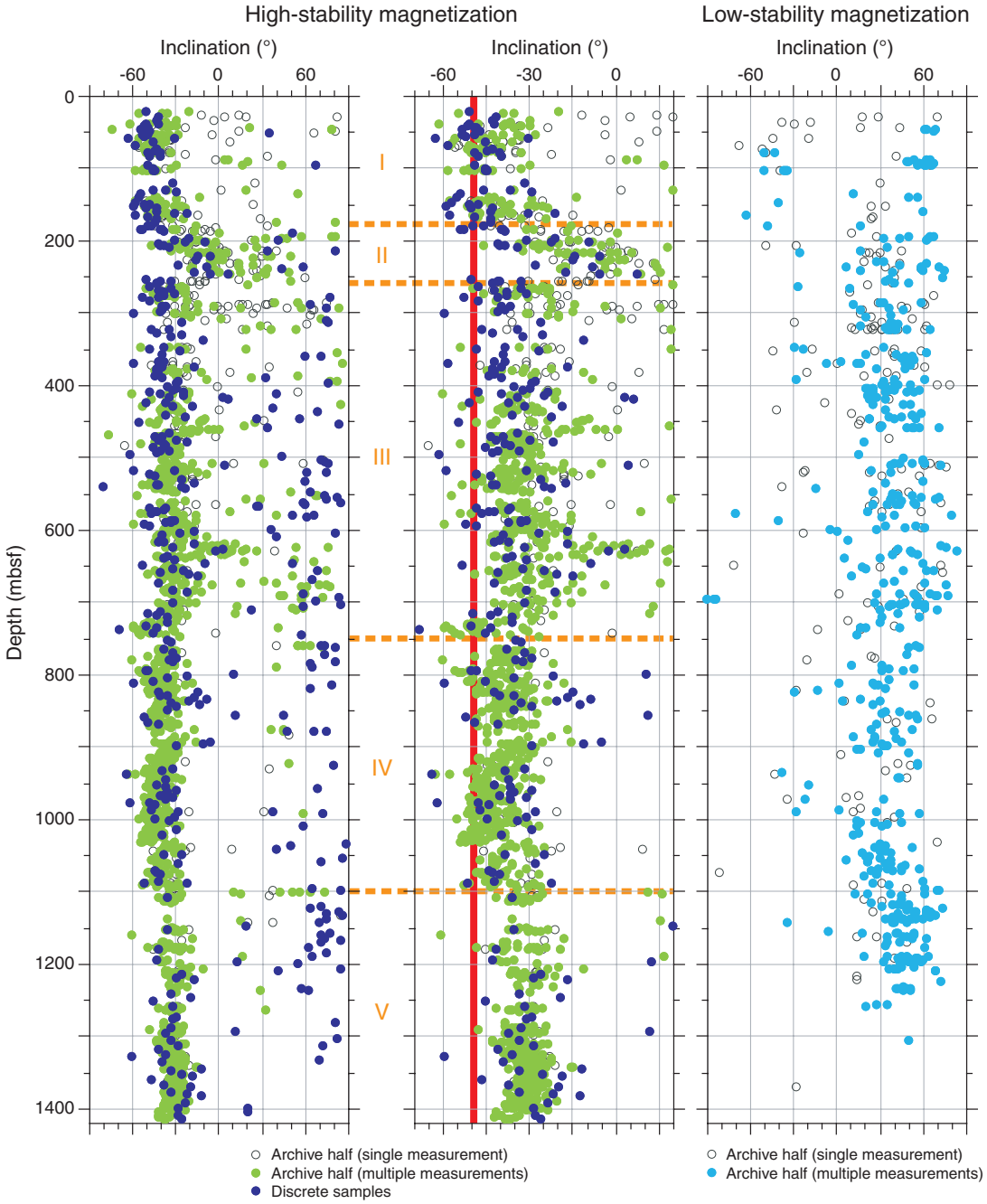

Figure F204. Remanence inclinations for Site U1309 for the inclination groups shown in Figure F203 (see also "Paleomagnetism"). Selection criteria for archive half core pieces are the same as in Figure F203 but include core pieces with a single measurement. High-stability (green) and low-stability (blue) magnetization components correspond to those shown in Figure F203. Discrete sample inclinations are shown only for samples with MAD angles <5°. Note that discrete sample data for inclination Group I include results from Hole U1309B. The mean inclinations (using the inclination only method of McFadden and Reid, 1982) for each group are based only on samples with negative inclinations.

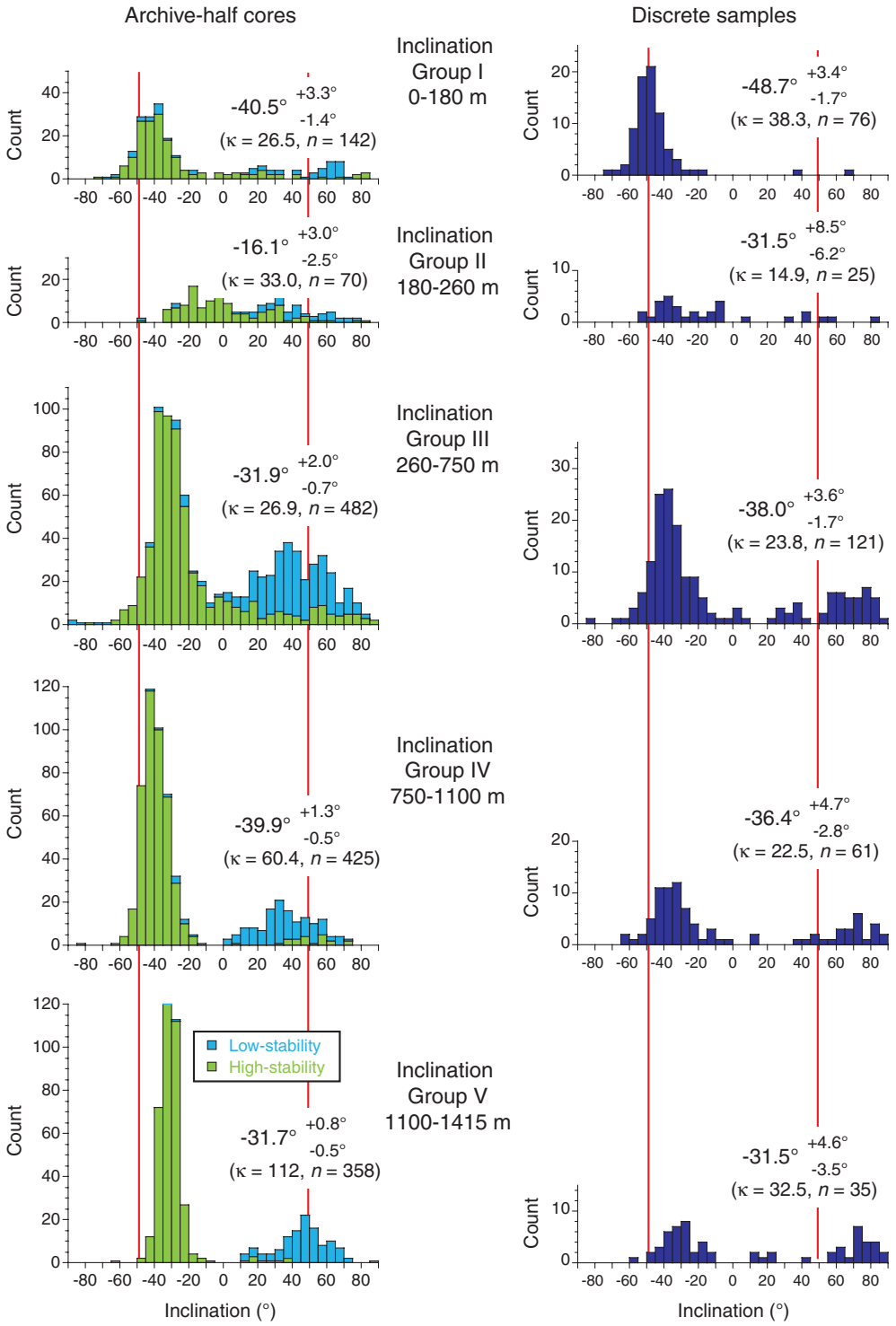

Figure F205. Lower hemisphere, equal area stereoprojections of poles to crystal-plastic and magmatic fabrics in a paleomagnetic (PMAG) reference frame for Holes (**A**) U1309B and (**B**) U1309D to 132 mbsf.

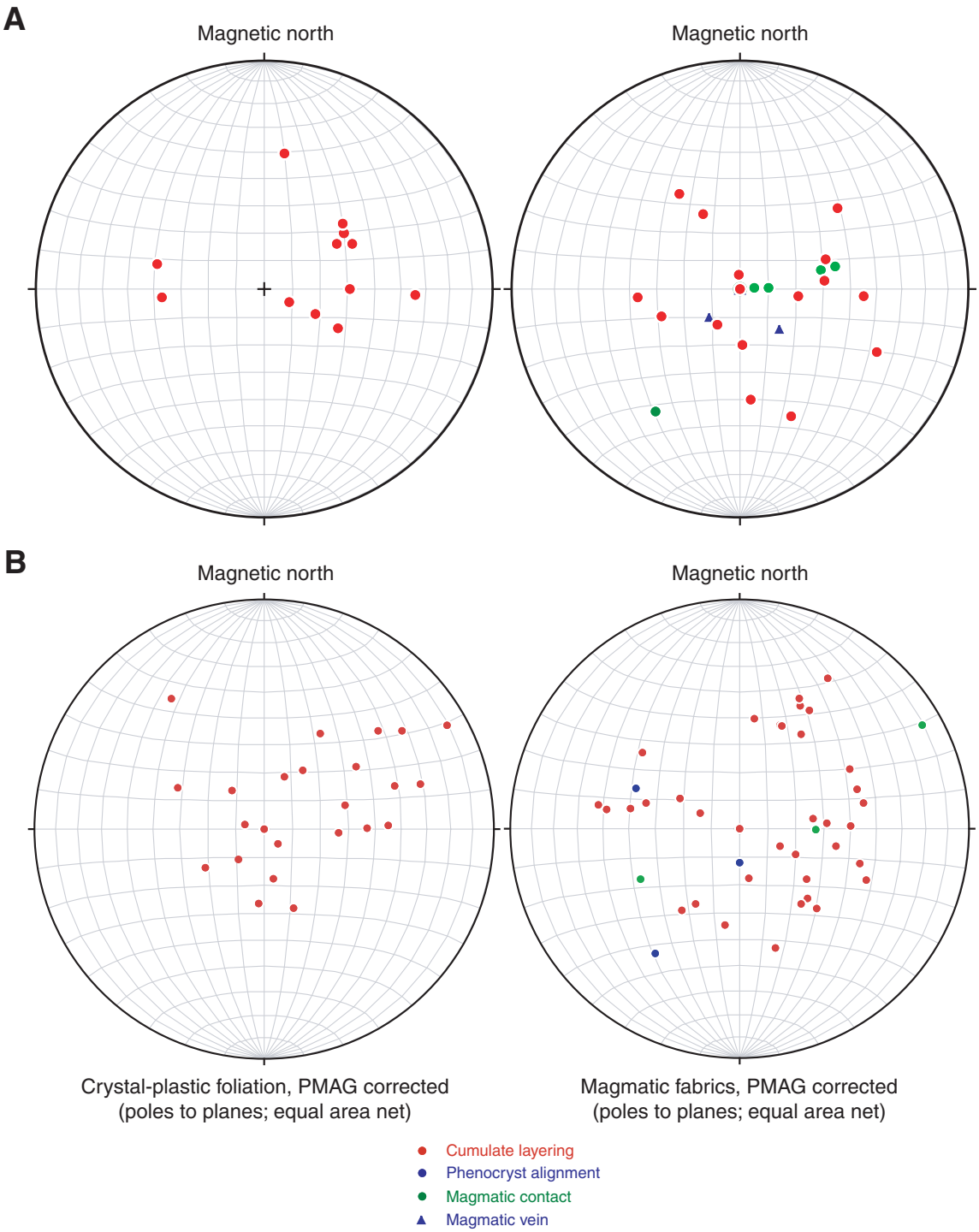

Figure F206. A. Lower hemisphere, equal area stereonet projection of orientations (poles to the planes) for all vein types observed in Holes U1309B and U1309D to 132 mbsf. Orientations have all been rotated to a common paleomagnetic reference frame. **B.** Stereonet plots comparing orientations of the three prominent vein types observed in Hole U1309B and the upper 130 mbsf of U1309D.

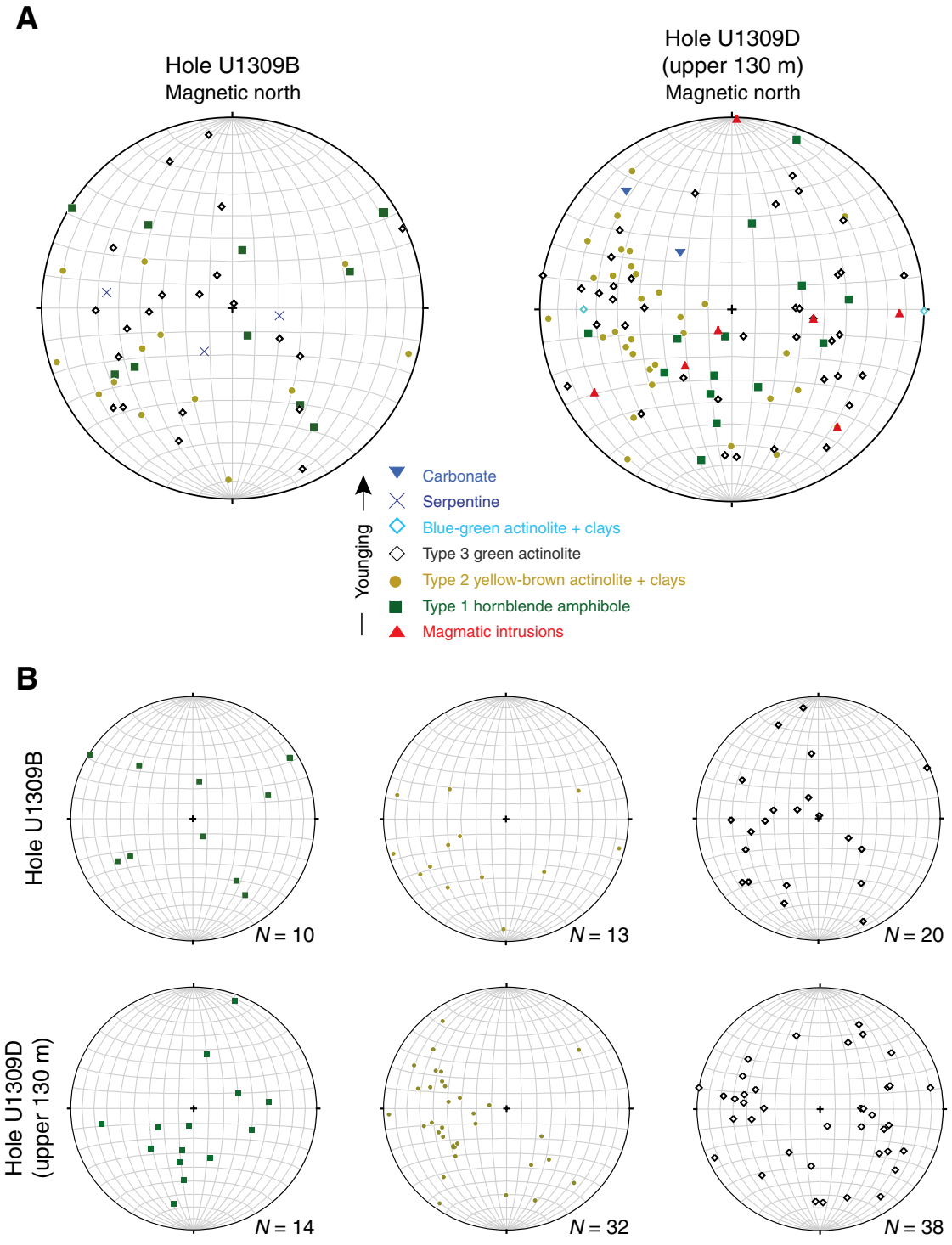

Figure F207. Lower hemisphere stereonet (equal area net) projections in a paleomagnetic reference frame. **A.** Orientations for Type 2 alteration veins observed from deeper than 50 mbsf in Hole U1309B. **B.** Orientations of Type 2 alteration veins observed between 50 and 80 mbsf in Hole U1309D. This subset of Figure F206 shows a clear preferred orientation, indicating more homogeneous stress in these intervals.

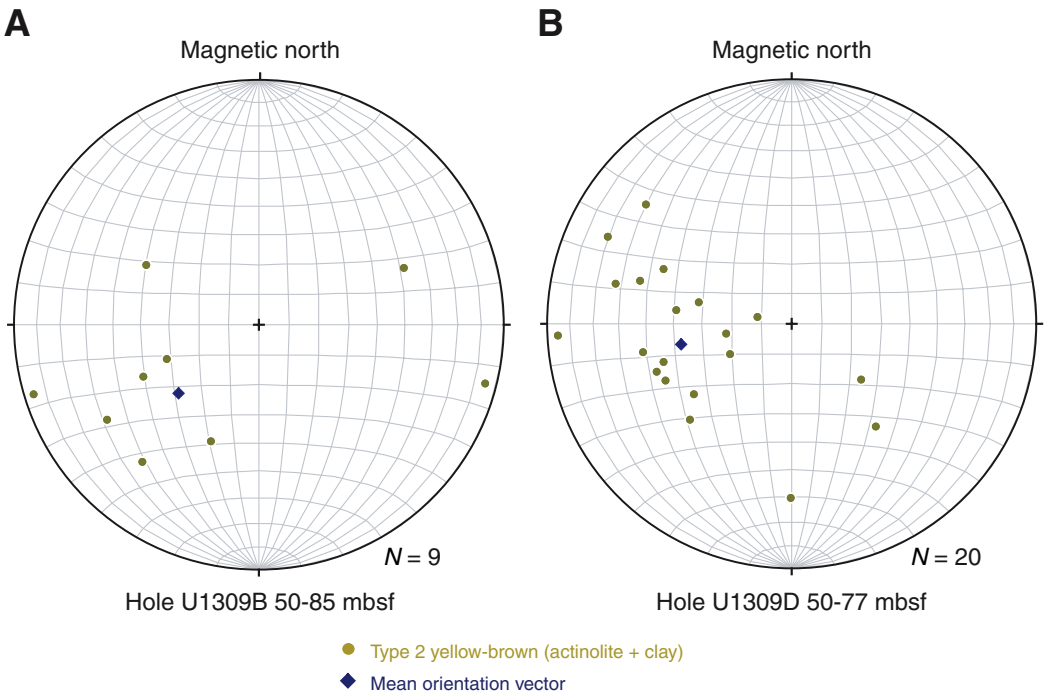

Figure F208. Lower hemisphere stereonet (equal area net) projections of orientations (poles to the planes) in Holes U1309B and U1309D to 132 mbsf. **A.** Cataclastic zones. **B.** Late-magmatic leucocratic cataclastic bands. **C.** Greenschist-grade cataclastic bands. **D.** Serpentine foliation. Orientations have all been rotated to a common paleomagnetic reference frame. Numbers are fault depths.

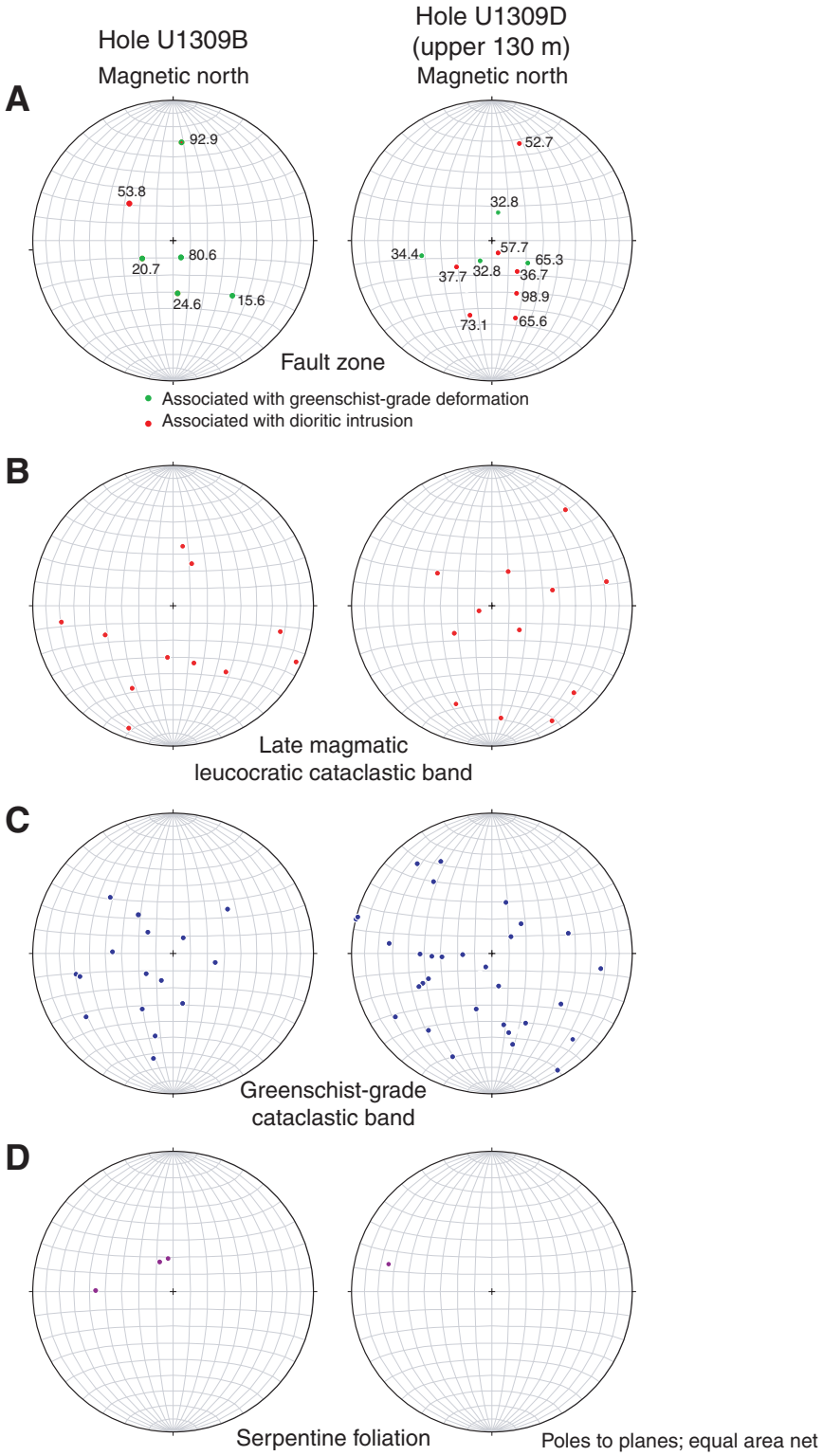

Figure F209. Downhole plots showing 5 m averaged intensities in Hole U1309D to 400 mbsf (Expedition 304). **A.** Magmatic fabrics. **B.** Crystal-plastic fabrics. **C.** Alteration veins. **D.** Cataclastic fabrics. Distribution of selected vein types is shown by solid bars adjacent to the lithologic column. Structural unit boundary (and subboundary) is indicated by solid red (and pink) line.

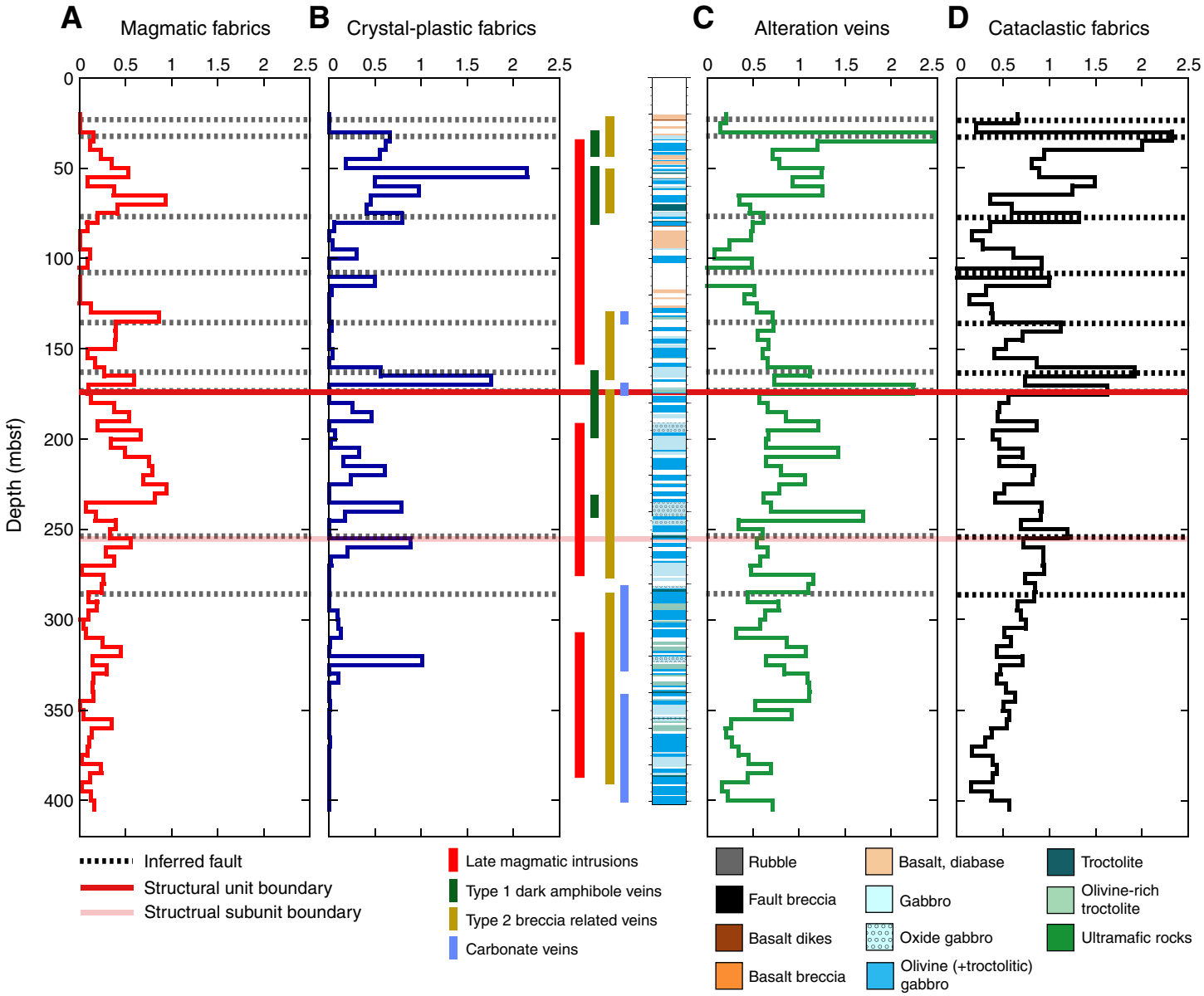

Figure F210. Same as Figure F209, with the addition of paleomagnetic inclination data measured on half cores.

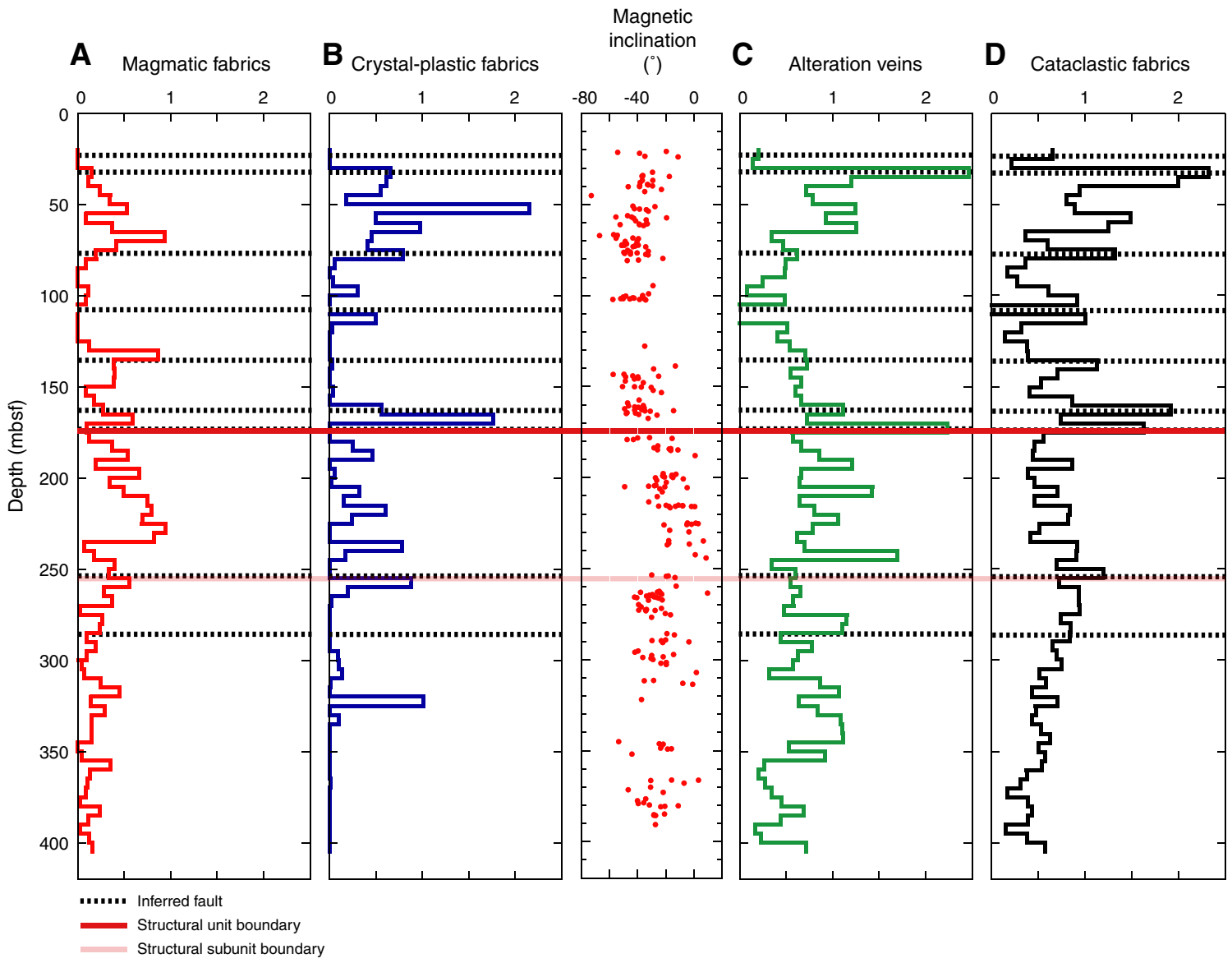

Figure F211. Summary of magmatic and structural trends in Hole U1309D. The top boundary of the middle magmatic unit (~600–1080 mbsf) is defined by magmatically strained troctolites, and the upper half of the unit contains common noritic gabbro and more abundant oxide gabbro (D). In this part of the unit, plastic strain culminates in plastic strain shear zones (660 mbsf). The lower part of the unit displays better magmatic strain, and the lower boundary is marked by the top of olivine-rich troctolites (F). An association of plastic strain shear zones and oxide gabbros similar to that at 660 mbsf occurs at ~1300 mbsf (G), possibly the top of another magmatic unit. Magmatic units are not clearly related to the structural units (see **"Definition of structural units"**). Structural Unit 1 seems to be associated with the suspected detachment fault exposed at the surface and is marked by talc-tremolite schist (A), abundant late, relatively undeformed diabase, high intensity of greenschist-grade alteration, and near present-day paleomagnetic inclination orientation. Recovered core shows pervasive static alteration and largely unmodified pseudomorphs of igneous textures. The Unit 1/Unit 2 boundary is marked by a low to moderately dipping crystal-plastic shear zone within gabbroic rocks, high veining intensity, strong cataclasis (B), and a ~2 m thick interval of altered ultramafic rocks including mantle harzburgite. Structural Unit 2 is marked by a high intensity of veining including sulfides, paleomagnetic inclinations that are 10°–30° shallower than present-day values, and varied lithology. The base of Unit 2 is defined by a decrease in whole-rock Mg# of gabbros and a series of greenschist-grade cataclastic fault zones (C) below which there is an abrupt decrease in the intensity of veining and cataclastic deformation. Structural Unit 3 is characterized by overall low intensity of cataclastic deformation, veining, and plastic deformation. (Continued on next page.)

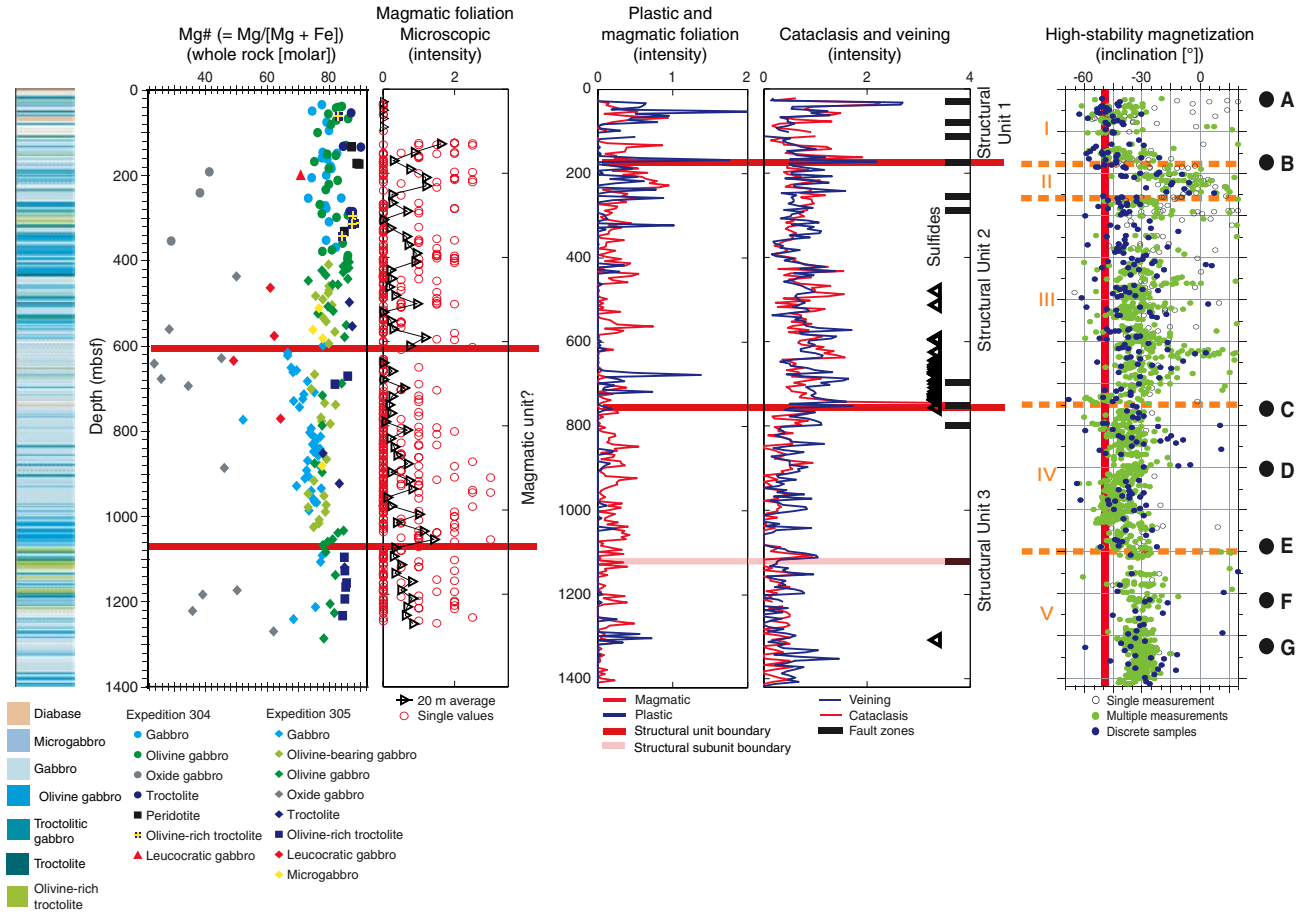

F211 (continued). Magmatic and structural features. **A.** Talc-tremolite schist in structural Unit 1 (304-U1309D-1R-3; 26 mbsf). **B.** Strong cataclasis in structural Unit 2 (304-U1309D-31R-2; 171 mbsf. **C.** Greenschist-grade cataclastic fault zones near the base of structural Unit 2 (304-U1309D-152R-1; 746 mbsf). **D.** Oxide gabbro abundant in the topmost part of the magmatic unit (304-U1309D-183R-2; 893 mbsf). **E.** Magmatic strain in the lower part of the magmatic unit (305-U1309D-222R-2; 1072 mbsf). **F.** Olivine-rich troctolites at the lower boundary of the magmatic unit (305-U1309D-248R-2; 1195 mbsf). **G.** Plastic strain shear zones and oxide gabbros that may mark the top of another magmatic unit (305-U1309D-270R-3; 1304 mbsf).

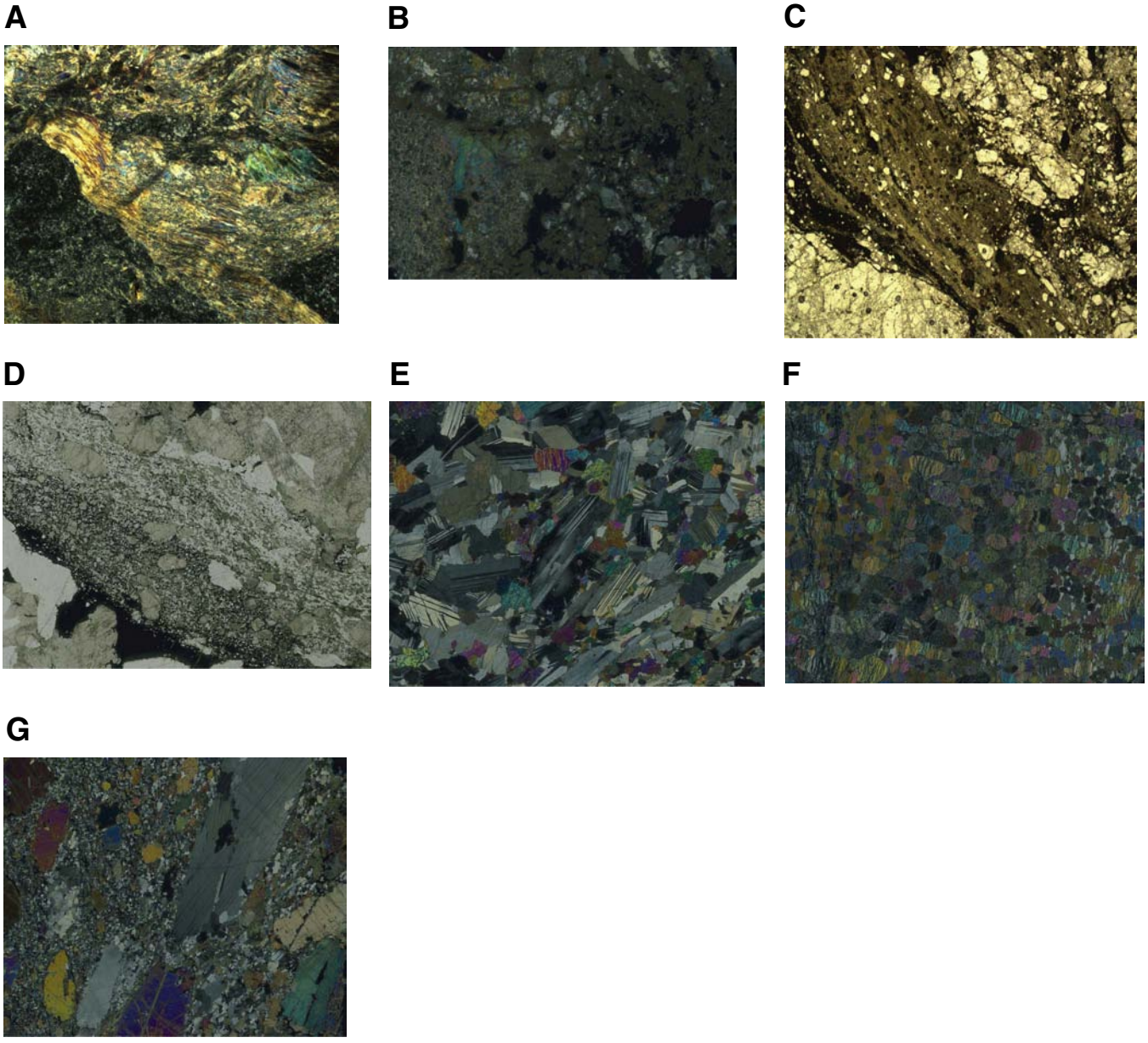

Figure F212. Structures recovered from Hole U1309B and the upper part of Hole U1309D and possible correlations. The tick marks on the inside margins of the lithology columns are qualitative projections of representative measurements onto the north-south section; red = phenocryst alignment, blue = crystal-plastic structures, black = brittle structures. Distribution of veins is shown schematically within the lithologic column, as are the other structures. The trace of the fault from Core 304-U1309B-16R and the dips of diabase units are inferred from the logging data and lithologic correlations, although there are other possible interpretations (indicated by dashed lines and question marks). The structural units are designated based upon changes in deformation intensity, and some faults are inferred at the unit boundaries. Specific observations relating to the ultramafic rocks and gabbro/troctolite contacts are schematic and keyed to the lithology columns.

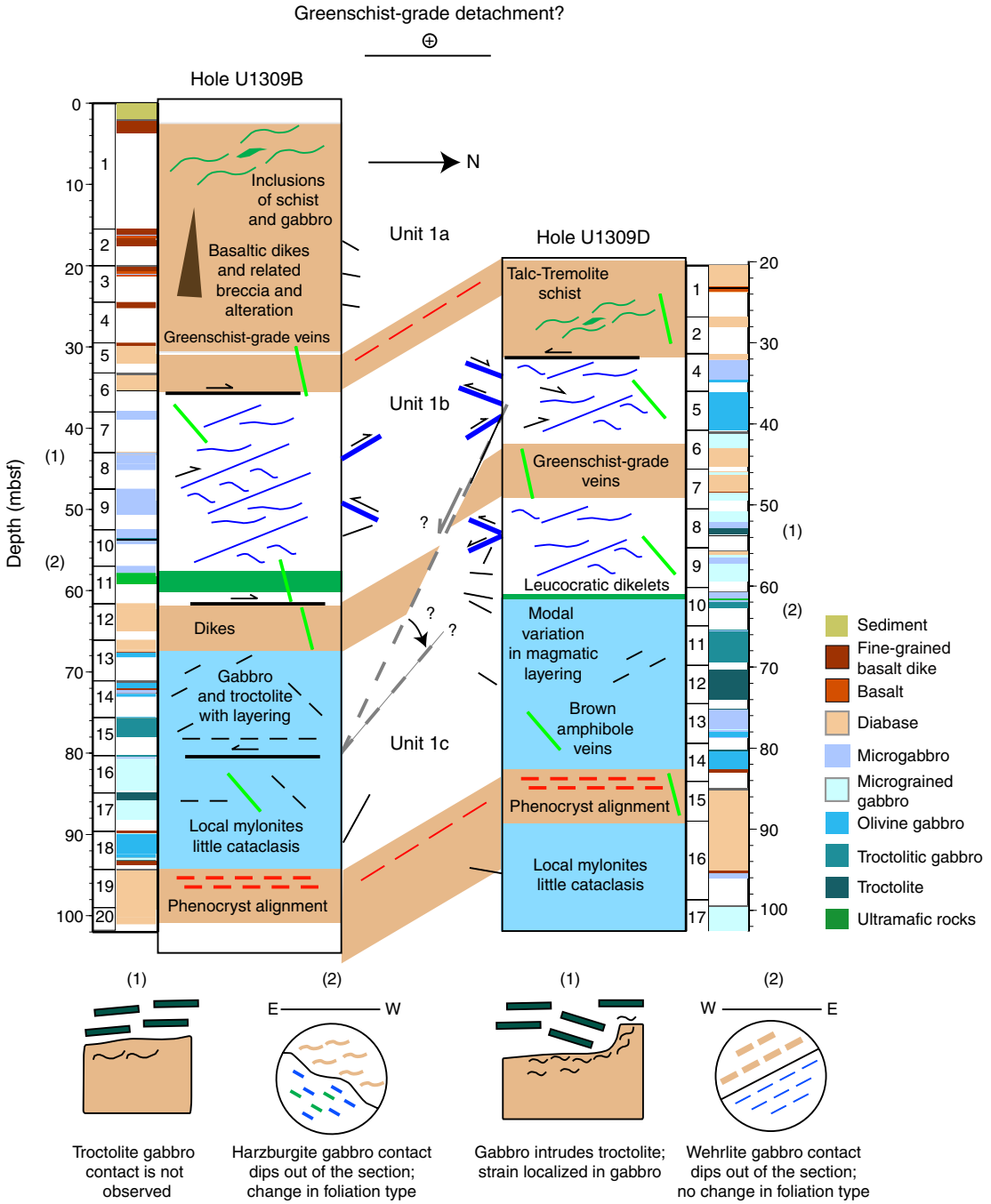

Figure F213. (**A**) H_2O versus SiO_2 and (**B**) CO_2 versus CaO for basalts, diabases, basalt breccia, gabbroic rocks, ultramafic rubble, and harzburgite from Hole U1309B and basalts, diabases, gabbros, and peridotites from Hole U1309D. Also shown for comparison are end-member compositions for lizardite, talc, tremolite, and actinolite (Deer et al., 1992) and ODP Site 920 serpentinites (Cannat, Karson, Miller, et al., 1995; Dilek et al., 1997).

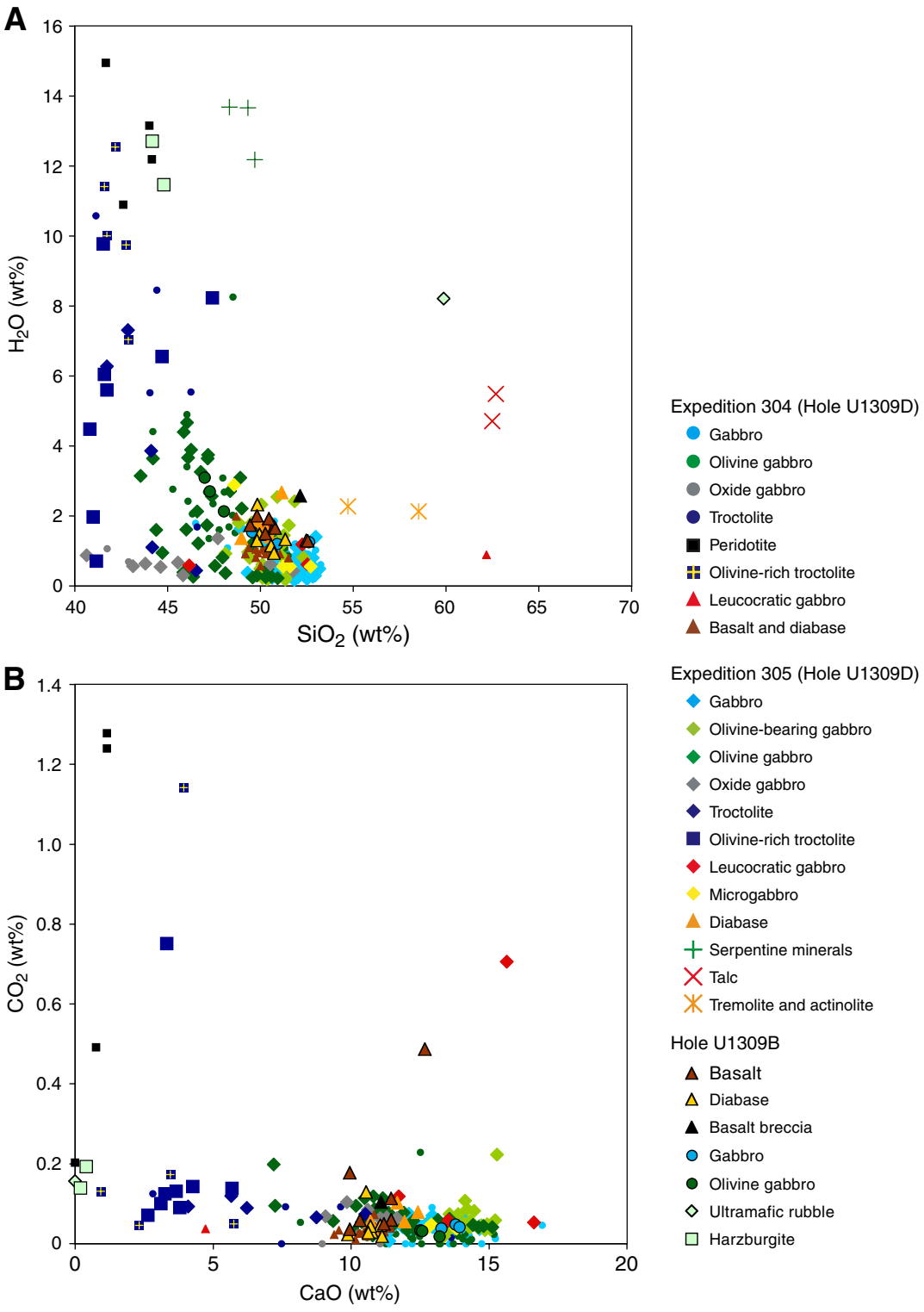

Figure F214. Volatile-free major element contents versus MgO for diabases and basalts from Holes U1309B and U1309D. **A.** SiO_2. **B.** Al_2O_3. **C.** Fe_2O_3. The composition, together with a compilation of Mid-Atlantic Ridge (MAR) volcanic glass compositions downloaded from PetDB in December 2004 (online at beta.www.petdb.org), are shown for comparison. **D.** CaO. **E.** Na_2O. **F.** TiO_2.

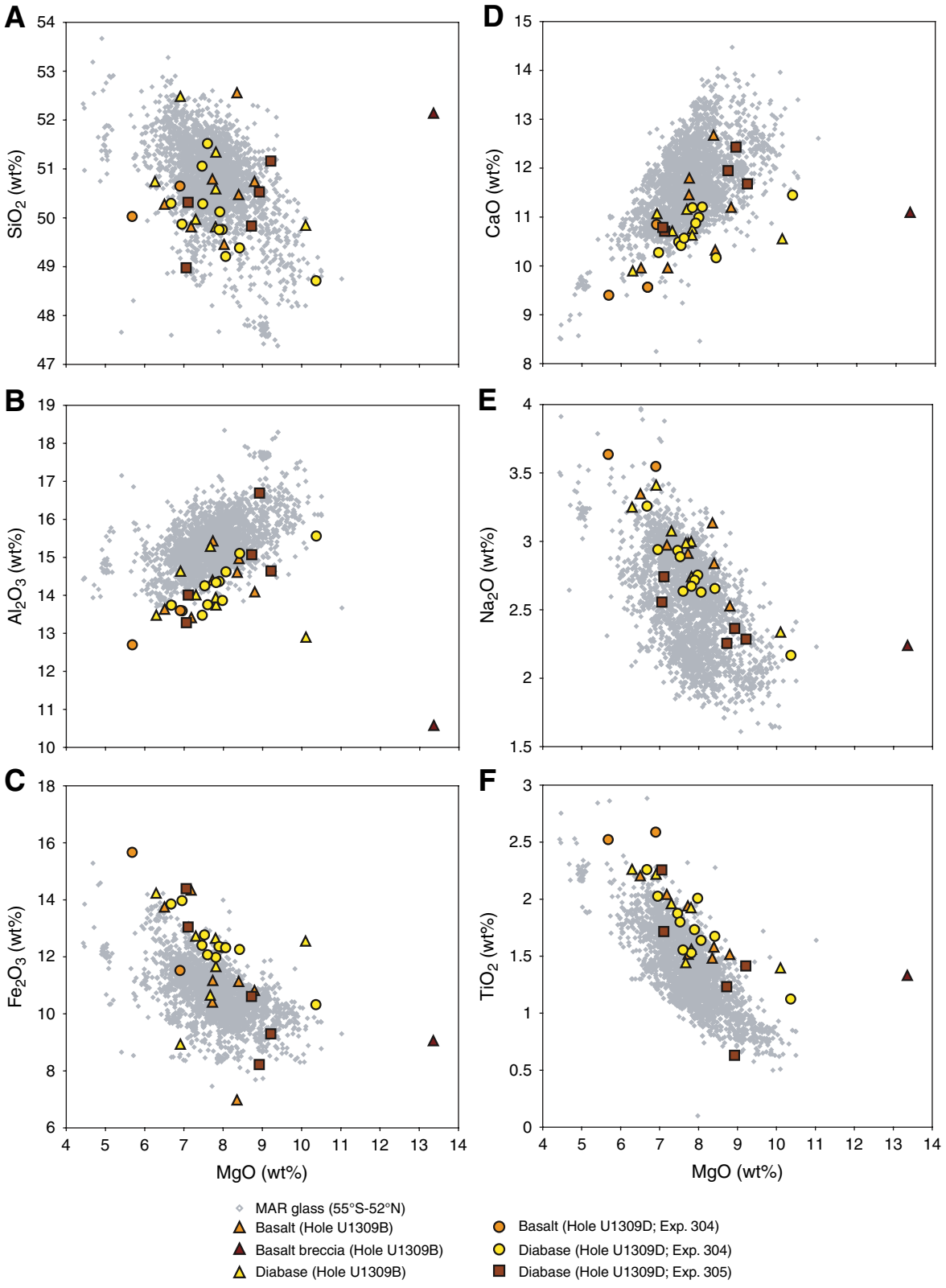

Figure F215. Volatile-free (**A**) Fe_2O_3, (**B**) Sr, (**C**) Sc, (**D**) Zr, and (**E**) V contents versus TiO_2 content for basalts and diabases from Holes U1309B and U1309D. The composition of Site U1309 basalts and diabases (beige diamonds), together with a compilation of Mid-Atlantic Ridge (MAR) volcanic glass compositions (open diamonds) downloaded from PetDB in December 2004 (online at **beta.www.petdb.org**), are shown for comparison.

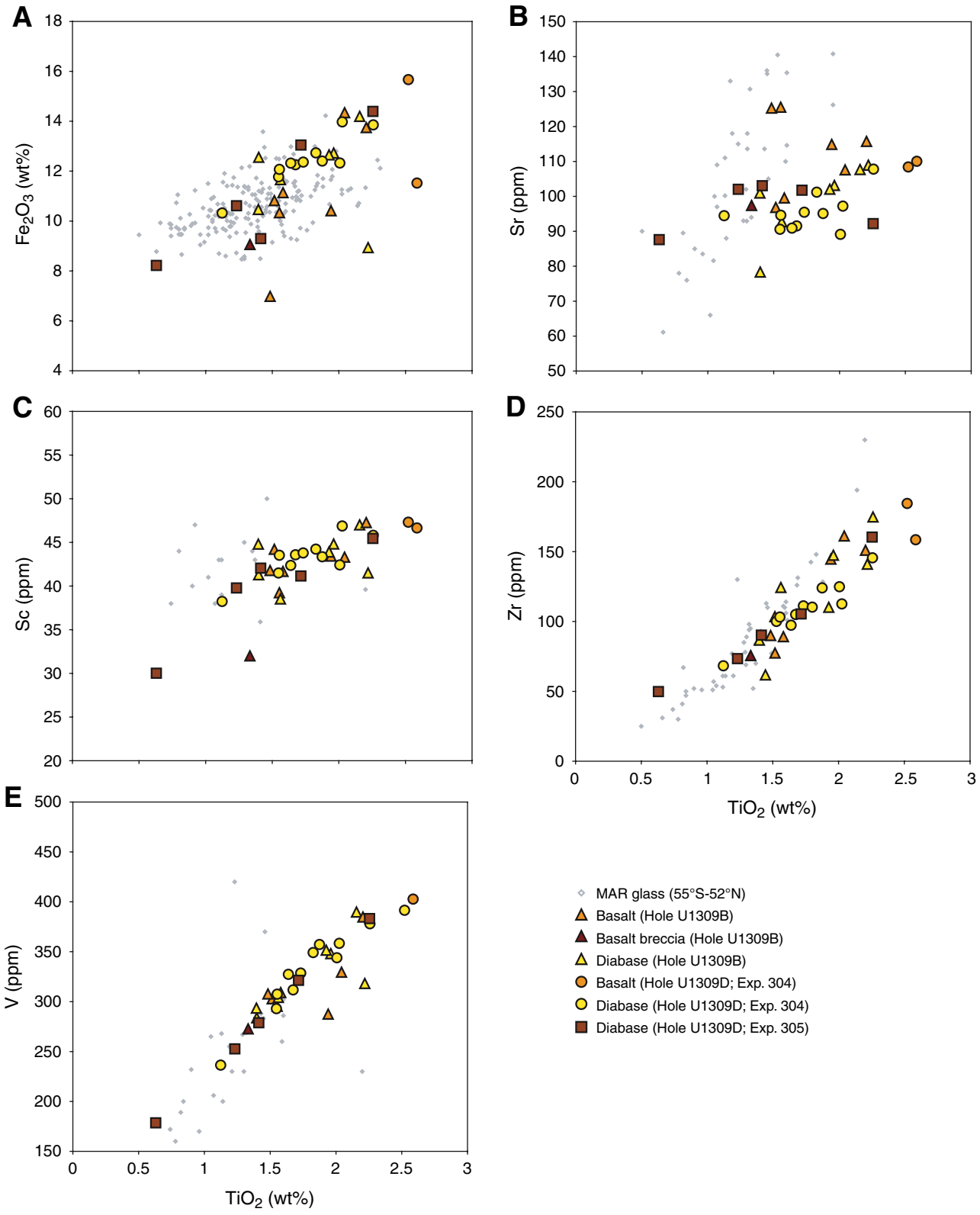

Figure F216. (**A**, **B**) V and (**C**, **D**) Sc versus TiO_2 anhydrous for gabbros, olivine gabbros, troctolites, orthopyroxene-bearing gabbros, oxide gabbros, and ultramafic rocks from Site U1309 (Expedition 304). The plots on the right side show a detailed view of the compositional variation of gabbros and wehrlite that is shown in the left plots. MAR = Mid-Atlantic Ridge.

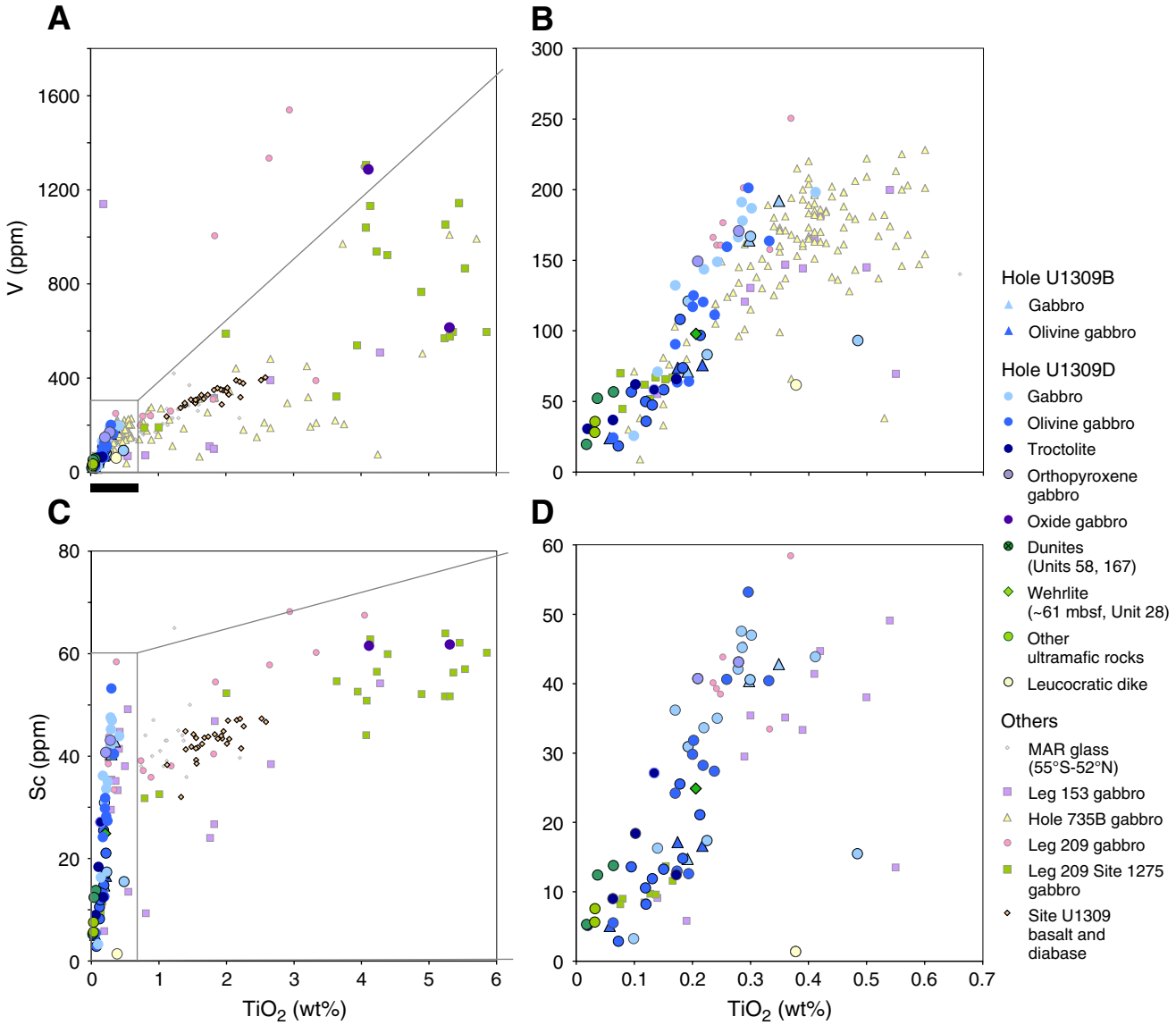

Figure F217. Volatile-free (**A**) Fe_2O_3 and (**B**) TiO_2 versus magnetic susceptibility for basalts, diabases, and basalt breccia from Site U1309 (Expedition 304). Lines join, in order of depth, the samples from the same diabase units (see **"Igneous petrology"**). DD2 = Hole U1309D Diabase D-2 (Units 5–6), DD3 = Hole U1309D Diabase D-3 (Units 12–14), DD5 = Hole U1309D Diabase D-5 (Units 42–44). UE = samples that have magnetic susceptibilities recognized as underestimates (see **"Physical properties"**).

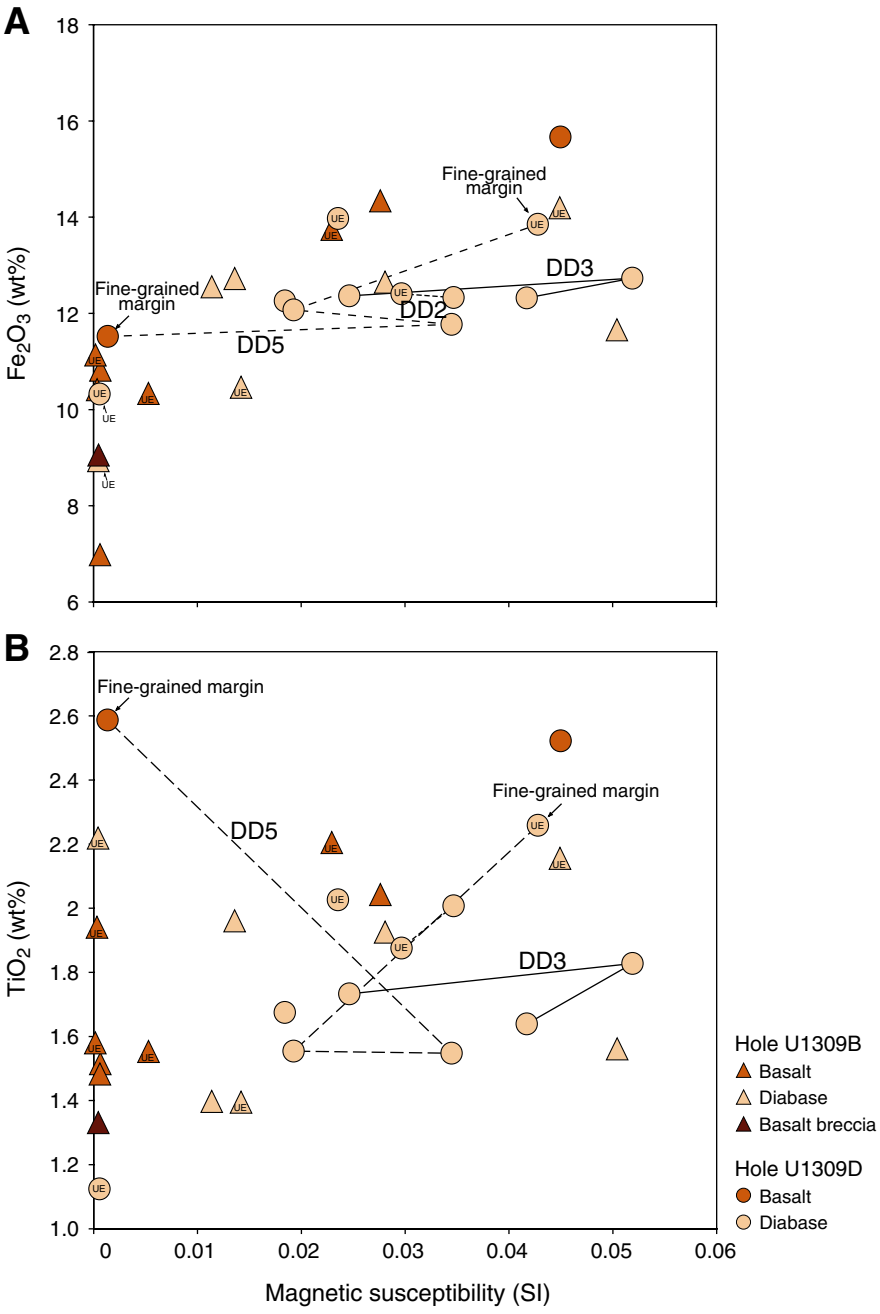

Figure F218. Downhole variation in H_2O between 400 and 1300 mbsf (Expedition 305) in Hole U1309D for peridotites, olivine-rich troctolites, gabbroic rocks, and diabases.

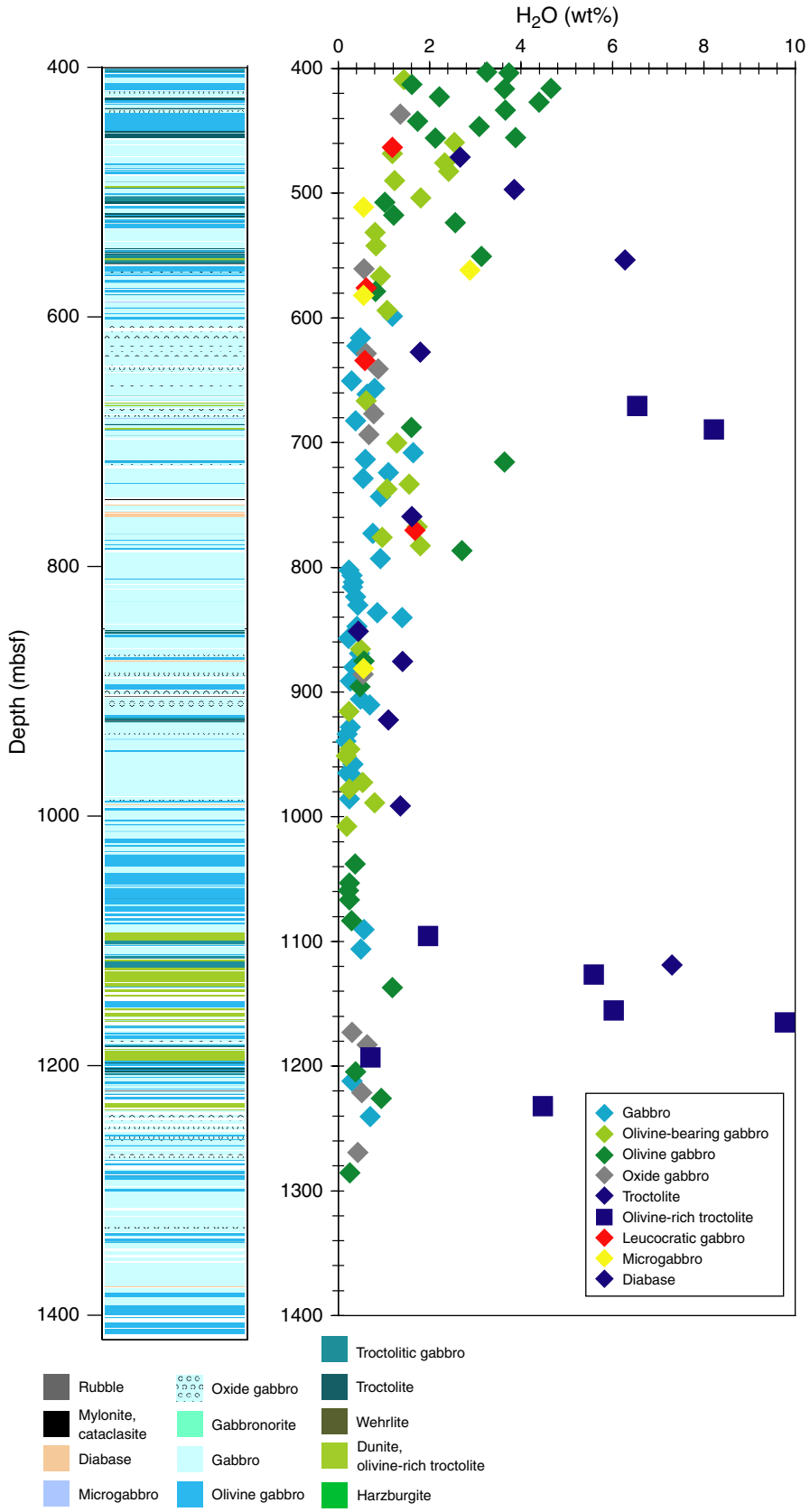

Figure F219. Volatile-free (**A**) MgO, (**B**) Fe_2O_3, (**C**) Al_2O_3, (**D**) CaO, (**E**) Na_2O, and (**F**) TiO_2 contents versus SiO_2 content for gabbros and olivine gabbros from Hole U1309B and gabbros, olivine gabbros, troctolites, orthopyroxene-bearing gabbros, oxide gabbros, wehrlite, and peridotites from Holes U1309B and U1309D. The composition of Site U1309 basalts and diabases (beige diamonds), together with a compilation of Mid-Atlantic Ridge (MAR) volcanic glass compositions (open diamonds) downloaded from PetDB in December 2004 (online at **beta.www.petdb.org**), are shown for comparison. Also shown for comparison are published data for Leg 153 gabbros (Agar et al., 1997), Hole 735B gabbros (Dick, Natland, Miller, et al., 1999), and Leg 209 gabbros (Kelemen, Kikawa, Miller, et al., 2004).

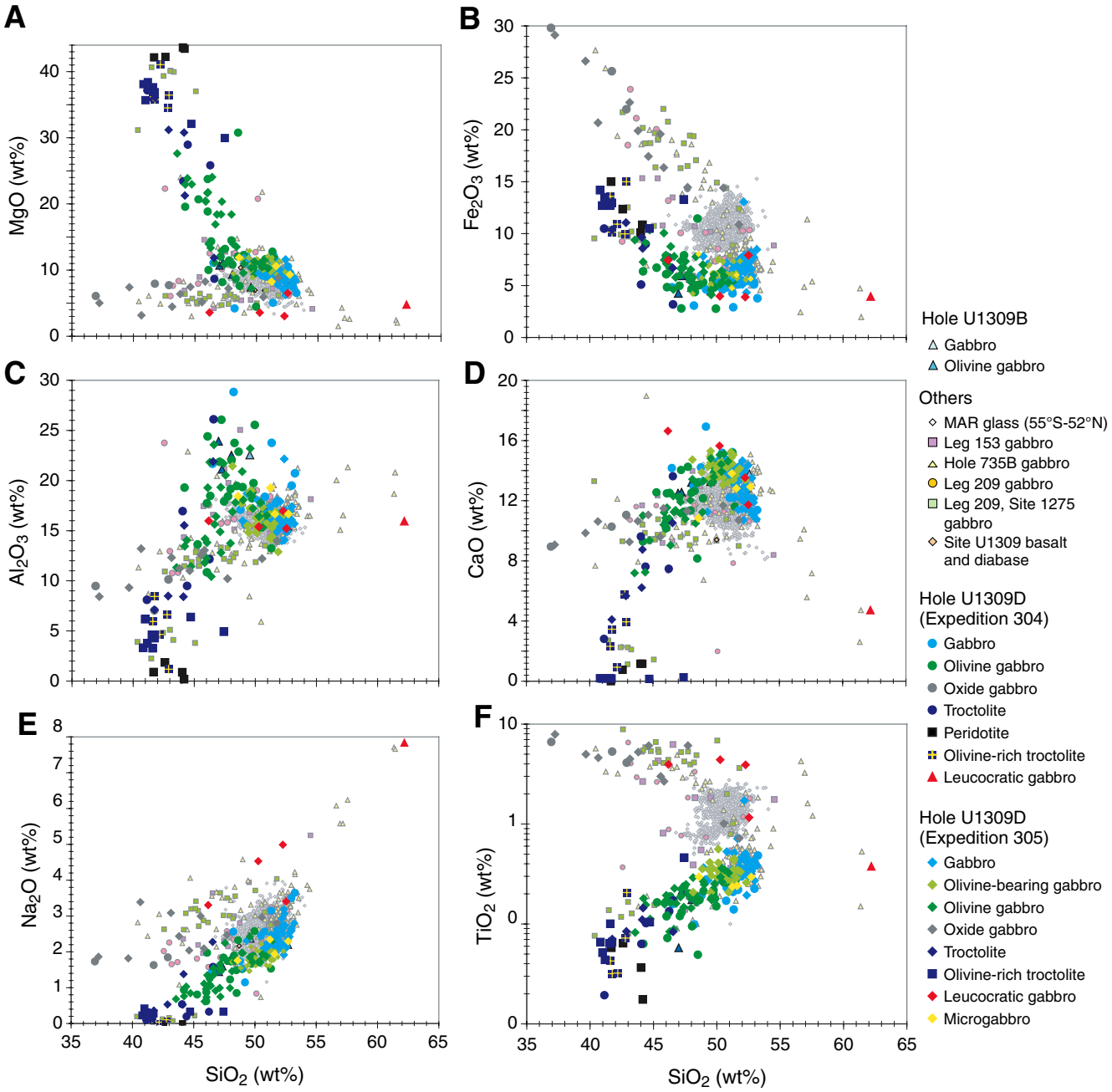

Figure F220. Volatile-free (**A**) SiO_2, (**B**) MnO, (**C**) Al_2O_3, (**D**) TiO_2, and (**E**) CaO contents versus Mg# for peridotites, olivine-rich troctolites, and gabbroic rocks from Hole U1309D.

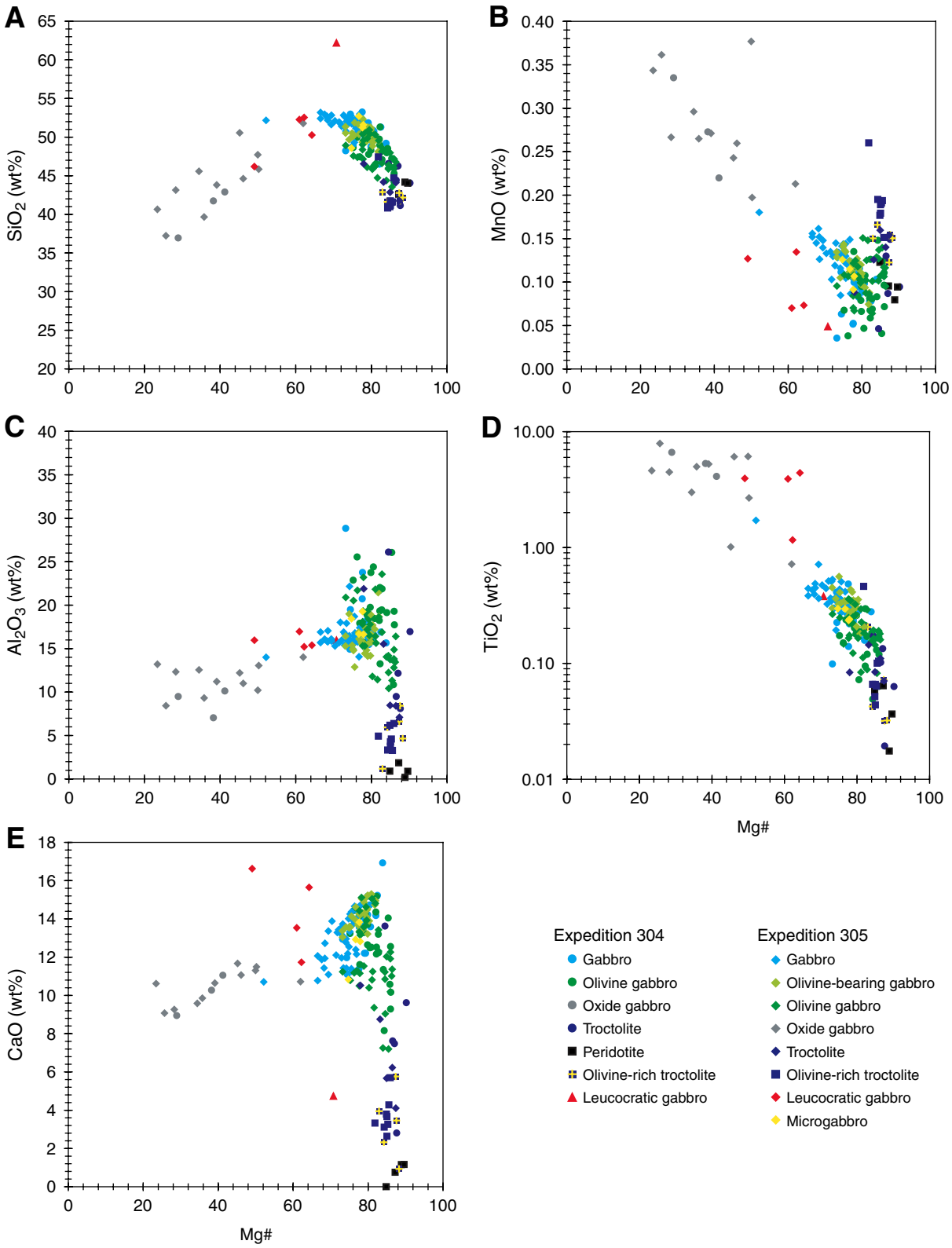

Figure F221. Volatile-free Fe_2O_3 content versus TiO_2 content for peridotites, olivine-rich troctolites, and gabbroic rocks from Hole U1309D. MAR = Mid-Atlantic Ridge.

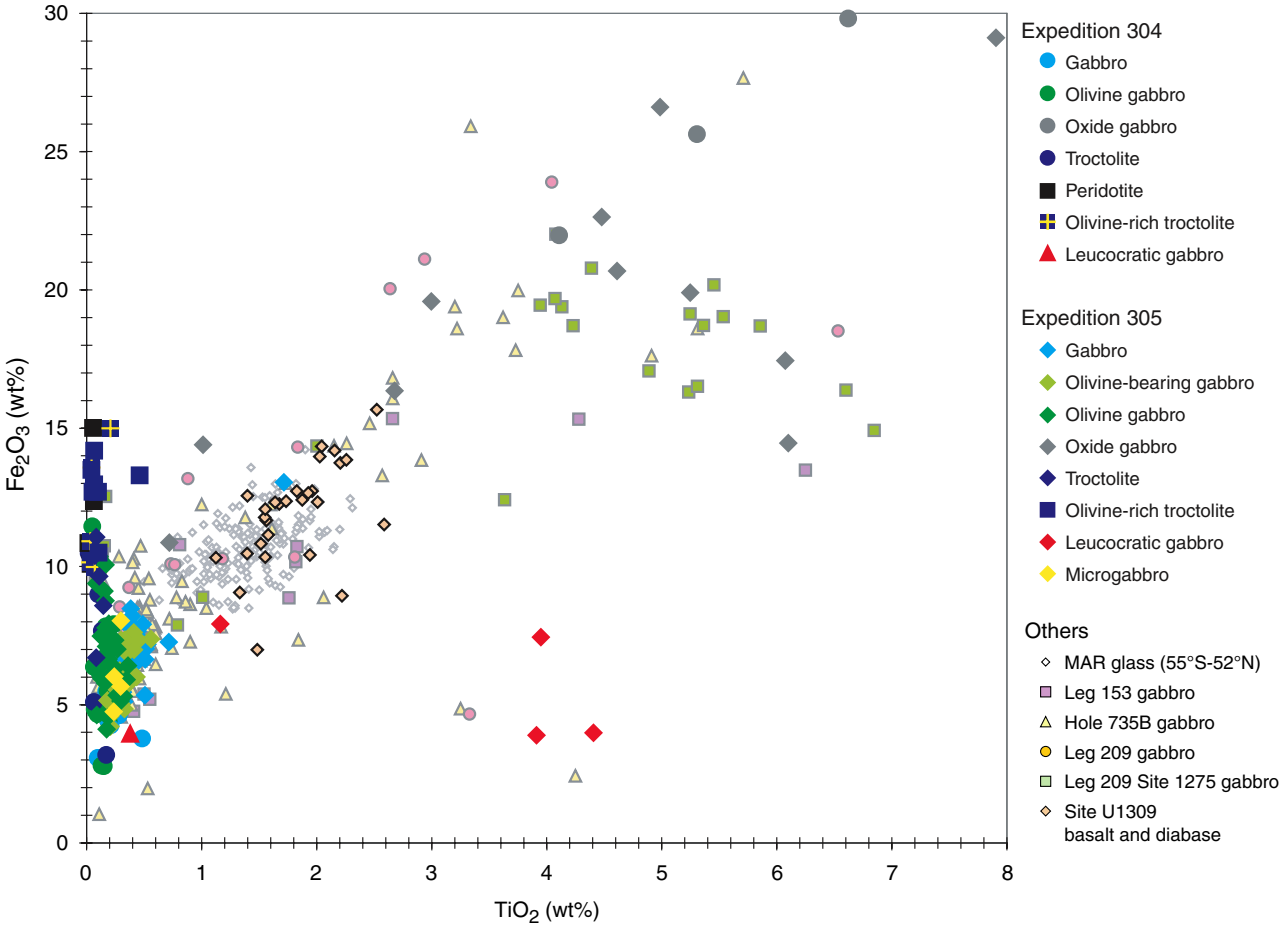

Figure F222. (**A**) Ni, (**B**) Cr, and (**C**) Sc versus Al_2O_3 anhydrous for gabbros, olivine gabbros, troctolites, orthopyroxene-bearing gabbros, oxide gabbros, and ultramafic rocks from Site U1309.

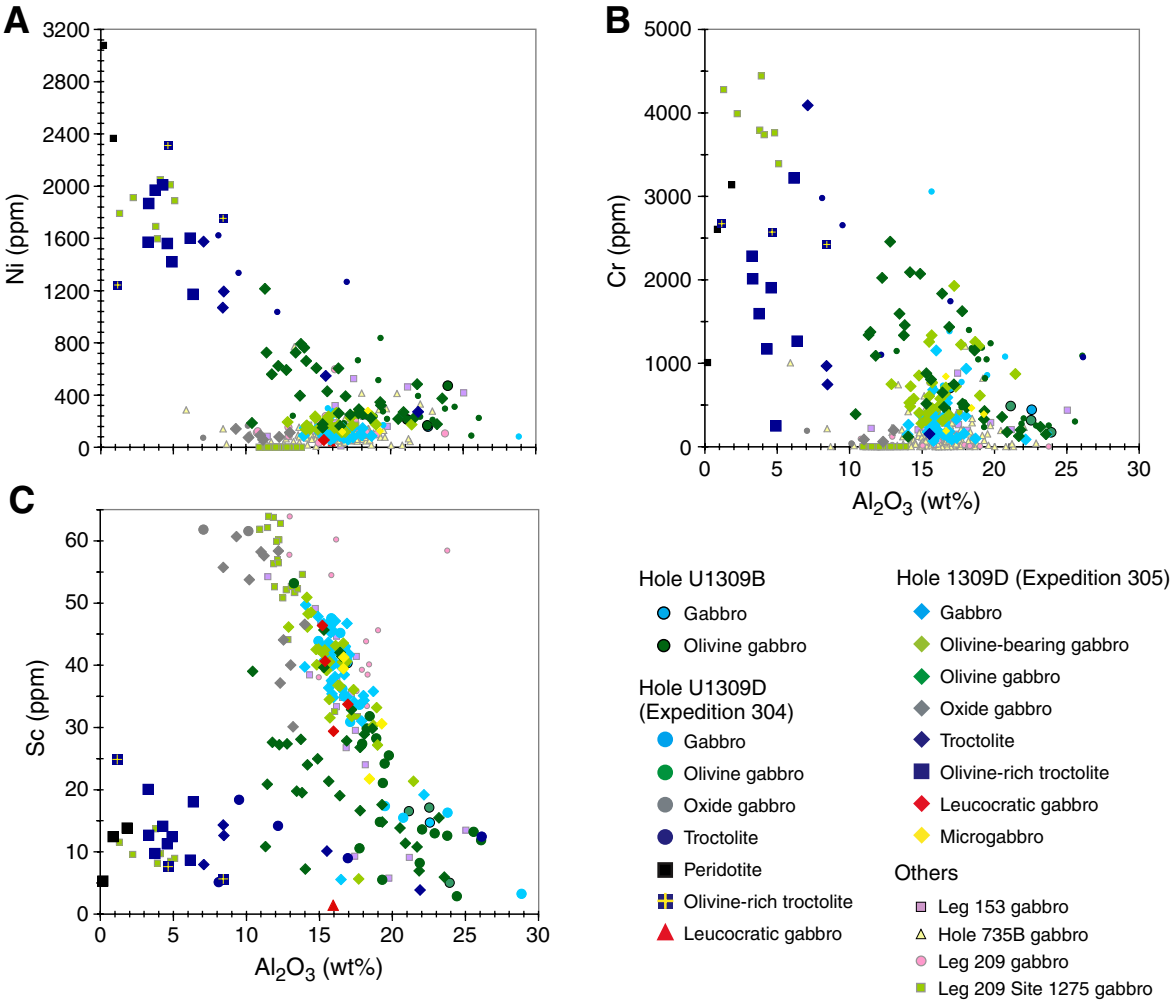

Figure F223. (**A**, **B**) Zr, (**C**, **D**) Y, and (**E**, **F**) Sr versus TiO_2 anhydrous for gabbros, olivine gabbros, troctolites, orthopyroxene-bearing gabbros, oxide gabbros, and ultramafic rocks from Site U1309. The plots on the right side show a detailed view of the compositional variation of gabbros and wehrlite shown in the left plots. MAR = Mid-Atlantic Ridge.

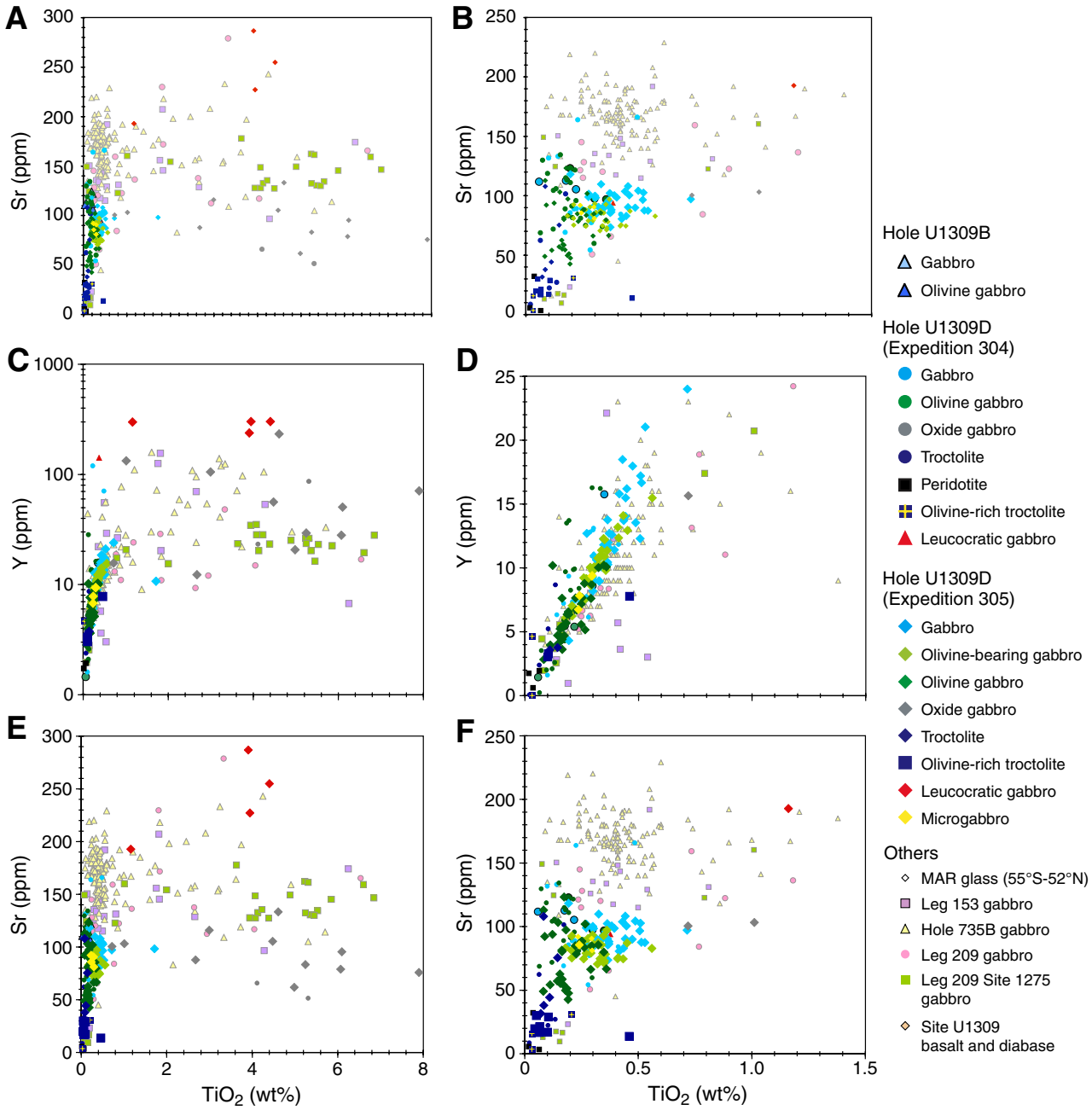

Figure F224. Zr versus Y for gabbros, olivine gabbros, troctolites, orthopyroxene-bearing gabbros, oxide gabbros, and ultramafic rocks from Site U1309. MAR = Mid-Atlantic Ridge.

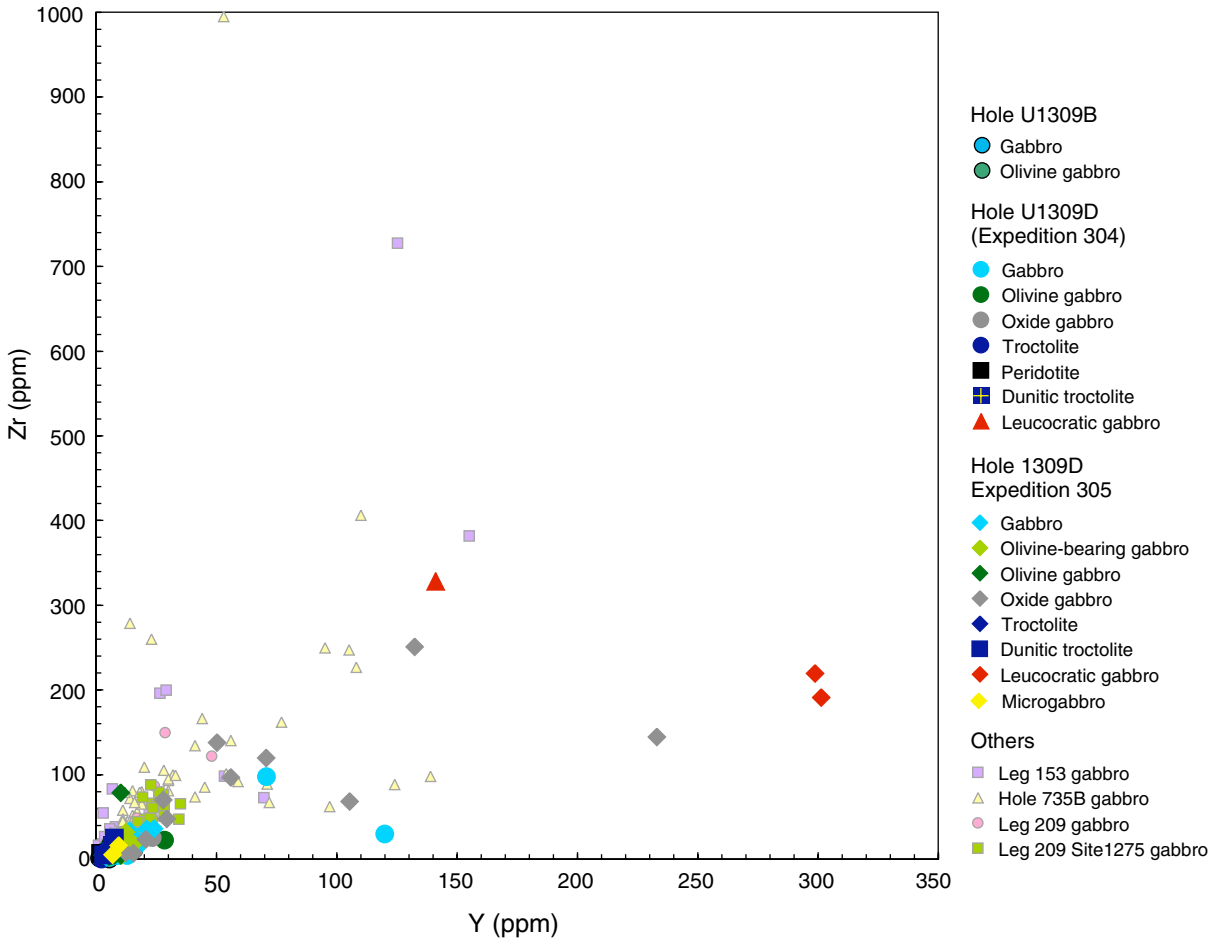

Figure F225. (**A**) Cr, (**B**) V, (**C**) Ni, and (**D**) Y versus Mg# (anhydrous) for peridotites, olivine-rich troctolites, and gabbroic rocks from Hole U1309D.

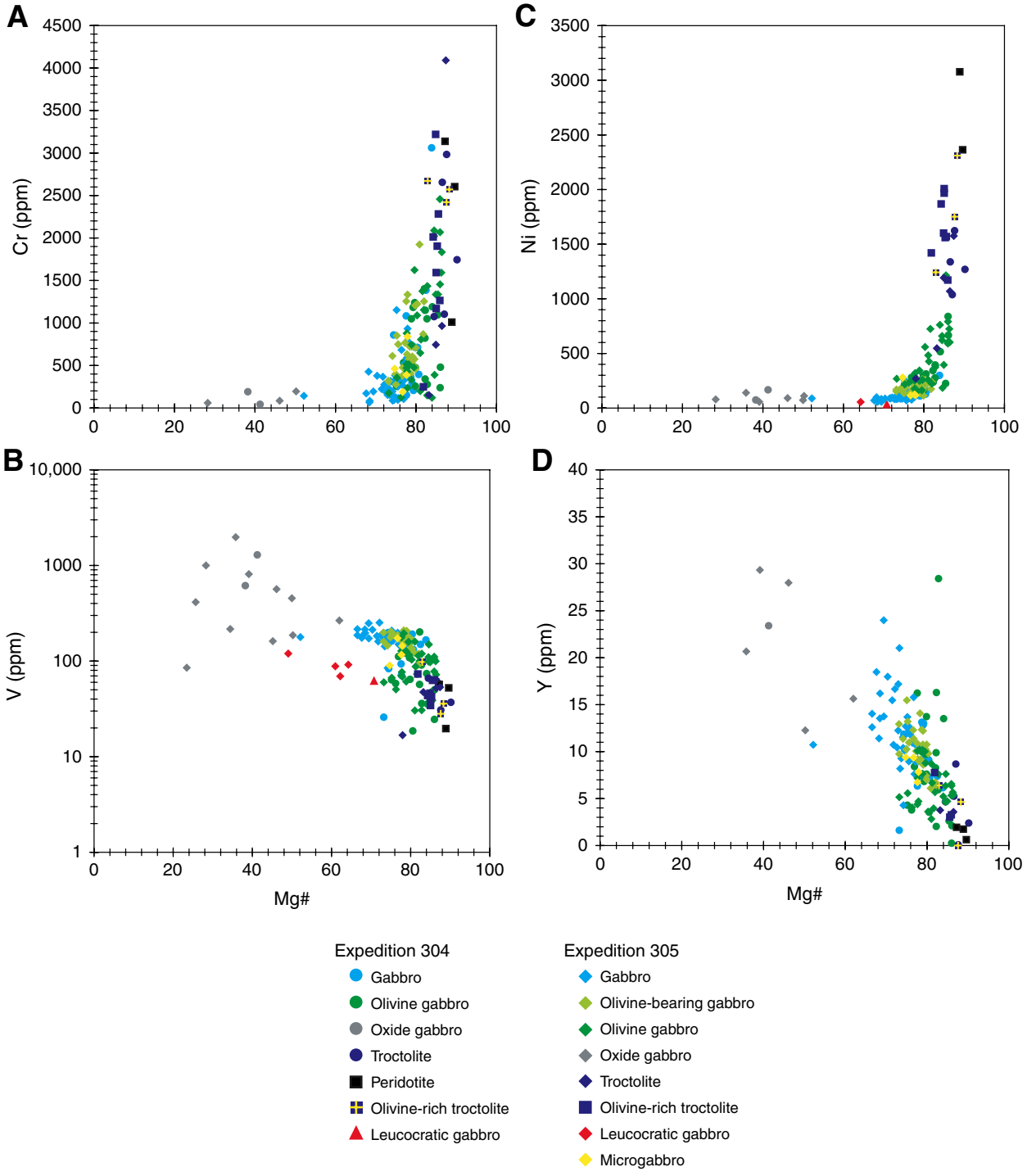

Figure F226. (**A**) Sc versus Al_2O_3 (anhydrous) and (**B**) Y versus TiO_2 for peridotites, olivine-rich troctolites, and gabbroic rocks from Hole U1309D. **C.** Sc versus Al_2O_3 for peridotites, olivine-rich troctolites, and gabbroic rocks from Hole U1309D.

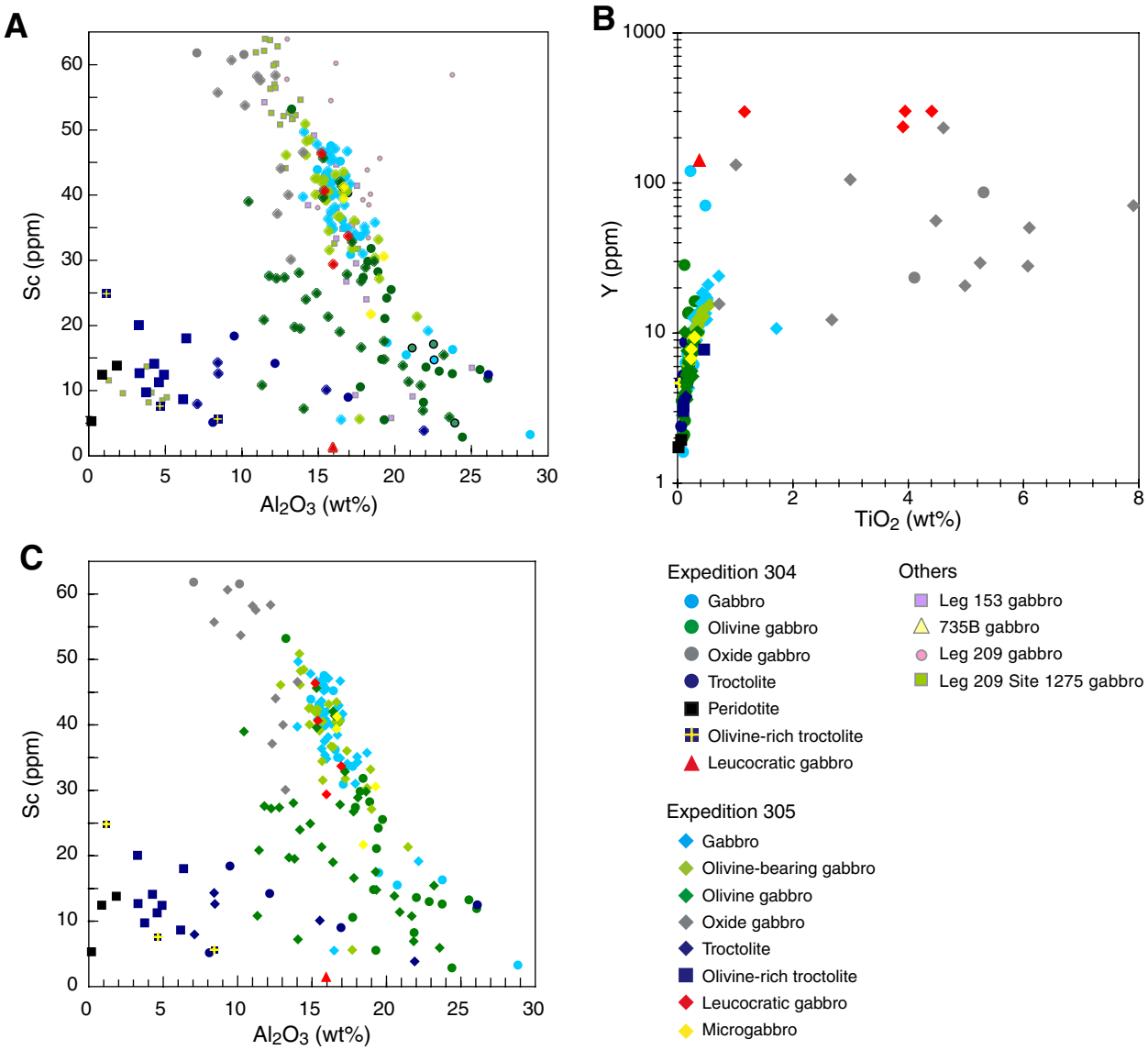

Figure F227. A. Anhydrous major element compositions of peridotites (green squares) and the ultramafic rubble (green diamonds) from Site U1309 (Expedition 304) compared to anhydrous compositions of end-member minerals (speciation is SiO_2, TiO_2, Al_2O_3, Cr_2O_3, FeO, MnO, MgO, CaO, Na_2O, K_2O, and P_2O_5, with all Fe as FeO). **B.** Expanded plot of A, with weight percent pyroxene proportions added. The composition of Site U1309 peridotites is consistent with 20%–25% orthopyroxene (opx) content as observed in thin section description. Ultramafic rubble approaches the composition of end-member talc.

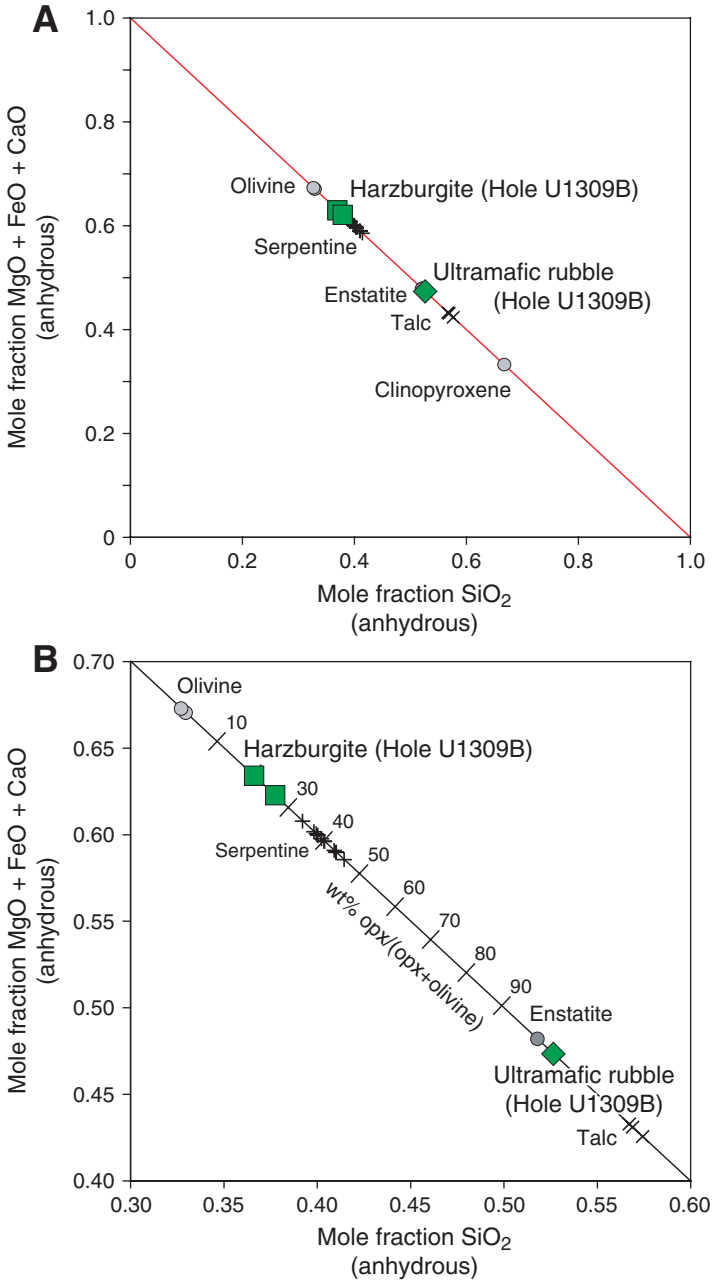

Figure F228. Volatile-free CaO versus Al_2O_3 for peridotites and ultramafic samples from Site U1309. Published data on Leg 153 Site 920 peridotites (Casey, 1997) and Leg 209 peridotites (Kelemen, Kikawa, Miller, et al., 2004) are shown for comparison. Solid line = bulk silicate earth (= primitive mantle) Al_2O_3/CaO ratio (Jagoutz et al., 1979; Hart and Zindler, 1986).

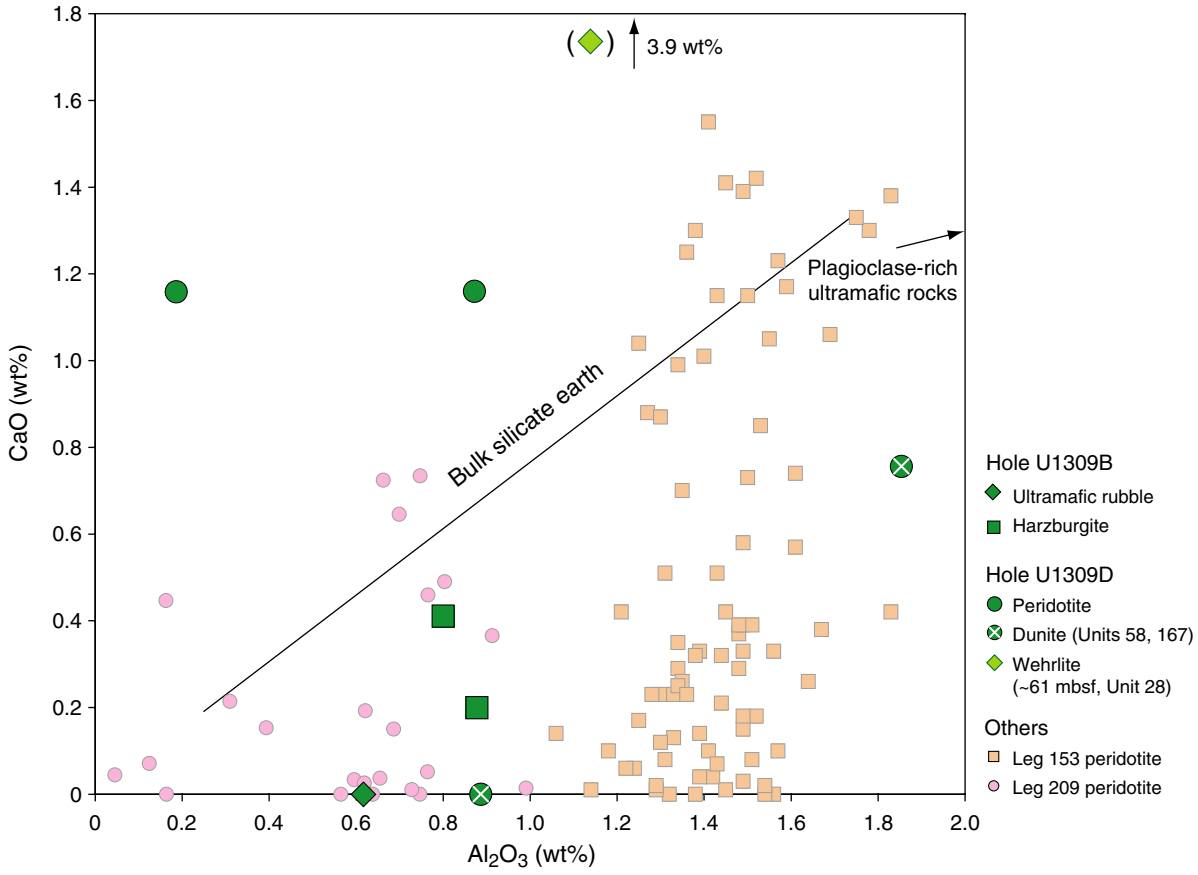

Figure F229. Ni versus Mg# (molar Mg/[Mg + Fe]) for gabbros, olivine gabbros, troctolites, orthopyroxene-bearing gabbros, oxide-gabbros, ultramafic rocks, and peridotites from Site U1309.

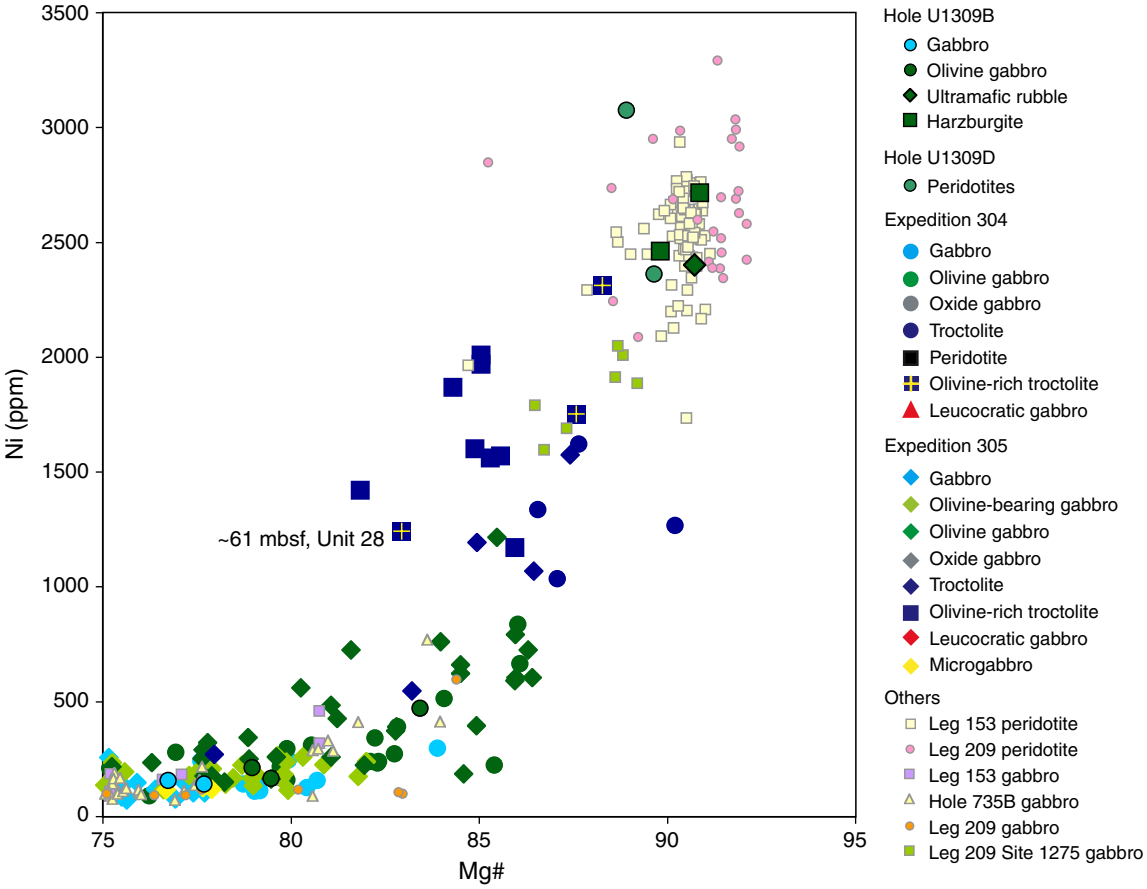

Figure F230. Volatile-free FeO versus MgO whole-rock concentrations of Site U1309 peridotites. Published data are also shown for comparison: Mid-Atlantic Ridge (MAR) peridotites from Leg 153 Site 920 (Casey, 1997), data from the Southwest Indian Ridge (SWIR) (Snow and Dick, 1995), drilled peridotites from the Izu-Bonin-Mariana (IBM) forearc (Parkinson and Pearce, 1998), East Pacific Rise (EPR) peridotites (Niu and Hekinian, 1997), Western Alps orogenic lherzolites and ophiolites (Lanzo; Bodinier, 1988), Internal Ligurides (IL) (Rampone et al, 1996), and Oman ophiolite (Godard et al, 2000; Gerbert-Gaillard, 2002; M. Godard, unpubl. data). Indonesia = from Monnier, 1996. Kane FZ = Kane Fracture Zone. Whole-rock compositions are presented on a volatile-free basis assuming all Fe is FeO. Solid black lines show olivine and orthopyroxene composition as a function of Fe/Mg. Fine gray lines show constant values of Mg# (Mg# = 100 × molar Mg/[Mg + Fe_{total}]).

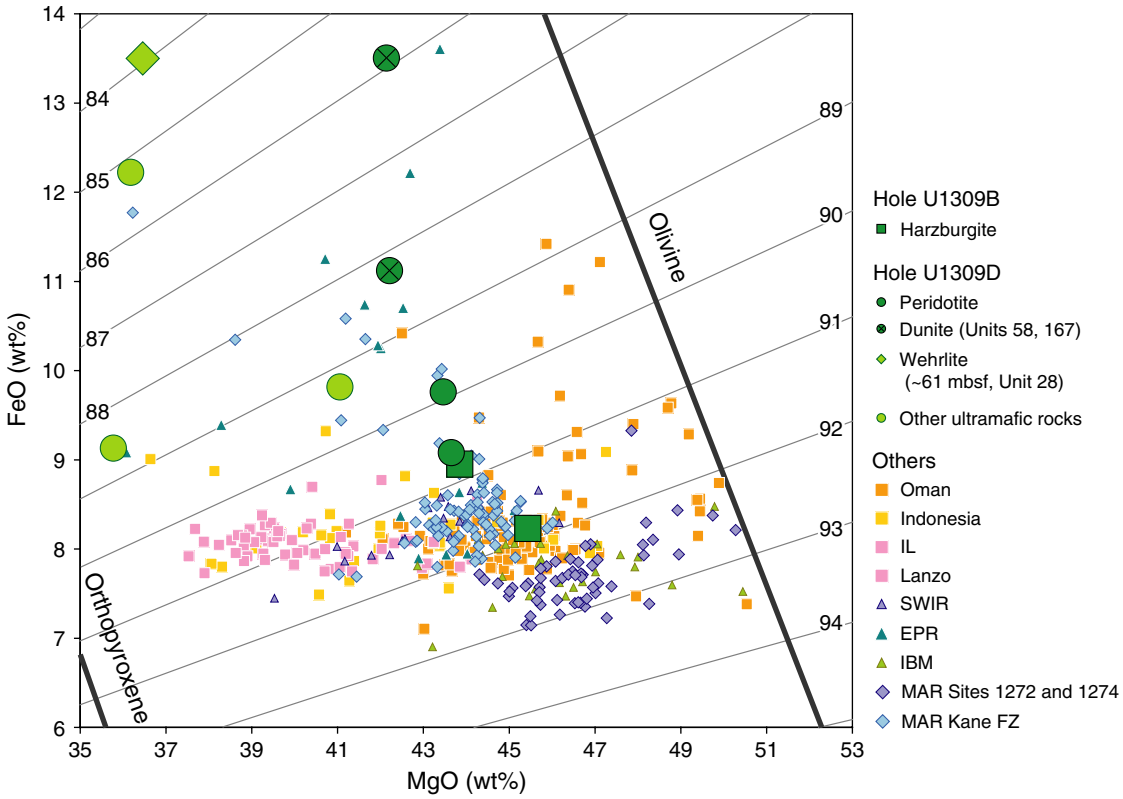

Figure F231. (**A**) V, (**B**) Sc, (**C**) Cr, (**D**) Y, and (**E**) Zr versus Al_2O_3 anhydrous for peridotites and ultramafic samples from Site U1309 (Expedition 304).

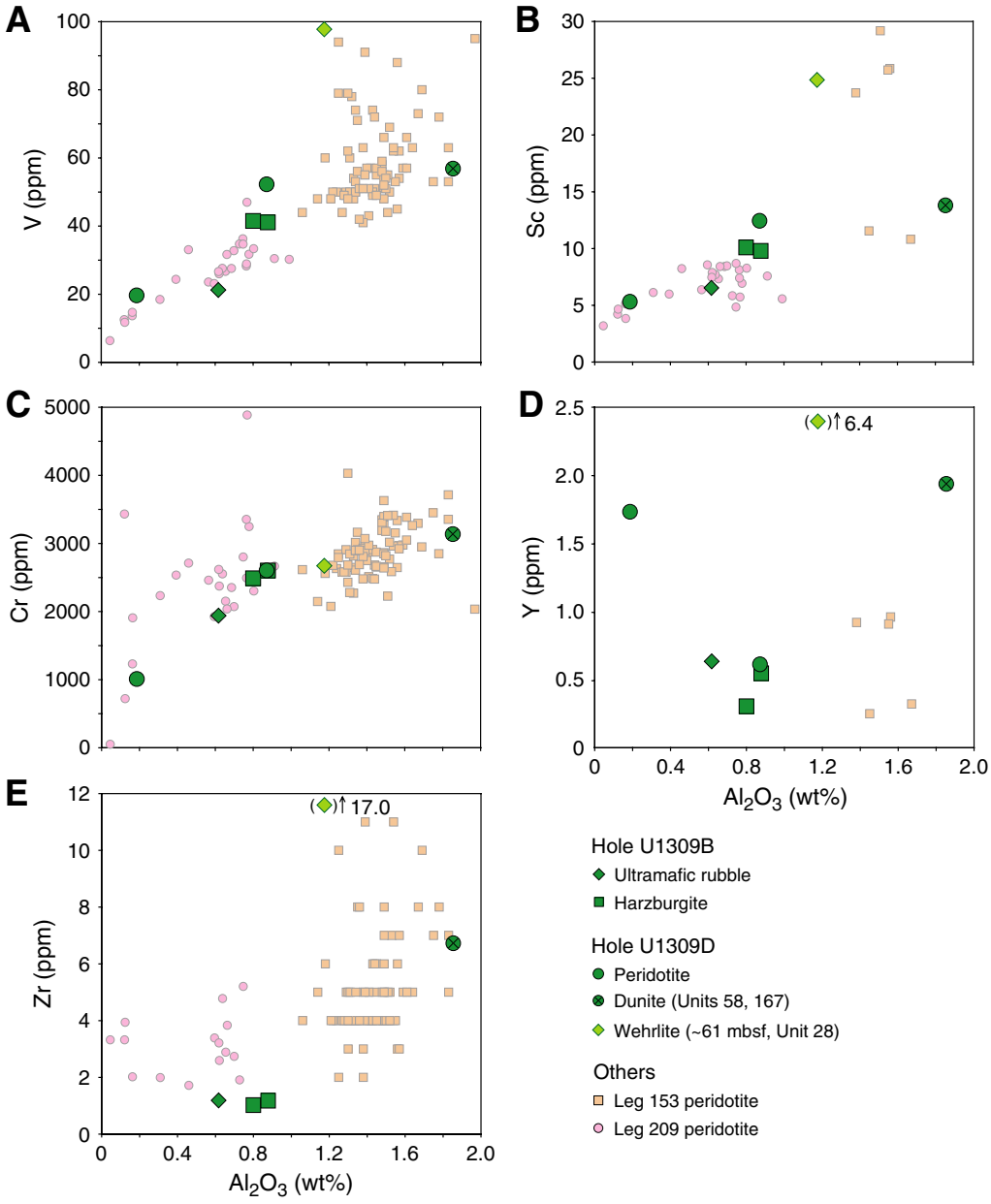

Figure F232. Zr/Y versus Zr (ppm) for basalts and diabases from Site U1309 (Expedition 304). Lines join same basaltic unit samples in order of depth at Site U1309 (see **"Igneous petrology"**). 1 = three samples from Hole U1309B Diabase D-1 (Units 20 and 22), 5 = five samples from Hole U1309D Diabase D-5 (Units 42 and 44). Plag = plagioclase, Cpx = clinopyroxene. MAR = Mid-Atlantic Ridge.

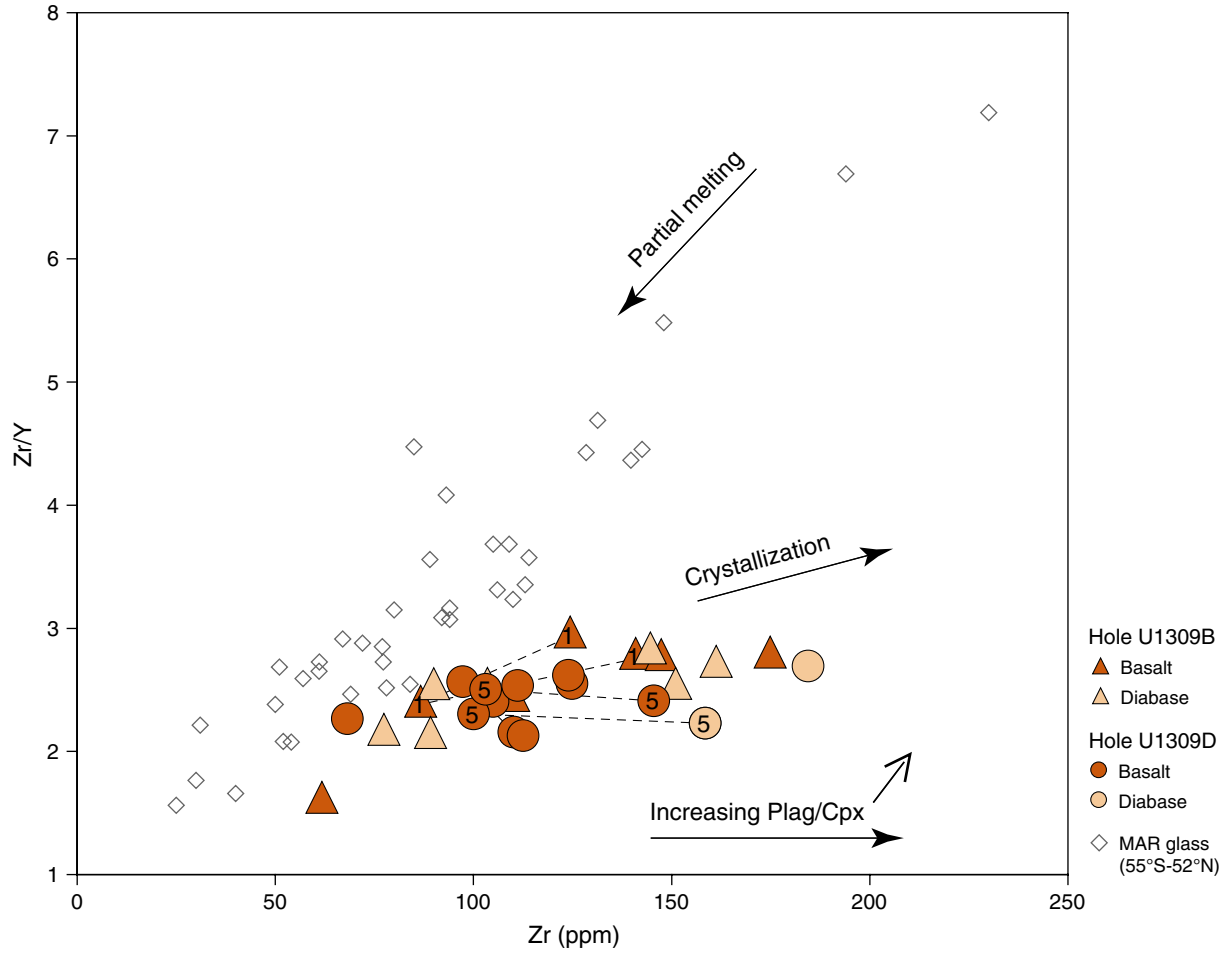

Figure F233. Volatile-free Fe_2O_3 versus MgO for peridotites, olivine-rich troctolites, and gabbroic rocks from Hole U1309D.

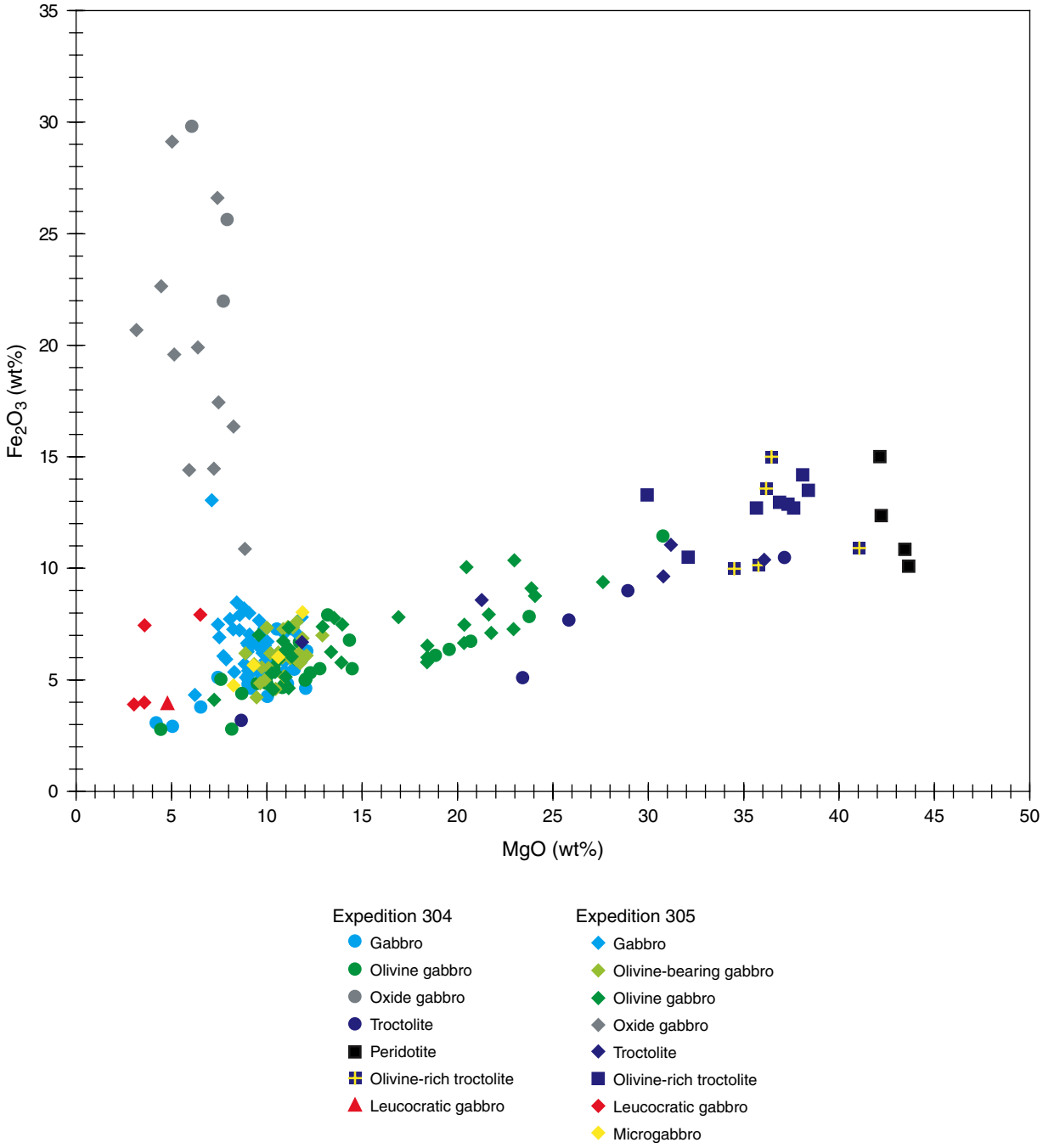

Figure F234. Downhole variations in (**A**) Mg# (anhydrous), (**B**) TiO_2 (anhydrous), and (**C**) MnO (anhydrous) for peridotites, olivine-rich troctolites, and gabbroic rocks from Hole U1309D. Horizontal solid lines show fault zones (see **"Structural geology"**).

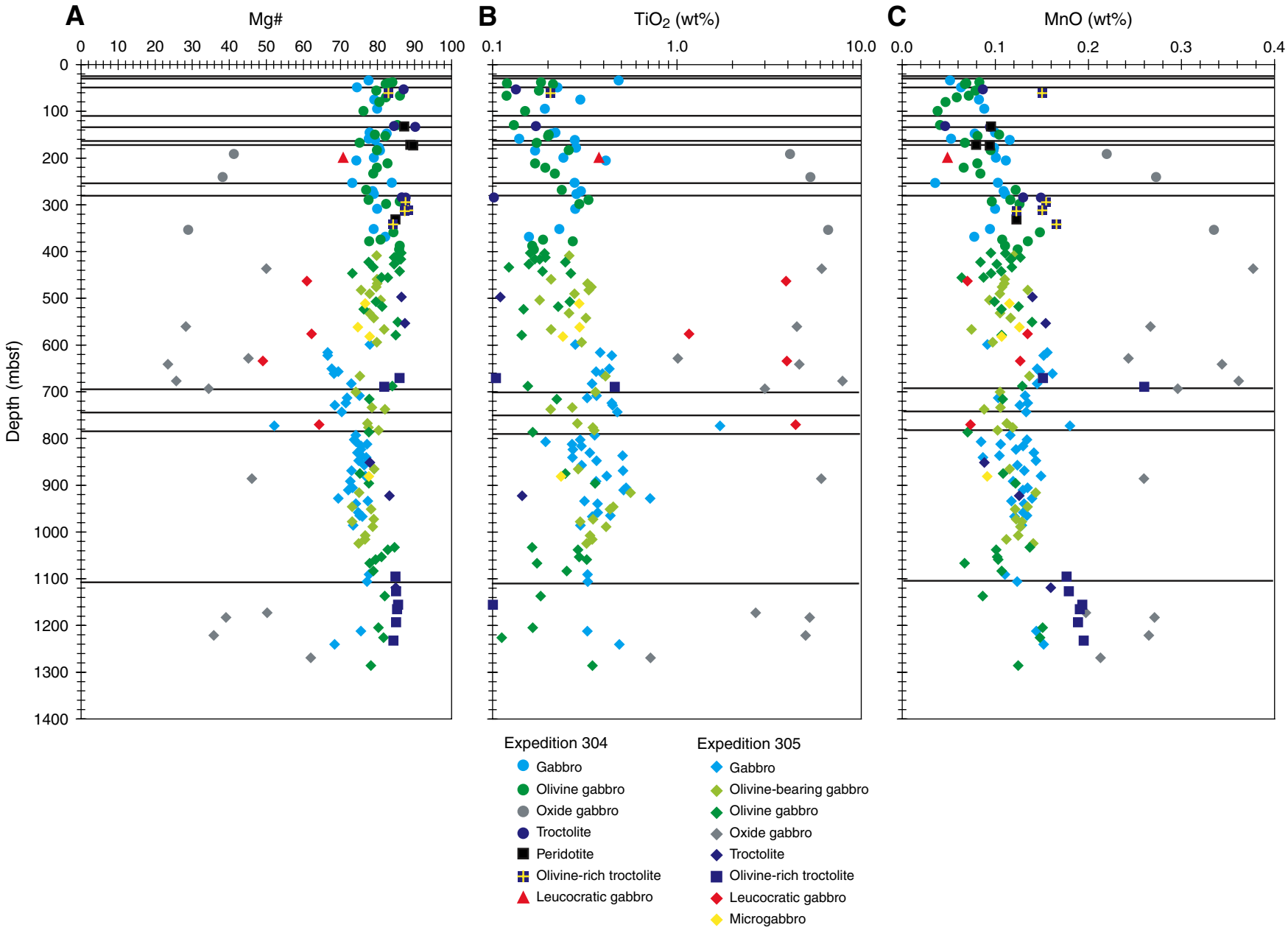

Figure F235. Downhole variation in Al_2O_3 (anhydrous) for peridotites, olivine-rich troctolites, and gabbroic rocks and modal abundance of plagioclase (from thin section description; see **"Igneous petrology"**) from Hole U1309D. Horizontal solid lines show fault zones (see **"Structural geology"**).

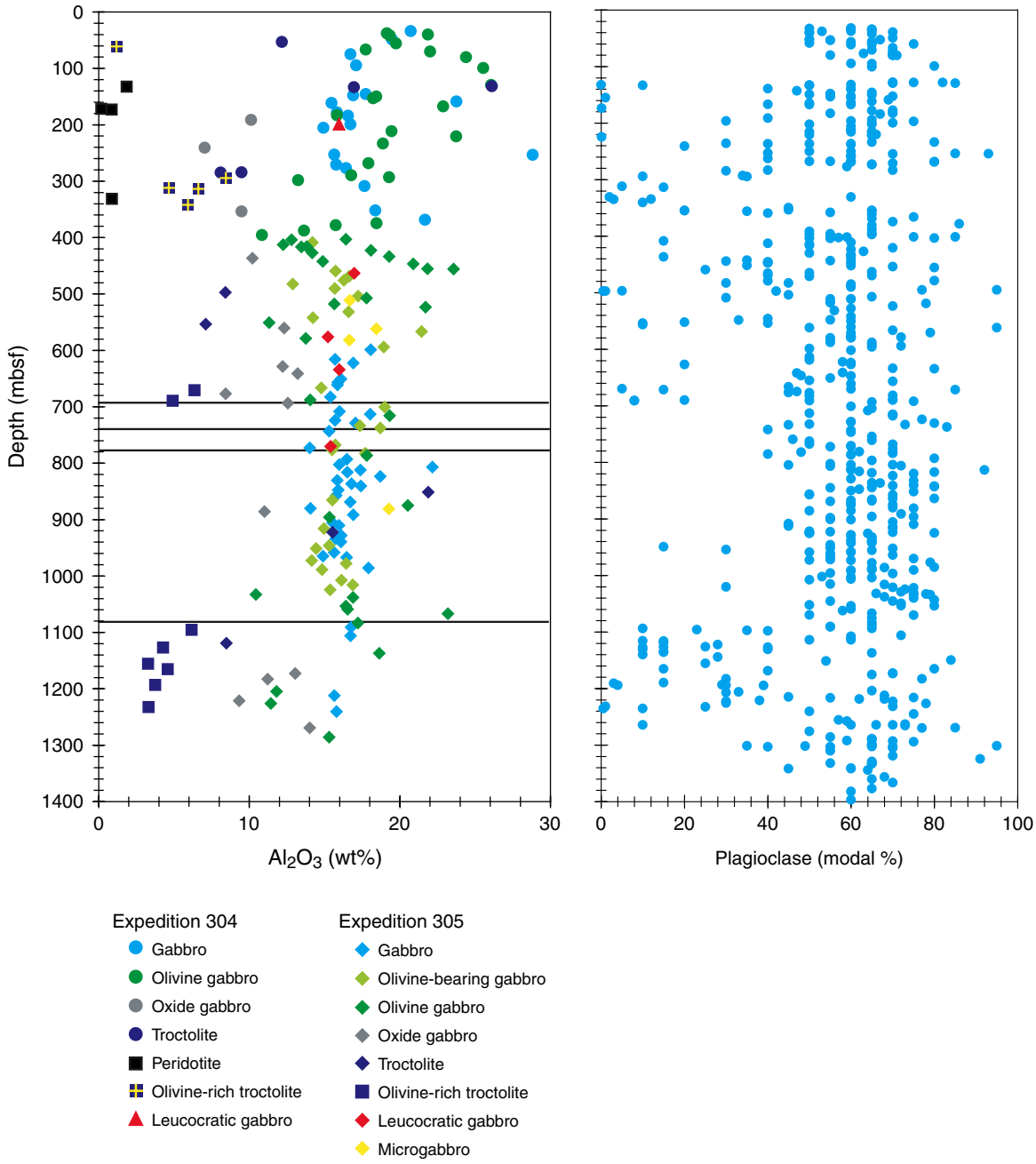

Figure F236. Mg# (100 × molar Mg/[Mg + Fe]) versus Ca# (100 × molar Ca/[Ca + Na]). Compositional fields of rocks from other locations at the Mid-Atlantic Ridge (MAR) (Leg 153; Casey, 1997), including Leg 209 (Kelemen, Kikawa, Miller, et al., 2004), and the Southwest Indian Ridge (SWIR) (Hole 735B; Dick et al., 2000) are shown for comparison.

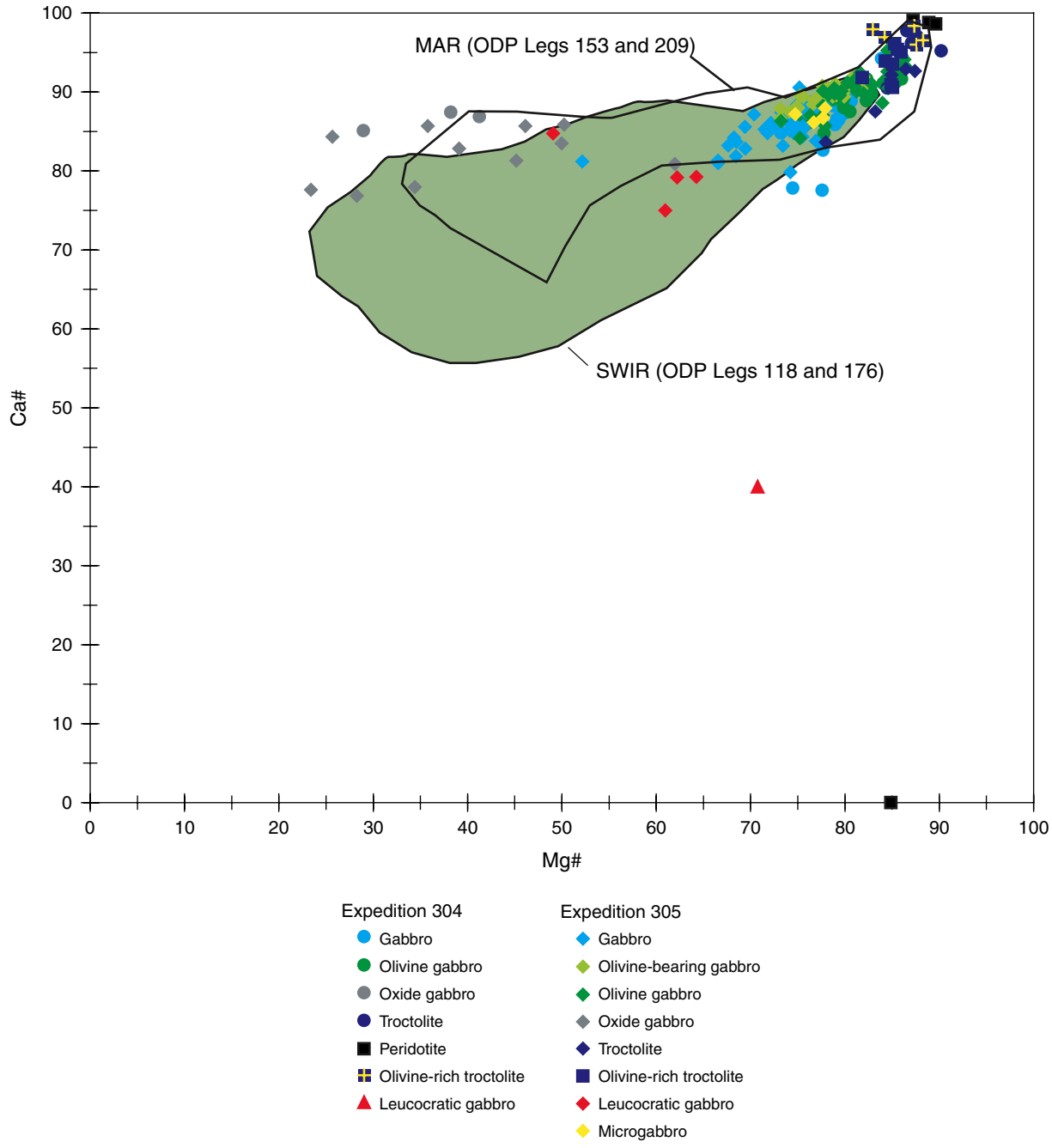

Figure F237. Summary of archive-half magnetic measurements (Expedition 304). Gray solid circles = NRM, blue open circles = remanence after 30 mT demagnetization. Volume magnetic susceptibility measured on the multisensor track. Note that susceptibility values are from whole-core measurements. Remanence and susceptibility data from within 4 cm of a piece end have been excluded. **A.** Hole U1309B. (Continued on next page.)

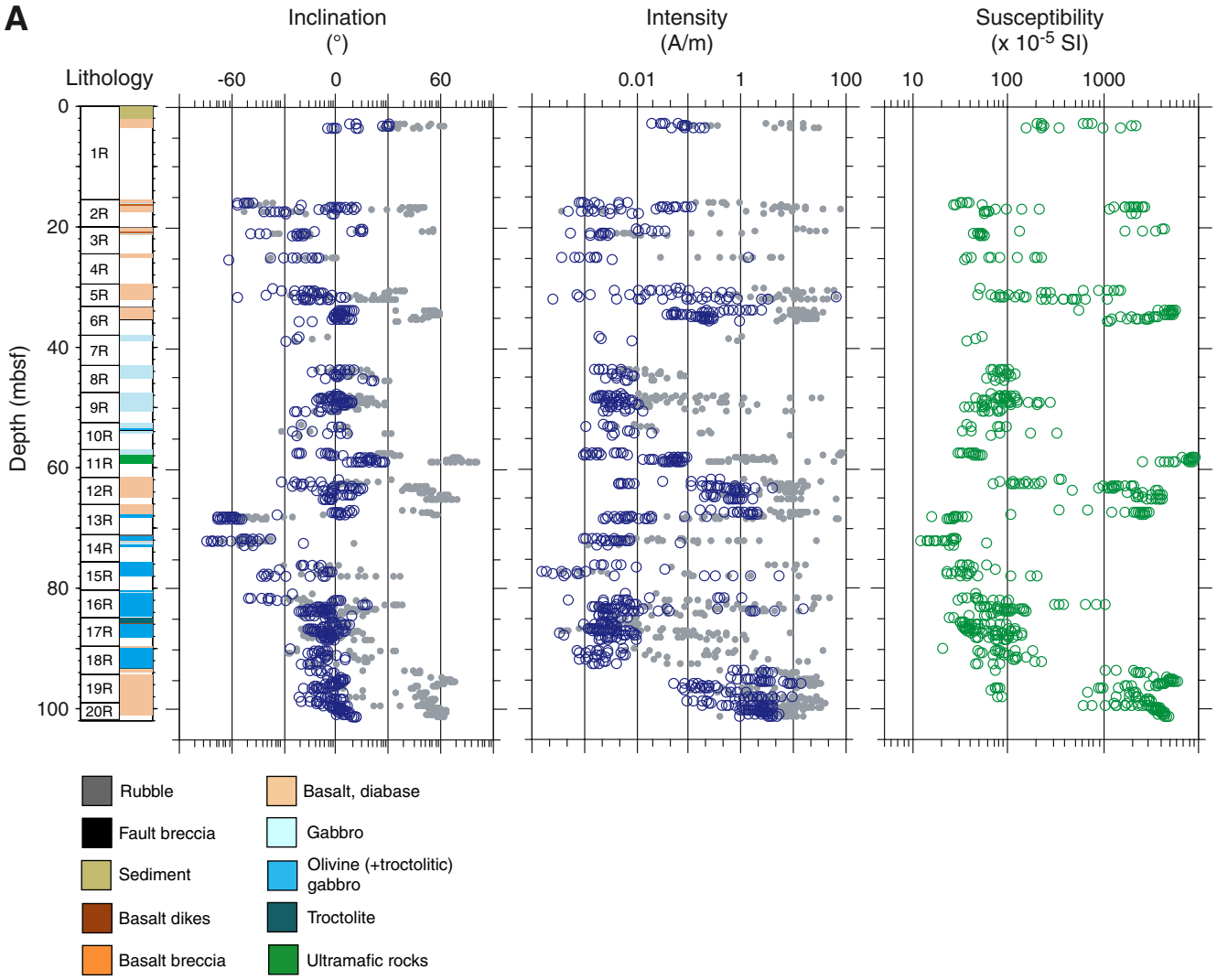

Figure F237 (continued). B. Hole U1309D.

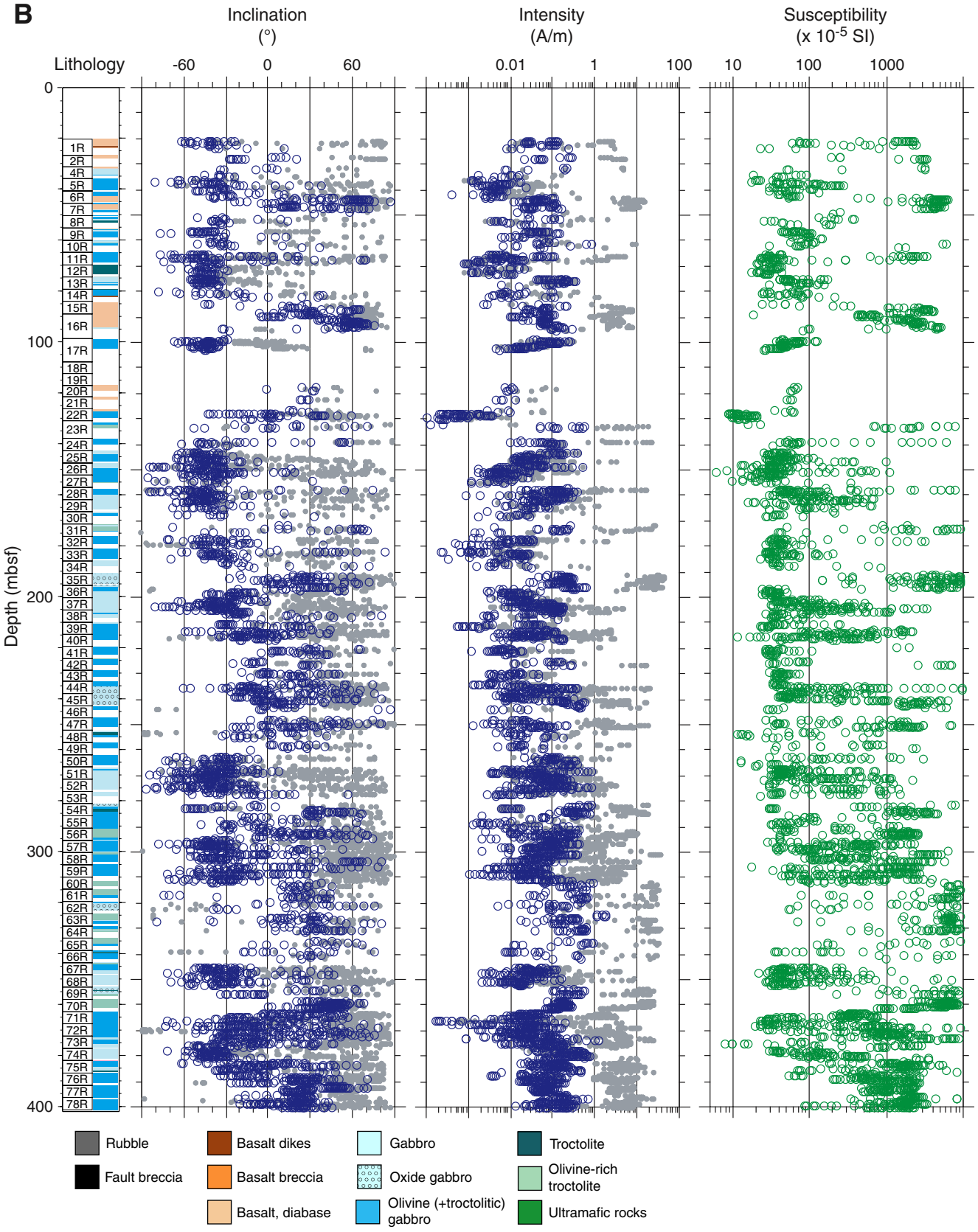

Figure F238. Natural remanent magnetization (NRM) intensity for various rock types from Site U1309 (Expedition 304) based on archive-half remanence measurements. Note that data with residual flux counts at the NRM level are included.

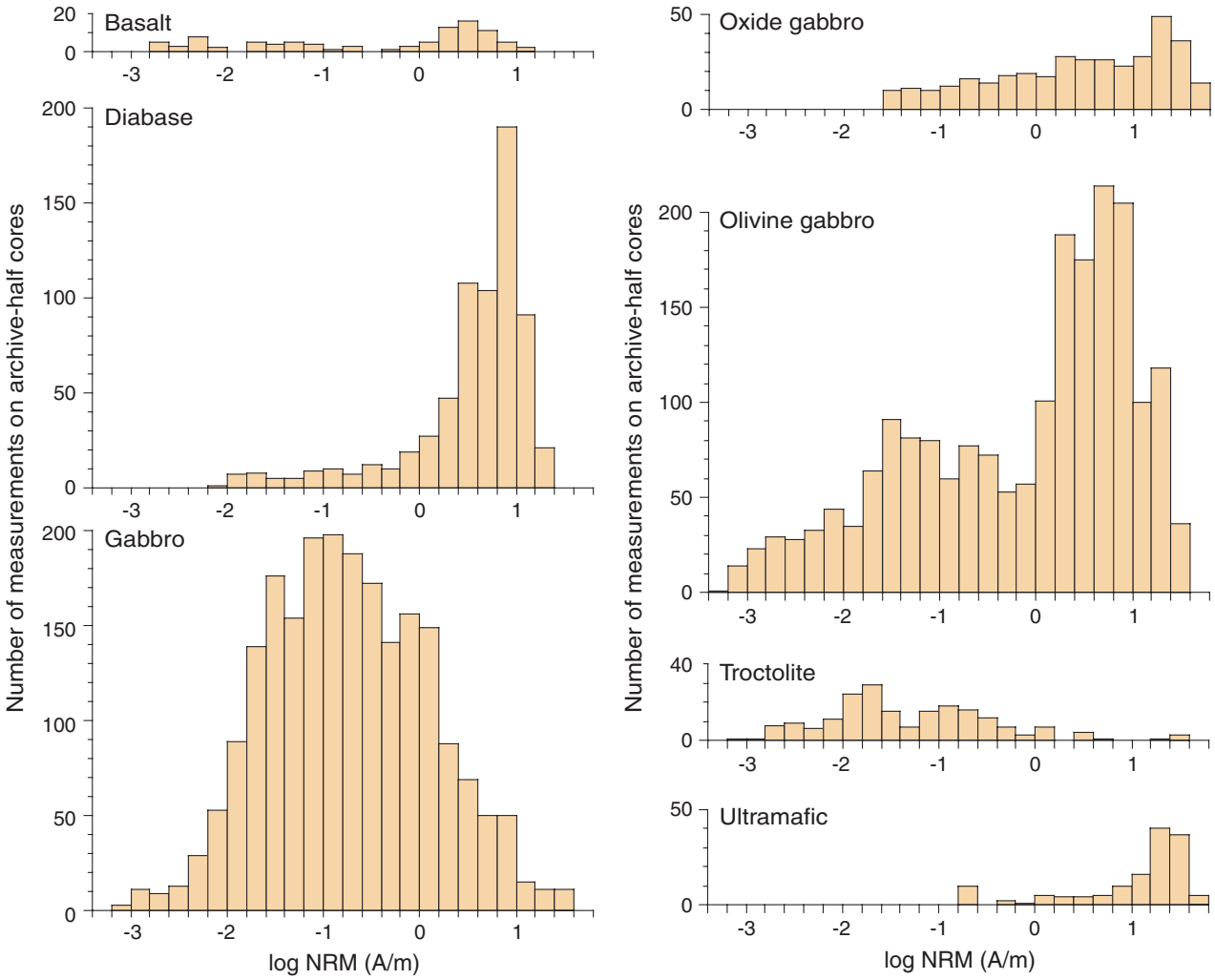

Figure F239. Representative demagnetization behavior for archive halves. **A.** High-stability reversed polarity component in olivine gabbro samples. Diabase samples exhibit a range of demagnetization behavior, including (**B**) intervals with apparently stable normal polarity vectors, (**C**) samples with magnetization vectors along great circle paths toward a reversed polarity direction, and (**D**) samples with a small stable reversed polarity component. Open circles in A, B, and D = projections of the remanence onto the north-south vertical plane, solid circles in A, B, and D = projections of the remanence onto the horizontal plane. Open circles in C = upper hemisphere projections. Solid circles in C = lower hemisphere projections. NRM = natural remanent magnetization.

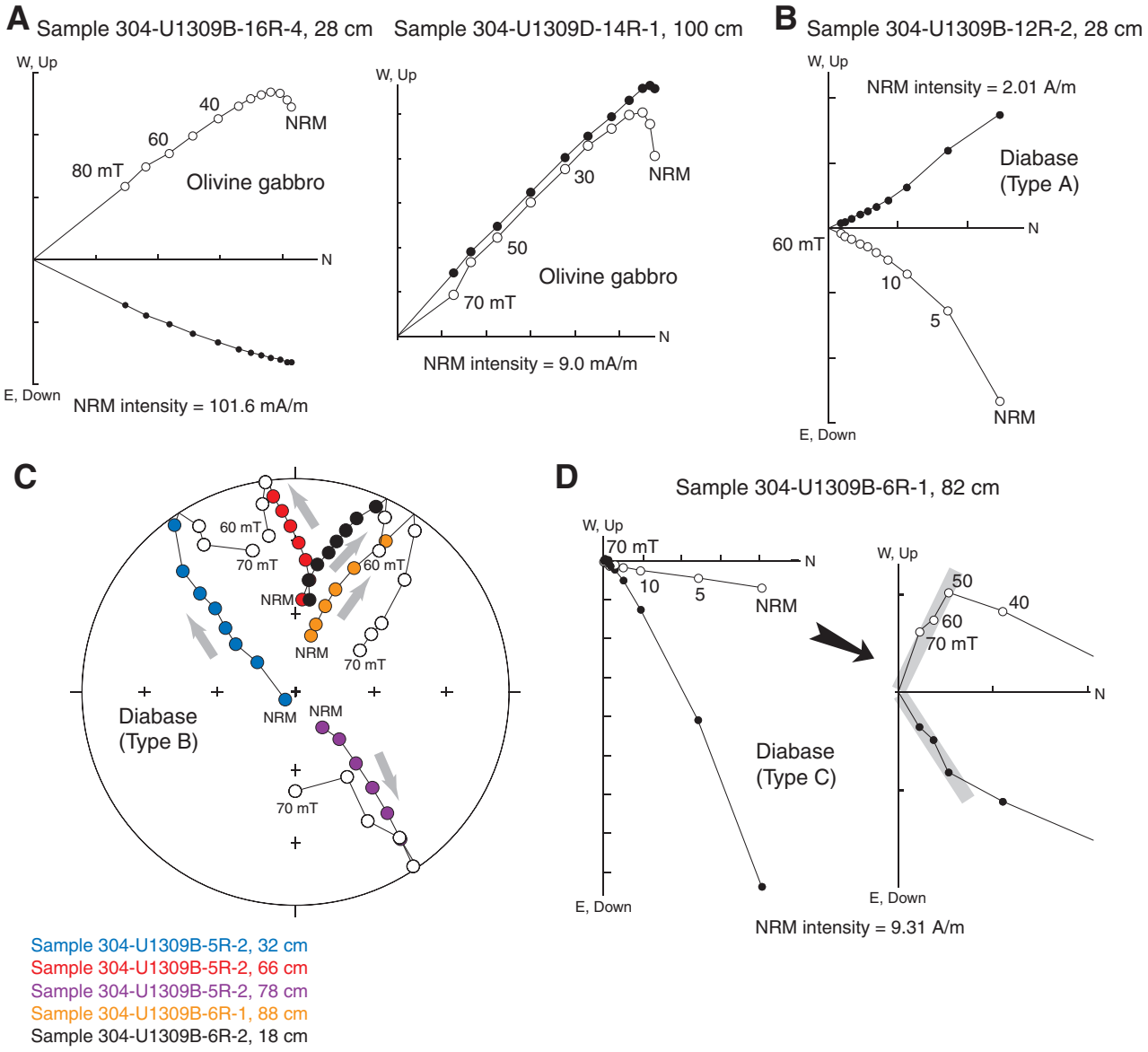

Figure F240. Distribution of characteristic remanence components from archive halves and discrete samples (Expedition 304). Negative inclination (reversed polarity) directions from both archive halves and discrete samples (red and blue) from both Holes (**A**) U1309B and (**B**) U1309D have random declinations as expected for azimuthally unoriented core pieces. Positive inclination (normal polarity) components for both types of samples from Holes (**C**) U1309B and (**D**) U1309D are biased toward +x (archive half) or –x (discrete samples) directions. All data are shown in the core reference frame. Note that the archive-half data are shown at the piece average level.

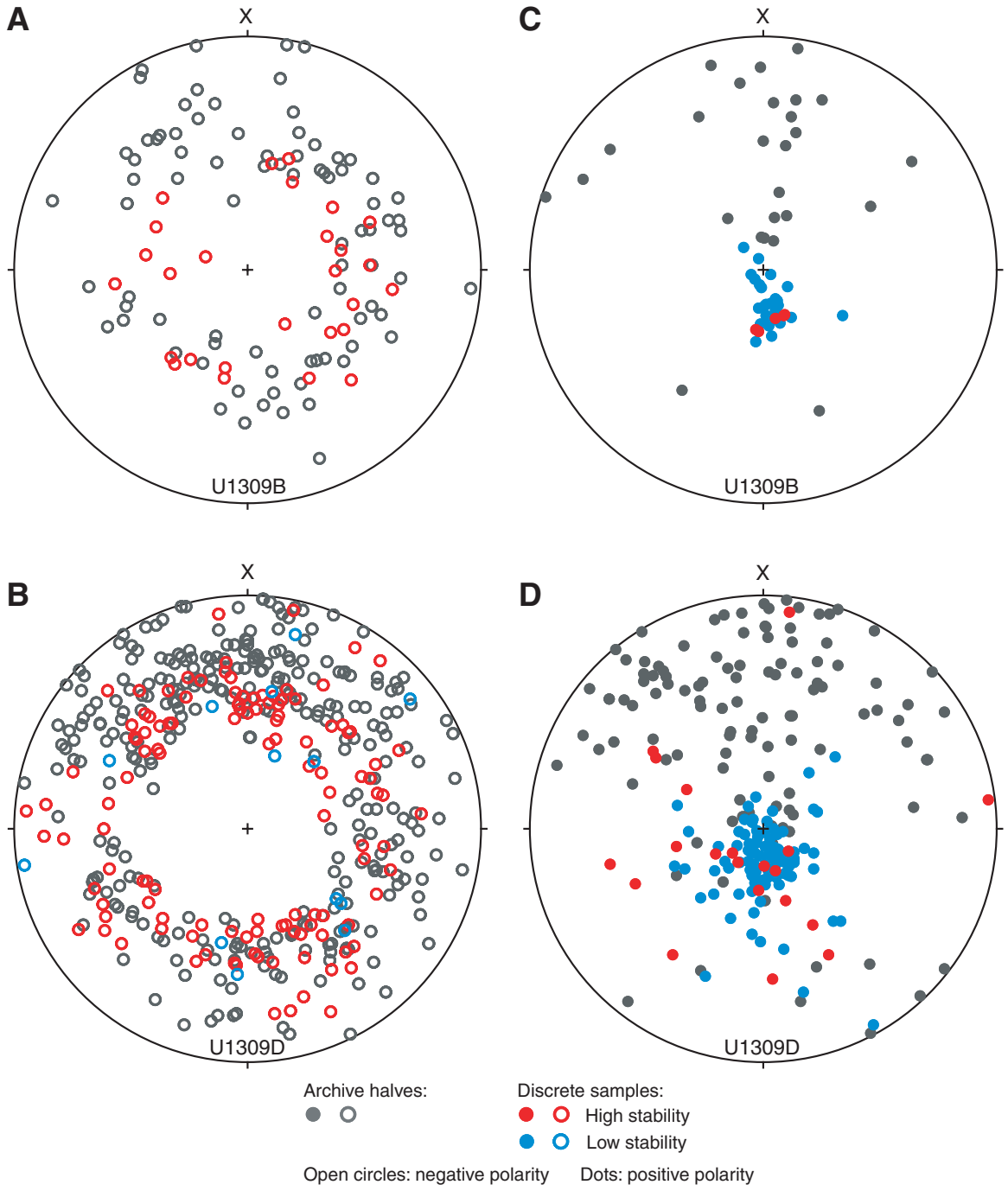

Figure F241. Representative vector endpoint diagrams for discrete samples with well-defined reversed polarity components. Open circles = projections of the remanence onto the north-south vertical plane, solid circles = projections of the remanence onto the horizontal plane. NRM = natural remanent magnetization.

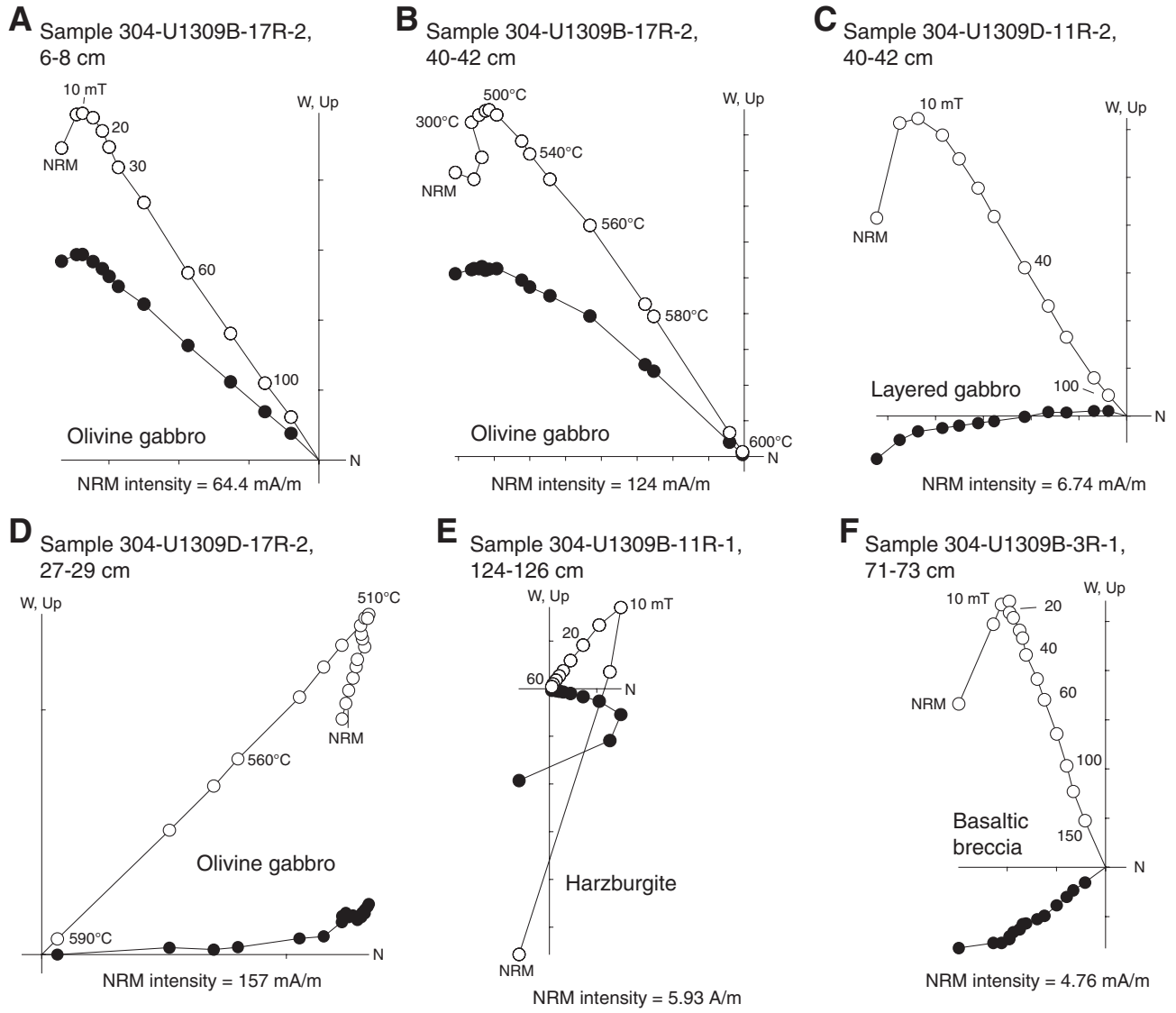

Figure F242. Inclinations of components from principal component analysis of archive-half and discrete sample demagnetization data. **A.** Hole U1309B. (Continued on next page.)

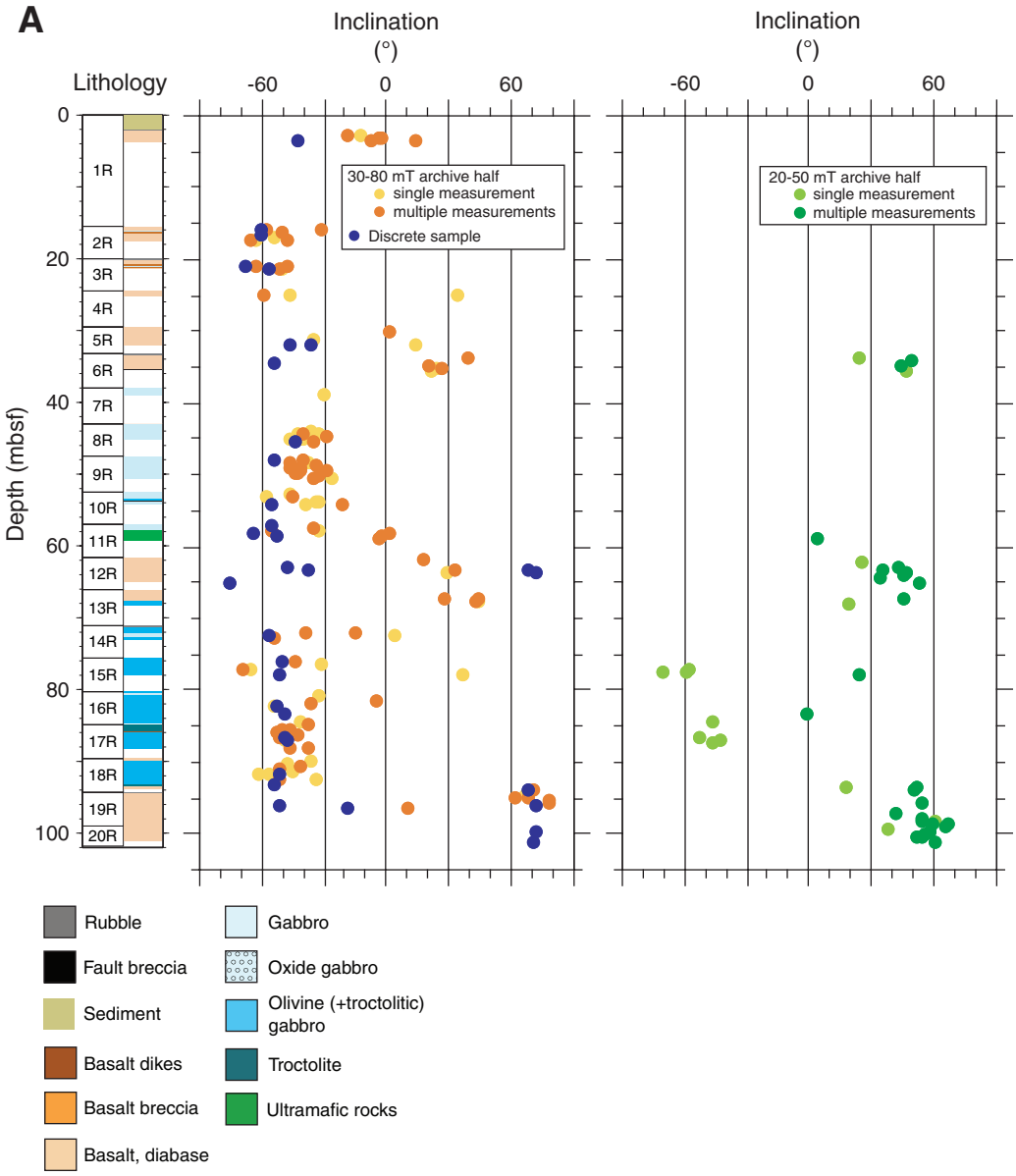

Figure F242 (continued). B. Hole U1309D (Expedition 304).

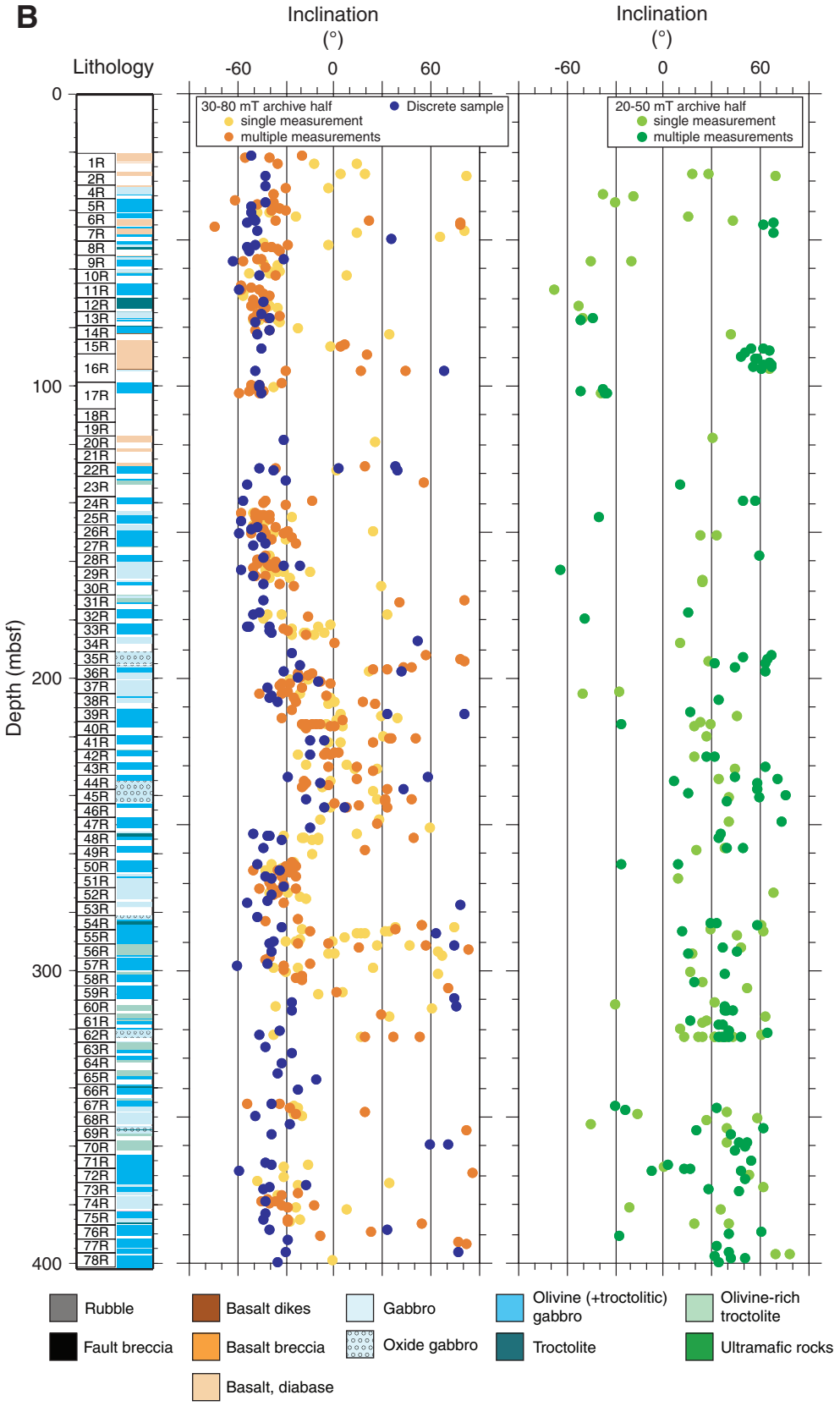

Figure F243. Comparison of stable remanence declinations determined from archive-half pieces and discrete samples taken from the corresponding working-half piece (Expedition 304). Archive-half data represent averages of all characteristic components picked from the archive-half piece.

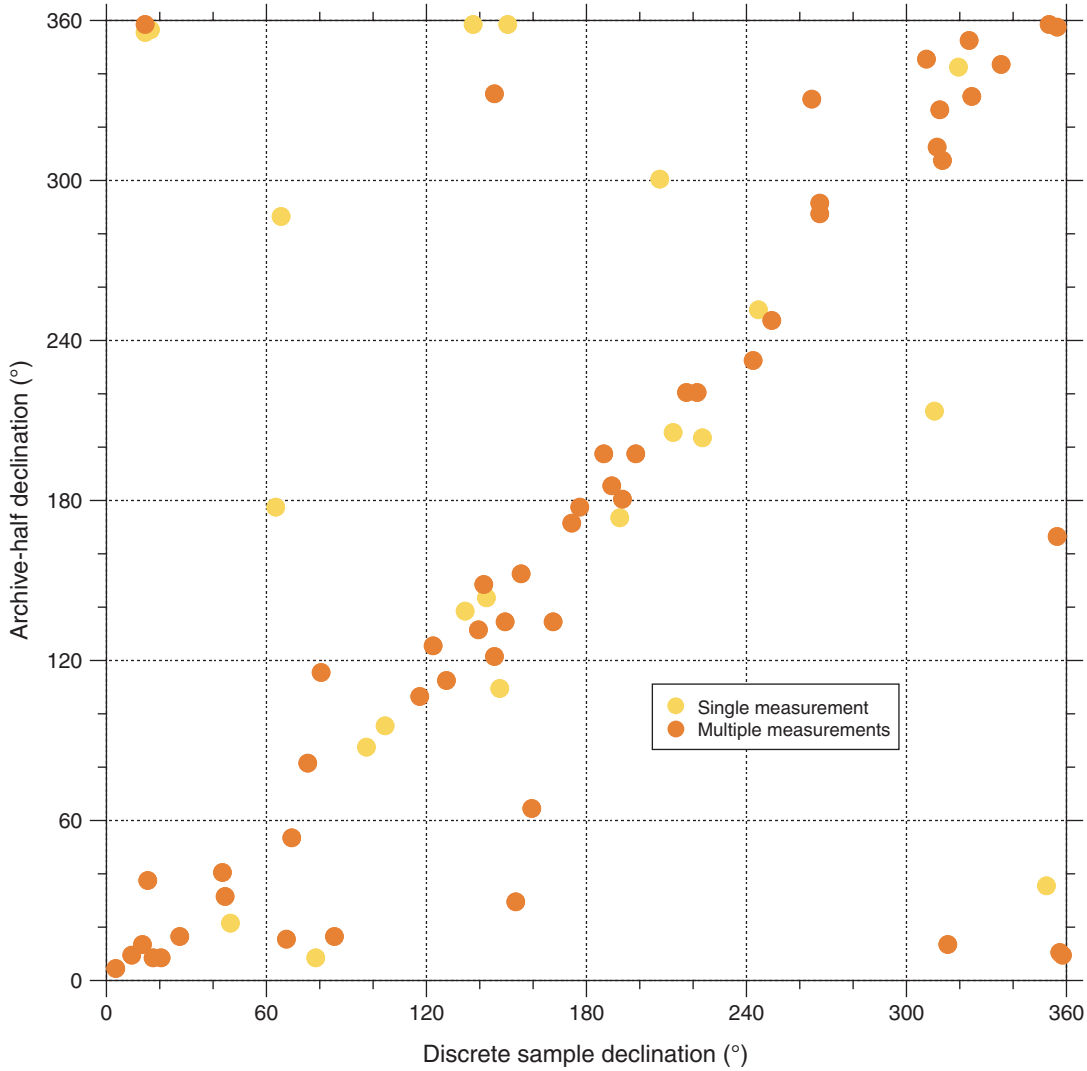

Figure F244. Inclinations of magnetization components identified by principal component analysis of archive-half data as a function of volume susceptibility (measured on the AMST). Note that samples with steep positive inclinations correlate with intervals of high magnetic susceptibility, presumably reflecting the abundance of coarse multidomain magnetite. The green lines indicate the normal (+49°) and reversed (–49°) inclinations expected from a geocentric axial dipole.

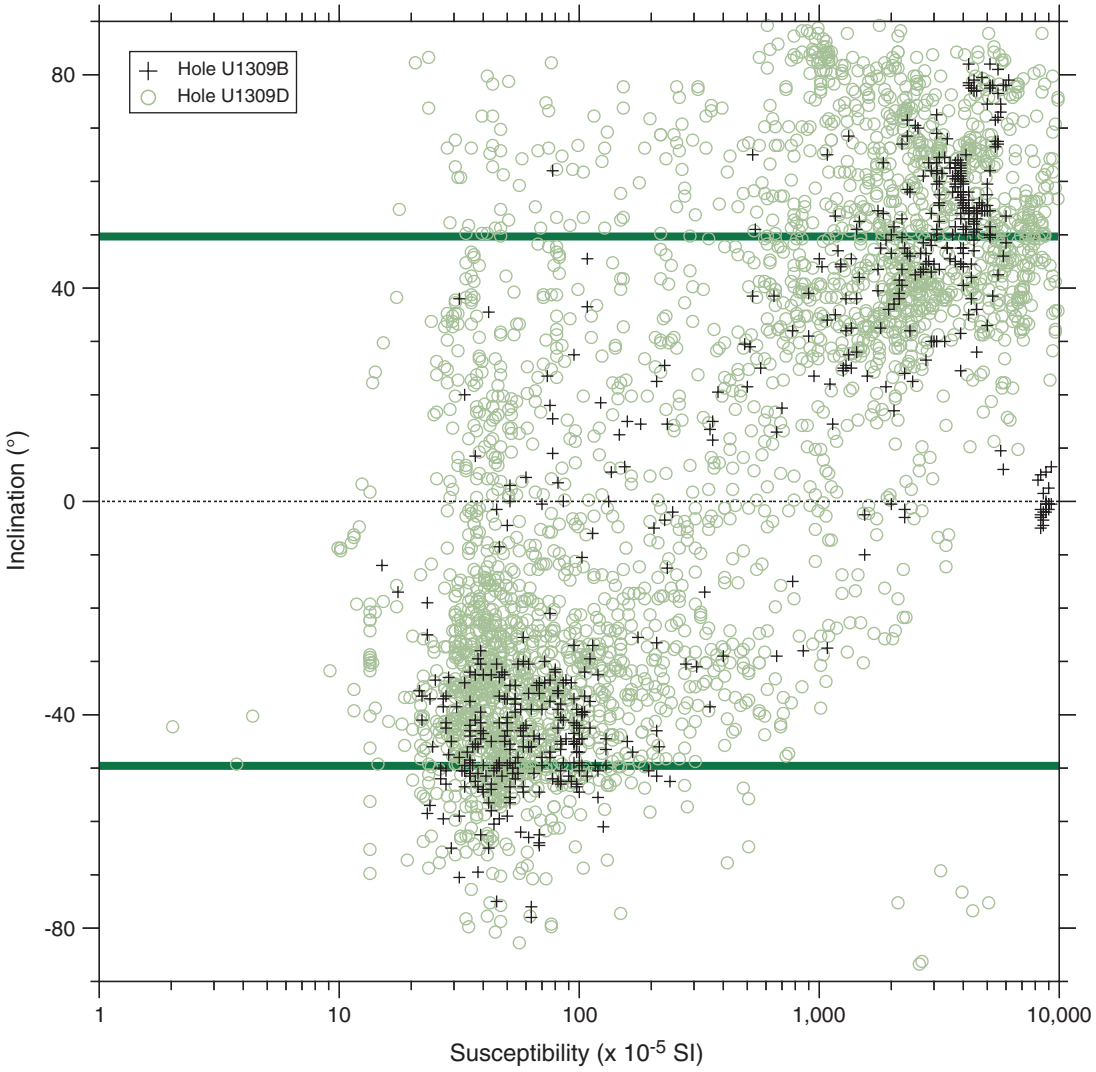

Figure F245. Comparison of different demagnetization treatments from discrete samples within a single diabase interval. **A, C, E.** In all cases, the natural remanent magnetization (NRM) is dominated by a steep normal polarity magnetization component, presumably related to drilling. Low-temperature treatment prior to alternating-field (AF) demagnetization (LTD steps in C) removes a large proportion of the normal polarity component, confirming that this is carried by coarse multidomain magnetite. **B, D.** A reversed polarity component (representing only a small fraction of the NRM) is isolated by demagnetization at high alternating fields. **E, F.** In contrast, thermal demagnetization isolates only a single, normal polarity component indistinguishable from the low-stability direction defined by AF demagnetization and with a maximum unblocking temperature close to the Curie temperature of magnetite. Open circles = projections of the remanence onto the north-south vertical plane, solid circles = projections of the remanence onto the horizontal plane.

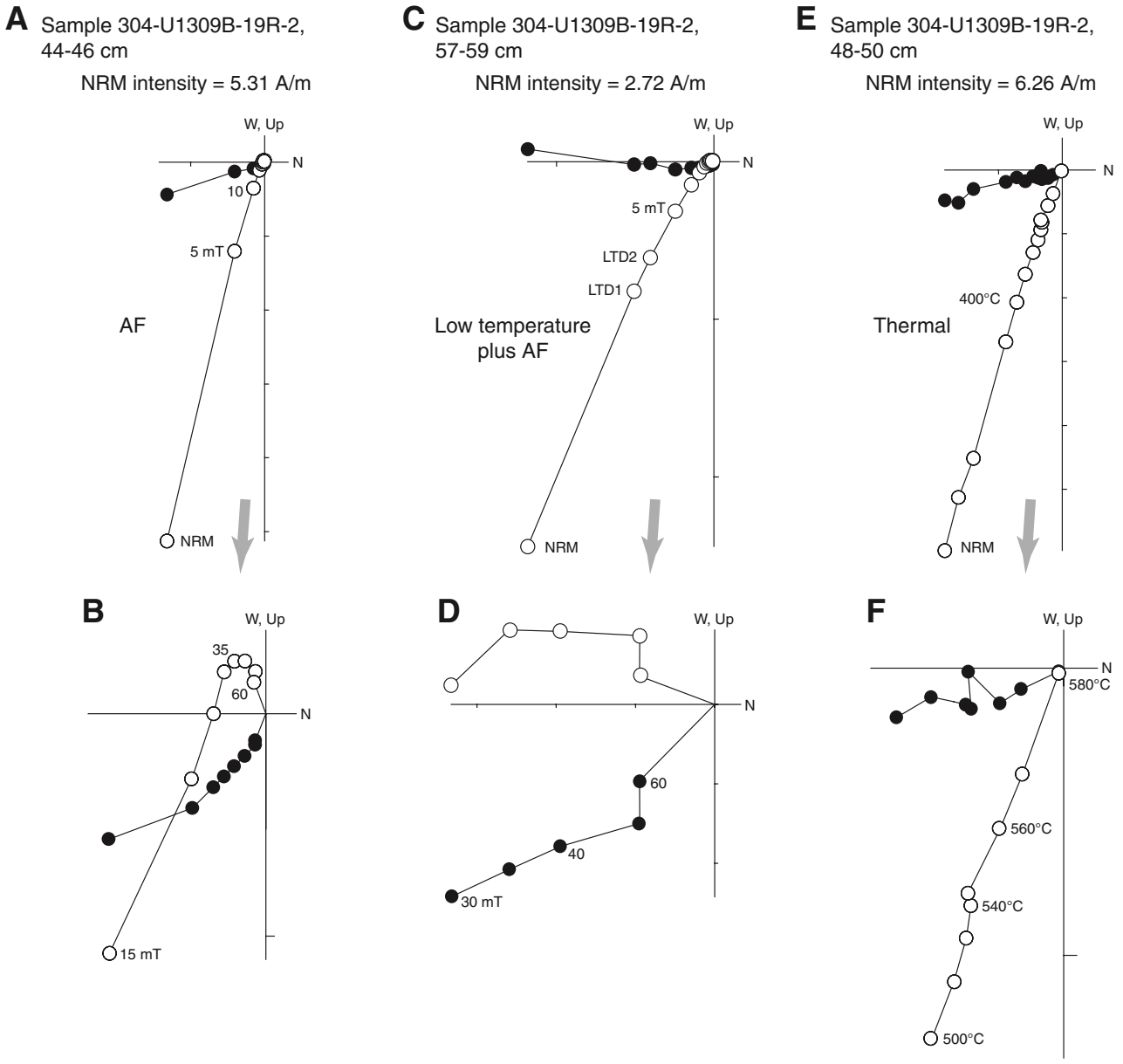

Figure F246. Archive-half data from Section 304-U1309D-22R-2, illustrating complex magnetic behavior presumably related to the presence of both normal and reversed polarity material. **A.** Scanned image of archive half and sketches of the archive and working halves, illustrating the principal lithologic and alteration features in the section. Red circles = discrete sample locations. Amph. = amphibole, DIS = digital imaging system, Pc = piece. **B.** Magnetic susceptibility data as measured on the Archive multisensor track (AMST) system. (**C**) Declination and (**D**) inclination variations determined from principal component analysis of the archive-half data (red circles). Larger blue dots = the results from thermally demagnetized discrete samples, smaller dots = AF demagnetization results from exterior chips of these same minicores. **E.** Median destructive field (MDF) calculated from the archive-half demagnetization data.

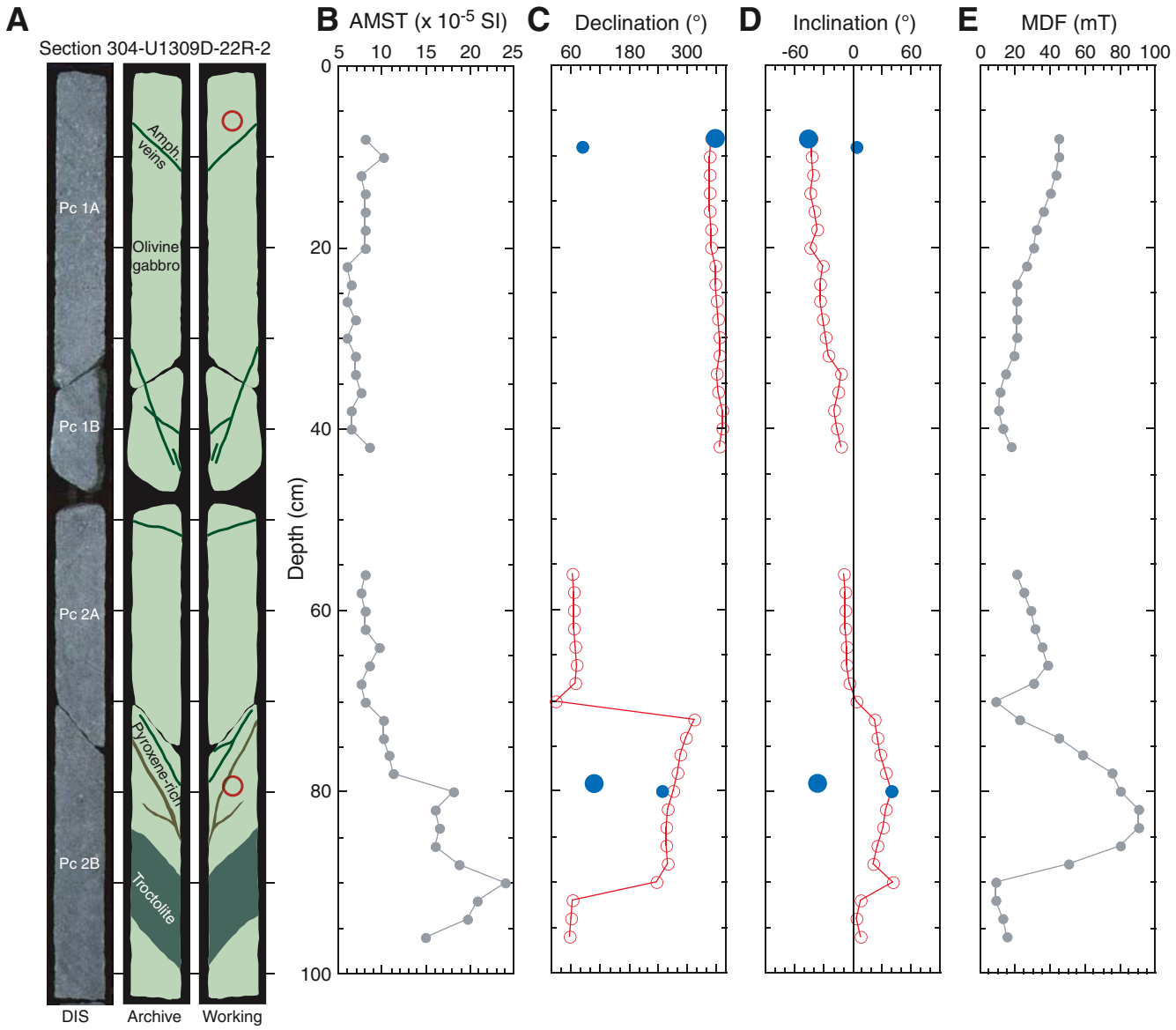

Figure F247. Demagnetization results from Section 304-U1309D-22R-2. **A.** Scanned image of archive halves and sketches of the archive and working halves illustrating the principal lithologic and alteration features in the section. Red circles = discrete sample locations. Amph. = amphibole, DIS = digital imaging system, Ps = piece. **B.** Thermal demagnetization results from a discrete sample in Section 304-U1309D-22R-2 (Piece 1) reveal a reversed polarity characteristic remanent magnetization (ChRM) with a lower stability normal polarity component stable up to temperatures of 520°C. **C.** AF demagnetization results from the corresponding interval of the archive half. **D.** Thermal demagnetization results from a discrete sample in the vicinity of later pyroxene-rich vein show a much larger normal polarity overprint (stable to 550°C). AF demagnetization results from both (**E**) the corresponding archive-half interval and (**F**) the exterior chip of the discrete sample; both have a high stability component of normal polarity similar to the normal polarity overprint isolated by thermal demagnetization of the discrete sample in D. Open circles = projections of the remanence onto the north-south vertical plane, solid circles = projections of the remanence onto the horizontal plane. NRM = natural remanent magnetization. Note that the ChRM directions have been rotated 180° for comparison between pieces.

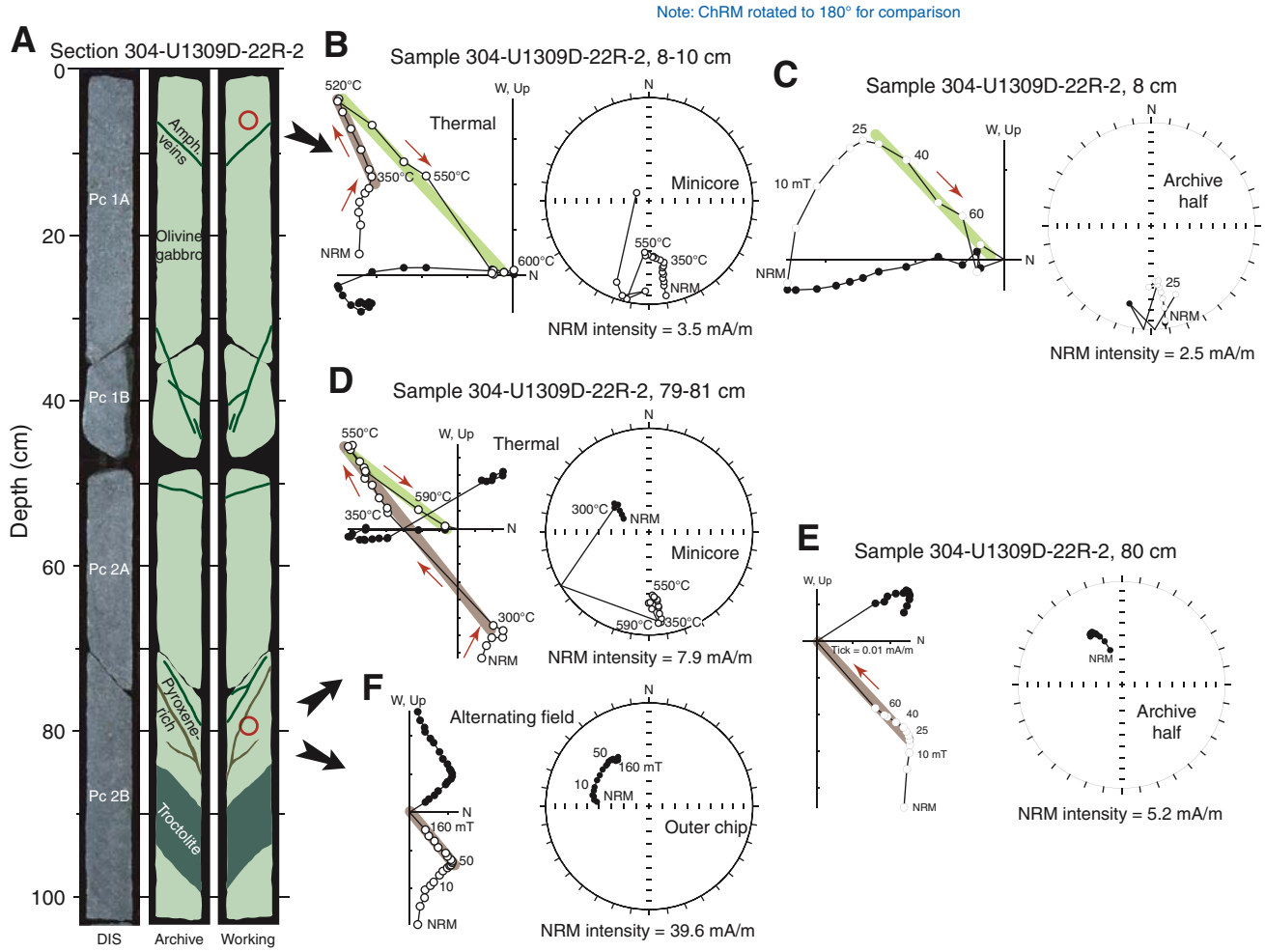

Figure F248. A–E. Examples of thermal demagnetization data illustrating multicomponent remanences from Hole U1309D (Expedition 304). For vector endpoint diagrams: open circles = projections of remanence onto north-south vertical plane, solid circles = projections of remanence onto horizontal plane. Arrows indicate the progressive removal of drilling-induced (blue arrows), normal polarity overprint (orange arrows), and high-temperature reversed polarity component (red arrows). Note that the sample shown in C has an additional reversed polarity overprint at lower temperatures (yellow arrow). The demagnetization data are also shown on the corresponding equal area projections, with insets showing the decay of the normalized remanence. For demagnetization data: solid circles = lower hemisphere, open circles = upper hemisphere. NRM = natural remanent magnetization.

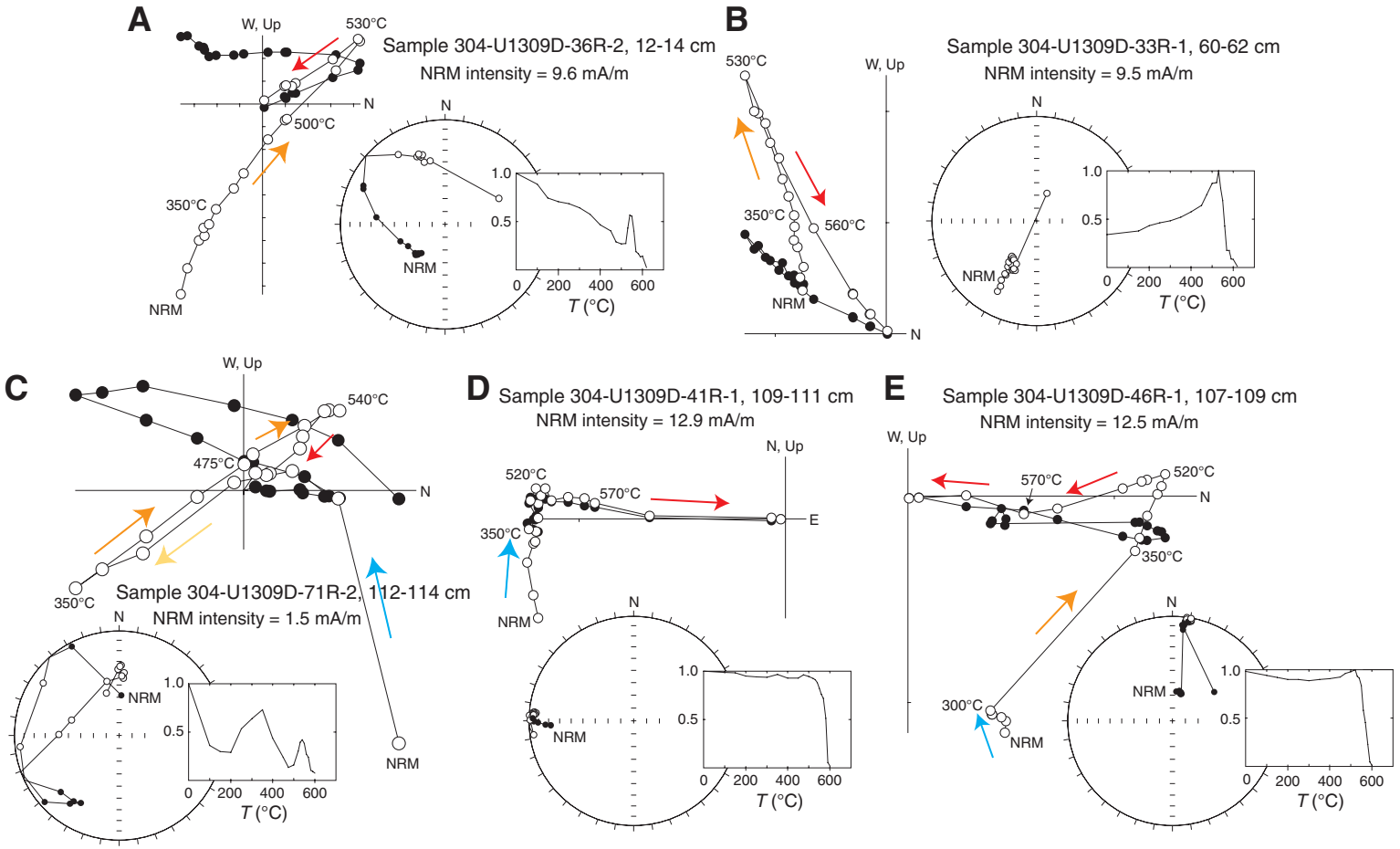

Figure F249. Anisotropy of magnetic susceptibility (AMS) for discrete samples from Site U1309 (Expedition 304). **A.** Data (in core coordinates) obtained from all discrete samples that have sufficiently high magnetic susceptibilities to allow accurate AMS determinations using the shipboard Kappabridge. **B.** Data restored to geographic reference frame using the remanent declination (see text) for all samples where a characteristic remanence direction could be isolated. **C.** AMS data from diabase and basalt intervals in the geographic reference frame. **D.** AMS data from serpentinized harzburgite and gabbroic samples restored to the geographic reference frame. **E.** Degree of anisotropy (P') versus shape factor (T).

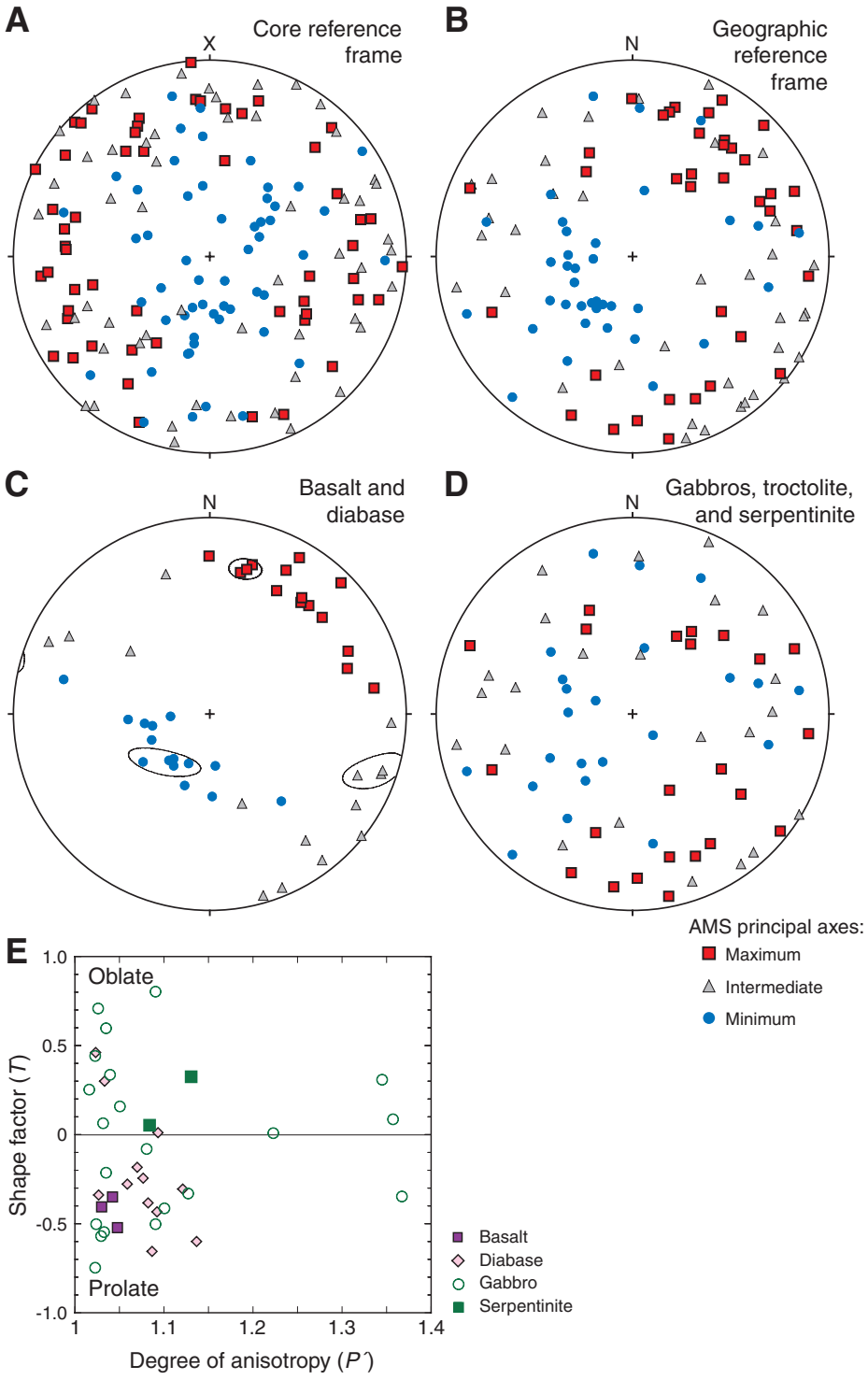

Figure F250. Comparison of sample magnetizations from recovered core and magnetic anomaly data acquired during logging. Remanence intensity from the archive halves is after 10 mT demagnetization. Average intensities used for modeling of the borehole magnetic field are shown by the heavy blue lines. Column 3 shows uncorrected horizontal (B_h) and vertical (B_v) magnetic anomaly profiles from run 1 of the GPIT tool. Magnetic anomalies calculated by subtracting the IGRF field values at the site (declination = –15.7°, inclination = 47.8°, intensity = 40,918 nT). Forward modeling results (heavier lines) based on the observed magnetization values from the core suggest large offsets of the fluxgate sensors. Column 4 shows anomaly profiles after removal of offsets of –1850 nT and +5150 nT from the horizontal and vertical anomaly components, respectively. An exponential fit to the magnetic anomaly from the drill pipe has also been removed from the vertical component.

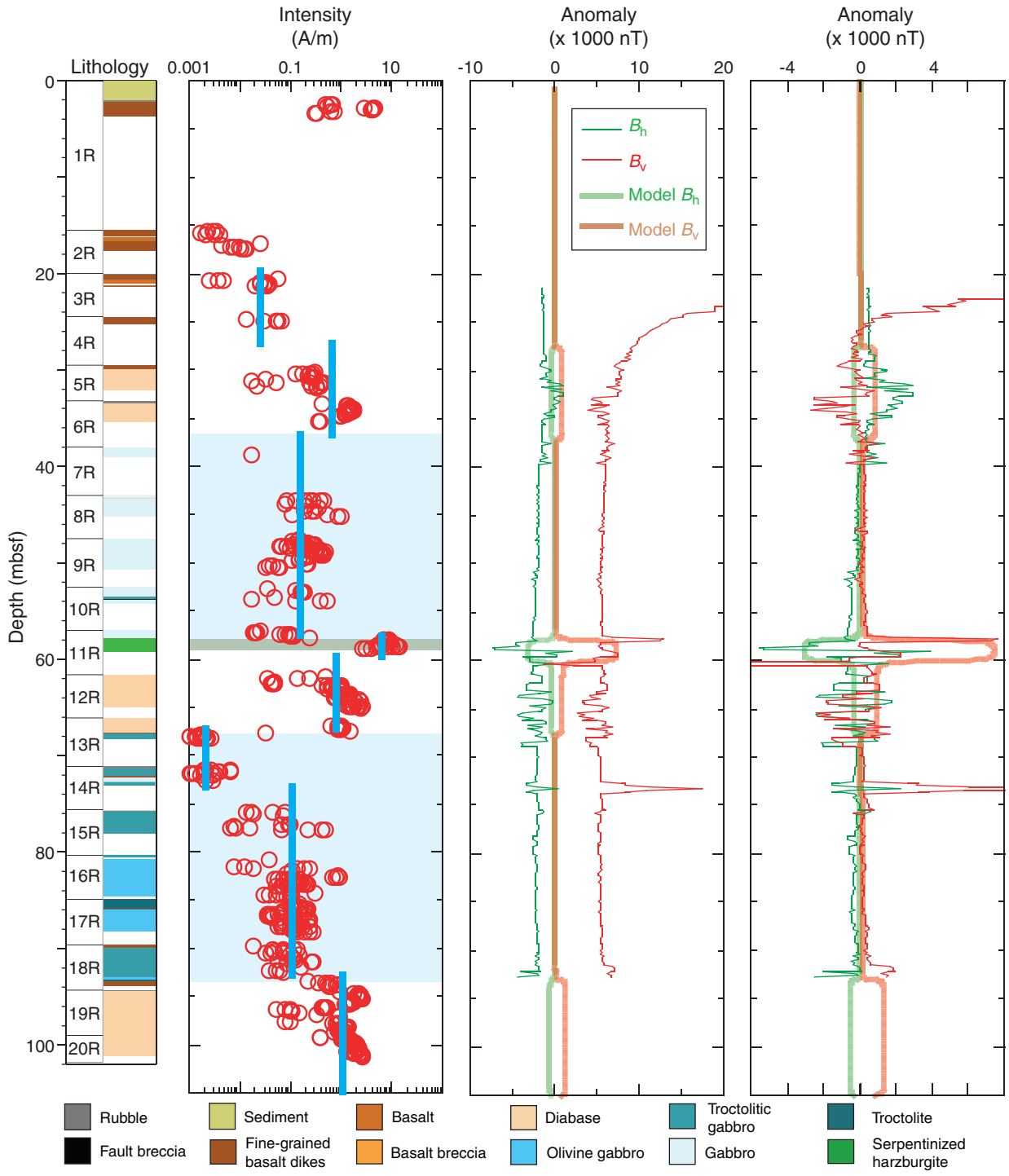

Figure F251. Summary of archive-half magnetic measurements and AMST susceptibility from Hole U1309D. Gray circles = NRM, purple and blue open circles = remanence after 30 mT demagnetization. (Continued on next nine pages.)

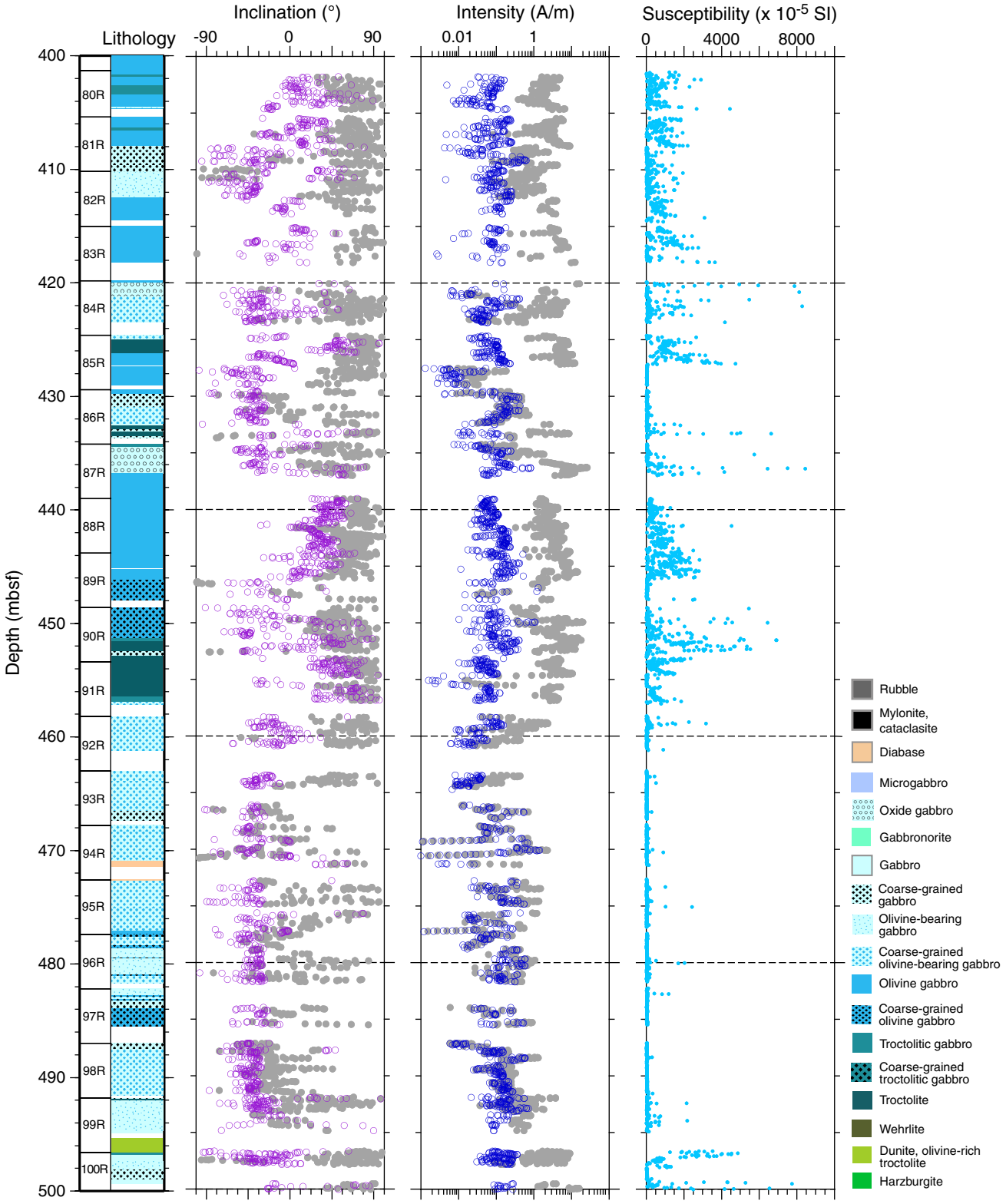

Figure F251 (continued).

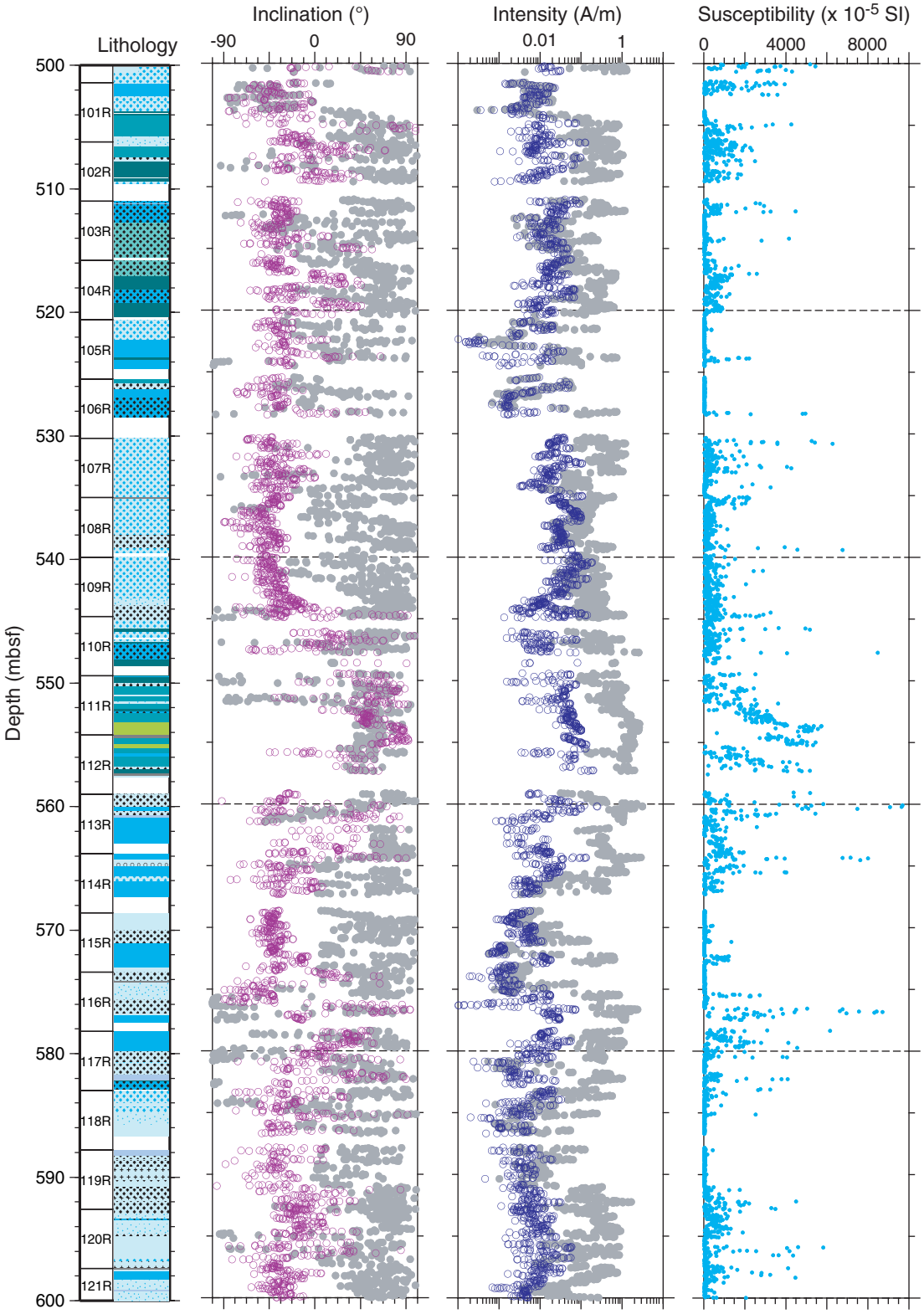

Figure F251 (continued).

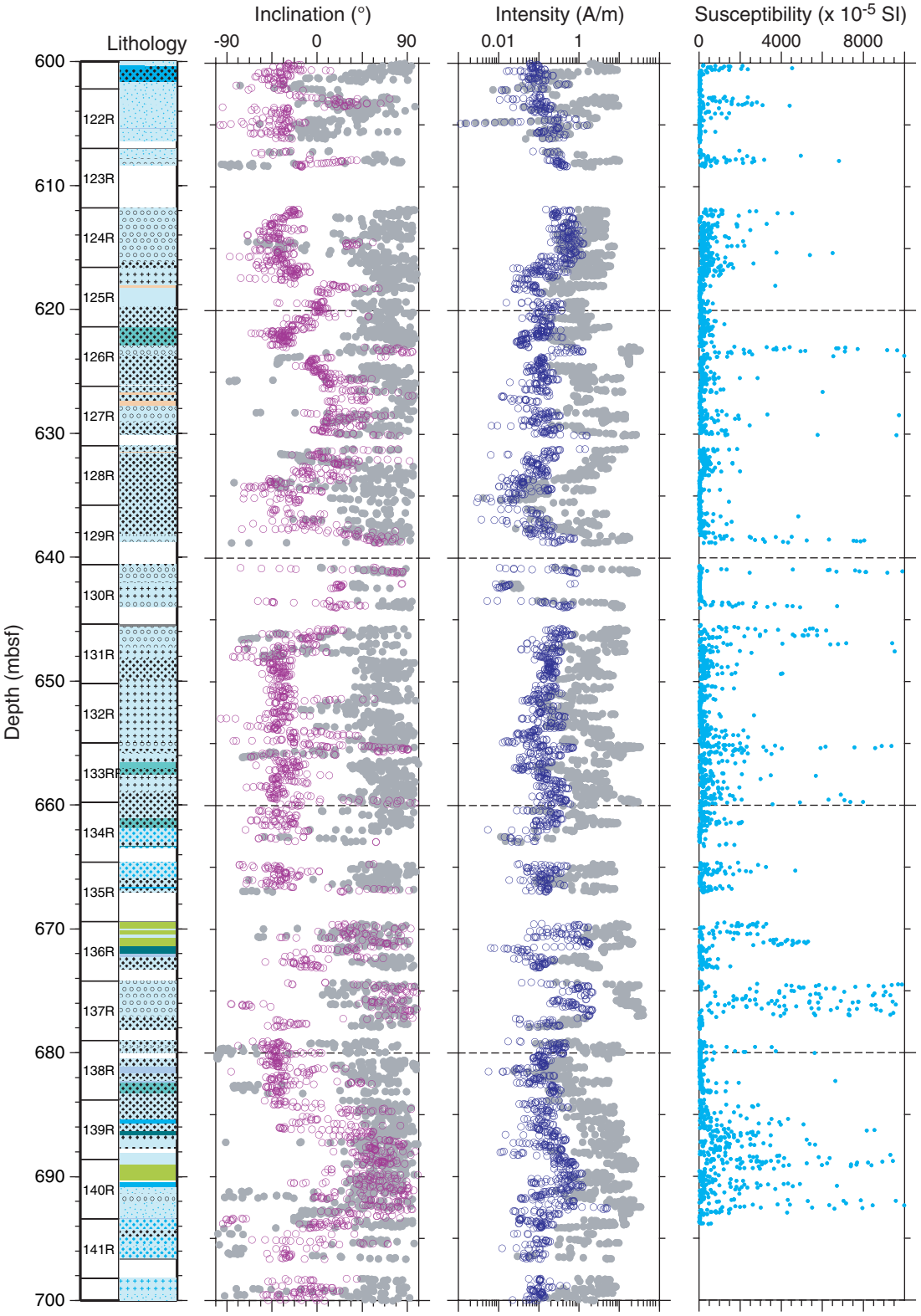

Figure F251 (continued).

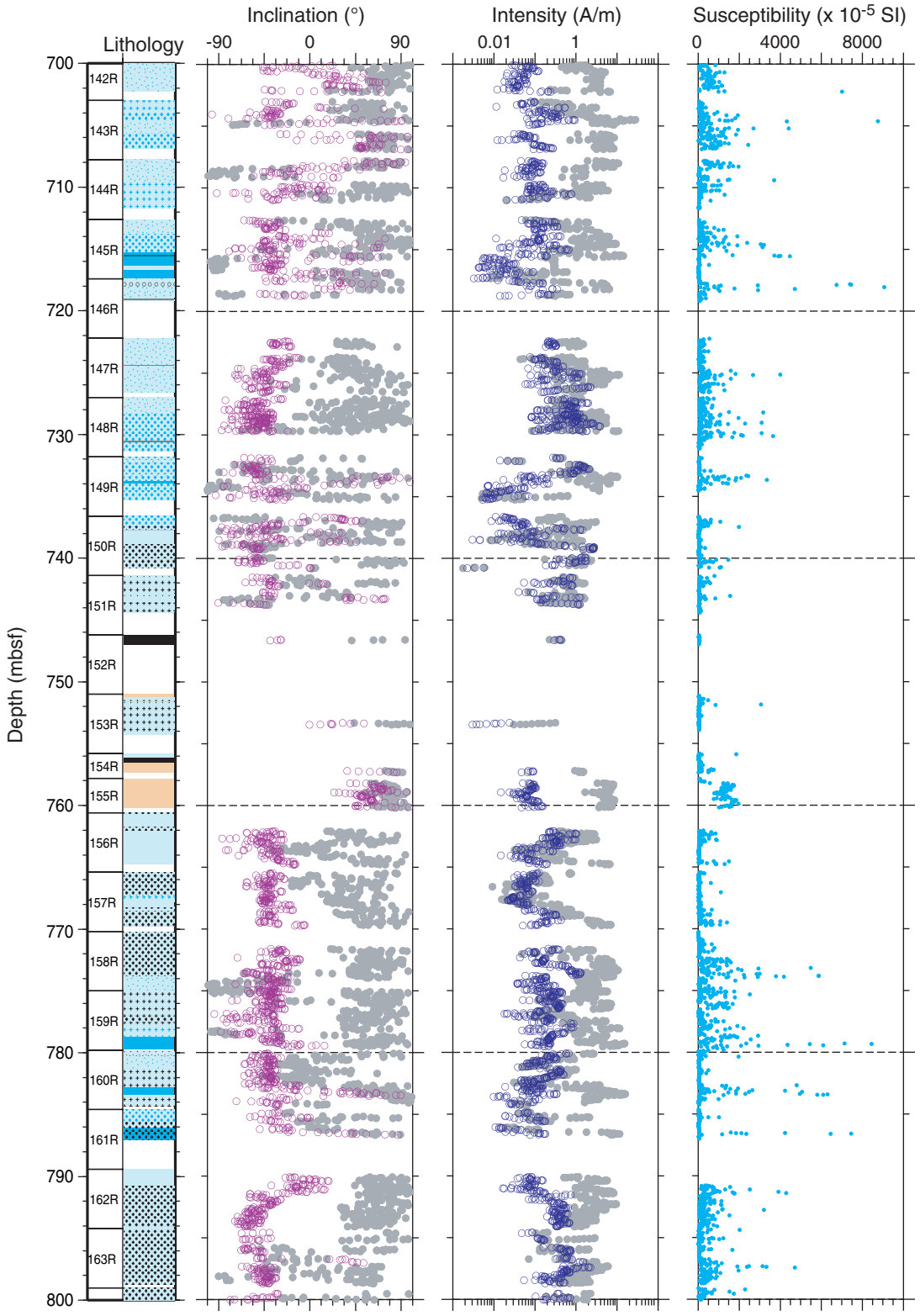

Figure F251 (continued).

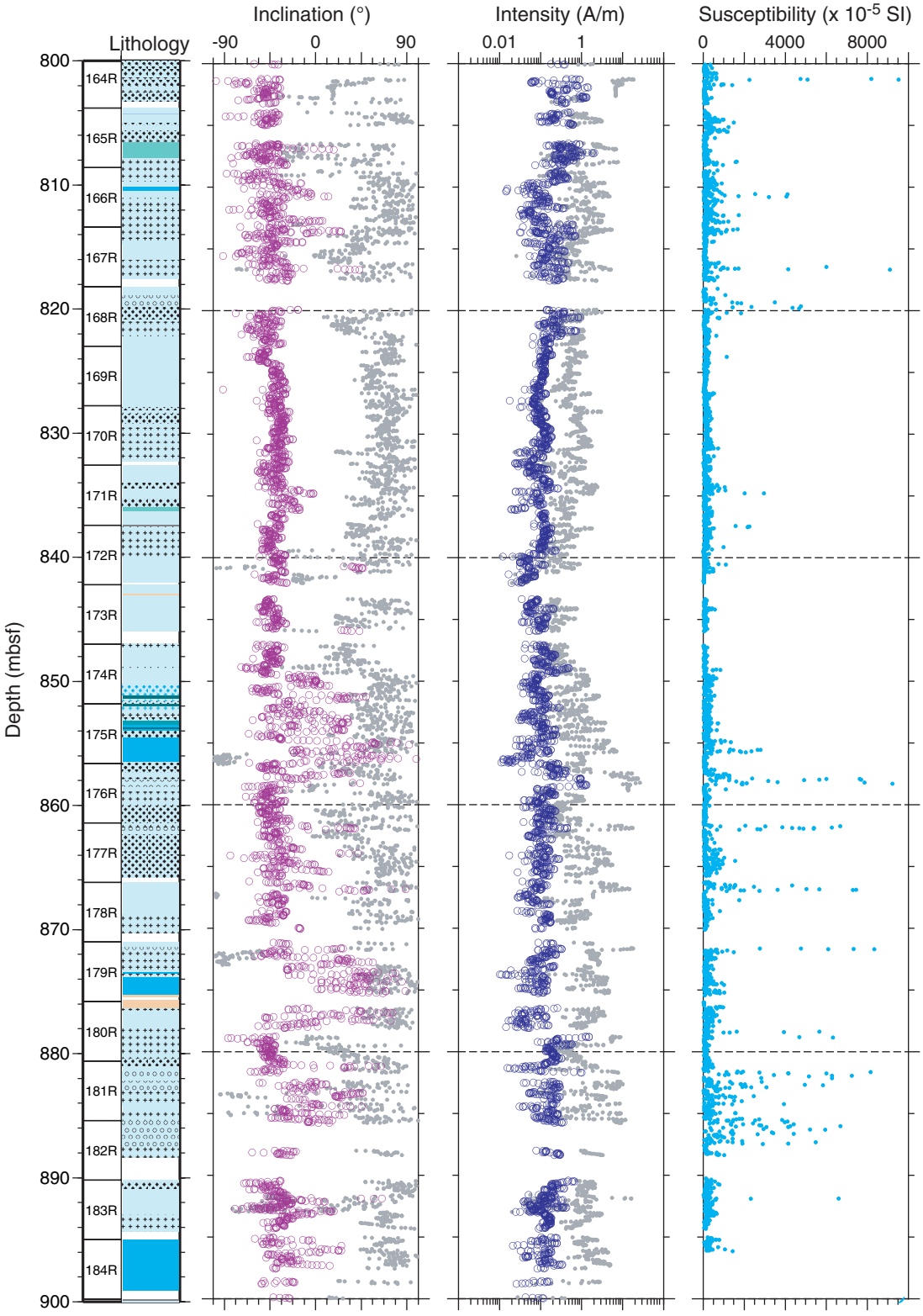

Figure F251 (continued).

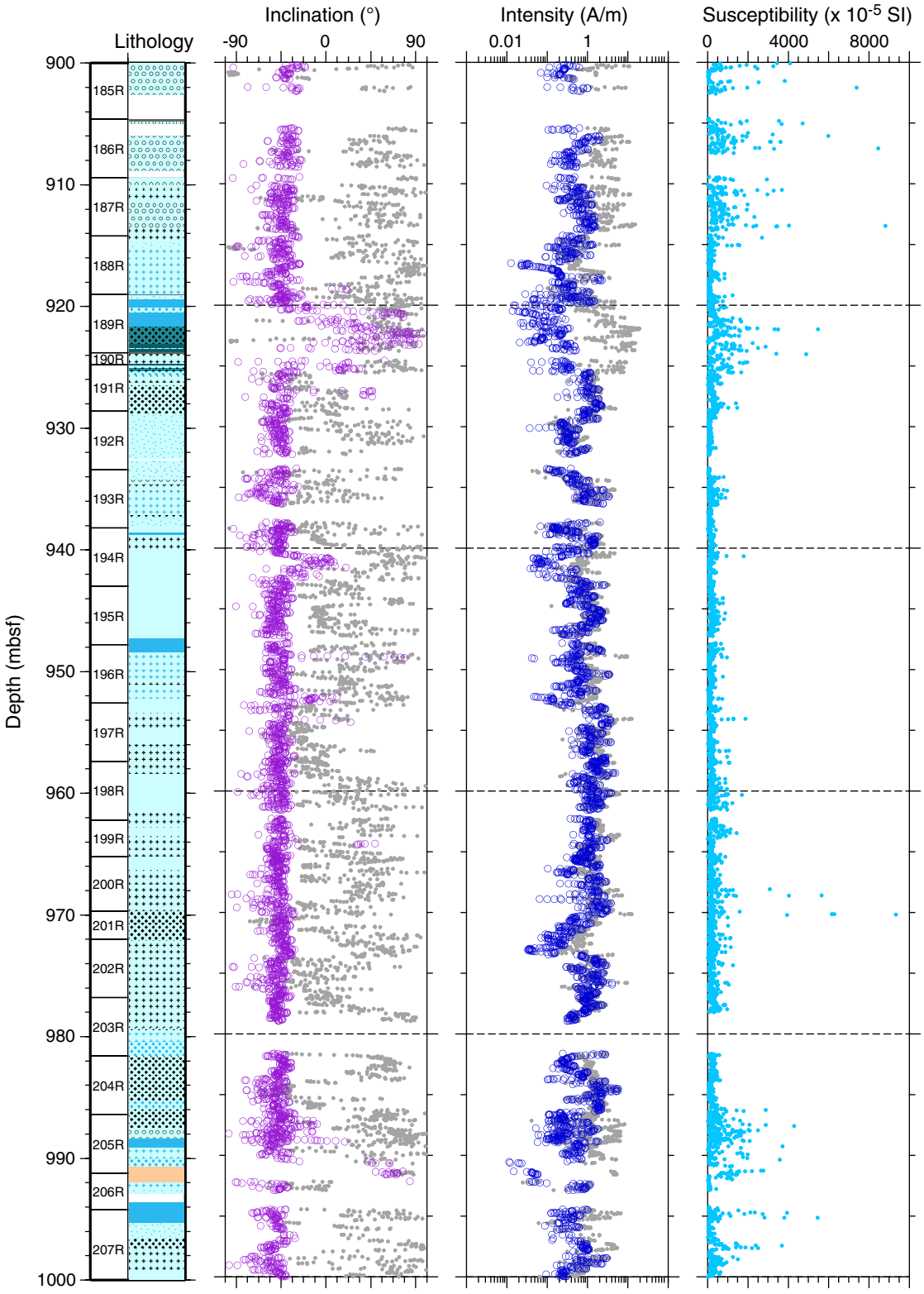

Figure F251 (continued).

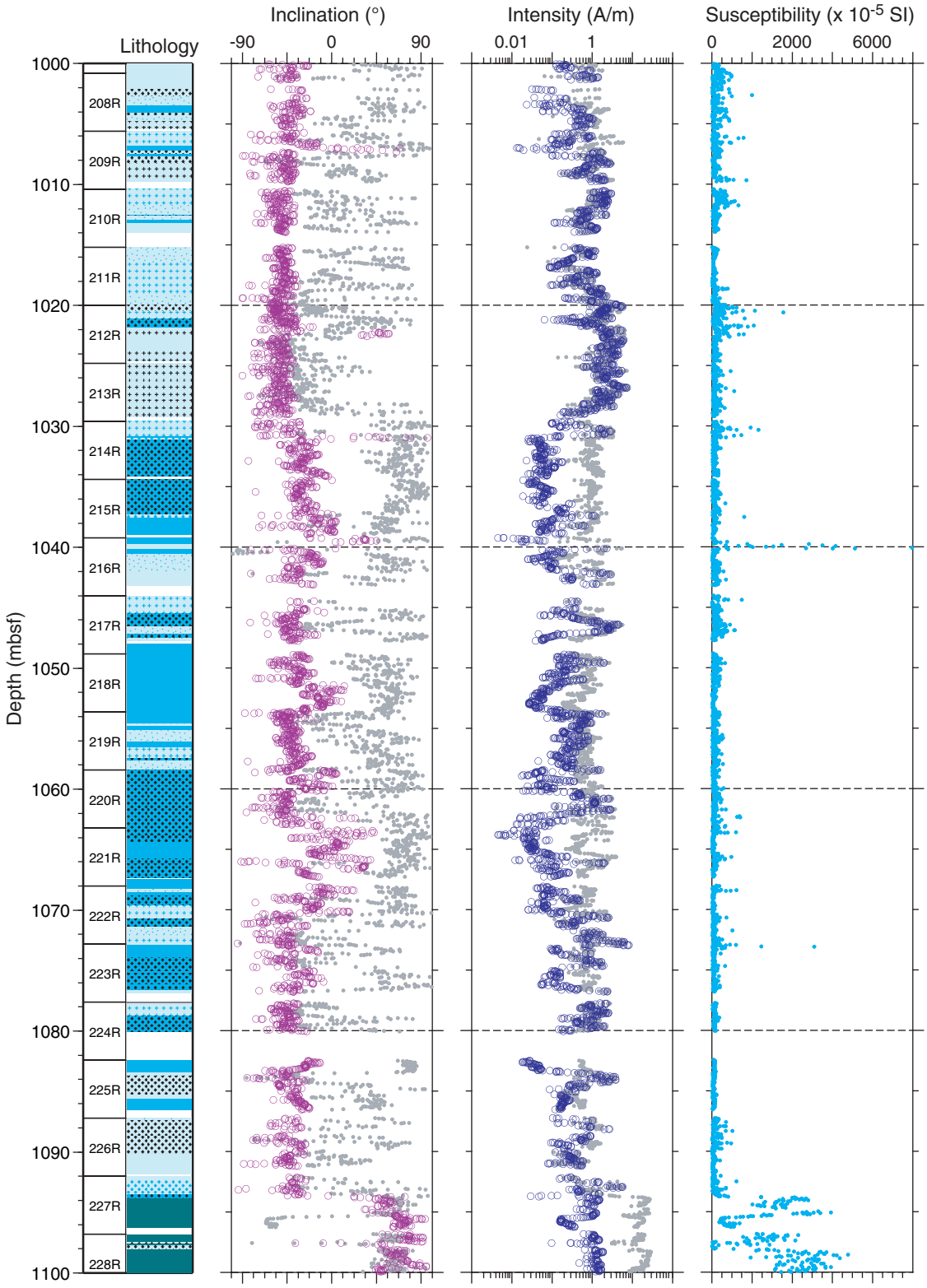

Figure F251 (continued).

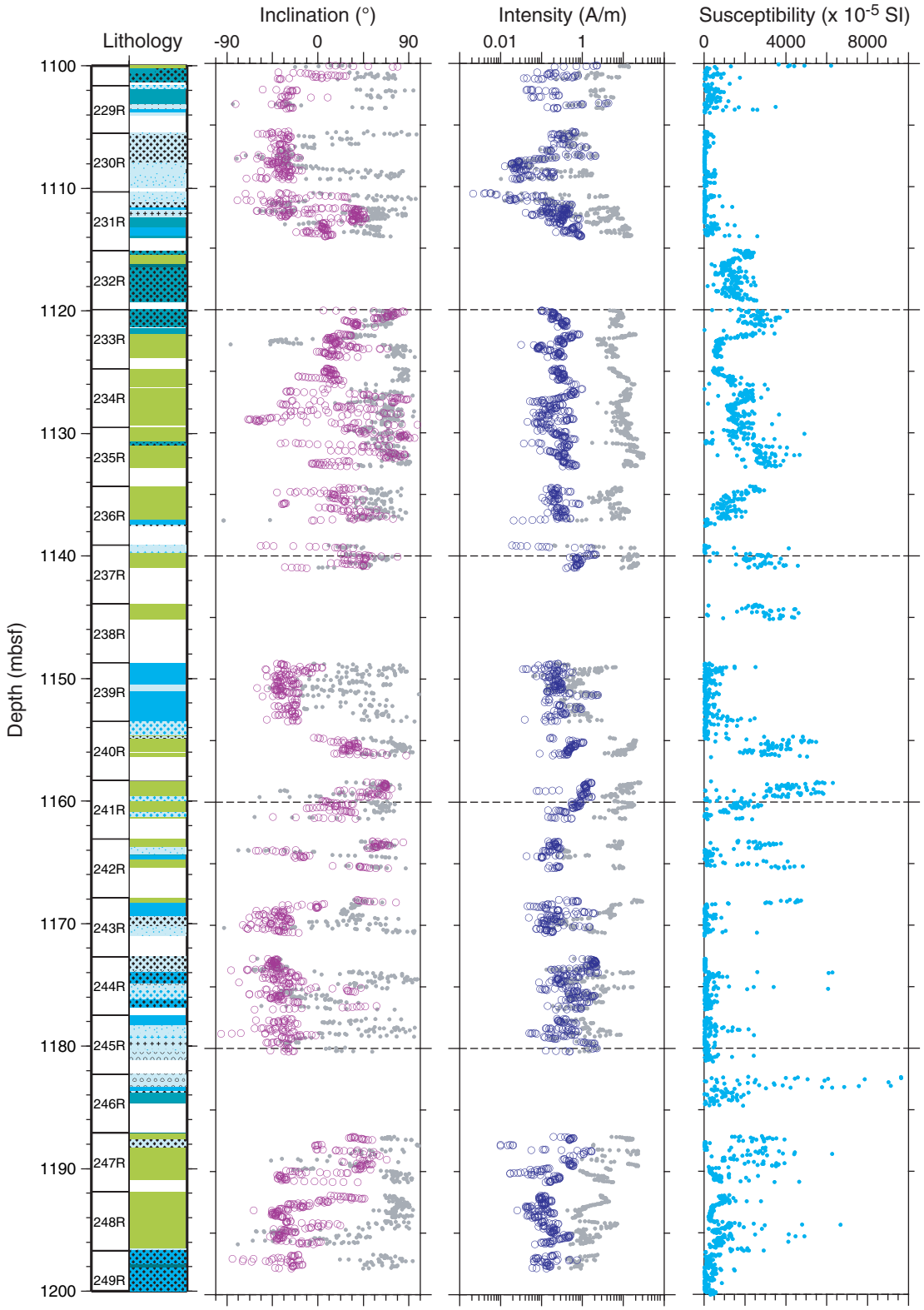

Figure F251 (continued).

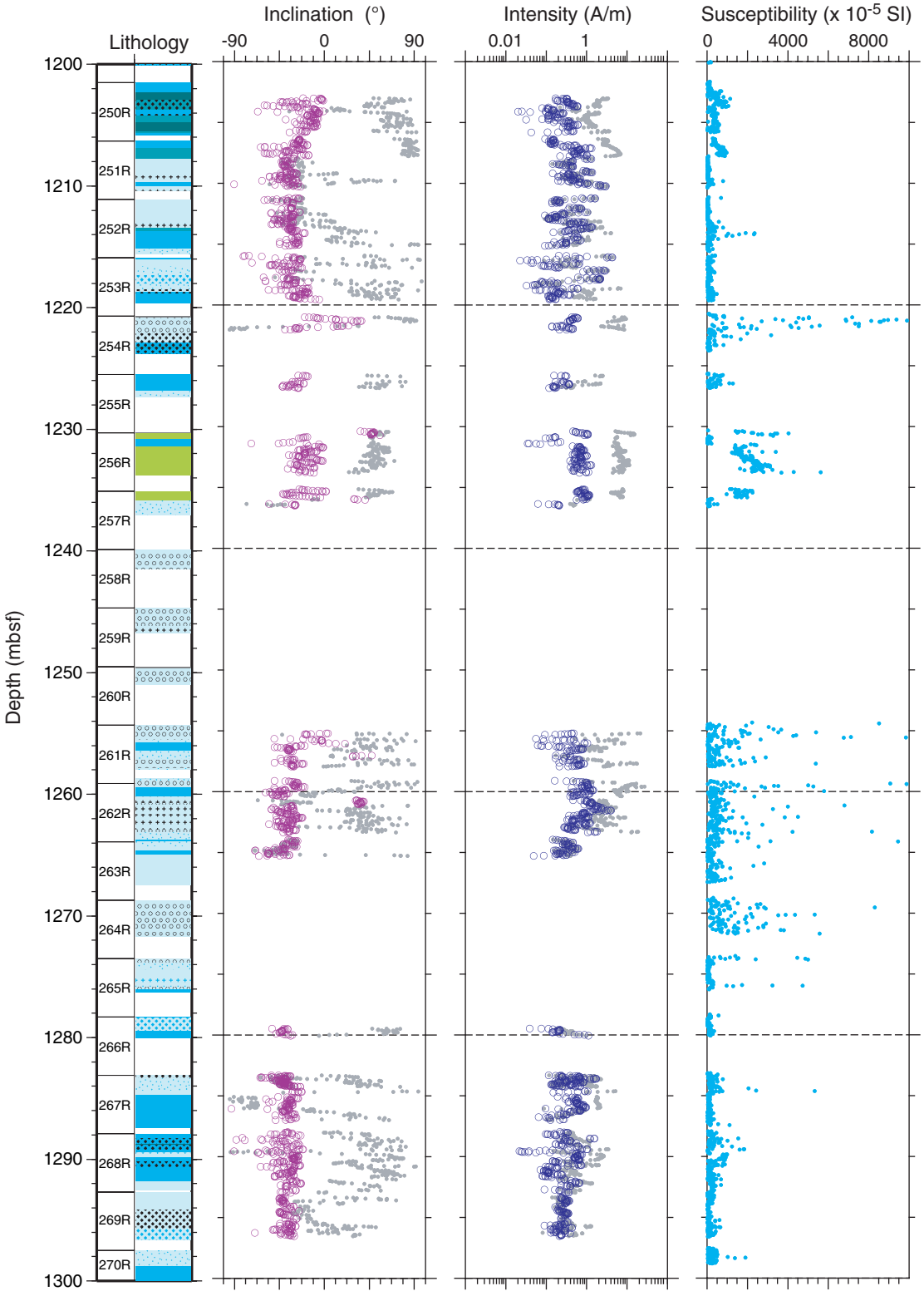

Figure F251 (continued).

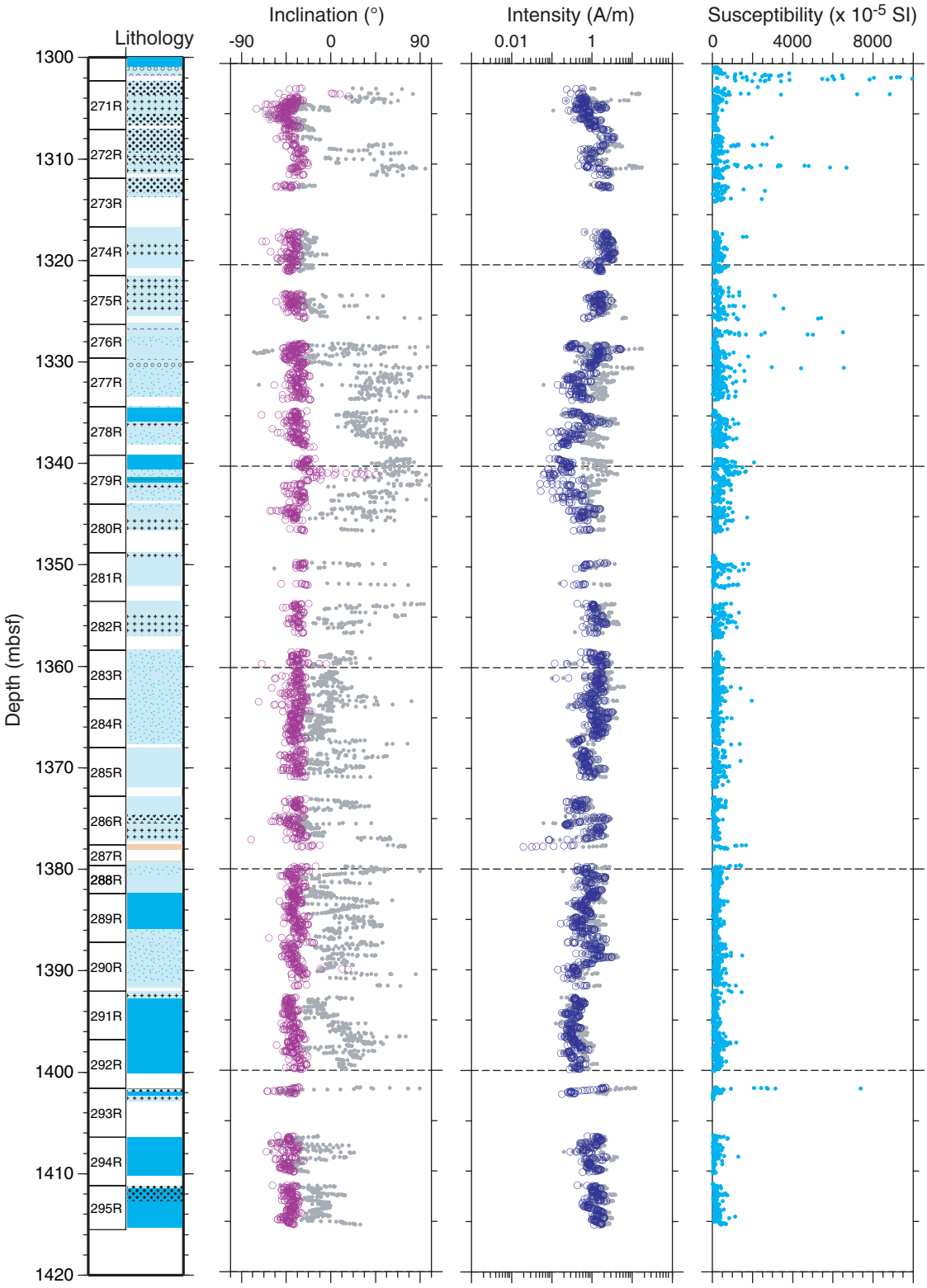

Figure F252. Inclination after 30 mT demagnetization for various rock types from Hole U1309D during Expedition 305, revealing clustering of reversed and normal polarities for individual lithologies.

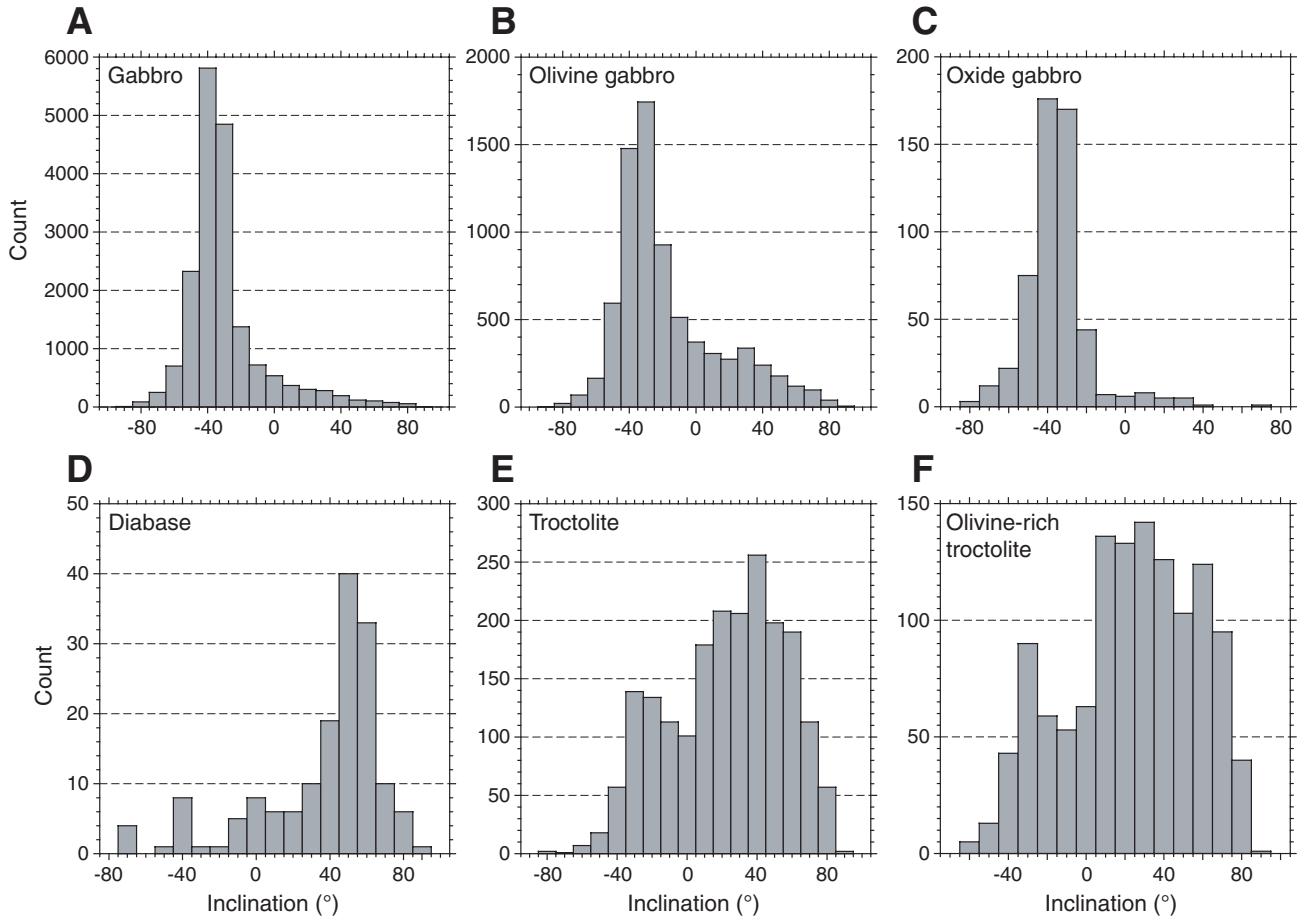

Figure F253. Inclination after 30 mT AF demagnetization and magnetic susceptibility (Expedition 305), showing that concentrations of samples with negative inclinations correlate with intervals of low magnetic susceptibility. Contours = 5, 10, 20, 50, 100, 200 (brightest).

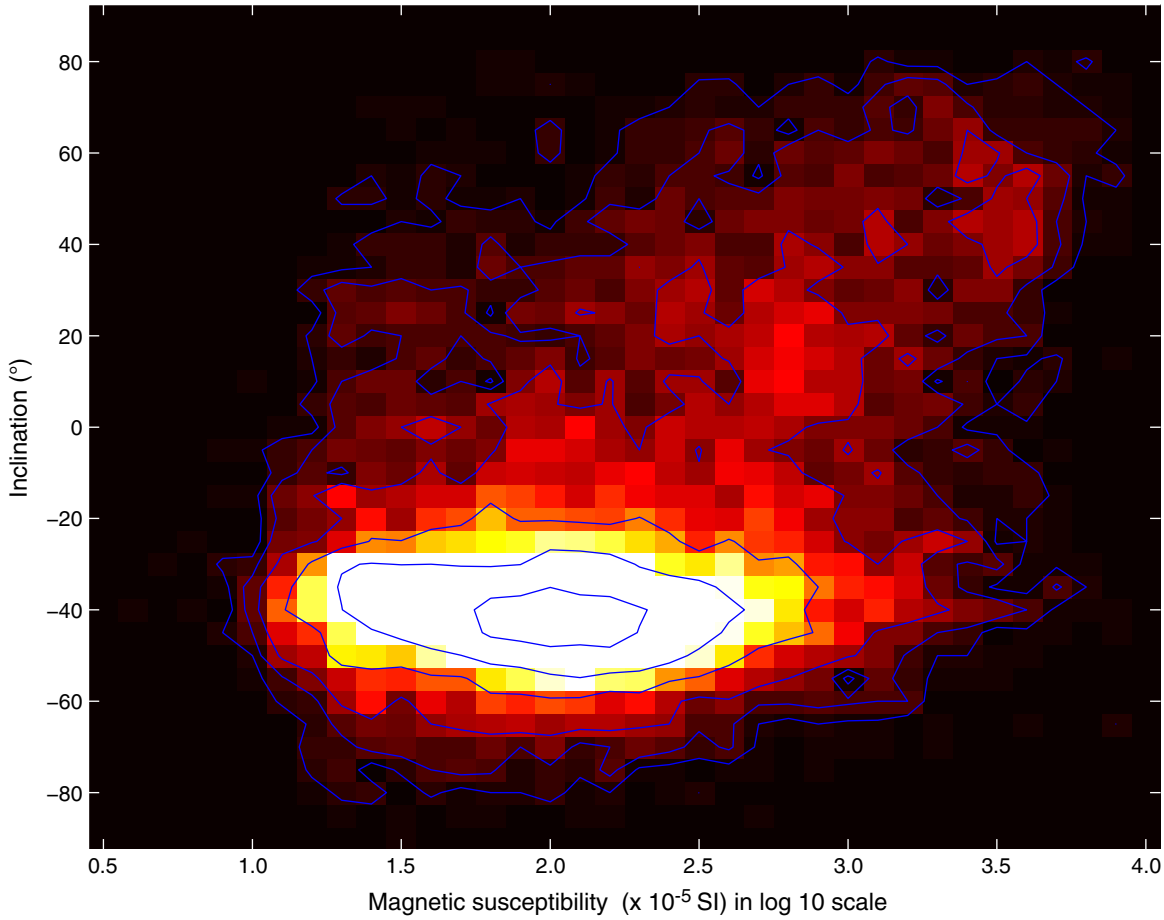

Figure F254. Representative vector endpoint diagrams for discrete samples with well-defined reversed and normal polarity ChRM magnetization. Solid circles = projection of the magnetization vector endpoints on the horizontal plane, open circles = projection of the magnetization vector endpoints on the vertical plane. NRM = natural remanent magnetization. **A.** AF demagnetization on reversely magnetized discrete samples. (Continued on next page.)

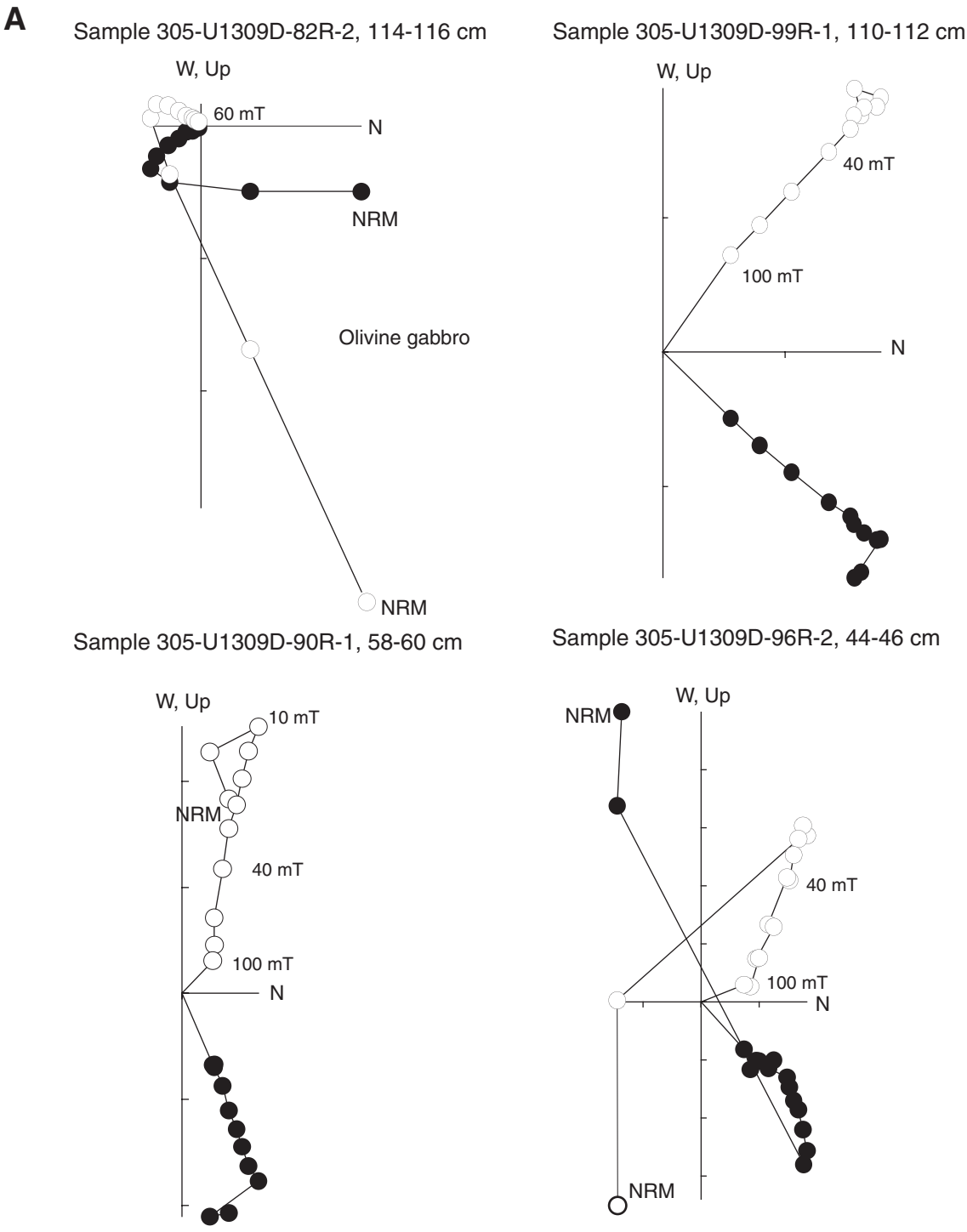

Figure F254 (continued). B. Thermal demagnetization on reversely and normally magnetized discrete samples.

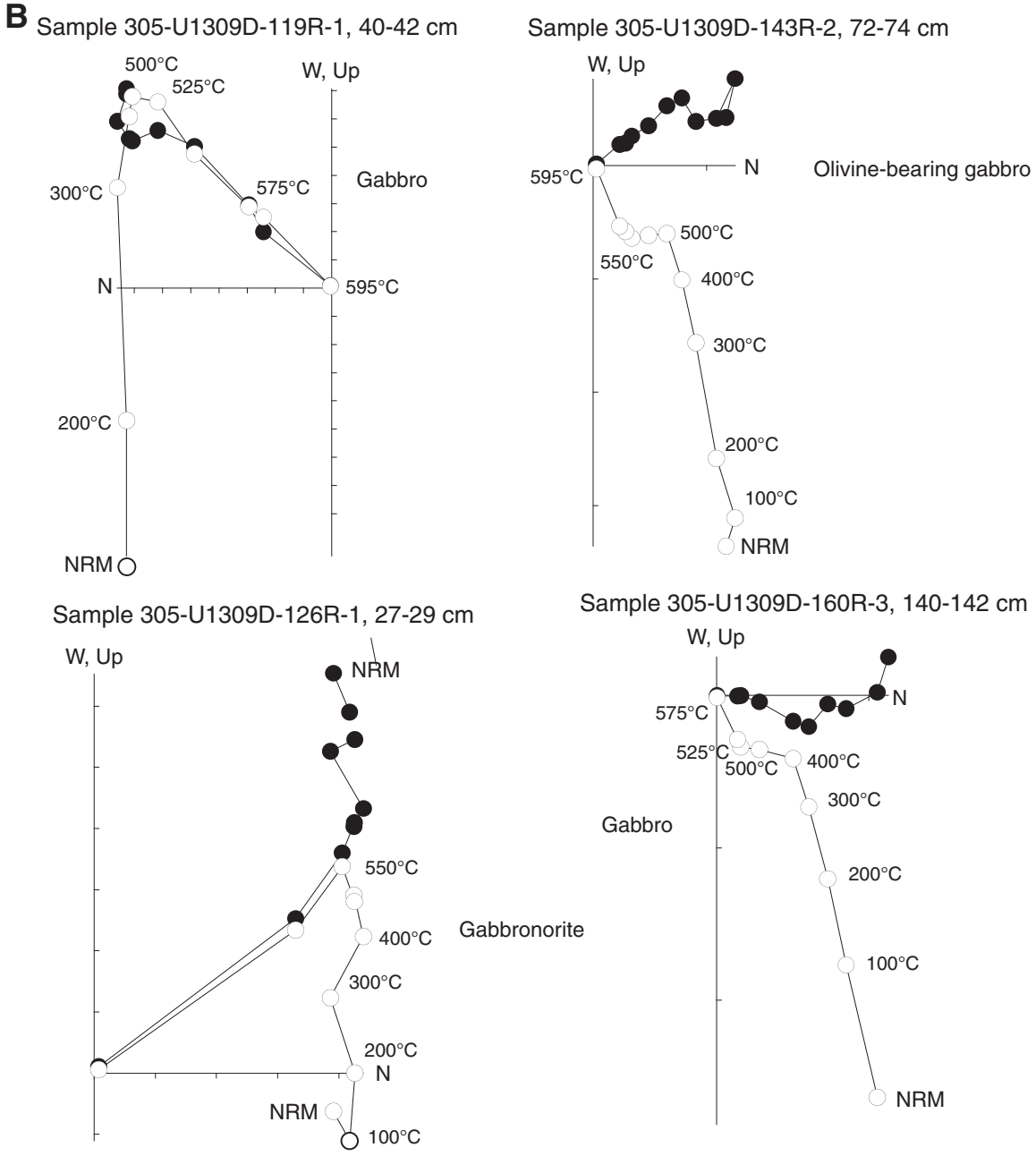

Figure F255. Downhole plot of (**A**) Königsberger ratios (*Q*) and (**B**) degree of anisotropy (from AMS) of rock samples from Hole U1309D below 400 mbsf (Expedition 305).

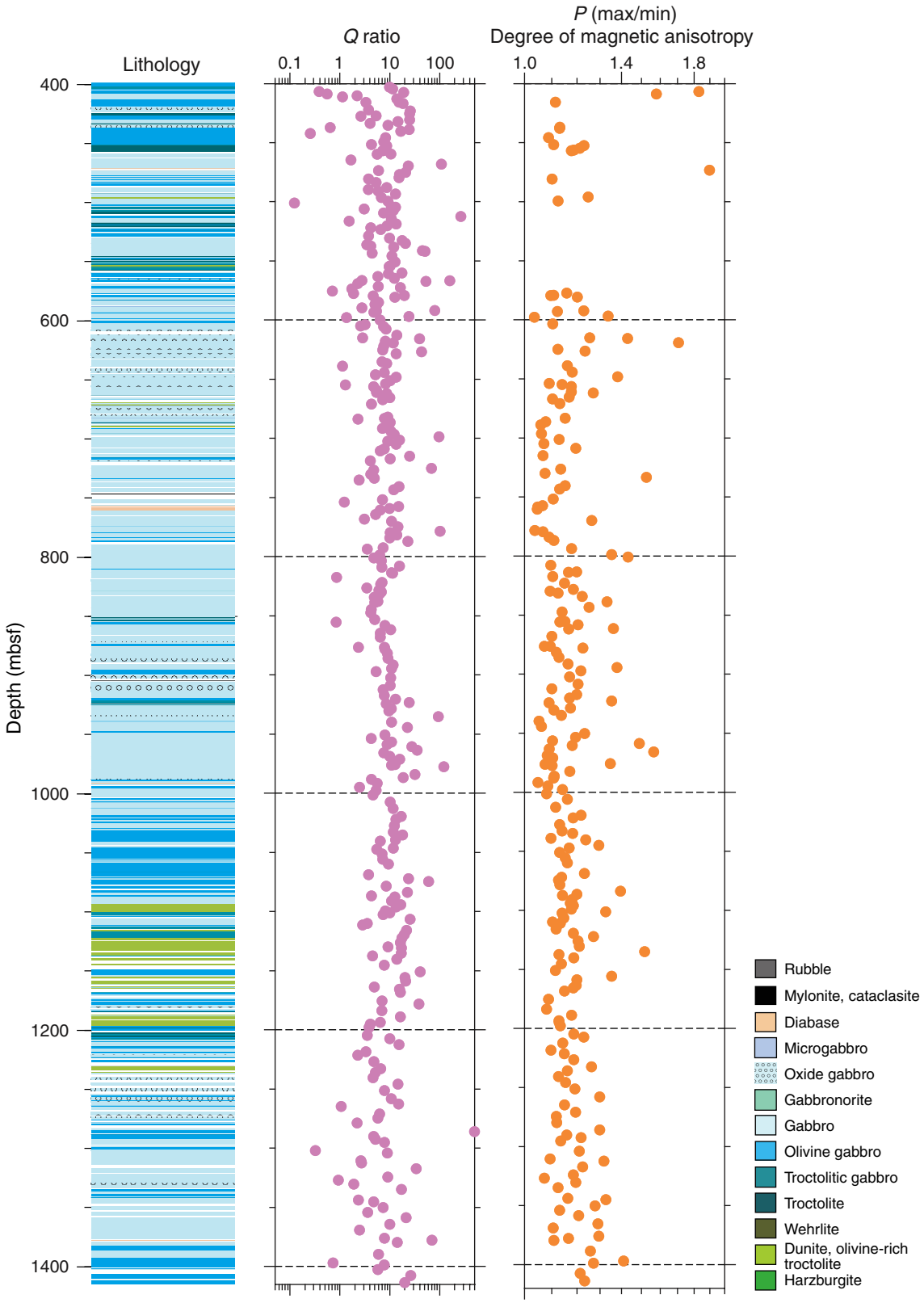

Figure F256. Magnetic susceptibility, electrical conductivity, thermal conductivity, compressional wave velocity, bulk density, and porosity for Hole U1309B.

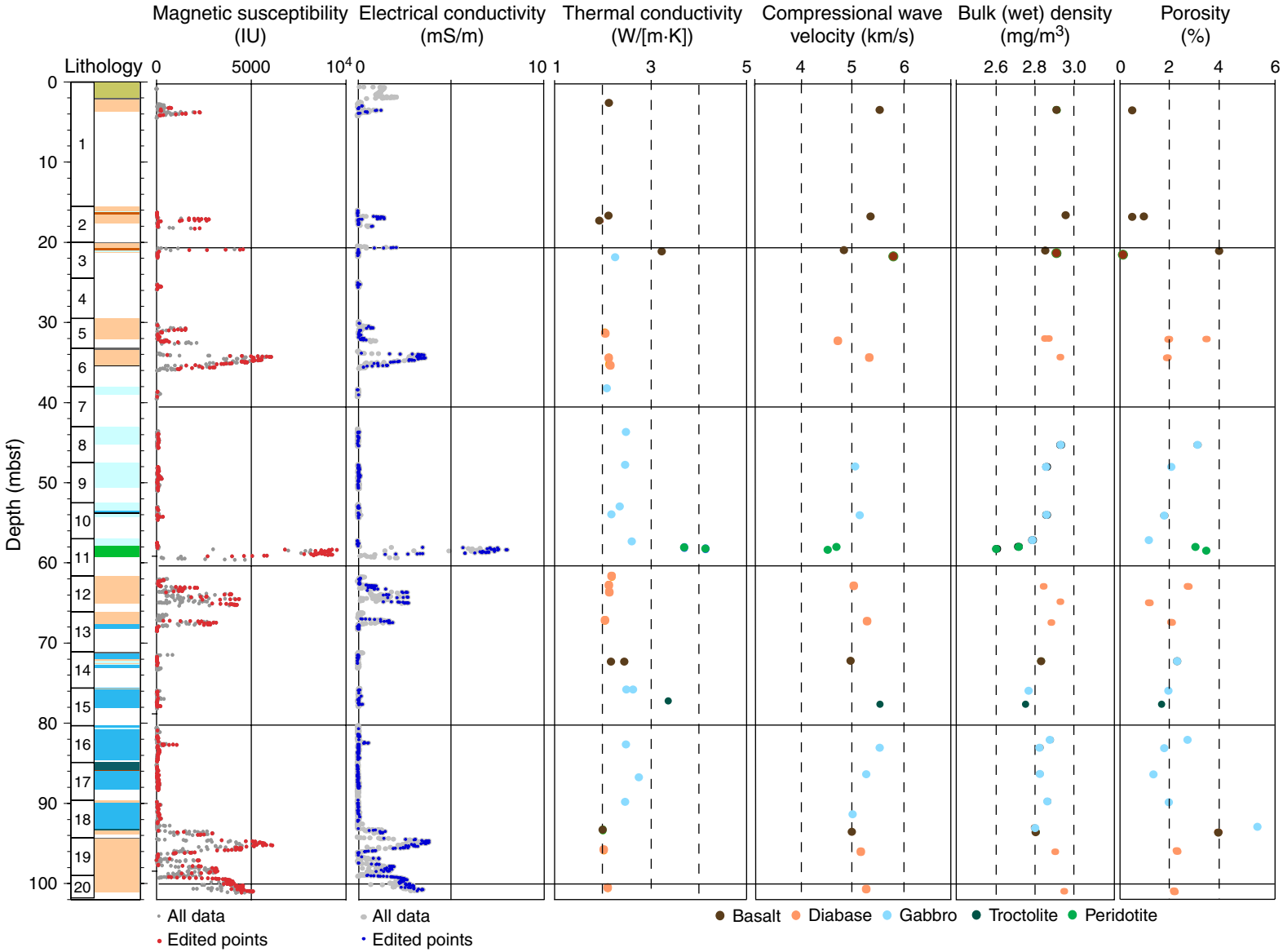

Figure F257. Compressional wave velocity versus bulk density for Hole U1309B. Also shown (gray symbols) are data from similar lithologies measured during Leg 209 (Kelemen, Kikawa, Miller, et al., 2004).

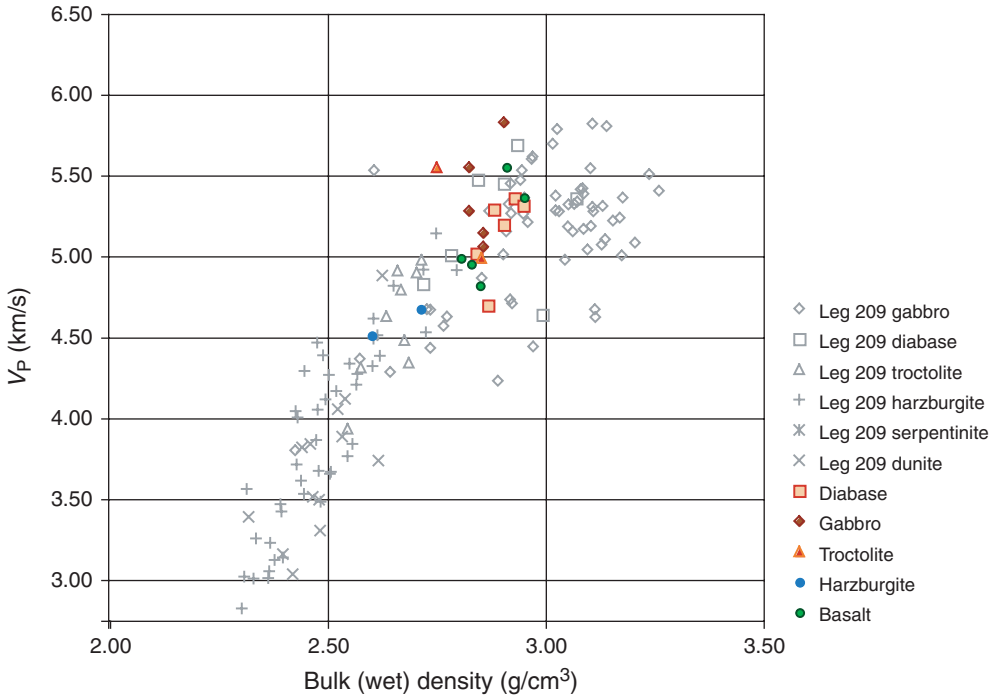

Figure F258. Magnetic susceptibility along Hole U1309B, Sections 304-U1309B-5R-1 through 6R-2, 12R-1 through 13R-1, and 19R-1 through 20R-2, showing variations within diabase Units 20, 33–35, and 62.

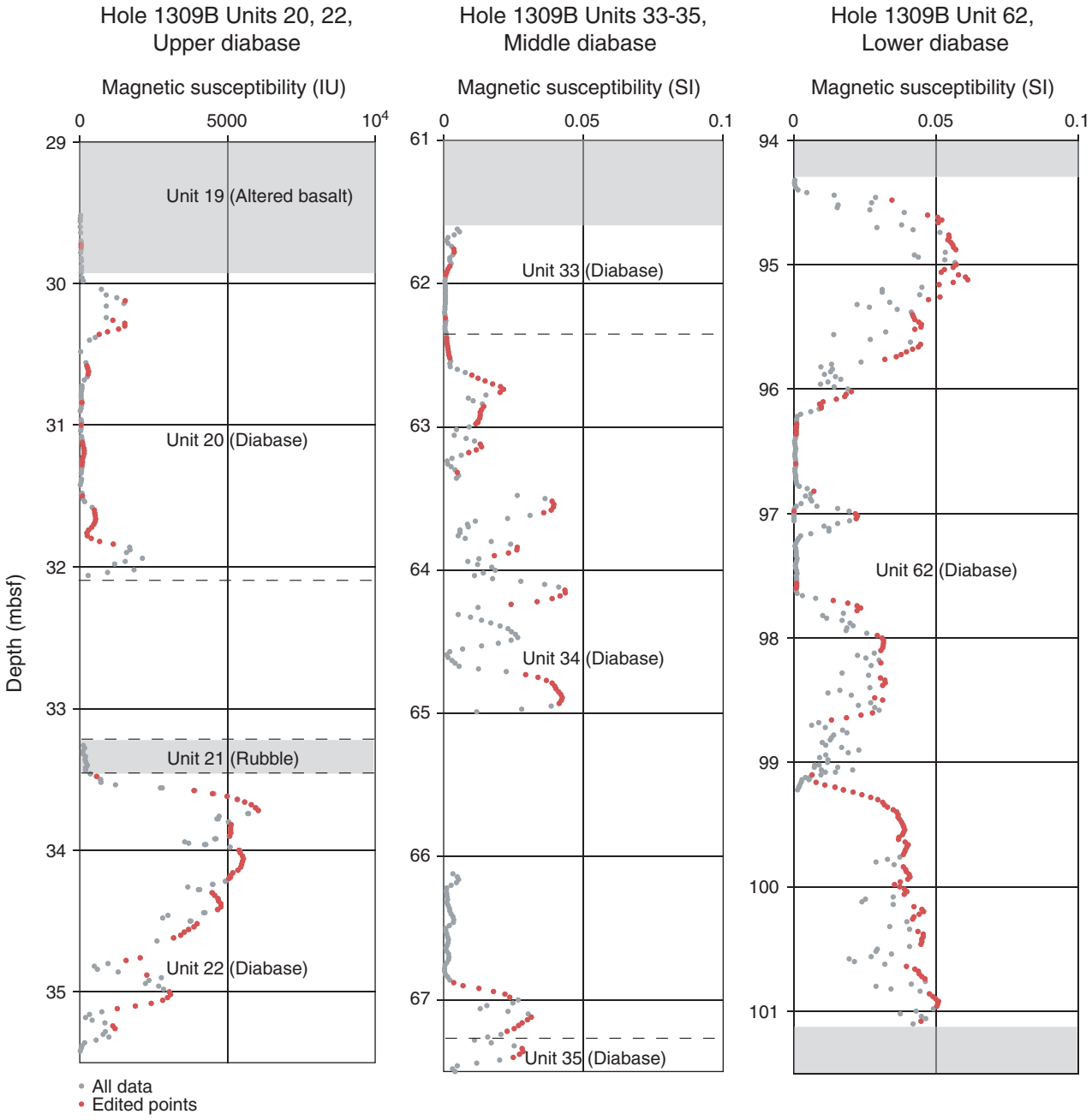

Figure F259. (**A**) Lithology of Hole U1309D plotted against (**B**) bulk density, (**C**) grain density, and (**D**) porosity.

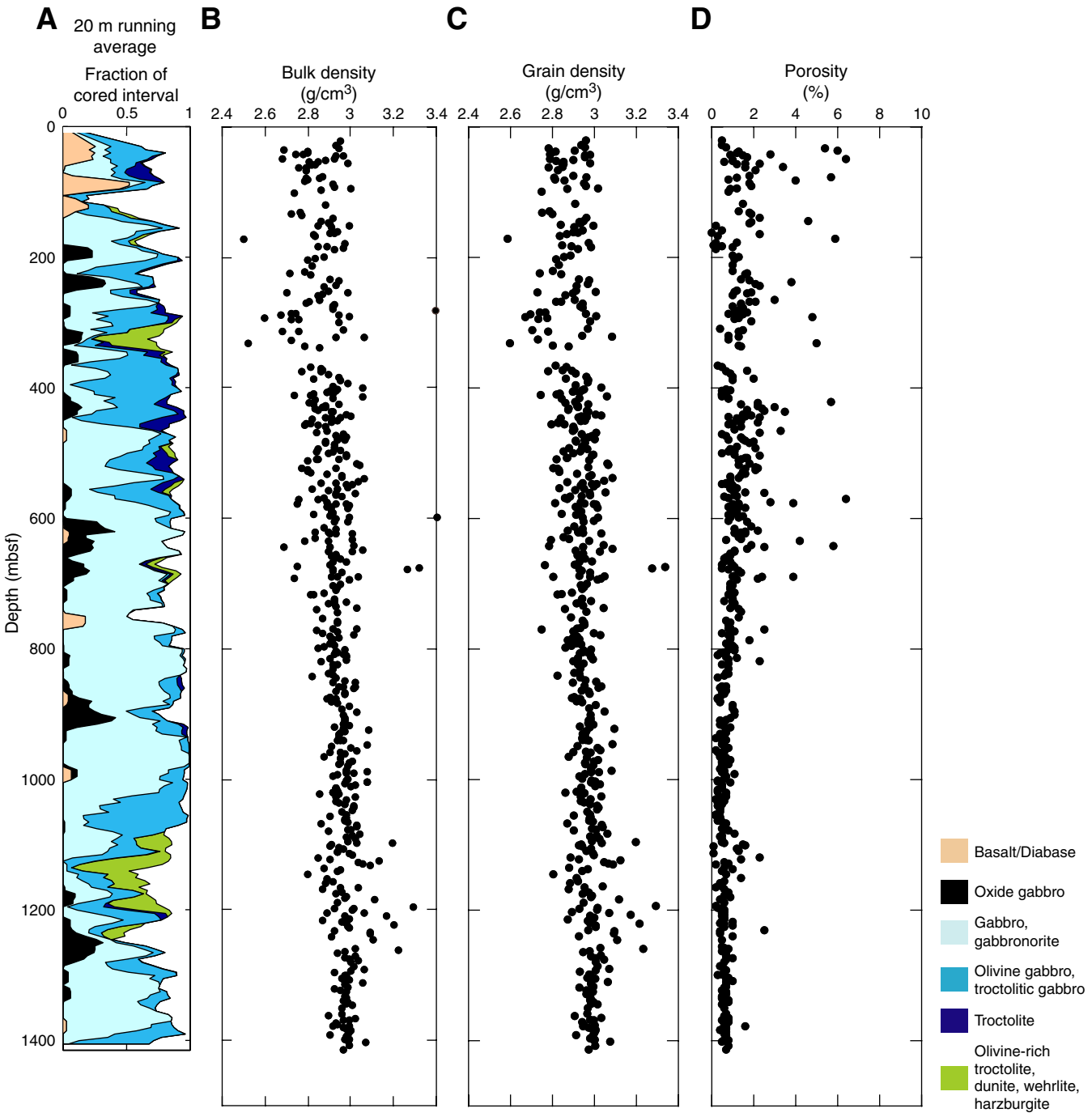

Figure F260. Cross-plot of bulk density determined by pycnometer and density estimated using calipers to define the wet volume of the rock cubes. Important sources of error include pycnometer problems and cubes with damaged edges or nonparallel faces. Despite the coarseness of the caliper measurement, the error in density is ~0.018 ± 0.001 g/cm³. In case of a complete pycnometer breakdown, it is practical to use method D for igneous rocks to determine moisture and density properties (see text).

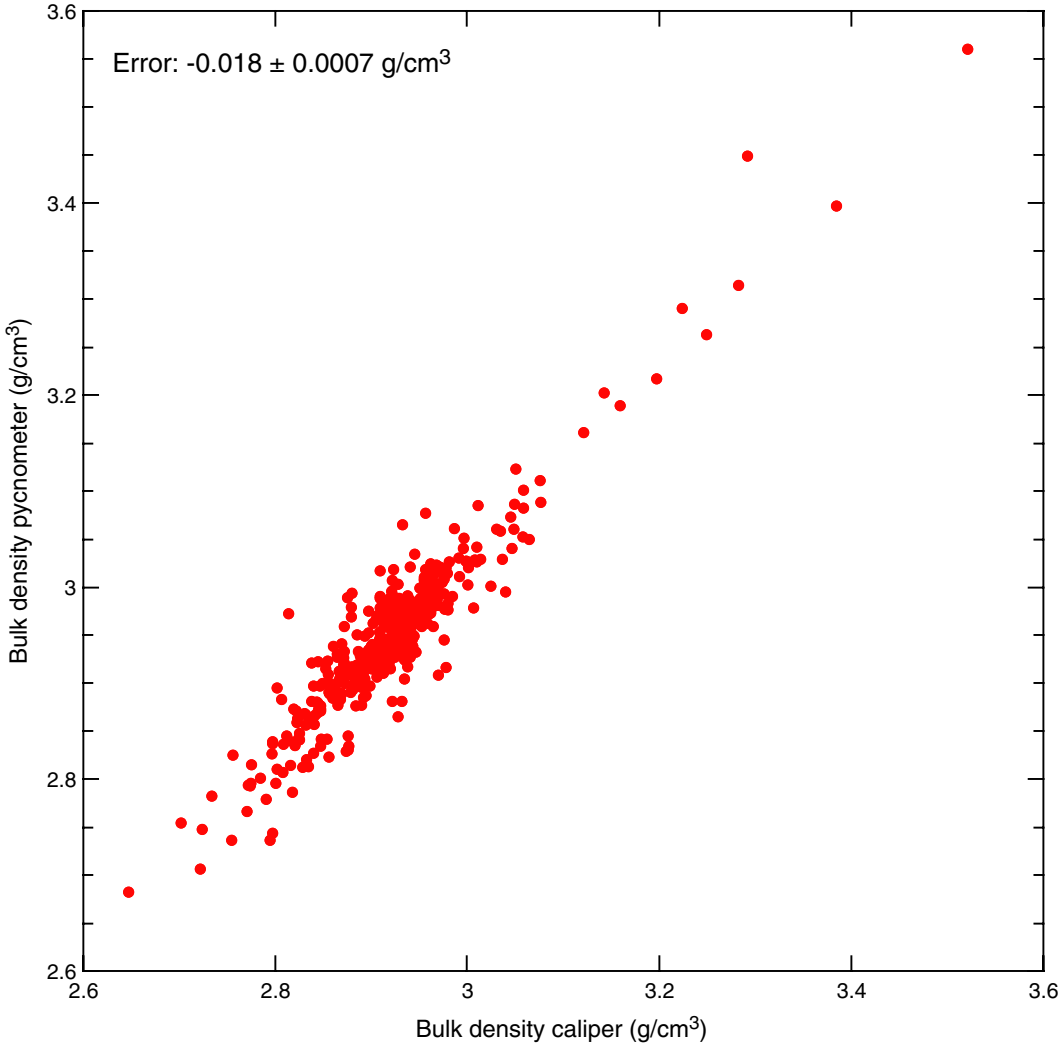

Figure F261. Seismic velocity, as measured from rock cubes using the *P*-wave sensor contact probe system, and vertical-horizontal and x-y anisotropy for Hole U1309D (Expedition 305).

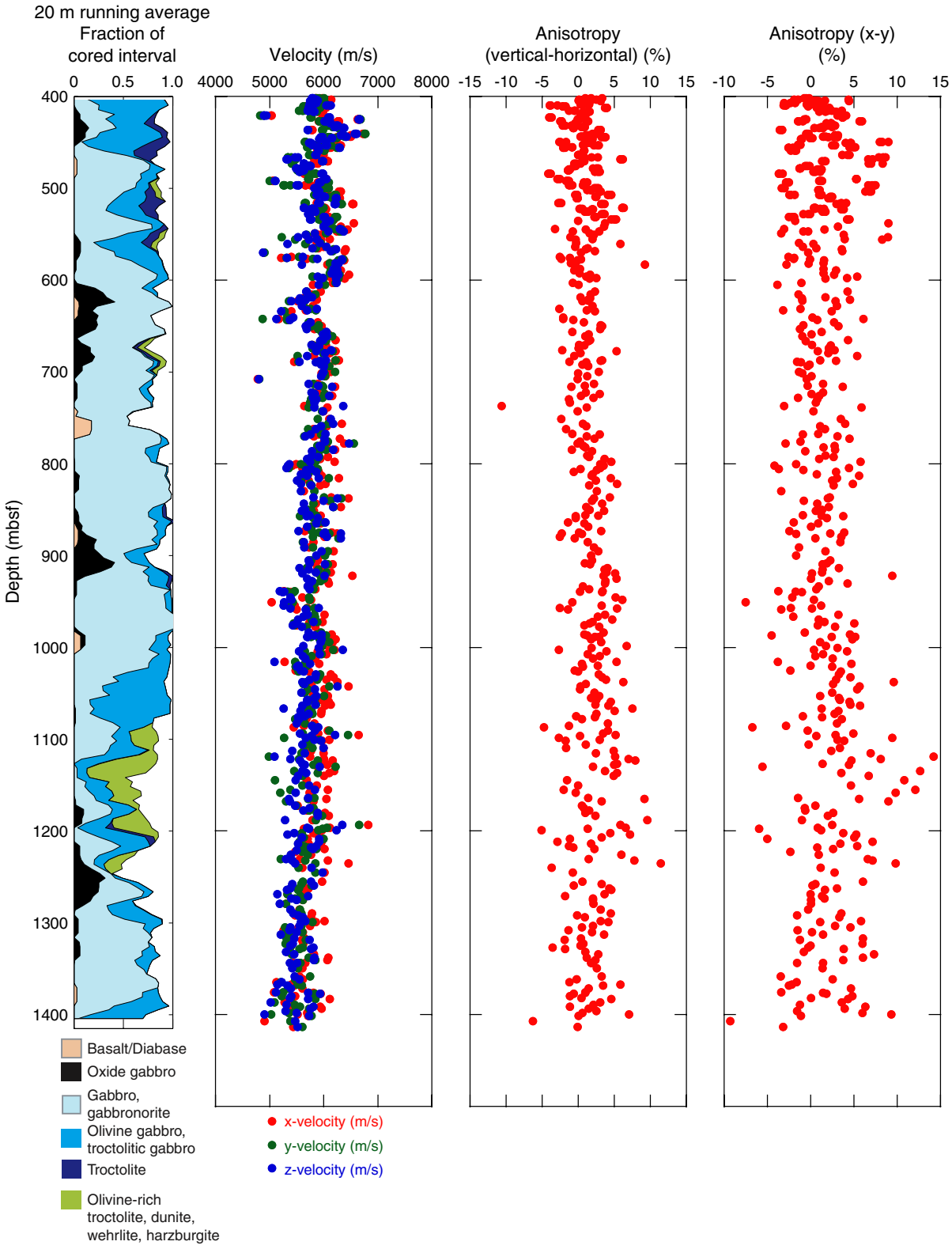

Figure F262. Precision determination of velocity measurements using the PWS-3 Hamilton Frame. Running average versus number of measurements for the x-direction of Sample 305-U1309D-107R-4, 48–50 cm. The plot limits of 6036.8 and 6105.2 m/s represent the maximum range of velocities measured on this sample. Convergence is reached with ~40–50 readings.

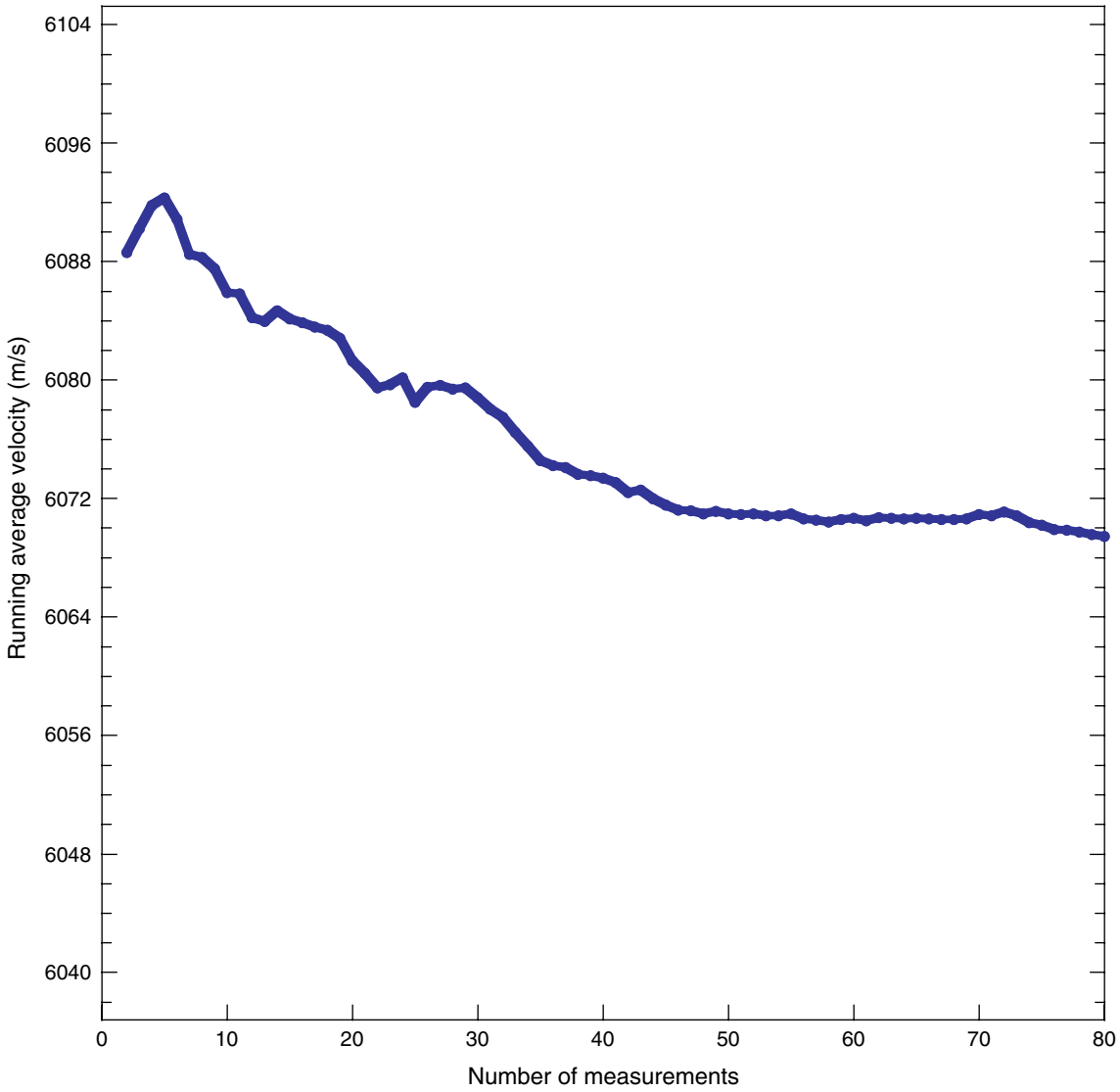

Figure F263. Seismic velocity, as measured from rock cubes using the *P*-wave sensor contact probe system, plotted with the lithology column for Hole U1309D.

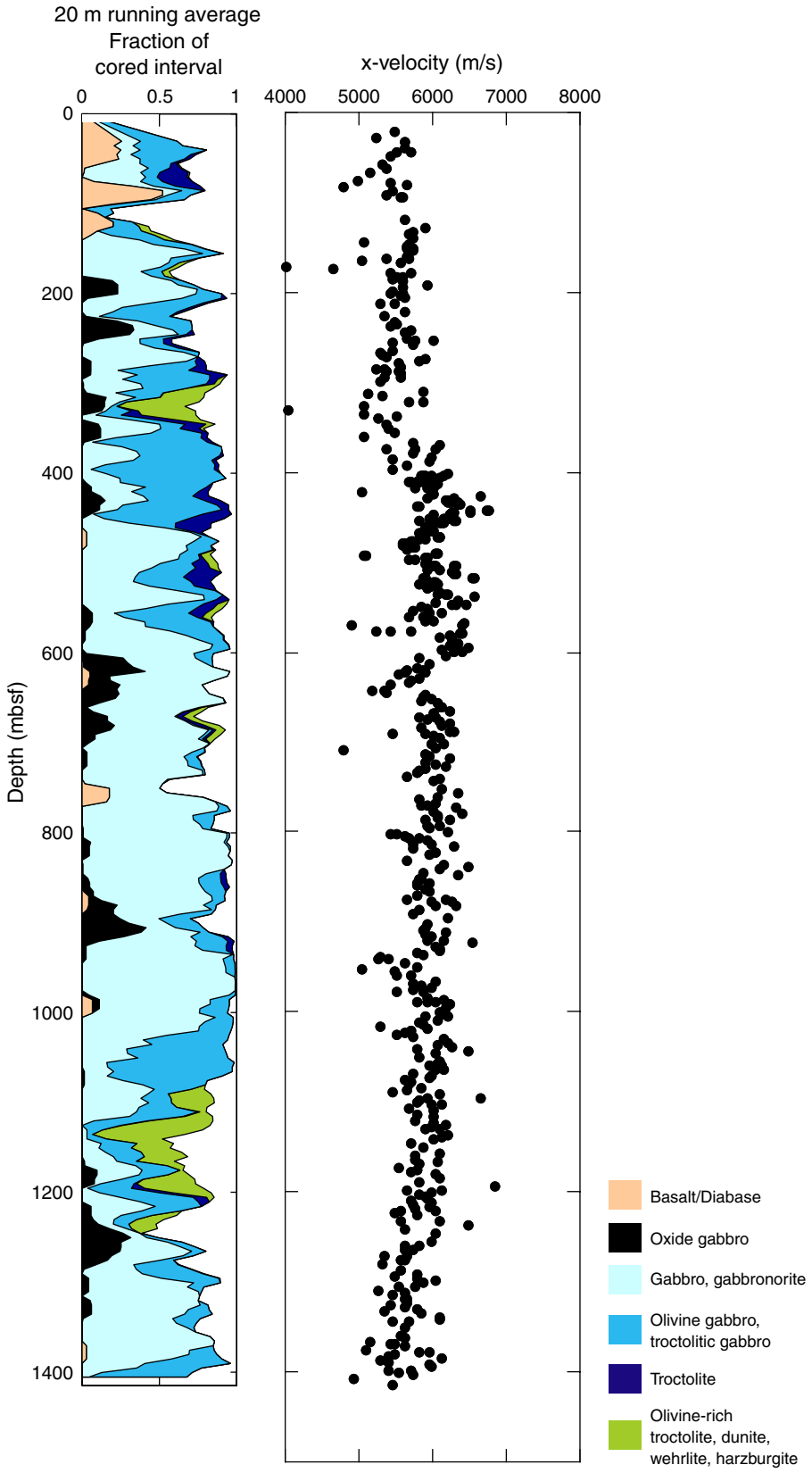

Figure F264. Moisture and density–determined bulk density plotted against x-direction velocity measured by the *P*-wave sensor contact probe system for Leg 209 (MAR, 15°20′N; Kelemen et al., 2004) and Expeditions 304 and 305 (Hole U1309D) for a range of rock types from oceanic crust.

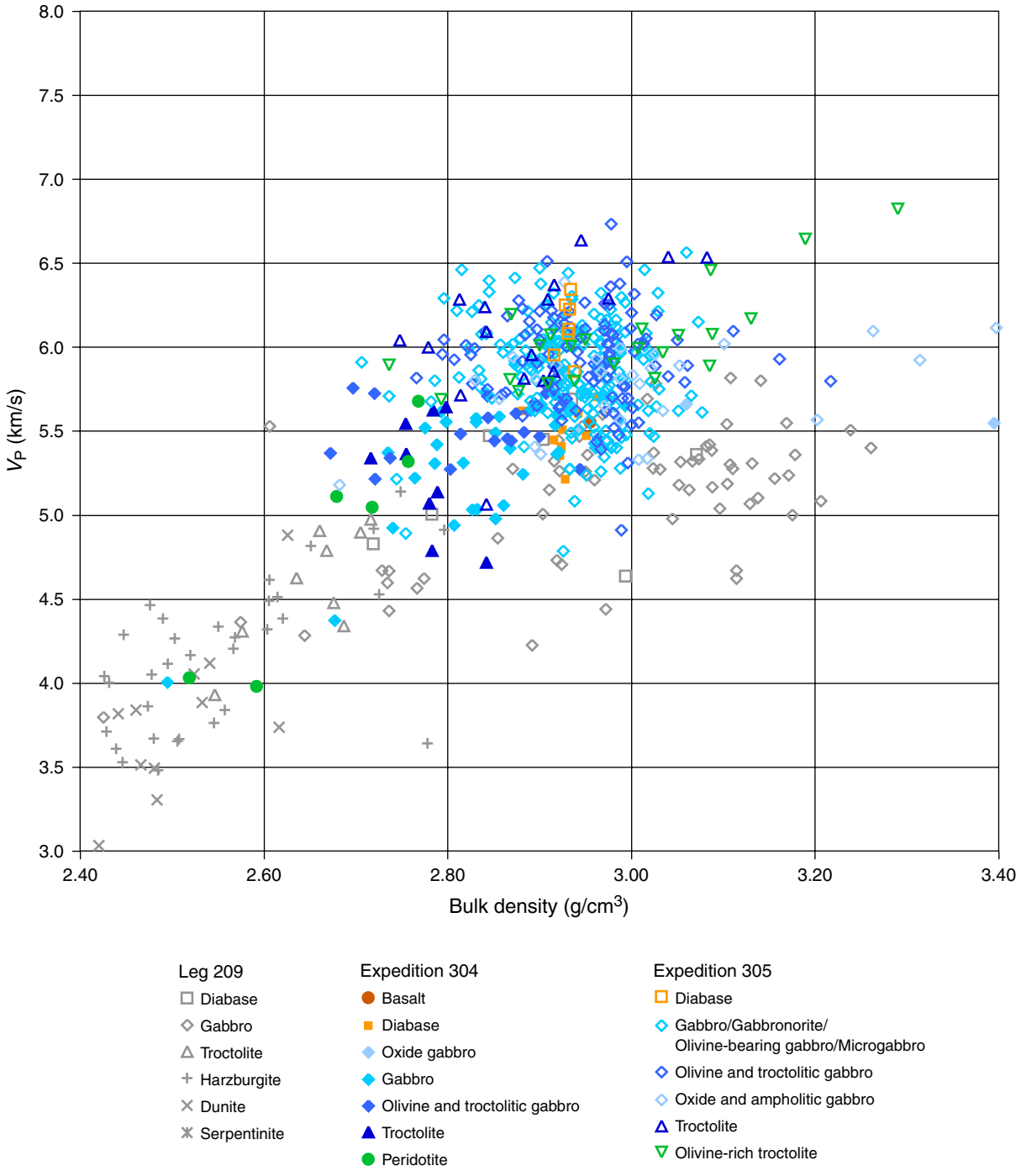

Figure F265. Comparison between logging seismic data (red and blue lines), PWS z-direction velocities (green dots), moisture and density–determined porosities, and fracture frequency for Hole U1309D. Red velocity line = Expedition 304 logging data, blue velocity line = Expedition 305 logging data, red porosity dots = Expedition 304, blue porosity dots = Expedition 305. For fracture frequency, see **"Structural geology."**

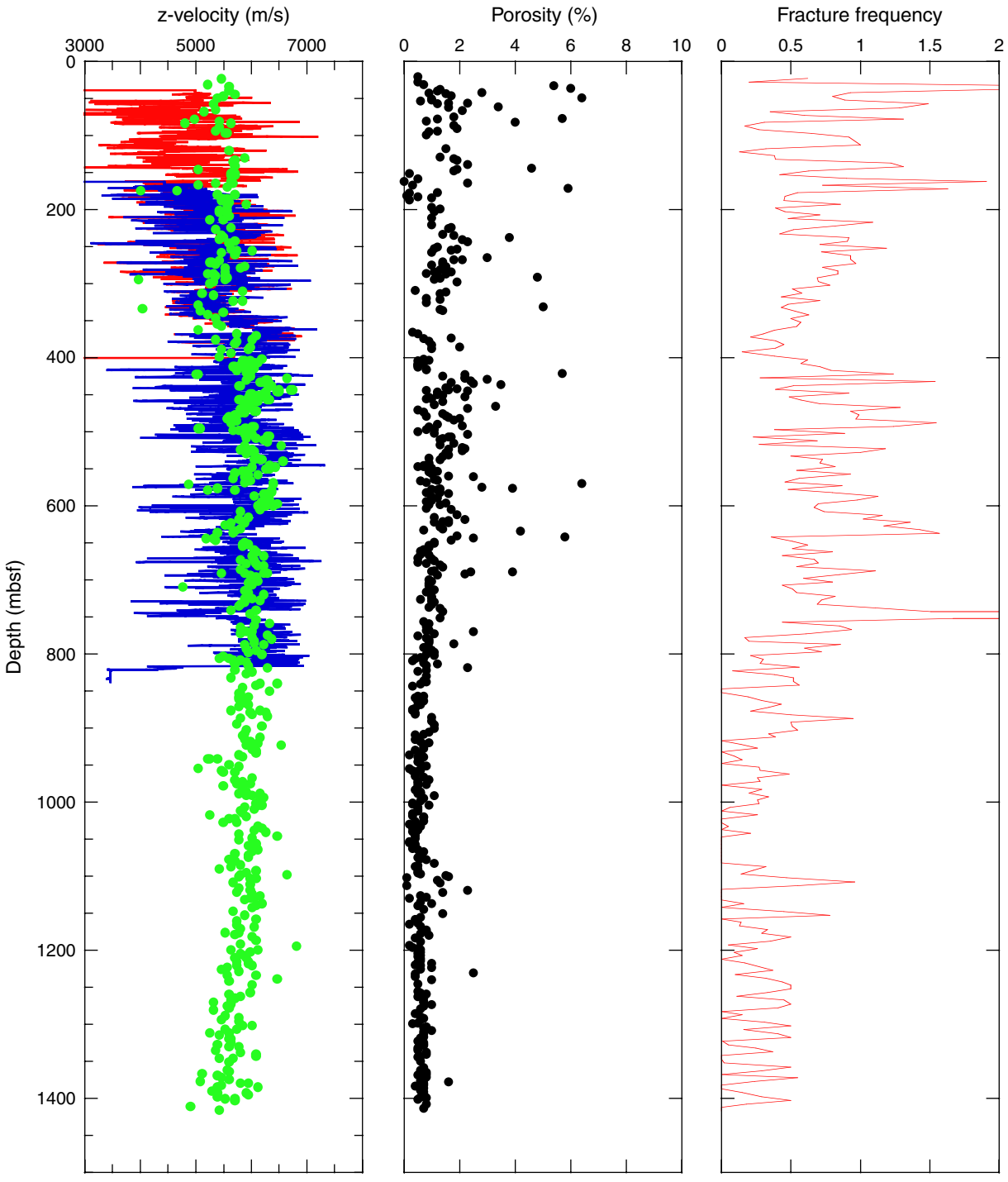

Figure F266. Thermal conductivity of samples as a function of depth and compared with the recovered lithology for Hole U1309D.

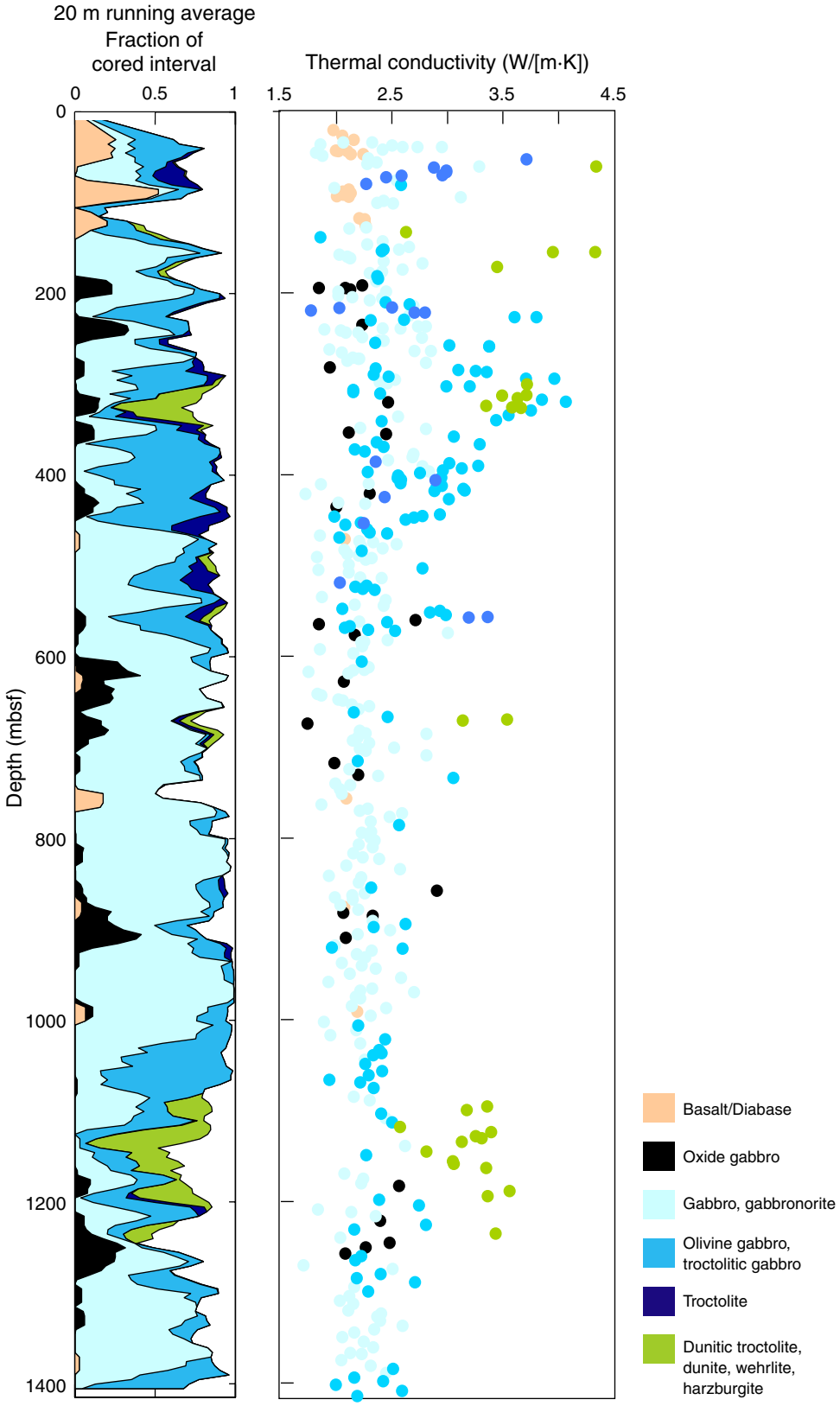

Figure F267. "Thermal tab" experiment, showing the before and after color change induced by the exposure of the tab to temperature for 24 h. The tab was placed in the physical properties laboratory oven, which is maintained at a temperature of 105° ± 5°C. The observed color change on the tab is consistent with an oven temperature between 98° and 104°C.

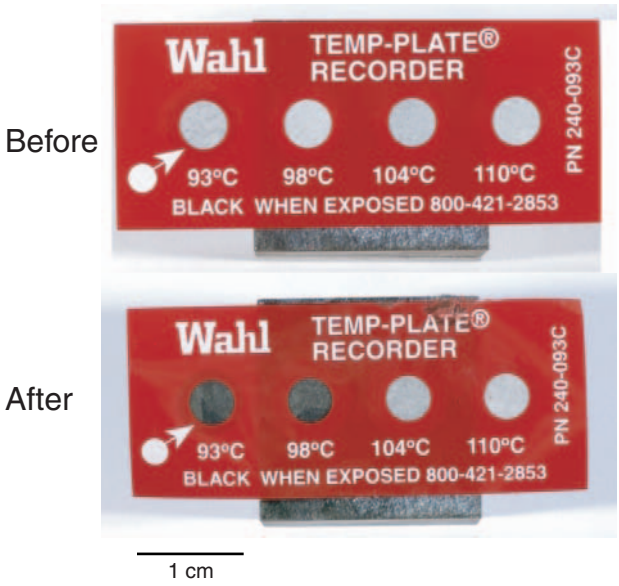

Figure F268. Predicted conductive temperature distribution for basal lithospheric heat flows in Hole U1309D consistent with 1 and 2 m.y. old oceanic crust. The measured distribution of thermal conductivities from Expeditions 304 and 305 coupled with Fourier's law were used to predict crustal temperatures as a function of depth. Maximum bottom hole temperatures (BHTs) are predicted to be 130°–145°C, consistent with various methods to obtain BHT during drilling operations. Because of fluid circulation during drilling, temperature measurements are considered a minimum. Thermal tabs (red circles) give minimum temperatures of 70° and 108°C at 1171 and 1220 mbsf, respectively. Triple combo TAP tool (yellow circles) = 52°C at 562 mbsf, 57°C at 700 mbsf, and 69°C at 754 mbsf. GBM magnetometer tool monitors temperature as a function of time both during descent (purple curve) and ascent (pink curve).

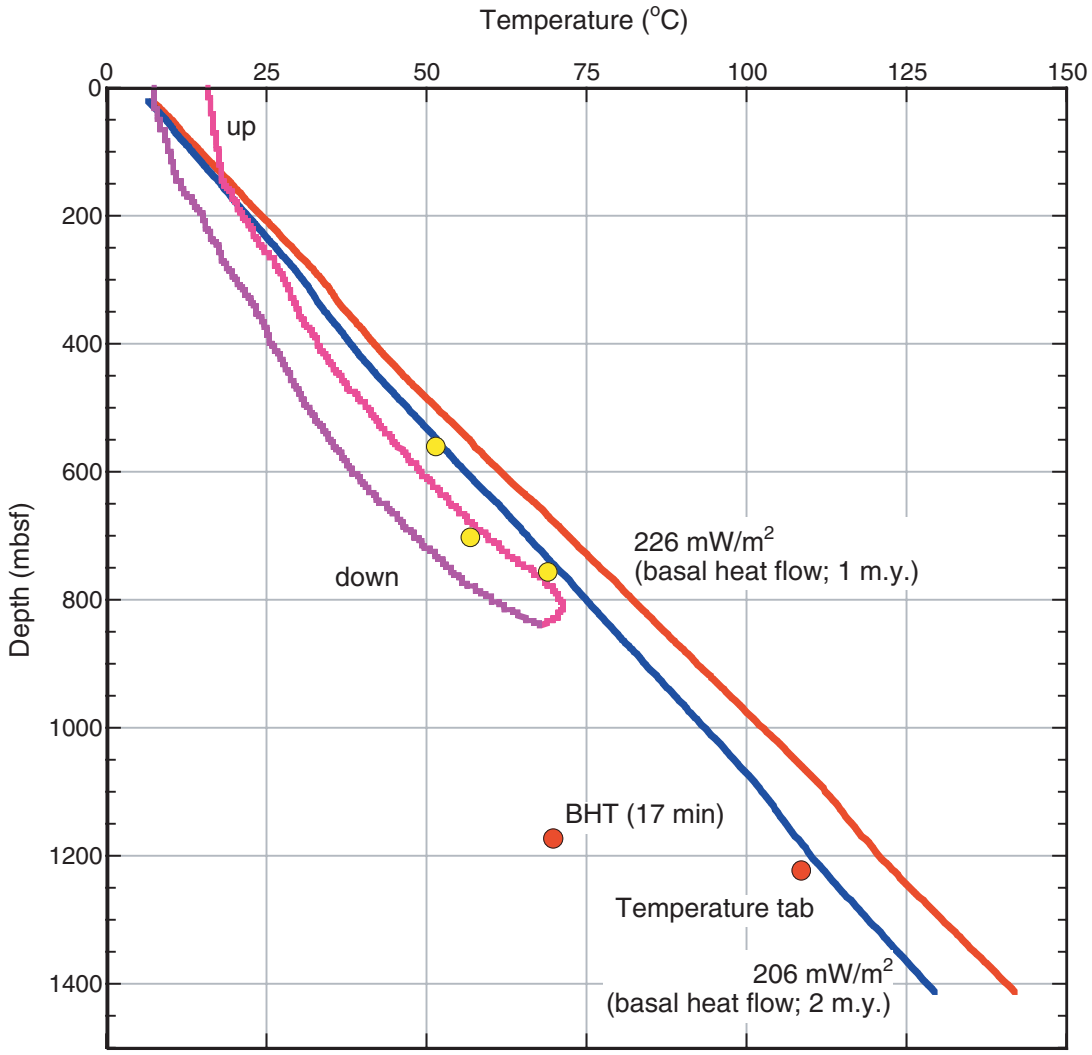

Figure F269. Comparison of magnetic susceptibility and inclination of the remanent vector as a function of depth for Hole U1309D. Data set has been filtered using a 51 point running average. The inclination data were determined after AF demagnetization of 50 mT. Green line = 0° inclination. Present-day field inclination = +48°. General correlation between high-amplitude magnetic susceptibility and positive inclination intervals suggests a way of dating serpentinization events and oxide precipitation episodes in Hole U1309D. However, positive inclination measurements must be interpreted with caution, as they may be drilling induced (see discussion in **"Paleomagnetism"**).

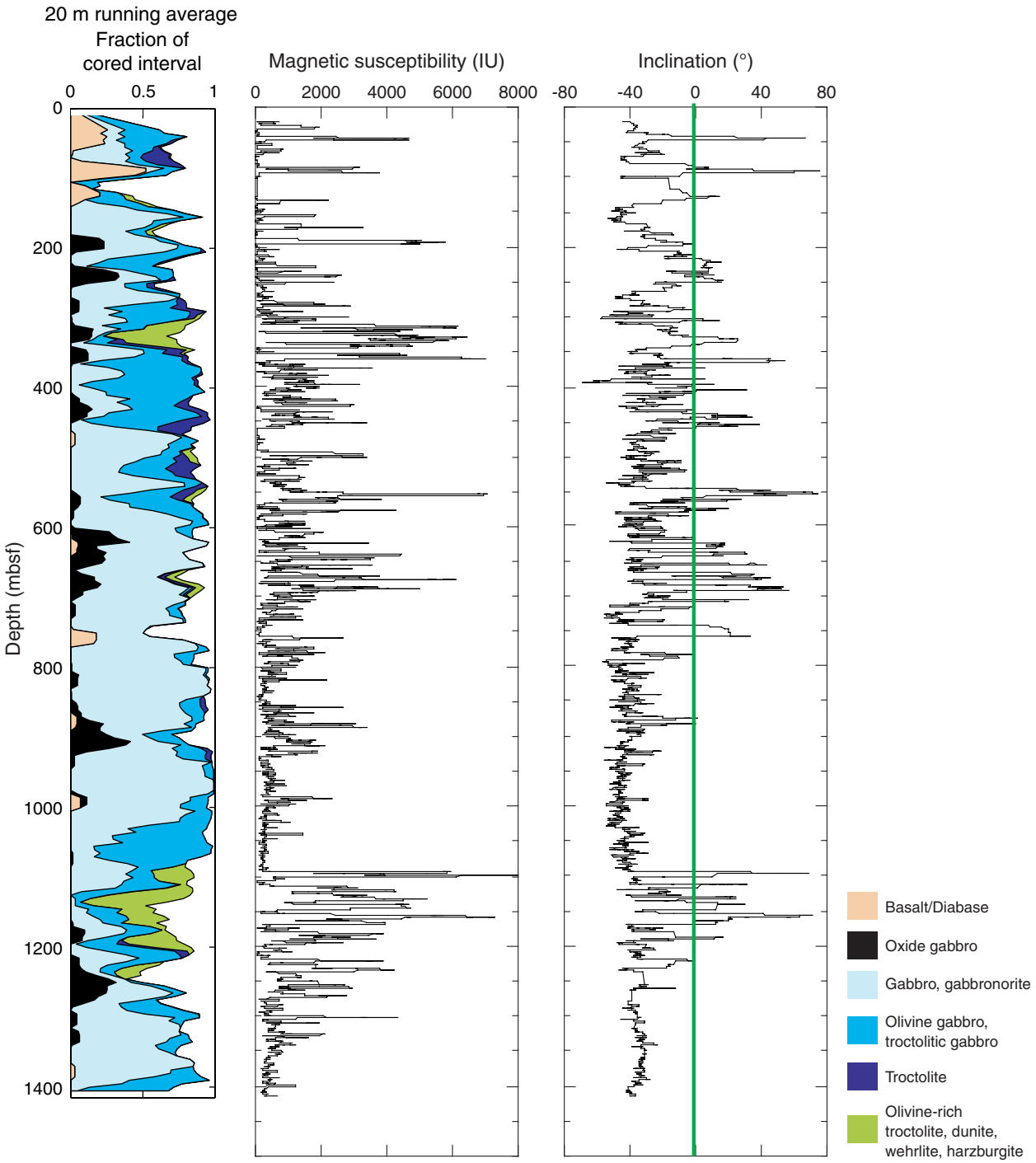

Figure F270. Magnetic susceptibility along diabase Units 1, 12, 14, and 44 (Hole U1309D), showing local variability within each unit.

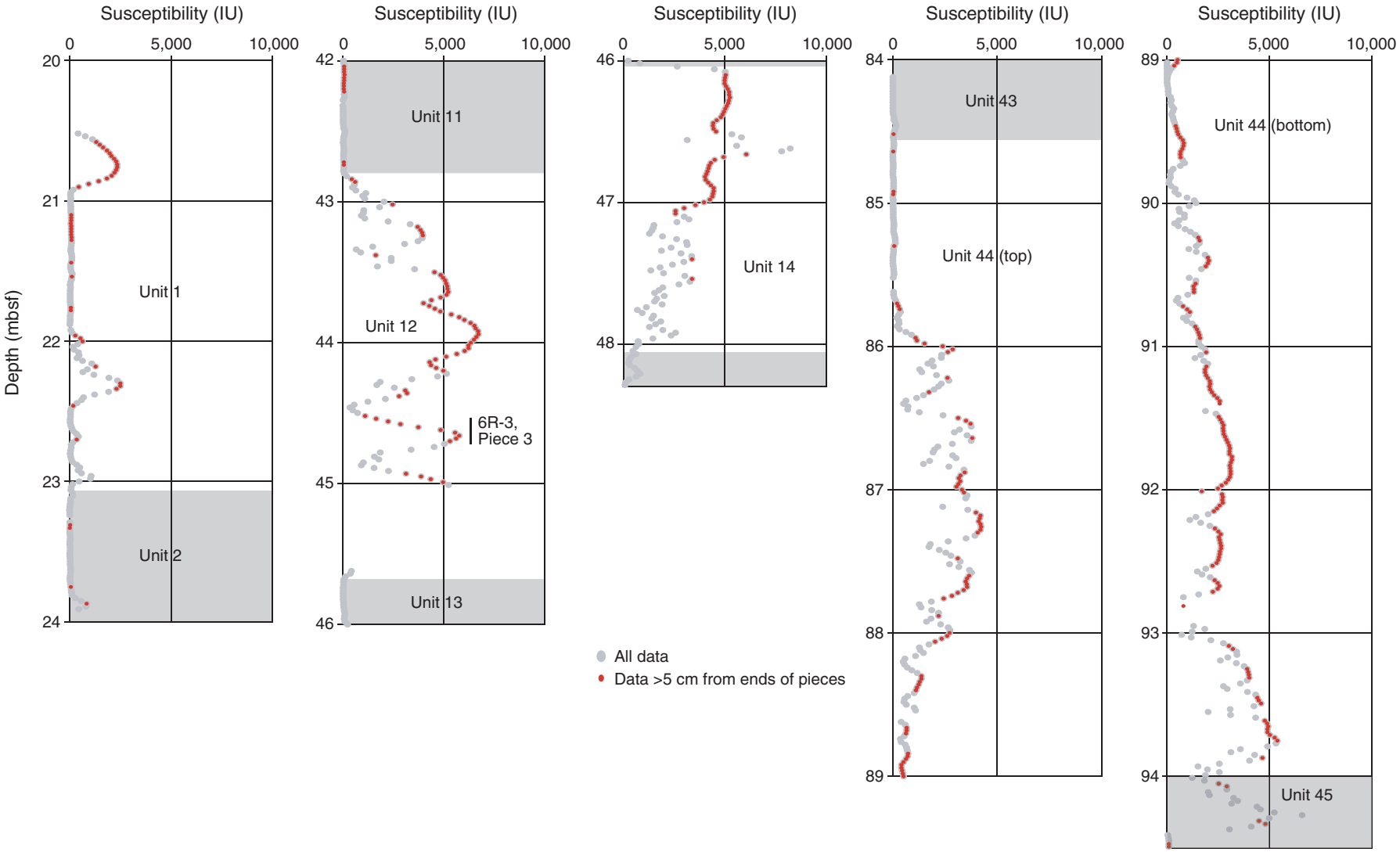

Figure F271. Magnetic susceptibility versus total iron content for basalts and diabases at Site U1309 (Expedition 304). Above a threshold of 10 wt% Fe_2O_3, susceptibility increases in proportion to iron content, suggesting the growth of iron-rich magnetic minerals (e.g., magnetite).

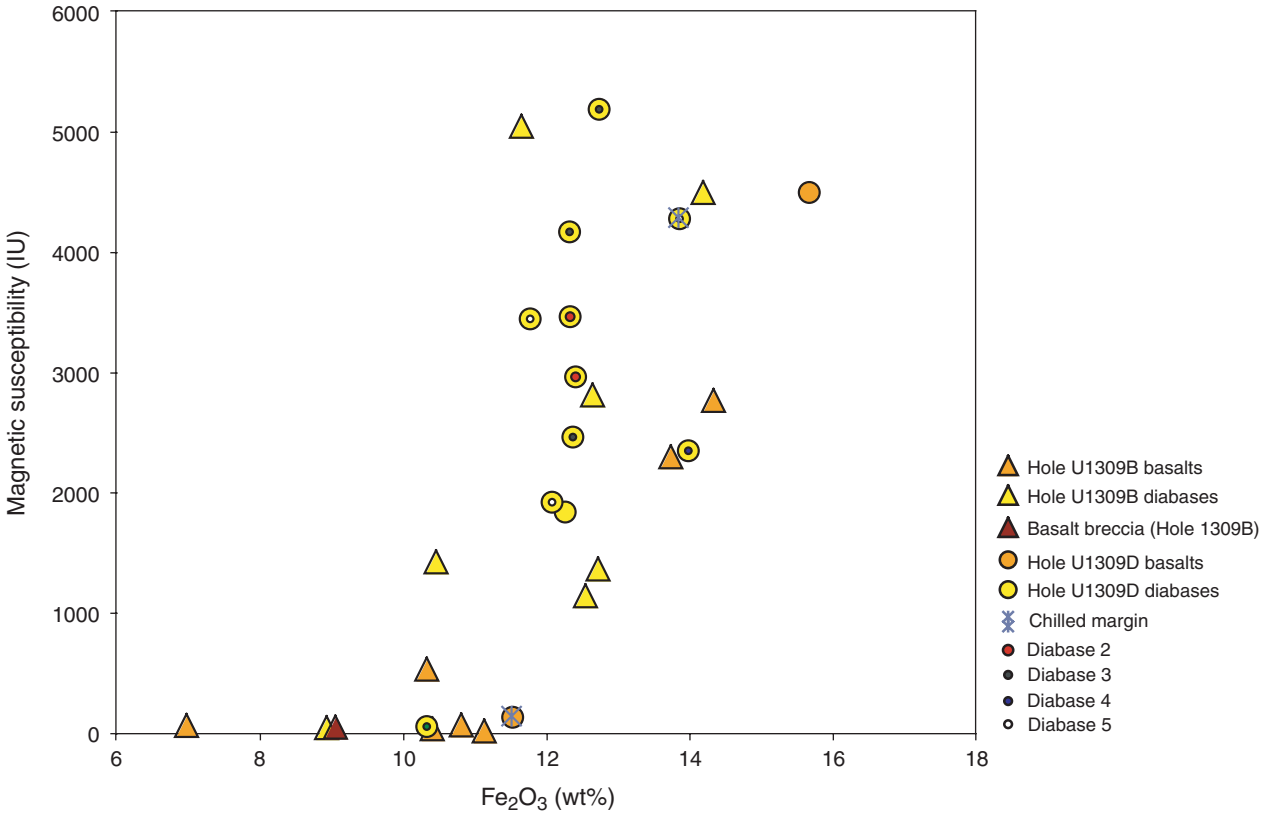

Figure F272. A relatively fresh magnetite grain from a moderate-susceptibility interval (top), compared with a magnetite from an adjacent very low susceptibility interval (bottom) where the magnetite (light tones) has largely been replaced by ilmenite (dark tones). Hole U1309B, lower diabase, Unit 62.

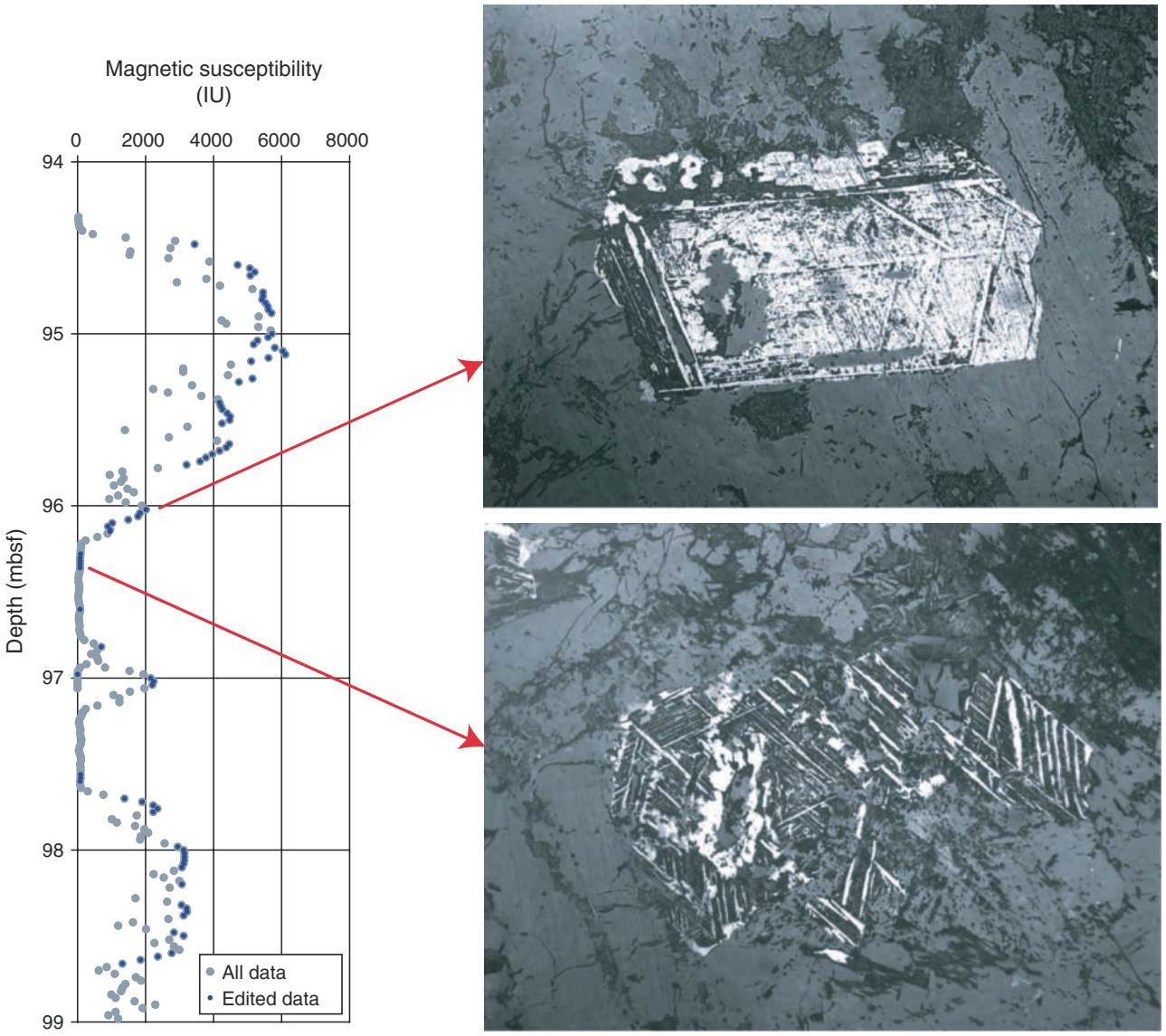

Figure F273. Raw (logged) magnetic susceptibility (red) and values adjusted for the loss of the least significant bit (blue) compared with electrical conductivity for a serpentinite in Hole U1309D. Conductivity curve scale has been adjusted to allow comparison to magnetic susceptibility.

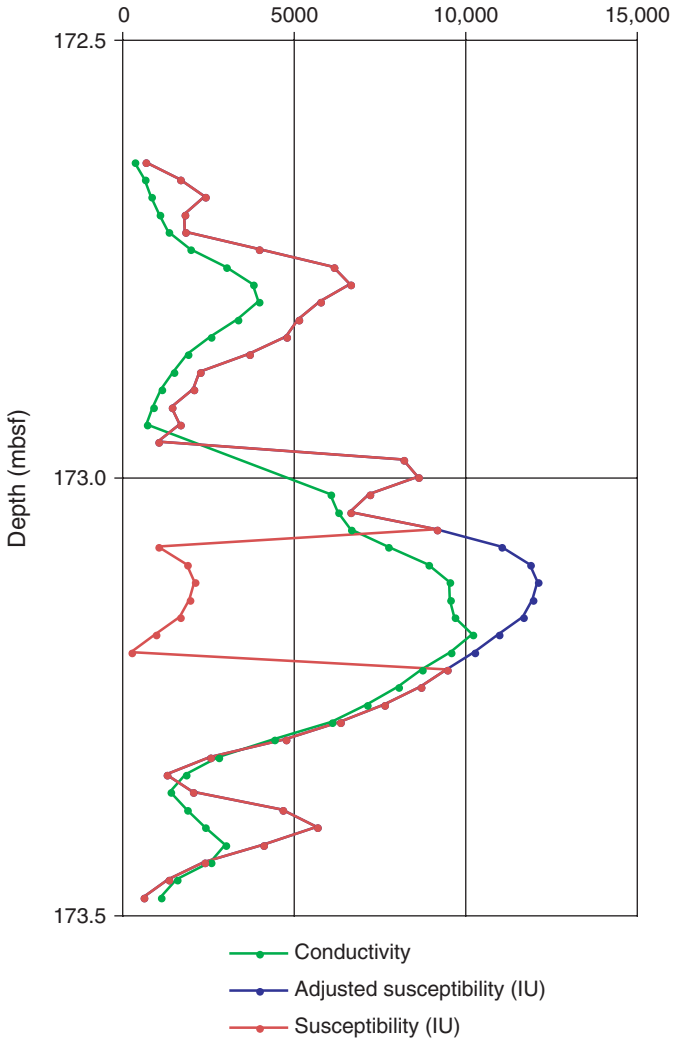

Figure F274. Magnetic susceptibility (blue) adjusted for the loss of the least significant bit by addition of 10,000 or 20,000 IU (green) compared with electrical conductivity (red) for oxide gabbros in Hole U1309D, Cores 304-U1309D-35R and 36R. Conductivity curve scale has been adjusted to allow comparison to magnetic susceptibility.

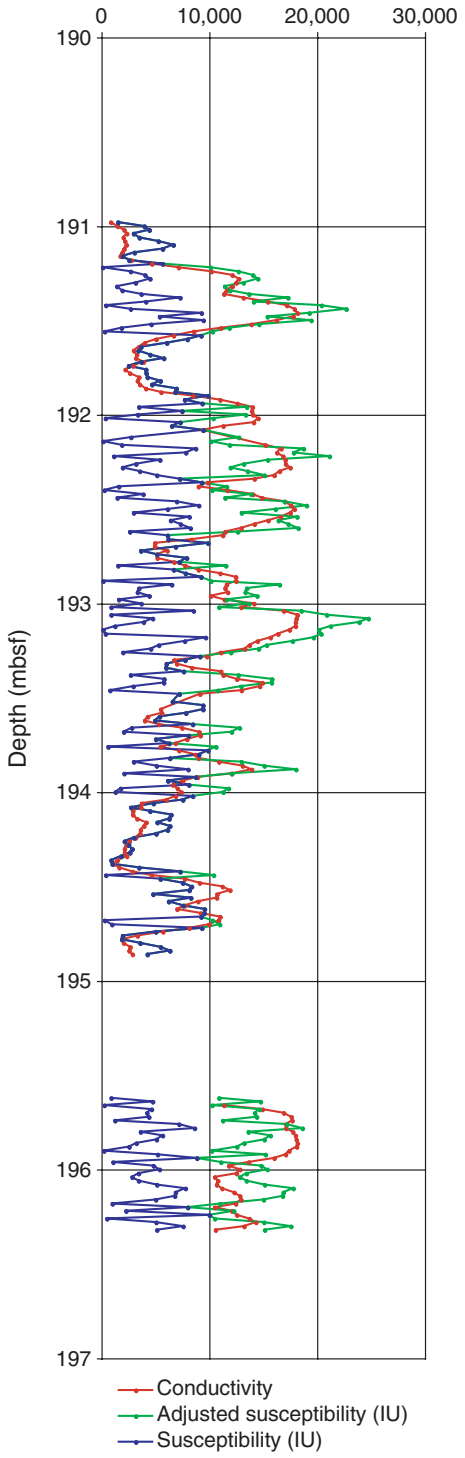

Figure F275. Magnetic susceptibility against lithology for part of Hole U1309D, showing extreme and rapid variability in magnetic susceptibility between and within lithologic units.

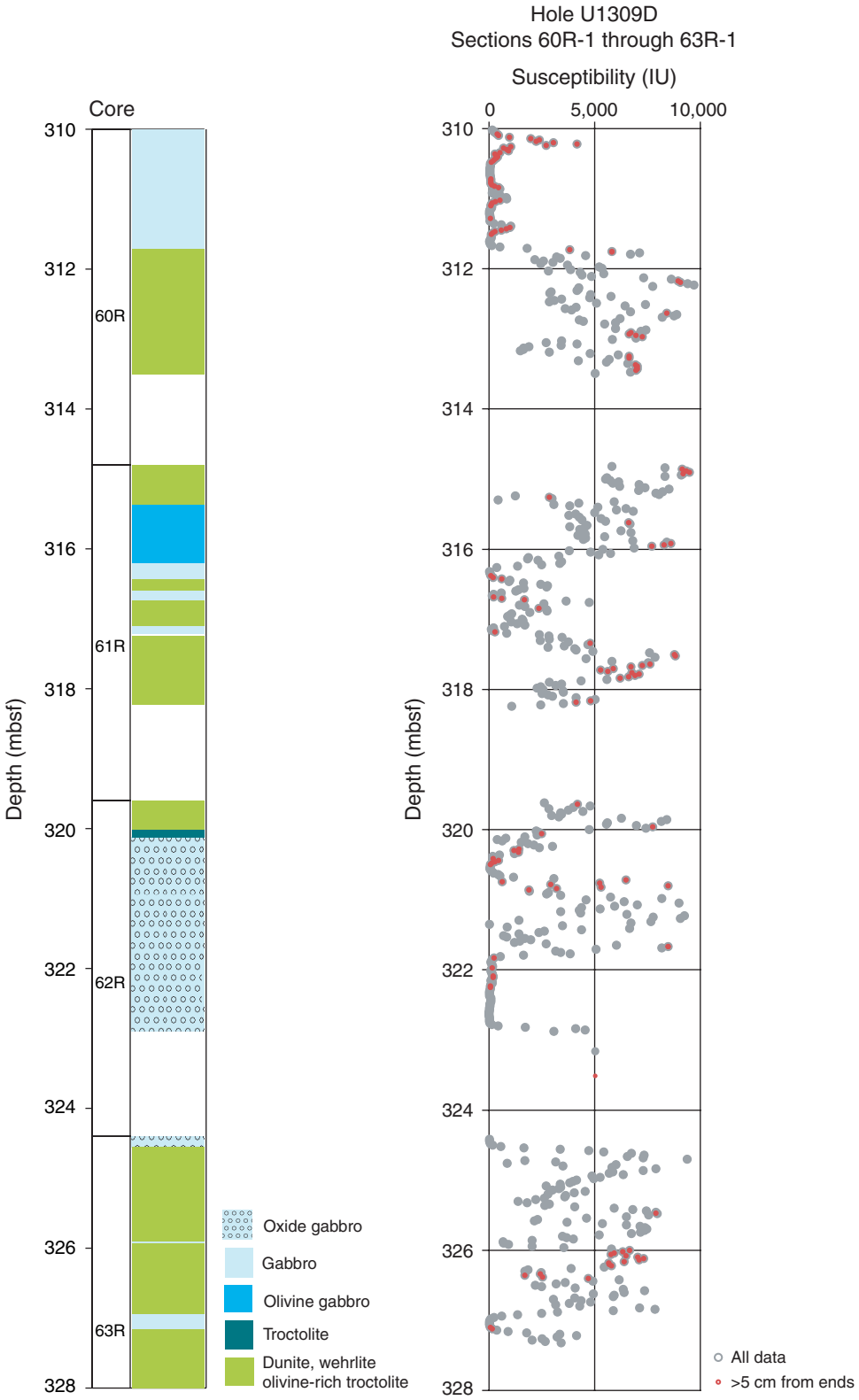

Figure F276. Magnetic susceptibility and electrical conductivity as a function of depth for Hole U1309D. All data sets have been filtered using a 51 point running average.

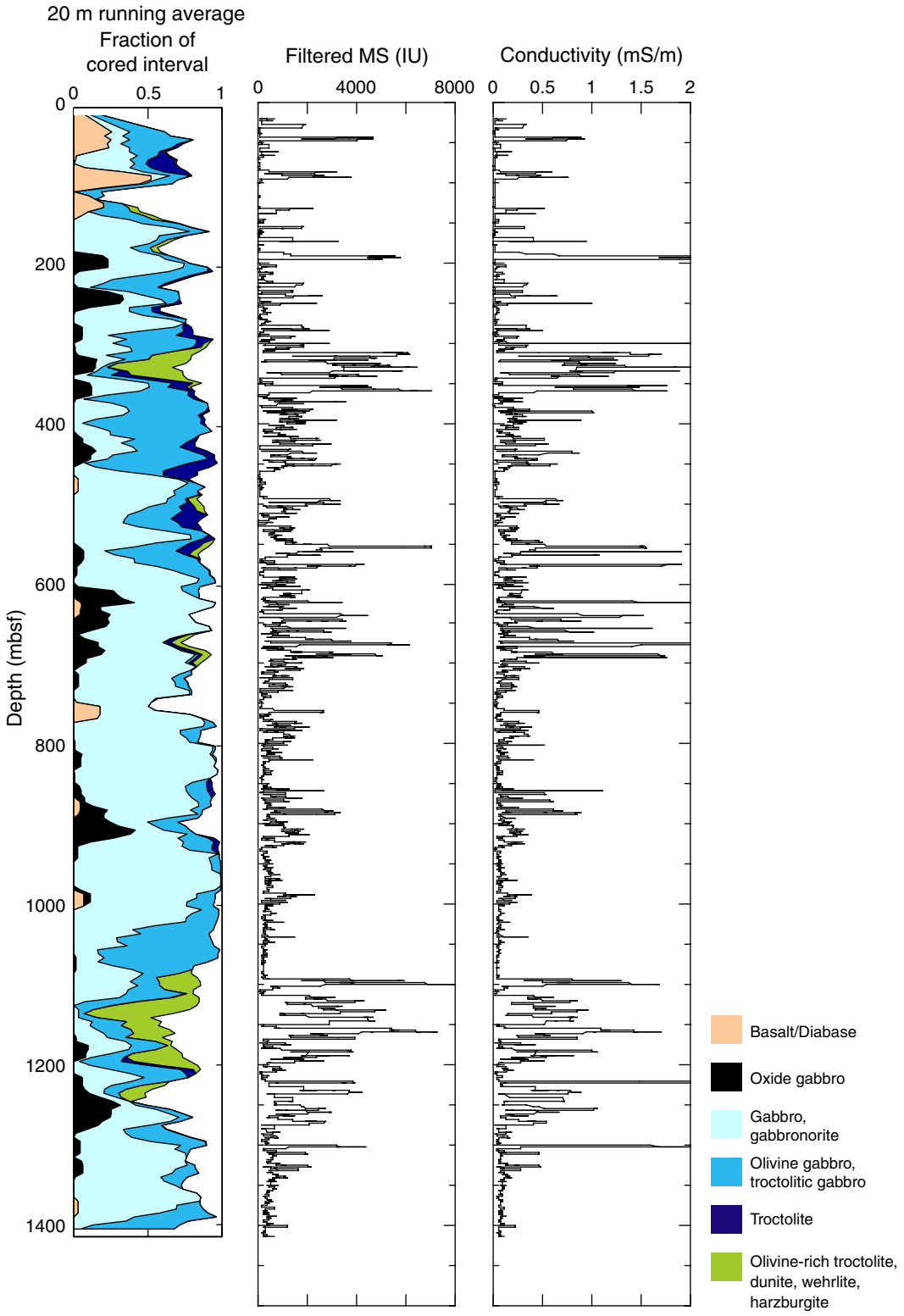

Figure F277. Voltage output from the noncontact resistivity (NCR) sensor on the multisensor track measured on olivine-bearing gabbro (Section 304-U1309D-57R-1 [Pieces 6 and 7]) following different degrees of saturation in seawater. Higher values of the NCR voltage represent more conductive values. The sample measurements extend from 5 to 105 cm; values beyond 110 cm were measured on empty core liner and give a measure of instrumental uncertainty. Diff = difference, SD = standard deviation.

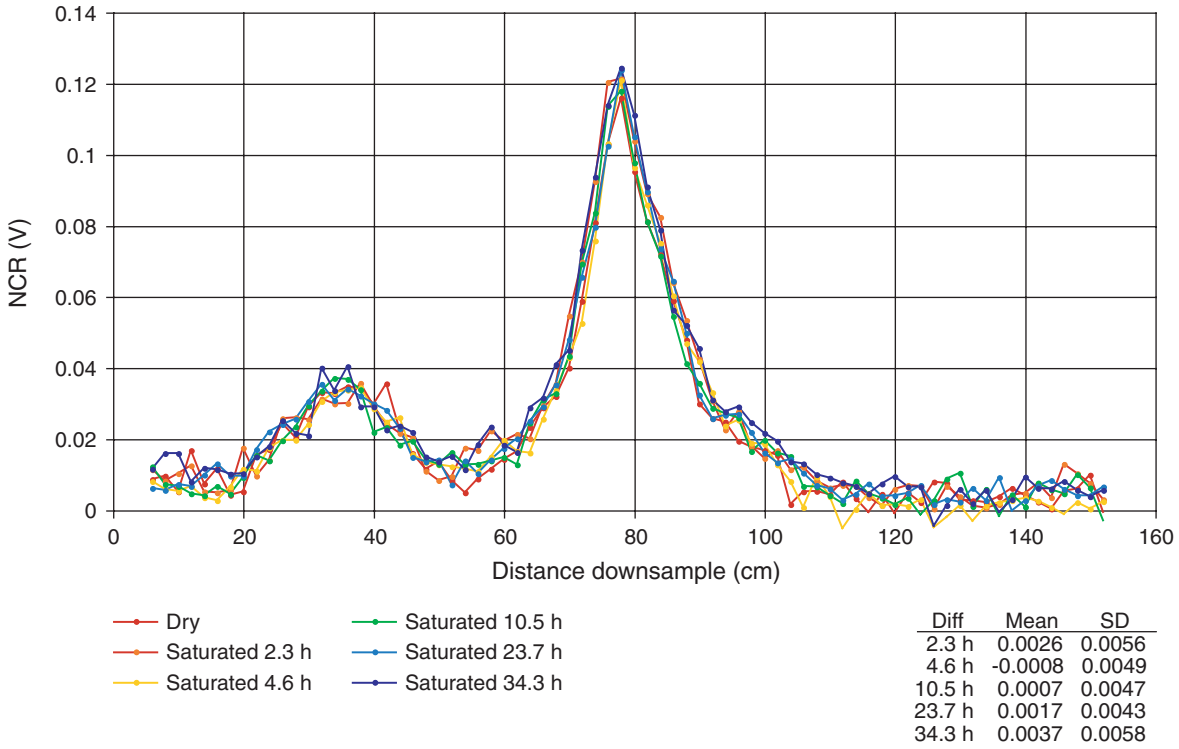

Diff	Mean	SD
2.3 h	0.0026	0.0056
4.6 h	-0.0008	0.0049
10.5 h	0.0007	0.0047
23.7 h	0.0017	0.0043
34.3 h	0.0037	0.0058

Figure F278. Natural gamma radiation (NGR), as measured by the MST, plotted as a function of depth compared with the recovered lithology for Hole U1309D. The variations in NGR are statistically not significantly different from background radiation levels.

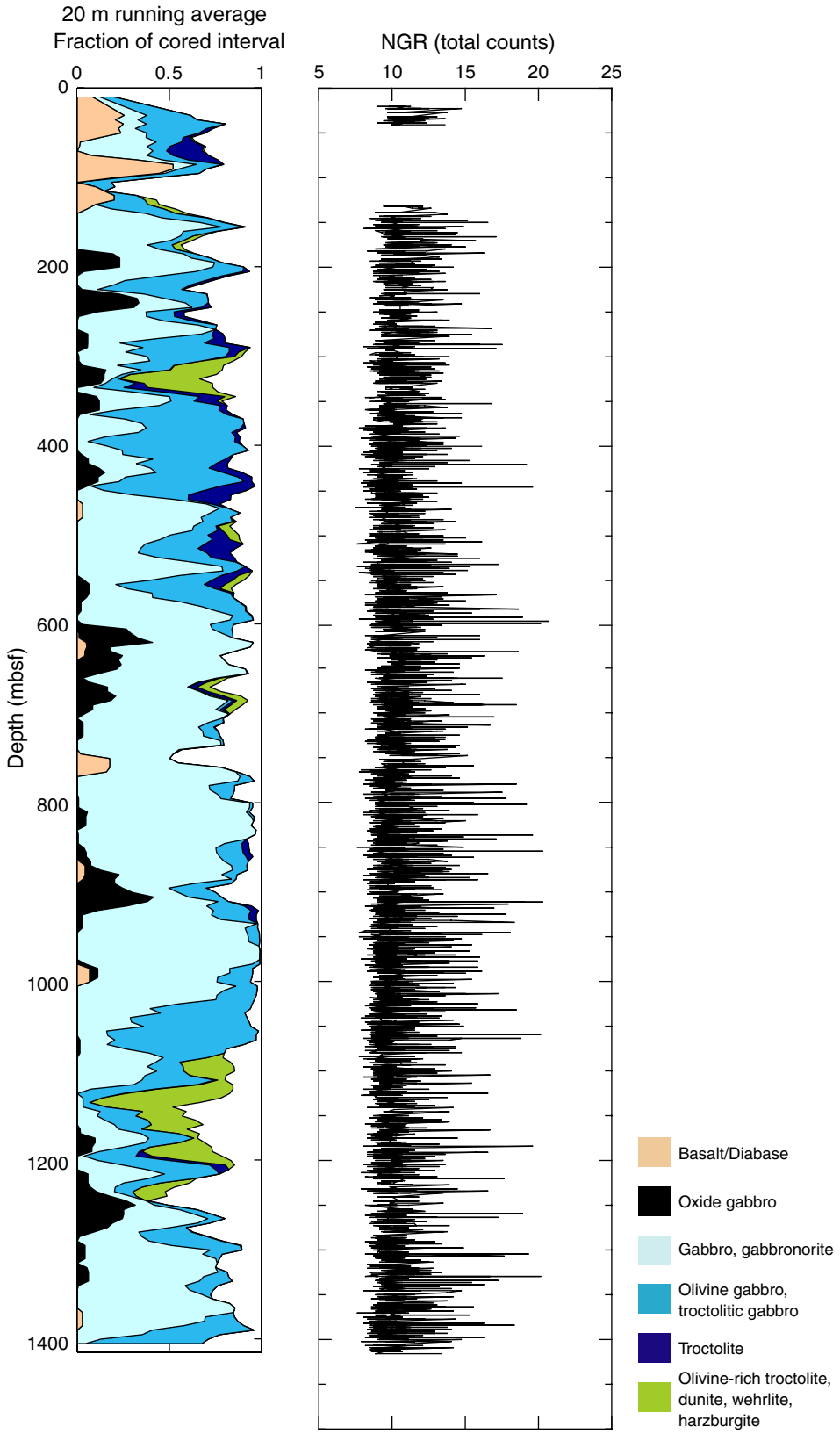

Figure F279. Epifluorescence microscopic image of microorganisms cultivated from igneous rock samples. Samples were stained with DAPI. **A.** Fluorescing particles from gabbro subsample (Sample 304-U1309B-16R-2, 0–8 cm) incubated at 65°C by using culture medium for methanogens. **B.** Cells and/or minerals radiating green light imaged with blue filter of wavelength 450–490 nm. Field of view = 60 µm. **C.** Fluorescing particles from gabbro subsample (Sample 304-U1309B-16R-2, 0–8 cm) incubated at 85°C by using culture medium for methanogens and stained with DAPI. **D.** Fluorescing particles from gabbro subsample (Sample 304-U1309B-16R-2, 0–8 cm) incubated at 37°C by using culture medium for heterotrophs. Scale bars = 10 µm.

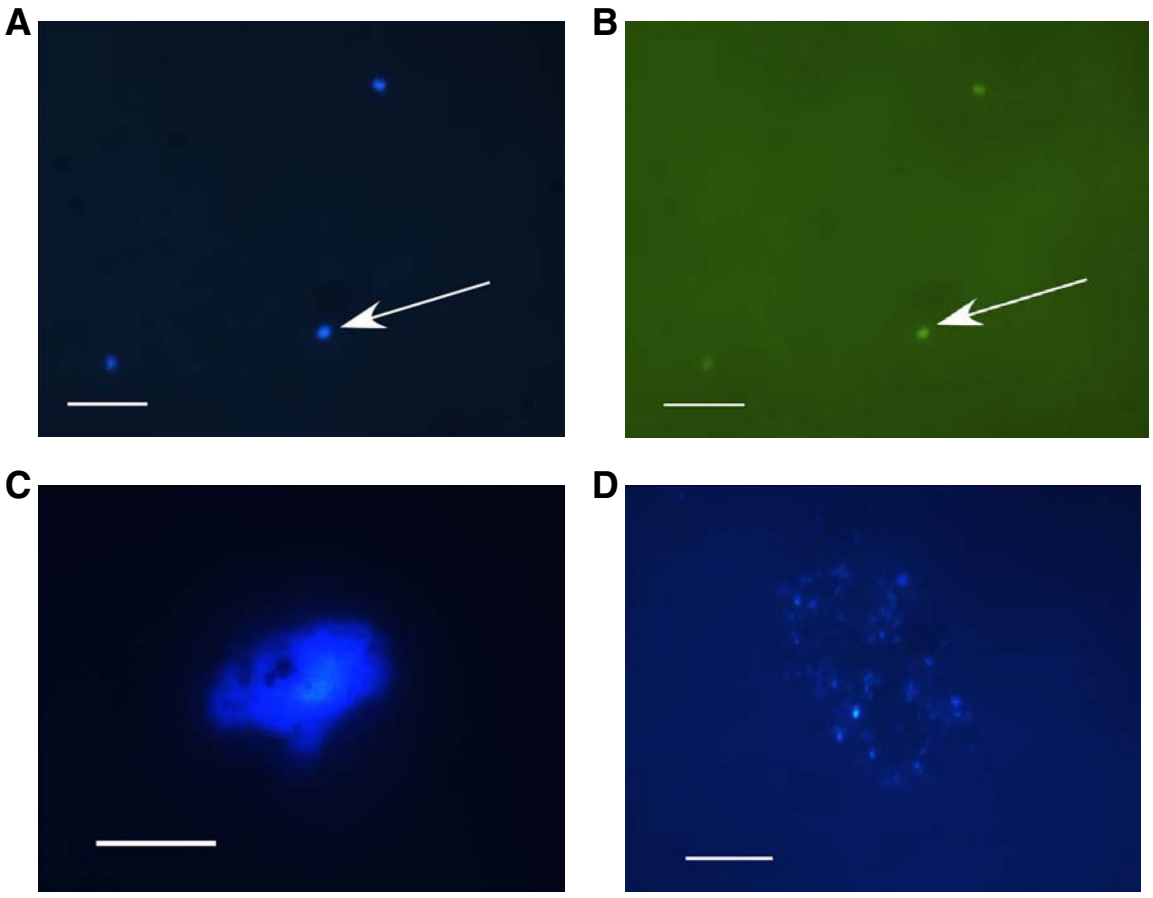

Figure F280. Epifluorescent image of cells grown on a marine agar 2216 plate (sample from Section 305-U1309D-80R-1) (field of view = 30 × 60 µm). Cells stained with acridine orange appear as light green spheres. Arrow indicates a cluster of cells.

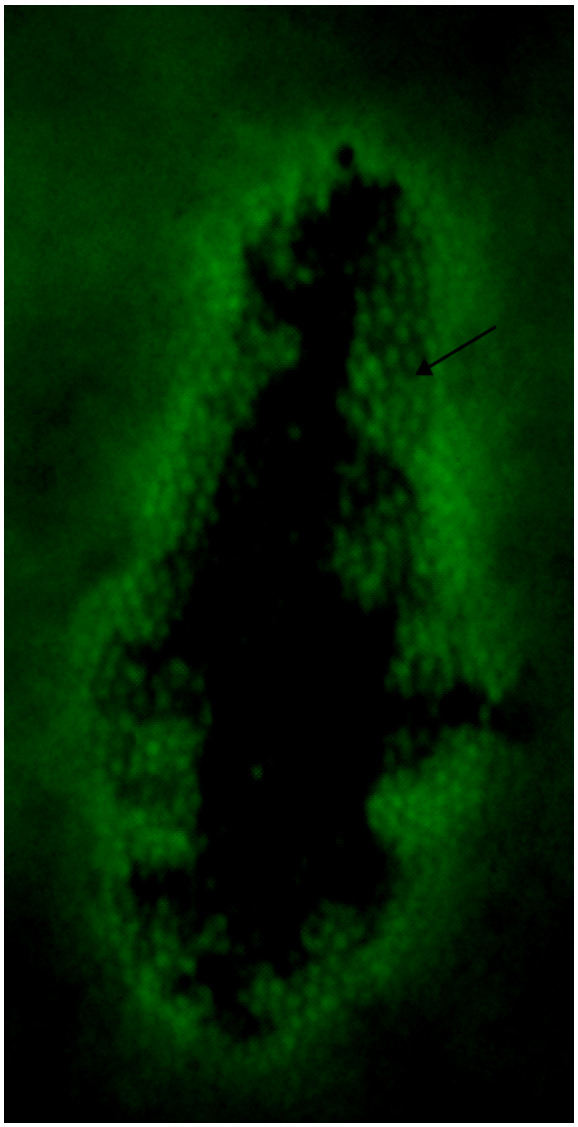

Figure F281. Epifluorescent image of an acridine orange–stained sample from methanogen enrichment media innoculated with an interior piece of Section 305-U1309D-122R-2. Red and green fluorescence of micrometer-sized particles may be indicative of the presence of microorganisms or of rock particles that autofluoresce (field of view = 175 × 135 µm.). Arrows indicate both green and red fluorescent cell-like structures.

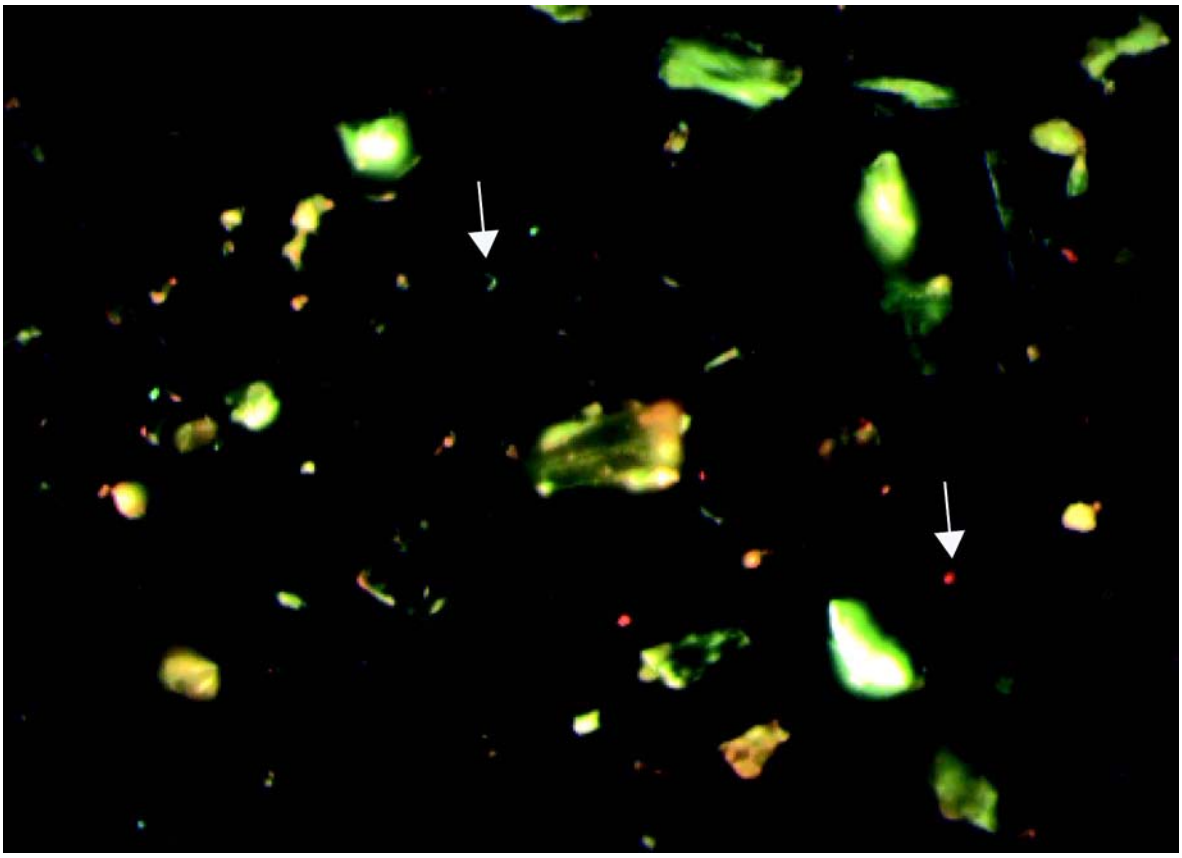

Figure F282. A. Detail of logging operations in Hole U1309B. The deployment of the SGT-GPIT tool string was devoted to the heave compensator tests. **B.** Detail of logging operations in Hole U1309D. Red lines = Expedition 304 runs, blue and green lines = Expedition 305 runs. Stars mark the clamping position of the check shot survey. HNGS = Hostile Environmental Gamma Ray Sonde, APS = Accelerator Porosity Sonde, HLDS = Hostile Environmental Litho-Density Sonde, DLL = Dual Laterolog, Triple Combo = triple combination, GPIT = General Purpose Inclinometry Tool, SGT = Scintillation Gamma Ray Tool, DSI = Dipole Sonic Imager, FMS = Formation MicroScanner, WST-3 = three-component Well Seismic Tool, UBI = Ultrasonic Borehole Imager, GBM = Goettingen Borehole Magnetometer.

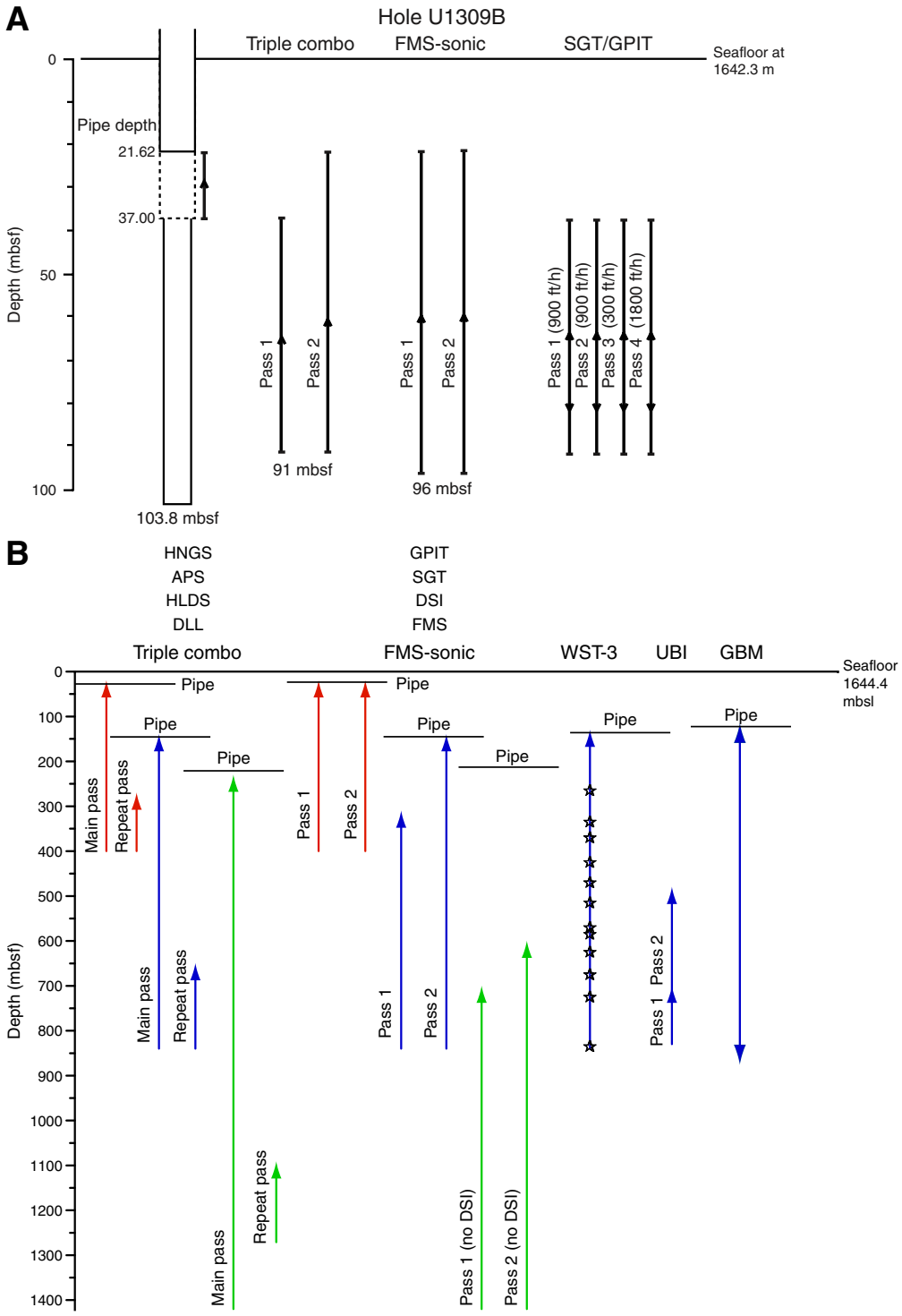

Figure F283. Results of selected measurements from Hole U1309B. The left column shows the core reference with the main lithologic units as derived from core descriptions. Circles in the neutron porosity and density panels represent shipboard measurements on core samples. DEVI = hole deviation, HNGS = Hostile Environment Gamma Ray Sonde, SGT = Scintillation Gamma Ray Tool, LLD = deep laterolog, LLS = shallow laterolog, RHOM = bulk density, HROM = high-resolution bulk density, APLC = neutron porosity, PEFL = photoelectric effect, SIGF = neutron capture cross section, FMS = Formation MicroScanner.

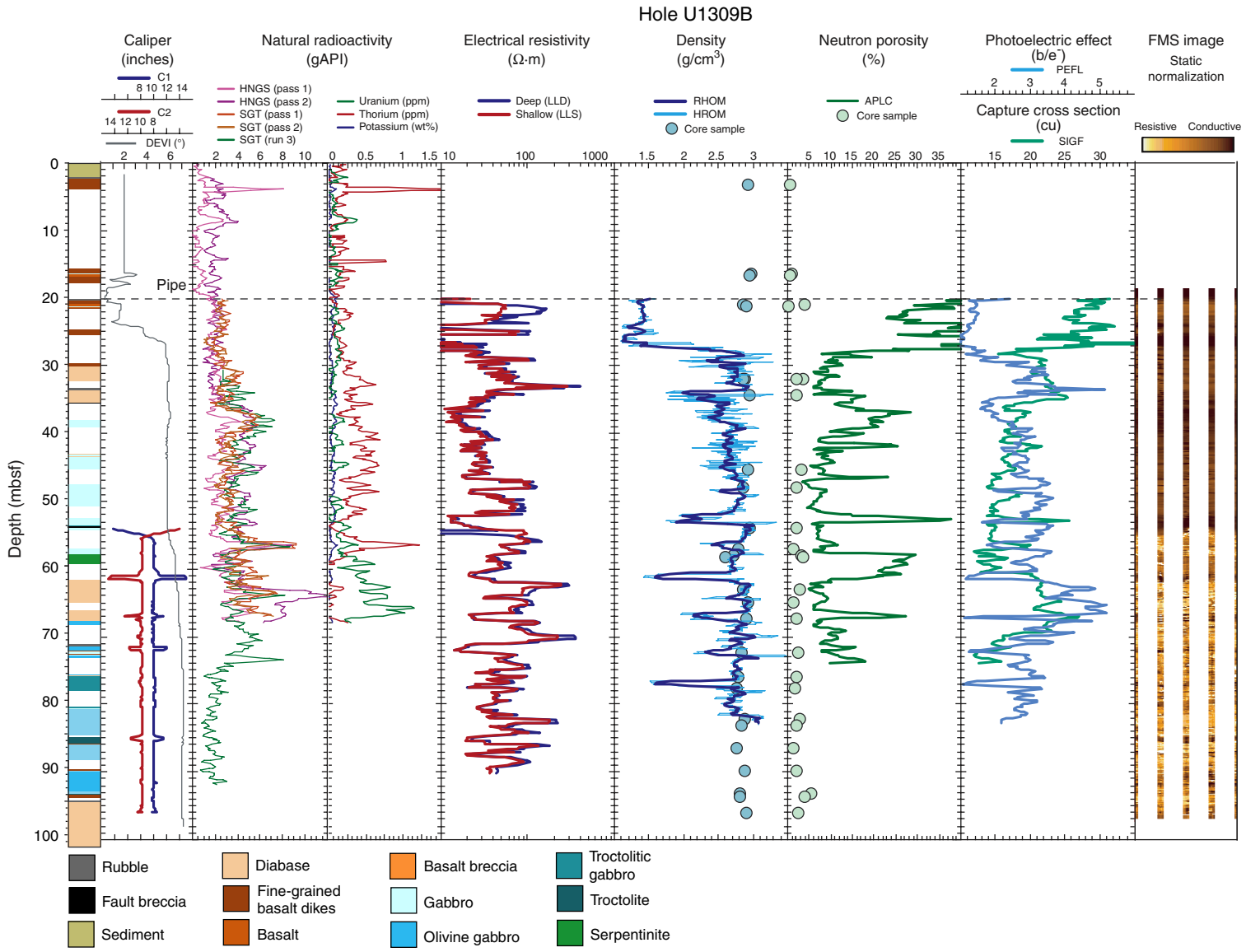

Figure F284. A. Results of selected measurements from Hole U1309D (<400 mbsf). Left column shows the core reference with the main lithologic units as derived from core descriptions. SGT = Scintillation Gamma Ray Tool, PEFL = photoelectric effect, HSGR = total gamma ray from the triple combo run. (Continued on next two pages.)

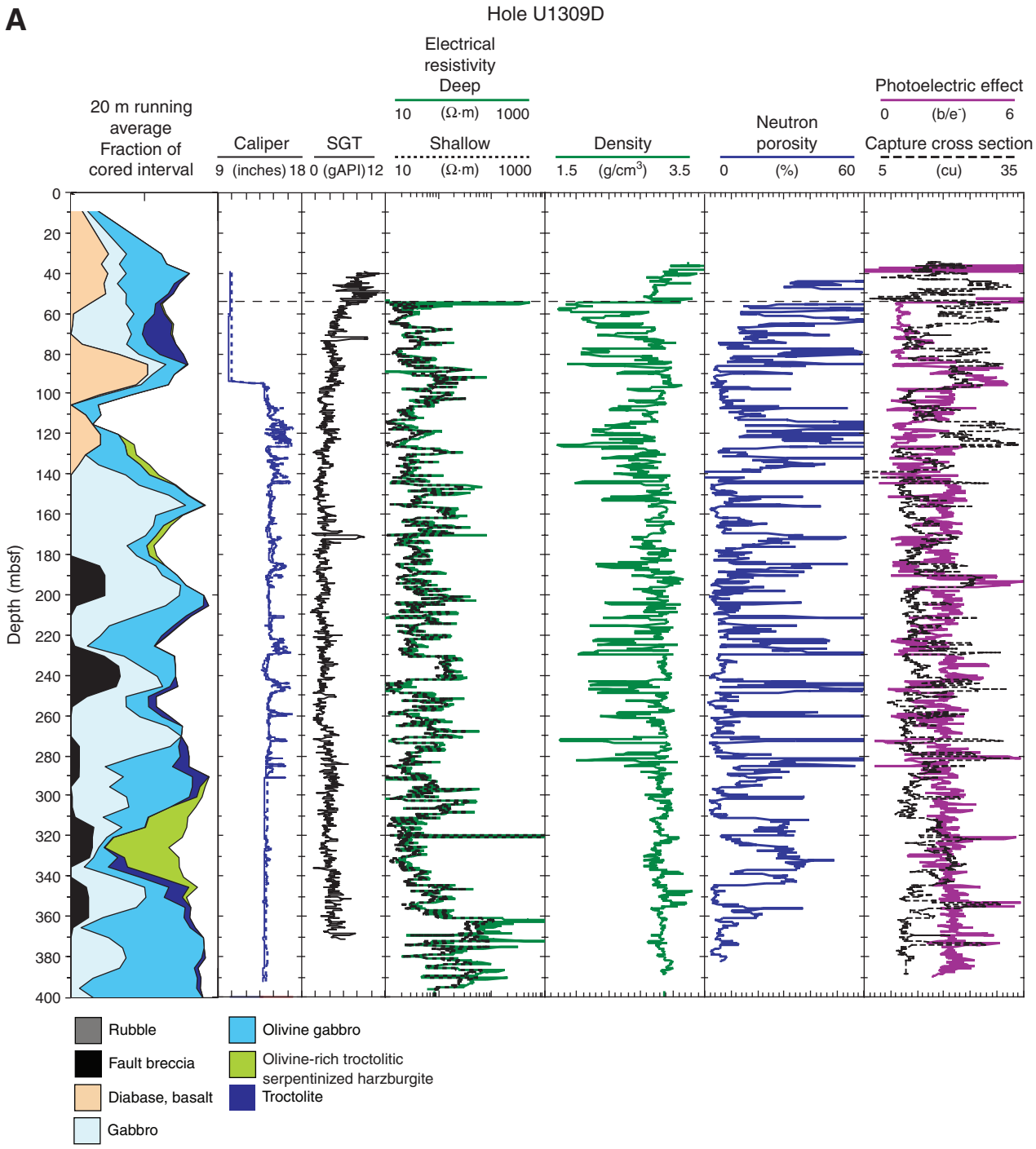

Figure F284 (continued). B. Results of selected logging measurements from Hole U1309D (100–840 mbsf). The right column shows the lithology running average based on the core description.

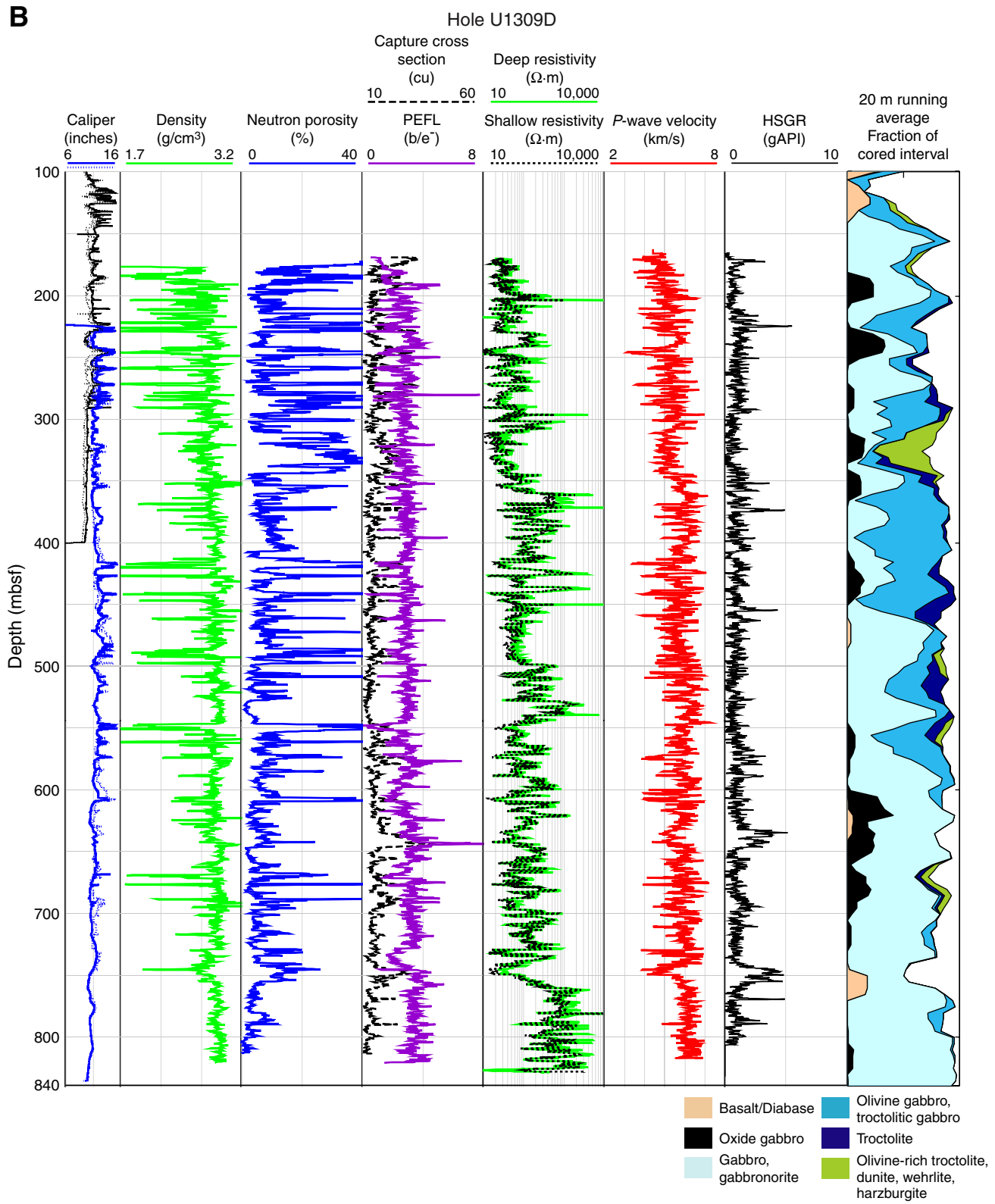

Figure F284 (continued). C. Results of selected logging measurements from Hole U1309D (800–1415.5 mbsf). Right column shows the lithology running average based on the core description. Logging velocity is missing due to failure of the DSI tool.

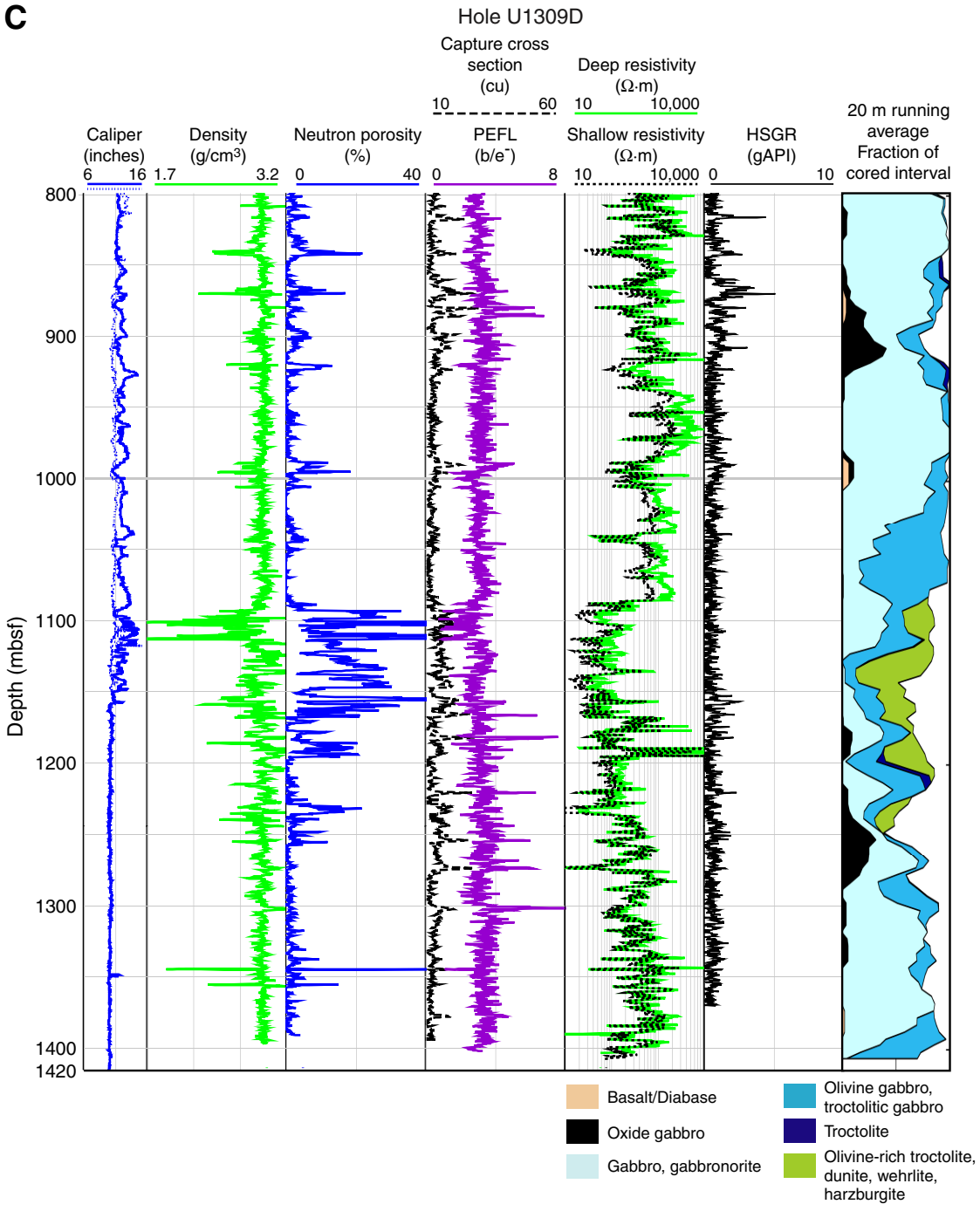

Figure F285. Raw three-component magnetometer data acquired by the GBM for uphole and downhole runs. Oscillation of horizontal components about the zero line in both runs is due to different angular rates of tool rotation that occurred while lowering and raising the GBM sonde within the hole.

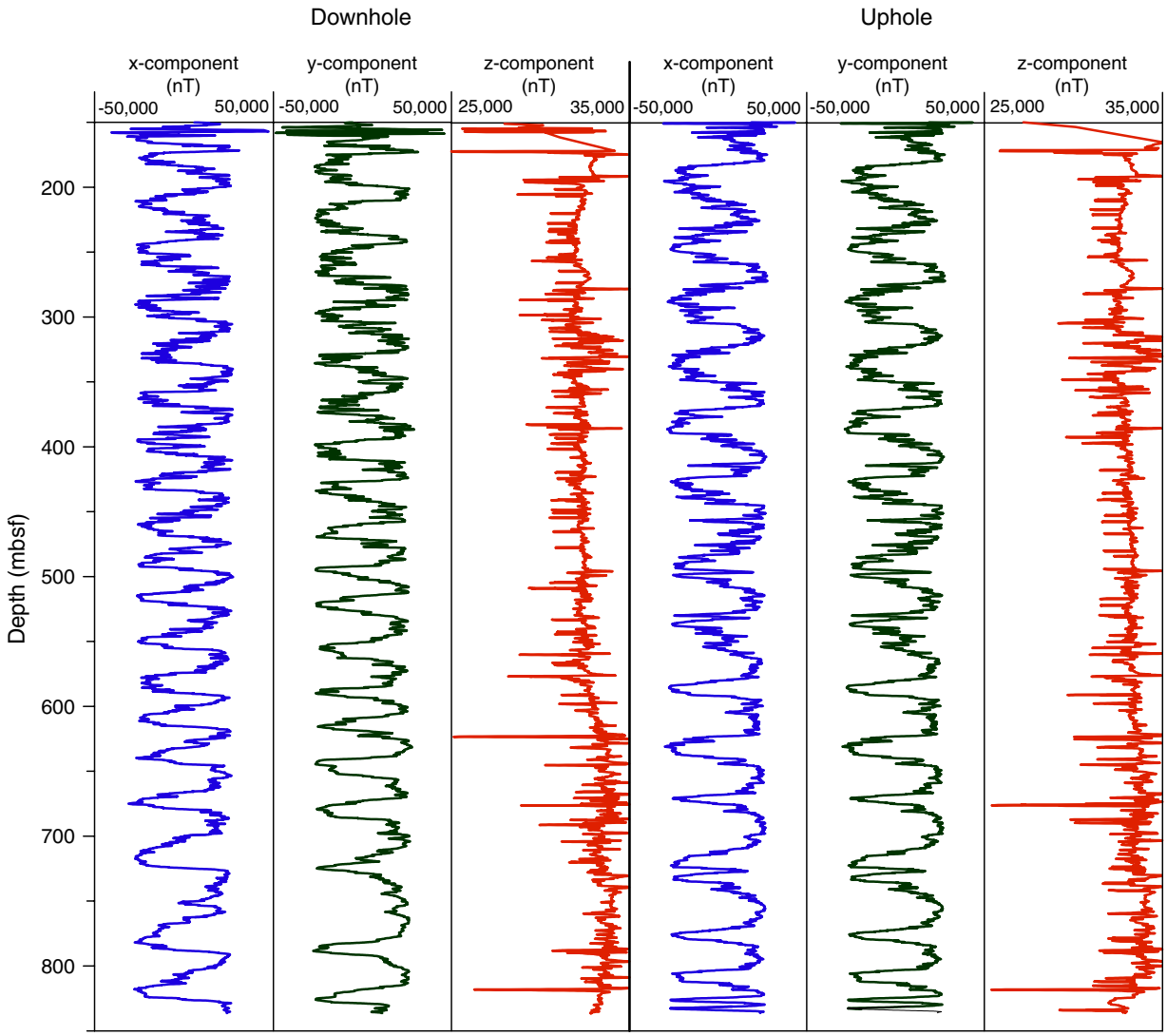

Figure F286. Comparison of Goettingen Borehole Magnetometer (GBM) and General Purpose Inclinometry Tool (GPIT) magnetic data showing similar patterns of relative highs and lows but differences in magnitude between instruments. Vertical components from both instruments show an offset from the recent field (International Geomagnetic Reference Field) expected for this latitude displayed as a constant line, as well as an offset with respect to each other.

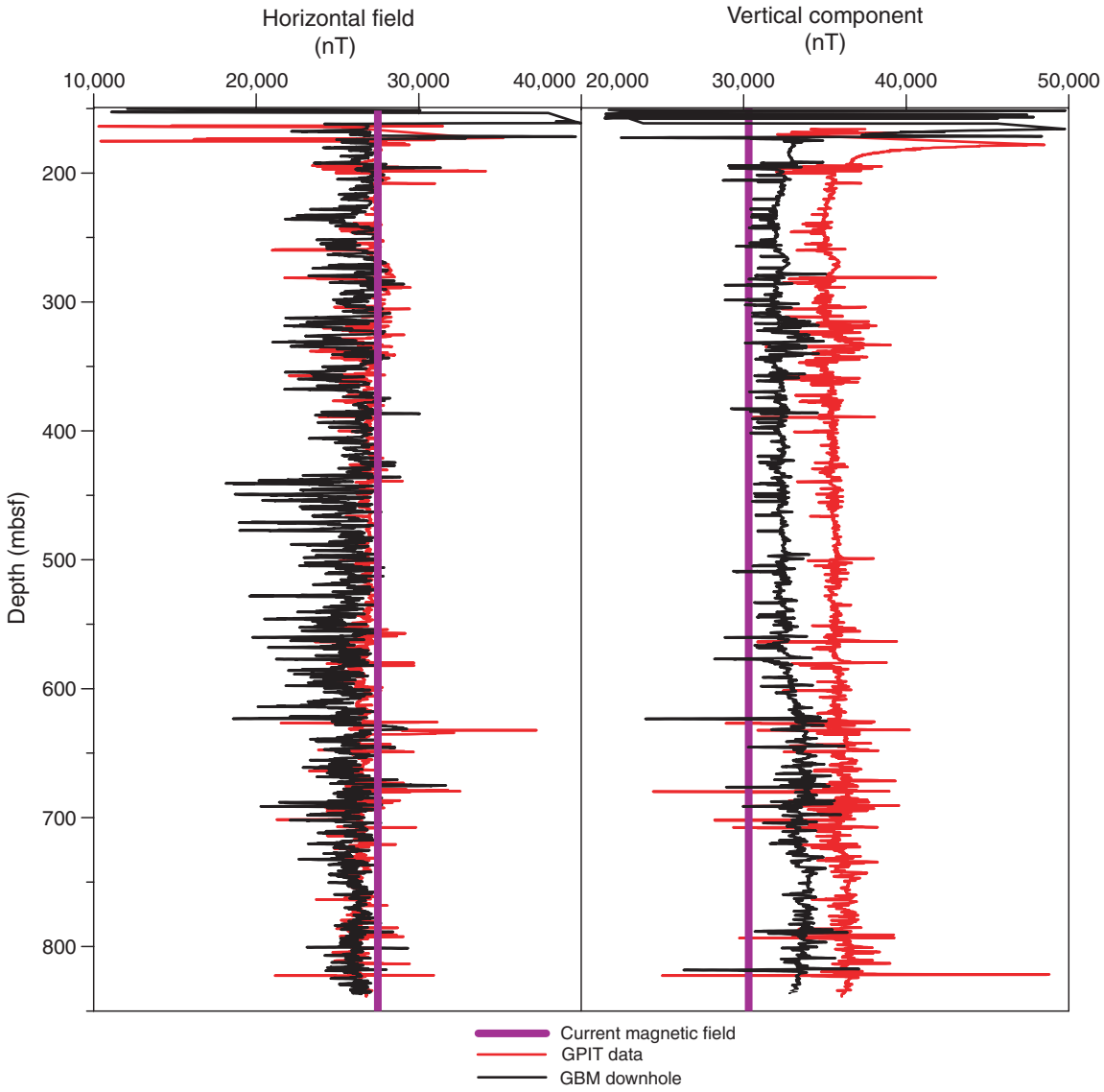

Figure F287. Comparison of the logging data and core petrophysical results. Triangles and diamonds = shipboard measurements on core samples (10 cm^3). All data follow a similar trend; however, the sample porosity is significantly lower than the neutron porosity (note the different scales) as expected (see text). PWS3 = *P*-wave sensor. **A.** Data from 400 to 820 mbsf. (Continued on next page.)

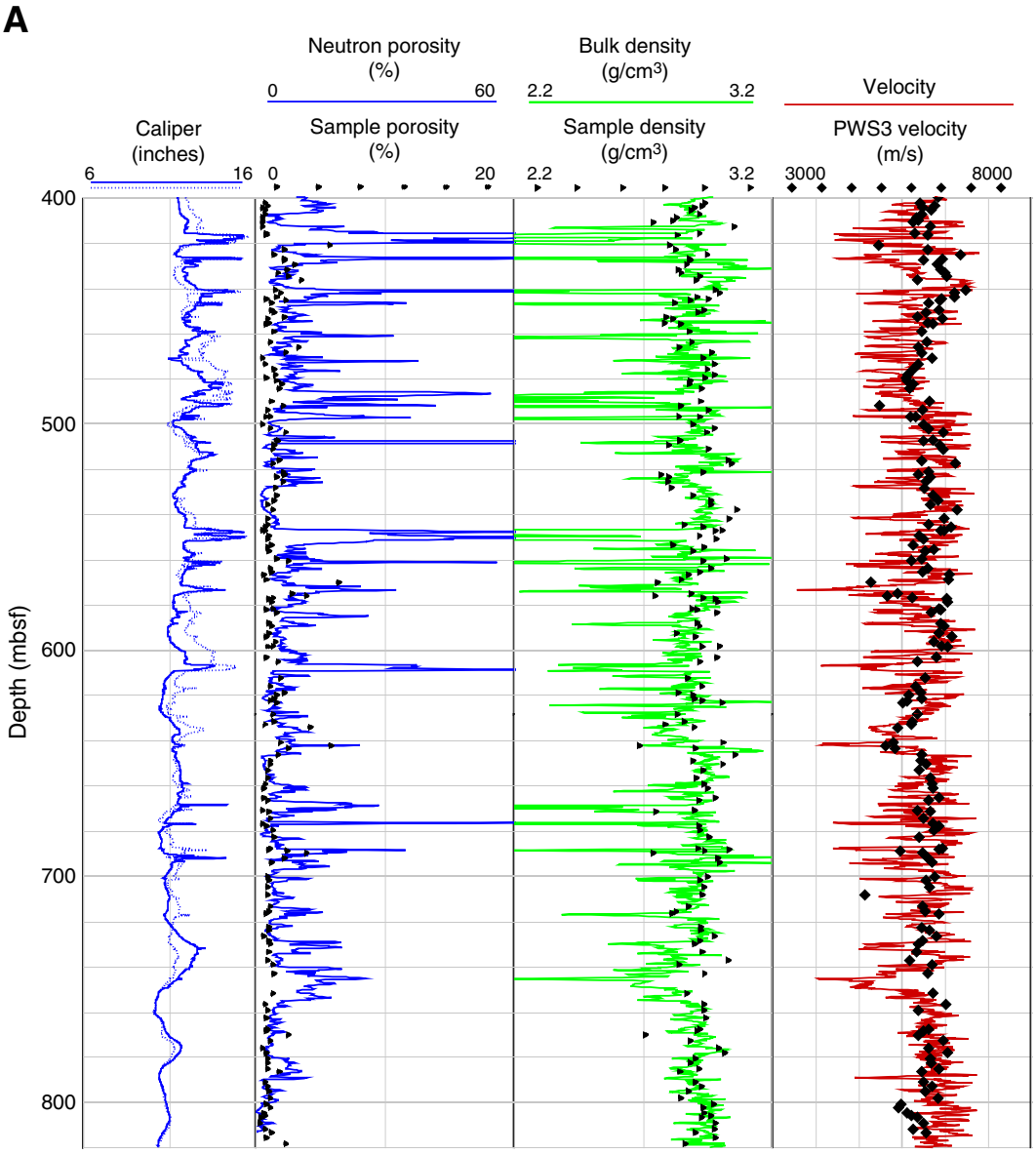

Figure F287 (continued). B. Data from 800 to 1415.5 mbsf.

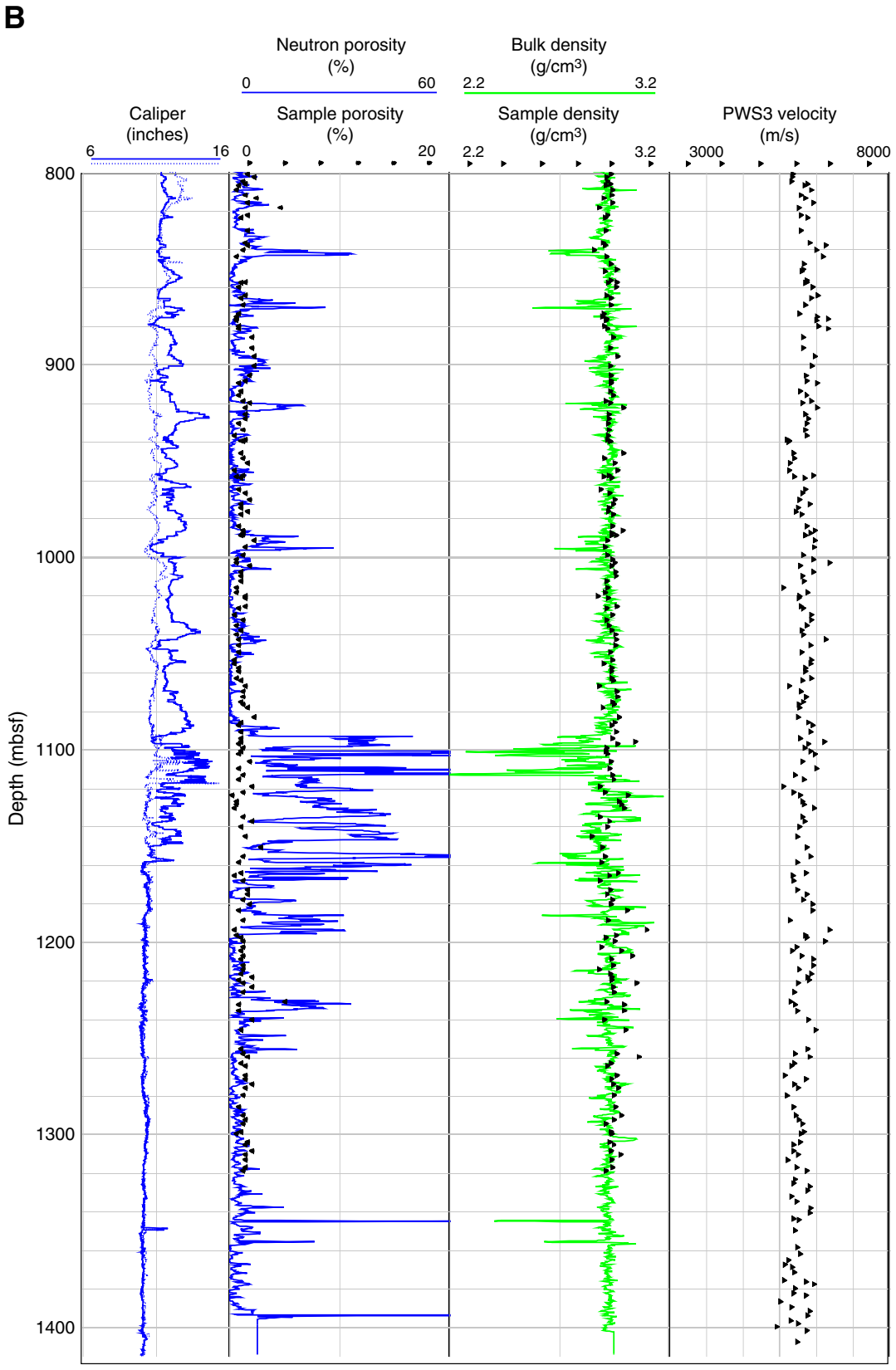

Figure F288. Detailed Formation MicroScanner (FMS) image displaying a typical gabbroic interval (365–368 mbsf) in Hole U1309D.

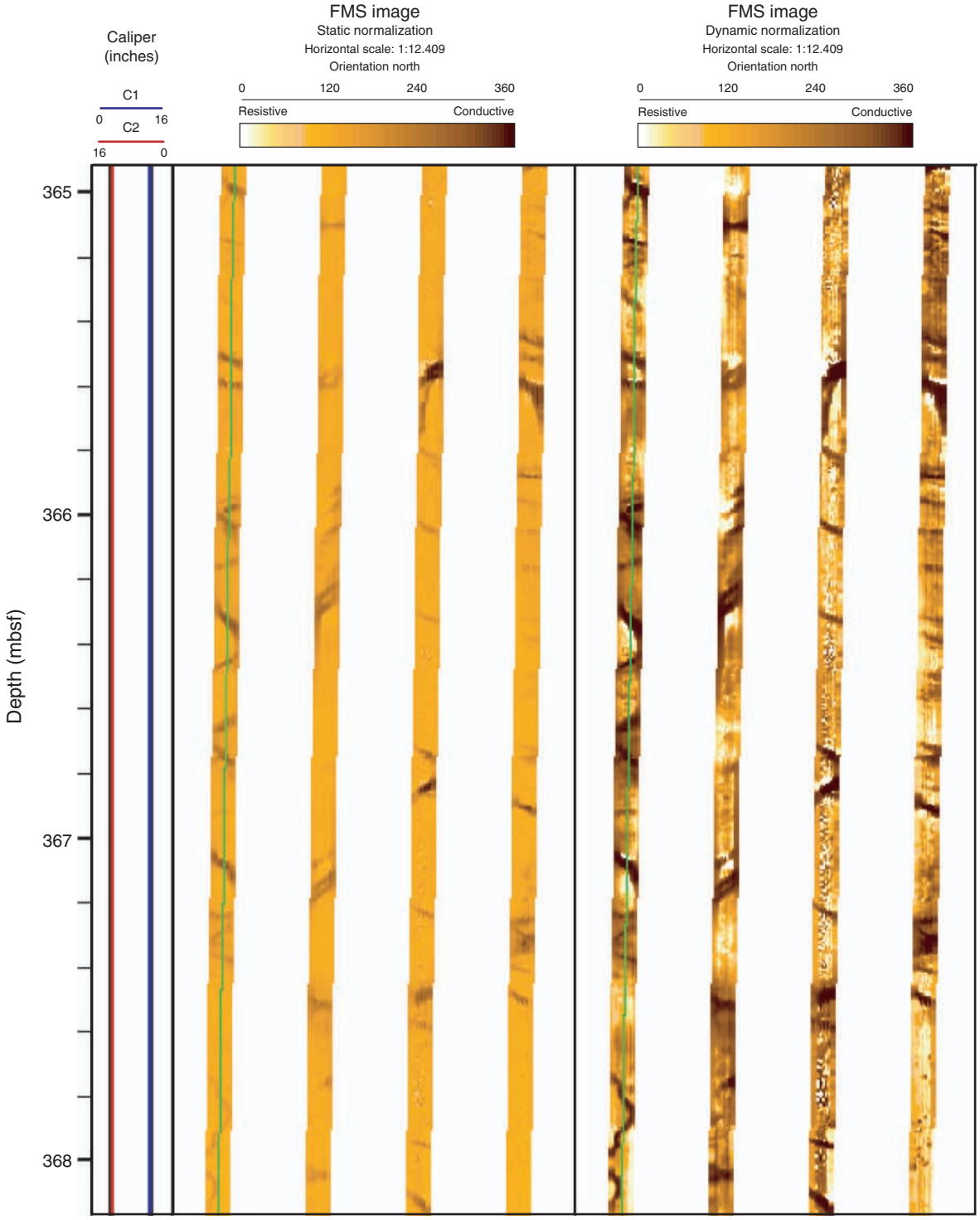

Figure F289. Detailed Formation MicroScanner (FMS) and Ultrasonic Borehole Imager (UBI) image displaying (**A**) the transition from a patchy looking coarse-grained olivine gabbro to an olivine gabbro, above, and (**B**) a steep fracture indicated by low resistivity (dark color), which is related to one appearing in Sections 305-U1309-120R-2 and 120R-3.

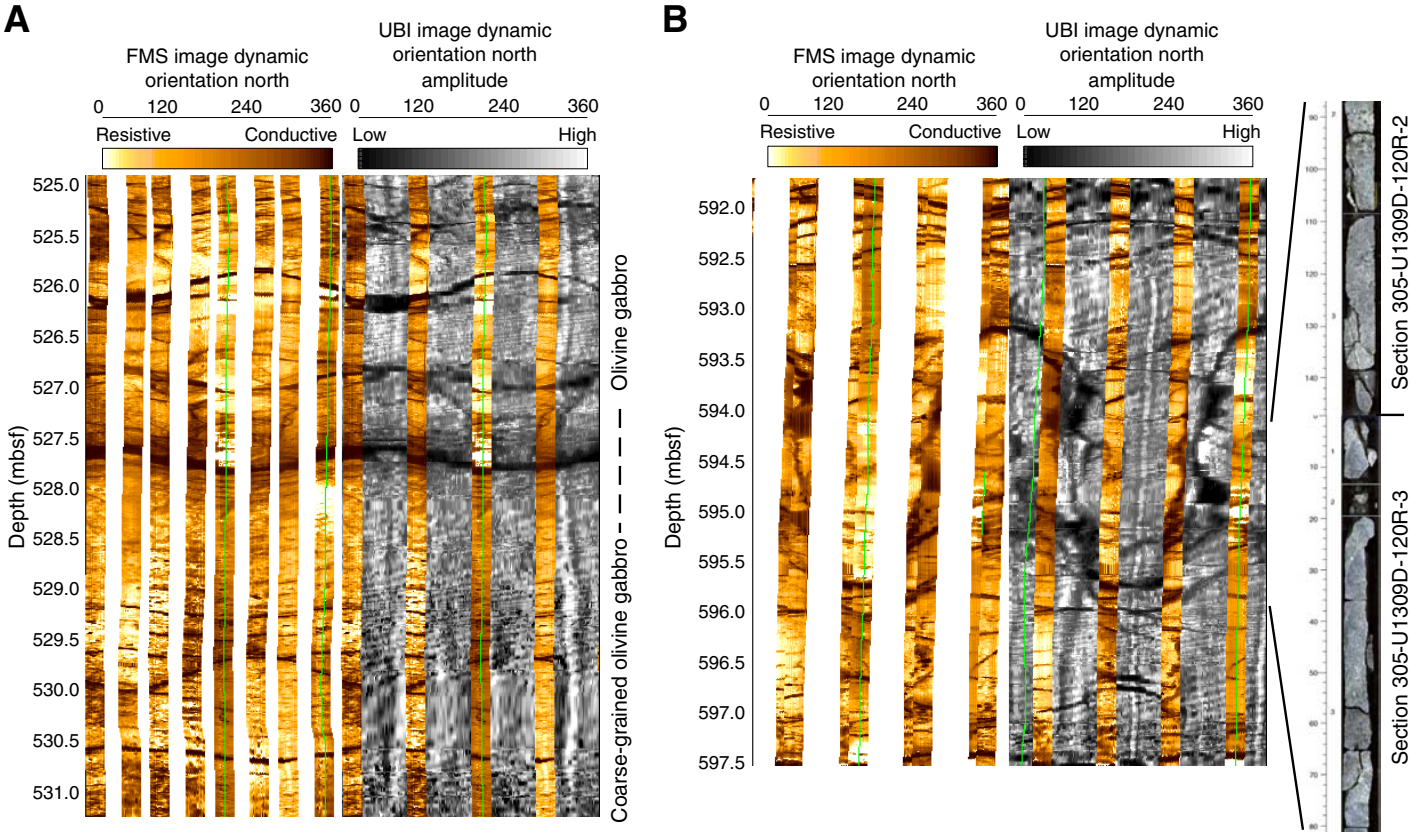

Figure F290. Detailed Formation MicroScanner (FMS) image displaying an oxide-rich layer (192–195 mbsf). Oxide minerals correspond to the black patches and are particularly abundant from 192.4 to 193.1 mbsf.

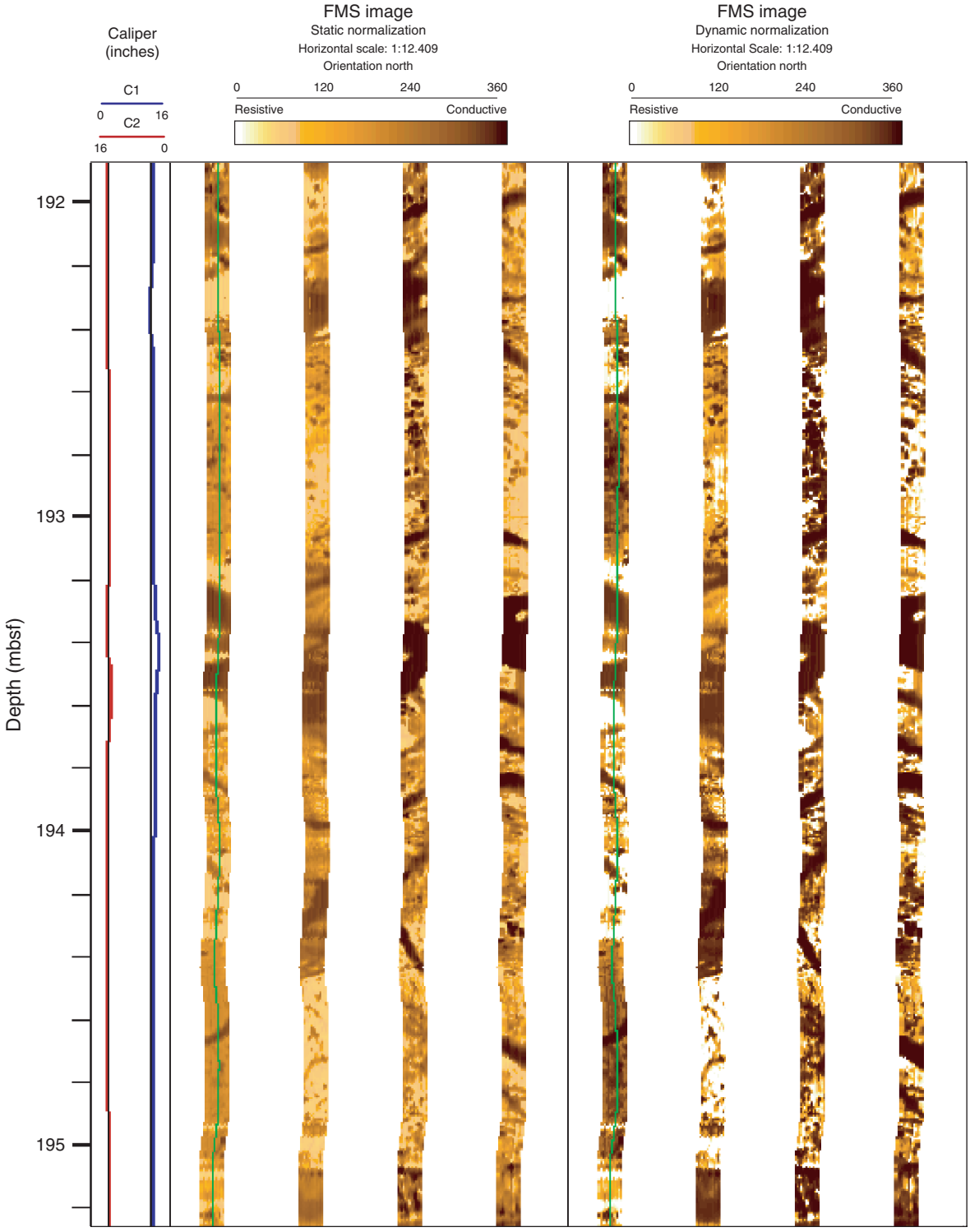

Figure F291. Preliminary structural interpretation of the Formation MicroScanner (FMS) images from Hole U1309B. FMS images are presented with a static and dynamic normalization. On the dynamic image, sinusoids that correspond to the mapped planes are shown by the red lines. The orientation tadpoles plot in the next column, where position along the horizontal axis indicates the dip (0°–90°) and the tadpole tail direction indicates the dip direction of the planar structure (south = down, north = up). Electrical resistivity (logarithmic scale), neutron porosity, density, photoelectric effect, and capture cross-section curves are also shown for comparison. In the lower right corner, the summary of the structural analysis of the FMS images is presented. The histogram shows the distribution of dip values, and the rosette diagram shows the dip direction of the planar structure identified on the FMS images. Good correlation is observed between fractured intervals on the FMS images (highly conductive intervals) and low density and electrical resistivity and high porosity.

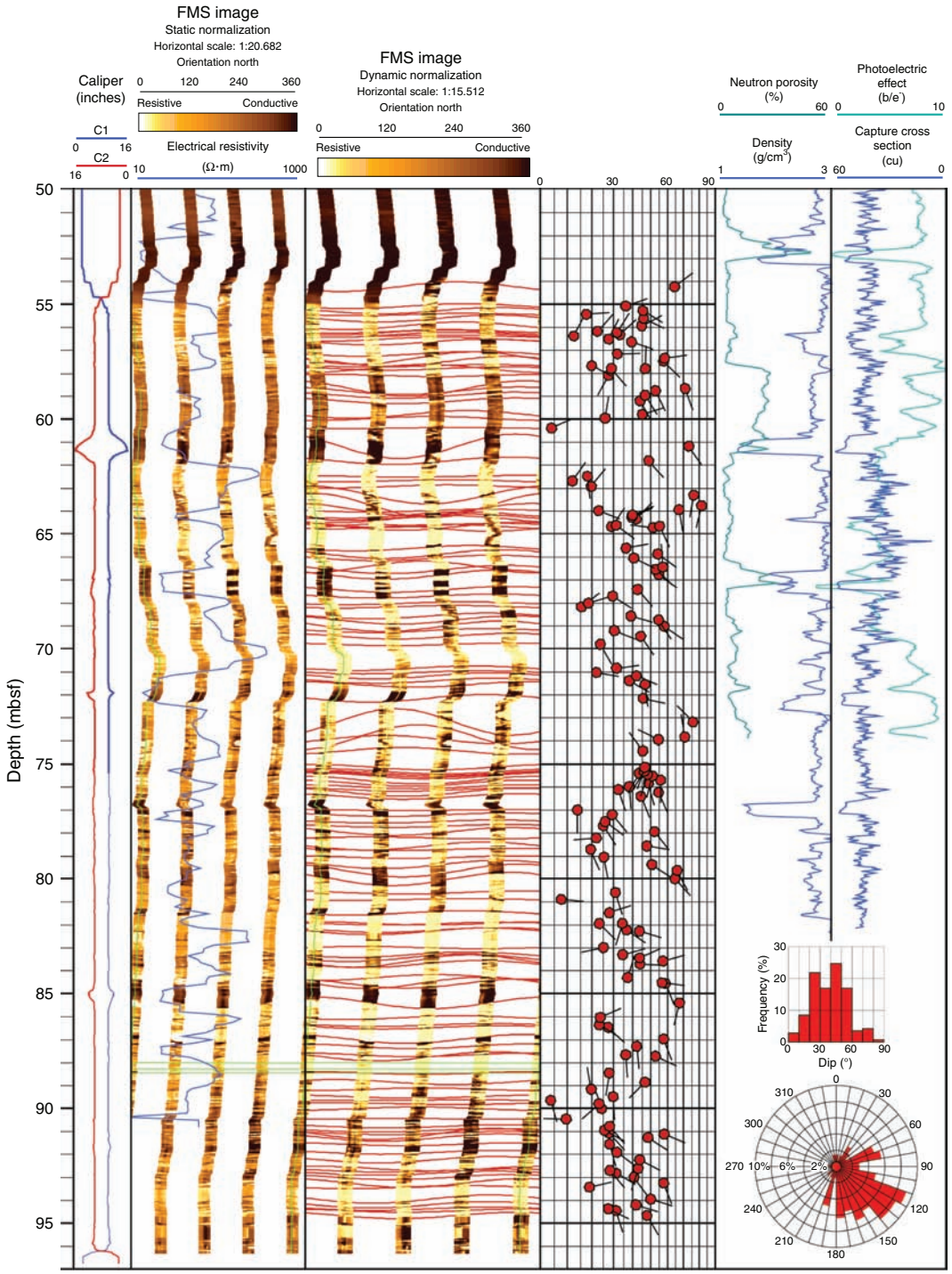

Figure F292. Detailed Formation MicroScanner (FMS) image displaying a brecciated interval (79.4–80 mbsf) in Hole U1309B. The breccia consists of heterogeneous material, with resistive material (white arrows) cemented in a conductive matrix.

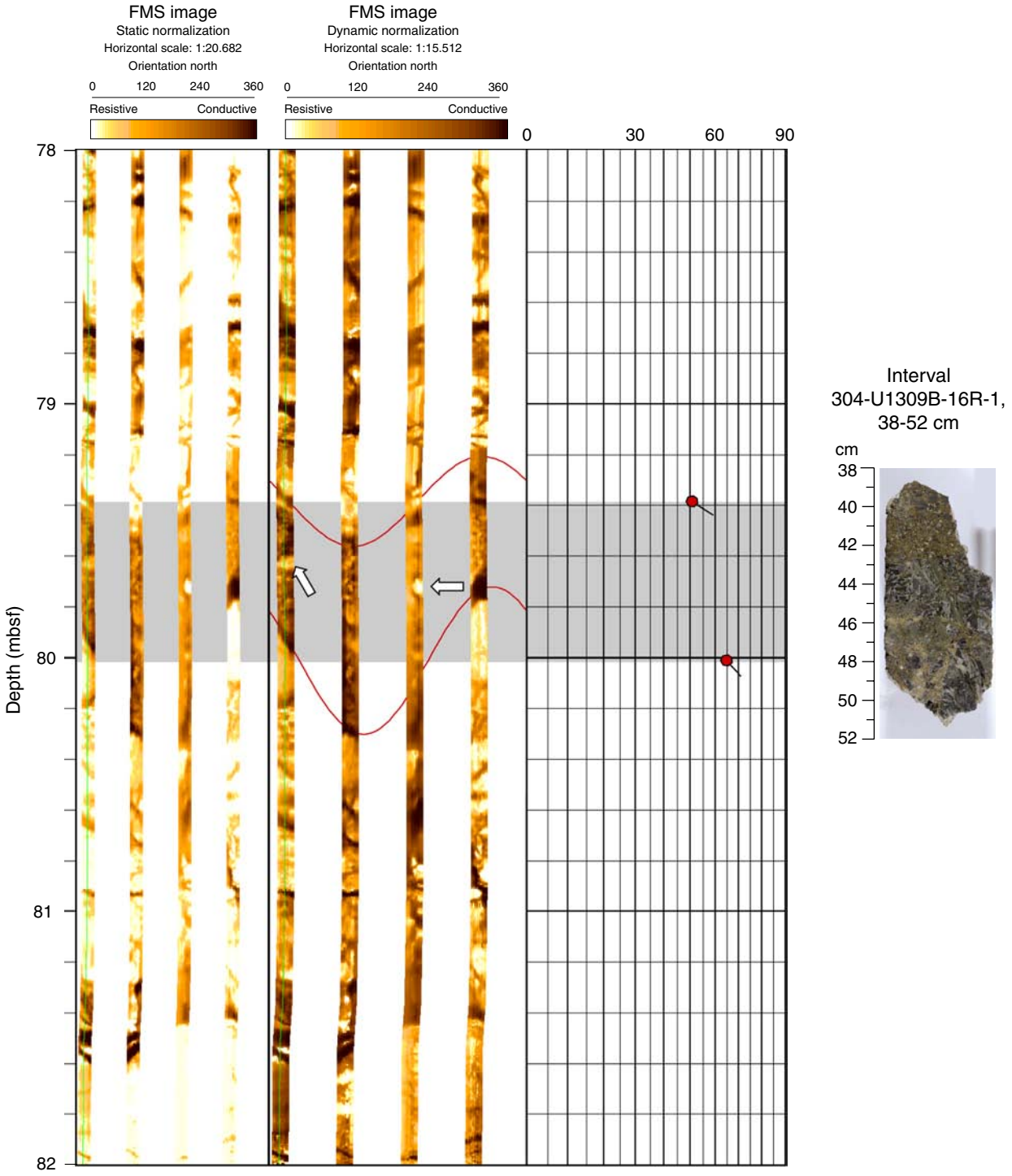

Figure F293. Hole U1309B static and dynamic Formation MicroScanner (FMS) images from 55 to 65 mbsf, showing a contact between highly resistive formation above 58 mbsf and a conductive formation (58–62 mbsf). This contact may correspond to the contact between the gabbros and serpentinized peridotite. At 61 mbsf, the borehole is enlarged and the electrical resistivity measured by the DLL decreases. This thin interval may correspond to a faulted zone.

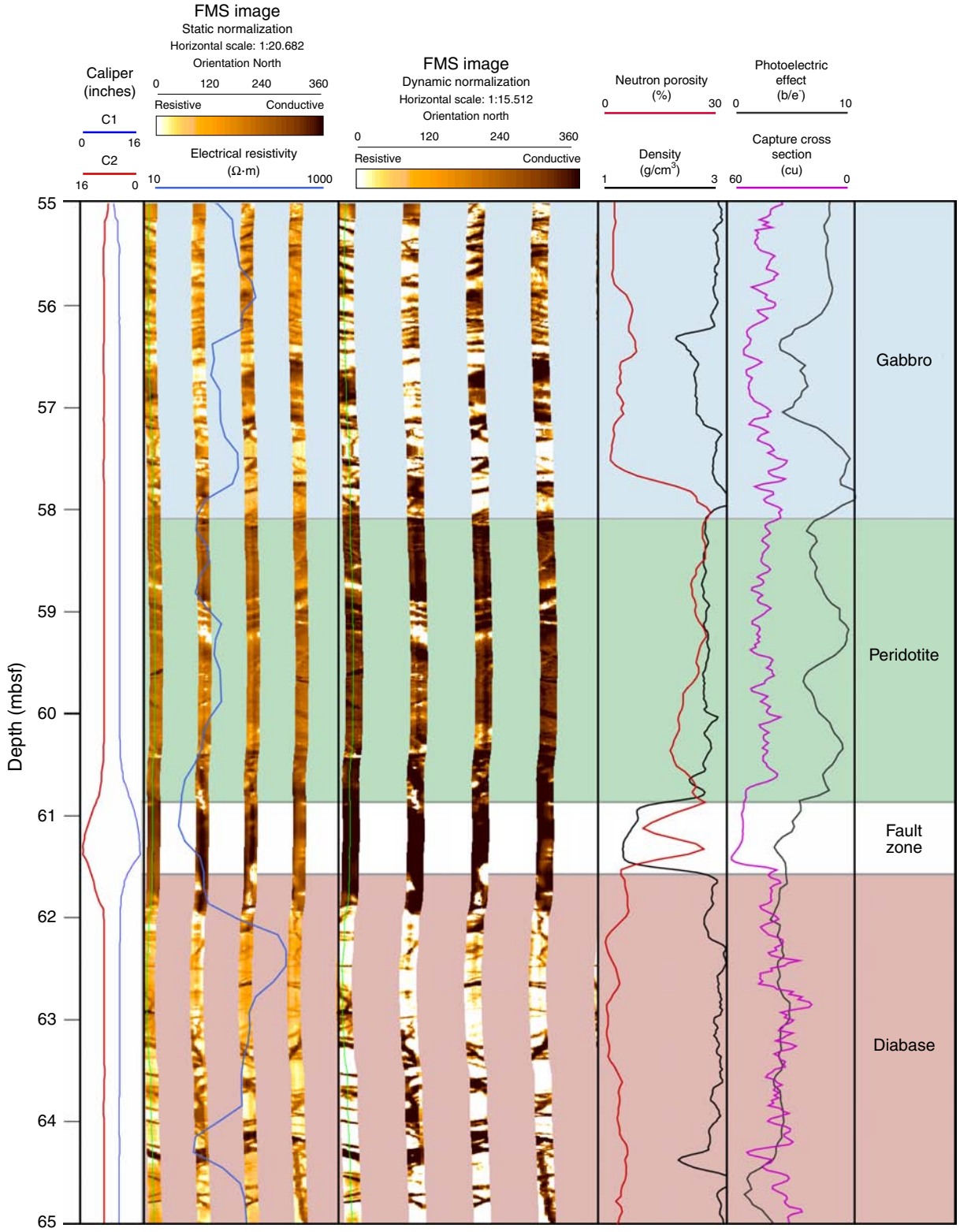

Figure F294. Detailed Formation MicroScanner (FMS) and UBI images displaying a fractured interval (772–783 mbsf) in Hole U1309D. Rose plot indicates that the conductive features are consistent in direction, with the shallow structures dipping toward north and the steep features dipping south.

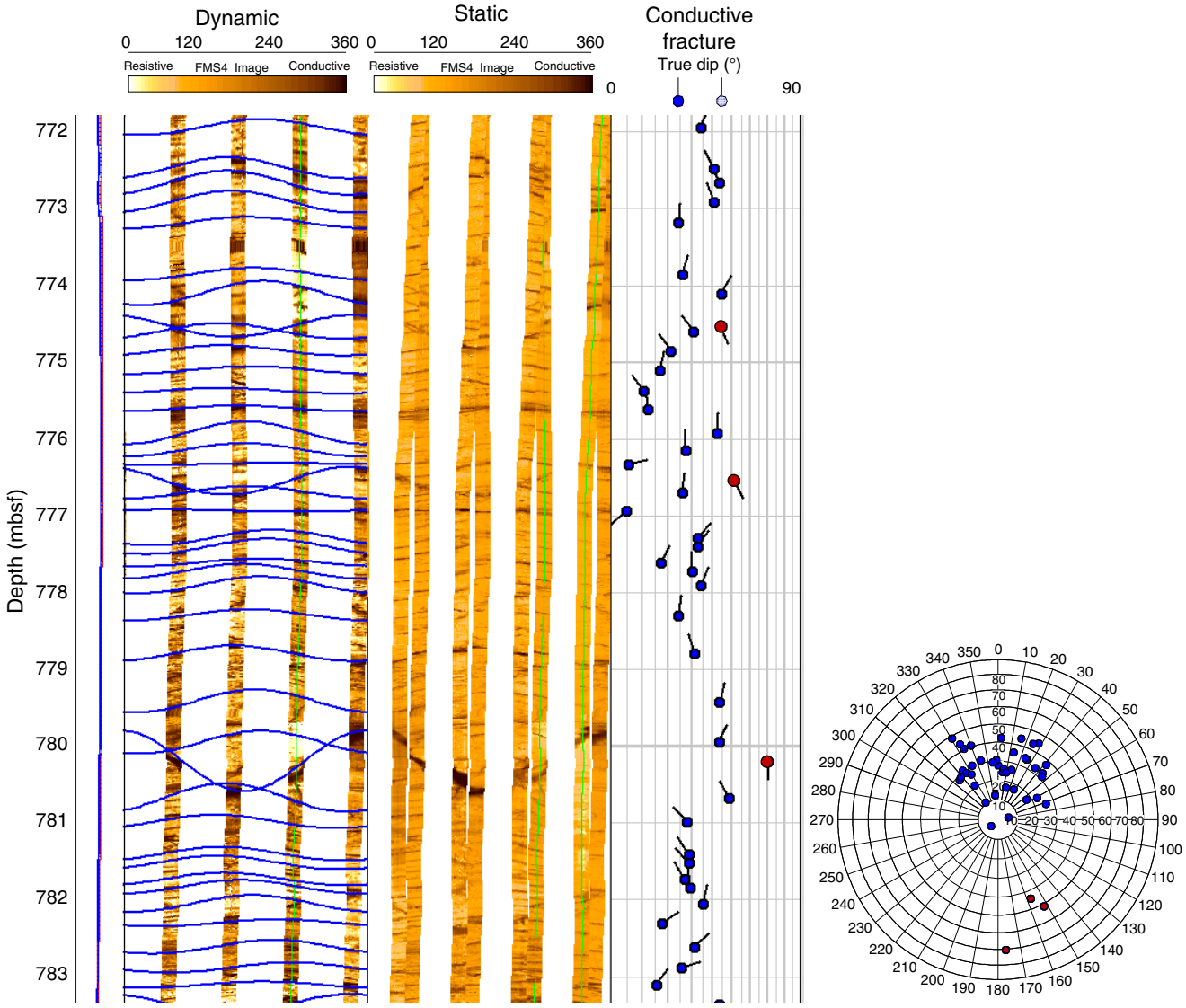

Figure F295. Detailed Formation MicroScanner (FMS) and Ultrasonic Borehole Imager (UBI) images displaying a fractured and sheared interval (667–673 mbsf). This interval may correspond to a wehrlite containing a mylonitic shear zone and, below, to a microgabbro and gabbro with steeply cutting veins described in Sections 305-U1309D-136R-1 through 136R-3.

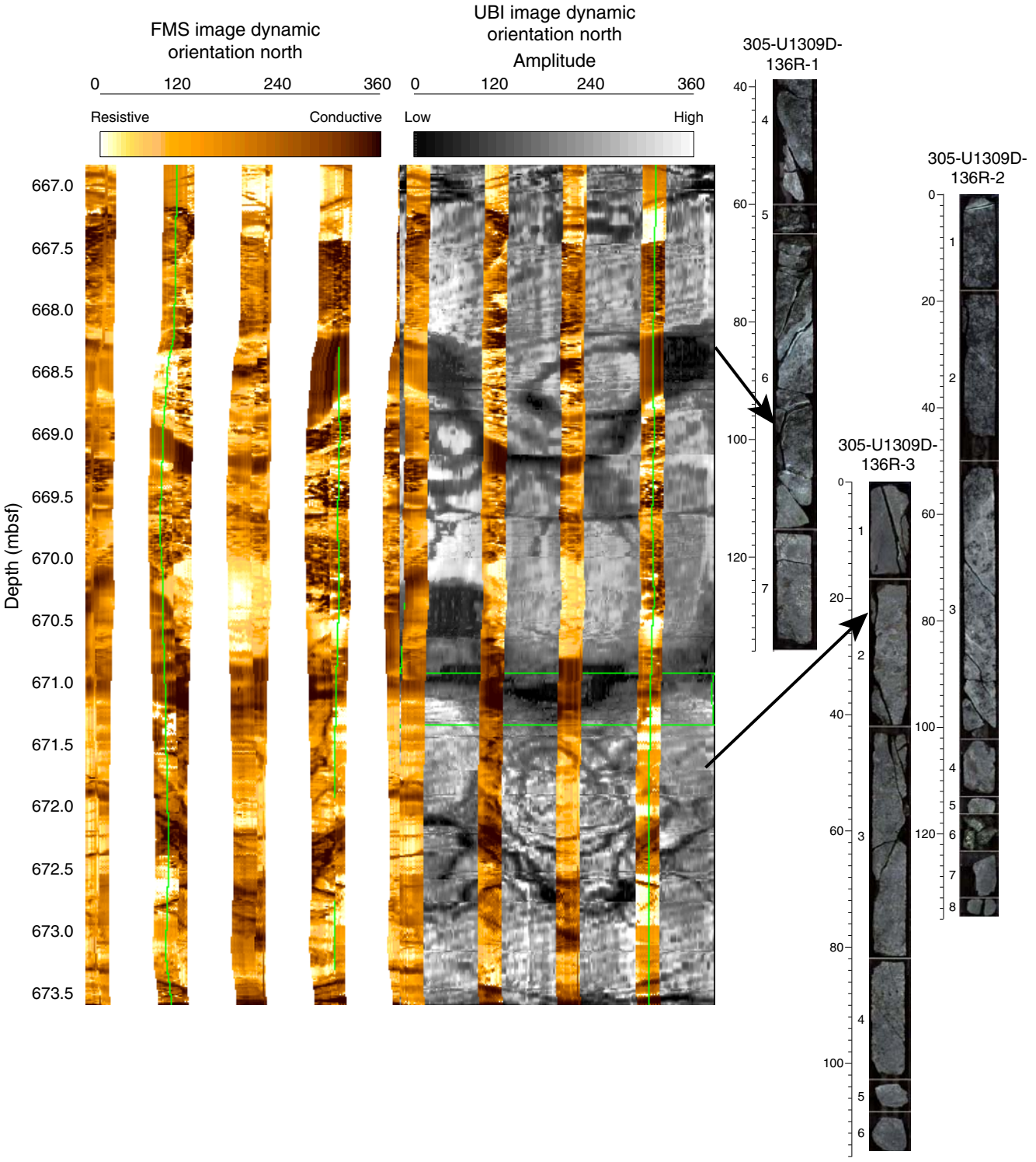

Figure F296. Comparison of logging data with vein and cataclastic intensity (600–836 mbsf) (see **"Structural geology"**).

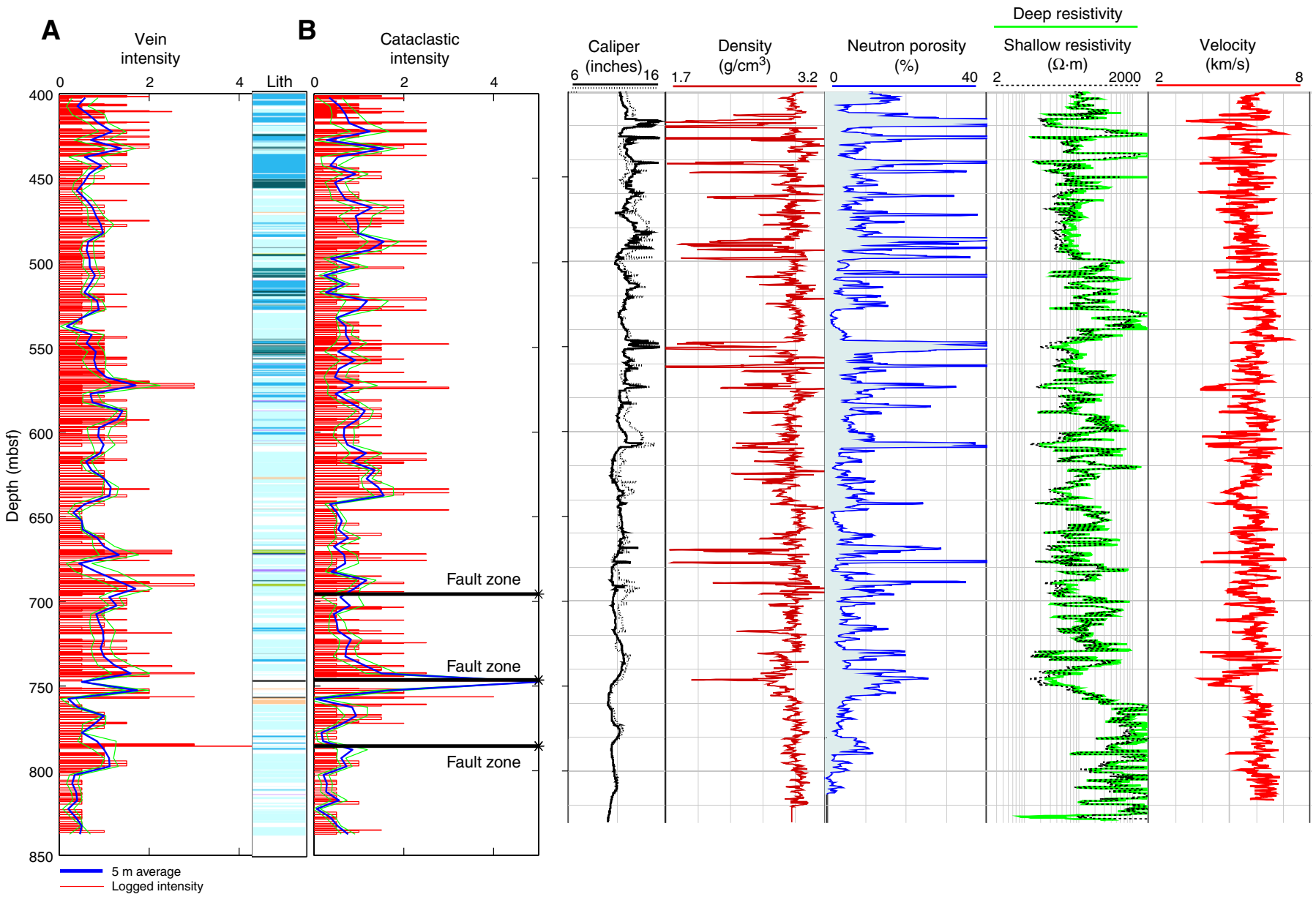

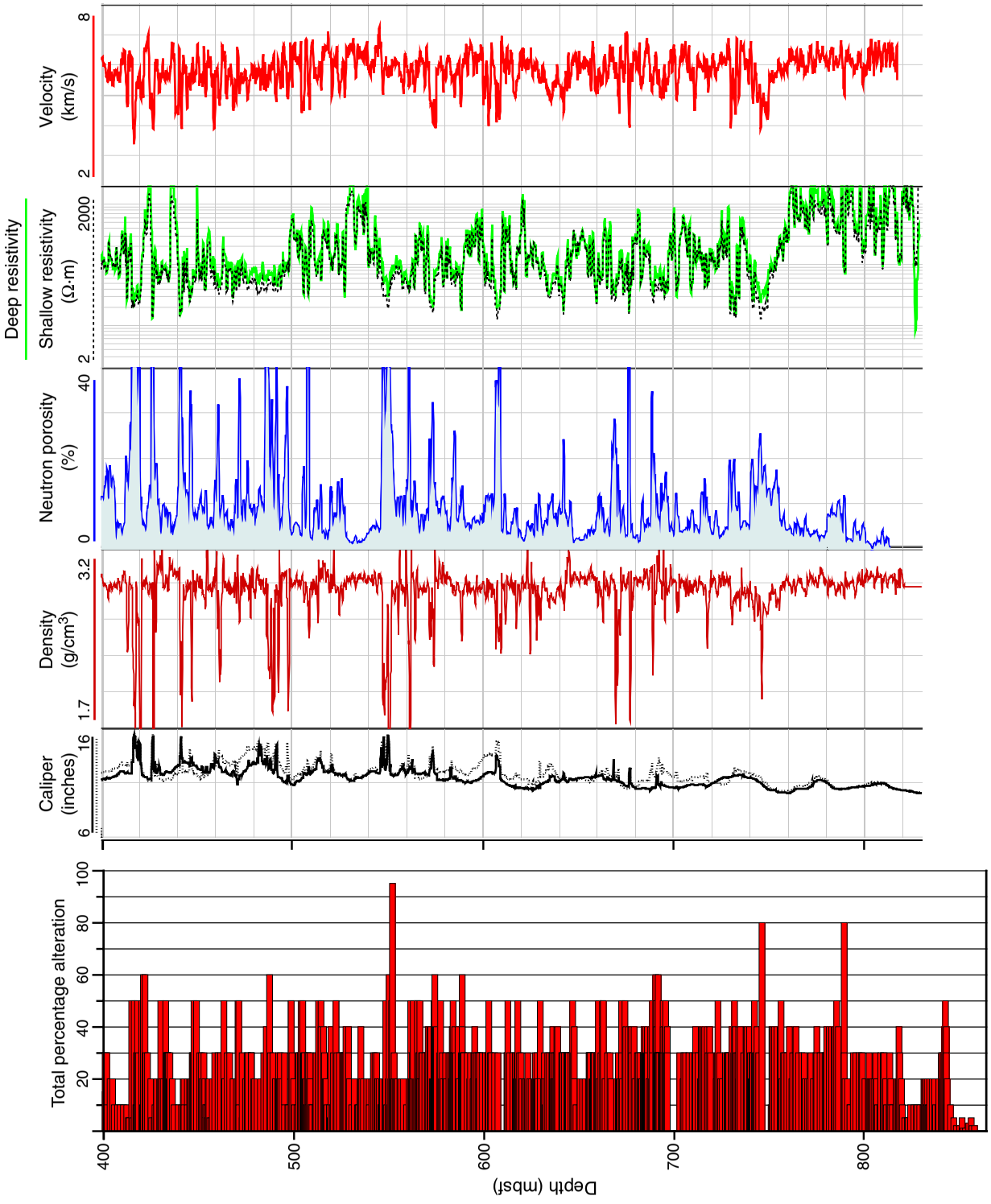

Figure F297. Comparison of logging data with alteration intensity (600–836 mbsf) (see "**Metamorphic petrology**").

Figure F298. The interval between 788.7 and 790 mbsf shows elevated neutron porosity and photoelectric factor (PEFL) and reduced resistivity and velocity values. In the Formation MicroScanner (FMS) image, it is seen as a low-resistivity layer with a dip of 25° to the northeast, which is probably related to missing rock in Core 305-U1309D-161R.

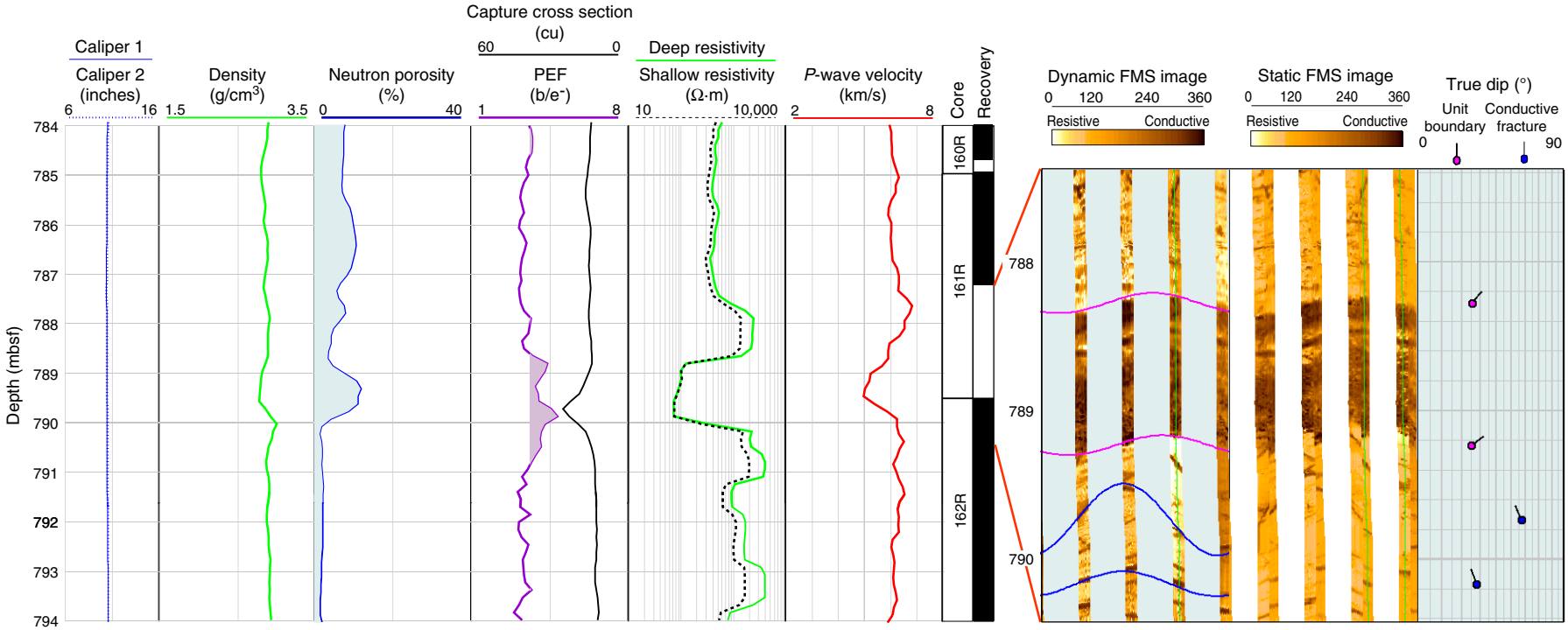

Figure F299. Detailed Formation MicroScanner (FMS) image displaying a serpentinized interval (300.2–301.9 mbsf). This serpentinized rock is surrounded by resistive gabbroic rocks. As for numerous serpentinized rocks, this interval is cut by resistive features (at 301 mbsf). This interval may correspond to the serpentinized dunite described in Section 304-U1309B-58R-1.

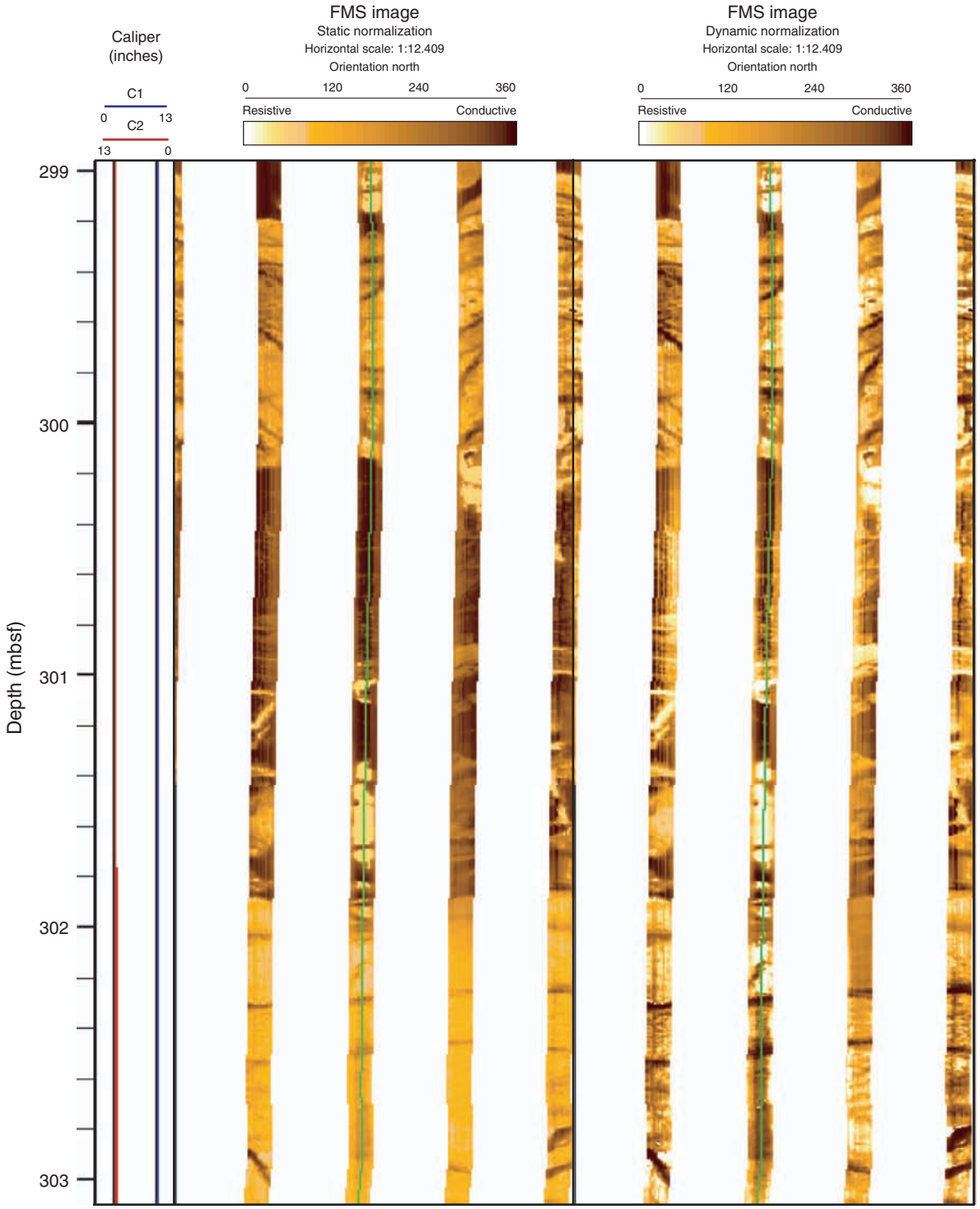

Figure F300. Selected depth interval from 720 to 780 mbsf showing the variation of log responses for a distinct fault zone. It appears the zone was not fully recovered in Core 305-U1309D-152R; logging data show the main zone at 747–750.5 mbsf (gray shading), but, based on increased total gamma ray, sigma, and neutron porosity, they also indicate that a larger depth interval (740–755 mbsf; dark gray shading) is affected by increased alteration. PEFL = photoelectric factor.

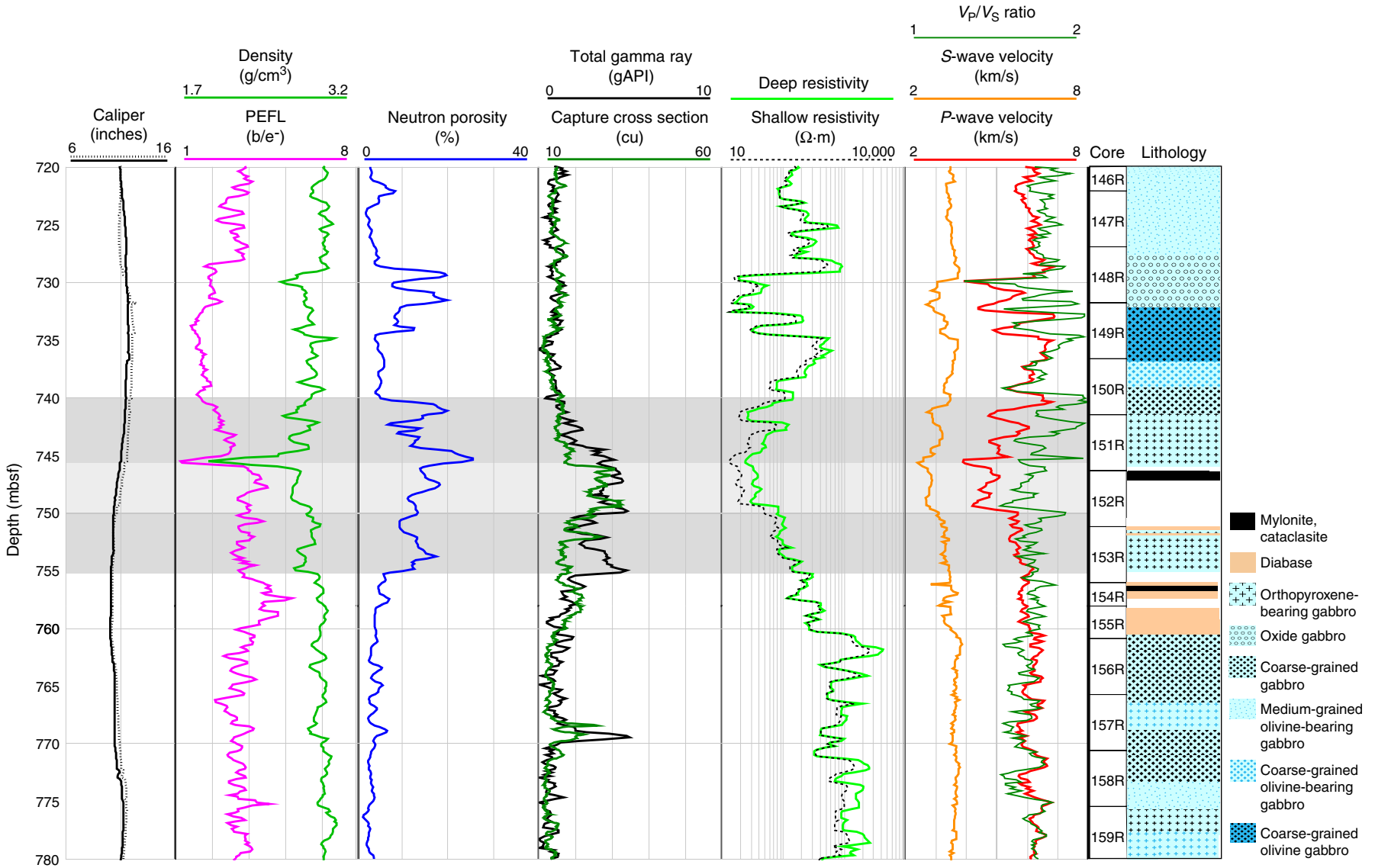

Figure F301. Comparison of vertical magnetic field component measured by the Goettingen Borehole Magnetometer (GBM) with photoelectric factor (PEFL) logging data and magnetic susceptibility measurements on cores (Hole U1309D). GBM data were averaged over 15 data points. The data reveal a correlation for high magnetic susceptibility in serpentinized cores (green) and oxide gabbros (gray) shading showing high PEFL values and high variations within the vertical magnetic flux density (z-component).

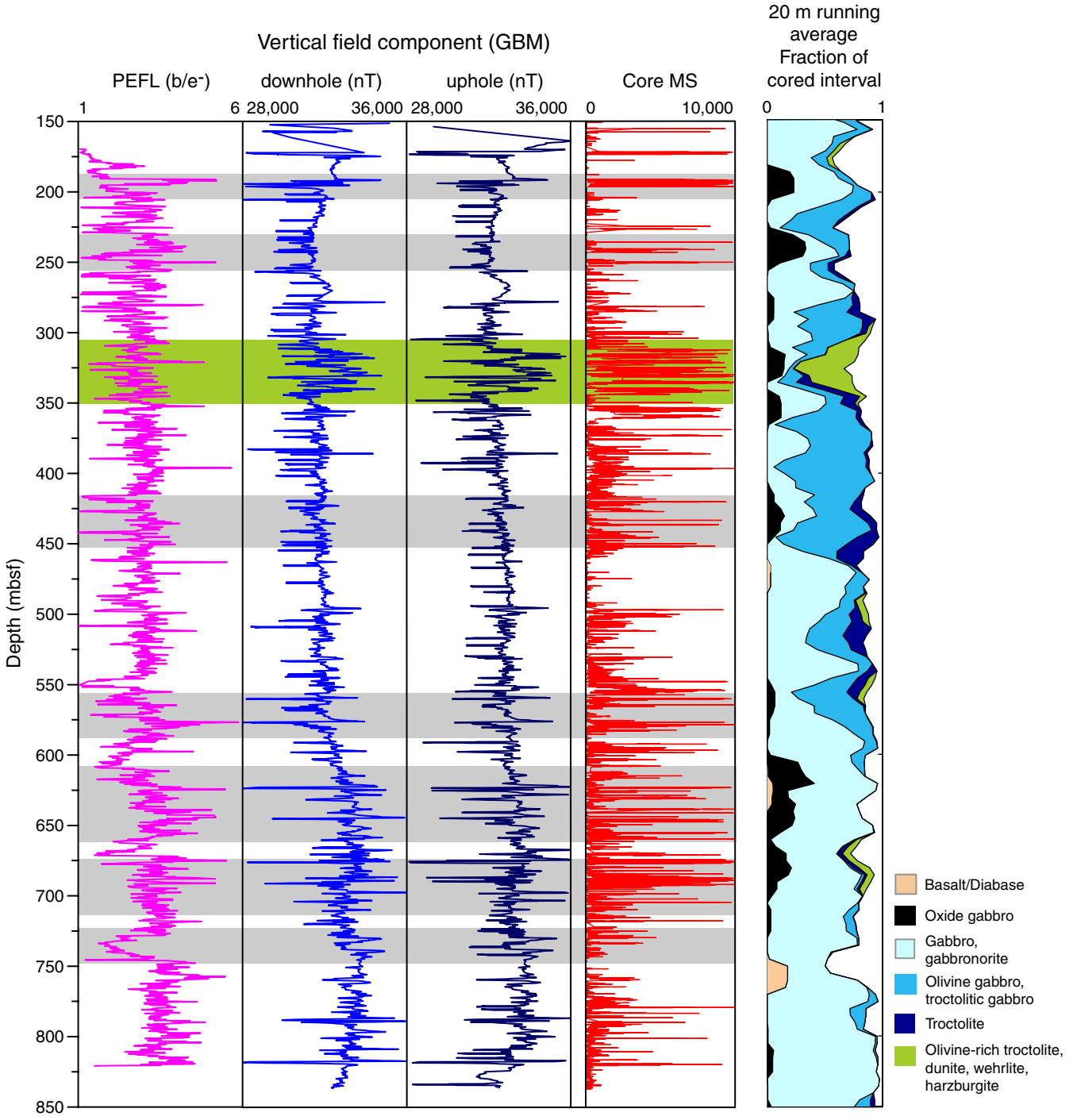

Figure F302. Composite seismic display of migrated MCS lines Meg-10 (left) and Meg-4 (right) (map view of lines is shown in Figure F2). The projection of Hole U1309D onto each line is shown. The green curve displayed represents the logging density. CDP = common depth point.

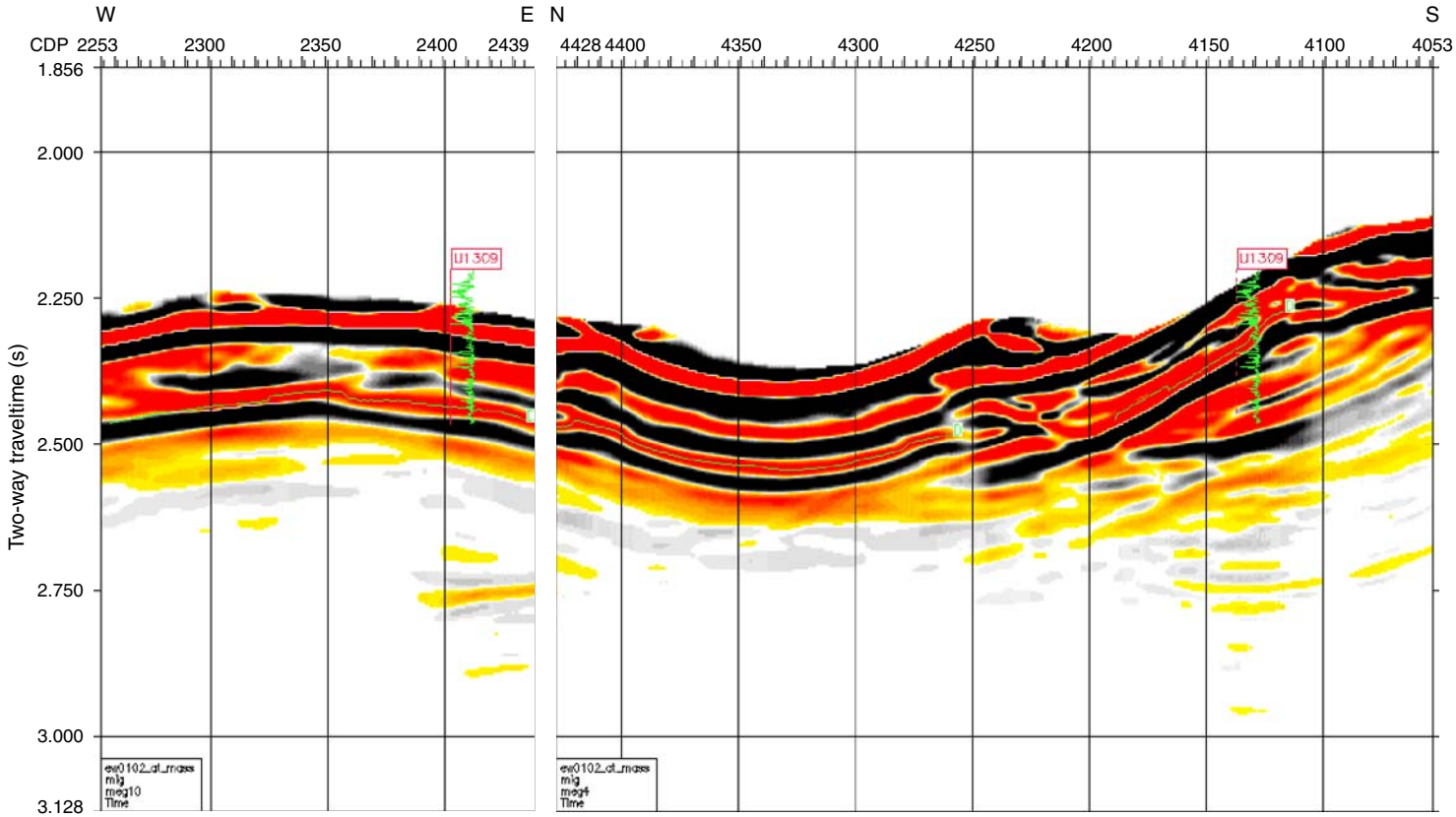

Figure F303. Comparison of two-way travel time (TWT) versus depth for three calculated data sets: check shot, integrated PWS measurements, and integrated sonic log. They agree very well and show no significant diversion. DTCO = compressional velocity, PP = PWS3 measurement on core sample.

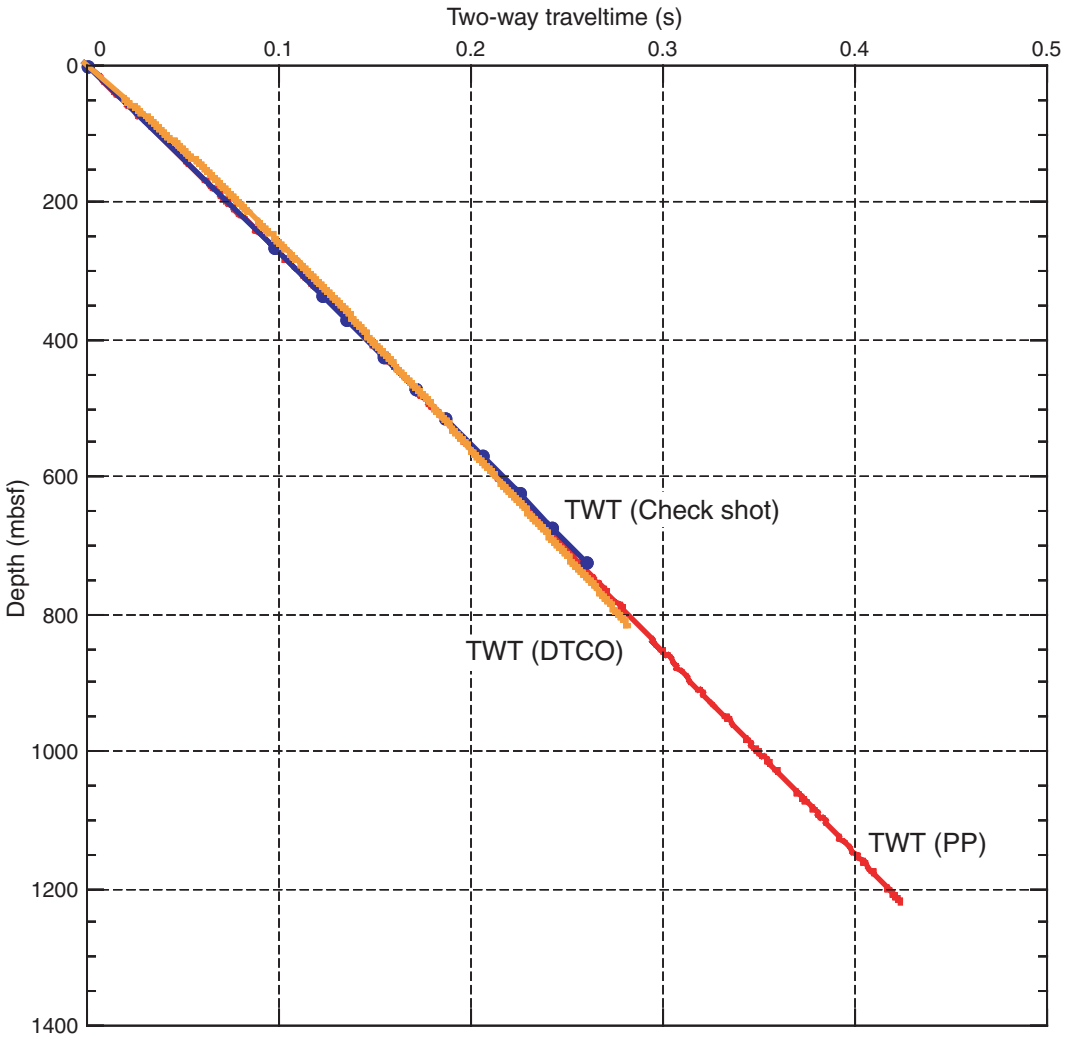

Figure F304. Map of Hole U1309D operations area developed from subsea camera survey observations. The initial survey began at 1842 h on 24 November 2004, following the expanding box pattern illustrated by the straight lines (the actual path of the camera is not plotted, but tracking the camera via sonar indicated the camera followed the ship's path). Seafloor hardware is not to scale. Cylinder in Hole U1309C represents ~25 m of casing left standing above the seafloor.

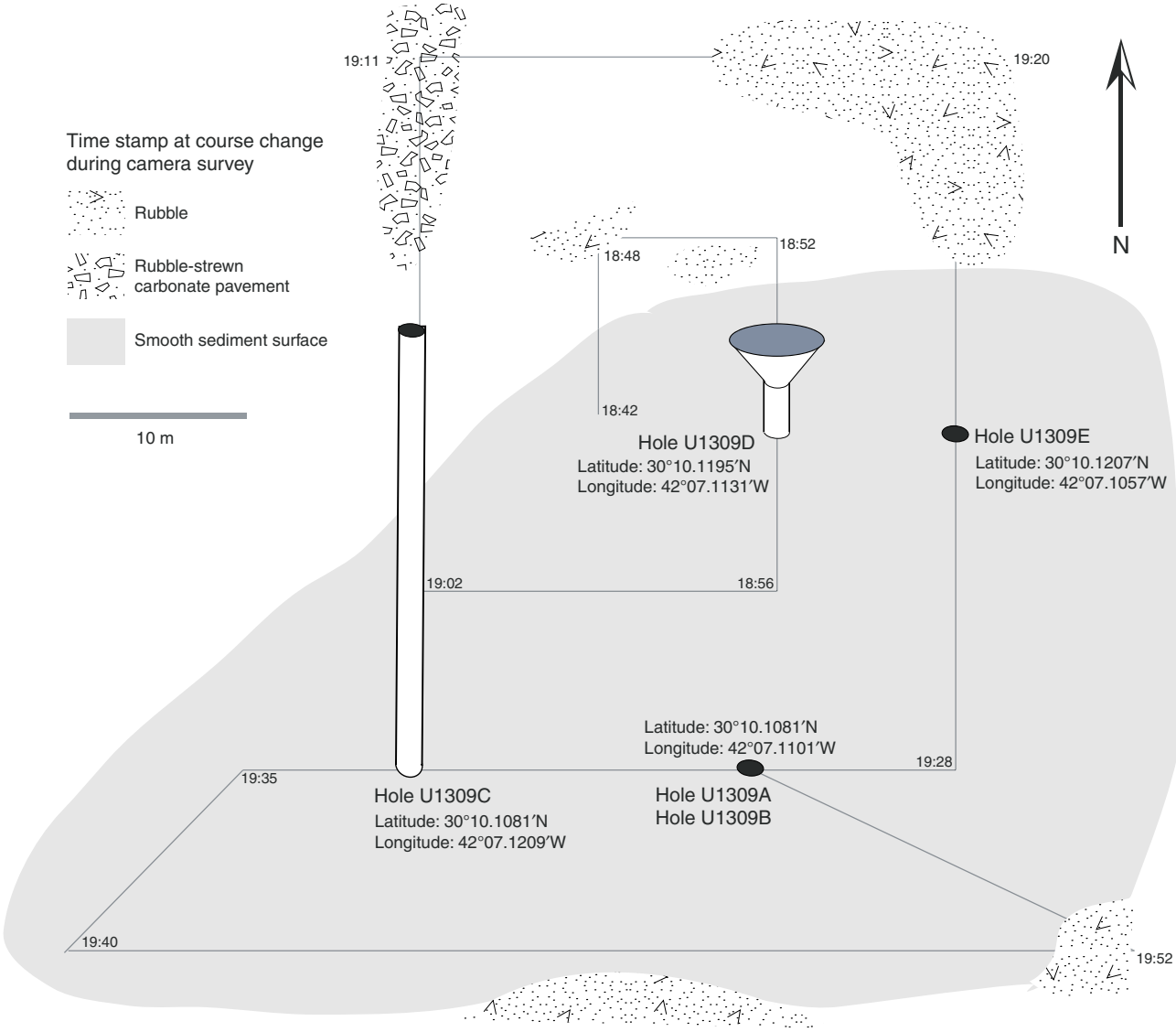

Table T1. Expedition 304 and 305 site summaries.

Hole	Latitude	Longitude	Seafloor depth (mbrf)	Cores (*N*)	Cored (m)	Recovered (m)	Recovery (%)	Drilled (m)	Total penetration (m)	Time on hole (h)	Time on hole (days)
U1309A	30°10.11′N	42°7.11′W	1653.4	1	2.0	1.9	96.0	0.0	2.0	14.75	0.6
U1309B	30°10.11′N	42°7.11′W	1653.4	20	101.8	46.7	45.9	0.0	101.8	152.83	6.4
U1309C	30°10.11′N	42°7.12′W	1646.0	0	0.0	0.0	0.0	6.0	6.0	47.83	2.0
U1309D	30°10.12′N	42°7.11′W	1656.0	294	1395.0	1043.3	74.8	20.5	1415.5	1400	59.4
U1309E	30°10.12′N	42°7.11′W	1656.0	1	3.8	5.6	147.4	0.0	3.8	3.25	0.1
U1309F	30°10.20′N	42°7.25′W	1656.0	1	4.8	6.1	126.9	0.0	4.8	14.58	0.6
U1309G	30°10.54′N	42°6.32′W	1885.0	1	3.5	0.9	76.0	0.0	3.5	16.92	0.7
U1309H	30°10.54′N	42°6.32′W	1885.0	1	4.0	0.2	4.8	0.0	4.0	4	0.15
		Site U1309 totals:		319	1514.9	1104.7	72.9	26.5	1541.4	1654.16	69.95
U1310A	30°11.49′N	42°3.93′W	2594.0	0	0.0	0.0	NA	12.0	12.0	115.42	4.8
U1310B	30°11.48′N	42°3.92′W	2594.0	2	23.0	1.3	5.7	0.0	23.0	66.67	2.8
U1311A	30°10.61′N	42°4.19′W	2552.0	2	12.0	1.7	14.3	0.0	12.0	57.33	2.4
U1311B	30°10.66′N	42°4.22′W	2516.0	0	0.0	0.0	0.0	10.6	10.6	37.42	1.6
		Site U1310 and U1311 totals:		4	35	3.0	8.6	22.6	57.6	276.8	11.5
		Expedition 304 and 305 totals:		323	1549.9	1107.7	71.5	49.1	1599	1930.96	81.45

Notes: Time on hole includes logging. NA = not available.

Table T2. Average modal compositions of gabbroic rocks determined by visual estimates from thin sections, Hole U1309B.

Rock type	*N*	Modal composition (%)		
		Plagioclase	Olivine	Clinopyroxene
Troctolite	3	61.0	38.3	0.7
Troctolitic gabbro	3	74.6	18.5	7.0
Olivine gabbro	4	62.3	21.5	16.3
Olivine-bearing gabbro	4	68.0	3.1	28.9
Gabbro	17	56.1	0.0	43.9

Notes: *N* = number of samples. This table is also available in **ASCII.**

Table T3. Lithologic proportions, Hole U1309D.

Lithology	Hole U1309D (%)	Comments
Peridotite	0.3	
Gabbroic series (total)	96.3	
Olivine-rich troctolite	5.4	
Troctolite	2.7	
Olivine gabbro	25.5	Including troctolitic gabbro
Gabbro	55.7	Including olivine-bearing gabbro, microgabbro, disseminated oxide gabbro, and gabbronorite
Gabbronorite	Included in gabbro	
Oxide gabbro	7.0	
Diabase	2.9	
Others	0.5	Including rubble and fault gouge

Notes: Proportions for Hole U1309D are from Expeditions 304 and 305. This table is also available in **ASCII.**

Table T4. Interpretation of X-ray diffraction patterns, Holes U1309B and U1309D, Expedition 304. (See table note. Continued on next two pages.)

Core, section, interval (cm)	Rock type	Preparation	Mineral phases		
			Main	Minor	Possible trace
304-U1309B-					
1R-3, 17–21	Rubble	Standard slide	Talc, serpentine (liz/ctl)	Pyrite/Chlorite	
1R-3, 114–116	Basalt	Standard slide	Plagioclase, amphiboles	Chlorite	
2R-1, 88–92	Basalt	Standard slide	Plagioclase, amphiboles		Clays
2R-2, 20–23	Basalt	Standard slide	Plagioclase, amphiboles	Chlorite	
3R-1, 60–63	Basalt	Standard slide	Plagioclase, amphiboles		
3R-1, 71–74	Basalt breccia	Standard slide	Plagioclase, amphiboles		Clays, pyroxene
5R-1, 127–129	Green vein in oxide diabase	Standard slide	Plagioclase, amphiboles		
5R-2, 55–56	Yellow patches in oxide diabase	Smear slide	Amphiboles	Saponite	Plagioclase, pyroxene
5R-2, 90–94	Oxide diabase	Standard slide	Plagioclase, amphiboles		Chlorite, pyroxene
6R-1, 97–102	Oxide diabase	Standard slide	Plagioclase, amphiboles	Chlorite	
8R-1, 37.5–38	Pale green patches in gabbro	Smear slide	Amphiboles	Chlorite	
8R-1, 115–118	Gabbro	Standard slide	Plagioclase, amphiboles	Chlorite	Magnetite
10R-1, 0–3	Gabbro	Standard slide	Plagioclase, amphiboles	Chlorite	
11R-1, 100–104	Harzburgite	Standard slide	Serpentine (liz/ctl), talc, olivine, pyroxene	Chlorite	Magnetite
11R-2, 68–70	Rubble (harzburgite)	Standard slide	Amphiboles		Magnetite
11R-2, 80–90	Harzburgite	Standard slide	Talc, serpentine (liz/ctl)	Magnetite, chlorite	Clays, olivine
12R-1, 126–13	Oxide diabase	Standard slide	Plagioclase, amphiboles		Pyroxene
13R-1, 120–125	Microdiabase	Standard slide	Plagioclase, amphiboles	Chlorite	Magnetite
14R-1, 67–70	Pale green cavity in troctolitic gabbro	Standard slide	Amphiboles		Clays (saponite?)
14R-1, 107–109	Basalt	Standard slide	Plagioclase, amphiboles	Chlorite	
15R-2, 80–84	Olivine gabbro	Standard slide	Plagioclase, chlorite	Amphiboles	
16R-3, 20–26	Olivine gabbro	Standard slide	Plagioclase, chlorite	Amphiboles	
17R-2, 5–9	Olivine gabbro	Standard slide	Plagioclase	Amphiboles, chlorite	
18R-1, 20–23	Basalt	Standard slide	Plagioclase, amphiboles		Chlorite
18R-2, 35–38	Olivine gabbro	Standard slide	Plagioclase, pyroxene	Amphiboles	Chlorite
18R-3, 110–112	Basalt	Standard slide	Plagioclase, pyroxene	Amphibole, chlorite	
19R-2, 38–40	Oxide diabase	Standard slide	Plagioclase	Pyroxene, amphiboles	Chlorite
20R-2, 72–74	Diabase	Standard slide	Plagioclase	Amphiboles	
304-U1309D-					
1R-1, 32–37	Diabase	Standard slide	Plagioclases, amphibole	Chlorite	
2R-1, 85–90	Diabase	Standard slide	Plagioclases, amphibole	Chlorite	
4R-1, 21–23	Fine-grained diabase	Standard slide	Plagioclases, amphibole		Chlorite
4R-2, 0–7	Matrix breccia in cataclastic gabbro	Smear slide	Amphibole	Clays (saponite?)	
4R-2, 112–113	Cataclastic gabbro	Standard slide	Plagioclases, amphibole		Chlorite
5R-2, 52–57	Troctolitic gabbro	Standard slide	Plagioclases, chlorite, amphibole		
5R-3, 114–118	Troctolitic gabbro	Standard slide	Plagioclases, chlorite, amphibole		
5R-4, 11–20 (1)	Green material in cavity around pink mineral in a troctolitic gabbro	Smear slide	Chlorite, amphibole, unknown mineral		
5R-4, 11–20 (2)	Pink mineral in cavity of troctolitic gabbro	Smear slide	Unknown mineral		
5R-4, 14–16	Pink mineral in cavity of troctolitic gabbro	Smear slide	Unknown mineral		
6R-1, 124–126	Olivine gabbro	Standard slide	Plagioclases, chlorite, amphibole		
6R-2, 70–73	Diabase	Standard slide	Plagioclases, amphibole	Chlorite	
6R-3, 16–21	Diabase	Standard slide	Plagioclase	Amphibole	Chlorite
7R-2, 26–33	Diabase	Standard slide	Plagioclase	Amphibole	Chlorite
7R-3, 102–105	Gabbro	Standard slide	Plagioclases, amphibole		Chlorite
8R-1, 120–127	Troctolitic gabbro	Standard slide	Saponite, amphibole		
8R-2, 56–57	Green cavity in troctolitic gabbro	Standard slide	Amphibole	Clay (saponite?)	
8R-2, 123–130	Troctolitic gabbro	Smear slide	Amphibole, chlorite	Talc(?)	Plagioclase
8R-3, 3–7	Vein in gabbro	Smear slide	Clay (saponite?)		

Table T4 (continued).

Core, section, interval (cm)	Rock type	Preparation	Mineral phases		
			Main	Minor	Possible trace
9R-1, 37–42	Fine-grained diabase	Standard slide	Plagioclase	Amphibole	
9R-1, 73–77	Olivine gabbro	Standard slide	Plagioclase	Amphibole, chlorite	
9R-2, 136–139	Brown vein in olivine gabbro	Standard slide	Plagioclases, amphibole, saponite	Calcite	
10R-1, 107–111	Harzburgite	Standard slide	Olivine, serpentine	Talc, magnetite	Amphibole
11R-2, 38–43	Olivine gabbro	Standard slide	Amphibole, chlorite	Plagioclase	
12R-1, 62–64	Olivine gabbro	Standard slide	Plagioclase	Amphibole, chlorite	
13R-1, 59–67	Gabbro	Standard slide	Plagioclase	Amphibole, chlorite	Talc
14R-1, 96–103	Troctolite	Standard slide	Plagioclase	Amphibole, chlorite	
14R-1, 107–109	Olivine gabbro	Standard slide	Plagioclase	Amphibole	Chlorite
14R-2, 128–132	Basalt	Standard slide	Plagioclase	Amphibole	Chlorite
15R-1, 140–142	Brown vein in fine-grained diabase	Standard slide	Amphibole, clay (saponite?)		
15R-2, 4–6	Brown fracture coating in diabase	Smear slide	Clay(?)		
15R-2, 72–74	Blue green vein in diabase	Standard slide	Amphibole? (cummingtonite?)		
15R-2, 125–131	Diabase	Standard slide	Plagioclase	Amphibole, chlorite	
16R-2, 62–68	Diabase	Standard slide	Plagioclases, amphibole	Chlorite	
16R-4, 90–92	Diabase	Standard slide	Plagioclases, amphibole		
16R-4, 136–140	Basalt	Standard slide	Plagioclases, amphibole		
16R-5, 18–26	Gabbro	Standard slide	Plagioclase	Amphibole, chlorite	Pyroxene
17R-1, 60–66	Olivine gabbro	Standard slide	Plagioclase	Amphibole, chlorite	
17R-3, 122–123	Blue-green vein in olivine gabbro	Smear slide	Amphibole	Chlorite, clays (saponite?)	
20R-1, 70–73	Fine-grained diabase	Standard slide	Plagioclases, amphibole	Chlorite	
22R-3, 43–49	Troctolitic gabbro	Standard slide	Plagioclase	Amphibole, chlorite	
23R-1, 79–84	Troctolitic gabbro	Standard slide	Plagioclase, chlorite	Amphibole	
23R-2, 0–4	Ultramafic cumulate	Standard slide	Serpentine, olivine, magnetite		
23R-2, 95–97	Ultramafic cumulate with troctolitic bands	Standard slide	Plagioclase, chlorite, amphibole		
25R-3, 24–31	Olivine-bearing gabbro	Standard slide	Plagioclase	Chlorite, amphibole	Talc
26R-1, 15–26	Orthopyroxene-bearing gabbro	Standard slide	Plagioclase	Chlorite, amphibole	Talc
26R-2, 127–134	Olivine-bearing gabbro	Standard slide	Plagioclase	Chlorite, amphibole	Talc
27R-1, 88–94	Olivine gabbro	Standard slide	Plagioclase	Chlorite, amphibole	Talc
28R-2, 70–74	Olivine-bearing gabbro	Standard slide	Plagioclase	Chlorite, amphibole	Talc
28R-4, 27–33	Orthopyroxene-bearing gabbro	Standard slide	Plagioclase, amphibole	Chlorite, talc	Pyroxene
30R-1, 58–65	Layered gabbro	Standard slide	Plagioclase	Chlorite, amphibole	
31R-1, 25–28	Dunite	Standard slide	Serpentine, magnetite		Talc, chlorite
31R-2, 11–17	Harzburgite	Standard slide	Serpentine, magnetite		Talc, chlorite
32R-2, 22–30	Olivine-bearing gabbro	Standard slide	Plagioclase	Chlorite, amphibole	Talc
33R-2, 55–64	Olivine-bearing gabbro	Standard slide	Plagioclase, chlorite	Amphibole, talc	Pyroxene
33R-3, 21–26	Vein in olivine-bearing gabbro	Standard slide	Plagioclase, chlorite, amphibole		
35R-1, 53–65	Oxide gabbro	Standard slide	Plagioclase, magnetite	Chlorite, amphibole	Pyroxene
36R-3, 80–82	Felsic/dioritic dike in olivine-gabbro	Standard slide	Plagioclase	Amphibole	
36R-3, 98–106	Olivine gabbro	Standard slide	Plagioclase	Chlorite, amphibole, talc	
38R-1, 45–51	Olivine-bearing gabbro	Standard slide	Plagioclase	Chlorite, amphibole, talc	
39R-2, 22–30	Olivine gabbro	Standard slide	Plagioclase, chlorite	Amphibole, talc	
41R-1, 116–124	Troctolite/Olivine gabbro	Standard slide	Plagioclase, chlorite, amphibole		
43R-2, 65–66	Vein in olivine gabbro	Smear slide	Calcite, clays (saponite?), amphibole		
44R-1, 22–29	Olivine gabbro	Standard slide	Plagioclase, chlorite, amphibole		
44R-1, 36–37	Vein in olivine gabbro	Smear slide	Amphibole, clays (saponite?)		
44R-1, 142–147	White patches in altered olivine from an olivine gabbro	Smear slide	Amphibole, talc, serpentine, tusodite?		
44R-4, 29–34	Vein in olivine-bearing gabbro	Smear slide	Amphibole, calcite	Plagioclase, clays (saponite?)	
45R-3, 18–24	Oxide gabbro	Standard slide	Plagioclase, amphibole, magnetite	Chlorite	
48R-1, 44–53	Gabbro with troctolite bands	Standard slide	Plagioclase, pyroxene	Chlorite, amphibole, talc	
48R-1, 111–119	Troctolite	Standard slide	Plagioclase	Chlorite, amphibole, talc	

Table T4 (continued).

Core, section, interval (cm)	Rock type	Preparation	Mineral phases		
			Main	Minor	Possible trace
50R-2, 54–55	Olivine gabbro	Smear slide	Amphibole, chlorite		
50R-2, 61–62	Olivine gabbro	Smear slide	Talc, amphibole, chlorite		Clays (saponite?)
51R-2, 50–53	Olivine-bearing gabbro	Standard slide	Plagioclase, chlorite, amphibole		
51R-4, 0–12	Olivine-bearing gabbro	Standard slide	Plagioclase	Amphibole, chlorite	Talc, pyroxene
52R-2, 72–75	Vein in gabbro (hydroscopic vein)	Smear slide	Calcite, clays (saponite?)		
52R-3, 15–16	Vein in gabbro (hydroscopic vein)	Smear slide	Calcite, clays (saponite?)		
53R-1, 52–59	Gabbro	Standard slide	Plagioclase	Chlorite, amphibole	
54R-3, 82–85	Olivine gabbro	Standard slide	Serpentine, magnetite	Chlorite, amphibole	
54R-3, 58–66	Olivine gabbro	Standard slide	Serpentine, magnetite	Chlorite, amphibole	
55R-2, 10–11	Vein in olivine gabbro (hydroscopic vein)	Smear slide	Calcite, clays (saponite?), celestine?		
55R-3, 81–87	Olivine-bearing gabbro	Standard slide	Plagioclase, chlorite, amphibole		Talc
56R-2, 106–114	Troctolitic gabbro	Standard slide	Plagioclase, chlorite, serpentine	Amphibole	
56R-3, 55–56	Vein in troctolitic gabbro	Smear slide	Calcite, clays (saponite?)	Serpentine	
56R-3, 93–100	Troctolitic gabbro	Standard slide	Serpentine, pyroxene, magnetite	Chlorite	
57R-2, 133–143	Olivine-bearing gabbro	Standard slide	Plagioclase, chlorite, talc	Amphibole	
59R-3, 99–109	Olivine-bearing gabbro	Standard slide	Plagioclase	Amphibole, chlorite	Talc
60R-2, 40–47	Dunite cumulate	Standard slide	Serpentine, magnetite, olivine		
60R-3, 56–64	Olivine gabbro cumulate	Standard slide	Serpentine, magnetite, olivine	Titanite	
64R-2, 82–87	Dunite cumulate	Standard slide	Serpentine, magnetite	Chlorite	
66R-3, 33–36	Troctolite	Standard slide	Serpentine, magnetite		
68R-3, 47–60	Olivine-bearing gabbro	Standard slide	Plagioclase	Amphibole, chlorite, talc	
69R-1, 66–72	Oxide gabbro	Standard slide	Plagioclase, magnetite	Amphibole, chlorite	
70R-2, 43–53	Serpentinized leucocratic troctolitic gabbro	Standard slide	Plagioclase, amphibole, magnetite		
72R-1, 72–81	Layered leucocratic olivine gabbro	Standard slide	Plagioclase, chlorite, amphibole		
73R-2, 75–85	Olivine gabbro	Standard slide	Plagioclase, chlorite, amphibole		
74R-1, 105–113	Gabbro	Standard slide	Plagioclase, chlorite, amphibole	Talc(?)	
76R-1, 93–102	Leucocratic olivine gabbro	Standard slide	Plagioclases, chlorite, amphibole		
77R-4, 41–48	Leucocratic olivine gabbro	Standard slide	Serpentine, plagioclase, magnetite	Chlorite	

Note: liz = lizardite, ctl = chrysotile.

Table T5. XRD data from veins, Hole U1309D, Expedition 305. (See table note. Continued on next two pages.)

Core, section, interval (cm)	Hand sample description/ scientist comments	Mineral phases		
		Main	Minor	Possible trace
305-U1309D-				
80R-1, 53–54	Soft, white vein	Chlorite, serpentine, clay		
80R-1, 89–90	Talc-carbonate	Chlorite, serpentine, clay		
80R-2, 6–7	Soft, white vein	Calcite	Amphibole	
80R-2, 50–51	Soft, white vein	Calcite, clay		
80R-2, 122–123	Vein	Chlorite, amphibole		
81R-1, 43–44	Talc-carbonate vein	Calcite, clay		
84R-1, 63–64	Vein	Quartz, calcite		Pyrite?, albite
84R-2, 16–18	Vein	Albite, tremolite		Augite
86R-1, 52–53	Vein	Albite, tremolite	Clinopyroxene	Pyrite?, ilmenite?
86R-2, 33–35	Vein	Albite, tremolite		
86R-3, 46–47	Vein	Plagioclase, clinopyroxene	Tremolite	
88R-5, 5–6	Messy talc vein	Chlorite, amphibole, talc, clay		
89R-1, 57–58	Messy talc vein	Calcite, amphibole, chlorite, clay		Talc
89R-2, 59–60	Sulfide-chlorite vein	Amphibole, augite	Plagioclase, clay	
90R-2, 55–56	Altered clinopyroxene	Amphibole, clinopyroxene, chlorite	Talc	
90R-4, 31–32	Calcite vein	Calcite		Clay
91R-1, 121–122	Albitized zone	Albite	Amphibole, chlorite	
93R-2, 72–73	Messy talc vein	Calcite, chlorite	Talc, amphibole	Albite, clay
93R-2, 123–124	Slip-fiber vein	Calcite, chlorite, amphibole		
94R-1, 52–53		Chlorite, amphibole, albite		
95R-1, 119–120	Slip-fiber	Tremolite, clay		
96R-1, 52–53	Magmatic vein	Tremolite, plagioclase (albite?)		
96R-1, 119–120	Slip-fiber	Tremolite, clay		
97R-1, 38–39	White vein	Quartz, calcite	Tremolite, chlorite	
100R-5, 37–38		Calcite, chlorite	Serpentine	
103R-2, 68–69	Talc vein	Chlorite, tremolite, clinopyroxene		Pyrite?
104R-2, 145–146	Talc	Bad pattern		
107R-2, 96–97	Magmatic vein	Albite	Chlorite	
109R-4, 6–7	Talc vein	Calcite, clay		
110R-3, 80–82	Slip-fiber vein	Calcite		Serpentine
111R-1, 90–92	Talc alteration zone	Talc, clay		
111R-2, 96–97	Vein in talc alteration zone	Chlorite, amphibole		
116R-1, 26–28	Altered leucogabbro	Plagioclase, amphibole, chlorite, clinopyroxene		
116R-4, 41–43	Slip-fiber vein	Tremolite, calcite	Chlorite	
117R-4, 24–28	ICP-AES?	Plagioclase, clinopyroxene	Amphibole, chlorite	
117R-4, 79–81	Slip fiber vein	Chlorite, tremolite, clay	Talc	
118R-3, 39–40	Slip fiber	Chlorite, tremolite, clay		
119R-1, 66–67	Dark green vein	Amphibole, plagioclase, clinopyroxene, clay		
119R-2, 40–41	Dark green vein	Amphibole, clay		
120R-2, 103–104	Carbonate-sulfide vein	Calcite, quartz, clay	Pyrite	
120R-3, 36–37		Calcite, quartz, pyrite		Plagioclase
124R-1, 83–84	Dark green vein	Chlorite, tremolite, clay	Calcite, plagioclase, clinopyroxene	
125R-1, 105–106	Dark green vein	Chlorite, amphibole, plagioclase, calcite, clinopyroxene, clay		
125R-3, 124–125	Calcite-chlorite vein	Calcite, quartz, pyrite, albite, clay		
130R-1, 125–126	Altered rock	Tremolite, plagioclase, clinopyroxene, clay		
130R-3, 40–41		Calcite	Chlorite	
134R-2, 122–123	Messy talc vein with calcite	Calcite	Talc, chlorite, pyrite	
136R-1, 73–74	Slip fiber	Calcite, talc, chlorite		
136R-2, 26–27	Quartz?	Serpentine		

Table T5 (continued).

Core, section, interval (cm)	Hand sample description/ scientist comments	Mineral phases		
		Main	Minor	Possible trace
139R-1, 113–116	Sulfide vein	Calcite, chlorite, pyrite	Amphibole, plagioclase	
139R-2, 125–127	Soft talc vein	Calcite, chlorite		
140R-2, 5–7	Altered magmatic dike in talc zone	Plagioclase, chlorite, amphibole, talc		
140R-2, 55–56	Altered diabase	Amphibole, cummingtonite	Chlorite	Illite
140R-2, 89–90	Frankenstein vein	Calcite		Clay
140R-3, 10–12	Soft talc vein	Bad pattern		
140R-4, 78–80	Soft talc vein	Serpentine, calcite, clay		
140R-4, 115–116	Altered igneous rock	Chlorite, amphibole	Plagioclase, clinopyroxene	
141R-2, 80–81	Metaigneous?	Clinopyroxene, amphibole, plagioclase		
145R-2, 110–111	Green vein	Tremolite		Clay
147R-1, 124–125	Green calcite vein	Calcite, amphibole		
149R-2	Funny green slip-fiber vein	Talc, tremolite, chlorite	Clay	
151R-1, 32–34	White, fibrous	Amphibole, chlorite, calcite, talc		
150R-3, 22–25	Big fluffy white vein	Anhydrite	Calcite	
157R-1, 112–114	Whitish vein	Amphibole		Clinopyroxene
164R-2, 16–17	Soapy vein with calcite	Serpentine, clay		
165R-2, 143–145	Talc-carbonate	Analcime, thomsonite/natrolite	Clay	
165R-3, 8–9	Soapy vein with calcite	Analcime, serpentine	Clinopyroxene	
168R-1, 59–60	Slip-fiber?	Albite, clay	Talc, amphibole	
171R-2, 94–95	Gouge with tremolite	Amphibole, clay	Plagioclase, clinopyroxene	
174R-2, 70–72	Waxy, dark green	Amphibole, talc, clay	Clinopyroxene, orthopyroxene, plagioclase	
177R-3, 46–48	Talc vein	Thomsonite, analcime, chrysotile	Plagioclase, clinopyroxene	
178R-1, 95–97	Zeolite	Plagioclase, amphibole, clinopyroxene		Natrolite
179R-4, 130–133	Chlorite?	Amphibole, plagioclase, clinopyroxene		
184R-1, 68–70	Slip fiber	Tremolite		
185R-1, 135–137	Greenish, earthy (gouge?)	Amphibole, clay, plagioclase, clinopyroxene		
186R-3, 61–64	White vein	Calcite, chlorite, amphibole, albite		
192R-1, 9–10	Talcose vein	Clay, chlorite, natrolite, analcime	Plagioclase, clinopyroxene	
202R-2, 12–13	Talc?-calcite vein	Clay, calcite,	Albite, thomsonite	
204R-3, 92–93	Talc? vein	Clay, talc, calcite, chlorite, amphibole, quartz	Plagioclase, clinopyroxene	
205R-4, 95–100	ICP-AES?	Amphibole	Plagioclase, clinopyroxene	
207R-5, 24–27	Talc vein	Clay, serpentine, clinopyroxene		Talc
207R-6, 11–14	Talc, very dark	Clay, serpentine, magnetite		
208R-2, 17–23	Talc, white stuff	Clay, thomsonite, analcime		
209R-1, 24–28	Strange calcite	Prehnite		
209R-2, 132–135	Talc-carbonate	Clay, serpentine, amphibole	Plagioclase, clinopyroxene	
213R-4, 42–47	Talc-carbonate	Clay, thomsonite, prehnite	Plagioclase, clinopyroxene, talc	
216R-2, 47–51	Talc-carbonate	Clay, thomsonite, prehnite	Plagioclase, clinopyroxene, ilmenite	
226R-1, 29–30	Zeolite	Clay, thomsonite, prehnite, talc		
226R-2, 38–39	Talc-carbonate	Clay, thomsonite	Plagioclase, clinopyroxene	
228R-1, 113–114	Pale green talc vein	Clay, calcite, serpentine		
228R-4, 51–51	Green talc vein	Clay, calcite	Clinopyroxene	
229R-1, 82–83	Talc-carbonate	Calcite, prehnite, chlorite		Zeolite, clay
229R-2, 62–63	Talc-carbonate	Calcite, clay		
230R-3, 86–87	Carbonate-zeolite	Clay, calcite, thomsonite		
231R-2, 55–56	Epidote-bearing	Chlorite, calcite, analcime, epidote		Clay, thomsonite
234R-2, 3–8	Tremolite near rodingite	Tremolite, calcite		
240R-1, 51–54	Soft vein	Clay, thomsonite, serpentine	Prehnite	Gibbsite
240R-1, 100–101	Soft green gel, heated to 200°C	Saponite	Calcite	
261R-2, 67–70	Green, slip-fiber vein	Tremolite, thomsonite, chlorite		Hydrogarnet
276R-2, 45–50	Calcite vein	Calcite, clay		

Table T5 (continued).

Core, section, interval (cm)	Hand sample description/ scientist comments	Mineral phases		Possible trace
		Main	Minor	
285R-1, 60–62	Soft, dark green vein	Chlorite, thomsonite, clay		
286R-1	Soft, dark green vein	Clay, chlorite		
289R-1, 73–76	Green vein	Actinolite, serpentine, thomsonite, prehnite, clay	Clinopyroxene	
290R-3, 52–55	Light green vein	Serpentine, albite, actinolite, thomsonite	Clay, clinopyroxene	
291R-2, 103–105	Soft, light green vein	Clay?		Weak pattern
291R-3, 100–102	Green and white vein	Thomsonite, saponite		
293R-1, 44–47	Green and white vein	Kutnahorite, clay		
293R-1, 79–81	Dark green vein	Chlorite, analcime, thomsonite, amphibole, prehnite	Clinopyroxene	

Note: ICP-AES = inductively coupled plasma–atomic emission spectroscopy.

Table T6. XRD data from whole-rock ICP-AES samples. (Continued on next two pages.)

Core, section, interval (cm)	Mineral phases		
	Main	Minor	Possible trace
305-U1309D-			
80R-2, 19–28	Plagioclase, chlorite, clinopyroxene, olivine, amphibole		
80R-2, 104–114	Plagioclase, clinopyroxene, chlorite, amphibole	Olivine	
81R-3, 33–43	Plagioclase, clinopyroxene	Chlorite, talc, amphibole	
82R-2, 101–110	Plagioclase, clinopyroxene, serpentine	Olivine	
83R-1, 98–108	Plagioclase, clinopyroxene, amphibole, talc, chlorite	Olivine	
83R-2, 32–42	Plagioclase, clinopyroxene, amphibole, olivine, serpentine	Chlorite, talc	
84R-3, 54–64	Plagioclase, clinopyroxene, amphibole, chlorite, talc		
85R-2, 116–125	Plagioclase, clinopyroxene, amphibole, serpentine, chlorite, talc	Olivine	
86R-3, 102–110	Plagioclase, clinopyroxene, amphibole, chlorite, talc	Olivine	Serpentine
87R-2, 80–93	Plagioclase, clinopyroxene, amphibole	Ilmenite	Cummingtonite?
87R-2, 80–93	Tremolite, plagioclase, clinopyroxene, ilmenite		
88R-4, 30–39	Plagioclase, clinopyroxene, olivine	Chlorite, amphibole, serpentine	
89R-2, 122–129	Chlorite, tremolite, plagioclase		Clinopyroxene
91R-2, 56–65	Chlorite, tremolite, plagioclase		
91R-2, 81–90	Plagioclase	Tremolite, chlorite	Clinopyroxene?, olivine?, magnetite?
92R-1, 104–116	Chlorite, talc, tremolite, plagioclase, clinopyroxene		
93R-1, 11–16	Plagioclase, clinopyroxene	Tremolite, clay	Pyrite
94R-1, 66–76	Chlorite, tremolite, plagioclase, clinopyroxene		
94R-3, 22–26	Chlorite, tremolite, plagioclase, clinopyroxene		
95R-3, 40–50	Chlorite, talc, tremolite, plagioclase		Clinopyroxene
98R-3, 20–43	Chlorite, tremolite, plagioclase	Talc, clinopyroxene	Pyrite
98R-3, 26–43	Chlorite, tremolite, quartz, plagioclase		
100R-1, 50–55	Serpentine, plagioclase, olivine, clinopyroxene		
103R-1, 15–23	Plagioclase, chlorite, tremolite, talc	Clinopyroxene	
104R-2, 37–47	Chlorite, talc, tremolite, plagioclase, clinopyroxene		Olivine
105R-3, 23–32	Chlorite, tremolite, plagioclase	Talc, augite	
107R-2, 35–44	Chlorite, talc, tremolite, plagioclase	Clinopyroxene	
109R-2, 77–95	Chlorite, talc, tremolite, plagioclase, clinopyroxene		
111R-2, 14–6	Chlorite, serpentine, olivine, plagioclase, clinopyroxene, tremolite		
111R-3, 131–138	Olivine, serpentine, plagioclase, clinopyroxene, brucite		
113R-2, 22–7	Chlorite, tremolite, plagioclase, clinopyroxene, ilmenite		
113R-2, 145–149	Chlorite, talc, tremolite, plagioclase, clinopyroxene		
114R-3, 29–37	Chlorite, talc, tremolite, plagioclase, clinopyroxene		
116R-2, 26–28	Plagioclase, amphibole, chlorite, clinopyroxene		
116R-3, 67–77	Plagioclase, amphibole, clinopyroxene		
117R-1, 41–51	Plagioclase, olivine, clinopyroxene	Amphibole, serpentine	
120R-2, 35–45	Plagioclase, chlorite, amphibole, clinopyroxene	Talc	
121R-2, 26–35	Chlorite, talc, amphibole, plagioclase, clinopyroxene		
124R-4, 49–59	Plagioclase, amphibole	Chlorite, talc, clinopyroxene	
126R-1, 94–104	Plagioclase, amphibole, clinopyroxene	Chlorite	
127R-2, 80–92	Plagioclase, amphibole, clinopyroxene		
128R-3, 38–48	Plagioclase, amphibole, clinopyroxene, epidote		
130R-1, 35–43	Plagioclase, clinopyroxene, amphibole, ilmenite, chlorite		Prehnite?
132R-1, 36–45	Plagioclase, clinopyroxene	Chlorite, talc, amphibole	
133R-2, 45–50	Plagioclase, clinopyroxene	Chlorite, talc, amphibole	
134R-2, 21–26	Plagioclase, clinopyroxene	Chlorite, talc, amphibole	
135R-2, 53–63	Plagioclase, clinopyroxene	Chlorite, talc, amphibole	Olivine
136R-2, 4–14	Serpentine, olivine, plagioclase, clinopyroxene	Chlorite, talc, amphibole	
138R-3, 69–79	Plagioclase, clinopyroxene, amphibole, orthopyroxene, chlorite, talc		
139R-3, 126–133	Serpentine, plagioclase, olivine		
140R-2, 11–19	Talc, amphibole, serpentine, chlorite	Plagioclase, calcite, clinopyroxene	
140R-3, 93–103	Plagioclase, amphibole	Chlorite, clinopyroxene	Prehnite
142R-2, 68–78	Plagioclase, clinopyroxene, amphibole, chlorite		
144R-2, 41–49	Plagioclase, clinopyroxene, amphibole, chlorite, talc		
145R-1, 64–74	Plagioclase, clinopyroxene, amphibole	Talc, chlorite	
145R-3, 28–36	Plagioclase, clinopyroxene, amphibole, chlorite, talc		Serpentine
147R-2, 24–30	Plagioclase, clinopyroxene, amphibole	Talc, chlorite	
148R-2, 34–44	Plagioclase, clinopyroxene, amphibole	Talc, chlorite	
149R-2, 10–20	Plagioclase, clinopyroxene, chlorite	Amphibole, talc	
150R-1, 72–82	Plagioclase, clinopyroxene	Amphibole, chlorite, talc,	
151R-2, 22–30	Plagioclase, clinopyroxene, amphibole	Talc, chlorite	
155R-2, 23–26	Plagioclase, clinopyroxene, amphibole, chlorite, ilmenite		
157R-2, 81–90	Plagioclase, clinopyroxene, amphibole, chlorite, talc		
158R-1, 11–18	Analcime, plagioclase, clinopyroxene	Epidote, thomsonite	
158R-3, 42–57	Plagioclase, clinopyroxene, amphibole, chlorite, talc		
159R-1, 110–117	Plagioclase, clinopyroxene	Chlorite, amphibole	
160R-2, 122–132	Plagioclase, clinopyroxene, amphibole, chlorite, talc		

Table T6 (continued).

Core, section, interval (cm)	Mineral phases		
	Main	Minor	Possible trace
161R-2, 51–60	Plagioclase, clinopyroxene, amphibole, chlorite, talc		
162R-3, 71–86	Plagioclase, clinopyroxene, amphibole, chlorite, talc		
164R-3, 115–123	Plagioclase, clinopyroxene	Amphibole	
165R-3, 18–28	Plagioclase, clinopyroxene, amphibole	Orthopyroxene	
166R-3, 45–55	Plagioclase, clinopyroxene	Olivine+D24	
167R-2, 99–109	Plagioclase, clinopyroxene	Amphibole, orthopyroxene	
169R-1, 50–60	Plagioclase, clinopyroxene, amphibole, talc		Orthopyroxene
170R-3, 20–30	Plagioclase, clinopyroxene, amphibole, talc		Orthopyroxene
171R-4, 18–30	Plagioclase, chlorite, amphibole, talc		
172R-3, 41–51	Plagioclase, clinopyroxene, amphibole, chlorite, talc		
174R-1, 52–60	Plagioclase, clinopyroxene	Amphibole, talc, orthopyroxene	
174R-4, 42–51	Plagioclase, olivine, clinopyroxene, amphibole		Serpentine
176R-1, 38–48	Plagioclase, clinopyroxene, orthopyroxene	Amphibole, talc	
177R-3, 127–137	Plagioclase, clinopyroxene, amphibole	Talc	
178R-3, 11–19	Plagioclase, clinopyroxene, amphibole, talc		Orthopyroxene
179R-4, 85–91	Plagioclase, olivine, clinopyroxene, amphibole		
180R-4, 84–94	Plagioclase, clinopyroxene, orthopyroxene, amphibole	Talc, chlorite	
181R-1, 56–62	Plagioclase, clinopyroxene, amphibole	Chlorite	
182R-1, 43–52	Plagioclase, clinopyroxene, amphibole, chlorite, ilmenite		
183R-1, 101–110	Plagioclase, clinopyroxene, orthopyroxene, amphibole, talc		
184R-1, 60–71	Plagioclase, amphibole, clinopyroxene, olivine		Orthopyroxene, serpentine
186R-1, 89–97	Plagioclase, clinopyroxene, amphibole, talc		Orthopyroxene
187R-1, 84–94	Plagioclase, clinopyroxene, amphibole, chlorite	Talc	
188R-2, 30–37	Plagioclase, clinopyroxene, olivine		
189R-3, 67–76	Plagioclase, clinopyroxene, olivine, serpentine		
191R-2, 65–83	Bad pattern		
191R-3, 55–66	Plagioclase, clinopyroxene, amphibole		
193R-1, 29–38	Plagioclase, clinopyroxene		Amphibole
194R-2, 50–60	Plagioclase, clinopyroxene		
195R-3, 44–54	Plagioclase, clinopyroxene	Amphibole	
196R-3, 55–62	Plagioclase, clinopyroxene	Amphibole	
198R-1, 62–72	Plagioclase, clinopyroxene	Amphibole, talc, chlorite	
199R-3, 55–68	Plagioclase, clinopyroxene	Amphibole	Orthopyroxene
200R-2, 40–50	Plagioclase, clinopyroxene	Amphibole	
202R-1, 44–56	Plagioclase, clinopyroxene	Amphibole, talc, chlorite	
203R-1, 83–92	Plagioclase, clinopyroxene		Olivine
204R-4, 15–26	Plagioclase, orthopyroxene	Clinopyroxene, amphibole, talc	
205R-2, 91–101	Plagioclase, clinopyroxene	Amphibole, talc, chlorite	
206R-1, 0–3	Plagioclase, clinopyroxene	Amphibole, talc, chlorite, ilmenite	
209R-2, 85–90	Plagioclase, clinopyroxene, olivine		Orthopyroxene
211R-1, 71–80	Plagioclase, clinopyroxene		
212R-4, 72–78	Plagioclase, clinopyroxene, olivine		
214R-3, 45–55	Plagioclase, clinopyroxene	Olivine	Orthopyroxene
215R-4, 37–45	Plagioclase, clinopyroxene, olivine		
218R-4, 55–63	Plagioclase, clinopyroxene, olivine		
220R-1, 70–80	Plagioclase, clinopyroxene, olivine		
221R-3, 91–99	Plagioclase, olivine		
225R-1, 76–85	Plagioclase, clinopyroxene, olivine		
226R-3, 45–55	Plagioclase, clinopyroxene	Amphibole, talc, serpentine	
227R-3, 73–78	Plagioclase, olivine, chromite, serpentine		
230R-1, 53–60	Plagioclase, clinopyroxene	Amphibole, talc	
232R-3, 110–117	Plagioclase, olivine, serpentine		Prehnite
234R-2, 63–68	Plagioclase, olivine, serpentine		
236R-2, 137–147	Plagioclase, clinopyroxene, olivine	Chlorite	
240R-2, 84–91	Olivine, serpentine, clinopyroxene	Plagioclase, amphibole	Hydrogarnet
242R-2, 83–91	Olivine, serpentine, clinopyroxene, amphibole	Plagioclase	Pyrrhotite
244R-1, 16–26	Plagioclase, clinopyroxene	Orthopyroxene, amphibole, talc	
246R-1, 60–69	Plagioclase, clinopyroxene, amphibole, ilmenite		
248R-2, 5–11	Olivine	Plagioclase, serpentine	
250R-3, 28–36	Plagioclase, clinopyroxene, olivine	Serpentine	
252R-1, 88–96	Plagioclase, clinopyroxene		Ilmenite
254R-1, 36–45	Plagioclase, clinopyroxene, amphibole, ilmenite		
255R-1, 28–35	Plagioclase, olivine, serpentine, clinopyroxene		
256R-2, 88–94	Plagioclase, serpentine, olivine		
258R-1, 34–39	Plagioclase, clinopyroxene, amphibole		Orthopyroxene
262R-3, 104–112	Plagioclase, clinopyroxene, olivine		
264R-1, 52–60	Plagioclase, clinopyroxene, amphibole		
267R-2, 111–120	Plagioclase, clinopyroxene	Olivine	

Table T6 (continued).

Core, section, interval (cm)	Mineral phases		
	Main	Minor	Possible trace
268R-2, 68–77	Plagioclase, olivine, serpentine, clinopyroxene		
270R-1, 96–105	Plagioclase, clinopyroxene	Chlorite, amphibole, talc	
271R-3, 44–52	Plagioclase, clinopyroxene, amphibole	Chlorite	
274R-3, 65–75	Plagioclase, clinopyroxene, amphibole, orthopyroxene	Chlorite, talc	
277R-2, 96–106	Plagioclase, clinopyroxene, orthopyroxene	Talc	
280R-1, 4–14	Plagioclase, clinopyroxene, amphibole, ilmenite		
287R-1, 0–3	Plagioclase, clinopyroxene, amphibole	Chlorite	Diabase

Table T7. Secondary mineral proportions in the thin section from Hole U1309D. (This table is available in an **oversized format.**)

Table T8. Vein minerals identified by XRD and in thin section, Hole U1309D. (This table is available in an **oversized format.**)

Table T9. Electron microprobe data. (This table is available in an **oversized format.**)

Table T10. Major and volatile compositions and trace element compositions of rocks, Holes U1309B and U1309D. (This table is available in an **oversized format.**)

Table T11. Major oxide and trace element compositions, Hole U1309D. (This table is available in an **oversized format.**)

Table T12. Lithologic variation of magnetic properties determined from archive-half data, Expedition 304.

Lithology	*N*	NRM (A/m)		MS ($\times 10^{-5}$ SI)	
		Mean	SD	Mean	SD
Basalt	96	0.34	1.21	324.2	0.76
Diabase	681	3.37	0.65	1806.7	0.54
Oxide gabbro	357	2.73	0.89	1032.4	0.75
Gabbro	2170	0.18	0.84	114.8	0.60
Olivine gabbro	1979	0.71	1.16	360.0	0.81
Troctolite	199	0.05	0.87	64.5	0.50
Ultramafic	139	10.35	0.65	3859.8	0.40

Notes: Mean = geometric mean with standard deviation (SD) given in log units. Natural remanent magnetization (NRM) values include core sections with residual flux counts. MS = magnetic susceptibility. *N* = number of samples. This table is also available in **ASCII.**

Table T13. Discrete sample remanence data, Holes U1309B and U1309D, Expedition 304. (See table notes. Continued on next three pages.)

Core, section, interval (cm)	Piece	Depth (mbsf)	Lithology	NRM			Principal component analysis							
				Declination (°)	Inclination (°)	Intensity (A/m)	Polarity	*N*	Type	MAD	Declination (°)	Inclination (°)	Demag (mT/°C) Low	Demag (mT/°C) High
304-U1309B-														
1R-3, 121	14	3.11	Plagioclase phyric basalt	192.5	74.7	7.55E+00	R	5	F	7.8	264.1	–43	20	50
2R-1, 30	3	15.80	Brecciated basalt	97.1	–18.0	2.48E–03	R	7	F	7.8	67	–60	35	100
2R-1, 90	8	16.40	Sparsely plagioclase phyric basalt	169.4	76.1	4.99E+00	R	2	A	1.3	90.9	–59	40	50
3R-1, 71	10	20.71	Aphyric basalt	151.2	–44.3	4.76E–03	R	11	F	1.6	145.3	–67	20	150
3R-1, 112	14	21.12	Gabbro	35.2	–50.3	5.34E–02	R	12	F	0.9	27.1	–55	15	150
5R-2, 90	5	31.84	Diabase	177.1	81.1	9.33E–01	R	7	F	5.7	150.4	–46	25	80
5R-2, 92	5	31.86	Diabase	130.6	84.0	2.36E+00	R	6	F	15.8	136.9	–35	25	60
6R-1, 99	9	34.19	Diabase	169.3	78.3	1.16E+01	R	6	F	5.5	53.6	–53	35	100
8R-2, 73	9	45.12	Gabbro	74.8	–35.3	1.02E+00	R	12	F	1.5	68.7	–43	5	100
9R-1, 35	3A	47.85	Gabbro	129.6	–43.2	2.45E–01	R	11	F	1.5	127.1	–53	10	100
10R-2, 7	1	53.94	Gabbro	293.7	–38.4	2.45E–01	R	10	F	0.6	295.3	–54	15	100
11R-1, 4	1A	57.04	Gabbro	185.2	–44.5	3.26E–02	R	8	F	1.1	193.1	–54	25	100
11R-1, 93	8	57.93	Harzburgite	250.0	67.8	4.97E+00	R	6	F	3.4	266.9	–63	20	50
11R-1, 124	9	58.24	Harzburgite	108.2	70.0	5.93E+00	R	8	F	1.3	13.1	–52	15	60
12R-1, 127	8	62.87	Diabase	154.3	76.2	5.14E+00	R	5	A	7.2	87.7	–47	25	50*
12R-1, 131	8A	62.91	Diabase	172.2	76.2	6.55E+00	D	10	F	7.6	184.1	68.3	400	580*
12R-1, 137	8A	62.97	Diabase	173.0	70.0	6.33E+00	R	5	A	11.8	97.9	–38	30	60*
12R-2, 46	4	63.50	Diabase	156.6	76.1	1.35E+01	D	8	F	3.7	155.9	72.6	500	580*
12R-3, 55	3	64.84	Diabase	158.8	79.0	1.08E+01	R	3	A	4.8	287.3	–75	35	50*
13R-1, 123	9A	67.33	Microdiabase	157.9	77.9	7.73E–01	—	—	—	—	—	—	—	—
14R-1, 107	10	72.17	Plagioclase phyric basalt	162.0	66.5	5.12E–02	R	5	F	4.8	78	–56	30	100
15R-1, 27	3	75.87	Layered gabbro	123.0	–35.3	1.58E–02	R	6	F	1.9	122	–50	25	100
15R-2, 76	6B	77.64	Layered gabbro	306.1	–44.0	3.24E–03	R	7	F	2.9	310.2	–51	20	100
16R-2, 27	5	82.04	Olivine gabbro	205.0	–5.1	1.65E–01	R	7	F	2.2	212.3	–53	20	100
16R-3, 22	1	83.10	Olivine gabbro	9.6	–16.6	1.21E–01	R	8	F	1.9	20.5	–48	20	120
17R-2, 6	1	86.40	Olivine gabbro	217.7	–43.8	6.44E–02	R	8	F	1.1	221	–49	20	120
17R-2, 40	1	86.74	Olivine gabbro	212.3	–39.7	1.24E–01	R	9	F	2.2	217.5	–48	520	600
18R-2, 44	5	91.45	Troctolite, olivine gabbro	190.2	–30.4	3.49E–01	R	8	F	1.5	192.2	–51	15	100
18R-3, 53	9	93.00	Basalt	279.4	–30.8	1.09E–01	R	8	F	3.5	278.6	–54	15	100
18R-3, 115	16	93.62	Basalt	156.3	78.1	8.72E+00	D	5	F	2.4	186.8	69	15	40*
19R-2, 44	4	96.02	Diabase	161.7	74.8	5.31E+00	R	3	A	4.7	108	–51	40	60
19R-2, 48	4A	96.06	Diabase	165.5	72.3	6.26E+00	D	14	F	1.7	166	72.7	0	580*
19R-2, 57	4B	96.15	Diabase	183.9	64.1	2.72E+00	R	4	A	7	136.9	–18	35	60
20R-1, 38	2B	99.38	Diabase	163.2	73.4	9.54E+00	D	11	F	2.6	154	72.8	300	580*
20R-2, 75	5	101.05	Diabase	165.5	74.1	1.18E+01	D	5	F	0.8	161.3	71.8	15	35*
304-U1309D-														
1R-1, 36	1	20.86	Diabase	168.3	82.3	3.82E+00	R	6	F	1.5	353.2	–50.6	30	100
2R-1, 86	8	27.66	Diabase	152.7	80.8	4.93E+00	R	7	F	5	169.5	–41.4	25	100
4R-1, 18	3	31.58	Diabase	219.3	84.2	6.21E+00	R	6	F	4.2	14.5	–42.5	30	100
5R-1, 54	5A	36.54	Troctolitic gabbro	65.2	–8.1	3.72E–02	R	6	F	5.5	74.8	–41.9	30	100
5R-2, 54	2B	37.95	Troctolitic gabbro	81.2	78.4	2.34E–02	R	8	F	5.1	14.9	–50.4	20	100
5R-3, 115	12	40.02	Troctolitic gabbro	146.5	–30.3	1.41E–02	R	9	F	1	141.9	–51.2	15	100
6R-1, 125	17A	42.05	Olivine gabbro	1.6	–40.3	6.66E–03	R	9	F	1.5	0.1	–49.1	15	100
6R-2, 70	8	43.00	Diabase	146.0	74.1	5.90E+00	R	4	A	6.3	15.5	–48.5	40	80
6R-3, 17	1	43.61	Diabase	168.1	76.9	1.19E+01	R	5	F	7.6	158.6	–53.4	35	80
7R-2, 28	1	46.86	Diabase	153.4	76.1	8.78E+00	R	6	F	6.1	207.1	–47.1	30	80
7R-3, 94	16	48.97	Olivine gabbro	176.3	73.4	9.04E–02	N	7	F	3.9	176.4	35.6	25	100*
8R-1, 59	8B	51.09	Olivine-bearing gabbro	315.4	61.1	4.16E–01	R	7	F	8.2	310.8	–48.8	15	60

Table T13 (continued).

Core, section, interval (cm)	Piece	Depth (mbsf)	Lithology	NRM			Principal component analysis							
				Declination (°)	Inclination (°)	Intensity (A/m)	Polarity	*N*	Type	MAD	Declination (°)	Inclination (°)	Demag (mT/°C) Low	Demag (mT/°C) High
8R-2, 19	2	52.15	Troctolite/Gabbro	186.5	–42.8	5.32E–03	R	7	F	1.3	188.8	–53.2	25	100
8R-2, 133	16	53.29	Troctolite	171.5	36.6	1.65E–01	R	6	F	4.9	180.5	–51.7	15	50
9R-1, 93	12A	56.23	Olivine gabbro/gabbro	242.8	–11.1	1.30E–01	R	7	F	1.5	248.6	–30.4	25	100
9R-2, 4	1	56.70	Gabbro	93.9	–58.7	5.70E–01	R	6	F	0.6	80.0	–62.7	30	100
10R-2, 44	6	62.02	Troctolitic gabbro	76.3	–29.5	2.99E–03	R	9	F	1.9	65.2	–45.3	15	100
11R-2, 40	2	66.69	Layered gabbro	170.3	–38.0	6.74E–03	R	9	F	1.1	173.7	–58.0	15	100
12R-1, 77	6	70.57	Troctolite	328.7	–36.8	2.88E–02	R	12	F	2.9	323.4	–42.9	300	580
13R-1, 64	4	75.14	Gabbro	8.8	66.4	2.88E–01	R	11	F	4.2	9.5	–44.3	15	120
13R-2, 89	7A	76.72	Gabbro	139.4	–19.0	2.78E–01	R	10	F	1.7	133.6	–40.0	15	100
13R-3, 30	5	77.56	Troctolitic gabbro	242.5	–42.3	4.70E–02	R	10	F	1	243.6	–48.6	15	120
14R-1, 98	15	80.38	Olivine gabbro	310.1	–30.9	1.13E–02	R	9	F	1.5	313.2	–39.6	20	120
14R-2, 129	13	82.03	Basalt	279.7	87.2	9.70E–01	R	6	A	5.8	311.6	–47.6	15	40
15R-2, 126	12	86.86	Diabase	159.9	77.7	8.25E+00	R	3	F	12.5	175.4	–44.4	35	50
16R-2, 63	5	91.13	Diabase	152.6	80.5	4.43E+00	—	—	—	—	—	—	—	—
16R-4, 140	12	94.33	Basalt dike	185.9	68.4	2.34E+00	D	13	F	1	184.7	68.4	2	60*
16R-5, 22	2	94.61	Gabbro	100.6	–9.3	2.06E–01	R	9	F	1.3	98.3	–48.8	20	120
17R-1, 61	5B	99.31	Olivine gabbro	177.6	–40.7	2.01E–01	R	10	F	1.5	176.8	–45.3	15	120
17R-2, 27	1	100.15	Olivine gabbro	352.7	–37.9	1.57E–01	R	6	F	1.4	356.2	–45.4	540	590
17R-3, 54	3	101.80	Olivine gabbro	18.2	–8.6	3.03E–02	R	5	F	3.9	14.0	–44.5	550	590
20R-1, 72	8	117.82	Microdiabase	105.8	61.6	7.16E–02	—	—	—	—	—	—	—	—
20R-1, 130	16	118.40	Microdiabase	150.5	53.6	3.87E–02	R	3	A	4.6	27.8	–31.2	520	540
22R-1, 87	11	127.17	Microdiabase	169.0	67.9	4.42E–02	N	4	F	14.3	152.6	39.0	10	25*
22R-2, 8	1	127.60	Troctolitic gabbro	345.9	–7.8	3.47E–03	R	3	A	2.3	355.6	–45.7	520	540
22R-2, 79	2	128.31	Troctolitic gabbro	225.9	67.3	7.89E–03	R	3	A	2.4	106.2	–36.4	530	570
22R-3, 45	4	129.43	Troctolitic gabbro	20.5	80.0	4.80E–04	—	—	—	—	—	—	—	—
23R-1, 82	15	131.82	Troctolitic gabbro	228.4	40.1	9.12E–04	R	4	F	5.4	238.2	–29.1	30	100
23R-2, 95	11	133.45	Serpentinized peridotite	172.5	62.5	1.16E+00	R	5	F	3.2	160.2	–53.6	20	40
24R-1, 125	15	139.15	Olivine gabbro	153.4	–26.3	2.54E–02	R	6	F	2.9	151.1	–55.3	40	140
25R-3, 26	2	145.81	Olivine-bearing gabbro	32.0	–20.8	2.32E–02	R	5	F	4.8	17.4	–57.0	50	140
26R-1, 16	4	147.76	Orthopyroxene-bearing gabbro	5.4	–46.3	7.19E–02	R	6	F	1.3	356.6	–47.4	40	140
26R-1, 91	9	148.51	Recrystallized gabbro	234.9	–46.0	4.89E–02	R	8	F	1.8	236.6	–50.8	540	620
26R-2, 130	9	149.99	Olivine-bearing gabbro	41.2	–26.8	3.66E–02	R	4	F	2.8	44.5	–59.0	50	100
26R-4, 34	1	151.48	Olivine-bearing gabbro	331.2	38.3	1.03E–02	R	7	F	10.8	307.1	–44.0	15	50
27R-1, 88	9	153.18	Olivine gabbro	353.9	24.9	4.32E–03	R	11	F	5.3	358.1	–42.5	15	120
27R-2, 53	5	154.17	Olivine gabbro	157.2	–97	4.37E–02	R	9	F	1.1	155.4	–50.1	530	620
28R-2, 61	1B	158.59	Olivine-bearing gabbro	288.4	–26.1	2.07E–01	R	13	F	3.4	293.1	–43.2	15	160
28R-4, 30	4	161.23	Orthopyroxene-bearing gabbro	149.7	–10.9	4.06E–01	R	3	A	2.6	166.8	–21.1	120	160
28R-4, 34	4	161.27	Orthopyroxene-bearing gabbro	135.2	54.8	8.58E–01	R	8	F	2.8	149.2	–30.2	540	620
28R-5, 11	1	162.46	Gabbro	155.3	72.9	7.65E–01	R	8	F	2.6	53.0	–57.3	35	160
29R-2, 134	14	164.68	Deformed gabbro	140.6	–2.4	9.72E–02	R	4	F	2.6	139.0	–49.1	80	160
30R-1, 60	9	167.30	Gabbro	355.4	–28.6	3.83E–02	R	4	F	1.7	3.0	–43.2	80	160
31R-2, 11	2	173.07	Serpentinized peridotite	176.9	62.9	9.62E+00	R	5	F	8.4	144.9	–43.5	25	50
32R-1, 101	13	177.31	Olivine-bearing gabbro	213.1	–30.6	2.51E–02	R	4	F	2.6	223.4	–46.0	60	130
32R-2, 27	2	177.89	Gabbro	145.1	27.0	4.25E–02	R	5	F	5.3	146.7	–49.3	60	160
33R-1, 60	6	181.70	Olivine gabbro	209.2	–24.2	9.48E–03	R	6	F	4	205.4	–52.3	560	620
33R-1, 76	6C	181.86	Olivine gabbro	188.4	–16.1	6.04E–03	R	5	F	2.2	175.0	–53.5	60	160
33R-1, 84	6	181.94	Olivine gabbro	125.9	57.7	7.27E–03	R	8	F	3	201.1	–39.1	540	620
33R-2, 46	2A	183.01	Olivine-bearing gabbro	69.9	3.4	2.51E–02	R	10	F	1.9	42.6	–39.6	25	160
33R-3, 37	4	184.28	Olivine-bearing gabbro	28.5	50.9	2.48E–02	R	10	F	4.3	15.9	–38.1	20	130

Table T13 (continued).

Core, section, interval (cm)	Piece	Depth (mbsf)	Lithology	NRM			Principal component analysis							
				Declination (°)	Inclination (°)	Intensity (A/m)	Polarity	*N*	Type	MAD	Declination (°)	Inclination (°)	Demag (mT/°C) Low	Demag (mT/°C) High
34R-1, 115	14A	187.15	Gabbro	159.6	78.6	1.22E–02	N	5	A	3.5	152.6	51.8	60	160*
35R-1, 45	7	191.25	Oxide gabbro	97.6	81.2	3.58E+01	R	5	F	16.2	85.0	–26.2	35	80
35R-3, 133	18	194.83	Oxide gabbro	189.7	81.5	1.37E+01	R	9	F	5.3	171.6	–20.9	15	80
36R-2, 12	1	197.21	Olivine-bearing gabbro	219.5	60.9	9.57E–03	R	7	F	3.6	338.5	–30.8	550	620
36R-2, 16	1	197.25	Olivine-bearing gabbro	251.9	74.4	1.55E–02	N	5	A	6.9	305.1	41.8	25	50*
36R-3, 102	10	199.51	Gabbro	243.9	32.3	9.95E–03	R	6	F	5.5	266.8	–22.2	40	120
37R-1, 26	4	200.66	Gabbro	19.1	62.5	3.98E–01	H	9	F	2.2	38.3	–9.3	20	100
37R-2, 122	9	203.12	Gabbro	190.2	–23.9	2.29E–02	R	10	F	2.1	184.8	–41.0	20	120
38R-1, 44	2	205.64	Gabbro	212.5	56.4	5.44E–01	R	8	F	2.9	253.9	–38.3	25	100
38R-1, 92	7	206.12	Gabbro	357.6	67.2	1.68E–02	R	6	F	4.2	46.3	–40.1	560	620
38R-2, 60	5	207.30	Gabbro	222.8	66.5	8.28E–03	R	6	F	4.9	311.7	–33.9	560	620
39R-2, 25	3	211.75	Olivine gabbro	200.6	69.3	7.65E–03	N	8	F	8.8	215.9	33.9	10	50*
39R-2, 64	8	212.14	Olivine gabbro	146.9	79.6	7.80E–02	D	3	F	0.8	152.9	81.2	0	10*
41R-1, 109	10A	220.59	Troctolite to gabbro layers	267.0	21.8	1.29E–02	H	7	F	2.9	274.5	–5.3	540	600
41R-1, 118	10B	220.68	Troctolite to gabbro layers	252.3	17.9	1.92E–02	R	5	F	10	267.9	–14.0	40	80
42R-1, 127	16	225.57	Olivine-bearing gabbro	158.7	–6.5	2.61E–02	R	9	F	5.4	155.5	–14.8	20	80
44R-1, 9	1	233.29	Olivine gabbro	62.0	84.2	1.38E–02	R	8	F	2.3	62.5	–27.7	530	600
44R-1, 25	1	233.45	Olivine gabbro	279.9	78.2	1.78E–02	N	4	F	3.6	258.3	58.7	15	30*
44R-2, 72	4	235.42	Disseminated oxide gabbro	257.0	75.3	1.47E+00	H	8	F	3.8	352.3	–8.1	20	70
44R-4, 7	1	237.65	Olivine-bearing/Oxide gabbro	151.4	78.8	1.57E+00	N	4	F	8.4	303.6	44.1	35	60*
45R-3, 24	2	240.94	Olivine-bearing/Oxide gabbro	135.1	76.3	1.10E+01	R	5	F	3	314.6	–17.0	60	140
46R-1, 102	12	243.82	Olivine-bearing gabbro	12.8	2.3	1.21E–02	H	11	F	1.7	11.8	–5.1	20	140
46R-1, 107	12	243.87	Olivine-bearing gabbro	16.8	66.8	1.25E–02	H	4	F	5.7	6.9	7.4	570	600
47R-3, 32	1	250.74	Olivine-bearing gabbro	301.7	82.8	1.01E+01	R	7	F	11.5	276.9	–13.9	15	50
48R-1, 48	6	252.88	Gabbro	255.7	73.7	2.02E–01	R	8	F	3.3	242.7	–49.9	15	60
48R-1, 93	13	253.33	Olivine gabbro	96.9	–28.4	2.43E–02	R	6	F	1.9	97.3	–40.8	550	600
48R-1, 116	15	253.56	Troctolite	78.5	–29.2	3.49E–02	R	14	F	2.8	76.1	–40.0	15	160
48R-2, 78	9	254.64	Olivine gabbro	144.1	4.8	6.94E–02	R	11	F	1.5	137.7	–32.5	25	160
49R-1, 60	9	257.80	Olivine gabbro	217.7	70.6	2.19E+00	R	5	F	4.3	220.7	–42.9	10	30
50R-1, 89	7	262.89	Olivine-bearing gabbro	103.6	–41.5	6.62E–02	R	6	F	2.7	104.2	–47.4	550	600
50R-3, 32	2	265.21	Olivine-bearing gabbro	140.9	–32.5	2.29E–01	R	14	F	1.9	141.4	–32.9	15	160
51R-1, 79	5	267.59	Gabbro/Fine-grained gabbro	13.4	–33.4	3.64E–02	R	10	F	1.3	11.0	–41.7	30	160
51R-2, 25	1A	268.08	Gabbro	302.1	–32.0	1.18E–01	R	6	F	3.7	309.0	–37.7	70	160
51R-4, 3	1	270.71	Gabbro	189.4	65.3	5.99E–01	R	4	F	7.4	242.3	–30.8	50	100
52R-2, 55	2	273.65	Gabbro	15.7	52.6	3.48E–01	R	12	F	2.3	335.0	–37.9	20	160
52R-3, 85	4	275.45	Gabbro	352.1	43.4	1.29E–02	R	13	F	6.6	355.0	–41.0	15	140
53R-1, 17	5	276.57	Gabbro	53.9	34.0	1.57E–02	R	6	F	4.9	34.1	–52.8	550	600
53R-1, 58	7	276.98	Gabbro	128.0	78.2	4.78E–02	D	3	F	1.8	131.1	78.2	0	10*
54R-1, 30	4B	281.5	Oxide-bearing gabbro	150.3	73.3	1.97E+01	R	3	A	3.1	4.0	–47.6	50	70
54R-3, 59	3	284.48	Olivine gabbro	179.0	75.4	1.05E+01	R	6	F	12.6	352.0	–32.5	25	60
55R-1, 107	15	287.07	Olivine gabbro	175.8	70.6	8.95E–02	N	6	F	2.6	162.5	63.7	15	40*
55R-3, 81	11	289.73	Olivine-bearing gabbro	206.2	54.4	1.98E–01	R	4	F	3.6	318.6	–36.4	40	80
55R-3, 102	13	289.94	Olivine-bearing gabbro	150.2	43.3	4.49E–02	R	6	A	6.6	156.3	–39.4	520	570
56R-1, 30	4	291.1	Dunite	147.0	5.1	2.44E–01	D	8	F	1.4	163.5	74.8	5	40*
56R-2, 108	4B	292.98	Gabbroic dike	59.8	65.5	2.26E+00	R	5	F	3.2	63.2	–38.5	20	40
57R-2, 7	1	297.05	Olivine-bearing gabbro	48.5	67.2	2.45E–01	R	5	F	1.8	20.1	–40.5	560	600
57R-2, 120	5A	298.18	Olivine-bearing gabbro	49.2	74.2	5.30E–02	R	7	F	6.4	14.1	–59.2	25	80
59R-3, 102	1A	309.02	Olivine-bearing gabbro	222.4	74.5	1.75E+00	D	4	F	1.8	216.7	75.5	0	15*
60R-1, 52	1	310.52	Olivine-bearing gabbro	248.6	34.4	8.82E–02	R	4	F	1	234.4	–25.8	570	600

Table T13 (continued).

Core, section, interval (cm)	Piece	Depth (mbsf)	Lithology	NRM			Principal component analysis							
				Declination (°)	Inclination (°)	Intensity (A/m)	Polarity	*N*	Type	MAD	Declination (°)	Inclination (°)	Demag (mT/°C) Low	Demag (mT/°C) High
60R-2, 43	3	311.76	Dunite cumulate	234.4	74.9	2.09E+01	D	5	F	1.5	232.0	76.5	0	20*
60R-3, 59	5	313.42	Olivine gabbro cumulate	274.0	66.7	1.35E+01	R	4	F	10.5	322.0	–25.7	20	35
62R-1, 81	10A	320.41	Oxide gabbro	279.2	80.3	1.26E+00	R	8	F	4.6	342.4	–33.8	20	70
62R-2, 66	12B	321.67	Oxide gabbro	243.9	56.1	2.10E+01	R	3	A	3.8	233.1	–46.1	40	60
63R-1, 107	15	325.47	Dunite cumulate	94.0	69.3	1.70E+01	R	4	A	7.2	39.3	–42.6	20	35
63R-3, 29	5	327.65	Troctolitic gabbro cumulate	174.2	48.0	1.78E+01	R	3	F	2	161.6	–25.3	580	600
64R-2, 84	8	331.27	Dunite cumulate	285.3	54.5	1.66E+01	R	4	F	0.9	330.0	–32.3	15	30
65R-1, 83	14	334.83	Troctolitic gabbro cumulate	191.2	61.6	2.54E+01	R	5	F	15.1	318.1	–34.4	25	50
65R-2, 115	13	336.65	Gabbroic dike	94.3	79.4	2.53E+00	R	4	F	1.6	30.5	–10.7	20	35
66R-2, 14	3	340.44	Troctolite cumulate	208.6	63.1	2.62E+01	R	4	F	11.3	288.2	–22.5	20	35
67R-2, 28	1D	345.3	Olivine-bearing gabbro	197.5	80.5	2.37E+00	R	6	F	8.2	117.0	–38.1	25	60
68R-1, 57	3	348.97	Gabbro	330.8	39.2	9.93E–02	R	6	F	1.8	153.0	–48.1	550	600
68R-3, 52	5	351.8	Olivine-bearing gabbro	148.3	3.0	3.06E–02	R	4	A	4.7	143.4	–26.5	50	80
69R-2, 103	4D	355.58	Oxide gabbro/troctolitic cumulate	235.4	79.7	2.86E+01	R	4	A	4.9	308.7	–38.7	35	60
70R-2, 35	1B	359.04	Troctolitic/Olivine gabbro domain cumulate	246.3	73.3	1.54E+01	N	9	F	6.3	297.4	59.8	520	600*
70R-2, 44	1B	359.13	Troctolitic/Olivine gabbro domain cumulate	248.2	70.7	2.60E+01	D	3	F	0.5	241.7	71.3	0	10*
71R-2, 112	3B	365.04	Leucocratic troctolitic/olivine gabbro domain cumulate	3.1	58.4	1.52E–03	R	7	F	6.9	6.3	–41.9	540	600
71R-3, 70	5	366.06	Leucocratic troctolitic/olivine gabbro domain cumulate	228.0	22.6	8.98E–04	R	9	A	8.5	270.0	–38.2	20	80
72R-1, 76	1C	368.36	Leucocratic troctolitic/olivine gabbro domain cumulate	179.0	80.2	2.61E+00	R	3	A	8.6	66.3	–58.3	25	35
73R-1, 29	4	372.69	Olivine gabbro/gabbro dike	184.4	63.6	7.54E+00	R	3	A	2.8	239.3	–16.7	30	40
73R-1, 108	8	373.48	Oxide gabbroic dike	84.5	66.9	3.63E–01	R	7	F	4.5	46.5	–39.4	20	60
73R-2, 70	6	374.55	Troctolitic gabbro	194.8	81.5	4.08E+00	R	4	A	5.5	67.4	–42.8	25	40
74R-1, 95	7	378.15	Gabbro	192.6	5.9	1.68E–01	R	10	F	1.4	185.7	–41.7	20	140
74R-1, 99	7	378.19	Gabbro	193.1	4.9	3.62E–01	R	6	F	1.5	198.3	–42.4	550	600
75R-1, 75	5A	382.75	Olivine gabbro	253.2	74.9	2.44E+00	R	5	F	2.8	319.6	–41.8	20	40
75R-3, 37	3	384.89	Gabbro	324.5	–24.3	2.93E–01	R	12	F	5.1	324.4	–43.6	10	140
76R-1, 105	4	387.95	Olivine gabbro	215.7	75.9	1.22E+00	N	9	F	5.7	256.9	33.3	520	600*
76R-1, 106	4	387.96	Olivine gabbro	205.6	72.3	1.24E+00	R	4	F	2.9	280.4	–39.3	25	40
77R-1, 12	2	391.82	Olivine gabbro	186.6	73.7	5.38E+00	R	5	F	4.3	227.7	–27.6	20	40
77R-4, 50	2	395.82	Olivine gabbro	180.3	78.6	9.18E+00	D	20	F	2.7	178.2	77.1	0	600*
77R-4, 52	2A	395.84	Olivine gabbro	67.1	5.6	5.45E+00	R	5	F	3.8	352.5	–29.1	15	35
78R-3, 41	2A	399.64	Olivine gabbro	346.9	72.7	1.64E+00	R	5	F	3	353.8	–35.0	20	40

Notes: Directions are reported in the core reference frame. Demag = demagnetization. R = reversed polarity, H = polarity uncertain, N = normal polarity, D = drilling-induced magnetization. F = free of origin, A = anchored. MAD = maximum angular deviation. * = not suitable for reorientation studies (poorly defined direction, drilling overprint, or normal polarity of uncertain origin). This table is also available in **ASCII.**

Table T14. Stable remanence data for core pieces, Holes U1309B and U1309D, Expedition 304. (See table notes. Continued on next four pages.)

Core, section (piece)	N	Average depth (mbsf)	CSD	Declination (°)	Inclination (°)
304-U1309B-					
1R-3 (7)	2	2.39	2.4	9.6	–18.1
1R-3 (9)	1	2.58	–1.0	289.4	–12.3
1R-3 (11)	3	2.74	2.9	332.2	–3.6
1R-3 (13)	3	2.96	2.6	347.0	–1.7
1R-3 (14)	2	3.13	7.9	330.9	–6.3
1R-3 (14)			7.8	264.1	–42.5
2R-1 (1)	2	15.57	5.6	101.7	–56.9
2R-1 (3)	2	15.83	1.9	16.0	–30.2
2R-1 (3)			7.8	67.0	–59.9
2R-1 (4)	2	15.95	3.5	9.9	–49.0
2R-1 (8)			1.3	90.9	–59.1
2R-1 (9)	1	16.68	–1.0	9.2	–52.8
2R-2 (1)	1	16.98	–1.0	204.3	–61.8
2R-2 (2)	3	17.14	6.8	205.6	–64.1
2R-2 (3)	3	17.30	2.7	257.1	–46.6
3R-1 (10)	3	20.70	7.7	122.5	–61.9
3R-1 (10)			1.6	145.3	–66.8
3R-1 (12)	4	20.91	3.1	70.9	–47.3
3R-1 (14)	3	21.10	3.6	17.2	–51.0
3R-1 (14)			0.9	27.1	–55.3
3R-1 (16)	1	21.24	–1.0	322.8	–49.1
4R-1 (4)	1	24.72	–1.0	38.5	–46.0
4R-1 (5)	7	24.90	10.0	251.1	–58.8
5R-1 (5)	2	29.73	1.9	16.0	1.6
5R-1 (18)	1	30.84	–1.0	332.1	–34.2
5R-2 (5)			5.7	150.4	–45.5
5R-2 (5)			15.8	136.9	–35.4
6R-1 (9)			5.5	53.6	–52.9
7R-1 (7)	1	38.72	–1.0	64.6	–29.4
8R-1 (10)	1	43.86	–1.0	70.6	–36.1
8R-1 (11)	2	43.99	1.8	108.5	–39.5
8R-1 (12)	1	44.10	–1.0	133.8	–42.6
8R-1 (13)	1	44.22	–1.0	263.8	–32.3
8R-2 (1)	2	44.48	1.2	349.0	–28.4
8R-2 (2)	1	44.59	–1.0	28.5	–39.1
8R-2 (6)	1	44.85	–1.0	62.4	–38.9
8R-2 (8)	1	45.01	–1.0	41.3	–46.3
8R-2 (9)	2	45.14	1.6	53.7	–33.9
8R-2 (9)			1.5	68.7	–43.1
9R-1 (1)	3	47.58	3.3	191.0	–39.1
9R-1 (3)	14	47.96	5.6	113.0	–46.2
9R-1 (3)			1.5	127.1	–53.3
9R-1 (4)	1	48.30	–1.0	155.4	–36.7
9R-1 (5)	3	48.44	3.8	75.5	–32.7
9R-1 (6)	5	48.68	2.8	43.2	–40.9
9R-1 (7)	4	48.87	6.3	36.1	–46.2
9R-2 (1)	4	49.05	1.3	313.9	–28.6
9R-2 (2)	2	49.23	2.1	298.9	–40.6
9R-2 (4)	3	49.46	1.4	106.5	–43.7
9R-2 (5)	2	49.63	2.0	330.5	–41.8
9R-2 (9)	2	49.99	3.7	325.3	–32.4
9R-2 (10)	2	50.19	0.8	93.2	–34.5
9R-2 (11)	1	50.32	–1.0	339.4	–25.3
10R-1 (3)	1	52.68	–1.0	168.0	–45.3
10R-1 (4)	1	52.80	–1.0	87.4	–56.6
10R-1 (5)	3	52.96	2.2	71.6	–44.2
10R-1 (13)	1	53.56	–1.0	115.1	–32.7
10R-1 (14)	1	53.66	–1.0	341.8	–32.2
10R-1 (16)	2	53.81	3.6	344.3	–21.1
10R-2 (1)			0.6	295.3	–54.2
10R-2 (2)	1	53.95	–1.0	308.6	–37.8
11R-1 (1)	5	57.10	3.7	181.1	–34.8
11R-1 (1)			1.1	193.1	–54.4
11R-1 (3)	9	57.44	3.5	240.5	–54.5
11R-1 (6)	1	57.74	–1.0	71.9	–32.3
11R-1 (8)	2	57.99	3.0	288.4	2.0
11R-1 (8)			3.4	266.9	–62.8
11R-1 (9)	9	58.18	3.0	14.2	–1.4
11R-1 (9)			1.3	13.1	–51.5
11R-2 (1)	4	58.63	1.5	9.9	–2.5
14R-1 (7)	4	71.69	2.4	38.9	–38.4
14R-1 (8)	2	71.99	5.0	159.2	–14.6
14R-1 (10)	1	72.18	–1.0	8.8	4.5
14R-1 (10)			4.8	78.0	–56.3
14R-1 (14)	2	72.47	7.4	166.7	–53.1
15R-1 (3)	5	75.84	5.0	126.0	–43.8
15R-1 (3)			1.9	122.0	–50.0
15R-1 (7)	1	76.20	–1.0	322.4	–30.3
15R-1 (16)	1	76.84	–1.0	348.4	–65.2
15R-2 (1)	2	77.05	2.7	60.4	–68.0
15R-2 (6)			2.9	310.2	–50.5
16R-1 (6)	1	80.70	–1.0	327.0	–31.8
16R-1 (16)	3	81.42	2.1	94.8	–4.7
16R-1 (17)	5	81.68	2.4	42.9	–35.7
16R-2 (5)	1	82.09	–1.0	205.6	–53.5
16R-2 (5)			2.2	212.3	–52.5
16R-3 (1)			1.9	20.5	–48.0
16R-3 (9)	1	84.14	–1.0	356.1	–41.0
16R-4 (3)	3	84.55	2.7	20.5	–37.4
17R-1 (6)	2	85.27	1.7	155.2	–45.2
17R-1 (7)	4	85.41	2.2	142.7	–49.8
17R-1 (8)	4	85.59	4.4	25.5	–52.6
17R-1 (9)	5	85.78	3.0	87.7	–45.8
17R-1 (12)	4	86.09	2.7	247.8	–42.2
17R-2 (1)	13	86.53	2.2	221.0	–51.1
17R-2 (1)			1.1	221.0	–48.6
17R-2 (1)			2.2	217.5	–47.6
17R-2 (2)	1	86.88	–1.0	139.1	–48.2
17R-2 (8)	2	87.71	2.3	166.1	–37.2
17R-3 (1)	4	87.93	6.2	23.4	–45.7
18R-1 (1)	1	89.66	–1.0	247.9	–35.3
18R-1 (10)	1	90.20	–1.0	184.2	–46.9
18R-1 (12)	2	90.39	3.8	173.5	–41.1
18R-1 (14)	2	90.61	3.0	145.4	–50.6
18R-2 (3)	1	91.29	–1.0	253.3	–44.9
18R-2 (4)	1	91.39	–1.0	74.6	–55.4
18R-2 (5)	1	91.49	–1.0	174.3	–61.0
18R-2 (5)			1.5	192.2	–50.6
18R-2 (16)	3	92.21	4.5	343.8	–50.4
18R-2 (17)	1	92.35	–1.0	314.4	–33.0
18R-3 (9)			3.5	278.6	–53.7
19R-2 (4)			4.7	108.0	–50.8
19R-2 (4)			7.0	136.9	–18.4
304-U1309D-					
1R-1 (1)	12	20.72	3.9	359.4	–19.8
1R-1 (1)			1.5	353.2	–50.6
1R-1 (3)	10	21.19	4.3	146.1	–54.5
1R-1 (9)	2	21.77	2.2	305.4	–38.9
1R-3 (1)	2	23.32	0.9	240.3	–35.0
1R-3 (6)	1	23.75	–1.0	168.4	–11.3
2R-1 (5)	1	27.22	–1.0	308.9	5.0
2R-1 (8)			5.0	169.5	–41.4
4R-1 (3)			4.2	14.5	–42.5
4R-1 (8)	1	31.92	–1.0	12.1	–3.3
4R-1 (11)	2	32.13	2.1	6.7	–29.6
4R-2 (18)	2	33.99	2.1	55.5	–36.5
4R-2 (19)	1	34.10	–1.0	265.2	–36.6
5R-1 (3)	5	36.30	6.3	89.9	–61.0
5R-1 (5)	2	36.59	3.1	81.9	–36.9
5R-1 (5)			5.5	74.8	–41.9
5R-2 (1)	4	37.56	6.4	201.9	–47.5
5R-2 (2)	5	37.77	5.0	38.5	–38.4

Table T14 (continued).

Core, section (piece)	N	Average depth (mbsf)	CSD	Declination (°)	Inclination (°)
5R-2 (2)			5.1	14.9	–50.4
5R-2 (12)	1	38.81	–1.0	115.0	–33.2
5R-3 (3)	3	39.09	2.7	340.3	–32.7
5R-3 (6)	2	39.38	0.9	132.6	–38.7
5R-3 (8)	2	39.60	1.4	323.1	–29.6
5R-3 (12)	1	40.01	–1.0	143.6	–38.9
5R-3 (12)			1.0	141.9	–51.2
5R-3 (13)	1	40.13	–1.0	80.7	–47.0
6R-1 (13)	1	41.62	–1.0	305.6	–23.2
6R-1 (17)			1.5	0.1	–49.1
6R-2 (5)	2	42.73	3.0	238.8	–35.2
6R-2 (8)			6.3	15.5	–48.5
6R-3 (1)			7.6	158.6	–53.4
6R-4 (2)	4	44.96	1.8	347.1	–73.4
7R-2 (1)			6.1	207.1	–47.1
8R-1 (4)	1	50.74	–1.0	336.5	–43.6
8R-1 (8)	3	51.06	1.9	313.3	–27.9
8R-1 (8)			8.2	310.8	–48.8
8R-1 (9)	1	51.24	–1.0	325.4	–3.6
8R-2 (2)	4	52.17	1.6	185.6	–42.6
8R-2 (2)			1.3	188.8	–53.2
8R-2 (3)	3	52.34	1.5	17.2	–38.8
8R-2 (7)	2	52.69	3.2	245.7	–34.0
8R-2 (16)			4.9	180.5	–51.7
8R-3 (1)	2	53.49	4.3	337.1	–32.6
9R-1 (11)	2	56.03	2.3	245.8	–47.4
9R-1 (12)	18	56.35	5.9	248.1	–44.9
9R-1 (12)			1.5	248.6	–30.4
9R-2 (1)	2	56.77	2.8	116.4	–55.7
9R-2 (1)			0.6	80.0	–62.7
9R-2 (9)	1	57.46	–1.0	106.3	–43.0
9R-3 (3)	1	58.31	–1.0	148.0	–34.1
9R-3 (9)	2	58.88	1.6	107.8	–41.6
10R-1 (3)	1	60.36	–1.0	333.4	–33.9
10R-1 (5)	1	60.50	–1.0	140.0	–33.3
10R-1 (6)	1	60.60	–1.0	349.1	–39.1
10R-1 (9)	1	60.90	–1.0	74.6	–52.7
10R-1 (10)	1	60.98	–1.0	107.7	–38.9
10R-1 (14)	2	61.47	1.8	208.3	–36.0
10R-2 (6)	1	62.02	–1.0	287.1	8.3
10R-2 (6)			1.9	65.2	–45.3
11R-1 (7)	9	65.36	7.3	107.6	–56.7
11R-1 (8)	5	65.64	5.2	125.8	–50.5
11R-2 (1)	8	66.42	4.3	194.2	–57.4
11R-2 (2)	3	66.67	5.3	171.7	–45.6
11R-2 (2)			1.1	173.7	–58.0
11R-2 (3)	1	66.77	–1.0	42.4	–54.7
11R-3 (7)	2	68.30	2.3	81.5	–43.6
11R-3 (8)	1	68.41	–1.0	188.3	–55.6
11R-3 (10)	9	68.67	3.1	349.8	–39.7
12R-1 (3)	1	69.98	–1.0	138.0	–40.6
12R-1 (4)	7	70.18	2.4	185.3	–49.2
12R-1 (6)	7	70.54	5.1	353.1	–43.1
12R-1 (6)			2.9	323.4	–42.9
12R-2 (3)	3	71.53	0.9	183.3	–48.1
12R-2 (7)	1	71.89	–1.0	100.5	–41.3
12R-2 (9)	5	72.07	3.2	238.4	–51.3
12R-2 (10)	1	72.23	–1.0	245.8	–39.8
12R-2 (11)	1	72.33	–1.0	156.4	–49.7
12R-3 (1)	7	72.70	2.6	154.6	–42.1
12R-3 (4)	2	72.99	2.7	170.8	–43.5
12R-3 (5)	1	73.08	–1.0	64.2	–34.5
13R-1 (4)	29	75.03	3.3	10.2	–47.4
13R-1 (4)			4.2	9.5	–44.3
13R-1 (6)	2	75.59	0.8	341.0	–32.6
13R-2 (1)	5	75.97	3.0	256.9	–45.4
13R-2 (2)	4	76.16	4.5	165.1	–50.1
13R-2 (3)	2	76.46	1.7	172.9	–40.6
13R-2 (7)	1	76.79	–1.0	139.4	–49.5
13R-2 (7)			1.7	133.6	–40.0
13R-2 (11)	1	77.13	–1.0	50.9	–45.3
13R-3 (1)	1	77.32	–1.0	346.6	–34.5
13R-3 (5)	1	77.54	–1.0	252.1	–32.7
13R-3 (5)			1.0	243.6	–48.6
14R-1 (3)	1	79.54	–1.0	0.0	–22.2
14R-1 (15)	3	80.38	2.8	308.0	–39.7
14R-1 (15)			1.5	313.2	–39.6
14R-1 (17)	3	80.62	2.1	106.4	–47.7
14R-2 (13)			5.8	311.6	–47.6
15R-2 (2)	3	85.72	6.8	349.7	7.6
15R-2 (4)	6	85.99	8.4	0.3	4.1
15R-2 (6)	1	86.22	–1.0	344.4	–1.4
15R-2 (12)			12.5	175.4	–44.4
16R-5 (1)	3	94.49	0.5	56.0	–29.3
16R-5 (2)			1.3	98.3	–48.8
17R-1 (4)	2	98.93	2.2	318.2	–32.4
17R-1 (5)	13	99.20	8.7	178.4	–45.7
17R-1 (5)			1.5	176.8	–45.3
17R-1 (7)	12	99.61	7.7	88.2	–50.8
17R-1 (8)	1	99.84	–1.0	169.2	–36.6
17R-2 (1)	17	100.14	2.6	357.9	–48.7
17R-2 (1)			1.4	356.2	–45.4
17R-2 (5)	17	100.72	3.6	118.3	–50.6
17R-2 (8)	1	101.14	–1.0	329.4	–43.7
17R-3 (1)	3	101.34	3.8	301.8	–42.8
17R-3 (2)	4	101.53	4.8	213.6	–52.3
17R-3 (3)	3	101.74	2.1	358.6	–45.8
17R-3 (3)			3.9	14.0	–44.5
17R-3 (4)	3	102.00	3.0	1.1	–57.9
20R-1 (16)			4.6	27.8	–31.2
22R-2 (1)	3	127.68	2.3	167.2	–35.1
22R-2 (1)			2.3	355.6	–45.7
22R-2 (1)			1.7	82.6	3.1
22R-2 (2)			2.4	106.2	–36.4
22R-2 (3)	1	128.80	–1.0	127.8	2.1
23R-1 (15)			5.4	238.2	–29.1
23R-2 (11)			3.2	160.2	–53.6
24R-1 (12)	2	138.59	3.0	52.7	–13.3
24R-1 (14)	4	138.83	5.6	264.1	–42.1
24R-1 (15)			2.9	151.1	–55.3
24R-2 (1)	10	139.40	7.9	322.1	–43.8
24R-2 (12)	2	140.22	1.5	53.3	–28.8
25R-1 (2)	9	142.94	6.5	319.7	–47.7
25R-1 (3)	1	143.14	–1.0	95.6	–50.0
25R-1 (4)	2	143.25	3.7	1.5	–57.7
25R-1 (6)	4	143.43	5.6	16.8	–39.6
25R-1 (10)	5	143.78	9.0	92.3	–46.1
25R-1 (11)	8	144.03	2.3	26.9	–43.7
25R-2 (1)	1	144.23	–1.0	18.1	–25.2
25R-2 (5)	6	144.57	2.6	304.1	–48.8
25R-2 (13)	8	145.39	4.4	22.5	–39.8
25R-3 (1)	1	145.71	–1.0	21.8	–42.6
25R-3 (2)	11	146.10	6.1	8.6	–47.2
25R-3 (2)			4.8	17.4	–57.0
25R-3 (8)	1	146.89	–1.0	157.5	–49.0
26R-1 (4)	3	147.80	1.2	11.4	–36.2
26R-1 (4)			1.3	356.6	–47.4
26R-1 (5)	8	148.17	7.2	172.0	–49.0
26R-1 (9)			1.8	236.6	–50.8
26R-2 (1)	10	148.94	9.2	2.2	–43.3
26R-2 (4)	3	149.53	7.6	247.5	–27.6
26R-2 (8)	3	149.87	1.4	149.5	–51.0
26R-2 (9)	2	150.02	4.7	31.8	–42.5
26R-2 (9)			2.8	44.5	–59.0
26R-3 (1)	1	150.19	–1.0	330.9	–37.6
26R-3 (2)	2	150.32	2.3	17.9	–30.5

Table T14 (continued).

Core, section (piece)	N	Average depth (mbsf)	CSD	Declination (°)	Inclination (°)
26R-4 (1)	9	151.36	10.0	346.5	–25.4
26R-4 (1)			10.8	307.1	–44.0
26R-4 (3)	1	151.90	–1.0	349.7	–29.1
26R-4 (5)	3	152.24	5.5	15.5	–38.3
27R-1 (9)	2	153.21	4.0	10.4	–23.2
27R-1 (9)			5.3	358.1	–42.5
27R-2 (5)			1.1	155.4	–50.1
28R-1 (2)	1	157.30	–1.0	227.6	–39.2
28R-1 (3)	12	157.77	9.2	15.3	–41.8
28R-2 (1)			3.4	293.1	–43.2
28R-2 (3)	3	158.84	3.5	305.7	–47.4
28R-3 (1)	2	159.50	6.3	94.3	–35.6
28R-3 (6)	2	160.20	7.6	31.1	–40.8
28R-3 (7)	2	160.34	1.6	326.9	–36.2
28R-3 (8)	4	160.52	3.7	298.2	–46.7
28R-3 (11)	4	160.82	8.2	33.6	–36.4
28R-4 (1)	1	161.03	–1.0	36.1	–42.3
28R-4 (4)	5	161.27	1.7	135.0	–39.7
28R-4 (4)			2.6	166.8	–21.1
28R-4 (4)			2.8	149.2	–30.2
28R-4 (6)	3	161.59	2.0	35.9	–35.6
28R-5 (1)			2.6	53.0	–57.3
29R-1 (1)	12	162.10	3.5	72.6	–49.5
29R-1 (6)	1	162.66	–1.0	329.9	–37.2
29R-1 (7)	1	162.78	–1.0	67.8	–42.3
29R-1 (11)	1	163.12	–1.0	169.9	–14.5
29R-1 (12)	1	163.24	–1.0	339.7	–35.0
29R-2 (1)	1	163.42	–1.0	251.7	–31.2
29R-2 (10)	2	164.25	3.9	185.7	–47.8
29R-2 (13)	2	164.51	1.6	194.1	–41.8
29R-2 (14)	4	164.65	2.9	132.5	–48.3
29R-2 (14)			2.6	139.0	–49.1
29R-3 (6)	1	165.23	–1.0	0.9	–39.4
29R-3 (10)	1	165.57	–1.0	3.2	–26.4
30R-1 (9)	2	167.31	2.2	4.9	–32.7
30R-1 (9)			1.7	3.0	–43.2
30R-1 (16)	3	168.04	5.2	341.9	–24.1
31R-2 (2)			8.4	144.9	–43.5
32R-1 (13)			2.6	223.4	–46.0
32R-2 (2)	1	177.90	–1.0	110.5	–31.7
32R-2 (2)			5.3	146.7	–49.3
32R-2 (3)	1	178.10	–1.0	135.8	–40.2
32R-2 (6)	5	178.38	4.7	46.2	–15.6
32R-3 (1)	1	178.99	–1.0	358.9	–43.3
33R-1 (5)	1	181.50	–1.0	30.4	–2.2
33R-1 (6)			4.0	205.4	–52.3
33R-1 (6)			2.2	175.0	–53.5
33R-1 (6)			3.0	201.1	–39.1
33R-1 (7)	1	182.08	–1.0	10.9	–8.8
33R-1 (10)	1	182.46	–1.0	325.7	–25.8
33R-2 (2)	15	182.94	5.7	41.4	–31.0
33R-2 (2)			1.9	42.6	–39.6
33R-2 (6)	7	183.49	4.2	44.1	–28.5
33R-3 (1)	1	183.99	–1.0	0.9	–16.5
33R-3 (3)	1	184.17	–1.0	297.1	–17.7
33R-3 (4)	1	184.29	–1.0	357.5	–5.7
33R-3 (4)			4.3	15.9	–38.1
33R-3 (7)	1	184.59	–1.0	349.8	–26.0
33R-3 (8)	1	184.69	–1.0	45.4	–11.4
33R-3 (11)	2	184.94	1.7	306.9	–16.5
34R-2 (3)	3	187.84	2.3	18.9	0.9
35R-1 (7)			16.2	85.0	–26.2
35R-3 (18)			5.3	171.6	–20.9
36R-2 (1)			3.6	338.5	–30.8
36R-2 (8)	4	197.72	3.5	25.4	–22.0
36R-2 (10)	4	198.00	4.6	325.8	–12.8
36R-3 (1)	3	198.59	2.3	287.4	–15.7
36R-3 (3)	1	198.85	–1.0	68.7	–22.3
36R-3 (6)	3	199.11	3.9	33.7	–22.1
36R-3 (7)	1	199.27	–1.0	40.5	–15.8
36R-3 (10)	6	199.58	3.5	291.7	–21.0
36R-3 (10)			5.5	266.8	–22.2
36R-3 (12)	1	199.85	–1.0	351.8	–15.0
36R-4 (1)	1	199.97	–1.0	2.2	–27.5
37R-1 (4)	2	200.61	4.3	45.9	–7.6
37R-1 (4)			2.2	38.3	–9.3
37R-1 (8)	2	201.12	6.3	327.4	–1.5
37R-1 (10)	4	201.38	4.3	329.8	–26.6
37R-1 (11)	15	201.68	6.5	356.2	–31.8
37R-2 (1)	11	202.10	7.6	86.1	–33.3
37R-2 (3)	10	202.51	4.9	52.1	–19.8
37R-2 (9)			2.1	184.8	–41.0
37R-3 (3)	10	204.34	3.5	341.3	–28.2
37R-3 (4)	4	204.60	2.3	5.5	–32.4
37R-4 (1)	5	204.83	9.6	127.0	–45.8
37R-4 (2)	1	205.01	–1.0	342.0	–20.8
38R-1 (1)	3	205.40	3.8	7.9	–4.8
38R-1 (2)			2.9	253.9	–38.3
38R-1 (6)	3	206.00	2.5	339.7	–24.4
38R-1 (7)	1	206.16	–1.0	22.0	–1.5
38R-1 (7)			4.2	46.3	–40.1
38R-2 (5)			4.9	311.7	–33.9
38R-2 (10)	2	207.71	1.1	314.1	–22.6
38R-2 (11)	1	207.84	–1.0	312.0	0.3
38R-2 (13)	1	208.04	–1.0	333.3	–3.5
39R-1 (3)	17	210.34	3.4	347.6	–26.2
39R-2 (1)	1	211.56	–1.0	9.2	4.4
39R-3 (2)	2	213.23	3.4	203.2	–32.3
39R-3 (6)	8	213.90	6.9	14.7	5.6
39R-3 (7)	1	214.16	–1.0	136.7	2.1
39R-4 (3)	9	214.99	1.0	328.3	–11.1
39R-4 (6)	2	215.26	2.1	309.7	–8.2
39R-4 (7)	2	215.36	1.2	327.7	–7.9
39R-4 (8)	3	215.41	8.8	304.1	–16.3
39R-4 (9)	2	215.62	1.4	47.0	–13.2
39R-4 (10)	1	215.65	–1.0	41.9	–17.9
39R-5 (10)	3	215.82	3.7	320.5	0.6
40R-1 (6)	3	215.16	4.4	189.2	–19.9
40R-1 (7)	1	215.34	–1.0	14.2	–3.9
40R-1 (10)	4	215.74	3.2	3.8	–1.7
40R-1 (11)	1	215.94	–1.0	218.1	6.4
40R-2 (2)	2	216.44	1.1	309.8	–17.0
41R-1 (10)			2.9	274.5	–5.3
41R-1 (10)			10.0	267.9	–14.0
41R-2 (4)	1	221.21	–1.0	281.6	–2.7
41R-2 (6)	1	221.39	–1.0	17.1	4.3
42R-1 (6)	3	224.78	0.9	313.2	–4.6
42R-1 (7)	2	224.93	2.4	152.3	1.3
42R-1 (9)	3	225.16	2.4	29.4	3.1
42R-1 (16)	2	225.57	0.8	153.5	–1.7
42R-1 (16)			5.4	155.5	–14.8
42R-1 (17)	2	225.69	3.7	335.8	–5.1
42R-2 (1)	1	225.86	–1.0	335.2	–21.4
43R-1 (1)	1	228.86	–1.0	190.7	–17.3
43R-1 (7)	1	229.36	–1.0	57.1	8.4
43R-1 (10)	2	229.75	1.7	337.8	–3.6
44R-1 (1)			2.3	62.5	–27.7
44R-1 (10)	2	234.55	1.7	320.2	–18.0
44R-2 (2)	1	234.90	–1.0	308.4	–1.2
44R-2 (3)	10	235.19	7.7	302.1	–17.3
44R-2 (4)			3.8	352.3	–8.1
44R-2 (7)	2	236.03	0.9	208.3	–18.0
44R-3 (2)	3	236.38	1.1	65.2	–3.3
44R-3 (3)	1	236.56	–1.0	100.8	–7.2
44R-3 (4)	4	236.81	3.5	87.0	–19.1
45R-3 (2)			3.0	314.6	–17.0

Table T14 (continued).

Core, section (piece)	N	Average depth (mbsf)	CSD	Declination (°)	Inclination (°)
45R-4 (1)	2	242.23	0.8	328.3	1.0
46R-1 (11)	1	243.70	–1.0	3.9	–1.6
46R-1 (12)			1.7	11.8	–5.1
46R-1 (12)			5.7	6.9	7.4
46R-1 (14)	2	244.03	3.1	347.0	8.7
47R-1 (1)	1	247.66	–1.0	298.6	–8.4
47R-3 (1)			11.5	276.9	–13.9
48R-1 (6)			3.3	242.7	–49.9
48R-1 (13)	1	253.36	–1.0	88.0	–30.2
48R-1 (13)			1.9	97.3	–40.8
48R-1 (15)			2.8	76.1	–40.0
48R-2 (1)	1	253.92	–1.0	116.5	–18.4
48R-2 (4)	1	254.12	–1.0	98.0	–19.7
48R-2 (6)	1	254.40	–1.0	139.9	–9.2
48R-2 (8)	1	254.56	–1.0	76.4	–9.7
48R-2 (9)			1.5	137.7	–32.5
48R-2 (11)	1	254.84	–1.0	294.4	–13.5
49R-1 (9)			4.3	220.7	–42.9
49R-2 (14)	1	259.48	–1.0	197.9	–12.7
50R-1 (4)	1	262.36	–1.0	62.8	–24.7
50R-1 (6)	2	262.67	0.9	359.0	–25.1
50R-1 (7)	1	262.92	–1.0	96.2	–38.2
50R-1 (7)			2.7	104.2	–47.4
50R-1 (8)	2	263.13	4.8	292.0	–23.9
50R-2 (4)	2	263.93	2.2	319.9	–23.0
50R-2 (6)	2	264.13	3.2	302.0	–29.7
50R-2 (10)	1	264.42	–1.0	129.9	–31.7
50R-2 (13)	1	264.66	–1.0	50.4	–30.7
50R-2 (14)	3	264.82	1.4	2.1	–29.0
50R-3 (1)	2	264.98	0.2	140.4	–33.9
50R-3 (2)	5	265.17	5.4	148.7	–49.6
50R-3 (2)			1.9	141.4	–32.9
50R-3 (3)	3	265.37	1.4	84.5	–28.4
50R-3 (5)	1	265.53	–1.0	47.6	–42.5
50R-3 (6)	4	265.68	2.2	13.9	–26.7
50R-3 (8)	1	265.87	–1.0	260.9	–40.8
50R-3 (11)	1	266.07	–1.0	13.3	–25.2
51R-1 (3)	2	267.05	0.1	31.7	–22.7
51R-1 (4)	3	267.24	4.5	332.1	–32.5
51R-1 (5)			1.3	11.0	–41.7
51R-2 (1)			3.7	309.0	–37.7
51R-3 (1)	4	269.44	5.2	234.1	–39.0
51R-3 (2)	10	269.70	5.0	219.7	–39.5
51R-3 (4)	8	270.04	5.4	251.0	–30.5
51R-4 (1)	13	270.94	4.3	232.7	–37.7
51R-4 (1)			7.4	242.3	–30.8
51R-4 (2)	9	271.42	9.7	213.4	–45.5
51R-4 (4)	2	271.69	1.5	106.0	–23.2
52R-1 (10)	2	272.35	1.0	341.8	–33.9
52R-1 (11)	1	272.50	–1.0	13.9	–34.6
52R-1 (13)	1	272.70	–1.0	145.0	–39.4
52R-1 (14)	1	272.84	–1.0	3.8	–27.8
52R-1 (15)	2	273.01	1.3	11.6	–34.3
52R-2 (2)	10	273.45	9.3	344.4	–36.9
52R-2 (2)			2.3	335.0	–37.9
52R-2 (4)	1	274.54	–1.0	338.4	–20.5
52R-3 (3)	1	275.24	–1.0	16.7	–16.8
52R-3 (4)			6.6	355.0	–41.0
53R-1 (5)			4.9	34.1	–52.8
53R-1 (9)	5	276.64	3.5	23.7	–30.3
54R-1 (4)			3.1	4.0	–47.6
54R-1 (6)	5	281.84	6.8	339.0	–22.1
54R-2 (1)	7	282.76	5.8	302.2	–41.5
54R-3 (3)			12.6	352.0	–32.5
54R-4 (4)	1	285.55	–1.0	144.3	–19.3
55R-1 (5)	3	286.30	3.6	298.7	–14.0
55R-2 (8)	1	288.24	–1.0	320.9	7.6
55R-3 (2)	1	289.04	–1.0	359.9	–20.2
55R-3 (7)	1	289.38	–1.0	305.3	–29.9
55R-3 (9)	1	289.54	–1.0	305.3	–23.4
55R-3 (11)	1	289.78	–1.0	343.5	–0.8
55R-3 (11)			3.6	318.6	–36.4
55R-3 (13)			6.6	156.3	–39.4
55R-3 (14)	3	290.10	0.9	61.5	–3.5
55R-3 (16)	1	290.28	–1.0	136.6	–22.2
55R-4 (1)	2	290.51	0.9	111.7	–22.3
56R-2 (4)			3.2	63.2	–38.5
56R-3 (2)	1	293.50	–1.0	47.2	1.4
56R-3 (4)	1	293.72	–1.0	5.6	–2.6
56R-4 (1)	2	295.09	3.0	49.7	–39.9
57R-1 (5)	2	295.85	0.4	108.1	–42.2
57R-1 (6)	13	296.12	5.2	68.3	–41.1
57R-2 (1)	2	297.07	0.7	8.9	–14.5
57R-2 (1)			1.8	20.1	–40.5
57R-2 (2)	4	297.59	3.9	107.7	–30.2
57R-2 (5)	1	298.34	–1.0	356.0	–21.9
57R-2 (5)			6.4	14.1	–59.2
57R-3 (2)	1	298.71	–1.0	145.8	–36.5
57R-3 (5)	3	299.19	1.7	352.0	–30.6
57R-4 (1)	1	299.86	–1.0	310.8	–29.3
58R-1 (6)	3	301.46	3.0	273.7	–19.7
58R-2 (1)	3	301.85	1.5	50.3	–23.6
58R-2 (3)	2	302.60	2.2	239.6	–19.7
59R-2 (6)	2	306.97	1.2	5.8	1.8
59R-2 (7)	1	307.10	–1.0	1.5	6.1
59R-2 (9)	1	307.68	–1.0	122.3	–9.0
60R-1 (1)			1.0	234.4	–25.8
60R-2 (1)	1	311.51	–1.0	306.7	–35.5
60R-3 (5)			10.5	322.0	–25.7
62R-1 (10)			4.6	342.4	–33.8
62R-2 (12)			3.8	233.1	–46.1
62R-2 (15)	1	321.83	–1.0	288.4	–37.5
63R-1 (15)			7.2	39.3	–42.6
63R-3 (5)			2.0	161.6	–25.3
64R-2 (8)			0.9	330.0	–32.3
65R-1 (14)			15.1	318.1	–34.4
65R-2 (13)			1.6	30.5	–10.7
66R-2 (3)			11.3	288.2	–22.5
67R-1 (16)	5	344.90	4.6	292.8	–53.8
67R-2 (1)	3	345.23	7.6	107.3	–33.6
67R-2 (1)			8.2	117.0	–38.1
67R-2 (5)	1	346.12	–1.0	8.7	–24.7
67R-3 (1)	1	346.36	–1.0	31.6	–22.0
67R-3 (2)	10	346.83	6.9	90.5	–27.5
68R-1 (2)	1	348.52	–1.0	336.1	–23.8
68R-1 (3)	7	348.78	5.2	30.1	–23.2
68R-1 (3)			1.8	153.0	–48.1
68R-1 (4)	1	349.08	–1.0	333.0	–18.8
68R-3 (5)			4.7	143.4	–26.5
69R-2 (4)			4.9	308.7	–38.7
71R-2 (3)			6.9	6.3	–41.9
71R-3 (5)			8.5	270.0	–38.2
71R-3 (6)	1	366.02	–1.0	293.8	–15.9
71R-3 (7)	1	366.34	–1.0	346.3	–30.9
72R-1 (1)			8.6	66.3	–58.3
72R-2 (8)	1	369.95	–1.0	100.0	–31.0
72R-3 (3)	1	371.34	–1.0	325.8	–46.9
72R-4 (4)	1	372.78	–1.0	353.7	–21.9
73R-1 (4)			2.8	239.3	–16.7
73R-1 (8)			4.5	46.5	–39.4
73R-2 (6)			5.5	67.4	–42.8
73R-3 (2)	4	375.52	9.8	183.5	–21.9
73R-3 (7)	1	376.35	–1.0	190.3	–34.4
73R-4 (1)	3	376.51	6.5	185.7	–31.7
74R-1 (3)	2	377.45	3.8	330.2	–40.4
74R-1 (7)	3	378.16	5.5	198.4	–44.4

Table T14 (continued).

Core, section (piece)	*N*	Average depth (mbsf)	CSD	Declination (°)	Inclination (°)
74R-1 (7)			1.4	185.7	–41.7
74R-1 (7)			1.5	198.3	–42.4
74R-1 (8)	10	378.51	4.9	333.5	–35.9
74R-2 (1)	13	378.92	4.2	216.7	–39.8
74R-2 (5)	23	379.72	4.4	359.0	–31.8
74R-3 (1)	6	380.14	2.1	17.8	–11.2
74R-3 (4)	3	380.53	7.5	321.7	–28.0
74R-3 (5)	1	380.71	–1.0	223.6	–23.7
74R-3 (7)	1	381.05	–1.0	354.2	8.1
75R-1 (5)			2.8	319.6	–41.8
75R-2 (4)	1	384.74	–1.0	184.3	–21.0
75R-3 (1)	3	385.06	0.9	154.4	–28.6
75R-3 (3)	5	385.32	3.2	332.1	–28.7
75R-3 (3)			5.1	324.4	–43.6
75R-3 (4)	1	385.54	–1.0	352.1	–27.4
76R-1 (4)			2.9	280.4	–39.3
76R-3 (2)	3	390.24	6.8	9.2	–7.6
77R-1 (2)			4.3	227.7	–27.6
77R-4 (2)			3.8	352.5	–29.1
78R-2 (3)	1	398.85	–1.0	313.4	–1.0
78R-3 (2)			3.0	353.8	–35.0

Notes: *N* = number of archive half core measurements used for piece average; blank if discrete sample. Average depth calculated from all reliable archive half core measurements in this piece. CSD = circular standard deviation for archive half cores or MAD angle for discrete samples. This table is also available in **ASCII.**

Table T15. Anisotropy of magnetic susceptibility data, Holes U1309B and U1309D, Expedition 304. (See table notes. Continued on next two pages.)

Core, section, interval (cm)	Piece	Depth (mbsf)	MS (SI)	Maximum			Intermediate			Minimum		
				k	Declination (°)	Inclination (°)	*k*	Declination (°)	Inclination (°)	*k*	Declination (°)	Inclination (°)
304-U1309B-												
1R-3, 121	14	3.11	2.61E–02	0.3409	165.1	16.5	0.3317	66.6	26.4	0.3274	283.6	58.2
2R-1, 30	3	15.80	4.09E–04									
2R-1, 90	8	16.40	3.08E–02	0.3422	316.0	6.3	0.3307	219.1	47.2	0.3271	51.7	42.1
3R-1, 71	10	20.71	4.22E–04									
3R-1, 112	14	21.12	5.58E–04	0.3357	256.3	38.6	0.3338	351.3	6.3	0.3306	89.0	50.7
5R-2, 90	5	31.84	7.90E–03	0.3493	12.7	26.2	0.3275	113.2	20.4	0.3231	236.4	55.8
5R-2, 92	5	31.86	2.66E–02	0.3580	6.1	25.5	0.3249	99.3	6.8	0.3171	203.0	63.5
6R-1, 99	9	34.19	5.50E–02	0.3453	272.9	27.5	0.3318	172.5	19.2	0.3229	52.1	55.5
8R-2, 73	9	45.12	1.36E–03									
9R-1, 35	3A	47.85	5.91E–04	0.3393	43.4	10.7	0.3325	309.3	20.6	0.3282	159.1	66.6
10R-2, 7	1	53.94	9.59E–04	0.3390	280.7	25.6	0.3347	15.5	10.1	0.3263	125.2	62.2
11R-1, 4	1A	57.04	2.81E–04									
11R-1, 93	8	57.93	9.96E–02	0.3512	155.0	12.2	0.3373	247.3	10.6	0.3115	17.2	73.7
11R-1, 124	9	58.24	9.01E–02	0.3465	321.5	4.3	0.3336	229.1	29.2	0.3198	59.1	60.4
12R-1, 127	8	62.87	1.79E–02	0.3420	76.9	16.9	0.3357	335.9	32.2	0.3223	190.3	52.7
12R-1, 131	8A	62.91	2.29E–02	0.3398	63.8	28.6	0.3370	317.5	27.2	0.3231	191.9	48.5
12R-1, 137	8A	62.97	2.21E–02	0.3407	76.3	21.9	0.3369	330.7	33.9	0.3224	192.7	47.9
12R-2, 46	4	63.50	4.24E–02	0.3367	354.4	0.7	0.3338	84.5	9.8	0.3295	260.3	80.2
12R-3, 55	3	64.84	4.32E–02	0.3383	93.1	1.9	0.3328	2.4	20.0	0.3288	188.1	69.9
13R-1, 123	9A	67.33	2.69E–02	0.3411	273.9	27.2	0.3316	18.2	25.6	0.3273	144.5	51.0
14R-1, 107	10	72.17	7.78E–04	0.3387	286.3	29.3	0.3320	58.2	49.9	0.3293	181.4	24.7
15R-1, 27	3	75.87	3.43E–04									
15R-2, 76	6B	77.64	2.23E–04									
16R-2, 27	5	82.04	1.08E–03	0.3383	233.5	14.6	0.3335	131.1	39.5	0.3282	339.6	46.8
16R-3, 22	1	83.10	8.32E–04	0.3552	356.6	21.8	0.3287	208.0	64.9	0.3160	91.4	11.8
17R-2, 6	1	86.40	3.12E–04									
17R-2, 40	1	86.74	4.86E–04	0.3387	8.8	49.1	0.3316	245.7	25.3	0.3297	140.1	29.8
18R-2, 44	5	91.45	1.38E–03	0.3363	305.1	11.1	0.3352	36.0	4.6	0.3285	148.3	78.0
18R-3, 53	9	93.00	8.42E–04	0.3496	128.0	52.7	0.3286	219.7	1.2	0.3218	310.6	37.3
18R-3, 115	16	93.62	3.15E–02	0.3452	106.2	22.5	0.3290	218.8	42.8	0.3258	356.8	38.7
19R-2, 44	4	96.02	2.37E–02	0.3467	332.8	22.1	0.3312	66.3	8.4	0.3221	175.7	66.2
19R-2, 48	4A	96.06	2.84E–02	0.3480	329.0	27.1	0.3299	69.6	19.8	0.3221	191.1	55.5
19R-2, 57	4B	96.15	1.30E–02	0.3498	331.1	25.0	0.3290	64.9	8.2	0.3212	171.8	63.5
20R-1, 38	2B	99.38	4.39E–02	0.3459	286.6	17.7	0.3332	192.5	12.7	0.3209	68.7	68.0
20R-2, 75	5	101.05	5.22E–02	0.3410	264.5	18.5	0.3308	359.8	15.4	0.3283	127.1	65.5
304-U1309D-												
1R-1, 36	1	20.86	2.23E–02	0.3381	203.0	9.1	0.3324	295.2	13.5	0.3296	80.0	73.7
2R-1, 86	8	27.66	3.55E–02	0.3482	17.5	18.2	0.3332	283.8	11.2	0.3186	163.8	68.5
4R-1, 18	3	31.58	3.76E–02	0.3543	232.9	25.5	0.3291	323.4	1.2	0.3165	55.9	64.4
5R-1, 54	5A	36.54	5.08E–04									
5R-2, 54	2B	37.95	1.82E–03	0.3428	321.4	31.9	0.3401	155.7	57.3	0.3171	55.4	6.5
5R-3, 115	12	40.02	3.05E–04									
6R-1, 125	17A	42.05	3.73E–04									
6R-2, 70	8	43.00	3.32E–02	0.3445	219.7	37.9	0.3294	309.9	0.3	0.3262	40.2	52.1
6R-3, 17	1	43.61	5.35E–02	0.3365	44.0	23.7	0.3345	136.1	4.8	0.3290	236.9	65.8
7R-2, 28	1	46.86	4.15E–02	0.3381	98.7	27.0	0.3344	190.8	4.2	0.3275	288.8	62.6
7R-3, 94	16	48.97	2.47E–03	0.3379	246.3	22.0	0.3327	154.9	3.5	0.3294	56.4	67.7
8R-1, 59	8B	51.09	2.37E–03	0.3834	327.9	36.8	0.3338	88.7	34.4	0.2827	206.9	34.6
8R-2, 19	2	52.15	1.99E–04									
8R-2, 133	16	53.29	1.83E–03	0.3411	248.9	23.9	0.3342	109.0	59.9	0.3247	346.8	17.2
9R-1, 93	12A	56.23	5.01E–04	0.3511	237.5	6.1	0.3289	144.6	25.9	0.3200	339.8	63.3
9R-2, 4	1	56.70	1.16E–03	0.3922	54.2	54.5	0.3191	185.1	25.1	0.2886	286.8	23.5
10R-2, 44	6	62.02	3.01E–04									
11R-2, 40	2	66.69	4.03E–04	0.3376	115.6	45.8	0.3317	248.1	33.3	0.3308	356.3	25.4
12R-1, 77	6	70.57	4.65E–04	0.3377	120.7	42.2	0.3355	330.6	43.7	0.3269	225.3	15.5
13R-1, 64	4	75.14	3.62E–03	0.3771	256.1	30.0	0.3411	157.4	14.7	0.2818	44.6	55.9
13R-2, 89	7A	76.72	1.28E–03	0.3671	132.0	17.4	0.3325	236.6	38.8	0.3004	23.0	46.1
13R-3, 30	5	77.56	4.00E–04	0.3364	212.7	23.9	0.3344	115.2	16.2	0.3292	354.2	60.5
14R-1, 98	15	80.38	2.91E–04									
14R-2, 129	13	82.03	1.86E–03	0.3452	85.7	28.0	0.3428	306.2	55.0	0.3121	186.3	19.2
15R-2, 126	12	86.86	3.69E–02	0.3437	355.0	20.7	0.3315	88.1	8.3	0.3248	198.8	67.6
16R-2, 63	5	91.13	2.10E–02	0.3416	296.6	0.7	0.3349	26.6	2.3	0.3236	189.2	87.6
16R-4, 140	12	94.33	5.57E–02	0.3511	314.8	3.6	0.3407	45.4	10.2	0.3082	205.4	79.2
16R-5, 22	2	94.61	8.50E–04	0.3465	104.4	12.4	0.3325	7.3	29.5	0.3210	214.6	57.5
17R-1, 61	5B	99.31	2.73E–04									

Table T15 (continued).

Core, section, interval (cm)	Piece	Depth (mbsf)	MS (SI)	Maximum			Intermediate			Minimum		
				k	Declination (°)	Inclination (°)	*k*	Declination (°)	Inclination (°)	*k*	Declination (°)	Inclination (°)
17R-2, 27	1	100.15	4.46E–04	0.3377	211.8	47.0	0.3321	94.1	23.5	0.3302	347.3	33.6
17R-3, 54	3	101.80	4.70E–04	0.3394	233.6	51.8	0.3315	332.8	7.2	0.3292	68.3	37.3
20R-1, 72	8	117.82	7.22E–04	0.3363	101.0	47.1	0.3328	300.6	41.2	0.3309	201.8	9.9
20R-1, 130	16	118.40	6.04E–04	0.3343	263.4	14.6	0.3329	29.5	66.2	0.3328	168.4	18.4
22R-1, 87	11	127.17	6.79E–04	0.3341	123.9	41.2	0.3334	217.7	4.3	0.3325	312.6	48.4
22R-2, 8	1	127.60	1.32E–04									
22R-2, 79	2	128.31	2.20E–04									
22R-3, 45	4	129.43	1.40E–04									
23R-1, 82	15	131.82	1.78E–04									
23R-2, 95	11	133.45	7.48E–03	0.3438	26.2	1.0	0.3400	295.8	17.7	0.3162	119.4	72.3
24R-1, 125	15	139.15	4.71E–04	0.3375	12.5	71.9	0.3330	199.6	18.0	0.3295	108.9	2.1
25R-3, 26	2	145.81	4.00E–04	0.3394	301.4	54.4	0.3340	74.4	26.1	0.3266	176.1	22.5
26R-1, 16	4	147.76	2.75E–04									
26R-1, 91	9	148.51	3.25E–04	0.3420	117.4	61.4	0.3330	237.9	15.5	0.3250	334.8	23.4
26R-2, 130	9	149.99	7.64E–04	0.3437	20.5	67.4	0.3303	166.8	19.1	0.3260	260.9	11.6
26R-4, 34	1	151.48	4.91E–04	0.3351	237.0	84.7	0.3342	9.7	3.6	0.3307	99.9	3.9
27R-1, 88	9	153.18	3.41E–04									
27R-2, 53	5	154.17	6.25E–04	0.3380	5.7	50.2	0.3317	192.0	39.7	0.3303	99.5	3.1
28R-2, 61	1B	158.59	9.79E–04	0.3541	123.3	19.4	0.3331	234.2	45.4	0.3127	17.2	38.2
28R-4, 30	4	161.23	1.60E–03	0.3582	307.7	2.5	0.3251	216.6	22.6	0.3166	43.7	67.2
28R-4, 34	4	161.27	7.26E–03	0.3833	125.0	18.5	0.3411	19.6	38.4	0.2756	235.1	45.7
28R-5, 11	1	162.46	5.99E–03	0.3817	278.7	19.1	0.3305	9.9	3.4	0.2878	109.5	70.6
29R-2, 134	14	164.68	8.31E–04	0.3408	11.0	10.9	0.3365	102.0	5.2	0.3227	217.3	77.9
30R-1, 60	9	167.30	3.70E–04	0.3395	205.1	33.2	0.3376	323.2	35.7	0.3228	85.8	36.8
31R-2, 11	2	173.07	1.10E–01	0.3448	209.1	12.8	0.3387	304.5	22.3	0.3165	91.4	63.9
32R-1, 101	13	177.31	2.91E–04	0.3451	288.6	7.6	0.3346	31.0	58.2	0.3203	194.1	30.7
32R-2, 27	2	177.89	5.39E–04	0.3426	177.4	6.1	0.3305	81.9	42.4	0.3270	274.0	47.0
33R-1, 60	6	181.70	3.38E–04	0.3554	356.6	62.4	0.3367	213.7	22.7	0.3079	117.3	14.9
33R-1, 76	6C	181.86	2.72E–04									
33R-1, 84	6	181.94	2.82E–04	0.3416	86.7	43.2	0.3324	206.5	27.9	0.3260	317.4	34.0
33R-2, 46	2A	183.01	4.17E–04	0.3434	71.6	14.3	0.3371	338.8	10.9	0.3196	212.7	71.9
33R-3, 37	4	184.28	6.16E–04	0.3396	64.1	0.7	0.3339	334.0	4.6	0.3265	162.4	85.3
34R-1, 115	14A	187.15	4.83E–04	0.3353	266.7	3.3	0.3327	173.3	44.8	0.3321	0.0	45.0
35R-1, 45	7	191.25	1.62E–01	0.3403	296.9	13.7	0.3330	171.5	67.1	0.3266	31.5	17.9
35R-3, 133	18	194.83	8.49E–02	0.3542	1.5	41.9	0.3327	192.1	47.6	0.3131	96.3	5.3
36R-2, 12	1	197.21	2.95E–04	0.3409	216.1	44.4	0.3305	29.1	45.4	0.3286	122.6	3.5
36R-2, 16	1	197.25	3.12E–04	0.3441	228.5	47.8	0.3302	3.4	32.6	0.3257	109.6	23.6
36R-3, 102	10	199.51	3.50E–04	0.3353	30.0	15.2	0.3348	270.2	61.4	0.3299	126.8	23.6
37R-1, 26	4	200.66	5.68E–03	0.3666	280.3	32.5	0.3319	70.9	53.8	0.3014	181.0	14.1
37R-2, 122	9	203.12	2.64E–04	0.3380	102.0	3.8	0.3338	192.3	4.3	0.3281	330.5	84.3
38R-1, 44	2	205.64	4.70E–03	0.3622	175.5	13.0	0.3270	282.2	51.1	0.3108	75.8	35.8
38R-1, 92	7	206.12	4.55E–04	0.3361	256.1	57.9	0.3346	130.0	20.3	0.3293	30.7	23.7
38R-2, 60	5	207.30	3.88E–04	0.3352	189.6	13.1	0.3334	282.5	12.3	0.3314	54.3	71.9
39R-2, 25	3	211.75	3.30E–04	0.3358	334.5	20.7	0.3343	105.0	59.7	0.3299	236.2	21.0
39R-2, 64	8	212.14	8.12E–04	0.3480	257.1	13.0	0.3322	73.4	77.0	0.3198	166.9	0.8
41R-1, 109	10A	220.59	2.69E–04	0.3369	108.5	34.5	0.3336	204.5	8.6	0.3295	306.5	54.2
41R-1, 118	10B	220.68	2.91E–04	0.3372	329.4	6.1	0.3348	180.0	82.9	0.3279	59.8	3.6
42R-1, 127	16	225.57	4.08E–04	0.3360	268.8	18.5	0.3336	167.8	29.5	0.3304	26.4	54.1
44R-1, 9	1	233.29	3.85E–04	0.3361	145.7	30.1	0.3328	12.6	49.8	0.3311	250.7	24.0
44R-1, 25	1	233.45	3.66E–04	0.3355	281.8	28.8	0.3332	182.0	17.3	0.3313	65.0	55.6
44R-2, 72	4	235.42	7.52E–03	0.3490	199.3	30.6	0.3321	305.7	25.6	0.3189	68.0	48.1
44R-4, 7	1	237.65	5.57E–03	0.3445	20.8	61.5	0.3398	166.1	24.1	0.3157	262.7	14.4
45R-3, 24	2	240.94	5.78E–02	0.3571	174.2	44.5	0.3385	52.7	28.0	0.3044	302.9	32.5
46R-1, 102	12	243.82	3.01E–04	0.3402	227.4	0.4	0.3360	317.8	42.4	0.3238	136.9	47.6
46R-1, 107	12	243.87	3.22E–04	0.3372	28.2	52.4	0.3333	251.2	29.4	0.3295	148.6	21.3
47R-3, 32	1	250.74	4.10E–02	0.3454	30.5	51.4	0.3313	278.9	16.4	0.3233	177.6	33.8
48R-1, 48	6	252.88	1.89E–03	0.3561	347.5	67.2	0.3282	217.7	15.0	0.3156	123.1	16.7
48R-1, 93	13	253.33	1.60E–04									
48R-1, 116	15	253.56	1.42E–04	0.3458	311.2	54.1	0.3298	168.7	29.9	0.3244	67.9	18.0
48R-2, 78	9	254.64	4.68E–04	0.3570	15.3	14.7	0.3314	179.0	74.7	0.3116	284.2	4.1
49R-1, 60	9	257.80	8.76E–03	0.3545	96.1	13.0	0.3315	208.1	58.3	0.3140	359.0	28.3
50R-1, 89	7	262.89	4.87E–04	0.3401	120.2	3.5	0.3370	27.8	34.6	0.3229	215.2	55.2
50R-3, 32	2	265.21	4.12E–04	0.3375	60.4	7.3	0.3349	327.2	23.7	0.3276	166.4	65.1
51R-1, 79	5	267.59	2.45E–04	0.3388	4.6	24.5	0.3319	97.7	6.7	0.3293	202.0	64.4
51R-2, 25	1A	268.08	3.54E–04									
51R-4, 3	1	270.71	3.75E–03	0.3568	261.1	19.3	0.3328	164.7	17.5	0.3104	35.6	63.4
52R-2, 55	2	273.65	2.48E–03	0.3737	79.9	27.2	0.3318	291.6	58.9	0.2945	177.2	14.0

Table T15 (continued).

Core, section, interval (cm)	Piece	Depth (mbsf)	MS (SI)	Maximum			Intermediate			Minimum		
				k	Declination (°)	Inclination (°)	*k*	Declination (°)	Inclination (°)	*k*	Declination (°)	Inclination (°)
52R-3, 85	4	275.45	4.27E–04	0.3389	18.5	12.2	0.3354	252.7	69.7	0.3257	112.1	16.0
53R-1, 17	5	276.57	4.16E–04	0.3382	26.0	40.3	0.3314	293.6	2.8	0.3305	200.3	49.6
53R-1, 58	7	276.98	3.43E–04									
54R-1, 30	4B	281.5	1.03E–01	0.3527	33.0	62.3	0.3343	153.8	15.0	0.3130	250.2	22.7
54R-3, 59	3	284.48	4.09E–02	0.3556	224.5	19.2	0.3310	116.1	42.1	0.3134	332.5	41.7
55R-1, 107	15	287.07	6.86E–04	0.3400	223.3	0.6	0.3364	313.6	21.7	0.3237	131.7	68.3
55R-3, 81	11	289.73	1.31E–03	0.3442	230.3	57.6	0.3341	66.5	31.4	0.3218	332.0	7.3
55R-3, 102	13	289.94	8.64E–04	0.3487	34.3	0.9	0.3349	124.5	13.9	0.3164	300.5	76.0
56R-1, 30	4	291.1	4.78E–03	0.3400	120.9	41.2	0.3333	296.5	48.8	0.3267	29.0	2.2
56R-2, 108	4B	292.98	1.73E–02	0.3588	293.5	19.0	0.3393	27.8	12.4	0.3019	149.1	67.0
57R-2, 7	1	297.05	2.56E–03	0.3537	103.2	26.9	0.3412	244.5	57.0	0.3050	3.9	17.7
57R-2, 120	5A	298.18	6.03E–04	0.3480	352.2	77.3	0.3341	248.8	3.0	0.3179	158.1	12.3
59R-3, 102	1A	309.02	8.28E–03	0.3486	295.0	37.2	0.3354	178.0	30.9	0.3160	60.7	37.6
60R-1, 52	1	310.52	6.66E–04	0.3493	338.5	16.8	0.3413	69.5	3.4	0.3094	170.6	72.8
60R-2, 43	3	311.76	8.65E–02	0.3555	267.3	59.9	0.3424	162.1	8.6	0.3021	67.4	28.6
60R-3, 59	5	313.42	7.54E–02	0.3557	332.6	16.8	0.3455	236.9	18.4	0.2987	102.3	64.6
62R-1, 81	10A	320.41	6.27E–03	0.3573	157.0	4.0	0.3290	250.0	37.5	0.3136	61.8	52.3
62R-2, 66	12B	321.67	1.12E–01	0.3713	276.1	42.2	0.3297	185.6	0.6	0.2990	95.0	47.8
63R-1, 107	15	325.47	9.12E–02	0.3562	74.0	26.9	0.3446	337.5	12.5	0.2992	225.0	59.9
63R-3, 29	5	327.65	8.86E–02	0.3603	203.8	28.5	0.3402	309.4	26.3	0.2995	74.5	49.3
64R-2, 84	8	331.27	1.31E–01	0.3629	188.7	22.1	0.3493	291.5	28.6	0.2878	66.7	52.5
65R-1, 83	14	334.83	1.03E–01	0.3612	167.9	32.9	0.3404	295.1	43.1	0.2984	56.7	29.2
65R-2, 115	13	336.65	1.80E–02	0.3537	87.5	2.5	0.3275	177.8	6.7	0.3188	337.5	82.8
66R-2, 14	3	340.44	8.45E–02	0.3647	160.9	11.7	0.3462	261.6	42.1	0.2891	58.6	45.6
67R-2, 28	1D	345.3	1.14E–02	0.3515	316.6	28.1	0.3317	54.6	14.6	0.3167	169.0	57.7
68R-1, 57	3	348.97	3.80E–04	0.3545	328.7	50.1	0.3378	112.8	34.2	0.3077	215.6	18.2
68R-3, 52	5	351.8	2.34E–04	0.3463	172.7	30.4	0.3310	50.2	42.5	0.3227	284.6	32.4
69R-2, 103	4D	355.58	1.29E–01	0.3504	310.0	38.8	0.3295	151.7	49.1	0.3202	48.9	10.9
70R-2, 35	1B	359.04	7.14E–02	0.3681	196.1	10.1	0.3480	293.5	35.8	0.2839	92.7	52.4
70R-2, 44	1B	359.13	8.91E–02	0.3672	199.1	15.8	0.3502	306.1	45.7	0.2826	95.4	40.0
71R-2, 112	3B	365.04	2.55E–04	0.3379	332.5	10.2	0.3345	66.8	22.9	0.3276	220.1	64.7
71R-3, 70	5	366.06	2.70E–04	0.3384	244.3	11.0	0.3351	151.6	13.6	0.3264	12.1	72.4
72R-1, 76	1C	368.36	7.49E–03	0.3791	213.9	5.9	0.3293	102.1	74.5	0.2916	305.4	14.3
73R-1, 29	4	372.69	2.37E–02	0.3518	124.3	35.0	0.3402	225.2	15.1	0.3079	334.6	51.0
73R-1, 108	8	373.48	3.07E–03	0.3622	126.9	27.3	0.3341	10.4	40.9	0.3037	239.7	36.9
73R-2, 70	6	374.55	1.49E–02	0.3550	235.6	44.0	0.3310	123.4	21.4	0.3141	15.4	38.3
74R-1, 95	7	378.15	1.11E–03	0.3563	295.1	78.5	0.3257	61.4	6.9	0.3180	152.5	9.2
74R-1, 99	7	378.19	2.07E–03	0.3617	213.3	52.5	0.3483	73.0	30.5	0.2900	330.9	19.6
75R-1, 75	5A	382.75	1.44E–02	0.3772	167.5	14.9	0.3276	263.5	21.7	0.2952	45.6	63.3
75R-3, 37	3	384.89	7.79E–04	0.3513	68.3	42.8	0.3367	201.2	36.4	0.3120	311.9	25.6
76R-1, 105	4	387.95	6.47E–03	0.3561	323.5	4.3	0.3263	231.6	23.8	0.3176	63.2	65.8
76R-1, 106	4	387.96	6.44E–03	0.3583	133.4	2.4	0.3255	225.2	37.0	0.3162	40.3	52.9
77R-1, 12	2	391.82	2.21E–02	0.3716	92.3	8.6	0.3181	351.9	50.1	0.3103	189.2	38.6
77R-4, 50	2	395.82	2.73E–02	0.3730	214.9	2.7	0.3179	114.1	75.9	0.3091	305.6	13.9
77R-4, 52	2A	395.84	3.13E–02	0.3748	215.6	7.5	0.3149	330.6	72.6	0.3104	123.5	15.6
78R-3, 41	2A	399.64	1.11E–02	0.3641	196.2	5.0	0.3314	288.9	27.9	0.3045	96.8	61.6

Notes: Blank lines indicate samples with susceptibility values too low to reliably determine AMS. MS = magnetic susceptibility. This table is also available in **ASCII.**

Table T16. Demagnetization results. (See table notes. Continued on next four pages.)

Core, section, interval (cm)	Depth (mbsf)	Demag type	Principal component analysis							
			Polarity	*N*	Type	MAD (°)	Declination (°)	Inclination (°)	Demag (mT/°C) Low	Demag (mT/°C) High
305-U1309D-										
80R-1, 82–84	402.12	—	—	—	—	—	—	—	—	—
80R-2, 35–37	402.96	AF	R	6	F	3.6	13.3	–29.3	15	60
80R-3, 25–27	404.36	AF	R	7	F	4.5	22.9	–31.9	20	60
81R-1, 103–105	406.43	—	—	—	—	—	—	—	—	—
81R-2, 46–48	407.30	AF	R	6	A	7.4	298.4	–23.6	25	60
81R-3, 27–29	408.61	Th	R	5	A	3	334.2	–47.7	500	550
81R-4, 25–27	410.09	AF	N	5	A	3.8	295.8	39.9	30	60
82R-1, 69–71	410.89	AF	R	5	A	1	125	–39.8	30	60
82R-2, 114–116	412.77	AF	R	6	F	4.1	149.2	–24.6	25	60
83R-1, 41–43	415.41	Th	H	3	A	5.8	132.2	3.1	540	600
83R-1, 65–67	415.65	Th	R	2	A	1.6	58.2	–33.9	480	600
83R-2, 36–38	416.51	AF	H	6	A	7.3	295.1	6.5	25	60
84R-2, 118–120	422.06	Th	R	4	F	6.7	208.9	–50.4	500	595
84R-3, 65–67	422.88	AF	R	5	F	2.8	285.5	–37	20	60
85R-1, 52–54	425.12	—	—	—	—	—	—	—	—	—
85R-2, 126–128	427.11	AF	R	6	F	6.9	230.1	–31.4	15	60
85R-3, 28–30	427.60	AF	R	4	F	6.2	259.7	–18.2	20	50
86R-1, 83–85	430.23	Th	N	5	A	1.3	177.5	38	300	600
86R-2, 77–79	431.67	—	—	—	—	—	—	—	—	—
86R-3, 89–91	433.28	—	—	—	—	—	—	—	—	—
87R-1, 93–95	435.13	Th	D	3	A	3	120.6	69	450	600
87R-2, 111–113	436.77	Th	D	7	F	13.8	260	76.1	400	600
88R-2, 55–57	440.78	AF	R	3	A	8.5	105.4	–36	30	50
88R-4, 20–22	442.20	AF	R	4	F	3.9	129.4	–22.4	20	50
88R-5, 64–66	444.10	Th	N	4	A	5.9	255	26.8	530	600
89R-2, 18–20	445.38	Th	N	8	F	7.7	144.2	57.2	520	620
90R-1, 58–60	449.18	AF	R	6	F	1.5	73.8	–54.7	10	40
90R-2, 120–122	451.30	Th	D	1	F	7.3	27	83.9	400	620
90R-3, 70–72	452.30	—	—	—	—	—	—	—	—	—
91R-1, 105–107	454.45	—	—	—	—	—	—	—	—	—
91R-2, 108–110	455.96	Th	N	9	F	7	305	34.9	500	620
91R-3, 32–34	456.70	—	—	—	—	—	—	—	—	—
92R-1, 120–122	459.40	—	—	—	—	—	—	—	—	—
92R-2, 4–6	459.65	Th	N	6	A	11.3	123.4	33.4	500	620
93R-1, 127–129	464.27	Th	R	4	F	2	191.9	–34.2	500	595
94R-1, 20–22	468.00	Th	R	4	F	2.2	289.1	–38.8	550	595
94R-2, 12–14	469.42	Th	R	3	F	1	268.2	–43.5	550	595
95R-1, 59–61	473.19	AF	R	4	F	3.9	69.6	–41.2	10	60
95R-2, 92–94	474.93	Th	R	5	F	0.7	342.1	–29.4	550	620
95R-3, 127–129	476.65	Th	R	4	F	2.5	144.7	–21.7	500	595
96R-2, 44–46	479.21	AF	R	9	F	2.3	36.7	–38	10	100
96R-3, 20–22	480.41	AF	R	3	F	8.9	131.9	–36.2	30	60
97R-1, 110–112	483.30	AF	R	8	F	1.7	30.2	–45.1	15	100
98R-1, 75–77	487.75	Th	R	5	F	2.1	147.5	–40.8	500	595
98R-2, 121–123	489.50	Th	R	4	F	9.3	39.6	–33.5	550	595
98R-3, 91–93	490.61	Th	R	4	F	3.1	191.8	–42.7	550	595
99R-1, 110–112	492.90	AF	R	7	F	7.3	50.7	–61.5	20	100
100R-1, 56–58	497.16	Th	N	4	F	3.6	262.8	44.5	570	620
100R-3, 111–113	500.59	Th	D	9	F	13.1	9.1	84.3	500	620
101R-1, 57–59	501.97	Th	D	6	F	7.8	346.1	71.3	400	595
101R-3, 116–118	504.98	Th	D	10	F	2.1	0.8	74.5	200	620
101R-4, 58–60	505.77	Th	D	10	F	5	316.5	76.3	200	620
101R-5, 53–55	507.00	—	—	—	—	—	—	—	—	—
102R-1, 81–83	507.01	Th	N	5	F	17.6	311.8	40	500	595
102R-2, 142–144	509.06	Th	H	4	F	5.4	9.9	4.5	550	600
103R-2, 144–146	513.89	—	—	—	—	—	—	—	—	—
103R-3, 102–104	514.97	Th	R	3	F	2.6	146.9	–30.7	575	595
104R-1, 32–34	516.12	Th	R	5	F	4.3	118.6	–58.9	500	595
104R-2, 112–114	518.24	Th	N	2	A	2.4	28.5	61.1	585	595
104R-3, 118–120	519.80	Th	D	8	F	7.5	40.9	75.2	300	620
105R-1, 94–96	521.54	Th	R	6	F	5.5	117.2	–47.9	525	620
105R-2, 106–108	523.04	Th	R	3	F	2.3	200.4	–43.4	575	595
106R-3, 53–55	528.42	Th	R	5	F	3.4	77.1	–25.7	500	595
107R-1, 14–16	530.34	Th	N	6	F	10	131.1	60.1	525	620
107Rv3, 22–24	532.45	Th	R	3	F	3.9	258.9	–17.2	575	595
107R-4, 137–139	534.89	Th	R	5	F	0.7	143.4	–41.2	500	595
108R-1, 109–111	536.09	Th	R	4	A	4.6	233.9	–42.9	550	620

Table T16 (continued).

Core, section, interval (cm)	Depth (mbsf)	Demag type	Principal component analysis							
			Polarity	*N*	Type	MAD (°)	Declination (°)	Inclination (°)	Demag (mT/°C) Low	Demag (mT/°C) High
108R-2, 113–115	537.28	Th	R	5	F	2.1	251.1	–80.5	500	595
108R-3, 77–79	538.16	Th	R	4	A	1	257.6	–24.8	550	595
109R-1, 123–125	541.03	—	—	—	—	—	—	—	—	—
109R-2, 36–38	541.51	Th	R	5	F	1.6	69.5	–22.3	500	595
109R-3, 77–79	543.16	Th	N	6	A	10.2	313.7	32.2	500	620
110R-1, 99–101	545.59	Th	N	7	F	7.4	17.7	64.7	400	620
111R-1, 118–120	550.58	Th	D	7	F	2.7	264.2	73.4	400	620
111R-4, 44–46	554.01	Th	D	9	F	8.3	341.3	82.7	150	595
112R-1, 26–28	554.46	Th	D	5	F	3.7	301	75.5	500	595
113R-1, 97–99	559.97	Th	N	8	F	4.8	292.4	59.7	300	620
113R-2, 100–102	561.32	Th	D	7	F	6	44.4	84.9	200	595
113R-4, 58–60	563.85	Th	N	5	F	7.2	82.8	60.6	500	595
114R-1, 52–54	564.32	Th	N	3	A	8.4	259.5	27	575	595
114R-2, 81–83	566.11	Th	N	4	F	3	256.6	27.7	525	600
114R-3, 72–74	567.12	Th	R	5	F	1.2	122.4	–36.5	500	595
115R-1, 20–22	568.80	Th	R	5	F	0.7	274.3	–47.9	500	595
115R-2, 140–142	571.23	Th	R	5	F	1.5	15.1	–37.2	500	595
115R-3, 86–88	572.16	Th	R	5	F	1.7	146	–42.3	500	595
115R-4, 47–49	573.21	Th	R	5	F	1.1	14.3	–43.7	500	595
116R-2, 39–41	575.18	Th	R	5	F	1.3	303.9	–46.4	500	595
116R-4, 33–35	577.04	Th	N	6	F	5.9	346.5	51.4	500	620
117R-1, 70–72	578.90	Th	D	5	F	2.3	201.6	66.9	500	595
117R-1, 107–109	579.27	Th	N	6	F	8.7	103.9	62.1	500	595
117R-2, 99–101	580.40	—	—	—	—	—	—	—	—	—
118R-1, 107–109	584.07	Th	R	5	F	3.8	301.2	–30.7	500	595
118R-2, 45–47	584.78	Th	R	5	F	2.6	312.1	–32.8	500	595
118R-3, 78–80	586.55	Th	R	5	A	5.5	284.1	–32.9	525	595
119R-1, 40–42	588.20	Th	R	5	F	4.8	223.5	–37	525	595
119R-2, 17–19	589.33	AF	R	5	F	2.2	25	–51.9	30	100
119R-3, 87–89	591.53	Th	R	4	F	4	227.4	–47.9	550	595
119R-4, 15–17	592.10	—	—	—	—	—	—	—	—	—
120R-1, 26–28	592.86	—	—	—	—	—	—	—	—	—
120R-3, 127–129	596.55	—	—	—	—	—	—	—	—	—
120R-4, 89–91	597.50	Th	N	6	A	7	158	36.9	500	620
121R-2, 113–115	599.51	Th	R	4	F	1.7	91.4	–16.3	500	585
122R-1, 117–119	603.37	Th	D	9	F	5.1	55.9	81.2	200	620
122R-2, 5–7	603.53	Th	R	5	F	3.2	144.7	–26.3	500	595
122R-3, 33–35	605.26	Th	R	3	F	1.3	266.1	–38.6	575	595
123R-1, 38–40	607.38	Th	N	4	F	2.3	35.9	39.9	550	620
124R-1, 67–69	612.47	Th	R	3	F	1.9	147.3	–40	550	600
124R-3, 56–58	614.93	AF	R	3	A	3.3	136.9	–41.7	60	100
124R-4, 12–14	615.52	AF	R	5	F	8	145.3	–37.2	30	100
125R-2, 41–43	618.17	Th	R	4	F	1.7	142	–16.7	550	620
125Rv3, 78–80	619.88	AF	H	8	A	12	92	4.3	0	595
126R-1, 27–29	621.67	Th	R	3	F	3.6	319.7	–31.5	550	600
126R-3, 61–63	624.92	Th	H	5	F	2.8	154.5	3.5	550	620
127R-1, 25–27	626.45	AF	H	6	F	2.9	226.6	–2.3	15	80
127R-2, 40–42	628.10	Th	N	6	F	11	338.6	58.3	400	600
128R-3, 88–90	634.79	Th	R	3	F	4.5	254.7	–35.6	550	600
129R-1, 63–65	636.43	Th	R	3	F	2.9	11.6	–37.6	550	600
129R-3, 34–36	638.76	AF	R	3	A	1.7	265.7	–30.6	60	100
130R-3, 56–57	643.99	Th	N	6	F	6.6	129.8	51.6	500	620
131R-1, 35–37	645.75	Th	H	3	A	3.7	128.4	–8.7	550	600
131Rv2, 117–119	648.00	Th	R	5	F	4.1	297.9	–53.2	500	595
132R-1, 97–99	651.17	Th	R	4	F	5.6	0	–31.9	525	600
132R-3, 136–138	654.02	Th	D	5	A	7.6	298	69.4	500	595
132R-4, 79–81	654.91	AF	R	5	F	6.5	101.8	–24.5	30	100
133R-1, 100–102	656.00	Th	R	3	F	1.2	346.1	–40.6	550	585
133R-3, 137–139	658.88	Th	R	4	A	5.6	304.8	–20.1	550	595
134R-1, 94–96	660.74	—	—	—	—	—	—	—	—	—
134R-2, 67–69	661.62	Th	R	4	F	3.4	348.6	–14.6	550	595
135R-1, 75–77	665.35	—	—	—	—	—	—	—	—	—
135R-2, 92–94	666.90	Th	D	5	F	1.7	229	65.8	550	620
136R-1, 123–125	670.63	AF	R	3	F	2.4	259.9	–41.8	60	100
138R-2, 130–132	681.80	Th	R	5	F	1.6	84.3	–31	500	595
138R-3, 106–108	682.97	Th	R	4	F	2.2	339.4	–21	550	595
139R-1, 97–99	684.77	AF	R	4	A	13.7	312.4	–33.5	40	100
139R-3, 76–78	687.32	Th	N	5	F	3.6	355.1	58.9	550	620

Table T16 (continued).

Core, section, interval (cm)	Depth (mbsf)	Demag type	Principal component analysis							
			Polarity	*N*	Type	MAD (°)	Declination (°)	Inclination (°)	Demag (mT/°C) Low	Demag (mT/°C) High
140R-3, 69–71	691.66	Th	D	9	F	7.3	264.6	83.8	200	600
141R-1, 28–30	693.68	—	—	—	—	—	—	—	—	—
141R-2, 140–142	696.22	Th	D	4	F	4.7	3.8	68.1	550	600
142R-1, 4–6	698.24	AF	R	4	F	1.6	357.2	–31.2	15	40
142R-2, 139–141	701.00	Th	D	9	F	3.5	86.3	85.3	200	600
142R-3, 82–84	701.87	—	—	—	—	—	—	—	—	—
143R-2, 72–74	704.76	Th	N	4	F	4.6	322.3	58.8	550	600
144R-1, 70–72	708.50	Th	N	6	F	6.5	260.2	22.7	500	600
144R-2, 118–120	710.45	AF	R	3	A	3	307.8	–40.8	60	100
145R-2, 82–84	714.92	Th	R	7	F	4.2	328.3	–49.5	500	620
145R-4, 7–9	716.77	AF	R	4	F	3.1	26.5	–43	30	80
146R-1, 131–133	718.71	Th	R	5	F	5.1	180.8	–35.7	500	595
147R-2, 113–115	724.83	—	—	—	—	—	—	—	—	—
147R-4, 6–8	726.37	Th	R	5	F	5.7	88.7	–35.5	525	600
148R-3, 17–19	729.91	Th	R	4	F	4.1	309.2	–50.3	550	600
149R-1, 141–143	733.21	Th	R	5	F	9	174.3	–43.1	525	600
149R-3, 27–29	734.83	Th	R	6	F	1.9	180.8	–68.2	400	595
150R-4, 37–39	740.39	Th	R	7	F	4.8	319	–45.1	500	620
151R-2, 13–15	743.03	Th	N	4	F	6	347	58.1	400	575
153R-1, 37–39	751.37	Th	R	3	F	1.3	28	–34.8	575	600
153R-2, 102–104	753.52	Th	R	5	F	5.8	148.8	–32.5	400	585
154R-2, 10–12	757.28	Th	D	5	F	0.8	11.6	72	400	585
155R-1, 104–106	758.84	Th	D	5	F	2.9	351.7	73.4	400	585
155R-2, 113–115	760.07	Th	D	5	F	4.5	269.1	81.9	400	585
156R-3, 68–70	764.07	Th	R	4	F	0.5	282.4	–37.7	400	595
157R-2, 113–115	767.90	Th	R	5	F	4.9	339.1	–31.6	500	600
157R-3, 138–140	769.65	Th	D	8	F	4.3	309.3	74.2	200	600
158R-4, 81–83	774.59	Th	R	5	F	1.9	6.9	–29	500	600
159R-3, 10–12	778.01	AF	R	4	F	2.2	340.4	–34.3	30	80
159R-4, 62–64	779.31	Th	D	8	F	2.8	334.3	81.4	200	600
160R-2, 6–8	781.36	AF	R	7	F	3.1	312	–32	15	100
160R-3, 104–106	783.82	Th	N	3	F	0.6	0.3	64.4	575	600
161R-2, 63–65	786.62	Th	N	7	F	2.6	346.3	64.8	300	600
162R-2, 130–132	792.05	AF	R	5	F	4.3	18.7	–48.4	20	80
162R-4, 14–16	793.44	Th	R	3	F	2.2	265.7	–49.9	575	595
163R-4, 7–9	798.53	Th	N	4	F	6.2	71.9	10.7	500	595
164R-2, 59–61	800.77	Th	R	4	F	4.4	350.9	–21.7	500	595
164R-4, 60–62	803.21	Th	R	6	F	4.2	29.4	–35.2	400	595
165R-3, 118–120	807.65	Th	R	4	F	5.6	205.2	–44.9	500	595
166R-1, 36–38	808.96	AF	R	6	F	4.1	138.6	–59.4	15	80
166R-4, 112–114	813.65	Th	D	5	F	14.7	78.1	69.6	400	595
167R-1, 10–12	813.50	Th	D	8	F	5.3	32	79.1	200	595
167R-3, 114–116	817.21	Th	N	8	F	5.4	38.7	63.8	200	595
168R-3, 49–57	821.29	Th	R	5	F	4.5	139.9	–41.9	500	595
169R-1, 19–21	823.19	Th	R	5	F	4.1	330.6	–14.5	500	595
169R-3, 57–59	826.45	AF	R	6	F	3.2	237.5	–40.4	15	80
170R-1, 69–71	828.49	AF	R	6	F	7.1	337	–35	20	100
170R-2, 131–133	829.98	Th	R	5	A	9.8	137.4	–16.7	500	595
170R-4, 48–50	831.81	Th	H	4	A	7.8	87.6	–8.2	500	585
171R-1, 131–133	833.91	Th	R	5	F	7.2	132.1	–20.1	500	595
171R-4, 109–111	837.40	AF	R	5	F	2.8	54	–32.9	20	80
172R-1, 107–109	838.47	Th	R	6	A	5.1	10.5	–12.3	525	595
173R-1, 106–108	843.26	Th	R	6	F	5.5	43.4	–28.7	525	595
174R-1, 7–9	847.07	Th	R	6	F	6	131.5	–35.3	525	595
175R-3, 118–120	855.37	Th	N	5	F	8.4	346	11.4	500	585
175R-4, 17–19	855.64	Th	N	6	F	4.5	306.1	45.2	500	595
176R-2, 14–16	857.85	AF	R	8	F	4.2	122.3	–51.8	10	100
176R-4, 122–124	861.24	—	—	—	—	—	—	—	—	—
177R-3, 15–17	864.24	Th	R	3	A	2.3	215.4	–49.1	575	595
178R-2, 26–28	867.77	Th	R	7	F	2.1	0.1	–40.9	500	595
180R-1, 58–60	876.38	Th	N	5	F	3.2	344.8	47.5	550	595
180R-1, 68–70	876.48	Th	D	9	F	5.6	336.9	74.9	300	595
180R-2, 131–133	877.91	Th	D	7	F	6.4	343.2	67	500	595
181R-1, 82–84	881.42	Th	H	5	F	15	99.6	2.6	500	595
182R-1, 12–14	885.52	—	—	—	—	—	—	—	—	—
183R-1, 113–115	891.33	Th	H	4	F	3	30.8	–4.9	550	595
183R-3, 122–124	894.20	Th	R	3	F	4.4	1.1	–10.7	500	595
184R-2, 64–66	896.80	Th	R	5	F	5.1	124.9	–28.8	500	595

Table T16 (continued).

Core, section, interval (cm)	Depth (mbsf)	Demag type	Principal component analysis							
			Polarity	*N*	Type	MAD (°)	Declination (°)	Inclination (°)	Demag (mT/°C) Low	Demag (mT/°C) High
185R-2, 68–70	901.90	Th	N	5	F	11.4	337.4	36.1	500	595
186R-3, 100–102	908.49	—	—	—	—	—	—	—	—	—
187R-3, 74–76	912.12	—	—	—	—	—	—	—	—	—
188R-3, 89–91	917.38	—	—	—	—	—	—	—	—	—
189R-1, 110–112	920.10	—	—	—	—	—	—	—	—	—
189R-3, 90–92	922.59	Th	D	7	F	2.9	26.5	80	300	595
190R-1, 28–30	924.08	Th	N	7	A	11	210.1	19.4	300	595
191R-3, 86–88	928.38	Th	R	5	F	5.4	180.4	–31.7	500	595
192R-1, 140–142	930.00	Th	R	3	F	2.6	324.6	–38.4	500	575
193R-2, 59–61	935.49	Th	R	6	F	9.9	68.8	–63.7	300	585
194R-2, 97–99	939.85	—	—	—	—	—	—	—	—	—
195R-1, 98–100	943.98	Th	R	5	F	4.8	160	–37	400	585
196R-3, 28–30	950.74	Th	R	4	F	6	149.2	–42.1	500	585
197R-1, 112–114	953.72	Th	R	5	F	4.7	203.1	–36.3	500	595
197R-4, 25–27	956.66	Th	D	7	F	5	293.1	68.9	200	595
198R-1, 108–110	958.48	Th	R	5	F	5.2	192.7	–29	500	595
198R-3, 101–103	960.39	Th	R	5	F	2.1	198.4	–35	400	620
199R-2, 42–44	963.96	Th	R	5	F	9.2	209.8	–36.5	500	595
200R-1, 44–46	965.64	Th	R	4	F	1.6	245.7	–40.3	550	595
200R-3, 100–102	968.58	AF	R	5	F	3.6	353.7	–31	30	100
201R-1, 112–114	970.82	Th	R	5	F	4.5	151.1	–36.7	500	595
202R-3, 52–54	975.33	Th	R	5	F	5.1	148	–47.6	500	595
202R-4, 8–10	975.97	Th	R	4	F	4.5	300.4	–61.7	550	595
203R-1, 5–7	976.85	Th	R	4	F	1.9	206.2	–43.8	550	595
204R-3, 52–54	984.60	Th	R	4	F	6	109.3	–46.7	550	595
204R-6, 40–42	988.70	AF	R	7	F	4.2	266.7	–27.7	15	100
205R-1, 117–119	987.57	Th	N	4	A	7.7	56.3	38.6	550	595
206R-1, 14–16	991.34	Th	D	5	F	2.1	355.2	73.3	500	595
207R-1, 93–95	995.13	Th	R	4	F	3.9	23.3	–30.8	550	595
207R-3, 68–70	997.88	Th	R	5	F	1.5	327.6	–44.2	500	595
208R-1, 18–20	1000.98	Th	R	4	F	3.5	8.8	–34.2	550	595
209R-2, 37–39	1007.13	Th	N	7	A	5.3	24.4	58.7	300	595
210R-1, 96–98	1011.36	—	—	—	—	—	—	—	—	—
210R-3, 3–5	1012.93	Th	R	5	F	3.6	327.5	–29.1	500	595
211R-5, 66–68	1021.09	Th	R	5	F	4.3	21	–39.3	500	595
212R-2, 37–39	1021.58	Th	R	4	F	11	99.3	–41	550	595
213R-2, 77–79	1027.02	Th	R	6	F	11.7	219.7	–37.5	500	620
214R-3, 36–38	1032.44	Th	D	7	F	6.2	189.7	89	300	595
215R-1, 28–30	1034.68	Th	N	6	F	5.1	315.4	50.3	400	595
215R-4, 141–143	1038.89	—	—	—	—	—	—	—	—	—
216R-1, 96–98	1040.16	Th	N	4	A	7.7	10.5	40	500	595
217R-2, 85–87	1046.26	AF	R	6	F	5	331	–38.2	20	100
217R-3, 38–40	1046.94	Th	R	4	F	3.9	160.2	–24.9	575	620
218R-3, 35–37	1051.78	Th	D	8	F	8.4	105.1	86.1	200	595
219R-2, 85–87	1055.77	Th	D	4	A	6	73.1	71.4	575	620
220R-1, 126–128	1059.66	AF	R	4	F	2.7	15.7	–27.8	20	60
222R-1, 117–119	1069.17	Th	R	5	F	2.3	164.2	–43.6	500	595
222R-4, 26–28	1072.45	AF	R	6	A	1.2	359.5	–42.7	15	80
223R-2, 37–39	1074.31	Th	R	5	F	4.1	235.2	–39.9	500	595
224R-1, 46–48	1078.06	—	—	—	—	—	—	—	—	—
225R-1, 120–122	1083.60	Th	R	5	F	3.9	334.1	–41.8	500	595
225R-3, 117–119	1086.36	Th	R	5	F	3.6	154	–22	500	595
226R-1, 3–5	1087.23	AF	R	6	F	5.2	167.3	–51.5	20	100
226R-3, 61–63	1090.71	Th	R	5	F	11.1	227.8	–35.3	500	595
227R-2, 46–48	1093.89	AF	D	6	F	3.1	214.9	65.8	10	60
227R-3, 90–92	1095.83	Th	D	8	F	6.3	286.1	84.6	200	595
228R-2, 92–94	1098.93	—	—	—	—	—	—	—	—	—
228R-4, 16–18	1100.86	Th	D	8	F	11.9	101.1	76.6	200	595
229R-1, 57–59	1102.17	Th	N	6	F	10.3	295.2	42.9	400	595
230R-1, 72–74	1106.22	AF	R	5	F	5.2	179.9	–35.5	20	80
230R-3, 128–130	1109.66	Th	H	6	F	13.4	165.1	3.1	400	595
231R-1, 65–67	1110.95	—	—	—	—	—	—	—	—	—
232R-1, 45–47	1115.55	—	—	—	—	—	—	—	—	—
232R-3, 123–125	1119.15	Th	D	8	F	3.6	342.2	71.8	200	595
233R-2, 60–62	1122.00	Th	N	8	F	4.9	53.2	64.5	200	595
234R-1, 122–124	1125.92	Th	D	8	F	2.4	340.3	84.5	200	595
234R-4, 23–25	1129.33	Th	D	5	F	3.2	332.4	75	500	595
235R-1, 78–80	1130.28	Th	D	8	F	3	168.4	86.8	200	595

Table T16 (continued).

Core, section, interval (cm)	Depth (mbsf)	Demag type	Principal component analysis							
			Polarity	*N*	Type	MAD (°)	Declination (°)	Inclination (°)	Demag (mT/°C) Low	Demag (mT/°C) High
236R-1, 59–61	1134.89	Th	D	8	F	5.9	82.9	75.4	200	595
236R-3, 6–8	1137.21	—	—	—	—	—	—	—	—	—
237R-1, 88–90	1139.98	Th	D	8	F	3.7	77.1	70.4	200	595
238R-1, 119–121	1145.09	Th	N	4	F	8.2	9.6	19.8	550	595
239R-2, 47–49	1150.60	Th	R	5	F	5.5	170.1	–35.2	500	595
240R-2, 80–82	1155.54	Th	D	8	F	3.6	10.9	78.1	200	595
241R-1, 21–23	1158.51	Th	D	8	F	1.5	73.8	71.1	200	595
242R-1, 30–32	1163.40	AF	D	8	F	1	224.2	74.6	5	80
242R-2, 95–97	1165.32	Th	D	8	F	3.1	354.7	85.1	200	595
243R-1, 13–15	1168.03	Th	D	9	F	8.4	107.4	72.1	100	595
244R-2, 113–115	1175.13	Th	N	4	F	4.3	48.7	63	550	595
245R-1, 40–42	1177.90	Th	R	5	F	2.8	101.2	–41.4	500	595
246R-1, 106–109	1183.36	Th	D	5	F	5.5	64	75.4	200	550
247R-2, 9–11	1188.58	Th	D	4	F	4.6	119.6	65.4	550	595
248R-2, 34–36	1193.48	AF	R	4	F	3.2	310.3	–42.4	30	80
248R-3, 45–47	1194.94	AF	N	5	F	6.2	342.8	12.9	30	80
249R-1, 94–96	1197.64	Th	N	4	F	4.7	113.2	55.5	575	620
250R-3, 23–25	1204.31	Th	D	7	F	6.7	131.4	84.7	300	595
251R-1, 85–87	1207.15	Th	N	6	F	6.8	28.7	42	400	595
252R-1, 100–102	1212.10	Th	R	6	F	5.6	88.3	–25.9	400	595
253R-2, 77–79	1218.14	Th	R	6	F	2.2	28.3	–28.5	400	595
254R-1, 48–50	1221.18	Th	R	4	A	2.4	331.6	–16.6	550	595
255R-1, 94–96	1226.44	Th	D	4	A	10.3	58.7	72.1	550	595
256R-2, 98–100	1232.42	Th	N	6	A	2.3	107.2	58.1	400	595
257R-1, 49–51	1235.59	Th	N	6	F	6.4	119	62.6	400	595
258R-1, 46–48	1240.36	Th	R	5	F	4.9	197.5	–33.2	500	595
259R-1, 93–95	1245.63	AF	R	6	F	5	354.8	–19.2	30	100
260R-1, 133–135	1250.83	AF	R	6	F	6.9	27.3	–45.1	30	100
261R-3, 83–85	1257.85	AF	R	7	F	9.7	330	–31.4	20	100
262R-3, 72–74	1262.67	Th	H	6	F	11.9	70.1	7.3	400	595
263R-1, 43–45	1264.33	Th	N	8	F	12.7	43.6	53.1	200	595
264R-2, 55–57	1270.75	Th	R	3	A	2	259.1	–29.2	575	595
265R-1, 85–87	1274.35	Th	R	4	F	3.3	62.2	–31.1	500	585
266R-2, 4–6	1279.49	Th	D	3	A	3.3	284	81.7	575	595
267R-2, 106–108	1285.60	Th	R	5	F	0.8	162.3	–32.6	500	595
268R-2, 61–63	1289.84	Th	N	8	F	16	278.8	53.5	200	595
268R-4, 23–25	1292.20	Th	N	5	F	9.3	140.5	11.8	500	595
269R-2, 74–76	1294.90	Th	R	6	F	3.6	293.9	–37	400	595
270R-3, 131–133	1301.59	Th	D	7	F	2.4	17.7	83.2	300	595
271R-2, 7–9	1303.76	Th	R	5	F	2.5	244.8	–33	500	595
272R-3, 28–30	1310.28	Th	D	6	F	2.8	55.5	72.2	400	595
273R-1, 12–14	1312.02	Th	R	4	F	0.7	327.7	–28.1	550	595
274R-1, 33–35	1317.03	Th	R	6	F	4.4	164.7	–40.9	400	595
275R-2, 116–118	1323.97	Th	R	5	F	2.1	246.6	–36	500	595
276R-1, 40–42	1326.70	Th	R	4	F	5.1	121.7	–59.5	575	620
277R-1, 61–63	1330.21	Th	D	9	F	8.8	6.8	70	100	595
278R-1, 26–28	1334.66	Th	R	5	F	2.3	34.1	–39	500	595
279R-4, 38–40	1343.56	Th	R	4	F	7	271.2	–11.3	500	585
280R-1, 92–94	1344.92	Th	R	5	F	2.8	257.6	–33.1	500	595
281R-1, 105–107	1349.85	Th	R	4	F	0.4	156.2	–25.3	550	595
282R-1, 30–32	1353.90	Th	R	5	F	1.8	319.5	–18.4	500	595
283R-1, 6–8	1358.46	Th	R	4	F	6.1	95.2	–46.2	550	595
284R-2, 80–82	1365.11	Th	R	4	F	3.9	148.1	–37.3	550	595
285R-1, 82–84	1368.82	Th	R	5	F	6.2	16	–19.6	500	595
286R-2, 134–136	1375.64	Th	R	5	F	7.4	332.8	–33	500	595
287R-1, 8–10	1377.68	Th	R	4	F	6.8	325.3	–21.3	550	595
288R-1, 15–17	1379.75	Th	R	5	F	7.1	156.3	–12.2	500	595
290R-2, 111–113	1389.45	Th	R	5	F	4.9	294.5	–23.1	500	595
291R-4, 118–120	1396.61	Th	N	6	A	9.9	273.4	20.6	400	595
292R-2, 59–61	1398.44	Th	R	5	F	3	184.6	–28.2	500	595
293R-1, 59–61	1402.19	Th	N	3	F	2	309.8	20.6	585	620
294R-1, 93–95	1407.33	AF	R	7	F	0.9	307.4	–27.7	15	100
295R-2, 70–72	1413.40	AF	R	7	F	2.1	342.7	–25.7	15	100

Notes: MAD = maximum angular deviation, Demag = demagnetization, *N* = number of demagnetization steps used in PCA, AF = alternating-field, Th = thermal, R = reversed, N = normal, H = polarity uncertain, D = drilling-induced magnetization, F = free of origin, A = anchored. This table is also available in **ASCII.**

Table T17. Königsberger ratios of rock samples, Hole U1309D, Expedition 305. (See table notes. Continued on next two pages.)

Core, section, interval (cm)	Depth (mbsf)	MS (x 10^{-6} SI)	NRM (A/m)	*Q* ratio
305-U1309D-				
80R-1, 82	402.12	3,055	0.132	1.33
80R-2, 35	402.95	1,175	0.374	9.78
80R-3, 25	404.36	8,870	3.24	11.20
81R-1, 103	406.43	21,720	0.268	0.38
81R-2, 46	407.30	7,330	4.44	18.60
81R-3, 27	408.61	1,105	0.0196	0.55
81R-4, 25	410.06	9,130	0.652	2.19
82R-1, 69	410.89	14,250	0.517	1.11
82R-2, 114	412.75	8,090	3.63	13.80
83R-1, 41	415.41	8,750	4.29	15.00
83R-1, 65	415.65	828	0.0883	3.28
83R-2, 36	416.51	8,923	5.27	18.10
84R-2, 118	422.06	1,592	0.194	3.74
84R-3, 65	422.88	833	0.692	25.50
85R-1, 52	425.12	9,110	7.30	24.60
85R-2, 126	427.11	47,310	8.14	5.28
85R-3, 28	427.45	300	0.0254	2.60
86R-1, 83	430.23	386	0.313	24.90
86R-2, 77	431.67	712	0.334	14.40
86R-3, 89	433.28	66,257	8.55	3.96
87R-1, 93	435.13	23,420	6.95	9.11
87R-2, 111	436.77	45,400	0.933	0.63
88R-2, 55	438.67	1,763	1.39	24.20
88R-4, 20	440.09	4,310	2.29	16.30
88R-5, 64	441.99	32,200	0.264	0.25
89R-2, 18	445.38	53,450	14.1	8.10
90R-1, 58	449.18	1,138	0.279	7.53
90R-2, 120	451.30	6,950	0.956	4.22
90R-3, 70	452.30	49,500	13.8	8.56
91R-1, 105	454.45	17,940	4.69	8.03
91R-2, 108	455.96	7,180	1.82	7.79
91R-3, 32	456.70	25,620	5.95	7.13
92R-1, 120	459.40	560	0.190	10.40
92R-2, 4	459.65	5,140	0.928	5.54
93R-1, 127	464.27	434	0.0234	1.65
94R-1, 20	468.00	428	1.50	107.00
94R-2, 12	469.42	996	0.756	23.30
95R-1, 59	473.19	432	0.0832	5.92
95R-2, 92	474.93	1,354	0.909	20.60
95R-3, 127	476.65	878	0.438	15.30
96R-2, 44	479.21	590	0.290	15.10
96R-3, 20	480.41	4,040	0.494	3.76
97R-1, 110	483.30	726	0.124	5.25
98R-1, 75	487.75	514	0.144	8.62
98R-2, 121	489.50	646	0.0771	3.67
98R-3, 91	490.61	724	0.1373	5.82
99R-1, 110	492.90	1,488	0.620	12.80
100R-1, 56	495.86	39,750	8.70	6.72
100R-3, 3	499.17	68,150	20.3	9.15
101R-1, 57	500.67	47,200	0.1862	0.12
101R-3, 116	503.68	30,100	10.4	10.60
101R-4, 58	504.47	23,900	9.99	12.80
101R-5, 53	505.70	41,800	4.121	3.03
102R-1, 81	507.01	9,160	3.4591	11.60
102R-2, 142	509.06	7,160	1.71	7.33
103R-1, 102	512.02	590	5.067	264.00
103R-2, 144	513.89	608	0.2109	10.70
104R-1, 32	516.12	5,710	0.28233	1.52
104R-2, 112	518.24	3,950	1.7228	13.40
104R-3, 118	519.80	11,310	3.18	8.64
105R-1, 94	521.54	1,480	0.199	4.13
105R-2, 106	523.04	1,290	0.271	6.46
106R-3, 53	528.42	406	0.0496	3.75
107R-1, 14	530.34	3,770	1.19	9.69
107R-3, 22	532.45	9,280	5.3211	17.60
107R-4, 137	534.89	960	0.6385	20.40
108R-1, 109	536.09	5,370	0.605	3.46
108R-2, 113	537.28	1,900	0.2553	4.13
108R-3, 77	538.16	2,430	0.9434	11.90
109R-1, 123	541.03	1,145	1.6543	44.40
109R-2, 36	541.51	2,315	3.7907	50.30
109R-3, 77	543.16	13,740	1.97	4.40
110R-1, 99	545.59	3,260	1.16	10.90
111R-1, 118	550.58	51,000	20.9	12.60
111R-4, 44	554.01	133,500	44.0	10.10
112R-1, 26	554.46	80,500	25.0	9.55
113R-1, 97	559.97	58,217	32.8	17.30
113R-2, 100	560.34	33,500	10.12	9.28
113R-4, 58	562.87	23,460	4.3633	5.71
114R-1, 52	564.32	71,333	28.489	12.30
114R-2, 81	566.11	406	0.0362	2.74
114R-2, 112	566.42	392	2.0169	158.00
114R-3, 72	567.12	183	0.31	52.00
115R-1, 20	568.80	520	0.03819	2.26
115R-2, 140	571.23	590	0.111	5.79
115R-3, 86	572.16	355	0.1872	16.20
115R-4, 47	573.21	435	0.02414	1.70
116R-2, 39	575.18	915	0.02082	0.70
116R-4, 33	577.04	46,300	2.79	1.85
117R-1, 70	578.90	34,220	21.6	19.40
117R-1, 107	579.27	64,750	9.7186	4.61
117R-2, 99	580.40	6,550	2.6449	12.40
118R-1, 107	584.07	460	0.08063	5.38
118R-2, 45	584.78	500	0.09594	5.89
118R-3, 78	586.55	565	0.0918	4.99
119R-1, 40	588.20	810	0.139	5.27
119R-2, 17	589.33	430	0.03803	2.72
119R-3, 87	591.53	590	1.503	78.20
119R-4, 15	592.10	24,200	4.1763	5.30
120R-1, 26	592.86	10,020	1.5601	4.78
120R-3, 127	596.55	8,460	6.5745	23.90
120R-4, 89	597.50	17,680	0.766	1.33
121R-2, 113	599.51	1,570	0.320	6.26
122R-1, 117	603.37	61,450	6.34	3.17
122R-2, 113	604.61	1,880	0.156	2.55
122R-3, 33	605.26	940	0.228	7.45
123R-1, 38	607.38	30,660	8.21	8.22
124R-1, 67	612.47	1,050	0.470	13.70
124R-3, 56	614.93	4,260	0.3937	2.84
124R-4, 12	615.52	4,890	6.2	38.90
125R-2, 41	617.40	928	0.243	8.04
125R-3, 78	619.11	2,640	1.0024	11.70
126R-1, 27	621.67	3,115	0.765	7.54
126R-3, 61	624.92	1,530	0.358	7.18
127R-1, 25	626.45	2,780	3.911	43.20
127R-2, 40	628.10	12,480	5.43	13.40
128R-3, 88	634.79	1,840	0.417	6.96
129R-1, 63	636.43	4,720	1.31	8.52
129R-3, 34	638.66	53,450	1.9554	1.12
130R-3, 56	643.99	37,700	9.45	7.70
131R-1, 35	645.75	36,400	6.03	5.09
131R-2, 117	648.00	4,310	1.8512	13.20
132R-1, 97	650.84	1,550	0.511	10.10
132R-3, 136	653.69	7,850	2.0725	8.11
132R-4, 79	654.58	40,200	1.6671	1.27
133R-1, 100	656.00	1,220	0.185	4.65
133R-3, 137	658.88	7,430	1.296	5.36
134R-1, 94	660.89	1,870	0.325	5.33
134R-2, 67	661.77	5,770	1.61	8.59
135R-1, 75	665.35	88,450	28.5	9.88
135R-2, 92	666.90	10,200	2.38	7.16
136R-1, 123	670.63	3,740	0.521	4.28
138R-2, 130	681.80	1,610	0.47358	9.03

Table T17 (continued).

Core, section, interval (cm)	Depth (mbsf)	MS (x 10^{-6} SI)	NRM (A/m)	Q ratio
138R-3, 106	682.97	3,390	0.855	7.74
139R-1, 97	683.52	86,800	6.4326	2.28
139R-3, 76	686.07	16,400	5.41	10.10
140R-3, 69	691.17	12,460	2.85	7.02
141R-1, 28	693.68	20,380	6.9159	10.40
141R-2, 140	696.22	8,120	3.20	12.10
142R-1, 4	698.24	620	1.9426	96.20
142R-2, 139	701.00	13,070	6.55	15.40
142R-3, 82	701.87	11,720	3.4538	9.05
143R-2, 72	704.76	8,340	3.58	13.20
144R-1, 70	708.50	10,060	2.51	7.68
144R-2, 118	710.45	1,230	0.257	6.41
145R-2, 82	714.92	1,450	1.17	24.70
145R-4, 7	716.77	480	0.1568	10.00
146R-1, 131	718.71	650	0.0859	4.06
147R-2, 113	724.83	2,195	4.8267	67.50
147R-4, 6	726.37	3,735	0.572	4.71
148R-3, 17	729.91	16,390	2.21	4.14
149R-1, 141	733.21	2,000	0.316	4.86
149R-3, 27	734.83	290	0.0227	2.40
150R-4, 37	740.40	2,330	1.15	15.20
151R-2, 13	743.03	22,560	8.78	12.00
153R-1, 37	751.37	7,010	1.61	7.05
153R-2, 102	753.52	765	0.0302	1.21
154R-2, 10	757.28	7,905	3.82	14.80
155R-1, 104	758.84	36,280	11.6	9.83
155R-2, 113	760.07	34,940	7.2663	6.39
156R-3, 68	764.07	700	0.118	5.16
157R-2, 113	767.90	547	0.0549	3.08
157R-3, 138	769.65	22,840	7.99	10.70
158R-4, 81	774.59	1,410	0.663	14.40
159R-3, 10	778.01	3,010	9.8725	101.00
159R-4, 62	779.31	86,950	28.7	10.10
160R-2, 6	781.36	1,370	0.61	13.70
160R-3, 104	783.82	9,380	3.05	9.97
161R-2, 63	786.62	55,350	40.7	22.60
162R-2, 130	792.05	10,700	2.521	7.24
162R-4, 14	793.44	6,720	0.766	3.50
163R-4, 7	798.53	6,600	1.33	6.21
164R-2, 59	800.77	4,390	0.678	4.74
164R-4, 60	803.21	1,450	0.3158	6.69
165R-3, 118	807.65	1,350	0.682	15.50
166R-1, 36	808.59	1,200	0.2648	6.78
166R-4, 112	813.28	6,800	2.37	10.70
167R-1, 10	813.50	10,600	3.92	11.30
167R-3, 114	817.21	8,360	0.2307	0.85
168R-3, 49	821.29	770	0.175	6.96
169R-1, 19	822.97	4,160	0.878	6.48
169R-3, 57	826.23	1,960	0.2194	3.44
170R-1, 69	827.97	3,205	0.6264	6.00
170R-2, 131	829.46	2,715	0.5926	6.70
170R-4, 48	831.29	3,740	0.753	6.18
171R-1, 131	833.91	3,175	0.500	4.84
171R-4, 109	837.40	1,790	0.3295	5.65
172R-1, 107	838.47	9,810	1.57	4.92
173R-2, 106	844.39	2,900	0.392	4.15
174R-1, 7	847.00	1,546	0.207	4.10
175R-1, 98	852.63	4,210	0.6769	4.94
175R-3, 118	855.22	29,160	0.793	0.84
176R-2, 14	857.85	8,330	2.13	7.85
176R-4, 122	861.24	1,914	0.641	10.30
177R-3, 15	864.24	14,490	3.00	6.35
178R-2, 26	867.77	1,625	0.336	6.34
180R-1, 58	876.28	14,510	3.64	7.70
180R-1, 68	876.38	11,320	0.859	2.33
180R-2, 131	877.81	6,680	1.72	7.89
181R-1, 82	881.27	2,310	0.668	8.87
182R-1, 12	885.52	54,050	16.1	9.15
183R-1, 113	891.33	7,960	2.96	11.40
183R-3, 122	894.20	1,978	0.689	10.70
184R-2, 64	896.80	1,755	0.301	5.26
185R-2, 68	901.90	6,030	2.02	10.30
186R-3, 100	908.49	7,795	2.56	10.10
187R-3, 74	912.12	20,100	4.74	7.24
188R-3, 89	917.05	9,630	2.40	7.65
189R-1, 110	920.10	5,900	2.49	13.00
189R-3, 90	922.79	13,540	10.6	24.10
190R-1, 28	924.08	10,390	2.84	8.39
191R-3, 86	928.38	8,920	3.10	10.70
192R-1, 140	930.15	1,150	0.356	9.50
193R-2, 59	934.82	836	2.52	92.60
194R-2, 97	939.68	2,906	1.01	10.70
195R-1, 98	943.98	3,218	2.35	22.40
196R-3, 28	950.19	6,620	1.70	7.87
197R-1, 112	953.29	10,400	1.41	4.16
197R-4, 25	956.23	31,480	11.1	10.80
198R-1, 108	958.37	5,405	1.53	8.67
198R-3, 101	960.28	4,855	4.29	27.10
199R-2, 42	963.21	2,836	3.21	34.80
200R-1, 44	965.64	3,106	0.758	7.49
200R-3, 100	968.58	22,140	7.092	9.84
201R-1, 112	970.82	4,190	2.14	15.70
202R-3, 52	975.43	5,030	2.07	12.70
202R-4, 8	976.07	6,320	2.205	10.70
203R-1, 5	977.20	1,878	7.34	120.00
204R-4, 52	983.74	2,906	2.98	31.50
204R-6, 40	986.39	1,900	1.137	18.40
205R-1, 117	987.85	13,390	1.86	4.28
206R-1, 14	991.34	27,480	4.90	5.47
207R-1, 93	994.56	15,240	1.21	2.45
207R-3, 68	997.31	4,490	0.77	5.27
208R-1, 18	1000.98	11,850	1.75	4.53
209R-2, 37	1007.13	1,908	0.624	10.10
210R-3, 3	1012.38	3,985	1.49	11.50
211R-5, 66	1019.33	9,400	5.11	16.70
212R-2, 37	1021.58	13,940	5.98	13.20
213R-2, 77	1027.02	2,780	1.11	12.30
214R-3, 36	1032.44	3,855	1.46	11.60
215R-1, 28	1034.68	1,384	0.800	17.70
215R-4, 141	1038.89	1,076	0.4529	12.90
216R-1, 96	1040.16	8,580	1.78	6.38
217R-2, 85	1046.26	5,465	2.062	11.60
217R-3, 38	1046.94	19,210	3.37	5.39
218R-3, 35	1050.90	2,265	0.512	6.95
219R-2, 85	1055.45	7,985	1.86	7.13
220R-1, 126	1059.60	2,672	0.809	9.30
222R-1, 117	1068.62	2,730	0.3318	3.73
222R-4, 26	1071.90	3,702	2.84	23.60
233R-2, 37	1074.31	1,996	3.87	59.50
224R-1, 46	1078.06	3,212	0.887	8.48
225R-1, 120	1083.60	1,364	1.002	22.60
225R-3, 117	1086.36	1,558	0.216	4.26
226R-1, 3	1087.23	2,194	0.892	12.50
226R-3, 61	1090.71	1,436	0.504	10.80
227R-2, 46	1093.89	82,300	44.0	16.40
227R-3, 90	1095.83	8,370	3.64	13.40
228R-2, 92	1098.93	94,850	24.873	8.05
228R-4, 16	1100.86	13,430	4.34	9.92
229R-1, 57	1102.17	4,775	1.13	7.27
230R-1, 72	1106.22	2,670	2.19	25.10
230R-3, 128	1109.66	6,090	0.690	3.48
231R-1, 65	1110.95	3,010	0.276	2.82
232R-1, 45	1115.55	41,700	28.91	21.30
232R-3, 123	1119.15	36,340	22.8	19.30
233R-2, 60	1122.00	36,800	20.5	17.10
234R-1, 122	1125.92	31,850	16.8	16.20
234R-4, 23	1129.33	38,100	11.38	9.17
235R-1, 78	1130.28	35,300	19.6	17.00

Table T17 (continued).

Core, section, interval (cm)	Depth (mbsf)	MS (x 10^{-6} SI)	NRM (A/m)	Q ratio
236R-1, 59	1134.89	35,500	19.3	16.70
236R-3, 6	1137.21	3,766	0.548	4.47
237R-1, 88	1139.98	55,850	24.8	13.60
238R-1, 119	1145.09	79,900	19.9	7.66
239R-2, 47	1150.60	868	1.15	40.50
240R-2, 80	1155.54	53,800	34.9	19.90
241R-1, 21	1158.51	101,200	68.5	20.80
242R-1, 30	1163.40	57,150	9.05	4.86
242R-2, 95	1165.32	78,750	39.6	15.40
243R-1, 13	1168.03	96,800	51.2	16.20
244R-2, 113	1175.13	2,005	0.452	6.93
245R-1, 40	1177.90	532	0.651	37.60
246R-1, 106	1183.36	10,520	2.34	6.84
247R-2, 9	1188.58	87,150	45.9	16.20
248R-2, 34	1193.48	6,730	1.39	6.36
248R-3, 45	1194.94	8,085	1.062	4.03
249R-1, 94	1197.64	7,130	0.8854	3.81
250R-3, 23	1204.31	14,050	1.591	3.48
251R-1, 85	1207.15	15,230	4.9263	9.93
252R-1, 100	1212.10	1,260	0.6185	15.10
253R-2, 77	1218.14	760	0.08119	3.28
254R-1, 48	1221.18	102,800	7.544	2.25
255R-1, 94	1226.44	13,970	2.179	4.79
256R-2, 98	1232.42	33,750	7.087	6.45
257R-1, 49	1235.59	36,800	6.056	5.05
258R-1, 46	1240.36	4,640	0.686	4.54
259R-1, 93	1245.63	5,040	2.358	14.40
260R-1, 133	1250.83	20,340	5.157	7.79
261R-3, 83	1257.85	11,140	3.819	10.50
262R-3, 72	1262.31	5,540	2.669	14.80
263R-1, 43	1264.33	7,455	0.2552	1.05
264R-2, 55	1270.75	16,540	3.3522	6.22
265R-1, 85	1274.35	910	0.1698	5.73
266R-2, 4	1278.34	3,450	0.245	2.18
267R-2, 106	1285.60	1,878	30.4	496.00
268R-2, 61	1289.84	14,300	2.167	4.65
268R-4, 23	1292.20	8,325	1.37	5.05
269R-2, 74	1294.90	942	0.2381	7.76
270R-3, 131	1301.59	78,130	0.8077	0.318
271R-2, 7	1303.76	3,655	1.047	8.80
272R-3, 28	1310.28	177,300	15.11	2.62
273R-1, 12	1312.02	14,220	1.252	2.70
274R-1, 33	1317.03	1,972	2.159	33.60
275R-2, 116	1323.97	7,285	2.1253	8.96
276R-1, 40	1326.91	168,500	5.016	0.91
277R-1, 61	1330.21	158,900	9.747	1.88
278R-1, 26	1334.66	912	0.501	16.90
279R-4, 38	1343.56	11,160	0.838	2.31
280R-1, 92	1344.92	6,090	0.9349	4.71
281R-1, 105	1349.85	5,640	1.329	7.24
282R-1, 30	1353.90	8,095	0.9341	3.54
283R-1, 6	1358.46	2,598	1.776	21.00
284R-2, 80	1364.00	5,770	1.8655	9.93
285R-1, 82	1368.82	11,550	0.925	2.46
286R-2, 134	1375.64	992	0.2507	7.76
287R-1, 8	1377.68	870	1.947	68.70
288R-1, 15	1379.28	5,910	2.7055	14.10
290R-2, 111	1389.45	3,970	0.7654	5.92
291R-4, 118	1396.61	11,390	0.2671	0.720
292R-2, 59	1398.44	2,670	0.6624	7.62
293R-1, 59	1402.19	7,625	1.4044	5.66
294R-1, 93	1407.33	1,745	1.469	25.90
295R-2, 70	1413.40	1,530	0.9802	19.70

Notes: MS = magnetic susceptibility, NRM = natural remanent magnetization, *Q* ratio = Königsberger ratio. This table is also available in **ASCII.**

Table T18. Anisotropy of magnetic susceptibility, Hole U1309D, Expedition 305. (See table notes. Continued on next three pages.)

Core, section, interval (cm)	Depth (mbsf)	Maximum			Intermediate			Minimum			P (max/min)
		k	Declination (°)	Inclination (°)	k	Declination (°)	Inclination (°)	k	Declination (°)	Inclination (°)	
305-U1309D-											
80R-2, 35	402.96	0.3527	75.7	48.8	0.3292	326.5	16.0	0.3181	224.2	36.7	1.11
81R-1, 103	406.43	0.4082	359.8	0.8	0.3683	269.1	39.5	0.2235	90.8	50.5	1.83
81R-3, 27	408.61	0.4047	122.0	75.7	0.3386	300.2	14.3	0.2567	30.3	0.4	1.58
83R-1, 41	415.41	0.3502	339.1	11.4	0.3349	94.7	65.0	0.3150	244.4	21.9	1.11
87R-2, 111	436.77	0.3512	316.1	26.4	0.3382	215.2	20.8	0.3107	91.9	55.2	1.13
88R-1, 64	437.53	0.3538	225.5	17.1	0.3328	322.3	21.1	0.3135	99.6	62.3	1.13
89R-2, 18	445.38	0.3442	148.7	2.2	0.3389	242.8	61.9	0.3169	57.6	28.0	1.09
90R-2, 120	451.30	0.3487	96.4	23.0	0.3357	3.7	6.3	0.3156	259.3	66.0	1.10
90R-3, 72	452.32	0.3641	272.3	64.1	0.3396	158.4	11.1	0.2963	63.6	23.0	1.23
91R-1, 105	454.45	0.3644	180.5	57.5	0.3344	280.2	6.1	0.3012	14.0	31.8	1.21
91R-2, 108	455.96	0.3614	174.2	6.7	0.3339	82.2	16.5	0.3047	285.6	72.1	1.19
91R-3, 32	456.70	0.3577	268.0	20.9	0.3380	156.7	43.5	0.3043	16.1	39.2	1.18
95R-1, 59	473.19	0.4176	53.8	45.3	0.3620	256.9	42.3	0.2204	155.9	11.8	1.90
96R-3, 20	480.41	0.3474	231.0	13.4	0.3368	321.4	1.5	0.3158	57.5	76.5	1.10
100R-1, 56	495.86	0.3666	359.6	3.4	0.3392	260.7	69.1	0.2942	90.9	20.6	1.25
100R-3, 111	499.29	0.3551	52.6	67.2	0.3287	159.2	6.8	0.3162	251.9	21.6	1.12
116R-4, 33	577.04	0.3546	177.6	37.8	0.3390	14.7	50.9	0.3064	274.2	8.4	1.16
117R-1, 72	578.92	0.3523	217.7	16.8	0.3291	124.5	10.6	0.3187	3.6	70.0	1.11
117R-1, 107	579.27	0.3524	319.0	57.4	0.3257	92.3	23.6	0.3219	192.0	21.1	1.09
117R-2, 99	580.40	0.3633	186.8	15.6	0.3340	286.2	30.3	0.3027	73.2	55.1	1.20
119R-4, 15	592.10	0.3616	24.5	4.1	0.3435	118.0	41.0	0.2949	289.9	48.7	1.23
120R-1, 26	592.86	0.3527	171.5	5.8	0.3324	78.9	23.7	0.3150	274.3	65.5	1.12
120R-3, 127	596.55	0.3803	182.0	25.7	0.3349	304.7	48.3	0.2848	75.7	30.3	1.34
120R-4, 89	597.50	0.3348	177.8	25.7	0.3317	310.7	54.7	0.3236	76.3	22.4	1.03
122R-1, 117	603.37	0.3507	142.3	4.2	0.3311	237.3	50.4	0.3182	48.8	39.3	1.10
124R-3, 56	614.93	0.3685	325.2	10.2	0.3374	232.0	17.2	0.2942	84.6	69.9	1.25
124R-4, 12	615.52	0.3958	194.4	8.5	0.3270	290.9	37.2	0.2772	93.5	51.5	1.43
125R-3, 78	619.11	0.4121	70.9	26.7	0.3462	175.5	26.6	0.2417	303.1	50.7	1.70
126R-3, 61	624.92	0.3514	51.4	11.9	0.3353	319.2	10.5	0.3132	188.7	74.1	1.12
127R-1, 25	626.45	0.3718	56.8	17.7	0.3264	196.7	67.3	0.3018	322.3	13.7	1.23
129R-3, 34	638.66	0.3637	301.7	30.1	0.3226	113.9	59.7	0.3137	209.7	3.4	1.16
130R-3, 56	643.99	0.3551	15.4	15.9	0.3438	264.6	51.4	0.3011	116.6	34.1	1.18
131R-2, 117	648.00	0.3880	300.8	33.8	0.3309	44.2	19.2	0.2812	158.5	49.8	1.38
132R-3, 136	653.69	0.3524	2.3	27.0	0.3241	191.4	62.7	0.3235	94.2	3.7	1.09
132R-4, 79	654.58	0.3558	328.3	38.3	0.3316	159.0	51.2	0.3126	62.4	5.2	1.14
133R-3, 137	656.37	0.3584	352.6	15.3	0.3322	246.1	46.0	0.3049	95.9	40.0	1.18
134R-1, 94	660.89	0.3573	31.6	33.7	0.3387	288.4	18.9	0.3040	174.3	50.0	1.18
134R-2, 67	661.77	0.3732	232.0	4.5	0.3324	111.6	81.1	0.2943	322.6	7.6	1.27
135R-1, 75	665.25	0.3593	312.1	28.9	0.3327	61.0	30.4	0.3081	187.8	45.6	1.17
135R-2, 92	666.90	0.3517	260.6	17.4	0.3290	51.7	70.2	0.3193	167.7	9.0	1.10
136R-1, 123	670.63	0.3499	24.2	3.2	0.3406	289.4	56.3	0.3096	116.4	33.5	1.13
138R-3, 106	682.97	0.3548	209.3	0.3	0.3370	299.9	67.4	0.3082	119.1	22.6	1.15
139R-3, 76	686.07	0.3483	356.2	40.1	0.3278	249.7	18.6	0.3239	140.7	44.0	1.08
140R-3, 69	688.80	0.3426	207.4	55.8	0.3335	350.9	28.7	0.3238	90.6	17.0	1.06
141R-2, 140	696.22	0.3423	64.0	22.1	0.3365	194.2	57.8	0.3231	324.5	22.2	1.06
142R-2, 139	701.00	0.3566	329.1	32.2	0.3269	226.7	18.8	0.3165	111.3	51.5	1.13
143R-2, 72	704.76	0.3428	327.6	54.6	0.3368	164.1	34.3	0.3204	68.7	7.8	1.07
144R-1, 70	708.50	0.3612	89.1	31.2	0.3363	226.3	50.5	0.3025	345.2	21.7	1.19
145R-2, 82	714.92	0.3444	65.7	35.5	0.3322	182.7	32.5	0.3234	302.3	37.7	1.07
147R-4, 6	726.37	0.3550	158.4	8.2	0.3317	68.0	2.7	0.3133	320.1	81.4	1.13
148R-3, 17	729.91	0.3458	2.3	21.4	0.3318	254.2	38.5	0.3224	114.4	43.8	1.07
149R-1, 141	733.21	0.4021	10.0	7.7	0.3342	129.2	74.5	0.2637	278.2	13.4	1.52
150R-4, 37	740.40	0.3552	154.9	11.3	0.3361	250.3	24.9	0.3087	42.5	62.3	1.15
151R-2, 13	743.03	0.3560	122.1	72.5	0.3288	257.4	12.6	0.3153	350.1	11.9	1.13
153R-1, 37	751.37	0.3534	206.8	12.4	0.3267	112.2	20.0	0.3200	326.7	66.2	1.10
154R-2, 10	757.28	0.3464	166.0	47.1	0.3282	261.2	4.8	0.3255	355.6	42.5	1.06
155R-1, 104	758.22	0.3393	56.7	23.4	0.3362	158.4	25.2	0.3244	289.5	54.4	1.05
155R-2, 113	760.07	0.3399	24.9	16.5	0.3348	293.3	5.5	0.3253	185.6	72.5	1.05
157R-3, 138	769.65	0.3808	308.5	4.4	0.3176	39.3	9.7	0.3016	194.3	79.3	1.26
159R-3, 10	778.01	0.3397	180.2	33.5	0.3321	326.3	51.4	0.3281	78.7	16.8	1.04
159R-4, 62	779.31	0.3432	307.1	5.1	0.3347	214.5	26.2	0.3222	47.3	63.2	1.07
160R-3, 104	783.82	0.3360	1.6	5.7	0.3350	254.3	71.3	0.3090	93.4	17.8	1.09
161R-2, 63	786.62	0.3498	15.0	5.1	0.3339	118.4	69.0	0.3163	283.1	20.3	1.11
162R-4, 14	793.44	0.3590	263.6	31.0	0.3357	140.5	42.3	0.3053	15.8	32.1	1.18
163R-4, 7	798.53	0.3864	118.9	4.2	0.3278	25.7	37.1	0.2858	214.4	52.5	1.35

Table T18 (continued).

Core, section, interval (cm)	Depth (mbsf)	Maximum			Intermediate			Minimum			*P* (max/min)
		k	Declination (°)	Inclination (°)	*k*	Declination (°)	Inclination (°)	*k*	Declination (°)	Inclination (°)	
164R-2, 59	800.77	0.3787	1.4	26.4	0.3594	96.2	9.6	0.2649	204.5	61.7	1.43
165R-3, 118	807.65	0.3508	42.4	11.1	0.3289	302.1	42.3	0.3204	143.9	45.5	1.09
166R-4, 112	813.28	0.3608	231.2	30.2	0.3379	330.5	15.6	0.3014	84.2	55.3	1.20
167R-1, 10	813.50	0.3590	199.3	26.7	0.3327	296.2	13.6	0.3084	50.5	59.5	1.16
167R-3, 114	817.21	0.3504	143.2	23.4	0.3315	30.5	41.7	0.3181	253.9	39.2	1.10
169R-1, 19	822.97	0.3584	6.8	20.9	0.3292	116.4	41.4	0.3124	257.1	41.3	1.15
170R-1, 69	827.97	0.3559	271.2	5.2	0.3434	1.4	2.8	0.3008	119.8	84.1	1.18
170R-2, 131	829.46	0.3487	198.5	2.0	0.3320	94.9	81.5	0.3194	288.8	8.2	1.09
170R-4, 48	831.29	0.3498	302.4	19.8	0.3386	91.4	67.2	0.3115	208.5	10.8	1.12
171R-1, 131	833.91	0.3706	123.9	45.6	0.3258	219.9	5.9	0.3036	315.6	43.8	1.22
172R-1, 107	838.47	0.3852	76.1	2.0	0.3254	167.8	41.0	0.2895	343.9	48.9	1.33
173R-1, 106	843.26	0.3708	81.0	24.9	0.3324	194.0	40.1	0.2968	328.4	39.7	1.25
174R-1, 7	847.00	0.3505	114.5	12.2	0.3414	257.7	74.9	0.3081	22.6	8.8	1.14
175R-3, 118	855.22	0.3560	34.6	34.8	0.3344	270.0	39.2	0.3096	149.9	31.5	1.15
175R-4, 17	855.49	0.3579	354.0	16.2	0.3254	193.0	72.9	0.3167	85.5	5.3	1.13
176R-2, 14	857.85	0.3566	288.8	30.5	0.3469	53.8	44.3	0.2965	178.7	30.4	1.20
176R-4, 122	861.22	0.3722	335.4	58.9	0.3540	193.6	25.4	0.2739	95.4	16.8	1.36
177R-3, 15	861.55	0.3576	131.0	2.3	0.3354	224.8	59.3	0.3070	39.7	30.6	1.16
178R-2, 26	867.77	0.3519	3.6	32.2	0.3277	111.1	25.5	0.3204	231.6	46.7	1.10
180R-1, 58	876.28	0.3420	274.8	26.5	0.3384	178.9	11.6	0.3197	67.5	60.7	1.07
180R-1, 68	876.38	0.3479	288.0	38.7	0.3338	30.6	15.1	0.3183	137.7	47.3	1.09
180R-2, 131	877.81	0.3618	27.8	49.8	0.3426	257.2	28.8	0.2956	152.0	25.4	1.22
181R-1, 82	881.27	0.3514	152.6	25.0	0.3337	254.2	23.3	0.3149	21.6	54.6	1.12
182R-1, 12	885.52	0.3495	216.8	16.0	0.3398	331.8	55.8	0.3107	117.5	29.3	1.13
183R-1, 113	891.33	0.3644	239.8	2.8	0.3220	135.3	78.9	0.3136	330.4	10.7	1.16
183R-3, 122	894.20	0.3726	61.4	7.9	0.3568	157.6	38.4	0.2706	321.7	50.5	1.38
184R-2, 64	896.80	0.3633	120.0	21.9	0.3375	2.2	49.3	0.2992	224.8	32.4	1.21
185R-2, 68	901.90	0.3619	357.1	25.1	0.3282	110.2	40.0	0.3099	244.3	39.6	1.17
186R-3, 100	908.49	0.3650	204.2	27.3	0.3316	313.5	32.7	0.3034	83.3	44.9	1.20
187R-3, 74	912.12	0.3438	272.0	11.8	0.3432	74.7	77.7	0.3130	181.3	3.6	1.10
188R-3, 89	917.05	0.3596	31.1	32.3	0.3399	233.5	55.6	0.3006	127.8	10.4	1.20
189R-1, 110	920.10	0.3588	267.3	33.4	0.3341	146.8	37.5	0.3071	24.5	34.8	1.17
189R-3, 90	922.59	0.3676	258.1	85.8	0.3603	8.8	1.5	0.2721	98.9	3.9	1.35
190R-1, 28	924.08	0.3453	218.6	45.1	0.3371	319.0	10.2	0.3176	58.7	43.1	1.09
191R-3, 86	928.38	0.3602	254.2	20.2	0.3324	349.1	13.0	0.3074	109.8	65.7	1.17
192R-1, 140	930.15	0.3521	355.9	18.2	0.3296	229.1	61.3	0.3183	93.4	21.4	1.11
193R-2, 59	934.82	0.3531	18.8	5.1	0.3358	128.4	75.0	0.3111	287.5	14.1	1.13
194R-2, 97	939.68	0.3428	89.2	42.9	0.3310	191.0	12.4	0.3261	293.5	44.5	1.05
195R-1, 98	943.98	0.3429	352.8	7.9	0.3337	261.0	12.8	0.3234	113.7	74.9	1.06
196R-3, 28	950.19	0.3627	173.1	42.6	0.3428	282.2	19.6	0.2945	30.2	41.0	1.23
197R-1, 112	953.29	0.3638	205.5	22.0	0.3309	107.6	18.7	0.3052	340.8	60.4	1.19
197R-4, 25	956.23	0.3501	326.4	33.8	0.3319	62.2	8.6	0.3180	164.7	54.8	1.10
198R-1, 108	958.37	0.3639	119.9	86.1	0.3639	119.9	86.1	0.2448	304.8	3.9	1.49
198R-3, 101	960.28	0.3562	217.9	26.0	0.3419	0.9	58.6	0.3019	119.7	16.4	1.18
199R-2, 42	963.21	0.3454	23.6	20.5	0.3373	222.4	68.5	0.3173	115.9	6.4	1.09
200R-3, 100	968.58	0.3474	224.9	35.0	0.3314	111.4	29.6	0.3212	352.0	40.8	1.08
200R-1, 44	965.64	0.3909	322.8	34.0	0.3592	211.8	27.4	0.2500	92.8	43.1	1.56
201R-1, 112	970.82	0.3500	225.5	45.5	0.3324	102.5	28.1	0.3176	353.6	31.2	1.10
202R-3, 52	975.43	0.3705	74.8	10.2	0.3539	336.6	38.4	0.2756	177.1	49.8	1.34
202R-4, 8	976.07	0.3458	39.7	10.3	0.3320	308.2	8.5	0.3222	179.1	76.6	1.07
203R-1, 5	977.20	0.3495	180.8	47.9	0.3325	73.8	14.8	0.3180	331.7	38.2	1.10
204R-3, 52	982.29	0.3602	152.2	4.1	0.3317	255.1	72.3	0.3081	60.9	17.2	1.17
204R-6, 40	986.39	0.3495	132.7	6.3	0.3349	238.0	67.2	0.3156	40.2	21.8	1.11
205R-1, 117	987.85	0.3526	178.1	14.2	0.3285	280.9	41.1	0.3190	73.2	45.4	1.11
206R-1, 14	991.34	0.3409	0.4	4.6	0.3337	91.1	9.4	0.3255	244.6	79.5	1.05
207R-1, 93	994.56	0.3493	68.9	16.1	0.3284	317.0	52.3	0.3224	169.7	33.1	1.08
207R-3, 68	997.31	0.3600	211.1	5.6	0.3242	302.0	8.3	0.3160	87.4	79.9	1.14
208R-1, 18	1000.98	0.3485	51.5	16.4	0.3285	319.4	7.1	0.3230	206.6	72.1	1.08
209R-2, 37	1005.97	0.3563	148.3	27.7	0.3364	250.1	21.2	0.3074	12.2	53.9	1.16
210R-3, 3	1012.38	0.3548	356.9	25.9	0.3265	158.2	62.8	0.3187	263.2	7.6	1.11
211R-5, 66	1019.23	0.3519	76.6	72.6	0.3501	308.8	10.9	0.2895	343.9	48.9	1.22
212R-2, 37	1021.58	0.3509	175.1	41.6	0.3337	58.6	26.7	0.2968	328.4	39.7	1.18
213R-2, 77	1027.02	0.3476	240.2	50.4	0.3306	338.4	6.8	0.3081	22.6	8.8	1.13
214R-3, 36	1032.44	0.3524	14.0	39.5	0.3439	189.7	50.4	0.3096	149.9	31.5	1.14
215R-1, 28	1034.58	0.3558			0.3429			0.3013			1.18
215R-4, 141	1038.89	0.3469	194.0	32.7	0.3310	298.2	20.9	0.3167	85.5	5.3	1.10
216R-1, 96	1040.16	0.3663	54.9	20.5	0.3416	160.4	35.5	0.2965	178.7	30.4	1.24
217R-2, 85	1044.85	0.3542	186.9	23.3	0.3250	96.6	0.7	0.2739	95.4	16.8	1.29

Table T18 (continued).

Core, section, interval (cm)	Depth (mbsf)	Maximum			Intermediate			Minimum			*P* (max/min)
		k	Declination (°)	Inclination (°)	*k*	Declination (°)	Inclination (°)	*k*	Declination (°)	Inclination (°)	
217R-3, 38	1046.94	0.3582	187.6	49.8	0.3261	76.7	16.8	0.3070	39.7	30.6	1.17
218R-3, 35	1050.90	0.3614	178.3	24.2	0.3390	4.5	65.6	0.3204	231.6	46.7	1.13
219R-2, 85	1055.45	0.3679	154.3	18.7	0.3381	48.4	38.9	0.3197	67.5	60.7	1.15
220R-1, 126	1059.60	0.3690	43.2	2.3	0.3575	303.2	76.9	0.3183	137.7	47.3	1.16
222R-1, 117	1068.62	0.3636	200.2	33.2	0.3265	96.3	20.1	0.2956	152.0	25.4	1.23
222R-4, 26	1071.90	0.3578	293.0	17.9	0.3357	184.5	44.5	0.3149	21.6	54.6	1.14
223R-2, 37	1074.31	0.3494	263.4	49.5	0.3360	62.0	38.5	0.3107	117.5	29.3	1.12
224R-1, 46	1078.06	0.3543	261.2	32.7	0.3279	155.7	22.7	0.3136	330.4	10.7	1.13
225R-1, 120	1083.60	0.3769	18.0	8.4	0.3452	261.3	71.8	0.2706	321.7	50.5	1.39
225R-3, 117	1086.36	0.3586	188.3	27.9	0.3234	291.2	22.9	0.2992	224.8	32.4	1.20
226R-1, 3	1087.23	0.3533	7.4	32.2	0.3270	98.0	0.9	0.3099	110.2	40.0	1.14
226R-3, 61	1090.71	0.3576	218.7	20.4	0.3382	325.3	37.6	0.3034	83.3	44.9	1.18
227R-2, 46	1093.89	0.3665	344.2	1.2	0.3440	252.4	54.7	0.3130	181.3	3.6	1.17
227R-3, 90	1095.83	0.3556	106.1	25.4	0.3265	198.3	4.6	0.3005	127.8	10.4	1.18
228R-2, 92	1098.93	0.3608	9.3	37.4	0.3533	183.6	52.4	0.3071	24.5	34.8	1.17
228R-4, 16	1100.86	0.3602	190.4	35.5	0.3569	311.2	35.7	0.2721	98.9	3.9	1.32
229R-1, 57	1102.17	0.3614	9.0	51.8	0.3417	132.4	23.4	0.3176	58.7	43.1	1.14
230R-1, 72	1106.22	0.3518	133.6	24.5	0.3265	42.4	2.4	0.3074	109.8	65.7	1.14
230R-3, 128	1109.66	0.3504	214.5	32.1	0.3396	329.0	33.5	0.3183	93.4	21.4	1.10
231R-1, 65	1110.95	0.3521	72.4	9.4	0.3336	169.6	37.3	0.3111	287.5	14.1	1.13
232R-1, 45	1115.55	0.3635	335.0	10.2	0.3403	227.2	59.7	0.3261	293.5	44.5	1.11
232R-3, 123	1119.15	0.3830	169.8	12.5	0.3502	7.4	77.0	0.3234	113.7	74.9	1.18
233R-2, 60	1122.00	0.3737	356.5	12.0	0.3589	257.0	37.9	0.2945	30.2	41.0	1.27
234R-1, 122	1125.92	0.3673	239.5	10.9	0.3265	338.6	39.4	0.3052	340.8	60.4	1.20
235R-1, 78	1130.28	0.3843	258.0	0.4	0.3292	349.2	73.0	0.3180	164.7	54.8	1.21
236R-1, 59	1134.89	0.3707	179.7	15.4	0.3554	301.0	62.2	0.2448	304.8	3.9	1.51
236R-3, 6	1137.21	0.3398	351.4	22.2	0.3339	252.8	20.1	0.3019	119.7	16.4	1.13
237R-1, 88	1139.98	0.3759	182.0	31.0	0.3614	299.3	37.4	0.3173	115.9	6.4	1.18
238R-1, 119	1145.09	0.3648	15.6	32.3	0.3465	176.6	56.2	0.3212	352.0	40.8	1.14
239R-2, 47	1150.60	0.3533	337.9	5.7	0.3322	224.5	75.8	0.3176	353.6	31.2	1.11
240R-2, 80	1155.54	0.3724	193.6	0.7	0.3512	99.1	80.9	0.2756	177.1	49.8	1.35
241R-1, 21	1158.51	0.3858	199.4	5.3	0.3615	301.6	66.1	0.3222	179.1	76.6	1.20
242R-1, 30	1163.40	0.3799	202.8	4.7	0.3475	315.2	77.9	0.3180	331.7	38.2	1.19
242R-2, 95	1165.32	0.3648	321.4	19.3	0.3342	58.4	19.3	0.3081	60.9	17.2	1.18
243R-1, 13	1168.03	0.3625	221.6	35.1	0.3504	337.4	31.8	0.3156	40.2	21.8	1.15
244R-2, 113	1175.13	0.3466	67.2	2.1	0.3327	159.5	47.9	0.3189	73.2	45.4	1.09
246R-1, 106	1183.36	0.3510	9.4	13.8	0.3311	262.4	49.9	0.3255	244.6	79.5	1.08
247R-2, 9	1188.58	0.3792	356.0	33.8	0.3651	90.8	7.2	0.3224	169.7	33.1	1.18
248R-2, 34	1193.48	0.3556	172.4	19.0	0.3408	263.8	4.2	0.3159	87.4	79.9	1.13
248R-3, 45	1194.94	0.3640	315.2	18.9	0.3515	221.9	9.5	0.3230	206.6	72.1	1.13
249R-1, 94	1197.64	0.3479	69.5	7.7	0.3355	333.2	39.3	0.3074	12.2	53.9	1.13
250R-3, 23	1204.31	0.3776	223.9	4.0	0.3363	324.7	69.5	0.3187	263.2	7.6	1.18
251R-1, 85	1207.15	0.3654	210.8	26.7	0.3322	329.3	43.5	0.2981	216.2	13.5	1.23
252R-1, 100	1212.10	0.3598	118.2	4.5	0.3321	240.3	81.6	0.3154	306.6	36.7	1.14
253R-2, 77	1218.14	0.3526	217.8	0.7	0.3295	127.1	46.7	0.3218	73.9	38.8	1.10
254R-1, 48	1221.18	0.3483	176.9	9.4	0.3342	290.7	67.7	0.3037	282.2	2.1	1.15
255R-1, 94	1226.44	0.3816	127.6	10.1	0.3304	217.8	0.9	0.3222	54.8	49.6	1.18
256R-2, 98	1232.42	0.3681	220.0	27.7	0.3577	328.3	30.8	0.2921	301.0	47.3	1.26
257R-1, 49	1235.59	0.3720	207.2	16.7	0.3457	308.3	32.6	0.3208	4.9	66.7	1.16
258R-1, 46	1240.36	0.3548	204.3	2.3	0.3367	295.5	27.3	0.3158	334.4	35.3	1.12
259R-1, 93	1245.63	0.3453	7.9	10.2	0.3364	270.0	37.3	0.2996	269.4	2.3	1.15
260R-1, 133	1250.83	0.3499	96.4	5.5	0.3333	359.2	52.2	0.2940	264.2	45.1	1.19
261R-3, 83	1257.85	0.3546	9.2	13.2	0.3442	106.1	27.2	0.2735	133.7	12.9	1.30
263R-1, 43	1264.33	0.3557	332.1	12.5	0.3407	228.5	46.8	0.3099	340.7	49.7	1.15
264R-2, 55	1270.75	0.3657	109.7	12.7	0.3254	201.9	9.6	0.3065	38.7	40.1	1.19
265R-1, 85	1274.35	0.3511	130.6	34.0	0.3263	12.1	35.3	0.3146	160.7	10.7	1.12
266R-2, 4	1279.49	0.3553	36.4	33.3	0.3263	304.6	2.8	0.3178	37.6	48.4	1.12
267R-2, 106	1285.60	0.3604	210.2	8.8	0.3248	324.2	69.3	0.2779	110.4	16.0	1.30
268R-2, 61	1289.84	0.3678	150.9	12.7	0.3414	59.7	5.4	0.3180	54.6	52.5	1.16
268R-4, 23	1292.20	0.3888	285.1	70.0	0.3171	93.2	19.6	0.3197	189.5	57.7	1.22
269R-2, 74	1294.90	0.3446	29.5	9.9	0.3350	140.4	64.0	0.3042	106.5	45.4	1.13
271R-2, 7	1303.76	0.3497	83.8	46.4	0.3338	309.5	33.6	0.2894	75.0	35.3	1.21
272R-3, 28	1310.28	0.3472	307.5	67.2	0.3337	204.3	5.5	0.3179	297.8	64.2	1.09
273R-1, 12	1312.02	0.3758	91.4	63.4	0.3346	290.1	25.4	0.2858	277.2	2.7	1.31
274R-1, 33	1317.03	0.3458	257.2	1.9	0.3294	166.3	25.1	0.2829	70.9	34.6	1.22

Table T18 (continued).

Core, section, interval (cm)	Depth (mbsf)	Maximum			Intermediate			Minimum			*P* (max/min)
		k	Declination (°)	Inclination (°)	*k*	Declination (°)	Inclination (°)	*k*	Declination (°)	Inclination (°)	
275R-2, 116	1323.97	0.3517	280.0	23.9	0.3439	44.2	51.8	0.2970	235.9	28.3	1.18
276R-1, 40	1326.55	0.3443	62.0	59.9	0.3327	312.1	11.2	0.3216	307.1	65.3	1.07
277R-1, 61	1330.21	0.3702	242.8	1.5	0.3261	152.5	9.1	0.3100	92.8	39.9	1.19
278R-1, 26	1334.66	0.3530	86.6	31.0	0.3283	182.8	10.1	0.3143	330.4	51.2	1.12
279R-4, 38	1343.56	0.3440	349.9	19.3	0.3328	250.8	24.4	0.2962	70.6	28.2	1.16
280R-1, 92	1344.92	0.3534	321.6	24.7	0.3311	219.6	24.2	0.2668	260.7	3.8	1.32
281R-1, 105	1349.85	0.3422	4.2	15.8	0.3340	106.7	37.5	0.2682	101.0	49.5	1.28
282R-1, 30	1353.90	0.3455	256.7	2.8	0.3351	0.6	78.5	0.3062	137.0	48.6	1.13
283R-1, 6	1358.46	0.3455	256.0	49.3	0.3413	346.5	0.5	0.2865	167.9	17.0	1.21
284R-2, 80	1365.11	0.3528	238.3	4.6	0.3311	329.2	10.9	0.2739	83.1	22.6	1.29
285R-1, 82	1368.82	0.3603	96.1	14.3	0.3393	194.6	30.2	0.3263	124.9	59.3	1.10
286R-2, 134	1375.64	0.3399	217.4	9.9	0.3339	101.2	68.5	0.2628	64.8	37.3	1.29
287R-1, 8	1377.68	0.3361	33.5	12.3	0.3348	300.3	14.5	0.2887	280.0	8.8	1.16
288R-1, 15	1379.28	0.3478	208.8	26.2	0.3432	311.3	23.8	0.3145	69.3	12.9	1.11
290R-2, 111	1388.31	0.3471	349.4	2.2	0.3324	81.4	42.9	0.2764	283.7	9.1	1.26
291R-4, 118	1396.61	0.3561	330.0	14.6	0.3340	235.8	15.6	0.2527	107.2	23.2	1.41
292R-2, 59	1398.44	0.3460	333.0	52.9	0.3397	65.8	2.1	0.2727	111.9	11.2	1.27
294R-1, 93	1407.33	0.3645	174.3	23.2	0.3241	293.3	48.4	0.3010	190	62.2	1.21
295R-2, 70	1413.40	0.3535	219.3	29.9	0.3284	126.5	4.8	0.2871	97.2	38.8	1.23

Notes: MS = magnetic susceptibility, max = maximum, min = minimum. This table is also available in **ASCII.**

Table T19. Summary of physical property data for major lithologies, Hole U1309B.

Lithology	MST MS (IU ~ x 10^{-5} SI)	MST NCR (Ω·m)	V_P (km/s)	Bulk density (g/cm^3)	Porosity (%)	Thermal conductivity (W/[m·K])
Basalt	Mean = ~530 Max = ~4600 (292)	Mean = ~150,000 Min = ~1,600 (262)	5.14 ± 0.33 *N* = 8	2.88 ± 0.06 *N* = 7	1.9 ± 1.4 *N* = 7	2.23 ± 0.52 *N* = 18
Diabase	Mean = ~1980 Max = ~6100 (745)	Mean = ~15,000 Min = ~900 (688)	5.20 ± 0.27 *N* = 10	2.89 ± 0.04 *N* = 8	2.1 ± 0.6 *N* = 8	2.09 ± 0.08 *N* = 23
Gabbro	Mean = ~60 Max = ~330 (408)	Mean = ~100,000 Min = ~18,000 (395)	4.99 ± 0.16 *N* = 4	2.88 ± 0.07 *N* = 4	2.0 ± 0.8 *N* = 4	2.36 ± 0.19 *N* = 20
Olivine/Troctolitic gabbro	Mean = ~60 Max = ~1100 (719)	Mean = ~130,000 Min = ~5,700 (700)	5.54 ± 0.30 *N* = 6	2.81 ± 0.06 *N* = 7	2.1 ± 1.6 *N* = 7	2.74 ± 0.35 *N* = 15
Troctolite	Mean = ~80 Max = ~460 (16)	Mean = ~70,000 Min = ~7,500 (16)	—	—	—	—
Peridotite	Mean = ~6400 Max = ~9500 (50)	Mean = ~2,400 Min = ~400 (50)	4.59 ± 0.12 *N* = 2	2.66 ± 0.08 *N* = 2	3.1 ± 0.3 *N* = 2	3.91 ± 0.30 *N* = 2

Notes: Magnetic susceptibility and electrical resistivity are not corrected for core diameter and spacer locations (see the **"Methods"** chapter). Numbers in parenthesis indicate number of measurements (MST data) or samples. SD = standard deviation. This table is also available in **ASCII.**

Table T20. Measurements of value, uncertainty, and directional dependence of thermal conductivity obtained, Hole U1309B.

Core, section, interval (cm)	Depth (midpoint) (mbsf)	Unit	Primary lithology	Thermal conductivity (W/[m·K])								
				Parallel		–35°		+35°		Average		Anisotropy (%)
				Mean	SD	Mean	SD	Mean	SD	Mean	SD	
304-U1309B-												
1R-3, 42–56	2.40	2	Plagioclase-phyric basalt	2.15	0.11	2.09	0.04	2.16	0.11	2.13	0.04	3
2R-1, 79–94	16.36	6	Sparsely plagioclase-phyric basalt	2.25	0.15	2.07	0.06	2.06	0.15	2.13	0.10	9
2R-2, 33–46	17.28	10	Plagioclase-phyric basalt	1.78	0.12	2.01	0.11	2.01	0.09	1.93	0.13	12
3R-1, 84–99	20.92	16	Aphyric basalt	3.24	0.09	3.29	0.12	3.16	0.07	3.23	0.06	4
4R-1, 27–41	24.77	19	Fine-grained altered basalt	2.27	0.12					2.27	0.12	
5R-2, 11–41	31.18	20	Diabase	2.04	0.01	2.04	0.07	2.06	0.04	2.05	0.01	1
6R-1, 107–127	34.36	22	Diabase	2.13	0.04	2.15	0.05	2.12	0.06	2.13	0.02	1
6R-2, 24–49	35.06	22	Diabase	2.12	0.04	2.15	0.07	2.10	0.02	2.12	0.02	2
7R-1, 0–17	38.10	24	Gabbro	2.05	0.05	2.09	0.07	2.10	0.03	2.08	0.02	2
8R-1, 48–57	43.53	28	Gabbro	2.61	0.11			2.31		2.46	0.21	
9R-1, 0–17	47.62	28	Gabbro	2.47	0.05	2.47	0.03	2.41	0.06	2.45	0.03	2
10R-1, 38–51	52.94	28	Gabbro	2.39	0.12	2.34	0.11	2.25	0.11	2.36	0.11	9
10R-2, 0–15	53.95	31	Gabbro	2.13	0.06	2.16	0.03	2.28	0.11	2.19	0.08	7
11R-1, 30–43	57.36	31	Gabbro	2.68	0.10	2.56	0.08	2.59	0.12	2.61	0.06	5
11R-1, 111–118	58.14	32	Harzburgite	3.70	0.12					3.70	0.12	
11R-1, 121–129	58.25	32	Harzburgite	4.12	0.09					4.12	0.09	
12R-1, 11–21	61.76	33	Diabase	2.19	0.09	2.19	0.04			2.19	0.00	
12R-1, 121–126	62.84	34	Diabase	2.12	0.06	2.12	0.17	2.16	0.02	2.14	0.02	2
12R-1, 121–126	62.84	34	Diabase					2.13	0.06	2.13	0.06	0
12R-2, 43–63	63.57	34	Diabase	2.11	0.08	2.16	0.07	2.11	0.06	2.13	0.02	2
13R-1, 95–118	67.16	34	Diabase	2.06	0.08	2.03	0.02	2.02	0.07	2.04	0.02	2
14R-1, 104–113	72.18	40	Plagioclase-phyric basalt	2.20	0.07	2.19	0.03	2.12	0.07	2.17	0.04	4
14R-1, 131–142	72.46	41	Troctolite	2.45	0.18	2.48	0.13	2.40	0.05	2.44	0.04	3
15R-1, 17–32	75.84	46	Layered gabbro	2.57	0.11	2.65	0.11	2.63	0.16	2.62	0.04	3
15R-1, 17–32	75.84	46	Layered gabbro					2.48	0.06	2.48	0.06	
15R-2, 54–60	77.45	46	Layered gabbro	3.41	0.09	3.33	0.07	3.31	0.15	3.35	0.05	3
16R-2, 92–98	82.72	50	Olivine gabbro	2.47	0.10	2.57	0.16	2.42	0.13	2.48	0.08	6
17R-2, 56–62	86.93	53	Olivine gabbro	2.71	0.10	2.78	0.08			2.74	0.06	3
18R-1, 43–49	90.06	56	Troctolite and olivine gabbro	2.42	0.07	2.52	0.19	2.43	0.07	2.46	0.05	4
18R-3, 97–103	93.47	60	Basalt	1.99	0.11					1.99	0.11	
19R-2, 37–52	96.02	62	Diabase	2.02	0.07					2.02	0.07	
20R-2, 29–43	100.66	62	Diabase	2.10	0.08					2.10	0.08	
			Average:	2.44	0.09	2.37	0.08	2.33	0.08	2.42	0.06	3.9
			Standard deviation:	0.53	0.03	0.37	0.05	0.33	0.04	0.50	0.04	2.9

Notes: SD = standard deviation. This table is also available in **ASCII.**

Table T21. Units displaying rapid transitions of magnetic susceptibility, Hole U1309B.

Unit	Core	Depth (mbsf)
	304-U1309B-	
20	5R-1	30.40, 31.82
34	12R-1	62.6
	12R-2	63.4
	13R-1	66.9
62	19R-2	96.2, 96.8
	19R-3	97.2, 97.65
	20R-1	99.1

Note: This table is also available in **ASCII.**

Table T22. Summary of physical property data for the major lithologies, Hole U1309D.

Lithology	MST MS (IU ~ 10^{-5} SI)	MST NCR (Ω·m)	V_P (km/s)	Bulk density (g/cm^3)	Porosity (%)	Thermal conductivity (W/[m·K])
Diabase/basalt	Mean = ~1,400 Max = ~8,200 *N* = 1,534	Mean = ~52,000 Min = ~700 *N* = 1,527	5.54 ± 0.39 *N* = 20	2.92 ± 0.05 *N* = 19	1.2 ± 0.9 *N* = 19	2.13 ± 0.19 *N* = 31
Oxide gabbro	Mean = ~2,200 Max = >10,000 *N* = 3,618	Mean = ~17,000 Min =~200 *N* = 3,575	5.68 ± 0.25 *N* = 37	3.02 ± 0.17 *N* = 34	1.4 ± 1.1 *N* = 34	2.21 ± 0.27 *N* = 40
Gabbro	Mean = ~470 Max = >10,000 *N* = 30,916	Mean = ~40,000 Min = ~200 *N* = 30,716	5.73 ± 0.32 *N* = 265	2.94 ± 0.17 *N* = 262	1.1 ± 0.9 *N* = 261	2.28 ± 0.27 *N* = 205
Olivine/troctolitic gabbro	Mean = ~720 Max = >10,000 *N* = 14,669	Mean = ~45,000 Min = ~200 *N* = 14,353	5.74 ± 0.35 *N* = 135	2.91 ± 0.09 *N* = 135	1.1 ± 0.9 *N* = 130	2.51 ± 0.39 *N* = 136
Troctolite	Mean = ~1,500 Max = >10,000 *N* = 1,538	Mean = ~30,000 Min = ~200 *N* = 1,514	5.81 ± 0.48 *N* = 19	2.84 ± 0.09 *N* = 18	1.3 ± 0.5 *N* = 17	2.82 ± 0.64 *N* = 18
Olivine-rich troctolite	Mean = ~3,600 Max = >10,000 *N* = 2,668	Mean = ~3,100 Min = ~200 *N* = 2,639	5.67 ± 0.43 *N* = 31	2.93 ± 0.16 *N* = 31	0.9 ± 1.1 *N* = 31	3.38 ± 0.33 *N* = 23
Peridotite	Mean = ~4,200 Max = >10,000 *N* = 252	Mean = ~1,600 Min = ~200 *N* = 243	4.85 ± 0.28 *N* = 2	2.74 ± 0.04 *N* = 3	2.0 ± 1.3 *N* = 3	3.72 ± 0.33 *N* = 7

Notes: Magnetic susceptibility (MS) and noncontact resistivity (NCR) are not corrected for core diameter and spacer locations (see the **"Methods"** chapter). *N* = number of measurements (multisensor track [MST] data) or samples. IU = instrument units. This table is also available in **ASCII.**

Table T23. Measurements of value, uncertainty, and directional dependence of thermal conductivity obtained for core from Hole U1309D.

Core, section, interval (cm)	Depth (midpoint) (mbsf)	Unit	Lithology	Thermal conductivity (W/[m·K]) Parallel Mean	Parallel SD	Oblique Angle (°)	Oblique Mean	Oblique SD	Difference (%)
304-U1309D-									
1R-1, 53–56	21.03	1	Diabase	1.99	0.08				
2R-1, 49–62	27.36	5	Diabase	2.05	0.09				
4R-1, 14–21	31.57	6	Diabase	2.16	0.04				
4R-2, 140–147	33.33	9	Gabbro	2.33	0.10				
4R-3, 10–17	34.55	?	Gabbro	2.06	0.05				
5R-1, 43–49	36.46	9	Gabbro	1.86	0.03				
5R-2, 49–56	37.93	9	Gabbro	2.50	0.07				
5R-3, 43–58	39.39	9	Gabbro	2.60	0.07				
5R-3, 71–77	39.62	9	Gabbro	2.73	0.17				
5R-3, 71–77	39.62	9	Gabbro	2.95	0.17				
6R-1, 120–130	42.05	11	Gabbro	2.42	0.06				
6R-2, 82–102	43.22	12	Diabase	2.00	0.04				
6R-3, 73–80	44.21	12	Diabase	2.02	0.04				
6R-3, 70–84	44.21	12	Diabase	2.10	0.05				
7R-1, 7–17	45.72	13	Gabbro	1.82	0.04				
7R-2, 90–101	47.54	14	Diabase	2.28	0.08	–35	2.28	0.08	1.6
7R-2, 90–101	47.54	14	Diabase	2.13	0.06				
7R-3, 95–101	49.01	16	Gabbro	1.88	0.05				
8R-1, 110–118	51.64	17	Gabbro	2.29	0.07	40	2.36	0.17	3.1
8R-2, 132–138	53.31	19	Troctolite	3.71	0.09				
9R-1, 114–121	56.48	24	Gabbro	2.36	0.04				
9R-3, 17–24	58.31	25	Gabbro	2.28	0.12				
10R-1, 90–95	61.12	27	Gabbro			–35	3.29	0.13	
10R-1, 95–100	61.18	27	Peridotite	4.34	0.18				
10R-2, 57–64	62.18	32	Troctolite/Olivine gabbro	2.88	0.09				
11R-1, 65–84	65.64	34	Troctolite/Olivine gabbro	2.99	0.09	70	3.02	0.17	0.8
11R-2, 69–83	67.05	34	Troctolite/Olivine gabbro	3.06	0.17	–35	2.97	0.11	–0.8
12R-1, 25–53	70.29	34	Troctolite/Olivine gabbro	2.96	0.11				
12R-1, 131–146	71.18	34	Troctolite/Olivine gabbro	2.59	0.02	40	2.47	0.16	–4.6
12R-3, 0–22	72.69	34	Troctolite	2.45	0.14				
13R-2, 45–70	76.41	35	Gabbro	2.54	0.04				
14R-1, 90–108	80.39	41	Troctolite	2.27	0.07				
14R-2, 58–71	81.38	41	Olivine gabbro	2.59	0.07				
15R-1, 38–47	84.53	44	Gabbro	1.98	0.06				
15R-2, 65–78	86.32	44	Diabase	2.12	0.08				
15R-4, 0–14	88.67	44	Diabase	2.06	0.04				
16R-1, 114–131	90.22	44	Diabase	2.13	0.06				
16R-3, 58–76	92.10	44	Diabase	2.06	0.04				
16R-4, 45–62	93.47	44	Diabase	2.00	0.02				
16R-4, 108–118	94.06	44	Diabase	2.06	0.08				
16R-5, 27–39	94.72	47	Gabbro	3.06	0.04				
17R-1, 16–29	98.92	49	Gabbro	2.43	0.07				
17R-2, 86–99	100.80	49	Gabbro	2.37	0.08				
17R-3, 0–14	101.33	49	Gabbro	2.51	0.06				
20R-1, 55–69	117.72	52	Diabase	2.21	0.06				
20R-2, 21–33	118.80	52	Diabase	2.26	0.05				
21R-1, 58–68	122.23	52	Diabase	2.26	0.09				
22R-1, 17–28	126.52	54	Diabase	2.27	0.03				
22R-2, 36–46	127.88	55	Gabbro	2.27	0.07				
22R-3, 42–58	129.48	55	Gabbro	2.12	0.07				
49R-2, 14–23	258.84	112	Olivine gabbro	3.38	0.17	–40	3.71	0.20	9.7
49R-2, 14–23	258.84	112	Olivine gabbro	3.38	0.17	40	3.59	0.12	6.2
68R-1, 7–19	348.53	178	Gabbro			–10	2.22	0.05	
69R-2, 80–86	355.38	182	Oxide gabbro			–10	2.45	0.08	
71R-2, 50–58	364.46	184	Leucocratic troctolitic/olivine gabbro domain cumulates	2.36	0.10	–35	2.36	0.10	
			Mean:	2.43	0.08		2.79	0.12	2.29
			Standard deviation:	0.50	0.04		0.55	0.05	4.67
			Number:	52	52		11	11	7

Notes: SD = standard deviation. Depths do not have shift applied. This table is also available in **ASCII.**

Table T24. Results of cultivation experiments at varying temperatures, Expedition 304.

Section	Methanogen (°)				Sulfate-reducing bacteria (°)				Heterotroph (°)	
	5	37	65	85	5	37	65	85	37	65
304-U1309A-										
1R-2	ND	—	—	—	ND	—	—	—	—	—
304-U1309B-										
2R-1	ND	ND	ND	*	ND	ND	ND	*	ND	ND
16R-2	ND	ND	*	*	ND	ND	ND	*	†	ND
304-U1309D-										
10R-1	ND	ND	ND	ND	ND	ND	ND	ND	ND	ND
12R-3	ND	ND	ND	*	ND	ND	ND	*	†	*
28R-4	ND	ND	ND	ND	ND	ND	ND	ND	ND	ND
37R-2	ND	ND	ND	ND	ND	ND	ND	ND	ND	ND
53R-1	ND	ND	ND	ND	ND	ND	ND	ND	ND	ND
58R-1	ND	ND	ND	ND	ND	ND	ND	ND	ND	ND
68R-1	ND	ND	ND	ND	ND	ND	ND	ND	ND	ND
78R-1	ND	ND	ND	ND	ND	ND	ND	ND	ND	ND

Notes: Bicarbonate and CO_2 gas were added to methanogen as a carbon source. Acetate was added to sulfate-reducing bacteria as a carbon source (final concentration = 2 mM). Yeast extract and pepton were added to heterotroph as a carbon source. * = difficulty in determining between microorganisms or minerals. † = microorganisms were observed in the culture bottle. ND = not detected.

Table T25. Check shot data acquired by WST-3 during intermediate logging run (400–800 mbsf).

Depth (mbrf)	OWT (ms)	Interval velocity (m/s)	Average velocity (m/s)
1920	1145.85	5225.7	5591.0
1990	1158.94	5349.9	5540.4
2025	1164.70	6071.8	5585.4
2080	1173.64	6153.4	5651.4
2125	1182.20	5256.0	5611.8
2170	1189.31	6330.0	5666.9
2224	1198.11	6136.4	5717.5
2279	1205.01	7971.0	5861.0
2329	1214.90	5055.6	5793.6
2380	1223.47	5951.0	5796.4
2440	1233.00	6295.9	4094.0

Notes: OWT = one-way traveltime. WST-3 = three-component Well Seismic Tool. Interval velocities were calculated after the Dix equation. This table is also available in **ASCII.**

Table T26. Expeditions 304 and 305 coring summary. (Continued on next six pages.)

Hole U1309A
Latitude: 30°10.11′N
Longitude: 42°7.11′W
Time on hole (h): 14.75
Seafloor (drill pipe measurement from rig floor, mbrf): 1653.4
Distance between rig floor and sea level (m): 11.1
Water depth (drill pipe measurement from sea level, m): 1642.3
Total depth (drill pipe measurement from rig floor, mbrf): 1655.4
Total penetration (meters below seafloor, mbsf): 101.8
Total length of cored section (m): 2
Total core recovered (m): 1.92
Core recovery (%): 96.0
Total number of cores: 1

Hole U1309B
Latitude: 30°10.11′N
Longitude: 42°7.11′W
Time on hole (days): 6.4
Seafloor (drill pipe measurement from rig floor, mbrf): 1653.4
Distance between rig floor and sea level (m): 11.1
Water depth (drill pipe measurement from sea level, m): 1642.3
Total depth (drill pipe measurement from rig floor, mbrf): 1755.2
Total penetration (meters below seafloor, mbsf): 101.8
Total length of cored section (m): 101.8
Total core recovered (m): 46.53
Core recovery (%): 45.7
Total number of cores: 20

Hole U1309C
Latitude: 30°10.11′N
Longitude: 42°07.12′W
Time on hole (days): 2
Seafloor (drill pipe measurement from rig floor, mbrf): 1649.0
Distance between rig floor and sea level (m): 11.1
Water depth (drill pipe measurement from sea level, m): 1637.7
Total depth (drill pipe measurement from rig floor, mbrf): 1655.0
Total penetration (meters below seafloor, mbsf): 6
Total length of cored section (m): 0
Total core recovered (m): 0
Core recovery (%): 0
Total number of cores: 1

Hole U1309D
Latitude: 30°10.12′N
Longitude: 42°7.11′W
Time on hole (days): 17.96
Seafloor (drill pipe measurement from rig floor, mbrf): 1656.0
Distance between rig floor and sea level (m): 11.1
Water depth (drill pipe measurement from sea level, m): 1644.9
Total depth (drill pipe measurement from rig floor, mbrf): 2057.3
Total penetration (meters below seafloor, mbsf): 401.3
Total length of cored section (m): 380.8
Total core recovered (m): 243.81
Core recovery (%): 64.0
Total number of cores: 78

Hole U1309E
Latitude: 30°10.12′N
Longitude: 42°7.11′W
Time on hole (h): 3.25
Seafloor (drill pipe measurement from rig floor, mbrf): 1656.0
Distance between rig floor and sea level (m): 11.6
Water depth (drill pipe measurement from sea level, m): 1644.4
Total depth (drill pipe measurement from rig floor, mbrf): 1659.8
Total penetration (meters below seafloor, mbsf): 3.8
Total length of cored section (m): 3.8
Total core recovered (m): 5.6
Core recovery (%): 147.4
Total number of cores: 1

Table T26 (continued).

Hole U1309F
Latitude: 30°10.20′N
Longitude: 42°7.25′W
Time on hole (h): 13.3
Seafloor (drill pipe measurement from rig floor, mbrf): 1656.0
Distance between rig floor and sea level (m): 11.7
Water depth (drill pipe measurement from sea level, m): 1644.3
Total depth (drill pipe measurement from rig floor, mbrf): 1660.8
Total penetration (meters below seafloor, mbsf): 4.8
Total length of cored section (m): 4.8
Total core recovered (m): 6.09
Core recovery (%): 126.9
Total number of cores: 1

Hole U1309G
Latitude: 30°10.54′N
Longitude: 42°6.32′
Time on hole (h): 16.9
Seafloor (drill pipe measurement from rig floor, mbrf): 1885.0
Distance between rig floor and sea level (m): 5.8
Water depth (drill pipe measurement from sea level, m): 1873.3
Total depth (drill pipe measurement from rig floor, mbrf): 1888.5
Total penetration (meters below seafloor, mbsf): 3.5
Total length of cored section (m): 3.5 m
Total core recovered (m): 0.91
Core recovery (%): 26.0
Total number of cores: 1

Hole U1309H
Latitude: 30°10.54′N
Longitude: 42°6.32′W
Time on hole (h): 23.4
Seafloor (drill pipe measurement from rig floor, mbrf): 1885.0
Distance between rig floor and sea level (m): 5.8
Water depth (drill pipe measurement from sea level, m): 1873.3
Total depth (drill pipe measurement from rig floor, mbrf): 1889.0
Total penetration (meters below seafloor, mbsf): 4
Total length of cored section (m): 4
Total core recovered (m): 0.19
Core recovery (%): 4.8
Total number of cores: 1

Hole U1309D
Latitude: 30°10.12′N
Longitude: 42°7.11′W
Time on site (h): 970.0
Seafloor (drill pipe measurement from rig floor, mbrf): 1656.0
Distance between rig floor and sea level (m): 11.1
Water depth (drill pipe measurement from sea level, m): 1644.9
Total depth (drill pipe measurement from rig floor, mbrf): 3071.5
Total penetration (meters below seafloor, mbsf): 1415.5
Total length of cored section (m): 1014.2
Total core recovered (m): 799.65
Core recovery (%): 78.8
Total number of cores: 216

Core	Date	Local time (h)	Depth (mbsf) Top	Depth (mbsf) Bottom	Length (m) Cored	Length (m) Recovered	Recovery (%)
304-U1309A-							
1R	24 Nov 2004	2315	0	2.0	2.0	1.92	96.0
			Cored totals:		2.0	1.92	96.0
304-U1309B-							
1R	26 Nov 2004	0215	0	15.5	15.5	3.77	24.3
2R	26 Nov 2004	1050	15.5	20.0	4.5	1.94	43.1
3R	26 Nov 2004	1810	20.0	24.5	4.5	1.20	26.7
4R	26 Nov 2004	2350	24.5	29.5	5.0	0.65	13.0
5R	27 Nov 2004	0650	29.5	33.2	3.7	2.21	59.7
6R	27 Nov 2004	1600	33.2	38.0	4.8	2.01	41.9
7R	27 Nov 2004	2020	38.0	43.0	5.0	0.81	16.2
8R	27 Nov 2004	2320	43.0	47.5	4.5	1.82	40.4
9R	28 Nov 2004	0400	47.5	52.5	5.0	3.08	61.6

Table T26 (continued).

Core	Date	Local time (h)	Depth (mbsf) Top	Depth (mbsf) Bottom	Length (m) Cored	Length (m) Recovered	Recovery (%)
10R	28 Nov 2004	0645	52.5	57.0	4.5	1.55	34.4
11R	28 Nov 2004	1000	57.0	61.6	4.6	2.12	46.1
12R	28 Nov 2004	1740	61.6	66.1	4.5	3.05	67.8
13R	28 Nov 2004	2255	66.1	71.1	5.0	1.90	38.0
14R	29 Nov 2004	0225	71.1	75.6	4.5	1.79	39.8
15R	29 Nov 2004	0535	75.6	80.3	4.7	1.90	40.4
16R	29 Nov 2004	0830	80.3	84.9	4.6	3.86	83.9
17R	29 Nov 2004	1100	84.9	89.6	4.7	3.19	67.9
18R	29 Nov 2004	1415	89.6	94.3	4.7	3.42	72.8
19R	29 Nov 2004	1920	94.3	99.0	4.7	4.30	91.5
20R	30 Nov 2004	0010	99.0	101.8	2.8	2.16	77.1
			Cored totals:		101.8	46.73	45.9
304-U1309C-							
1	2 Dec 2004	2030	0.0	6.0	0	0	0.0
			Cored totals:		0	0	0.0
304-U1309D-							
1R	6 Dec 2004	1900	20.5	26.8	6.3	2.84	45.1
2R	7 Dec 2004	0240	26.8	31.3	4.5	1.35	30.0
3G	7 Dec 2004	0540	31.3	31.4	0.1	0.12	120.0
4R	7 Dec 2004	0835	31.4	36.0	4.6	2.55	55.4
5R	7 Dec 2004	1120	36.0	40.8	4.8	4.10	85.4
6R	7 Dec 2004	1530	40.8	45.6	4.8	3.56	74.2
7R	7 Dec 2004	1925	45.6	50.5	4.9	3.07	62.7
8R	7 Dec 2004	2215	50.5	55.3	4.8	2.42	50.4
9R	8 Dec 2004	0040	55.3	60.2	4.9	2.93	59.8
10R	8 Dec 2004	0245	60.2	64.9	4.7	1.74	37.0
11R	8 Dec 2004	0510	64.9	69.8	4.9	3.55	72.4
12R	8 Dec 2004	0750	69.8	74.5	4.7	3.23	68.7
13R	8 Dec 2004	0955	74.5	79.4	4.9	3.15	64.3
14R	8 Dec 2004	1225	79.4	84.1	4.7	2.37	50.4
15R	8 Dec 2004	1650	84.1	89.0	4.9	4.14	84.5
16R	9 Dec 2004	0150	89.0	98.7	9.7	5.53	57.0
17R	9 Dec 2004	0610	98.7	107.9	9.2	3.90	42.4
18R	9 Dec 2004	0910	107.9	112.4	4.5	0.00	0
19R	9 Dec 2004	1250	112.4	117.1	4.7	0.06	1.3
20R	9 Dec 2004	1550	117.1	121.6	4.5	1.78	39.6
21R	9 Dec 2004	1900	121.6	126.3	4.7	0.74	15.7
22R	9 Dec 2004	2215	126.3	131.0	4.7	3.19	67.9
23R	22 Dec 2004	2030	131.0	137.9	6.9	2.02	29.3
24R	22 Dec 2004	2305	137.9	142.7	4.8	2.04	42.5
25R	23 Dec 2004	0150	142.7	147.6	4.9	4.25	86.7
26R	23 Dec 2004	0540	147.6	152.3	4.7	4.77	101.5
27R	23 Dec 2004	0815	152.3	157.1	4.8	2.55	53.1
28R	23 Dec 2004	1055	157.1	161.9	4.8	4.97	103.5
29R	23 Dec 2004	1320	161.9	166.7	4.8	3.17	66.0
30R	23 Dec 2004	1710	166.7	171.5	4.8	1.23	25.6
31R	23 Dec 2004	1955	171.5	176.3	4.8	2.45	51.0
32R	23 Dec 2004	2230	176.3	181.1	4.8	2.56	53.3
33R	24 Dec 2004	0055	181.1	186.0	4.9	3.39	69.2
34R	24 Dec 2004	0340	186.0	190.8	4.8	1.93	40.2
35R	24 Dec 2004	0720	190.8	195.6	4.8	3.58	74.6
36R	24 Dec 2004	1005	195.6	200.4	4.8	4.10	85.4
37R	24 Dec 2004	1245	200.4	205.2	4.8	4.50	93.8
38R	24 Dec 2004	1530	205.2	210.0	4.8	2.70	56.3
39R	24 Dec 2004	1855	210.0	214.8	4.8	5.40	112.5
40R	24 Dec 2004	2155	214.8	219.5	4.7	1.68	35.7
41R	25 Dec 2004	0125	219.5	224.3	4.8	2.77	57.7
42R	25 Dec 2004	0430	224.3	228.8	4.5	1.98	44.0
43R	25 Dec 2004	0855	228.8	233.2	4.4	2.35	53.4
44R	25 Dec 2004	1345	233.2	238.0	4.8	4.41	91.9
45R	25 Dec 2004	1915	238.0	242.8	4.8	4.04	84.2
46R	26 Dec 2004	2150	242.8	247.6	4.8	1.24	25.8
47R	26 Dec 2004	0010	247.6	252.4	4.8	3.00	62.5
48R	26 Dec 2004	2100	252.4	257.2	4.8	2.21	46.0
49R	26 Dec 2004	2335	257.2	262.0	4.8	1.89	39.4
50R	27 Dec 2004	0240	262.0	266.8	4.8	3.68	76.7
51R	27 Dec 2004	0515	266.8	271.6	4.8	4.89	101.9
52R	27 Dec 2004	0815	271.6	276.4	4.8	3.71	77.3

Table T26 (continued).

Core	Date	Local time (h)	Depth (mbsf) Top	Depth (mbsf) Bottom	Length (m) Cored	Length (m) Recovered	Recovery (%)
53R	27 Dec 2004	1135	276.4	281.2	4.8	1.71	35.6
54R	27 Dec 2004	1520	281.2	286.0	4.8	4.40	91.7
55R	27 Dec 2004	1830	286.0	290.8	4.8	4.14	86.3
56R	27 Dec 2004	2100	290.8	295.6	4.8	4.12	85.8
57R	27 Dec 2004	2340	295.6	300.4	4.8	4.37	91.0
58R	28 Dec 2004	0215	300.4	305.2	4.8	3.34	69.6
59R	28 Dec 2004	0500	305.2	310.0	4.8	4.17	86.9
60R	28 Dec 2004	0705	310.0	314.8	4.8	2.95	61.5
61R	28 Dec 2004	0930	314.8	319.6	4.8	2.91	60.6
62R	28 Dec 2004	1210	319.6	324.4	4.8	2.69	56.0
63R	28 Dec 2004	1515	324.4	329.2	4.8	3.07	64.0
64R	28 Dec 2004	1830	329.2	334.0	4.8	1.92	40.0
65R	28 Dec 2004	2050	334.0	338.8	4.8	2.16	45.0
66R	28 Dec 2004	2310	338.8	343.6	4.8	2.61	54.4
67R	29 Dec 2004	0140	343.6	348.4	4.8	4.09	85.2
68R	29 Dec 2004	0505	348.4	353.2	4.8	3.61	75.2
69R	29 Dec 2004	0810	353.2	358.0	4.8	2.83	59.0
70R	29 Dec 2004	1055	358.0	362.8	4.8	3.36	70.0
71R	29 Dec 2004	1455	362.8	367.6	4.8	5.48	114.2
72R	29 Dec 2004	1915	367.6	372.4	4.8	5.00	104.2
73R	29 Dec 2004	2200	372.4	377.2	4.8	4.14	86.3
74R	30 Dec 2004	0040	377.2	382.0	4.8	3.66	76.3
75R	30 Dec 2004	0410	382.0	386.9	4.9	4.18	85.3
76R	30 Dec 2004	0800	386.9	391.7	4.8	3.64	75.8
77R	30 Dec 2004	1100	391.7	396.5	4.8	4.60	95.8
78R	30 Dec 2004	1415	396.5	401.3	4.8	4.88	101.7
			Cored totals:		380.8	243.81	64.0
304-U1309E-							
1R	31 Dec 2004	0100	0	3.8	3.8	5.60	147.4
			Cored totals:		3.8	5.60	147.4
304-U1309F-							
1R	31 Dec 2004	0855	0	4.8	4.8	6.09	126.9
			Cored totals:		4.8	6.09	126.9
304-U1309G-							
1X	1 Jan 2005	1535	0	3.5	3.5	0.91	26.0
			Cored totals:		3.5	0.91	26.0
304-U1309H-							
1R	3 Jan 2005	1915	0	4.0	4.0	0.19	4.8
			Cored totals:		4.0	0.19	4.8
305-U1309D-							
80R	17 Jan 2005	1045	401.3	405.4	4.1	3.12	76.1
81R	17 Jan 2005	1330	405.4	410.2	4.8	4.50	93.8
82R	17 Jan 2005	1615	410.2	415.0	4.8	4.36	90.8
83R	17 Jan 2005	1850	415.0	419.8	4.8	2.80	58.3
84R	17 Jan 2005	2105	419.8	424.6	4.8	3.66	76.2
85R	17 Jan 2005	2355	424.6	429.4	4.8	4.14	86.2
86R	18 Jan 2005	0250	429.4	434.2	4.8	3.91	81.5
87R	18 Jan 2005	0545	434.2	439.0	4.8	2.68	55.8
88R	18 Jan 2005	0800	439.0	443.8	4.8	6.65	138.5
89R	18 Jan 2005	1005	443.8	448.6	4.8	3.69	76.9
90R	18 Jan 2005	1240	448.6	453.4	4.8	4.52	94.2
91R	18 Jan 2005	1545	453.4	458.2	4.8	3.40	70.8
92R	18 Jan 2005	1830	458.2	463.0	4.8	2.71	56.5
93R	18 Jan 2005	2100	463.0	467.8	4.8	3.77	78.5
94R	18 Jan 2005	2340	467.8	472.6	4.8	3.11	64.8
95R	19 Jan 2005	0145	472.6	477.4	4.8	4.18	87.1
96R	19 Jan 2005	0345	477.4	482.2	4.8	3.69	76.9
97R	19 Jan 2005	0545	482.2	487.0	4.8	2.74	57.1
98R	19 Jan 2005	0825	487.0	491.8	4.8	4.08	85.0
99R	19 Jan 2005	1045	491.8	496.6	4.8	2.80	58.3
100R	19 Jan 2005	1330	496.6	501.4	4.8	3.75	78.1
101R	19 Jan 2005	1710	501.4	506.2	4.8	5.70	118.8
102R	19 Jan 2005	2000	506.2	511.0	4.8	3.13	65.2
103R	19 Jan 2005	2215	511.0	515.8	4.8	4.14	86.2
104R	20 Jan 2005	0130	515.8	520.6	4.8	4.45	92.7
105R	20 Jan 2005	0355	520.6	525.4	4.8	3.75	78.1

Table T26 (continued).

Core	Date	Local time (h)	Depth (mbsf) Top	Depth (mbsf) Bottom	Length (m) Cored	Length (m) Recovered	Recovery (%)
106R	20 Jan 2005	0645	525.4	530.2	4.8	2.81	58.5
107R	20 Jan 2005	0930	530.2	535.0	4.8	4.73	98.5
108R	21 Jan 2005	0100	535.0	539.8	4.8	4.42	92.1
109R	21 Jan 2005	0315	539.8	544.6	4.8	4.86	101.3
110R	21 Jan 2005	0555	544.6	549.4	4.8	3.78	78.8
111R	21 Jan 2005	0850	549.4	554.2	4.8	4.45	92.7
112R	21 Jan 2005	1145	554.2	559.0	4.8	2.94	61.2
113R	21 Jan 2005	1440	559.0	563.8	4.8	4.29	89.4
114R	21 Jan 2005	1745	563.8	568.6	4.8	3.25	67.7
115R	21 Jan 2005	2100	568.6	573.4	4.8	4.62	96.2
116R	22 Jan 2005	0040	573.4	578.2	4.8	3.89	81.0
117R	22 Jan 2005	0340	578.2	583.0	4.8	4.36	90.8
118R	22 Jan 2005	0555	583.0	587.8	4.8	3.40	70.8
119R	22 Jan 2005	0825	587.8	592.6	4.8	4.63	96.5
120R	22 Jan 2005	1120	592.6	597.4	4.8	4.63	96.5
121R	22 Jan 2005	1450	597.4	602.2	4.8	4.63	96.5
122R	22 Jan 2005	1750	602.2	607.0	4.8	3.92	81.7
123R	22 Jan 2005	2030	607.0	611.8	4.8	1.36	28.3
124R	22 Jan 2005	2340	611.8	616.6	4.8	5.01	104.4
125R	23 Jan 2005	0245	616.6	621.4	4.8	5.04	105.0
126R	23 Jan 2005	0605	621.4	626.2	4.8	4.38	91.2
127R	23 Jan 2005	0920	626.2	631.0	4.8	3.59	74.8
128R	23 Jan 2005	1210	631.0	635.8	4.8	4.45	92.7
129R	23 Jan 2005	1530	635.8	640.6	4.8	2.67	55.6
130R	23 Jan 2005	1830	640.6	645.4	4.8	3.20	66.7
131R	24 Jan 2005	1100	645.4	650.2	4.8	4.29	89.4
132R	24 Jan 2005	1405	650.2	655.0	4.8	4.84	100.8
133R	24 Jan 2005	1750	655.0	659.8	4.8	4.60	95.8
134R	24 Jan 2005	2030	659.8	664.6	4.8	3.05	63.5
135R	24 Jan 2005	2330	664.6	669.4	4.8	2.36	49.2
136R	25 Jan 2005	0210	669.4	674.2	4.8	3.50	72.9
137R	25 Jan 2005	0600	674.2	679.0	4.8	3.50	72.9
138R	25 Jan 2005	0855	679.0	683.8	4.8	4.10	85.4
139R	25 Jan 2005	1210	683.8	688.6	4.8	4.80	100.0
140R	25 Jan 2005	1530	688.6	693.4	4.8	5.11	106.5
141R	25 Jan 2005	1900	693.4	698.2	4.8	2.87	59.8
142R	25 Jan 2005	2210	698.2	703.0	4.8	3.68	76.7
143R	26 Jan 2005	0135	703.0	707.8	4.8	3.73	77.7
144R	26 Jan 2005	0440	707.8	712.6	4.8	3.70	77.1
145R	26 Jan 2005	0730	712.6	717.4	4.8	4.53	94.4
146R	26 Jan 2005	1045	717.4	722.2	4.8	1.60	33.3
147R	26 Jan 2005	1410	722.2	727.0	4.8	4.22	87.9
148R	26 Jan 2005	1710	727.0	731.8	4.8	4.00	83.3
149R	26 Jan 2005	1940	731.8	736.6	4.8	3.14	65.4
150R	26 Jan 2005	2150	736.6	741.4	4.8	3.85	80.2
151R	26 Jan 2005	2355	741.4	746.2	4.8	2.65	55.2
152R	27 Jan 2005	0210	746.2	751.0	4.8	0.73	15.2
153R	27 Jan 2005	0550	751.0	755.8	4.8	2.70	56.2
154R	27 Jan 2005	2310	755.8	757.8	2.0	1.30	65.0
155R	28 Jan 2005	0345	757.8	760.6	2.8	2.20	78.6
156R	28 Jan 2005	0745	760.6	765.4	4.8	3.74	77.9
157R	28 Jan 2005	1035	765.4	770.2	4.8	4.07	84.8
158R	28 Jan 2005	1340	770.2	775.0	4.8	4.67	97.3
159R	28 Jan 2005	1640	775.0	779.8	4.8	4.53	94.4
160R	28 Jan 2005	2100	779.8	784.6	4.8	4.38	91.2
161R	29 Jan 2005	0110	784.6	789.4	4.8	2.28	47.5
162R	29 Jan 2005	0430	789.4	794.2	4.8	4.40	91.7
163R	29 Jan 2005	0750	794.2	799.0	4.8	4.00	83.3
164R	29 Jan 2005	1030	799.0	803.8	4.8	4.17	86.9
165R	29 Jan 2005	1330	803.8	808.6	4.8	4.15	86.5
166R	29 Jan 2005	1745	808.6	813.4	4.8	4.93	102.7
167R	29 Jan 2005	2115	813.4	818.2	4.8	4.09	85.2
168R	30 Jan 2005	0130	818.2	823.0	4.8	4.30	89.6
169R	30 Jan 2005	0500	823.0	827.8	4.8	4.62	96.2
170R	30 Jan 2005	0855	827.8	832.6	4.8	4.86	101.3
171R	30 Jan 2005	1230	832.6	837.4	4.8	4.41	91.9
172R	3 Feb 2005	0100	837.4	842.2	4.8	4.50	93.8
173R	3 Feb 2005	0345	842.2	847.0	4.8	3.57	74.4

Table T26 (continued).

Core	Date	Local time (h)	Depth (mbsf) Top	Depth (mbsf) Bottom	Length (m) Cored	Length (m) Recovered	Recovery (%)
174R	3 Feb 2005	0705	847.0	851.8	4.8	4.62	96.2
175R	3 Feb 2005	1015	851.8	856.6	4.8	4.80	100.0
176R	3 Feb 2005	1400	856.6	861.4	4.8	4.72	98.3
177R	3 Feb 2005	1745	861.4	866.2	4.8	4.30	89.6
178R	3 Feb 2005	2125	866.2	871.0	4.8	3.71	77.3
179R	4 Feb 2005	0145	871.0	875.8	4.8	4.22	87.9
180R	4 Feb 2005	0525	875.8	880.6	4.8	4.58	95.4
181R	4 Feb 2005	0910	880.6	885.4	4.8	4.72	98.3
182R	4 Feb 2005	1400	885.4	890.2	4.8	2.72	56.7
183R	4 Feb 2005	1800	890.2	895.0	4.8	4.01	83.5
184R	4 Feb 2005	2200	895.0	899.8	4.8	3.77	78.5
185R	5 Feb 2005	0215	899.8	904.6	4.8	2.50	52.1
186R	5 Feb 2005	0615	904.6	909.4	4.8	3.59	74.8
187R	5 Feb 2005	1020	909.4	914.2	4.8	4.15	86.5
188R	5 Feb 2005	1530	914.2	919.0	4.8	5.27	109.8
189R	6 Feb 2005	0915	919.0	923.8	4.8	4.61	96.0
190R	6 Feb 2005	1040	923.8	924.8	1.0	0.85	85.0
191R	6 Feb 2005	1410	924.8	928.6	3.8	3.73	98.2
192R	6 Feb 2005	1800	928.6	933.4	4.8	3.53	73.5
193R	6 Feb 2005	2150	933.4	938.2	4.8	5.11	106.5
194R	7 Feb 2005	0225	938.2	943.0	4.8	4.77	99.4
195R	7 Feb 2005	0535	943.0	947.8	4.8	4.22	87.9
196R	7 Feb 2005	0845	947.8	952.6	4.8	4.76	99.2
197R	7 Feb 2005	1210	952.6	957.4	4.8	4.85	101.0
198R	7 Feb 2005	1540	957.4	962.2	4.8	4.12	85.8
199R	7 Feb 2005	1945	962.2	965.2	3.0	3.57	119.0
200R	7 Feb 2005	2345	965.2	969.7	4.5	4.33	96.2
201R	8 Feb 2005	0200	969.7	972.0	2.3	2.31	100.4
202R	8 Feb 2005	0505	972.0	976.8	4.8	4.94	102.9
203R	8 Feb 2005	0815	976.8	981.6	4.8	2.09	43.5
204R	8 Feb 2005	1115	981.6	986.4	4.8	7.05	146.9
205R	8 Feb 2005	1505	986.4	991.2	4.8	4.20	87.5
206R	8 Feb 2005	2000	991.2	994.2	3.0	1.48	49.3
207R	9 Feb 2005	0130	994.2	1000.8	6.6	6.56	99.4
208R	9 Feb 2005	1730	1000.8	1005.6	4.8	4.14	86.2
209R	9 Feb 2005	2030	1005.6	1010.4	4.8	4.08	85.0
210R	9 Feb 2005	2330	1010.4	1015.2	4.8	3.54	73.8
211R	10 Feb 2005	0330	1015.2	1020.0	4.8	6.25	130.2
212R	10 Feb 2005	0635	1020.0	1024.8	4.8	4.55	94.8
213R	10 Feb 2005	0920	1024.8	1029.6	4.8	4.29	89.4
214R	10 Feb 2005	1215	1029.6	1034.4	4.8	4.42	92.1
215R	10 Feb 2005	1645	1034.4	1039.2	4.8	4.47	93.1
216R	10 Feb 2005	2010	1039.2	1044.0	4.8	3.75	78.1
217R	10 Feb 2005	2250	1044.0	1048.8	4.8	3.56	74.2
218R	11 Feb 2005	0245	1048.8	1053.6	4.8	5.26	109.6
219R	11 Feb 2005	0645	1053.6	1058.4	4.8	4.86	101.3
220R	11 Feb 2005	0935	1058.4	1063.2	4.8	4.68	97.5
221R	11 Feb 2005	1315	1063.2	1068.0	4.8	3.10	64.6
222R	11 Feb 2005	1715	1068.0	1072.8	4.8	5.13	106.9
223R	11 Feb 2005	2040	1072.8	1077.6	4.8	3.74	77.9
224R	11 Feb 2005	2325	1077.6	1082.4	4.8	2.38	49.6
225R	12 Feb 2005	0230	1082.4	1087.2	4.8	3.97	82.7
226R	12 Feb 2005	0520	1087.2	1092.0	4.8	4.24	88.3
227R	12 Feb 2005	0805	1092.0	1096.8	4.8	4.07	84.8
228R	12 Feb 2005	1055	1096.8	1101.6	4.8	4.12	85.8
229R	13 Feb 2005	0220	1101.6	1105.5	3.9	2.16	55.4
230R	13 Feb 2005	0440	1105.5	1110.3	4.8	4.02	83.8
231R	13 Feb 2005	0735	1110.3	1115.1	4.8	3.17	66.0
232R	13 Feb 2005	0950	1115.1	1119.9	4.8	4.00	83.3
233R	13 Feb 2005	1200	1119.9	1124.7	4.8	3.74	77.9
234R	13 Feb 2005	1500	1124.7	1129.5	4.8	4.39	91.5
235R	13 Feb 2005	1825	1129.5	1134.3	4.8	3.08	64.2
236R	13 Feb 2005	2100	1134.3	1139.1	4.8	2.84	59.2
237R	13 Feb 2005	2300	1139.1	1143.9	4.8	1.72	35.8
238R	14 Feb 2005	0125	1143.9	1148.7	4.8	1.12	23.3
239R	14 Feb 2005	0345	1148.7	1153.5	4.8	4.41	91.9
240R	14 Feb 2005	0710	1153.5	1158.3	4.8	2.56	53.3
241R	14 Feb 2005	0945	1158.3	1163.1	4.8	2.92	60.8

Table T26 (continued).

Core	Date	Local time (h)	Depth (mbsf) Top	Depth (mbsf) Bottom	Length (m) Cored	Length (m) Recovered	Recovery (%)
242R	14 Feb 2005	1230	1163.1	1167.9	4.8	2.20	45.8
243R	14 Feb 2005	1610	1167.9	1172.7	4.8	2.84	59.2
244R	14 Feb 2005	2100	1172.7	1177.5	4.8	3.97	82.7
245R	14 Feb 2005	2350	1177.5	1182.3	4.8	3.12	65.0
246R	15 Feb 2005	0330	1182.3	1187.1	4.8	2.03	42.3
247R	15 Feb 2005	0600	1187.1	1191.9	4.8	3.47	72.3
248R	15 Feb 2005	0910	1191.9	1196.7	4.8	4.43	92.3
249R	15 Feb 2005	1215	1196.7	1201.5	4.8	3.02	62.9
250R	15 Feb 2005	1515	1201.5	1206.3	4.8	4.03	84.0
251R	15 Feb 2005	1935	1206.3	1211.1	4.8	3.81	79.4
252R	15 Feb 2005	2230	1211.1	1215.9	4.8	4.14	86.2
253R	16 Feb 2005	0215	1215.9	1220.7	4.8	3.55	74.0
254R	16 Feb 2005	0545	1220.7	1225.5	4.8	2.81	58.5
255R	17 Feb 2005	0155	1225.5	1230.3	4.8	1.65	34.4
256R	17 Feb 2005	0435	1230.3	1235.1	4.8	3.40	70.8
257R	17 Feb 2005	0705	1235.1	1239.9	4.8	1.75	36.5
258R	17 Feb 2005	0955	1239.9	1244.7	4.8	1.37	28.5
259R	17 Feb 2005	1340	1244.7	1249.5	4.8	1.75	36.5
260R	17 Feb 2005	1845	1249.5	1254.3	4.8	1.28	26.7
261R	17 Feb 2005	2215	1254.3	1259.1	4.8	3.28	68.3
262R	18 Feb 2005	0300	1259.1	1263.9	4.8	4.92	102.5
263R	18 Feb 2005	0635	1263.9	1268.7	4.8	3.09	64.4
264R	18 Feb 2005	1000	1268.7	1273.5	4.8	2.71	56.5
265R	18 Feb 2005	1315	1273.5	1278.3	4.8	2.41	50.2
266R	18 Feb 2005	1650	1278.3	1283.1	4.8	1.57	32.7
267R	18 Feb 2005	2030	1283.1	1287.9	4.8	4.00	83.3
268R	18 Feb 2005	2315	1287.9	1292.7	4.8	4.36	90.8
269R	19 Feb 2005	0245	1292.7	1297.5	4.8	3.60	75.0
270R	19 Feb 2005	0555	1297.5	1302.3	4.8	4.00	83.3
271R	19 Feb 2005	0910	1302.3	1307.1	4.8	4.16	86.7
272R	19 Feb 2005	1240	1307.1	1311.9	4.8	3.81	79.4
273R	19 Feb 2005	1600	1311.9	1316.7	4.8	1.59	33.1
274R	19 Feb 2005	2000	1316.7	1321.5	4.8	3.75	78.1
275R	20 Feb 2005	0110	1321.5	1326.3	4.8	3.55	74.0
276R	20 Feb 2005	1630	1326.3	1329.6	3.3	3.02	91.5
277R	20 Feb 2005	1940	1329.6	1334.4	4.8	3.47	72.3
278R	20 Feb 2005	2330	1334.4	1339.2	4.8	3.62	75.4
279R	21 Feb 2005	0340	1339.2	1344.0	4.8	4.04	84.2
280R	21 Feb 2005	0730	1344.0	1348.8	4.8	2.45	51.0
281R	21 Feb 2005	1015	1348.8	1353.6	4.8	2.84	59.2
282R	21 Feb 2005	1310	1353.6	1358.4	4.8	2.90	60.4
283R	21 Feb 2005	1625	1358.4	1363.2	4.8	4.47	93.1
284R	21 Feb 2005	1955	1363.2	1368.0	4.8	4.23	88.1
285R	21 Feb 2005	2315	1368.0	1372.8	4.8	3.58	74.6
286R	22 Feb 2005	0255	1372.8	1377.6	4.8	4.05	84.4
287R	22 Feb 2005	1030	1377.6	1379.6	2.0	0.41	20.5
288R	22 Feb 2005	1355	1379.6	1382.4	2.8	3.01	107.5
289R	22 Feb 2005	1720	1382.4	1387.2	4.8	4.66	97.1
290R	22 Feb 2005	2045	1387.2	1392.0	4.8	4.15	86.5
291R	22 Feb 2005	2340	1392.0	1396.8	4.8	4.50	93.8
292R	23 Feb 2005	0240	1396.8	1401.6	4.8	3.05	63.5
293R	23 Feb 2005	0505	1401.6	1406.4	4.8	1.24	25.8
294R	23 Feb 2005	0730	1406.4	1411.2	4.8	3.61	75.2
295R	23 Feb 2005	1015	1411.2	1415.5	4.3	3.98	92.6
			Cored totals:		1014.2	799.65	78.8

Figure AF1. Magnetic moments measured by the x- and y-SQUID sensors for an approximately axial dipole standard aligned parallel to the z-SQUID sensor. **A.** Results for rotation of the standard about the magnetometer z-axis with the standard sample in approximately the center of the measurement region (position used for discrete sample measurements). Note that the mean of the x-component is significantly offset toward –x. **B.** Corresponding results when standard is positioned in the bottom of the sample tray (to simulate measurement of archive halves). In this position, the x-component is significantly offset toward +x.

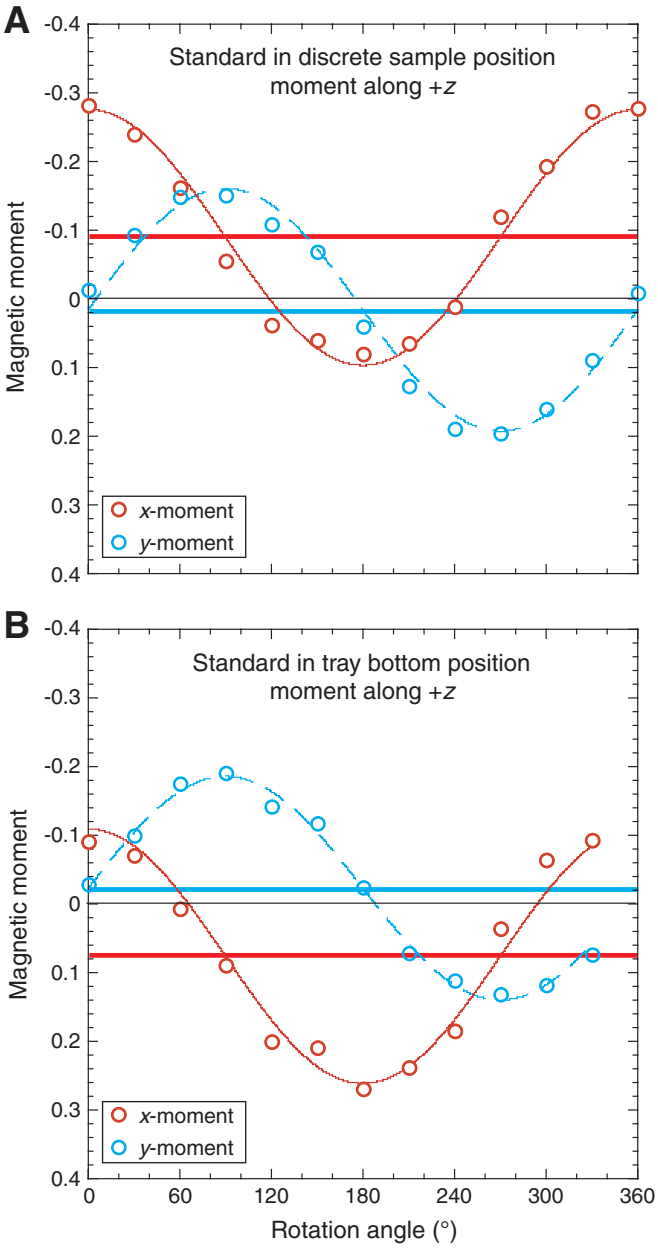

Table AT1. Composition of water samples, Site U1309.

Sample	pH	Alkalinity (mM)	Salinity (g/kg)
Coil sample	7.73	2.16	35.5
Overflow 1 (bottle 6)	7.81	2.45	34.5
Overflow 2 (bottle 6)	7.78	2.45	34.5

Notes: All samples taken from seafloor on 24 November 2004. This table is also available in **ASCII.**

Table AT2. Bottom water samples, Hole U1309D.

Date (2005)	Depth (mbsf)	Salinity (‰)	pH	Alkalinity (mM)	
				Corrected	Uncorrected
17 Jan	396	36	7.7	6.1	6.9
16 Feb	1215	36	7.4	2.0	2.3

Note: This table is also available in **ASCII.**